

The Nuclear Magnetic Resonance  
Society of Japan *Editor*

# Experimental Approaches of NMR Spectroscopy

Methodology and Application to Life  
Science and Materials Science



# Experimental Approaches of NMR Spectroscopy

The Nuclear Magnetic Resonance Society of Japan  
Editor

# Experimental Approaches of NMR Spectroscopy

Methodology and Application to Life Science  
and Materials Science



Springer

*Editor*  
The Nuclear Magnetic Resonance Society  
of Japan  
Kobe  
Japan

ISBN 978-981-10-5965-0            ISBN 978-981-10-5966-7 (eBook)  
<https://doi.org/10.1007/978-981-10-5966-7>

Library of Congress Control Number: 2017950018

© Springer Nature Singapore Pte Ltd. 2018

This work is subject to copyright. All rights are reserved by the Publisher, whether the whole or part of the material is concerned, specifically the rights of translation, reprinting, reuse of illustrations, recitation, broadcasting, reproduction on microfilms or in any other physical way, and transmission or information storage and retrieval, electronic adaptation, computer software, or by similar or dissimilar methodology now known or hereafter developed.

The use of general descriptive names, registered names, trademarks, service marks, etc. in this publication does not imply, even in the absence of a specific statement, that such names are exempt from the relevant protective laws and regulations and therefore free for general use.

The publisher, the authors and the editors are safe to assume that the advice and information in this book are believed to be true and accurate at the date of publication. Neither the publisher nor the authors or the editors give a warranty, express or implied, with respect to the material contained herein or for any errors or omissions that may have been made. The publisher remains neutral with regard to jurisdictional claims in published maps and institutional affiliations.

Printed on acid-free paper

This Springer imprint is published by Springer Nature  
The registered company is Springer Nature Singapore Pte Ltd.  
The registered company address is: 152 Beach Road, #21-01/04 Gateway East, Singapore 189721, Singapore

## **Member of the Editorial Board**

**Akira Naito** (Editor in Chief) Graduate School of Engineering, Yokohama National University, Yokohama, Japan

**Tetsuo Asakura** Department of Biotechnology, Tokyo University of Agriculture and Technology, Tokyo, Japan

**Ichio Shimada** Graduate School of Pharmaceutical Science, University of Tokyo, Tokyo, Japan

**Kiyonori Takegoshi** Graduate School of Science, Kyoto University, Kyoto, Japan

**Yasuhiko Yamamoto** Department of Chemistry, University of Tsukuba, Tsukuba, Japan

# Preface

This book describes the advanced developments in methodology and applications of NMR spectroscopy to life science and materials science. Experts who are leaders in the development of new methods and applications of life science and materials science have contributed an exciting range of topics that cover recent advances in structural determination and dynamic characterization of biological and material molecules, and development of novel NMR techniques, including resolution and sensitivity enhancement. First, this book particularly emphasizes the experimental details for new researchers to use NMR spectroscopy and also to pick up the potentials of NMR spectroscopy. Second, the book is designed for those who are involved in either developing the techniques or expanding the NMR application fields by applying them to specific samples. Third, the Nuclear Magnetic Resonance (NMR) Society of Japan has organized this book not only for NMR members of Japan but also for worldwide readers who are interested in using NMR spectroscopy extensively.

This book consists of two parts: methodology and application to life science and materials science. In Part I (Chaps. 1–9: Methodology), first, new concept of NMR experiment such as high pressure NMR and isotope-aided NMR methods are described. Second, advances in NMR data acquisition and processing methods are introduced. Third, advances in NMR hardware such as dynamic nuclear polarization (DNP), photoirradiation and microwave irradiation NMR spectroscopies are emphasized. Fourth, recently developed solid-state NMR spectroscopy under ultrafast magic angle spinning (MAS) is focused in this book. Fifth, dynamics of biological molecules using relaxation dispersion NMR spectroscopy is particularly emphasized. Sixth, structure-determination experiments of biological molecules utilizing paramagnetic lanthanide probe methods and solid-state NMR spectroscopy are particularly highlighted.

In Part II (Chaps. 10–22: Application to Life Science and Materials Science), advanced application to life science and materials science is described. First, as applications of solid-state NMR spectroscopy to materials science, studies on silk materials, polymer materials, functional materials and gaseous molecules in polymer materials are extensively described. Second, as applications of advanced NMR

techniques to life science, studies of natural products, glycoproteins and ribonucleic acid (RNA) are widely accounted. Third, metabolic profiling for small molecular complexity is introduced. Fourth, this book focuses on NMR studies of paramagnetic compounds. Fifth, NMR spectroscopy of quadrupole nuclei in organic compounds and inorganic materials is described. Sixth, advanced NMR spectroscopies are focused on characterization of protein–ligand interaction and determination of protein structure and dynamics.

Kobe, Japan  
June 2017

The NMR Society of Japan  
Editorial board  
Akira Naito (Editor in Chief)  
Tetsuo Asakura  
Ichio Shimada  
Kiyonori Takegoshi  
Yasuhiko Yamamoto

## Acknowledgements

We are deeply grateful to Dr. Tomohide Saio for completing Chap. 8 succeeded from late Prof. Fuyuhiko Inagaki. Unfortunately, Prof. Inagaki had passed away during the course of writing this book. Professor Inagaki was excited to write a chapter in this book and encouraged us to publish this book. We, therefore, sincerely dedicate this book to the late Prof. Inagaki.

We would also like to acknowledge the council member of the NMR Society of Japan for their devoted help in the process of editing this book.

Finally, we would like to thank Ms. Risa Takizawa and Mr. Shinichi Koizumi of the Springer Japan for their encouragement and assistance in editing the book.

# Contents

## Part I Methodology

<b>1 Protein Studies by High-Pressure NMR . . . . .</b>	<b>3</b>
Kazuyuki Akasaka	
<b>2 Isotope-Aided Methods for Biological NMR Spectroscopy: <i>Past, Present, and Future</i> . . . . .</b>	<b>37</b>
Masatsune Kainoshio, Yohei Miyanoiri and Mitsuhiro Takeda	
<b>3 Advances in NMR Data Acquisition and Processing for Protein Structure Determination . . . . .</b>	<b>63</b>
Teppei Ikeya and Yutaka Ito	
<b>4 Advances in High-Field DNP Methods . . . . .</b>	<b>91</b>
Yoh Matsuki and Toshimichi Fujiwara	
<b>5 Photoirradiation and Microwave Irradiation NMR Spectroscopy . . . . .</b>	<b>135</b>
Akira Naito, Yoshiteru Makino, Yugo Tasei and Izuru Kawamura	
<b>6 Solid-State NMR Under Ultrafast MAS Rate of 40–120 kHz . . . . .</b>	<b>171</b>
Yusuke Nishiyama	
<b>7 Elucidating Functional Dynamics by <math>R_{1\rho}</math> and <math>R_2</math> Relaxation Dispersion NMR Spectroscopy . . . . .</b>	<b>197</b>
Erik Walinda and Kenji Sugase	
<b>8 Structural Study of Proteins by Paramagnetic Lanthanide Probe Methods . . . . .</b>	<b>227</b>
Tomohide Saio and Fuyuhiko Inagaki	
<b>9 Structure Determination of Membrane Peptides and Proteins by Solid-State NMR . . . . .</b>	<b>253</b>
Izuru Kawamura, Kazushi Norisada and Akira Naito	

**Part II Application to Life Science and Materials Science**

<b>10 NMR Studies on Silk Materials</b>	297
Tetsuo Asakura and Yugo Tasei	
<b>11 NMR Studies on Polymer Materials</b>	313
Atsushi Asano	
<b>12 Solid-State <math>^2\text{H}</math> NMR Studies of Molecular Motion in Functional Materials</b>	341
Motohiro Mizuno	
<b>13 NMR Spectral Observations of the Gases in Polymer Materials</b>	365
Hiroaki Yoshimizu	
<b>14 NMR Studies on Natural Product—Stereochemical Determination and Conformational Analysis in Solution and in Membrane</b>	383
Nobuaki Matsumori and Michio Murata	
<b>15 Technical Basis for Nuclear Magnetic Resonance Approach for Glycoproteins</b>	415
Koichi Kato, Saeko Yanaka and Hirokazu Yagi	
<b>16 NMR Studies on RNA</b>	439
Taiichi Sakamoto, Maina Otsu and Gota Kawai	
<b>17 NMR Analysis of Molecular Complexity</b>	461
Jun Kikuchi	
<b>18 NMR of Paramagnetic Compounds</b>	491
Yasuhiko Yamamoto and Tomokazu Shibata	
<b>19 NMR of Quadrupole Nuclei in Organic Compounds</b>	519
Kazuhiko Yamada	
<b>20 Quadrupole Nuclei in Inorganic Materials</b>	545
Toshikazu Takahashi	
<b>21 Protein–Ligand Interactions Studied by NMR</b>	579
Hidekazu Hiroaki and Daisuke Kohda	
<b>22 Protein Structure and Dynamics Determination by Residual Anisotropic Spin Interactions</b>	601
Shin-ichi Tate	

# **Part I**

## **Methodology**

# Chapter 1

## Protein Studies by High-Pressure NMR

Kazuyuki Akasaka

**Abstract** High-pressure NMR spectroscopy is a method that allows NMR measurements of any target samples under variable pressure. When applied to proteins, the method extends the conformational space that NMR spectroscopy can handle, from the space limited to the basic folded paradigm into the extensive conformational space that spans the entire high-energy paradigm of protein structure from the folded to the unfolded. The success of the experiment is ensured by the strong coupling between the volume and the conformation of a protein such that *the partial molar volume of a protein decreases in parallel with the loss of its conformational order* (the “volume theorem of protein”) as advocated by Akasaka). The validity of this principle arises from the fact that a globular protein generally has a significant vacant space (sometimes called “void” or “cavities”) inside its folded architecture into which water molecules may penetrate to reduce its partial molar volume and its conformational order simultaneously. Thanks to this principle, pressure provides a simple, clean, systematic and often efficient means of investigating the high-energy conformers of a protein, which is essential for understanding its folding, function, interaction, fibrillation, adaptation and evolution.

**Keywords** Partial molar volume · Conformational order · Cavity hydration  
High-energy paradigm · Protein function and evolution

### 1.1 Introduction

This chapter draws attention to the new paradigm of protein structure that has not hitherto been the direct target of NMR spectroscopic observation, but could be crucially important for function, adaptation and evolution of proteins, namely the “high-energy paradigm” of proteins. To explore this paradigm with NMR, the author found, a couple of decades ago, that the best means to advance our

---

K. Akasaka (✉)  
Kyoto Prefectural University of Medicine, Kyoto, Japan  
e-mail: akasakak@koto.kpu-m.ac.jp

knowledge in this respect is the combination of NMR spectroscopy with pressure perturbation. In this chapter, I begin with reviewing the relevant thermodynamics that proteins obey, emphasizing their unique volumetric properties that are decisive for the successful high-pressure NMR experiments on proteins. Techniques and applications will follow.

As unit of pressure, both “bar” and “MPa” will be used in this text, which are related by

$$1 \text{ bar} = 0.1 \text{ MPa}, 1 \text{ kbar} = 100 \text{ MPa}, \text{ or } 1 \text{ MPa} = 10 \text{ bar}, 100 \text{ MPa} = 1 \text{ kbar}, 1 \text{ GPa} = 10 \text{ kbar.}$$

The pressure in our natural environment is at most  $\sim 1$  kbar or 0.1GPa at the deepest part of the ocean, while our high-pressure NMR experiments are performed in the pressure range within several kbars.

### ***1.1.1 The NMR Spectroscopy and Its Limitation***

Since its discovery in 1946 [1, 2], the NMR spectroscopy has made several dramatic transformations into high-resolution spectroscopy of all kinds of molecules in solid and in solution. In particular, thanks to the slow spin relaxation of spin 1/2 nuclei, the time-domain spin technology [3] has revolutionized NMR spectroscopy into unprecedented versatility and utility where the information is selected or enhanced to meet the variety of needs and choice of the experimentalist [4]. A variety of combination with external perturbations such as rapid sample rotation (see Chap. 6 by Nishiyama), photo-illumination (see Chap. 5 by Naito), concentration-jump and temperature-jump have also been employed along with the spin technology and the isotope-labeling techniques (see Chap. 2 by Kainosho) to enhance or select the information to meet the individual needs.

With regard to the NMR application to protein studies, following the discovery of “Anfinsen’s dogma” [5] such that “the functional structure of a protein is thermodynamically determined in solution to be in the Gibbs energy minimum state,” the determination of protein structures in solution by expressing them in average atomic coordinates has gained the major attention and become the major accomplishment in NMR spectroscopy of proteins [6]. The consequence gives an overwhelmingly “static” image of protein structure such that “the polypeptide chain is folded to give a tightly interlocking, rigid molecule” [7], the small fluctuations of which give rise to function.

On the other hand, the life as we see daily in nature is distinctly dynamic and this dynamism depends largely on the dynamism of protein molecules (see Fig. 1.1), namely the “kicking and screaming stochastic molecules in which fluctuations are frequent and dramatic” [7], which, in turn, is closely connected to the dynamism of water molecules filling the earthy environment, even a tiny space within a protein molecule [8]. The necessity for overcoming the limitation of the “single conformer” concept and “static” picture of protein structure, as unduly enhanced by the astonishing elegance of X-ray crystallography and modern NMR spectroscopy,

must be replaced with a new dynamic concept of protein structure to face *directly* with the dynamic reality of life.

In an effort to gain information on the dynamics of a protein structure, a number of important contributions have been made from different experimental approaches, including those from compressibility [9], enzyme kinetics [10] and hydrogen exchange, to the recent relaxation dispersion method (see Chap. 7 by Sugase), a major conflict still remains between the two concepts of proteins; the one confined largely to a “single” major conformer and the other basically allowing “multiple” conformational transitions over the entire allowed conformational space. Now we wish to overcome the conflict with a new experimental approach based possibly on a simple general principle that governs the protein conformation and its fluctuation in the entire allowed conformational space from the folded to the unfolded.

Before going into our strategies in solving the conflict, one should first realize the basic property of NMR spectroscopy per se, which places strong limitation on our visibility of dynamic events in proteins, in two ways both originating from the small magnetism of nuclear spins:

(1) Limitation due to the *long* spin relaxation times:

NMR is intrinsically a “slow” spectroscopy with long spin relaxation times, so that the effects of any “*rapid fluctuations*” with  $\tau \ll ms$  disappear during acquisition of free induction decay signals, leaving practically “no trace” in the resultant spectrum.

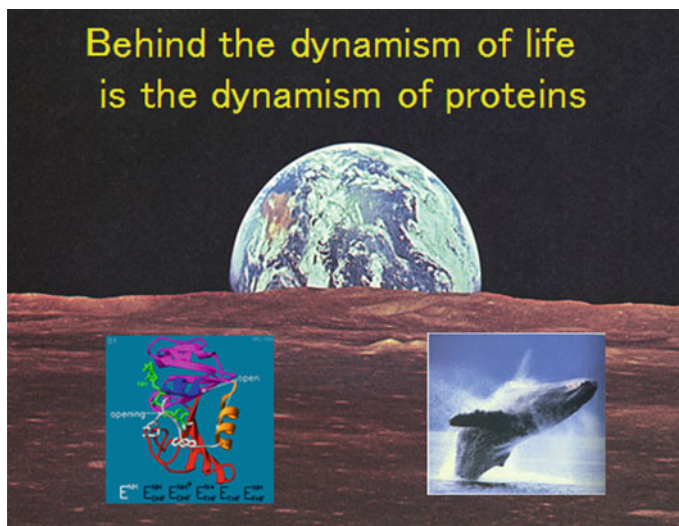


**Fig. 1.1** Astonishing “dynamism of life” on earth has its origin in the “dynamism of protein molecules,” which is only realized in collaboration with water molecules

(2) Limitation due to the *low* sensitivity of detection:

The current NMR spectroscopy per se would fail to detect or identify signals from “rare” or “minor” conformers that might exist in equilibrium with the major conformer and the “transient” species that might appear transiently in protein folding and/or unfolding.

### 1.1.2 *Overcoming the Limitation with Pressure*

Over the past decades, the new inventions in NMR spectroscopy have been made primarily in spin technologies producing advanced spectroscopy, such as multi-dimensional NMR spectroscopy and high-resolution solid-state NMR. This all done, but apparently has not been sufficient to reach the dynamic entirety of proteins controlling the dynamism of life. Proteins are the molecules not just with chemical bonding, but are *the molecules of life* that have adapted themselves to the natural environment on earth for billions of years, long before the human evolution. Namely they are the molecules that have survived by fitting to the natural environment on earth, obeying the laws of thermodynamics and statistics, so that they function under the control of these laws, namely under the choice of *temperature* and *pressure*, in addition to the choice of other conditions.

Of the two, temperature is a “reality,” to which proteins have delicately adjusted themselves to function, from below the freezing point in anti-arctic to the boiling bath of a hot spring. What about pressure? It varies from 1 bar to 1.1 kbar in the deepest ocean, but most proteins on earth have adapted themselves to the low-pressure environment close to 1 bar. Thus, pressure over 1 kbar is a “non-reality” for most proteins, as they would have seldom experienced it in their long history of evolution, but the general belief that *pressure at kbars is energetically a much more strong perturbation to proteins than temperature, is wrong*. In most pressure experiments where the experiments are performed after the temperature rise due to adiabatic compression is removed, the energetic contribution is very subtle compared to that by temperature, so that the structures in high-energy sub-states remain practically unchanged from those at 1 bar. Furthermore, in contrast to temperature, the rewarding properties of pressure perturbation on protein solution are that (1) pressure is transferred uniformly over the entire sample solution upon applying pressure (Pascal’s rule) and (2) pressure causes practically no aggregation of proteins under applied pressure or even upon removal of pressure if experiments are carefully done.

In 1972 and 1974, Yamada proposed high-pressure NMR up to ~200 MPa on solution samples by using a “pressure-resisting cell” made of glass capillaries [11, 12]. By utilizing techniques, Morishima [13] and Wagner [14] performed some pioneering and stimulating works on selected topics of protein dynamics in early 1980’s before the two-dimensional NMR techniques came into use.

In 1990s, Jonas pioneered the field of high-pressure NMR studies of proteins with his “autoclave type” high-pressure NMR apparatus operable up to 850 MPa and started protein structure and unfolding studies under pressure with 1D  $^1\text{H}$  NMR spectroscopy successfully [15, 16]. However, because of the lack in sufficient field homogeneity and versatility in pulse sequence, the extension of his “autoclave” technique into two-dimensional high-pressure NMR spectroscopy of proteins turned out to be unsuccessful.

A few years later in 1990s, Akasaka and Yamada came up with hand-made pressure-resistive synthetic quartz cells, in conjunction with a high-field NMR spectrometer (750 MHz for  $^1\text{H}$ ) [17], started high-pressure NMR spectroscopy of proteins with excellent high resolution in the pressure range up to 200–400 MPa. Since then, Akasaka and co-workers and later independently Kalbitzer and coworkers [18] have opened a “new paradigm” of NMR spectroscopy of proteins with pressure as variable, as summarized in a number of review articles hitherto published [19–34] that describe high-pressure NMR techniques for the study of protein dynamics, folding and aggregation. In recent years, easy-handling ceramic cells made of zirconia became commercially available, which has changed the world landscape of high-pressure NMR studies of proteins for its expansion to the next decades [34].

### 1.1.3 *Turning NMR “Invisible” Conformers into NMR “Visible” with Pressure*

To simply illustrate what the high-pressure NMR spectroscopy can do in contrast to the conventional NMR spectroscopy limited to 1 bar, we show below two typical cases of *turning the NMR “invisible” conformers to NMR “visible”* by pressure perturbation.

#### Case 1. $^1\text{H}$ NMR spectra: hen lysozyme between 3 and 400 MPa [35].

Take a look at Fig. 1.2 for the case of 1D  $^1\text{H}$  NMR spectrum of hen lysozyme (pH 2.0) at  $-5^\circ\text{C}$  using a quartz cell (low temperature is chosen to enhance the pressure effect). The bottom spectrum is the only spectrum that we can observe at 0.1 MPa (1 bar), assignable to the basic folded structure of the protein. When we apply pressure at 0.1–300 MPa, the spectrum starts to undergo dramatic changes (*chemical shift changes with some broadening*) until finally at 400 MPa (the highest pressure available in this experiment) the high-field shifted methyl proton signals (0 to  $-1\text{ ppm}$ ) coming from the folded protein core disappear and are replaced by a new combined methyl signals at around  $0.9\text{ ppm}$ , characteristic of unfolding. Chemical shift positions of most other signals are also closer to those of fully unfolded conformer (U) in 8 M urea, but the broadness of their signals at 400 MPa suggests that their side-chain motions are restricted, characteristic of a molten globule state (MG).

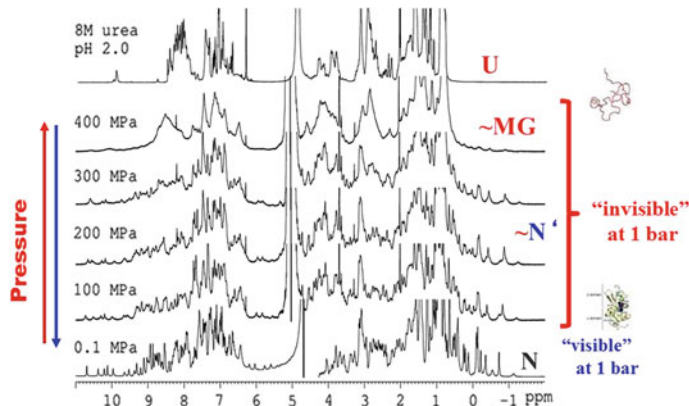


**Fig. 1.2** Pressure turns the “invisible” conformer to “visible” in hen lysozyme [35]

Qualitatively, the spectral changes with continuous chemical shift changes occurring in the pressure range of 0.1–300 MPa indicate a rapid ( $\tau \ll \text{ms}$ ) conformational fluctuations (compaction of the core) within the folded manifold ( $N-N'$ ), whereas the jumping of signal positions represented by intensity changes at 300–400 MPa indicates the slow ( $\tau \gg \text{ms}$ ) transition of the folded conformation ( $N-N'$ ) into the unfolded, molten globule ( $MG$ ) state at 400 MPa.

The important point here is that *the entire spectral changes at 0.1–400 MPa are fully reversible with pressure*: It is not likely that pressure has produced newly conformers like  $N'$  and  $MG$  from  $N$ ; rather, the conformers  $N'$  and  $MG$  preexist before applying pressure. Pressure merely increases their populations to such a level that they can be detected by NMR. This supports the notion that all the conformational species from  $N$  to  $MG$  (at least) exist in equilibrium in the entire pressure range studied (0.1–400 MPa), despite the fact that at 0.1 MPa, only the signals from the dominant conformer  $N$  are observed. Here we see “*the magical power of pressure*” that turns the “invisible” to “visible” in NMR spectroscopy. In other words, it “dramatically increases the NMR sensitivity” of “rare conformers” in proteins.

A series of 1D  $^1\text{H}$  NMR spectra of hen lysozyme (1.7 mM protein, pH 2.0) observed under applied hydrostatic pressures between 0.1 and 400 MPa [35]. The spectra between 100 and 400 MPa were obtained at  $-5^\circ\text{C}$  at 800 MHz using a pressure-resisting quartz capillary tube [17] whereas the reference spectra at the bottom (0.1 MPa) and the top (in 8 M urea) were obtained at 600 MHz at  $25^\circ\text{C}$ . At 0.1 MPa, only the basic folded conformer  $N$  is “visible” in the NMR spectrum, while the conformers between 100 and 300 MPa are likely the folded conformers with different degrees of compaction of the core, here designated by  $N'$ . The conformer at 400 MPa may be assigned to  $MG$  (molten globule) (cf. the fully unfolded conformer  $U$  in 8 M urea at 0.1 MPa). All the spectral changes are reversible with pressure, suggesting that the  $N'$  and  $MG$  conformers preexist at 0.1 MPa in

equilibrium with  $N$  at “invisibly small fractions,” but becomes “visible” at higher pressures simply because the equilibrium is shifted to  $N'$  and  $MG$  at elevated pressures (adapted from Fig. 2 in [35]).

**Case 2.  $^1\text{H}/^{15}\text{N}$  HSQC spectra: apomyoglobin between 3 and 300 MPa [36].**

A more delicate and dramatic spectral change occurs for the case of two-dimensional NMR spectroscopy ( $^{15}\text{N}/^1\text{H}$  HSQC) of apomyoglobin. We observe here an entire process of its transition from the folded  $N$  at 3 MPa to the fully unfolded conformer  $U$  at 300 MPa. At the lowest pressure (here 30 bar), only the folded species  $N$  is observable. By increasing pressure (3–120 MPa), individual signals undergo continuously chemical shift changes  $\epsilon$  ( $\tau \ll \text{ms}$ ), and, by further increasing the pressure (150–300 MPa), individual cross-peaks jump to new positions ( $\tau \gg \text{ms}$ ). When the pressure is reduced back to 3 MPa, the spectrum returns essentially to that of the original, suggesting again that the  $I$  and  $MG$  conformers preexist at 0.1 MPa in equilibrium with  $N$  at “invisibly small fractions,” but becomes “visible” at higher pressures simply because the equilibrium is shifted to  $I$  and  $MG$  at elevated pressures, as exactly in the case of hen lysozyme.

$^1\text{H}/^{15}\text{N}$  HSQC spectra of apomyoglobin at various pressures from 3 to 300 MP at 35 °C (3 MPa instead of 0.1 MPa to avoid bubbling in the solution). Adapted from Fig. 5 of Ref. [21].

The observation is again consistent with the notion that all different conformers of apomyoglobin, designated tentatively by the symbol  $N$ ,  $I$ ,  $MG$ ,  $U$ , coexist in equilibrium at any pressure between 3 and 300 MPa. Namely the equilibrium



holds at whatever the pressure chosen. At 3 MPa, only the basic folded conformer  $N$  is “visible” by NMR spectroscopy, while, at elevated pressures, all conformers  $I$ ,  $MG$  and  $U$ , which are “invisible” at 3 MPa, become visible on NMR at high pressures. In this way, we can observe all conformers existing between  $N$  and  $U$  directly with NMR under pressure. Here, *pressure does not produce any new conformers, but rather simply shifts the equilibrium (1.1) to the right by increasing the populations of conformers already existing at 0.1–3 MPa according to the Le Chatelier’s principle*. Or alternately, *an equilibrium structure stabilized at high pressure should correspond to one of the fluctuated structures at the ambient pressure [8]*.

Thus, the essential new feature that these two experiments depict is that, in reality, *a protein exists in solution as a fluctuating equilibrium mixture of “multiple-conformations”* rather than confined to a “single conformation” as hitherto has been believed. This feature, generally observed in globular proteins under variable pressure, should be accepted as a reality of proteins existing in nature today.

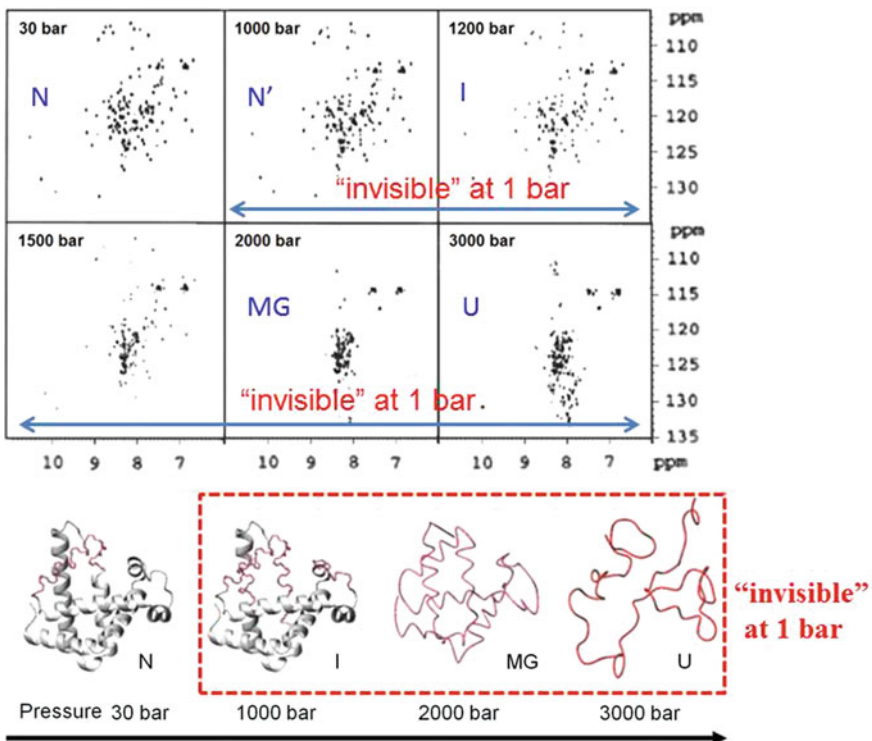


**Fig. 1.3** Pressure turns the “invisible” conformer to “visible” in 2D  $^{15}\text{N}/^1\text{H}$ NMR

In the next section, we will discuss the thermodynamic background on how one can visualize this reality on NMR spectroscopy using pressure perturbation.

## 1.2 The Thermodynamic Background

### 1.2.1 Effect of Pressure on the Protein Conformational Equilibrium

Proteins are the molecules for maintaining the dynamism of life on the earth environment at relatively mild temperature and pressure. Thus, their structures must have been made to be sufficiently mobile under the control of thermodynamic laws. Thus, a folded protein molecule under physiological conditions existing mainly in the basic folded state  $N$  may actually exist in dynamic equilibrium with other conformational states under physiological conditions, say with the unfolded state  $U$  or any conformer other than  $N$ . The equilibrium constant  $K = [U]/[N]$ , say

between the two conformers  $N$  and  $U$  conformational states is governed by the Gibbs energy difference ( $\Delta G$ ) between the two states

$$\Delta G = G_U - G_N = -RT \ln K. \quad (1.2)$$

In most variable-pressure experiments in which we vary pressure while we keep the temperature constant ( $T = T_x$ ), we have the following basic relation to  $p$  up to the second order [20, 37, 38]

$$\Delta G = \Delta G_x^0 + \Delta V^0(p - p_0) + \frac{\Delta\kappa}{2}(p - p_0)^2 + \Delta\alpha(p - p_0)(T_x - T_0) \quad (1.3)$$

and

$$\Delta V = V_U - V_N = \Delta V_0 + \Delta\alpha(T - T_0). \quad (1.4)$$

Equation (1.3) depicts that the pressure dependence of the equilibrium between  $U$  and  $N$  of a protein depends on four parameters  $\Delta G^0$ ,  $\Delta V^0$ ,  $\Delta\kappa$  and  $\Delta\alpha$ , which are  $\Delta G^0$ :  $\Delta U(T_x) - T_x \Delta S(T_x)$ ; the stability difference at 1 bar at  $T_x$  ( $>0$  except at extreme  $T_x$ )

$\Delta V^0$ : the volume difference under standard conditions (a significantly large negative value  $<0$ )

$\Delta\kappa$ : the compressibility difference ( $\sim$  small for low pressures)

$\Delta\alpha$ : the expansivity difference (a significantly positive value  $> 0$ )

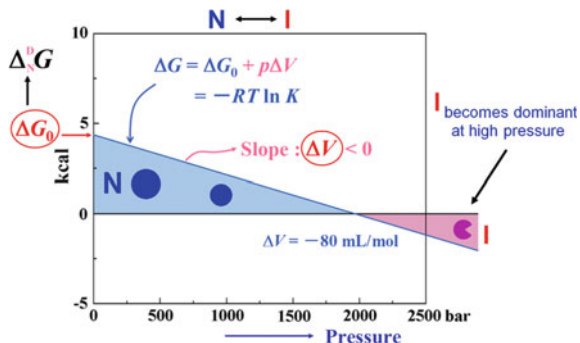
Granted that  $\Delta\kappa$  is negligible for  $p <$  a few kbar, Eq. (1.4) is simplified to (1.5);

$$\Delta G = \Delta G^0 + \Delta V(p - p_0). \quad (1.5)$$

In high-pressure NMR experiments, where pressure is varied at a fixed temperature, the equilibrium constant  $K$  between any two conformational sub-states (e.g.,  $N$  and  $U$ ) is reduced from the intensities of individual sub-states or from chemical shift changes for each pressure, from which  $\Delta G$  is calculated from Eq. (1.2). For a series of pressures chosen, we get  $\Delta G$  values as a function of pressure, which then is fitted to Eq. (1.5) to obtain the best-fit values of  $\Delta G^0$  and  $\Delta V$ . The general procedure is illustrated in Fig. 1.4. Here by fitting Eq. (1.5) to the experimental data [plot of  $\Delta G$  vs.  $p$ ], we obtain  $\Delta V_{IN} = -80$  mL/mol from the slope and  $\Delta G_{IN}^0 \sim 4$  kcal/mol or  $\sim 16$  kJ/mol by extrapolating  $\Delta G$  to  $p_0 = 1$  bar. In this case, the excess stability of  $N$  over  $I$  ( $\Delta G^0 > 0$ ), which turns out to be marginal for most functional proteins, decreases further with increasing pressure, making conformer  $I$  to increase by  $\sim 1000$ -fold, making it more dominant than  $N$  above  $\sim 200$  MPa. *The dramatic conversion from  $N$  to  $I$  occurs as a result of small positive  $\Delta G^0 > 0$  and significantly negative  $\Delta V_{IN} < 0$ .* Thus,  $\Delta V$  is the decisive factor, along with  $\Delta G^0$ , in each step of the equilibrium (1.1).

In practice, as long as the experiment is carried out under physiological conditions,  $\Delta V$  is considerably negative, giving  $\Delta V_{UN} = -30$  to  $-100$  ml/mol for small

**Fig. 1.4** Illustration how the thermodynamic Eq. (1.5) will explain the shift of conformational equilibrium  $N \rightleftharpoons I$  in equilibrium (1.1.) for a typical case when  $\Delta G^0$  is  $\sim 4$  kcal/mol and  $\Delta V$  is  $\sim -80$  mL/mol



globular proteins and considerably larger for larger proteins. Because in Eq. (1.4)  $\Delta V$  depends on temperature and  $\Delta\alpha$  is known to be positive, the negative  $\Delta V$  value tends to diminish at higher temperature. Thus, to realize a larger negative  $\Delta V$  and to explore the high-energy sub-states of proteins with high-pressure NMR effectively, a temperature at physiological or lower is preferred. Furthermore, as the  $\Delta G^0$  value in Eq. (1.5) tends to decrease with temperature (toward cold denaturation), the low-temperature effect is further increased.

Our experience tells that, when the temperature is close to 0 °C or even lower, pressure within  $\sim 4$  kbar is usually sufficient to find the onset of unfolding in the equilibrium (1.1) in a globular protein. Likewise, under pressure of 2 kbar, one can even realize the cold denaturation of ubiquitin, which does not denature within 4 kbar at 25 °C.

### 1.2.2 “Volume” Decreases as “Cavity” Hydration Increases

We now must understand how the sign of  $\Delta V$  is determined in each step of the equilibrium (1.1).

The “volume” of the protein we deal with is actually the “partial molar volume” of a protein in solution (water as solvent), which is given approximately by the three major contributions (cf. Fig. 1.5a [39]):

$$V = V_{\text{atom}} + V_{\text{cav}} + \Delta V_{\text{sol}} \quad (1.6)$$

- $V_{\text{atom}}$  the sum of the *van der Waals volume* of all the constitutive atoms of the protein (Fig. 1.5a)
- $V_{\text{cav}}$  the solvent-excluded “void” volume or the space occupied by “cavities” (Fig. 1.5a)
- $\Delta V_{\text{sol}}$  the volume change due to the *solvation* of the protein in water; This includes the *volume change*  $\Delta V_{\text{hvd}}$ , due to “hydration of the protein” (both the main chain and side chains) as well as the *thermal volume*,  $V_T$ , which results from

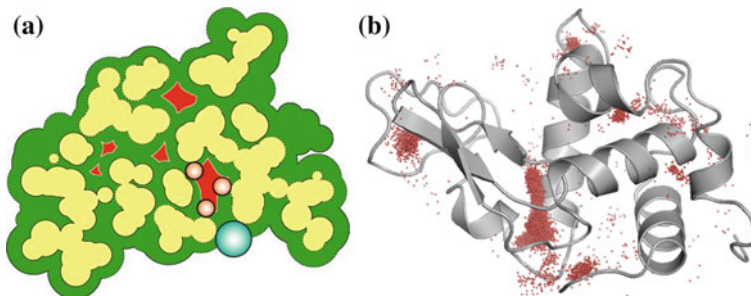


**Fig. 1.5** Atoms, cavities and water in proteins. **a** Schematic cross-sectional view of a protein, illustrating the *van der Waals volume* ( $V_{\text{atom}}$ , green) and the *cavities* ( $V_{\text{cav}}$ , red), estimated by rolling the blue sphere and the pink sphere, respectively, on the van der Waals surface (adapted from Fig. 2 of Ref. [39] by permission of Gekko). **b** Penetration of water molecules into the interior of hen lysozyme at 1 bar as obtained by M.D. simulation (adapted from Fig. 2 in [40] by permission of Elsevier). The figure shows water molecules (red dots) getting in and out of the cavities, located mainly in the hinge region between  $\alpha$  and  $\beta$  domains and in the loop region of the  $\beta$  domain

thermally induced molecular fluctuation between the solute and the solvent (i.e., the average empty space around the solute due to imperfect packing of the solvent).

Then, the molar volume difference  $\Delta V$  between any two conformational states of a protein becomes, as  $V_{\text{atom}}$  largely cancels

$$\Delta V = \Delta V_{\text{cav}} + \Delta V_{\text{sol}}. \quad (1.7)$$

The term  $V_{\text{cav}}$  results when a polypeptide chain folds into the N state, the packing of the side chains is not generally perfect and leave some “defect” or extra space unoccupied by atoms within the folded protein architecture. The location and the size of the cavities are found in crystal structures by scrolling a probe of a sphere of  $1.0 \sim 1.4 \text{ \AA}$  inside the protein molecule and by finding the space left out by the probe. Recent studies indicate that cavities are always found in a variety of globular proteins and further that the size and density of cavities vary greatly from protein to protein apparently related to their function [19]. In the case of lysozyme, cavities are found always in the same strategic positions common to all lysozymes from different biological species [41]. These observations support the notion that cavities, large or small, are the essential elements in globular proteins for creating function.

The cavities are haunted by solvent water even at ambient pressure as the M.D. simulated figure (Fig. 1.5b) shows. As pressure is increased, more water molecules occupy cavities and void inside, eliminating their space further. Namely at each step of the equilibrium (1.1),  $V_{\text{cav}}$  decreases ( $\Delta V_{\text{cav}} < 0$ ).

On the other hand, the term  $\Delta V_{\text{sol}}$  is contributed at least by two factors ( $\Delta V_{\text{hyd}}$  and  $\Delta V_T$ ); the term  $\Delta V_{\text{hyd}}$  is likely to decrease as hydration proceeds, whereas the thermal volume  $\Delta V_T$  is likely to contribute a considerably larger positive value at higher temperature as  $\Delta \alpha > 0$  in Eq. (1.4), and may even cancel the negative

contribution from  $\Delta V_{\text{cav}}$ . Thus, in order to cover a wide range of conformational order of the protein by varying pressure, it would generally be better to perform the experiment at a relatively low temperature. An additional merit of choosing a lower temperature is that we will have decreased  $\Delta G^0$  value closer to cold denaturation, so that full unfolding within a few kbar pressure would become easier. For example, one can bring the extremely stable protein ubiquitin to undergo cold denaturation by applying pressure at 2 kbar [42].

As each step of the equilibrium (1.1) is characterized with increased hydration of the polypeptide chain and  $\Delta V < 0$ . All the globular proteins so far studied with high-pressure NMR have been found to follow this general rule. Values of  $\Delta V = -30$  to  $-100$  ml/mol are reported for small globular proteins [43], and significantly larger values ( $\Delta V >$  a few hundred ml/mol) for larger proteins and membrane proteins.

### 1.2.3 The “Volume Theorem” of Protein and the High-Pressure NMR Experiment

When a protein in solution exists in a dynamic mixture of various conformerl substates differing in Gibbs energy and in partial molar volume, a conformational transition like that in Fig. 1.4 may occur between any two substates, and, as we increase the pressure, consecutively in the decreasing conformational order  $N \rightarrow I \rightarrow \text{MG} \rightarrow U$ . Provided that the  $\Delta G^0$  value is marginal and the  $\Delta V$  values

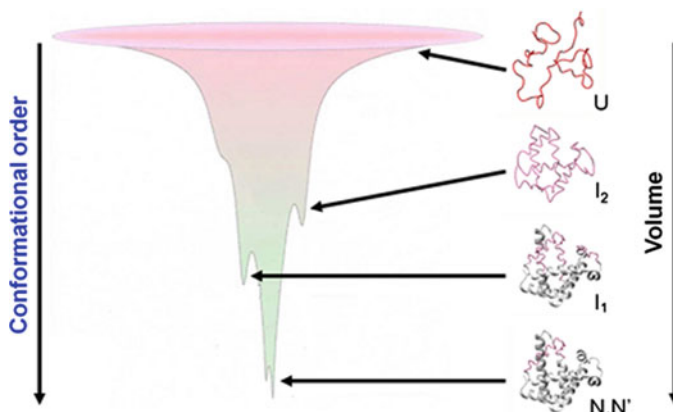


**Fig. 1.6** The “volume theorem” of protein-a general rule for globular proteins [20]. The Volume Rule of Protein “the partial molar volume of a protein decreases in parallel with the loss of its conformational order” as advocated by Akasaka [20]. The funnel is drawn schematically for a hypothetical globular protein, with five major conformational sub-ensembles, placed in decreasing conformational order; the native ( $N$ ), the low-lying excited states ( $N'$ ), intermediate states ( $I_1$ ,  $I_2$ ) and the unfolded state ( $U$ ), in parallel with decreasing partial molar volume,  $N > N' > I_1 > I_2 > U$

are significantly negative, we may scan the entire conformational space allowed for a protein from the fully ordered native ( $N$ ) to the totally disordered conformer ( $U$ ) *with pressure as sole variable*.

Here the underlying principle that makes this possible is that “*the partial molar volume of a protein decreases in parallel with the loss of its conformational order*” (the “volume theorem” of protein), as advocated by Akasaka globular proteins [20] (Fig. 1.6). The “volume theorem” assures us to observe NMR signals of all relevant high-energy conformers of a protein in decreasing conformational order as we increase the hydrostatic pressure to a sufficiently high level.

In principle, by stably trapping each of these conformers at appropriate pressures, we may determine the average structure of each intervening conformer in detail with NMR, if possible with atom-based resolution, and by extrapolating the signals to 1 bar (as in Fig. 1.4), we may find out its equilibrium population under the physiological condition. This does not necessarily mean that all these intervening species give separately observable spectra as we increase the pressure, but some are separate and others appear mixed, depending on how rapidly they mutually exchange. Only when the exchange rate is much slower than the chemical shift separations of their signals, the two spectra are separately observed. But in general, the exchange rate between conformers becomes slower under pressure, because of the positive activation volume governing the transition. However, when they exchange rapidly, the mixing would be sensed as nonlinear pressure dependence of chemical shift [19].

In this way, *pressure provides a simple, clean and often efficient means of shifting the population distribution among fluctuating conformers of a protein in solution at the will of the experimenter* [24].

### 1.3 Apparatus for High-Pressure NMR Experiments

Traditionally, there have been two basic methods for performing NMR measurements under variable pressure. One is to use an *autoclave (pressure vessel)* inside of which the NMR detection coil and the sample cell containing the target solution are housed [44]. The other is to use a commercial NMR probe into which a *pressure-resisting sample cell* is inserted, just like the way the conventional NMR measurement at 1 bar is performed, but the pressure within the cell is controlled by a pressure generator (e.g., a pump) placed outside the magnet [18]. The latter method is now almost exclusively used for protein and biopolymer studies, because of the  $H_0$  and  $H_1$  homogeneity that assures high-resolution NMR signals and allows the use of a variety of pulse sequences that standard NMR measurement of protein structure may need, despite the drawback such as the limitation in the applicable pressure to avoid cell burst.

### 1.3.1 *The Autoclave Method*

The autoclave (the pressure vessel) method started as early as in 1954 when Benedek and Purcell [45] measured spin relaxation and self-diffusion of small molecules up to  $\sim 1000$  MPa ( $\sim 1$  GPa). Jonas extended the technique [16] to study proteins under pressure followed by Markley et al. [46]. The autoclave method utilizes a pressure-resisting vessel (autoclave) made of nonmagnetic materials, inside of which the NMR detection coils and the sample solution are housed. Pressure is applied from the remotely located pump often with, for example, silicone oil as the pressure mediator, and fills the inner space of the autoclave containing the detection coil.

The autoclave method is not extensively used today for studying proteins in solution, because of its low spectral resolution and the inability of carrying out multi-dimensional experiments with sophisticated pulse sequences. However, the utility of the autoclave method continues in studying dynamics of simple liquids and other substances in a wider pressure range ( $\sim 1$  GPa or more).

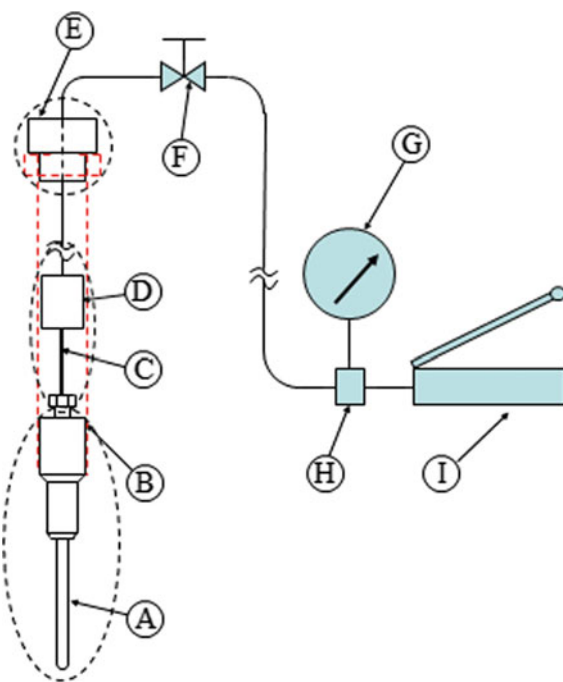
### 1.3.2 *The Pressure-Resisting Cell Method*

The other design is “the pressure-resisting cell method,” by which only the sample solution within a specially manufactured cylindrically shaped pressure-resisting cell is under pressure, while the NMR probe itself, usually from a commercial NMR spectrometer, is kept at ambient pressure throughout the measurement [12, 46–49]. The cell is connected with an external pressure line through which the pressure of the sample solution is varied (Fig. 1.7). Pressure is mediated, through a high-pressure line filled with a pressure-mediating liquid, either mineral oil, silicone oil or water, to the protein solution in the sample tube placed in the NMR probe. An example of the block diagram is shown in (Fig. 1.7). To avoid mixing of the sample solution with the pressure-mediating liquid, usually a barrier is provided, either with a synthetic membrane or with a tiny plastic piston [17, 47, 48].

Once the sample solution is set under pressure, measurements can be carried out, just like the measurement at ambient pressure with the versatility of pulse sequences as long as the signal-to-noise permits.

The only concern is how to set up the high-pressure NMR measuring system with a reliable pressure-resisting cell. The crucial factors for the pressure-resisting cells for use in high-pressure NMR is (1) the sufficient pressure-resistance at least 2 kbar or preferably higher (up to 4 kbar or more), besides easy handling and safety and (2) a sufficient magnetic homogeneity to assure high-resolution signals and to allow for multi-dimensional NMR spectroscopy (particularly for protein studies). It is for factor 1 that recently focus is on ceramic materials like zirconia with high shear strength, although factor 2 is not a trivial factor to overcome with ceramic

**Fig. 1.7** An example of the block diagram of the high-pressure NMR ceramic cell system. A ceramic cell; B cell holder; C connecting tube; D tube to tube connector; E cell suspender (to be placed on top of the magnet bore); F stop valve; G pressure gauge; H tee; and I pressure generator (pump)



cells compared to glass or quartz cells for which high resolution is relatively easily attained.

### Cells made of glass

In 1974, Yamada introduced a “hand-made” glass capillary tube that can fit to a commercial NMR probe and endure pressure between 0.1 and 200 MPa for pressure shift measurement of organic compounds [52]. Luedemann employed the method for studying dynamics of simple liquids, and later Wagner applied it for the first time to study protein dynamics (ring-flip motions) in a protein BPTI [14]. Earlier, Yamada had introduced a “one-by-one” type pressure-resisting glass cell (pressure is produced within a sealed glass tube by an expansion of an organic liquid) [11], which Morishima employed for his high-pressure NMR studies of heme proteins [13].

### Cells made of synthetic quartz (Fig. 1.8)

In 1996, Akasaka and Yamada, started high-resolution high-pressure NMR studies of proteins at 750 MHz with a hand-made pressure-resisting cell made of synthetic quartz (Fig. 1.8). The synthetic quartz cells extended the resistivity to ~4 kbar and gave extremely high magnetic field homogeneity inside the cell [cf. Fig. 3, 50]. Because of the excellent high resolution along with the high Q value of the detection coil system, the sensitivity was surprisingly high despite of the small quantity (~40 µL) of the sample solution in the NMR active part of the coil.

## High pressure NMR with pressure-resisting cells

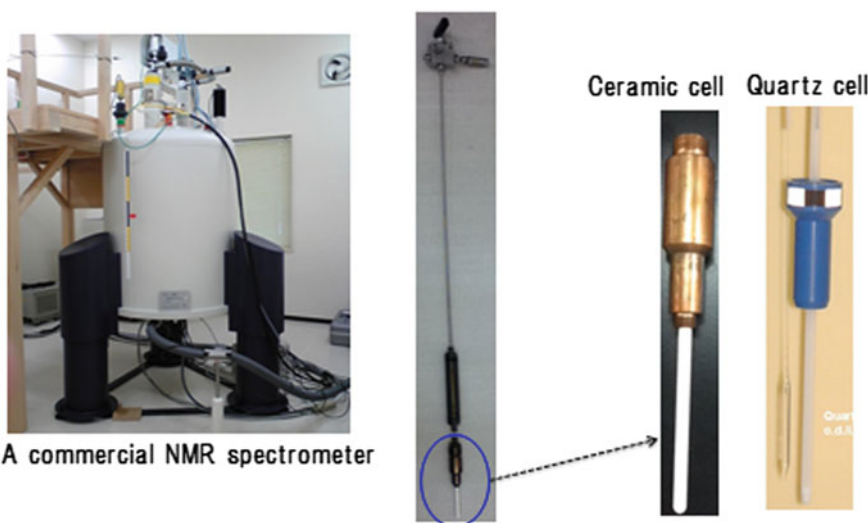


**Fig. 1.8** Photograph of a system for the high-pressure NMR measurement, with a ceramic cell or a quartz cell

In 1997, the first paper using the quartz cell was published, showing details of the *diamagnetic* chemical shift changes in the  $^1\text{H}$  NMR spectrum within the folded manifold of hen lysozyme upon applying pressure [46]. Since then, the technique was applied to a number of proteins, in one-dimensional  $^1\text{H}$  and heteronuclear two-dimensional NMR spectroscopy under varying pressure up to 200–400 MPa, and produced a number of new findings on protein structure and dynamics extending into the hitherto unexplored *high-energy paradigm of protein structure*, as summarized in a series of review articles by Akasaka and collaborators [18–30, 50] and briefly in [53].

The major drawback of this method is that these cells are not commercially available, but must be hand-made by following the detailed procedure reported by Yamada et al. [17]. Moreover, a special procedure must be followed to introduce the sample solution into the cell also. On the other hand, it has some excellence over other sample cells such that, besides the high resolution of the recorded spectra, an accidental breakage of the cell during measurement causes no damage to the NMR probe a small device, because a special device is designed to protect the sample solution from spilling out of the cell in case of a sudden cell damage.

### Cells made of sapphire

For measurements at relatively low pressure range ( $\leq 2$  kbar), cells made of sapphire can also be used. Wand and co-workers report sapphire cell designs for a multi-dimensional NMR study of proteins for a relatively low pressure range ( $\sim$  up to 1 kbar) [47]. Kalbitzer and co-workers designed sapphire cells to be used for up to  $\sim 2$  kbar [54].

In terms of availability and handiness, sapphire cells may be useful for some applications, where an extreme high pressure is not required.

### Cells made of zirconia (Fig. 1.8)

Zirconia cells are currently favored by many researchers because of its sturdiness as well as handiness, and importantly commercial availability, as described below. In general, cells made of zirconia, particularly those of aluminum toughened, are stronger in tensile strength and thus preferred over the other materials for the cell materials for studying proteins. The major question is how to shape them into cylindrical cells with high magnetic homogeneity along with high stability against pressure.

Zirconia cells are now commercially available from Daedalus Innovations, which changed the landscape of high-pressure NMR researches in the world as many new researchers have come into this area by using the commercial cells to study proteins with high-pressure NMR. A few groups have independently developed zirconia cells for their own research [51, 55] in particular. Akasaka et al. [30] have developed zirconia cells based on their own design with a special protection system against an accidental cell burst. One of the merits of the ceramic cell is that, because of its simple cylindrical shape, one can use it for systems other than soluble proteins, for example, the suspension of bacterial spores under pressure [55].

Since the wall of the zirconia cells requires a minimum thickness for keeping the pressure, the inner diameter of the sample cell is limited to 2–3 mm for the 5-mm probe, the filling factor, and therefore the NMR sensitivity is a few to several times lower than that of a glass-made normal sample tube for conventional NMR spectroscopy at 1 bar. Therefore, the use of NMR spectrometer with high sensitivity is preferred, if available, for the high-pressure NMR study of proteins using the ceramic and other pressure-resisting cells. The principles of the design and performance of an aluminum-toughened zirconia cell from Akasaka's group will be reported elsewhere.

## 1.4 Application to Protein Studies

The NMR spectroscopic study of proteins with pressure as variable over a couple of decades has allowed exploration of protein structures in the conformational space of proteins hitherto unexplored by conventional NMR spectroscopy, namely the paradigm of high-energy conformers having Gibbs energies higher than that of the basic folded conformer N [20, 24, 29, 33]. In contrast to the basic folded paradigm of protein, the high-energy paradigm of protein may consist of a variety of conformers from those close to *N* to those close to *U* with varying partial molar

volumes, whose populations may be increased systematically by applying pressure and structures analyzed by employing established NMR techniques.

Application may be divided into three major categories according to the extent of conformational changes involved:

1. Rapid ( $\ll \mu\text{s} \sim \text{ms}$ ) conformational fluctuations within the folded state:  $N \rightleftharpoons N'$ ;
2. Conformational fluctuations (in  $\mu\text{s} \sim \text{ms}$ ) involving high-energy sub-states:  $N1 \rightleftharpoons N2 \rightleftharpoons I$ ;
3. Slow conformational fluctuations (in  $\gg \text{ms} \sim \text{s}$ ) involving the unfolded and fibril or aggregated states:  $N \rightleftharpoons MG \rightleftharpoons U \rightleftharpoons \text{Fibril}$ .

### 1.4.1 Fluctuations within the Basic Folded Ensemble

In this section, we discuss the simple case where the fluctuation is restricted largely within a single sub-ensemble of conformers (the case in which higher energy conformers are far distant and the protein remains in the native ensemble “ $N$ ” or “ $N'$ ”). On applying pressure on the native ensemble “ $N$ ,” its partial molar volume (protein molecule + hydration layer) responds to pressure, but on the NMR spectrum, one can detect signals only from the protein part of the structure as residue-specific chemical shift changes of  $^1\text{H}$ ,  $^{15}\text{N}$  or  $^{13}\text{C}$  nuclei with pressure.

Macroscopically, the compressibility measurements of folded proteins have long been the primary source of conformational fluctuation of proteins [39]. The compressibility of proteins in their native states is known to be positive [ $\kappa > 0$ , Eqs. (1.2) and (1.3)] [9], suggesting that the interatomic distances should decrease, on average, within the native fold at high pressure.

Importantly, the *compressibility* (coefficient  $\beta$ ) of the volume  $V$  of a protein is related to its mean-square *fluctuation* ( $\langle (\delta V)^2 \rangle$ ) through the relation

$$\langle (\delta V)^2 \rangle = \beta V k_B T \quad (1.8)$$

where  $V$  is the partial molar volume of the protein system,  $\beta$  is the isothermal compressibility coefficient,  $k_B$  is the Boltzmann’s constant and  $T$  is the absolute temperature [7].

This relation indicates that the information on the volume fluctuation of a protein can be estimated from its compressibility measurement, which traditionally has been obtained from ultrasonic sound velocity measurements of proteins, the adiabatic part of which giving RMS fluctuations of volume on the order of  $\sim 0.3\%$  for most globular proteins [9]. By using high-pressure NMR, the *compressibility* of the protein part can be measured, in principle, *at individual residue sites*, e.g., at individual hydrogen bonds, through residue-specific chemical shift changes of  $^1\text{H}$ ,  $^{15}\text{N}$  or  $^{13}\text{C}$  nuclei with pressure, as will be shown later.

Since most covalent bond lengths are practically invariant under pressure at least within kilo-bar ranges, within the protein structure, compression arises from changes in individual weak chemical bonds (hydrogen bonds, ionic bonds, van der Waals interactions) accompanied by changes in individual  $\phi$ ,  $\Psi$  or  $\chi$  torsional angles [49], which are manifested most sensitively in pressure-induced chemical shifts of individual  $^1\text{H}$ ,  $^{15}\text{N}$  and  $^{13}\text{C}$  nuclei from the main chain as well as the side chains.

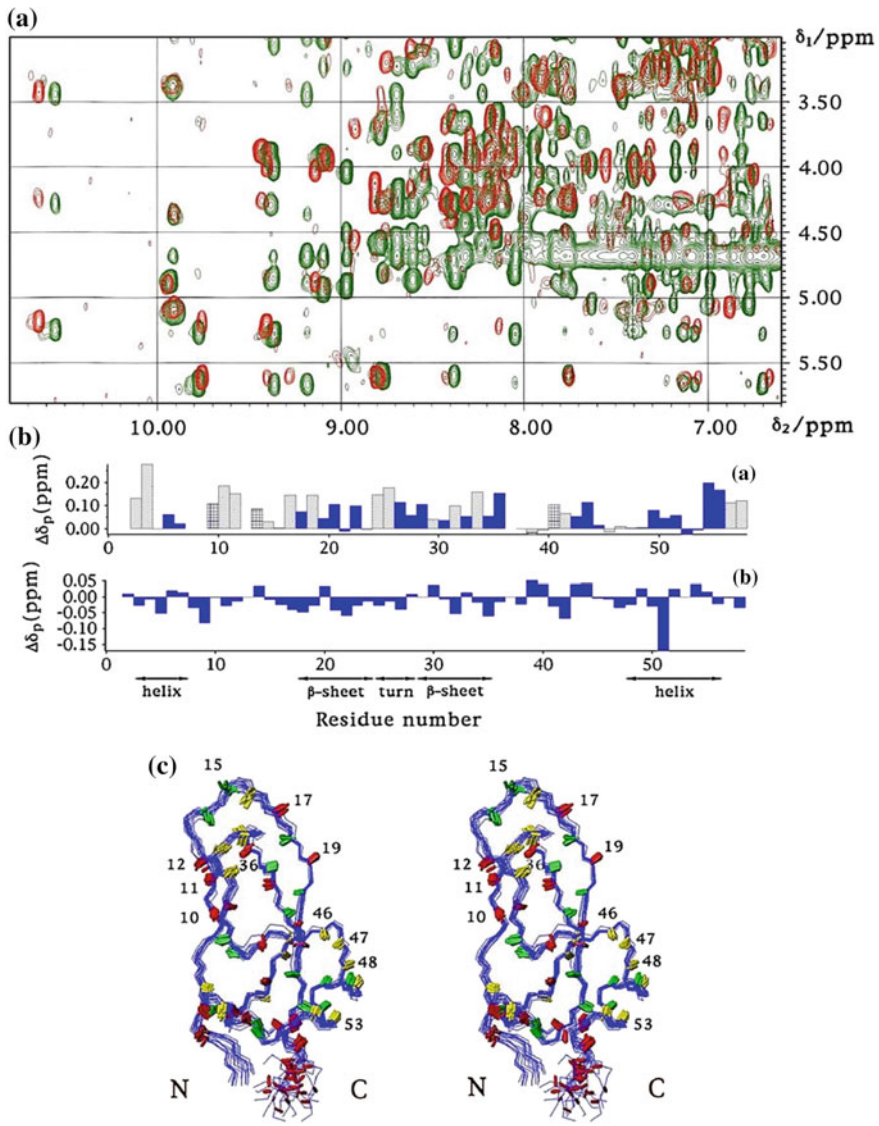
#### 1.4.1.1 Fluctuation in Individual Hydrogen Bonds Detected by $^1\text{H}$ Pressure Shifts

Pressure-induced changes in chemical shift of individual amide ( $^1\text{HN}$ ) protons can be measured either on  $^1\text{H}/^1\text{H}$  two-dimensional spectra (e.g., nuclear Overhauser effect spectroscopy (NOESY) (Fig. 1.9a) and total correlation spectroscopy (TOCSY) or on  $^{15}\text{N}/^1\text{H}$  two-dimensional heteronuclear single-quantum correlation spectra (HSQC) (for the uniformly  $^{15}\text{N}$ -labeled samples) in an  $^1\text{H}_2\text{O}$ -rich environment (e.g., 90%  $^1\text{H}_2\text{O}$ /10%  $^2\text{H}_2\text{O}$ ) at neutral to low pH in the pressure range 1–2000 bar [18, 27, 49, 56–57].

The low field shift trend of amide  $^1\text{H}$  and  $^{15}\text{N}$  signals are generally observed (Fig. 1.9b), which may be understood as arising from a decreased shielding of the magnetic field on these nuclei due to an increased polarization of the peptide N–H bond and also from the increased susceptibility effect from the increased proximity of the C=O group at high pressure. Therefore, the pressure-induced shifts of amide  $^1\text{H}$  and  $^{15}\text{N}$  signals give at least a qualitative measure of the pressure-induced changes (compaction in general) of individual N–H $\cdots$ O=C hydrogen bond distances [57].

The pressure-induced shifts of individual amide ( $^1\text{HN}$ ) protons are quite linear in BPTI in the pressure range up to 200 MPa, but heterogeneous in magnitude over individual ( $^1\text{HN}$ ) protons, indicating that the compressions of the hydrogen bonds occur actually quite heterogeneously over the hydrogen bonds of the protein molecule [57]. The larger the change in distance denotes the larger the fluctuation of the hydrogen bond. The observed low-field shifts of  $^1\text{HN}$  protons averaged over all of the NH $\cdots$ O hydrogen bonds of BPTI correspond to a shortening of N–H distances on average by  $\sim 0.020$  Å (or by  $\sim 1\%$ ) at 2 kbar for those engaged in the internal (NH $\cdots$ O=C) hydrogen bonding, as estimated from the empirical shift-distance relationship (see [23, 27, 57]). The results indicate that the compression is not uniform but rather heterogeneous over the folded molecule.

Despite the heterogeneity in fluctuation among hydrogen bonds within a single protein molecule, the average degree of fluctuations of hydrogen bonds over a protein molecule, as represented by the linear response part of the pressure shift, are similar to each other among different globular proteins. On the other hand, in many



proteins, nonlinearity in  $^1\text{H}$  and  $^{15}\text{N}$  shifts against pressure are rather commonly observed, the degree of which vary from protein to protein. The nonlinearity of pressure shift shows a good correlation with the density of cavities large enough to accommodate water molecules in the folded protein structure and is likely to be

◀Fig. 1.9 Pressure effect on individual hydrogen bond in BPTI. **a** Fingerprint ( $\text{NH}-\text{C}\alpha\text{H}$ ) regions of the NOESY spectra of BPTI, measured at 750 MHz at 36 °C and at 1 bar (green) and 2000 bar (red). **b** Histograms of pressure-induced chemical shifts [ $\Delta\delta_p = \delta(2 \text{ kbar}) - \delta(1 \text{ bar})$ ] for individual peptide NH and  $\text{C}\alpha$  protons of BPTI. The filled columns are for the 28 NH protons hydrogen bonded to carbonyls, the cross-hatched columns for the 4 NH protons hydrogen bonded to internal water molecules which can be identified with X-ray diffraction, and the dotted columns for the 20 NH protons forming no hydrogen bonds to any of the above. **c** Cross-eyed stereoview of the backbone atoms with positions and directions of the NH bonds, derived from 20 NMR structures (PDB ID: 1PIT) and drawn with the program MOLMOL. The N–H bonds are colored into three groups with different ranges of the pressure-induced shifts ( $\Delta\delta_p$ ) of the NH protons:  $\Delta\delta_p > 0.09 \text{ ppm}$  (red),  $0.03 < \Delta\delta_p < 0.09 \text{ ppm}$  (green) and  $\Delta\delta_p < 0.03 \text{ ppm}$  (yellow). Reproduced from Fig. 1.1 of [57] by permission of Elsevier

correlated with increased cavity hydration at elevated pressures leading to transition into high-energy states of proteins [19]. The  $^1\text{H}$  and  $^{15}\text{N}$  pressure-shift data for various proteins are summarized in a review article [28], while the role of cavities in protein dynamics is discussed, for example, in [31].

#### 1.4.1.2 Residue-Specific Fluctuations of the Polypeptide Chain Conformation Detected by $^{15}\text{N}/^1\text{H}$ Pressure Shifts

Fluctuations of  $N \rightleftharpoons N'$  in the polypeptide main chain can be manifested sensitively in pressure-induced  $^{15}\text{N}/^1\text{H}$  chemical shift changes in  $^{15}\text{N}/^1\text{H}$  HSQC spectra. For example, in  $^{15}\text{N}$ -labeled hen lysozyme in its folded state or in the “non-functional” hen lysozyme.

Interestingly, in the folded hen lysozyme (Fig. 1.10 right, a; left, a), measured over the pressure range of 3–200 MPa [59], all the cross-peaks exhibit shifts with pressure, indicating that at all residue sites the hydrogen bonds and possibly  $\phi$ ,  $\psi$  torsion angles change in response to pressure [49]. In contrast, the same protein in the 8 M urea-denatured state (in the “non-functional” hen lysozyme) shows monotonous shifts for all residues (Fig. 1.10 left, b).

The pressure-induced  $^{15}\text{N}$  and  $^1\text{H}$  shifts are plotted for almost all individual residues, for the folded and urea-denatured hen lysozyme (Fig. 1.10 right, a–d). Most individual  $^1\text{H}$  and  $^{15}\text{N}$  signals of folded “functional” hen lysozyme (Fig. 1.10 right, a, b) show characteristic shifts to low field with increasing pressure, the average pressure shifts being  $0.069 \pm 0.101 \text{ ppm}$ . ( $^1\text{H}$ ) and  $0.51 \pm 0.36 \text{ ppm}$ . ( $^{15}\text{N}$ ). The shifts indicate that the hydrogen bonds formed to carbonyl groups or water molecules by the backbone amides are, on average, shortened by  $\approx 0.02 \text{ \AA}$  as a result of pressure. In contrast, the pressure-induced  $^1\text{H}$  and  $^{15}\text{N}$  shifts for “non-functional” lysozyme denatured in 8 M urea (Fig. 1.10 right, c, d) are much more uniform over the residues, with average backbone amide shifts of  $0.081 \pm 0.029 \text{ ppm}$ . ( $^1\text{H}$ ) and  $0.57 \pm 0.14 \text{ ppm}$ . ( $^{15}\text{N}$ ), merely representing compaction of hydrogen bonding distances of the peptide NH with bulk water.

Interestingly, in the folded “functional” hen lysozyme (Fig. 1.10 right, a, b), six residues show anomalously large nonlinear  $^{15}\text{N}$  and  $^1\text{H}$  shifts (circled in red),

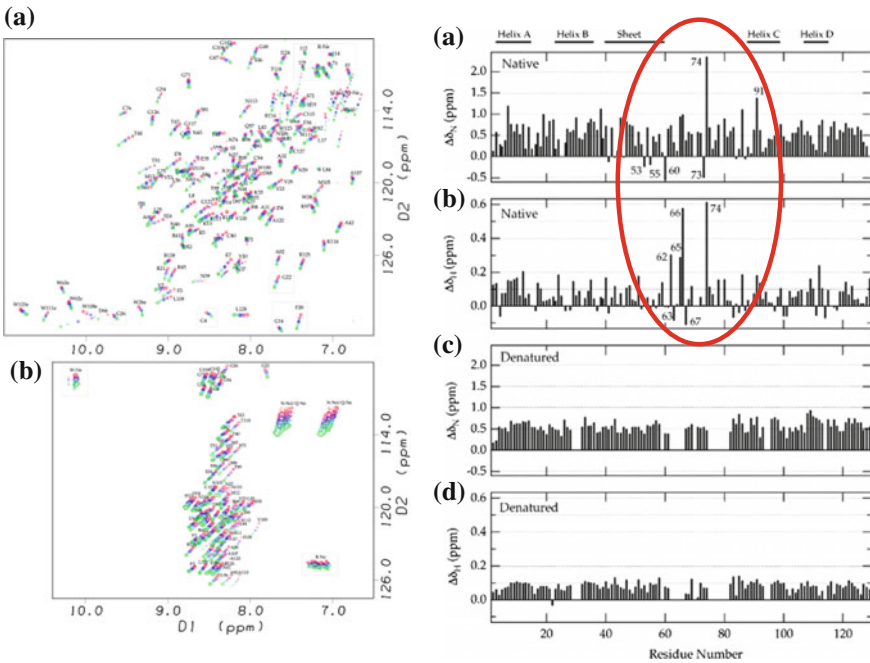


**Fig. 1.10** Left, panel **a**, **b** Superposition of <sup>15</sup>N/<sup>1</sup>H HSQC NMR spectra of <sup>15</sup>N-labeled hen lysozyme in its native state (panel **a**) and in 8 M urea-denatured state (panel **b**), in the pressure range of 3–200 MPa. Right, panel **a–d** Pressure-induced <sup>15</sup>N and <sup>1</sup>H shifts at 200 MPa for individual residues of hen lysozyme in the folded (**a**, **b**) and urea-denatured (**c**, **d**) state [59] (adapted from Figs. 1 and 3 in [59] by permission of Elsevier Inc.)

suggesting that particularly large fluctuations in  $\phi$ ,  $\Psi$  torsional angles or locally activated conformational fluctuations take place in the polypeptide backbone around these residues [48, 49]. Figure 1.11a, b shows that these residues exist in the  $\beta$  domain or at the  $\alpha/\beta$  domain interface close to the water-containing cavities o (circled in red). Both the <sup>1</sup>H and <sup>15</sup>N anomalous pressure shifts suggest strongly that the cavity hydration is intimately correlated with the peculiar conformational fluctuations in the “functional” hen lysozyme. This expectation is supported by the M.D. simulation showing water molecules getting in and out in the similar region [40].

It is further intriguing to find that cavities are located in the same positions in all lysozyme molecules from different biological species [41]. The coincidence of the cavity positions among lysozymes of different biological species supports strongly the hypothesis that the cavities are evolutionarily preserved in all lysozymes of different biological species for producing the mobility required for the common enzymatic activity. In short, whether the protein is “alive” or “dead” may easily be recognized by measuring <sup>15</sup>N/<sup>1</sup>H pressure shifts.

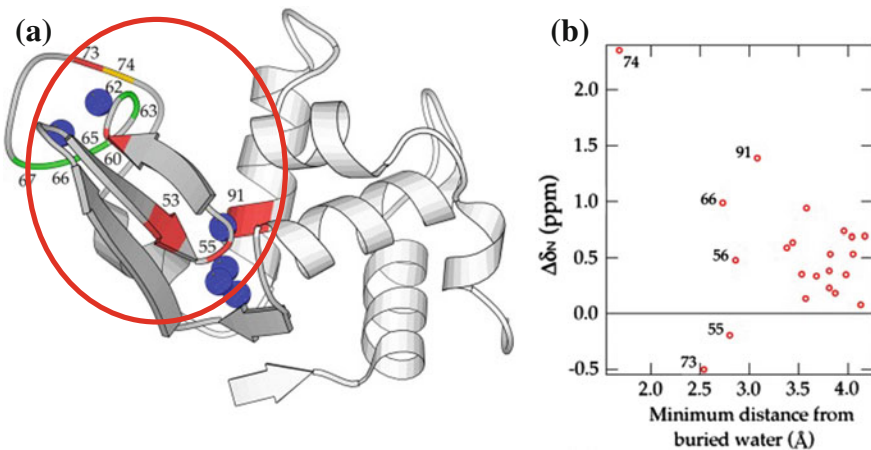


**Fig. 1.11** Mobile region of hen lysozyme disclosed by high-pressure NMR. **a** Locations of the six residues with anomalous  $^5\text{N}$  pressure shifts in hen lysozyme. **b** Plots of the anomalous shifts against the distance of respective residues from any of the water molecules (purple) in the cavities (adapted from Fig. 5 in [59] by permission of Elsevier Inc.)

#### 1.4.1.3 Slow Cooperative Fluctuations Detected by Ring-Flip Motions

Beside the local nature of rapid fluctuations such as in hydrogen bonding or torsion angles in the main chain occurring within  $\text{ps} \sim \text{ns}$ , much less frequent ( $\tau \sim \text{ms}$ ) and cooperative motions exist in a globular protein.

In 1980, using the glass capillary  $^1\text{H}$  high-pressure NMR method, Wagner studied the pressure effect on the flip-flop motions of Phe and Tyr rings about their  $C\beta \sim C\gamma$  axes in BPTI and found that the rates are significantly retarded by pressure [14]. Later, the same phenomenon was examined closely by performing two-dimensional  $^1\text{H}/^1\text{H}$  TOCSY NMR measurements under varying pressure by Li et al. [56]; Fig. 1.12c shows the TOCSY slice spectra for the (3,5) ring protons of Tyr-35, which vary dramatically between 30 and 2000 bar. Spectral simulation determines the flip rate of Tyr-35, which is slowed down from  $620 \text{ s}^{-1}$  at 30 bar to only  $12 \text{ s}^{-1}$  at 2000 bar by nearly two orders of magnitude.

Furthermore, the result gave an activation volumes Tyr-35 and Phe-45 ring-flips,  $\Delta V^\ddagger = 51.2$  and  $27.7 \text{ ml/mol}$ , respectively, at  $57^\circ\text{C}$  (Fig. 1.12e). This means that the core of the protein undergoes extremely infrequent, but large amplitude fluctuation, transiently creating an internal void of  $50\text{--}80 \text{ \AA}^3$  around these rings (Fig. 1.12b), much larger than the statistically expected volume fluctuation for BPTI of  $\sim 30 \text{ \AA}^3$ . A similar phenomenon has been observed in another protein HPr [60]. The clear presence of such ample but rare fluctuations in this “tightly” folded protein such as BPTI is surprising. Although the total view and its biological significance are yet to be clarified, the result gives undeniable evidence that even a globular protein, well-known for its “exceptionally high stability and rigidity”, has such a large volume fluctuation in its tertiary structure.

### 1.4.2 Fluctuations into Alternately Folded Conformer

In the case of ubiquitin, all the  $^{15}\text{N}/^1\text{H}$  HSQC NMR cross-peaks showed reversible shifts with pressure (Fig. 1.13, upper left), out of which some signals showed clearly sigmoidal changes (Fig. 1.13, upper right), suggesting a two-state transition probably from one folded conformer ( $N_1$ ) dominant at 1 bar to another folded conformer ( $N_2$ ) dominant at high pressure [61], carried out the three-dimensional structure determination of the protein conformation for the first time at high pressure (300 MPa) using NOE distance and torsion angle constraints to create average atomic coordinates of ubiquitin (Fig. 1.13) [23]. Since the two states undergo mutual transitions at sub-microsecond time range [61], the coordinates show the first NMR-based “snapshots” of a fluctuating protein structure in solution (ubiquitin at pH 4.6 at 20 °C).

While  $N_1$  takes a well-known folded conformation,  $N_2$  shows a partly open conformation with the helix swinging away by more than 0.3 nm. The partial molar volume difference  $\Delta V = V_{N_2} - V_{N_1} = -24 \text{ ml/mol}$ , suggesting a significant water penetration in  $N_2$ , which is detected in a molecular dynamic simulation (Imai and Sugita 2010) [62]. The open form  $N_2$  is identified as close to the active form of ubiquitin in its binding to the target protein  $E1$ , giving a clear evidence that the high-energy conformer  $N_2$  is the functional conformer rather than the basic folded conformer  $N_1$ .

In closing this section, I anticipate that, in future, the time will come when most of the protein structures are expressed by a series of snapshots of fluctuating conformers, possibly each with average coordinates, rather than by a single, static conformer as we have today, although not all high-energy conformers may be expressed in average coordinates, as some of them may contain disordered regions.

### 1.4.3 Conformational Fluctuations Involving Fibril Formation and Dissociation

In this section, we consider the unfolded conformer  $U$  or those close to  $U$ . The conformer  $U$  is present even under physiological conditions, but well controlled in population. In this sense, *all the proteins are “intrinsically denatured” proteins*.

These high-energy conformers are reactive in two ways: firstly, they are the reactive species causing aggregation or fibrillation, which might lead to amyloidosis. Secondly, they receive proteolysis and easily degraded into smaller peptides. Because of these properties, the equilibrium concentration of the unfolding or closely unfolding species is evolutionally controlled usually at an extremely low level under physiological conditions by strictly selecting their amino acid sequences.

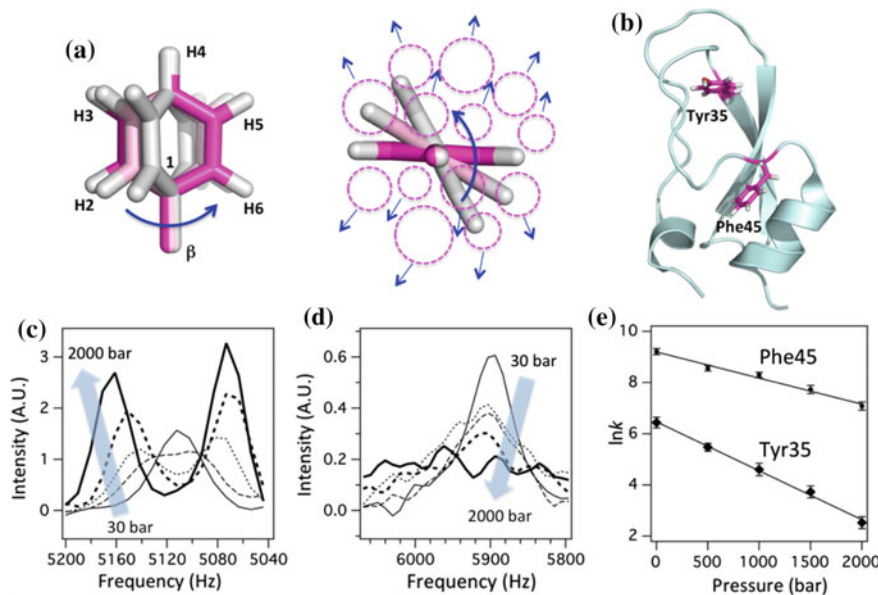


**Fig. 1.12** Slow breathing motions of BPTI by pressure. **a** Illustration of the aromatic ring-flip motion taking Phe as an example. The aromatic ring undergoes 180° flip motion along its  $C_\beta-C_1$  axis. The right panel shows the view from along  $C_\beta-C_1$  axis. The dotted circles represent the atoms around Phe schematically. **b** A ribbon model for BPTI with locations of Tyr35 and Phe45. **c** Superposition of the 3H and 5H region of the TOCSY slice spectra taken at 2H resonance position of Tyr35 measured at 57 °C at five different pressures. **d** Superposition of the 3H and 5H region of the TOCSY slice spectra taken at 2H resonance position of Phe45 measured at 57 °C at five different pressures. In (c) and (d), the slice spectra at different pressures superimposed: 1 bar (line), 500 bar (dotted line), 1000 bar (dashed line), 1500 bar (thick dotted line) and 2000 bar (thick line). **e** Logarithmic plot of the flip-flop rate of the ring,  $k$  (in  $\text{s}^{-1}$ ), for Tyr35 and Phe45 against pressure (adapted from Fig. 5 in [56] by permission of Elsevier Inc.)

#### 1.4.3.1 Cause for Familial Amyloidotic Polyneuropathy

Transthyretin amyloidosis is a fatal disease for a family with a single mutation, e.g., V30M in their transthyretin. Comparison of its crystal structure with the wild type gives no hint of difference. However, we found, by utilizing high-pressure NMR, that, under physiological conditions, a single familial mutation V30M in human transthyretin causes a dramatic increase in the equilibrium concentration of the *unfolded species* by a factor of 1000 compared to its wild type. The increase in the reactive unfolded species is considered to be the main reason why a single mutation V30M causes the familial amyloidotic polyneuropathy [63]. It is easy to compare the effect of each mutation on the equilibrium concentration of the reactive species U under physiological conditions by using high-pressure NMR spectroscopy. The mechanism (increase in the equilibrium concentration of the reactive species U)

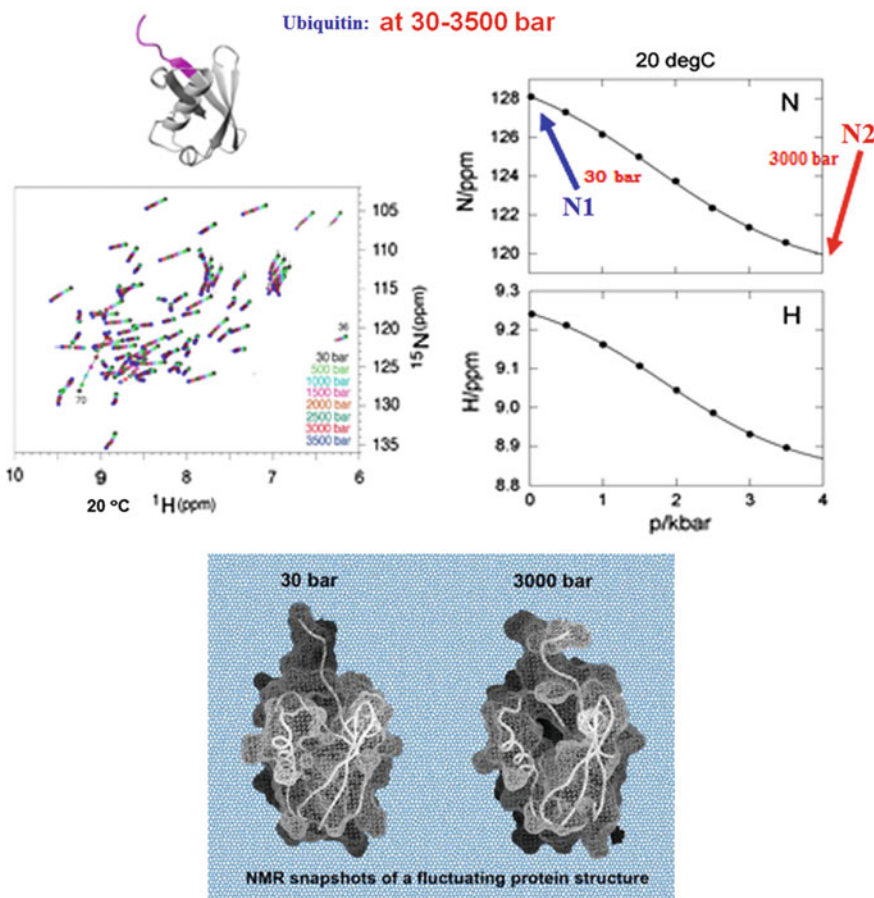


**Fig. 1.13** The low pressure ( $N_1$ ) and the high-pressure ( $N_2$ ) structures of ubiquitin [61]. *Upper figure*  $^{15}\text{N}/^1\text{H}$  HSQC NMR spectra of  $^{15}\text{N}$ -labeled ubiquitin and a sigmoidal  $^{15}\text{N}$ -chemical shift change with pressure suggesting a conformational equilibrium between  $N_1$  and  $N_2$ . *Lower figure* molecular surface of ubiquitin (pH 4.6, 20 °C) at 30 bar (PDB 1V80) and at 3000 bar (PDB 1V81)

appears to be common to many amyloid diseases known to be caused by single mutations.

#### 1.4.3.2 Conformational Fluctuations in Prion Protein and Drugs to Prevent Fibrillation

The unfolded form of a globular protein often becomes the source of aggregation or fibril formation, depending on the concentration and the solution condition (temperature, pH, etc.). Amyloid diseases are caused by the fibril formation from proteins dominantly unfolded states.

Prion protein ( $\text{PrP}^C$ ) is a well-known protein, of which the fibril ( $\text{PrP}^{SC}$ ) formation is considered a cause for the prion disease (Fig. 1.14). To find the equilibrium concentration of the unfolded conformer or possible reactive species in equilibrium with  $\text{PrP}^C$ , we have carried out high-pressure  $^1\text{H}-^{15}\text{N}$  HSQC measurement of rPrP (90-231) (pH 5.2) as a function of pressure and temperature (Fig. 1.14) [64].

In the experiment shown in Fig. 1.14,  $\text{PrP}^C$  stable at 30 bar at 30 °C changes into an intermediate conformer  $\text{PrP}^*$  at 2–2.5 kbar (with helices B and C preferentially disordered) and by lowering temperature the totally unfolded conformer  $\text{PrP}^U$  is also observed, suggesting an equilibrium among the three monomeric conformers of the protein

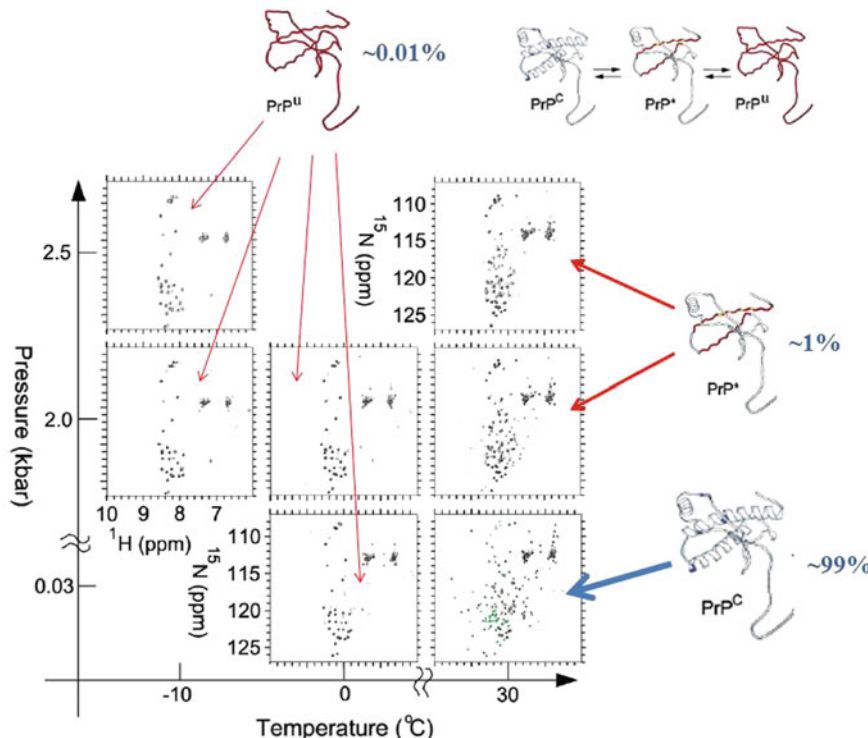
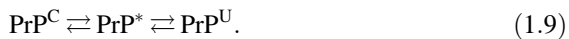


**Fig. 1.14** Spectral changes in  $^1\text{H}-^{15}\text{N}$  HSQC of rPrP (90-231) (pH 5.2) observed as a function of pressure and temperature. The spectrum of the intact prion protein  $\text{PrP}^C$  is shown at the bottom right corner (at 30 bar and 30 °C), with the signals from intrinsically disordered residues 90–128 colored green. The cross-peaks from the folded core region of  $\text{PrP}^C$  decrease with pressure and almost disappear at 2500 bar. The transition of  $\text{PrP}^C$  into  $\text{PrP}^U$  is observed by decreasing temperature (cold denaturation)

The conformer PrP\* has a unique structure with crucial helices B and C preferentially disordered. We postulate that the peculiar conformer PrP\*, existing in a relatively high concentration ( $\sim 1\%$ ) at 30°C, is likely to be the precursor to PrP<sup>SC</sup> (fibrils), the pathogenic form of the prion protein. In fact, Kuwata et al. named the preferentially disordered region of PrP\* as “hot spot” of prion protein and succeeded in designing a compound that preferentially binds to the “hot spot”, which prohibited the pathogenic conversion of the prion protein [65].

#### 1.4.3.3 Amyloid Fibril Is a High-Volume State

However, in the experiment in Fig. 1.14 we could not follow any reaction of turning monomers PrP\* or PrP<sup>U</sup> into fibrils (PrP<sup>SC</sup>). The reason becomes clear in a separate, but related experiment using the disulfide-deletion mutant of hen lysozyme (OSS). Namely, *when OSS forms protofibrils, its partial molar volume increases dramatically ( $\Delta V = -570 \text{ ml/mol}$ )* [66]. Since all matured fibrils should consist of bundles of protofibrils, we expect that even the matured fibrils of the prion protein (PrP<sup>SC</sup>) should also be in high-volume state. Therefore, the reaction (1.9) would not proceed further to the right under high-pressure conditions, because the fibrils would be unstable under pressure.

#### 1.4.3.4 Fibril Formation Is Part of the Intrinsic Conformational Fluctuation of Proteins

To find whether the formation of the pathogenic mature fibril PrP<sup>SC</sup> (fibrils) is an irreversible process (1.10a) or a reversible process as in (1.10b), we must prepare PrP<sup>SC</sup> (fibrils) first and then apply pressure to see if PrP<sup>SC</sup> (fibrils) dissociates into monomers.

The experiment to check this idea is carried out as shown in Fig. 1.15, but the direct observation of the reaction by high-pressure NMR is abandoned, because of the small quantity of the sample, but the dissociation of fibrils is examined by observing whether the fibrils become PK-degradable PrP<sup>C</sup> monomers due to dissociation or not.

The results in Fig. 1.15a show that above 300 MPa PrP<sup>SC</sup> fibrils(AFM, left) is digested fully by the enzyme protease K, which is taken to give a proof that the fibrils of PrP<sup>SC</sup> are dissociated into monomeric PrP<sup>C</sup> by pressure (AFM, right). This dramatic event that the well-known “protease K-resistant” fibrils (the contagious scrapie form of the prion protein) is dissociated into monomeric state indicates that the entire process is essentially an equilibrium process represented by (1.10).

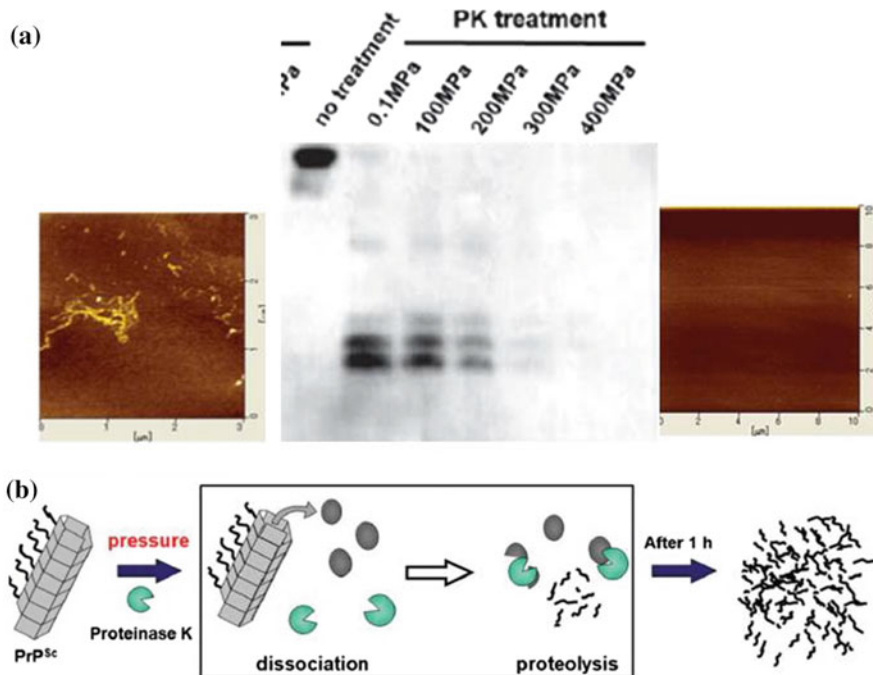


**Fig. 1.15** Pressure dissociation and proteolysis of prion fibrils. **a** The experimental results in the upper part show that prion fibrils, which are protease K-resistant at ambient pressure, can be degraded by protease K under the applied pressure of 400 MPa. **b** The figure shows what happens in the experiment; the prion fibrils are dissociable into monomers of prion protein [67]



The high-pressure experiment disclosed that even *the fibril formation is part of the intrinsic conformational fluctuation of a protein in solution*.

#### 1.4.4 Exploring the Protein Folding Pathway with High-Pressure NMR

High-pressure NMR can also be used to study kinetic pathways of protein folding. Although a close identity of a pressure-stabilized intermediate with a kinetic intermediate in protein folding has been noted in a small protein like ubiquitin [68], detailed pathways of folding may be monitored more directly by real-time NMR, if one could slow down the reaction sufficiently. This could be realized by taking advantage of the fact that activation volumes of folding/unfolding are often positive. The interesting attempts are being successful recently by Roche, Roumestand and Royer, and readers are referred to their review articles [69].

## 1.5 Summary: Perspectives of High-Pressure NMR Spectroscopy

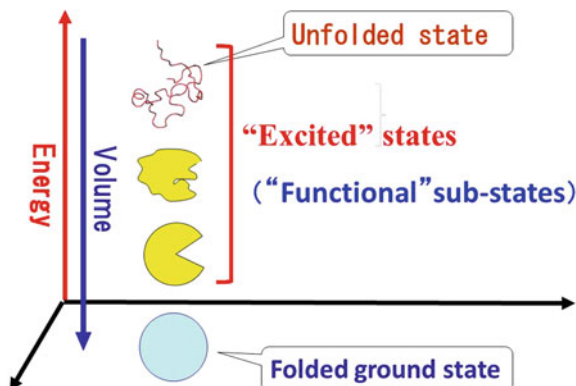
Figure 1.16 depicts schematically the new dynamic view of proteins that has emerged from the high-pressure NMR studies of proteins carried out in the author's laboratory during the last couple of decades [21, 24, 26]. Here, the excited-states form the *high-energy paradigm*, which is considered the *functional paradigm of proteins* rather than the folded ground-state paradigm itself.

Perhaps, the most important contribution of the high-pressure NMR spectroscopy to study proteins is that it provides, for the first time, a systematic spectroscopic means of exploring the high-energy paradigm of proteins, which has not hitherto been the direct target of systematic or intensive investigation, except perhaps by the method of spin relaxation dispersion targeting the  $\mu$ s-ms dynamics [70].

It just happened that the “partial molar volume” of a protein in aqueous solution is intimately coupled to its “conformation” and therefore that, by manipulating the volumetric state of a protein with pressure, one can manipulate its conformational state as well. The intimate coupling between the “volume” and the conformation of a protein in aqueous environment (embedded in the “volume theorem”), which is mediated by the cavities and their hydration, forms the basis for both the *conceptual and practical simplicity* of high-pressure NMR experiments on proteins.

Since pressure allows the investigator to “trap” any of the excited-state conformers of a protein rather stably, the method gives a good opportunity for investigating their structures, dynamics and thermodynamics with up-dated NMR spectroscopic techniques. Such studies are expected to disclose the delicate couplings of thermodynamics with structure that occur preferentially in high-energy paradigm for each protein to perform its function, adaptation and evolution. Such information is considered crucial in advancing our knowledge on protein beyond the concept so far established for its thermodynamics and folding [5] and for its structure in the basic folded paradigm [6].

**Fig. 1.16** A new dynamic view of protein emerging from high-pressure NMR experiments



Alternately, in terms of the biotechnological view point, we have acquired the power of choosing sub-states of a protein according to our specific needs by finely tuning pressure. For these reasons and with further development of the experimental techniques anticipated in near future, high-pressure NMR spectroscopy will grow to be an indispensable tool not only in protein studies, but also in a wide range of biosciences for many years to come.

## References

1. Bloch, F.: Nuclear induction. *Phys. Rev.* **70**(7–8), 460–474 (1946)
2. Purcell, E.M., Torrey, H.C., Pound, R.V.: Resonance absorption by nuclear magnetic moments in a solid. *Phys. Rev.* **69**(1–2), 37–38 (1946)
3. Hahn, E.L.: Spin echoes. *Phys. Rev.* **80**(4), 580–594 (1950)
4. Ernst, R.R., Bodenhausen, G., Wokaun, A.: Principles of Nuclear Magnetic Resonance in One and Two Dimensions (International Series of Monographs on Chemistry), Oxford Univ. Press, London/New York (1991)
5. Anfinsen, C.B.: Principles that govern the folding of protein chains. *Science* **181**(4096), 223–230 (1973)
6. Wüthrich, K.: NMR of Proteins and Nucleic Acids. Wiley, Hoboken (1986)
7. Cooper, A.: Thermodynamic fluctuations in protein molecules. *Biochemistry* **73**(8), 2740–2741 (1976)
8. Hirata, F., Akasaka, K.: Structural fluctuation of proteins induced by thermodynamic perturbation. *J. Chem. Phys.* **142**(4), 44110 (2015)
9. Gekko, K., Hasegawa, Y.: Compressibility–structure relationship of globular proteins. *Biochemistry* **25**(21), 6563–6571 (1986)
10. Frauenfelder, H., et al.: Proteins and pressure. *J. Phys. Chem.* **94**, 1024–1037 (1990)
11. Yamada, H.: High resolution NMR measurement under high pressure and pressure dependence of the proton chemical shifts. *Chem. Lett.* **1**(9), 747–750 (1972)
12. Yamada, H.: Pressure-resisting glass cell for high pressure, high resolution NMR measurement. *Rev. Sci. Instrum.* **45**(5), 640–642 (1974)
13. Morishima, I., Hara, M.: High-pressure NMR studies of hemoproteins. Pressure-induced structural changes in the heme environments of cyanometmyoglobin. *J. Am. Chem. Soc.* **104**(24), 6833–6834 (1982)
14. Wagner, G.: Activation volumes for the rotational motion of interior aromatic rings in globular proteins determined by high resolution  $^1\text{H}$  NMR at variable pressure. *FEBS Lett.* **112**(2), 280–284 (1980)
15. Jonas, J., Jonas, A.: High-pressure NMR spectroscopy of proteins and membranes. *Annu. Rev. Biophys. Biomol. Struct.* **23**(1), 287–318 (1994)
16. Jonas, J., Ballard, L., Nash, D.: High-resolution, high-pressure NMR studies of proteins. *Biophys. J.* **75**(1), 445–452 (1998)
17. Yamada, H., Nishikawa, K., Honda, M., Shimura, T., Akasaka, K., Tabayashi, K.: Pressure-resisting cell for high-pressure, high-resolution nuclear magnetic resonance measurements at very high magnetic fields. *Rev. Sci. Instrum.* **72**(2), 1463 (2001)
18. Akasaka, K., Yamada, H.: On-line cell high-pressure nuclear magnetic resonance technique: application to protein studies. *Methods Enzymol.* **338**, 134–158 (2001)
19. Akasaka, K., Li, H.: Low-lying excited states of proteins revealed from nonlinear pressure shifts in  $^1\text{H}$  and  $^{15}\text{N}$  NMR. *Biochemistry* **40**(30), 8665–8671 (2001)
20. Akasaka, K.: Exploring the entire conformational space of proteins by high-pressure NMR. *Pure Appl. Chem.* **75**(7), 927–936 (2003)

21. Akasaka, K.: Highly fluctuating protein structures revealed by variable-pressure nuclear magnetic resonance. *Biochemistry* **42**(37), 10875–10885 (2003)
22. Kamatari, Y., Kitahara, R., Yamada, H., Yokoyama, S., Akasaka, K.: High-pressure NMR spectroscopy for characterizing folding intermediates and denatured states of proteins. *Methods* **34**(1), 133–143 (2004)
23. Li, H., Akasaka, K.: Conformational fluctuations of proteins revealed by variable pressure NMR. *Biochim. Biophys. Acta Proteins Proteom.* **1764**(3), 331–345 (2006)
24. Akasaka, K.: Probing conformational fluctuation of proteins by pressure perturbation. *Chem. Rev.* **106**(5), 1814–1835 (2006)
25. Lassalle, M.W., Akasaka, K.: The use of high-pressure nuclear magnetic resonance to study protein folding. *Methods Mol. Biol.* **350**, 21–38 (2007)
26. Akasaka, K.: High pressure NMR study of proteins-seeking roots for function, evolution, disease and food applications. *High Press. Res.* **30**(4), 453–457 (2010)
27. Akasaka, K., Kitahara, R., Kamatari, Y.O.: Exploring the folding energy landscape with pressure. *Arch. Biochem. Biophys.* **531**(1–2), 110–115 (2013)
28. Kitahara, R., Hata, K., Li, H., Williamson, M.P., Akasaka, K.: Pressure-induced chemical shifts as probes for conformational fluctuations in proteins. *Prog. Nucl. Magn. Reson. Spectrosc.* **71**, 35–58 (2013)
29. Akasaka, K.: Pressure and protein dynamism. *High Press. Res.* **34**(2), 222–235 (2014)
30. Akasaka, K.: High pressure NMR spectroscopy. In: Akasaka, K., Matsuki, H. (eds.) *High Pressure Bioscience-Basic Concepts, Applications and Frontiers*, pp. 707–721. Springer, Amsterdam (2015)
31. Kalbitzer, H.R.: High pressure NMR methods for characterizing functional substates in proteins. In: Akasaka, K., Matsuki, H. (eds.) *High Pressure Bioscience-Basic Concepts, Applications and Frontiers*, pp. 179–197. Springer, Amsterdam (2015)
32. Kremer, W.: High pressure NMR studies in proteins. In: *Annual Reports on NMR Spectroscopy*, **57**, 177–203. Elsevier, Amsterdam (2006)
33. Fourme, R., Girard, E., Akasaka, K.: High-pressure macromolecular crystallography and NMR: status, achievements and prospects. *Curr. Opin. Struct. Biol.* **22**(5), 636–642 (2012)
34. Nguyen, L.M., Roche, J.: High-pressure NMR techniques for the study of protein dynamics, folding and aggregation. *J. Magn. Reson.* **277**(April), 179–185 (2017)
35. Maeno, A., Matsuo, H., Akasaka, K.: The pressure–temperature phase diagram of hen lysozyme at low pH. *BIOPHYSICS (J. Biophys. Soc. Japan)* **5**, 1–9 (2009)
36. Kitahara, R., Yamada, H., Akasaka, K., Wright, P.E.: High pressure NMR reveals that apomyoglobin is an equilibrium mixture from the native to the unfolded. *J. Mol. Biol.* **320**(2), 311–319 (2002)
37. Hawley, S.A.: Reversible pressure–temperature denaturation of chymotrypsinogen. *Biochemistry* **10**(13), 2436–2442 (1971)
38. Smeller, L.: Protein denaturation on p-T axes-thermodynamics and analysis. In: Akasaka, K., Matsuki, H. (eds.) *High Pressure Bioscience-Basic Concepts, Applications and Frontiers*, pp. 19–39. Springer, Amsterdam (2015)
39. Gekko, K.: Volume and compressibility of proteins. In: Akasaka, K., Matsuki, H. (eds.) *High Pressure Bioscience-Basic Concepts, Applications and Frontiers*, pp. 75–108. Springer, Amsterdam (2015)
40. Soda, K., Shimbo, Y., Seki, Y., Taiji, M.: Structural characteristics of hydration sites in lysozyme. *Biophys. Chem.* **156**(1), 31–42 (2011)
41. Kamatari, Y.O., Smith, L.J., Dobson, C.M., Akasaka, K.: Cavity hydration as a gateway to unfolding: An NMR study of hen lysozyme at high pressure and low temperature. *Biophys. Chem.* **156**(1), 24–30 (2011)
42. Kitahara, R., Okuno, A., Kato, M., Taniguchi, Y., Yokoyama, S., Akasaka, K.: Cold denaturation of ubiquitin at high pressure. *Magn. Reson. Chem.* **44**(S1), S108–S113 (2006)
43. Royer, C.A.: Revisiting volume changes in pressure-induced protein unfolding. *Biochim. Biophys. Acta* **1595**(1–2), 201–209 (2002)

44. Kalbitzer, H.R., Görler, A., Li, H., Dubovskii,, P.V., Hengstenberg, W., Kowollik, C., Yamada, H., Akasaka, K.:  $^{15}\text{N}$  and  $^1\text{H}$  NMR study of histidine containing protein (HPr) from *Staphylococcus carnosus* at high pressure. *Protein Sci.* **9**:693–703 (2000)
45. Benedek, G.B., Purcell, E.M.: Nuclear magnetic resonance in liquids under high pressure. *J. Chem. Phys.* **22**(12), 2003–2012 (1954)
46. Royer, C.A., et al.: Effects of amino acid substitutions on the pressure denaturation of staphylococcal nuclease as monitored by fluorescence and nuclear magnetic resonance spectroscopy. *Biochemistry* **32**(19), 5222–5232 (1993)
47. Akasaka, K., Tezuka, T., Yamada, H.: Pressure-induced changes in the folded structure of lysozyme. *J. Mol. Biol.* **271**, 671–678 (1997)
48. Refaei, M., Tezuka, T., Akasaka, K., Williamson, M.P.: Pressure-dependent changes in the solution structure of hen egg-white lysozyme. *J. Mol. Biol.* **327**(4), 857–865 (2003)
49. Urbauer, J.L., Ehrhardt, M.R., Bieber, R.J., Flynn, P.F., Wand, A.J.: High-resolution triple-resonance NMR spectroscopy of a novel calmodulin, peptide complex at kilobar pressures. *J. Amer. Chem. Soc.* **118**, 11329–11330 (1996)
50. Akasaka, K., Yamada, H.: On-line cell high-pressure nuclear magnetic resonance technique: application to protein studies. *Methods Enzymol.* **338**, 134–158 (2001)
51. Erlach, M.B., et al.: Ceramic cells for high pressure NMR spectroscopy of proteins. *J. Magn. Reson.* **204**(2), 196–199 (2010)
52. Yamada, H.: Pressure-resistant glass cell for high pressure, high resolution NMR measurement. *45*, 640–642 (1974)
53. Akasaka, K.: High pressure NMR spectroscopy. In: Akasaka, K., Matsuki, H. (eds.) *High Pressure Bioscience-Basic Concepts, Applications and Frontiers*, pp. 707–721. Springer, Amsterdam (2015)
54. Arnold, M.R., Kalbitzer, H.R., Kremer, W.: High-sensitivity sapphire cells for high pressure NMR spectroscopy on proteins. *J. Magn. Reson.* **161**(2), 127–131 (2003)
55. Akasaka, K., Maeno, A., Yamazaki, A.: Direct high-pressure NMR observation of dipicolinic acid leaking from bacterial spore: a crucial step for thermal inactivation. *Biophys. Chem.* (2017) Apr 19. doi: [10.1016/j.bpc.2017.04.008](https://doi.org/10.1016/j.bpc.2017.04.008)
56. Li, H., Yamada, H., Akasaka, K.: Effect of pressure on the tertiary structure and dynamics of folded basic pancreatic trypsin inhibitor. *Biophys. J.* **77**, 2801–2812 (1999)
57. Li, H., Yamada, H., Akasaka, K.: Effect of pressure on individual hydrogen bonds in proteins. Basic pancreatic trypsin inhibitor. *Biochemistry* **37**(5), 1167–1173 (1998)
58. Akasaka, K., Naito, A., Imanari, M.: Novel method for NMR spectral correlation between the native and the denatured states of a protein. Application to ribonuclease A. *J. Am. Chem. Soc.* **113**(12), 4688–4689 (1991)
59. Kamatari, Y.O., Yamada, H., Akasaka, K., Jones, J.A., Dobson, C.M., Smith, L.J.: Response of native and denatured hen lysozyme to high pressure studied by  $(15)\text{N}/(1)\text{H}$  NMR spectroscopy. *Eur. J. Biochem.* **268**(6), 1782–1793 (2001)
60. Hattori, M., et al.: Infrequent cavity-forming fluctuations in HPr from *Staphylococcus carnosus* revealed by pressure- and temperature-dependent tyrosine ring flips. *Protein Sci.* **13** (12), 3104–3114 (2004)
61. Kitahara, R., Yokoyama, S., Akasaka, K.: NMR snapshots of a fluctuating protein structure: ubiquitin at 30 bar–3 kbar. *J. Mol. Biol.* **347**(2), 277–285 (2005)
62. Imai, T., Sugita, Y: Dynamic correlation between pressure-induced protein structural transition and water penetration. *J. Phys. Chem. B* **114**(6), 2281–2286 (2010)
63. Niraula, T.N., Haraoka, K., Ando, Y., Li, H., Yamada, H., Akasaka, K.: Decreased thermodynamic stability as a crucial factor for familial amyloidotic polyneuropathy. *J. Mol. Biol.* **320**(2), 333–342 (2002)
64. Kuwata, K., Li, H., Yamada, H., Legname, G., Prusiner, S.B., Akasaka, K., James, T.L.: Locally Disordered Conformer of the Hamster Prion Protein: A Crucial Intermediate to  $\text{PrP}^{\text{Sc}}?$ . *Biochemistry* **41**(41), 12277–12283 (2002)
65. Kuwata, K. et al.: Hot spots in prion protein for pathogenic conversion. *Proc. Natl. Acad. Sci. (USA)* **104**(29), 11921–11926 (2007)

66. Akasaka, K., Latif, A.R.A., Nakamura, A., Matsuo, K., Tachibana, H., Gekko, K.: Amyloid protofibril is highly voluminous and compressible. *Biochemistry* **46**(37), 10444–10450 (2007)
67. Akasaka, K., et al.: Pressure-assisted dissociation and degradation of proteinase K-resistant fibrils prepared by seeding with scrapieinfected hamster prion protein. *Prion* **8**(4), 314–318 (2014)
68. Kitahara, R., Akasaka, K.: Close identity of a pressure-stabilized intermediate with a kinetic intermediate in protein folding. *Proc. Natl. Acad. Sci. USA* **100** (6), 3167–3172 (2003)
69. Roche, J., Dellarole, M., Royer, C. A., Roumestand, C.: Exploring the protein folding pathway with high-pressure NMR: Steady-state and kinetics studies. In: Akasaka, K., Matsuki, H. (eds.) *High Pressure Bioscience-Basic Concepts, Applications and Frontiers*, pp. 261–278 Springer, Amsterdam (2015)
70. Vallurupalli, P., Hansen, D.F., Kay, L.E.: Structures of invisible, excited protein states by relaxation dispersion NMR spectroscopy. *Proc Natl Acad Sci USA.* **105**(33):11766–11771 (2008)

# **Chapter 2**

## **Isotope-Aided Methods for Biological NMR Spectroscopy: *Past, Present, and Future***

**Masatsune Kainosho, Yohei Miyanoiri and Mitsuhiro Takeda**

**Abstract** This chapter starts by providing a historical background of our research endeavors over the past half-century to develop various isotope-aided methods in biological NMR spectroscopy, since innovations bloom only on the rich ground cultivated by previous investigators. We then focused on the stereo-array isotope-labeling (SAIL) method, one of our recent accomplishments, which culminates the isotope-aided NMR technologies for structural studies of proteins from various aspects: accurate structural determinations of large proteins, elaboration for automated structural determination, highly efficient and versatile residue-selective methyl labeling with newly developed auxotrophic *E. coli* strains, large-amplitude slow-breathing motion (LASBM) as revealed by the aromatic ring flipping of the residues in ligand-binding interfaces, and applications of the deuterium-induced <sup>13</sup>C-NMR isotope shift to investigate the hydrogen exchange phenomena of side-chain polar groups. Meanwhile, the expected role of NMR spectroscopy has been rapidly shifting from structure determinations to dynamics studies of biologically interesting targets, such as membrane proteins and larger protein complexes. The dynamic aspects of protein–protein and protein–ligand interactions are closely related to their biological functions and can be efficiently studied by using proteins residue selectively labeled with amino acids bearing optimized labeling

---

M. Kainosho (✉)

Graduate School of Science and Engineering, Tokyo Metropolitan University,

1-1 Minami-ohsawa, Hachioji 192-0397, Tokyo, Japan

e-mail: kainosho@tmu.ac.jp

M. Kainosho · Y. Miyanoiri

Structural Biology Research Center, Graduate School of Science, Nagoya University,

Furo-cho, Chikusa-ku, Nagoya 464-8602, Japan

e-mail: y-miyanoiri@protein.osaka-u.ac.jp

Y. Miyanoiri

Research Center for State-of-the-Art Functional Protein Analysis, Institute for Protein Research, Osaka University, 3-2 Yamadaoka, Suita 565-0871, Osaka, Japan

M. Takeda

Department of Structural BioImaging, Faculty of Life Sciences, Kumamoto University, 5-1, Oe-honmachi, Chuo-ku, Kumamoto 862-0973, Japan

e-mail: takeda@structbiol.com

patterns, prepared by cellular expression. We are absolutely confident that biological NMR spectroscopy will continually develop with further innovations of isotope-labeling technologies in the coming era, featuring ultrahigh field spectrometers beyond 1 GHz.

**Keywords** Isotope-aided NMR method •  $^{13}\text{C}$ ,  $^{15}\text{N}$  double labeling  
SAIL method • Aromatic ring flipping • Stereo-specific methyl labeling  
Hydrogen exchange rates of polar groups • Deuterium-induced  $^{13}\text{C}$  isotope shift

## 2.1 Historical Background of Our Research to Develop Isotope-Aided NMR Methods

Over the past half-century, we have exploited isotope-aided NMR methods to investigate biological molecules, such as amino acids, peptides, proteins, and nucleic acids. Many of our results were initially presented at the annual meetings of the NMR Society of Japan, and some of our novel techniques are still being used worldwide. One of the prominent features of our approach is utilizing site- and stereo-specifically isotope-labeled amino acids and nucleosides, which can be efficiently prepared by combining microbial fermentations, enzymatic reactions, and chiral organic syntheses—all areas in which Japan has world-leading technological expertise. In this chapter, after a brief recollection of the early days in the development of isotope-aided biological NMR methods, we describe some of the past and current advances achieved mostly in our laboratory. However, because of the space limitation, the methods for studying nucleic acids are not included.

At the first annual symposium of the NMR Society of Japan, which was held in Tokyo, 1961, two papers on NMR studies of amino acids were presented. Namely, Fujiwara et al. reported the 56.4 MHz  $^1\text{H}$ -NMR spectra of aqueous solutions of various amino acids and Takeuchi et al. reported the 40 MHz  $^1\text{H}$ -NMR spectra of threonine and *allo*-threonine. To the best of our knowledge, these were the first biological NMR applications ever reported in Japan. At that time, there was no systematic NMR research on proteins, except for a short communication on ribonuclease A [1]. Unfortunately, the reported 40 MHz spectrum showed only four broad overlapped signals and did not provide detailed structural information. It was obvious that some groundbreaking methodologies were absolutely necessary to investigate proteins by NMR. Jardetzky proposed an excellent idea at the “International Symposium on Nuclear Magnetic Resonance,” which was held in Tokyo, 1965, aiming to settle the problem [2]. In this very exciting international meeting, gathering many of the eminent NMR pioneers, he explained a perspective of biosynthetic selective deuteration to simplify the  $^1\text{H}$ -NMR spectra of proteins for obtaining structural information related to their biological functions. Surprisingly, it was only three years later when his colleagues published the first 100 MHz  $^1\text{H}$ -NMR spectra of selectively deuterated nucleases, clearly showing that the

proposed strategy actually works well [3]. This enlightening work strongly motivated us to further develop isotope-labeling technologies for NMR studies of biological systems ever since [4].

### 2.1.1 Stereo-Specific Deuteration of Prochiral Methylene Protons—Conformational Analysis of Amino Acids and Peptides

Until the early 1970s, most biological NMR studies were still focused on small molecules, such as amino acids and oligopeptides. One of the crucial issues to be addressed in those days was the unambiguous discrimination of the side-chain  $\beta$ -methylene proton signals. Without the explicit stereo-specific assignments for the prochiral methylene protons, the two gauche conformations around the  $C_\alpha-C_\beta$  bonds of amino acids, estimated by the Karplus relationship for the vicinal  $^1\text{H}-^1\text{H}$  coupling constants, could not be distinguished unambiguously. We solved this long-standing problem for the first time by using amino acids with one of the prochiral methylene protons stereo-specifically deuterated, prepared by either enzymatic reactions or organic syntheses. By using stereo-specifically deuterated

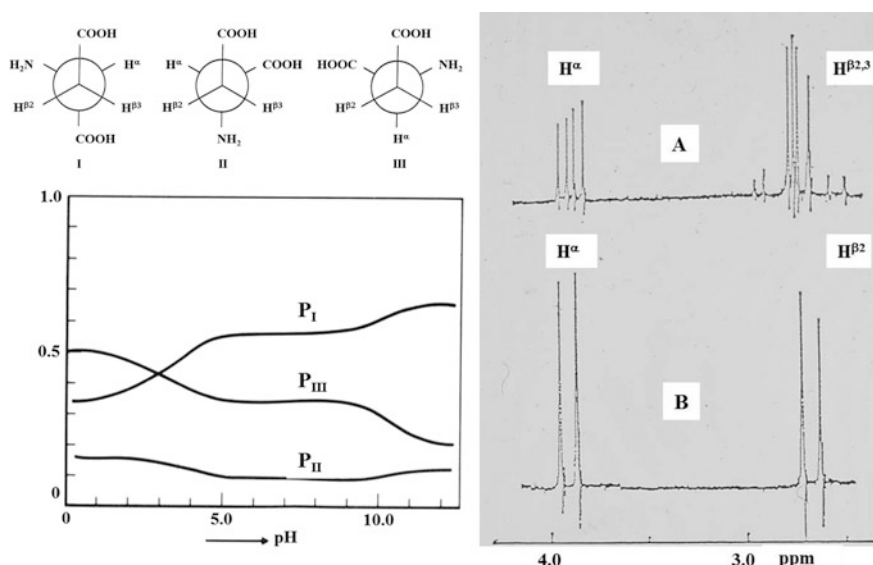


**Fig. 2.1** Conformational analysis of aspartic acid using L-Asp and L-[ $\beta_3$ -D]-Asp at various pHs. The relative populations of the three conformers were estimated at various pHs, by using the vicinal  $^1\text{H}-^1\text{H}$  spin coupling constants with the stereo-specifically assigned  $\beta$ -protons and  $\alpha$ -proton. 100 MHz continuous-wave  $^1\text{H}$ -NMR spectra: A L-Asp; B L-[ $\beta_3$ -D]Asp under deuterium decoupling using the deuterium lock channel [6]

amino acids, we established the stereo-specific assignments for the prochiral  $\beta$ -methylene proton signals and thus discriminated the two gauche conformations for various amino acids and small peptides [5, 6] (Fig. 2.1). Despite our efforts, the approach along this line could not be extended for studying larger peptides or proteins, since no practical experimental methods to incorporate stereo-specifically deuterated amino acids into peptides or proteins were established at that time. As a matter of fact, more than 30 years after our early work, the idea blossomed into the stereo-array isotope-labeling (SAIL) method with the help of two emerging key technologies: chiral organic synthesis and recombinant DNA methods for protein expression [4].

### **2.1.2 Selective $^{13}\text{C}$ , $^{15}\text{N}$ Double-Labeling Method for the Sequential Assignment of Backbone Amide NMR Signals in Large Proteins**

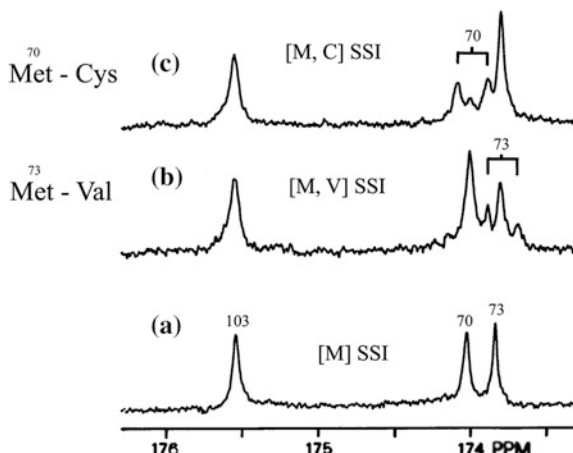
During the 1970s, there was a multidisciplinary collaborative research group, known as the “Research Consortium on *Streptomyces* Subtilisin Inhibitor (SSI),” which focused on SSI as a shared target, aiming to promote biophysical and biochemical protein research activities in Japan. SSI, which was isolated from the culture broth of *Streptomyces albogriseolus*, is a 23-kDa dimeric protein composed of two identical subunits, and it strongly inhibits serine proteinases, especially subtilisin family proteinases. One of the controversial issues for proteinase–inhibitor interactions in the late 1970s was the state of the active site peptide bond, i.e., the “scissile bond,” in the inhibitors complexed with proteinases. X-ray crystallographic analyses of various proteinase–inhibitor complexes initially concluded the existence of the “tetrahedral intermediate,” which was thought to be formed by a covalent bond between the active site Ser O $_{\gamma}$  of a proteinase and the carbonyl of a scissile bond. It was assumed that the tetrahedral intermediate was trapped due to the overwhelming stabilization by the “oxy-anion hole” of serine proteinases, which serves as a molecular device to enormously accelerate the enzymatic hydrolysis of substrate peptides. However, this remarkable model, which was cited in most of the biochemistry textbooks at that time to highlight the beauty of the enzymatic functions of proteinases, was becoming dubious. Namely, as higher-resolution X-ray structures became available, they revealed that the atomic distance between the Ser O $_{\gamma}$  and the carbonyl carbon atom of the scissile bond was apparently a little too long to form the covalent bond. In addition to this serious concern, others still remained about the state of the proteinase–inhibitor complex, which could not be solved by crystallographic studies, such as the following: Does it exist in solution as a single intermediate or as an equilibrium mixture of multiple intermediates? Is the scissile peptide bond in the complexes planar, as usually found for peptide bonds, or distorted by the effect of the nearby Ser O $_{\gamma}$ ? In principle, all of these questions could be investigated by solution NMR spectroscopy. However, it was difficult to

think that such work was feasible since the molecular weight of the SSI–subtilisin complex, 78 kDa, was too large. We overcame this problem by a unique isotope-labeling strategy, as described below [7].

Since the scissile peptide bond of SSI is formed between Met<sup>73</sup> and Val<sup>74</sup>, its state in the proteinase complex would be precisely manifested by the <sup>13</sup>C-NMR signal for the carbonyl carbon of Met<sup>73</sup>, if we could observe a single <sup>13</sup>C-NMR signal for the 78-kDa protein. Although each of the two identical SSI subunits contains three Met residues, i.e., Met<sup>70</sup>, Met<sup>73</sup>, and Met<sup>103</sup>, their C-terminal neighbors are all different, i.e., Cys<sup>71</sup>, Val<sup>74</sup>, and Asn<sup>104</sup>, respectively. Taking advantage of this sequential diversity, we contrived the <sup>13</sup>C, <sup>15</sup>N double-labeling method to sequentially assign the three carbonyl carbon signals. By using SSI samples doubly labeled with [<sup>1-13</sup>C]Met and [<sup>15</sup>N]Cys, and with [<sup>1-13</sup>C]Met and [<sup>15</sup>N]Val, we should be able to discriminate the carbonyl <sup>13</sup>C signals of Met<sup>70</sup> and Met<sup>73</sup> through the spin couplings between the directly bonded <sup>13</sup>C and <sup>15</sup>N, which are known to be about 15 Hz. As illustrated in Fig. 2.2, this strategy based solely on the amino acid sequence information worked perfectly [7]. In addition to the unambiguous assignment, this method provided even more crucial information about the state of the scissile bond in the SSI–subtilisin complex, through the <sup>13</sup>C chemical shift of Met<sup>73</sup> and the <sup>13</sup>C–<sup>15</sup>N spin coupling values between Met<sup>73</sup> and Val<sup>74</sup>. We finally proved that the Michaelis complex with the intact, undistorted scissile bond is the only stable form of the SSI–subtilisin complex in solution [8, 9].

The idea of the sequential assignment for the backbone carbonyl carbons by the selective <sup>13</sup>C, <sup>15</sup>N double-labeling method was extended to assign the peptide <sup>15</sup>N and side-chain <sup>13</sup>C signals, through the <sup>13</sup>C–<sup>15</sup>N and <sup>13</sup>C–<sup>13</sup>C connectivities [10, 11]. The method can be regarded as the historic prototype of triple-resonance sequential assignment methods, using uniformly <sup>13</sup>C, <sup>15</sup>N double-labeled proteins. We were actually one of the first groups to suggest the idea of establishing sequential assignment methods by extending the <sup>13</sup>C, <sup>15</sup>N double-labeling method, which was presented at the XI ICMRBS in Goa, India, in 1984 [12].

**Fig. 2.2** Sequence-specific assignment of the carbonyl <sup>13</sup>C signals for the three Met residues in *Streptomyces* subtilisin inhibitor (SSI) by the selective <sup>13</sup>C, <sup>15</sup>N double-labeling method. 75 MHz <sup>13</sup>C-NMR spectra of SSI labeled with **a** [<sup>1-13</sup>C]Met; **b** [<sup>1-13</sup>C]Met/[<sup>15</sup>N]Val; **c** [<sup>1-13</sup>C]Met/[<sup>15</sup>N]Cys [7]



### 2.1.3 Revisiting the Stereo-Specific Isotope-Labeling Approach for Studying Proteins: A Long March to the SAIL Method

In 1997, with financial support from the newly launched grant “Core Research and Evolutional Science and Technology,” also known as CREST, aiming to promote basic sciences in Japan, we started a 5-year project to develop a breakthrough isotope-aided NMR technology for studying large proteins. At that time, NMR technologies using uniformly  $^{13}\text{C}$ ,  $^{15}\text{N}$  double-labeled proteins were firmly established, but they could only be applied to determine the three-dimensional structures of small proteins. However, a variety of key technologies, which were not available back in the 1970s, facilitated further innovations of isotope-aided NMR methods. For example, multinuclear multidimensional NMR spectroscopy, chiral organic syntheses, and protein expression using recombinant DNA techniques were all quite mature techniques by then. Therefore, we had a unique opportunity to revisit the old idea to explore cutting-edge methods for studying larger proteins. In order to encompass the advents of various multidimensional NMR methods, we exploited novel synthetic routes for the regio- and stereo-specifically D,  $^{13}\text{C}$ ,  $^{15}\text{N}$  triple-labeled amino acids. With the help of state-of-the-art chiral organic synthetic methods, together with enzymatic reactions and microbial fermentations, we actually successfully synthesized all of the protein component amino acids with a variety of labeling patterns [13–15]. Fortunately, with further support from a second CREST grant for another five years, we completed the development of the “stereo-array isotope-labeling (SAIL) method” by using those labeled amino acids. Although it took more than 30 years after our early work on the stereo-specific deuteration of amino acids and peptides, the SAIL method has been proven to be extremely useful for studying the structures as well as the dynamics of larger proteins, for which previous NMR methods were difficult to apply [16–19].

## 2.2 The SAIL Method: An Optimized Isotope-Labeling Strategy for the Structural Study of Proteins by NMR Spectroscopy

NMR spectra of larger proteins are typically characterized by numerous overlapped signals, which are severely broadened by dipolar interactions between nearby protons. Therefore, it was difficult to obtain sufficient amounts of NMR information for proteins larger than 20–25 kDa, even with sophisticated multidimensional methods. For example, for a long time it was thought to be virtually impossible to analyze the prochiral methylene proton signals, especially for large proteins, even

though the information is absolutely required for accurately determining the side-chain conformations, as described above for amino acids [5, 6]. Conceptually, however, we may not necessarily need all of the NMR data for the determination of protein structures, since many of the amino acid side chains contain somewhat redundant information. For example, if we could stereo-specifically observe either one of the prochiral groups, i.e., methyls and methylenes, we could compensate for the missing information about the geminal counterparts. The SAIL method creates this type of situation for all of the amino acid residues in proteins, by trimming away the redundant information by the optimized isotope-labeling patterns, as described below [20, 21].

Our original labeling design concepts for the SAIL amino acids were the following: (1) stereo-specific labeling for one of the methylene protons by deuterium, i.e.,  $^{13}\text{C}^*\text{HD}$ ; (2) stereo-specific labeling for the geminal methyl groups of Leu and Val residues with  $^{13}\text{CHD}_2$  and  $^{12}\text{CD}_3$ ; (3) alternating the labeling of aromatic rings with  $^{13}\text{CH}$  and  $^{12}\text{CD}$ ; and (4)  $^{13}\text{C}$  labeling for the methine groups of Ile, Leu, and Val. Therefore, all of the methyl, methylene, and methine groups labeled with  $^{13}\text{C}$  have a single proton, i.e.,  $^{13}\text{CHD}_2$ ,  $^{13}\text{C}^*\text{HD}$ , and  $^{13}\text{CH}$ . In addition to these labeling patterns, all of the nitrogens and the carbonyl carbons are labeled with  $^{15}\text{N}$  and  $^{13}\text{C}$ , respectively. We successfully synthesized the 20 protein component amino acids based on these design concepts, as shown in Fig. 2.3 [20]. The SAIL labeling patterns preserve the through-bond  $^{13}\text{C}$ – $^{13}\text{C}$  and  $^{13}\text{C}$ – $^{15}\text{N}$  connectivity paths for the backbone and side-chain sequential assignments and completely eliminate the ambiguity of stereo-specific assignments for prochiral groups. More importantly, the density of the remaining protons attached to the  $^{13}\text{C}$  atoms in a SAIL protein, which is exclusively composed of the SAIL amino acids, is reduced down to 50–60% as compared to that of a fully protonated protein. The significantly decreased proton density for a SAIL protein mitigates the spin diffusion and thus facilitates the acquisition of accurate inter-proton NOEs, even for larger proteins. One might recollect at this point that a traditional strategy using “random fractional deuteration” was used a while ago, to reduce the NMR line widths of the remaining proton signals [22]. However, the random fractional deuteration results in an enormous number of isotopomer proteins with chemical shift heterogeneities and the concomitant loss of intensities for the remaining signals. All of these problems are completely eliminated by the SAIL method. It is quite important to emphasize that, even though the level of deuteration is as high as that of random fractionally deuterated proteins, there is always a single isotopomer for a SAIL protein. Therefore, the proton concentrations for the protonated sites are not decreased at all. Actually, the terminology “stereo-array isotope labeling” seeks to highlight this striking feature of the SAIL method.

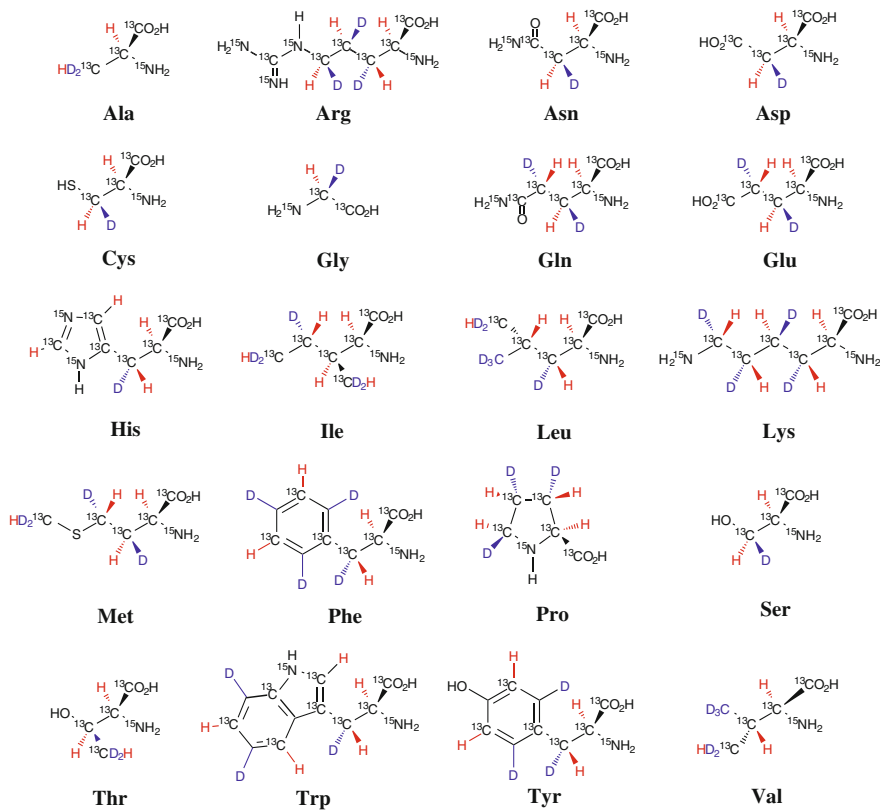


**Fig. 2.3** Structures of the SAIL amino acids with the original isotope-labeling patterns [20]. There are many other SAIL and SAIL-related amino acids with various labeling patterns optimized for obtaining specific information, as described in this chapter

### 2.2.1 Cell-Free Expression and NMR Spectra of SAIL Proteins

As described above, the SAIL method facilitates structural analyses of larger proteins, through the rational isotope-labeling design for the component amino acid residues. Therefore, it is necessary to incorporate SAIL amino acids into a target protein while preserving their original labeling patterns. In this respect, conventional cellular protein expression using recombinant DNA may not be a good choice, since metabolic scrambling reactions and isotope dilution with unlabeled amino acids are not completely avoidable for some amino acid residues. All these problems are largely circumvented by using *in vitro* expression systems. Fortunately for us, the *in vitro* protein expression using the *E. coli* cell-free extract

became available at around the time we nearly completed the synthesis of the SAIL amino acids. By using the cell-free extract prepared from the *E. coli* cells, we successfully prepared a sufficient amount of a SAIL protein for an NMR study. SAIL proteins, which are composed exclusively of SAIL amino acids, are typically obtained with ~10 wt% yields calculated from the amount of the amino acid mixture and show virtually no isotopic dilution or metabolic scrambling [23–25].

The NMR spectra of SAIL proteins actually exhibit profoundly better sensitivity and resolution, as compared to those of conventional  $^{13}\text{C}$ ,  $^{15}\text{N}$  uniformly labeled (UL) proteins. Figure 2.4 shows such superior NMR features for the case of 17-kDa SAIL calmodulin (SAIL-CaM) [20]. By comparing the  $^1\text{H}$ - $^{13}\text{C}$  ct-HSQC spectra for SAIL- and UL-CaM, it becomes obvious that the  $^1\text{H}$ - $^{13}\text{C}$  cross-peaks are considerably sharper and well dispersed for SAIL-CaM (Fig. 2.4a) than for UL-CaM (Fig. 2.4d). A closer comparison of the methyl (Fig. 2.4b, e) and methylene regions (Fig. 2.4c, f) of the two proteins reveals that only one of the prochiral pairs shows up as an NMR signal in SAIL-CaM. The benefit of the universal stereo-specific deuteration for the methylene groups in the SAIL method can be illustrated for the  $\delta$ -methylene signals of the six Arg residues in SAIL- and UL-CaM (Fig. 2.4g–i). Since the  $\delta_3$  methylene proton is stereo-specifically deuterated in SAIL-CaM, the six observed  $\delta$ -CH signals can be unambiguously assigned to  $\delta_2$ -CH (Fig. 2.4g), while in UL-CaM, most of the Arg  $\delta$ -CH<sub>2</sub> signals are completely overlapped for both the  $^1\text{H}$  and  $^{13}\text{C}$  dimensions, except for Arg-37 and 106, for which no facile stereo-specific assignment methods could be envisaged (Fig. 2.4h). Since similar problems are ubiquitously encountered in UL proteins for the methylene groups in other amino acid residues, only SAIL proteins provide accurate structural information for the side-chain moieties. The complete spectral analyses of SAIL proteins are usually quite straightforward, by using the standard triple-resonance pulse sequences with slight modifications [15].

The analyses of aromatic ring signals in proteins are generally very cumbersome or infeasible for UL proteins, due to their complex  $^{13}\text{C}$ ,  $^1\text{H}$  spin systems. The situation becomes even more complicated when the flipping rates of aromatic rings influence the signal shapes. Nevertheless, the information about the bulky aromatic rings, which tend to be embedded in the hydrophobic cores, is extremely important for structural studies of proteins. Therefore, we expended a great deal of effort toward optimizing the isotope-labeling patterns of aromatic amino acids, to obtain all of the structural information for aromatic rings in straightforward manners [26–28]. Figure 2.5 illustrates the application of SAIL Phe with various labeling patterns, aiming toward analyses of the ring  $^1\text{H}$ - $^{13}\text{C}$  signals, as exemplified by the assignment of the 12 Phe residues in *E. coli* peptidyl prolyl cis-trans isomerase b (EPPIb) [27]. The aromatic  $^1\text{H}$ - $^{13}\text{C}$  region of the ct-HSQC spectrum for EPPIb labeled with UL Phe (Fig. 2.5d) gives virtually no detailed information, due to the overcomplicated spin systems. In contrast, each of the HSQC spectra for EPPIbs, selectively labeled with  $\delta$ -,  $\varepsilon$ -, or  $\zeta$ -SAIL Phe, shows clean, well-resolved signals (Fig. 2.5e–g). The  $\delta$ -,  $\varepsilon$ -, and  $\zeta$ -CH could be readily assigned by the NOE

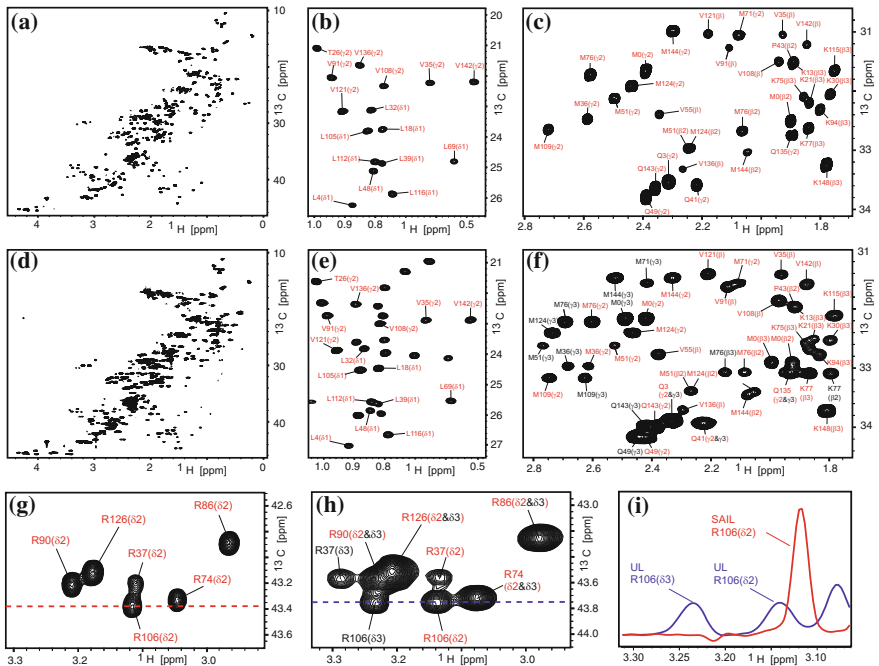


**Fig. 2.4** 800 MHz  $^1\text{H}$ - $^{13}\text{C}$  ct-HSQC spectra of calmodulin (CaM). **a** SAIL-CaM, aliphatic region; **b** SAIL-CaM, methyl region; **c** SAIL-CaM, methylene region; **d** UL-CaM, aliphatic region; **e** UL-CaM, methyl region; **f** UL-CaM, methylene region; **g** SAIL-CaM, Arg  $\delta$  region; **h** UL-CaM, Arg  $\delta$  region; **i** Cross sections from (g) and (h). The spectra for SAIL-CaM and UL-CaM were recorded under identical conditions and scaled for equal noise levels [20]

correlations between the  $\delta$ - $^1\text{H}$  and  $\beta_3$ - $^1\text{H}$ , HBCB(CG)HE, and HBCB(CGCZ)HZ sequences, respectively (Fig. 2.5a–c). The most significant advantage of the SAIL Phe can be realized by comparing the spectra between the  $\zeta$ -SAIL-labeled (Fig. 2.5g) and the  $\delta$ -,  $\varepsilon$ -SAIL-labeled EPPIb (Fig. 2.5e, f). The  $\zeta$ -CH signals in  $\zeta$ -SAIL Phe-labeled EPPIb have line shapes that are invariant against the flipping rates, because the  $\zeta$ -CH bond lies along the  $\text{C}_\beta$ - $\text{C}_\gamma$  bond, and thus they appeared as 12 discrete signals with almost the same intensities (Fig. 2.5g). In contrast, in the  $\delta$ - and  $\varepsilon$ -SAIL Phe-labeled EPPIb, the  $^1\text{H}$ - $^{13}\text{C}$  HSQC spectra show very weak or no visible signals for F27, F110, and F123 (Fig. 2.5e, f). The results clearly indicated that the ring-flipping rates for these three residues are relatively slow, as compared to the chemical shift differences for the two  $\delta$ - and  $\varepsilon$ -CH atoms on the opposite side of the ring. As the aromatic ring-flipping motions are perfectly degenerated conformational exchange phenomena, which can only be manifested by the NMR line-shape analysis, these SAIL aromatic amino acids are extremely valuable for studying large-amplitude dynamics in proteins (see Sect. 2.3.2).

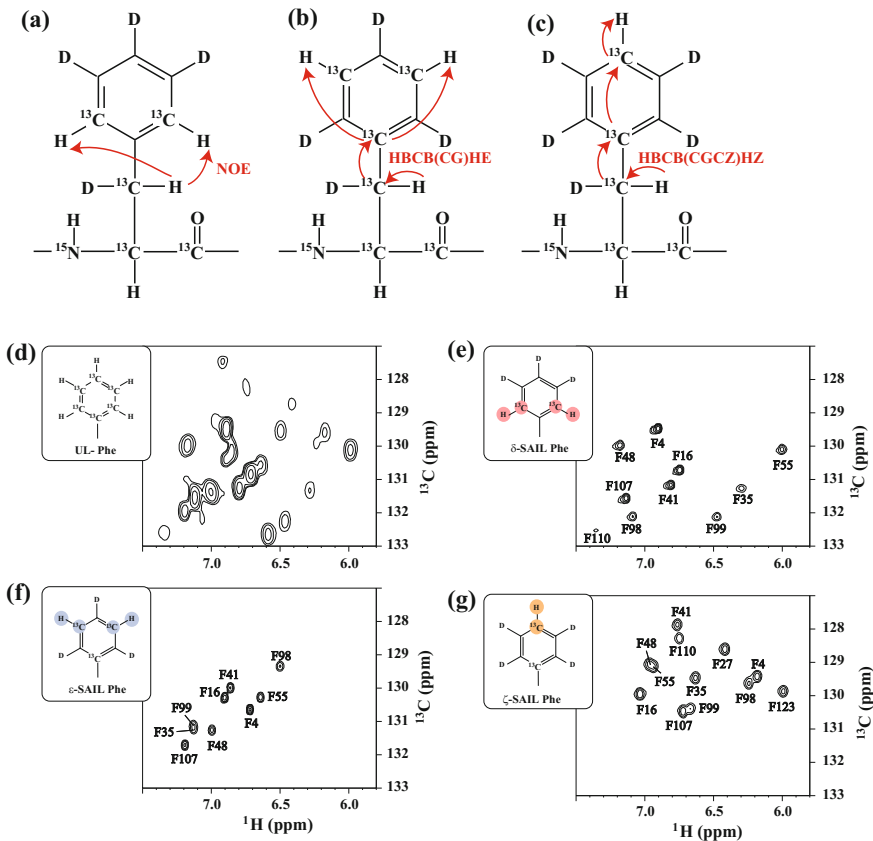


**Fig. 2.5** Assignment of aromatic ring CH signals of the 12 Phe residues in EPPIb using various SAIL Phes. Structures of **a**  $\delta$ -SAIL Phe, **b**  $\epsilon$ -SAIL Phe and **c**  $\zeta$ -SAIL Phe. The arrows indicate the magnetization transfer pathways for making the ring CH signal assignments, starting from the  $\beta$ -proton that can be assigned by the conventional sequential assignment protocols. 600 MHz  $^1\text{H}$ - $^{13}\text{C}$  HSQC spectra with the assignments of EPPIbs specifically labeled with **d** [ $\text{U}-^{13}\text{C}$ ]Phe; **e**  $\delta$ -SAIL Phe; **f**  $\epsilon$ -SAIL Phe; and **g**  $\zeta$ -SAIL Phe [27]

## 2.2.2 Structural Determination of SAIL Proteins

As described above, SAIL proteins provide unmatched chemical shift data quality for the backbone and aliphatic/aromatic side chains, including the full stereo-specific assignments for prochiral groups. Therefore, SAIL proteins facilitate the automated assignment of the  $^{13}\text{C}$ - and  $^{15}\text{N}$ -edited NOESY spectra, with the concurrent structure refinement using the CYANA program adapted to SAIL proteins (SAIL-CYANA). It is important to mention that the substantially reduced

proton density in SAIL proteins allows the use of a longer mixing time for collecting long-range NOE constraints, without spin diffusion problems. Taking advantage of the improved distance constraints and the unequivocal stereo-specific assignments for prochiral groups, the structures determined for SAIL proteins are accurate, as illustrated in Fig. 2.6 for some of the structures determined by the SAIL-CYANA method [20, 21].

The marked improvement in the overall quality of the NMR spectra obtained for SAIL proteins further encouraged us to use the FLYA program for automated backbone and side-chain resonance assignments. The chemical shift data obtained by FLYA can then be used as the input data for the NOESY spectral analysis and the structure calculation by CYANA. This two-step automated structure determination using the FLYA-CYANA program works well for small SAIL proteins, without additional human participation [29, 30]. We also tried to develop a fully automated structure determination method exclusively based on NOESY data, obviating the need to measure any other spectra than those necessary for the

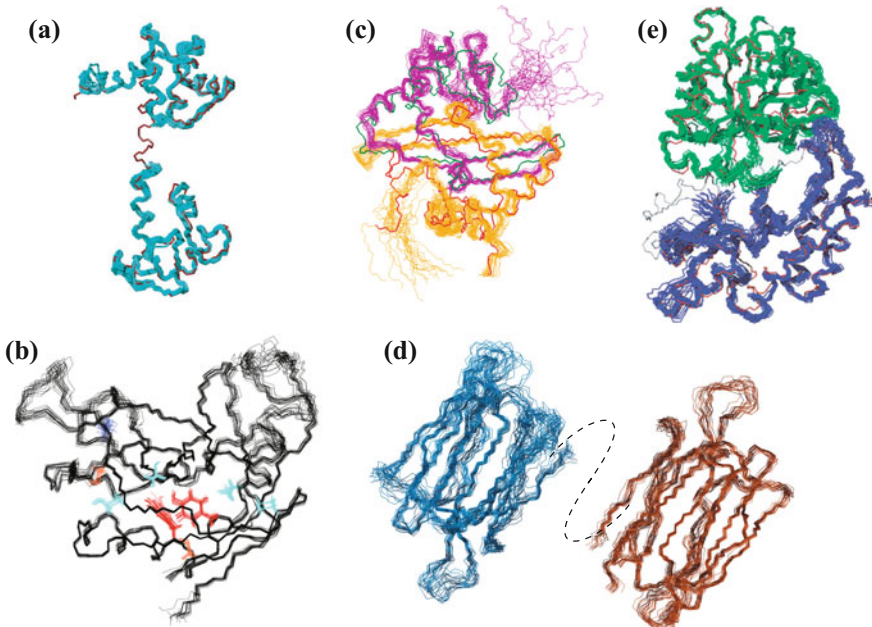


**Fig. 2.6** Backbone structures of proteins determined by the SAIL-NMR method. **a** Calmodulin in cyan, overlaid with the X-ray structure in red [20]; **b** EPPIb in black, which was refined using additional NOEs involving slowly exchanging side-chain polar groups: the side chains of Ser, Thr in cyan, Cys in pink and Tyr in red [48]; **c** C-terminal dimerization domain of SARS coronavirus nucleocapsid protein. The two subunits of the homodimer are shown in pink and yellow, and the overlaid X-ray structures are shown in green and red, respectively [51]; **d** the putative protein At3g16450.1, encoded by the *Arabidopsis thaliana* gene, composed of the N-terminal domain in cyan and the C-terminal domain in brown [52]; **e** maltose-binding protein (MBP): the N-domain in green and C-domain in blue, overlaid with the X-ray structure in red [20]

resonance assignment. This ambitious automated approach, which would be useful for determining a large number of structures as efficiently as possible, was actually utilized for two small SAIL proteins and yielded well-defined structures that coincide closely with those determined by the conventional method [31].

## 2.3 Recent Trends in the Isotope-Aided NMR Methods for Studying Proteins

We described above our early studies on isotope-aided NMR techniques and then introduced a recent achievement, the SAIL method. However, the prospective roles of NMR in structural biology are rapidly changing, especially because other methods, such as X-ray crystallography and cryo-electron microscopy, have been overwhelmingly employed for the structural determinations of biologically important proteins, such as membrane proteins or extraordinarily large protein complexes. Obviously, NMR cannot be a competitive structural determination tool for those targets. Instead, a variety of alternative applications are envisaged for NMR spectroscopy, to bridge the gap between protein structures and their biological functions. In principle, NMR could afford unique information for this purpose, even if the proteins are too large for structure determination by NMR. Actually, in many cases, one could start with the three-dimensional structures previously determined by the other methods and focus on the structures and dynamics of the selected regions of interest, which could be precisely manifested by NMR. For that purpose, it is necessary to develop a method to observe and assign the NMR signals for any regions of the selected amino acid residues in such proteins. Recently, there have been major advances in NMR signal observations for larger proteins. Wuethrich et al. exploited transverse relaxation-optimized spectroscopy (TROSY) for observing the backbone amide  $^1\text{H}^{15}\text{N}$  signals in deuterated proteins and the aromatic ring  $^1\text{H}^{13}\text{C}$  signals for uniformly  $^{13}\text{C}$ -labeled proteins [32, 33]. Kay et al. developed a method to observe the Ile, Leu, and Val (ILV)  $^{13}\text{CH}_3$  signals, utilizing them as NMR probes for studying protein structures and dynamics [34]. The  $^1\text{H}^{15}\text{N}$  TROSY and methyl observation methods can be applied for proteins as large as 1 MDa and are routinely used for studying larger proteins in solution [35].

Since the backbone amides and the side-chain methyl groups ( $^{13}\text{CH}_3$ ) cover considerable portions of larger proteins, their NMR signals provide valuable structural information. However, it may not be sufficient for analyzing the precise side-chain conformations and dynamics for the selected residues in order to understand the molecular basis of biological functions, which we expect to obtain by solution NMR. This is where sophisticated isotope-aided methods such as SAIL come in. We have exploited methods to observe NMR signals for any parts of

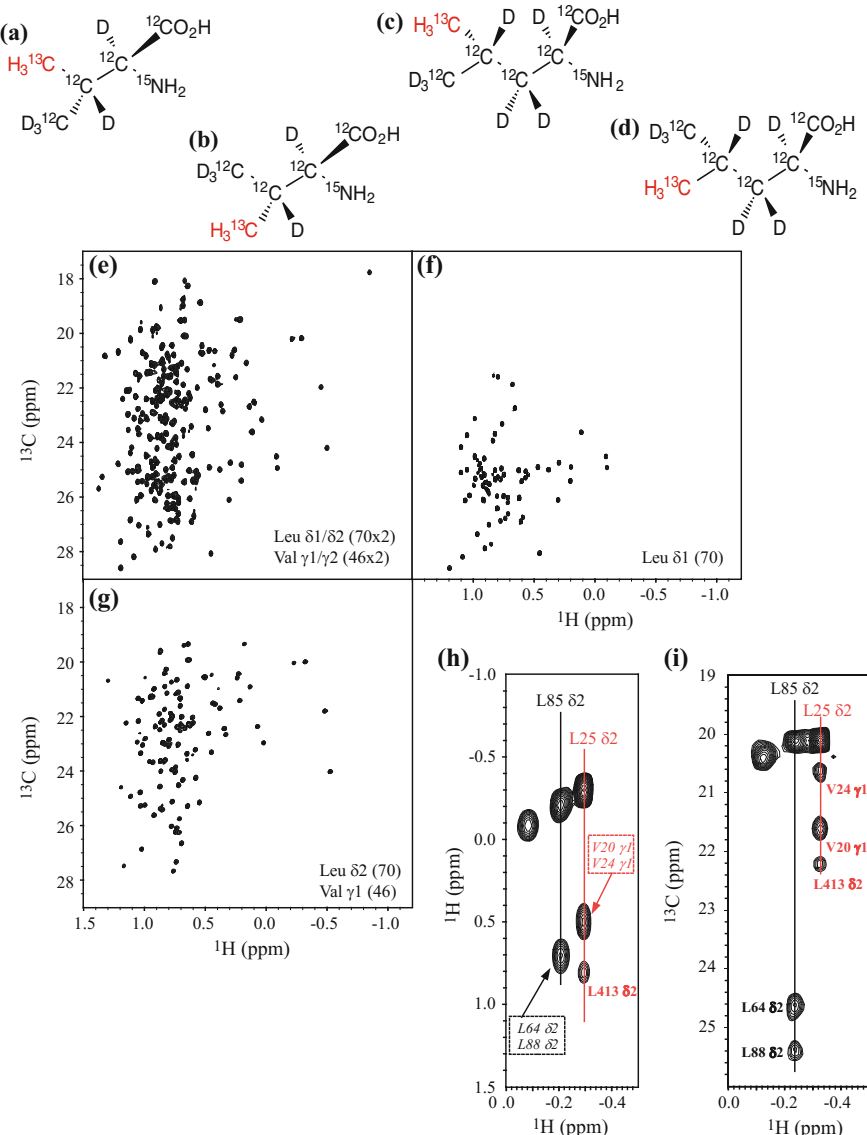
aliphatic and aromatic side chains in a protein, by further optimizing the isotope-labeling patterns of the original SAIL design concepts. In the following, we describe some of our recent work along this line, in order to provide an outline of our current research endeavors.

### 2.3.1 Residue- and Stereo-Specific Labeling Method: The Case for Leu and Val Methyl Labeling of Larger Proteins

Larger proteins have numerous methyl groups in their Ala, Thr, Met, Ile, Leu, and Val (ATMILV) residues, which are widely distributed on their surface and interior regions. Therefore, the methyl signals are valuable probes for studying the structures and dynamics of proteins and protein complexes, if the individual methyl signals could be observed. However, this is not trivial especially for larger proteins, since they have so many ATMILV residues. For example, the 82-kDa protein malate synthase G (MSG) has 289 ATMILV residues that comprise approximately 40% of its 723 residues. Among them, the 160 ILV residues are especially useful as NMR probes, since the total of 317 ILV methyls accounts for as many as ~70% of the 446 methyl signals. Therefore, extensive efforts have been exerted to develop robust methods to observe and assign ILV methyl signals in larger proteins. Most of them employ region-specifically  $^{13}\text{C}$ , D-labeled precursors, such as [4- $^{13}\text{C}$ ;3,3-D<sub>2</sub>]- $\alpha$ -ketobutyrate and [3- $^{13}\text{CH}_3$ ;3,4,4,4-D<sub>4</sub>]- $\alpha$ -ketoisovalerate ( $\alpha$ -KIV), for preparing fully deuterated proteins except for the Ile ( $\delta_1$ ), Val ( $\gamma_1/\gamma_2$ ), and Leu ( $\delta_1/\delta_2$ ) methyls, which are to be labeled with  $^{13}\text{CH}_3$  [36, 37]. However, since the racemic  $\alpha$ -KIV precursor labels both of the prochiral methyls in Leu and Val residues, the observable number of methyl signals cannot be decreased, and the labeling rates are 50% or less. Therefore, the signal congestion for Leu/Val methyls could not be improved and the methyl–methyl NOEs are significantly reduced. In order to compensate for the drawbacks of this Leu/Val precursor, a few new precursors for the stereo-specific methyl labeling of Leu/Val residues have been developed [38]. However, it is difficult to use labeled precursors to prepare any desired combinations for either one of the prochiral methyls in Val and Leu, since Val is converted to Leu biosynthetically, as shown in the metabolic map.

In the SAIL method, we synthesized SAIL Leu/Val, in which one of the prochiral methyls is stereo-specifically labeled with  $^{13}\text{CHD}$  and the other one with CD<sub>3</sub>. The SAIL Val/Leu can be incorporated into proteins by the in vitro expression system, using the *E. coli* cell-free extract (vide supra). Using the same protocols, we synthesized all four of the Leu and Val residues, in which either one of  $\delta_1/\delta_2$  or  $\gamma_1/\gamma_2$  in Leu and Val, respectively, is stereo-specifically labeled with  $^{13}\text{CH}_3$ , and all of the other protons are fully deuterated, as shown in Fig. 2.7 [39]. These four

stereo-specifically methyl-labeled Val and Leu, designated as  $\gamma_1$ -Val (a),  $\gamma_2$ -Val (b),  $\delta_1$ -Leu (c), and  $\delta_2$ -Leu (d), could be incorporated into proteins in any combinations by the conventional cellular expression using the *E. coli* BL21 (DE3) strain. The incorporation rate for the labeled Leu into MSG at a 20 mg/L concentration was  $\sim 90\%$ , but that for the labeled Val at 100 mg/L was only close to 80%. In order to increase the incorporation rates for Leu and Val at lower amino acid concentrations, we have recently developed an auxotrophic *E. coli* BL21 (DE3) strain [40]. The mutant was derived from the BL21 (DE3) strain by deleting the *ilvD* and *leuB* genes encoding dihydroxy acid dehydratase and  $\beta$ -isopropylmalate dehydrogenase, respectively; therefore, it cannot survive in the absence of Ile, Leu, and Val. Using this auxotrophic *E. coli* strain, the incorporation rates of isotope-labeled Leu, Val, and also Ile into MSG were found to be higher than 95% even at a 10 mg/L concentration of each of the stereo-specifically methyl-labeled Leu or Val, or the region-specifically methyl-labeled Ile, without any observable scrambling [41]. The usefulness of the stereo-specifically methyl-labeled Leu and Val is clearly illustrated in Fig. 2.7e–g. Figure 2.7e shows the methyl region of the  $^1\text{H}$ – $^{13}\text{C}$  HMQC spectrum of deuterated MSG labeled with a conventional precursor, [3- $^{13}\text{C}$ ] $_3$ ;4,4,4-D<sub>4</sub>]- $\alpha$ -ketoisovalerate. The spectrum showed 232 considerably overlapped methyl signals, including the  $\delta_1$ ,  $\delta_2$  methyls of 70 Leu residues (including one extra Leu in the His tag at the C-terminus) and the  $\gamma_1$ ,  $\gamma_2$  methyls of 46 Val residues. In contrast, the spectra in Fig. 2.7f, g for deuterated MSG labeled by  $\delta_1$ -Leu or  $\delta_2$ -Leu +  $\gamma_1$ -Val, respectively, show almost no signal overlap. It may not be apparent from the spectra, but the methyl signals observed for the MSGs labeled by  $\delta_1$ -Leu,  $\delta_2$ -Leu +  $\gamma_1$ -Val showed increased sensitivities, as compared to the MSG labeled by the  $\alpha$ -KIV precursor, by a factor of 2. It is important to mention that any single-residue-labeled MSGs and also any combinatorially dual-residue-labeled MSGs can be prepared by using the four different stereo-specifically methyl-labeled Leus and Vals. The combinatorial methyl-labeling method using stereo-specifically isotope-labeled Leu and Val is especially useful for collecting the inter-residue methyl–methyl NOEs at higher sensitivities, by a factor of 4, as compared to the precursor method. Actually, the Val  $\gamma_1$  and Leu  $\delta_2$  combinatorially labeled MSG gave highly sensitive inter-residue methyl–methyl NOE signals. Even if the signal overlap remains in the 2D  $^1\text{H}$ – $^1\text{H}$  plane of the 3D  $^{13}\text{C}$ -edited NOESY-HMQC spectrum for a combinatorially labeled protein, as illustrated in Fig. 2.7h, the 3D HMQC-NOESY-HMQC should have better resolution, as shown for the 2D  $^1\text{H}$ – $^{13}\text{C}$  plane, making good use of the wider dispersion in the  $^{13}\text{C}$  dimension (Fig. 2.7i). Obviously, further extensions of the combinatorial labeling method involving multiple regio- and stereo-specifically isotope-labeled amino acid residues would eventually approach the concept of the SAIL method.



### 2.3.2 Large-Amplitude Dynamics of Proteins as Probed by Aromatic Ring-Flipping Motions—The Case for the Interface Between FKBP and Drug Complexes

Nowadays, it is generally accepted that folded proteins occasionally undergo large-amplitude slow-breathing motions (LASBMs) under physiological

**►Fig. 2.7** Residue- and stereo-specific isotope labeling for the Leu and Val methyl groups in the 82-kDa protein malate synthase G (MSG) using stereo-specifically methyl-labeled amino acids. Structures of the stereo-specifically  $^{13}\text{CH}_3$ -labeled, otherwise uniformly deuterated, valines and leucines: **a** [ $\gamma_1$ - $^{13}\text{CH}_3$ ;  $\alpha$ - $^{15}\text{N}$ ; D<sub>5</sub>]-valine, “ $\gamma$ 1-Val”; **b** [ $\gamma_2$ - $^{13}\text{CH}_3$ ;  $\alpha$ - $^{15}\text{N}$ ; D<sub>5</sub>]-valine, “ $\gamma$ 2-Val”; **c** [ $\delta_1$ - $^{13}\text{CH}_3$ ;  $\alpha$ - $^{15}\text{N}$ ; D<sub>7</sub>]-leucine, “ $\delta$ 1-Leu”; **d** [ $\delta_2$ - $^{13}\text{CH}_3$ ;  $\alpha$ - $^{15}\text{N}$ ; D<sub>7</sub>]-leucine, “ $\delta$ 2-Leu.” 900 MHz 2D  $^1\text{H}$ - $^{13}\text{C}$  HMQC spectra of labeled MSGs: **e** Leu/Val selectively labeled MSG expressed by *E. coli* BL21 (DE3) using the precursor [3- $^{13}\text{CH}_3$ ; 3,4,4,4-D<sub>4</sub>]- $\alpha$ -ketoisovalerate; **f** Leu-specific,  $\delta_1$ -methyl-specific-labeled MSG prepared by the *ΔilvD/ΔleuB* *E. coli* mutant using “ $\delta$ 1-Leu” and deuterated Ile/Val; **g**  $\gamma_1/\delta_2$ - $^{13}\text{CH}_3$ -labeled MSG prepared by the *ΔilvD/ΔleuB* *E. coli* mutant using “ $\gamma$ 1-Val,” “ $\delta$ 2-Leu” and deuterated Ile. Shown in **(h)** and **(i)** are the 2D planes at the  $^{13}\text{C}$  chemical shift of 20.1 ppm, which corresponds to the  $\delta_2$  methyls of L25 and L85, of the 3D  $^{13}\text{C}$ -edited NOESY-HMQC and 3D HMQC-NOESY-HMQC spectra, respectively, measured for a 0.2-mM solution of the  $\gamma_1/\delta_2$ - $^{13}\text{CH}_3$  specifically labeled, otherwise fully deuterated MSG. Ambiguous NOE signal assignments are labeled in *italics* [40]

conditions. Since the frequency of LASBMs is within the millisecond to second region, such motions have attracted the interests of biophysicists in the context of biological functions and protein dynamics. The LASBM was initially implicated by the intriguing observations that the  $\delta$ - and  $\epsilon$ -protons for the Phe and Tyr aromatic rings in proteins showed time-averaged NMR signals. It was quite surprising, especially for most of the crystallographers back in the 1970s, that such bulky aromatic rings flip about the  $\text{C}_\beta$ - $\text{C}_\gamma$  axis so frequently, since they are often deeply embedded in the hydrophobic core, which was thought to be the most solid part of a protein [41, 42]. Ironically, until recently there have only been few cases in which the aromatic rings show discrete signals for the  $\delta$ - and  $\epsilon$ -nuclei of Phe and Tyr, due to slow ring-flipping rates [43]. Theoretically, it might be possible that the  $^1\text{H}$  and  $^{13}\text{C}$  nuclei at the  $\delta$ - and  $\epsilon$ -positions incidentally have identical, or nearly identical, chemical shifts and thus appear as a time-averaged single peak regardless of the flipping rates, although it is quite unlikely that such situations happen very often. Taking advantage of the simplified spin systems of the SAIL Phe and Tyr, we revisited the ring-flipping phenomena and found that there are actually many more cases showing flipping rate-dependent aromatic ring signals. Apparently, the aromatic rings in conventional protein samples have such complicated spin networks that such cases are rarely identified. Therefore, proteins selectively labeled by  $\delta$ -,  $\epsilon$ -SAIL Phe and Tyr would provide unprecedented opportunities to investigate LASBMs through the widely distributed aromatic rings in the hydrophobic interior and on the ligand-binding surface. In the following, we illustrate the application of the aromatic ring-flipping phenomena for characterizing the LASBMs within the binding interface in FKBP12-ligand complexes [44].

The tight complexes FKBP12 forms with immunosuppressive drugs, such as FK506 and rapamycin, have long been used as models for developing various approaches to structure-based drug design. The regions of rapamycin and FK506 that bind FKBP are very similar to each other, but the opposite sides of them, which are referred to as the effector regions, are entirely different for the two drugs. Rapamycin and FK506 can bind to their targets, mTOR and calcineurin, only if they are complexed with FKBP12. Therefore, it is very interesting to understand the

molecular mechanism by which FKBP12 activates these drugs to trigger their diversified biological functions by forming the ternary complexes. The aromatic ring cluster in FKBP12 forms an extremely hydrophobic, concave binding pocket, composed of Trp59, Tyr26, Phe99, Phe46, and Phe48, for the immunosuppressive drugs, such as rapamycin or FK506, with high affinities (Fig. 2.8). Although the interfaces between FKBP12 and these drugs are well defined structurally and are almost identical in the crystallographic structures of various complexes, our NMR studies have clearly revealed the existence of substantial large-amplitude motions in the FKBP12–ligand interfaces that strongly depend on the nature of the drug. We have monitored these motions by measuring the rates of Tyr and Phe aromatic ring flips, and hydroxyl proton exchange for Tyr residues clustered within the FKBP12–ligand interface. To do so, we prepared FKBP12 proteins selectively labeled by  $\delta$ -,  $\epsilon$ -,  $\zeta$ -SAIL Tyr and by  $\delta$ -,  $\epsilon$ -SAIL Phe. Free in solution, all of the Phe and Tyr residues in the ligand-binding pocket of FKBP12 show time-averaged signals for their  $\delta$ - and  $\epsilon$ -CHs, due to their rapid ring-flipping rates. In contrast, in the ligand bound states, Tyr26 and Phe99 give two separated signals for their  $\delta$ - and  $\epsilon$ -CHs, due to the slow ring-flipping rates of these residues. In addition, significant decreases in the ring-flipping rates were observed for all of the other Tyr and Phe residues in the binding pocket, namely, Tyr82, Phe36, Phe46, and Phe48, as illustrated for the FKBP12–rapamycin complex (Fig. 2.8). The rates of hydroxyl proton exchange were also measured for  $\zeta$ -SAIL Tyr-labeled FKBP12 in the drug complexes, using the method described in the next paragraph. Pairwise comparisons between FKBP12 complexed with rapamycin and FK506 revealed that the hydroxyl proton exchange and the ring-flipping rates for Tyr26 are much slower in

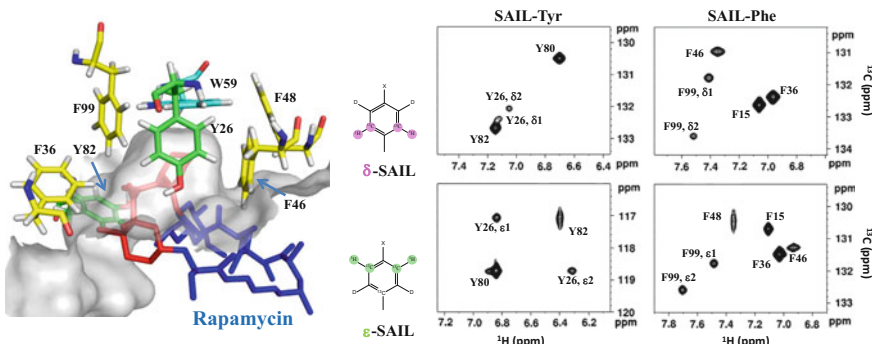


**Fig. 2.8** Ligand-binding interface structure of the FKBP12–rapamycin complex in the crystalline state (PDB entry 2DG3), in which the FKBP binding motif of the rapamycin backbone is shown red, and the aromatic ring  $^1\text{H}$ – $^{13}\text{C}$  correlation signals in the 600 MHz HSQC spectra at 20 °C for the rapamycin bound FKBP12s, which are residue specifically labeled with  $\delta$ -,  $\epsilon$ -SAIL Phe and  $\delta$ -,  $\epsilon$ -SAIL Tyr, respectively. The ring-flipping rates of the aromatic rings of Phe and Tyr residues in the primary binding concave surface, namely Trp59, Phe46, Phe48, Phe99 and Tyr26, were significantly slowed down, as shown by the line shapes of either or both  $\delta$ - and  $\epsilon$ -CH. Similarly, the ring-flipping rates of Phe48, in juxtaposition with Phe46, and Tyr82, which forms a hydrogen bond with the carbonyl oxygen at C8 of rapamycin, were also slowed down [44].

the FK506 complex than in the rapamycin complex, whereas the ring-flipping rates for Phe48 and Phe99 are significantly faster in the FK506 complex than in the rapamycin complex. The apparent rate differences observed for the interfacial aromatic residues in the two complexes confirm that these dynamic processes occur without ligand dissociation. We attribute the differential interface dynamics for these complexes to a single hydrogen bond between the  $\zeta$ -hydrogen of Phe46 and the C32 carbonyl oxygen of rapamycin, which is not present in the FK506 complex. This newly identified Phe46  $\zeta$ -hydrogen bond in the rapamycin complex imposes motional restriction on the surrounding hydrophobic cluster and subsequently regulates the dynamics within the protein–ligand interface. Such information concerning large-amplitude dynamics at drug-target interfaces has the potential to provide novel clues for drug design [44].

### **2.3.3 Deuterium-Induced Isotope Shifts for Measuring Hydrogen Exchange Rates of Polar Side-Chain Groups in Proteins: Facile Screening of the Polar Groups Involved in Hydrogen Bond Networks**

The hydrogen exchange phenomena of the backbone amides in aqueous solutions are among the most intensively studied protein dynamics by NMR spectroscopy. The exchange rates are usually estimated by a time course of the amide proton signal intensity changes for a protein freshly dissolved in D<sub>2</sub>O. The information has made crucial contributions toward understanding the backbone dynamics and the folding–unfolding processes of proteins in solution. In contrast, the hydrogen exchange rates for the polar side-chain groups, such as hydroxyl (OH) or sulfhydryl (SH), have not been studied extensively, because they are usually too rapid to be measured by the method used for the backbone amides. We have exploited an alternative approach for the facile screening of the slowly exchanging polar side-chain groups and the estimation of their hydrogen exchange rates with the surrounding water. We adapted our previous method for detecting slowly exchanging backbone amide hydrogens by the steady-state line shapes of the amide carbonyl <sup>13</sup>C signals, in a protein dissolved in a 1:1 mixture of H<sub>2</sub>O and D<sub>2</sub>O [7, 8, 45]. In such an environment, the line shape of the amide carbonyl of the *i*th residue depends on the isotope shift values induced by deuteration for both of the (*i* + 1)th and *i*th amides and also on their hydrogen–deuterium exchange rates [45].

Since the <sup>13</sup>C chemical shift differences for the carbons directly bonded to side-chain OH or SH groups measured in H<sub>2</sub>O and D<sub>2</sub>O are usually a little greater than 0.1 ppm, we could use these relatively large isotope shifts for the facile screening of the slowly exchanging polar groups. To do so, we prepared proteins selectively labeled by  $\zeta$ -SAIL Tyr, [3-<sup>13</sup>C; 3,3'-D<sub>2</sub>]-Ser, [3-<sup>13</sup>C; 3-D]-Thr, or [3-<sup>13</sup>C; 3,3'-D<sub>2</sub>]-Cys. These labeled proteins gave extremely sharp 1D <sup>13</sup>C-NMR signals for the C <sub>$\zeta$</sub>  or C <sub>$\beta$</sub>  under deuterium decoupling and thus were quite useful for

estimating the isotope shifts on the C<sub>ζ</sub> or C<sub>β</sub> and then the hydrogen exchange rates for the slowly exchanging polar groups by the EXSY experiment. We found that quite a few Tyr, Ser, Thr, and Cys residues in various proteins, dissolved in a 1:1 H<sub>2</sub>O–D<sub>2</sub>O mixture, actually exhibit slow hydrogen–deuterium exchanging rates for their side-chain hydroxyl or sulfhydryl groups. Interestingly, all of the polar groups identified by this method as having very slow hydrogen exchange rates form hydrogen bonds and give <sup>1</sup>H-NMR signals in H<sub>2</sub>O [46–49]. Therefore, this approach is useful for screening slowly exchanging polar functional groups that are likely to play important structural roles in proteins. A typical example of a search for the Tyr residues in a protein, which might have slowly exchanging hydroxyl groups, is illustrated as follows.

In order to search for the Tyr residue with a slowly exchanging hydroxyl group, if any exist, we prepared proteins selectively labeled by ζ-SAIL Tyr (Fig. 2.9a). This particular type of SAIL Tyr has the optimal labeling pattern for observing the <sup>13</sup>C signals of ζ-carbons most efficiently and is also convenient for making sequential assignments through the NOE and HSQC correlations between H<sub>β3</sub> and C<sub>ζ</sub>, as shown by the red and blue arrows. The three Tyr residues in the 18.2-kDa protein EPPIb labeled by ζ-SAIL Tyr gave three sharp signals in H<sub>2</sub>O and D<sub>2</sub>O solutions with the sequential assignment (Fig. 2.9b, top and bottom). The chemical shifts for the <sup>13</sup>C<sub>ζ</sub> signals in H<sub>2</sub>O appeared ~0.1 ppm downfield as compared to those in D<sub>2</sub>O, due to the two-bond isotope shift induced by the deuteration of hydroxyl groups in D<sub>2</sub>O. In a 1:1 H<sub>2</sub>O–D<sub>2</sub>O mixture, the <sup>13</sup>C<sub>ζ</sub> of Tyr36 and Tyr30 appeared as two separate signals with equal intensities, corresponding to the Tyr residues with a protonated and a deuterated hydroxyl group, respectively. In

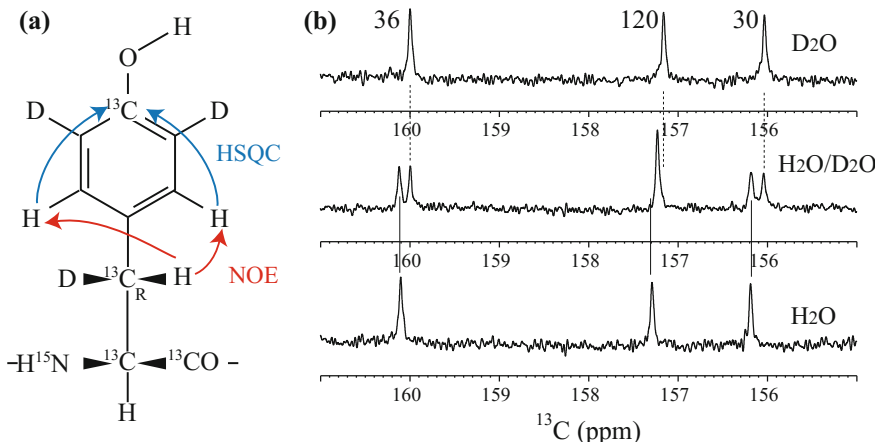


**Fig. 2.9** Deuterium isotope effect on the <sup>13</sup>C<sub>ζ</sub> chemical shifts of Tyr residues in EPPIb. **a** Structure of ζ-SAIL Tyr and the magnetization transfer pathway to make the sequential assignments of the <sup>13</sup>C<sub>ζ</sub> signals. **b** Proton-decoupled <sup>13</sup>C-NMR (125 MHz, 40 °C) spectra of EPPIb selectively labeled with ζ-SAIL Tyr under conditions of 100% D<sub>2</sub>O (top), 1:1 H<sub>2</sub>O–D<sub>2</sub>O mixture (middle) and 100% H<sub>2</sub>O (bottom) [46]

contrast, the  $^{13}\text{C}_{\delta}$  of Tyr120 showed a single peak just in the middle of the chemical shifts observed in  $\text{H}_2\text{O}$  and  $\text{D}_2\text{O}$  solutions (Fig. 2.9b, middle). The results clearly show that the hydrogen exchange rates of the hydroxyl groups in Tyr30 and Ty36 are much slower than the isotope shift difference, while Tyr120 has a rapidly exchanging hydroxyl group. It is interesting to mention that we identified the hydrogen bonds involving the hydroxyl groups of Tyr30 and Tyr36 by NOEs, but Tyr120 is on the surface of EPPIb. We could also observe the hydroxyl proton signals for Tyr30 and Tyr36 in  $\text{H}_2\text{O}$  at the chemical shifts identified by the NOE experiment [46].

## 2.4 Future Perspectives of the Isotope-Aided NMR Method

The SAIL method has become well known worldwide as a state-of-the-art isotope-aided NMR technology. However, it is clear that further efforts are required to make it a standard practice among the international biological NMR communities. The substantially high cost of the SAIL amino acids is certainly one of the obstacles, but they will be more affordable if the SAIL method becomes routinely used. Cell-free protein expression, which is necessary to prepare proteins exclusively composed of SAIL amino acids, seems to be another barrier for most NMR laboratories with no such experience. However, the *E. coli* cell-free kit for preparing isotope-labeled protein samples for NMR is now available commercially at a moderate cost. Therefore, there are no major hurdles to trying out the SAIL method for structure studies of proteins. The SAIL method could be extended for solving precise structures of proteins as large as 100 kDa or even more, by further optimization of the relaxation properties of SAIL amino acids (Miyanoiri et al., unpublished). The applications of the SAIL method to solid-state NMR spectroscopy are also interesting, but they have just started [50].

Meanwhile, the expected role of NMR spectroscopy in structural biology seems to be rapidly shifting from structure determinations to dynamics studies of biologically interesting targets, such as membrane proteins and larger protein complexes. The dynamic aspects of protein–protein and protein–ligand interactions are closely related to their biological functions and can be efficiently studied by using proteins residue selectively labeled with amino acids bearing optimized labeling patterns, prepared with conventional cellular expression systems. It is therefore quite important for the NMR community to explore the stable isotope-labeling technology to its full potentials. We are absolutely confident that biological NMR spectroscopy will be continually developing with further innovations of isotope-labeling methods in the coming era, featuring ultrahigh field spectrometers beyond 1 GHz.

**Acknowledgements** None of our work cited in this review could have been accomplished without the seminal contributions of numerous students and collaborators over the last

half-century. We sincerely regret that we could not mention most of their important accomplishments, simply because of the space limitation. Needless to mention, our research activities were not possible without the generous, persistent financial support from various government organizations and funding agencies, although we cannot mention them individually.

## References

1. Saunders, M., Wishnia, A., Kirkwood, J.G.: The nuclear magnetic resonance spectrum of ribonuclease. *J. Am. Chem. Soc.* **79**, 3289–3290 (1957)
2. Jardetzky, O.: An approach to the determination of the active site of an enzyme by nuclear magnetic resonance spectroscopy. In: Proceeding of International Conference on Magnetic Resonance, Tokyo, N3-14 (1965)
3. Markley, J.L., Putter, I., Jardetzky, O.: High-resolution nuclear magnetic resonance spectra of selectively deuterated staphylococcal nuclease. *Science* **161**, 1249–1251 (1968)
4. Kainosho, M.: Developing stable-isotope-aided NMR technologies for biological systems. In: *Encyclopedia of Magnetic Resonance*, pp. 1–4. doi:[10.1002/9780470034590.emrhp1026](https://doi.org/10.1002/9780470034590.emrhp1026) (2012)
5. Kainosho, M., Ajisaka, K., Kamisaku, M., Murai, A., Kyogoku, Y.: Conformational analysis of amino acids and peptides using specific isotope substitution. I. Conformation of L-phenylalanylglycine. *Biochem. Biophys. Res. Commun.* **64**, 425–432 (1975)
6. Kainosho, M., Ajisaka, K.: Conformational analysis of amino acids and peptides using specific isotope substitution. II. Conformation of serine, tyrosine, phenylalanine, aspartic acid, asparagine, aspartic acids β-methyl ester in various ionization states. *J. Am. Chem. Soc.* **97**, 5630–5631 (1975)
7. Kainosho, M., Tsuji, T.: Assignment of the three methionyl carbonyl carbon resonances in *Streptomyces* subtilisin inhibitor by a <sup>13</sup>C and <sup>15</sup>N double labeling technique. A new strategy for structural studies of proteins in solution. *Biochemistry* **24**, 6273–6279 (1982)
8. Kainosho, M., Tsuji, T.: <sup>13</sup>C-NMR Study of the SSI-subtilisin BPN' complex. In: Hiromi, K., Akasaka, K., Mitsui, Y., Tonomura, B., Murao, S. (eds.) *Protein Proteinase Inhibitor—The Case of Streptomyces Subtilisin Inhibitor (SSI)*, pp. 322–331. Elsevier, Amsterdam (1985)
9. Miyake, Y., Kainosho, M.: Nuclear magnetic resonance studies on *Streptomyces* subtilisin inhibitor and its complexes with proteinases. In: Fukui, T., Soda, K. (eds.) *Molecular Aspects of Enzyme Catalysis*, pp. 37–53. Kodansha-VCH, Tokyo (1994)
10. Westler, W.M., Kainosho, M., Nagao, H., Tomonaga, N., Markley, J.L.: Two-dimensional NMR strategies for carbon-carbon correlations and sequence-specific assignments in <sup>13</sup>C labeled proteins. *J. Am. Chem. Soc.* **110**, 4093–4095 (1988)
11. Westler, W.M., Stockman, B.J., Hosoya, Y., Miyake, Y., Kainosho, M., Markley, J.L.: Correlation of <sup>13</sup>C and <sup>15</sup>N chemical shifts in selectively and uniformly labeled proteins by heteronuclear two-dimensional NMR spectroscopy. *J. Am. Chem. Soc.* **110**, 6256–6258 (1988)
12. Kainosho, M., Nagao, H., Imamura, Y., Nakamura, Y., Tomonaga, N., Uchida, K., Tsuji, T.: A new strategy for the prediction of solution structure of proteins using specific isotope labeling techniques. In: Govil, G., Khetrapal, C.L., Saran, A. (eds.) *Magnetic Resonance in Biology and Medicine*, pp. 27–34. Tata-McGraw Hill, New York (1985)
13. Terauchi, T., Kobayashi, K., Okuma, K., Oba, M., Nishiyama, K., Kainosho, M.: Stereoselective synthesis of triply isotope-labeled Ser, Cys, and Ala: Amino acids for stereo-array isotope labeling (SAIL) technology. *Org. Lett.* **10**, 2785–2787 (2008)
14. Okuma, K., Ono, A.M., Tsuchiya, S., Oba, M., Nishiyama, K., Kainosho, M.: Asymmetric synthesis of (2S,3R)- and (2S,3S)-[2-<sup>13</sup>C;3-<sup>2</sup>H]glutamic acid. *Tetrahedron Lett.* **50**, 1482–1484 (2009)

15. Terauchi, T., Kamikawai, T., Vinogradov, M.G., Starodubtseva, E.V., Takeda, M., Kainosho, M.: Synthesis of stereo-array isotope labeled (SAIL)-lysine *via* the head-to-tail conversion of SAIL-glutamic acid. *Org. Lett.* **13**, 161–163 (2011)
16. Oki, S.-Y., Kainosho, M.: Recent developments in stable-isotope-aide methods for protein NMR spectroscopy. In: Webb, G.A. (ed.) *Modern Magnetic Resonance Part 1*, pp. 211–218. Springer, Dordrecht (2006)
17. Oki, S.-Y., Kainosho, M.: Stable isotope labeling methods for protein NMR spectroscopy. *Prog. Nucl. Magn. Reson. Spectrosc.* **53**, 208–226 (2008)
18. Miyanoiri, Y., Takeda, M., Kainosho, M.: Stereo-array isotope labeling method for studying protein structure and dynamics. In: Atreya, H.S. (ed.) *Isotope Labeling Methods for Biomolecular NMR Spectroscopy. Advances in Experimental Medicine and Biology*, vol. 992, pp. 83–93. Springer, Berlin (2012)
19. Miyanoiri, Y., Takeda, M., Kainosho, M.: Stable-isotope-aided NMR spectroscopy. In: Webb, G.A. (ed.), *Modern Magnetic Resonance*, 2nd edn. Springer, Berlin. doi:[10.1007/978-3-319-28275-6](https://doi.org/10.1007/978-3-319-28275-6) (2017)
20. Kainosho, M., Torizawa, T., Iwashita, Y., Terauchi, T., Ono, A.M., Güntert, P.: Optimal isotope labelling for NMR protein structure determinations. *Nature* **440**, 52–57 (2006)
21. Kainosho, M., Güntert, P.: SAIL-Stereo-array isotope labeling. *Q. Rev. Biophys.* **42**, 247–300 (2009)
22. Kalbitzer, H.R., Leberman, R., Wittnighofer, A.:  $^1\text{H}$ -NMR spectroscopy on elongation factor Tu from *Escherichia coli*. Resolution enhancement by perdeuteration. *FEBS Lett.* **180**, 40–42 (1985)
23. Torizawa, T., Shimizu, M., Taoka, M., Miyano, H., Kainosho, M.: Efficient production of isotopically labeled proteins by cell-free synthesis: a practical protocol. *J. Biomol. NMR* **30**, 311–325 (2004)
24. Takeda, M., Kainosho, M.: Cell-free protein production for NMR studies. In: Shekhtman, A., Burz, D.S. (eds.) *Protein NMR Techniques*, 3rd edn. *Methods in Molecular Biology*, vol. 831, pp. 71–84. Humana Press, Springer Protocols, New York (2012)
25. Takeda, M., Kainosho, M.: Cell-free protein synthesis using *E. coli* cell extract for NMR studies. In: Atreya, H.S. (ed.) *Isotope Labeling Methods for Biomolecular NMR Spectroscopy. Advances in Experimental Medicine and Biology*, vol. 992, pp. 167–177. Springer, Berlin (2012)
26. Torizawa, T., Ono, A.M., Terauchi, T., Kainosho, M.: NMR assignment methods for the aromatic ring resonances of phenylalanine and tyrosine residues in proteins. *J. Am. Chem. Soc.* **127**, 12620–12626 (2005)
27. Takeda, M., Ono, A.M., Terauchi, T., Kainosho, M.: Application of SAIL phenylalanine and tyrosine with alternative isotope-labeling patterns for protein structure determination. *J. Biomol. NMR* **46**, 45–49 (2010)
28. Miyanoiri, Y., Takeda, M., Jee, J.-G., Ono, A.M., Okuma, K., Terauchi, T., Kainosho, M.: Alternative SAIL-Trp for robust aromatic signal assignment and determination of the  $\chi(2)$  conformation by intra-residue NOEs. *J. Biomol. NMR* **51**, 425–435 (2011)
29. Takeda, M., Ikeya, T., Güntert, P., Kainosho, M.: Automated structure determination of proteins with the SAIL-FLYA NMR method. *Nat. Protoc.* **2**, 2896–2902 (2007)
30. Ikeya, T., Takeda, M., Yoshida, H., Terauchi, T., Jee, J.-G., Kainosho, M., Güntert, P.: Automated NMR structure determination of stereo-array isotope labeled ubiquitin from minimal sets of spectra using the SAIL-FLYA system. *J. Biomol. NMR* **44**, 261–272 (2009)
31. Ikeya, T., Jee, J.-G., Shigemitsu, Y., Hamatsu, J., Mishima, M., Ito, Y., Kainosho, M., Güntert, P.: Exclusively NOESY-based automated NMR assignment and structure determination of proteins. *J. Biomol. NMR* **50**, 137–146 (2011)
32. Pervushin, K., Riek, R., Wider, G., Wüthrich, K.: Attenuated  $T_2$  relaxation by mutual cancellation of dipole-dipole coupling and chemical shift anisotropy indicates an avenue to NMR structures of large biological macromolecules in solution. *Proc. Natl. Acad. Sci. USA* **94**, 12366–12371 (1997)

33. Pervushin, K., Riek, R., Wider, G., Wüthrich, K.: Transverse relaxation-optimized spectroscopy (TROSY) for NMR studies of aromatic spin systems in  $^{13}\text{C}$ -labeled proteins. *J. Am. Chem. Soc.* **120**, 6394–6400 (1998)
34. Tugarinov, V., Kay, L.E.: Ile, Leu, and Val methyl assignments of the 723-residue malate synthase G using a new labeling strategy and novel NMR methods. *J. Am. Chem. Soc.* **125**, 13868–13878 (2003)
35. Ruschak, A.M., Kay, L.E.: Proteasome allosteric as a population shift between interchanging conformers. *Proc. Natl. Acad. Sci. USA* **109**, E3454–E3462 (2012)
36. Gardner, K.H., Kay, L.E.: Production and incorporation of  $^{15}\text{N}$ ,  $^{13}\text{C}$ ,  $^2\text{H}$  ( $^1\text{H}$ - $\delta_1$  methyl) isoleucine into proteins for multidimensional NMR studies. *J. Am. Chem. Soc.* **119**, 7599–7600 (1997)
37. Goto, N.K., Gardner, K.H., Mueller, G.A., Willis, R.C., Kay, L.E.: A robust and cost-effective method for the production of Val, Leu, Ile ( $\delta_1$ ) methyl-protonated  $^{15}\text{N}$ -,  $^{13}\text{C}$ -,  $^2\text{H}$ -labeled proteins. *J. Biomol. NMR* **13**, 369–374 (1999)
38. Gans, P., Hamelin, O., Sounier, R., Ayala, I., Durá, M.A., Amero, C.D., Noirclerc-Savoye, M., Franzetti, B., Plevin, M.J., Boibouvier, J.: Stereospecific isotopic labeling of methyl groups for NMR spectroscopic studies of high-molecular-weight proteins. *Angew. Chem. Int. Ed. Engl.* **49**, 1958–1962 (2010)
39. Miyanoiri, Y., Takeda, M., Okuma, K., Ono, A.M., Terauchi, T., Kainosh, M.: Differential isotope-labeling for Leu and Val residues in a protein by *E. coli* cellular expression using stereo-specifically methyl labeled amino acids. *J. Biomol. NMR* **57**, 237–249 (2013)
40. Miyanoiri, Y., Ishida, Y., Takeda, M., Terauchi, T., Inouye, M., Kainosh, M.: Highly efficient residue-selective labeling with isotope-labeled Ile, Leu, and Val using a new auxotrophic *E. coli* strain. *J. Biomol. NMR* **65**, 109–119 (2016)
41. Wagner, G., Wüthrich, K.: Dynamic model of globular protein conformations based on NMR studies in solution. *Nature* **275**, 247–248 (1978)
42. Wagner, G.: Characterization of the distribution of internal motions in the basic pancreatic trypsin inhibitor using a large number of internal NMR probes. *Q. Rev. Biophys.* **16**, 1–57 (1983)
43. Skalicky, J.J., Mills, J.L., Sharma, S., Szypersky, T.: Aromatic ring-flipping in supercooled water: implications for NMR-based structural biology of proteins. *J. Am. Chem. Soc.* **123**, 388–397 (2001)
44. Yang, C.-J., Takeda, M., Terauchi, T., Jee, J.-G., Kainosh, M.: Differential large-amplitude breathing motions in the interface of FKBP12-Drug complexes. *Biochemistry* **54**, 6983–6995 (2015)
45. Markley, J.L., Kainosh, M.: Stable isotope labelling and resonance assignments in larger proteins. In: Roberts, G.C.K. (ed.) *NMR of Macromolecules. A Practical Approach*, pp. 101–152. Oxford University Press, Oxford (1993)
46. Takeda, M., Jee, J.-G., Ono, A.M., Terauchi, T., Kainosh, M.: Hydrogen exchange rate of tyrosine hydroxyl groups in proteins as studied by the deuterium isotope effect on  $\text{C}_\zeta$  chemical shifts. *J. Am. Chem. Soc.* **131**, 18226–18562 (2009)
47. Takeda, M., Jee, J.-G., Terauchi, T., Kainosh, M.: Detection of the sulphydryl groups in proteins with slow hydrogen exchange rates and determination of their proton/deuteron fractionation factors using the deuterium-induced effects on the  $^{13}\text{C}_\beta$  NMR signals. *J. Am. Chem. Soc.* **132**, 6254–6260 (2010)
48. Takeda, M., Jee, J.-G., Ono, A.M., Terauchi, T., Yang, C.-J., Kainosh, M.: Hydrogen exchange study on the hydroxyl groups of serine and threonine residues in proteins and structure refinement using NOE restraints with polar side-chain groups. *J. Am. Chem. Soc.* **133**, 17420–17427 (2011)
49. Takeda, M., Miyanoiri, Y., Terauchi, T., Kainosh, M.: Use of H/D isotope effects to gather information about hydrogen bonding and hydrogen exchange rates. *J. Magn. Reson.* **241**, 148–154 (2014)
50. Wang, S., Parthasarathy, S., Nishiyama, Y., Endo, Y., Nemoto, T., Yamauchi, K., Asakura, T., Takeda, M., Terauchi, T., Kainosh, M., Ishii, Y.: Nano-mole scale sequential signal

- assignment by  $^1\text{H}$ -detected protein solid-state NMR by ultra-fast magic-angle spinning and stereo-array isotope labeling. *Chem. Commun.* **51**, 15055–15058 (2015)
51. Takeda, M., Chang, C.-K., Ikeya, T., Güntert, P., Chang, Y.-H., Hsu, Y.-L., Huang, T.-H., Kainosho, M.: Solution structure of the C-terminal dimerization domain of SARS coronavirus nucleocapsid protein solved by the SAIL-NMR method. *J. Mol. Biol.* **380**, 608–622 (2008)
52. Takeda, M., Sugimori, N., Torizawa, T., Terauchi, T., Ono, A.M., Yagi, H., Yamaguchi, Y., Kato, K., Ikeya, T., Jee, J.-G., Güntert, P., Aceti, D.J., Markley, J.L., Kainosho, M.: Structure of the putative 32 kDa myrosinase binding protein from *Arabidopsis* (At3g16450.1) determined by SAIL-NMR. *FEBS J.* **275**, 5873–5884 (2008)

# Chapter 3

## Advances in NMR Data Acquisition and Processing for Protein Structure Determination

Teppei Ikeya and Yutaka Ito

**Abstract** Solution NMR has become an indispensable technique in studying the physical properties and functions of biomacromolecules at near physiological conditions. However, biomolecular systems are often extraordinarily large, dynamic, and possess low solubility, which complicates the acquisition and analysis of NMR spectra. Together this results in severe signal overlapping and low signal to noise, which demands longer total experimental time. NMR spectroscopists must consider how to improve spectral resolution and sensitivity to extract the maximum structural information from imperfect data within reasonable measurement times. Recent advances in multi-dimensional NMR acquisition and computation methods overcome these problems and enable the investigation of larger and more complicated biomolecular systems. This chapter first reviews conventional and then state-of-the-art methodologies for NMR data collection, signal processing, and protein structure data analysis. In the first section, we survey the basics of multi-dimensional NMR and present rapid measurement techniques such as non-uniform sampling and spectrum reconstruction algorithms. In the second half, we illustrate the conventions of protein structure determination using chemical shift and NOE data to obtain interatomic distances, dihedral angles, and dynamics information. We also briefly introduce the currently popular hybridisation of NMR with solution angle scattering for 3D structure analysis.

**Keywords** Non-uniform sampling · Maximum entropy · Compressed sensing  
Protein structure determination · Bayesian inference

---

T. Ikeya · Y. Ito (✉)

Department of Chemistry, Tokyo Metropolitan University, Tokyo, Japan  
e-mail: ito-yutaka@tmu.ac.jp

T. Ikeya

e-mail: tikeya@tmu.ac.jp

### 3.1 Advances in Processing of Multi-dimensional NMR Spectra, and Their Application to Rapid NMR Measurements

#### 3.1.1 *Multi-dimensional NMR Takes Time*

Protein NMR spectra suffer from signal overlapping, and thus, the extension of their dimensionality to 3D (and sometimes 4D) is required. Employing conventional methods to record multi-dimensional (nD) NMR data increases experimental time drastically. An additional indirect dimension itself increases the experimental time proportional to the data points introduced for the dimension. It takes a couple of hours to days for 3D experiments and days to a week for 4D experiments. Moreover, for each indirect data point, we need to repeat experiments to implement coherence selection and frequency discrimination methods.

Multiple scans, phase cycling, and time between scans (recycle delay) which are required in acquisition of each FID are part of the reason for the long experimental time. Protein NMR studies frequently face a problem of low solubility of target proteins, and thus, multiple scans are required from the signal-to-noise ratio (S/N) point of view. For instance, we would need to collect four times as many scans so as to achieve the same S/N expected for that of a sample with twice the concentration. This is because S/N increases proportional to the root of number of scans [signal grows additively ( $I_{\text{signal}} \propto n$ ), while noise more slowly ( $I_{\text{noise}} \propto n/\sqrt{2}$ )]. Multiple scans are also required for phase cycling, which is used for selecting favourable coherence transfer pathways and suppressing various artefacts. Recycle delay is required in order to recover the magnetisation to near equilibrium condition (steady state) at the beginning of each scan. Recycle delay depends on the longitudinal relaxation time ( $T_1$ ) of the observed nuclei, and typically 1–1.3 s are required in  $^1\text{H}$ -detected experiments of protein samples. For example, when measuring a 3D triple-resonance experiment with eight scans, 1-s recycle delay, and 64 ( $^{13}\text{C}$ )  $\times$  24 ( $^{15}\text{N}$ ) complex points for indirect dimensions, it requires roughly  $8 \times 1 \times 64 \times 2 \times 24 \times 2 = 49,152$  s ( $\sim 14$  h).

Rovnyak et al. [1] reported that optimal resolution for indirect dimensions can be achieved with an acquisition time of  $3 \times$  transverse relaxation time ( $T_2$ ) of the observed nuclei, while optimal S/N can be achieved with the acquisition time of  $1.6 \times T_2$ . Although higher magnetic fields create better resolution, increasing the number of points collected in the indirect dimensions is more essential for obtaining highly resolved spectra. For a 3D HNCO experiment, on a 600 MHz spectrometer, of a  $^{13}\text{C}/^{15}\text{N}$ -labelled protein comprised of less than 100 amino acids, for which carbonyl  $^{13}\text{C}$  and  $^{15}\text{N}$   $T_2$  relaxation times are roughly estimated in a range of 100–150 ms and 150–250 ms, respectively, optimal resolution would be achieved with  $\sim 300$  and  $\sim 600$  ms acquisition times for carbonyl  $^{13}\text{C}$  and  $^{15}\text{N}$  dimensions, respectively. Similarly,  $\sim 200$  and  $\sim 400$  ms acquisition times are required for

optimal S/N for carbonyl  $^{13}\text{C}$  and  $^{15}\text{N}$  dimensions, respectively. However, when utilising a standard pulse sequence,  $^{15}\text{N}$  acquisition time is restricted to approximately 20–24 ms because of the constant-time evolution periods in the pulse sequence. Carbonyl  $^{13}\text{C}$  is observed with conventional (decaying) evolution period, but at most 256 complex points ( $\sim 150$  ms acquisition) are usually observed. Generally speaking, with conventional acquisition protocols for acquiring indirect dimensions, data sampling is rarely performed beyond  $0.4 \times T_2$ , and extending acquisition times for indirection dimensions would result in ridiculously long experimental times.

In reality, in our group, a HNCO experiment with conventional acquisition protocols is usually performed with 128 (carbonyl  $^{13}\text{C}$ ) and 24 ( $^{15}\text{N}$ ) complex points, in which acquisition of indirect dimensions is heavily truncated.

### 3.1.2 Processing of Multi-dimensional NMR Spectra

Heavy truncation in indirect dimensions in nD NMR data causes serious artefacts in Fourier transformed spectra, and thus, “apodisation” functions have to be applied prior to Fourier transform (FT). On the other hand, from the spectral resolution point of view, apodisation functions broaden peak lineshapes. To overcome the problem, linear prediction (LP) [2] is often used, with which cosine/sine functions are fitted to recorded data and points missing after the truncation are predicted. The LP-predicted data are then apodised, zero-filled, and Fourier transformed. Note that the apodisation after LP often still influences linewidth. The procedure to perform LP calculations to indirect dimensions of 3D/4D spectra is rather complicated with successive application of inverse Fourier transforms, Hilbert transforms to produce imaginary data, etc. This is because LP is applied to one-dimensional time-domain data and the other dimensions of the spectra are needed to be frequency domains. In comparison with the ordinary 3D FT procedure (Fig. 3.1a), a typical procedure for LP calculations of 3D NMR data is shown in Fig. 3.1b. A 3D HNCO spectrum processed with LP (Fig. 3.1e) is compared with the corresponding 3D FT-processed spectrum (Fig. 3.1d).

Maximum-entropy (MaxEnt) reconstruction [3, 4] has been also utilised for processing of truncated data. MaxEnt algorism guesses a mock spectrum based on the information theory principle of maximum entropy, which compares its inverse Fourier transformed data with the observed data points. MaxEnt processing is relatively more tolerant of extreme data truncation than LP, and the resulting spectra are not influenced by apodisation. Unlike LP, MaxEnt processing of 3D/4D NMR is rather straightforward. Figure 3.1c shows a typical procedure for 2D MaxEnt processing of 3D NMR data. For comparison with 3D FT-processed and LP-processed spectra, a 2D  $^{13}\text{C}$ – $^{15}\text{N}$  slice from the MaxEnt-processed 3D HNCO spectrum is also shown in Fig. 3.1f.

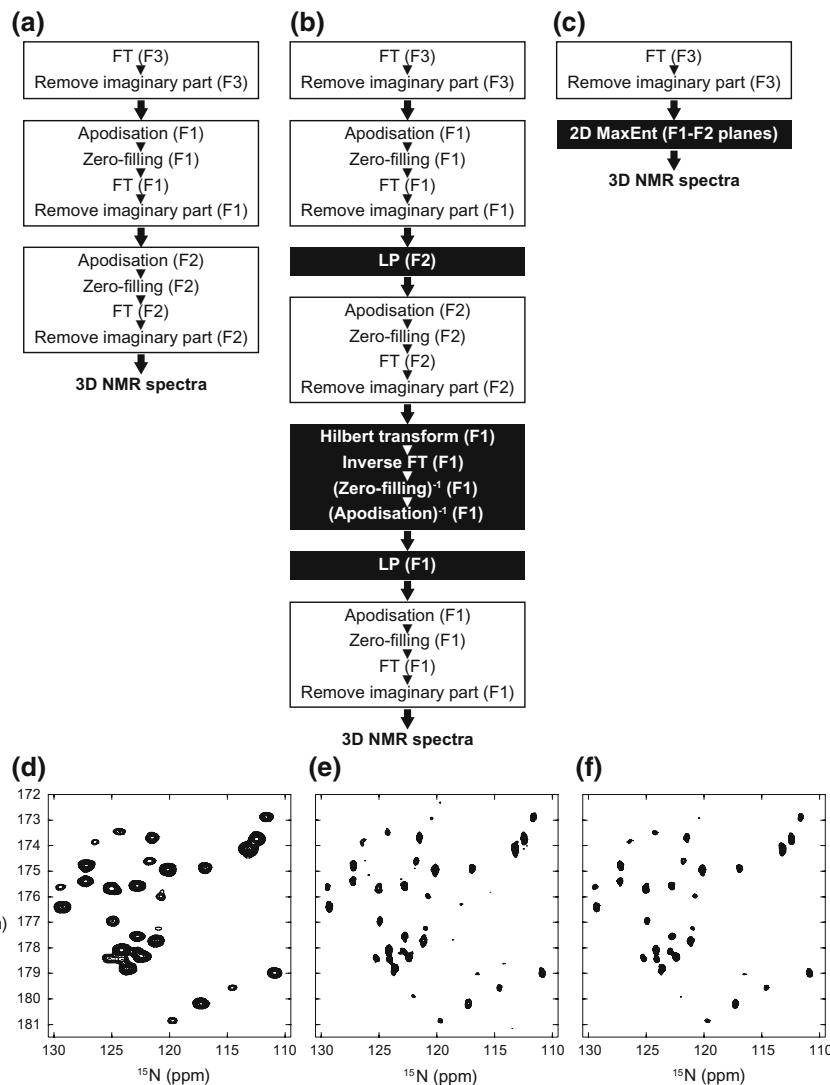


**Fig. 3.1** Schematic representations of typical processing procedures for 3D NMR data using conventional FT (a), LP (b) and 2D MaxEnt (c). In the LP procedures,  $(\text{Zero-filling})^{-1}$  and  $(\text{Apodisation})^{-1}$  represent the reduction in the zero-filled points from the later part of the interferogram and the application of the inverse window function, respectively.  $F_1({}^{13}\text{C})-F_2({}^{15}\text{N})$  cross sections at  $F_3({}^1\text{H}^{\text{N}}) = 8.35$  ppm from conventional FT-processed (d), LP-processed (e), and MaxEnt-processed (f) 3D TROSY-HNCO spectra of uniformly  ${}^2\text{H}/{}^{13}\text{C}/{}^{15}\text{N}$ -labelled *E. coli* NikA protein. The data were acquired with a total of 1024 ( $t_3$ ,  ${}^1\text{H}^{\text{N}}$  acquisition)  $\times$  24 ( $t_1$ ,  ${}^{15}\text{N}$ )  $\times$  64 ( $t_2$ ,  ${}^{13}\text{C}$ ) complex points. The data were processed using the AZARA 2.8 software suite (W. Boucher, <http://www.bio.cam.ac.uk/azara/>)

### 3.1.3 Rapid Measurement of Multi-dimensional NMR Spectra

As described so far, acquiring nD NMR spectra takes time, and thus, new acquisition schemes for speeding up multi-dimensional NMR experiments are required for dramatic improvements in both sensitivity and resolution. Many approaches have been proposed [5, 6], which can be largely grouped into three main types.

The first group consists of approaches to optimise radio frequency pulses, etc. to achieve rapid acquisition of nD spectra within the conventional sampling strategy for indirect dimensions. Brügel and co-workers have reported pulse sequences called band-selective optimised flip angle short-transient (SOFAST)-HMQC [7, 8] and related 3D triple-resonance experiments [9, 10], e.g., band-selective excitation short-transient (BEST)-HNCA, enabling the drastic reduction in recycle delays, thus speeding up the experiments. These experiments employ band-selective  $^1\text{H}$  pulses which are optimised to ensure rapid recovery of steady state magnetisation based on the observations that the selective manipulation of a subset of  $^1\text{H}$  spins yields significantly shortened longitudinal relaxation times [11]. In short, the non-perturbed  $^1\text{H}$  spins act as a “sink” for polarised spins through dipole–dipole interactions. Typically, 2D  $^1\text{H}$ – $^{15}\text{N}$  SOFAST-HMQC experiments are performed with  $\sim 0.2$ -s recycling delay, resulting in approximately 150–200% increase in S/N per unit time depending on the size of proteins and the magnetic field strength.

Projection reconstruction (PR) [12, 13], G-matrix Fourier Transform (GFT)-NMR [14], automated projection spectroscopy (APSY) [15], and non-uniform sampling (NUS, also known as nonlinear sampling) methods [16–18] compose the second group in which alternative sampling schemes for indirect dimensions are employed. The basic concept of PR-related approaches including GFT-NMR and APSY is as follows. In 3D HNCO spectra, chemical shifts of intraresidue amide  $^{15}\text{N}$  and carbonyl  $^{13}\text{C}$  of previous residue are correlated with each amide  $^1\text{H}^{\text{N}}$  resonance. For  $^1\text{H}^{\text{N}}$  resonances which are not overlapped in the  $^1\text{H}$  (acquisition) dimension, a whole 3D HNCO experiment is not necessary, since 2D  $^{13}\text{C}'$ – $^1\text{H}^{\text{N}}$  and  $^{15}\text{N}$ – $^1\text{H}^{\text{N}}$  projection experiments can provide required information. When two  $^1\text{H}^{\text{N}}$  resonances are overlapped in the acquisition dimension, the 2D projections, however, provide two possible chemical shifts in both  $^{15}\text{N}$  and  $^{13}\text{C}$  dimensions, thus requiring an additional “tilted” projection for distinguishing the correct chemical shift combination. The tilted projection spectra can be acquired by a combination of indirect dimension frequencies instead of sampling them independently. In PR, the acquired 2D projections are utilised for reconstructing the 3D spectrum by employing tomography-type processing procedures. In contrast, in the GFT-NMR, APSY-type methods, peak picking is directly performed for the projections, and the obtained peak information is utilised to calculate the chemical shifts. The advantage of PR-related approach is that this concept can be easily extended for the experiments with even higher dimensionality. However, we experienced that tomography-type reconstruction often produces poor spectra particularly for the spectra of larger proteins. The reconstruction process can be improved by

employing statistical methods such as MaxEnt. PR may, however, be regarded essentially similar to the below-mentioned NUS with the exception of utilising off-Nyquist grid sampling, if such statistical methods come into frequent use.

The third group utilised conceptually new approaches for acquiring indirect dimensions, in which single-scan NMR [19, 20] and Hadamard spectroscopy [5, 21] can be categorised.

### 3.1.4 Non-uniform Sampling

NUS has been shown to be a robust technique, in which sampling points on Nyquist grid for indirect dimensions are decimated. Since discrete Fourier transform (DFT) cannot be used for processing NUS-sampled data, various “non-FT” processing methods have been utilised for reconstruction of nD NMR spectra. When NUS was applied for the first time to 2D NMR experiments, an exponential weighted function was employed for selecting sampling points in the decaying indirect dimension [16]. Later, Wagner, Hyberts, and their co-workers have contributed significantly to the applications of NUS to 3D and 4D NMR experiments [17].

As a “non-FT” processing method for data processing, MaxEnt has been used since the beginning of NUS. As an improved version of MaxEnt, forward maximum-entropy reconstruction [22, 23] has also been proposed. Recently, we have introduced another improvement of MaxEnt, quantitative maximum entropy (QME) [24]. For most of the nD NMR spectra, MaxEnt and QME provide very similar results. However, it was demonstrated that QME has the advantage in producing spectra with much better accuracy than MaxEnt, particularly when the spectra contain signals with wide dynamic range [24, 25]. Besides adopting a Bayesian framework around the principle of maximum entropy, QME uses a novel holistic reconstruction approach where the entire nD spectrum is reconstructed in one iteration, which has been discussed to be beneficial for the accurate reconstructions.

Apart from MaxEnt and related methods, non-uniform Fourier transform [26, 27] and decomposition algorithms for multi-way arrays, such as multi-dimensional decomposition (MDD) [28], rMDD [29], coMDD [30], and SHIFT [31], have been proposed. More recently,  $L_p$ -norm ( $0 < p \leq 1$ ) minimisation referred to as compressed sensing (CS) was introduced to the NMR field [32, 33]. So far, many algorithms of convex optimisation for L1- or L0-norm minimisation have been developed, such as iterative soft thresholding (IST) [34, 35], iteratively reweighted least squares (IRLS) [32], NESTA [36], and sparse multi-dimensional iterative lineshape-enhanced (SMILE) [37]. Since most of these software packages are freely available for academic use, researchers can compare their performances on their own NMR data. We have compared QME, MaxEnt in AZARA software suite

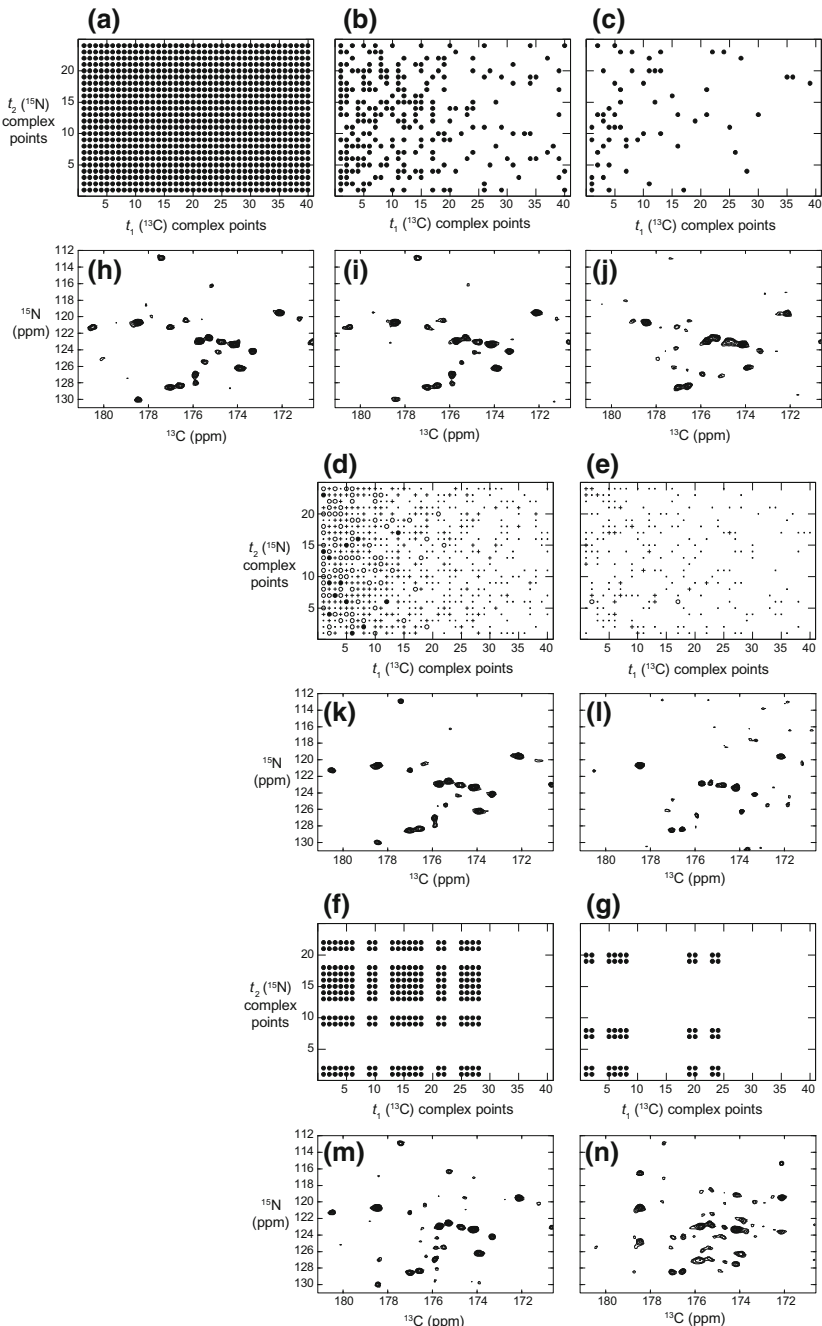
(W. Boucher, <http://www.bio.cam.ac.uk/azara/>), MDD, IST, and IRLS in the MDDNMR software [32, 38] in reconstructing 3D NOESY data acquired with various sparse sampling schedules and found that MaxEnt, QME, and IRLS provided spectra with slightly better quality than those processed by MDD or IST, over almost the entire range of sampling data points.

### 3.1.5 NUS Sampling Schemes

For NUS sampling schemes, Wagner and co-workers have suggested to apply an exponentially weighted sampling for conventional (decaying) evolution periods, while a randomly distributed sampling is suitable for constant-time evolution periods [17]. Figure 3.2 shows various sampling schedules and the corresponding 3D NMR spectra processed with MaxEnt. Figure 3.2b, c illustrates sampling schemes in which 1/4 (3.2b) and 1/16 (3.2c) of the hypercomplex points were selected in a pseudo-random fashion from the conventional regularly spaced grid of  $t_1, t_2$  points (Fig. 3.2a). The resulting spectra (Fig. 3.2i, j) show the usefulness of this approach. Generally speaking, “randomness” is required in the sampling schemes, since “regularity” tends to cause artefacts (e.g., dropping points gives rise to aliasing artefacts). On the other hands, NUS/MaxEnt processing shows robustness even with so-called block sampling. Indeed, we could obtain 3D triple-resonance NMR spectra on human mitochondrial ABCB6 C-terminal ATP binding cassette (ABC) domain with reasonable quality, even though “block” sampling had to be used because of the Azara software limitation at that time [39]. Figure 3.2f, g demonstrates examples of block sampling with 1/4 and 1/16 reduction in hypercomplex points, respectively. Although block sampling is still effective for collecting data with 1/4 reduction in sampling points (Fig. 3.2m), the block-sampled data with 1/16 reduction (Fig. 3.2n) do not provide analysable spectra, suggesting that more “randomness” is indeed needed.

Recently, further flexibility has been introduced in data sampling, in which the selection of quadrature components is also randomised (partial-component sampling [40]). Unlike DFT, it is noteworthy that two quadrature components for each complex point are not necessarily required for statistical processing algorithms. Figure 3.2d, e shows examples of partial-component sampling with 1/4 and 1/16 reduction in total FIDs, respectively. The resulting spectra are shown in Fig. 3.2k, l, respectively. More recently, this approach has been extended in combination with CS processing to the indirect dimensions with  $P$ -type/ $N$ -type selection, for which addition and subtraction are required to construct ordinary complex data [41]. These “hyper” random sampling approaches introduce extra flexibility in employing sampling schedules and enable further reduction in experimental time, particularly for 4D and higher-dimensional NMR experiments.

Large gaps between data points and those biased distributions in NUS sampling schedules sometimes cause undesirable artefacts. To minimise the artefacts, Hyberts



◀Fig. 3.2 Sampling schemes and reconstructed spectra for the indirect dimensions of 3D HNCO data of  $^{13}\text{C}/^{15}\text{N}$ -labelled *Thermus thermophilus* HB8 RecO. For the evaluation of artefacts arising from the employment of each sampling scheme, data sets with various randomly sampled points in the indirect dimensions were prepared from the conventionally acquired 3D HNCO data. Schematic illustration of the conventional full sampling (**a**), the NUS schemes with 1/4 (**b**, **d**), 1/16 (**c**, **e**) randomly selected data points, 1/4 (**f**) and 1/16 (**g**) block-sampled data points. *Filled circles*, *outlined circles*, *pluses*, and *dots* represent that four, three, two, and one FIDs, respectively, are selected for the hypercomplex points. In schemes **b** and **c**, all selected hypercomplex points have four FIDs (corresponding to quadrature components for both indirect dimensions). In schemes **d** and **e**, selection of quadrature components is also randomised. A representative  $F_1(^{13}\text{C}) - F_2(^{15}\text{N})$  cross section at  $F_3(^1\text{H}^N) = 8.39$  ppm of the MaxEnt-processed 3D HNCO spectra reconstructed from the data collected according to the schemes shown in **a–g** is shown in **h–n**, respectively

et al. proposed a sparse sampling scheme collecting data points along with a sinusoidal-weighted Poisson distribution or Poisson-gap sampling [42, 43]. It produces a sampling list with less dependency on random number generators, preventing coincidental inappropriate random numbers for the Nyquist theorem.

### 3.1.6 Semi-constant-Time Evolution Periods

Constant-time evolution periods limit the maximum sampling points. Figure 3.3a shows a typical pulse sequence for 3D HNCO experiments. Constant-time evolution of the  $t_1$  ( $^{15}\text{N}$ ) dimension is achieved by shifting the simultaneous  $^{15}\text{N}$  and  $^{13}\text{C}'$  180° pulses, while keeping the total duration of the  $^{13}\text{C}'$  to  $^{15}\text{N}$  INEPT period constant (enclosed in a box), and thus, the evolution must be terminated when the pulses reach the end of the INEPT period (Fig. 3.3b). Semi-constant-time evolution is a useful trick to achieve a longer acquisition and resulting high resolution in the indirect dimensions. In the pulse sequence,  $^{15}\text{N}$ -evolution is performed by increasing a newly introduced duration  $T_{NA}$ , which starts at the minimum possible duration, with following the relation:  $IN(T_{NA}) = IN(t_1) - IN(T_{NB})$ , where  $IN(T_{NA})$  and  $IN(t_1)$  represent increment steps of  $T_{NA}$  and  $t_1$ , respectively, while  $IN(T_{NB})$  is a decrement step of  $T_{NB}$  (Fig. 3.3c). Figure 3.3d shows the final stage of  $^{15}\text{N}$ -evolution, where  $T_{NB}$  reaches to zero. Combined with NUS, semi-constant-time evolution data collection can achieve very wide sampling space within realistic experimental durations. An example of this sampling strategy is shown in Fig. 3.4b in contrast to the conventional method (Fig. 3.4a). Both  $t_1$  and  $t_2$  indirect acquisition periods are extended fourfold, while the total number of observed FIDs is kept equal to the conventional sampling scheme by employing 1/16 NUS. The resulting spectrum (Fig. 3.4d, f) achieves very high resolution in the  $^{13}\text{C}-^{15}\text{N}$  dimensions.

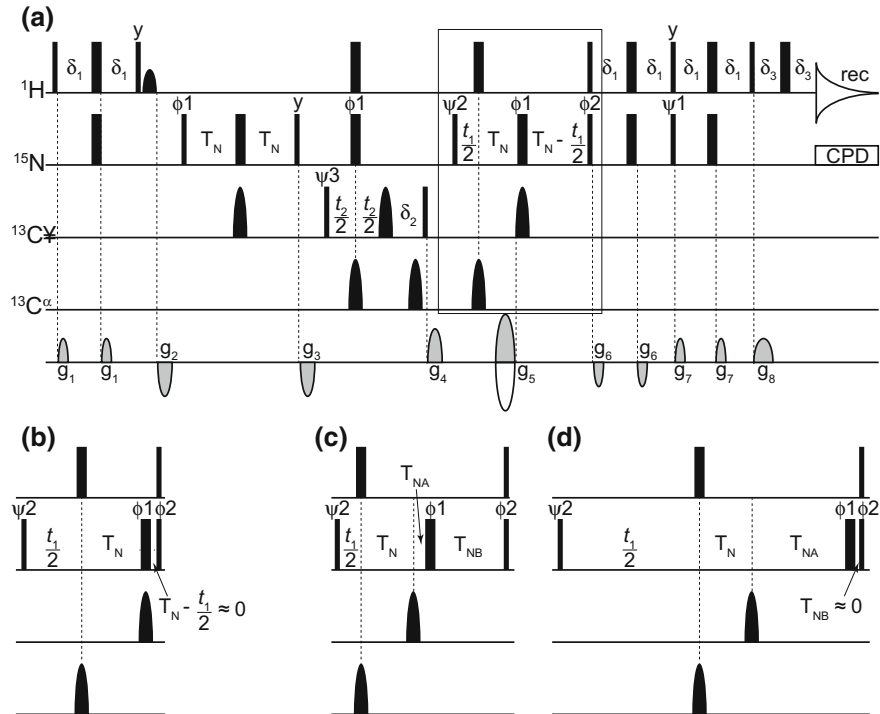


**Fig. 3.3** **a** An experimental scheme for 3D HNCO. Rectangular 90° and 180° pulses are indicated by thin and thick vertical bars, respectively, and phases are indicated above the pulses. All proton pulses are applied with a field strength of ~22 kHz with the exception of a shaped E-SNOB pulse for water flip back. For 600 MHz NMR spectrometers, all rectangular 90°  $^{13}\text{C}^\alpha$  pulses have a length of 53  $\mu\text{s}$  to provide an excitation null at the corresponding  $^{13}\text{C}^\alpha$  frequencies. The shaped 180°  $^{13}\text{C}^\alpha$  and  $^{13}\text{C}'$  pulses are applied with rSNOB and SEDUCE-1 profiles, respectively. Delay durations:  $\delta_1 = 2.35$  ms;  $\delta_3 = 1.1$  ms;  $T_N = 12$  ms.  $\delta_2$  was set so as to refocus  $^{13}\text{C}'$  chemical shift evolution at the starting point of the experiment. Phase cycling used:  $\phi_1 = 4(x)$ ,  $4(-x)$ ;  $\phi_2 = 2(x)$ ,  $2(-x)$ ;  $\psi_1 = 2(y)$ ,  $2(-y)$ ;  $\psi_2 = y$ ;  $\psi_3 = x$ ,  $-x$ ; receiver =  $x$ ,  $2(-x)$ ,  $x$ ,  $-x$ ,  $2(x)$   $-x$ . Where no radio frequency phase is marked, the pulse is applied along  $x$ . The relative power for  $g_5$  and  $g_8$  gradient pulses is given by the gyromagnetic ratios  $g_5/g_8 = \gamma_{\text{H}}/\gamma_{\text{N}}$ . Quadrature detection in the  $t_2$  ( $^{13}\text{C}'$ ) dimension is achieved using States-TPPI of  $\psi_3$ , while in the  $t_1$  ( $^{15}\text{N}$ ) dimension a phase-sensitive spectrum is obtained by recording a second FID for each increment of  $t_1$  with the inversion of phase  $\psi_1$  and the sign of  $g_5$  gradient pulse. For each successive  $t_1$  increment,  $\psi_2$  and the phase of the receiver are incremented by 180°, and the data are processed as described by Kay et al. [44]. **b** The pulse sequence at the final stage of  $t_1$  ( $^{15}\text{N}$ ) evolution. Only the  $^{13}\text{C}'$  to  $^{15}\text{N}$  INEPT transfer period enclosed in the box in (a) is shown. **c** A modified HNCO scheme with semi-constant-time  $t_1$   $^{15}\text{N}$  evolution period (c), and its final stage of  $t_1$  ( $^{15}\text{N}$ ) evolution (d). Initial  $T_{\text{NB}}$  is set slightly larger than  $T_N$  so as to refocus  $^{15}\text{N}$  chemical shift evolution at the starting point of the experiment

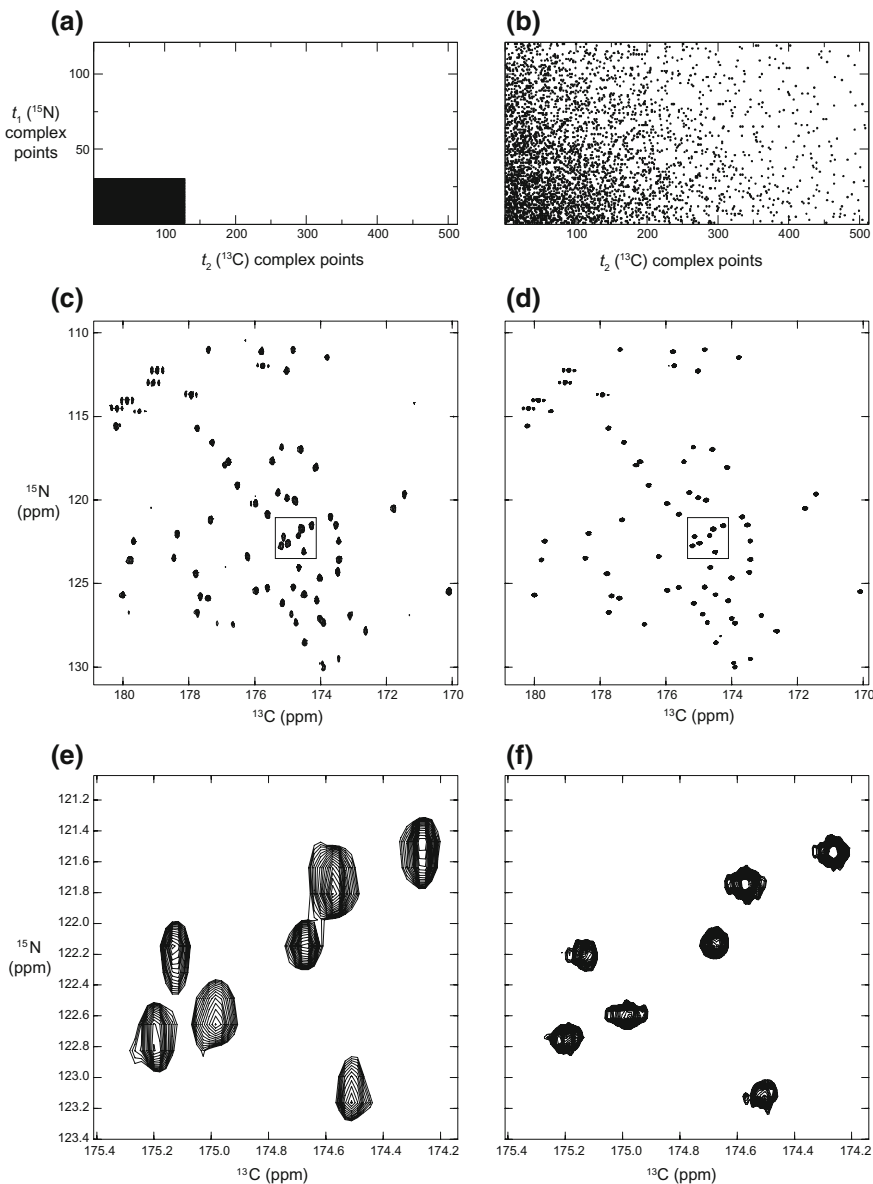


**Fig. 3.4** Sampling schemes and reconstructed spectra for the indirect dimensions of 3D HNCO data of  $^{13}\text{C}/^{15}\text{N}$ -labelled human ubiquitin. Schematic illustration of the conventional full sampling (a) and NUS schemes with 1/16 randomly selected data points in a sampling space for which both  $t_1$  and  $t_2$  dimensions are extended fourfold. Overlay of  $F_1$  ( $^{13}\text{C}$ )– $F_2$  ( $^{15}\text{N}$ ) cross sections from the MaxEnt-processed 3D HNCO spectra reconstructed from the data collected according to the schemes shown in a and b is shown in c and d, respectively. Panels e and f represent magnified inlays of panels c and d, respectively

### 3.1.7 *Conclusions*

Rapid nD NMR measurement in combination with advanced processing algorithms opens a new avenue for investigating NMR samples which are intractable by conventional approaches. NUS is the most promising approach and has come into widespread use as a robust method. One of the major criticisms to NUS in combination with non-FT methods has been their questionable reliability in reproducing cross-peaks with proper signal intensity, especially in the case of signals with a wide dynamic range as in NOESY-type experiments. With increasing efficiency of non-FT algorithms, researchers have started using NUS in experiments where quantitative peak analysis is required. As NMR maintains an indispensable role in molecular sciences, further methodological improvements are eagerly awaited in this field.

## 3.2 Data Analysis for Protein Structure Determination

In biomolecular NMR, the subsequent processes of spectrum reconstruction and resonance assignment are required to extract structural information from peak positions, intensities, and linewidths in order to determine three-dimensional (3D) structures of biomacromolecules. It is necessary to accurately deduce structural information from experimental data with its imperfections and uncertainties and to convert it into 3D conformations by NMR structure calculation. Representative data for the structure analysis in current biomolecular NMR include chemical shifts, *J*-couplings, nuclear Overhauser effects (NOEs), paramagnetic effects such as paramagnetic relaxation enhancement (PRE) and pseudocontact shift (PCS), and residual dipolar couplings (RDC). These data can be converted to atom–atom distances, dihedral angles, angles of a bond vector relative to the external magnetic field, and dynamics. Along with the rapid progress of high-performance computing, many NMR structure analysis and data-assisted modelling methods have been proposed for treating the data efficiently. This chapter reviews several methodologies for protein structure data analysis. Since the paramagnetic effects and RDCs are explained in detail in the other chapters, we focus on the data handling for chemical shifts and NOEs, and the currently popular hybrid method with small- and wide-angle scattering (SAXS and WAXS) and small-angle neutron scattering (SANS).

### 3.2.1 *Chemical Shift Data Analysis*

The chemical shift is the most basic and widely used NMR data which is obtained at an early stage of structure analysis. Compared to other NMR data, it can be

measured accurately and with high reproducibility. It has long been recognised that the chemical shift is highly sensitive to local structural differences and useful for 3D molecular structure analysis. However, the accurate structural interpretation of chemical shifts is still a major challenge on account of its intricate dependency on many physical properties. Its interpretation corresponds to an unconstrained inverse problem with an infinite number of solutions. Accordingly, the analysis requires some prior information to restrict the solutions, i.e., empirical knowledge and statistics from a database. Most methods for estimating 3D structure information from chemical shifts are based on statistics of the Protein Data Bank (PDB) and the Biological Magnetic Resonance Data Bank (BMRB).

The most common 3D information derived from chemical shifts is dihedral angle ranges for the protein backbone. Several approaches to deduce dihedral angles have been proposed based on statistical analysis. The chemical shift index (CSI) [45] is a straightforward and widely used method, defining the correlation between chemical shifts and the secondary structure of proteins. The basic strategy of CSI is to identify secondary structure elements by comparing observed shift values to a reference table which is empirically obtained from a set of proteins. CSI converts chemical shifts into an index with three values,  $-1$ ,  $0$ , or  $1$ , based on the difference with the reference. The sequence of the ternary digits describes the segments of  $\alpha$ -helix, random coil, or  $\beta$ -strand, respectively. Although the original CSI used only  $^1\text{H}^\alpha$  chemical shifts [46], the current method employs all backbone atoms of proteins,  $^1\text{H}^\alpha$ ,  $^{13}\text{C}^\alpha$ ,  $^{13}\text{C}^\beta$ ,  $^{13}\text{C}'$ ,  $^1\text{H}^\text{N}$ , and  $^{15}\text{N}$ , for more accurate prediction. Not only a simple classification in terms of the three secondary structure types, but also a more detailed prediction of  $\phi$  and  $\psi$  torsion angles is available from the backbone chemical shifts [47]. Moreover, the approach that takes into account amino acid sequence has been proposed for more accurate chemical shift prediction. It is instructive to employ the information of adjacent amino acids in addition to a given residue so that chemical shift strongly correlates with chemical bonds to different nuclear species. Cornilescu et al. developed the program TALOS that predicts protein backbone torsion angles by searching a database for a sequence containing three residues, a given and its adjacent amino acids, and their chemical shifts. The same group has released improved versions of the software, such as TALOS+ [48] and TALOS-N [49], and hence, using dihedral angle restraints produced by these programs is currently one of the standard approaches for NMR structure calculation.

To extract further information including tertiary structure data from chemical shifts is one of the most difficult issues in current chemical shift analysis. In principle, quantum chemical calculation can provide theoretically computed chemical shift values. Indeed, modern quantum chemical calculation methods are remarkably sensitive to the structural changes of small peptides [50]. However, the approach entails heavy computational cost, which exceeds for macromolecules even the capabilities of current high-performance computing. In addition, it is not trivial to perform the quantum chemical calculation taking account of the large dynamical motions of biomacromolecules that also contribute to chemical shifts. Thus, currently empirical approaches are more realistic candidates to predict the

chemical shifts of proteins. Software using the empirical approach mostly models the chemical shift  $\delta_{\text{pred}}$  as a sum composed of the following terms,

$$\delta_{\text{pred}} = \delta_n + \delta_{\text{aa}} + \delta_{\text{ring}} + \delta_{\text{2nd}} + \delta_{\omega 1} + \delta_{\omega 2} + \delta_{\text{hb}} \quad (3.1)$$

where  $\delta_n$ ,  $\delta_{\text{aa}}$ ,  $\delta_{\text{ring}}$ ,  $\delta_{\text{2nd}}$ ,  $\delta_{\omega 1}$ ,  $\delta_{\omega 2}$ , and  $\delta_{\text{hb}}$  are the contributions of nuclear type, amino acid type, ring current shift, secondary structure, backbone and side-chain torsion angles, and hydrogen bonds, respectively. Some software employs additional contribution terms such as accessible surface area (ASA) and disulphide bonds.

The program SHIFTX2 is one of the most popular software applications for chemical shift prediction from 3D protein structures. It achieved accurate chemical shift prediction with root-mean-square errors (RMSE) of 1.1 ( $^{15}\text{N}$ ),  $\sim 0.5$  ( $^{13}\text{C}$ ), 0.17 ( $^1\text{H}^{\text{N}}$ ), and 0.12 ( $^1\text{H}^{\alpha}$ ) ppm by using additional features to Eq. (3.1), such as pH and temperature. It uses a machine learning algorithm for parameter optimisation in a multiple-regression model, the so-called Bagging ensemble. A high-quality data set containing more than 190 protein structures with known chemical shifts was used for the training of these feature vectors. As an additional function, the software directly exploits chemical shift values in the BMRB when highly homologous proteins exist in the database. The final prediction is obtained by combining two chemical shifts independently predicted based on multiple regression and sequence similarity.

Another representative software, the program SPARTA+, employs an artificial neural network as machine learning algorithm on the basis of known structures and chemical shifts. In addition to the feature terms of Eq. (3.1), it takes account of the N–H-order parameter  $S^2$  for the prediction. Validation with a set of 11 proteins showed RMSEs of 2.45 ( $^{15}\text{N}$ ), 1.09 ( $^{13}\text{C}'$ ), 0.94 ( $^{13}\text{C}^{\alpha}$ ), 1.14 ( $^{13}\text{C}^{\beta}$ ), 0.49 ( $^1\text{H}^{\text{N}}$ ), and 0.25 ( $^1\text{H}^{\alpha}$ ) ppm. According to a comparison by the authors of SHIFTX2, the performance of SPARTA+ for a test set of 61 proteins was comparable with that of SHIFTX2.

An ultimate goal of the chemical shift back calculation is to extract structural information and obtain tertiary structures from chemical shift data. However, up to date structural information derived exclusively from chemical shifts is not sufficient to define the 3D structure of a protein because of its large conformational space. Combining it with molecular dynamics simulation (MD) or structural modelling, on the other hand, may yield tertiary structure models. Those approaches adopt a target function representing the agreement between experimental and predicted chemical shifts, and the force field or statistical data describing the properties of proteins. The program CamShift is a chemical shift back-calculation method aimed at integration with MD [51]. In MD combined with chemical shift prediction, the residual term of the target function requires the shift values computed from atomic coordinates in each MD step, which is generally a very complicated or discrete function. The discontinuous function does not permit to compute its derivate, which is essential

for obtaining the forces and accelerations for the MD calculation. Meanwhile, the target function of CamShift is defined exclusively by a polynomial expansion of the interatomic distances, allowing to rapidly calculate the derivative from the residuals of chemical shifts. Despite using a “naive” equation, the chemical shifts predicted by CamShift are accurate and sensitive to conformational changes. Several protein simulations with MD guided by CamShift show intriguing outcomes, e.g., the characterisation of free-energy landscapes of proteins [51].

A major drawback of MD structure modelling is the high computational cost as a consequence of extensive conformational searching, which exclusively limits the approach to small peptides. Also, the target function consisting of the force field and residual term for chemical shifts is generally not sufficient to define the 3D structure, particularly for larger target proteins. Thus, it is useful to exploit likely conformations predicted statistically from the amino acid sequence because the statistic tendency of 3D structures considerably restricts the conformational space of proteins. CS-Rosetta is the most successful software to obtain tertiary structures based on chemical shift data [52]. Rosetta [53] was originally developed as software for knowledge-based de novo protein structure prediction and has been remarkably successful in the Critical Assessment of Techniques for Protein Structure Prediction (CASP) competition [54, 55]. The basic strategy of Rosetta is to reconstruct global protein structures by assembling short fragments of known protein structures with Monte Carlo sampling, so-called fragment assembly. Shen et al. improved the Rosetta algorithm by combining it with SPARTA chemical shift prediction (CS-Rosetta). The basic flow of Rosetta for protein structure prediction consists of the creation of a large number of candidate conformations and the subsequent selection of the best structures from this ensemble. CS-Rosetta achieves highly accurate modelling assisted by chemical shift prediction with SPARTA in the above two steps of the Rosetta procedure. In the original article, its evaluation with 16 proteins of 56–129 residues showed that it yielded accurate structures with RMSD of 0.7–1.8 Å [52].

### 3.2.2 NOE Data Analysis

Interatomic distance restraints derived from NOE peak intensities are the most important experimental data for NMR structure determination. They employ the relationship that the NOE peak intensity  $I_{ij}$  is proportional to the inverse sixth power of the interproton distance  $r_{ij}$ , scaled by a calibration constant  $\gamma$ ,

$$I_{ij} = \gamma r_{ij}^{-6} \quad (3.2)$$

This straightforward model suggests that the atom distance can be easily estimated from the NOE intensity with the calibration constant. In practical applications, however, it is not trivial to determine the calibration constant on account of

the contribution of several other physical factors. The model neglects spin diffusion, anisotropic global rotational motion, internal dynamics of molecules, signal overlap (ambiguous NOE assignments), the interaction with water molecules, and other experimental errors such as magnetic field inhomogeneity. Thus, many methods of NMR structure determination employ a simple approximation which categorises peak intensities into a few classes with certain distance ranges, e.g., short-, middle-, and long-distance restraints. As another simple approach to obtain NOE distances, the program CYANA [56, 57], which is widely used for NMR structure calculations as well as occasionally for molecular modelling in de novo design of proteins, determines the calibration constant by an assumption that the median intensity in an NOE data set corresponds to a given distance, with a default value of 4.0 Å. Even using these simple approximations, the collection of a sufficient number of distance restraints compensates for the ambiguity of individual data, and this standard method of NMR structure determination is able to determine adequately accurate structures.

For structure refinement or the case that one cannot obtain a sufficient number of NOEs, it is worthwhile to analyse NOE in detail for the acquisition of more exact interproton distances by considering spin diffusion and dynamics.

Taking into account the spin diffusion effect permits to extract distance information from NOEs more accurately. A 2D NOESY cross-peak intensity  $I_{ij}$  derived from a dipolar interaction between spin  $i$  and  $j$  is described as

$$I_{ij} = I_0^j \exp(-\mathbf{R}t_m) \quad (3.3)$$

where  $I_{ij}$  is the cross-peak intensity,  $t_m$  is the mixing time,  $I_0^j$  is the peak intensity of the spin  $j$  when the mixing time is zero, and  $\mathbf{R}$  is the Solomon relaxation matrix. An off-diagonal element in the matrix represents the cross-relaxation rate between the two spins,

$$R_{ij} = \frac{1}{4} (\gamma_H^2 \hbar)^2 (6J_{ij}(2\omega_H) - J_{ij}(0)) \quad (3.4)$$

where  $\gamma_H$  is the gyromagnetic ratio,  $\omega_H$  the Larmor frequency of protons,  $\hbar$  is the reduced Planck constant, and  $J_{ij}(\omega)$  is the power spectral density function. For a vector  $\vec{ij}$  in a molecular tumbling as a symmetric top, the spectral density function is described as,

$$J_{ij}(\omega) = \frac{2}{5} \sum_{k=-2}^2 \frac{\tau_k}{1 + \omega^2 \tau_k^2} \frac{|Y_2^k(\theta_{ij}, \phi_{ij})|^2}{r_{ij}^6} \quad (3.5)$$

where  $\tau_k$  is the correlation time,  $Y_2^k$  are spherical harmonics, and  $r_{ij}$ ,  $\theta_{ij}$ , and  $\phi_{ij}$  are the polar coordinates describing the vector between spins  $i$  and  $j$ . Assuming that there is no internal dynamics, the spectral density function is simplified as

$$J_{ij}(\omega) = \frac{1}{4\pi r_{ij}^6} \frac{\tau_c}{1 + (\omega\tau_c)^2} \quad (3.6)$$

where  $\tau_c$  is the rotational correlation time that can be determined by other experimental methods such as the NMR relaxation measurements. Thus, it is possible to more accurately estimate the peak intensities from the relaxation matrix with the correction of the spin diffusion.

ARIA is one of the most popular software packages for protein structure determination [58]. It includes a function that rapidly calculates an approximate relaxation matrix by iteratively building up the peak intensity from the NOE at  $t_m = 0$ .

$$I(t_m) = (\mathbf{E} - \mathbf{R}\Delta t)^n I(0) \quad (3.7)$$

where  $n\Delta t = t_m$ ,  $\mathbf{E}$  is the identity matrix.  $I(0)$  is a diagonal matrix which is set to the number of equivalent protons attached to a methyl carbon, e.g., three for a methyl group. The authors performed this process for an NOE data set of a pleckstrin homology (PH) domain with 80-ms mixing time in the final step of structure calculation. They demonstrated that structural quality measures such as Ramachandran map statistics and scores of some validation software (WHATCHECK [59], PROCHECK [60], PROSA-II [61], etc.) clearly improved.

Vögeli et al. proposed a method that enables to extract more accurate distance information from NOEs in terms of both experimental and analytical aspects, so-called exact NOEs (eNOE) [62, 63]. This method determines the homonuclear cross-relaxation rate by performing several 3D HMQC-NOESY experiments with different mixing times and converts them into distances based on the model of a rigid molecule. Using the HMQC-NOESY permits to regard as identical relaxation for the diagonal and every of its NOESY cross-peaks since those signals are observed by passing through the same magnetisation pathway. Assuming a rigid target molecule, the interproton distance can be extracted from cross-relaxation rates obtained from NOE peak intensities relative to the reference at  $t_m = 0$ , and a rotational correlation time derived from  $T_1$  and  $T_2$  relaxation experiments. The authors obtained highly accurate interproton distances with an experimental error of  $\sim 0.07$  Å from  $^{15}\text{N}$ -resolved HMQC-NOESY experiments of ubiquitin. The eNOE-derived distances were in excellent agreement with the X-ray structure for distances up to 5 Å but underestimated the ones over 5 Å particularly in loop regions. The authors discussed that this difference attributes to dynamics or conformational artefacts by crystal packing.

### 3.2.3 NMR Protein Structure Determination Based on Bayesian Inference

Conventional NMR structure calculation is an optimisation method which searches the conformational model that best-fits to the experimental data. It neglects the uncertainty resulting from spin diffusion, dynamics, interactions with water and ions, signal overlaps, and noise. Analysing the relaxation matrix as noted above, it is possible to interpret the spin diffusion and dynamics to some extent. However, it remains the ambiguity from uncertain physical factors as well as various experimental artefacts. Those hinder to extract more accurate structure information from the data, as it would be crucial especially in case that one cannot easily obtain a sufficient number of experimental measurements, such as larger or unstable proteins that degrade or precipitate rapidly. In contrary to the optimisation approach, Bayesian probability estimation takes unknown factors into account as the spread of the probability distribution of an explanatory variable. Nilges and co-workers presented an NMR structure calculation method based on Bayes theorem, so-called inferential structure determination (ISD) [64, 65]. Whereas the explanatory variables are fixed to user-defined values in the conventional methods, the Bayesian method can deduce them with a statistical model by parameter sampling schemes. It provides the posterior distribution of conformational ensembles instead of the target function. Moreover, it estimates the contributions of prior and likelihood from the data without a predefined explicit weight factor. Based on the framework of ISD, we also developed Bayesian-assisted structure determination in the program CYANA (CYBAY) [25, 66].

The target function  $T$  of the conventional method consists of the  $\chi^2$ -term between predicted and observed data, the physical potential energy  $E$ , and a weight factor  $w$ ,

$$T(\theta) = \chi^2(\theta) + wE(\theta), \quad (3.8)$$

where  $\theta$  denotes the set of torsion angles used to describe the protein structure. In the framework of Bayes' theorem, the target function can be replaced by the posterior probability for the evaluation of an ensemble of conformations,

$$P(\theta|D) \propto P(\theta)P(D|\theta) \quad (3.9)$$

where  $D$  is the experimental data. Our approach treats NOE data in the framework of Bayesian inference, while the other experimental data are treated in conventional form, e.g., dihedral angle restraints. The likelihood function is described by a lognormal distribution

$$I_{kl} = \frac{\gamma}{r_{kl}^6} \quad (3.10)$$

$$P(I|\theta) = \prod_{i=1}^n L(I_{k_il_i}|\theta) \quad (3.11)$$

$$L(I_{kl}|\theta) = \frac{1}{\sqrt{2\pi\sigma^2 I_{kl}}} \exp\left(-\frac{1}{2\sigma^2} \ln^2\left(\frac{I_{kl}}{\mu}\right)\right) \quad (3.12)$$

where  $I_{kl}$  and  $r_{kl}$  are an NOE intensity and distance derived from spin  $k$  and  $l$ , respectively,  $n$  is the number of peaks,  $\sigma$  is the standard deviation, and  $\mu$  is an expected peak intensity. The prior probability distribution of the Bayesian modelling is

$$P(\sigma, \theta, \gamma) = P(\sigma)P(\theta)P(\gamma) \quad (3.13)$$

$$P(\theta) = \frac{1}{Z(\beta)} \exp(-\beta E(\theta)) \quad (3.14)$$

$$\begin{aligned} \sigma &\sim G[a, b] \\ \gamma &\sim LN[\mu_\gamma, \sigma_\gamma] \end{aligned}$$

where  $a$  and  $b$  are shape and scale parameters of the gamma function  $G$ , respectively,  $LN$  is the lognormal distribution, and  $P(\theta)$  is described as the canonical ensemble of molecular structures with partition function  $Z$  and inverse temperature  $\beta$ .

The sampling algorithm for obtaining the  $\sigma$  and  $\gamma$  parameters is based on Markov chain Monte Carlo (MCMC) with the Gibbs sampler, while the sampling for the canonical ensemble of conformations uses MD because several reports demonstrated that the sampling of protein conformations is far superior to MC due to covalent structure restrictions and the tightly packed globular shape [67, 68]. The target function  $T(\theta)$  in MD is composed of the physical potential  $E(\theta)$  and a pseudo energy  $L(\theta, \gamma, \sigma)$  with  $\gamma$  and  $\sigma$ , which are sampled by the Gibbs sampler,

$$T(\theta) = \beta E(\theta) + L(\theta, \gamma, \sigma) \quad (3.15)$$

$$E(\theta) = \sum E_{\text{dihedral}} + \sum E_{\text{vdw}} + \sum E_{\text{vdw14}} + \sum E_{\text{electro}} + \sum E_{\text{electro14}} + \sum E_{\text{GB}}$$

$$L(\theta, \gamma, \sigma) = \frac{1}{2\sigma^2} \sum_{i=1}^n \ln\left(\frac{V_i r_i^6}{\gamma}\right)$$

where  $E_{\text{dihedral}}$ ,  $E_{\text{vdw}}$ ,  $E_{\text{vdw14}}$ ,  $E_{\text{electro}}$ ,  $E_{\text{electro14}}$ , and  $E_{\text{GB}}$  are energy terms for dihedral angles, van der Waals, 1–4 van der Waals, electrostatic, 1–4 electrostatic, and generalised Born (GB) implicit water model interactions.

In the case of an ambiguously assigned distance restraint with  $m$  assignment possibilities, the distance  $r_i$  is replaced by

$$\bar{r} = \left( \sum_{j=1}^m r_{kj}^{-6} \right)^{-1/6} \quad (3.16)$$

The MD calculation for the conformational sampling adopts torsion angle molecular dynamics (TAMD) that enables to obtain converged structures quickly with longer step-sizes than MD in Cartesian coordinate space. The potential energy of CYANA is a physical force field optimised for torsion angle space derived from the Cartesian space force field of the MD program Amber [69] and with a generalised Born (GB) implicit water model [70]. The physical force field and water model can achieve a more accurate estimation of the prior distribution of the structure ensemble, while TAMD reduces the computational cost for obtaining the marginal likelihood as well as molecular conformations.

We validated the method with NOE peak lists simulated from 3D structures of the proteins ubiquitin and TTHA1718 (PDB accession code 1D3Z and 2ROE). Structure calculations using either the conventional CYANA-OPALp approach or the Bayesian refinement were independently performed with these data sets. First, we tested the peak lists of  $^{13}\text{C}$ -,  $^{15}\text{N}$ -, and  $^{13}\text{C}$ -separated aromatic NOESY spectra derived from ubiquitin structures with arbitrary  $\gamma$  and  $\sigma$  values by CYANA and the Bayesian method. Assuming that the peak intensities reflect not only distance information but also various other physical properties and noise, these peaks were simulated with fluctuations given by a normal distribution with standard deviation  $\sigma$ . The means and standard deviations of the logarithm of the  $\gamma$  values were set to  $22.87 \pm 2.29$ ,  $16.46 \pm 3.75$ , and  $18.14 \pm 4.67$  for producing the  $^{13}\text{C}$ -,  $^{15}\text{N}$ -, and  $^{13}\text{C}$ -aromatic NOE peaks, respectively. Figure 3.5 shows the structures and distributions of the calibration constants  $\gamma$  of ubiquitin computed by the two methods (Fig. 3.5c). The Bayesian calculation was done with a sufficient number of Gibbs sampler MC steps to converge well as indicated by (1) frequent exchange among the 18 different runs (replicas) at all temperatures sampled and (2) that the negative logarithm of the posterior was on average stationary (data not shown). The results demonstrate that the Bayesian method predicts those parameters with fairly accurate distributions for all spectra of ubiquitin. There is no  $\sigma$  in the CYANA calculations because  $\gamma$  values were determined such that the median value of all peak intensities, in a given NOESY spectrum, corresponds to a predefined distance of 4.0 Å. The  $\gamma$  values predicted by CYANA are also relatively accurate despite the fairly naïve assumption for obtaining the distances (Fig. 3.5c, green arrows). Nevertheless, the Bayesian method almost perfectly reconstructs the original distribution of peak intensities in all spectra.

While the conventional method selects 10 or 20 lowest target function structures from 100 conformers, the Bayesian approach predicts the posterior distribution and allows selection of an ensemble from the estimated distribution due to a wider search of the conformational space satisfying current experimental data by MCMC. For graphical representation of the structures, we randomly selected 20% of the total conformers from trajectories run at 300 K. Even showing 180 conformers of

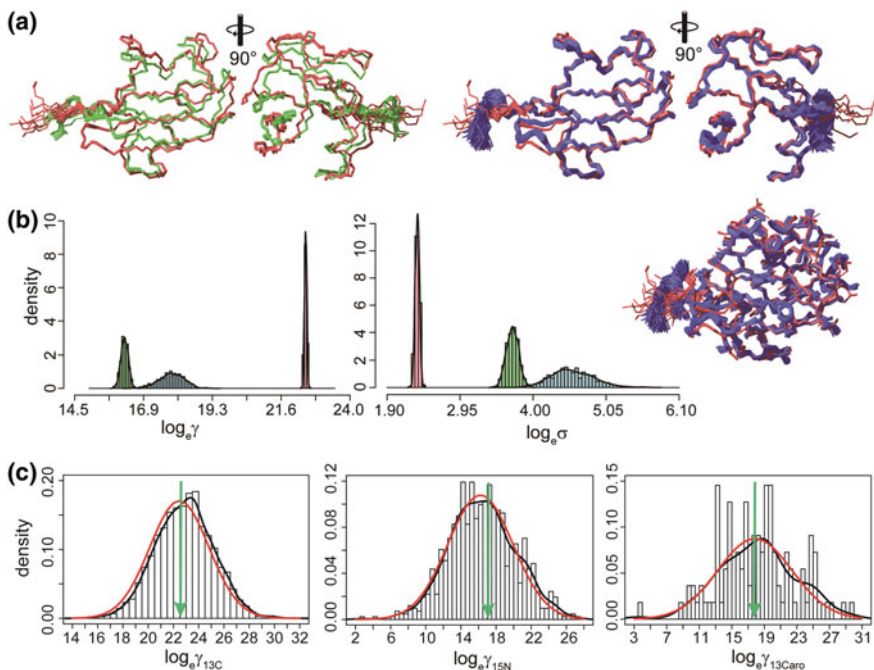


**Fig. 3.5** Bayesian structure calculations with fully simulated ubiquitin NMR data. **a** Superpositions of the 10 reference structures (PDB 1D3Z, red) with ensembles calculated by the conventional CYANA (green) or Bayesian methods (blue). Only the backbone (N, C $\alpha$ , C') atoms are visible. *Lower right* is the superposition of reference and Bayesian conformers with visible side-chain atoms. **b** Distributions of  $\gamma$  and  $\sigma$  for the  $^{13}\text{C}$ -separated NOESY (red),  $^{15}\text{N}$ -separated NOESY (green), and  $^{13}\text{C}$ -separated aromatic NOESY (blue). **c** Histograms and distribution curves of  $\gamma$  for the  $^{13}\text{C}$ -,  $^{15}\text{N}$ -, and  $^{13}\text{C}$ -separated aromatic NOESY spectra. The distributions of  $\gamma$  in the input peaks (black) and predicted by the Bayesian method (red), as well as the values determined by CYANA (green arrows), are shown

ubiquitin in Fig. 3.5a, the structure bundle is well converged, and much closer to the reference structure deposited in the PDB than those of the conventional CYANA method. The RMSDs of the backbone and all heavy atoms were 1.94 and 2.13 Å, respectively, from the reference structure, whereas the Bayesian approach yielded backbone and all heavy atom RMSDs of 0.72 and 1.05 Å, respectively.

We repeated the calculations with reduced peak lists of ubiquitin and TTHA1718, in which 221 and 159 peaks were used, respectively (Fig. 3.6). We selected 20% of the final conformers equal to 20 from the conventional method and 200 from the Bayesian trajectories. Again, the Bayesian method is better converged and closer to the reference PDB for both proteins—as clearly demonstrated by the tube models depicting the C $\alpha$  atom coordinates (Fig. 3.6). Whereas the CYANA calculation yielded backbone RMSDs for ubiquitin and TTHA1718 as 2.73 and 2.22 Å compared to the respective reference structures, the Bayesian approach

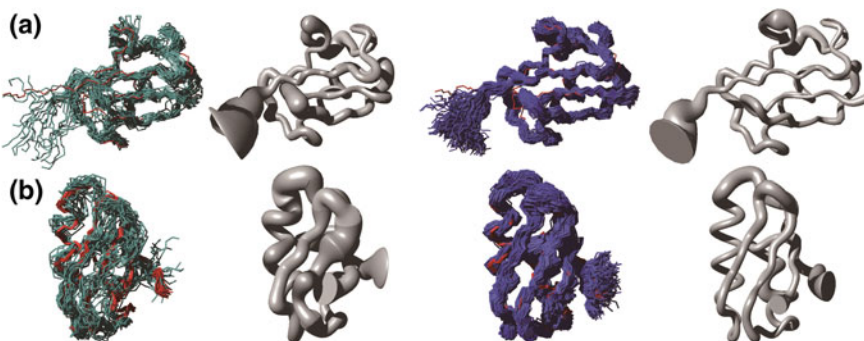


**Fig. 3.6** Structures bundles of two proteins calculated from reduced data sets by the conventional CYANA method (green) and Bayesian refinement (blue) superimposed on conventionally determined reference structures from the full data set (red). **a** ubiquitin. **b** TTHA1718. Deviations of  $C^\alpha$  atoms in the Bayesian-refined conformers are shown as tube models

improved the backbone RMSDs to 2.05 and 1.55 Å, respectively. This shows that the Bayesian approach is also noteworthy for data sets with an insufficient number of peaks and/or imperfect peak intensities.

### 3.2.4 Hybrid Method with Small-Angle Scattering (SAS)

Conventional NMR structure determinations with NOE and chemical shift data may, in rare cases, yield severe conformational errors when the data are not sufficient or include a huge number of noise signals. It is not trivial to circumvent this problem because those methods reconstruct global structures by collecting short-distance and local structure information. This affects in particular the structure determination of larger molecules which requires the reduction in the number of  $^1\text{H}$  nuclei by deuteration, resulting in a severe shortage of distance and dihedral angle restraints. It is necessary to employ additional data which is complementary to the short-range structure information derived from NOEs and chemical shifts. RDC, PRE, and PCS are very sensitive techniques for refining and validating structures on account of their long-range distance information. For the particularly importance for structural analysis, these data are discussed separately in detail in the other chapters. Meanwhile, in the analysis of molecules larger than 100 kDa one encounters a further severe shortage of structural information due to fast transverse relaxation or as a result of perdeuteration for avoiding this relaxation. Even using the state-of-the-art NMR methodology, there are substantial difficulties in determining the global structure of such larger proteins exclusively by solution NMR. Therefore, several groups have developed hybrid NMR structure determination for large molecules by combining NMR data with the data of X-ray and neutron scattering (SAS).

In isotropic molecules, the averaged scattering intensity is observed in all orientations of the molecules with respect to X-ray or neutron beams. The common model describing the scattered intensity is the Debye equation,

$$I(q) = \sum_{i=1}^N \sum_{j=1}^N f_i(q) f_j(q) \frac{\sin(qr_{ij})}{qr_{ij}} \quad (3.17)$$

$$q = \frac{4\pi \sin \theta}{\lambda}$$

where  $\lambda$  is the wavelength of the beam,  $2\theta$  is the scattering angle,  $r_i$  is the atomic coordinate of the atom  $i$ ,  $N$  is the number of atoms in the system, and  $f_i$  is the atomic form factor. The target function for SAS data is described as a  $\chi^2$  statistics,

$$\chi^2 = \frac{1}{N_d - 1} \sum_{k=1}^{N_d} \left[ \frac{I_{\text{exp}}(q_k) - c_k I_{\text{pred}}(q_k)}{\sigma(q_k)} \right]^2 \quad (3.18)$$

where  $N_d$  is the number of data points,  $\sigma$  is the standard deviation of data,  $I_{\text{exp}}$  is the experimental scattering intensity,  $I_{\text{pred}}$  is the scattering intensity computed from a conformation, and  $c_k$  is the scale factor. The atomic form factor is the Fourier transform of the electron distribution around a nucleus of a given atom. To simplify the calculation, the atomic form factor is defined as a constant scalar value, or described by a solvent-corrected model.

$$f_i(q) = f_{v,i}(q) - f_{s,i}(q) \quad (3.19)$$

where  $f_{v,i}$  and  $f_{s,i}$  are the atomic factors of a particular atom in vacuum and solvent, respectively. These atomic factors are given by

$$f_{v,i}(q) = \sum_{i=1}^4 a_i \exp(-b_i(q/4\pi)^2) + c$$

$$f_{s,i}(q) = \rho V \exp(-q^2 V^{2/3}/4\pi)$$

where  $a_i$ ,  $b_i$ ,  $c$  are the Cromer–Mann coefficients for a given atom and  $V$  is the solvent volume. Thus, it is possible to compute the gradient of  $\chi^2$  with respect to the atomic coordinates in a MD calculation and optimise a structure along with conformational restraints derived from NMR data in a structure calculation. Approximate global structures can thus be defined with the score function obtained from SAS data. For instance, multiple-domain proteins can be targets of this approach in that NMR data provide the local structure information within each domain and SAS restricts the relative orientation of the domains.

Venditti et al. [71] have recently applied the hybrid method to the structural analysis of a large system, enzyme I (EI). EI is a  $\sim 128$ -kDa dimer that consists of

two domains (EIN and EIC), and its complex with the histidine phosphocarrier (HPr) has a molecular mass of  $\sim 146$  kDa. The EIN domain is further divided into two subdomains,  $EIN^{\alpha/\beta}$  containing the active site of phosphoryl transfer and  $EIN^\alpha$  interacting with HPr. Three crystal structures of intact EI from different organisms showed strongly different orientations of the  $EIN^\alpha$  subdomain relative to  $EIN^{\alpha/\beta}$ , even though the EIC domains were almost identical. The authors studied the domain orientation in solution by using RDC, small- and wide-angle scattering (SAXS and WAXS), and small-angle neutron scattering (SANS). As the initial structure for structure calculation, the phosphorylated intact crystal structure (PDBID:2HWG) and EIN domain in the EIN–HPr complex determined by NMR (PDBID:3EZA) were used. The EIN and EIC domains were fixed as rigid bodies, and the linker between them was allowed to vary degrees of freedom in the simulated annealing calculations with restraints derived from experimental data. The resulting structure did not agree with the three crystal structures, and the residuals between observed and back-calculated scattering data from the X-ray structures were relatively large. These results suggested that crystal packing artefacts disturbed the domain orientation between  $EIN^\alpha$  and  $EIN^{\alpha/\beta}$  in the crystal structure and offered new insight into large-scale interdomain conformational transitions in solution using the hybrid method with NMR, and X-ray and neutron scattering.

### 3.2.5 Conclusions

In this chapter, we reviewed the data analysis for chemical shifts, NOEs, and the hybrid method with SAS data for NMR protein structure determination. Since the raw NMR experimental data are not direct structural information, it is necessary to convert the NMR data into restraints on distances and dihedral angles by relations that are based on physical principles with some explanatory parameters. In addition, the analysis of sparse or noisy data requires prior information derived from the physical principles and/or statistics from the PDB and BMRB databases, and extensive search of conformations and the explanatory variables. State-of-the-art statistical mathematics and optimisation algorithms along with the acceleration of computational performance can overcome these problems. These technologies provide efficient data analysis which allows to extract more accurate structure information from NMR data and enhance the possible applications of NMR spectroscopy.

**Acknowledgements** The authors thank Dr. Youhei Kawabata for useful discussions regarding solution scattering and Dr. Joshua James Ziarek and Prof. Peter Güntert for a critical reading of this manuscript. We gratefully acknowledge financial supports by Scientific Research on Innovative Areas (JP26102538, JP25120003, JP16H00779 to T.I., and JP15H01645, JP16H00847 to Y.I.) and Grants-in-Aid for Scientific Research (JP15K06979 to T.I.) from the Japan for the Promotion of Science (JSPS) and by the Funding Program for Core Research for Evolutional Science and Technology (CREST JPMJCR13M3) from Japan Science and Technology Agency (JST).

## References

1. Rovnyak, D., Hoch, J.C., Stern, A.S., Wagner, G.: Resolution and sensitivity of high field nuclear magnetic resonance spectroscopy. *J. Biomol. NMR* **30**, 1–10 (2004). doi:[10.1023/B:JNMR.0000042946.04002.19](https://doi.org/10.1023/B:JNMR.0000042946.04002.19)
2. Barkhuijsen, H., Debeer, R., Bovee, W.M.M.J., Vanormondt, D.: Retrieval of frequencies, amplitudes, damping factors, and phases from time-domain signals using a linear least-squares procedure. *J. Magn. Reson.* **61**, 465–481 (1985). doi:[10.1016/0022-2364\(85\)90187-8](https://doi.org/10.1016/0022-2364(85)90187-8)
3. Laue, E.D., Mayer, M.R., Skilling, J., Staunton, J.: Reconstruction of phase-sensitive two-dimensional NMR spectra by maximum entropy. *J. Magn. Reson.* **68**, 14–29 (1986). doi:[10.1016/0022-2364\(86\)90312-4](https://doi.org/10.1016/0022-2364(86)90312-4)
4. Hoch, J.A., Stern, A.S.: NMR Data Processing. Wiley, New York (1996)
5. Kupce, E., Freeman, R.: Fast multi-dimensional Hadamard spectroscopy. *J. Magn. Reson.* **163**, 56–63 (2003). doi:[10.1016/S1090-7807\(03\)00036-3](https://doi.org/10.1016/S1090-7807(03)00036-3)
6. Hyberts, S.G., Arthanari, H., Robson, S.A., Wagner, G.: Perspectives in magnetic resonance: NMR in the post-FFT era. *J. Magn. Reson.* **241**, 60–73 (2014). doi:[10.1016/j.jmr.2013.11.014](https://doi.org/10.1016/j.jmr.2013.11.014)
7. Schanda, P., Brutscher, B.: Very fast two-dimensional NMR spectroscopy for real-time investigation of dynamic events in proteins on the time scale of seconds. *J. Am. Chem. Soc.* **127**, 8014–8015 (2005). doi:[10.1021/ja051306e](https://doi.org/10.1021/ja051306e)
8. Schanda, P., Kupce, E., Brutscher, B.: SOFAST-HMQC experiments for recording two-dimensional heteronuclear correlation spectra of proteins within a few seconds. *J. Biomol. NMR* **33**, 199–211 (2005). doi:[10.1007/s10858-005-4425-x](https://doi.org/10.1007/s10858-005-4425-x)
9. Schanda, P., Van Melckebeke, H., Brutscher, B.: Speeding up three-dimensional protein NMR experiments to a few minutes. *J. Am. Chem. Soc.* **128**, 9042–9043 (2006). doi:[10.1021/ja062025p](https://doi.org/10.1021/ja062025p)
10. Lescop, E., Schanda, P., Brutscher, B.: A set of BEST triple-resonance experiments for time-optimized protein resonance assignment. *J. Magn. Reson.* **187**, 163–169 (2007). doi:[10.1016/j.jmr.2007.04.002](https://doi.org/10.1016/j.jmr.2007.04.002)
11. Pervushin, K., Vogeli, B., Eletsky, A.: Longitudinal <sup>1</sup>H relaxation optimization in TROSY NMR spectroscopy. *J. Am. Chem. Soc.* **124**, 12898–12902 (2002). doi:[10.1021/ja027149q](https://doi.org/10.1021/ja027149q)
12. Kupce, E., Freeman, R.: Projection-reconstruction of three-dimensional NMR spectra. *J. Am. Chem. Soc.* **125**, 13958–13959 (2003). doi:[10.1021/Ja038297z](https://doi.org/10.1021/Ja038297z)
13. Kupce, E., Freeman, R.: Projection-reconstruction technique for speeding up multidimensional NMR spectroscopy. *J. Am. Chem. Soc.* **126**, 6429–6440 (2004). doi:[10.1021/Ja049432q](https://doi.org/10.1021/Ja049432q)
14. Kim, S., Szyperski, T.: GFT NMR, a new approach to rapidly obtain precise high-dimensional NMR spectral information. *J. Am. Chem. Soc.* **125**, 1385–1393 (2003). doi:[10.1021/Ja028197d](https://doi.org/10.1021/Ja028197d)
15. Hiller, S., Fiorito, F., Wuthrich, K., Wider, G.: Automated projection spectroscopy (APSY). *Proc. Natl. Acad. Sci. USA* **102**, 10876–10881 (2005). doi:[10.1073/pnas.0504818102](https://doi.org/10.1073/pnas.0504818102)
16. Barna, J.C.J., Laue, E.D., Mayer, M.R., Skilling, J., Worrall, S.J.P.: Exponential sampling, an alternative method for sampling in two-dimensional NMR experiments. *J. Magn. Reson.* **73**, 69–77 (1987). doi:[10.1016/0022-2364\(87\)90225-3](https://doi.org/10.1016/0022-2364(87)90225-3)
17. Schmieder, P., Stern, A.S., Wagner, G., Hoch, J.C.: Improved resolution in triple-resonance spectra by nonlinear sampling in the constant-time domain. *J. Biomol. NMR* **4**, 483–490 (1994). doi:[10.1007/BF00156615](https://doi.org/10.1007/BF00156615)
18. Rovnyak, D., Frueh, D.P., Sastry, M., Sun, Z.Y., Stern, A.S., Hoch, J.C., Wagner, G.: Accelerated acquisition of high resolution triple-resonance spectra using non-uniform sampling and maximum entropy reconstruction. *J. Magn. Reson.* **170**, 15–21 (2004). doi:[10.1016/j.jmr.2004.05.016](https://doi.org/10.1016/j.jmr.2004.05.016)

19. Frydman, L., Scherf, T., Lupulescu, A.: The acquisition of multidimensional NMR spectra within a single scan. *Proc Natl Acad Sci USA* **99**, 15858–15862 (2002). doi:[10.1073/pnas.252644399](https://doi.org/10.1073/pnas.252644399)
20. Frydman, L., Lupulescu, A., Scherf, T.: Principles and features of single-scan two-dimensional NMR spectroscopy. *J. Am. Chem. Soc.* **125**, 9204–9217 (2003). doi:[10.1021/ja030055b](https://doi.org/10.1021/ja030055b)
21. Kupce, E., Freeman, R.: Two-dimensional Hadamard spectroscopy. *J. Magn. Reson.* **162**, 300–310 (2003). doi:[10.1016/S1090-7807\(02\)00196-9](https://doi.org/10.1016/S1090-7807(02)00196-9)
22. Hyberts, S.G., Heffron, G.J., Tarragona, N.G., Solanky, K., Edmonds, K.A., Luithardt, H., Fejzo, J., Choref, M., Aktas, H., Colson, K., Falchuk, K.H., Halperin, J.A., Wagner, G.: Ultrahigh-resolution  $(^1\text{H})$ - $(^{13}\text{C})$  HSQC spectra of metabolite mixtures using nonlinear sampling and forward maximum entropy reconstruction. *J. Am. Chem. Soc.* **129**, 5108–5116 (2007). doi:[10.1021/ja068541x](https://doi.org/10.1021/ja068541x)
23. Hyberts, S.G., Frueh, D.P., Arthanari, H., Wagner, G.: FM reconstruction of non-uniformly sampled protein NMR data at higher dimensions and optimization by distillation. *J. Biomol. NMR* **45**, 283–294 (2009). doi:[10.1007/s10858-009-9368-1](https://doi.org/10.1007/s10858-009-9368-1)
24. Hamatsu, J., O'Donovan, D., Tanaka, T., Shirai, T., Hourai, Y., Mikawa, T., Ikeya, T., Mishima, M., Boucher, W., Smith, B.O., Laue, E.D., Shirakawa, M., Ito, Y.: High-resolution heteronuclear multidimensional NMR of proteins in living insect cells using a baculovirus protein expression system. *J. Am. Chem. Soc.* **135**, 1688–1691 (2013). doi:[10.1021/ja310928u](https://doi.org/10.1021/ja310928u)
25. Ikeya, T., Ikeda, S., Kigawa, T., Ito, Y., Güntert, P.: Protein NMR structure refinement based on Bayesian inference. *J. Phys: Conf. Ser.* **699**, 012005 (2016). doi:[10.1088/1742-6596/699/1/012005](https://doi.org/10.1088/1742-6596/699/1/012005)
26. Kazmierczuk, K., Zawadzka, A., Kozminski, W., Zhukov, I.: Random sampling of evolution time space and Fourier transform processing. *J. Biomol. NMR* **36**, 157–168 (2006). doi:[10.1007/s10858-006-9077-y](https://doi.org/10.1007/s10858-006-9077-y)
27. Stanek, J., Kozminski, W.: Iterative algorithm of discrete Fourier transform for processing randomly sampled NMR data sets. *J. Biomol. NMR* **47**, 65–77 (2010). doi:[10.1007/s10858-010-9411-2](https://doi.org/10.1007/s10858-010-9411-2)
28. Jaravine, V.A., Orekhov, V.Y.: Targeted acquisition for real-time NMR spectroscopy. *J. Am. Chem. Soc.* **128**, 13421–13426 (2006). doi:[10.1021/ja062146p](https://doi.org/10.1021/ja062146p)
29. Jaravine, V., Ibraghimov, I., Orekhov, V.Y.: Removal of a time barrier for high-resolution multidimensional NMR spectroscopy. *Nat. Methods* **3**, 605–607 (2006). doi:[10.1038/Nmeth900](https://doi.org/10.1038/Nmeth900)
30. Mayzel, M., Rosenlow, J., Isaksson, L., Orekhov, V.Y.: Time-resolved multidimensional NMR with non-uniform sampling. *J. Biomol. NMR* **58**, 129–139 (2014). doi:[10.1007/s10858-013-9811-1](https://doi.org/10.1007/s10858-013-9811-1)
31. Matsuki, Y., Eddy, M.T., Herzfeld, J.: Spectroscopy by integration of frequency and time domain information for fast acquisition of high-resolution dark spectra. *J. Am. Chem. Soc.* **131**, 4648–4656 (2009). doi:[10.1021/ja807893k](https://doi.org/10.1021/ja807893k)
32. Kazmierczuk, K., Orekhov, V.Y.: Accelerated NMR spectroscopy by using compressed sensing. *Angew. Chem. Int. Ed. Engl.* **50**, 5556–5559 (2011). doi:[10.1002/anie.201100370](https://doi.org/10.1002/anie.201100370)
33. Holland, D.J., Bostock, M.J., Gladden, L.F., Nietlispach, D.: Fast multidimensional NMR spectroscopy using compressed sensing. *Angew. Chem. Int. Ed. Engl.* **50**, 6548–6551 (2011). doi:[10.1002/anie.201100440](https://doi.org/10.1002/anie.201100440)
34. Stern, A.S., Donoho, D.L., Hoch, J.C.: NMR data processing using iterative thresholding and minimum  $\ell(1)$ -norm reconstruction. *J. Magn. Reson.* **188**, 295–300 (2007). doi:[10.1016/j.jmr.2007.07.008](https://doi.org/10.1016/j.jmr.2007.07.008)
35. Hyberts, S.G., Milbradt, A.G., Wagner, A.B., Arthanari, H., Wagner, G.: Application of iterative soft thresholding for fast reconstruction of NMR data non-uniformly sampled with multidimensional Poisson Gap scheduling. *J. Biomol. NMR* **52**, 315–327 (2012). doi:[10.1007/s10858-012-9611-z](https://doi.org/10.1007/s10858-012-9611-z)

36. Sun, S., Gill, M., Li, Y., Huang, M., Byrd, R.A.: Efficient and generalized processing of multidimensional NUS NMR data: the NESTA algorithm and comparison of regularization terms. *J. Biomol. NMR* **62**, 105–117 (2015). doi:[10.1007/s10858-015-9923-x](https://doi.org/10.1007/s10858-015-9923-x)
37. Ying, J., Delaglio, F., Torchia, D.A., Bax, A.: Sparse multidimensional iterative lineshape-enhanced (SMILE) reconstruction of both non-uniformly sampled and conventional NMR data. *J. Biomol. NMR* (2016). doi:[10.1007/s10858-016-0072-7](https://doi.org/10.1007/s10858-016-0072-7)
38. Orekhov, V.Y., Jaravine, V.A.: Analysis of non-uniformly sampled spectra with multi-dimensional decomposition. *Prog. Nucl. Magn. Reson. Spectrosc.* **59**, 271–292 (2011). doi:[10.1016/j.pnmrs.2011.02.002](https://doi.org/10.1016/j.pnmrs.2011.02.002)
39. Kurashima-Ito, K., Ikeya, T., Senbongi, H., Tochio, H., Mikawa, T., Shibata, T., Ito, Y.: Heteronuclear multidimensional NMR and homology modelling studies of the C-terminal nucleotide-binding domain of the human mitochondrial ABC transporter ABCB6. *J. Biomol. NMR* **35**, 53–71 (2006). doi:[10.1007/s10858-006-9000-6](https://doi.org/10.1007/s10858-006-9000-6)
40. Schuyler, A.D., Maciejewski, M.W., Stern, A.S., Hoch, J.C.: Nonuniform sampling of hypercomplex multidimensional NMR experiments: dimensionality, quadrature phase and randomization. *J. Magn. Reson.* **254**, 121–130 (2015). doi:[10.1016/j.jmr.2015.02.015](https://doi.org/10.1016/j.jmr.2015.02.015)
41. Bostock, M.J., Holland, D.J., Nietlispach, D.: Improving resolution in multidimensional NMR using random quadrature detection with compressed sensing reconstruction. *J. Biomol. NMR* (2016). doi:[10.1007/s10858-016-0062-9](https://doi.org/10.1007/s10858-016-0062-9)
42. Kazimierczuk, K., Zawadzka, A., Kozminski, W.: Optimization of random time domain sampling in multidimensional NMR. *J. Magn. Reson.* **192**, 123–130 (2008). doi:[10.1016/j.jmr.2008.02.003](https://doi.org/10.1016/j.jmr.2008.02.003)
43. Hyberts, S.G., Takeuchi, K., Wagner, G.: Poisson-gap sampling and forward maximum entropy reconstruction for enhancing the resolution and sensitivity of protein NMR data. *J. Am. Chem. Soc.* **132**, 2145–2147 (2010). doi:[10.1021/ja908004w](https://doi.org/10.1021/ja908004w)
44. Kay, L.E., Keifer, P., Saarinen, T.: Pure absorption gradient enhanced heteronuclear single quantum correlation spectroscopy with improved sensitivity. *J. Am. Chem. Soc.* **114**(26), 10663–10665 (1992). doi:[10.1021/ja00052a088](https://doi.org/10.1021/ja00052a088)
45. Wishart, D.S., Case, D.A.: Use of Chemical Shifts in Macromolecular Structure Determination, Vol. 338. *Methods Enzymol.* Elsevier, New York (2001). doi:[10.1016/s0076-6879\(02\)38214-4](https://doi.org/10.1016/s0076-6879(02)38214-4)
46. Wishart, D.S., Sykes, B.D., Richards, F.M.: The chemical shift index: a fast and simple method for the assignment of protein secondary structure through NMR spectroscopy. *Biochemistry* **31**, 1647–1651 (1992). doi:[10.1021/bi00121a010](https://doi.org/10.1021/bi00121a010)
47. Beger, R.D., Bolton, P.H.: Protein phi and psi dihedral restraints determined from multidimensional hypersurface correlations of backbone chemical shifts and their use in the determination of protein tertiary structures. *J. Biomol. NMR* **10**, 129–142 (1997). doi:[10.1023/A:1018302105638](https://doi.org/10.1023/A:1018302105638)
48. Shen, Y., Delaglio, F., Cornilescu, G., Bax, A.: TALOS+: a hybrid method for predicting protein backbone torsion angles from NMR chemical shifts. *J. Biomol. NMR* **44**, 213–223 (2009). doi:[10.1007/s10858-009-9333-z](https://doi.org/10.1007/s10858-009-9333-z)
49. Shen, Y., Bax, A.: Protein backbone and sidechain torsion angles predicted from NMR chemical shifts using artificial neural networks. *J. Biomol. NMR* **56**, 227–241 (2013). doi:[10.1007/s10858-013-9741-y](https://doi.org/10.1007/s10858-013-9741-y)
50. Sumowski, C.V., Hanni, M., Schweizer, S., Ochsenfeld, C.: Sensitivity of ab initio vs empirical methods in computing structural effects on NMR chemical shifts for the example of peptides. *J. Chem. Theory Comput.* **10**, 122–133 (2014). doi:[10.1021/ct400713t](https://doi.org/10.1021/ct400713t)
51. Granata, D., Camilloni, C., Vendruscolo, M., Laio, A.: Characterization of the free-energy landscapes of proteins by NMR-guided metadynamics. *Proc. Natl. Acad. Sci. USA* **110**, 6817–6822 (2013). doi:[10.1073/pnas.1218350110](https://doi.org/10.1073/pnas.1218350110)
52. Shen, Y., Lange, O., Delaglio, F., Rossi, P., Aramini, J.M., Liu, G., Eletsky, A., Wu, Y., Singarapu, K.K., Lemak, A., Ignatchenko, A., Arrowsmith, C.H., Szyperski, T., Montelione, G.T., Baker, D., Bax, A.: Consistent blind protein structure generation from NMR chemical shift data. *Proc. Natl. Acad. Sci. USA* **105**, 4685–4690 (2008). doi:[10.1073/pnas.0800256105](https://doi.org/10.1073/pnas.0800256105)

53. Bradley, P., Misura, K.M., Baker, D.: Toward high-resolution de novo structure prediction for small proteins. *Science* **309**, 1868–1871 (2005). doi:[10.1126/science.1113801](https://doi.org/10.1126/science.1113801)
54. Moult, J., Pedersen, J.T., Judson, R., Fidelis, K.: A large-scale experiment to assess protein structure prediction methods. *Proteins* **23**, ii–v (1995). doi:[10.1002/prot.340230303](https://doi.org/10.1002/prot.340230303)
55. Kryshtafovych, A., Monastyrskyy, B., Fidelis, K.: CASP11 statistics and the prediction center evaluation system. *Proteins* **84**(Suppl 1), 15–19 (2016). doi:[10.1002/prot.25005](https://doi.org/10.1002/prot.25005)
56. Guntert, P., Mumenthaler, C., Wuthrich, K.: Torsion angle dynamics for NMR structure calculation with the new program DYANA. *J. Mol. Biol.* **273**, 283–298 (1997). doi:[10.1006/jmbi.1997.1284](https://doi.org/10.1006/jmbi.1997.1284)
57. Guntert, P.: Automated NMR protein structure calculation. *Prog. Nucl. Mag. Res. Spectrosc.* **43**, 105–125 (2003). doi:[10.1016/S0079-6565\(03\)00021-9](https://doi.org/10.1016/S0079-6565(03)00021-9)
58. Rieping, W., Habeck, M., Bardiaux, B., Bernard, A., Malliavin, T.E., Nilges, M.: ARIA2: automated NOE assignment and data integration in NMR structure calculation. *Bioinformatics* **23**, 381–382 (2007). doi:[10.1093/bioinformatics/btl589](https://doi.org/10.1093/bioinformatics/btl589)
59. Hooft, R.W., Vriend, G., Sander, C., Abola, E.E.: Errors in protein structures. *Nature* **381**, 272 (1996). doi:[10.1038/381272a0](https://doi.org/10.1038/381272a0)
60. Laskowski, R.A., MacArthur, M.W., Moss, D.S., Thornton, J.M.: Procheck—a program to check the stereochemical quality of protein structures. *J. Appl. Crystallogr.* **26**, 283–291 (1993). doi:[10.1107/S0021889892009944](https://doi.org/10.1107/S0021889892009944)
61. Sippl, M.J.: Recognition of errors in three-dimensional structures of proteins. *Proteins* **17**, 355–362 (1993). doi:[10.1002/prot.340170404](https://doi.org/10.1002/prot.340170404)
62. Vogeli, B., Segawa, T.F., Leitz, D., Sobol, A., Choutko, A., Trzesniak, D., van Gunsteren, W., Riek, R.: Exact distances and internal dynamics of perdeuterated ubiquitin from NOE buildups. *J. Am. Chem. Soc.* **131**, 17215–17225 (2009). doi:[10.1021/ja905366h](https://doi.org/10.1021/ja905366h)
63. Vogeli, B., Kazemi, S., Guntert, P., Riek, R.: Spatial elucidation of motion in proteins by ensemble-based structure calculation using exact NOEs. *Nat. Struct. Mol. Biol.* **19**, 1053–1057 (2012). doi:[10.1038/nsmb.2355](https://doi.org/10.1038/nsmb.2355)
64. Rieping, W., Habeck, M., Nilges, M.: Inferential structure determination. *Science* **309**, 303–306 (2005). doi:[10.1126/science.1110428](https://doi.org/10.1126/science.1110428)
65. Habeck, M., Nilges, M., Rieping, W.: Bayesian inference applied to macromolecular structure determination. *Phys. Rev. E* **72**, 031912 (2005). doi:[10.1103/PhysRevE.72.031912](https://doi.org/10.1103/PhysRevE.72.031912)
66. Ikeya, T., Hanashima, T., Hosoya, S., Shimazaki, M., Ikeda, S., Mishima, M., Guntert, P., Ito, Y.: Improved in-cell structure determination of proteins at near-physiological concentration. *Sci. Rep.* **6**, 38312 (2016). doi:[10.1038/srep38312](https://doi.org/10.1038/srep38312)
67. Northrup, S.H., McCammon, J.A.: Simulation methods for protein structure fluctuations. *Biopolymers* **19**, 1001–1016 (1980). doi:[10.1002/bip.1980.360190506](https://doi.org/10.1002/bip.1980.360190506)
68. Yamashita, H., Endo, S., Wako, H., Kidera, A.: Sampling efficiency of molecular dynamics and Monte Carlo method in protein simulation. *Chem. Phys. Lett.* **342**, 382–386 (2001). doi:[10.1016/S0009-2614\(01\)00613-3](https://doi.org/10.1016/S0009-2614(01)00613-3)
69. Duan, Y., Wu, C., Chowdhury, S., Lee, M.C., Xiong, G., Zhang, W., Yang, R., Cieplak, P., Luo, R., Lee, T., Caldwell, J., Wang, J., Kollman, P.: A point-charge force field for molecular mechanics simulations of proteins based on condensed-phase quantum mechanical calculations. *J. Comput. Chem.* **24**, 1999–2012 (2003). doi:[10.1002/jcc.10349](https://doi.org/10.1002/jcc.10349)
70. Baker, N.A.: Improving implicit solvent simulations: a Poisson-centric view. *Curr. Opin. Struct. Biol.* **15**, 137–143 (2005). doi:[10.1016/j.sbi.2005.02.001](https://doi.org/10.1016/j.sbi.2005.02.001)
71. Venditti, V., Schwieters, C.D., Grishaev, A., Clore, G.M.: Dynamic equilibrium between closed and partially closed states of the bacterial Enzyme I unveiled by solution NMR and X-ray scattering. *Proc. Natl. Acad. Sci. USA* **112**, 11565–11570 (2015). doi:[10.1073/pnas.1515366112](https://doi.org/10.1073/pnas.1515366112)

# Chapter 4

## Advances in High-Field DNP Methods

Yoh Matsuki and Toshimichi Fujiwara

**Abstract** Magic-angle sample spinning NMR (MAS NMR) spectroscopy is a powerful tool for studying atomic resolution structure and dynamics of insoluble and/or non-crystalline molecular systems such as membrane proteins and amyloid fibrils, but suffers from its low sensitivity. Dynamic nuclear polarization (DNP) is an emerging technique that enhances the NMR sensitivity by transferring large electron spin polarization to the nuclei of interest through a high-power microwave irradiation, enabling aforementioned molecular structural and dynamical studies at unprecedented signal receptivity. Despite the remarkable advances achieved in the past two decades, the current high-field DNP-MAS NMR method still endures a number of limitations and difficulties. This thus calls for a further sophistication of the method, especially for implementing it at very high-field conditions, which is crucial for high-resolution studies targeting systems with ever-increasing size and complexity. This chapter aims at providing an overview on the contemporary high-field DNP instruments and methods. Together with the current success, the authors highlight the remaining technical issues and limitations to give a baseline for the future development and innovation. Detailed description of the instruments as well as the DNP samples should provide a useful piece of information for managers of DNP spectrometers for avoiding/solving day-to-day technical problems, as well as for users to improve their sample setups, or to design a new research plan.

**Keywords** Dynamic nuclear polarization (DNP) · Sensitivity enhancement  
Magic-angle spinning solid-state NMR · High-field condition · Microwave

---

Y. Matsuki · T. Fujiwara (✉)  
Institute for Protein Research, Osaka University, Osaka, Japan  
e-mail: tfjwr@protein.osaka-u.ac.jp

## 4.1 Introduction

Magic-angle spinning NMR (MAS NMR) is one of the most powerful tools for studying structure and dynamics of not only crystalline, but also amorphous molecular systems including polymers [1, 2], inorganic materials [3] and bio-macromolecules [4] at atomic resolution, but suffers from its low sensitivity. Dynamic nuclear polarization (DNP) enables orders of magnitude sensitivity enhancement of MAS NMR by transferring high electron spin polarization to the nuclei of interest with an irradiation of strong microwave at the frequency near the electron spin resonance (ESR). Although the phenomenon of DNP has been known almost for the entire history of the NMR itself that dates back to 1940s, the key breakthrough toward high-field ( $B_0 > 5$  T), high-resolution application of DNP was only achieved in 1993, in which a vacuum electron device, gyrotron, was introduced as a new radiation source for DNP [5]. Since then, the following two decades have witnessed rapid advances of high-field DNP in both the instruments and methodologies that include the development of the cross-effect (CE)-based DNP methods [6], biradical polarizing agents that efficiently drive the CE-DNP [7–9], high-frequency gyrotrons [10–13] and NMR probes. To date, the DNP-enhanced MAS NMR is receiving growing popularity under the field conditions of up to 9.4 T and has been applied to many different types of samples.

At even higher magnetic field, however, the popularity seems to relax partly due to the relative inefficiency of the current CE-based DNP process as compared with at lower fields. In combating these issues, hardware innovation should play a key role, and so far, tremendous efforts have been made on the development of advanced gyrotrons [14–17], more competent DNP-NMR probes [18–21], efficient cryogenic MAS systems [22, 23] and the pulse DNP instruments [20], for which research level innovations are most actively undertaken at Massachusetts Institute of Technology (MIT), USA, and at Institute for Protein Research (IPR), Osaka University, Japan. Based on these efforts, high-field DNP-MAS NMR spectrometers are now operative at  $B_0 = 5$  T (212 MHz  $^1\text{H}$  frequency), 11.7 T (500 MHz), 14.1 T (600 MHz), 16.4 T (700 MHz) and 18.7 T (800 MHz), and many commercial spectrometers [24] are up and running worldwide.

Although impressive were the technical advances in the past decades, the contemporary high-field DNP method still endures a number of limitations, and a further sophistication is called for in its all aspects including the instruments, polarizing agents and the methodologies. This chapter aims at providing a detailed overview on the current high-field DNP instruments and methods, discussing their merits and drawbacks from a practical point of view and providing a baseline for the future developments. Details given here are at a level not required for mere users, especially when the aforementioned commercial DNP spectrometers are operated, but will still provide an idea for managers of DNP spectrometers for avoiding/solving day-to-day technical problems. Understanding molecular details of successful (and also unsuccessful) DNP samples and the elemental DNP processes taking place in a sample will be helpful also for users for improving their

sample setups, or for designing a new research plan. Furthermore, looking to alternative NMR vendors in the future that will possibly participate manufacturing DNP spectrometers at various levels of system flexibility, we believe that a summary of the current status with basic and practical caveats should be instructive for the future users. The next section (Sect. 4.2) takes a glance at the essential components of the high-field DNP system, and the following sections (Sects. 4.3–4.6) separately discuss each part in greater detail. Finally, a short section (Sect. 4.7) concludes the chapter with a future outlook.

## 4.2 Overview of a DNP-NMR System

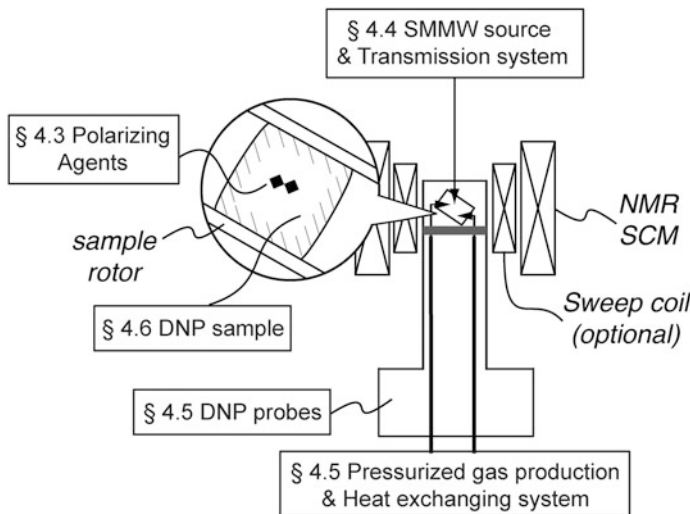
The ESR frequency for  $g \sim 2$  electron under “high-field” condition in the contemporary NMR sense ( $B_0 = 14.1\text{--}28.2$  T for 600–1200 MHz  $^1\text{H}$  frequency) corresponds to  $\omega_e/2\pi = 395\text{--}790$  GHz. This high-frequency wave falls between the radio waves and infrared light, whose wavelength is 0.76–0.38 mm. Thus, they are called variously in the literatures such as “submillimeter waves,” “terahertz waves” or somewhat loosely high-frequency “microwave”. In the following text, we adopt “submillimeter wave (SMMW)” when high fields are concerned, and “microwave” in more general statements.

Figure 4.1 overviews the essential components in a contemporary DNP-NMR system. They involve a polarizing agent as the electron source (Sect. 4.3), a SMMW source and its transmission system (Sect. 4.4), a DNP-NMR probe together with a cryogenic spinner gas generation system (Sect. 4.5). The sample setup will be discussed in Sect. 4.6.

## 4.3 DNP Mechanisms and Polarizing Agents

In this section, the basic accounts on the DNP mechanisms and on relevant polarizing agents are given in mainly qualitative terms. The question of why biradicals perform better than monomeric radicals at high fields will also be briefly addressed.

The phenomenon of DNP has already come to an inception of Albert Overhauser in the beginning of 1952 [25], soon after the discovery of the NMR itself. His idea was later experimentally confirmed by Charles Slichter at very low field condition (0.03 T) for Li metal powder sample [26]. The field strength in this case was limited by the skin depth of the metallic sample. The mechanism for the electron to nuclear (e–n) polarization transfer in action was the one now known as the Overhauser effect (OE). The same effect acting between two nuclear spins is well known as the “nuclear Overhauser effect (NOE)”. In this mechanism, the polarization of the electron spin leaks into the hyperfine-coupled nuclear spin via the cross-relaxation process, upon perturbation on the electron spin. Naturally, for this pathway to work,



**Fig. 4.1** Essential components of a DNP-NMR system. Each component will be discussed in the section indicated. The superconducting “sweep coil” could become unnecessary if the SMMW source goes fully frequency-tunable (see Sect. 4.4.3)

a stochastic fluctuation of the local field is necessary in the background whose spectral density is nonzero at the frequency of the DQ or ZQ transitions in an electron–nuclear (e–n) two-spin system (Fig. 4.2a). In the two-spin system, the transitions in question are located near the ESR frequency ( $\omega_e/2\pi$ ) and thus require fast field fluctuations in the order of  $\omega_e/2\pi$  (1/s). It follows that the DNP via OE is most effective in metals [26] and solution samples [27], where the motion of the free electrons or the Brownian molecular motion provides the necessary time dependence. In a same token, OE-DNP should be inefficient at high fields ( $B_0 > 5$  T) where the rate of the required fluctuation tends to be too high ( $\sim 10^{11}$  1/s), and the spectral density approaches to zero due to the absence of such fast motion in a sample. Nevertheless, some research groups have recently reported a significant OE-DNP signal enhancement in liquid samples at field conditions of up to 9.2 T [28–31] and suggested a need for further investigation on the mechanism. Even more surprising was the discovery of the OE-DNP phenomenon in insulating solids (no metal, no solution!) at very high fields (9.4–18.8 T) [32]. Detailed accounts on these new observations are still awaited, calling for more experimental data and theoretical development to clarify the physics underlining the phenomenon.

From 1960s to 1970s, two more DNP mechanisms, namely the solid effect (SE) [33, 34] and cross-effect (CE) [35–39] have been put forth and characterized. They both assume no inherent time dependence and work through a stationary hyperfine coupling, thus in solid samples. In the late 1980s, the SE was combined with MAS NMR at low fields ( $\sim 1.4$  T) and has found some use in chemical and

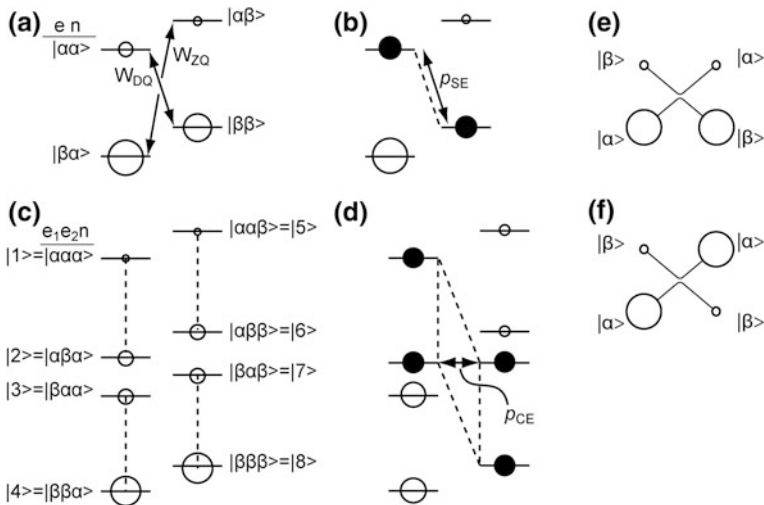


**Fig. 4.2** Energy level diagrams for the OE, SE and CE-DNP mechanisms. **a, b** Four energy levels for an e-n two-spin system. In **a** the DQ and ZQ cross-relaxation rates are indicated. In **b** the DQ transition is irradiated for a positive SE-DNP enhancement. The populations driven to saturation by the SMMW irradiation are indicated by the dashed lines and filled circles. **c, d** Eight levels for an  $e_1-e_2-n$  three-spin system. In **d** the low-frequency electron ( $e_2$ ) is irradiated for a positive CE-DNP enhancement. **e, f** Energy levels at a level anti-crossing (LAC) shown for the adiabatic (**e**) and non-adiabatic crossing (**f**)

polymer sciences [40–43]. The field condition was now mainly limited by the availability of suitable light source for the ESR excitation. The SE-DNP is also explained with a hyperfine-coupled e-n two-spin system (Fig. 4.2b). At high fields, the relevant four spin states are all close to the direct product states except for the slight admixture of the state  $|\alpha\alpha\rangle$  with  $|\alpha\beta\rangle$ , and  $|\beta\alpha\rangle$  with  $|\beta\beta\rangle$  due to the hyperfine coupling. These states are separated by the nuclear Zeeman energy in the order of >600 MHz for protons at high fields and thus difficult to mix with moderate hyperfine coupling (usually  $\sim 50$  MHz or less). A resultant slight admixture of the spin states weakly allows the originally forbidden DQ and ZQ transitions. Thus, the SMMW irradiation at the frequency

$$\omega_{SMMW} = \omega_e \pm \omega_n, \quad (4.1)$$

where  $\omega_e$  and  $\omega_n$  are the electron and nuclear Larmor frequencies, drives the DQ/ZQ transition toward the saturation, resulting in the positively/negatively enhanced nuclear polarization. Figure 4.2b shows the result of the DQ irradiation for the positive SE-DNP (denoted as SE-DNP(+)). The enhancement maxima for DNP(+) and (-) are thus separated by *twice* the nuclear Zeeman frequency, which is often identified as a characteristic of the SE-DNP phenomenon. If the EPR line is broader than the nuclear Zeeman frequency, the positive and negative effects start to cancel to each other; thus, the SE-DNP requires narrow-line radicals  $\delta$ ,  $\Delta < \omega_n$ ,

where  $\delta$  and  $\Delta$  are the homogeneous and inhomogeneous ESR linewidth. So far, 1,3-bis(diphenylene)-2-phenylallyl (BDPA), trityl radical, and some transition metal ion complexes have been used for SE-DNP (Fig. 4.3).

The DQ/ZQ transition probability  $p_{SE}$  is proportional to the SMMW amplitude  $\omega_{te}$ , pseudo-secular hyperfine coupling  $h_{xz}$ , and the nuclear Zeeman frequency  $\omega_n$  as  $p_{SE} \propto (\omega_{te} h_{xz}/\omega_n)^2$ . It follows that the efficiency of the SE-DNP degrades with the external field in proportion to  $1/B_0^2$ . Also, it is seen that strong SMMW is required for a significant transition rate. As a consequence, a high signal enhancement (>100) at high fields (>5 T) has only been observed so far for a sample contained in a capillary, and irradiated in a coiled TE<sub>011</sub> cavity [20]. Much more moderate enhancements have been obtained at 9 T using Mn/Gd–DOTA complexes [44, 45], where DOTA stands for the octadentate chelating ligand 1,4,7,10-tetraazacyclododecane-1,4,7,10-tetraacetic acid. Still, SE-DNP can remain to be interesting or potentially important mechanism at very high fields ( $\gg 10$  T) because the linewidth of the central transition of non-Kramers metal ions, for example, is governed by the second-order zero-field splitting (ZFS), and can become progressively narrower with increasing external field, allowing more efficient electron saturation at higher fields. This is in contrast to the situation for the CE-based DNP.

The CE-DNP is described in an  $e_1$ – $e_2$ –n three-spin system. The resultant eight spin states are again almost in the direct product states (Fig. 4.2c), except for the central four states |2), |3), |6), |7) weakly perturbed under the influence of the

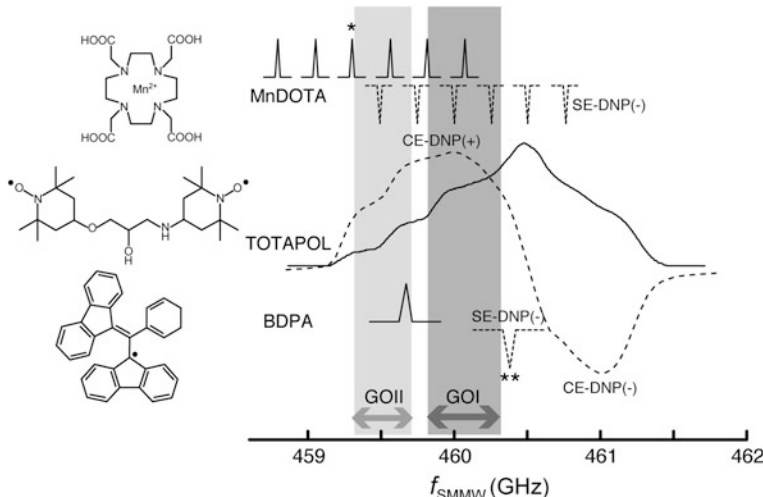


**Fig. 4.3** Chemical structures and schematic ESR spectra (solid lines) of some popular polarizing agents used in high-field DNP. Typical DNP frequency profiles are shown with broken lines. Only the negative DNP effect (DNP $(-)$ ) is shown for Mn–DOTA and BDPA.  $B_0 = 16.4$  T is assumed. Typical SMMW frequency ranges of two tunable gyrotrons operating at Osaka University (called GOI and GOII) are shaded

second-order off-diagonal element from the hyperfine as well as the e–e dipolar couplings. The perturbation is maximized when two levels, e.g., |2⟩ and |7⟩ are nearly degenerate (Fig. 4.2d), which is realized when the differential electron Zeeman frequency matches the nuclear Zeeman frequency as

$$\pm\omega_n = |\omega_{e1} - \omega_{e2}|, \quad (4.2)$$

where  $\omega_{e1}$  and  $\omega_{e2}$  are the ESR frequencies of the electron 1 and 2. This “frequency matching” condition drives an intriguing e<sub>1</sub>–e<sub>2</sub>–n three-spin flips, providing a path for the electron polarization to flow into the nuclei. In other words, in the CE-DNP, the energy quanta produced by the differential electron Zeeman energy act as a springboard for an efficient delivery of the electron polarization to the nucleus at high fields; this springboard effect did not exist for the SE-DNP. The probability of the three-spin flip  $p_{CE}$  is proportional to  $(d_{ee} h_{xz}/\omega_n)^2$ , where  $d_{ee}$  is the electron–electron dipolar coupling constant. Note that in comparison with  $p_{SE}$ ,  $\omega_{1e}$  is replaced with  $d_{ee}$  for the CE-DNP. Since the e–e dipolar coupling can be much stronger ( $\sim 30$  MHz or more for biradicals) than the SMMW amplitude (usually  $<1$  MHz), the CE-DNP is generally more efficient than SE-DNP. Also, because the CE-DNP is initiated with the allowed electron transition, a high signal enhancement is obtained with much weaker SMMW irradiation than for SE.

Overall, as illustrated in Fig. 4.2d, upon irradiation of, for example, the lower-frequency electron (e<sub>2</sub>), all the connected spin states |1⟩–|2⟩–|7⟩–|8⟩ are driven toward saturation, and a net positively enhanced nuclear polarization is produced. Similarly, an irradiation of the higher frequency electron (e<sub>1</sub>) will result in the negative nuclear spin enhancement from a saturation of the spin states |5⟩–|7⟩–|2⟩–|4⟩. The positive and negative maxima of the CE-DNP enhancements are thus separated by  $\omega_n$ , which is often identified as a characteristic for the CE-DNP phenomenon.

The electron pair satisfying the CE frequency matching is conveniently realized by a use of broad-line radicals (Fig. 4.3), for which  $\Delta > \omega_n$ . For instance, the breadth of the nitroxide radicals such as (2,2,6,6-tetramethylpiperidin-1-yl)oxyl (TEMPO) and 1-(TEMPO-4-oxy)-3-(TEMPO-4-amino)propan-2-ol (TOTAPOL) is dominated by the g-anisotropy and easily exceeds  $\omega_n$ . Thus, with randomly oriented TEMPO, a finite number of spin isochromats always satisfy the matching condition. Biradical polarizing agents provide an improved solution to this: Two nitroxide radicals are covalently bound so that the frequency matching isochromats are always under the influence of strong e–e dipolar coupling. Indeed, biradicals such as bis-TEMPO-2-ethyleneglycol (BT2E) and TOTAPOL has improved the then maximum enhancement of  $\varepsilon_{on/off} \sim 40$  obtained with 40 mM monomeric TEMPO to  $\sim 180$  at  $B_0 = 5$  T [7, 9]. An additional merit is that biradicals can work at low concentration ( $\sim 5$  mM) and thus less prone to the paramagnetic signal broadening. In 2008, the first biradical bis-TEMPO-bisketal (bTbK) aiming also at

optimizing the frequency matching condition based on a rigidly twisted molecular structure was proposed [8] and stimulated a number of subsequent applications and developments [46–48]. To date, various types of nitroxide biradicals, such as so-called AMUPol, TEKPol, either water-soluble or hydrophobic, have been designed and synthesized [49], and still under an intense research and development.

Above description of the CE-DNP should be slightly modified under MAS, where the electron  $g$ -tensor rotates with the sample rotation. This causes the energy levels shown in Fig. 4.2 a periodic modulation with the amplitude set by the  $g$ -anisotropy. As a result, the energy levels  $|2\rangle, |3\rangle, |6\rangle, |7\rangle$  might cross each other (often more than once) in a rotor revolution. In fact, however, the levels mediated by nonzero off-diagonal elements do not cross to each other, but form the level anti-crossing (LAC) [50]. At a LAC, if the levels go by sufficiently slowly (i.e., adiabatically) so that the off-diagonal element has enough time to act, then the spin-state population can follow the energy levels as if it is bounced by the gap at the LAC (Fig. 4.2e). On the other hand, if it is too fast, the population will stick to the same spin state as if it goes across the gap (Fig. 4.2f). For an elementary example, consider the electron excitation with the SMMW: In a rotating frame of the SMMW frequency, the two energy levels nearly cross each other at the ESR condition; if the SMMW of amplitude  $\omega_{1e}$  have enough time ( $>1/\omega_{1e}$ ) close to the resonance, the spin population in the down-spin state will be transferred to the up spin adiabatically (electron spin excitation). If the sweep is too fast, no excitation occurs. In a similar manner, the electron excitation as well as the three-spin flip occurs instantaneously and sequentially at corresponding LACs during a sample rotation. The overall efficiency of the DNP process is then governed by the probability of the adiabatic population transfer at these LACs,  $p_{\text{exc}}$  and  $p_{\text{CE\_MAS}}$ , respectively, as well as the electron relaxation between LACs. The approximate probability is given in the Landau-Zener formulation [51],

$$p_{\text{exc}} \propto \frac{\omega_{1e}^2}{\partial \omega_e / \partial t}, \quad (4.3a)$$

$$p_{\text{CE\_MAS}} \propto \frac{d^2 h_{xz}^2}{\omega_n^2 \partial(\omega_{e1} - \omega_{e2}) / \partial t}. \quad (4.3b)$$

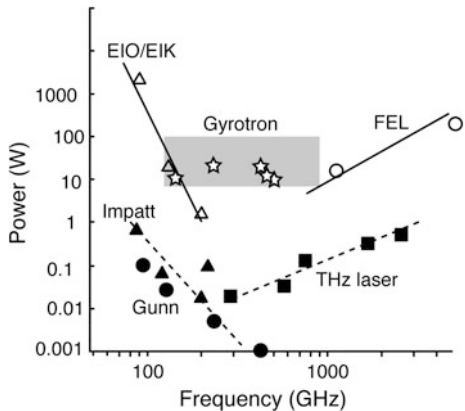
From these expressions, it can be seen that the efficiency of the CE-DNP under MAS may degrade with increasing external field faster than  $1/B_0$ , since the CE transition imposes stronger bottleneck, being proportional to  $1/B_0^3$  (Eq. 4.3b), than the electron excitation proportional to  $1/B_0$  (Eq. 4.3a). Experimental CE-DNP enhancement factors observed at  $T \sim 90$  K using TOTAPOL,  $\varepsilon_{\text{on/off}} \sim 180$  @5 T,  $\sim 100$  @9.4 T,  $\sim 60$  @14.1 T,  $\sim 40$  @16.4 T and  $\sim 20$  @18.8 T, roughly correspond to the trend  $1/B_0^p$ , with  $p = 1-1.5$ .

## 4.4 SMMW Sources and Transmission Systems

### 4.4.1 Various Light Sources and Gyrotron

The SMMW required for the high-field DNP experiments falls on the frequency range of 0.1–1 THz. This is, by unfortunate coincidence, one of the most “troublesome” frequency ranges, where the practical technology for generating and detecting the radiation is strongly underdeveloped. For example, a plot of the average output power versus frequency for the conventional wave sources exhibits a dip or the so-called THz-gap in the very frequency range we concern for DNP (Fig. 4.4). This is because the conventional microwave tubes and laser equipment have the limited power extraction efficiency at this frequency range owing to the unfavorable interaction structure (as detailed below) or low individual photon energy, respectively. The average power from the free electron lasers (FEL) is often limited by the low duty factor as well as the high wiggler  $K$  factor required for longer wavelength output that reduces the gain. The maximum power output from the solid-state sources such as Gunn and IMPATT diodes combined with an amplifier multiplier chain (AMC) only reaches  $\sim 200$  mW at 264 GHz (for 400 MHz DNP-NMR). Although this has enabled some DNP measurements at very low sample temperatures [52], the signal enhancement was low especially at moderate temperatures such as  $T \sim 90$  K due to the insufficient power delivered to the sample. Considering the rapid power drop at even higher frequencies (e.g.,  $\sim 15$  mW at 460 GHz), these sources are not promising at the moment for high-field DNP. The conventional “slow-wave” vacuum electron devices (VED) such as extended interaction klystron (EIK), traveling-wave tube (TWT) and backward-wave oscillators (BWO) follow a similar trend. In these devices, a linear beam interacts with a periodic circuit, which supports slow electromagnetic waves. The periodic structure slows down the electromagnetic waves to a subluminous speed (i.e., the phase velocity  $<$  speed of light) to make them synchronous with an electron beam. One can think of the periodic structure as presenting obstacles to the propagation of the electromagnetic wave to slow it down. The period of these obstacles is typically a fraction of the operating wavelength, and hence, these structures become very fragile at millimeter and submillimeter wavelengths. This is the main reason for the difficulty in generating SMMW with high power and ensuring a long lifetime of the device. A “fast-wave” VED, gyrotron, on the other hand uses a periodic beam (gyrating beam) with a smooth circuit, which supports fast waves (phase velocity  $>$  speed of light). In other words, the gyrotron transfers part of the complexity of operating at higher frequency from the circuit to the electron beam by requiring a periodic beam: The electrons in the beam have to gyrate at a cyclotron frequency that is either equal to or a subharmonic of the desired output frequency. The smooth wall circuit makes also fabrication easier and increases thermal handling capability, and favors the device lifetime. Furthermore, the gyrotron can operate selectively in a higher-order mode of the resonator, thus allowing larger transverse dimensions and higher power handling capability at the

**Fig. 4.4** A plot of the average/CW output power versus frequency for the conventional solid-state (*filled symbols*) and vacuum electron devices (*open symbols*). A region relevant to the high-field DNP is *shaded*



frequency range in question enabling  $\gg 10$  W output at 460 GHz. Since it was introduced in 1993, gyrotron still remains to be the primary source of choice for DNP-NMR spectroscopy.

The need of high-power output is due to the dimensional mismatch between the NMR sample (e.g., 5 mm length by 2.4 mm diameter in a  $3.2\varphi$  rotor) and the SMMW wavelength ( $\ll 1$  mm); it is difficult to construct any resonator structure around a sample, leading to very poor power-to- $B_{1e}$  conversion efficiency. Alternatively, the sample could be irradiated at a low field (e.g., 0.35 T) to hyperpolarize the nuclear spins and then transferred to a higher field for high-resolution observation. This mode of operation has been adopted in some solution-DNP setups in which a sample tube can travel back and forth between two magnetic fields [53, 54] and in the “dissolution” DNP setups in which a frozen sample is polarized at a low field (3.5 T often at 1.5 K using 95 GHz wave), and then is dissolved before being transferred to high-field solution-NMR or MRI magnets [55, 56]. Although it mitigates the technical challenge in the electron excitation, it generates other challenges due to the need for the mechanical sample shuttling over distance. Therefore, this mode is unsuited for experiments requiring repetitive scans such as multi-dimensional NMR and/or those requiring stable MAS, and for samples sensitive to the huge temperature cycle such as biological samples.

Gyrotrons have been extensively used in plasma heating where most often they have been operated at low frequencies  $< 200$  GHz and high power of up to 1 megawatt. In introducing gyrotron into the spectroscopy use, the challenges included the requirement for much higher frequency (up to 1 THz), very high stability of the power ( $< 1\%$ ) and frequency ( $< 1$  ppm) for long term (for weeks) in a continuous wave (CW) mode. Although the required power (10–100 W) is not high compared to the larger and higher power gyrotrons (megawatt level) used in nuclear fusion applications, it is important to have very good cooling and temperature control of the cavity to ensure high frequency stability as the thermal expansion of

the gyrotron cavity will lead to a frequency reduction. These rather stringent criteria for the DNP-NMR spectroscopy have been addressed in the past decades, making gyrotron a viable source for DNP as discussed in the following.

#### 4.4.2 Principles of Gyrotron

The principle of gyrotron oscillation is briefly summarized here. The detailed theory and quantitative treatment is found in many review articles [57, 58] and textbooks such as [59]. In brief, a gyrotron generates SMMW by converting the rotational (transverse) kinetic energy of the electrons in a gyrating motion into electromagnetic radiation. By synchronizing the relativistic cyclotron frequency of the gyrating electrons with a resonant transverse electric (TE) mode in the cavity, the kinetic energy of the electron beam can be used to excite an absolute instability (gyrotron oscillator in which the background noise in the cavity serves as an input) or a convective instability in which a weak input signal is amplified (gyrotron amplifier). Figure 4.5 compiles the essential components: (a) the vacuum tube that holds a resonator cavity (b) in the middle, an electron gun (c) that supplies the electrons beam on the one end and a collector (d) that collects the spent electrons on the other

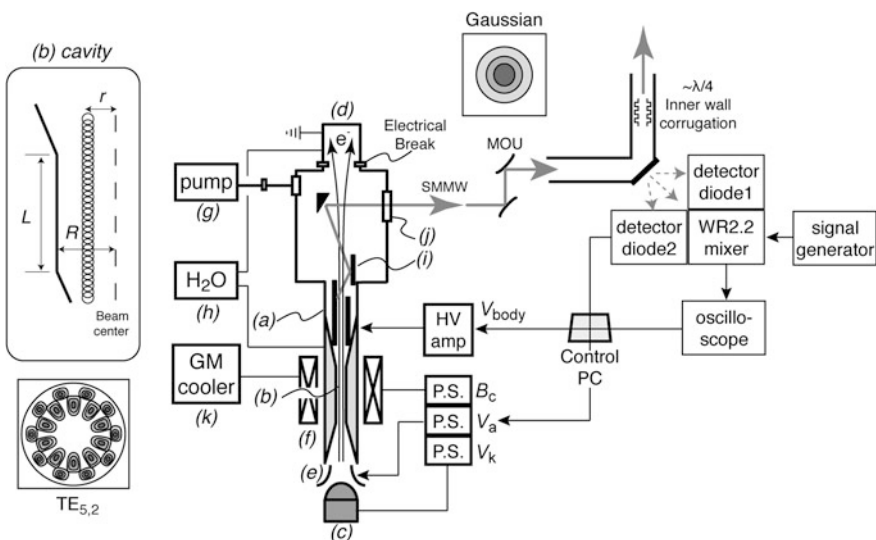


**Fig. 4.5** Essential components of a DNP gyrotron. The system for the real-time frequency and power monitoring/feedback control is shown on the right. *a* gyrotron tube, *b* resonant cavity, *c* electron gun, *d* collector, *e* modulation anode, *f* SCM, *g* vacuum pump, *h* chilled water circulator, *i* internal mode converter, *j* output window and cryo-cooler for the SCM (*k*). A typical cavity structure is illustrated in the *inset* on the left. Contour plots of the  $E$ -field amplitude for the TE<sub>5,2</sub> mode in the cavity (*b*) and the Gaussian mode after the mode convertor (*i*) are also shown

end. Beside the electron gun that works as a cathode, there is a modulation anode (e) if a triode electron gun is employed. The cylindrical cavity consists of a short straight section ( $L \sim 20$  mm) terminated with up tapers at both input and output ends forming an open-ended resonator (Fig. 4.5b, inset). The magnetic field  $B_c$  at the cavity (roughly 7–15 T for the high-field DNP) produced by a superconducting magnet (SCM) (f) guides the electrons through the cavity and determines the frequency of the cyclotron motion in the cavity. The turbo-molecular pump or ion pump (g) evacuates the tube to  $10^{-6}$  Pa or less. The cavity and the collector are actively cooled with a chilled water flow (h). The SMMW generated at the cavity is shaped using the internal mode converter (i) and then radiated through the window (j) while the spent electrons go on to the collector, where the electrons energy is converted to heat. The beam shape often receives further correction using an external matching optic unit (MOU).

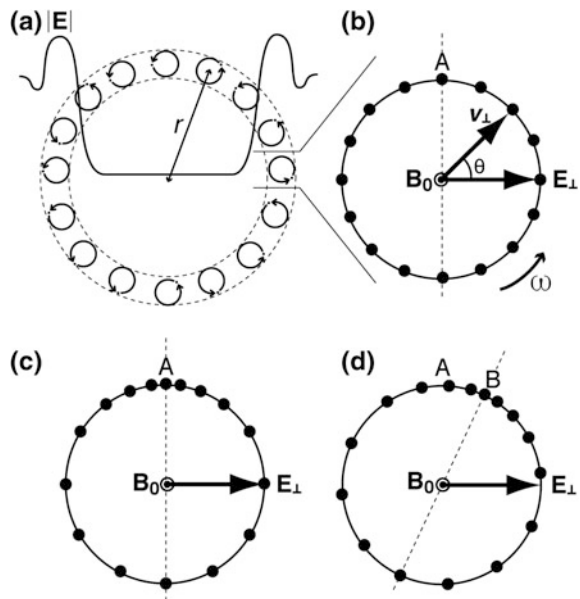
The electrons are thermionically emitted from a ring-shaped emitting region on the electron gun and then accelerated at the cathode voltage  $V_k$  toward the collector at the ground level. The initial trajectory of the emitted electron can be precisely controlled with the anode voltage  $V_a$  (if available) relative to  $V_k$ . The accelerated electrons form a hollow annular beam, in which electrons gyrate in a helical cyclotron motion along the tube axis (Fig. 4.5b inset; Fig. 4.6a). The beam radius  $r$  is compressed while drifting toward the magnet center, where the cavity is located, with increasing magnetic field. The compression ratio (aka mirror ratio) is proportional to  $F_m = B_c/B_k$ , where  $B_k$  and  $B_c$  is the field strength at the gun and at the cavity. Thus, a user can control the beam radius in the cavity by changing  $B_k$ , often employing an auxiliary magnet installed around the electron gun. Alternatively, the beam radius is modulated by adjusting  $V_a$  if available. Another key factor that determines the power extraction efficiency is the transverse velocity  $v_\perp$  of the electron helical motion in the cavity, which is proportional to  $V_k F_m$ . Thus,  $v_\perp$  is under user's control through the balance between  $V_k$ ,  $B_k$  and  $B_c$ . Usually, the ratio of the transverse to vertical electron velocity  $\alpha = v_\perp/v_\parallel = 1.5\text{--}2$  gives the best result.

In the beam, the electrons gyrate in many small beamlets (Fig. 4.6a). At the input edge of the cavity, the electron motion is random in phase and starts interacting with the “noise” field existing in the resonant cavity in the form of the blackbody radiation. The noise contains all frequencies, but due to the boundary conditions, a cavity only supports some resonant waves at discrete frequencies on the following dispersion relation:

$$\omega = c \sqrt{\left(\frac{v_{m,p}}{R}\right) + \left(\frac{q\pi}{L}\right)}, \quad (4.4)$$

where  $v_{m,p}$  is the  $p$ th zero of the  $m$ th-order Bessel function,  $R$  is cavity radius,  $L$  is the cavity length (Fig. 4.5b, inset). Only the radius  $R$  is under user's control during experiment. Each mode sets up a characteristic field pattern in the cavity, which is denoted by  $\text{TE}_{m,p,q}$ , where  $m$ ,  $p$  and  $q$  specify the number of the azimuthal, transverse and the axial nodes (see Fig. 4.5 for the pattern of  $\text{TE}_{5,2}$  mode, for

**Fig. 4.6** Hollow and annular electron beam in the cavity (a) and a rotating frame representation of the electrons orbiting in a beamlet (b). In (a), the amplitude of a representative cavity-resonant electric field  $|E|$  is plotted. In (b–d), vectors for the transverse electric field  $E_{\perp}$ , static magnetic field directed out of the paper  $B_0$  and the electron transverse velocity  $v_{\perp}$  are illustrated



example). The beam radius is usually adjusted to match one of the  $E$ -field maxima of the resonant wave to maximize the beam-wave interaction (Fig. 4.6a). This ability that the beam radius can be adjusted to selectively interact with a desired mode is unique to gyro devices. The slow-wave devices use a linear beam, which has a finite size on axis and hence does not offer this mode selectivity by the choice of beam radius. It is true that the size of the gyrotron cavity will decrease with increasing frequency (or decreasing wavelength) just in the same rate as that in the slow-wave devices. However, the ability to operate at higher-order modes (hence larger cavity dimensions) mitigates the problem of the downsizing of the structure dimensions with increasing frequency.

For an efficient energy exchange between the beam and the wave, the electrons cyclotron frequency

$$\Omega_c \approx \frac{B_c e}{m_0 \gamma_c}, \quad (4.5)$$

or its  $s$ th harmonic  $s\Omega_c$  should approach one of the cavity mode frequencies  $\omega$ . This is reminiscent of the rotating RF field that most effectively influences the nuclear magnetization vector at the magnetic resonance condition. In Eq. (4.5),  $e$  is the electron charge,  $m_0$  is the rest mass of electron,  $\gamma_c$  is the relativistic gamma:  $\gamma_c = 1 + V_k/511$  ( $V_k$  in kV), where  $B_c$  and  $V_k$  are under user's control. At the synchrony, both  $v_{\perp}$  and  $E_{\perp}$  become stationary in a rotating frame representation (Fig. 4.6b), and the rate of the energy exchange will be given by

$$\begin{aligned}\frac{dW}{dt} &= -ev_{\perp} \cdot \mathbf{E}_{\perp} \\ &= -e|v_{\perp}| |E_0| \cos \vartheta.\end{aligned}\tag{4.6}$$

From this, it is clear that the electrons in the right half of the orbit will lose their energy (negative energy flow), while those in the left half will gain. Due to the mildly relativistic electron motion, the energy-losing electrons lose its mass and thus gain the gyration speed while those gain energy lose its speed. As the result, while drifting along the cavity axis the electrons start to bunch up toward the point A (Fig. 4.6c). At this point still, there is no net energy extraction, and the final missing piece is provided by the “detuning” of the gyration speed: If the cyclotron frequency (Eq. 4.5) is tuned slightly lower than the resonant wave frequency (Eq. 4.4), the whole electrons start to slowly slip to the right in the beamlet toward the point B, i.e., into the electron decelerating phase (Fig. 4.6d). In this way, the majority of the electrons are forced to be in the energy-emitting phase before leaving the cavity. The resonant wave will be continuously affected by fresh electrons coming one after another into the cavity, pumped repeatedly and amplified, and this results in a steady-state radiation near the cyclotron frequency. Overall, gyrotrons generate  $(28 s/\gamma_c)$  GHz wave per Tesla of magnetic field. Most modern DNP-NMR gyrotrons operate in the second harmonic ( $s = 2$ ), which reduces the required  $B_c$  by a factor of two. Thus, a 460 GHz, second harmonic gyrotron operating at  $V_k = 20$  kV requires  $B_c \sim 8.53$  T. The efficiency of gyrotrons decreases strongly with the increase in harmonic number  $s$  and operation above second harmonic is not efficient and quite challenging.

#### 4.4.3 Operation of Gyrotron

As became clear now, conventional gyrotrons are basically fixed-frequency oscillator, whose radiation frequency is set by the cavity radius and the resonator modes, and one can only hop between the frequencies corresponding to separate modes by adjusting  $B_c$ . This is the reason why the high-field DNP originally employed a fixed-frequency SMMW and optimized the NMR field up and down for maximizing the signal enhancement. In this configuration, however, it is required at least once at the installation of the system a careful optimization of the NMR field for the best DNP enhancement. Fine-tuning of the main NMR field to a desired value needs skill, experience (especially for taking into account the subsequent field drift) and a lot of liquid helium, and thus is usually not to be done by users routinely. For a user desiring to work with only one polarizing agent (e.g., TOTAPOL) for a long term, the above inconvenience can be justified or perhaps be tolerated. In general, the optimization is desired at every measurement since the enhancement depends on the  $g$ -factor of the polarizing agents chosen for the experiment, on how reproducible is the gyrotron output frequency every day, and strictly speaking on the sample

temperature as well from the competition of the DNP mechanisms. Thus, from the practical demand, the NMR magnet often has an integrated superconducting auxiliary coil (the so-called sweep coil, Fig. 4.1), allowing routine DNP conditioning. Nevertheless, this original configuration also invites some drawbacks: It raises the cost of the magnet/the whole system; especially at very high fields, it is a challenge to build a magnet with an integral sweep coil while preserving the bore size and the field homogeneity. Also, it makes difficult to retrofit an existing MAS NMR spectrometer to a DNP-capable machine.

To overcome these issues, a gyrotron whose output frequency is smoothly tunable was strongly desired. Several groups have built and characterized tunable gyrotrons, for which a similar principle relying on the excitation of high-order axial modes (HOAM,  $q > 1$ ) has been adopted [14, 15]. Slightly longer cavity helps the excitation of HOAMs at the magnetic field just above that required for  $\text{TE}_{m,p,1}$  mode. And due to the lower Q factor of the cavity, the HOAMs are made significantly overlapped with each other, enabling smooth transition between the modes, and thus the output frequency. Figure 4.7 shows that the SMMW frequency can be smoothly tuned over  $\sim 1$  GHz in function of  $B_c$  with a gyrotron (called FU CW VI) operating at Osaka University [60]. Note that changing  $B_c$  is quick and easy, simply done by operating the power supply for the gyrotron SCM (Fig. 4.5), and its utility has been reported in the 395 GHz–600 MHz DNP-NMR measurement [60]. The “FU CW series” gyrotrons are developed in Research Center for Development of Far-Infrared Region at University of Fukui, and four of them (FU CW IIA, VI, GOI and GOII) are operating in the DNP-NMR laboratory at Osaka University [61]. Some other tunable gyrotrons have also been integrated into the actual DNP-NMR spectrometers [16, 60]. In the above DNP setup in Osaka indeed, a standard 600 MHz MAS NMR spectrometer whose SCM has no sweep coil has been retrofit to a DNP system empowered by the tunable gyrotron. A current technical shortcoming of a tunable gyrotron setup is its uneven power spectrum across the frequency sweep (Fig. 4.7c); the higher-order axial modes have larger number of nodes along the cavity, resulting in the lower energy extraction efficiency. Active feedback control of the output power should enable a power spectrum completely flat over the required frequency range, but needs a continuous power monitoring system and an advanced controlling software (Sect. 4.4.5).

By understanding the oscillation principles, a set of operational tips can be identified; a gyrotron is not a black box anymore! This often enables fine-tuning of the SMMW frequency and power to suite the experimental needs. Tips include: (1) higher electron beam current  $I_b$ , higher output power with more thermionic electrons that pumps the wave; (2) higher acceleration voltage  $V_k$ , higher power from larger  $\alpha$  and Eq. (4.6), and lower frequency from Eq. (4.5); (3) a tweak on  $B_k$  or on the anode voltage  $V_a$  (if available) modulating the output power by modifying the beam radius; (4) higher oscillation duty or higher beam current, lower frequency from cavity dilation (larger  $R$ ) by ohmic heating from Eq. (4.4); and (5) lower cavity cooling water temperature, higher frequency from cavity contraction (Eq. 4.4). In Fig. 4.3, typical tunable ranges are shown for the two 460 GHz gyrotrons FU CW GOI and GOII. For example, these gyrotrons oscillate at

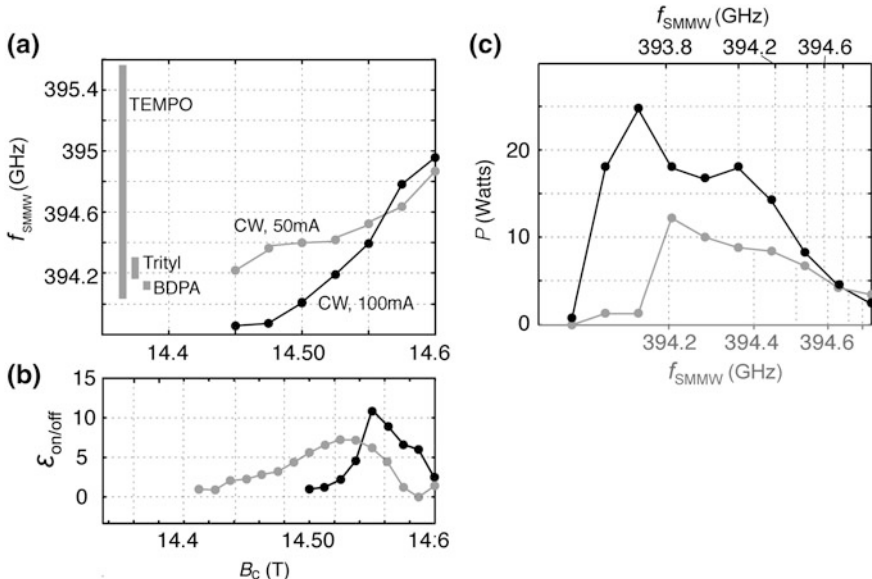


**Fig. 4.7** SMMW frequency (**a**), and signal enhancement factor (**b**) versus gyrotron field  $B_c$ . The output power over the tunable range is shown in (**c**). The beam current  $I_b$  of 50 and 100 mA was used for data shown in gray and black, respectively. In (**a**), the ESR frequencies of some popular radical polarizing agents are indicated with gray bars. Data taken with the 600 MHz DNP-NMR system at Osaka University

$f_{\text{SMMW}} = 459.8\text{--}460.5$  GHz (GOI) and  $459.3\text{--}459.7$  GHz (GOII) with typical beam parameters,  $V_k/V_a = 16/8$  kV,  $I_b = 200$  mA,  $B_c = 8.50\text{--}8.54$  T at second harmonic condition  $s = 2$ . An extension toward slightly lower frequency to irradiate one of the hyperfine-split ESR lines from the Mn–DOTA complex at 459.27 GHz (marked with \* in Fig. 4.3) was possible with a use of higher  $V_k$  (17 kV for larger  $\gamma_c$ ) and higher  $I_b$  (270 mA for larger  $R$ ). Both lend to a high-power output from an increased  $\alpha$  and thermions. Frequency extension to high side was also possible. For example, an irradiation of the SE-DNP(–) condition of BDPA at 460.35 GHz (marked with \*\* in Fig. 4.3) was possible using higher  $B_c$  (8.55 T for higher  $\Omega_c$ ) together with the increase of  $V_a$  (11.8 kV) and  $V_k$  (18 kV) to preserve the beam quality, and high  $I_b$  (400 mA) for enough power output.

For safety of users, several precautions and procedures are necessary with a gyrotron as it uses high voltage ( $\sim 20$  kV) and very high magnetic fields. The electron acceleration voltage is supplied to a gyrotron via a high-voltage cable from a power supply rack, which is usually a few meters away from the gyrotron magnet. For the feedback frequency regulation that will be discussed below, the tube body itself is also maintained at a high voltage of up to 1 kV from the ground. These high-voltage areas must be sequestered, and appropriate interlocks must be installed to prevent accidental contact with high voltage. Also, there is a reasonable X-ray production due to a small number of fast electrons accelerated during the interaction

process to well above 50 kV. The users must be stationed at a safe distance to prevent exposure to X-rays or a proper X-ray shield (like a lead barrier) should be installed around the collector. Unlike many NMR magnets, the gyrotron magnets are often unshielded or only partially shielded and have a strong stray field. Magnetic tools, nuts/bolts and the scopes need to be kept away; in particular, the gyrotron window should be properly protected when adjusting the waveguide and other components nearby. The wave coming out of the gyrotron window can be extremely intense and easy to burn human eyes and skin. Gaussian beam has its power concentrated at its center and propagates fairly straight even in the open air; it easily burns the room wall meters away. If the beam hits some metallic parts located near gyrotron, it bounces around in pretty unexpected directions. Many plastic tubes installed for supplying cooling water or gas for pneumatic valves are common around a gyrotron, and the stray SMMW beam can easily melt and disrupt them. For a temporally power damp, a simple and inexpensive tool is an open box with a cone-shaped structure inside, whose diameter is made bigger than the beam size. Their surface should be all covered with crumpled aluminum foil so that the beam is scattered to random directions in the box, and absorbed at the wall. To stop the beam permanently, more elaborate structure can be designed such as water-cooled Teflon blocks in a thermostatic container. The gyrotron tube vacuum needs continuous surveillance either during the operation or while it is resting; needs to make sure that it is high enough ( $<10^{-6}$  Pa) before start heating the electron gun. At a low vacuum, it will be difficult to draw enough electrons, or at worse the heat will poison the electron gun. In the very initial stage of the tube operation, or when operating after a while of off time, or in a new cavity mode, the tube vacuum tends to spike quite unexpectedly; thus, it is a usual practice to setup a mechanical interlock on the high voltages from a vacuum gauge. Power outage either planned or unexpected also causes a considerable threat to the gyrotron operation. To protect the tube vacuum even at unexpected power outage, automatic pneumatic vacuum shutter can be set up on the pumps. Power outage on the chiller water circulators is devastating if it is during operation since the electron beam will easily cut a hole on an uncooled collector. A cryogen-free magnet often used for gyrotron uses electrical cryo-coolers (Fig. 4.5k), whose compressor unit needs air or water cooling. With impaired water flow, the cryo-cooler halts and the superconductor fails. If the magnet fails during operation, the beam will not be properly guided through the cavity and hits an unexpected area in the tube that is not water-cooled. This can lead to pitting and melting of that region and even a loss of vacuum, which is always catastrophic. The main power supply for those devices with outdoor heat exchanger unit should be planned with enough margins, taking the seasonal fluctuation of the power consumption into account. A mechanical interlock on the water flow meter tripping the high voltages is also an indispensable part for a safe operation.

In summary, with the high-frequency and high-power capability, as well as the flexibility in frequency and power tuning upon legitimate parameter choice, gyrotron is a handy and powerful light source in pursuing DNP at very high fields. With proper precautions and advanced control software combined with the

mechanical/logistic interlocks, it is a safe and easy-to-use laboratory tool. It is robust either for continuous operation or for high-power short pulses for a long signal averaging. The mechanical duration is very high, and with appropriate care, a single gyrotron tube should run for decades without decay of its performance. With actively ongoing developments on both hardware and software, gyrotrons should become even cheaper, smaller and easier to use [17]. A step toward gyrotrons that can be installed in the NMR magnet bore has also been reported recently [62].

#### **4.4.4 Transmission of SMMW**

The SMMW should be transferred with a minimum loss toward the NMR sample in the probe. Since the wavelength is usually much smaller than the passive components used for the transmission, the quasi-optical treatment can be used. Due to the compactness and robustness, transmission through the closed oversized metallic waveguides is convenient. To efficiently couple the SMMW to the waveguide, the beam oscillated in the high-order TE mode in the cavity needs to be converted to the Gaussian-like TEM<sub>00</sub> mode, which is round in shape with the power concentrated at the beam center (Fig. 4.5). This mode efficiently couples with the HE<sub>11</sub> waveguide mode in a corrugated waveguide. A gyrotron tube often has an integral mode convertor to create a free space Gaussian-like output beam from the higher-order cavity mode [63]. An external matching optics unit (MOU) may be added if higher mode purity and/or flatter phase front are desired, and for the correction of the beam waist size. The coupling coefficient to the waveguide is maximized when the beam is input exactly to the waveguide center, with the beam axis perfectly aligned to the waveguide axis, and with the waist size matched to 64.3% of the waveguide radius. Deviation from the complete alignment results in a considerable power loss: For example, when coupling 460 GHz wave to 19 mm diameter waveguide, the axis offset must be <0.6 mm, and the beam tilt must be <0.06° to maintain the mode conversion loss at the input to less than 1%. The HE<sub>11</sub> mode is most efficiently transmitted in a waveguide whose inner wall is corrugated at the pitch size and depth of ~1/4 of the wavelength (Fig. 4.5). Typical transmission loss of a straight section is negligible (<0.01 dB/m), and the ohmic and mode conversion loss occurring at a miter bend, a component that bends the beam with a flat mirror reflection, usually dominates the transmission loss (~0.1 dB each). Thus, it is important to minimize the number of bends. The waveguides need to be strictly straight along the beam; even a slight bend or curvature will lead to a power loss and thus must be held on a stiff and stable support structure. Still, a typical total transmission can be made fairly high; for example, in a system operating at Osaka University, for a ~12 m transmission of the 460 GHz wave involving six miter bends, two 3 dB hybrids and two Notch filters in between (Bridge12 Technologies, Inc.) have resulted in ~2.2 dB loss (i.e., 60% transmission) between a gyrotron and the NMR magnet. Transmission in the TE<sub>01</sub>/TE<sub>11</sub> mode that does not require corrugated waveguides has also been recently proposed

for a simpler alternative [64], which is to be tested experimentally. A polarization rotator or a universal polarizer made of a pair of grated mirrors is useful for conditioning the  $\mathbf{B}_{1e}$  direction perpendicular to  $\mathbf{B}_0$  of NMR at the sample [65]. The circularly polarized beam has been reported to improve the enhancement by  $\sim 20\%$  at maximum [66].

#### 4.4.5 *Feedback Regulation of SMMW*

The frequency of the SMMW needs to be set very precisely. For example, to irradiate at the center of the EPR line of a narrow-line radical (FWHH  $\sim 10$  MHz), the frequency accuracy of 0.5 MHz or better ( $\sim 1$  ppm for the 460 GHz wave) is required for maximizing the enhancement. Also, this optimal frequency needs to be maintained for several days or a week during the NMR measurement. In another example, the user wants to sweep the SMMW frequency as fine as desired to record the frequency dependence of the enhancement to investigate, e.g., the DNP mechanism. For this purpose, the SMMW power level needs to be constant over the frequency sweep as well. The ability to continuously and precisely monitor the SMMW frequency and power in real time during DNP measurement will be a basis for these demanding requirements. In one of the DNP systems at MIT (250 GHz–380 MHz), a quartz beam splitter plate was inserted in the middle of the transmission line at an angle of 45° to the beam axis to intercept a few % of the transmitting power to a branch line, on which a detector diode was installed for a signal detection [67]. Since the diode detection is sensitive to the direction of the SMMW polarization, the diode mount was to be manually rotated to maximize the signal. The 460 GHz–700 MHz DNP-NMR system developed at Osaka University also intercepts a small part of the transmitting SMMW for a power measurement, but utilizes a miter bend mirror bearing three  $\sim 1$  mm- $\varphi$  coupling holes. The power coupling coefficient at the hole was measured to be about  $-50$  dB at 460 GHz, i.e., only 10 ppm of the power is intercept for the signal detection. The power from one of the holes was coupled to a diode mixer (Virginia Diode, WR2.2EHM) for a heterodyne frequency measurement, and the power from the other two holes were input to the zero-bias GaAs power detection diodes (Pacific millimeter, Model HD) as shown in Fig. 4.5 on the right. The latter two diodes were installed at the right angle to each other so that the measurement does not depend on the beam polarization. The RF signal ( $\sim 460$  GHz) was mixed with a LO signal ( $\sim 38$  GHz) down to  $\sim 1$  GHz IF signal and detected on a spectrum analyzer (Agilent, N1996A) or high-sensitivity digital oscilloscope (Agilent, DSO9204H). The power loss of the LO signal on the cable has impeded the detection of the small RF signal even when a doubly shielded extra low-loss coaxial cable (Insulated Wire Inc.) was employed if it was longer than 1.5 m. This constrained the location of the local oscillator in the room, and in turn the signal detecting mirror. Affordable amplifiers (such as Agilent, 87405B) are readily available for the low frequency IF signal. The detected IF signal was Fourier transformed on the oscilloscope, and the frequency data were

communicated to the central PC via TCP-IP line. A LabVIEW software written in-house (Fig. 4.8a) takes care of the PID signal conditioning vis-à-vis a user-set target frequency, and an analog signal was output via a DAQ device (National Instruments, NI-USB 6009). Two 460 GHz gyrotrons FU CW GVI and GVIA (also called as GOI and GOII in the Osaka laboratory) have the fast power and frequency modulation/stabilization capability through modulation of the anode and body voltage, respectively [68, 69]. Based on this, the PID regulated analog signal was fed into a high-voltage amplifier (TREK, model 2210) that controls gyrotron's body potential  $V_{\text{body}}$  to modulate the electron acceleration as  $V_k + V_{\text{body}}$ , and thus the output frequency [70]. The gyrotron body is isolated from the collector using a ceramic break (isolator). Figure 4.8b, c shows the SMMW frequency versus time with and without the feedback stabilization. The natural frequency fluctuation of  $\sim 20$  MHz (Fig. 4.8c) with a time period of about 15 min may come from the period of the room AC, or that of the electric chiller water circulator, or some other external sources. The natural fluctuation is completely suppressed with the feedback control of  $V_{\text{body}}$ , resulting in the frequency stability of less than 1 ppm ( $<0.5$  MHz) (Fig. 4.8b).

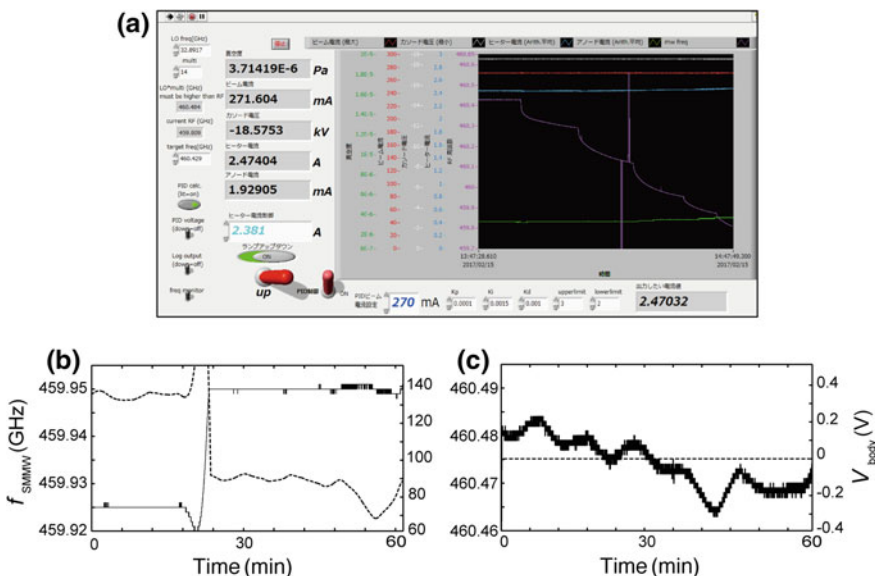


**Fig. 4.8** SMMW frequency feedback stabilization. **a** Interface of a home-written gyrotron control software. High voltages  $V_k$  (white), tube vacuum (green), filament heater current  $I_h$  (blue), beam current  $I_b$  (red) and the SMMW frequency  $f_{\text{SMMW}}$  (purple) are plotted in real time. Feedback regulation on  $I_b$  and  $f_{\text{SMMW}}$  can be set on the same interface (using the fields on the left). In **b**, **c**,  $f_{\text{SMMW}}$  (solid line) and the gyrotron body voltage  $V_{\text{body}}$  (dashed line) are plotted over time with **(b)** and without **(c)** the feedback regulation. In **b**, the target  $f_{\text{SMMW}}$  was manually changed at time  $\sim 20$  min from 459.924 to 459.950 GHz

In the power detection as well, the signal level from the GaAs diodes was low being in  $\sim 1$  mV range, and specially shielded semirigid coaxial cables (Pasternack Enterprises) were required. A simple DC amplifier may be constructed with transistors for further sensitivity. A similar feedback circuit can be constructed from the detected power to the heater filament on the electron gun and/or the anode voltage  $V_a$  that modulates the beam radius. Ideally, simultaneous feedback control on the power and frequency is implemented [71].

#### 4.4.6 Double SMMW Irradiation

Besides the efforts toward safe and stable SMMW irradiation, more innovative developments have also been pursuit. In the 700 MHz DNP system at Osaka University, for example, two 460 GHz gyrotrons (GOI and GOII) are integrated into a single DNP system for a compound SMMW irradiation (Fig. 4.9a) [72]. Both gyrotrons oscillate at the second harmonic resonance ( $s = 2$ ), and produce over 10 W output, and are widely frequency-tunable (Fig. 4.3). The ability to use two SMMWs with independent power and frequency opens up many interesting possibilities in practicality and innovation. The outputs from the two gyrotrons are combined with a custom-designed power combiner (Fig. 4.9b, Bridge12 Technologies Inc.); then, a resultant dichromic SMMW is sent to the NMR. The combiner integrates the two beams without mutual interference or disturbance of the polarization of each beam and with minimal insertion loss. Therefore, the timing of the SMMW irradiation can be freely chosen from in turn to simultaneous. Potential application is manifold: Improvement in the DNP efficiency from the twice more power delivered to the sample [72], or utilizing the alternate excitation of the positive and negative DNP (DNP(+)) and DNP(−)) with a rotor-synchronized SMMW and RF pulses, molecular geometrical analysis from uneven polarization distribution emphasized by the alternating DNP(+)–(−) excitations, spectral editing by exciting polarizing agents with distinct  $g$ -factors localized in different phases or location of a system, as well as the recently proposed “electron-decoupling” for reducing the paramagnetic quenching [73].

For such advanced double-frequency DNP experiments, the timing of the SMMW outputs must be precisely controlled from a pulse program. This can be done using a semiconductor (MOSFET) switch that is able to rapidly turn the electron acceleration voltage on and off, based on the TTL signals from the NMR console. The typical temporal resolution is at  $\mu\text{s}$  or faster, being fast enough for a rotor-synchronized, multi-pulse NMR experiments.

Precise control on the SMMW phase that enables fully coherent “pulse DNP” experiment proves to be a more challenging endeavor. However, remembering the benefit the NMR has gained by going from the CW to pulse FT version, and DNP would also have to be evolved to “pulse DNP” in the near future. In principle, gyrotron picks up the radiation from the noise signal as described in Sect. 4.4.2, and it does not have an active control on the wave phases. One of the ongoing

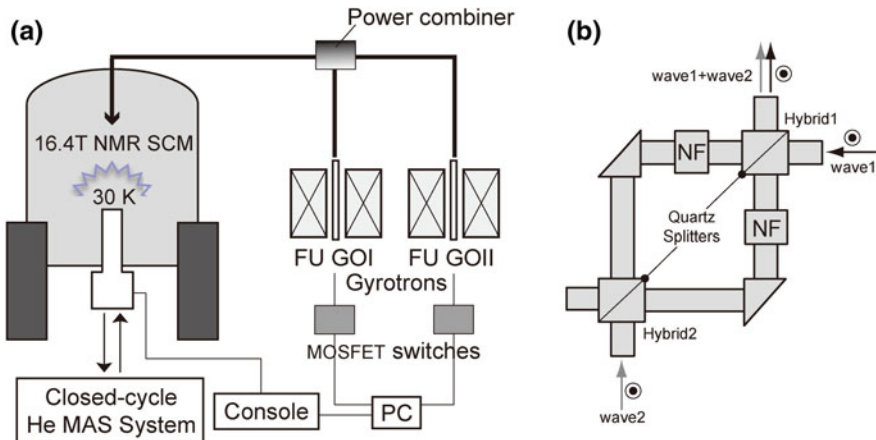


**Fig. 4.9** The double-gyrotron DNP setup (a), and the custom-designed SMMW power combiner (b). Waves 1 and 2 are split at the 3 dB hybrids and then reflected or passes through, respectively, the notch filters if the notch is tuned to the frequency of wave 1, resulting in a combined beam. The wave polarization is preserved before and after the power combination

developments at MIT involves a 140 and 250 GHz gyro-amplifiers that can amplify the seed SMMW in 100 mW level into the desirable 10–100 W wave. The source SMMW can be generated with a phase-stable low-power diode sources and amplifier multiplier cascade. Some basic results toward the pulse-based DNP have been published already at low fields [74, 75], but its integration to high-field DNP-NMR still needs some more time for technical maturation.

## 4.5 DNP-NMR Probes and Low-Temperature Facilities

Only two essential requirements for a DNP-NMR probe are (1) the heat insulation to protect the magnet bore from freezing and to stably obtain sample temperature of  $\sim 100$  K or less and (2) a path to deliver the SMMW to the sample. Low temperature not only increases the electron thermal polarization, but also elongates the electron and nuclear  $T_1$  to improve the DNP efficiency itself.

### 4.5.1 MAS at Cryogenic Temperatures

Figure 4.10 illustrates two examples of the DNP-NMR probes in actual use in Osaka University. In the simpler setup shown in (a), only the gas lines delivering the spinner gases and the variable temperature (VT) gas were vacuum insulated, but not the probe itself. Between the heat exchanger and the probe/NMR SCM,

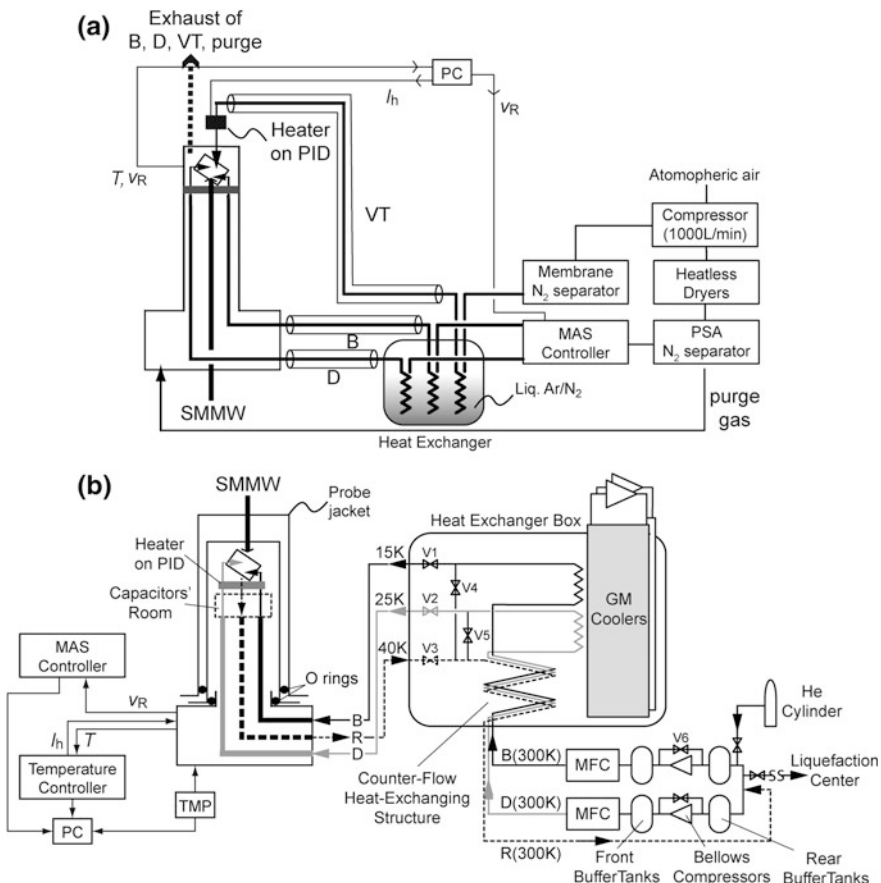


**Fig. 4.10** Schematic diagrams of a simple (a), and advanced (b) cryogenic MAS DNP-NMR probe systems. In (a), dry  $\text{N}_2$  gas is separated from the air, then cooled with liquid cryogen. In (b), pure He gas is introduced from a gas cylinder, cooled with the electric gas chillers and circulated in a completely closed loop comprising the NMR probe

vacuum-jacketed flexible transfer tubes were employed, while in the probe/SCM bore, the gas lines were simply wrapped with a foam insulator such as the Aerogel blanket ( $\kappa \sim 0.02 \text{ W/mK}$ , Takumi Sangyo, Inc.) and further by Mylar® film (Dupont Teijin Films, Ltd.). To protect the magnet bore from freezing, and to avoid condensation on the probe surface, the inside the probe body was flushed with a flow of ambient temperature “purge gas”. With an input of the cold spinner and VT  $\text{N}_2$  gas streams at  $\sim 90 \text{ K}$  from the heat exchanger, the sample temperature of  $\sim 120 \text{ K}$  was stably obtained for a 4 mm rotor spinning at  $v_R \sim 7 \text{ kHz}$ . With a controlled addition of a few percent of oxygen in the VT gas, the sample temperature could be reduced to  $\sim 105 \text{ K}$ . Oxygen liquefies in the heat exchanger and evaporates during the transfer. Since liquid cryogen has a greater specific heat than

that of gas ( $\sim 2$  kJ/kg K for liquid O<sub>2</sub>, and about half for the gas), lower VT gas temperature is obtained at the sample. The same technique is not applicable to the spinner gases, since the MAS rate is sensitive to even a partial liquefaction. Since, in this setup, the temperature of the spinner gas was much higher than the VT gas, the use of zirconia rotor with low thermal conductivity was required for the lowest sample temperature.

For more advanced heat insulation, each path for the spinner gases in the probe was also insulated with an independent vacuum jacket (Fig. 4.10b). In addition, the whole cylindrical part of the probe body in the magnet bore was enclosed with a vacuum layer formed between the probe body and the jacket. The vacuum must be kept in the order of  $10^{-2}$  Pa or better throughout the measurement; thus, the probe base box is equipped with a service port for a continuous pumping. Many turbo-molecular pumps (TMP) and vacuum gauges can operate in a stray field of the NMR magnet (often <50 G) without problem. Some cold cathode gauges show systematic error in the reading in a stray field and thus better to be calibrated with and without the magnetic field. Crystal ion gauges seem to be too sensitive to the repetitive relief of the vacuum and thus not very suited if the vacuum section needs to be broken frequently, e.g., at the time of every sample exchange.

A MAS DNP probe should soon incorporate the cold preamplifier and duplexer for reducing the thermal noise as well. Since in a DNP probe, the sample and a part of the RF circuit is already kept cold, cooling of some additional RF components together should be relatively straightforward. And a reward is sweet: e.g., the signal enhancement of  $\sim 100$  from DNP should be boosted to the total sensitivity gain of  $\sim 400$  from the fourfold noise reduction currently established. The bore of the NMR magnet is often assumed to be “wide” (e.g., 89 mm for the diameter) for providing enough space for the SMMW transmission and for accommodating good heat insulation structure, but narrow-bore DNP probe should also be envisaged as well. More specific design to be explored would include: a DNP probe with a 0.75 mm MAS module for proton detected DNP, a 1 GHz DNP probe for sensitivity-enhanced <sup>17</sup>O (quadrupolar) NMR and that with X and/or Y broadband channels for material applications.

#### 4.5.2 SMMW Irradiation of Sample

The waveguide system in the probe is similar to that used between the SMMW source and the NMR magnet, but usually much smaller in diameter (e.g., 4 mm vs. 20 mm) due to the space limitation. Regardless of the existence of the wall corrugation, the transmission loss of the oversized waveguide rapidly increases as the diameter is reduced ( $d/\lambda \rightarrow 1$ ), and thus poses a significant technical challenge. By coupling power from top of the probe, a larger diameter waveguide can be accommodated compared to the case when the waveguide is built into the probe assembly. This reduces the loss in the waveguide and also simplifies the probe design. For a small waveguide, inner-wall corrugation by direct machining will

become difficult. Other suitable alternatives include a helical tap corrugation and corrugation using the electroforming techniques. For the former, the corrugations are not circumferentially independent anymore, and this will rotate the polarization of the SMMW during transmission, degrading the orthogonality between the SMMW  $\mathbf{B}_{1e}$  and the NMR  $\mathbf{B}_0$  at the sample. However, according to a calculation [67], the effect is minimal if the guide is not too long. An emerging alternative is the stacked-ring method, in which two metal rings with different inner diameter are stacked in a cylindrical sleeve to produce the corrugation (Swissto12 SA). Although this has been adopted in some commercial systems, it remains underused due to its high commercial price (\$40 k–\$80 k/m, depending on the SMMW frequency). A use of  $TE_{01}/TE_{11}$  mode as an alternative to  $HE_{11}$  that requires no corrugation on the waveguide for a similar transmission loss for a straight section has also been proposed [64].

The configuration for the sample irradiation in the MAS module is still a source of debate. Figure 4.11 shows two possible configurations: transverse and axial, for which the SMMW can be delivered either with a bent waveguide or a focusing mirror set. The axial setup needs precise alignment of the beam to the rotor axis every time the sample exchange and usually difficult to directly optimize it from outside the probe after the sample cooling, for example, by looking at the enhancement factor. It also blocks the way out of the rotor and makes the pneumatic sample insertion/ejection practically impossible. In addition, the final mirror is far from the sample (e.g., >20 mm, for a 3.2 mm rotor), and the plastic spacers and caps in the rotor can attenuate the power delivered to the sample. Also, when the top part of the sample absorbs the SMMW, it transmits less to the bottom, producing an inhomogeneously illuminated sample. One attractive feature of the axial

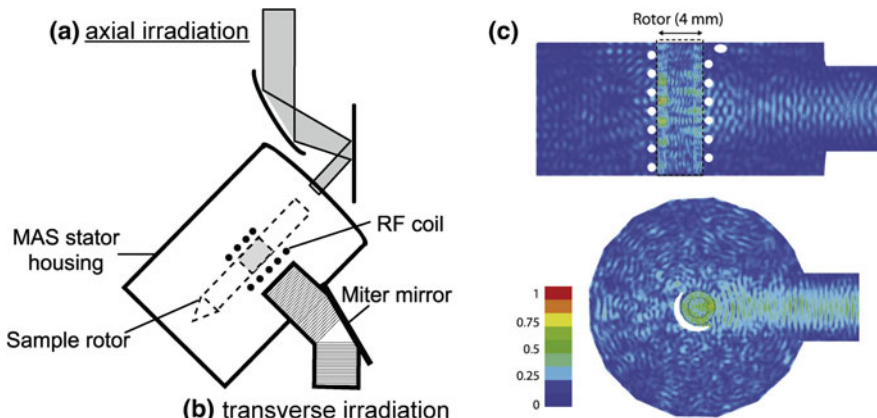


**Fig. 4.11** Two major configurations for the SMMW irradiation of an NMR sample: axial (a), and transverse (b). c A result of an EM wave simulation around the NMR sample under the transverse irradiation in the presence of the RF coil and rotor sleeve. The normalized SMMW magnetic field intensity is color-coded. Reproduced from [76] with permission

irradiation is that the wave is not deranged by the RF coil. This is, on the other hand, the major bottleneck for the transverse irradiation scheme. Since the metallic coil surfaces are almost completely reflective to the SMMW, the transverse irradiation might appear an inefficient approach at first glance. A compromise can be made, however, by winding the RF coil less tightly than required for the best RF efficiency and/or by employing higher gauge wire, since the sensitivity gain from DNP overwhelms the loss owing to the suboptimal RF efficiency. Figure 4.11b shows an example of the EM wave simulation (Ansys HFSS) around the sample under the transverse irradiation. The wave is scattered and reflected at the coil and the rotor wall, forming multiple of standing waves in and around the sample, but significant fraction of the wave diffracts into the coil and reaches the sample. According to the calculation, a probe-in power of  $\sim 5$  W achieves the average electron nutation frequency of about 0.8 MHz in the rotor [76]. In the transverse scheme, it is also easy to illuminate a long sample homogeneously with a beam elongated along the rotor axis, ensuring absolute sensitivity. The rotor wall thickness can be optimized for the wave transmission based on the dielectric constant of the rotor material, and can lead to  $\sim 30\%$  increase in the enhancement for a sapphire rotor [76].

Regardless of the irradiation scheme, axial or transverse, the resonant cavity structure is difficult to build, since the sample is usually way larger than the wavelength of the relevant SMMW. A highly overmoded Fabry–Perot-type resonator in a MAS module may be conceived, but the insertion loss from the RF coil and sample rotor in the resonator usually rejects this idea. Still, the SMMW scattered by the coil or sample rotor could be partly reflected back toward the sample using a silver coating of the inner wall of the MAS module, but resulted in a small (20%) improvement in the enhancement factor [76, 77]. In the axial irradiation scheme, a reflecting silver foil placed at the bottom of the sample also made a minor improvement. In both cases, the  $\mathbf{B}_{1e}$  field of the reflected wave does not necessarily add up at the location of the sample. Recently, it was reported that a sample packed with many small dielectric particles seems to cause a factor of two-improvement in the enhancement factor [78]. Detailed EM wave simulation has revealed that the small spaces formed randomly between the particles partly acted as a sort of resonator, and concentrated the SMMW power. This interesting phenomenon, however, does not lend to the practical sensitivity gain, since the volume of the dielectric particle excludes the sample of interest in the rotor. As described in this section, the sample illumination system is highly underdeveloped section in a DNP probe and with a full of future challenge. Since improved irradiation efficiency should eventually transform the requirement for the SMMW source and will have a considerable impact on the overall efficiency of the system.

Selection of the rotor material is also an important factor for maximizing the DNP efficiency. Although for very fast MAS, the material strength matters most, but usually toughness is more important for DNP using moderate MAS rates at cryogenic temperatures. Sapphire is fragile (flexural strength of only  $\sigma \sim 20$  MPa), although hard, and thus shatters from time to time upon careless MAS operation. Ceramics such as  $\text{ZrO}_2$  and  $\text{Si}_3\text{N}_4$  are much tougher (usually

$\sigma \sim 1000$  MPa) and more reliable, although the inherent microcracks may cause statistical failure. For DNP, transmission of the SMMW through the rotor wall is of the paramount importance. Sapphire and  $\text{Si}_3\text{N}_4$  are transparent with relatively low dielectric constants ( $\epsilon_r = 8\text{--}10$ ) at SMMW range, while  $\text{ZrO}_2$  is a lot worse ( $\epsilon_r \sim 30$ ). For visible light transmission, sapphire is the best (transparent), although  $\text{ZrO}_2$  (white) is fairly good when the wall is thin (such as 0.5 mm), and  $\text{Si}_3\text{N}_4$  (black) is the worst. The SMMW heating of the sample is problematic since the DNP enhancement is a strong function of the sample temperature. The loss tangent for the glycerol/water matrix was measured to be very small at 77 K ( $\sim 50 \times 10^{-4}$ ) at 140 GHz [76], being comparable to that for sapphire  $20 \times 10^{-4}$  (@35 GHz) and  $\text{Si}_3\text{N}_4$   $3 \times 10^{-4}$  (@300 GHz), while the loss of  $\text{ZrO}_2$  is particularly worse being  $1000 \times 10^{-4}$  (@50 GHz), and thus not preferred. The SMMW scattered by the coil and the rotor will hit the inner wall of the MAS module often made of lossy plastics and heats the atmosphere within the MAS module. The heat produced at the sample and the rotor should be dissipated relying on the thermal conductivity of the rotor material and cooled by the cryogenic spinner gases. Figure 4.12a, b plots the time course of the sample temperature  $T_{\text{KBr}}$  as well as that of the sample room  $T_S$  before and after the SMMW irradiation. Both  $T_{\text{KBr}}$  and  $T_S$  jumped up at the onset of the SMMW irradiation and then slowly came back down with the drop of the probe heater, which is PID controlled from  $T_S$ . It is interesting to see that  $T_{\text{KBr}}$  does not return to the original temperature since the heat is confined due to the finite thermal conductivity of the rotor material. The average temperature rise  $\Delta T$  was found to be 1.6 K for  $\text{ZrO}_2$  and 0.8 K for  $\text{Si}_3\text{N}_4$ , and 0.1 K for sapphire rotor, which is clearly anti-correlated with the thermal conductivity of the rotor material: 3 W/mK for  $\text{ZrO}_2$ ,  $\sim 30$  for  $\text{Si}_3\text{N}_4$  and  $>40$  for sapphire (Fig. 4.12c). More interestingly, the DNP enhancement factor observed using a  $\text{Si}_3\text{N}_4$  and sapphire rotor was 15 and 20% higher than that with a  $\text{ZrO}_2$  rotor at 100 K (Fig. 4.12d). Also, this trend intensified at lower temperature (85 K): The enhancement for the sapphire rotor was 60% better than that in  $\text{ZrO}_2$  rotor, suggesting a greater impact of the heat at lower set temperatures. This maintains the preference for sapphire rotor even if the visible light is unnecessary for the experiment, and  $\text{Si}_3\text{N}_4$  rotor should come as a good compromise. In the future development, tougher and highly heat-conductive materials should receive more attention.

#### 4.5.3 Production of Cryogenic Spinner Gas

Cost-effective generation of cold spinner and VT gases poses another instrumental challenge. For  $T > 90$  K, liquid  $\text{N}_2$  is often preferred to other cryogens such as helium (He) due to its lower commercial price. Still, even with “cheap”  $\text{N}_2$ , providing all the spinner and VT gases from a simple boil-off of liquid  $\text{N}_2$  is unrealistically costly for a long-term experiment lasting days to weeks, which is routine for biological NMR. Even with a probe with reasonably good heat insulation, the required spinner and VT gas altogether amounts to 200–400 L/min, i.e., 400–800

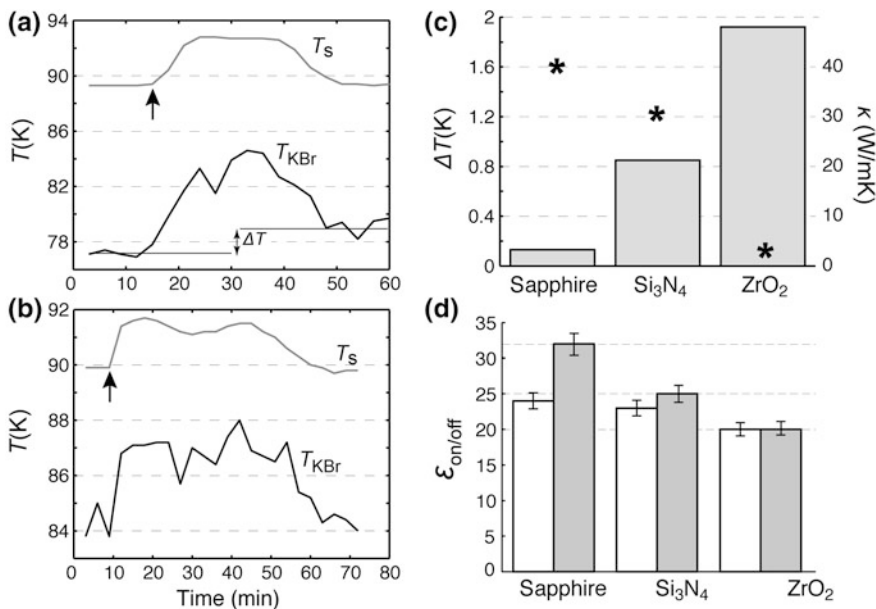


**Fig. 4.12** Effect of the rotor material on the DNP efficiency. **a, b** Sample temperature ( $T_{\text{KBr}}$ ) and sample room temperature ( $T_{\text{S}}$ ) measured over time for  $\text{ZrO}_2$  (**a**) and sapphire rotor (**b**). At the arrow, the SMMW ( $\sim 8$  W probe-in) was turned on. **c** Average temperature increase  $\Delta T$  due to the SMMW heating (left scale), and the thermal conductivity (asterisks (\*), right scale) for different rotor materials. **d** Enhancement factor measured at 100 K (white bars) and 85 K (gray bars). The MAS rate was made less than 1 kHz to minimize the frictional heating. The sample temperature  $T_{\text{KBr}}$  was measured from the  $T_1$  time of  ${}^{79}\text{Br}$ .

L/day of liquid N<sub>2</sub>. A more realistic approach thus will be to separate dry N<sub>2</sub> gas from the atmosphere. The latter strategy in turn needs careful quality control on the gas purity (removal of oxygen that easily liquefy during heat exchange) and dryness (ice formation from air moisture can accumulate in the gas line over time, and eventually block it). A setup developed by the Osaka group involves an oil-free gas compressor, PSA (pressure-swing adsorption)-type heatless dryers and a PSA-N<sub>2</sub> separator (Kuraray Chemical Co. Ltd., MA2-5.5-7 K), and produces pure (>99.9%) and dry (dew point < 60 °C) N<sub>2</sub> gas in good amount (160 L/min) (Fig. 4.10a). In this setup, the power consumption of the air compressor (200 kWh/day) dominates the production cost, which is, however, significantly less expensive than the liquid boil-off method.

The N<sub>2</sub> gas thus produced can be heat exchanged with liquid N<sub>2</sub> to  $\sim 80$  K to achieve the sample temperatures of 85–110 K, depending on the efficiency of the heat insulation on the probe side. Usually, a heat exchanger consists of two to three lines (for spinner and VT gases) of helical copper tubings immersed into a liquid N<sub>2</sub> bath, where average liquid N<sub>2</sub> consumption for the heat exchange is typically 3–5 L/h (or <120 L/day). Two major challenges in cooling N<sub>2</sub> gas against liquid N<sub>2</sub> are:

(1) easy liquefaction of the pressurized (usually <0.3 MPa) spinner gas that may crush the rotor and (2) the MAS rate and temperature drift/instability owing to the slowly decreasing liquid N<sub>2</sub> level and/or disturbance at the Dewar fill. In a viable approach, the heat-exchanging copper helix is enclosed into a pressurized metallic canister structure, where the inner canister pressure is independently controlled to regulate the liquid N<sub>2</sub> level in the canister to avoid liquefaction [79]. Since the MAS rate and sample temperature depend on the canister pressure, a care should be taken to stabilize it throughout the measurement. Alternatively, liquid argon (b.p. 87 K) can be used for the heat exchange instead of liquid N<sub>2</sub> (b.p. 77 K). This inherently avoids liquefaction of the spinner gas N<sub>2</sub> and obviates the canister structure and the additional N<sub>2</sub> gas pressure line [72].

DNP experiments at  $T \ll 90$  K are desired for an improved DNP efficiency (Sect. 4.6.3). Liquid He boil-off is the simplest approach for the generation of the pressurized cold spinner gas streams at  $T < 40$  K [23, 80–84], but very costly: Typical liquid He consumption was  $\sim 144$  L/day [23]. Alternatively, cold He gas can be used only for the VT gas, but N<sub>2</sub> gas for the MAS [21]. This reduced the He consumption to 48 L/day, but made the recycling of the spent He gas difficult since in the MAS module the VT and spinner gases mix up. An elegant and highly effective solution to this issue has recently been proposed by the Osaka group, reporting the first completely closed-cycle He MAS system [22]. It consists of oil-free gas compressors, a heat-exchanging vessel with two electrical gas chillers (GM coolers, Sumitomo Heavy Industries, RDK-408S) and a dedicated NMR probe that guarantees a complete He hermeticity throughout the gas input/output paths, and in the sample room. Also, the probe design must incorporate significant thermal insulation (Fig. 4.10b) to reduce the size and number of the gas compressors and cryo-coolers to be reasonable for a use in a typical NMR laboratory. With this system, excellent long-term (>2 weeks) stability was obtained for the sample temperature ( $\pm 0.5$  K) and the MAS rate ( $\pm 3$  Hz). Also, the probe is RF arcing-free with a careful circuit design (Japanese and International patents are pending). Any sample temperature between 24 and 300 K, and the MAS rate between 6 kHz (@28 K) and 25 kHz (@280 K) are stably obtained as of writing (February, 2017). The primary running cost arises from the electricity for the gas chillers (384 kWh/day), and the overall cost with this setup is the lowest of the above-described methods for both N<sub>2</sub> and He MAS. Although highly promising, achieving faster MAS and lower temperatures is still a challenge that entails further modification of the MAS module, bearing structure and turbine blades taking the temperature-dependent kinematic viscosity of the spinner gas into account, and needs further researches. The system may also be optimized for a use exclusively in higher temperature range such as >80 K, enabling an even more compact and inexpensive system. In the near future, the closed-cycle MAS system can become “staple” equipment for DNP-NMR, as well as regular MAS NMR at low temperatures.

## 4.6 DNP Samples and Recent Applications

### 4.6.1 Basic Setup

In a most basic sample setup, the molecule of interest (protein, organic compound, etc.) and a polarizing agent are sparsely and homogeneously dissolved in an organic matrix. The electron spin polarization is first transferred to nearby protons, and then distributed to the bulk matrix through the  $^1\text{H}$ - $^1\text{H}$  spin diffusion (Fig. 4.13). In fact, it seems that only the polarization directly transmitted to the protons outside the “diffusion barrier” surrounding the polarizing agent is successfully diffused to the bulk [85], which has a fundamental meaning in both the theory and application. In any case, no specific association between the radical and the molecules of interest is assumed for the DNP to work, and this ensures the high generality of the method. The enhanced bulk polarization can be accumulated to the matrix for a time roughly set by  $T_{1\text{H}}$  of the matrix. The enhanced proton polarization that reached the solute molecule of interest is often transferred to the rare spins, such as  $^{13}\text{C}$  or  $^{15}\text{N}$ , via cross-polarization (CP) for observation.

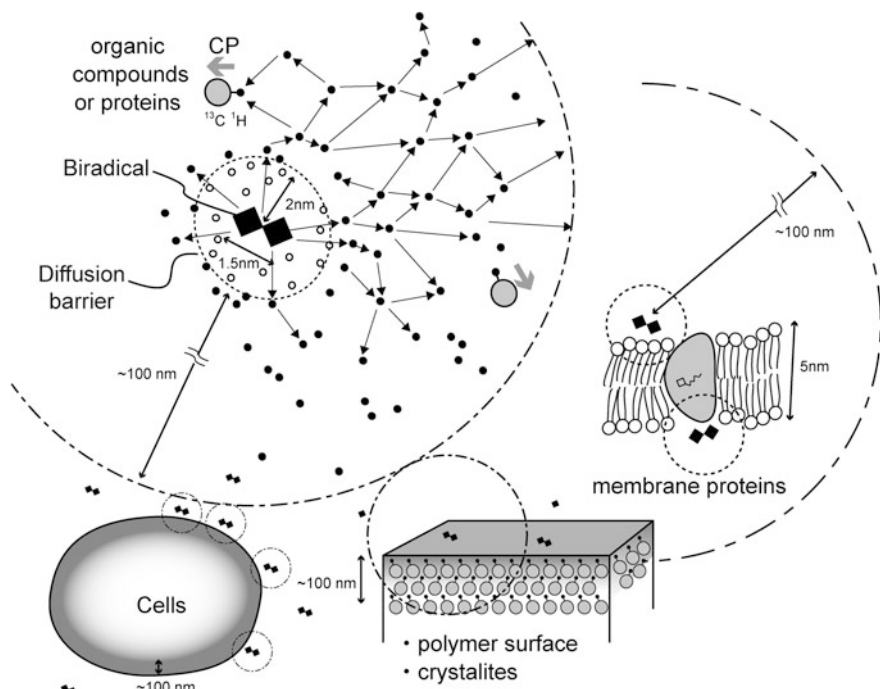
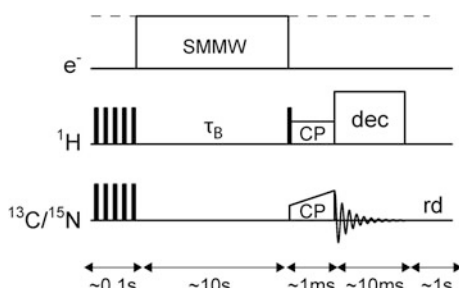


**Fig. 4.13** A microscopic description of various DNP samples, emphasizing the role of the  $^1\text{H}$ - $^1\text{H}$  spin diffusion and its spatial scale. The diffusion barrier and the typical diffusion limit is shown by dashed and dash-dot line, respectively. Approximate length scale is shown in nm. Black dots for the water/matrix molecules

Figure 4.14 shows the basic pulse scheme used in the DNP experiments. To accurately measure the  $^1\text{H}$  polarization enhancement, the initial  $^1\text{H}$  and  $^{13}\text{C}$  polarizations are erased with  $\sim 120^\circ$ -pulse train on both channels. Normally, 3–10 pulses suffice to dissipate the polarization down to the thermal noise level. This is followed by the polarization buildup/accumulation time,  $\tau_B$ , and then CP before the observation. The same measurement is repeated with and without SMMW irradiation for recording the so-called on signal and off signal to calculate the simplistic signal enhancement factor by  $\varepsilon_{\text{on/off}} = I_{\text{on}}/I_{\text{off}}$ , where  $I_{\text{on}}$  and  $I_{\text{off}}$  are the  $^{13}\text{C}$  NMR signal intensities taken with the SMMW on and off, respectively. The SMMW may be made on only during  $\tau_B$  to reduce the radiation heating of the sample, but usually it has a minor effect especially when the high thermal conductivity material is used for the sample rotor (Sect. 4.5.2). As long as the buildup time constant is identical for the on and off signals, the same enhancement factor is obtained at any  $\tau_B$ . Otherwise, each intensity may be measured at respective  $T_{1\text{H}}$  time, or both intensities at plateau  $\tau_B > 5*T_{1\text{H}}$ . Any experiment in either 1D or  $N$ -dimensional ( $N$ -D) can be converted to the DNP-enhanced version with a simple addition of the polarization buildup time  $\tau_B$  before the initial CP period. For  $N$ -D acquisition,  $\tau_B$  is often minimized for increasing the repetition rate, while  $\tau_B \sim 1.26*T_{1\text{H}}$  should yield the optimal unit-time sensitivity. Usually,  $T_{1\text{H}}$  does not increase significantly with decreasing temperature for a doped sample, and stays in the order of 1–10 s at  $T \sim 90$  K. The increase of  $T_{1\text{H}}$  is especially modest when the sample contains methyl groups, lingering around 5 s even at 30 K.

Various techniques exist for packing the often liquid-state or wet DNP sample to a MAS rotor. The sample must be center-packed using top/bottom spacers for typically 5–10 mm in length, so that the whole part could be evenly illuminated with the SMMW. Fluorinated resins such as Kel-F and Teflon having no  $^1\text{H}$ – $^{13}\text{C}$  direct bonds are popular for the spacer material, but polyimides and polyamideimides such as Vespel and Torlon are sometimes preferred for precision machining. For packing the sample liquid-tight, very tight spacers are required. To avoid compression of the air into the rotor, the tight spacers should have a vent hole at the center, which may be made as small as possible ( $<0.1$  mm- $\varphi$ ) to avoid sample leakage, or tapped so that a small plastic screw can be used to close it after packing. The spacer itself can have a hollow structure to contain some powdered KBr for an in situ temperature measurement (Figs. 4.12 and 4.16) [86, 87]. Alternatively, the

**Fig. 4.14** A basic pulse scheme for DNP. Typical time range is shown below



sample may be contained in a separate rotor insert with a liquid-tight cap. The sample insert will decrease the rotor-filling factor, thus to be avoided for measurements critical in sensitivity.

#### 4.6.2 Sample Preparation and DNP Efficiency

The currently most popular glass matrices include glycerol–water, DMSO–water mixtures for hydrophilic samples, and tetrachloroethane (TCE) sometimes added with a hint of methanol for hydrophobic compounds. The solubility of the radical molecule into the matrix is a key for the DNP efficiency, since even microscopic aggregation of the radical molecules significantly reduces the enhancement factor. Thus, hydrophilic and hydrophobic radicals are to be chosen depending on the molecule of interest. In the sample preparation, the use of sonication and mild heat may be tolerated for many of the stable radicals, but should be minimized. Techniques for dissolving hydrophobic radicals into water-based matrix using micelles [88] and cyclodextrins [47] have also been reported. These organic matrices are all liquid at room temperature, allowing easy dissolution of the solute and radical, but form a rigid and homogeneous glassy matrix at  $T \sim 110\text{--}150\text{ K}$ . The glass formation avoids the water crystallization, thus concomitant radical aggregation, as well as protects (biological) molecules from cold denaturation/damage. In addition, the rigid matrix is required for an efficient spin diffusion process. Some organic glass formers, such as ortho-terphenyl (OTP), stay rigid even at room temperature [89], but they require considerable heats for melting it and for dissolving the solutes, and thus are incompatible with biological or heat-sensitive samples. Matrices with the high glass transition temperature as well as low melting temperature (ideally at room temperature) are desirable for more general use and under an extensive research in the authors' laboratory. The quality of the glass often depends on the cooling rate and requires  $\sim 1000\text{ K/min}$  or faster for a good glass. Thus, loading the sample to a probe kept at cryogenic temperature is always preferred to a slow cooling of a sample rotor from the ambient temperature. Reduction in paramagnetic oxygen in the sample has been reported to improve the enhancement factor for some polymer films without methyl groups [90], but could be generally important at very low temperatures  $T < 30\text{ K}$ , where the methyl group rotation is restricted.

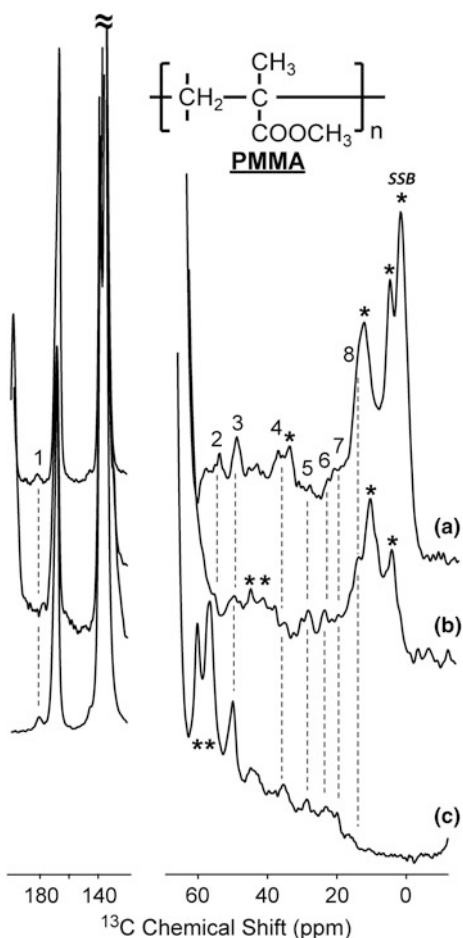
More generally, the molecule of interest should not necessarily be soluble/monodispersed in the matrix, but can be any form of molecular assembly such as crystals [72, 91, 92] (amyloid) fibrils [93, 94], membrane proteins embedded in a lipid bilayer [95–99], cell debris/whole cell [100, 101], polymer debris and material particles [102, 103]. These substances can simply be suspended to or wet by the radical-containing matrix (Fig. 4.13). As long as these molecular assemblies are populated with protons, the polarization will sink into them by spin diffusion even if the radical molecule itself cannot permeate it. On the other hand, if the sample is scarce in protons such as for inorganic materials, the general DNP

methods described previously are not directly applicable, and require the development of specific new methods. The efficiency of the spin diffusion increases with the effective proton density in the matrix at a given MAS rate. At an unduly high proton density, however, the polarization will be shared among too many matrix protons and reduces the dividend received by the molecule of interest. The optimal matrix proton density has been systematically studied for the glycerol–water and DMSO–water mixtures at  $T \sim 90$  K, and it was determined for the glycerol matrix as  $d_8$ -glycerol/ $D_2O/H_2O \sim 6/3/1$  w/w/w. The impact of the optimized deuteration level of a target protein molecule itself has also been investigated [104].

Assuming the typical spin diffusivity of  $\sim 1$  nm<sup>2</sup>/ms determined in many organic polymers also for the frozen DNP matrix, the enhanced polarization travels over  $\sim 100$  nm away from the radical molecule in  $\sim 10$  s, the typical  $^1H$   $T_1$  of the matrix (radical-doped organic glass matrix) at  $T \sim 100$  K. Even at a very low radical concentration (say  $\sim 0.1$  mM), the average inter-radical distance is smaller than 100 nm by assuming a homogeneous radical distribution. This means that at the typical radical concentration used in many DNP experiments (1–20 mM), the solute molecules should receive the polarization from much more than one surrounding radical molecules, leading to the high DNP efficiency. From another point of view, it is understood that a strategy for obtaining molecular geometrical information based on uneven signal enhancement within a molecule/molecular assembly will work only for the systems whose size is in the order of 100 nm or larger. Naturally, some previous attempts to detect the uneven enhancement distribution on a protein molecule whose diameter were only  $<5$  nm or so resulted in a limited success [98]. Even with a use of the direct  $^{13}C$ -DNP, the spin diffusion was too fast in a uniformly  $^{13}C$ -labeled protein molecule to detect the enhancement distribution clearly [45]. As a contrasting example, a 7-residue peptide GNNQQNY forms a needle-shaped microcrystal with the lateral dimension of  $\sim 200$  nm, for which the polarization distribution was suggested to be strongly non-uniform, resulting in a much lower stationary polarization at the crystal core [92]. A large multi-lamellar liposomal vesicle would become similar in size, and the polarization at its core would also be spin diffusion-limited. The similar limitation applies to an attempt to polarize the cytoplasm of a cell using radicals located outside the cell, since the cell diameter often exceeds 1  $\mu$ m even for bacterial cells. In an example trying to polarize the functional surface coating of a polymer film (Fig. 4.15), the ability of polarizing only  $\sim 100$  nm deep from the film surface was utilized as an advantage for zooming into the functional coating.

In polarizing molecular systems suspended in the matrix, the affinity of the matrix to the surface of the molecular system of interest seems to have a critical impact on the DNP efficiency. For example, in polarizing the GNNQQNY microcrystals above (5 T, 90 K, 5 kHz MAS), observed average enhancement was considerably lower than expected from the theory assuming a continuous flow of the matrix polarization into the crystal by spin diffusion. The authors suggested that some kind of “bottleneck” for the spin diffusion exists at the matrix–crystal interface. This is presumably due to the microscopic molecular segregation at the system interface although the effect was mild in this case since the peptide in question was

**Fig. 4.15** Surface-enhancing DNP on polyacrylate-coated PET film. The DNP-enhanced  $^{13}\text{C}$ -spectrum obtained using TEKPol in TCE (a), and TOTAPOL in glycerol/D<sub>2</sub>O/H<sub>2</sub>O (b). The acquisition time was  $\sim 20$  min for each. c Spectrum taken without DNP, but with  $100\times$  longer acquisition time at room temperature. Signals 1–4 seem to be more strongly enhanced in TCE matrix than in glycerol.  $B_0 = 16.4$  T,  $T = 100$  K,  $v_R = 11$  kHz. The asterisks (\*) indicate the spinning side bands. Sample was provided by Fuji Film Corporation



fairly hydrophilic. This notion is further corroborated by the following recent observations: (a) For a microcrystal of a tri-peptide, MLF, absolutely no DNP enhancement was observed (16.4 T, 100 K, 3 kHz MAS) when wet by glycerol/water matrix, to which it is highly insoluble. (b) Similarly, a microcrystal of glucose showed no enhancement (14.1 T, 100 K, 5 kHz MAS) when suspended to the ethanol glass, to which it is fairly insoluble. (c) On the other hand, the same glucose crystal was very efficiently polarized (14.1 T, 100 K, 5 kHz MAS) [72] in the glycerol/water matrix, to which it is soluble. (d) And finally, in polarizing the PET film with a 1  $\mu\text{m}$  hydrophobic polyacrylate surface coating, some surface signals have received considerably higher enhancement (16.4 T, 100 K, 11 kHz MAS) when it was wet by hydrophobic matrix and radical (Fig. 4.15a: TCE + TEKPol), than with the water-based matrix (Fig. 4.15b: glycerol/water +TOTAPOL). The enhancement factor was difficult to evaluate since the off signal was not seen for this sample. Instead, Fig. 4.15c shows a spectrum taken for the

same film packed to a 3.2 mm rotor, averaged over a day and half at room temperature for a similar S/N to the DNP-enhanced spectrum. From this, roughly ~100-fold time saving, i.e., the overall signal enhancement of ~10 was deduced.

Other noteworthy examples include the matrix-free DNP, targeted DNP and DNP with endogenous polarizing agent. In the matrix-free approach [105, 106], the sample of the cell wall debris were mixed with a TOTAPOL water solution and then dried out [107]. Due to the specific association between TOTAPOL and the peptidoglycan on the cell wall surface, TOTAPOL did not form aggregation even without glassy matrix. So far, this approach is of interest only for a limited range of samples, but clarified an interesting possibility for the future development. In the recently proposed “target-DNP” approach, a ligand peptide was spin-labeled with TOTAPOL, and used to selectively polarize its binding partner protein in an overwhelming background from the cellular lysate [108]. This approach delivers the enhanced polarization based on the biologically meaningful protein-protein associations and can provide a powerful means for detecting key biological events in unpurified samples. Some DNP experiments on molecular systems with endogenous polarizing agents have also been reported, for which the paramagnetic center was directly attached to the molecule of interest or its close surroundings. For example, biomolecules with an intrinsic metal- [109] or chlomophore-coordinating site [110] or proteins recombinantly modified for a site-specific spin labeling have been investigated. In the membrane protein setups, the lipid molecules were labeled with radicals so that the polarization is predominantly delivered to the transmembrane proteins [99, 106]. As mentioned above, it is difficult to retrieve precise geometrical information relative to the coordination site from the DNP effect; they still provided important examples of the viable sample setup. An additional feature with these setups is that a rotor can be fully filled with the sample of interest without the matrix, lending to the absolute sensitivity; the polarization can be delivered to the target through the direct molecular contact. However, in such cases one can expect potential signal broadening from the direct/close association of the radial and target molecule.

The incipient impregnation or sample wetting procedure has a similar merit of reducing the matrix volume for an increased absolute sensitivity and has somewhat wider applicability. In these methods, the sample is pestled with a minimum amount of radical-containing solution, or the sample is suspended in the matrix then thoroughly drained before packing to a rotor. The matrix solution that does not dissolve the sample itself is suited for this approach. This was first applied to the DNP of surface-modified material particles and pharmaceutical formulations, in which finely grinded powder sample was “impregnated” with a TCE solution of hydrophobic radicals (TEKPol, bCTbk, etc.) [103, 111]. Similarly, in polarizing GNNQQNY, the protein crystals were washed with glycerol/water solution of TOTAPOL and drained [92]. Liposome sample containing membrane protein have also been treated in a similar fashion, for which the pelleted membrane fraction was re-suspended to the glycerol/water solution of radical, then spun down before packing [95, 96]. In a report, a membrane sample in a rotor was wetted with drops of the radical solution from the top and equilibrated [97]. In these preparations

described here, the radical molecules do not penetrate into the molecular assembly of interest, and the spectrum is minimally affected by the paramagnetic broadening. This was clearly evidenced by the high resolution observed for the active site of bacteriorhodopsin (bR), for which the loaded radical molecules were sequestered outside the membrane [112].

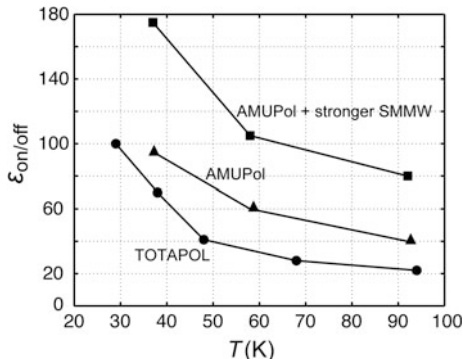
For evaluating the absolute sensitivity gain, it is important to take account of the effect of the signal quenching. A finite number of solute molecules directly surrounding the radical molecule experience strong paramagnetic shift and broadening, and thus escape the NMR detection. Thus, this will reduce the absolute signal intensity of the radical-doped sample when measured without SMMW irradiation [73]. A distinct depolarization path that is specific to a spinning sample doped with the broad-line radicals (aka Thurber effect) was also proposed [113]. Due to the quenching and/or the Thurber effect, the off-signal intensity is normally in artificially reduced state, and leads to an overestimation of the sensitivity gain by DNP if one is only based on the simplistic enhancement factor  $\varepsilon_{\text{on/off}}$ . Ultimately, the absolute sensitivity should take an account of the quenching/Thurber effect together with the reduced CP efficiency due to the shorter  $T_{1\rho}$  for a doped sample, slower data collection due to the longer  $T_{1H}$  at low temperatures, reduced sample filling factor due to the glass matrix for the sensitivity losses, but, on the other hand, the smaller thermal noise and greater Curie magnetization at low temperatures together with the DNP signal enhancement for the gains. Usually, the gain overwhelms the loss.

The large signals from the glassy matrix can cause unwanted problems in application studies. The  $^{13}\text{C}$  signals of glycerol ( $\sim 65$  and  $75$  ppm), TCE ( $\sim 80$  ppm) and DMSO ( $\sim 40$  ppm) can partly overlap with the aliphatic signals of interest. If the molecule of interest is isotopically labeled with  $^{13}\text{C}$  and/or  $^{15}\text{N}$ , multi-dimensional measurement easily escapes this problem by resolving the interesting cross-peaks to the off-diagonal spectral regions, while the matrix signals stay on the diagonal. If the molecule under test is unlabeled, or only 1D measurement is sought, a possible work-around is the use of the  $^{12}\text{C}$ -enriched matrix. At the moment,  $^{12}\text{C}$ -enriched glycerol is commercially available. If the sample of interest is compatible with the matrix-free setup, or with the matrix impregnation method, the matrix signal should annoy the measurement much less.

#### **4.6.3 DNP Enhancement Factor and Temperature**

For combating the diminishing DNP efficiency at high fields, the choice of lower temperatures can be an effective strategy. Figure 4.16 shows the DNP enhancement factor measured at  $B_0 = 16.4$  T as a function of the sample temperature. The sample was  $^{13}\text{C}$ -urea dissolved in glycerol/water matrix. The closed-cycle He MAS system was used [22]. Clearly, the enhancement factor rapidly increases with the lowering temperature. With TOTAPOL and AMUPol, the enhancement factor exceeded 100 at  $T = 28$  K and  $v_R = 6$  kHz, with roughly a few watts of SMMW at the sample.

**Fig. 4.16** Enhancement factor versus sample temperature recorded at  $B_0 = 16.4$  T. Sample was 1M  $^{13}\text{C}$ -urea in  $d_8$ -glycerol/ $\text{D}_2\text{O}/\text{H}_2\text{O}$  matrix. The MAS rate was 6 kHz, except for the 38 and 28 K data, for which  $v_R \sim 4$  kHz. The sample temperature was measured from  $T_1$  of  $^{79}\text{Br}$  co-packed in the rotor



Together with the increased Curie polarization by a factor of  $\sim 10$  ( $=300/30$  K), reduced thermal noise level by 30% from the cold RF coil and capacitors, and the measured 50% signal loss from the CP efficiency plus the quenching effect, the absolute sensitivity gain was determined as  $100*10*1.3*0.5 = 600$  at 30 K for TOTAPOL (circles, Fig. 4.16). With AMUPol, although a factor of 1.5–2 larger enhancement was obtained (triangles), the quenching effect was found to be severer than with TOTAPOL: The off signal intensity was found to be only  $\sim 30\%$  of undoped sample. Thus, overall sensitivity turned out to be similar to the one with TOTAPOL at 30 K. Also shown in Fig. 4.16 for AMUPol is the enhancement factor obtained with several-fold higher SMMW power (rectangles). The  $\epsilon_{on/off}$  was almost doubled to be  $\sim 175$  at 38 K, leading to the overall gain of  $\sim 175*7.9$  ( $=300/38$  K)\*1.3\*0.3 = 540. These overall gains are considerably higher than that reported at the same field condition, but conventional temperature  $T \sim 85$  K [16, 114]:  $40*3.5*0.5 = 70$ , where the same quenching factor from our measurement was assumed.

## 4.7 Summary and Outlook

This chapter discussed the current methods and instruments for the high-field DNP technique for sensitizing the high-resolution MAS NMR spectroscopy. After decades since the “big bang” brought by the seminal paper published in 1993, the field of high-field DNP is still rapidly evolving and expanding, and will continue to do so. Thus, together with the current success, the authors have emphasized a number of remaining technical issues and current limitations to give a baseline for the future development and innovation. It is the authors’ belief that the overall sensitivity gain of MAS NMR should exceed a factor of 10,000 in several years with a use of lower temperatures, better polarizing agents, more sophisticated SMMW irradiation schemes and the cryogenic signal receiving systems. Along the way, the high-field DNP is expected to open up new avenues to in-cell structural biology at

physiological concentration, studies on supramolecular membrane assemblies as well as (unlabeled) ligand conformation and dynamics of membrane receptors, and even to fully isotope labeling-free structural biology. Besides the biological systems, the unprecedented sensitivity will enable detection and structural analysis of trace amount of natural products or pharmaceutical contamination, polymer terminals, organo-functionalized material surfaces and minor metabolites.

Other interesting scope of high-field DNP includes the quadrupolar DNP, especially on  $^{17}\text{O}$  NMR spectroscopy of proteins,  $^{35}\text{Cl}$  NMR in the chlorine pumps,  $^{43}\text{Ca}$  NMR of the organic–inorganic domain interface in bones and  $^{27}\text{Al}$  NMR in various material samples. With the high spin polarization exceeding  $\sim 50\%$ , the high temperature approximation would start to sway at high fields. Novel NMR techniques based on the considerably nonlinear equilibrium spin states should be explored for application. Combined with the optically excited electrons, the nuclear polarization way exceeding that relying on the electron's thermal equilibrium will be available for high-resolution MAS NMR spectroscopy. The sensitivity gain itself would be phenomenal, but also this would lend to the molecular mechanistic understandings of the electron transfer phenomena, and eventually to the development of artificial photosynthetic systems in a long term.

Engineering effort should be directed, for example, to a DNP probe with the cold signal receiving system, 1 GHz DNP spectrometer,  $^1\text{H}$  detection DNP probe with fast MAS, ultra-fast helium MAS DNP probe, table-top gyrotron employing the high- $T_c$  bulk superconductors, integral gyrotron in the NMR magnet, high-power non-gyrotron SMMW sources for  $f_{\text{SMMW}} \gg 300$  GHz, RF coils transparent to the SMMW, phase-controllable SMMW pulse generator for the coherent pulse DNP and SMMW resonator structure compatible with the MAS NMR samples. Chemically, more advances on the polarizing agents are hoped for those utilizing transition metals, those being able to promote the OE-DNP in insulating solids, a pair of narrow-line radicals directly matching the CE frequency condition and 20 K-optimized radicals. Development of the sample preparation methods for increasing the low-temperature spectral resolution, and of the numerical approaches, at the same time, for extracting information from overlapped signals should also be an important part of the future innovation.

**Acknowledgements** We thank Drs. Toshitaka Ideahra and Jagadishwar R. Sirigiri for a careful reading of the manuscript.

## References

1. Hansen, M.R., Graf, R., Spiess, H.W.: Interplay of structure and dynamics in functional macromolecular and supramolecular systems as revealed by magnetic resonance spectroscopy. *Chem. Rev.* **116**, 1272–1308 (2016)
2. Kazmierski, S., Pawlak, T., Jeziorna, A., Potrzebowski, M.J.: Modern solid state NMR techniques and concepts in structural studies of synthetic polymers. *Polym. Adv. Technol.* **27**, 1143–1155 (2016)

3. Howarth, A.J., Peters, A.W., Vermeulen, N.A., Wang, T.C., Hupp, J.T., Farha, O.K.: Best practices for the synthesis, activation, and characterization of metal-organic frameworks. *Chem. Mater.* **29**, 26–39 (2017)
4. Polenova, T., Gupta, R., Goldbourt, A.: Magic angle spinning NMR spectroscopy: a versatile technique for structural and dynamic analysis of solid-phase systems. *Anal. Chem.* **87**, 5458–5469 (2015)
5. Becerra, L.R., Gerfen, G.J., Temkin, R.J., Singel, D.J., Griffin, R.G.: Dynamic nuclear-polarization with a cyclotron-resonance maser at 5 T. *Phys. Rev. Lett.* **71**, 3561–3564 (1993)
6. Rosay, M., Weis, V., Kreischer, K.E., Temkin, R.J., Griffin, R.G.: Two-dimensional  $^{13}\text{C}$ - $^{13}\text{C}$  correlation spectroscopy with magic angle spinning and dynamic nuclear polarization. *J. Am. Chem. Soc.* **124**, 3214–3215 (2002)
7. Hu, K.N.: Polarizing agents and mechanisms for high-field dynamic nuclear polarization of frozen dielectric solids. *Solid State Nucl. Magn. Reson.* **40**, 31–41 (2011)
8. Matsuki, Y., Maly, T., Ouari, O., Karoui, H., Le Moigne, F., Rizzato, E., Lyubenova, S., Herzfeld, J., Prisner, T., Tordo, P., Griffin, R.G.: Dynamic nuclear polarization with a rigid biradical. *Angew. Chem. Int. Ed.* **48**, 4996–5000 (2009)
9. Song, C.S., Hu, K.N., Joo, C.G., Swager, T.M., Griffin, R.G.: TOTAPOL: A biradical polarizing agent for dynamic nuclear polarization experiments in aqueous media. *J. Am. Chem. Soc.* **128**, 11385–11390 (2006)
10. Bajaj, V.S., Hornstein, M.K., Kreischer, K.E., Sirigiri, J.R., Woskov, P.P., Mak-Jurkauskas, M.L., Herzfeld, J., Temkin, R.J., Griffin, R.G.: 250 GHz CW gyrotron oscillator for dynamic nuclear polarization in biological solid state NMR. *J. Magn. Reson.* **189**, 251–279 (2007)
11. Hornstein, M.K., Bajaj, V.S., Griffin, R.G., Temkin, R.J.: Continuous-wave operation of a 460-GHz second harmonic gyrotron oscillator. *IEEE Trans. Plasma Sci. IEEE Nucl. Plasma Sci. Soc.* **34**, 524–533 (2006)
12. Hornstein, M.K., Bajaj, V.S., Griffin, R.G., Temkin, R.J.: Efficient low-voltage operation of a CW gyrotron oscillator at 233 GHz. *IEEE Trans. Plasma Sci.* **35**, 27–30 (2007)
13. Idehara, T., Tatematsu, Y., Yamaguchi, Y., Khutoryan, E.M., Kuleshov, A.N., Ueda, K., Matsuki, Y., Fujiwara, T.: The development of 460 GHz gyrotrons for 700 MHz DNP-NMR spectroscopy. *J. Infrared Millim. Terahertz Waves* **36**, 613–627 (2015)
14. Chang, T.H., Idehara, T., Ogawa, I., Agusu, L., Kobayashi, S.: Frequency tunable gyrotron using backward-wave components. *J. Appl. Phys.* **105**, 063304 (2009)
15. Hornstein, M.K., Bajaj, V.S., Griffin, R.G., Kreischer, K.E., Mastovsky, I., Shapiro, M.A., Sirigiri, J.R., Temkin, R.J.: Second harmonic operation at 460 GHz and broadband continuous frequency tuning of a gyrotron oscillator. *IEEE Trans. Electron Devices* **52**, 798–807 (2005)
16. Barnes, A.B., Nanni, E.A., Herzfeld, J., Griffin, R.G., Temkin, R.J.: A 250 GHz gyrotron with a 3 GHz tuning bandwidth for dynamic nuclear polarization. *J. Magn. Reson.* **221**, 147–153 (2012)
17. Idehara, T., Mudiganti, J.C., Agusu, L., Kanemaki, T., Ogawa, I., Fujiwara, T., Matsuki, Y., Ueda, K.: Development of a compact sub-THz gyrotron FU CW CI for application to high power THz technologies. *J. Infrared Millim. Terahertz Waves* **33**, 724–744 (2012)
18. Barnes, A.B., Mak-Jurkauskas, M.L., Matsuki, Y., Bajaj, V.S., Van Der Wel, P.C.A., Derocher, R., Bryant, J., Sirigiri, J.R., Temkin, R.J., Lugtenburg, J., Herzfeld, J., Griffin, R.G.: Cryogenic sample exchange NMR probe for magic angle spinning dynamic nuclear polarization. *J. Magn. Reson.* **198**, 261–270 (2009)
19. Markhasin, E., Hu, J., Su, Y., Herzfeld, J., Griffin, R.G.: Efficient, balanced, transmission line RF circuits by back propagation of common impedance nodes. *J. Magn. Reson.* **231**, 32–38 (2013)
20. Smith, A.A., Corzilius, B., Bryant, J.A., Derocher, R., Woskov, P.P., Temkin, R.J., Griffin, R.G.: A 140 GHz pulsed EPR/212 MHz NMR spectrometer for DNP studies. *J. Magn. Reson.* **223**, 170–179 (2012)

21. Thurber, K.R., Potapov, A., Yau, W.M., Tycko, R.: Solid state nuclear magnetic resonance with magic-angle spinning and dynamic nuclear polarization below 25 K. *J. Magn. Reson.* **226**, 100–106 (2013)
22. Matsuki, Y., Nakamura, S., Fukui, S., Suematsu, H., Fujiwara, T.: Closed-cycle cold helium magic-angle spinning for sensitivity-enhanced multi-dimensional solid-state NMR. *J. Magn. Reson.* **259**, 76–81 (2015)
23. Matsuki, Y., Ueda, K., Idehara, T., Ikeda, R., Ogawa, I., Nakamura, S., Toda, M., Anai, T., Fujiwara, T.: Helium-cooling and -spinning dynamic nuclear polarization for sensitivity-enhanced solid-state NMR at 14 T and 30 K. *J. Magn. Reson.* **225**, 1–9 (2012)
24. Rosay, M., Blank, M., Engelke, F.: Instrumentation for solid-state dynamic nuclear polarization with magic angle spinning NMR. *J. Magn. Reson.* **264**, 88–98 (2016)
25. Slichter, C.P.: The discovery and demonstration of dynamic nuclear polarization: a personal and historical account. *Phys. Chem. Chem. Phys.* **12**, 5741–5751 (2010)
26. Carver, T.R., Slichter, C.P.: Polarization of nuclear spins in metals. *Phys. Rev.* **92**, 212–213 (1953)
27. Carver, T.R., Slichter, C.P.: Experimental verification of the Overhauser nuclear polarization effect. *Phys. Rev.* **102**, 975–980 (1956)
28. Kryukov, E.V., Pike, K.J., Tam, T.K., Newton, M.E., Smith, M.E., Dupree, R.: Determination of the temperature dependence of the dynamic nuclear polarisation enhancement of water protons at 3.4 Tesla. *Phys. Chem. Chem. Phys.* **13**, 4372–4380 (2011)
29. Neugebauer, P., Krummenacker, J.G., Denysenkov, V.P., Parigi, G., Luchinat, C., Prisner, T.F.: Liquid state DNP of water at 9.2 T: an experimental access to saturation. *Phys. Chem. Chem. Phys.* **15**, 6049–6056 (2013)
30. Prandolini, M.J., Denysenkov, V.P., Gafurov, M., Endeward, B., Prisner, T.F.: High-field dynamic nuclear polarization in aqueous solutions. *J. Am. Chem. Soc.* **131**, 6090–6092 (2009)
31. Armstrong, B.D., Han, S.: A new model for Overhauser enhanced nuclear magnetic resonance using nitroxide radicals. *J. Chem. Phys.* **127**, 104508 (2007)
32. Can, T.V., Caporini, M.A., Mentink-Vigier, F., Corzilius, B., Walish, J.J., Rosay, M., Maas, W.E., Baldus, M., Vega, S., Swager, T.M., Griffin, R.G.: Overhauser effects in insulating solids. *J. Chem. Phys.* **141**, 064202 (2014)
33. Jefferies, C.D.: Polarization of nuclei by resonance saturation in paramagnetic crystals. *Phys. Rev.* **106**, 164–165 (1957)
34. Jefferies, C.D.: Polarization of nuclei by forbidden transitions in paramagnetic resonance. *Phys. Rev.* **117**, 1056–1069 (1960)
35. Hwang, C.F., Hill, D.A.: New effect in dynamic polarization. *Phys. Rev. Lett.* **18**, 110 (1967)
36. Kessenikh, A.V., Lushchikov, V.I., Manenkov, A.A., Taran, Y.V.: Proton polarization in irradiated polyethylenes. *Sov. Phys. Solid State* **5**, 321–329 (1963)
37. Kessenikh, A.V., Manenkov, A.A., Pyatnitskii, G.I.: On explanation of experimental data on dynamic polarization of protons in irradiated polyethylenes. *Sov. Phys. Solid State* **6**, 641–643 (1964)
38. Wollan, D.S.: Dynamic nuclear polarization with an inhomogeneously broadened ESR line. I. Theory. *Phys. Rev. B: Condens. Matter* **13**, 3671–3685 (1976)
39. Wollan, D.S.: Dynamic nuclear polarization with an inhomogeneously broadened ESR line. II. Experiment. *Phys. Rev. B: Condens. Matter* **13**, 3686–3696 (1976)
40. Afeworki, M., Schaefer, J.: Mechanism of DNP-enhanced polarization transfer across the interface of polycarbonate polystyrene heterogeneous blends. *Macromolecules* **25**, 4092–4096 (1992)
41. Maresch, G.G., Kendrick, R.D., Yannoni, C.S., Galvin, M.E.: Dynamic nuclear polarization via confined electrons in bulk solids. *J. Magn. Reson.* **82**, 41–50 (1989)
42. Singel, D.J., Seidel, H., Kendrick, R.D., Yannoni, C.S.: A spectrometer for EPR, DNP, and multinuclear high-resolution NMR. *J. Magn. Reson.* **81**, 145–161 (1989)

43. Wind, R.A., Duijvestijn, M.J., Van Der Lugt, C., Manenschijn, A., Vriend, J.: Applications of dynamic nuclear polarization in  $^{13}\text{C}$  NMR in solids. *Prog. Nucl. Magn. Reson. Spectrosc.* **17**, 33–67 (1985)
44. Corzilius, B., Smith, A.A., Barnes, A.B., Luchinat, C., Bertini, I., Griffin, R.G.: High-field dynamic nuclear polarization with high-spin transition metal ions. *J. Am. Chem. Soc.* **133**, 5648–5651 (2011)
45. Kaushik, M., Bahrenberg, T., Can, T.V., Caporini, M.A., Silvers, R., Heiliger, J., Smith, A. A., Schwalbe, H., Griffin, R.G., Corzilius, B.: Gd(III) and Mn(II) complexes for dynamic nuclear polarization: small molecular chelate polarizing agents and applications with site-directed spin labeling of proteins. *Phys. Chem. Chem. Phys.* **18**, 27205–27218 (2016)
46. Salnikov, E., Rosay, M., Pawsey, S., Ouari, O., Tordo, P., Bechinger, B.: Solid-state NMR spectroscopy of oriented membrane polypeptides at 100 K with signal enhancement by dynamic nuclear polarization. *J. Am. Chem. Soc.* **132**, 5940–5941 (2010)
47. Mao, J., Akhmetzyanov, D., Ouari, O., Denysenkov, V., Corzilius, B., Plackmeyer, J., Tordo, P., Prisner, T.F., Glaubitz, C.: Host-guest complexes as water-soluble high-performance DNP polarizing agents. *J. Am. Chem. Soc.* **135**, 19275–19281 (2013)
48. Kiesewetter, M.K., Corzilius, B., Smith, A.A., Griffin, R.G., Swager, T.M.: Dynamic nuclear polarization with a water-soluble rigid biradical. *J. Am. Chem. Soc.* **134**, 4537–4540 (2012)
49. Kubicki, D.J., Casano, G., Schwarzwaldar, M., Abel, S., Sauvee, C., Ganesan, K., Yulikov, M., Rossini, A.J., Jeschke, G., Copret, C., Lesage, A., Tordo, P., Ouari, O., Emsley, L.: Rational design of dinitroxide biradicals for efficient cross-effect dynamic nuclear polarization. *Chem. Sci.* **7**, 550 (2016)
50. Landau, L.D., Lifshitz, L.M.: Quantum Mechanics. Butterworth-Heinemann, Oxford (1981)
51. Thurber, K.R., Tycko, R.: Theory for cross effect dynamic nuclear polarization under magic-angle spinning in solid state nuclear magnetic resonance: The importance of level crossings. *J. Chem. Phys.* **137**, 084508 (2012)
52. Thurber, K.R., Yau, W.M., Tycko, R.: Low-temperature dynamic nuclear polarization at 9.4 T with a 30 mW. *J. Magn. Reson.* **204**, 303–313 (2010)
53. Krahn, A., Lottmann, P., Marquardsen, T., Tavernier, A., Turke, M.T., Reese, M., Leonov, A., Bennati, M., Hoefer, P., Engelke, F., Griesinger, C.: Shuttle DNP spectrometer with a two-center magnet. *Phys. Chem. Chem. Phys.* **12**, 5830–5840 (2010)
54. Reese, M., Turke, M.T., Tkach, I., Parigi, G., Luchinat, C., Marquardsen, T., Tavernier, A., Hofer, P., Engelke, F., Griesinger, C., Bennati, M.:  $^1\text{H}$  and  $^{13}\text{C}$  dynamic nuclear polarization in aqueous solution with a two-field (0.35 T/14 T) shuttle DNP spectrometer. *J. Am. Chem. Soc.* **131**, 15086–15087 (2009)
55. Ardenkjær-Larsen, J.H.: On the present and future of dissolution DNP. *J. Magn. Reson.* **264**, 3–12 (2016)
56. Ardenkjær-Larsen, J.H., Fridlund, B., Gram, A., Hansson, G., Hansson, L., Lerche, M.H., Servin, R., Thaning, M., Golman, K.: Increase in signal-to-noise ratio of >10,000 times in liquid-state NMR. *Proc. Natl. Acad. Sci. USA* **100**, 10158–10163 (2003)
57. Felch, K.L., Danly, B.G., Jory, H.R., Kreischer, K.E., Lawson, W., Levush, B., Temkin, R. J.: Characteristics and applications of fast-wave gyrodevices. *Proc. IEEE* **87**, 752–781 (1999)
58. Chu, K.R.: The electron cyclotron maser. *Rev. Mod. Phys.* **76**, 489–540 (2004)
59. Nusinovich, G.S.: Introduction to the Physics of Gyrotrons. Johns Hopkins University Press, Baltimore (2004)
60. Matsuki, Y., Ueda, K., Idehara, Toshitaka, Ikeda, R., Kosuga, K., Ogawa, I., Nakamura, S., Toda, M., Anai, T., Fujiwara, T.: Application of continuously frequency-tunable 0.4 THz gyrotron to dynamic nuclear polarization for 600 MHz solid-state NMR. *J Infrared Milli Terahz Waves* **33**, 745–755 (2012)
61. Idehara, T., Sabchevski, S.P.: Gyrotrons for high-power terahertz science and technology at FIR UF. *J. Infrared Millim. Terahertz* **38**, 62–86 (2017)
62. Ryan, H., Van Bentum, J., Maly, T.: A ferromagnetic shim insert for NMR magnets: towards an integrated gyrotron for DNP-NMR spectroscopy. *J. Magn. Reson.* **277**, 1–7 (2017)

63. Vlasov, S.N., Orlova, I.M.: Quasioptical transformer which transforms the waves in a waveguide having a circular cross section into a highly directional wave beam. *Radiophys. Quantum Electron.* **17**, 115–119 (1974)
64. Maly, T., Sirigiri, J.R.: Simplified THz instrumentation for high-field DNP-NMR spectroscopy. *Appl. Magn. Reson.* **43**, 181–194 (2012)
65. Thumm, M.K., Kasperek, W.: Passive high-power microwave components. *IEEE Trans. Plasma Sci.* **30**, 755–786 (2002)
66. Thurber, K., Tycko, R.: Low-temperature dynamic nuclear polarization with helium-cooled samples and nitrogen-driven magic-angle spinning. *J. Magn. Reson.* **264**, 99–106 (2016)
67. Woskov, P.P., Bajaj, V.S., Hornstein, M.K., Temkin, R.J., Griffin, R.G.: Corrugated waveguide and directional coupler for CW 250-GHz gyrotron DNP experiments. *IEEE Trans. Microw. Theory Tech.* **53**, 1863–1869 (2005)
68. Idehara, T., Khutoryan, E.M., Tatematsu, Y., Yamaguchi, Y., Kuleshov, A.N., Dumbrajs, O., Matsuki, Y., Fujiwara, T.: High-speed frequency modulation of a 460-GHz gyrotron for enhancement of 700-MHz DNP-NMR spectroscopy. *J. Infrared Millim. Terahertz Waves* **36**, 819–829 (2015)
69. Khutoryan, E.M., Idehara, T., Kuleshov, A.N., Tatematsu, K., Yamaguchi, Y., Matsuki, Y., Fujiwara, T.: Simultaneous stabilization of gyrotron frequency and power by PID double feedback control on the acceleration and anode voltages. *J. Infrared Milli. Terahertz Waves* (2017). doi:[10.1007/s10762-10017-10374-10761](https://doi.org/10.1007/s10762-10017-10374-10761)
70. Idehara, T., Pereyaslavets, M., Nishida, N., Yoshida, K., Ogawa, I.: Frequency modulation in a submillimeter wave gyrotron. *Phys. Rev. Lett.* **81**, 1973–1976 (1998)
71. Idehara, T., Khutoryan, E.M., Ogawa, I., Matsuki, Y., Fujiwara, T.: Modulation and stabilization of the output power and frequency of FU series gyrotrons. *Int. J. Terahrz Sci. Tech.* **9**, 117–130 (2016)
72. Matsuki, Y., Idehara, T., Fukazawa, J., Fujiwara, T.: Advanced instrumentation for DNP-enhanced MAS NMR for higher magnetic fields and lower temperatures. *J. Magn. Reson.* **264**, 107–115 (2016)
73. Corzilius, B., Andreas, L.B., Smith, A.A., Ni, Q.Z., Griffin, R.G.: Paramagnet induced signal quenching in MAS-DNP experiments in frozen homogeneous solutions. *J. Magn. Reson.* **240**, 113–123 (2014)
74. Can, T.V., Walish, J.J., Swager, T.M., Griffin, R.G.: Time domain DNP with the NOVEL sequence. *J. Chem. Phys.* **143**, 054201 (2015)
75. Mathies, G., Jain, S., Reese, M., Griffin, R.G.: Pulsed dynamic nuclear polarization with trityl radicals. *J. Phys. Chem. Lett.* **7**, 111–116 (2016)
76. Nanni, E.A., Barnes, A.B., Matsuki, Y., Woskov, P.P., Corzilius, B., Griffin, R.G., Temkin, R.J.: Microwave field distribution in a magic angle spinning dynamic nuclear polarization NMR probe. *J. Magn. Reson.* **210**, 16–23 (2011)
77. Rosay, M., Zeri, A.C., Astrof, N.S., Opella, S.J., Herzfeld, J., Griffin, R.G.: Sensitivity-enhanced NMR of biological solids: dynamic nuclear polarization of Y21M fd bacteriophage and purple membrane. *J. Am. Chem. Soc.* **123**, 1010–1011 (2001)
78. Kubicki, D.J., Rossini, A.J., Purea, A., Zagdoun, A., Ouari, O., Tordo, P., Engelke, F., Lesage, A., Emsley, L.: Amplifying dynamic nuclear polarization of frozen solutions by incorporating dielectric particles. *J. Am. Chem. Soc.* **136**, 15711–15718 (2014)
79. Allen, P.J., Creuzet, F., Degroot, H.J.M., Griffin, R.G.: Apparatus for low-temperature magic-angle spinning NMR. *J. Magn. Reson.* **92**, 614–617 (1991)
80. Condicstre, M., Johannessen, O.G., Carignani, E., Geppi, M., Levitt, M.H.: Magic-angle spinning NMR of cold samples. *Acc. Chem. Res.* **46**, 1914–1922 (2013)
81. Hackmann, A., Seidel, H., Kendrick, R.D., Myhre, P.C., Yannoni, C.S.: Magic-angle spinning NMR at near-liquid-helium temperatures. *J. Magn. Reson.* **79**, 148–153 (1988)
82. Macho, V., Kendrick, R., Yannoni, C.S.: Cross polarization magic-angle spinning NMR at cryogenic temperatures. *J. Magn. Reson.* **52**, 450–456 (1983)
83. Hall, D.A., Maus, D.C., Gerfen, G.J., Inati, S.J., Becerra, L.R., Dahlquist, F.W., Griffin, R.G.: Polarization-enhanced NMR spectroscopy of biomolecules in frozen solution. *Science* **276**, 930–932 (1997)

84. Samoson, A., Tuherm, T., Past, J., Reinhold, A.: New horizons for magic-angle spinning NMR. *Topic Curr. Chem.* **246**, 15–31 (2004)
85. Smith, A.A., Corzilius, B., Barnes, A.B., Maly, T., Griffin, R.G.: Solid effect dynamic nuclear polarization and polarization pathways. *J. Chem. Phys.* **136**, 015101 (2012)
86. Mieville, P., Vitzthum, V., Caporini, M.A., Jannin, S., Gerber-Lemaire, S., Bodenhausen, G.: A spinning thermometer to monitor microwave heating and glass transitions in dynamic nuclear polarization. *Magn. Reson. Chem.* **49**, 689–692 (2011)
87. Thurber, K.R., Tycko, R.: Measurement of sample temperatures under magic-angle spinning from the chemical shift and spin-lattice relaxation rate of  $^{79}\text{Br}$  in KBr powder. *J. Magn. Reson.* **196**, 84–87 (2009)
88. Kiesewetter, M.K., Michaelis, V.K., Walish, J.J., Griffin, R.G., Swager, T.M.: High field dynamic nuclear polarization NMR with surfactant sheltered biradicals. *J. Phys. Chem. B* **118**, 1825–1830 (2014)
89. Tateishi, K., Negoro, M., Kagawa, A., Kitagawa, M.: Dynamic nuclear polarization with photoexcited triplet electrons in a glassy matrix. *Angew. Chem. Int. Ed.* **52**, 13307–13310 (2013)
90. Le, D., Ziarelli, F., Phan, T.N., Mollica, G., Thureau, P., Aussena, F., Ouari, O., Gigmes, D., Tordo, P., Viel, S.: Up to 100% improvement in dynamic nuclear polarization solid-state NMR sensitivity enhancement of polymers by removing oxygen. *Macromol. Rapid Commun.* **36**, 1416–1421 (2015)
91. Marker, K., Pingret, M., Mouesca, J.M., Gasparutto, D., Hediger, S., De Paepe, G.: A new tool for NMR crystallography: complete  $^{13}\text{C}/^{15}\text{N}$  assignment of organic molecules at natural isotopic abundance using DNP-enhanced solid-state NMR. *J. Am. Chem. Soc.* **137**, 13796–13799 (2015)
92. Van Der Wel, P.C.A., Hu, K.N., Lewandowski, J., Griffin, R.G.: Dynamic nuclear polarization of amyloidogenic peptide nanocrystals: GNNQQNY, a core segment of the yeast prion protein Sup35p. *J. Am. Chem. Soc.* **128**, 10840–10846 (2006)
93. Bayro, M.J., Debellochina, G.T., Eddy, M.T., Birkett, N.R., Macphee, C.E., Rosay, M., Maas, W.E., Dobson, C.M., Griffin, R.G.: Intermolecular structure determination of amyloid fibrils with magic-angle spinning and dynamic nuclear polarization NMR. *J. Am. Chem. Soc.* **133**, 13967–13974 (2011)
94. Debellochina, G.T., Bayro, M.J., Fitzpatrick, A.W., Ladizhansky, V., Colvin, M.T., Caporini, M.A., Jaroniec, C.P., Bajaj, V.S., Rosay, M., Macphee, C.E., Vendruscolo, M., Maas, W.E., Dobson, C.M., Griffin, R.G.: Higher order amyloid fibril structure by MAS NMR and DNP spectroscopy. *J. Am. Chem. Soc.* **135**, 19237–19247 (2013)
95. Bajaj, V.S., Mak-Jurkauskas, M.L., Belenky, M., Herzfeld, J., Griffin, R.G.: Functional and shunt states of bacteriorhodopsin resolved by 250 GHz dynamic nuclear polarization-enhanced solid-state NMR. *Proc. Natl. Acad. Sci. USA* **106**, 9244–9249 (2009)
96. Mak-Jurkauskas, M.L., Bajaj, V.S., Hornstein, M.K., Belenky, M., Griffin, R.G., Herzfeld, J.: Energy transformations early in the bacteriorhodopsin photocycle revealed by DNP-enhanced solid-state NMR. *Proc. Natl. Acad. Sci. USA* **105**, 883–888 (2008)
97. Becker-Baldus, J., Bamann, C., Saxena, K., Gustmann, H., Brown, L.J., Brown, R.C., Reiter, C., Bamberg, E., Wachtveitl, J., Schwalbe, H., Glaubitz, C.: Enlightening the photoactive site of channelrhodopsin-2 by DNP-enhanced solid-state NMR spectroscopy. *Proc. Natl. Acad. Sci. USA* **112**, 9896–9901 (2015)
98. Koers, E.J., Van Der Cruijsen, EaW, Rosay, M., Weingarth, M., Prokofyev, A., Sauvee, C., Ouari, O., Van Der Zwan, J., Pongs, O., Tordo, P., Maas, W.E., Baldus, M.: NMR-based structural biology enhanced by dynamic nuclear polarization at high magnetic field. *J. Biomol. NMR* **60**, 157–168 (2014)
99. Smith, A.N., Caporini, M.A., Fanucci, G.E., Long, J.R.: A method for dynamic nuclear polarization enhancement of membrane proteins. *Angew. Chem. Int. Ed.* **54**, 1542–1546 (2015)
100. Renault, M., Pawsey, S., Bos, M.P., Koers, E.J., Nand, D., Tommassen-Van Boxtel, R., Rosay, M., Tommassen, J., Maas, W.E., Baldus, M.: Solid-state NMR Spectroscopy on

- cellular preparations enhanced by dynamic nuclear polarization. *Angew. Chem. Int. Ed.* **51**, 2998–3001 (2012)
101. Yamamoto, K., Caporini, M.A., Im, S.C., Waskell, L., Ramamoorthy, A.: Cellular solid-state NMR investigation of a membrane protein using dynamic nuclear polarization. *Biochim. Biophys. Acta* **1848**, 342–349 (2015)
102. Lelli, M., Gajan, D., Lesage, A., Caporini, M.A., Vitzthum, V., Mieville, P., Heroguel, F., Rascon, F., Roussey, A., Thieuleux, C., Boualleg, M., Veyre, L., Bodenhausen, G., Coperet, C., Emsley, L.: Fast characterization of functionalized silica materials by silicon-29 surface-enhanced NMR spectroscopy using dynamic nuclear polarization. *J. Am. Chem. Soc.* **133**, 2104–2107 (2011)
103. Lesage, A., Lelli, M., Gajan, D., Caporini, M.A., Vitzthum, V., Mieville, P., Alauzun, J., Roussey, A., Thieuleux, C., Mehdi, A., Bodenhausen, G., Coperet, C., Emsley, L.: Surface enhanced NMR spectroscopy by dynamic nuclear polarization. *J. Am. Chem. Soc.* **132**, 15459–15461 (2010)
104. Akbey, U., Franks, W.T., Linden, A., Lange, S., Griffin, R.G., Van Rossum, B.J., Oschkinat, H.: Dynamic nuclear polarization of deuterated proteins. *Angew. Chem. Int. Ed.* **49**, 7803–7806 (2010)
105. Takahashi, H., Lee, D., Dubois, L., Bardet, M., Hediger, S., De Paepe, G.: Rapid natural-abundance 2D  $^{13}\text{C}$ – $^{13}\text{C}$  correlation spectroscopy using dynamic nuclear polarization enhanced solid-state NMR and matrix-free sample preparation. *Angew. Chem. Int. Ed.* **51**, 11766–11769 (2012)
106. Fernandez-De-Alba, C., Takahashi, H., Richard, A., Chenavier, Y., Dubois, L., Maurel, V., Lee, D., Hediger, S., De Paepe, G.: Matrix-free DNP-enhanced NMR spectroscopy of liposomes using a lipid-anchored biradical. *Chemistry* **21**, 4512–4517 (2015)
107. Takahashi, H., Ayala, I., Bardet, M., De Paepe, G., Simorre, J.P., Hediger, S.: Solid-state NMR on bacterial cells: selective cell wall signal enhancement and resolution improvement using dynamic nuclear polarization. *J. Am. Chem. Soc.* **135**, 5105–5110 (2013)
108. Viennet, T., Viegas, A., Kuepper, A., Arens, S., Gelev, V., Petrov, O., Grossmann, T.N., Heise, H., Etzkorn, M.: Selective protein hyperpolarization in cell lysates using targeted dynamic nuclear polarization. *Angew. Chem. Int. Ed.* **55**, 10746–10750 (2016)
109. Wenk, P., Kaushik, M., Richter, D., Vogel, M., Suess, B., Corzilius, B.: Dynamic nuclear polarization of nucleic acid with endogenously bound manganese. *J. Biomol. NMR* **63**, 97–109 (2015)
110. Maly, T., Cui, D., Griffin, R.G., Miller, A.F.:  $^1\text{H}$  dynamic nuclear polarization based on an endogenous radical. *J. Phys. Chem. B* **116**, 7055–7065 (2012)
111. Valla, M., Rossini, A.J., Caillot, M., Chizallet, C., Raybaud, P., Digne, M., Chaumonnot, A., Lesage, A., Emsley, L., Van Bokhoven, J.A., Coperet, C.: Atomic description of the interface between silica and alumina in aluminosilicates through dynamic nuclear polarization surface-enhanced NMR spectroscopy and first-principles calculations. *J. Am. Chem. Soc.* **137**, 10710–10719 (2015)
112. Barnes, A.B., Corzilius, B., Mak-Jurkauskas, M.L., Andreas, L.B., Bajaj, V.S., Matsuki, Y., Belenky, M.L., Lugtenburg, J., Sirigiri, J.R., Temkin, R.J., Herzfeld, J., Griffin, R.G.: Resolution and polarization distribution in cryogenic DNP/MAS experiments. *Phys. Chem. Chem. Phys.* **12**, 5861–5867 (2010)
113. Thurber, K.R., Tycko, R.: Perturbation of nuclear spin polarizations in solid state NMR of nitroxide-doped samples by magic-angle spinning without microwaves. *J. Chem. Phys.* **140**, 184201 (2014)
114. Barnes, A.B., Markhasin, E., Daviso, E., Michaelis, V.K., Nanni, E.A., Jawla, S.K., Mena, E.L., Derocher, R., Thakkar, A., Woskov, P.P., Herzfeld, J., Temkin, R.J., Griffin, R.G.: Dynamic nuclear polarization at 700 MHz/460 GHz. *J. Magn. Reson.* **224**, 1–7 (2012)

# Chapter 5

## Photoirradiation and Microwave Irradiation NMR Spectroscopy

Akira Naito, Yoshiteru Makino, Yugo Tasei and Izuru Kawamura

**Abstract** In situ photoirradiation solid-state nuclear magnetic resonance (NMR) spectroscopy is designed for optical irradiation from the top part of a zirconia rotor through a glass cap, which makes it possible to efficiently irradiate the inside of the rotor. This experimental method has made it possible to observe photo-intermediates of sensory rhodopsins, such as sensory rhodopsin I (SRI) and sensory rhodopsin II (SRII), and bacteriorhodopsin (bR) Y185F mutant. In SRI, green light generates M-intermediates, which exhibit positive phototaxis, while blue light generates P-intermediates, which exhibit negative phototaxis. In SRII, green light generates M-intermediates and blue light generates O-intermediates. In Y185F-bR, O-intermediates were first observed using solid-state NMR spectroscopy. The microwave irradiation NMR spectrometer was developed in-house by modification of a commercial NMR spectrometer. A flat long copper ribbon was used as a capacitor and a half turn of copper ribbon at the edge was used as an inductor for the microwave resonance circuit, which was coaxially inserted inside the radiofrequency induction coil and allowed NMR signals to be observed under microwave irradiation conditions. The temperature of *N*-(4-methoxybenzylidene)-4-butylaniline (MBBA) during microwave irradiation was estimated by measuring the temperature-dependent chemical shifts, whereby different protons were found to indicate significantly different temperatures in the molecule. Liquid

---

A. Naito (✉) · I. Kawamura

Faculty of Engineering, Yokohama National University,  
79-5 Hodogayaku Tokiwadai, Yokohama 240-8501, Japan  
e-mail: naito@ynu.ac.jp

I. Kawamura

e-mail: izuruk@ynu.ac.jp

Y. Makino · Y. Tasei

Graduate School of Engineering, Yokohama National University,  
79-5 Hodogayaku Tokiwadai, Yokohama 240-8501, Japan  
e-mail: makino-yoshiteru-yj@ynu.jp

Y. Tasei

e-mail: tasei-yugo-db@ynu.jp

crystalline-isotropic phase correlation 2D NMR spectra were observed using pulsed microwave irradiation for rapid temperature jump experiments.

**Keywords** Photoirradiation • Microwave irradiation • Photoreceptor membrane protein • Liquid crystal

## 5.1 Introduction

Nuclear magnetic resonance (NMR) spectroscopy provides important information on molecular structure and dynamics in biological and material systems. External perturbation can be combined with NMR spectroscopy to obtain molecular information. Photoirradiation NMR spectroscopy is a useful technique for understanding the photoactivation mechanisms associated with the biological functions of photoreceptor membrane proteins. Microwave irradiation NMR spectroscopy is also a useful tool for elucidating the heating and activation mechanisms of organic reactions. In this chapter, the experimental details of photoirradiation and microwave irradiation as external perturbations for NMR measurements are described.

### 5.1.1 *Photoirradiation Solid-State NMR Spectroscopy*

Photoirradiation solid-state NMR spectroscopy is particularly useful for the study of photoreceptor retinal-binding membrane proteins, detection of photo-intermediates, and for elucidation of photoreaction cycles and photoactivated structural changes. However, such experiments cannot be performed easily because photoirradiation systems for solid-state NMR are quite difficult to incorporate due to the complex nature of magic angle spinning (MAS) probe assemblies. Most of the early experiments were performed with photoirradiation from outside the probe and with freezing of the sample, followed by transfer to the NMR probe for measurement of the signals derived from the trapped photoactivated intermediates (freeze-trapping). The light-adapted state and M- and N-intermediates of bacteriorhodopsin (bR) have been characterized using photoirradiation solid-state NMR spectroscopy [1–4]. The metarhodopsin-I photo-intermediate of rhodopsin was characterized using the photoirradiation method in combination with double-quantum solid-state NMR [5]. The metarhodopsin II photo-intermediate of the visual receptor rhodopsin was also trapped and characterized [6, 7].

An *in situ* photoirradiation solid-state NMR spectrometer has also been described, in which light passes through an optical fiber to the probe and the sample is irradiated from outside the rotor tube [8, 9]. This system was used to characterize an early M-intermediate,  $M_0$ , and a late M-intermediate,  $M_n$ , in the bR photocycle [8, 9]. The L-intermediate of bR was trapped by irradiation of the light-adapted state

(LA) with  $>610$  nm light in the temperature range of  $-95$  to  $-130$  °C for at least 2 h [10].

By combination with the dynamic nuclear polarization (DNP) method, the heterogeneity of dark-adapted bR and distortion in the K-intermediate were revealed, and four discrete L-intermediates were detected [11, 12]. Recently, the photoactive site of channel rhodopsin-2 was revealed using DNP-enhanced photoirradiation solid-state NMR [13].

Another *in situ* photoirradiation solid-state NMR apparatus has been developed, in which the sample is irradiated from inside the rotor tube through a glass rod inserted into the rotor [14–19]. This allows irradiation of the sample with extremely high efficiency and enables observation of the photo-intermediates and photoreaction processes of photoreceptor membrane proteins [17, 18]. *In situ* photoirradiation is particularly useful for the study of the photocycles of retinal proteins such as sensory rhodopsin I (SRI) [16] and sensory rhodopsin II (SRII), which is also identified as pharaonis phoborhodopsin (ppR) [15, 17].

### 5.1.2 *Microwave Irradiation NMR Spectroscopy*

Microwave heating is widely used to accelerate organic reactions [20–29], to reduce polymerization times [30–33], and to enhance the activity of enzymes [34, 35]. The major reason for acceleration of the reactions in this manner is the thermal effect of microwaves [36]. However, non-thermal effects have also been identified and it has been reported that the thermal and non-thermal effects of microwaves can be separated [37]. Non-thermal effects have recently been demonstrated by an observed increase in the rate of polymerization reactions under an electric field but a decrease under a magnetic field [33]. Microwave thermal effects are attributed to an increase in the solvent temperature due to dielectric loss [23, 24, 38, 39]. Electric dipoles of the solvent molecule will align under an applied electric field, and in the case of microwave irradiation, the applied field will oscillate. As the dipoles attempt to realign with this alternating electric field, energy is released by molecular friction and collisions. Ions also translate along the oscillating electric field, generating collisions or friction with other molecules in the sample matrix to produce additional thermal energy. However, details of the molecular mechanisms associated with the microwave heating effect on chemical reaction rates have not yet been fully elucidated. One of the most important phenomena associated with microwave irradiation is non-equilibrium localized heating, defined as the generation of isolated regions with much higher temperatures than the bulk solution. This has been reported to occur in liquid–solid systems in response to microwave irradiation, such as in the case of dimethyl sulfoxide (DMSO) molecules in contact with Co particles under microwave irradiation [40].

In this chapter, *in situ* microwave irradiation solid-state NMR spectroscopy is described with the aim of characterizing microwave heating mechanisms. Recently, microwave-induced heating mechanism was observed in liquid crystalline systems

[41, 42]; local heating effects were observed in a liquid crystalline phase, where a locally isotropic phase appeared under microwave irradiation. Furthermore, molecular temperatures were measured by observing chemical shifts for individual protons to determine different temperatures within a molecule under microwave irradiation [42]. Microwave heating allows rapid temperature jump experiments to be performed. This technique is used to obtain state-correlated two-dimensional (SC-2D) NMR spectra. This allows for the high-resolution observation of  $^1\text{H}$  dipolar patterns in  $^1\text{H}$  NMR spectra in the liquid state rather than in the liquid crystalline state. Using this method, the local dipolar interactions of individual protons in the liquid crystalline state can be examined via high-resolution resonances in the isotropic phase [43–47] and the resulting data may also be used to obtain SC-2D NMR spectra of protein in both their native and denatured states [48].

## 5.2 Experimental Details for Photoirradiation Solid-State NMR Spectroscopy

### 5.2.1 Photoirradiation System for Solid-State NMR

An *in situ* photoirradiation system was developed for solid-state NMR measurements under the MAS condition. *In situ* continuous photoirradiation with a light-emitting diode (LED) light source was conducted using an optical fiber passed from outside the magnet through a tightly sealed cap made of a glass rod glued to a zirconia rotor (Fig. 5.1). Photoirradiation was performed from the top of the spinner without touching the optical fiber to the cap of the spinner. The tip of the glass rod was grained so as to provide irradiation perpendicular to the rotor wall, to which the fluid membrane proteins were attached on the side wall as a thin film. Therefore, light is directed perpendicular from inside the spinner to the rotor wall. If the irradiation is not perpendicular to the rotor wall, then it will be completely reflected off the surface of the film sample and will not penetrate into the sample. Thus, the irradiation efficiency is significantly improved when the light is provided from the inside. It is important for light to penetrate into the sample, especially when the absorbance is quite large. Using a solid-state NMR spectrometer (CMX Infinity-400, Chemagnetics) equipped with this photoirradiation system, it is possible to efficiently irradiate samples in the rotor with 150 mW of green (520 nm), orange (590 nm) and blue (365 nm) LED lights.

### 5.2.2 Photoirradiation NMR Measurements

For *in situ* photoirradiation solid-state NMR measurements, 100  $\mu\text{L}$  (50 mg) each of photoreceptor membrane protein samples were placed into the zirconia rotor and

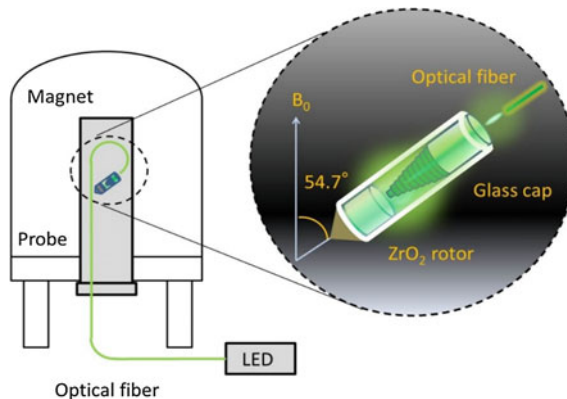


**Fig. 5.1** Schematic illustration of the in situ photoirradiation solid-state NMR spectrometer. An optical fiber is guided from the outside of the magnet and connected to an LED light source (520, 595 and 365 nm, 150 mW). The optical fiber is guided from the bottom to the top of the probe head and accurately aligned along the top of the MAS rotor. The top part of the zirconia rotor is capped by a glass rod, in which the tip part is ground to provide illuminate perpendicular to the spinner axis, so that strong light irradiates the sample from inside the sample tube [16]

sealed with the glass rod as a cap. A cross-polarization-magic angle spinning (CP-MAS) pulse sequence was used with a contact time of 1 ms, followed by acquisition with 50 kHz two-pulse phase modulated (TPPM) proton decoupling pulses (Fig. 5.2a). It was noted that the  $^{13}\text{C}$  NMR signals of [20- $^{13}\text{C}$ ] retinal were only observed with the CP pulse sequence because the retinal is located deep inside the core part of the membrane and is immobile. The MAS frequency was set to 4 kHz, and the temperature was set to 0, -20 and -40 °C using a gas flow temperature controller system. Typically, 20,000 transients were accumulated for dark and light experiments. Samples could be continuously irradiated with three different LED wavelengths (365, 520, and 595 nm) during NMR measurements. The LED continuous irradiation does not increase sample temperature.

### 5.2.3 Detection of Photo-Intermediates in the Photoreaction Cycles

When retinal-binding membrane proteins such as SR-II are irradiated with LED light, retinal absorbs the light energy and is excited from the G-state to the K-intermediate, subsequently relaxes to L-, M-, and O-intermediates and finally returns to the G-state as follows  $\text{G} \rightarrow \text{K} \rightarrow \text{L} \rightarrow \text{M} \rightarrow \text{O} \rightarrow \text{G}$ , which is referred to as the photocycle (Fig. 5.2b). If the M-intermediate exhibits a slightly longer half-life than the other states, then M-intermediates can be stationary trapped under continuous light irradiation because the production rate of M-intermediate is

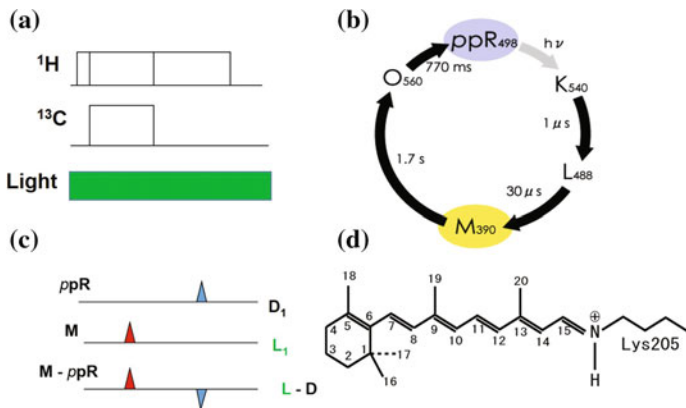


**Fig. 5.2** **a** Pulse sequence for photoirradiation CP-MAS NMR spectroscopy. **b** Photocycle for SRII (ppR). **c** NMR spectra of dark state (*D*<sub>1</sub>). NMR spectrum under photoirradiation (*L*<sub>1</sub>). Difference spectrum between dark state and irradiation state (*L*<sub>1</sub>-*D*<sub>1</sub>). **d** All-trans configuration of retinal

possibly faster than its relaxation rate. Thus, in a system with a photocycle, CP-MAS NMR spectra can be observed under dark condition and subsequently under irradiation with LED using the same experimental parameter such as the temperature (Fig. 5.2c). The difference spectrum between the dark and light conditions provides a background-free spectrum in which reactant species exhibit negative peaks and product species exhibit positive peaks (Fig. 5.2c). Thus, the photoreaction pathways can be clearly characterized. It is also possible to switch the photoreaction pathways by changing the wavelength of the LED light. In the SRII (ppR) system, the pathway of the M-intermediate may switch from M(390) → O(560) to M(390) → SRII under irradiation with blue light (365 nm).

### 5.3 Photoreaction Cycle for SRI as Revealed by In Situ Photoirradiation Solid-State NMR

SRI functions as a color-discriminating receptor in halobacterial phototaxis [49]. SRI has seven transmembrane  $\alpha$ -helices with an all-trans retinal chromophore [50]. SRI forms a 2:2 complex with its cognate transducer protein, HtrI [51]. The essential photocycle of SRI from *Halobacterium salinarum* (HsSRI) proceeds as follows: SRI<sub>G</sub>(587) → (hv) → SRI<sub>K</sub>(625) → SRI<sub>P</sub>(540) → SRI<sub>M</sub>(373) → SRI<sub>G</sub>(587) (Fig. 5.3a). Here, the SRI<sub>P</sub>(520)-intermediate is produced from the M-intermediate by absorption of a second photon from near-UV light as a back reaction: SRI<sub>M</sub>(373) → (hv) → SRI<sub>P</sub>(520) → SRI<sub>G</sub>(587) [52]. During the photocycle, the M- and P-intermediates are thought to be essential for positive and negative phototaxis, respectively (Fig. 5.3a). Little is known about the structural

change or the signal relay mechanism for this type of phototaxis because HsSRI is unstable under various conditions and its inherent instability hampers the elucidation of its molecular mechanism.

Recently, a novel SRI protein from the eubacterium *Salinibacter ruber* (SrSRI) was cloned and characterized. SrSRI was the first eubacterial SRI identified as a functional protein [53]. SrSRI has an all-trans retinal configuration as a chromophore in the dark and an absorption maximum at a longer wavelength (557 nm) than SRII (500 nm), and a slower photocycle than the light-driven ion-pumping rhodopsin [bR and halorhodopsin (HR)], which indicates that it is similar to *Halobacterium salinarum* (Hs)SRI [54].

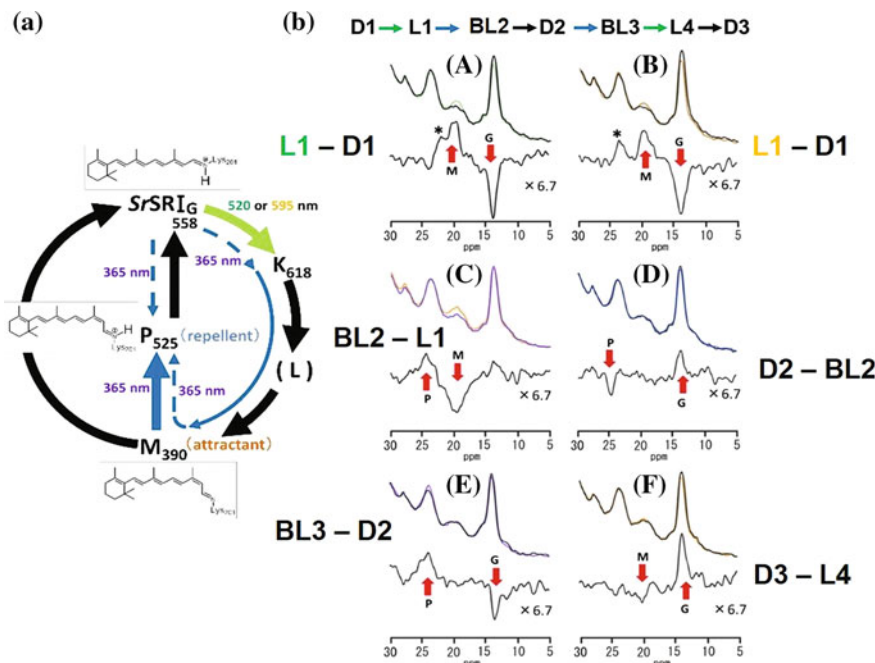


**Fig. 5.3** **a** Estimated photoreaction cycle for SrSRI and retinal configurations. The two photoactivated pathways from the G-state to the P-intermediate under blue light irradiation were revealed to be single- and double-photon processes. The retinal configuration of the P-intermediate was determined to be 13-cis, 15-anti. **b** <sup>13</sup>C CP-MAS NMR signals for the [20-<sup>13</sup>C]-Ret-SrSRI-PG system under dark condition (D1) (black) and under irradiation with 520 nm (L1) (green) and 595 nm (L1) (orange) LED light (A- and B-top), and difference spectra between the light and dark states (L1-D1) (A- and B-bottom). <sup>13</sup>C CP-MAS NMR signals for irradiation of the M-intermediate with 595 nm (L1) (orange) and 365 nm (BL2) (blue) LED light (C, top), and difference spectra between the M- and P-intermediates (BL2-L1) (C, bottom), and relaxation process (D2-BL2) from the p-intermediate (BL2) (blue) to the G-state (D2) (black) (D, top). <sup>13</sup>C CP-MAS NMR signals under dark conditions (D2) (black) and under irradiation 365 nm (BL3) (blue) to G-state (E, top) and difference spectrum between blue light and dark states (BL3-D2) (bottom) (E, bottom), and relaxation process (D3-L4) from the M-intermediate (L4) to the G-state (D3) (F, bottom) [16]

The individual intermediates of the SrSRI photocycle have been observed using *in situ* photoirradiation solid-state NMR spectroscopy [16].  $^{13}\text{C}$  CP-MAS NMR signals from the [20- $^{13}\text{C}$ ]-retinal of the long-lived M- and P-intermediates and pathways from the G-state to the photo-intermediates were observed, thereby providing insight into the mechanism of the SrSRI photocycle.

First, *in situ* photo-irradiated  $^{13}\text{C}$  solid-state NMR spectra, as shown in Fig. 5.3b, were collected by irradiating the G-state of [20- $^{13}\text{C}$ ]-retinal-SrSRI with 520 or 595 nm LED light at  $-40\text{ }^{\circ}\text{C}$ . The lipid signals overlapped heavily, so that difference spectra could be obtained to resolve the light-induced changes. The difference spectrum between the dark and light state clearly indicated that the  $^{13}\text{C}$ -NMR signal of the G-state at 13.8 ppm (negative peak) decreased and that of the M-intermediate at 19.8 ppm (positive peak) increased [Fig. 5.3b(L1–D1)]. The signals in the figure marked with an asterisk (\*) could be derived from lipids that changed in intensity during photoirradiation. These data indicated that the G-state with all-trans retinal transforms into the M-intermediate with a 13-cis, 15-anti retinal configuration and deprotonated Schiff base (SB) bonding (Fig. 5.3a). These configuration of the SrSRI retinal could be clearly determined by comparison of the  $^{13}\text{C}$  chemical shifts for [20- $^{13}\text{C}$ ]-retinal with those for ppR [15] and bR [1, 12, 55], as summarized in Table 5.1.

The M-intermediate was trapped in a stationary state by irradiation with 520 nm LED light (stationary trapping) and was subsequently irradiated with 365 nm LED light at  $-40\text{ }^{\circ}\text{C}$  to examine the double-photon process. As shown in Fig. 5.3b(BL2–L2), the signal from the M-intermediate at 19.8 ppm decreased while that for the P-intermediate at 24.8 ppm increased. This result indicates that the M-intermediate transformed into the P-intermediate by absorption of the second irradiation with 365 nm LED light (blue) and that the half-life of the P-intermediate should be

**Table 5.1** Chemical shift values for [20- $^{13}\text{C}$ ]-retinal proteins (ppm)

Retinal proteins	G-state	M-intermediate	P-intermediate	N-intermediate	O-intermediate
SrSRI ( $-40\text{ }^{\circ}\text{C}$ )	13.8 <sup>a</sup> (all-trans)	19.8 <sup>a</sup> (13-cis)	24.8 <sup>a</sup> (13-cis, 15-anti)		
ppR ( $0\text{ }^{\circ}\text{C}$ ) ( $-20\text{ }^{\circ}\text{C}$ )	13.3 <sup>b</sup> 13.5 <sup>b</sup> (all-trans)	22.3 <sup>b</sup> 24.1, 22.5, 21.7 <sup>b</sup> (13-cis, 15-anti)			
ppR/pHtrII ( $0\text{ }^{\circ}\text{C}$ ) ( $-20\text{ }^{\circ}\text{C}$ ) ( $-40\text{ }^{\circ}\text{C}$ )	13.6 <sup>b</sup> 13.5 <sup>b</sup>	22.7 <sup>b</sup> 23.5, 22.3 21.3 <sup>b</sup> (13-cis, 15-anti)		23.9 (13-cis)	16.4 (all-trans)

<sup>a</sup>Ref. [16], <sup>b</sup>Ref [15]

sufficiently long to enable a high population to remain at  $-40^{\circ}\text{C}$ . The 24.8 ppm  $^{13}\text{C}$  chemical shift for the P-intermediate from [20- $^{13}\text{C}$ ]-retinal suggests a 13-cis, 15-anti configuration of retinal based on the chemical shifts of ppR [15] and bR [1, 12, 55] (Table 5.1). In addition, the significant difference between the chemical shifts of the P- and M-intermediates is indicative of a rather large conformational change, which may in turn be responsible for the significant changes in protein interaction that lead to the functional switch between positive and negative phototaxis [56].

After the P-intermediate was trapped in a stationary state by irradiation with 365 nm LED light, the irradiation was stopped and a change in the intensity of the P-intermediate was observed, as shown in Fig. 5.3b(D2–BL2). The signal intensity of the P-intermediate at 24.8 ppm decreased and that of the G-state at 13.8 ppm increased, which indicates that the P-intermediate relaxes to reach the G-state. Therefore, it was concluded that the P-intermediate returns directly to the G-state via a thermal process under dark conditions. Although the P-intermediate relaxed within a half day at  $-40^{\circ}\text{C}$ , it was trapped stationary under irradiation with 365 nm LED light [Fig. 5.3b(BL3–D2)], which indicates that the P-intermediate and G-state are in equilibrium under irradiation with 365 nm LED light. Thus, to examine the direct pathway of transformation from the G-state to the P-intermediate, the G-state was irradiated with 365 nm LED light [Fig. 5.3b(BL3–D2)]. The result indicated a decrease in the G-state and simultaneous increase in the P-intermediate, which clearly revealed that the P-intermediate is directly generated from the G-state upon irradiation with 365 nm LED light.

In contrast, the M-intermediate was thermally transformed into the G-state under dark condition, as shown in Fig. 5.3b(D3–L4). In addition, the half-life of the M-intermediate was as long as 1 day at  $-40^{\circ}\text{C}$ . This result confirmed the normal pathway of the single photon photocycle under irradiation with green light rather than UV light.

In summary, the photoreaction cycle and possible configuration of retinals in the intermediates of SrSRI were revealed (Fig. 5.3a). In this photoreaction cycle, the M-intermediate is trapped stationary in an attractant state under irradiation with green light (520 nm), and the P-intermediate is subsequently trapped stationary by a second irradiation with UV light (365 nm), acting in a repellent state. The configuration of the M- and P-intermediates was determined to be 13-cis, 15-anti with deprotonation and protonation of the SB, respectively. The pathway from the G-state to the P-intermediate was also observed by irradiation with UV light at 365 nm. SrSRI has been shown to function in both positive and negative phototaxis with color-discriminating manner.

## 5.4 The Photoreaction Cycle of *Pharaonis* Phoborhodopsin (SRII) as Revealed by Photoirradiation Solid-State NMR Spectroscopy

*Pharaonis* phoborhodopsin (ppR or SRII) is a negative phototoxic receptor of *Natronomonas pharaonis*. The ppR protein forms a 2:2 complex with the cognate transducer pHtrII, which transmits a photosignal into the cytoplasm [57]. Light absorption by ppR initiates trans-cis photoisomerization of the retinal chromophore, followed by a cyclic chemical reaction that consists of several intermediates (K, L, M, and O) [58], as shown in Fig. 5.4a (thick arrows).

The K(540)-intermediate has a 1  $\mu$ s half-life and a 13-cis, 15-anti retinal configuration. The L(488)-intermediate can be transformed from the K-intermediate and has a 30 ns half-life and a 13-cis, 15-anti retinal configuration. Subsequent to formation of the L-intermediate, a proton is removed from the SB to form the M (390)-intermediate, which has a long half-life of 1.7 s. The M-intermediate has a 13-cis, 15-anti retinal configuration with a deprotonated SB. By accepting protons, the M-intermediate transforms into the O(560)-intermediate, which has a 770 ms

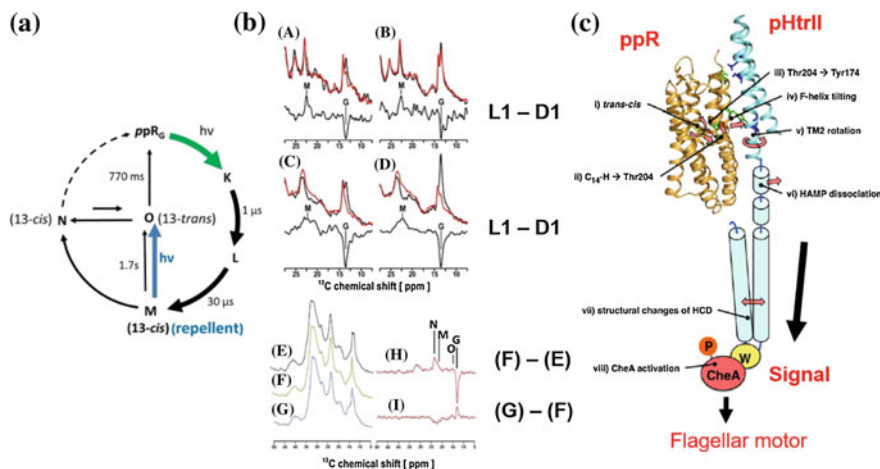


**Fig. 5.4** **a** Photoreaction cycle of the ppR/pHtrII complex and retinal configurations for the M, N, and O-intermediates. **b** <sup>13</sup>C-CP-MAS NMR spectra of [20-<sup>13</sup>C]-Ret-ppR and -ppR/pHtrII complex taken at 0, -20 and -40 °C. The top spectra were obtained from the light (red) and dark (black) state of ppR (A) and the ppR/pHtrII complex (B) at 0 °C. The bottom spectra in each panel show the differences between the light (L1) (red) and dark (D1) (black) spectra (L1-D1). Peaks labeled M and G indicate the <sup>13</sup>C-CP-MAS signals for [20-<sup>13</sup>C]-Ret in the M-intermediate and the G-state, respectively. Middle spectra were obtained for ppR (C) and ppR/pHtrII complex (D) at -20 °C. Spectra for the ppR/pHtrII complex obtained (E) in the dark, and under irradiation with (F) 520 nm (green) and (G) 365 nm (blue) light at -40 °C. (H) Difference spectrum for (F)-(E), where G, O, M, and N indicate the signals of the G-state and O-, M-, and N-intermediates, respectively. (I) Difference spectrum of (G)-(F). The M-intermediate is converted to the O-intermediate [15, 18]. **c** Signal transduction mechanism model of ppR-pHtrII complex system [50]

half-life. The M- and O-intermediates are considered to be the active states for signal transduction.

The crystal structure of the *ppR/pHtrII* complex suggests the formation of two specific hydrogen bonds, between Tyr199<sup>pPR</sup> and Asn74<sup>pHtrII</sup> and between Thr189<sup>pPR</sup> and Glu43<sup>pHtrII</sup>/Ser62<sup>pHtrII</sup> [59]. Thr204 is an important residue for color tuning and the photocycle kinetics of *ppR* (Fig. 5.4c) [60], and further observation have provided additional information regarding the important role of Thr204 in the negative phototaxis function of the *ppR/pHtrII* complex [61]. Steric hindrance between the C14-H of retinal and Thr204 occurs upon formation of the K-intermediate [62]. At the same time, a specific hydrogen bonding alteration occurs between Thr204 and Tyr174 in a *pHtrII*-dependent manner [63]. Several groups have suggested that helix movement in *ppR* and outward tilting of helix F occur during the photocycle [64–66], and these steps are considered essential for the activation of *pHtrII*. However, no helix tilting was observed in the crystal structure of the M-intermediate of the *ppR/pHtrII* complex [67]. TM2 helical rotation occurs during the formation of the M-intermediate, which transfers the signal to the phosphorylation cascade to initiate rotation of the bacterial flagellum motor and results in negative phototaxis (Fig. 5.4c). Thus, the structural changes that occur upon formation of the active M-intermediate continue to be an exciting topic of research [68, 69].

In situ photoirradiation CP-MAS solid-state NMR experiments were performed on a sample of [20-<sup>13</sup>C]-retinal-*ppR* in egg phosphatidylcholine (PC) under near physiological condition at 0 and -20 °C [Fig. 5.4b(A) and (C)] [15]. In addition to the long half-life of the M(390)-intermediate (1.7 s), the relatively long-lived O (560)-intermediate (0.77 s) was irradiated with 520 nm LED light. In the G-state, a peak corresponding to the 20-C in retinal appeared at 13.5 ppm, and the signal shifted to 22.4 ppm for the M-intermediate at 0 °C [Fig. 5.4b(A)(L1–D1)]. At least three distinct M-intermediates appeared at 24.1 (M3), 22.5 (M2), and 21.7 ppm (M1) in photo-irradiated *ppR* at -20 °C (Fig. 5.4b(C)(L1–D1); Table 5.1). The overall yields of the M-intermediates were 40 and 80% at 0 and -20 °C, respectively. This difference in yield can be attributed to the longer half-life of the M-intermediate at the lower temperature. The multiple signals at -20 °C could be attributed to the occurrence of several different interactions between retinal and the protein.

The M-intermediates were also trapped for the [20-<sup>13</sup>C]-retinal-*ppR/pHtrII* complex (which exhibits signal transduction activity), as revealed by the appearance of a <sup>13</sup>C-NMR peak at 22.6 ppm at 0 °C [Fig. 5.4b(B)] and three distinct peaks at 23.5, 22.3, and 21.3 ppm at -20 °C [Fig. 5.4b(D)] (Table 5.1). Thus, multiple M-intermediates were also observed in the *ppR/pHtrII* complex at -20 °C. Note that the signal from the M-intermediate for *ppR* was slightly different from that of the *ppR/pHtrII* complex, which indicates that the interaction of retinal with *ppR* alone differs from the interaction with the *ppR/pHtrII* complex.

When the *ppR/pHtrII* complex was irradiated with 520 nm green light at -40 °C, the G-state [Fig. 5.4b(E)] was converted to the O-, M-, and N-intermediates [Fig. 5.4b(F)]. After the M-intermediates of the *ppR/pHtrII* complex were trapped at

–40 °C in a stationary manner by irradiation with 520 nm green light [Fig. 5.4b(F)], irradiation with the LED light was switched to 365 nm blue light [Fig. 5.4b(G)]. In this process, the intensities of the M-intermediates decayed, while the intensities of the O-intermediate and G-state increased [Fig. 5.4b(I)(G–F)]. In contrast, the N-intermediate did not decay over the same period. Furthermore, the G-state was transformed to the O- and N-intermediates following irradiation with 365 nm blue light [Fig. 5.4b(I)]. The M-intermediate is reportedly transformed back to the G-state by irradiation with blue light (356 nm) [70], as the M-intermediate has a maximum absorbance of 390 nm. However, the M-intermediate was converted to the O-intermediate under irradiation with 365 nm blue light [Fig. 5.4b(H)]. Spectroscopic evidence for the formation of an N-intermediate was recently determined in a transient absorption study [71], which reported that decay of the M-intermediate produces an O-intermediate that is in equilibrium with the N-intermediate. Thus, by taking into account the results of photoirradiation solid-state NMR experiments, the photoreaction cycle of *ppR/pHtrII* is presented in Fig. 5.4a. The M-intermediate is converted to the O-intermediate under irradiation with 365 nm blue light through a double-photon process, and the O-intermediate is then converted to the N-intermediate and reaches an equilibrium state in which the intensity of the N-intermediate is higher than that of the O-intermediate.

## 5.5 The Photoreaction Pathway for the Bacteriorhodopsin Y185F Mutant

The ordered sequence of conformational changes that occur in bR as a result of light absorption is known as the photocycle, which is initiated in a dark-adapted state such as the all-trans (AT is the same as bR-568) and 13-cis, 15-syn (CS is the same as bR-548) states and consists of at least five additional major distinct states (i.e., the K-, L-, M-, N-, and O-intermediates) characterized by changes in the maximum absorbance wavelength, and finally returns back to the AT state [72–75]. The retinal configuration in dark-adapted bR consists of AT and CS configurations at a molar ratio close to 1. Upon irradiation with 560 nm light, the population of the AT increases, a condition known as the light-adapted state. The light-adapted state is excited to the K-intermediate (13-cis, 15-anti) and consequently relaxed through the L- (13-cis, 15-anti), M- (13-cis, 15-anti), N- (13-cis, 15-anti), and O- (all-trans) intermediates before returning to the AT (bR-568) state.

In the Y185F-bR mutant, the CS/AT molar ratio in the dark-adapted state is 3:1 [76]. Light adaptation produces the AT state and the O-intermediate [77]. Photoexcitation of the O<sup>Y185F</sup>-intermediate at 170 and 250 K produces an N-intermediate, but no M-intermediate [78]. In the process of transition from the O-intermediate to the AT state, a H<sup>+</sup> is transported from Asp85 to a proton release group (PRG) through the Y185F-bR hydrogen bond network, which consists of

Asp212 and Tyr185. However, breakdown of the hydrogen bond network prevents H<sup>+</sup> transport, so that the half-life of the O-intermediate is predicted to be significantly increased [79].

The photoreaction pathways for Y185F-bR were examined using in situ photoirradiation solid-state NMR spectroscopy [19]. <sup>13</sup>C-CP-MAS NMR spectra were acquired at -40 °C in the dark (D1), under irradiation with 520 nm light (L1), subsequently in the dark (D2), and again under irradiation with 520 nm light (L2). Between D1 and L1, the CS (bR-548) state changed to a CS\*- (13-cis, 15-syn) intermediate, which was highly stable at -40 °C, and was similar to the batho-13-cis-bR [80] and K-intermediate [81] [Fig. 5.5a(A)(L1–D2)]. The AT (bR-568) state transformed to an N-intermediate. Under the D2 condition, the N-intermediate transformed to an O-intermediate, which was also highly stable at

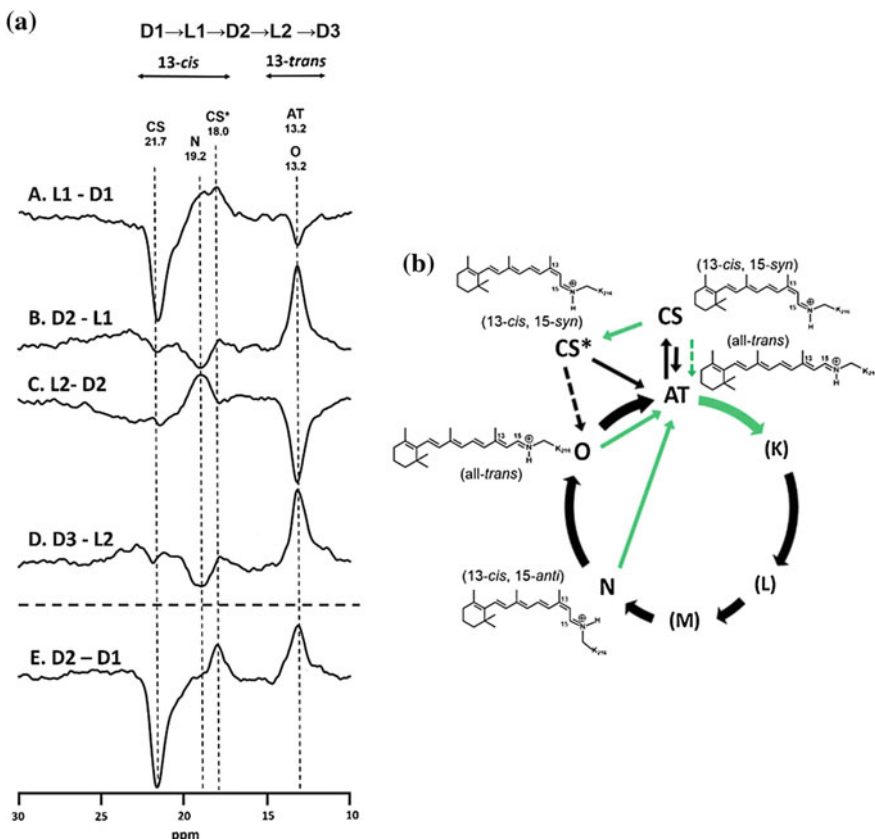


**Fig. 5.5** **a** Difference spectra for [20-<sup>13</sup>C]Ret-Y185F-bR at -40 °C in the pathway from (A. L1–D1) D1 to L1, (B. D2–L1) L1 to D2, (C. L2–D2) D2 to L2, (D. D3–L2) L2 to D3, and (E. D2–D1) D1 to D2. **b** Photoreaction pathway of Y185F-bR. *Solid green arrows* indicate the photoreaction pathway under irradiation with 520 nm light. *Solid black arrows* indicate thermal relaxation pathways. *Broken arrows* indicate hydrothermal pathways [19]

**Table 5.2**  $^{13}\text{C}$  Chemical shifts (ppm) for the various states of [ $20\text{-}^{13}\text{C}$ ]Ret-, [ $14\text{-}^{13}\text{C}$ ]Ret-, and [ $15\text{-}^{13}\text{C}$ ]Ret-bR and Y185F as determined using photoirradiation solid-state NMR spectroscopy

State	$20\text{-}^{13}\text{C}$	$14\text{-}^{13}\text{C}$	$15\text{-}^{13}\text{C}$	$^{15}\text{N}_\zeta$	Configuration
AT (bR568)	13.3 <sup>a</sup>	122.0 <sup>a</sup>	160.0 <sup>a</sup>	165.2 <sup>e</sup>	13-trans, 15-anti
CS (bR548)	22.0 <sup>a</sup>	110.5 <sup>a</sup>	163.2 <sup>a</sup>	173.5 <sup>e</sup>	13-cis, 15-syn
K		118.2 <sup>d</sup>	160.2 <sup>d</sup>	156.5 <sup>e</sup>	13-cis, 15-anti
L165	15.5 <sup>d</sup>		163.0 <sup>d</sup>	165.2 <sup>e</sup>	13-cis, 15-anti
L174		123.3 <sup>d</sup>	162.9 <sup>d</sup>	174.3 <sup>e</sup>	13-cis, 15-anti
L181	24.0 <sup>d</sup>	116.2 <sup>d</sup>	162.5 <sup>d</sup>	181.2 <sup>e</sup>	13-cis, 15-anti
L185	24.5 <sup>d</sup>	116.2 <sup>d</sup>	162.7 <sup>d</sup>	184.9 <sup>e</sup>	13-cis, 15-anti
M <sub>0</sub>	21.5 <sup>d</sup> 19.5 <sup>g</sup>	124.5 <sup>d</sup>	165.4 <sup>d</sup>	318.4 <sup>e</sup>	13-cis, 15-anti
M <sub>n</sub>	17.8 <sup>g</sup>	124.6 <sup>c</sup>		312.0 <sup>e</sup>	13-cis, 15-anti
N		115.2 <sup>b</sup>		150.7 <sup>b</sup>	13-cis, 15-syn
AT (Y185F)	13.2 <sup>f</sup>	123.1 <sup>f</sup>	159.4 <sup>f</sup>		13-trans, 13-anti
CS (Y185F)	21.7 <sup>f</sup>	110.0 <sup>f</sup>	165.4 <sup>f</sup>		13-cis, 15-syn
CS*(Y185F)	18.0 <sup>f</sup>	115.0 <sup>f</sup>	162.2 <sup>f</sup>		13-cis, 15-syn
N (Y185F)	19.2 <sup>f</sup>	125.4 <sup>f</sup>	163.8 <sup>f</sup>		13-cis, 15-anti
O (Y185F)	13.2 <sup>f</sup>	123.1 <sup>f</sup>	159.4 <sup>f</sup>		13-trans, 15-anti

<sup>a</sup>Ref. [1], <sup>b</sup>Ref. [4], <sup>c</sup>Ref. [8], <sup>d</sup>Ref. [13], <sup>e</sup>Ref. [11], <sup>f</sup>Ref. [19], <sup>g</sup>Ref. [9]

$-40^\circ\text{C}$  in the dark [Fig. 5.5a(B)(D2–L1)]. Consequently, the O-intermediate transformed to the N-intermediate through the AT state, whereas the CS\*-intermediate did not change under irradiation with 520 nm light. The CS\*-intermediate was converted to the AT state after the temperature was increased to  $-20^\circ\text{C}$ . Upon subsequent increase in the temperature to  $20^\circ\text{C}$ , the AT state was converted to the CS state until equilibrium was reached. In this experiment, the chemical shift of [ $20\text{-}^{13}\text{C}$ ,  $14\text{-}^{13}\text{C}$ ]-retinal provided the 13-C=C and 15-C=N configurations (Fig. 5.2d). From these data (Table 5.2), the configuration of the AT and CS states, and the CS\*, N-, and O-intermediates were determined as (13-trans, 15-anti), (13-cis, 15-syn), (13-cis, 15-syn), (13-cis, 15-anti), and (13-trans, 15-anti), respectively. In situ photoirradiation solid-state NMR spectroscopy thus revealed the photoreaction pathways and structures for the AT and CS states, and the CS\*, N-, and O-intermediates of the Y185F-bR mutant (Fig. 5.5b) [19].

## 5.6 Experimental Details for Microwave Irradiation NMR Spectroscopy

### 5.6.1 In Situ Microwave Irradiation NMR Spectrometer

The microwave irradiation solid-state NMR spectrometer was developed in-house by modification of a solid-state NMR spectrometer (CMX Infinity 400, Chemagnetics) [41], as schematically shown in Fig. 5.6. A flat 4-mm-wide and

38-mm-long copper ribbon was used as a capacitor and a half turn of copper ribbon at the edge was used as an inductor for the microwave resonance circuit (Fig. 5.6b), which was coaxially inserted inside the 7-mm-diameter and 18-mm-wide radio frequency induction coil (Fig. 5.6c). The dimensions of the microwave and radio frequency circuits increase the isolation between the microwave and radio frequency resonance circuits, which allows the NMR signals to be observed under microwave irradiation conditions. Although the sensitivity of the NMR signals is reduced, it is important for the capacitor part of the microwave resonance circuit to be wound inside the radio frequency coil. If the radio frequency coil is located inside of the microwave circuit, then strong arcing would occur and the radio frequency coil would be immediately disrupted. The microwave circuit was appropriately tuned to 2.45 GHz by adjusting the capacitor part of the copper ribbon space outside of the sample tube, and the radio frequency circuit was tuned to 398 MHz by adjusting variable capacitors to match and tune using a sweep generator. NMR spectra were recorded at 398 MHz on the NMR spectrometer (CMX infinity 400 MHz, Chemagnetics), which was equipped with a microwave generator (IDX, Tokyo Electronics Co., Ltd) capable of transmitting 1.3 kW pulsed and continuous wave (CW) microwave irradiation at a frequency of 2.45 GHz. Microwaves were transmitted from the microwave generator to near the magnet through a waveguide, and transferred from the waveguide to a coaxial cable. The coaxial cable was guided to the resonance circuit at the probe head. Microwave pulses were controlled by a gating pulse produced by the pulse programmer of the NMR spectrometer. The sample was cooled down to the temperature of the liquid crystalline phase using a gas flow temperature controller. Samples were filled into a 3 mm outer diameter (OD) and 35 mm long inner glass tube (Shigemi Co., Ltd) for NMR measurements to insulate from thermal contact with a 6 mm OD and 38 mm long outer glass tube (Shigemi Co., Ltd) for NMR measurements without the use of any protection apparatus for high-temperature experiments (Fig. 5.6).

### 5.6.2 Temperature Measurements

It is important to measure the temperature of a sample directly in the NMR probe to observe microwave heating effects. Therefore, the temperature dependence of the  $^1\text{H}$  chemical shifts was observed for sample molecules using the temperature control system in the spectrometer. In the case of liquid-state NMR, the difference in the chemical shift  $\Delta\delta$ , between  $\text{CH}_3$  and OH protons of methanol and glycol, has been commonly used as a thermometer [82, 83]. Although,  $\Delta\delta$  for methanol is not linearly dependent on temperature represented over a wide temperature range, the coefficient of the quadratic term is small, so a straight line approximation will not cause a large temperature error. Moreover,  $\Delta\delta$  for glycol is perfectly linear within the error of 0.3 K within the range 310–410 K. In the case of solid-state NMR, the temperature dependence of the  $^{207}\text{Pb}$  chemical shift in MAS spectra is linear within the range –130 to +150 °C [84]. Paramagnetic lanthanide complexes also show a

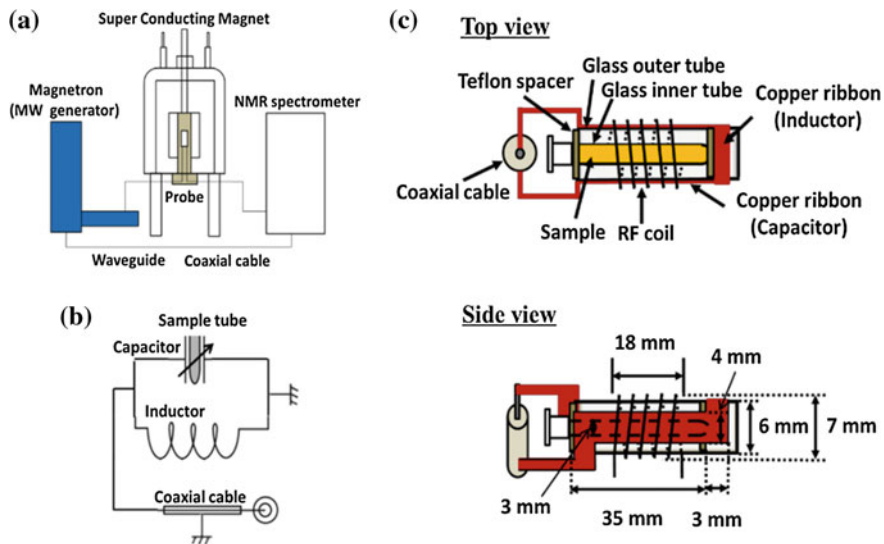


**Fig. 5.6** **a** Schematic diagram of the *in situ* microwave irradiation solid-state NMR spectrometer (CMX Infinity 400, Chemagnetics) equipped with a microwave transmitter (IDX, 1.3 kW, Tokyo Electron Co., Ltd.). CW and pulsed microwaves are gated by a pulse from the pulse programmer of the NMR spectrometer. Microwaves are transmitted from the microwave transmitter via a waveguide and coaxial cable and finally introduced to the microwave resonance circuit in the probe. **b** The equalizing microwave resonance circuit consists of an inductor and capacitor. The sample is inserted into the capacitor in the microwave resonance circuit, and radio frequency inductor. The inner glass tube (Shigemi) filled with the samples is inserted into an outer glass tube, so that the gas flow on the surface of the outer glass tube (Shigemi) is mostly insulated from the inner sample tube. The microwave resonance circuit is attached to the surface of the outer glass tube [41]

linear temperature dependence over a narrow temperature range [85]. In this Sect. 5.6,  $\delta$  values for individual protons in the sample were measured with respect to H<sub>2</sub>O protons at 20 °C in the temperature range from 50 to 95 °C. The temperature of the sample under microwave irradiation was thus evaluated based on the slope of this temperature dependence.

### 5.6.3 Microwave Temperature Jump Experiments

Microwave heating can also increase the sample temperature rapidly, which enables temperature jump experiments. In such experiments, a microwave pulse is applied to the probe, which is controlled by the pulse programmer of the NMR spectrometer. A 15 °C temperature jump within 100 ms was thus established for water by microwave irradiation at 1.3 kW.

## 5.7 Microwave Heating Effect of MBBA

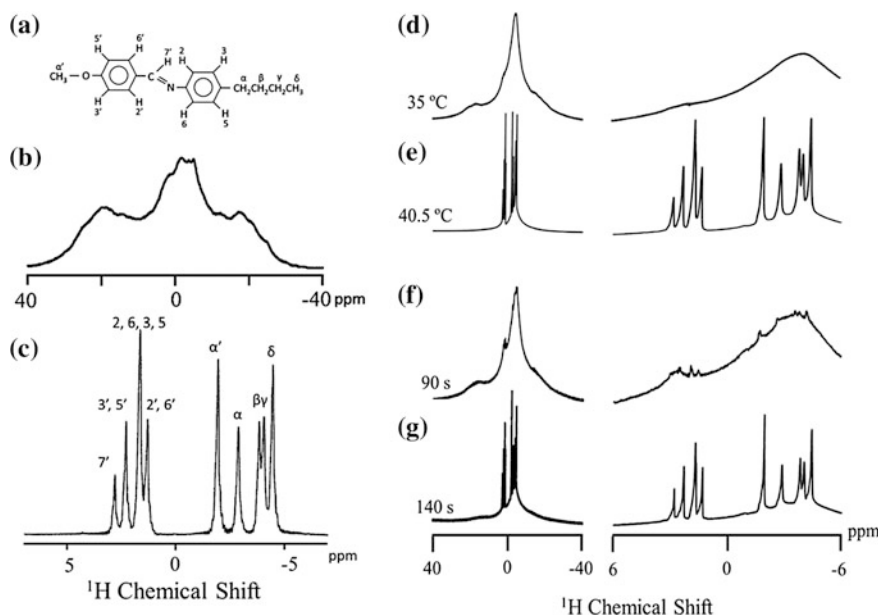
### 5.7.1 *Microwave Heating Effect of MBBA in the Liquid Crystalline State*

Figure 5.7a shows the molecular structure of *N*-(4-methoxybenzylidene)-4-butylaniline (MBBA), and Fig. 5.7b shows  $^1\text{H}$  NMR spectra of MBBA in the liquid crystalline state at 35 °C, which is 6 °C below the phase transition temperature ( $T_c$ ) of 41 °C. A broad  $^1\text{H}$  NMR spectrum with a 20 kHz linewidth was obtained for the liquid crystalline sample due to  $^1\text{H}$ - $^1\text{H}$  dipolar couplings. MBBA molecules are aligned in the magnetic field in the liquid crystalline phase, therefore, residual  $^1\text{H}$ - $^1\text{H}$  dipolar interactions cause a number of transitions with various dipolar interactions and this generates the observed line broadening. These dipolar interactions can provide information concerning the order parameter of liquid crystals. Figure 5.7c shows a high-resolution  $^1\text{H}$  NMR spectrum of MBBA in the isotropic phase that was obtained at 43 °C, in which numerous proton signals were resolved and assigned to the various protons in the molecule.

In subsequent trials, the MBBA temperature was increased from 20.0 °C below  $T_c$  to 40.5 °C, which was performed using the temperature control unit of the spectrometer. As shown in Fig. 5.7, the  $^1\text{H}$  NMR signals of the liquid crystalline phase appeared alone at 35 °C. At 40.0 °C, the liquid crystalline phase had partly transitioned to the isotropic phase (Fig. 5.7d). The temperature of the liquid crystalline and isotropic phases was observed to be almost the same. It was also evident that the signals obtained at this temperature were broader than those of the fully isotropic phase, which may be attributed to interaction of the isotropic and liquid crystalline phases. This phase transition was completed at 40.5 °C (Fig. 5.7e), which indicates that the liquid crystalline and isotropic phases coexisted near the phase transition temperature.

The instrument temperature was then set at 20 °C, (20.5 °C below  $T_c$ ), followed by application of CW microwave irradiation at 130 W for 90 s, which generated weak isotropic phase signals (representing approximately 2% of the bulk sample) among the liquid crystalline phase signals (Fig. 5.7f). Based on the temperature dependence of the linewidths, the temperature of the liquid crystalline phase was estimated to be 35 °C from assessment of the NMR linewidths (Fig. 5.7d, f). Such signals would not typically be expected until the temperature of the sample is close to its isotropic phase transition temperature of 40.5 °C as observed in the setting of a temperature control unit. This result indicates that microwave irradiation generated localized heating in the sample to form a region of the higher temperature isotropic phase.

The temperature of the sample was successfully determined using *in situ* microwave irradiation NMR because the temperature of the liquid crystal MBBA is correlated with the NMR signal linewidths. As noted, microwave irradiation generated a small fraction of the isotropic phase in the bulk liquid crystal at 35 °C, even



**Fig. 5.7** **a** Molecular structure of *N*-(4-methoxybenzylidene)-4-butylaniline (MBBA). <sup>1</sup>H NMR spectra of MBBA at **b** 35 °C in the liquid crystalline phase and **c** 45 °C in the isotropic phase, together with signal assignments for the individual protons. <sup>1</sup>H NMR spectra (*left*) and expanded spectra (*right*) of MBBA at **d** 35 and **e** 40.5 °C and setting the temperature at 20 °C under 130 W CW microwave irradiation for **f** 90 and **g** 140 s [42]

though this is 5.5 °C lower than the phase transition temperature of 40.5 °C, which suggests a non-equilibrium localized heating within the sample [42].

### 5.7.2 Microwave Heating Effect of MBBA in the Isotropic State

The chemical shifts for individual protons were determined as a function of temperature for MBBA in the isotropic phase, as shown in Fig. 5.8. The chemical shifts did not vary significantly with temperature, when the temperature was increased by 30 °C, for example, a higher field shift of only 0.06 ppm was observed for the aromatic protons. Interestingly, the chemical shifts for different protons also had very different temperature variation. However, the chemical shift did exhibit a linear temperature dependence for each different proton and thus it was possible to estimate the effective temperature of MBBA in the isotropic phase as induced by microwave irradiation.

Figure 5.8 presents the increase in the MBBA sample temperature in response to CW microwave irradiation. Application of CW microwave irradiation at 65 W

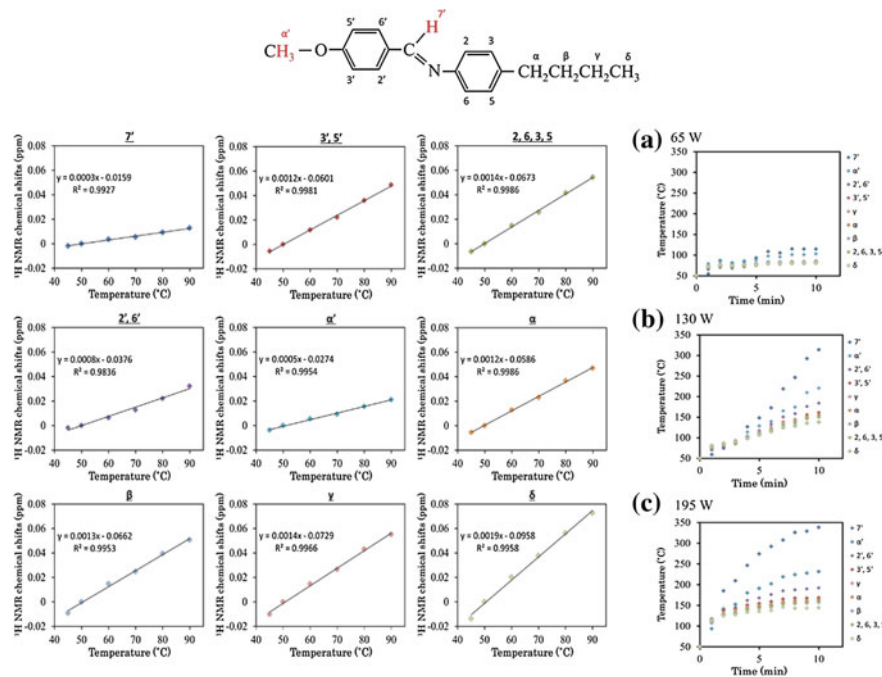


**Fig. 5.8** Plots of temperatures against microwave irradiation time at microwave powers of **a** 65, **b** 130 and **c** 195 W. Temperatures were determined using the slopes obtained for the individual protons as shown in the *left side* [42]

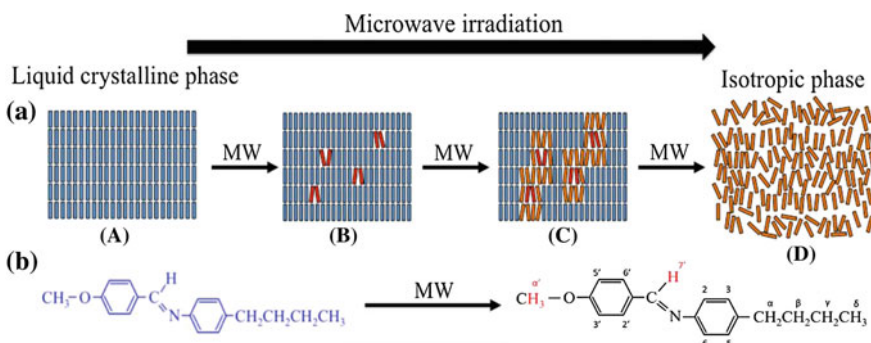
increased the temperature from 50 to 70 °C within 2 min based on the majority of proton data, after which the temperature plateaued. However, there were significant variations in the apparent temperature; 7' and α' protons indicated 110 and 80 °C, respectively. When CW microwave irradiation was applied at 130 W, the temperature increased to 140 °C, according to the majority of the proton data, although values of 210 and 330 °C were indicated by the α' and 7' protons, respectively, and 8 min was required to obtain a stable temperature. The temperature of the 7' and α' protons deviated more significantly from those of the other protons. Application of CW microwave irradiation at 195 W increased the temperature to 160 °C within 5 min, although again the α' and 7' protons were discrepant and indicated temperatures of 220 and 350 °C, respectively. Thus, at this microwave power level, large temperature variations were evident among protons in the same molecule, which indicated that individual protons within the same molecule experienced different temperatures.

Figure 5.8 makes it evident that the 7' and α' protons experienced much higher temperatures than those of other protons in the same molecule. However, the temperature indicated by protons other than 7' and α' was all very similar and they are thus considered to represent the temperature of the bulk isotropic state. The temperature at a power of 65 W could be determined accurately, because the

chemical shifts were within the range of the experimentally determined values using the temperature control unit of the spectrometer.

### 5.7.3 Mechanism for Microwave Heating of Liquid Crystalline MBBA

The microwave-induced local heating phenomena observed in liquid crystalline MBBA is shown schematically in Fig. 5.9. Heating the liquid crystalline phase below its phase transition temperature to a temperature near  $T_c$ , by microwave (MW) irradiation generates a small amount of the isotropic phase inside the sample (Fig. 5.9a(B)). The dielectric loss for the isotropic phase is expected to be higher than that for the liquid crystalline phase; therefore, the isotropic phase is heated more efficiently by microwave irradiation, which induces a relatively high temperature in the isotropic phase region. This phenomenon can be considered to be due to a type of non-equilibrium localized heating state. The isotropic phase form small particles and the surfaces of these particles interact with the surrounding liquid crystals to generate different linewidths than those produced by the bulk isotropic phase. This non-equilibrium heating state can be maintained over long time spans because the rate at which heat is obtained by the small isotropic phase particles by the absorption of microwave energy is balanced with the rate at which heat is dissipated to the bulk liquid crystalline phase. At higher microwave power level, the bulk isotropic phase appears (Fig. 5.9a(C)) and, eventually, the entire sample transitions to the isotropic phase (Fig. 5.9a(D)).



**Fig. 5.9** **a** Schematic diagrams showing the proposed (A, B, C and D) microwave (MW) heating processes within the liquid crystalline state. During microwave irradiation, a small fraction of the liquid crystalline domain changes to the isotropic phase (image B). The rate of temperature increase in this isotropic phase domain is higher than in the liquid crystalline phase because the dielectric loss for the isotropic phase is larger than that for the liquid crystalline phase. This is considered to represent a non-equilibrium localized heating state. **b** When microwave is irradiated in the isotropic phase,  $\text{CH}_3-$  and  $\text{H}-\text{C}=\text{N}$  protons showed higher than the other protons [42]

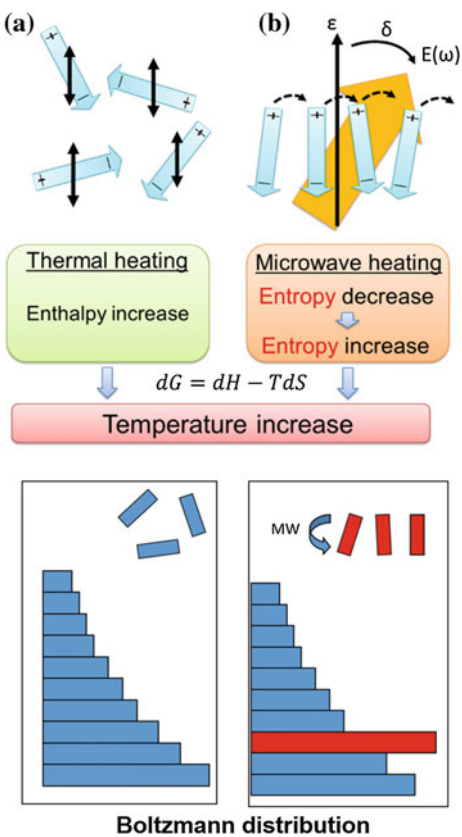
Microwave irradiation of MBBA generated a non-equilibrium localized heating state that could be maintained for long time spans, in which an isotropic phase was present within the near liquid crystalline state, solely as the result of microwave irradiation.

#### **5.7.4 Mechanism for Microwave Heating of Isotropic Phase MBBA**

It is of interest to consider the reason why the  $\gamma'$  and  $\alpha'$  protons of the MBBA molecule showed significantly different chemical shifts from the other protons. Both protons are with the polar bonds of the H–C=N– and CH<sub>3</sub>–O– functional groups. Microwave irradiation of the MBBA sample produces a strong alternating electric field that may induce an ordered state (Fig. 5.10b-top). This state can be described by a non-Boltzmann distribution (Fig. 5.10b-bottom). It is important to note that these states reduce the entropy term of the system and cannot be achieved by a thermal heating process, i.e., microwave energy is absorbed by the liquid crystalline system by reducing entropy term, which can be expressed as entropy driven energy flow. Polar groups interact with each other to generate electric polarization in the polar group due to the electric dipolar interaction that is not eliminated in the presence of an alternating electric field of microwave. This reduction of the entropy term may provide additional energy to the system which has gained thermal energy due to the molecular friction that increase the entropy term. Consequently, the electron density experienced by the  $\gamma'$  and  $\alpha'$  protons increases slightly, which produces higher field chemical shifts during microwave irradiation. It should be noted that microwave energy at 2.45 GHz is far from that which would affect the electric density through excitation of the electric state. This change in the electron density may in turn affect the rates of various chemical reactions. This type of temperature increase for particular protons bonded to polar groups may thus be discussed as a distinct effect of microwave irradiation.

In summary, the temperatures indicated by the  $\gamma'$  and  $\alpha'$  protons of the MBBA molecules were significantly higher than those for the other protons. These protons are bonded to polar functional groups, and thus it is possible that microwave irradiation induced an increase in electron polarization in the associated bonds. This polarization would result in changes in the chemical shifts and may partly explain the mechanism by which organic reactions are accelerated through distinct microwave effects.

**Fig. 5.10** **a** Energy flow pathway under thermal heating and associated Boltzmann distribution. **b** Energy flow pathway under microwave heating. Polar molecules are oriented in the electric field and can be described as a non-Boltzmann distribution



## 5.8 Experimental Details for SC-2D NMR Spectroscopy

The pulse sequence used in state-correlated two-dimensional (SC-2D) NMR spectroscopy is essentially the same as that for a 2D exchange or a nuclear Overhauser effect (NOE) experiment (Fig. 5.11). The first  $90^\circ$  pulse prepares the transverse magnetization from thermal equilibrium. During the evolution period, the temperature of the sample is kept constant to maintain the nematic phase so that the  $^1\text{H}$  spins evolve under strong dipolar interaction between protons in the nematic phase. After a period of  $t_1$ , a second  $90^\circ$  pulse is applied to establish the magnetization along the  $z$ -axis. During the transition period, a microwave pulses are applied for a short time to increase the sample temperature so that the nematic phase can be transformed into an isotropic phase. It is stressed that the transition period should be shorter than the spin-lattice relaxation time for  $^1\text{H}$  nuclei to retain the spin memory. Any remaining transverse magnetization is assumed to dipose within a couple of milliseconds during the transition period under strong dipolar interactions. To study the spin diffusion processes, a mixing time  $\tau_m$ , is inserted in the

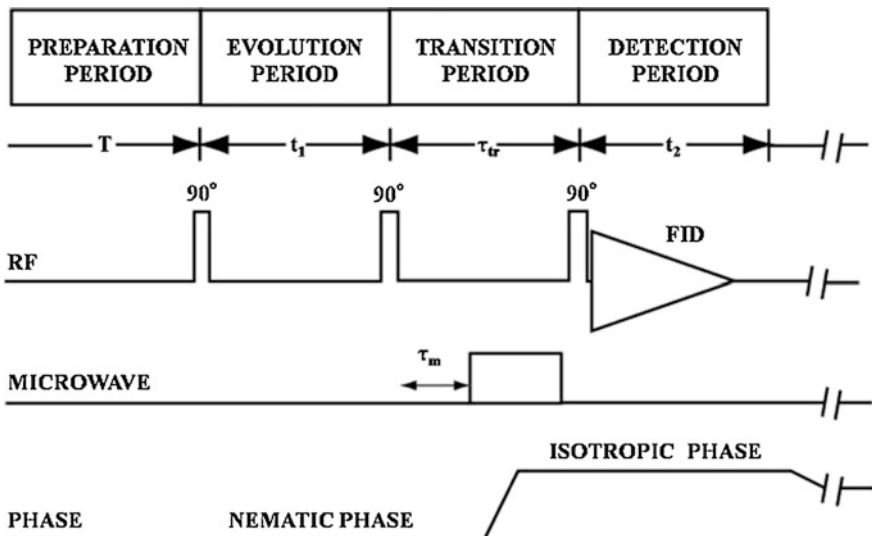


**Fig. 5.11** Pulse sequence for the SC-2D NMR experiments. The mixing time  $\tau_m$  is increased at the beginning of the transition period to examine the spin diffusion properties

beginning of the transition period. After the third  $90^\circ$  pulse, a free induction decay is acquired in the detection period,  $t_2$ , during which the system experiences magnetic interactions in the isotropic phase. After the temperature jump, the sample is cooled down to produce the nematic phase using a gas flow temperature controller to repeat the experiment for signal averaging. The free induction decay signal is recorded as functions of  $t_1$  and  $t_2$  and is double Fourier-transformed to generate the 2D NMR spectrum that correlate the nematic with isotropic phases.

## 5.9 SC-2D NMR Spectra of Liquid Crystalline Samples

### 5.9.1 SC-2D NMR Measurements of APAPA

Static 1D  $^1\text{H}$  NMR spectra of 4'-methoxybenzylidene-4-acetoxyaniline (APAPA) in the isotropic phase at 110 °C and in the nematic phase at 108 °C are shown in Fig. 5.12a [44]. The proton signals in the isotropic phase are very narrow, and multiplet patterns due to spin–spin couplings are clearly observed. Therefore, all the peaks were unambiguously assigned to individual protons as shown in Fig. 5.12a-top. In contrast, the signals in the nematic phase at 108 °C are very broad and overlapped with each other, as shown in Fig. 5.12a-bottom, and thus the  $^1\text{H}$  NMR pattern was not assigned to individual protons.

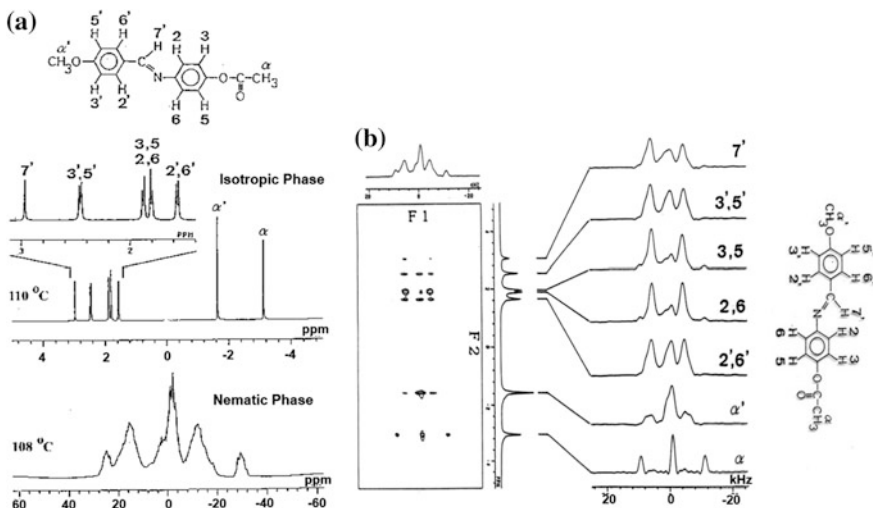


**Fig. 5.12** **a** Static <sup>1</sup>H NMR spectra of 4'-methoxybenzylidene-4-acetoxyaniline (APAPA) measured at 110 and 108 °C. **b** Nematic-isotropic SC-2D NMR spectrum of APAPA with cross-sectional patterns by application of microwave pulses of 10 ms durations

A nematic/isotropic SC-2D NMR spectrum of APAPA (Fig. 5.12b) was obtained using the pulse sequence shown in Fig. 5.11 with  $\tau_m = 0$  and a microwave pulse of 10 ms duration. The temperature before the transition was kept at 108 °C, and a repetition time of 120 s was used for the system to completely return to the initial nematic phase. The NMR spectrum for the nematic phase appeared in the  $\omega_1$  dimension and that for the isotropic phase in the  $\omega_2$  dimension. The cross sections along the  $\omega_1$  axis clearly showed different dipolar coupling patterns for individual resonances separated in the  $\omega_2$  axis [44].

In particular, a triplet pattern with an intensity ratio of 1:2:1 and a splitting frequency of 10.2 kHz appeared for the  $\alpha$ -methyl protons. This indicates the presence of three protons with equal values of dipolar coupling. On the other hand, a broad singlet pattern was observed for the  $\alpha'$ -methyl protons, with minor satellite signals on both sides of the central peak. This observation indicates that the dipolar coupling constant for the  $\alpha'$ -methyl protons was much smaller than that for the  $\alpha$ -methyl protons. The satellite lines are attributable to aromatic protons and are caused by the exchange of longitudinal magnetization due to cross-relaxation and/or spin diffusion during the transition period under the influence of strong dipolar interactions in the nematic phase.

Doublet patterns were observed for 2.6 and 3.5 protons with a splitting frequency of 9.7 kHz. Doublet patterns were also observed for 2', 6' and 3', 5' protons, although they were mixed with the dipolar patterns for the  $\alpha'$ -methyl and 7' protons produced by spin exchange. It is noted that the doublet patterns for 2', 6' and 3', 5' protons have splitting frequencies slightly different from those for 2, 6 and 3, 5 protons.

To determine the origin of the spectral mixing, SC-2D NMR spectra were recorded with varying  $\tau_m$  values as shown in Fig. 5.13. It is clear that the mixing patterns are dependent on  $\tau_m$  values. When  $\tau_m$  was 100 ms, the central lines due to the  $\alpha'$  protons grew considerably in the resonance patterns for the 2, 6 and 3, 5 protons. On the other hand, mixing of signals from 2', 6' and 3', 5' protons did not significantly change even for  $\tau_m = 600$  ms, because an equilibrium state had already been established at  $\tau_m = 100$  ms. It is also noted that the sum of the cross sections shown at the top of the 2D spectrum is invariant during the course of the  $\tau_m$  variation. These results indicate that spectral mixing occurs more efficiently within the aromatic ring protons, which are considered to constitute a core group of the liquid crystalline molecule, than between the aromatic and the  $\alpha'$ -methyl protons. Furthermore, spectral mixing between aromatic and the  $\alpha$ -methyl protons is very slow, and thus the spectral patterns are different even at  $\tau_m = 600$  ms.

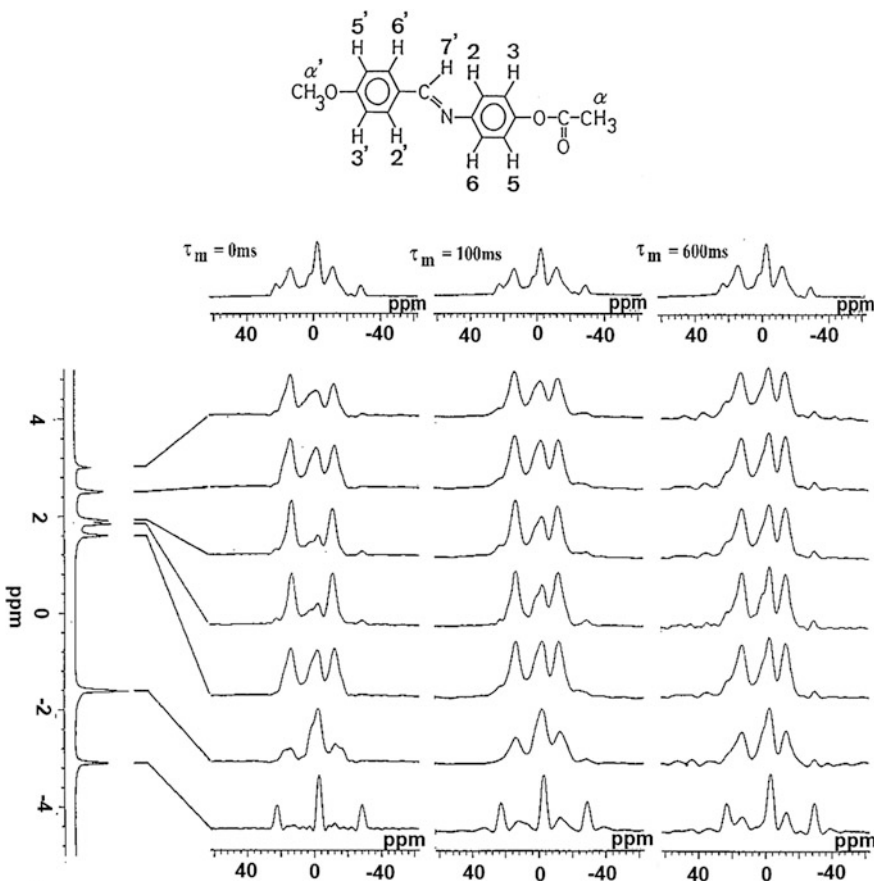


**Fig. 5.13** Dependence of the cross-sectional patterns on mixing time  $\tau_m$  in the SC-2D NMR spectra of APAPA [44]

### 5.9.2 Interpretation of the Cross-sectional Spectra from SC-2D NMR Experiments

The cross sections of the SC-2D NMR spectra of APAPA are considered in terms of a limited number of spin interactions (subspin system) in the nematic phase. First, it is assumed that the signals in the  $F_2$  dimension are well separated so that transverse magnetizations of individual protons  $I_y^k$  ( $k = 1, 2, \dots, n$ ) are detected separately. To obtain the  $k$ -th cross section, we follow the method by Schuff et al. [86], for the case of a dipolar-coupled spin system in a crystal, and calculate the  $t_1$  variation of the component of the  $k$ -th spin by

$$\begin{aligned} \langle I_y^k(t_1) \rangle &= \text{Tr}\{\rho(t_1)I_y^k\} \\ &= \text{Tr}\{\exp(-iH_1t_1)\rho(0)\exp(iH_1t_1)I_y^k\}, \end{aligned} \quad (5.1)$$

with

$$\begin{aligned} \rho(0) &= \sum_l I_y^l \\ H_1 &= -\sum_i v_L^i I_{zi} - 2 \sum_{ij} A_{ij} \left[ I_{zi} I_{zj} - \left( I_i^+ I_j^- + I_i^- I_j^+ \right) \right] / 4 \\ A_{ij} &= (\gamma^2 h / 4\pi r_{ij}^3) \langle 3 \cos^2 \theta_{ij} - 1 \rangle. \end{aligned}$$

Here,  $\rho(0)$  is the density matrix at the start of the evolution period, which evolves under the Hamiltonian in the nematic phase,  $H_1$ , to  $\rho(t_1)$  at the end of the evolution period  $t_1$ . We consider the Zeeman interaction,  $v_L$ , and the secular part of the homonuclear dipolar interaction in  $H_1$ , where  $\theta_{ij}$  represents the angle between the internuclear vector connecting nuclei  $i$  and  $j$  and the static external magnetic field. The cross section of the SC-2D NMR spectrum for the  $k$ -th proton,  $S_k(\omega_1)$ , is then obtained by a Fourier transform,  $I_y^k(t_1)$ , i.e.,

$$S_k(\omega_1) = \int dt_1, I_y^k(t_1) \cdot \exp(-i\omega_1 t_1). \quad (5.2)$$

Figure 5.14 shows calculated and experimental SC-2D NMR spectra for the methyl protons and the 2, 3, 5, 6 ring protons, both of which were calculated as a 7 spin system consisting of  $\alpha$ -methyl protons and 2, 3, 5, 6 ring protons, with effective dipolar coupling parameters of  $A_{\alpha,\alpha} = -3410$  Hz,  $A_{\alpha,3} = 400$  Hz,  $A_{\alpha,2} = 50$  Hz,  $A_{3,2} = 3250$  Hz,  $A_{3,5} = -400$  Hz, and  $A_{3,6} = -100$  Hz. Calculations with a Lorentzian half-width of 500 Hz showed good agreement with the experimentally obtained cross-sectional spectra (Fig. 5.14b), except for the central portion of the cross section for the 2, 3, 5, 6 protons, which would originate predominantly from the  $\alpha'$ -methyl protons by spin diffusion in the finite transition time of the

experiment (Fig. 5.14c). While this result points to the necessity of further shortening the transition time to completely isolate each spectrum, it is also recognized in the calculated spectra that, even at the zero transition time for which the calculations are performed, some mixing should occur in the cross-sectional patterns. Furthermore, when a Lorentzian half-width of 100 Hz was applied, complex fine structures appeared in the calculated spectra. This fine structure for the  $\alpha$ -methyl protons match well with the fine structure that appears in the central portion of the 1D spectrum measured separately at high resolution (Fig. 5.14a), which indicates that the fine structure is real. An interesting point is that some emissive patterns also appear in the calculated spectra (Fig. 5.14a). This is a common characteristic of a 2D correlation spectrum for a strongly coupled spin system, such as a J-coupled spin system in a solution [87] or a dipolar-coupled spin system in a solid [86]. However, the resolution of the present SC-2D NMR spectrum did not allow for direct experimental observation of the emission.

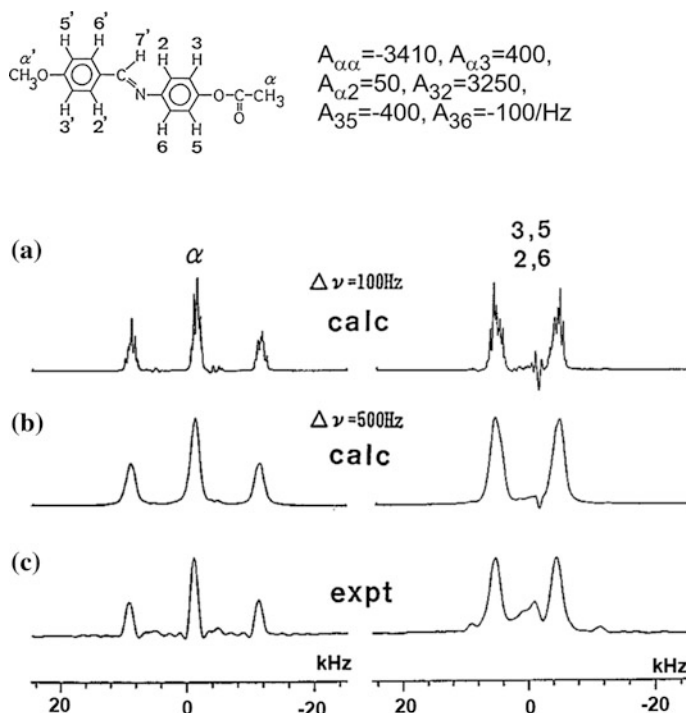


**Fig. 5.14** Experimental and simulated cross-sectional patterns for  $\alpha$ -protons and 3,5/2,6 protons in the SC-2D NMR spectrum of APAPA. **a** Simulated patterns calculated with the parameters of  $A_{\alpha\alpha} = -3410$ ,  $A_{\alpha 3} = 400$ ,  $A_{\alpha 2} = 50$ ,  $A_{32} = 3250$ ,  $A_{35} = -400$ , and  $A_{36} = -100$  Hz, and a Lorentzian half-width of 100 Hz. **b** The simulated pattern with the same parameter as (b) but with a half-width of 500 Hz. **c** The experimental pattern [44]

### 5.9.3 Interpretation of the Dipolar Patterns of the Aromatic and Methyl Protons

In the cross section of the aromatic protons, doublet patterns with a splitting of 9.7 kHz were commonly observed. The splitting frequency for two strongly coupled aromatic protons is given by

$$\Delta\nu = 3\gamma^2 h/(4\pi r^3)(3 \cos^2 \beta - 1)S, \quad (5.3)$$

with

$$S = \langle(3 \cos^2 \zeta - 1)/2\rangle,$$

where  $S$  is the long-range order parameter for the molecular axis and  $\beta$  is the angle of the director inclined to the proton internuclear vectors.  $S$  is a statistical value and  $\zeta$  represents the angle between the static magnetic field and the director vector. In this expression, the molecular axis and the director of the liquid crystal are considered to be parallel. When  $r = 2.45$  Å and  $\beta = 10^\circ$ , as calculated from X-ray diffraction data, are adopted with  $\Delta\nu = 9.7$  kHz, we obtain  $S = 0.41$  for aromatic protons in APAPA at 108 °C.

The cross section of the SC-2D NMR spectrum of APAPA indicates a large difference in dipolar couplings between two types of methyl protons. Protons in a methyl group with mutually equivalent dipolar coupling constants will generally show a triplet pattern with an intensity ratio of 1:2:1, for which the splitting frequency is given by

$$\Delta\nu = (-1/2)3\gamma^2 h/(4\pi r^3)(3 \cos^2 \beta' - 1)S. \quad (5.4)$$

Here, the value of  $-1/2$  comes from the rapid rotation of the proton internuclear vector for the methyl protons about the C3 axis of the methyl group to make an angle of  $90^\circ$ .  $\beta'$  is the angle between the C3 axis and the molecular axis. For a methyl proton,  $\Delta\nu$  was determined from Fig. 9.12c to be  $-10.2$  kHz. The inter-nuclear distance was estimated to be 1.66 Å using neutron diffraction data. Putting these values together with the order parameter for the molecular axis,  $S = 0.41$ , as evaluated from the splitting of the aromatic protons of APAPA, into Eq. (5.4) [88], the angle  $\beta'$  was determined to be  $29^\circ$ . On the other hand, the  $\Delta\nu$  value for  $\alpha'$ -methyl protons was estimated to be close to zero, and hence, the  $\beta'$  value must be close to the magic angle. Therefore, it can be concluded that the large difference in the dipolar coupling constants between the  $\alpha$ - and  $\alpha'$ -methyl protons can be attributed to the differences in the angle between the molecular axis and the C<sub>3</sub> axis.

### 5.9.4 Interpretation of the Cross-Sectional Patterns

The first mutually different cross-sectional patterns were observed in the SC-2D NMR spectrum when  $\tau_m$  was chosen to be 0 ms, which indicates that both the inter- and intramolecular cross-relaxation rates and spin flip-flop rates between interacting pairs of protons are relatively slow. This can be understood if the dipolar interactions are considered to be partially averaged out by fast translational and rotational molecular motions in the liquid crystalline phase in contrast to that in the solid phase.

However, spectral mixing does occur among different cross sections, particularly with larger  $\tau_m$  values. To understand the degree of mixing among the cross-sectional pattern for an SC-2D NMR spectrum more quantitatively, we must find the equation that governs the exchange of longitudinal magnetization within the homonuclear spin system during the mixing time. The results shown in Fig. 5.15a indicate that the exchange occurs in the liquid crystalline phase and suggests that it must arise from the static and time-dependent parts of the dipolar coupling Hamiltonian. It can be analyzed by starting with a Solomon type equation for a dipolar-coupled homonuclear spin system, which can be expressed in a compact form as

$$\frac{d\langle I_z \rangle}{dt} = R\langle I_z \rangle \quad (5.5)$$

Here,  $I_z$  denotes the longitudinal magnetization vector of the homonuclear spin system with components  $I_{z1}, I_{z2}, \dots$  etc. for individual protons and  $R$  denotes the relaxation matrix. For an exact estimation of the relaxation matrix elements, we require details not only on the conformation of the molecule, but also on the molecular motion, which are presently unknown. Thus, a phenomenological approach is taken under a reasonable simplification. The spin-lattice relaxation rates are entirely neglected, which are in the order of a second at a proton resonance frequency of 400 MHz and as the first approximation are unimportant for consideration of the spectral patterns, and take only the exchange of magnetizations into account. The elements of the relaxation matrix should then follow the relation

$$R_{ij} = - \sum_j R_{ij} (i \neq j) \quad (5.6)$$

with

$$R_{ij} = R_{ji} (i \neq j).$$

Now the element  $R_{ij}$  simply denotes the rate of exchange of magnetizations between two protons,  $i$  and  $j$ , due to mutual dipolar coupling. In the SC-2D NMR experiments using the pulse sequence shown in Fig. 5.11, the transverse magnetization  $\langle I_y(t_1) \rangle$  that has evolved for  $t_1$  under the nematic phase Hamiltonian is transformed into  $\langle I_z(t_1) \rangle = \sum_k \langle I_z^k(t_1) \rangle$  by the second 90° pulse. During the mixing

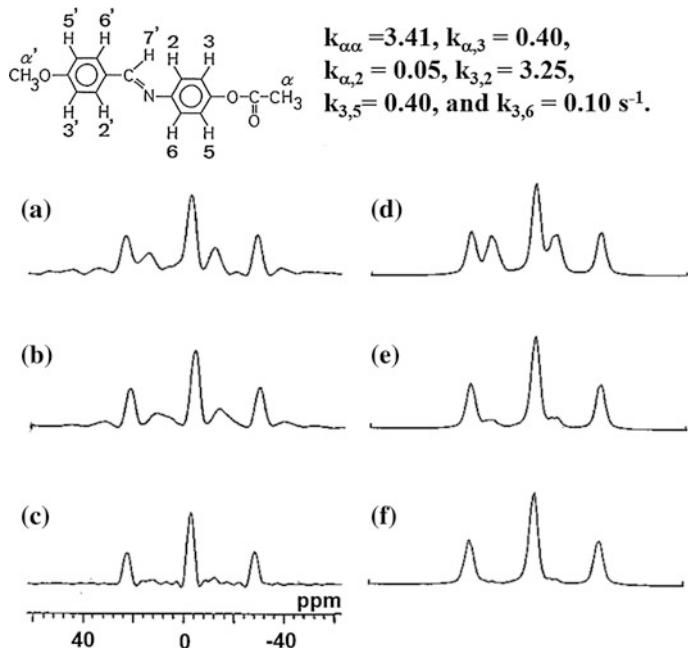


**Fig. 5.15** Experimental and simulated SC-2D NMR spectra for  $\alpha$ -protons in APAPA. Experimental patterns with  $\tau_m = \mathbf{a}$  600 ms,  $\mathbf{b}$  100 ms, and  $\mathbf{c}$  0 s. Simulated pattern with  $\mathbf{d} \tau_m = 600$  ms,  $\mathbf{e} \tau_m = 100$  ms, and  $\mathbf{f} \tau_m = 0$  s. Simulations were performed using elements of the exchange matrix of  $k_{\alpha\alpha} = 3.41$ ,  $k_{\alpha,3} = 0.40$ ,  $k_{\alpha,2} = 0.05$ ,  $k_{3,2} = 3.25$ ,  $k_{3,5} = 0.40$ , and  $k_{3,6} = 0.10 \text{ s}^{-1}$  [44]

time  $\tau_m$ , the longitudinal magnetization further evolves by the exchange obeying the following equation

$$\langle I_z(t_1, \tau_m) \rangle = \exp(\tau_m \mathbf{R}) \langle I_z(t_1) \rangle \quad (5.7)$$

Of which the component of the  $k$ -th proton is given by

$$\langle I_z^k(t_1, \tau_m) \rangle = \sum_l [\exp(\tau_m \mathbf{R})]_{kl} \langle I_z^l(t_1) \rangle. \quad (5.8)$$

The matrix  $\exp(\tau_m \mathbf{R})$  can be obtained numerically after diagonalization of  $\mathbf{R}$ . The longitudinal magnetization  $\langle I_z^k(t_1, \tau_m) \rangle$  can then be transformed into  $\langle I_y^k(t_1, \tau_m) \rangle$  by the third  $90^\circ$  pulse. Finally, the resonance lines for the  $k$ -th proton  $S_k(\omega_1, t_m)$  mixed with other proton resonances can be obtained by a Fourier transformation of  $\Sigma_l [\exp(\tau_m \mathbf{R})]_{kl} \langle I_{1z}(t_1) \rangle$ , i.e.,

$$S_k(\omega_1, \tau_m) = \sum_l [\exp(\tau_m \mathbf{R})]_{kl} \int dt_1 \left\langle I_y^l(t_1) \right\rangle \exp(i\omega t_1). \quad (5.9)$$

In the actual calculation of the mixing pattern for the  $\alpha$ -methyl protons, seven protons were included and the exchange rates for the individual proton pairs were determined from Fig. 5.15. The 3', 5'/2', 6', 7 and  $\alpha'$ -methyl protons are far from the  $\alpha$ -methyl protons and only mixing with the 3, 5/2, 6 protons was observed in Fig. 5.15; therefore, a subspin system consisting of  $\alpha$ -methyl and 3, 5/2, 6 protons was considered in the simulation. Figure 5.15 shows the experimentally obtained and best-fit simulated cross sections for protons with mixing times of 0, 100, and 600 ms. The results of the calculation indicate that the cross-relaxation rate from aromatic to  $\alpha$ -protons is only  $0.40 \text{ s}^{-1}$ , which is far lower than that expected in solids. This low rate of exchange clearly explains why proton NMR spectra of nematic liquid crystals are inhomogeneously broadened unlike those in solids.

## 5.10 Conclusions

In situ photoirradiation NMR spectroscopy has been demonstrated to be a very useful means of elucidating the photoreaction cycles of photoreceptor membrane proteins. In the SRI system, M-intermediates were stationary trapped and exhibit a negative phototaxis state under green light irradiation, and the P-state was stationary trapped and exhibited negative phototaxis under blue light irradiation. In the SRII system, M-intermediates were stationary trapped and exhibited negative phototaxis. In the system of the Y185F-bR mutant, N-intermediates were stationary trapped under green light irradiation and O-intermediate could be trapped in a subsequent dark state.

An in situ microwave irradiation NMR spectrometer was successfully developed, and the microwave-induced heating mechanism was revealed. In the liquid crystalline state, local heating states were observed under microwave irradiation. In the isotropic state, different temperatures were observed within the same molecule under microwave irradiation. This can be explained by the low entropy state induced by microwave energy which induced an orientationally ordered state. This ordered state induces electric dipolar interaction which results in an additional chemical shift to the polar group in the molecule.

Microwave irradiation makes it possible to achieve rapid temperature jump in a liquid crystalline sample, which allows liquid-state isotropic state SC-2D NMR spectroscopy to be performed and provides the  ${}^1\text{H}-{}^1\text{H}$  local dipolar field in the resolution of the isotropic state. Thereby, the order parameters for liquid crystalline systems can be accurately determined.

**Acknowledgements** This work was supported by grants-in-aid for Scientific Research in an Innovative Area (16H00756 to AN and 16H00828 to IK), and by a grant-in-aid for Scientific Research (C) (15K06963 to AN) and Research (B) (15H04336 to IK) from the Ministry of Education, Culture, Sports, Science and Technology of Japan.

## References

- Smith, S.O., de Groot, H.J.M., Gebhard, R., Courtin, J., Lugtenburg, J., Herzfeld, J., Griffin, R.G.: Structure and protein environment of the retinal chromophore in ligand- and dark-adapted bacteriorhodopsin studied by solid-state NMR. *Biochemistry* **28**, 8897–8904 (1989)
- McDermott, A.E., Thompson, L.K., Winkel, C., Farrar, M.R., Pelletier, S., Lugtenburg, J., Herzfeld, J., Griffin, R.G.: Mechanism of proton pumping in bacteriorhodopsin by solid-state NMR: the protonation state of tyrosine in the light-adapted and M state. *Biochemistry* **30**, 8366–8371 (1991)
- Farrar, M.R., Lakshmi, K.V., Smith, S.O., Brown, R.S., Raap, J., Lugtenburg, J., Griffin, R.G., Herzfeld, J.: Solid state NMR study of [ $\varepsilon$ -<sup>13</sup>C]Lys-bacteriorhodopsin: schiff base photoisomerization. *Biophys. J.* **65**, 310–315 (1993)
- Lakshmi, K.V., Farrar, M.R., Raap, J., Lugtenburg, J., Griffin, R.G., Herzfeld, J.: Solid state <sup>13</sup>C and <sup>15</sup>N NMR investigations of the N intermediate of bacteriorhodopsin. *Biochemistry* **33**, 8853–8857 (1994)
- Feng, X., Verdegem, P.J.E., Eden, M., Sandstrom, D., Lee, Y.K., Bovee-Geurts, P.H.M., de Grip, W.J., Lugtenburg, J., de Groot, H.J.M., Levitt, M.H.: Determination of a molecular torsional angle in the metarhodopsin-I photointermediate of rhodopsin by double-quantum solid-state NMR. *J. Biomol. NMR* **16**, 1–8 (2000)
- Crocker, E., Eilers, M., Ahuja, S., Hornak, V., Hirshfeld, A., Sheves, M., Smith, S.O.: Location of Trp265 in metarhodopsin II: implications for the activation mechanism of the visual receptor rhodopsin. *J. Mol. Biol.* **357**, 163–172 (2006)
- Ahuja, S., Crocker, E., Eilers, M., Hornak, V., Hirshfeld, A., Ziliox, M., Syrett, N., Reeves, P.J., Khorana, H.G., Sheves, M., Smith, S.O.: Location of the retinal chromophore in the Activated state of rhodopsin. *J. Biol. Chem.* **284**, 10190–10201 (2009)
- Hu, J.G., Sun, B.Q., Bizounok, M., Hatcher, M.E., Lansing, J.C., Raap, J., Verdegen, P.J.E., Lugtenburg, J., Griffin, R.G., Herzfeld, J.: Early and late M intermediates in the bacteriorhodopsin photocycle: a solid-state NMR study. *Biochemistry* **37**, 8088–8096 (1998)
- Petkova, A.T., Hatanaka, M., Jaroniec, C.P., Hu, J.G., Belenky, M., Verhoeven, M., Lugtenburg, J., Griffin, R.G., Herzfeld, J.: Tryptophan interaction in bacteriorhodopsin: a heteronuclear solid-state NMR study. *Biochemistry* **41**, 2429–2437 (2002)
- Hu, J.G., Sun, B.Q., Petkova, A.T., Griffin, R.G., Herzfeld, J.: The predischarge chromophore in bacteriorhodopsin: a <sup>15</sup>N solid-state NMR study of the L photointermediate. *Biochemistry* **36**, 9316–9322 (1997)
- Mak-Jurkauskas, M.L., Bajaj, V.S., Hornstein, M.K., Blenky, M., Griffin, R.G., Herzfeld, J.: Energy transformations early in the bacteriorhodopsin photocycle revealed by DNP-enhanced solid-state NMR. *Proc. Natl. Acad. Sci. U S A* **105**, 883–888 (2008)
- Bajaj, V.S., Mak-Jurkauskas, M.L., Belenky, M., Herzfeld, J., Griffin, R.G.: Functional and shunt state of bacteriorhodopsin resolved by 250 GHz dynamic nuclear polarization-enhanced solid-state NMR. *Proc. Natl. Acad. Sci. U S A* **106**, 9244–9249 (2009)
- Becker-Baldus, J., Bamann, C., Saxena, K., Gustmann, H., Brown, L.J., Brown, R.C.D., Reiter, C., Bamberg, E., Wachtveitl, J., Schwalbe, H., Glaubitz, C.: Enlightening the photoactive site of channelrhodopsin-2 by DNP-enhanced solid-state NMR spectroscopy. *Proc. Natl. Acad. Sci. U S A* **112**, 9896–9901 (2015)

14. Kawamura, I., Kihara, N., Ohmine, M., Nishimura, K., Tuzi, S., Saitô, H., Naito, A.: Solid-state NMR studies of two backbone conformations at Tyr185 as a function of retinal configurations in the dark, light, and pressure adapted bacteriorhodopsin. *J. Am. Chem. Soc.* **129**, 1016–1017 (2007)
15. Tomonaga, Y., Hidaka, T., Kawamura, I., Nishio, T., Ohsawa, K., Okitsu, T., Wada, A., Sudo, Y., Kamo, N., Ramamoorthy, A., Naito, A.: An active photoreceptor intermediate revealed by *in situ* photoirradiated solid-state NMR spectroscopy. *Biophys. J.* **101**, L50–L52 (2011)
16. Yomoda, H., Makino, Y., Tomonaga, Y., Hidaka, T., Kawamura, I., Okitsu, T., Wada, A., Sudo, Y., Naito, A.: Color-discriminating retinal configurations of sensory rhodopsin I by photo-irradiation solid-state NMR spectroscopy. *Angew. Chem. Int. Ed.* **53**, 6960–6964 (2014)
17. Naito, A., Kawamura, I.: Photoactivated structural changes in photoreceptor membrane proteins as revealed by *in situ* photoirradiation solid-state NMR spectroscopy. In: Separovic, F., Naito, A. (eds.) *Advances in Biological Solid-State NMR: Proteins and Membrane Active Peptides*, pp. 387–404. Royal Society of Chemistry, London (2014)
18. Naito, A., Kawamura, I., Javkhlanlus, N.: Recent solid-state NMR studies of membrane-bound peptides and proteins. *Annu. Rep. NMR Spectrosc.* **86**, 333–411 (2015)
19. Oshima, K., Shigeta, A., Makino, Y., Kawamura, I., Okitsu, T., Wada, A., Tuzi, S., Iwasa, T., Naito, A.: Characterization of photo-intermediates in the photo-reaction pathways of a bacteriorhodopsin Y185F mutant using *in situ* photo-irradiation solid-state NMR spectroscopy. *Photochem. Photobiol. Sci.* **14**, 1694–1702 (2015)
20. Gedye, R., Smith, F., Westaway, K., All, H., Baldisers, L., Laberge, L., Rousell, J.: The use of microwave ovens for rapid organic synthesis. *Tetrahedron Lett.* **27**, 279–282 (1986)
21. Giguere, R.J., Bray, T.L., Duncan, S.M., Majetich, G.: Application of commercial microwave ovens to organic synthesis. *Tetrahedron Lett.* **27**, 4945–4948 (1986)
22. Adam, D.: Out of the kitchen. *Nature* **421**, 571–572 (2003)
23. Perreux, L., Loupy, A.: Attentative rationalization of microwave effects in organic synthesis according to the reaction medium, and mechanistic considerations. *Tetrahedron* **57**, 9199–9223 (2001)
24. Lidström, P., Tiemey, J., Wathey, B., Westman, J.: Microwave assisted organic synthesis. *Tetrahedron* **57**, 9235–9283 (2001)
25. Bogdal, D., Lukasiewicz, M., Pielichowski, J., Miciak, A., Begdarz, Sz.: Microwave-assisted oxidation of alcohols using magtrieve. *Tetrahedron* **59**, 649–653 (2003)
26. Kappe, G.O.: Controlled microwave heating in modern organic synthesis. *Angew. Chem. Int. Ed.* **43**, 6250–6284 (2004)
27. Yoshimura, Y., Shimizu, H., Hinou, H., Nishimura, S.-I.: A novel glycosylation concept: microwave-assisted acetal-exchange type glycosylation from methyl glycosides as donors. *Tetrahedron Lett.* **46**, 4701–4705 (2005)
28. Shimizu, H., Yoshimura, Y., Hinou, H., Nishimura, S.-I.: A new glycosylation method part 3: study of microwave effects at low temperatures to control reaction pathways and reduce byproducts. *Tetrahedron* **64**, 10091–10096 (2008)
29. Kappe, C.O., Pieber, B., Dallinger, D.: Microwave effect in organic synthesis: myth or reality. *Angew. Chem. Int. Ed.* **52**, 1088–1094 (2013)
30. Hoogenboom, R., Wiesbrock, F., Huang, H., Leenen, M.A.M., Thijis, H.M.L., van Nispen, S. F.G.M., van der Loop, M., Fustin, C.-A., Jonas, A.M., Gohy, J.-F., Schubert, U.S.: Microwave-assisted cationic ring-opening polymerization of 2-oxazolines: a powerful method for the synthesis of amphiphilic triblock copolymers. *Macromolecules* **39**, 4719–4725 (2006)
31. Iwamura, T., Ashizawa, K., Sakaguchi, M.: Efficient and echo-friendly anionic polymerization of acrylamide under microwave irradiation and hydrolysis of the obtained polymers by microwave irradiation. *Macromolecules* **42**, 5001–5006 (2009)
32. Kajiwara, Y., Nagai, A., Chujo, Y.: Microwave-assisted synthesis of poly(2-hydroxyethyl methacrylate)(HEMA)/Silica hybrid using *in situ* polymerization method. *Polymer J.* **41**, 1080–1084 (2009)

33. Yamada, S., Takasu, A., Takayama, S., Kawamura, K.: Microwave-assisted solution polycondensation of L-lactic acid using a Dean-Stark apparatus for a non-thermal microwave polymerization effect induced by the electric field. *Polym. Chem.* **5**, 5283–5288 (2014)
34. Pramanik, B.N., Mirza, U.A., Ing, Y.H., Liu, Y.-H., Bartner, P.L., Weber, P.C., Bose, A.K.: Microwave-enhanced enzyme reaction for protein mapping by mass spectrometry: a new approach to protein digestion in minutes. *Protein Sci.* **11**, 2676–2687 (2002)
35. Huang, W., Xia, Y.-M., Gao, H., Fang, T.-J., Wang, Y., Fang, Y.J.: Enzymatic esterification between n-alcohol homologs and n-caprylic acid in non-aqueous medium under microwave irradiation. *Mol. Catal.* **35**, 115–116 (2005)
36. Herrero, M.A., Kremsner, J.M., Kappe, C.O.: Nonthermal microwave effects revised: on the importance of internal temperature monitoring and agitation in microwave chemistry. *J. Org. Chem.* **73**, 36–49 (2008)
37. Obermayer, D., Gutmann, B., Kappe, C.O.: Microwave chemistry in silicon carbide reaction vials: separating thermal from nonthermal effects. *Angew. Chem. Int. Ed.* **48**, 8321–8324 (2009)
38. Tanaka, M., Sato, M.: Microwave heating of water, ice, and saline solution: molecular dynamic study. *J. Chem. Phys.* **126**, 034509 (2007)
39. Kanno, M., Nakamura, K., Kanai, K., Hoki, K., Kono, H., Tanaka, M.: Theoretical verification of nonthermal microwave effects on intramolecular reactions. *J. Phys. Chem. A* **116**, 2177–2183 (2012)
40. Tsukahara, Y., Higashi, A., Yamauchi, T., Nakamura, T., Yasuda, M., Baba, A., Wada, Y.: In situ observation of nonequilibrium local heating as an origin of spherical effect of microwave on chemistry. *J. Phys. Chem. C* **114**, 8965–8970 (2010)
41. Tasei, Y., Yamakami, T., Kawamura, I., Fujito, T., Ushida, K., Sato, M., Naito, A.: Mechanism for microwave heating of 1-(4'-cyanophenyl)-4-propylcyclohexane characterized by in situ microwave irradiation NMR spectroscopy. *J. Magn. Reson.* **254**, 27–34 (2015)
42. Tasei, Y., Tanigawa, F., Kawamura, I., Fujito, T., Sato, M., Naito, A.: The microwave heating mechanism of N-(4-methoxybenzylidene)-4-butylaniline in liquid crystalline and isotropic phases as determined using in situ microwave irradiation NMR spectroscopy. *Phys. Chem. Chem. Phys.* **17**, 9082–9089 (2015)
43. Naito, A., Imanari, M., Akasaka, K.: Separation of local magnetic fields of individual protons in nematic phase by state-correlated 2D NMR spectroscopy. *J. Magn. Reson.* **92**, 85–93 (1991)
44. Naito, A., Imanari, M., Akasaka, K.: State-correlated two-dimensional NMR spectroscopy: separation of local dipolar fields of protons in nematic phase of 4'-methoxybenzylidene-4-acetoxyaniline. *J. Chem. Phys.* **105**, 4502–4510 (1996)
45. Akasaka, K., Kimura, M., Naito, A., Kawahara, H., Imanari, M.: Local order, conformation, and interaction in nematic 4-(n-pentyloxy)-4'-cyanobiphenyl and its one-to-one mixture with 1-(4'-cyanophenyl)-4-propylcyclohexane. A study by state-correlated 1H two-dimensional NMR spectroscopy. *J. Phys. Chem.* **99**, 9523–9529 (1995)
46. Naito, A., Ramamoorthy, A.: Structural studies of liquid crystalline materials using a solid state NMR technique. *Thermotropic Liquid Crystal: Recent Advances*, pp. 85–116, Springer, Berlin (2007)
47. Naito, A., Tasei, Y.: Separation of local fields of individual protons in nematic phase of 4'-ethoxybenzylidene-4-n-butylaniline by microwave heating 2D NMR spectroscopy. *Mater. Sci. Technol. (MS&T)* **2010**, 2886–2894 (2010)
48. Akasaka, K., Naito, A., Imanari, M.: Novel method for NMR spectral correlation between the native and the denatured states of a protein. Application to ribonuclease A. *J. Am. Chem. Soc.* **113**, 4688–4689 (1991)
49. Spudich, J.L., Bogomolni, R.A.: Mechanism of colour discrimination by a bacterial sensory rhodopsin. *Nature* **312**, 509–513 (1984)
50. Suzuki, D., Irieda, H., Honma, M., Kawagishi, I., Sudo, Y.: Phototactic and chemotactic signal transduction by transmembrane receptors and transducers in microorganisms. *Sensors* **10**, 4010–4039 (2010)

51. Chen, X., Spudich, J.L.: Demonstration of 2:2 stoichiometry in the functional SRI-HtrI signaling complex in *Halobacterium* membrane by gene fusion analysis. *Biochemistry* **41**, 3891–3896 (2002)
52. Szundi, I., Swartz, T.E., Bogomoni, R.A.: Multicolored protein conformation state in the photocycle of transducer-free sensory rhodopsin-I. *Biophys. J.* **80**, 469–479 (2001)
53. Kitajima-Ihara, T., Furutani, Y., Suzuki, D., Ihara, K., Kandori, H., Honma, M., Sudo, Y.: Salinibacter sensory rhodopsin: sensory rhodopsin I-like protein from a eubacterium. *J. Biol. Chem.* **283**, 23533–23541 (2008)
54. Suzuki, D., Sudo, Y., Furutani, Y., Takahashi, H., Honnma, M., Kandori, H.: Structural changes of salinibacter sensory rhodopsin I upon formation of the K and M photointermediates. *Biochemistry* **47**, 12750–12759 (2008)
55. Harbison, G.S., Smith, S.O., Pardoen, J.A., Mudder, P.P.J., Lugtenburg, J., Herzfeld, J., Mishien, G.S., Griffin, R.G.: Solid-state  $^{13}\text{C}$  NMR studies of retinal in bacteriorhodopsin. *Biochemistry* **23**, 2662–2687 (1984)
56. Sineshchekov, O.A., Sasaki, J., Philip, S.B.J., Spudich, J.L.: A Schiff base connectivity switch in sensory rhodopsin signaling. *Proc. Natl. Acad. Sci. U S A* **105**, 16159–16164 (2008)
57. Spudich, J.L., Luecke, H.: Sensory rhodopsin II: functional insight from structure. *Curr. Opin. Struct. Biol.* **12**, 540–546 (2002)
58. Kamo, N., Shimono, K., Iwamoto, M., Sudo, Y.: Photochemistry and photoinduced proton-transfer by pharaonis phoborhodopsin. *Biochemistry (Mosc.)* **66**, 1277–1282 (2001)
59. Gordelly, V.L., Labahn, J., Moukhambetzianov, R., Efremov, R., Granzin, J., Schlesinger, R., Büldt, G., Sevopol, T., Scheldig, A.J., Klarr, J.P., Engelhart, M.: Molecular basis of transmembrane signalling by sensory rhodopsin II-transducer complex. *Nature* **419**, 484–487 (2002)
60. Shimono, K., Hayashi, T., Ikebara, Y., Sudo, Y., Iwamoto, M., Kamo, N.: Importance of the broad regional interaction for spectral tuning in *Natronobacterium pharaonis* phoborhodopsin (sensory rhodopsin II). *J. Biol. Chem.* **278**, 23882–23889 (2003)
61. Sudo, Y., Furutani, Y., Kandori, H., Spudich, J.L.: Functional importance of the interhelical hydrogen bond between Thr204 and Tyr174 of sensory rhodopsin II and its alteration during the signalling process. *J. Biol. Chem.* **281**, 34239–34245 (2006)
62. Sudo, Y., Furutani, Y., Wada, A., Ito, M., Kamo, N., Kandori, H.: Steric constraint in the primary photoproduct of an archaeal rhodopsin from regiospecific perturbation of C-D stretching vibration of the retinyl chromophore. *J. Am. Chem. Soc.* **127**, 16036–16037 (2005)
63. Furutani, Y., Kamada, K., Sudo, Y., Shimono, K., Kamo, N., Kandori, H.: Structural changes of the complex between pharaonis phoborhodopsin and its cognate transducer upon formation of the M photointermediate. *Biochemistry* **44**, 2909–2915 (2005)
64. Wagner, A.-A., Chzhov, I., Engelhard, M., Steinhoff, H.-J.: Time-resolved detection of transient movement of helix F in spin-labelled pharaonic sensory rhodopsin II. *J. Mol. Biol.* **301**, 881–891 (2000)
65. Spudih, J.I.: Variations on a molecular switch: transport and sensory signalling by archaeal rhodopsin. *Mol. Microbiol.* **28**, 1051–1058 (1998)
66. Yoshida, H., Sudo, Y., Shimono, K., Iwamoto, M., Kamo, N.: Transient movement of helix F revealed by photo-induced inactivation by reaction of a bulky SH-reagent to cysteine-introduced pharaonis phoborhodopsin (sensory rhodopsin II). *Photochem. Photobiol. Sci.* **3**, 537–542 (2004)
67. Moukhambetzianov, R., Klare, J.P., Efremov, R., Baeken, C., Göppner, A., Labahn, J., Engelhard, M., Büldt, G., Gordelly, V.I.: Development of the signal in sensory rhodopsin and its transducer to the cognate transducer. *Nature* **440**, 115–119 (2006)
68. Etzkorn, M., Seidel, K., Li, L., Martell, S., Geyer, M., Engelhard, M., Baldus, M.: Complex formation and light activation in membrane-embedded sensory rhodopsin II as seen by solid-state NMR spectroscopy. *Structure* **18**, 293–300 (2010)
69. Kawamura, I., Yoshida, H., Ikeda, Y., Yamaguchi, S., Tuzi, S., Saitô, H., Kamo, N., Naito, A.: Dynamic change of phoborhodopsin and transducer by activation: study using D75N

- mutant of the receptor by site-directed solid-state  $^{13}\text{C}$  NMR. *Photochem. Photobiol.* **84**, 921–930 (2008)
- 70. Roy, S., Kikukawa, T., Sharma, P., Ksmo, N.: All-optical switching in pharaonic phorhodopsin protein molecules. *IEEE Trans. Nanobiosci.* **5**, 178–187 (2006)
  - 71. Tateishi, Y., Abe, T., Tamogami, J., Nakano, Y., Kikukawa, T., Kamo, N., Unno, M.: Spectroscopic evidence for the formation of an N intermediate during the photocycle of sensory rhodopsin II (phorhodopsin) from *Natronobacterium pharaonicum*. *Biochemistry* **50**, 2135–2143 (2011)
  - 72. Lanyi, J.K.: Proton transfers in the bacteriorhodopsin photocycle. *Biochim. Biophys. Acta* **1757**, 1012–1018 (2006)
  - 73. Lanyi, J.K.: Molecular mechanism of ion transport in bacteriorhodopsin: insights from crystallographic, spectroscopic, kinetic, and mutational studies. *J. Phys. Chem. B* **48**, 11441–11448 (2000)
  - 74. Morgan, J.E., Vakkasoglu, A.S., Lanyi, J.K., Lugtenburg, J., Gennis, R.B., Maeda, G.A.: Structure changes upon deprotonation of the proton release group in the bacteriorhodopsin photocycle. *Biophys. J.* **103**, 444–452 (2012)
  - 75. Nango, E., Royant, A., Kubo, M., Nakane, T., Wlckstrand, C., Kimura, T., Tanaka, T., Tono, K., Soug, C., Tanaka, R., et al.: A three-dimensional movie of structural changes in bacteriorhodopsin. *Science* **354**, 1552–1557 (2016)
  - 76. Duriaich, M., Marti, T., Khorana, H.G., Rothchild, K.J.: UV-visible spectroscopy of bacteriorhodopsin mutants: substitution of Arg-82, Asp-85, Tyr-185, and Asp-212 results in abnormal light-dark adaptation. *Proc. Natl. Acad. Sci. U S A* **87**, 9873–9877 (1990)
  - 77. Sonar, S., Krebs, M.P., Khorana, H.G., Rothchild, K.J.: Static and time-resolved absorption spectroscopy of the bacteriorhodopsin mutant Tyr185 → Phe: evidence for an equilibrium between bR570 and O-like species. *Biochemistry* **32**, 2223–2271 (1993)
  - 78. Rath, P., Krebs, M.P., He, Y., Khorana, H.G., Rothchild, K.J.: Fourier transform raman spectroscopy of the bacteriorhodopsin mutant Tyr185 → Phe: formation of a stable O-like species during light adaptation and detection of its transient N-like photoproduct. *Biochemistry* **32**, 2272–2281 (1993)
  - 79. Richter, H.-T., Needleman, R., Lanyi, J.K.: Perturbed interaction between residues 85 and 204 in Tyr185 → Phe and Asp85 → Glu bacteriorhodopsin. *Biophys. J.* **71**, 3392–3398 (1996)
  - 80. Iwasa, T., Tokunaga, F., Yoshizawa, T.: Photochemical reaction of 13-cis-bacteriorhodopsin studied by low temperature spectroscopy. *Photochem. Photobiol.* **33**, 539–545 (1981)
  - 81. Roepe, P.D., Ahl, P.L., Herzelfeld, J., Lugtenburg, J., Rothchild, K.J.: Tyrosine protonation changes in bacteriorhodopsin, a Fourier transform infrared study of BR648 and its primary photoproduct. *J. Biol. Chem.* **263**, 5110–5117 (1988)
  - 82. Van Greet, A.L.: Calibration of the methanol and glycol nuclear magnetic resonance thermometers with a static thermistor probe. *Anal. Chem.* **40**, 2227–2229 (1968)
  - 83. Van Greet, A.L.: Calibration of methanol nuclear magnetic resonance thermometer at low temperature. *Anal. Chem.* **42**, 679–680 (1970)
  - 84. Bielecki, A., Burum, D.P.: Temperature dependence of  $^{207}\text{Pb}$  MAS spectra of solid lead nitrate. An accurate, sensitive thermometer for variable-temperature MAS. *J. Magn. Reson. A* **116**, 215–220 (1995)
  - 85. Zuo, C.S., Metz, K.R., Sun, Y., Sherry, A.D.: NMR temperature measurements using a paramagnetic Lanthanide complex. *J. Magn. Reson.* **133**, 53–60 (1998)
  - 86. Schuff, N.: Haeberlen, 2D Correlation spectroscopy in homonuclear dipolar-coupled solids. *J. Magn. Reson.* **52**, 267–281 (1983)
  - 87. Bodenhausen, G., Freeman, R., Morris, G.A., Turner, D.L.: NMR spectra of some simple spin systems studied by two-dimensional Fourier transformation of spin echoes. *J. Magn. Reson.* **31**, 75–95 (1978)
  - 88. Prasad, J.S.: Orientational order parameters and conformation of nematic p-ethoxybenzylidene-p-n-butylaniline. *J. Chem. Phys.* **65**, 941 (1976)

# Chapter 6

## Solid-State NMR Under Ultrafast MAS Rate of 40–120 kHz

Yusuke Nishiyama

**Abstract** With the recent advances in magic-angle spinning (MAS) technology, MAS rates faster than 100 kHz can now be achieved in commercially available probes. The very fast MAS system is comprised of tiny rotors of diameter less than 1 mm, very small sample volume less than 1  $\mu\text{L}$ , very strong rf field strength close to 1 MHz, etc. Because of such extreme features, the very fast MAS measurements require a careful handling of hardware and proper setting of experimental conditions. To this end, the main objective of this chapter is to provide a comprehensive practical guide to set up fundamental experimental conditions (both sample-independent and sample-dependent conditions) associated with very fast MAS technique. The art of shimming, magic-angle adjustment, rf field strength calibration, frequency referencing, repetition delay, and fluctuations in spinning rate are discussed in detail. In addition, two widely used two-dimensional (2D) measurements of  $^1\text{H}$  homonuclear double-quantum/single-quantum (DQ/SQ) correlations and  $^1\text{H}/\text{X}$  cross-polarization heteronuclear single-quantum coherence (CP-HSQC) experiments are introduced.

**Keywords** Fast MAS •  $^1\text{H}$  indirect detection • Homonuclear correlation  
Heteronuclear correlation

### 6.1 Overview

In general, limited resolution and sensitivity of NMR spectra of solids have always been major roadblocks for widespread applications of solid-state NMR. The presence of orientation-dependent NMR spin anisotropic interactions like chemical shift

---

Y. Nishiyama (✉)  
JEOL RESONANCE Inc., Akishima, Tokyo 196-8558, Japan  
e-mail: yunishiy@jeol.co.jp

Y. Nishiyama  
RIKEN CLST-JEOL Collaboration Center,  
Yokohama, Kanagawa 230-0045, Japan

anisotropy (CSA), dipolar couplings, and quadrupolar couplings, results in broad and featureless NMR spectra of static samples [1, 2]. Magic-angle sample spinning (MAS), which averages out anisotropic interactions to enhance resolution and sensitivity of NMR spectra, serves as an essential technique to study rigid solids [3, 4]. While with the available probe technology the maximum attainable MAS frequency (120 kHz) is larger than the size of the most spin interactions, MAS frequency >120 kHz can still be beneficial in isotopically enriched and naturally abundant chemical, material and biological samples. One of the major advantages of the very fast MAS technique is the reduced broadening of  $^1\text{H}$  NMR resonances due to suppression of  $^1\text{H}$ - $^1\text{H}$  homonuclear dipolar interactions in rigid  $^1\text{H}$  networks, which is inversely proportional to the sample spinning frequency [5, 6]. Consequently, a combination of the very fast MAS, high natural abundance, and high sensitivity of protons allows the  $^1\text{H}$  indirect observation of X nuclei with enhanced sensitivity [7–16]. The application of very fast MAS to the systems with large anisotropies like quadrupolar nuclei, heavy spin-1/2 nuclei, paramagnetic systems is shown to be very efficient for their structural characterization by several research groups [17–23]. Many excellent review articles on very fast MAS NMR technique can be found in the literature that introduce the engineering improvement, giving the theoretical backgrounds and discussing the practical applications [5, 24–35]. However, it is not straightforward to use very fast MAS techniques especially for researchers with non-NMR background. In this regard, the purpose of this chapter is not to provide a comprehensive review of the very fast MAS technique, rather to introduce the practical hands-on guide to researchers using this technique for structural and dynamics studies of rigid solid samples.

The very fast MAS probes with a diameter of 0.7–2 mm have several advantages and disadvantages over the commonly used slow to moderate MAS systems with a diameter of 3–5 mm. Advantages are (a1) faster MAS rate [36–47], (a2) smaller sample volume, (a3) stronger rf field strength with the same rf input, (a4) high sensitivity per unit volume, (a5) smaller temperature increase due to friction loss at the same MAS rate, (a6) use of low power sequences [48–52], and (a7) less E-field heating for lossy samples. The disadvantages are (d1) lower absolute sensitivities at the same experimental conditions, (d2) difficulty in sample and probe handling, (d3) limited temperature range, and (d4) generally more expensive. It is crucial to choose the appropriate sample rotors depending on the system of interest, considering the above-mentioned advantages and disadvantages. Nowadays, the probes with a capability of MAS rate faster than 100 kHz are commercially available (a1). Since the spinning frequency is typically limited by the speed at the surface which is close to the speed of sound at the maximum attainable MAS rate, the practical solution to achieve faster MAS is to make the sample rotor smaller. This accompanies with the small sample volume (a2). The very fast MAS probe for 100+ kHz MAS rate needs the rotor diameter of 0.7–0.75 mm with the sample volume less than 0.5  $\mu\text{L}$ , which is hundred times smaller than that of standard MAS rotor (ca 50  $\mu\text{L}$  for 4 mm). Although the tiny sample volume accompanies with the limited absolute sensitivity, the capability of volume limited sample analysis dramatically reduces the barrier to prepare and analyze costly samples such as fully isotopically labeled protein

samples, natural products, tissues samples. Moreover, the smaller diameter allows the micro-sized sample coil. This achieves the high  $B_1$  field with a given rf field input to the probe (a3). Such characteristics of the probe design is particularly useful to reduce the rf input for given  $B_1$  field and to maximize the  $B_1$  field to excite broad spectral range of quadrupolar nuclei, heavy spin-1/2 nuclei, paramagnetic samples, etc. For example, the rf field strength for  $^1\text{H}$  can be close to 1 MHz at 100 W input. From the reciprocal relationship, the sensitivity from a given induced  $B_1$  field is maximized (a4). This maximizes the sensitivity if the available sample amount is limited. In addition, speed at the surface is proportional to the diameter of sample rotor. This reduces the friction heating at a given MAS frequency (a5). At the MAS frequency >40 kHz, the most spin interactions are averaged out because the size of most spin interactions is smaller than the MAS frequency. This changes the spin dynamics dramatically and allows the use of the so-called low power sequences like decoupling, recoupling, cross-polarization (CP) (a6). This is particularly beneficial to heat-sensitive samples like biomolecules with the additional advantage of less friction heating (a5) and high rf efficiency (a3). It is also important to note that low power sequences like decoupling at very fast MAS reduces the complexity in setting up experiments in comparison with their counterparts at slow MAS that require high-power rf pulses. Therefore, an extra care should be taken to avoid any damage to the probe while setting such experiments at slow MAS. On the other hand, the limited sample volume is problematic due to the low sensitivity (d1) of the NMR spectra. Therefore, the measurements using moderate or large rotors are advisable if very fast MAS rate is not required and the available sample volume is enough to fill these larger rotors. In addition, the sample packing for the very fast MAS probe takes much longer time (typically 10–30 min) than the standard rotor, potentially reducing the overall throughput (d2). Since the operating temperature range of very fast MAS probes is limited (typically –50 to +50 °C) compared to the conventional MAS systems (typically –100 to 200 °C), the range of sample temperature is also limited (d3). The initial and maintenance cost, including rotors, caps, consumables, of very fast MAS probes is typically more expensive than those of the conventional MAS probes (d4), and therefore, only selected laboratories across the world have privilege to such facilities.

On the basis of our own experiences at our research laboratory, we will introduce the practical setup of experimental conditions at very fast MAS rate in this chapter. While the basic setup is the same as the standard MAS systems, there are several points which one should take care under the very fast MAS conditions. The following sections highlight the practical aspects of very fast MAS experiments. First, we focus on the basic setup of very fast MAS probes, including magic-angle adjustment, shimming, referencing, and rf field calibration. These setups are not sample dependent and can be adjusted using standard samples whenever one starts very fast MAS experiments. The sample-dependent optimizations of repetition delay and hardware handlings are also summarized. Finally, basic 2D experiments,  $^1\text{H}$  double-quantum (DQ)/single-quantum (SQ) correlations and  $^1\text{H}$ -detected cross-polarization heteronuclear single-quantum coherence (CP-HSQC) measurements are introduced.

## 6.2 Setup of Sample-independent Factors

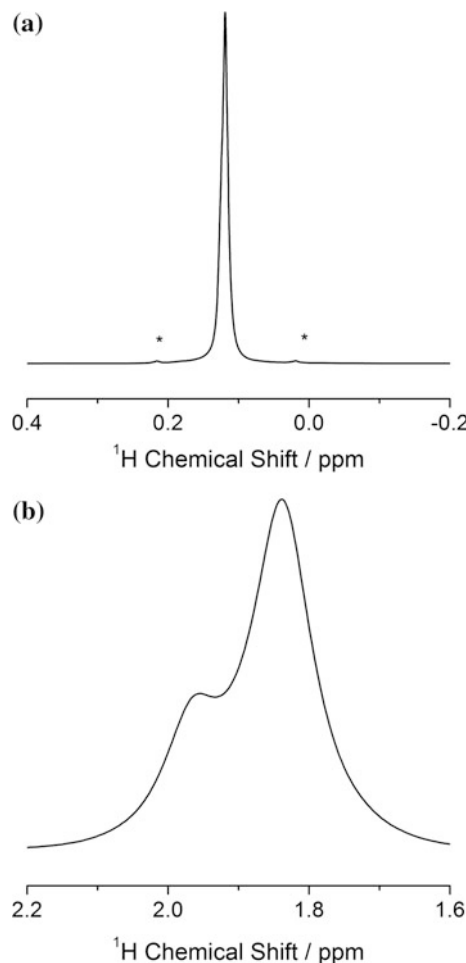
### 6.2.1 Shimming

Homogeneous static magnetic field is crucial for all the high-resolution NMR experiments. Since the NMR lines are usually broad in rigid solids, the contributions to the line broadening from the inhomogeneous static field were considered to be insignificant in the past. However, such effects now can no longer be treated as insignificant due to recent developments of probe technology and methods to achieve high resolution in solid-state NMR including  $^1\text{H}$  NMR at very fast MAS. The field variations are adjusted by the corrective magnetic fields. In the modern NMR spectrometer, it is achieved by additional electromagnets, i.e., shim coils [53]. The source of inhomogeneity comes from both sample-independent factors, including inhomogeneity from the main magnet, effect of probe components, and sample-dependent factors, including magnetic susceptibility broadening. Therefore, the shim-coil current basically must be optimized for sample to sample. In the solution NMR, the shim values can be automatically adjusted by the field gradient methods [54–56], which allow optimization within minutes for every sample. On the other hand, the susceptibility broadening in solid-state NMR is largely suppressed by MAS in solid-state NMR [57–59]. This avoids the need to optimize shim values sample to sample and the same shim values can be retained for all the samples. The automatic shimming in MAS NMR is recently introduced using the field gradient produced by the shim coil [60]. However, these field gradients are not sufficiently strong enough to apply to short samples used in very fast MAS experiments. Thus, the fast MAS probe still requires manual shimming to achieve high resolution.

In the solution NMR, shimming can be done by changing the values along  $z$ -axis including,  $Z_1$ ,  $Z_2$ ,  $Z_3$ . This is because the inhomogeneity along the  $x$ - and  $y$ -axes is averaged by sample spinning along the  $z$ -axis and only results in spinning sidebands. In the solid-state NMR, the axis of sample spinning is different from that of solution NMR, making different set of shim terms effective [61, 62]. Assuming the axis of sample spinning lies in the  $YZ$  plane, the first-order shimming can be done by  $Z_1$  and  $Y_1$  and the second-order by  $YZ$  and  $X_2-Y_2$  ( $X_2$ ). It should be noted that  $Z_2$  does not give any effect on lineshape. Generally,  $Z_1$  is more efficient than  $Y_1$ ; thus, we can safely use  $Z_1$  for the first-order shimming. However, if  $Z_1$  is not strong enough,  $Y_1$  can additionally be used. Since the two bearings are located at the both end of the sample rotors, large second-order terms are required. Typically either  $YZ$  or  $X_2-Y_2$  alone is not sufficiently strong enough. The combined use of these two terms is recommended. It should be noted that care must be taken on the sign of  $YZ$  and  $X_2-Y_2$  terms, otherwise  $YZ$  and  $X_2-Y_2$  may cancel out each other. Usually, the first- and second-order terms are enough to obtain sufficient resolution. The orthogonal field inhomogeneity with respect to sample spinning axis can be neglected because of the very fast MAS rate.

The manual shimming is typically done by monitoring NMR signal lineshape. Adamantane is commonly used for shimming by monitoring  $^{13}\text{C}$  (CP)MAS lineshape for the most solid-state NMR setup. However, the very fast MAS probe requires the other sample for shimming because of its limited sensitivity.  $^1\text{H}$  NMR spectrum of a piece of silicone rubber wherein molecular motions mostly average out anisotropic interactions is useful for shimming because of high resolution and sensitivity in the presence of very slow MAS (2–5 kHz). Even much faster MAS can also be used without any harmful effects. The  $^1\text{H}$  NMR spectra of silicone rubber at 20 kHz MAS is shown in Fig. 6.1a. The shimming should be done to minimize not only the full width at half maxima but also the width at the foot of the peak. The  $^1\text{H}$  NMR linewidth at half maxima is 0.011 ppm and at 0.55% is 0.1 ppm for silicone rubber. Alternatively,  $^1\text{H}$  NMR of adamantane can be used (Fig. 6.1b at 80 kHz MAS). Because of intermolecular  $^1\text{H}$ – $^1\text{H}$  dipolar interaction, faster MAS

**Fig. 6.1** **a**  $^1\text{H}$  NMR spectra of silicone rubber under 20 kHz MAS and **b** adamantane under 80 kHz MAS. The spectra were measured at 14.1 T. Asterisks (\*) in (a) indicate the carbon satellites

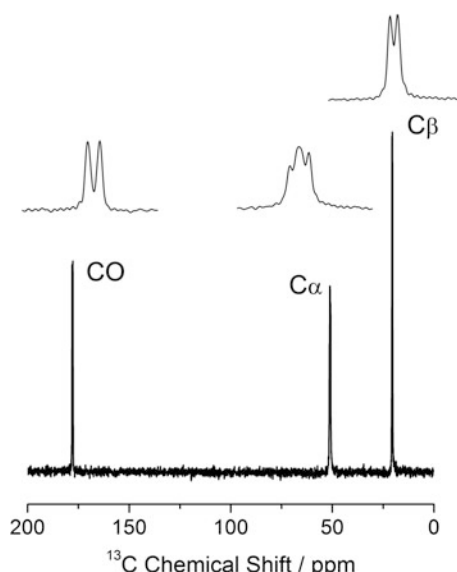


>80 kHz is required for this case, where  $^1\text{H}$  NMR of CH and  $\text{CH}_2$  starts to be resolved. In addition, the magic angle should be adjusted. Thus, iterative adjustment is required between shimming and magic-angle adjustment for adamantane.

### 6.2.2 Magic-Angle Adjustment

The precise magic-angle adjustment is required for all the MAS NMR experiments. The satellite transitions of  $^{79}\text{Br}$  of KBr are widely used to adjust magic angle at a MAS frequency of 5–10 kHz [63]. Following the similar approach, the magic angle in the very fast MAS probes can be adjusted by using  $^{27}\text{Al}$  of simple compounds like kaolin. Alternatively,  $^{13}\text{C}_3$ ,  $^{15}\text{N}$  L-alanine can be used for the precise magic-angle adjustment. The  $^{13}\text{C}$  CPMAS peaks are resolved by  $^{13}\text{C}$ – $^{13}\text{C}$  homonuclear J-coupling and immune to  $^{13}\text{C}$ – $^{13}\text{C}$  homonuclear dipolar interactions at the MAS frequency >30 kHz [20]. The CO carbon, which shows large  $^{13}\text{C}$  CSA, gives lineshape, which is very sensitive to the magic angle. Thus, the magic angle can be precisely adjusted by maximizing the depth of splittings of the CO peak. While the splitting comes from homonuclear J-interactions (ca. 55 Hz), which is immune to the magic angle, the line broadening due to residual CSA is very sensitive to the magic angle. Thus, the depth of the splitting gives good measure of the magic angle. The spectra after MAS adjustment are shown in Fig. 6.2. It should be noted that this splitting is also sensitive to shim, and therefore, iterative optimization of shimming and magic-angle adjustment is required for getting the best output. The other carbons also show splitting but are much less sensitive to magic angle.

**Fig. 6.2**  $^{13}\text{C}$  CPMAS spectrum of  $^{13}\text{C}_3$ ,  $^{15}\text{N}$  L-alanine measured at 14.1 T under 70 kHz MAS. Insets are expansion of each peak with a spectral width of 4 ppm. While  $^{13}\text{C}$ – $^{13}\text{C}$  J-couplings give major splittings, the  $^{15}\text{N}$ – $^{13}\text{C}$  J-coupling also affects the splitting of the  $\text{C}\alpha$  carbon signal

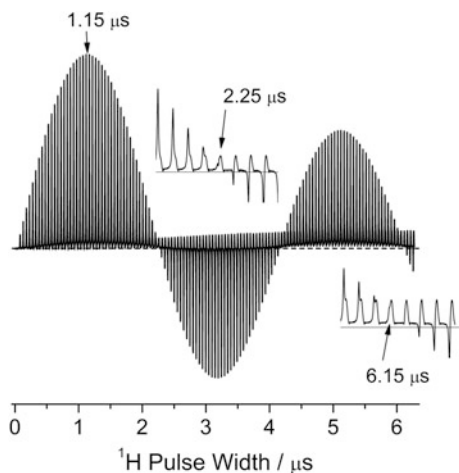


### 6.2.3 rf Field Strength Calibration

The rf magnetic field strength ( $B_1$ ) calibration is one of the fundamental adjustments in experimental NMR setup. It can be usually measured by the nutation curve (mostly sinusoidal), which is a set of single-pulse NMR spectra recorded with varying the excitation pulse width. The  $90^\circ$  and  $180^\circ$  pulse width can be measured from the first maxima and null point, respectively. The rf field strength is calculated from either  $90^\circ$  or  $180^\circ$  pulse width. However, such procedure may result in some error in the rf field strength estimation due to rf transients (amplitude and phase) in very fast MAS probes. The amplitude and phase transients are created at the rising and falling edges of the pulses in high-Q NMR probes and can be significant in very short pulses. As a result, noticeable elongation of  $90^\circ$  and  $180^\circ$  pulse widths is observed, which is reflective of error in the calculated rf field strength. To avoid such complexities, nutation curve up to a pulse width  $540^\circ$  is recommended in the pulse width calibration measurement; i.e., nutation curve should at least have three null points. The  $90^\circ$  and  $180^\circ$  pulse widths are determined from the first maxima and null point, respectively. These values already include the effect of pulse transients, and, thus, can safely be used for  $90^\circ$  and  $180^\circ$  pulses. The difference between  $540^\circ$  and  $180^\circ$  pulse widths removes the effect of pulse transient effects, allowing the estimation of rf field strength in continuous irradiations. This value can be safely used to set up the continuous or semi-continuous rf irradiations, including decoupling/recoupling sequences, CP.

The  $^1\text{H}$  rf field calibration can be done by any sample containing hydrogen. An example of nutation curves is shown in Fig. 6.3 using  $^{13}\text{C}_3, ^{15}\text{N}$  L-alanine. The repetition delay should be sufficiently (~three times) longer than  $^1\text{H}$   $T_1$  relaxation time. Shorter repetition time shifts the first maxima toward shorter length, resulting in underestimation of  $90^\circ$  pulse width, while the position of null points is immune to the repetition delay. Thus,  $180^\circ$  pulse width, which is determined by the first null point, can be used for rough estimation of rf field strength even with shorter repetition delays. Since this phenomenon occurs due to the residual magnetization from the previous scans, instead of long repetition delay, saturation pulses to suppress the residual magnetization just before the repetition delay can be used with the const of low sensitivity. Care must be taken when the null point is evaluated; the null points should be taken from the pulse length where the signal intensity from the sample is minimized with respect to the background signal rather than where the signal intensity becomes zero. Figure 6.3 shows visible background signals, and the narrow hump and the broad baseline originating from signals from caps and static component (MAS stator, capacitor, etc.), respectively. Since background signals feel much weaker rf field strength than that from the sample, these signals keep growing with increase in the pulse width. This results in deviation of baseline from zero-intensity line (shown as dotted line in Fig. 6.3). If null point is taken from the position where the signal intensities are zero, the signal is already negative compared to the baseline, overestimating the  $180^\circ$  and  $540^\circ$  pulse lengths. In the present case, the  $90^\circ$ ,  $180^\circ$ , and  $540^\circ$  can be measured as 1.15, 2.25, and 6.15  $\mu\text{s}$ ,

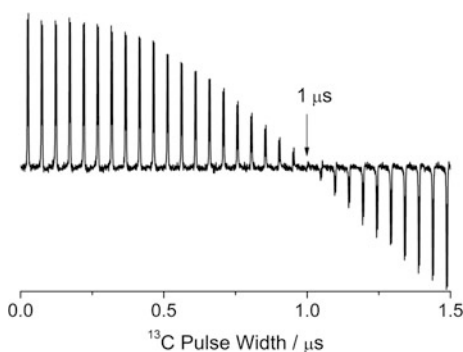
**Fig. 6.3**  $^1\text{H}$  nutation curve of the  $\text{NH}_3^+$  signal of  $^{13}\text{C}_3, ^{15}\text{N}$  L-alanine at 70 kHz. The insets are expansion around  $180^\circ$  and  $540^\circ$  pulses (first and third null point). The zero-intensity line is shown by the dotted line



respectively. The rf field strength for CW irradiations can be obtained as  $1/(6.15 - 2.25 \mu\text{s}) = 256 \text{ kHz}$ . The calculated  $180^\circ$  and  $540^\circ$  pulses can be expected to be two and six times longer than  $90^\circ$  pulse, respectively, and, however, are shorter than observed from the nutation curve. In the other words, the observed  $90^\circ$  and  $180^\circ$  pulse lengths are longer than those expected from the rf field strength (0.98 and 1.95  $\mu\text{s}$ ). This is because the pulse transients elongate the observed  $90^\circ$  and  $180^\circ$  pulse widths. Moreover, long rf irradiation selects the homogeneous  $B_1$  field region, which typically gives the stronger rf field.

In a similar way, the  $^{13}\text{C}$  rf field strength can also be measured.  $^{13}\text{C}_3, ^{15}\text{N}$  L-alanine is useful sample because of short  $T_1$  relaxation time of  $\text{CH}_3$ . Instead,  $^{13}\text{C}$  CPMAS experiments with additional  $^{13}\text{C}$  pulse right after the CP can be used to overcome the long  $^{13}\text{C}$   $T_1$  relaxation time. This results in cosine sinusoidal curve and  $90^\circ$  pulse width can be obtained from the first null point (Fig. 6.4).

**Fig. 6.4**  $^{13}\text{C}$  cosine nutation curve observed by  $^{13}\text{C}$  CPMAS with the additional  $^{13}\text{C}$  pulse with various pulse lengths right after CP. CO signal of  $^{13}\text{C}_3, ^{15}\text{N}$  L-alanine at 14.1 T under 70 kHz MAS is plotted



In the very fast MAS experiments, wide range of rf field strengths is required for recoupling and decoupling interactions. In addition, shaped pulses also require various rf field outputs. It is very time-consuming process to calibrate the wide variety for rf field strength. Fortunately, the modern NMR spectrometers are equipped with very high linear amplifiers and some spectrometers have calibration table to compensate the residual nonlinear responses of high-power amplifiers. This avoids the need of rf field strength calibration at various output levels. Instead, the calculated value from a certain rf-output level can safely be used.

### 6.2.4 Reference

The solid-state NMR spectra can be referenced by the external reference, because shift in peak position is not expected from one sample to another unlike solution NMR. The useful reference material should have the following characteristics: (1) sharp lineshape, (2) less temperature dependence, (3) fine powder, (4) short  $T_1$  relaxation time, (5) high sensitivity, and (6) non toxic. The list of standard samples for  $^1\text{H}$ ,  $^{13}\text{C}$ , and  $^{15}\text{N}$  secondary references are listed in Table 6.1. For the practical use, we recommend  $^{13}\text{C}_3$ ,  $^{15}\text{N}$  L-alanine because it can be used for multiple purpose including magic-angle adjustment, CP setup, rf field calibrations. However, the linewidths of  $^{13}\text{C}_3$ ,  $^{15}\text{N}$  L-alanine are somewhat broad; thus, the other samples can be useful for fine referencing.

**Table 6.1** List of samples for peak shift reference

Nucleus	Sample	Shift (ppm)
$^1\text{H}^{\text{a}}$	Silicone rubber	0.119 [64]
	Adamantane (CH)	1.84
	Adamantane (CH <sub>2</sub> )	1.95
	$^{13}\text{C}_3$ , $^{15}\text{N}$ L-alanine (CH <sub>3</sub> )	1.5
	$^{13}\text{C}_3$ , $^{15}\text{N}$ L-alanine (CH)	3.9
	$^{13}\text{C}_3$ , $^{15}\text{N}$ L-alanine (NH <sub>3</sub> <sup>+</sup> )	8.6
$^{15}\text{N}^{\text{b}}$	NH <sub>4</sub> Cl	39.3 [65]
	$^{13}\text{C}_3$ , $^{15}\text{N}$ L-alanine	42.7
$^{13}\text{C}^{\text{c}}$	Adamantane (CH)	29.45 [66]
	$^{13}\text{C}_3$ , $^{15}\text{N}$ L-alanine (CH <sub>3</sub> )	20.55 <sup>d</sup>
	$^{13}\text{C}_3$ , $^{15}\text{N}$ L-alanine (CH)	51.11 <sup>d</sup>
	$^{13}\text{C}_3$ , $^{15}\text{N}$ L-alanine (COOH)	177.88 <sup>d</sup>

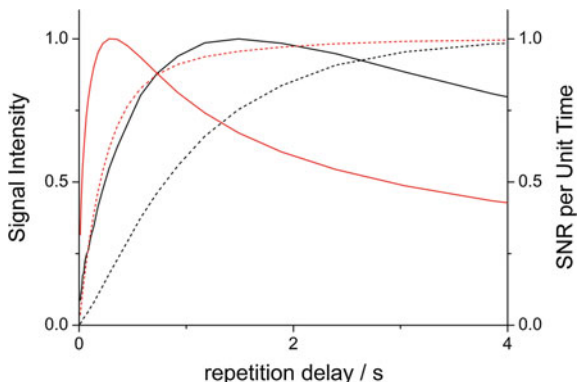
With respect to <sup>a</sup>TMS, <sup>b</sup>liquid NH<sub>3</sub>, and <sup>c</sup>TMS, <sup>d</sup>peak positions are calculated at the center of gravities of the peaks

## 6.3 Sample-Dependent Setup

### 6.3.1 Relaxation Delay

For time-effective NMR measurements, it is crucial to optimize the relaxation delay, or an idle time between the consecutive scans to relax the spin system toward its thermal equilibrium state. The signal intensity per scan is maximized when spins achieve the Boltzmann distribution at thermal equilibrium; however, the number of scans per unit time is minimized at the same time, leading to low signal to noise ratio (SNR) per unit time. Each scan includes (a) noise—a random process whose magnitude is constant for every scans, and (b) signal—whose magnitude depends on the repetition delay. Therefore, the SNR per unit time heavily relies on repetition delay. Assuming the mono-exponential relaxation, the SNR is maximized when the repetition delay is equal to 1.26 times of  $T_1$  relaxation time. Since the SNR per unit time drops very rapidly when the repetition delay is shorter than its optimal value, it is recommended to use slightly longer repetition time than the theoretical maximum. 1.5–2 times of the  $T_1$  relaxation time can be good compromise between the time efficiency and any underestimation of the  $T_1$  relaxation time. The  $T_1$  relaxation can be measured either by the saturation or inversion recovery methods. The inversion recovery measurements give higher sensitivity, thus better accuracy, than saturation recovery because the signal intensity varies from  $-M$  to  $+M$  for former on the other hand from 0 to  $+M$  for latter. However, the relaxation delay should be longer than 3–5 times of  $T_1$  relaxation time in inversion recovery experiments, since the spin systems should be close to the thermal equilibrium before each scan. This complicates the setup of inversion recovery experiments, since the  $T_1$  relaxation time is not known before measurements. In practical use, saturation recovery is recommended because the repetition delay can be set to zero or very short value regardless of the  $T_1$  relaxation time. The  $T_1$  relaxation sometimes does not follow the single exponential curve, making 1.26 times rule ineffective. In such a case, application of  $\sqrt{\tau}$  window function is advisable, where  $\tau$  denotes the recovery duration between the saturation pulses and the read pulse. This window function gives SNR per unit time as a signal intensity in saturation recovery curve. Of course, it can be applied to mono-exponential curve as well, giving maxima at 1.26 times of the  $T_1$  relaxation time (Fig. 6.5). Moreover, the  $\sqrt{\tau}$  window function can be used not only for saturation recovery but also for any other sequence with varying repetition delay, wherever the pulse schemes saturate magnetization after the measurements. This is particularly useful when only a part of NMR signal contributes to the final results. For example, in the  $^1\text{H} \rightarrow ^{13}\text{C} \rightarrow ^1\text{H}$  filtering experiments, the appropriate repetition delay should be determined by the recovery curve of  $^1\text{H}$ , which is directly attached to  $^{13}\text{C}$ . However, it is not straightforward to monitor the recovery curve of  $^1\text{H}(-^{13}\text{C})$ , since the  $^1\text{H}(-^{13}\text{C})$  signals are buried with the  $^1\text{H}$  signals, which are connected to  $^{12}\text{C}$  in the samples at natural abundance.

**Fig. 6.5**  $^1\text{H}$  saturation recovery curves with (solid) and without (dotted)  $\sqrt{\tau}$  window function of  $\text{NH}_3^+$  (red) and  $\text{CH}_2$  (black) signals of  $\alpha$ -glycine at 70 kHz MAS under 14.1 T. The mono-exponential curve fitting gives the  $^1\text{H}$   $T_1$  relaxation times of 0.32 s for  $\text{NH}_3^+$  and 1.0 s for  $\text{CH}_2$



Moreover, the  $T_1$  relaxation time between these  $^1\text{H}$ s can be different because of presence/absence of  $^{13}\text{C}$  neighbor. It should be noted that the combination of the  $\sqrt{\tau}$  window function and actual pulse sequences like  $^1\text{H} \rightarrow ^{13}\text{C} \rightarrow ^1\text{H}$  filtering experiments requires enough number of prescans since it is assumed that the system reaches to the steady state.

The  $^1\text{H}$   $T_1$  relaxation time is assumed to be uniform at the moderate MAS rate because of rapid spin diffusion among  $^1\text{H}$ s, which smears the difference of intrinsic  $^1\text{H}$   $T_1$  relaxation time. However, the very fast MAS slows down the spin diffusion, reintroducing the variation of  $^1\text{H}$   $T_1$  [67]. It is also illustrated in Fig. 6.5;  $\text{NH}_3^+$  and  $\text{CH}_2$  protons of  $\alpha$ -glycine give different recovery behaviors in saturation recovery experiments. These phenomena are frequently observed at the very fast MAS rate and can be problematic to set up optimal repetition delay, especially if the peak of interest has long  $T_1$  relaxation time than that of the other  $^1\text{H}$ s. For example, the  $T_1$  relaxation time of  $^1\text{H}$ s among the same molecule can vary from several to hundreds seconds at the very fast MAS rate. To overcome this problem,  $^1\text{H}$ – $^1\text{H}$  spin diffusion can be turned on during the repetition delay by applying rf driven recoupling (RFDR) schemes shown in Fig. 6.6 [68, 69]. RFDR transfers the magnetization from the rapidly relaxing components to slow relaxing components, utilizing rapid relaxation mechanism several times between consecutive scans. It should also be noted that the efficiency depends on the phase cycling (Fig. 6.7). The optimization can be done by (1) optimization of integer  $m$  and  $n$  shown in Fig. 6.6, and (2) optimization of repetition delay using the  $\sqrt{\tau}$  function with saturation recovery schemes. The optimization should be repeated iteratively until convergence. The initial  $\tau$  can be determined by the optimal repetition delay for the shortest  $T_1$  component. This sensitivity enhancement is particularly useful for NH and OH measurements, which are typically isolated from the other  $^1\text{H}$ s and tend to show longer  $T_1$  relaxation time.

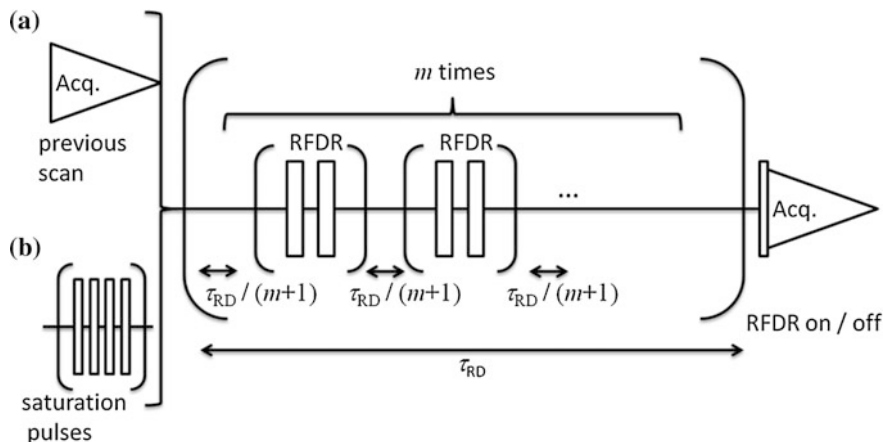


**Fig. 6.6** Pulse schemes used in the **a** general experiments and **b** saturation recovery experiments. The equally spaced  $m$  RFDR trains can be applied during  $\tau_{RD}$ . While  $\pi/2$  pulse is applied just before the acquisition in the single-pulse experiments and saturation recovery experiments, any pulse scheme can be applied after  $\tau_{RD}$  delay. Reproduced from Ref. [69] with permission from Elsevier

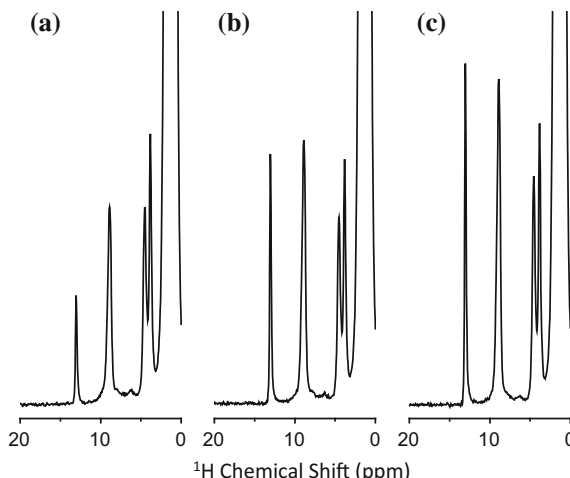


**Fig. 6.7** Single-pulse  ${}^1\text{H}$  NMR spectra of a powder  $N$ -acetyl- ${}^{15}\text{N}$ -L-valyl- ${}^{15}\text{N}$ -L leucine (NAVL) sample obtained at 100 kHz MAS without fp-RFDR (**a**), with fp-RFDR of  $(\text{XY}8)^4$  (**b**), and with fp-RFDR of  $(\text{XY}4)^4$  (**c**) during the recycle delay. A relaxation delay of 2.2 s and rf field strength of 467 kHz for fp-RFDR were used. Number of fp-RFDR cycles (3 for **b** and 6 for **c**) and duration of each fp-RFDR (1.92 ms for **b** and 6.4 ms for **c**) were optimized such that the carbonyl proton peak (13 ppm) is maximized. Reproduced from Ref. [70] with permission from Elsevier

### 6.3.2 *Hardware Treatment*

Since the very fast MAS probe consists of very precise micro-engineering parts, contamination with very tiny dust particles, lint, even moisture causes fatal crush. Thus, the maximum attention should be paid to avoid this by following the procedure written each instruction manual. The same level of attention should be paid for sample packing as well.

Here, we discuss the stability of MAS. Some of recoupling sequences need two separated rf irradiations synchronous to sample spinning. One example can be seen in D-HMQC experiments [70, 71], which are widely used in  $^1\text{H}$ - $^{14}\text{N}$  correlation measurements [72–74] at the very fast MAS conditions. The other example can be found in  $^1\text{H}$  DQ/SQ correlation experiments (see Sec. 6.4.1). The synchronization can be done by either calculating the pulse timing from the spinning frequency, or actively synchronizing the pulse scheme by feeding the spinning signal to the spectrometer. In both cases, even slight fluctuation of sample spinning causes huge  $t_1$  noise, which comes from the mismatch of rotor phases in two recoupling sequences for the former case and from the introduction of variable time delay for the latter case. This short-term stability cannot be evaluated by monitoring the frequency counter of MAS controller, which only shows the averaged frequency over much longer time period (100 ms to 1 s). The short-term stability is more important at faster MAS, since faster MAS amplifies the rotor phase deviation from the expected phase. For example, while the 1% deviation at 10 kHz MAS introduces only 0.1 rotation ( $=36^\circ$ ) of sample rotor after 1 ms, it results in 1 rotor ( $=360^\circ$ ) changes of rotor phase at 100 kHz. This is because the rotor spins 10 times within 1 ms at 10 kHz, on the other hand the sample rotor rotates 100 times during the same time period at 100 kHz MAS. It shows that 10 times more stable spinning at 100 kHz is required than 10 kHz MAS. The short-term fluctuations can be experimentally monitored by digital oscilloscopes. The oscilloscope is first triggered, and the signal is observed after several ms of triggering. The persistent display mode allows to monitor the fluctuation of sample spinning. If the sample spinning is perfectly stable, we should not see any fluctuation of the waveform. The fluctuations appear as a jitter on the screen. The picture shown in Fig. 6.8 is taken with 1 ms delayed trigger and shows  $\pm 0.5 \mu\text{s}$  variation, which corresponds to 250 ppm variation of MAS rate. Such level of stability is typically required in D-HMQC experiment. Note that the fluctuations that are obtained from MAS controller display should be in the range  $\pm 10 \text{ Hz}$  (140 ppm) and smaller than the short-term fluctuations. The very different short-term stability can be observed even with the same read of MAS controller, since the short- and long-term stability is partially independent on each other. This emphasizes the importance of checking the short-term stability by monitoring the oscilloscope when significant  $t_1$  noise appears in D-HMQC experiments.

The sample insertion to the stator can be problematic and time-consuming for very tiny rotors  $\sim 0.75 \text{ mm}$ , since the rotor can stick on the stator wall due to the electrostatic force. To check the proper insertion of the sample rotor in the MAS

**Fig. 6.8** Snapshot of the oscilloscope screen at 70 kHz MAS. The spinning signal is monitored after 1 ms trigger with the persistent mode. The jitter ( $\pm 0.5 \mu\text{s}$ ) represents the spinning fluctuations of 250 ppm



stator and hence to save time, it is advisable to use the oscilloscope. When the rotor is properly inserted into the stator, the spinning detector observes some signals, otherwise it gives no signal.

## 6.4 Setup of 2D Measurements

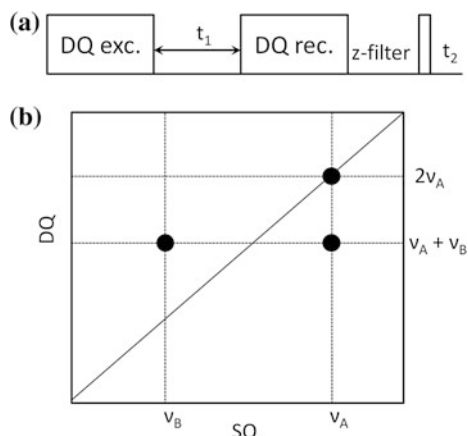
### 6.4.1 $^1\text{H}$ DQ/SQ Correlation

Homonuclear and heteronuclear correlation experiments are very informative experiments in NMR measurements. While the internuclear correlations are established using internuclear interactions, very fast MAS suppresses these interactions. Even though, using the residual interactions or reintroducing interactions by rf irradiations, the internuclear correlations can be easily made. At very fast MAS,  $^1\text{H}$ - $^1\text{H}$  correlation measurements are useful for practical applications because of high sensitivity and information content [17]. Since  $^1\text{H}$  is highly abundant nuclei with large gyromagnetic ratio, it is straightforward to obtain  $^1\text{H}$ - $^1\text{H}$  correlations. Moreover, since  $^1\text{H}$  is located on the surface of the molecules,  $^1\text{H}$ - $^1\text{H}$  correlations give insight into the intermolecular interactions in addition to intramolecular interactions. In particular,  $^1\text{H}$  DQ/SQ correlation is useful for such information. While the SQ/SQ experiments always give strong diagonal autocorrelation peaks in addition to cross-peaks, DQ/SQ experiments only give internuclear cross-peaks. The experiments and spectra are similar to INADEQUATE, which gives  $^{13}\text{C}$  DQ/SQ correlation through J-coupling. The major difference between  $^{13}\text{C}$  INADEQUATE and  $^1\text{H}$  DQ/SQ experiment is the interactions used to correlate nuclei. This results in different behavior at diagonal peaks; while J-based INADEQUATE does not give any diagonal peak,  $^1\text{H}$  DQ/SQ experiment gives. The diagonal peak in  $^1\text{H}$  DQ/SQ spectra is direct evidence of proximity between

same kinds of nuclei. The schematic representations of DQ/SQ pulse sequence and correlation spectrum are shown in Fig. 6.9. First, the DQ coherence is prepared by the initial excitation block and then evolves during the  $t_1$  period. The resultant DQ coherence is back-transferred to the z magnetization by the reconversion block. The residual transversal coherence is removed either by the phase cycling or z-filtering. Finally, the magnetization is excited by the 90° pulse and observed during the  $t_2$  period. The Fourier transformation to both dimensions gives DQ/SQ correlation spectra. The cross-peak between two nuclei (A and B) appears along the SQ axis. While the DQ coherence evolves at the sum of two resonance frequencies,  $v_A + v_B$ , the SQ coherence thus obtained shows frequencies  $v_A$  and  $v_B$ . This results in the 2D correlations at (DQ, SQ) = ( $v_A + v_B$ ,  $v_A$ ) and ( $v_A + v_B$ ,  $v_B$ ). These peaks appear symmetrically with respect to the diagonal line with a slope of 2. If two nuclei have the identical chemical shift, the correlation peak appears on the diagonal line at  $2v_A$ . The DQ/SQ spectrum in Fig. 6.9b shows the presence of (A, A) and (A, B) correlations and the absence of (B, B) correlations. It should be noted that the DQ/SQ correlation spectra not only give proximity between  $^1\text{H}$ s but also impart additional resolution, which is advantageous for practical applications.

The excitation and reconversion blocks can be comprehended by the first-order and higher-order average Hamiltonians [75–83]. The former includes back-to-back (BABA), symmetry-based pulses, while latter uses dipolar homonuclear homogeneous Hamiltonian (DH<sup>3</sup>) terms, which come from higher-order perturbations in the INADEQUATE sequence. The use of the first-order recoupling allows quick buildup and reconversion of DQ coherences, minimizing the relaxation decay during excitation/reconversion blocks. In addition, the dipolar truncation removes remote correlations, limiting the correlation for short-range (~4 Å) proximities. This feature is useful to understand the local  $^1\text{H}$ – $^1\text{H}$  network structures. The use of the first-order average Hamiltonian induces peak position shift/splitting at an integer multiple of the spinning frequency in the DQ dimension [84]. To avoid such complexity, the excitation and reconversion block should be exactly synchronized to the sample spinning; i.e., increments in the  $t_1$  dimension must be an integer

**Fig. 6.9** Schematic representation of  $^1\text{H}$  DQ/SQ pulse sequence (a) and spectrum (b)



multiple of the cycle time of the sample spinning. It is noteworthy that the requirement of the rotor synchronization of the  $t_1$  dimension induces  $t_1$  noise in the presence of spinning fluctuations. This can be avoided by utilizing the higher-order average Hamiltonian with the sequence exactly same as INADEQUATE. Although INADEQUATE requires only J-coupling, the  $DH^3$  terms can be used throughout the dipolar-based  $^1\text{H}$  network [75]. The use of the  $DH^3$  terms allows non-rotor-synchronous acquisition in the  $t_1$  dimension and, therefore, is less sensitive toward spinning fluctuations. However, the overall sensitivity in general is lower than that of the first-order recoupling sequences.

Here, we demonstrate the experimental setup of  $^1\text{H}$  DQ/SQ correlation measurements. BABA-xy16 [72] is recommended for the DQ recoupling sequence due to its high efficiency and robustness toward experimental imperfections. The cycle time of BABA-xy16 is  $8\tau_r$ , where  $\tau_r$  is the cycle time of sample spinning, and enough long to reach the plateau of buildup curve for  $^1\text{H}-^1\text{H}$  homonuclear coupled systems. Thus, one cycle of BABA-xy16 can be safely used without any optimization. The only adjustable parameter is the  $90^\circ$  pulse width used in the BABA recoupling sequence. This is easily optimized by monitoring  $^1\text{H}$  DQ filtered spectra with varying pulse widths in the BABA recoupling, using the sequence shown in Fig. 6.9a with  $t_1 = 0$ . Although theoretically the optimal flip angle is  $90^\circ$ , the experimentally obtained maxima always appear at a pulse length shorter than the  $90^\circ$  pulse width. This is because of higher-order recoupling in the BABA sequences. This effect becomes smaller at faster MAS rate because it is higher-order effect; thus, the optimization should be done at every MAS rate. Since the spin system can also affect this phenomenon, it is advisable to optimize conditions for each sample. However, the dependence to samples is generally small for most organic molecules, and optimization can be skipped. The optimal  $90^\circ$  pulses used in the BABA sequences are typically found in the range of  $40^\circ$  to  $90^\circ$  pulse widths. DQ filtering efficiency can be evaluated by comparing the  $^1\text{H}$  single pulse spectrum and the DQ filtered spectrum. The efficiency is strongly dependent on sample and in general lies between 20 and 40% of the intensities of  $^1\text{H}$  single-pulse spectra. This allows quick measurements of  $^1\text{H}$  DQ/SQ correlation spectra with reasonable sensitivities. The measurement time is dominated by the number of  $t_1$  points and the phase cycling rather than the sensitivity because of the high efficiency. To minimize the indirect spectral points, thus experimental time, the  $^1\text{H}$  offset should be set to the center of the SQ  $^1\text{H}$  spectral width. The indirect spectral width should be larger than twice of the maximum  $^1\text{H}$  chemical shift separation in the SQ dimension and synchronized to the sample spinning. The number of phase cycling can be minimized to 4 for each  $t_1$  slice by z-filtering (typically 1 ms) for the coherence selection after the reconversion block. However, this procedure can introduce additional peaks due to spin diffusion during the z-filtering. This problem can be avoided by removing z-filtering with the additional phase cycling (at least 12 scans).

The experimental optimization is demonstrated on  $^{13}\text{C}_3, ^{15}\text{N}$  L-alanine at 70 kHz MAS (shown in Fig. 6.10). The maximum appears at 0.56  $\mu\text{s}$ , which is corresponding to  $44^\circ$  pulse length. The 2D DQ/SQ correlation spectrum of L-histidine·HCl·H<sub>2</sub>O is shown in Fig. 6.11. Since L-histidine·HCl·H<sub>2</sub>O is very small

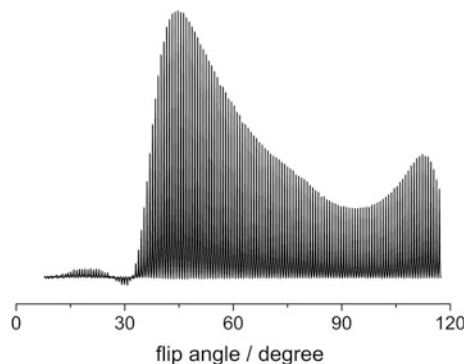


**Fig. 6.10**  $^1\text{H}$  DQ filtered spectra of  $^{13}\text{C}_3$ ,  $^{15}\text{N}$ , L-alanine at 70 MHz MAS under 14.1 T. BABA-xy16 of  $\tau_{\text{exc}} = \tau_{\text{rec}} = 114 \mu\text{s}$  with various flip angles is applied during excitation and reconversion period. The  $90^\circ$  pulse length measured from the first maxima is  $1.15 \mu\text{s}$  and used to calculate the flip angle

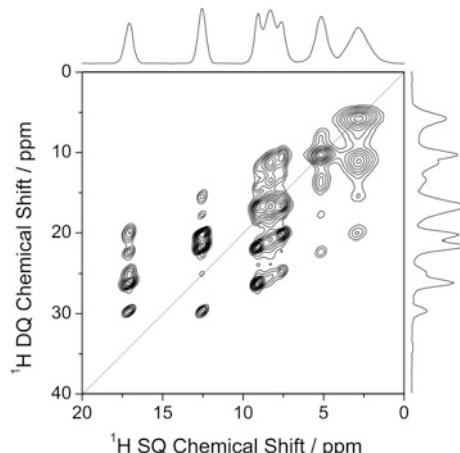


**Fig. 6.11**  $^1\text{H}$  DQ/SQ correlation spectrum of L-histidine·HCl·H<sub>2</sub>O under 70 kHz MAS at 14.1 T using BABA-xy16 recoupling sequence with  $\tau_{\text{exc}} = \tau_{\text{rec}} = 114 \mu\text{s}$ . z-filter was not applied to avoid unwanted spin diffusion and 12 scans are collected with the phase cycling to select the proper coherence pathway. While the pulse length in the BABA sequence is optimized to  $0.56 \mu\text{s}$ , the  $90^\circ$  pulse length of  $1.15 \mu\text{s}$ , which is obtained from the first maxima of  $^1\text{H}$  nutation curve, is used for the excitation pulse just before the signal acquisition. The indirect spectral width is set to 35 kHz so that the  $t_1$  evolution time and two BABA sequences are synchronized to sample spinning. 64 hypercomplex  $t_1$  points are collected using the states-TPPI approach. The total acquisition time is 2.1 h with a repetition delay of 5 s

molecule, most of the possible  $^1\text{H}$ – $^1\text{H}$  correlations are observed except for auto-correlation of NH at (DQ, SQ) = (34.2 ppm, 17.1 ppm). It is interesting to see the very weak intermolecular autocorrelation between NHs (4.8 Å apart) at (DQ, SQ) = (25.0 ppm, 12.5 ppm).

### 6.4.2 $^1\text{H}$ -detected $^1\text{H}/\text{X}$ CP-HSQC

Very fast MAS dramatically improves the efficiency of  $^1\text{H}$  indirectly detected heteronuclear correlation (idHETCOR) experiments on rigid solids [7–16]. The  $^1\text{H}$  indirect observation is widely used as sensitivity enhancement methods in solution NMR. In the  $^1\text{H}$  indirect detection scheme, first,  $^1\text{H}$  magnetization is transferred to X nuclei, followed by the time evolution of X magnetization. Finally, X magnetization is back-transferred to  $^1\text{H}$  for detection. The sensitivity in  $^1\text{H}$  indirect detection is basically independent to the gyromagnetic ratio of X nuclei; thus, the sensitivity enhancement factor is greatly improved for low gamma X nuclei as

$$\frac{\text{SNR}_{\text{indirect}}}{\text{SNR}_{\text{direct}}} = f \left( \frac{\Delta_X}{\Delta_H} \right) \left( \frac{\gamma_H}{\gamma_X} \right)^{3/2} \quad (6.1)$$

where  $f$  is various experimental factors including probe Q factors, magnetization transfer efficiency,  $\Delta_{X(H)}$  and  $\gamma_{X(H)}$  are apparent linewidth in the X ( $^1\text{H}$ ) dimension and gyromagnetic ratio of X( $^1\text{H}$ ), respectively [7]. This equation well illustrates the necessity of the very fast MAS in rigid solids as the  $^1\text{H}$  linewidth due to  $^1\text{H}$ – $^1\text{H}$  dipolar interactions is inversely proportional to the MAS frequency. It also avoids the difficulty associated with probe ringing, which is more prevalent in the case of quadrupolar nuclei. In addition, the folding of spinning sideband in solid-state MAS NMR with the rotor-synchronized  $t_1$  acquisition enhances the sensitivity along with removal of spinning sidebands in systems with large anisotropies. The sequence includes two-way magnetization transfer of  $^1\text{H} \rightarrow \text{X} \rightarrow ^1\text{H}$ . There are several different mechanisms of magnetization transfer including CP, refocused-INEPT, J/D-HMQC and complete list can be found in the literature [35]. X nucleus can be either spin-1/2 or quadrupolar nuclei including  $^{14}\text{N}$ . When X is spin-1/2 nuclei, e.g.,  $^{13}\text{C}$  and  $^{15}\text{N}$ , indirect detection HETCOR (HSQC) approaches are useful because  $^1\text{H}$  decoupling can be applied during the  $t_1$  period. In the CP-HSQC pulse sequence, the first  $^1\text{H} \rightarrow \text{X}$  transfer is achieved by CP while the second  $\text{X} \rightarrow ^1\text{H}$  transfer can be achieved either by CP or refocused-INEPT [15]. Basically, CP and refocused-INEPT transfer gives through-space and bond correlation, respectively. However, both CP and refocused-INEPT give similar results if the contact time of the second CP is sufficiently short at the very fast MAS conditions. This results in pseudo through-bond correlation even with CP for both magnetization transfers [47]. For the simplicity of experimental setup, we here focus on CP/CP-HSQC experiments, where CP is utilized for both  $^1\text{H} \rightarrow \text{X}$  and  $\text{X} \rightarrow ^1\text{H}$  magnetization transfers (Fig. 6.12). First, X magnetization is prepared by the first CP from the  $^1\text{H}$  magnetization followed by the time evolution under  $^1\text{H}$  decoupling during the  $t_1$  period. The X transversal magnetization is stored along the z-axis to halt the time evolution. The residual  $^1\text{H}$  magnetization is suppressed by the HORROR  $^1\text{H}$ – $^1\text{H}$  recoupling [85]. This irradiation also removes residual solvent signals if present [86]. Finally, the X magnetization is back-transferred to  $^1\text{H}$  by the second  $\text{X} \rightarrow ^1\text{H}$  CP followed by the  $^1\text{H}$  observation under the X decoupling during

**Fig. 6.12** Schematic representation of  $^1\text{H}/\text{X}$  CP/CP-HSQC correlation measurements

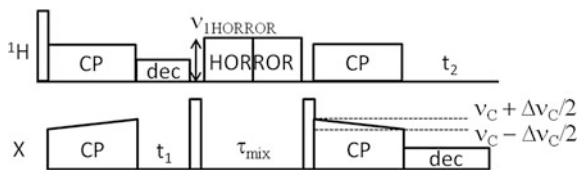


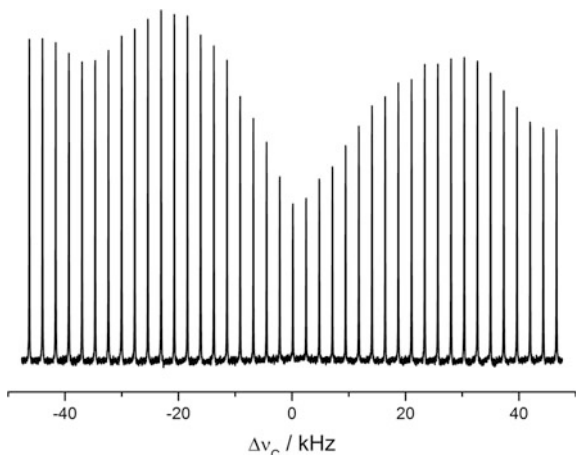
**Table 6.2** Building blocks in the CP/CP-HSQC experiments with optimization strategy

Blocks	Optimization
CPs	Standard sample (contact time can be optimized with the sample of interest)
HORROR	Sample of interest
X decoupling	Standard sample
$^1\text{H}$ decoupling	Standard sample

the  $t_2$  period. Even if X is a rare nucleus, X decoupling is mandatory because  $^1\text{H}$  nucleus observed in this sequence always accompanies the X nucleus. Each building blocks used in the sequence can be optimized separately by using standard samples (Table 6.2) as well as sample of interest.

$^{13}\text{C}_3$ ,  $^{15}\text{N}$  L-alanine can be used as a standard sample to set up experimental conditions. The HORROR condition can be roughly calculated by setting the rf field strength equal to  $v_R/2$  and fine optimization is achieved by minimizing the residual signal after spinlock (1–5 ms). The HORROR duration for natural abundance samples can be long (20–100 ms) to suppress the residual signal and, however, cannot be longer than the  $t_1$  relaxation time of X to avoid signal loss due to longitudinal relaxation. The CP conditions are roughly adjusted by  $^{13}\text{C}$  CPMAS. The shaped CP schemes are recommended to maximize the efficiency. While RAMP CP on the  $^{13}\text{C}$  channel can be recommended for simplicity [87], other schemes like tangential CP can be used alternatively. The RAMP on  $^1\text{H}$  instead of  $^{13}\text{C}$  can also be used without significant difference in efficiency after proper optimizations. It should be noted that unlike moderate MAS CP conditions, the sense of RAMP greatly affects the magnetization transfer efficiency and should be optimized (Fig. 6.13). In this example,  $^{13}\text{C}$  rf field strength  $v_C$  is linearly varied from  $v_C - \Delta v_C/2$  to  $v_C + \Delta v_C/2$  and the optimal condition is found at the negative ramp (descending rf field strength) with  $\Delta v_C = -23$  kHz. Indeed, the signal intensity at  $\Delta v_C = 23$  kHz gives only ca 80% of the maximum at  $\Delta v_C = -23$  kHz. Very fast MAS allows to use low power CP conditions. A great care must be taken to avoid any recoupling conditions. The DQ CP ( $n = 1$ ) condition [88] with  $v_C \sim 2v_R/3$  and  $v_H \sim v_R/3$  is generally recommended to cover the wider  $^{13}\text{C}$  chemical shift range than  $^1\text{H}$ . The fine optimization should be done by monitoring  $^1\text{H} \rightarrow ^{13}\text{C} \rightarrow ^1\text{H}$  1D CP/CP-HSQC signal intensities. Although the contact time of two CP transfers can be different, the symmetric RAMP CP generally gives the best efficiency from our personal experience; the positive ramp on the first CP and negative ramp on the

**Fig. 6.13**  $^{13}\text{C}$  CPMAS signal intensities of the CH moiety of  $^{13}\text{C}_3, ^{15}\text{N}$  L-alanine with various  $\Delta\nu_{\text{C}}$ . The rf fields of  $\nu_{\text{C}} = 51 \text{ kHz}$  and  $\nu_{\text{H}} = 19 \text{ kHz}$  are used



second CP, and vice versa. This is most probably due to the time-reversible behavior of spin systems. While the contact time of the first CP is typically 1–2 ms, that of the second CP can be 0.3–0.5 ms. Even with such a short second CP, the efficient magnetization transfer is achieved due to dipolar truncation effect. The longer contact time of the second CP may introduce remote  $^1\text{H}$ – $^{13}\text{C}$  correlations and should be avoided if pseudo through-bond correlations are needed. Both  $^1\text{H}$  and  $^{13}\text{C}$  decoupling can be performed by WALTZ at 10 kHz rf field strength without further optimization [89]. While the two-way  $^1\text{H} \rightarrow ^{13}\text{C} \rightarrow ^1\text{H}$  magnetization efficiency of the CH moiety of  $^{13}\text{C}_3, ^{15}\text{N}$  L-alanine is about 30–40%; it can be improved in the natural abundance samples.

## 6.5 Conclusions

In this chapter, the practical hands-on guides for setups of the fast MAS experiments are presented. While very fast MAS probes offer an attractive set of experiments for structural analysis at the atomic scale, those also require careful setup of experimental conditions compared to the moderate MAS rate probes. First, sample-independent factors are discussed including shimming, magic-angle adjustment, rf field strength calibrations, and referencing. It is discussed how to overcome the difficulties associated with the weak signal intensity due to the limited sample volume, very short pulses, etc. The discussions on sample-dependent factors such as relaxation delay and spinning fluctuations are followed.  $^1\text{H}$  relaxation times are no longer uniform at very fast MAS rate and special care must be taken to set up the repetition delay. The spinning fluctuations can be critical factor to reduce the  $t_1$  noise in rotor-synchronous experiments and should be monitored by oscilloscopes. Finally, two practically useful homonuclear and heteronuclear correlation experiments are introduced together with experimental setups.

In spite of the limited sample volume,  $^1\text{H}$  indirectly detected heteronuclear experiments and  $^1\text{H}/^1\text{H}$  homonuclear correlation experiments achieve high-throughput solid-state NMR measurements at very fast MAS rate. I believe the application of very fast MAS will spread very quickly and widely, and enhance the ability of solid-state NMR in various applications. I am hoping this chapter will help these improvements.

**Acknowledgements** We thank Dr. Manoj Kumar Pandey of Indian Institute of Technology Ropar for careful reading of the manuscript and helpful discussions.

## References

1. Schmidt-Rohr, K., Spiess, H.W.: Multidimensional Solid-State NMR and Polymers. Academic Press, London (1994)
2. Livitt M.H.: Spin Dynamics, 2 edn. Wiley, London (2008)
3. Andrew, E.R., Bradbury, A., Eades, R.G.: Nuclear magnetic resonance spectra from a crystal rotated at high speed. *Nature* **182**, 1659 (1958)
4. Lowe, I.J.: Free induction decays of rotating solids. *Phys. Rev. Lett.* **2**, 285 (1959)
5. Zorin, V.E., Brown, S.P., Hodgkinson, P.: Origins of line width in  $^1\text{H}$  magic-angle spinning NMR. *J. Chem. Phys.* **125**, 144508 (2006)
6. Brunner, E., Freude, D., Gerstein, B.C., Pfeifer, H.: Residual linewidths of NMR spectra of spin-1/2 systems under magic-angle spinning. *J. Magn. Reson.* **90**, 90–99 (1990)
7. Ishii, Y., Tycko, R.: Sensitivity enhancement in solid state  $^{15}\text{N}$  NMR by indirect detection with high-speed magic angle spinning. *J. Magn. Reson.* **142**, 199–204 (2000)
8. Ishii, Y., Yesinowski, J.P., Tycko, R.: Sensitivity enhancement in solid-state  $^{13}\text{C}$  NMR of synthetic polymers and biopolymers by  $^1\text{H}$  NMR detection with high-speed magic angle spinning. *J. Am. Chem. Soc.* **123**, 2921–2922 (2001)
9. Paulson, E.K., Morcombe, C.R., Gaponenko, V., Dancheck, B., Byrd, R.A., Zilm, K.W.: Sensitive high resolution inverse detection NMR spectroscopy of proteins in the solid-state. *J. Am. Chem. Soc.* **125**, 15831–15836 (2003)
10. Reif, B., Griffin, R.G.:  $^1\text{H}$  detected  $^1\text{H}$ ,  $^{15}\text{N}$  correlation spectroscopy in rotating solids. *J. Magn. Reson.* **160**, 78–83 (2003)
11. Zhou, D.H., Rienstra, C.M.: Rapid analysis of organic compounds by proton-detected heteronuclear correlation NMR spectroscopy with 40 kHz magic-angle spinning. *Angew. Chem. Int. Ed.* **47**, 7328–7331 (2008)
12. Zhou, D.H., Shah, G., Cormos, M., Mullen, C., Sandoz, D., Rienstra, C.M.: Proton-detected solid-state NMR spectroscopy of fully protonated proteins at 40 kHz magic-angle spinning. *J. Am. Chem. Soc.* **129**, 11791–11801 (2007)
13. Zhou, D.H., Shea, J.J., Nieuwkoop, A., Franks, W.T., Wylie, B.J., Mullen, C., Sandoz, D., Rienstra, C.M.: Solid state protein structure determination with proton detected triple resonance 3D magic angle spinning NMR spectroscopy. *Angew. Chem. Int. Ed.* **46**, 8380–8383 (2007)
14. Wiench, J.W., Bronnimann, C.E., Lin, V.S.-Y., Pruski, M.: Chemical shift correlation NMR spectroscopy with indirect detection in fast rotating solids: studies of organically functionalized mesoporous silicas. *J. Am. Chem. Soc.* **129**, 12076–12077 (2007)
15. Mao, K., Pruski, M.: Directly and indirectly detected through-bond heteronuclear correlation solid-state NMR spectroscopy under fast MAS. *J. Magn. Reson.* **201**, 165–174 (2009)

16. Althaus, S.M., Mao, K., Stringer, J.A., Kobayashi, T., Pruski, M.: Indirectly detected heteronuclear correlation solid-state NMR spectroscopy of naturally abundant  $^{15}\text{N}$  nuclei. *Solid State Nucl. Magn. Reson.* **57–58**, 17–21 (2014)
17. Ishii, Y., Wickramasinghe, N.P., Chimon, S.: A new approach in 1D and 2D  $^{13}\text{C}$  high-resolution solid-state NMR spectroscopy of paramagnetic organometallic complexes by very fast magic-angle spinning. *J. Am. Chem. Soc.* **125**, 3438–3439 (2003)
18. Wickramasinghe, N.P., Shaibat, M., Ishii, Y.: Enhanced sensitivity and resolution in  $^1\text{H}$  solid-state NMR spectroscopy of paramagnetic complexes under very fast magic angle spinning. *J. Am. Chem. Soc.* **127**, 5796–5797 (2005)
19. Wickramasinghe, N.P., Shaibat, M.A., Jones, C.R., Casabianca, L.B., de Dios, A.C., Harwood, J.S., Ishii, Y.: Progress in  $^{13}\text{C}$  and  $^1\text{H}$  solid-state nuclear magnetic resonance for paramagnetic systems under very fast magic angle spinning. *J. Chem. Phys.* **128**, 052210 (2008)
20. Parthasarathy, S., Nishiyama, Y., Ishii, Y.: Sensitivity and resolution enhanced solid-state NMR for paramagnetic systems and biomolecules under very fast magic angle spinning. *Acc. Chem. Res.* **46**, 2127–2135 (2013)
21. Shen, M., Trebosc, J., Lafon, O., Gan, Z.H., Pourpoint, F., Hu, B.W., Chen, Q., Amoureux, J. P.: Solid-state NMR indirect detection of nuclei experiencing large anisotropic interactions using spinning sideband-selective pulses. *Solid State Nucl. Magn. Reson.* **72**, 104–117 (2015)
22. Pöppler, A.-C., Demers, J.-P., Malon, M., Singh, A.P., Roesky, H.W., Nishiyama, Y., Lange, A.: Ultra-fast magic angle spinning: benefits for the acquisition of ultra-wideline NMR spectra of heavy spin-1/2 nuclei. *ChemPhysChem* **17**, 812–816 (2016)
23. Rossini, A.J., Hanrahan, M.P., Thuot, M.: Rapid acquisition of wideline MAS solid-state NMR spectra with fast MAS, proton detection, and dipolar HMQC pulse sequences. *Phys. Chem. Chem. Phys.* **18**, 25284–25295 (2016)
24. Samoson, A., Tuherm, T., Gan, Z.: High-field high-speed MAS resolution enhancement in  $^1\text{H}$  NMR spectroscopy of solids. *Solid State Nucl. Magn. Reson.* **20**, 130–136 (2001)
25. Deschamps, M.: Ultrafast magic angle spinning nuclear magnetic resonance. *Annu. Rep. NMR Spectrosc.* **81**, 109–144 (2014)
26. Brown, S.P.: Probing proton–proton proximities in the solid state. *Prog. Nucl. Magn. Reson. Spectrosc.* **50**, 199–251 (2007)
27. Samoson, A., Tuherm, T., Past, J., Reinhold, A., Heinmaa, I., Anupold, T., Smith, M.E., Pike, K.J.: Fast Magic-Angle Spinning: Implications, *Encyclopedia of Magnetic Resonance*, pp. 1–20. Wiley, Chichester (2010)
28. Samoson, A.: Magic-angle spinning extensions. In: Harris, R.K., Grant, D.M. (eds.) *Encyclopedia of Nuclear Magnetic Resonance*, pp. 59–64. Wiley, Chichester (2002)
29. Zhou, D.H.: Fast Magic Angle Spinning for Protein Solid-State NMR Spectroscopy, *Encyclopedia of Magnetic Resonance*, pp. 331–342. Wiley, Chichester (2007)
30. Brown, S.P.: Applications of high-resolution  $^1\text{H}$  solid-state NMR. *Solid State Nucl. Magn. Reson.* **41**, 1–27 (2012)
31. Demers, J.-P., Chevelkov, V., Lange, A.: Progress in correlation spectroscopy at ultra-fast magic-angle spinning: Basic building blocks and complex experiments for the study of protein structure and dynamics. *Solid State Nucl. Magn. Reson.* **40**, 101–113 (2011)
32. Hodgkinson, P.: High-resolution  $^1\text{H}$  NMR spectroscopy of solids. *Annu. Rep. NMR Spectrosc.* **72**, 185 (2011)
33. Su, Y.C., Andreas, L., Griffin, R.G.: In: Kornberg, R.D. (ed) *Annual Review of Biochemistry*, vol. 84, pp. 465–497 (2015)
34. Mote, K.R., Madhu, P.K.: Proton-detected solid-state NMR spectroscopy of fully protonated proteins at slow to moderate magic-angle spinning frequencies. *J. Magn. Reson.* **261**, 149–156 (2015)
35. Nishiyama, Y.: Fast magic-angle sample spinning solid-state NMR at 60–100 kHz for natural abundance samples. *Solid State Nucl. Magn. Reson.* **78**, 24–36 (2016)
36. Kobayashi, T., Mao, K., Paluch, P., Nowak-Krol, A., Sniechowska, J., Nishiyama, Y., Gryko, D.T., Potrzebowski, M.J., Pruski, M.: Study of intermolecular interactions in the corrole

- matrix by solid-state NMR under 100 kHz MAS and theoretical calculations. *Angew. Chem. Int. Ed.* **52**, 14108–14111 (2013)
- 37. Agarwal, V., Penzel, S., Szekely, K., Cadalbert, R., Testori, E., Oss, A., Past, J., Samoson, A., Ernst, M., Bockmann, A., Meier, B.H.: De novo 3D structure determination from sub-milligram protein samples by solid-state 100 kHz MAS NMR spectroscopy. *Angew. Chem. Int. Ed.* **53**, 12253–12256 (2014)
  - 38. Zhou, D.H., Shea, J.J., Nieuwkoop, A.J., Franks, W.T., Wylie, B.J., Mullen, C., Sandoz, D., Rienstra, C.M.: Solid-state protein-structure determination with proton-detected triple-resonance 3D magic-angle-spinning NMR spectroscopy. *Angew. Chem. Int. Ed.* **46**, 8380–8383 (2007)
  - 39. Barbet-Massin, E., Pell, A.J., Retel, J.S., Andreas, L.B., Jaudzems, K., Franks, W.T., Nieuwkoop, A.J., Hiller, M., Higman, V., Guerry, P., Bertarello, A., Knight, M.J., Felletti, M., Le Marchand, T., Kotelovica, S., Akopjana, I., Tars, K., Stoppini, M., Bellotti, V., Bolognesi, M., Ricagno, S., Chou, J.J., Griffin, R.G., Oschkinat, H., Lesage, A., Emsley, L., Herrmann, T., Pintacuda, G.: Rapid proton-detected NMR assignment for proteins with fast magic angle spinning. *J. Am. Chem. Soc.* **136**, 12489–12497 (2014)
  - 40. Penzel, S., Smith, A.A., Agarwal, V., Hunkeler, A., Org, M.L., Samoson, A., Bockmann, A., Ernst, M., Meier, B.H.: Protein resonance assignment at MAS frequencies approaching 100 kHz: a quantitative comparison of J-coupling and dipolar-coupling-based transfer methods. *J. Biomol. NMR* **63**, 165–186 (2015)
  - 41. Lafon, O., Wang, Q., Hu, B.W., Vasconcelos, F., Trebosc, J., Cristol, S., Deng, F., Amoureux, J.-P.: Indirect detection via spin-1/2 nuclei in solid state NMR spectroscopy: application to the observation of proximities between protons and quadrupolar nuclei. *J. Phys. Chem. A* **113**, 12864–12878 (2009)
  - 42. Hung, I., Zhou, L.N., Pourpoint, F., Grey, C.P., Gan, Z.: Isotropic high field NMR spectra of Li-Ion battery materials with anisotropy >1 MHz. *J. Am. Chem. Soc.* **134**, 1898–1901 (2012)
  - 43. Gan, Z., Amoureux, J.-P., Trebosc, J.: Proton-detected 14N MAS NMR using homonuclear decoupled rotary resonance. *Chem. Phys. Lett.* **435**, 163–169 (2007)
  - 44. Cavadini, S., Abraham, A., Bodenhausen, G.: Proton-detected nitrogen-14 NMR by recoupling of heteronuclear dipolar interactions using symmetry-based sequences. *Chem. Phys. Lett.* **445**, 1–5 (2007)
  - 45. Wiench, J.W., Bronnimann, C.E., Lin, V.S.Y., Pruski, M.: Chemical shift correlation NMR spectroscopy with indirect detection in fast rotating solids: studies of organically functionalized mesoporous silicas. *J. Am. Chem. Soc.* **129**, 12076–12077 (2007)
  - 46. Nishiyama, Y., Kobayashi, T., Malon, M., Singappuli-Arachchige II, D., Slowing, M., Pruski: Studies of minute quantities of natural abundance molecules using 2D heteronuclear correlation spectroscopy under 100 kHz MAS. *Solid State Nucl. Magn. Reson.* **66–67**, 56–61 (2015)
  - 47. Shishovs, M., Rummieks, J., Diebolder, C., Jaudzems, K., Andreas, L.B., Stanek, J., Kazaks, A., Kotelovica, S., Akopjana, I., Pintacuda, G., Koning, R.I., Tars, K.: Structure of AP205 coat protein reveals circular permutation in ssRNA bacteriophages. *J. Mol. Biol.* **428**, 4267–4279 (2016)
  - 48. Ernst, M., Samoson, A., Meier, B.H.: Low-power decoupling in fast magic-angle spinning NMR. *Chem. Phys. Lett.* **348**, 293–302 (2001)
  - 49. Ernst, M., Samoson, A., Meier, B.H.: Low-power XiX decoupling in MAS NMR experiments. *J. Magn. Reson.* **163**, 332–339 (2003)
  - 50. Kotecha, M., Wickramasinghe, N.P., Ishii, Y.: Efficient low-power heteronuclear decoupling in <sup>13</sup>C high-resolution solid-state NMR under fast magic angle spinning. *Magn. Reson. Chem.* **45**, S221–S230 (2007)
  - 51. Lange, A., Scholz, I., Manolikas, T., Ernst, M., Meier, B.H.: Low-power cross polarization in fast magic-angle spinning NMR experiments. *Chem. Phys. Lett.* **468**, 100–105 (2009)
  - 52. Vijayan, V., Demers, J.-P., Biernat, J., Mandelkow, E., Becker, S., Lange, A.: Low-power solid-state NMR experiments for resonance assignment under fast magic-angle spinning. *ChemPhysChem* **10**, 2205–2208 (2009)

53. Romeo, F., Hoult, D.I.: Magnetic field profiling: analysis and correcting coil design. *Magn. Reson. Med.* **1**, 4–65 (1984)
54. Prammer, M.G., Haselgrove, J.C., Shinnar, M., Leigh, J.S.: A new approach to automatic shimming. *J. Magn. Reson.* **77**, 40–52 (1988)
55. Barjat, H., Chilvers, P.B., Fetler, B.K., Horne, T.J., Morris, G.A.: A practical method for automated shimming with normal spectrometer hardware. *J. Magn. Reson.* **125**, 197–201 (1997)
56. van Zijl, P.C.M., Sukumar, S., O’Neil Johnson, M., Webb, P., Hurd, R.E.: Optimized shimming for high-resolution NMR using three-dimensional image-based field mapping. *J. Magn. Reson. A* **111**, 203–207 (1994)
57. Vanderhart, D.L., William, L., Garroway, A.N.: Resolution in <sup>13</sup>C NMR of organic solids using high-power proton decoupling and magic-angle sample spinning. *J. Magn. Reson.* **44**, 361–401 (1981)
58. Kubo, A., Spaniol, T.P., Terao, T.: The effect of bulk magnetic susceptibility on solid state NMR spectra of paramagnetic compounds. *J. Magn. Reson.* **133**, 330–340 (1998)
59. Elbayed, K., Bourdonneau, M., Furrer, J., Richert, T., Raya, J., Hirschinger, J., Piotto, M.: Origin of the residual NMR linewidth of a peptide bound to a resin under magic angle spinning. *J. Magn. Reson.* **136**, 127–129 (1999)
60. Nishiyama, Y., Tsutsumi, Y., Utsumi, H.: MAGIC SHIMMING: gradient shimming under magic angle sample spinning. *J. Magn. Reson.* **216**, 197–200 (2012)
61. Sodickson, A., Cory, D.G.: Shimming a high-resolution MAS probe. *J. Magn. Reson.* **128**, 87–91 (1997)
62. Piotto, M., Elbayed, K., Wieruszkeski, J.-M., Lippens, G.: Practical aspects of shimming a high resolution magic angle spinning probe. *J. Magn. Reson.* **173**, 84–89 (2005)
63. Frye, J.S., Maciel, G.E.: Setting the magic angle using a quadrupolar nuclide. *J. Magn. Reson.* **48**, 125–131 (1982)
64. Hayashi, S., Hayamizu, K.: Chemical shift standards in high-resolution solid-state NMR (1) <sup>13</sup>C, <sup>29</sup>Si, and <sup>1</sup>H nuclei. *Bull. Chem. Soc. Jpn.* **64**, 685–687 (1991)
65. Bertani, P., Raya, J., Bechinger, B.: <sup>15</sup>N chemical shift referencing in solid state NMR. *Solid State Nucl. Magn. Reson.* **61–62**, 15–18 (2014)
66. Morcombe, C.R., Zilm, K.W.: Chemical shift referencing in MAS solid state NMR. *J. Magn. Reson.* **162**, 479–486 (2003)
67. Nishiyama, Y., Frey, M.H., Mukasa, S., Utsumi, H.: <sup>13</sup>C solid-state NMR chromatography by magic angle spinning <sup>1</sup>H T1 relaxation ordered spectroscopy. *J. Magn. Reson.* **202**, 135–139 (2010)
68. Ye, Y.Q., Malon, M., Martineau, C., Taulelle, F., Nishiyama, Y.: Rapid measurement of multidimensional <sup>1</sup>H solid-state NMR Spectra at ultra-fast MAS frequencies. *J. Magn. Reson.* **239**, 75–80 (2014)
69. Nishiyama, Y., Zhang, R., Ramamoorthy, A.: Finite-pulse radio frequency-driven recoupling with phase cycling for 2D <sup>1</sup>H/<sup>1</sup>H correlation at ultrafast MAS frequencies. *J. Magn. Reson.* **243**, 25–32 (2014)
70. Lafon, O., Wang, Q., Hu, B., Vasconcelos, F., Trébosc, J., Cristol, S., Deng, F., Amoureaux, J.-P.: Indirect detection via spin-1/2 nuclei in solid state NMR spectroscopy: application to the observation of proximities between protons and quadrupolar nuclei. *J. Phys. Chem. A* **113**, 12864–12878 (2009)
71. Tricot, G., Trébosc, J., Pourpoint, F., Gauvin, R., Delevoye, L.: The D-HMQC MAS-NMR technique: an efficient tool for the editing of through-space correlation spectra between quadrupolar and spin-1/2 (<sup>31</sup>P, <sup>29</sup>Si, <sup>1</sup>H, <sup>13</sup>C) Nuclei. *Annu. Rep. NMR Spectrosc.* **81**, 145–184 (2014)
72. Gan, Z., Amoureaux, J.-P., Trébosc, J.: Proton-detected <sup>14</sup>N MAS NMR using homonuclear decoupled rotary resonance. *Chem. Phys. Lett.* **435**, 163–169 (2007)
73. Cavadini, S., Abraham, A., Bodenhausen, G.: Proton-detected nitrogen-14 NMR by recoupling of heteronuclear dipolar interactions using symmetry-based sequences. *Chem. Phys. Lett.* **445**, 1–5 (2007)

74. Nishiyama, Y., Endo, Y., Nemoto, T., Utsumi, H., Yamauchi, K., Hioka, K., Asakura, T.: Very fast magic angle spinning  $^{1}\text{H}$ - $^{14}\text{N}$  2D solid-state NMR: submicro-liter sample data collection in a few minutes. *J. Magn. Reson.* **208**, 44–48 (2011)
75. Feike, M., Demco, D.E., Graf, R., Gottwald, J., Hafner, S., Spiess, H.W.: Broadband multiple-quantum NMR spectroscopy. *J. Magn. Reson. A* **122**, 214–221 (1996)
76. Schnell, I., Spiess, H.W.: High-resolution  $^{1}\text{H}$  NMR spectroscopy in the solid state: very-fast sample rotation and multiple-quantum coherences. *J. Magn. Reson/Adv. Magn. Reson.* **151**, 153–227 (2001)
77. Carravetta, M., Edén, M., Zhao, X., Brinkmann, A., Levitt, M.H.: Symmetry principles for the design of radiofrequency pulse sequences in the nuclear magnetic resonance of rotating solids. *Chem. Phys. Lett.* **321**, 205–215 (2000)
78. Levitt, M.H.: Symmetry-based pulse sequences in magic-angle spinning solid state NMR. In: Grant, D.M., Harris, R.K. (eds.) *Encyclopedia of Magnetic Resonance*, vol. 9, pp. 165–196. Wiley, Chichester (2002)
79. Brown, S.P., Spiess, H.W.: Advanced solid-state NMR methods for the elucidation of structure and dynamics of molecular, macromolecular, and supramolecular systems. *Chem. Rev.* **101**, 4125–4155 (2001)
80. Saalwächter, K., Lange, F., Matyjaszewski, K., Huang, C.-F., Graf, R.: BaBa-xy16: robust and broadband homonuclear DQ recoupling for applications in rigid and soft solids up to the highest MAS frequencies. *J. Magn. Reson.* **212**, 204–215 (2011)
81. Hu, B., Wang, Q., Lafon, O., Trébosc, J., Deng, F., Amoureaux, J.P.: Robust and efficient spin-locked symmetry-based double-quantum homonuclear dipolar recoupling for probing  $^{1}\text{H}$ - $^{1}\text{H}$  proximity in the solid-state. *J. Magn. Reson.* **198**, 41–48 (2009)
82. Wang, Q., Hu, B., Lafon, O., Trébosc, J., Deng, F., Amoureaux, J.-P.: Homonuclear dipolar recoupling under ultra-fast magic-angle spinning: Probing  $^{19}\text{F}$ - $^{19}\text{F}$  proximities by solid-state NMR. *J. Magn. Reson.* **203**, 113–128 (2010)
83. Deschamps, M., Fayon, F., Cadars, S., Rollet, A.-L., Massiot, D.:  $^{1}\text{H}$  and  $^{19}\text{F}$  ultra-fast MAS double-quantum single-quantum NMR correlation experiments using three-spin terms of the dipolar homonuclear Hamiltonian. *Phys. Chem. Chem. Phys.* **13**, 8024–8030 (2011)
84. Geen, H., Titman, J.J., Gottwald, J., Spiess, H.W.: Spinning sidebands in the fast-MAS multiple-quantum spectra of protons in solids. *J. Magn. Reson. A* **114**, 264–267 (1995)
85. Nielsen, N.C., Bildsøe, H., Jakobsen, H.J., Levitt, M.H.: Double-quantum homonuclear rotary resonance: Efficient dipolar recovery in magic-angle spinning nuclear magnetic resonance. *J. Chem. Phys.* **101**, 1805 (1994)
86. Zhou, D.H., Rienstra, C.M.: High-performance solvent suppression for proton detected solid-state NMR. *J. Magn. Reson.* **192**, 167–172 (2008)
87. Metz, G., Wu, X., Smith, S.O.: Ramped-amplitude cross polarization in magic-angle-spinning NMR. *J. Magn. Reson. A* **110**, 219–227 (1994)
88. Laage, S., Sachleben, J.R., Steuernagel, S., Pierattelli, R., Pintacuda, G., Emsley, L.: Fast acquisition of multi-dimensional spectra in solid-state NMR enabled by ultra-fast MAS. *J. Magn. Reson.* **196**, 133–141 (2009)
89. Wickramasinghe, A., Wang, S., Matsuda, I., Nishiyama, Y., Nemoto, T., Endo, Y., Ishii, Y.: Evolution of CP/MAS under fast magic-angle-spinning at 100 kHz and beyond. *Solid State Nucl. Magn. Reson.* **72**, 9–16 (2015)

# Chapter 7

## Elucidating Functional Dynamics by $R_{1\rho}$ and $R_2$ Relaxation Dispersion NMR Spectroscopy

Erik Walinda and Kenji Sugase

**Abstract** NMR spectroscopy is the method of choice to measure protein and nucleic acid dynamics on a variety of timescales. Picosecond to nanosecond dynamics can be precisely probed by quantifying  $R_1$  and  $R_2$  relaxation rates and heteronuclear NOE values, whereas residual dipolar couplings (RDCs) are sensitive to motion on a wide range of timescales from submicrosecond to milliseconds. Even slower dynamics can be assessed by hydrogen exchange experiments. In a biochemical context, relaxation dispersion NMR spectroscopy is particularly valuable, because it reports on the biologically important timescale from micro- to milliseconds, encompassing the conformational rearrangements of ligand binding, enzymatic reactions, and base pair transitions. From relaxation dispersion measurements, it is possible to obtain structural, kinetic, and thermodynamic information about energetically excited conformational minor states beyond the ground state structure. Here, we review the two methods of  $R_{1\rho}$  and  $R_2$  relaxation dispersion, focusing on recent developments in pulse sequence design and data processing techniques, as well as applications of the methods to resolve protein–protein interactions.

**Keywords** Protein dynamics • Conformational exchange • Protein–ligand interactions • Transverse relaxation

---

E. Walinda

Department of Molecular and Cellular Physiology,  
Graduate School of Medicine, Kyoto University,  
Yoshida Konoe-cho, Sakyo-ku, Kyoto 606-8501, Japan  
e-mail: walinda.erik.6e@kyoto-u.ac.jp

K. Sugase (✉)

Department of Molecular Engineering,  
Graduate School of Engineering, Kyoto University,  
Kyoto-Daigaku Katsura, Nishikyo-ku, Kyoto 615-8510, Japan  
e-mail: sugase@molen.kyoto-u.ac.jp

## 7.1 Relaxation Dispersion

Accurate function of biomolecules such as proteins, carbohydrates, and nucleic acids is central to all cellular processes. Although the function of many proteins and nucleic acids would seem to be explained by a single static structure, many biomacromolecules such as enzymes are extremely dynamic. This dynamical character means that the proteins in fact sample many conformations to exert their physiological function in solution. The static ground state structure of a protein can be obtained from X-ray crystallography, NMR spectroscopy, or cryo-electron microscopy; however, the dynamics beyond this ground state structure remain hidden. Because these “invisible” transient dynamic conformations cannot be observed directly, specialized methods are needed that can detect the energetically excited minor states in solution.

Relaxation dispersion NMR spectroscopy is the method of choice to detect and quantify such functionally relevant motion in biomolecules on a timescale from microseconds to milliseconds. Indeed, relaxation dispersion has provided unprecedented insight, with an astonishing level of detail, into the mechanisms of protein binding [1, 2], enzymatic activity [3–9], base pair exchange [10, 11], post-translational modifications [12], protein folding [13, 14], protein intermediate structures [15], intrinsically disordered proteins [1, 2, 16, 17], and transcriptional activators [18]. This great degree of detail arises (i) because relaxation dispersion provides site-specific information at atomic resolution; and (ii) because the extracted information has such high diversity. The method allows the extraction of structural (chemical shift difference between the major and minor states,  $\Delta\omega$ ), kinetic (lifetime of the excited states,  $1/k_{ex}$ ), and thermodynamic (relative populations of the states,  $p_i$ ) information about the excited states. Although none of these parameters is directly measurable, the information can be obtained by quantifying the broadening of NMR resonance lines, which is caused by the conformational exchange process.

Relaxation dispersion can be measured by two main methods:  $R_2$  relaxation dispersion and  $R_{1\rho}$  relaxation dispersion. In the  $R_2$  relaxation dispersion experiment, the effective transverse relaxation rate is measured as a function of the delay between two successive refocusing pulses in a Carr–Purcell–Meiboom–Gill (CPMG) pulse sequence [19–21]. In the  $R_{1\rho}$  relaxation dispersion experiment, the effective rotating-frame relaxation rate is probed as a function of either the amplitude or the offset of an applied spin-lock radiofrequency (RF) field [22–29]. The relaxation rates resulting from either method can then be plotted as a function of the applied field (Fig. 7.1). In the  $R_{1\rho}$  relaxation dispersion experiment, the relaxation rates can also be plotted as a function of the spin-lock offset. In either case, fitting of the data points of the relaxation dispersion profile to a theoretical model enables the relevant structural, kinetic, and thermodynamic parameters to be extracted.

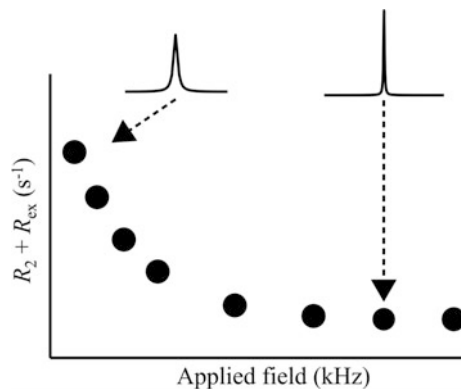


**Fig. 7.1** Schematic relaxation dispersion profile. In the presence of chemical exchange (shown), broad signals (large effective  $R_2$ ) are obtained at weak applied fields, whereas strong fields refocus the magnetization leading to sharp lines (small effective  $R_2$ ). In the absence of exchange (not shown), the relaxation rates are equal at all applied fields and a flat profile is obtained

In this chapter, we briefly review the two relaxation dispersion methods and then discuss several recent theoretical and practical developments. To this end, we focus on protein–ligand interactions and the automation of relaxation dispersion measurements and processing.

## 7.2 Accessible Information

The kind of information that can be extracted from relaxation dispersion depends on the exchange regime in question. Assuming the simplest model to describe the exchange between two conformational states A and B in a biomolecule, a two-state exchange model is:



If the exchange between A and B is slow on the chemical shift timescale (slow exchange regime), fitting of the relaxation rates as a function of the applied field strength to a theoretical model yields the chemical shift difference  $\Delta\omega$  between the two states, the exchange rate of the process  $k_{\text{ex}} = k_{\text{AB}} + k_{\text{BA}}$ , and the populations of the major ( $p_A$ ) and minor state ( $p_B$ ) [30]. If the exchange process is fast on the chemical shift timescale (fast exchange regime), unfortunately it is not possible to separate  $p_A$ ,  $p_B$ , and  $\Delta\omega$  [29, 31]; in this case, only  $k_{\text{ex}}$ ,  $R_2^0$  (the intrinsic transverse relaxation rate in absence of exchange), and the site of the exchange can be derived and interpreted.

## 7.3 $R_{1\rho}$ Relaxation Dispersion

### 7.3.1 General Aspects

Spin-lock-based relaxation dispersion experiments are called  $R_{1\rho}$  relaxation dispersion experiments because, during the relaxation block of the pulse sequence, a magnetization decays at the rotating-frame relaxation rate  $R_{1\rho}$ . In proteins, relaxation of the  $^{15}\text{N}$  amide nucleus is most frequently studied [20, 32–34]; however, applications of relaxation dispersion to  $^1\text{H}$  and  $^{13}\text{C}$  nuclei have also been described in the literature [35, 36]. For simplicity, here we focus on the  $^{15}\text{N}$  nucleus.

Whether it is possible to resolve a given exchange process by  $R_{1\rho}$  relaxation dispersion depends on the exchange rate  $k_{\text{ex}}$  relative to the applied field strength [29]. That is, the exchange rate  $k_{\text{ex}}$  should be of the same order as the experimentally applicable effective field amplitudes:

$$\omega_e = \sqrt{\omega_1^2 + \Omega^2}, \quad (7.2)$$

where  $\omega_e$  is the effective field amplitude (in units of  $\text{rad s}^{-1}$ ).  $\omega_1$  and  $\Omega$  denote the RF field amplitude and the offset of a given resonance from the spin-lock carrier frequency, respectively. In other words, the experimentally applicable field strength directly determines the time window of the dynamical process that can be studied by  $R_{1\rho}$  relaxation dispersion. In general, higher effective fields can be used in spin-lock ( $R_{1\rho}$  relaxation dispersion) experiments than in CPMG ( $R_2$  relaxation dispersion) experiments; however, spin-lock experiments present other challenges such as accurate field calibration [37], sample heating, and offset effects that are not critical issues with CPMG-type experiments. The spectrometer hardware (amplifier and probe) may impose additional constraints.

When using the  $^{15}\text{N}$  amide nucleus as a probe to study the conformational dynamics of a protein, spin-locking fields as high as  $\omega_1/2\pi \approx 6 \text{ kHz}$  can be applied [38]. Such strong fields refocus rapidly exchanging magnetization, and thus, very fast chemical exchange processes can be resolved. The spin-lock field can be applied near-resonance ( $\Omega \simeq 0$ ), on-resonance ( $\Omega = 0$ ), or off-resonance ( $\Omega \neq 0$ ). The effective relaxation rate depends on both  $\omega_1$  and  $\Omega$ . Thus, either  $\omega_1$  or  $\Omega$ , or both, can be varied between experiments to obtain spin-lock power (on-resonance  $R_{1\rho}$  [28, 39]) or spin-lock offset (off-resonance  $R_{1\rho}$  [40, 41])-dependent relaxation dispersion profiles.

Early  $^{15}\text{N}$   $R_{1\rho}$  relaxation dispersion experiments were carried out in a relatively conventional manner; in other words, data were obtained as a series of 2D  $^1\text{H}$ – $^{15}\text{N}$  experiments in which a near-resonance spin-lock relaxation building block was included [27, 28, 40, 42]. However, the dependence of the relaxation rate  $R_{1\rho}$  on the offset from the spin-lock carrier frequency  $\Omega$  posed challenges. In particular, because the amide resonances in a protein have different  $^{15}\text{N}$  chemical shifts, all resonances experience the effect of the spin lock at different offsets. Thus, these experiments were called “near-resonance” experiments, rather than on-resonance

experiments. The offset dependence imposes the limitation that weak spin-locking fields cannot be used owing to the resulting tilt  $\theta$  of the effective field toward the  $z$ -axis when  $\omega_1$  becomes small relative to the offset  $\Omega$ :

$$\tan \theta = \frac{\omega_1}{\Omega}. \quad (7.3)$$

A highly tilted effective field maximizes the contribution of  $R_1$  and minimizes the contribution of  $R_2$ . This is not useful, however, because  $R_1$  does not report on the exchange process in question: Only the transverse relaxation rate  $R_2$  contains an exchange contribution [43]:

$$R_2 = \overline{R_2^0} + R_{\text{ex}}, \quad (7.4)$$

where the line above  $R_2^0$  indicates that in the case of fast exchange, the relaxation rate will be population-averaged.

In 2005, Kay and coworkers suggested that it would be more beneficial to probe only one of the amide resonances of a protein at a time [25]. An equivalent strategy was also used by Al-Hashimi and coworkers to probe  $^{13}\text{C}$  spins in nucleic acids [22]. This strategy eliminates the problem of the differential off-resonance effects of the spins of a protein because only one spin is studied at a time, which is particularly advantageous for off-resonance experiments [25]. Moreover, if desired, the spin lock can be applied completely on-resonance ( $\Omega = 0$ ) in all experiments [44]. To probe a single spin at a time, the pulse sequences utilize Hartmann–Hahn cross-polarization (CP) transfer for selective coherence transfer. Although the number of spectra to be obtained is markedly increased in this scheme, experimental time can be somewhat conserved by recording the experiments as a series of 1D NMR spectra.

When the spin lock is applied on-resonance, accurate spin locking can be achieved even with very weak  $\omega_1$  fields. This extends the time window of dynamics that can be studied by  $R_{1\rho}$  relaxation dispersion for the study of slow exchange processes, because this window depends on the value of  $\omega_e$  relative to  $k_{\text{ex}}$ . Moreover, in this approach,  $^1\text{H}$  decoupling during the duration of the spin lock is simplified, thereby avoiding potential problems arising from  $J$ -coupling and cross-correlation between dipole–dipole interactions and chemical shift anisotropy whenever  $^{15}\text{N}$  transverse coherence is present [25].

### 7.3.2 Pulse Sequence of the $R_{1\rho}$ Relaxation Dispersion Experiment

The pulse sequence of a typical  $R_{1\rho}$  relaxation dispersion experiment is shown in Fig. 7.2. Equilibrium proton magnetization is excited and transferred to the scalar-coupled amide  $^{15}\text{N}$  spin by Hartmann–Hahn cross-polarization [45]. To this

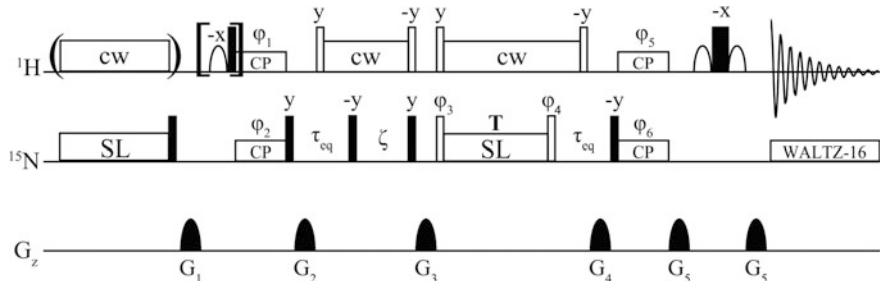


**Fig. 7.2**  $R_{1\rho}$  relaxation dispersion. Shown is a pulse sequence to probe micro- to millisecond dynamics by <sup>15</sup>N  $R_{1\rho}$  relaxation dispersion [22, 44]. Pulses are applied with  $x$  phase, unless noted otherwise in the diagram. The filled rectangles denote non-selective 90° pulses. A WATERGATE scheme is used for water suppression [85]. The open rectangles represent pulses with variable tip angles as described previously [25]. <sup>15</sup>N decoupling during acquisition is achieved by the WALTZ-16 sequence [86]. The block in square brackets can be replaced by a selective excitation pulse (E-BURP-1 shape, 5 ms). Phase cycle:  $\varphi_1 = 8(y), 8(-y); \varphi_2 = x, -x; \varphi_5 = 4(x), 4(-x); \varphi_6 = 2(x), 2(-x); \varphi_{rec} = x, -x, -x, x, x - x, -x, x, x, -x, x, -x, -x, x$ ; for more details, see ref. [44]. Gradients:  $G_1$  (1 ms, 3 G/cm),  $G_2$  (1 ms, 40 G/cm),  $G_3$  (1 ms, 15 G/cm),  $G_4$  (0.5 ms, 27.5 G/cm),  $G_5$  (1 ms, 10 G/cm). Abbreviations CP cross-polarization, cw continuous wave irradiation, SL spin lock

end, RF fields of matched frequency are applied on both the <sup>1</sup>H and the <sup>15</sup>N channels. The selectivity of this transfer depends on the amplitude of the matched applied RF fields, which is termed  $\omega_{CP}$ . In general, it is possible to select a single amide resonance, that is a single cross-peak in a <sup>1</sup>H<sup>15</sup>N-heteronuclear single-quantum coherence (HSQC) spectrum using this technique with very weak matched CP fields, which may be as weak as [46]:

$$\frac{\omega_{CP}}{2\pi} = \frac{\sqrt{3}}{4} J. \quad (7.5)$$

If the resonance in question is sufficiently isolated in the <sup>1</sup>H<sup>15</sup>N-HSQC spectrum, slightly stronger matched CP fields may be applied. By using the program SIMPSON [47], it is possible to simulate the selectivity of this transfer. For example, matched CP fields of  $\omega_{CP}/2\pi = 93$  Hz  $\approx |J_{HN}|$  cause coherence transfer in an approximate range of  $\pm 100$  Hz around the target resonance at a static field of 16.4 T [44]. After CP, the resulting <sup>15</sup>N in-phase coherence is stored on the  $z$ -axis and a  $z$ -filter is applied to dephase all resonances except the single resonance of interest.

While the coherence of interest is still stored on the  $z$ -axis, an equilibration time ( $\tau_{eq}$ ) on the order of 5 ms is employed. In some circumstances, the initial population of each state may differ from the expected value if this equilibration period is omitted. Consider a given spin that exchanges between two conformational states A and B, where A is the major state (population  $p_A \simeq 0.99$ ) and B is the minor state (population  $p_B \simeq 0.01$ ). For the given spin, the separation in chemical shift ( $\Delta\omega_{AB}$ )

between states A and B is relatively large. Thus, when the spin of interest is subjected to selective CP, only the spins of the molecules in which the spin is in state A will feel the effect of selective CP. In other words, only spins in state A transfer their coherence by CP from  $^1\text{H}$  to  $^{15}\text{N}$ . The subsequent  $z$ -filter dephases all other resonances, including the spins in state B. Thus, the relative populations of A and B will have been perturbed to  $p_A = 1.0$  and  $p_B = 0$ . The additional equilibration delay  $\tau_{\text{eq}}$  makes sure that, at the beginning of the relaxation period (spin lock), the respective populations  $p_A$  and  $p_B$  are restored to their appropriate equilibrium values. This is important because the populations appear in the theoretical equations that describe  $R_{1\rho}$ . Because of this dependence, accurate values of  $p_A$  and  $p_B$  are critical to ensure a good agreement between theory and experiment. For small values of  $\Delta\omega_{AB}$ , the influence of  $\tau_{\text{eq}}$  may be limited because spins in state B will be affected by selective CP; however, for  $\Delta\omega_{AB}$  values that fall outside the range of the CP coherence transfer profile, the experiment is expected to perform better when a sufficient equilibration delay  $\tau_{\text{eq}}$  is used.

Next, the target magnetization is flipped back to the transverse plane, where the optional delay  $\zeta$  separates a target on-resonance coherence ( $^{15}\text{N}$  chemical shift  $\Omega = 0$ ) and a CP-excited nearby unwanted coherence ( $^{15}\text{N}$  chemical shift  $\Omega \neq 0$ ). If the target coherence is sufficiently isolated in the  $^1\text{H}^{15}\text{N}$ -HSQC spectrum or CP selectivity is sufficient, a value of  $\zeta = 0$  may be set: Because  $\zeta$  is on the order of milliseconds, setting  $\zeta$  to 0 will maximize sensitivity. The subsequent gradient  $G_3$  dephases the unwanted off-resonance coherences, whereas the target coherence is stored on the  $z$ -axis. Whenever  $^{15}\text{N}$  transverse coherence is present,  $^1\text{H}$  decoupling is achieved by applying on-resonance continuous wave fields [25].

As a result, only the single target desired coherence is retained at the beginning of the relaxation period in which the spin lock of variable power and/or offset is applied. After the relaxation block, another equilibration delay is employed and coherence is transferred back from  $^{15}\text{N}$  to  $^1\text{H}$  for detection as a 1D experiment.

The effective rotating-frame relaxation rate is then obtained according to:

$$R_{1\rho} = -\frac{1}{T} \ln \left( \frac{I}{I_0} \right), \quad (7.6)$$

where  $T$  is the duration of the spin lock, typically 30–50 ms;  $I$  is the peak intensity in an experiment in which a spin lock is applied; and  $I_0$  is a reference intensity from an experiment in which the spin-lock block is omitted (by setting  $T = 0$ ). Note that, because of the dependence of  $R_{1\rho}$  on  $\omega_1$ , the experimentally applied  $B_1$  fields must be rigorously calibrated and their actual values should be measured directly [37].

### 7.3.3 Automation of $R_{1\rho}$ Relaxation Dispersion Measurements and Data Processing

Performing the  $R_{1\rho}$  relaxation dispersion experiment separately for one site at a time, as described in the previous section, has many advantages because very weak  $\omega_1$  fields can be used. However, this approach means that a large number of free-induction decays (FIDs) must be recorded, processed, and integrated before the relaxation rates can be calculated and fitted to a theoretical model. The number of FIDs is  $n \times (m + r)$ , where  $n$  is the number of probed resonances;  $m$  is the number of varied parameters, that is, spin-lock power  $\omega_1$  or offset  $\Omega$  (i.e.,  $m$  is the number of  $R_{1\rho}$  relaxation rates (data points) in the final relaxation dispersion profile); and  $r$  is the number of reference data recorded. Thus, even for a small protein such as ubiquitin (76 residues; ~72 resolved cross-peaks in the  $^1\text{H}^{15}\text{N}$ -HSQC spectrum), approximately 1600 ( $n = 72$ ;  $m = 20$ ;  $r = 2$ ) FIDs would have to be recorded, processed, and peak-picked before the  $R_{1\rho}$  relaxation rates can be calculated and compared with a theoretical model of the exchange process. It is very likely that many researchers have shied away from this approach to relaxation dispersion owing to its apparently labor-intensive procedure.

It is, however, relatively straightforward to make the acquisition and processing of the data more convenient by considering the following points:

1. Not all amino acids in a protein report on conformational exchange.
2.  $R_{1\rho}$  relaxation dispersion-positive residues can be easily identified.
3. Acquisition and processing can be automated.

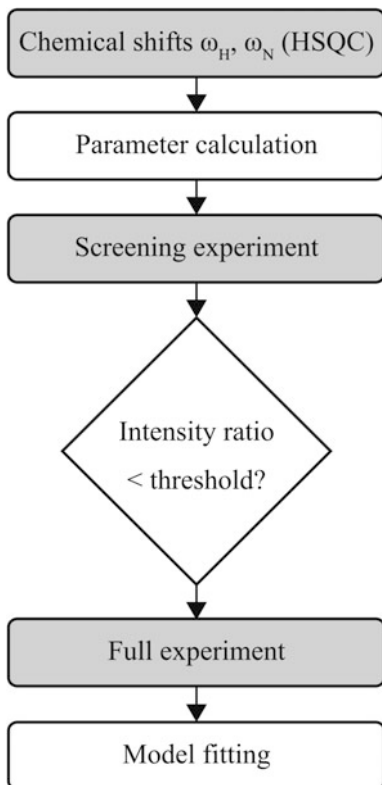
Based on these three considerations, the acquisition and processing of  $R_{1\rho}$  relaxation dispersion data have been recently automated through the development of the *Amaterasu* (automated  $R_{1\rho}$  analysis utility) pipeline (Fig. 7.3) [24].

#### 7.3.3.1 Experimental Setup

A dedicated spreadsheet included in the *Amaterasu* package ([http://www.moleng.kyoto-u.ac.jp/~moleng\\_01/amaterasu](http://www.moleng.kyoto-u.ac.jp/~moleng_01/amaterasu)) calculates all of the acquisition parameters that are required to set up the experiment. The acquisition pulse program is implemented in such a way that the entire dataset, comprising  $n$  residues  $\times (m + r)$  residue-specific FIDs, is acquired in a single run (i.e., a single acquisition dataset). This type of implementation is termed a “pseudo-2D” experiment and means that only a single experiment needs to be set up at the spectrometer. The acquisition of all residues with all power/offset values is handled entirely by the pulse program.

First, a conventional  $^1\text{H}^{15}\text{N}$ -HSQC spectrum is acquired. The spectrum is semi-automatically peak picked in a spectrometer acquisition program, such as Bruker TopSpin. The chemical shifts of all resonances of interest are then copied to the *Amaterasu* spreadsheet. At this stage, resonances such as tryptophan side chain

**Fig. 7.3** Workflow of *Amaterasu*. Gray boxes, experimental steps; white boxes, steps automated by the pipeline



peaks can be discarded if desired. After the basic pulse lengths and powers ( $^1\text{H}$  and  $^{15}\text{N}$  hard pulses) are entered, the spreadsheet automatically calculates all parameters necessary to perform the  $R_{1\rho}$  relaxation dispersion experiment, including CP, spin lock, water-flip back, decoupling pulses, and the optional delay  $\zeta$ . The chemical shifts  $\omega_{\text{H}}$ ,  $\omega_{\text{N}}$ , the delay  $\zeta$ , and the spin-lock power or offset values are passed to the pulse program as simple text files. Once these text files are created, the spreadsheet can be closed.

### 7.3.3.2 Screening

In almost all known cases, not all residues of a protein will report on conformational exchange on the micro- to millisecond timescale; therefore, it is not recommended that relaxation dispersion profiles are acquired for all residues of a protein, because a great deal of spectrometer time will be spent on acquiring essentially meaningless flat profiles. Instead, an efficient spectroscopist will first identify the dynamic residues of the protein by performing a quick screening experiment in which only two spectra are recorded for all resonances. Each

resonance is probed by a weak and a strong spin-lock field  $\omega_1$ . For ubiquitin, for example, the  $\sim 72$  cross-peaks of its  $^1\text{H}^{15}\text{N}$ -HSQC spectrum would be picked and two spectra would be acquired for each: one with  $\omega_1/2\pi \simeq 50$  Hz and one with  $\omega_1/2\pi \simeq 3000$  Hz. If the residue in question does not exhibit chemical exchange, the two spectra will show peaks of equal intensity. Conversely, if the resonance does exhibit micro- to millisecond conformational dynamics, a lower peak intensity will be observed in the spectrum corresponding to the weak spin-lock experiment. In summary, a screening experiment will collect only the first and the last data point of a relaxation dispersion profile (Fig. 7.1), with the exception that no reference spectrum is acquired, and thus, the relaxation rate  $R_{1\rho}$  is not actually calculated.

If the ratio of these two intensities indicates the presence of chemical exchange, *Amaterasu* will select the resonance for acquisition of a full relaxation dispersion profile. Unpromising resonances can be discarded at this stage to save acquisition time, except for special cases in which a flat profile is particularly desired (e.g., negative control experiments).

### 7.3.3.3 Processing

The software package *Amaterasu* performs the entire processing procedure from the raw FIDs (in Bruker spectrometer format) to model fitting of the final  $R_{1\rho}$  relaxation dispersion profile in a fully automated manner. First, it splits the pseudo-2D dataset into the respective 1D data. Second, it reads all acquisition parameters and, for each FID, conducts apodization, zero filling, 1D Fourier transform (FT), and automatic phase correction. All processing steps are carried out using the Python library nmrglue [48]. For phase correction, the entropy of the spectrum is minimized as described by Chen and coworkers [49]. Third, *Amaterasu* performs peak picking on all spectra. Because the chemical shift of each given resonance is known a priori, the program can easily recognize the correct peak based on the known chemical shift. It is also possible to plot all spectra to check for the presence of artifacts arising from peak overlap or erroneous phases. After all of the peaks are integrated, the resulting peak intensities as a function of  $\omega_1$  and/or  $\Omega$  are passed to the relaxation dispersion data-fitting program GLOVE [50]. The output files of GLOVE will then contain the kinetic and thermodynamic parameters that govern the exchange process, along with the fitted relaxation dispersion profile. For a small protein ( $\sim 100$  amino acids), *Amaterasu* completes its pipeline, from reading the raw FIDs to the final output of the relaxation dispersion profiles, in less than 1 min on a standard desktop PC (e.g., Mac mini, 2015). Examples of relaxation dispersion profiles obtained with *Amaterasu* are shown in Fig. 7.4.

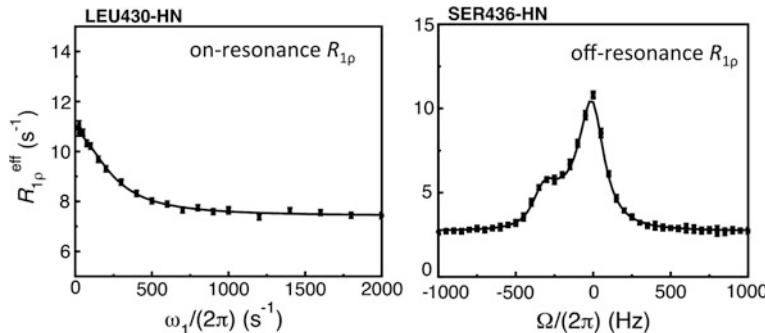


**Fig. 7.4**  $^{15}\text{N}$   $R_{1\rho}$  relaxation dispersion profiles of amide resonances of the ubiquitin-associated (UBA) domain of the autophagy receptor protein p62 as obtained with *Amaterasu* and GLOVE [24, 50]. *Left*, on-resonance  $R_{1\rho}$  relaxation dispersion experiment; *right*, off-resonance  $R_{1\rho}$  relaxation dispersion experiment. Reproduced with permission from ref. [24]

## 7.4 $R_2$ Relaxation Dispersion

### 7.4.1 General Aspects

Application of a spin-lock pulse is not the only method to keep a coherence from dephasing during a fixed relaxation delay  $T$ . A Carr–Purcell–Meiboom–Gill (CPMG) pulse sequence [19–21] refocuses a given coherence by repetitive execution of the spin-echo sequence ( $\tau$ — $180^\circ$ — $2\tau$ — $180^\circ$ — $\tau$ ) $_n$ . Here,  $n$  is an integer and the spacing between the two successive  $180^\circ$  pulses,  $2\tau$ , is called  $\tau_{\text{CP}}$ . In general, chemical exchange can be detected by  $R_2$  relaxation dispersion if the exchange rate  $k_{\text{ex}}$  is of the same order as  $1/\tau_{\text{CP}}$ . As with spin-lock experiments, CPMG experiments may cause sample heating at high values of  $n$ , which may also interfere with theoretical treatments of the experiment because the pulse lengths of the refocusing pulses are assumed to be negligible in these models [41, 43].

In principle, the evolution of both in-phase and anti-phase coherences during the CPMG time must be considered. It has been shown, however, that it is beneficial to average the differential contributions of in-phase and anti-phase coherences to  $R_2$  in the experiment by including a relaxation-compensating (RC) element in the pulse sequence (Fig. 7.5). The RC element interconverts in-phase and anti-phase coherences in the middle of the relaxation period, which eliminates any artifacts that may arise from different relaxation rates of in-phase and anti-phase coherences of a spin. For simplicity, the sequence in Fig. 7.5 shows only the pulse sequence during the relaxation time  $T_{\text{CPMG}}$  including the RC element. In a full sequence, the experiment begins from equilibrium proton magnetization using an INEPT element to obtain the anti-phase  $^{15}\text{N}$  coherence  $-2\text{H}_z\text{N}_y$ . This coherence is then continuously rephased by the CPMG spin-echo sequence while exhibiting transverse relaxation and imprinting the exchange contribution  $R_{\text{ex}}$  onto the intrinsic transverse relaxation rate  $R_2$ . In the middle of the pulse sequence, the anti-phase coherence  $-2\text{H}_z\text{N}_y$

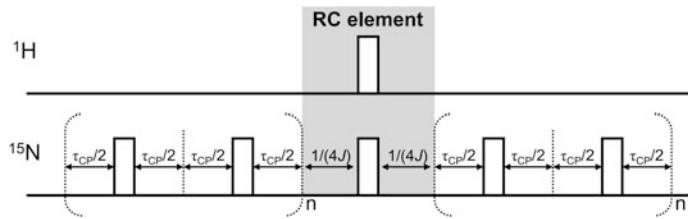


**Fig. 7.5**  $R_2$  relaxation dispersion. Shown are pulse sequence elements of a CPMG relaxation dispersion experiment for evolution through the relaxation block of length  $T_{\text{CPMG}}$ . The sequence starts from an initial coherence described by  $-2H_zN_y$ , which can be obtained by an INEPT sequence. Open rectangles indicate  $180^\circ$  pulses. The relaxation compensation (RC) element interchanges anti-phase to in-phase coherence.  $J$  is the amide  $^1J_{\text{HN}}$ -coupling

encounters the RC element and is thus converted to the in-phase coherence  $N_x$ ; moreover, the RC element suppresses cross-correlation arising from chemical shift anisotropy and dipole–dipole interaction. After passing the RC element, the in-phase coherence  $N_x$  relaxes for the remainder of  $T_{\text{CPMG}}$ , thereby averaging the effect of in-phase and anti-phase coherence relaxation during  $T_{\text{CPMG}}$ .  $^{15}\text{N}$  frequency labeling during  $t_1$  and acquisition during  $t_2$  conclude the experiment.

In the  $^{15}\text{N}$  CPMG experiment, problems can arise from  $^1J_{\text{HN}}$ -coupling, offset effects, and pulse imperfections, which can lead to erroneous estimation of the effective transverse relaxation rate  $R_2^{\text{eff}}$ . These problems can be largely alleviated by applying continuous wave decoupling on the  $^1\text{H}$  channel during  $T_{\text{CPMG}}$  [51, 52].

#### 7.4.2 Quantifying Protein–Ligand Interactions by $R_2$ Relaxation Dispersion

Interestingly, relaxation dispersion has not only been used to study the dynamics of a single protein, but it can also probe interactions between a protein and other molecules [31].

When the interaction between a protein and a ligand is in intermediate or slow exchange on the NMR timescale, then the observed chemical shifts do not appear as population averages between the free and bound states in the experiment. In this situation, therefore, other methods that assume fast exchange conditions, such as chemical shift titration or transferred  $R_1$  and  $R_2$  experiments [53–56], are not applicable. For example, for a binding process in the slow exchange regime, the NMR signal of a protein or a ligand does not move during a titration experiment; accordingly, it is not possible to simply obtain a titration curve (chemical shift difference as a function of protein–ligand ratio) to extract the dissociation constant  $K_D$ .

In recent years, multiple NMR methods have been developed to study the kinetic rates of slow and intermediate exchange systems. In principle,  $R_{1\rho}$  dispersion [28],  $R_2$  dispersion [20, 32, 57, 58], ZZ-exchange [59–61], CEST [62, 63], and DEST

[64] techniques can all be applied to this end; each of these methods has the potential to derive the kinetic rates of interconversion between the states, even though one of the states is not directly measurable because of its low population and a large transverse relaxation rate (due to the additive contribution of  $R_{\text{ex}}$ ).

#### 7.4.2.1 Theory

Consider the interaction between a protein (A) and a ligand (B):



It has been shown that it is possible to determine  $[B]k_{\text{on}}$  and  $k_{\text{off}}$  by relaxation dispersion in an analogous way to determination of the kinetic rates of conformational exchange in a single molecule. Note, however, that  $[B]$  is unknown and must be determined. Although it is possible to determine  $K_D$  from isothermal titration calorimetry (ITC), to measure  $k_{\text{off}}$  by NMR, and then to calculate  $k_{\text{on}}$  from  $K_D = k_{\text{off}}/k_{\text{on}}$  [65], here we discuss the determination of  $k_{\text{on}}$  and  $k_{\text{off}}$  without any prior information on  $K_D$  by using  $R_2$  relaxation dispersion [1].

If the exchange process—that is, the association–dissociation equilibrium—occurs on the timescale of milliseconds with a comparably large chemical shift change  $\Delta\omega$ , we can assume that the effective transverse relaxation rate  $R_2$  of the free and the bound resonances will increase by an additional relaxation rate  $R_{\text{ex}}$ , as described by Eq. 7.4.  $R_2^{\text{eff}}$  can be obtained from the  $R_2$  relaxation dispersion experiment, thereby allowing extraction of the rate  $k_{\text{ex}}$  of the association–dissociation process. In addition, structural information in form of the chemical shift difference  $\Delta\omega$  between the free and bound states can be obtained.  $R_2^{\text{eff}}$  can be accurately described by numerical solution of the Bloch–McConnell equations [66, 67]. Alternatively, we can assume a simple two-state exchange model and describe  $R_2^{\text{eff}}$  as follows [68]:

$$\begin{aligned} R_2^{\text{eff}} &= R_2^0 + \frac{1}{2} \left\{ k_{\text{ex}} - \frac{1}{\tau_{\text{cp}}} \cosh^{-1} [D_+ \cosh(\eta_+) - D_- \cos(\eta_-)] \right\} \\ D_{\pm} &= \frac{1}{2} \left[ \pm 1 + \frac{\Psi + 2\Delta\omega^2}{\sqrt{\Psi^2 + \xi^2}} \right] \\ \eta_{\pm} &= \tau_{\text{cp}} \sqrt{\frac{1}{2} (\pm \Psi + \sqrt{\Psi^2 + \xi^2})} \\ \Psi &= k_{\text{ex}}^2 - \Delta\omega^2 \\ \xi &= 2\Delta\omega([B]k_{\text{on}} - k_{\text{off}}) \\ k_{\text{ex}} &= [B]k_{\text{on}} + k_{\text{off}}, \end{aligned} \quad (7.8)$$

where  $R_2^0$  is the intrinsic relaxation rate in the absence of exchange and is assumed to be identical for the free and bound states; and  $\tau_{\text{CP}}$  is the delay between two successive  $180^\circ$  pulses in the CPMG pulse train.  $\tau_{\text{CP}}$  is thus a known, preset

parameter when the experiment is performed. If the interaction between protein and ligand is in the intermediate or slow exchange regime, it is possible to separate the parameter  $k_{\text{ex}}$  into  $[B]k_{\text{on}}$  and  $k_{\text{off}}$ .

In general, the concentration of unbound ligand—namely, the concentration of free B—is described by:

$$[B] = \frac{1}{2} \left\{ -K_D - [A]_0 + [B]_0 + \sqrt{(K_D + [A]_0 - [B]_0)^2 + 4[B]_0 K_D} \right\}, \quad (7.9)$$

where  $[A]_0$  and  $[B]_0$  are the total concentrations of A and B, respectively. To separate  $[B]k_{\text{on}}$  in order to calculate  $k_{\text{on}}$ , we notice that  $[B]$  depends on  $[A]_0$  and  $[B]_0$ . As a result, multiple samples with varying total amounts of  $[A]_0$  and/or  $[B]_0$  can be prepared, and global fits of the  $R_2$  relaxation dispersion profiles can be performed for the various samples. In most cases, it is wise to keep one of the concentrations constant, ideally the concentration  $[A]_0$  of the isotope-labeled protein, to obtain relaxation dispersion profiles with similar sensitivity from different measurements. Thus, it is most feasible to vary the total concentration of the unlabeled ligand  $[B]_0$ . As described in detail in ref. [31], it is necessary to include the total concentrations  $[A]_0$  and  $[B]_0$  as variable fitting parameters in the fitting procedure under realistic experimental conditions; otherwise, a 5% mismatch of the concentration can lead to a twofold error in the final  $K_D$  value. Moreover, the NMR samples for these experiments must be prepared with extreme care—preferably by dilution from single respective concentrated stock solutions—to obtain accurate concentration ratios. Taken together, relaxation dispersion is measured for multiple samples with multiple concentration ratios using a modified version of Eq. 7.9, in which the parameter  $a$  is introduced as follows:

$$[B] = \frac{1}{2} \left\{ -K_D - [A]_0 + a[B]_0 + \sqrt{(K_D + [A]_0 - a[B]_0)^2 + 4a[B]_0 K_D} \right\}. \quad (7.10)$$

#### 7.4.2.2 Example 1: Interaction Between the pKID Domain of CREB and the KIX Domain of CBP/p300

The method to obtain  $K_D$  by  $R_2$  relaxation dispersion was originally applied to study the phosphorylated kinase-inducible domain (pKID), an intrinsically disordered protein that forms part of the transcription factor CREB. pKID binds to the KIX domain of CBP/p300 [1]. To study the affinity of the two proteins, a  $[^{15}\text{N}]$ -labeled sample of pKID was prepared and relaxation dispersion profiles were obtained for samples with concentration ratios (KIX/pKID) of 0.95, 1.00, 1.05, and 1.10 at two distinct static magnetic fields of 500 and 800 MHz (Fig. 7.6).

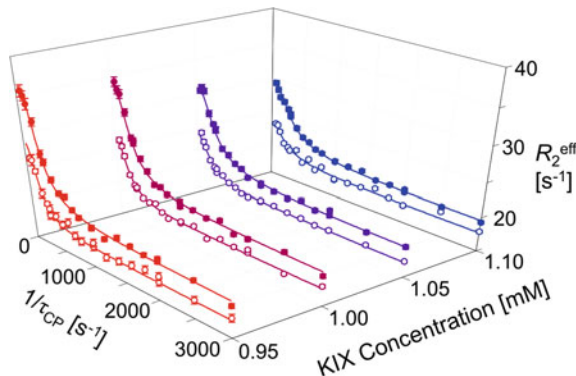
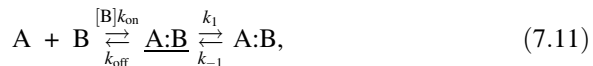


**Fig. 7.6** Protein–ligand ratio-dependent  $R_2$  relaxation dispersion profiles. The relaxation dispersion profiles were obtained at 800 MHz (filled circles) and 500 MHz (open circles). The data (reproduced with permission from [1]) show  $\text{Arg}^{124}$  of 1 mM pKID in the presence of 0.95, 1.00, 1.05, and 1.10 mM KIX. A global fit of the relaxation dispersion data provided the values of  $k_{\text{on}}$ ,  $k_{\text{off}}$ ,  $k_1$ ,  $k_{-1}$ , and  $K_D$ , as well as chemical shift differences between the distinct states

The induced fit model was used to fit all relaxation dispersion data (4 concentration ratios, 2  $B_0$  values) as follows:



where the underline indicates that the conformation of the state A:B is different from the final bound state A:B. For each residue, the chemical shift differences were defined as global parameters. The folding ( $k_1$ ) and unfolding ( $k_{-1}$ ) rates were considered as global parameters for all residues falling within the same cluster, that is, residues that are in close proximity in the same secondary structure element and thus presumably fold/unfold in a cooperative manner. As a result, it was possible to obtain site-specific  $K_D$  values for the binding of pKID to KIX. Strikingly, the mean  $K_D$  value obtained from the site-specific analysis showed excellent agreement with the global, macroscopic dissociation constant obtained by ITC [69]. Based on the relaxation dispersion data combined with chemical shift titrations, it was concluded that pKID engages with KIX, while it is unfolded through the formation of non-specific encounter complexes; upon KIX binding, pKID adopts a partially folded intermediate, which subsequently evolves toward a fully folded bound state. In other words, this model consists of four distinct states: free pKID, a non-specific encounter complex, a bound-folding intermediate, and the final bound-folded state. Note that this model assumes that the exchange between the free state and the encounter complex is too fast to be traceable by  $R_2$  relaxation dispersion. In summary, relaxation dispersion deciphered the coupled folding and binding mechanism of an intrinsically disordered protein.

#### 7.4.2.3 Example 2: Interaction Between the Transactivation Domain of c-Myb and KIX

The transactivation domain of c-Myb, a transcription factor, also binds the KIX domain. Similar to pKID, the transactivation domain of c-Myb is an intrinsically disordered protein [16]. Again, the mechanism of binding has been resolved in great molecular detail by  $R_2$  relaxation dispersion. In essence, it was deduced that the N-terminal region of c-Myb binds to KIX while already in a principally folded conformation. Conversely, the C-terminal region of c-Myb folds after binding to KIX, and again this binding is explained by an induced fit mechanism.

## 7.5 Fitting of the Relaxation Rates to a Theoretical Model

The theoretical model used for fitting depends on the exchange regime and the number of exchange sites. A vast amount of work has been done in the development of analytical equations to describe relaxation dispersion (Table 7.1). These equations can be used to fit the experimental relaxation dispersion profiles. Fitting can be performed by implementing a selected equation in commercial or free packages such as Mathematica, MatLab, SciLab, or similar software. Alternatively, a relaxation dispersion-dedicated free software package such as GLOVE ([http://www.scripps.edu/wright/?page\\_id=17](http://www.scripps.edu/wright/?page_id=17)) can be used. In the following, we illustrate both theoretical and practical aspects of fitting of relaxation dispersion data by GLOVE.

### 7.5.1 Least-Squares Fitting in GLOVE

GLOVE is a dedicated relaxation dispersion data-fitting software, although it also supports several other NMR experiments such as  $R_1$ ,  $R_2$ , and CLEANEX-PM [70].

**Table 7.1** Reports of analytical equations to approximate relaxation dispersion

Method	Exchange process	Reference
$R_{1\rho}$	2-Site fast exchange	[87]
$R_{1\rho}$	2-Site fast exchange	[88]
$R_{1\rho}$	2-Site exchange	[89]
$R_{1\rho}$	2-Site exchange	[90]
$R_{1\rho}$	2-Site exchange	[91]
$R_{1\rho}$	2-Site exchange	[26]
$R_{1\rho}$	$N$ -Site exchange	[92]
$R_2$	2-Site fast exchange	[93]
$R_2$	2-Site exchange	[94]
$R_2$	2-Site exchange	[87]
$R_2$	2-Site exchange	[68]
$R_2$	2-Site exchange	[95]

It solves nonlinear least square problems by using the algorithm of Levenberg–Marquardt. GLOVE is written in C++, which assures rapid fitting of the data. To fit the relaxation dispersion profiles, the GLOVE software attempts to minimize the statistical variable  $\chi^2$  in an iterative manner.  $\chi^2$  is given as a function of the experimental and calculated effective  $R_2$  rates:

$$\chi^2 = \sum_{i=1}^N \left( \frac{R_2^{i,\text{exp}} - R_2^{i,\text{calc}}}{\sigma^i} \right)^2. \quad (7.12)$$

where the variables  $R_2^{i,\text{exp}}$  and  $R_2^{i,\text{calc}}$  denote the experimental and calculated values of  $R_2^{\text{eff}}$ , respectively; and the parameter  $\sigma^i$  represents the experimental error.

To minimize the function iteratively, initial parameters must be provided. In GLOVE, there are five distinct methods to provide the initial parameters. Importantly, it is possible to run multiple methods or to repeat the same method. The program stores the parameter set corresponding to the lowest obtained value of  $\chi^2$  and replaces this set if a better fit (a lower value of  $\chi^2$ ) is found.

The method named *ONE* is a minimization routine that starts from the lowest limit or an optionally specified value. As soon as the minimization routine finds a local minimum, the fitting process stops. *ONEEX* is equivalent to *ONE*, with the exception that the fitting process does not stop until both global and local parameters (optimized separately) have converged into local minima. When global fitting of parameters is desired, it is advisable to use *ONEEX* even though the fit converges more slowly. The methods *GRID*, *RANDOM*, and *MCMIN* stop when they reach the same condition as described for *ONE*; however, they explore the parameter space much more rapidly at the earlier stages of the fitting procedure.

As indicated by its name, *GRID* represents a grid search. Initially, the global parameters are fixed (to a given grid point) and the local parameters of each dataset are varied using a grid search algorithm. Next, the fix on the global parameters is removed, and then, all parameters including global parameters are optimized. The procedure is iterated to explore all grid points of the parameter space of the global parameters.

Lastly, the methods *RANDOM* and *MCMIN* represent a random search and minimization by a Monte Carlo algorithm, respectively. *RANDOM* uses a random number generator to choose a random initial value from a range of parameters, and  $\chi^2$  is subsequently minimized by other iterative methods as specified by the user. Thus, *RANDOM* can be used to quickly find good starting values to determine the global minimum from the entire range of specified parameters. Conversely, *MCMIN* achieves a more accurate determination of the global minimum after initial establishment of the fit parameter set provided by *RANDOM* and other methods. This Monte Carlo implementation in GLOVE is described in detail in the next section.

### 7.5.2 Monte Carlo Minimization Algorithm in GLOVE

Monte Carlo minimization is a popular method in molecular simulations. For example, it has been used to find the global energy minimum during the folding of a peptide structure by randomly varying the dihedral angles in order to overcome large energy barriers [71]. In a protein-folding context, the Metropolis criterion is used to compare the newly energy-minimized structure with a previous conformation [72, 73]. In the minimization context of GLOVE, the initial parameter values are the currently available best-fit parameters to which positive or negative random numbers, which follow a Gaussian distribution, are added. This enables the parameter set to overcome the barriers of a local minimum. The newly obtained parameter set can then be minimized by using conventional least-squares methods as described above. If the new  $\chi^2$  is smaller than the previous value, the Monte Carlo step is accepted.

Monte Carlo minimization (*MCMIN*) runs until no better parameter set is found for a total number of iterations as specified by the user; in general, this number is higher than 5. Moreover, if a lower value of  $\chi^2$  is obtained, the iteration counter is reset to 0. The magnitude of the Monte Carlo trial steps can be controlled by the user by specifying a scaling factor in the input file to GLOVE. For efficient minimization of  $\chi^2$ , it is important to choose this factor judiciously. In particular, a too small scaling factor would not overcome the barriers of a local minimum efficiently. Conversely, if the scaling factor is too large, resulting in a large Monte Carlo step, the new set of parameters may be completely different from the current best parameter set, which may lead to a marked increase in the value of  $\chi^2$ . An efficient protocol to determine the global minimum most accurately and rapidly is therefore to run *MCMIN* multiple times with successively smaller scaling factors. Because the fitting parameters are far from the best-fit solution at the early stages of fitting, the *MCMIN* scaling factor should be set to a comparably large value. The parameters can be varied very finely by using a small scaling factor in the final stages of the fitting in order to determine the global minimum most accurately.

### 7.5.3 Two-State Exchange

For simplicity, we describe the most common model used to fit relaxation dispersion data; however, many additional published equations, including two- and three-state exchanges, are available within GLOVE. A relaxation dispersion profile, which reports on a two-state exchange process (Eq. 7.1), is described by the equation of Carver and Richards [68] for all exchange regimes under realistic

experimental conditions. The Carver and Richards equation calculates the effective transverse relaxation constant  $R_2^{\text{eff}}$  as:

$$\begin{aligned}
 R_2^{\text{eff}} &= \frac{1}{2} \left\{ R_{2A}^0 + R_{2B}^0 + k_{AB} + k_{BA} - \frac{1}{\tau_{\text{CP}}} \cosh^{-1} [D_+ \cosh(\eta_+) - D_- \cos(\eta_-)] \right\} \\
 D_{\pm} &= \frac{1}{2} \left[ \pm 1 + \frac{\Psi + 2\Delta\omega^2}{\sqrt{\Psi^2 + \zeta^2}} \right] \\
 \eta_{\pm} &= \tau_{\text{CP}} \sqrt{\frac{1}{2} \left( \pm \Psi + \sqrt{\Psi^2 + \zeta^2} \right)} \\
 \Psi &= (R_{2A}^0 - R_{2B}^0 + k_{AB} - k_{BA})^2 - \Delta\omega^2 + 4k_{AB}k_{BA} \\
 \zeta &= 2\Delta\omega(R_{2A}^0 - R_{2B}^0 + k_{AB} - k_{BA}).
 \end{aligned} \tag{7.13}$$

Equation 7.13 resembles Eq. 7.8 but has a more general nature. In Eq. 7.13,  $\Delta\omega$  denotes the difference in chemical shift between the states A and B and has the units  $\text{rad s}^{-1}$ ; and  $R_{2A}^0$  and  $R_{2B}^0$  are the transverse relaxation rates of the respective states A and B. Note that Eq. 7.13 considers that these values differ: In principle, the intrinsic transverse relaxation rates may be different; however, in practice, they are usually assumed to be the same. Thus,

$$R_2^0 = R_{2A}^0 = R_{2B}^0. \tag{7.14}$$

Importantly, this assumption does not have a large effect on the analysis of the exchange process in the case that the rate of the exchange is larger than the difference between  $R_{2A}^0$  and  $R_{2B}^0$  (i.e., if  $k_{\text{ex}} \gg |R_{2A}^0 - R_{2B}^0|$ ). Moreover, we reduce the parameter space by defining  $k_{\text{ex}}$  as the sum of the reaction rates of the forward and backward reaction. Thus,

$$k_{\text{ex}} = k_{AB} + k_{BA}. \tag{7.15}$$

In addition, the product of  $p_A \times p_B$  is treated as a single fitting parameter  $a = p_A p_B$ . After fitting,  $p_B$  (the population of the minor state) can then be calculated as:

$$p_B = \frac{\sqrt{1 - 4a}}{2}. \tag{7.16}$$

This further enhances the efficiency and stability of the calculation. In summary, the Carver and Richards equation [68] is implemented in GLOVE as:

$$\begin{aligned}
 R_2^{\text{eff}} &= R_2^0 + \frac{1}{2} \left\{ k_{\text{ex}} - \frac{1}{\tau_{\text{CP}}} \cosh^{-1} [D_+ \cosh(\eta_+) - D_- \cos(\eta_-)] \right\} \\
 D_{\pm} &= \frac{1}{2} \left[ \pm 1 + \frac{\Psi + 2\Delta\omega^2}{\sqrt{\Psi^2 + \xi^2}} \right] \\
 \eta_{\pm} &= \tau_{\text{CP}} \sqrt{\frac{1}{2} \left( \pm \Psi + \sqrt{\Psi^2 + \xi^2} \right)} \\
 \Psi &= k_{\text{ex}}^2 - \Delta\omega^2 \\
 \xi &= 2\Delta\omega k_{\text{ex}} \sqrt{1 - 4p_{\text{AP}}p_{\text{B}}}.
 \end{aligned} \tag{7.17}$$

Note that GLOVE calculates the partial derivatives of  $R_2^{\text{eff}}$  (required by the least-squares minimization algorithm) with respect to the fitting parameters analytically instead of numerically, which helps to speed up the calculation.

#### 7.5.4 Workflow for Processing Relaxation Dispersion Data in GLOVE

In this section, a practical approach to processing relaxation dispersion data using the software package GLOVE is presented. First, the relaxation dispersion spectra are measured. In the case of  $R_{1\rho}$  relaxation dispersion data, *Amaterasu* can be used, which will automatically pass the relaxation rates and spin-lock powers to GLOVE.

In the case of  $R_2$  relaxation dispersion data, additional steps are necessary. Initially, all spectra are processed by exactly the same processing parameters, including the functions for solvent suppression, apodization, Fourier transform, zero- and first-order phase correction, and baseline correction. It is advisable to use a low order for the baseline correction function in order not to perturb the intensities of relatively small signals. It is not feasible to apply linear prediction because it may interfere with quantitative analysis of the NMR data. However, it is possible to reduce the acquisition time of relaxation dispersion datasets by nonlinear sampling methods [74]. Next, it is necessary to obtain the integrated peak intensities to calculate the effective transverse relaxation rates. This is done by using the tool *pkfit*, which is included in the GLOVE package. The experimental error in the peak intensity is calculated from the standard deviation of the amplitudes of the noise in each spectrum and the deviation between peak intensities in duplicated data. Thus, after running *pkfit*, the output file contains the static magnetic field  $B_0$  (MHz), the relaxation time  $T_{\text{CPMG}}$  (s), and the peak intensities of all resonances as a function of  $1/\tau_{\text{CP}}$  ( $\text{s}^{-1}$ ). The delay  $\tau_{\text{CP}}$  in the pulse sequence is the time between two  $180^\circ$  pulses of the CPMG pulse train. Note that some groups use a different notation by defining  $\tau_{\text{CPMG}}$  as half the delay between two  $180^\circ$  pulses; in this case, the relaxation rates are plotted as a function of  $v_{\text{CPMG}} = 1/(4\tau_{\text{CPMG}})$  instead of  $1/\tau_{\text{CP}}$ .

Although the horizontal axis differs in the two representations, it is straightforward to convert  $v_{\text{CPMG}}$  to  $1/\tau_{\text{CP}}$  according to:

$$1/\tau_{\text{CP}} = 2v_{\text{CPMG}}. \quad (7.18)$$

In complete analogy to Eq. 7.6, the effective  $R_2^{\text{eff}}$  relaxation rates are then calculated according to:

$$R_2^{\text{eff}}(\tau_{\text{CP}}) = -\frac{1}{T_{\text{CPMG}}} \ln \left( \frac{I(\tau_{\text{CP}})}{I_0} \right), \quad (7.19)$$

where  $I(\tau_{\text{CP}})$  is the peak intensity in the spectrum corresponding to a particular value of  $\tau_{\text{CP}}$ ; and  $I_0$  is the intensity in a reference spectrum in which the relaxation block is omitted (by setting  $T_{\text{CPMG}} = 0$ ). This calculation is carried out by the tool *cpmg2glove* in the GLOVE package. Moreover, the experimental error in  $R_2^{\text{eff}}$  is calculated from the spectral RMSD noise according to [75]:

$$\sigma^i = \frac{\varepsilon_I}{I(\tau_{\text{CP}}) \times T_{\text{CPMG}}}, \quad (7.20)$$

where  $\varepsilon_I$  is the RMSD noise of the spectrum. The output of the tool *cpmg2glove* is the input file for GLOVE and contains all data necessary to perform curve fitting of the relaxation dispersion profile. The file may contain only one measurement or multiple different measurements (e.g., under different values of  $B_0$ , temperatures or ligand concentrations).

After fitting of the  $R_{1\rho}$  or  $R_2$  relaxation dispersion data, GLOVE writes an output file containing a summary of the results and plots of the fitted relaxation dispersion profile in the format Xmgr or Grace. An Xmgr file for each resonance of the dataset is created, but it is possible to combine all of these plots in a single PDF file for convenience. This is achieved by the tool *mplot*, which is included in the GLOVE package. During the fitting process, GLOVE will write the reduced value of  $\chi^2$ , which is  $\chi^2$  divided by the number of degrees of freedom of the fitting model, to the standard output (typically, the console), enabling the user to monitor the convergence of the fit in real time. Uncertainties in the resulting fitting parameters can be calculated by standard deviation, Monte Carlo, and/or jackknife methods [76, 77].

### 7.5.5 Examples of Relaxation Dispersion Curve Fitting by GLOVE

Here, we illustrate curve fitting of relaxation dispersion data by fitting the  $R_2$  relaxation dispersion profiles of KIX. In total, 110  $R_2$  relaxation dispersion profiles (55 resonances; 2 values of  $B_0$ ) were subjected to analysis. KIX exhibits a two-state exchange between its native and a non-native conformation [78]. The relaxation

dispersion profiles were obtained at two distinct magnetic fields on a Bruker DRX600 and a Bruker DMX750 spectrometer at a temperature of 25 °C using a [<sup>15</sup>N]-labeled sample of KIX (concentration: 0.5 mM) [74]. Spectra were acquired for  $\tau_{\text{CP}}$  values of 10, 5, 3.33, 2.5, 2.0, 1.66, 1.43, 1.25, 1.0, 0.83, 0.71, 0.63, 0.55, 0.5, 0.4, and 0.33 ms at a relaxation time,  $T_{\text{CPMG}}$ , of 40 ms.

The performance of GLOVE was evaluated on an Apple iMac (Intel Core i7 dual core, 3.4 GHz) with the GLOVE executable file compiled by using the Intel C++ compiler [50]. The speed and accuracy of the fit were evaluated by using the directives *ONE*, *ONEEX*, and *GRID*. In addition, the combinations *GRID + ONEEX*, *RANDOM + ONEEX*, *MCMIN + ONEEX*, and *RANDOM + MCMIN + ONEEX* were tested. A combined workflow of *RANDOM + MCMIN + ONEEX* was found to yield the best results [50].

The relaxation dispersion profiles of KIX were subjected to a global fit using the Carver and Richards equation [68]. The exchange rate  $k_{\text{ex}}$  and the product of the populations  $p_{APB}$  were specified as global parameters. The possible range of the parameters was specified as [100–2500] for  $\Delta\omega$ , [5–4000] for  $k_{\text{ex}}$ , and [0.005–0.09] for the product  $p_{APB}$ . The initial parameter value of  $R_2^0$  was taken from the lowest value of  $R_2^{\text{eff}}$  (the right-most data point in the relaxation dispersion profile). For the minimization routines *ONE*, *ONEEX*, and *MCMIN*, the calculation starts from the lower limits of the parameter range. In the evaluation study, grid sizes from 2 to 20 were evaluated for the method *GRID* for the parameters  $\Delta\omega$ ,  $k_{\text{ex}}$ ,  $p_{APB}$  [50]. In *MCMIN*, the scaling factor was sequentially reduced from 0.1 to a final value of 0.001. Note that, because *RANDOM* and *MCMIN* rely on random number generators, they provide a different result at each execution. Thus, methods relying only on *RANDOM* or *MCMIN* alone were repeated 10 times to evaluate the average and standard deviation of each fit.

The 110 relaxation dispersion profiles of KIX were subjected to a global fit, where the overall lowest value of  $\chi^2$ , reached by many methods, was 1.45047, indicating that it represents the global minimum. At this value of  $\chi^2$ , the global parameters of the exchange rate  $k_{\text{ex}}$  converged to  $600 \pm 5 \text{ s}^{-1}$ . Moreover, the product of  $p_{APB}$  converged to  $0.0343 \pm 0.0002$ . Examples of the corresponding relaxation dispersion profiles are shown in Fig. 7.7. Note that these plots were obtained directly from GLOVE and no further adjustment of the image to obtain publication quality was necessary.

The global minimum was not found by *ONE*, which means that relaxation dispersion profile fitting has the intrinsic problem of becoming trapped in local minima (Table 7.2). Thus, good initial values, or alternatively multiple fits starting from different initial parameters, are necessary to find the global minimum. *ONEEX* found a smaller  $\chi^2$  value; however, it did not locate the global minimum either. The *GRID* method with a grid size of 11 resulted in a  $\chi^2$  value of 1.45056, which is very near to the global minimum. Moreover, when *ONEEX* was followed by *GRID*, the global minimum was always found. Thus, *ONEEX* is very useful at the last stages of the fit to converge to the global minimum. Importantly, fitting strategies that used only *RANDOM* or *MCMIN* alone did not find the global minimum. Conversely,

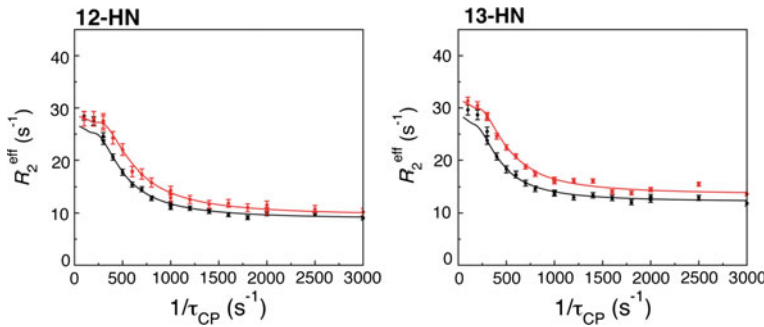


**Fig. 7.7** Relaxation dispersion profiles for KIX as fitted by GLOVE. The *best-fit curves* are shown for a dataset collected at a  $^{15}\text{N}$  frequency of 60.83 MHz (black line) and 76.01 MHz (red line), respectively. Residue numbers are indicated at the *top* (-HN)

**Table 7.2** Relaxation dispersion curve-fitting methods in GLOVE

Method	Reduced $\chi^2$ value <sup>a</sup>
ONE	14.9719
ONEEX	9.82986
RANDOM + ONEEX	2.06638 → 1.45047
RANDOM + MCMIN + ONEEX	3.70891 → 1.45052 → 1.45047
MCMIN + ONEEX	9.54153 → 8.93963

Additional details are given in Ref. [50]

<sup>a</sup>The initial reduced  $\chi^2$  was 88.7611

when applying *ONEEX* after *RANDOM*, the global minimum was always found. Likewise, the combination *RANDOM + MCMIN + ONEEX* always found the global minimum and was computationally faster than other methods.

## 7.6 Outlook

Without a doubt, both  $R_{1\rho}$  and  $R_2$  relaxation dispersion will continue to contribute to the elucidation of a myriad of functionally important dynamical processes in the life of biomolecules such as proteins and nucleic acids. If sufficiently accurate relaxation dispersion profiles are obtained, standard desktop computers are now fast enough to solve Bloch–McConnell equations numerically without relying on approximate methods (Table 7.1). Application of relaxation dispersion to larger molecules

remains challenging because of signal overlap and other complications; however, methods are continuously being developed to tackle these challenges [79–82].

The great wealth of information provided by relaxation dispersion sometimes overshadows the most important question in this context. What *is* the excited state? Even if relaxation dispersion can be unambiguously detected for a specific site in a biomolecule, initially it is often unknown what the dynamical process in question is. In other words, it is necessary to “assign” the excited state unambiguously.

If  $\Delta\omega$  can be successfully derived in terms of both sign and magnitude, the chemical shift of the excited state may provide hints about its structural nature. A combination of relaxation dispersion with chemical shift-based methods such as CS-ROSETTA is particularly useful in this case [83]. Alternatively, the excited state chemical shift determined from  $\Delta\omega$  may be compared with database reference chemical shifts from known structures or chemical shifts calculated by density functional theory [11]. Although the millisecond timescale exceeds the computational cost of most current laboratories for direct visualization of the dynamics by molecular dynamics (MD) simulations, visualization of possible dynamical processes by steered MD simulations is a potential computationally inexpensive approach [11]. In addition, comparison of the experimental relaxation dispersion-derived kinetic–thermodynamic data obtained from relaxation dispersion profiles acquired at different temperatures with theoretical free-energy calculations seems to be a successful strategy [11]. Lastly, it has been demonstrated that including additional biophysical methods such as single-molecule Förster resonance energy transfer (FRET), time-resolved X-ray crystallography, and principle component analysis (PCA) of conventional MD trajectories can successfully establish dynamical models of protein function over a wide range of timescales [84].

## References

1. Sugase, K., Dyson, H.J., Wright, P.E.: Mechanism of coupled folding and binding of an intrinsically disordered protein. *Nature* **447**, 1021–1025 (2007)
2. Sugase, K., Lansing, J.C., Dyson, H.J., Wright, P.E.: Tailoring relaxation dispersion experiments for fast-associating protein complexes. *J. Am. Chem. Soc.* **129**, 13406–13407 (2007)
3. Boehr, D.D., McElheny, D., Dyson, H.J., Wright, P.E.: The dynamic energy landscape of dihydrofolate reductase catalysis. *Science* **313**, 1638–1642 (2006)
4. Henzler-Wildman, K.A., Thai, V., Lei, M., Ott, M., Wolf-Watz, M., Fenn, T., Pozharski, E., Wilson, M.A., Petsko, G.A., Karplus, M., Hübner, C.G., Kern, D.: Intrinsic motions along an enzymatic reaction trajectory. *Nature* **450**, 838–844 (2007)
5. Eisenmesser, E.Z., Millet, O., Labeikovsky, W., Korzhnev, D.M., Wolf-Watz, M., Bosco, D. A., Skalicky, J.J., Kay, L.E., Kern, D.: Intrinsic dynamics of an enzyme underlies catalysis. *Nature* **438**, 117–121 (2005)
6. Whittier, S.K., Hengge, A.C., Loria, J.P.: Conformational motions regulate phosphoryl transfer in related protein tyrosine phosphatases. *Science* **341**, 899–903 (2013)
7. Bhabha, G., Lee, J., Ekiert, D.C., Gam, J., Wilson, I.A., Dyson, H.J., Benkovic, S.J., Wright, P.E.: A Dynamic knockout reveals that conformational fluctuations influence the chemical step of enzyme catalysis. *Science* **332**, 234–238 (2011)

8. Harada, E., Sugishima, M., Harada, J., Fukuyama, K., Sugase, K.: Distal regulation of heme binding of heme oxygenase-1 mediated by conformational fluctuations. *Biochemistry* **54**, 340–348 (2015)
9. Sprangers, R., Gribun, A., Hwang, P.M., Houry, W.A., Kay, L.E.: Quantitative NMR spectroscopy of supramolecular complexes: dynamic side pores in ClpP are important for product release. *Proc. Natl. Acad. Sci. U S A* **102**, 315–320 (2005)
10. Kimsey, I.J., Petzold, K., Sathyamoorthy, B., Stein, Z.W., Al-Hashimi, H.M.: Visualizing transient Watson–Crick-like mispairs in DNA and RNA duplexes. *Nature* **519**, 315–320 (2015)
11. Nikolova, E.N., Kim, E., Wise, A.A., O’Brien, P.J., Andrecioaei, I., Al-Hashimi, H.M.: Transient Hoogsteen base pairs in canonical duplex DNA. *Nature* **470**, 498–502 (2011)
12. Morimoto, D., Walinda, E., Fukada, H., Sugase, K., Shirakawa, M.: Ubiquitylation directly induces fold destabilization of proteins. *Sci. Rep.* **6**, 1–9 (2016)
13. Meinhold, D.W., Wright, P.E.: Measurement of protein unfolding/refolding kinetics and structural characterization of hidden intermediates by NMR relaxation dispersion. *Proc. Natl. Acad. Sci. U S A* **108**, 9078–9083 (2011)
14. Yanagi, K., Sakurai, K., Yoshimura, Y., Konuma, T., Lee, Y.-H., Sugase, K., Ikegami, T., Naiki, H., Goto, Y.: The monomer–seed interaction mechanism in the formation of the  $\beta$ 2-microglobulin amyloid fibril clarified by solution NMR techniques. *J. Mol. Biol.* **422**, 390–402 (2012)
15. Neudecker, P., Robustelli, P., Cavalli, A., Walsh, P., Lundstrom, P., Zarrine-Afsar, A., Sharpe, S., Vendruscolo, M., Kay, L.E.: Structure of an intermediate state in protein folding and aggregation. *Science* **336**, 362–366 (2012)
16. Arai, M., Sugase, K., Dyson, H.J., Wright, P.E.: Conformational propensities of intrinsically disordered proteins influence the mechanism of binding and folding. *Proc. Natl. Acad. Sci. U S A* **112**, 9614–9619 (2015)
17. Schneider, R., Maurin, D., Communie, G., Kragelj, J., Hansen, D.F., Ruigrok, R.W., Jensen, M.R., Blackledge, M.: Visualizing the molecular recognition trajectory of an intrinsically disordered protein using multinuclear relaxation dispersion NMR. *J. Am. Chem. Soc.* **137**, 1220–1229 (2015)
18. Tzeng, S.R., Kalodimos, C.G.: Dynamic activation of an allosteric regulatory protein. *Nature* **462**, 368–372 (2009)
19. Carr, H.Y., Purcell, E.M.: Effects of diffusion on free precession in nuclear magnetic resonance experiments. *Phys. Rev.* **94**, 630–638 (1954)
20. Loria, J.P., Rance, M., Palmer, A.G.: A relaxation-compensated Carr–Purcell–Meiboom–Gill sequence for characterizing chemical exchange by NMR spectroscopy. *J. Am. Chem. Soc.* **121**, 2331–2332 (1999)
21. Meiboom, S., Gill, D.: Modified spin-echo method for measuring nuclear relaxation times. *Rev. Sci. Instrum.* **29**, 688–691 (1958)
22. Hansen, A.L., Nikolova, E.N., Casiano-Negrón, A., Al-Hashimi, H.M.: Extending the range of microsecond-to-millisecond chemical exchange detected in labeled and unlabeled nucleic acids by selective carbon  $R_{1p}$  NMR spectroscopy. *J. Am. Chem. Soc.* **131**, 3818–3819 (2009)
23. Hansen, D.F., Vallurupalli, P., Kay, L.E.: Using relaxation dispersion NMR spectroscopy to determine structures of excited, invisible protein states. *J. Biomol. NMR* **41**, 113–120 (2008)
24. Walinda, E., Morimoto, D., Nishizawa, M., Shirakawa, M., Sugase, K.: Efficient identification and analysis of chemical exchange in biomolecules by  $R_{1p}$  relaxation dispersion with *Amaterasu*. *Bioinformatics* **32**, 2539–2541 (2016)
25. Korzhnev, D.M., Orekhov, V.Y., Kay, L.E.: Off-resonance  $R_{1p}$  NMR studies of exchange dynamics in proteins with low spin-lock fields: an application to a Fyn SH3 domain. *J. Am. Chem. Soc.* **127**, 713–721 (2005)
26. Miloushev, V.Z., Palmer, A.G.:  $R_{1p}$  relaxation for two-site chemical exchange: general approximations and some exact solutions. *J. Magn. Reson.* **177**, 221–227 (2005)

27. Massi, F., Grey, M.J., Palmer, A.G.: Microsecond timescale backbone conformational dynamics in ubiquitin studied with NMR  $R_{1p}$  relaxation experiments. *Protein Sci.* **14**, 735–742 (2005)
28. Massi, F., Johnson, E., Wang, C., Rance, M., Palmer, A.G.: NMR  $R_{1p}$  rotating-frame relaxation with weak radio frequency fields. *J. Am. Chem. Soc.* **126**, 2247–2256 (2004)
29. Palmer, A.G., Kroenke, C.C., Loria, J.P.: Nuclear magnetic resonance methods for quantifying microsecond-to-millisecond motions in biological macromolecules. *Methods Enzymol.* **339**, 204–238 (2001)
30. Bothe, J.R., Nikolova, E.N., Eichhorn, C.D., Chugh, J., Hansen, A.L., Al-Hashimi, H.M.: Characterizing RNA dynamics at atomic resolution using solution-state NMR spectroscopy. *Nat. Methods* **8**, 919–931 (2011)
31. Furukawa, A., Konuma, T., Yanaka, S., Sugase, K.: Quantitative analysis of protein–ligand interactions by NMR. *Prog. Nucl. Magn. Reson. Spectrosc.* **96**, 47–57 (2016)
32. Loria, J.P., Rance, M., Palmer, A.G.: A TROSY CPMG sequence for characterizing chemical exchange in large proteins. *J. Biomol. NMR* **15**, 151–155 (1999)
33. Tollinger, M., Skrynnikov, N.R., Mulder, F.A., Forman-Kay, J.D., Kay, L.E.: Slow dynamics in folded and unfolded states of an SH3 domain. *J. Am. Chem. Soc.* **123**, 11341–11352 (2001)
34. Skrynnikov, N.R., Mulder, F.A., Hon, B., Dahlquist, F.W., Kay, L.E.: Probing slow time scale dynamics at methyl-containing side chains in proteins by relaxation dispersion NMR measurements: application to methionine residues in a cavity mutant of T4 lysozyme. *J. Am. Chem. Soc.* **123**, 4556–4566 (2001)
35. Ishima, R., Torchia, D.A.: Extending the range of amide proton relaxation dispersion experiments in proteins using a constant-time relaxation-compensated CPMG approach. *J. Biomol. NMR* **25**, 243–348 (2003)
36. Orekhov, V.Y., Korzhnev, D.M., Kay, L.E.: Double-and zero-quantum NMR relaxation dispersion experiments sampling millisecond time scale dynamics in proteins. *J. Am. Chem. Soc.* **126**, 1886–1891 (2004)
37. Guenneugues, M., Berthault, P., Desvaux, H.: A method for determining  $B_1$  field inhomogeneity: are the biases assumed in heteronuclear relaxation experiments usually underestimated? *J. Magn. Reson.* **136**, 118–126 (1999)
38. Ban, D., Gossert, A.D., Giller, K., Becker, S., Griesinger, C., Lee, D.: Exceeding the limit of dynamics studies on biomolecules using high spin-lock field strengths with a cryogenically cooled probehead. *J. Magn. Reson.* **221**, 1–4 (2012)
39. Szyperski, T., Luginbühl, P., Otting, G., Güntert, P., Wüthrich, K.: Protein dynamics studied by rotating frame  $^{15}\text{N}$  spin relaxation times. *J. Biomol. NMR* **3**, 151–164 (1993)
40. Mulder, F.A., de Graaf, R.A., Kaptein, R., Boelens, R.: An off-resonance rotating frame relaxation experiment for the investigation of macromolecular dynamics using adiabatic rotations. *J. Magn. Reson.* **131**, 351–357 (1998)
41. Zinn-Justin, S., Berthault, P., Guenneugues, M., Desvaux, H.: Off-resonance RF fields in heteronuclear NMR: application to the study of slow motions. *J. Biomol. NMR* **10**, 363–372 (1997)
42. Akke, M., Palmer, A.G.: Monitoring macromolecular motions on microsecond to millisecond time scales by  $R_{1p}$ – $R_1$  constant relaxation time NMR spectroscopy. *J. Am. Chem. Soc.* **118**, 911–912 (1996)
43. Cavanagh, J., Fairbrother, W.J., Palmer, A.G., Skelton, N.J.: *Protein NMR Spectroscopy: Principles and Practice*. Academic Press, New York (1996)
44. Walinda, E., Morimoto, D., Shirakawa, M., Sugase, K.: Practical considerations for investigation of protein conformational dynamics by  $^{15}\text{N}$   $R_{1p}$  relaxation dispersion. *J. Biomol. NMR* **67**, 201–209 (2017)
45. Hartmann, S., Hahn, E.: Nuclear double resonance in the rotating frame. *Phys. Rev.* **128**, 2042–2053 (1962)
46. Pelupessy, P., Chiarparin, E.: Hartmann–Hahn polarization transfer in liquids: an ideal tool for selective experiments. *Concepts Magn. Reson.* **12**, 103–124 (2000)

47. Bak, M., Rasmussen, J.T., Nielsen, N.C.: SIMPSON: a general simulation program for solid-state NMR spectroscopy. *J. Magn. Reson.* **213**, 366–400 (2011)
48. Helmus, J.J., Jaroniec, C.P.: Nmrglue: an open source Python package for the analysis of multidimensional NMR data. *J. Biomol. NMR* **55**, 355–367 (2013)
49. Chen, L., Weng, Z., Goh, L., Garland, M.: An efficient algorithm for automatic phase correction of NMR spectra based on entropy minimization. *J. Magn. Reson.* **158**, 164–168 (2002)
50. Sugase, K., Konuma, T., Lansing, J.C., Wright, P.E.: Fast and accurate fitting of relaxation dispersion data using the flexible software package GLOVE. *J. Biomol. NMR* **56**, 275–283 (2013)
51. Vallurupalli, P., Hansen, D.F., Kay, L.E.: Structures of invisible, excited protein states by relaxation dispersion NMR spectroscopy. *Proc. Natl. Acad. Sci. U S A* **105**, 11766–11771 (2008)
52. Jiang, B., Yu, B., Zhang, X., Liu, M., Yang, D.: A  $^{15}\text{N}$  CPMG relaxation dispersion experiment more resistant to resonance offset and pulse imperfection. *J. Magn. Reson.* **257**, 1–7 (2015)
53. LaPlante, S.R., Aubry, N., Déziel, R., Ni, F., Xu, P.: Transferred  $^{13}\text{C}$   $T_1$  relaxation at natural isotopic abundance: a practical method for determining site-specific changes in ligand flexibility upon binding to a macromolecule. *J. Am. Chem. Soc.* **122**, 12530–12535 (2000)
54. Su, X.-C., Jergic, S., Ozawa, K., Burns, N.D., Dixon, N.E., Otting, G.: Measurement of dissociation constants of high-molecular weight protein–protein complexes by transferred  $^{15}\text{N}$ -relaxation. *J. Biomol. NMR* **38**, 65–72 (2007)
55. Williamson, M.P.: Using chemical shift perturbation to characterise ligand binding. *Prog. Nucl. Magn. Reson. Spectrosc.* **73**, 1–16 (2013)
56. Walinda, E., Morimoto, D., Sugase, K., Konuma, T., Tochio, H., Shirakawa, M.: Solution structure of the ubiquitin-associated (UBA) domain of human autophagy receptor NBR1 and its interaction with ubiquitin and polyubiquitin. *J. Biol. Chem.* **289**, 13890–13902 (2014)
57. Hansen, D.F., Vallurupalli, P., Kay, L.E.: An improved  $^{15}\text{N}$  relaxation dispersion experiment for the measurement of millisecond time-scale dynamics in proteins. *J. Phys. Chem. B* **112**, 5898–5904 (2008)
58. Vallurupalli, P., Hansen, D.F., Stollar, E., Meirovitch, E., Kay, L.E.: Measurement of bond vector orientations in invisible excited states of proteins. *Proc. Natl. Acad. Sci. U S A* **104**, 18473–18477 (2007)
59. Farrow, N.A., Zhang, O., Forman-Kay, J.D., Kay, L.E.: A heteronuclear correlation experiment for simultaneous determination of  $^{15}\text{N}$  longitudinal decay and chemical exchange rates of systems in slow equilibrium. *J. Biomol. NMR* **4**, 727–734 (1994)
60. Sahu, D., Clore, G.M., Iwahara, J.: TROSY-based z-exchange spectroscopy: application to the determination of the activation energy for intermolecular protein translocation between specific sites on different DNA molecules. *J. Am. Chem. Soc.* **129**, 13232–13237 (2007)
61. Li, Y., Palmer, A.G.: TROSY-selected ZZ-exchange experiment for characterizing slow chemical exchange in large proteins. *J. Biomol. NMR* **45**, 357–360 (2009)
62. Vallurupalli, P., Bouvignies, G., Kay, L.E.: Studying “invisible” excited protein states in slow exchange with a major state conformation. *J. Am. Chem. Soc.* **134**, 8148–8161 (2012)
63. Bouvignies, G., Kay, L.E.: A 2D  $^{13}\text{C}$ -CEST experiment for studying slowly exchanging protein systems using methyl probes: an application to protein folding. *J. Biomol. NMR* **53**, 303–310 (2012)
64. Fawzi, N.L., Ying, J., Ghirlando, R., Torchia, D.A., Clore, G.M.: Atomic-resolution dynamics on the surface of amyloid- $\beta$  protofibrils probed by solution NMR. *Nature* **480**, 268–272 (2011)
65. Demers, J.P., Mittermaier, A.: Binding mechanism of an SH3 domain studied by NMR and ITC. *J. Am. Chem. Soc.* **131**, 4355–4367 (2009)
66. McConnell, H.M.: Reaction rates by nuclear magnetic resonance. *J. Chem. Phys.* **28**, 430–431 (1958)

67. Korzhnev, D.M., Salvatella, X., Vendruscolo, M., Di Nardo, A.A., Davidson, A.R., Dobson, C.M., Kay, L.E.: Low-populated folding intermediates of Fyn SH3 characterized by relaxation dispersion NMR. *Nature* **430**, 586–590 (2004)
68. Carver, J.P., Richards, R.E.: A general two-site solution for the chemical exchange produced dependence of  $T_2$  upon the Carr–Purcell pulse separation. *J. Magn. Reson.* **6**, 89–105 (1969)
69. Goto, N.K., Zor, T., Martinez-Yamout, M., Dyson, H.J., Wright, P.E.: Cooperativity in transcription factor binding to the coactivator CREB-binding protein (CBP). The mixed lineage leukemia protein (MLL) activation domain binds to an allosteric site on the KIX domain. *J. Biol. Chem.* **277**, 43168–43174 (2002)
70. Hwang, T.-L., van Zijl, P.C., Mori, S.: Accurate quantitation of water-amide proton exchange rates using the phase-modulated CLEAN chemical EXchange (CLEANEX-PM) approach with a Fast-HSQC (FHSQC) detection scheme. *J. Biomol. NMR* **11**, 221–226 (1998)
71. Li, Z., Scheraga, H.A.: Monte Carlo-minimization approach to the multiple-minima problem in protein folding. *Proc. Natl. Acad. Sci. U S A* **84**, 6611–6615 (1987)
72. Metropolis, N., Rosenbluth, A.W., Rosenbluth, M.N., Teller, A.H., Teller, E.: Equation of state calculations by fast computing machines. *J. Chem. Phys.* **21**, 1087–1092 (1953)
73. Kirkpatrick, S., Gelatt, C.D., Vecchi, M.P.: Optimization by simulated annealing. *Science* **220**, 671–680 (1983)
74. Matsuki, Y., Konuma, T., Fujiwara, T., Sugase, K.: Boosting protein dynamics studies using quantitative nonuniform sampling NMR spectroscopy. *J. Phys. Chem. B* **115**, 13740–13745 (2011)
75. Ishima, R., Torchia, D.A.: Error estimation and global fitting in transverse-relaxation dispersion experiments to determine chemical-exchange parameters. *J. Biomol. NMR* **32**, 41–54 (2005)
76. Press, W.H.: Numerical Recipes 3rd edition: The Art of Scientific Computing. Cambridge University Press, Cambridge (2007)
77. Mosteller, F., Tukey, J.W.: Data analysis, including statistics. *Handbook of Social Psychology*, pp. 80–203 (1968)
78. Schanda, P., Brutscher, B., Konrat, R., Tollinger, M.: Folding of the KIX domain: characterization of the equilibrium analog of a folding intermediate using  $^{15}\text{N}/^{13}\text{C}$  relaxation dispersion and fast  $^1\text{H}/^2\text{H}$  amide exchange NMR spectroscopy. *J. Mol. Biol.* **380**, 726–741 (2008)
79. Konuma, T., Harada, E., Sugase, K.: Extracting protein dynamics information from overlapped NMR signals using relaxation dispersion difference NMR spectroscopy. *J. Biomol. NMR* **63**, 367–373 (2015)
80. Korzhnev, D.M., Kloiber, K., Kanelis, V., Tugarinov, V., Kay, L.E.: Probing slow dynamics in high molecular weight proteins by methyl-TROSY NMR spectroscopy: application to a 723-residue enzyme. *J. Am. Chem. Soc.* **126**, 3964–3973 (2004)
81. Toyama, Y., Osawa, M., Yokogawa, M., Shimada, I.: NMR method for characterizing microsecond-to-millisecond chemical exchanges utilizing differential multiple-quantum relaxation in high molecular weight proteins. *J. Am. Chem. Soc.* **138**, 2302–2311 (2016)
82. Walinda, E., Morimoto, D., Shirakawa, M., Sugase, K.:  $F_1F_2$ -selective NMR spectroscopy. *J. Biomol. NMR* **68**, 41–52 (2017)
83. Lange, O.F., Rossi, P., Sgourakis, N.G., Song, Y., Lee, H.-W., Aramini, J.M., Ertekin, A., Xiao, R., Acton, T.B., Montelione, G.T., Baker, D.: Determination of solution structures of proteins up to 40 kDa using CS-Rosetta with sparse NMR data from deuterated samples. *Proc. Natl. Acad. Sci. U S A* **109**, 10873–10878 (2012)
84. Henzler-Wildman, K.A., Lei, M., Thai, V., Kerns, S.J., Karplus, M., Kern, D.: A hierarchy of timescales in protein dynamics is linked to enzyme catalysis. *Nature* **450**, 913–916 (2007)
85. Piotto, M., Šaudek, V., Sklenář, V.: Gradient-tailored excitation for single-quantum NMR spectroscopy of aqueous solutions. *J. Biomol. NMR* **2**, 661–665 (1992)
86. Shaka, A., Keeler, J., Freeman, R.: Evaluation of a new broadband decoupling sequence: WALTZ-16. *J. Magn. Reson.* **53**, 313–340 (1969)

87. Davis, D., Perlman, M., London, R.: Direct measurements of the dissociation-rate constant for inhibitor-enzyme complexes via the  $T_{1\rho}$  and  $T_2$  (CPMG) methods. *J. Magn. Reson. B* **104**, 266–275 (1994)
88. Deverell, C., Morgan, R., Strange, J.: Studies of chemical exchange by nuclear magnetic relaxation in the rotating frame. *Mol. Phys.* **18**, 553–559 (1970)
89. Abergel, D., Palmer, A.G.: On the use of the stochastic Liouville equation in nuclear magnetic resonance: application to  $R_{1\rho}$  relaxation in the presence of exchange. *Concepts Magn. Reson. Part A* **19**, 134–148 (2003)
90. Trott, O., Palmer, A.G.:  $R_{1\rho}$  relaxation outside of the fast-exchange limit. *J. Magn. Reson.* **154**, 157–160 (2002)
91. Trott, O., Abergel, D., Palmer, A.G.: An average-magnetization analysis of  $R_{1\rho}$  relaxation outside of the fast exchange limit. *Mol. Phys.* **101**, 753–763 (2003)
92. Koss, H., Rance, M., Palmer, A.G.: General expressions for  $R_{1\rho}$  relaxation for  $N$ -site chemical exchange and the special case of linear chains. *J. Magn. Reson.* **274**, 36–45 (2017)
93. Luz, Z., Meiboom, S.: Nuclear magnetic resonance study of the protolysis of trimethylammonium ion in aqueous solution—order of the reaction with respect to solvent. *J. Chem. Phys.* **39**, 366–370 (1963)
94. Ishima, R., Torchia, D.A.: Estimating the time scale of chemical exchange of proteins from measurements of transverse relaxation rates in solution. *J. Biomol. NMR* **14**, 369–372 (1999)
95. Bloom, M., Reeves, L., Wells, E.: Spin echoes and chemical exchange. *J. Chem. Phys.* **43**, 1615–1624 (1965)

# **Chapter 8**

## **Structural Study of Proteins by Paramagnetic Lanthanide Probe Methods**

**Tomohide Saio and Fuyuhiko Inagaki**

**Abstract** Long-range structural information provided by the paramagnetic lanthanide probe methods is invaluable in the structural analysis of proteins, particularly protein complexes and multi-domain proteins. The application of paramagnetic lanthanide probe methods in protein structural analysis is expanding, owing to recent developments in lanthanide-binding tags. Here, we describe paramagnetic effects observed in the presence of paramagnetic lanthanide ions, which can be exploited to obtain structural information about proteins. We also illustrate practical aspects of the experiments and analyses utilizing the paramagnetic lanthanide probe methods. Applications in structure determination of protein–protein complexes and visualization of conformational changes in multi-domain proteins are also described.

**Keywords** Lanthanide ion • Paramagnetic effect • Pseudocontact shift  
Paramagnetic relaxation enhancement • Residual dipolar coupling  
Lanthanide-binding tag • Protein structure • Conformational change  
Long-range structural information

---

Fuyuhiko Inagaki: Deceased.

---

T. Saio (✉)  
Department of Chemistry, Faculty of Science, Hokkaido University,  
Kita 10, Nishi 8, Kita-ku 060-0810, Sapporo, Japan  
e-mail: saio@sci.hokudai.ac.jp

T. Saio  
PRESTO, JST, Tokyo 135-0063, Japan

F. Inagaki  
Department of Structural Biology, Faculty of Advanced Life Science,  
Hokkaido University, N-21, W-11, Kita-ku 001-0021, Sapporo, Japan

## 8.1 Introduction

Paramagnetic lanthanide ions with unpaired electrons in the  $4f$  orbital enable NMR to exploit long-range structural information that is derived from paramagnetic effects induced by through-space interaction between an electron and a nuclear spin. Since the magnetic moment of an electron is 658 times greater than that of proton, a single unpaired electron can induce significant effects on NMR spectra, which are utilized in paramagnetic lanthanide probe methods. Paramagnetic lanthanide probe methods were originally used to study the structure and conformation of small molecules [1–3], but in the past few decades the method has been increasingly applied to protein structural analyses [4]. Long-range structural information obtained by paramagnetic lanthanide probe methods is important in protein NMR, especially in the analysis of large proteins, multi-domain proteins, and their complexes [5]. Because of the recent developments in isotope labeling techniques, including deuterium labeling [6], methyl-specific labeling [7], and stereo-array isotope labeling (SAIL) [8], NMR studies of proteins over several hundred kDa [9] and large membrane proteins [10] are becoming feasible. However, the structural analyses of large proteins still suffer from a shortage of structural information; especially when the proton density is decreased by deuterium labeling, short-range distance information from the inter-proton nuclear Overhauser effect (NOE) tends to be insufficient. High sensitivity and resolution of NMR spectra can be achieved for large proteins by deuteration, but a shortage of structural information prevents detailed structural study.

Here, we illustrate paramagnetic lanthanide probe methods that provide long-range structural information. A paramagnetic lanthanide ion fixed in a protein frame induces several paramagnetic effects on the observed nuclei in the protein, depending on the relative position of the nuclei to the paramagnetic lanthanide ion. Analysis of the paramagnetic effects provides quantitative long-range distance and angular information that can be exploited in the structural study of large proteins and their complexes [4]. Owing to the recent developments of lanthanide-binding tags, paramagnetic lanthanide probe methods are no longer limited to metal-binding proteins. We describe practical aspects of paramagnetic lanthanide probe methods, including the usage of lanthanide-binding tags and analysis of the magnetic susceptibility tensor, and provide examples of applications for structural analysis.

## 8.2 Structural Information Obtained from Paramagnetic Lanthanide Probe Methods

A paramagnetic lanthanide ion fixed in a protein induces several paramagnetic effects and thus provides unique structural information that can improve both the quality and efficiency of structural analysis by NMR. Whereas NOEs yield

short-range ( $\sim 5 \text{ \AA}$ ) distance information, paramagnetic effects provide long-range ( $\sim 40 \text{ \AA}$ ) quantitative distance and angular information [4, 11] that is important for the structural analysis of large proteins and their complexes [12]. The long-range structural information includes distance and angular information from pseudocontact shifts (PCSs), angular information from residual dipolar couplings (RDCs), and distance information from paramagnetic relaxation enhancements (PREs) [13]. These paramagnetic effects can be observed by simple NMR measurements once a paramagnetic lanthanide ion is attached to the target protein [14]. Details of each paramagnetic effect are described below.

### 8.2.1 Pseudocontact Shift (PCS)

PCS is a chemical shift change that depends on the relative position of the observed nucleus with respect to the lanthanide ion (Fig. 8.1a–c), thus containing distance and angular information. PCS arises from through-space interaction between the nucleus and the unpaired electrons in the paramagnetic lanthanide ion and can be observed within the range of  $\sim 40 \text{ \AA}$  from the ion [15]. The PCS value,  $\Delta\delta^{\text{PCS}}$ , is given by Eq. 8.1,

$$\Delta\delta^{\text{PCS}} = \frac{1}{12\pi r^3} \left[ \Delta\chi_{\text{ax}}(3\cos^2\theta - 1) + \frac{3}{2}\Delta\chi_{\text{rh}}\sin^2\theta\cos 2\phi \right] \quad (8.1)$$

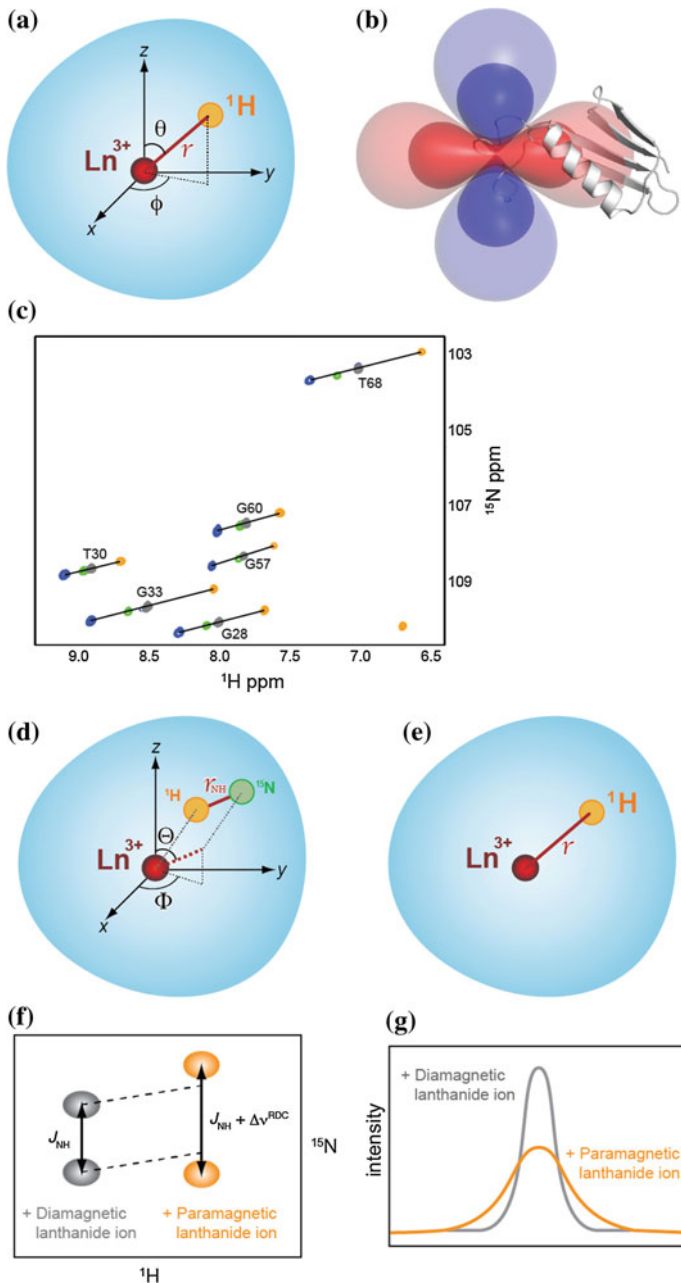
where  $\Delta\delta^{\text{PCS}}$  is the PCS value,  $r$ ,  $\theta$ , and  $\phi$  are the polar coordinates of the nucleus with respect to the principal axes of the magnetic susceptibility tensor, and  $\Delta\chi_{\text{ax}}$  and  $\Delta\chi_{\text{rh}}$  are the axial and rhombic components of the magnetic susceptibility tensor, respectively, as defined by Eq. 8.2.

$$\Delta\chi_{\text{ax}} = \chi_{zz} - \frac{\chi_{xx} + \chi_{yy}}{2} \quad \text{and} \quad \Delta\chi_{\text{rh}} = \chi_{xx} - \chi_{yy} \quad (8.2)$$

Among several paramagnetic effects of the lanthanide ion, PCSs provide particularly useful long-range structural information that is easily measured with high accuracy, usually based on simple two-dimensional (2D) spectra.

### 8.2.2 Residual Dipolar Coupling (RDC)

RDC originates from dipolar interaction between nuclei and depends on the orientation of the vector connecting the two coupled nuclei with respect to the static magnetic field  $B_0$  [16]. Usually, RDCs between directly bonded nuclei such as  $^{1}\text{H}^{\text{N}}$  and  $^{15}\text{N}$  in amide groups are measured and used to extract structural information (Fig. 8.1d and f). In normal solution, RDCs are not observed, because molecular



◀Fig. 8.1 Schematic representation of structural information derived from paramagnetic effects. **a** Distance and angular information obtained from PCS. PCS depends on the location of the observed nuclei in the principal frame of  $\Delta\chi$ -tensor. **b** Isosurfaces depicting the PCSs of  $\pm 2.5$  and  $\pm 0.6$  ppm induced by  $\text{Tb}^{3+}$  fixed in LBT-GB1 [47] (2rpv.pdb). **c** Overlay of a selected region of  $^1\text{H}-^{15}\text{N}$  HSQC spectra of  $^{15}\text{N}$ -labeled LBT-GB1 in complex with  $\text{La}^{3+}$  (gray),  $\text{Er}^{3+}$  (green),  $\text{Tm}^{3+}$  (blue), and  $\text{Tb}^{3+}$  (orange). Chemical shift difference between paramagnetic state (in the presence of  $\text{Er}^{3+}$ ,  $\text{Tm}^{3+}$ , or  $\text{Tb}^{3+}$ ) and diamagnetic state (in the presence of  $\text{La}^{3+}$ ) is PCS. **d** Angular information from RDC. **e** Distance information from PRE. **f** Schematic representation of RDC measurement. **g** Schematic representation of PRE observed as line broadening

tumbling makes the orientation term averaged to zero. However, if the molecule is partially aligned with respect to  $B_0$ , the dipolar couplings are not completely averaged, and thus, “residual” dipolar couplings can be measured. In addition to alignment media such as Pf1 filamentous bacteriophage [17] or poly(ethylene glycol) [18], a paramagnetic lanthanide ion fixed in a protein induces partial molecular alignment [19]. The different energies for each orientation of the protein with respect to the  $B_0$  cause different probabilities of the orientation of the protein, thus resulting in self-orientation. The principle axes of the alignment tensor coincide with those of the  $\Delta\chi$ -tensor, therefore, the RDC value,  $\Delta\delta^{\text{RDC}}$ , can be represented by Eq. 8.3,

$$\Delta\nu^{\text{RDC}}(\text{Hz}) = -\frac{hB_0^2\gamma_{\text{N}}\gamma_{\text{H}}}{240k_{\text{B}}T\pi^3r_{\text{NH}}^3} \left[ \Delta\chi_{\text{ax}}(3\cos^2\Theta - 1) + \frac{3}{2}\Delta\chi_{\text{rh}}\sin^2\Theta\cos 2\Phi \right] \quad (8.3)$$

where  $\Delta\nu^{\text{RDC}}$  is the RDC value,  $h$  is Planck’s constant,  $B_0$  is the magnetic field strength,  $\gamma_{\text{N}}$  and  $\gamma_{\text{H}}$  are the magnetogyric ratios of  $^{15}\text{N}$  and  $^1\text{H}$ , respectively,  $k_{\text{B}}$  is the Boltzmann constant,  $T$  is the absolute temperature,  $r_{\text{NH}}$  is the inter-nuclear distance between  $^{15}\text{N}$  and  $^1\text{H}^{\text{N}}$  and is usually fixed, and  $\Theta$  and  $\Phi$  are the polar angles describing the orientation of the vector connecting the coupled nuclei, such as  $^{15}\text{N}$  and  $^1\text{H}^{\text{N}}$  (Fig. 8.1d). RDCs are not related to the distance from the lanthanide ion and thus provide angular information without a distance limitation.

### 8.2.3 Paramagnetic Relaxation Enhancement (PRE)

Whereas PCS and RDC are anisotropic paramagnetic effects, paramagnetic relaxation enhancement (PRE) is an isotropic paramagnetic effect that is proportional to the inverse of the 6th power of the metal-to-nucleus distance (Fig. 8.1e, g) [20]. In the case of paramagnetic lanthanide ions, PRE arises from direct dipole–dipole interactions and due to the Curie spin relaxation mechanism [21]. Trivalent paramagnetic lanthanide ions other than the gadolinium ion ( $\text{Gd}^{3+}$ ) have very short electron relaxation time ( $10^{-12}$  to  $10^{-14}$  s) with respect to the rotational correlation time  $\tau_r$ , and thus, the Curie spin relaxation mechanism is predominant [22]. In the

case of  $\text{Gd}^{3+}$  whose electron relaxation time is relatively long ( $10^{-8}$  to  $10^{-9}$  s), the dipole–dipole relaxation mechanism is predominant.

PRE in the transverse relaxation rate through the Curie spin relaxation,  $R_{2,\text{Curie}}^{\text{PRE}}$ , is represented by Eq. 8.4,

$$R_{2,\text{Curie}}^{\text{PRE}} = \frac{1}{5} \left( \frac{\mu_0}{4\pi} \right)^2 \frac{\omega_H^2 g_J^4 \mu_B^4 J^2 (J+1)^2}{(3k_B T)^2 r^6} \left[ 4\tau_{\text{Curie}} + \frac{3\tau_{\text{Curie}}}{1 + (\omega_H \tau_{\text{Curie}})^2} \right] \quad (8.4)$$

where  $\mu_0$  is the permeability of vacuum,  $\omega_H$  is the Larmor frequency of the proton,  $g_J$  is the  $g$ -factor of the lanthanide free ion,  $\mu_B$  is the Bohr magneton,  $J$  is the total angular momentum quantum number,  $r$  is the distance between the nuclear spin and the paramagnetic center, and  $\tau_{\text{Curie}}$  is defined in Eq. 8.5,

$$1/\tau_{\text{Curie}} = 1/\tau_r + 1/\tau_M \quad (8.5)$$

where  $\tau_r$  is the rotational correlation time and  $\tau_M$  is exchange correlation time.

For the dipole–dipole relaxation mechanism, PRE in the transverse relaxation rate,  $R_{2,\text{Dip}}^{\text{PRE}}$ , is expressed by Eq. 8.6.

$$R_{2,\text{Dip}}^{\text{PRE}} = \frac{1}{15} \left( \frac{\mu_0}{4\pi} \right)^2 \frac{\gamma_H^2 g_J^2 \mu_B^2 J(J+1)}{r^6} \left[ 4\tau_c + \frac{3\tau_c}{1 + (\omega_H \tau_c)^2} + \frac{13\tau_c}{1 + (\omega_S \tau_c)^2} \right] \quad (8.6)$$

The correlation time  $\tau_c$  is defined in Eq. 8.7,

$$1/\tau_c = 1/\tau_r + 1/\tau_s + 1/\tau_M \quad (8.7)$$

where  $\tau_s$  is the effective electron correlation time.

Owing to the strong PRE, the NMR signals of the nuclei close to the paramagnetic ion are easily broadened beyond detection. However, PRE depends on the inverse of the 6th power of metal-to-nucleus distance and decays much more rapidly with increasing distance from the paramagnetic center than that of PCS which depends on the inverse of the 3rd power of the distance. Thus, in general, PCS can be observed within the range of 12–40 Å from the paramagnetic lanthanide ion.

### 8.3 Various Magnetic Properties of Lanthanide Ions

Among paramagnetic metal ions, one of the most important advantages of lanthanide ions is the availability of various magnetic properties. The trivalent lanthanide ions, except  $\text{La}^{3+}$  and  $\text{Lu}^{3+}$ , have unpaired electrons in the  $4f$  orbital that are located inside of the  $5s$  and  $5p$  electrons. Consequently, the  $4f$  electrons do not participate in bonding, and thus, the chemical properties of the lanthanide ions are similar to each other. In contrast, variety in the  $4f$  orbital results in various magnetic

properties [23, 24]. Different lanthanide ions have various magnitudes and signs of the  $\Delta\chi$ -tensor due to the difference in the number of  $4f$  electrons. Lanthanide ions with smaller magnitudes of the  $\Delta\chi$ -tensor generate smaller PCSs, but simultaneously generate less PREs, which is suitable for obtaining structural information for the region close to the ion. Lanthanide ions with larger magnitudes of the  $\Delta\chi$ -tensor provide stronger PREs as well as PCSs; thus, signals near the lanthanide ion become too broad to be detected, but PCSs can be detected from the nuclei located further away from the ion. There are also diamagnetic lanthanide ions ( $\text{La}^{3+}$  and  $\text{Lu}^{3+}$ ) that serve as diamagnetic references. Use of diamagnetic lanthanide ions is important because all paramagnetic effects are measured as the difference between the data sets measured in the paramagnetic and diamagnetic states.  $\text{Gd}^{3+}$  has the longest electronic relaxation time of all the lanthanide(III) ions, and thus,  $\text{Gd}^{3+}$  generates strong PREs through the dipole–dipole relaxation mechanism and provides no PCS. PREs caused by  $\text{Gd}^{3+}$  are larger than those caused by nitroxide spin labels and as large as those arising from  $\text{Mn}^{2+}$ , reaching up to  $\sim 35 \text{ \AA}$  from the ion.

## 8.4 Application of the Paramagnetic Lanthanide Probe in Protein Structural Studies

For application of the paramagnetic lanthanide probe methods, a lanthanide ion has to be fixed in a protein frame. A number of important applications have been performed on metal-binding proteins in which their natural metals such as  $\text{Ca}^{2+}$  and  $\text{Mg}^{2+}$  have been replaced by lanthanide ions. For example, PCS/RDC-based structure refinement [15, 25–29], structure determination of a protein–protein complex [30] and a protein–ligand complex [31], conformational and dynamical analysis of multi-domain proteins [32–36], and structure-based NMR signal assignment [14, 37] have been reported. Application of the paramagnetic lanthanide probe to non-metalloproteins requires a rigid lanthanide-binding tag, because the mobility of the tag averages out the anisotropic paramagnetic effects of the lanthanide ion, thus limiting the accuracy and reliability of the structural information. For this purpose, several lanthanide-binding tags have been developed [11]. These tags are classified into two types: lanthanide-binding peptide tags and lanthanide-chelating synthetic tags. Peptide tags can be attached to a target protein by N- or C-terminal fusion [38–42], a disulfide bond [43, 44], loop insertion [45, 46], or double anchoring via N- or C-terminal fusion and a disulfide bridge [47–50]. The synthetic tags can be attached through disulfide bond(s) [38, 51–65], thioether bond(s) [66–70], or by the introduction of an unnatural amino acid of *p*-azido-L-phenylalanine (AzF) conjugated to the tag via triazole [71]. Because of the suppressed mobility of the tag, two-armed tags such as Caged Lanthanide NMR Probe 5 (CLaNP-5) [63, 64] and two-point anchored lanthanide-binding peptide tag (LBT) [47–50] are becoming widely used in the protein structural studies. Below, we describe details regarding the two major tags.

### 8.4.1 Caged Lanthanide NMR Probe 5 (CLaNP-5)

In addition to the mobility, another major issue for synthetic tags was peak splitting due to the enantiomeric conformers of the lanthanide-substituted tag. Keizers et al. [63, 64] have overcome the issue by CLaNP-5, in which two pyridine-N-oxides are attached to the DOTA (1,4,7,10-tetraazacyclododecane-1,4,7,10-tetraacetic acid)-based chelating tag having two arms for disulfide bridges with the protein (Fig. 8.2a). Double linkage of the tag in C-2 symmetric architecture enables strong anisotropic paramagnetic effects without peak splitting. CLaNP-5 can be efficiently ligated to the protein by mixing the tag with the protein. A lanthanide ion is loaded to the tag prior to the ligation. Another advantage of CLaNP-5 is that the tag can be introduced in principle anywhere on the surface of the protein as long as the two cysteine mutations are properly designed. The mutations can be designed based on the structure of the target protein. We follow the three criteria below in choosing two residues for cysteine mutations:

1. The two residues should be located on a rigid part of the protein, e.g., a region forming secondary structures.
2. The side chains should be exposed on the surface of the protein.
3. The two residues should be separately located at an appropriate distance.

Mutations can be designed on the basis of the distance between the  $C_\beta$  atoms: If the distance between the  $C_\beta$  atoms is too short ( $<\sim 6 \text{ \AA}$ ) or too long ( $>\sim 11 \text{ \AA}$ ), the structure of the protein can be distorted, which can be judged by chemical shift perturbations in the  $^1\text{H}-^{15}\text{N}$  HSQC spectrum of the protein after the ligation of CLaNP-5 containing a diamagnetic lanthanide ion (Fig. 8.2b–d).

If the two cysteine residues are properly located, CLaNP-5 can be ligated at high yield and strong paramagnetic effects without peak splitting are observed. Low yield of the ligation is another indication of improper positions of the cysteine mutations. The magnetic susceptibility tensor for the paramagnetic lanthanide ions coordinated in CLaNP-5 are near-axial symmetric, as represented by small rhombic component of  $\Delta\chi$ -tensor [63, 64, 72] (Table 8.1). This symmetric feature of the  $\Delta\chi$ -tensor is consistent with the symmetric coordination of the lanthanide ion in CLaNP-5 (Fig. 8.2a).

Several derivatives of CLaNP-5 also have been reported, such as CLaNP-7, in which a net charge of the tag in complex with the trivalent lanthanide ion is decreased from +3 (CLaNP-5) to +1 to limit the impact on the surface potential of the protein [65], and CLaNP-9, which has a net charge of +1 and two arms decorated with  $\alpha$ -bromoacetamide-pyridine-N-oxides, thus allowing formation of thioether linkages that are stable under reducing conditions [66].

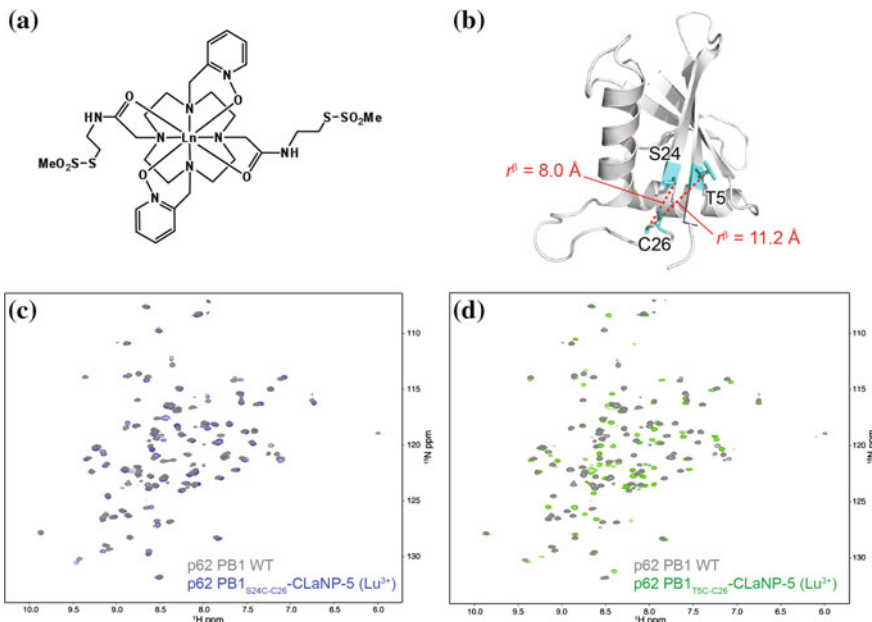


**Fig. 8.2** Design and evaluation of the construct for the use of double-arm synthetic tag CLaNP-5. **a** Chemical structure of CLaNP-5 [63, 64]. **b** The structure of p62 PB1 [92] (2kkc.pdb) with the amino acids used for the ligation of CLaNP-5 drawn in stick representation. **c**  $^1\text{H}$ - $^{15}\text{N}$  HSQC spectrum of  $^{15}\text{N}$ -labeled p62 PB1<sub>S24C-C26</sub> ( $r^\beta = 8.0 \text{ \AA}$ )-CLaNP-5 ( $\text{Lu}^{3+}$ ) overlaid with the spectrum of  $^{15}\text{N}$ -labeled wild-type p62 PB1. The perturbations are small and the perturbed resonances are only from the residues located close to the tag, suggesting that the introduction of CLaNP-5 has negligible effect to the protein structure. **d**  $^1\text{H}$ - $^{15}\text{N}$  HSQC spectrum of  $^{15}\text{N}$ -labeled p62 PB1<sub>T5C-C26</sub> ( $r^\beta = 11.2 \text{ \AA}$ )-CLaNP-5 ( $\text{Lu}^{3+}$ ) overlaid with the spectrum of  $^{15}\text{N}$ -labeled wild-type p62 PB1. Larger chemical shift perturbations from broad region of the protein imply possible structural distortion by CLaNP-5

**Table 8.1** Magnetic susceptibility tensors of lanthanide ions in CLaNP-5 attached to MurD domain 1-2 E260C/K262C [72]

Lanthanide	$\Delta\chi_{\text{ax}}^{\text{a}}$	$\Delta\chi_{\text{rh}}^{\text{a}}$	$\alpha^{\text{b}}$	$\beta^{\text{b}}$	$\gamma^{\text{b}}$
Yb <sup>3+</sup>	$8.45 \pm 0.46$	$0.56 \pm 0.70$	137.0	69.3	22.5
Tm <sup>3+</sup>	$47.01 \pm 2.30$	$8.48 \pm 5.18$	137.0	72.2	59.1

<sup>a</sup> $\Delta\chi_{\text{ax}}$  and  $\Delta\chi_{\text{rh}}$  values are in  $10^{-32} \text{ m}^3$  and error estimates were obtained by Monte-Carlo protocol using the 100 partial PCS data sets in which 30% of the input data were randomly deleted

<sup>b</sup>The Euler angles ( $\alpha$ ,  $\beta$ ,  $\gamma$ ) are represented in ZYZ convention in degrees

#### 8.4.2 Two-Point Anchored Lanthanide-Binding Peptide Tag (LBT)

One drawback of the synthetic tags is their limited availability: Compounds generated through multiple steps of synthetic reactions are not always easy for

structural biologists to prepare by themselves. Another option is two-point anchored lanthanide-binding peptide tag (LBT) in which the lanthanide-binding peptide (CYVDTNNDGAYEGDEL) derived from the EF-hand motif and optimized for binding to the lanthanide ions [43, 44, 73, 74] is attached to a target protein via two anchoring points, a disulfide bridge and an N- or C-terminal fusion [47] (Fig. 8.3a). Since the tag can be introduced by a simple genetic modification of the expression construct, the two-point anchored LBT is easily available to structural biologists.

Sample preparation is simple and efficient. The LBT sequence is fused to the N/C-terminus of a target protein with a spacer consisting of 3–5 amino acids [47, 50], and one cysteine residue is introduced to the surface of the protein by mutagenesis (Fig. 8.3a). Criteria for the design of a cysteine mutation and spacer length are as follows [47, 50].

1. A cysteine residue should be introduced on a rigid part of the protein, e.g., a region forming secondary structures.
2. The side chains should be exposed on the surface of the protein.
3. The  $C_\alpha$  atom of the cysteine residue should be located 5–10 Å away from that of the N/C-terminus. The minimal spacer length between LBT and the N/C-terminus is three residues if the distance between  $C_\alpha$  atoms is ~6 Å, or four residues if the distance is ~10 Å. The amino acid composition of the spacer is arbitrary.

After protein preparation under the reducing conditions, the disulfide bridge between the cysteines is efficiently formed by the addition of 5,5'-dithiobis (2-nitrobenzoic acid) (DTNB). The lanthanide ion is coordinated by LBT by the addition of 1 equivalent of lanthanide ion to the protein. The  $K_d$  between the lanthanide ion and LBT is ~50 nM [73], which is sufficiently strong to generate significant paramagnetic effects but low enough to allow exchange of the lanthanide ion between the NMR experiments. Two-point anchoring of LBT suppresses the mobility of the tag, thereby producing strong paramagnetic anisotropic effects that can be used for structural analysis of protein–protein [47, 50] and protein–ligand complexes [49], and resonance assignment. Peak doubling in complex with the paramagnetic lanthanide ion is an indication of the fact that the spacer length is too short [47] (Fig. 8.3b). Paramagnetic lanthanide ions coordinated in LBT provides  $\Delta\chi$ -tensor with large rhombic component [50] (Table 8.2), which is advantageous for obtaining structural information, especially from the region on the  $x$ – $y$  plane of the principal axes of the  $\Delta\chi$ -tensor. Another advantage of the two-point anchored LBT is that the direction of the principal axes of the  $\Delta\chi$ -tensor and the metal position relative to the target protein can be conveniently modulated by modifying the spacer length between LBT and the protein [50] so that another orthogonal data set can easily be obtained (see Sect. 8.6.1).

The paramagnetic lanthanide probe methods are now widely available for non-metalloproteins by the use of lanthanide-binding tags including CLaNP-5 and the two-point anchored LBT. In the following sections, we describe practical aspects of the experiments and analyses for the use of paramagnetic lanthanide probe with paramagnetic lanthanide tags.

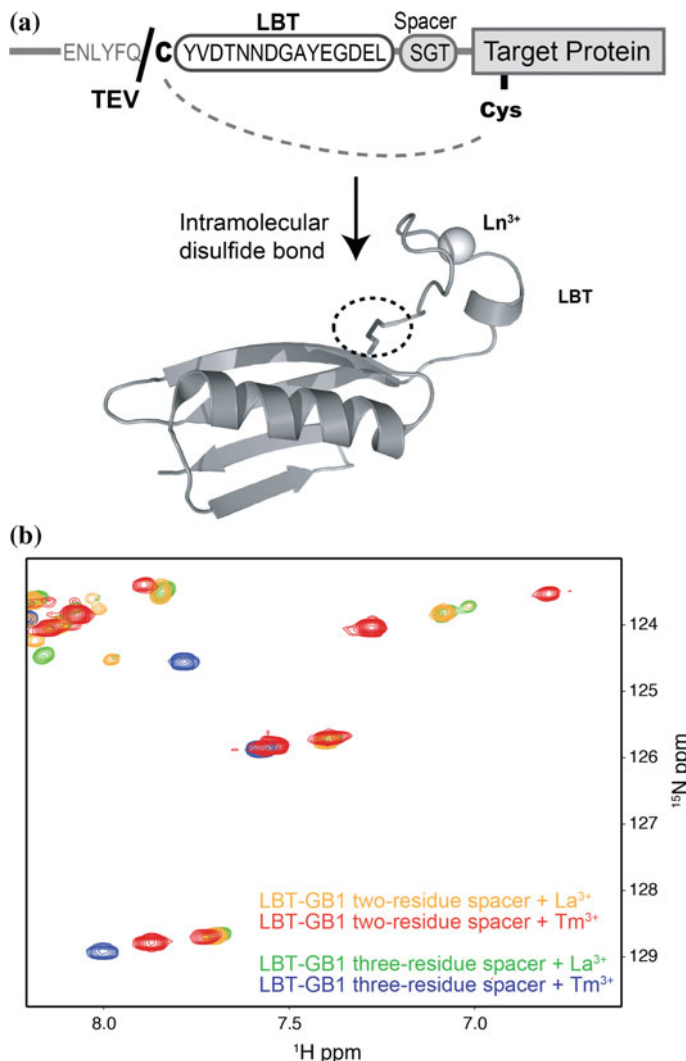


**Fig. 8.3** Design and evaluation of the construct for the use of the two-point anchored LBT. **a** Scheme of the two-point attachment of the LBT [47]. The LBT sequence is fused to the target protein with a spacer sequence, and the second anchoring point is made by disulfide bond between cysteine residues at the N/C-terminus of LBT and on the surface of the protein. The affinity tag at the N-terminus can be cleaved off by the tobacco etch virus (TEV) protease. **b** Overlay of a selected region of the  $^1\text{H}$ - $^{15}\text{N}$  HSQC spectra of  $^{15}\text{N}$ -labeled GB1 attached with the two-point anchored LBT with two- and three-residue spacer. LBT-GB1 with two-residue spacer showed peak doubling indicating the spacer is too short. Spacers with more than three residues showed no peak doubling

**Table 8.2** Magnetic susceptibility tensors of lanthanide ions in complex with LBT-FKBP12-rapamycin, LBT-GB1, LBT-p62 PB1, LBT-Grb2 SH2 [48, 50]

Protein (anchoring points)	$C_{\alpha}$ - distance <sup>c</sup> [Å]	Minimal spacer length	Lanthanide ion	$\Delta\chi_{ax}^a$	$\Delta\chi_{rh}^a$	$\alpha^b$	$\beta^b$	$\gamma^b$
FKBP12 (V2-T75C)	5.6	3	Dy <sup>3+</sup>	23.1 (±1.8)	20.2 (±1.2)	49	106	31
			Tb <sup>3+</sup>	34.0 (±2.5)	13.4 (±2.1)	53	106	17
		4	Dy <sup>3+</sup>	23.1 (±1.6)	19.0 (±0.7)	33	77	38
			Tb <sup>3+</sup>	29.2 (±1.2)	17.9 (±0.5)	35	69	9
	6.1	3	Tm <sup>3+</sup>	-18.5 (±0.9)	-18.0 (±0.4)	66	148	149
			Tb <sup>3+</sup>	39.2 (±1.0)	15.9 (±2.1)	97	145	158
			Er <sup>3+</sup>	-9.4 (±0.7)	-7.0 (±0.2)	71	138	136
		4	Tm <sup>3+</sup>	-23.6 (±1.2)	-20.0 (±0.7)	85	127	160
			Tb <sup>3+</sup>	41.8 (±2.3)	20.4 (±0.6)	94	125	153
			Er <sup>3+</sup>	-9.3 (±0.8)	-8.4 (±0.4)	74	115	145
p62 PB1 (S3-C26)	6.0	3	Dy <sup>3+</sup>	28.6 (±1.5)	21.7 (±1.0)	34	108	127
			Tb <sup>3+</sup>	40.8 (±1.1)	20.7 (±0.9)	29	106	105
		4	Tm <sup>3+</sup>	-27.2 (±1.3)	-18.9 (±0)	24	107	92
			Er <sup>3+</sup>	-10.4 (±0.3)	-9.1 (±0.2)	24	107	104
	9.9	4	Dy <sup>3+</sup>	22.7 (±1.3)	17.6 (±0.7)	106	57	53
			Tb <sup>3+</sup>	29.2 (±1.7)	16.9 (±0.5)	97	52	34
			Tm <sup>3+</sup>	-17.5 (±1.6)	-17.1 (±0.5)	99	65	27
		5	Dy <sup>3+</sup>	25.1 (±2.2)	21.0 (±1.2)	113	41	51
			Tb <sup>3+</sup>	30.2 (±2.6)	21.1 (±1.0)	100	42	37
			Tm <sup>3+</sup>	-19.0 (±1.7)	-19.1 (±1.0)	97	45	34

<sup>a</sup> $\Delta\chi_{ax}$  and  $\Delta\chi_{rh}$  values are in  $10^{-32}$  [m<sup>3</sup>] and error estimates were obtained by the Monte-Carlo protocol using 100 partial PCS data sets in which 30% of the input data were randomly deleted

<sup>b</sup>The Euler angles ( $\alpha$ ,  $\beta$ ,  $\gamma$ ) are represented in ZYZ convention in degrees

<sup>c</sup>The distance between  $C_{\alpha}$  atoms of the cysteine mutation and N/C-terminus of the protein

## 8.5 Measurement and Analysis of Anisotropic Paramagnetic Effects

All paramagnetic effects are measured as the difference between paramagnetic and diamagnetic states. Among several paramagnetic effects, we describe here how to measure PCSs that provide the most useful information for protein structural analysis. The two ions in the lanthanide group, La<sup>3+</sup> and Lu<sup>3+</sup>, are diamagnetic and thus are used to obtain the references. PCS is observed as a chemical shift change induced via a through-space interaction between observed nuclei and unpaired electrons in the lanthanide ion. The most popular way to measure PCS is to use 2D NMR spectra such as <sup>1</sup>H–<sup>15</sup>N HSQC. Since the <sup>1</sup>H and <sup>15</sup>N atoms of each amide group are close in space, both nuclei experience similar paramagnetic effects from the lanthanide ion, thereby resulting in similar PCS values in both <sup>1</sup>H and <sup>15</sup>N dimensions. Thus, in the overlaid spectra, the shifted resonances from the same amide group align in a straight line (Fig. 8.1c). This linearity aids in assignment of PCSs on the basis of the assignments for the diamagnetic state: Large PCSs can be tracked by the use of the paramagnetic lanthanide ions with weaker anisotropic paramagnetic effects, thus inducing smaller PCSs. For larger proteins containing > 100 amino acid residues, unambiguous PCS assignment is often difficult because of resonance overlap. The use of amino acid selective <sup>15</sup>N-labeling [14, 48, 72], inverse labeling [50], segment labeling [75, 76], or methyl-specific isotope labeling [7] decreases the number of resonances in the spectra so that even large PCSs can be tracked without ambiguity. Subtraction of the chemical shift of diamagnetic resonance from that of paramagnetic resonance yields PCS. In the case of backbone <sup>1</sup>H–<sup>15</sup>NHSQC spectra, PCS values for both <sup>1</sup>H<sup>N</sup> and <sup>15</sup>N are obtained.

The  $\Delta\chi$ -tensor can be determined on the basis of the observed PCSs and the three-dimensional (3D) coordinates of the protein.  $\Delta\chi$ -tensor is responsible for the characterization of anisotropic paramagnetic effects including PCS and RDC. Determination of the  $\Delta\chi$ -tensor is essential for the quantitative use of the anisotropic paramagnetic effects. Given the availability of the 3D structure of the protein, the  $\Delta\chi$ -tensor can be determined in principle by only eight PCSs where the parameters of  $\Delta\chi_{ax}$ ,  $\Delta\chi_{rh}$ , Euler angles ( $\alpha$ ,  $\beta$ ,  $\gamma$ ), and metal position ( $x$ ,  $y$ ,  $z$ ) are determined. Larger numbers of PCSs enable more reliable analysis, but PCSs from flexible regions of the protein (e.g., loop or terminal regions) can hinder the fitting. PCSs should be collected from the resonances from the rigid regions of the protein. PCS-based tensor fitting is supported by several programs such as Numbat [77], Echidna [78], FANTEN [79], and Olivia (Yokochi et al. <http://fermi.pharm.hokudai.ac.jp/olivia/>). The fitting often depends on initial parameters, thus fitting from approximate values for parameters such as  $\Delta\chi_{ax}$ ,  $\Delta\chi_{rh}$ , and metal position ( $x$ ,  $y$ ,  $z$ ) may be necessary to obtain more reliable results. The paramagnetic lanthanide ion fixed at different positions by the same lanthanide-binding tag should yield similar tensor parameters given that the tag is well fixed in the protein frame. Thus, the initial parameters for  $\Delta\chi_{ax}$  and  $\Delta\chi_{rh}$  can be taken from the previous reports using two-point anchored LBT

[47–50] or CLaNP-5 [63, 64, 72, 80]. The initial metal position can be set at one of the side chain atoms of the residue mutated to cysteine for fixation of the tag. Tensor fitting based on the data from multiple lanthanide ions makes the result more reliable, because the number of variables in the fitting can be decreased assuming that all of the lanthanide ions coordinated in the same tag have a shared position. Back-calculated PCSs based on the fitted tensor aid in identifying additional PCSs assignments, especially those from crowded regions of the spectra. Although the  $\gamma$  term in the Euler angles, which define the relative orientation of the principal axes of the  $\Delta\chi$ -tensor with respect to the protein frame, tends to vary by lanthanide ion, the lanthanide ions in the same tag generally have similar  $\alpha$  and  $\beta$  (Tables 8.1 and 8.2).

## 8.6 Use of Paramagnetic Effects in Protein Structural Studies

Long-range distance and angular information from paramagnetic effects especially from PCSs is highly useful in protein structural analysis and drug design. Most of the major structure calculation programs can now handle paramagnetic restraints such as PCS, RDC, and PRE. Patches for paramagnetic restraints in structure calculation have been developed in Bertini's group from the early stage, and PARA restraints for Xplor-NIH [81] and paramagnetic DYANA/CYANA [82] are available. An increasing number of programs are being upgraded to incorporate paramagnetic restraints in their calculations. For example, paramagnetic restraints are implemented in CYANA3.0 [83], HADDOCK [84], PCS-Rosetta [85], and GPS-Rosetta [86, 87]. Among a number of important examples of structural studies exploiting the paramagnetic lanthanide probe methods, including the studies on protein–protein complexes [12, 30, 48, 50, 88], protein–ligand complexes [24, 49, 89, 90], and multi-domain proteins [72, 91], we here describe a few examples of structural analysis of protein–protein complexes [48, 50] and a multi-domain protein [72].

### 8.6.1 PCS-Based Docking for Protein–Protein Complexes

If a paramagnetic lanthanide ion is fixed on one protein in a complex, the paramagnetic effects such as PCSs can also be observed from the binding partner, thus providing a wealth of structural information for the complex. The usefulness of PCSs in structural analysis of protein–protein complexes has been demonstrated with the dimer of p62 PB1 (Phox and Bem1) domain [48] and the complex of FKBP12 (FK-506 binding protein 12) and mTOR (mammalian target of rapamycin) FRB (FKBP12 rapamycin binding) domain [50]. As a first example, PCS-based rigid-body docking of a 10 kDa domain at the N-terminus of p62, PB1 domain, has

been presented. The PB1 domain of p62 forms a homo oligomer in a head-to-tail manner. For the structural study by solution NMR, DR mutant (D67A/D69R) and KE mutant (K7E/R94A), forming 1:1 DR-KE dimer, were designed [48, 92], and a lanthanide ion was fixed on DR by the two-point anchored LBT. As a second example, docking of the complex of the FKBP12-rapamycin and mTOR FRB domain has been presented [50], and a lanthanide ion was fixed on FKBP12 by the use of the two-point anchored LBT. For both cases, the  $\Delta\chi$ -tensors were determined for the paramagnetic lanthanide ions in complex with isolated LBT-DR or LBT-FKBP12 (Table 8.2). On the basis of the  $\Delta\chi$ -tensor determined for LBT-DR or LBT-FKBP12, the PCSs observed from the binding partner are readily translated into the structural information for the complex, more specifically, information regarding the relative position of the binding partner with respect to LBT-DR or LBT-FKBP12. Based on the PCSs as well as  $\Delta\chi$ -tensor parameters, rigid-body docking calculations were performed using Xplor-NIH [93] equipped with PARA restraints for Xplor-NIH [81]. The rigid-body docking calculations solely based on PCS restraints resulted in degenerate solutions, in which the binding partner is distributed in multiple positions [48, 50]. This degeneracy is due to the symmetry of the  $\Delta\chi$ -tensor as seen in Eq. 8.1 and Fig. 8.1a, b. In principle, a calculation based on PCSs from a single paramagnetic lanthanide ion results in eight degenerate solutions [50]. The degeneracy can be eliminated by the use of multiple PCS data sets from different paramagnetic lanthanide ions, because the x and y directions of the principal axes of the  $\Delta\chi$ -tensor, represented as the  $\gamma$  term of the Euler angles, tend to vary among the lanthanide ions even in the same coordination (Table 8.2). The combined use of PCSs from  $Tb^{3+}$  and  $Dy^{3+}$ , whose x and y directions of principal axes differed by 20°–30°, eliminated the degeneracy and yielded four degenerate solutions (Fig. 8.4a). To fully overcome the degeneracy, another orthogonal restraints, such as contact-surface restraints derived from chemical shift perturbation mapping [48] (Fig. 8.4b) or another orthogonal set of PCSs derived from the paramagnetic ion fixed at another position [50] (Fig. 8.4d), are needed. To obtain contact-surface restraints based on chemical shift perturbation mapping, the contact residues are selected according to the following criteria:

1. Significant chemical shift perturbation is observed upon binding.
2. At least one or two atoms of the residue are exposed on the surface of the protein.
3. The contact residue is located in a cluster of residues on a contiguous, single binding surface.

The combined use of contact-surface restraints resolves the degeneracy, as shown by docking of the p62 PB1 DR-KE dimer (Fig. 8.4c). Another choice is to use multiple sets of PCSs: For two-point anchored LBT, obtaining another orthogonal set of PCSs is quite easy, because the metal position can be readily modified by changing the length of the spacer between LBT and the protein [50] (Fig. 8.3a). In the case of FKBP12, the two constructs with the three- and four-residue spacers resulted in the metal positions ~5 Å apart and the direction of the principal axes of  $\Delta\chi$ -tensor differed by 30°–40° (Fig. 8.4d) (Table 8.2). The use of PCS data sets

from lanthanide ions at two different positions successfully resolved the degeneracy [50] (Fig. 8.4e). Furthermore, using orthogonal sets of PCSs is powerful not only in the docking calculation but also in de novo determination of the 3D fold of the protein [85, 86, 94, 95].

### 8.6.2 Evaluation of the Conformational Changes in a Multi-domain Protein

Long-range, quantitative distance and angular information from PCSs is also useful in the analysis of conformational changes, particularly drastic conformational changes in multi-domain proteins [72, 91]. If the lanthanide ion is fixed in one of

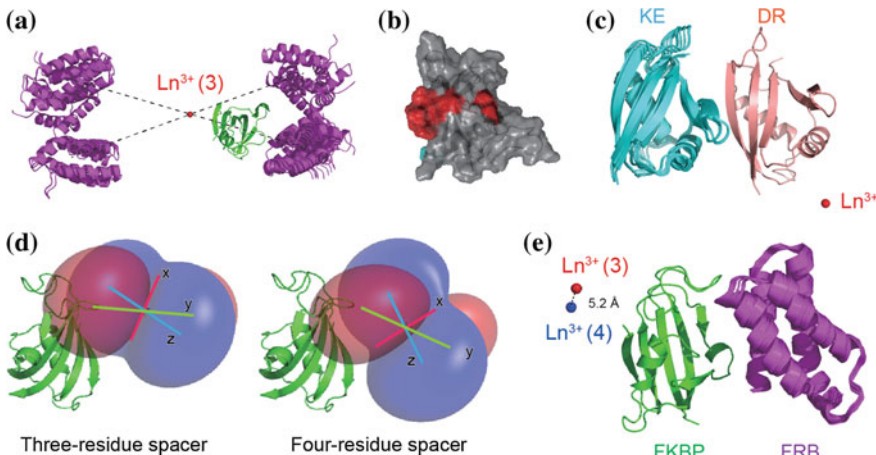


**Fig. 8.4** PCS-based docking for protein–protein complexes. **a** Docking of FKBP12 and FRB domain solely based only on the PCSs derived from  $\text{Dy}^{3+}$  and  $\text{Tb}^{3+}$  coordinated in LBT-FKBP with three-residue spacer [50]. The metal position is represented as red sphere. FKBP and FRB domain are colored in green and purple, respectively. Due to the symmetry of  $\Delta\gamma$ -tensor, FRB domain is distributed in the four distinct locations. **b** Mapping of the interfacial residues on p62 PB1 KE. The residues showing significant chemical shift perturbation ( $\Delta\delta > 0.5 \text{ ppm}$ ) upon binding to LBT-DR at a ratio of 1:1 and fulfilling the other two criteria (see main text) are colored red and defined as “contact residues” in the docking calculation [48]. A residue colored in cyan, Asp90, showed large chemical shift perturbation but did not satisfy the criterion #3 (see main text). **c** The docking structures of p62 PB1 DR-KE complex, calculated based on PCSs derived from  $\text{Tm}^{3+}$  and  $\text{Tb}^{3+}$  coordinated in LBT-DR with three-residue spacer as well as the contact-surface restraints [48]. The metal position is represented as red sphere. **d** PCS isosurfaces of  $\text{Dy}^{3+}$  coordinated in LBT-FKBP12 with three- or four-residue spacer [50]. Positive and negative PCSs are represented by blue and red, respectively. **e** The docking structures of FKBP12-FRB domain complex, calculated based on PCSs derived from  $\text{Dy}^{3+}$  and  $\text{Tb}^{3+}$  coordinated in LBT-FKBP12 with three- and four-residue spacers. The metal positions in LBT-FKBP12 with three- and four-residue spacers are represented as red and blue spheres, respectively

the domains, PCSs from the other domains reflect the orientation of the domains relative to the one with the lanthanide ion fixed. PCS-based evaluation of ligand-driven conformational changes in a multi-domain protein has been demonstrated with a 47 kDa bacterial protein MurD consisting of three domains [72]. A lanthanide ion was fixed on domain 2 by CLaNP-5 [63, 64] and the conformational changes of domain 3 by the addition of ADP, the ATP analogue adenylylimidodiphosphate (AMP-PNP), Mg<sup>2+</sup>, and UDP-N-acetyl muramoyl-l-alanine (UMA) in various combinations were monitored by PCSs (Fig. 8.5a–c). The resonances from domain 3 indicated large PCS changes by the addition of the ligands, indicating drastic conformational changes in MurD upon the binding to the ligands (Fig. 8.5b, c). In the absence of these ligands, the observed PCSs were consistent with the crystal structure of MurD in the open form [96] (1e0d.pdb), thus indicating that apo MurD is in the open form as seen in the crystal structure. PCSs in the presence of ADP, Mg<sup>2+</sup>, and UMA, or the inhibitor indicated that MurD in complex with these ligands is in the closed conformation, as seen in the crystal structure [97] (3uag.pdb). Interestingly, PCS analysis identified a novel conformational state of MurD, a semi-closed form in the presence of AMP-PNP and Mg<sup>2+</sup> or ADP and Mg<sup>2+</sup>. Rigid-body calculations based on the PCSs observed for MurD in complex with AMP-PNP and Mg<sup>2+</sup> indicated that the semi-closed form has domain 3 located in between the open and closed forms (Fig. 8.5d). Despite a number of crystal structures reported in the absence or presence of various ligands, no crystal structure has been reported for MurD in complex with ATP or its analogue, and thus, the semi-closed form had been veiled in the previous crystallographic studies for a long time. Structural information by solution NMR exploiting the paramagnetic lanthanide probe is exceptionally useful for unbiased structural characterization of multi-domain proteins. Furthermore, evaluation of the conformational states of a protein by PCSs can be powerful in drug screening in which the drug candidates are evaluated on the basis of “activity” in inducing conformational changes in the target protein. In fact, the known inhibitors of MurD strongly induced closed conformation as detected by PCSs (Fig. 8.5c). In addition to binding affinity, the conformational changes in the target protein can be another indicator for estimating the efficacy of drug candidates.

### 8.6.3 *Further Applications of Paramagnetic Lanthanide Probe Methods*

Since the paramagnetic effects can be obtained on the basis of simple 2D spectra with high sensitivity, the use of paramagnetic lanthanide probe methods expands the range of the NMR targets, especially in terms of concentration, lifetime, throughput, and size. Structural information obtainable from dilute protein solutions is beneficial for structural studies of membrane proteins [95] or proteins in living cells [98, 99]. Structure determination in living cells is challenging because of the

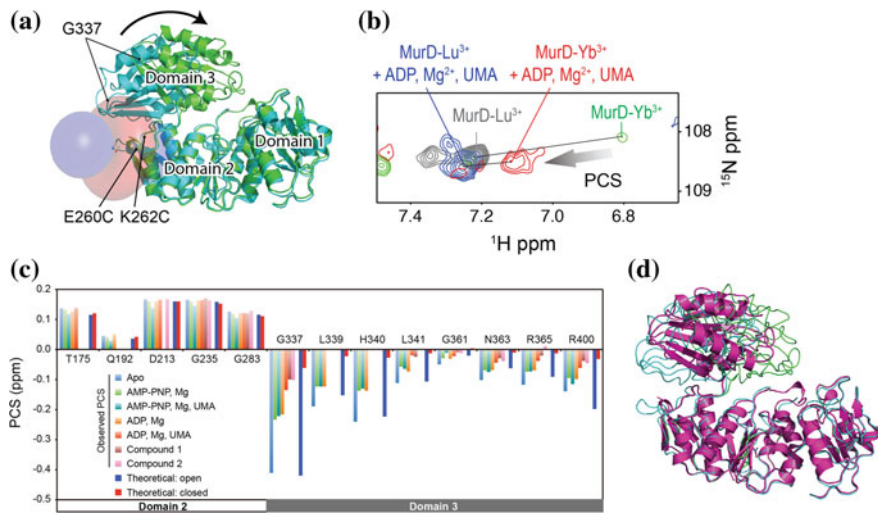


**Fig. 8.5** PCS-based analysis of conformational changes in a multi-domain protein MurD [72]. **a** PCS isosurfaces of Yb<sup>3+</sup> coordinated in CLaNP-5 fixed on MurD domain 1-2 E260C/K262C [72]. Conformational changes of domain 3 can be detected by PCSs observed from domain 3. Positive and negative PCSs are represented by blue and red, respectively. **b** Overlay of the <sup>1</sup>H-<sup>15</sup>N HSQC spectra of <sup>15</sup>N-labeled MurD E260C/K262C-CLaNP-5 in the presence and absence of the ligands. A region for the resonance of G337 is selected. **c** PCSs observed for the backbone amide proton resonances from domain 2 and 3 in the presence or absence of the ligands. Theoretical values for open and closed state are also displayed. **d** PCS-based model of semi-closed state (*purple*) calculated based on PCSs. The model is superimposed with crystal structures of MurD in the open [96] (1e0d.pdb, *cyan*) and closed [97] (3uag.pdb, *green*) conformations

limited concentration of the protein incorporated in the cell as well as the limited lifetime of the cell. Reducing conditions in the cytosol have prevented application of the paramagnetic lanthanide probe in in-cell NMR, because most of the lanthanide-binding tags are attached to the protein through disulfide bonds. Recent developments of the high-affinity lanthanide-binding tags attached through nonreducible thioether bond(s) [66–69] have enabled the use of the paramagnetic probe in the living cells. Even in the absence of NOE restraints, the PCS restraints combined with advanced structure calculation software such as PCS-Rosetta [85] and GPS-Rosetta [86, 87] have succeeded in determining the 3D structures of proteins in living cells [98, 99]. Structural information obtained from sensitive 2D spectra is also useful in the structure determination of short-lived protein species. Chen et al. [100] have reported PCS-based structure determination of an intermediate of an enzyme Sortase A whose half-life is ~2.5 h. The structural information provided by paramagnetic effects can also be exploited in ligand screening and drug design, particularly in fragment-based drug design (FBDD), in which small compounds are screened for binding to specific sites of a target protein and hit compounds are combined and optimized to increase the affinity and specificity. Saio et al. [49] have proposed a hybrid method that screens ligands bound to a specific

binding site on a target protein by  $\text{Gd}^{3+}$ -induced PRE and then performs rapid PCS-based docking for the protein–ligand complex.

Long-range quantitative information from PCSs is also useful in structural studies of large proteins and their complexes. One of the advantages of the paramagnetic lanthanide probe methods using a tag is that the  $\Delta\chi$ -tensor can be predicted because the paramagnetic properties are mostly determined by local environment, such as coordination of the lanthanide ion [64, 88]. Even if one protein in the complex is too large to yield sufficient sensitivity of NMR resonances, the tensor parameters can be predicted on the basis of the parameters determined for other proteins, and structural information of the complex can be obtained from the transferred PCSs observed from the binding partner. One example has been shown by Keizers et al. [88], in which the paramagnetic lanthanide ion was fixed at two positions on  $\sim 50$  kDa adrenodoxin reductase, and PCSs and PREs were observed from the binding partner adrenodoxin (4-108). Predicted  $\Delta\chi$ -tensor parameters were used, so that the PCSs observed from adrenodoxin were translated into structural information of the complex [88]. The ambiguity of the predicted tensor parameters was compensated by the use of multiple sets of PCSs.

The structural information of PCSs extracted from chemical shifts is also attractive in Carr–Purcell–Meiboom–Gill sequence (CPMG) relaxation dispersion experiments to obtain structural information of the minor state. Vallurupalli et al. [101] have demonstrated the use of RDCs as well as residual chemical shift anisotropies, which were measured by the use of external alignment media to obtain structural information for the minor state of the protein. In principle, PCSs as well as RDCs of the minor state can be observed through the use of paramagnetic lanthanide ions in relaxation dispersion experiments. Another advantage of the use of paramagnetic lanthanide ions in relaxation dispersion experiments is the magnification of relaxation dispersion due to PCS differences between the states. Several examples have been reported for metal-binding proteins substituted by lanthanide ions [36] or a cobalt ion [35]. However, applications for non-metalloproteins using lanthanide-binding tags currently seem difficult because the motion of the tag interferes with the relaxation dispersion originating from the protein dynamics [102, 103].

## 8.7 Concluding Remarks

The 3D structures of proteins provide important information for unveiling the detailed mechanisms of the proteins. However, proteins are intrinsically flexible and mobile, and their structure and dynamics change as the proteins undergo their functional processes. Thus, it is difficult to fully unveil the mechanisms based only on snapshots of the protein structure. A lack of information about interactions, structural changes, and dynamics often obscures the mechanism of the protein even after structure determination. A technique that enables comprehensive structural analysis has been desired. Solution NMR equipped with a paramagnetic lanthanide

probe can be one of the best tools. The long-range quantitative structural information derived from the paramagnetic lanthanide probe is useful not only for structure determinations but also for analyses of interactions, dynamics, and structural changes [4]. If the lanthanide ion is fixed in a target protein, the structure of the complex [24, 30, 48–50] as well as structural changes in the protein [72, 91] can be immediately characterized on the basis of paramagnetic effects such as PCSs, RDCs, and PREs. Dynamic properties of a complex can also be characterized according to the paramagnetic effects [32, 33]. By exploiting the paramagnetic lanthanide probe methods, the structure, interactions, and successive structural and dynamical changes in a protein through the functional process can be quantitatively analyzed. Such analyses can scarcely be addressed only by X-ray crystallography or conventional NOE-based NMR structure determination. Even for large proteins or their complexes, whose NMR spectra tend to be crowded with broad signals, lanthanide probe experiments can be applied with the use of advanced isotope labeling techniques, including selective labeling and deuterium labeling. The quantitative information on protein structure and dynamics can be extracted from the limited number of NMR signals.

The lack of an efficient method for fixing the lanthanide ion to a protein has prevented general application of the lanthanide probe method, but recent developments in lanthanide-binding tags have enabled the application of the paramagnetic lanthanide probe methods to any proteins of interest [11]. Practical applications of the lanthanide probe method have just been started. The NMR techniques, bolstered by the use of the paramagnetic lanthanide probe, will shed light on multiple aspects of biological systems that have not been revealed by other methods.

**Acknowledgements** We would like to thank Dr. Yoshihiro Kobashigawa for providing the data for Fig. 8.4 and Dr. Hiromasa Yagi for helpful comments and careful reading of the manuscript. A part of this work was supported by Creation of Innovation Centers for Advanced Interdisciplinary Research Areas Program, Ministry of Education, Culture, Sports, Science and Technology, Japan. This work was also partly supported by JSPS KAKENHI Grant Number 15H01624 and 15K20829 and by JST, PRESTO.

## References

1. Inagaki, F., Miyazawa, T.: NMR analyses of molecular conformations and conformational equilibria with the lanthanide probe method. *Progr. Nuclear Magn. Reson. Spectrosc.* **14**, 67–111 (1980)
2. Hinckley, C.C.: Paramagnetic shifts in solutions of cholesterol and the dipyridine adduct of trisdipivalomethanatoeuropium(III). A shift reagent. *J. Am. Chem. Soc.* **91**, 5160–5162 (1969)
3. Barry, C.D., North, A.C.T., Glasel, J.A., Williams, R.J.P., Xavier, A.V.: Quantitative determination of mononucleotide conformations in solution using lanthanide ion shift and broadening NMR Probes. *Nature* **232**, 236–245 (1971)

4. Nitsche, C., Otting, G.: Pseudocontact shifts in biomolecular NMR using paramagnetic metal tags. *Progr. Nuclear Magn. Reson. Spectrosc.* **98–99**, 20–49 (2017)
5. Göbl, C., Madl, T., Simon, B., Sattler, M.: NMR approaches for structural analysis of multidomain proteins and complexes in solution. *Progr. Nuclear Magn. Reson. Spectrosc.* **80**, 26–63 (2014)
6. Matthews, S.: Perdeuteration/site-specific protonation approaches for high-molecular-weight proteins. In: Kristina Downing, A. (ed.) *Protein NMR Techniques*, pp. 035–046. Humana Press, New Jersey (2004)
7. Tugarinov, V., Kanelis, V., Kay, L.E.: Isotope labeling strategies for the study of high-molecular-weight proteins by solution NMR spectroscopy. *Nat. Protoc.* **1**, 749–754 (2006)
8. Kainoshio, M., Torizawa, T., Iwashita, Y., Terauchi, T., Ono, A.M., Güntert, P.: Optimal isotope labelling for NMR protein structure determinations. *Nature* **440**, 52–57 (2006)
9. Sprangers, R., Kay, L.E.: Quantitative dynamics and binding studies of the 20S proteasome by NMR. *Nature* **445**, 618–622 (2007)
10. Kofuku, Y., Ueda, T., Okude, J., Shiraishi, Y., Kondo, K., Mizumura, T., Suzuki, S., Shimada, I.: Functional dynamics of deuterated  $\beta$  2-adrenergic receptor in lipid bilayers revealed by NMR spectroscopy. *Angew. Chem. Int. Ed.* **53**, 13376–13379 (2014)
11. Koehler, J., Meiler, J.: Expanding the utility of NMR restraints with paramagnetic compounds: background and practical aspects. *Progr. Nuclear Magn. Reson. Spectrosc.* **59**, 360–389 (2011)
12. Hass, M.A., Ubbink, M.: Structure determination of protein–protein complexes with long-range anisotropic paramagnetic NMR restraints. *Curr. Opin. Struct. Biol.* **24**, 45–53 (2014)
13. Otting, G.: Protein NMR using paramagnetic ions. *Annu. Rev. Biophys.* **39**, 387–405 (2010)
14. Pintacuda, G., Keniry, M.A., Huber, T., Park, A.Y., Dixon, N.E., Otting, G.: Fast structure-based assignment of  $^{15}\text{N}$  HSQC spectra of selectively  $^{15}\text{N}$ -labeled paramagnetic proteins. *J. Am. Chem. Soc.* **126**, 2963–2970 (2004)
15. Allegrozzi, M., Bertini, I., Janik, M.B.L., Lee, Y.M., Liu, G., Luchinat, C.: Lanthanide-induced pseudocontact shifts for solution structure refinements of macromolecules in shells up to 40 Å from the metal ion. *J. Am. Chem. Soc.* **122**, 4154–4161 (2000)
16. Tjandra, N., Bax, A.: Direct measurement of distances and angles in biomolecules by NMR in a dilute liquid crystalline medium. *Science* **278**, 1111–1114 (1997)
17. Hansen, M.R., Mueller, L., Pardi, A.: Tunable alignment of macromolecules by filamentous phage yields dipolar coupling interactions. *Nat. Struct. Mol. Biol.* **5**, 1065–1074 (1998)
18. Rückert, M., Otting, G.: Alignment of biological macromolecules in novel nonionic liquid crystalline media for NMR experiments. *J. Am. Chem. Soc.* **122**, 7793–7797 (2000)
19. Tolman, J.R., Flanagan, J.M., Kennedy, M.A., Prestegard, J.H.: Nuclear magnetic dipole interactions in field-oriented proteins: information for structure determination in solution. *PNAS* **92**, 9279–9283 (1995)
20. Clore, G.M., Iwahara, J.: Theory, practice, and applications of paramagnetic relaxation enhancement for the characterization of transient low-population states of biological macromolecules and their complexes. *Chem. Rev.* **109**, 4108–4139 (2009)
21. Bertini, I., Luchinat, C., Parigi, G., Ravera, E.: Relaxation. In: *Solution NMR of Paramagnetic Molecules*, pp. 77–126. Elsevier, Amsterdam (2017)
22. Bertini, I., Luchinat, C., Parigi, G., Ravera, E.: Lanthanoids and actinoids: shift and relaxation. In: *Solution NMR of Paramagnetic Molecules*, pp. 255–276. Elsevier, Amsterdam (2017)
23. Bertini, I., Janik, M.B.L., Lee, Y.M., Luchinat, C., Rosato, A.: Magnetic susceptibility tensor anisotropies for a lanthanide ion series in a fixed protein matrix. *J. Am. Chem. Soc.* **123**, 4181–4188 (2001)
24. Pintacuda, G., John, M., Su, X.-C., Otting, G.: NMR structure determination of protein–ligand complexes by lanthanide labeling. *Acc. Chem. Res.* **40**, 206–212 (2007)

25. Bentrop, D., Bertini, I., Cremonini, M.A., Forsén, S., Luchinat, C., Malmendal, A.: Solution structure of the paramagnetic complex of the N-terminal domain of calmodulin with two Ce<sup>3+</sup> ions by <sup>1</sup>H NMR. *Biochemistry* **36**, 11605–11618 (1997)
26. Bertini, I., Janik, M.B.L., Liu, G., Luchinat, C., Rosato, A.: Solution structure calculations through self-orientation in a magnetic field of a cerium(III) substituted calcium-binding protein. *J. Magn. Reson.* **148**, 23–30 (2001)
27. Bertini, I., Donaire, A., Jiménez, B., Luchinat, C., Parigi, G., Piccioli, M., Poggi, L.: Paramagnetism-based versus classical constraints: an analysis of the solution structure of Ca Ln calbindin D9k. *J. Biomol. NMR* **21**, 85–98 (2001)
28. Rinaldelli, M., Ravera, E., Calderone, V., Parigi, G., Murshudov, G.N., Luchinat, C.: IUCr: simultaneous use of solution NMR and X-ray data in REFMAC5 for joint refinement/detection of structural differences. *Acta Crystallogr. D Biol. Crystallogr.* **70**, 958–967 (2014)
29. Carlon, A., Ravera, E., Hennig, J., Parigi, G., Sattler, M., Luchinat, C.: Improved accuracy from joint X-ray and NMR refinement of a protein–RNA complex structure. *J. Am. Chem. Soc.* **138**, 1601–1610 (2016)
30. Pintacuda, G., Park, A.Y., Keniry, M.A., Dixon, N.E., Otting, G.: Lanthanide Labeling offers fast NMR approach to 3D structure determinations of protein–protein complexes. *J. Am. Chem. Soc.* **128**, 3696–3702 (2006)
31. John, M., Pintacuda, G., Park, A.Y., Dixon, N.E., Otting, G.: Structure determination of protein–ligand complexes by transferred paramagnetic shifts. *J. Am. Chem. Soc.* **128**, 12910–12916 (2006)
32. Bertini, I., Del Bianco, C., Gelis, I., Katsaros, N., Luchinat, C., Parigi, G., Peana, M., Provenzani, A., Zoroddu, M.A.: Experimentally exploring the conformational space sampled by domain reorientation in calmodulin. *PNAS* **101**, 6841–6846 (2004)
33. Bertini, I., Gupta, Y.K., Luchinat, C., Parigi, G., Peana, M., Sgheri, L., Yuan, J.: Paramagnetism-based NMR restraints provide maximum allowed probabilities for the different conformations of partially independent protein domains. *J. Am. Chem. Soc.* **129**, 12786–12794 (2007)
34. Russo, L., Maestre-Martinez, M., Wolff, S., Becker, S., Griesinger, C.: Interdomain dynamics explored by paramagnetic NMR. *J. Am. Chem. Soc.* **135**, 17111–17120 (2013)
35. Wang, X., Srisailam, S., Yee, A.A., Lemak, A., Arrowsmith, C., Prestegard, J.H., Tian, F.: Domain–domain motions in proteins from time-modulated pseudocontact shifts. *J. Biomol. NMR* **39**, 53–61 (2007)
36. Eichmüller, C., Skrynnikov, N.R.: Observation of  $\mu$ s time-scale protein dynamics in the presence of Ln<sup>3+</sup> ions: application to the N-terminal domain of cardiac troponin C. *J. Biomol. NMR* **37**, 79–95 (2006)
37. John, M., Schmitz, C., Park, A.Y., Dixon, N.E., Huber, T., Otting, G.: Sequence-specific and stereospecific assignment of methyl groups using paramagnetic lanthanides. *J. Am. Chem. Soc.* **129**, 13749–13757 (2007)
38. Gaponenko, V., Sarma, S.P., Altieri, A.S., Horita, D.A., Li, J., Byrd, R.A.: Improving the accuracy of NMR structures of large proteins using pseudocontact shifts as long-range restraints. *J. Biomol. NMR* **28**, 205–212 (2004)
39. Wöhner, J., Franz, K.J., Nitz, M., Imperiali, B., Schwalbe, H.: Protein alignment by a coexpressed lanthanide-binding tag for the measurement of residual dipolar couplings. *J. Am. Chem. Soc.* **125**, 13338–13339 (2003)
40. Martin, L.J., Hähnke, M.J., Nitz, M., Wöhner, J., Silvaggi, N.R., Allen, K.N., Schwalbe, H., Imperiali, B.: Double-lanthanide-binding tags: design, photophysical properties, and NMR applications. *J. Am. Chem. Soc.* **129**, 7106–7113 (2007)
41. Ma, C., Opella, S.J.: Lanthanide ions bind specifically to an added “EF-Hand” and orient a membrane protein in micelles for solution NMR spectroscopy. *J. Magn. Reson.* **146**, 381–384 (2000)

42. Zhuang, T., Lee, H.S., Imperiali, B., Prestegard, J.H.: Structure determination of a Galectin-3-carbohydrate complex using paramagnetism-based NMR constraints. *Protein Sci.* **17**, 1220–1231 (2008)
43. Su, X.-C., Huber, T., Dixon, N.E., Otting, G.: Site-specific labelling of proteins with a rigid lanthanide-binding tag. *ChemBioChem* **7**, 1599–1604 (2006)
44. Su, X.C., McAndrew, K., Huber, T., Otting, G.: Lanthanide-binding peptides for NMR measurements of residual dipolar couplings and paramagnetic effects from multiple angles. *J. Am. Chem. Soc.* **130**, 1681–1687 (2008)
45. Barthelmes, K., Reynolds, A.M., Peisach, E., Jonker, H.R.A., DeNunzio, N.J., Allen, K.N., Imperiali, B., Schwalbe, H.: Engineering encodable lanthanide-binding tags into loop regions of proteins. *J. Am. Chem. Soc.* **133**, 808–819 (2010)
46. Barb, A.W., Subedi, G.P.: An encodable lanthanide binding tag with reduced size and flexibility for measuring residual dipolar couplings and pseudocontact shifts in large proteins. *J. Biomol. NMR* **64**, 75–85 (2016)
47. Saio, T., Ogura, K., Yokochi, M., Kobashigawa, Y., Inagaki, F.: Two-point anchoring of a lanthanide-binding peptide to a target protein enhances the paramagnetic anisotropic effect. *J. Biomol. NMR* **44**, 157–166 (2009)
48. Saio, T., Yokochi, M., Kumeta, H., Inagaki, F.: PCS-based structure determination of protein–protein complexes. *J. Biomol. NMR* **46**, 271–280 (2010)
49. Saio, T., Ogura, K., Shimizu, K., Yokochi, M., Burke Jr., T.R., Inagaki, F.: An NMR strategy for fragment-based ligand screening utilizing a paramagnetic lanthanide probe. *J. Biomol. NMR* **51**, 395–408 (2011)
50. Kobashigawa, Y., Saio, T., Ushio, M., Sekiguchi, M., Yokochi, M., Ogura, K., Inagaki, F.: Convenient method for resolving degeneracies due to symmetry of the magnetic susceptibility tensor and its application to pseudo contact shift-based protein–protein complex structure determination. *J. Biomol. NMR* **53**, 53–63 (2012)
51. Su, X.-C., Man, B., Beeren, S., Liang, H., Simonsen, S., Schmitz, C., Huber, T., Messerle, B.A., Otting, G.: A dipicolinic acid tag for rigid lanthanide tagging of proteins and paramagnetic NMR spectroscopy. *J. Am. Chem. Soc.* **130**, 10486–10487 (2008)
52. Dvoretzky, A., Gaponenko, V., Rosevear, P.R.: Derivation of structural restraints using a thiol-reactive chelator. *FEBS Lett.* **528**, 189–192 (2002)
53. Haberz, P., Rodriguez-Castañeda, F., Junker, J., Becker, S., Leonov, A., Griesinger, C.: Two new chiral EDTA-based metal chelates for weak alignment of proteins in solution. *Org. Lett.* **8**, 1275–1278 (2006)
54. Pintacuda, G., Moshref, A., Leonchiks, A., Sharipo, A., Otting, G.: Site-specific labelling with a metal chelator for protein–structure refinement. *J. Biomol. NMR* **29**, 351–361 (2004)
55. Prudêncio, M., Rohovec, J., Peters, J.A., Tocheva, E., Boulanger, M.J., Murphy, M.E.P., Hupkes, H.J., Kosters, W., Impagliazzo, A., Ubbink, M.: A caged lanthanide complex as a paramagnetic shift agent for protein NMR. *Chem. Eur. J.* **10**, 3252–3260 (2004)
56. Ikegami, T., Verdier, L., Sakhaii, P., Grimme, S., Pescatore, B., Saxena, K., Fiebig, K.M., Griesinger, C.: Novel techniques for weak alignment of proteins in solution using chemical tags coordinating lanthanide ions. *J. Biomol. NMR* **29**, 339–349 (2004)
57. Leonov, A., Voigt, B., Rodriguez Castañeda, F., Sakhaii, P., Griesinger, C.: Convenient synthesis of multifunctional EDTA-based chiral metal chelates substituted with an *S*-mesylcysteine. *Chem. Eur. J.* **11**, 3342–3348 (2005)
58. Gaponenko, V., Altieri, A.S., Li, J., Byrd, R.A.: Breaking symmetry in the structure determination of (large) symmetric protein dimers. *J. Biomol. NMR* **24**, 143–148 (2002)
59. Vlasie, M.D., Comuzzi, C., van den Nieuwendijk, A.M.C.H., Prudêncio, M., Overhand, M., Ubbink, M.: Long-range-distance NMR effects in a protein labeled with a lanthanide–DOTA chelate. *Chem. Eur. J.* **13**, 1715–1723 (2007)
60. Häussinger, D., Huang, J.-R., Grzesiek, S.: DOTA-M8: an extremely rigid, high-affinity lanthanide chelating tag for PCS NMR spectroscopy. *J. Am. Chem. Soc.* **131**, 14761–14767 (2009)

61. Swarbrick, J.D., Ung, P., Su, X.-C., Maleckis, A., Chhabra, S., Huber, T., Otting, G., Graham, B.: Engineering of a bis-chelator motif into a protein  $\alpha$ -helix for rigid lanthanide binding and paramagnetic NMR spectroscopy. *Chem. Commun.* **47**, 7368–7370 (2011)
62. Swarbrick, J.D., Ung, P., Chhabra, S., Graham, B.: An iminodiacetic acid based lanthanide binding tag for paramagnetic exchange NMR spectroscopy. *Angew. Chem. Int. Ed.* **50**, 4403–4406 (2011)
63. Keizers, P.H.J., Desreux, J.F., Overhand, M., Ubbink, M.: Increased paramagnetic effect of a lanthanide protein probe by two-point attachment. *J. Am. Chem. Soc.* **129**, 9292–9293 (2007)
64. Keizers, P.H.J., Saragliadis, A., Hiruma, Y., Overhand, M., Ubbink, M.: Design, synthesis, and evaluation of a lanthanide chelating protein probe: ClaNp-5 yields predictable paramagnetic effects independent of environment. *J. Am. Chem. Soc.* **130**, 14802–14812 (2008)
65. Liu, W.-M., Keizers, P.H.J., Hass, M.A.S., Blok, A., Timmer, M., Sarris, A.J.C., Overhand, M., Ubbink, M.: A pH-sensitive, colorful, lanthanide-chelating paramagnetic NMR probe. *J. Am. Chem. Soc.* **134**, 17306–17313 (2012)
66. Liu, W.-M., Skinner, S.P., Timmer, M., Blok, A., Hass, M.A.S., Filippov, D.V., Overhand, M., Ubbink, M.: A two-armed lanthanoid-chelating paramagnetic NMR probe linked to proteins via thioether linkages. *Chem. Eur. J.* **20**, 6256–6258 (2014)
67. Yang, Y., Li, Q.F., Cao, C., Huang, F., Su, X.-C.: Site-specific labeling of proteins with a chemically stable, high-affinity tag for protein study. *Chem. Eur. J.* **19**, 1097–1103 (2013)
68. Li, Q.F., Yang, Y., Maleckis, A., Otting, G., Su, X.-C.: Thiol–ene reaction: a versatile tool in site-specific labelling of proteins with chemically inert tags for paramagnetic NMR. *Chem. Commun.* **48**, 2704–2706 (2012)
69. Yang, Y., Wang, J.-T., Pei, Y.-Y., Su, X.-C.: Site-specific tagging proteins via a rigid, stable and short thioether tether for paramagnetic spectroscopic analysis. *Chem. Commun.* **51**, 2824–2827 (2015)
70. Hikone, Y., Hirai, G., Mishima, M., Inomata, K., Ikeya, T., Arai, S., Shirakawa, M., Sodeoka, M., Ito, Y.: A new carbamidemethyl-linked lanthanoid chelating tag for PCS NMR spectroscopy of proteins in living HeLa cells. *J. Biomol. NMR* **66**, 99–110 (2016)
71. Loh, C.T., Ozawa, K., Tuck, K.L., Barlow, N., Huber, T., Otting, G., Graham, B.: Lanthanide tags for site-specific ligation to an unnatural amino acid and generation of pseudocontact shifts in proteins. *Bioconjugate Chem.* **24**, 260–268 (2013)
72. Saio, T., Ogura, K., Kumeta, H., Kobashigawa, Y., Shimizu, K., Yokochi, M., Kodama, K., Yamaguchi, H., Tsujishita, H., Inagaki, F.: Ligand-driven conformational changes of MurD visualized by paramagnetic NMR. *Sci. Rep.* **5**, 16685 (2015)
73. Nitz, M., Franz, K.J., Maglathlin, R.L., Imperiali, B.: A powerful combinatorial screen to identify high-affinity terbium(III)-binding peptides. *ChemBioChem* **4**, 272–276 (2003)
74. Nitz, M., Sherawat, M., Franz, K.J., Peisach, E., Allen, K.N., Imperiali, B.: Structural origin of the high affinity of a chemically evolved lanthanide-binding peptide. *Angew. Chem. Int. Ed.* **43**, 3682–3685 (2004)
75. Iwai, H., Züger, S.: Protein ligation: applications in NMR studies of proteins. *Biotechnol. Genet. Eng. Rev.* **24**, 129–146 (2007)
76. Kobashigawa, Y., Kumeta, H., Ogura, K., Inagaki, F.: Attachment of an NMR-invisible solubility enhancement tag using a sortase-mediated protein ligation method. *J. Biomol. NMR* **43**, 145–150 (2009)
77. Schmitz, C., Stanton-Cook, M.J., Su, X.-C., Otting, G., Huber, T.: Numbat: an interactive software tool for fitting  $\Delta\chi$ -tensors to molecular coordinates using pseudocontact shifts. *J. Biomol. NMR* **41**, 179–189 (2008)
78. Schmitz, C., John, M., Park, A.Y., Dixon, N.E., Otting, G., Pintacuda, G., Huber, T.: Efficient  $\chi$ -tensor determination and NH assignment of paramagnetic proteins. *J. Biomol. NMR* **35**, 79–87 (2006)

79. Rinaldelli, M., Carlon, A., Ravera, E., Parigi, G., Luchinat, C.: FANTEN: a new web-based interface for the analysis of magnetic anisotropy-induced NMR data. *J. Biomol. NMR* **61**, 21–34 (2014)
80. Bertini, I., Calderone, V., Cerofolini, L., Fragai, M., Geraldes, C.F.G.C., Hermann, P., Luchinat, C., Parigi, G., Teixeira, J.M.C.: The catalytic domain of MMP-1 studied through tagged lanthanides. *FEBS Lett.* **586**, 557–567 (2012)
81. Banci, L., Bertini, I., Cavallaro, G., Giachetti, A., Luchinat, C., Parigi, G.: Paramagnetism-based restraints for Xplor-NIH. *J. Biomol. NMR* **28**, 249–261 (2004)
82. Banci, L., Bertini, I., Huber, J.G., Luchinat, C., Rosato, A.: Partial orientation of oxidized and reduced cytochrome b5 at high magnetic fields: magnetic susceptibility anisotropy contributions and consequences for protein solution structure determination. *J. Am. Chem. Soc.* **120**, 12903–12909 (1998)
83. Güntert, P.: Automated NMR structure calculation with CYANA. In: Kristina Downing, A. (ed.) Protein NMR Techniques, pp. 353–378. Humana Press, New Jersey (2004)
84. Schmitz, C., Bonvin, A.M.J.J.: Protein–protein HADDocking using exclusively pseudo-contact shifts. *J. Biomol. NMR* **50**, 263–266 (2011)
85. Schmitz, C., Vernon, R., Otting, G., Baker, D., Huber, T.: Protein structure determination from pseudocontact shifts using ROSETTA. *J. Mol. Biol.* **416**, 668–677 (2012)
86. Yagi, H., Pilla, K.B., Maleckis, A., Graham, B., Huber, T., Otting, G.: Three-dimensional protein fold determination from backbone amide pseudocontact shifts generated by lanthanide tags at multiple sites. *Structure* **21**, 883–890 (2013)
87. Pilla, K.B., Otting, G., Huber, T.: Pseudocontact shift-driven iterative resampling for 3D structure determinations of large proteins. *J. Mol. Biol.* **428**, 522–532 (2016)
88. Keizers, P.H.J., Mersinli, B., Reinle, W., Donauer, J., Hiruma, Y., Hannemann, F., Overhand, M., Bernhardt, R., Ubbink, M.: A solution model of the complex formed by adrenodoxin and adrenodoxin reductase determined by paramagnetic NMR spectroscopy. *Biochemistry* **49**, 6846–6855 (2010)
89. Guan, J.-Y., Keizers, P.H.J., Liu, W.-M., Löhr, F., Skinner, S.P., Heeneman, E.A., Schwalbe, H., Ubbink, M., Siegal, G.: Small-molecule binding sites on proteins established by paramagnetic NMR spectroscopy. *J. Am. Chem. Soc.* **135**, 5859–5868 (2013)
90. Künze, G., Köhling, S., Vogel, A., Rademann, J., Huster, D.: Identification of the glycosaminoglycan binding site of interleukin-10 by NMR spectroscopy. *J. Biol. Chem.* **291**, 3100–3113 (2016)
91. de la Cruz, L., Nguyen, T.H.D., Ozawa, K., Shin, J., Graham, B., Huber, T., Otting, G.: binding of low molecular weight inhibitors promotes large conformational changes in the dengue virus NS2B–NS3 protease: fold analysis by pseudocontact shifts. *J. Am. Chem. Soc.* **133**, 19205–19215 (2011)
92. Saio, T., Yokochi, M., Inagaki, F.: The NMR structure of the p62 PB1 domain, a key protein in autophagy and NF-κB signaling pathway. *J. Biomol. NMR* **45**, 335–341 (2009)
93. Schwieters, C.D., Kuszewski, J.J., Tjandra, N., Marius Clore, G.: The Xplor-NIH NMR molecular structure determination package. *J. Magn. Reson.* **160**, 65–73 (2003)
94. Li, J., Pilla, K.B., Li, Q., Zhang, Z., Su, X., Huber, T., Yang, J.: Magic angle spinning NMR structure determination of proteins from pseudocontact shifts. *J. Am. Chem. Soc.* **135**, 8294–8303 (2013)
95. Crick, D.J., Wang, J.X., Graham, B., Swarbrick, J.D., Mott, H.R., Nietlispach, D.: Integral membrane protein structure determination using pseudocontact shifts. *J. Biomol. NMR* **61**, 197–207 (2015)
96. Bertrand, J.A., Fanchon, E., Martin, L., Chantalat, L., Auger, G., Blanot, D., van Heijenoort, J., Dideberg, O.: “Open” structures of MurD: domain movements and structural similarities with folylpolyglutamate synthetase. *J. Mol. Biol.* **301**, 1257–1266 (2000)
97. Bertrand, J.A., Auger, G., Martin, L., Fanchon, E., Blanot, D., Le Beller, D., van Heijenoort, J., Dideberg, O.: Determination of the MurD mechanism through crystallographic analysis of enzyme complexes. *J. Mol. Biol.* **289**, 579–590 (1999)

98. Pan, B.-B., Yang, F., Ye, Y., Wu, Q., Li, C., Huber, T., Su, X.-C.: 3D structure determination of a protein in living cells using paramagnetic NMR spectroscopy. *Chem. Commun.* **52**, 10237–10240 (2016)
99. Müntener, T., Häussinger, D., Selenko, P., Theillet, F.-X.: In-cell protein structures from 2D NMR experiments. *J. Phys. Chem. Lett.* **7**, 2821–2825 (2016)
100. Chen, J.-L., Wang, X., Yang, F., Cao, C., Otting, G., Su, X.-C.: 3D structure determination of an unstable transient enzyme intermediate by paramagnetic NMR spectroscopy. *Angew. Chem. Int. Ed.* **55**, 13744–13748 (2016)
101. Vallurupalli, P., Hansen, D.F., Kay, L.E.: Structures of invisible, excited protein states by relaxation dispersion NMR spectroscopy. *Proc. Natl. Acad. Sci. U.S.A.* **105**, 11766–11771 (2008)
102. Hass, M.A.S., Keizers, P.H.J., Blok, A., Hiruma, Y., Ubbink, M.: Validation of a lanthanide tag for the analysis of protein dynamics by paramagnetic NMR spectroscopy. *J. Am. Chem. Soc.* **132**, 9952–9953 (2010)
103. Hass, M.A.S., Liu, W.-M., Agafonov, R.V., Otten, R., Phung, L.A., Schilder, J.T., Kern, D., Ubbink, M.: A minor conformation of a lanthanide tag on adenylylate kinase characterized by paramagnetic relaxation dispersion NMR spectroscopy. *J. Biomol. NMR* **61**, 123–136 (2015)

# Chapter 9

## Structure Determination of Membrane Peptides and Proteins by Solid-State NMR

Izuru Kawamura, Kazushi Norisada and Akira Naito

**Abstract** Solid-state nuclear magnetic resonance (NMR) spectroscopy provides useful information on the structure, topology, and orientation of peptides and proteins bound to lipid bilayers. The structure and orientation of membrane-associated peptides and proteins can be elucidated by analyzing structural constraints obtained from anisotropic chemical-shift interactions, nuclear dipolar interactions, or a combination of these interactions. Detailed structures of various peptides and proteins in their membrane-bound states can be studied by analyzing anisotropic chemical-shift interactions by, for example, chemical-shift oscillation analysis, and nuclear dipolar interactions using techniques such as polarity index slant angle wheel analysis. Magic-angle spinning (MAS) experiments coupled with cross-polarization (CP) and high-power decoupling (CP-MAS) techniques provide high-resolution  $^{13}\text{C}$  and  $^{15}\text{N}$  NMR signals for selectively or uniformly labeled membrane-bound peptides and proteins in solid-state NMR. Furthermore, homonuclear and heteronuclear dipolar interactions can be recoupled using various spin manipulation pulse sequences under MAS conditions. These experiments enable the correlation of  $^{13}\text{C}$ - $^{13}\text{C}$  and  $^{13}\text{C}$ - $^{15}\text{N}$  signals, allowing their assignment to specific amino acid residues and ultimately determination of the high-resolution structure of membrane-bound peptides and proteins.

**Keywords** Membrane peptide • Membrane protein • Chemical-shift interaction  
Nuclear dipolar interaction • Solid-state NMR

---

I. Kawamura (✉) · A. Naito

Faculty of Engineering, Yokohama National University,  
79-5 Hodogayaku Tokiwadai, Yokohama 240-8501, Japan  
e-mail: izuruk@ynu.ac.jp

A. Naito

e-mail: naito@ynu.ac.jp

K. Norisada

Graduate School of Engineering, Yokohama National University,  
79-5 Hodogayaku Tokiwadai, Yokohama 240-8501, Japan  
e-mail: k\_norisada@iic.ihi.co.jp

## 9.1 Introduction

Elucidation of both the structure and orientation of the membrane-bound structures of membrane-associated, biologically active peptides and proteins is important for full understanding of their biological functions and activities. These structures and orientations can be determined using structural and orientational constraints derived from magnetically anisotropic interactions, studied by solid-state NMR spectroscopy [1–6]. One such interaction is chemical-shift anisotropy (CSA), which typically appears as a dynamically averaged chemical-shift pattern. Using CSA interaction, the orientation of peptides and proteins in a lipid-bilayer environment can be derived [7]. Another interaction to be considered as a structural constraint is nuclear dipolar interaction between coupled nuclei. This type of interaction can be combined with chemical-shift constraints to provide detailed structural information regarding membrane-associated peptides and proteins [8]. Taken together, these constraints provide the dynamic structures, including detailed local structure, topology, and orientation of membrane-associated peptides and proteins [9]. However, complete structural information has only been determined for a limited number of these compounds.

Solid-state NMR analyses of biomolecules are typically performed using  $^{13}\text{C}$  and  $^{15}\text{N}$  nuclei, which exhibit spin-1/2. Solid-state NMR spectra yield enormously broadened signals, with line widths on the order of 20 kHz. Magic-angle spinning (MAS) experiments combined with cross-polarization (CP) and high-power decoupling (CP-MAS) provide high-resolution  $^{13}\text{C}$  and  $^{15}\text{N}$  NMR signals for selectively or uniformly labeled membrane-bound peptides and proteins. In solid-state NMR, homonuclear and heteronuclear dipolar interactions can be recoupled using various pulse sequences combined with multidimensional NMR techniques under MAS conditions. These experiments enable the correlation of  $^{13}\text{C}$  and  $^{15}\text{N}$  signals for assignment to amino acid residues and chemical shifts and distance constraints. These data can then be used to determine the high-resolution structure of membrane-associated peptides and proteins [10, 11].

In this review, we describe the experimental approaches used in solid-state NMR methods to determine the membrane-bound structures and orientations of antimicrobial peptides and membrane proteins.

## 9.2 Experimental Approaches Used in Solid-State NMR Spectroscopy

The broadened signals of spin-1/2 nuclei, including  $^{13}\text{C}$  and  $^{15}\text{N}$ , arise from nuclear interactions such as nuclear dipolar interactions and chemical-shift anisotropy (CSA), which are on the order of 20 kHz. A wealth of structural data in relation to interatomic distances and nuclear orientation to the applied magnetic field is contained in such broadened NMR signals in both the crystalline and non-crystalline

state and should be carefully analyzed in a site-specific manner using site-specific isotropic labeling. It is useful to orient the sample along the magnetic field, leading to relatively high-resolution signals. High-resolution signals can also be obtained by rotating the sample about an axis tilted by  $54.7^\circ$  to the magnetic field, called the magic angle. This high-resolution technique is combined with a recoupling technique to obtain further structural information on biologically significant molecules.

### ***9.2.1 Experimental Details for Obtaining the Structures of Membrane-Associated Peptides and Proteins Using Anisotropic Interactions***

#### **9.2.1.1 Orientation Dependence of Chemical-Shift Interaction**

The orientations of peptides bound to magnetically aligned lipid bilayers can be determined by analyzing the  $^{13}\text{C}$  CSA of the carbonyl carbon in the peptide chain. Chemical-shift tensors for the carbonyl carbons can be clearly discerned from the spectral line shape, as shown in Fig. 9.1. When the peptide is completely rigid, 150 ppm of anisotropy will be observed in a low-temperature experiment (Fig. 9.1a, f). In contrast, when the temperature is increased above the liquid crystalline-to-gel phase-transition temperature ( $T_c$ ), the molecules exhibit a large-amplitude rotational motion about the bilayer normal (Fig. 9.1A, C). In this case, an axially symmetric powder pattern is observed, as shown in Fig. 9.1b, g. Since bilayers tend to align with the magnetic field, narrow signals appear at either the  $\delta_{||}$  or  $\delta_{\perp}$  position when  $\alpha$ -helical peptide molecules rotate about the bilayer parallel or bilayer normal (Fig. 9.1B(d), C(e), respectively). A slow MAS experiment can break down the alignment to exhibit an axially symmetric powder pattern (Fig. 9.1b, g). The molecule actually exhibits a reorientational motion about the bilayer normal (Fig. 9.1C) as evidenced by the axially symmetric pattern observed in dimyristoylphosphatidylglycerol (DMPG)-melittin bilayers (Fig. 9.1g) [7, 12].

When the rotor stops spinning, DMPG-melittin lipid-bilayer systems spontaneously orient with the magnetic field, and the membrane-bound molecules also align with the magnetic field. In most cases, membrane-bound biomolecules rotate about the membrane normal due to lateral diffusion of the lipid molecules in the liquid-crystalline phase (Fig. 9.1C). In the case of melittin, the entire molecule forms an  $\alpha$ -helix in the membrane-bound state, and the helical axis rotates about the bilayer normal with tilt angle  $\zeta$  and phase angle  $\gamma$  (Fig. 9.1A). In this case, the  $^{13}\text{C}$  NMR signals of carbonyl carbons in the magnetically oriented lipid bilayer appear at the  $\delta_{\perp}$  position (Fig. 9.1e, h) of the axially symmetric powder pattern (Fig. 9.1b, g). However, it must be stressed that the  $\alpha$ -helix does not rotate about the helical axis.

The helical axis rotates rapidly about the bilayer normal, as shown in Fig. 9.1A, C; thus, Euler rotation matrices are used to transform the  $^{13}\text{C}$  chemical-shift tensors from the principal-axis frame (PAF) to the helical molecular frame (HMF), then to

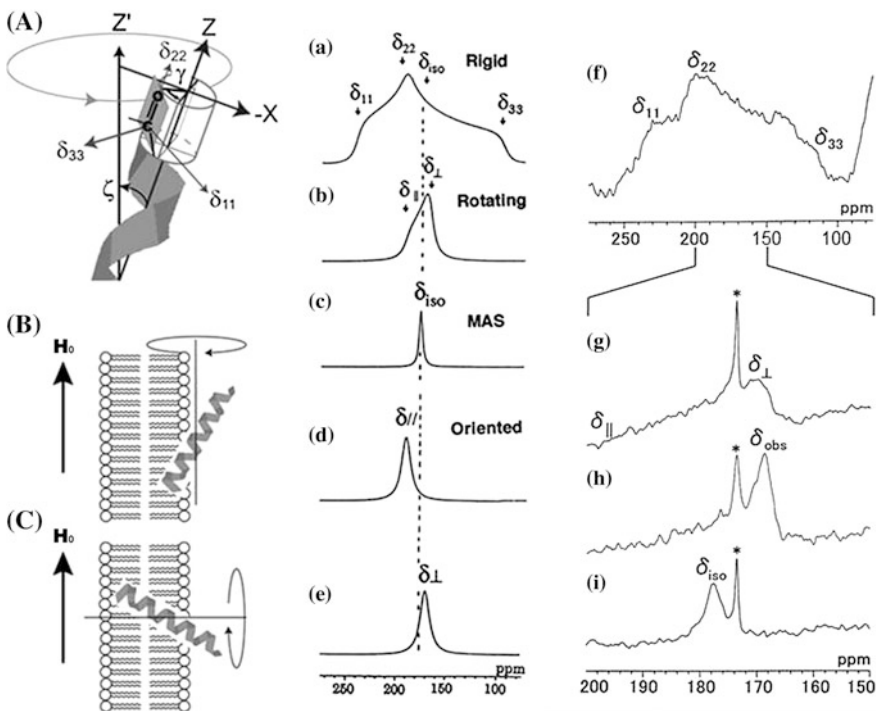
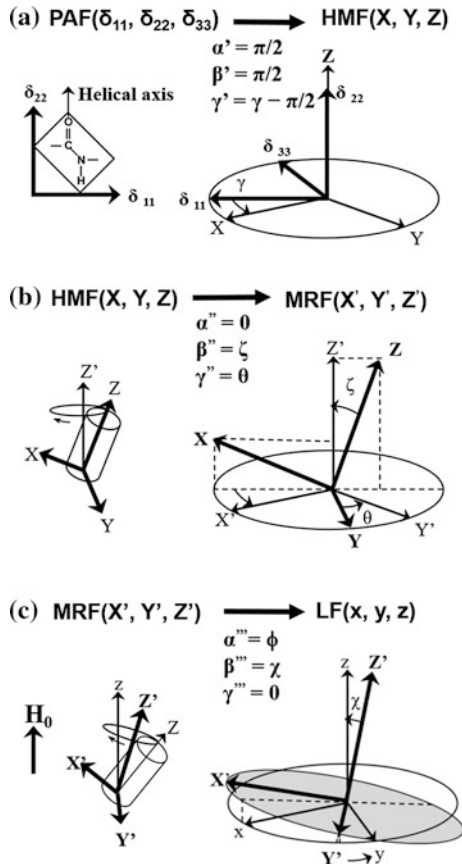


**Fig. 9.1** **A** Direction of the principal axis of the  $^{13}\text{C}$  chemical-shift tensor of the C=O group. **B** The helical axis rotates about the magnetic field ( $H_0$ ). **C** The helical axis rotates about the bilayer normal.  $^{13}\text{C}$ -NMR spectral patterns of the C=O carbons corresponding to the orientation of the  $\alpha$ -helix with respect to the surface of the magnetically oriented lipid bilayers. Simulated spectra were calculated using  $\delta_{11} = 241$ ,  $\delta_{22} = 189$ , and  $\delta_{33} = 96$  ppm for the rigid case (a), rotation about the unique axis without orienting to the magnetic field (slow MAS condition) (b), MAS (c), rotation about the magnetic field (d), and rotation about the bilayer normal (e).  $^{13}\text{C}$  NMR of [ $1-^{13}\text{C}$ ]Ile4-melittin-DMPG bilayer system in the rigid state at  $-60$  °C (f), in the slow MAS condition at  $40$  °C (g), in the oriented condition at  $40$  °C (h), and in the fast MAS condition at  $40$  °C (i) [4]

the molecular rotating frame (MRF), and finally to the laboratory frame (LF), using a three-step transformation (Fig. 9.2) to analyze the dynamic structures of melittin bound to membranes. Assuming that the  $\delta_{zz}$ -axis for the carbonyl carbon is parallel to the helical axis (the Z-axis) of melittin (Fig. 9.2a) for a transformation from the PAF ( $\delta_{11}$ ,  $\delta_{22}$ ,  $\delta_{33}$ ) to the HMF ( $X$ ,  $Y$ ,  $Z$ ), the matrix  $R_1$  for the Euler rotation is given by:

$$R_1(\alpha', \beta', \gamma') = R_1\left(\frac{\pi}{2}, \frac{\pi}{2}, \gamma - \frac{\pi}{2}\right) = \begin{bmatrix} \cos \gamma & 0 & -\sin \gamma \\ -\sin \gamma & 0 & -\cos \gamma \\ 0 & 1 & 0 \end{bmatrix}, \quad (9.1)$$

**Fig. 9.2** Coordinate conversion using Euler rotation angles for description of the rotational motion of  $\alpha$ -helical melittin bound to the membrane. **a** Rotation from the principal-axis frame (*PAF*) to the helical molecular frame (*HMF*). **b** Rotation from the *HMF* to the molecular rotation frame (*MRF*). **c** Rotation from the *MRF* to the laboratory frame (*LF*)



where  $\gamma$  is a constant and the helical axis is directed from the N- to the C-terminus. When the helical axis rotates about the  $Z'$ -axis at a constant tilt angle of  $\zeta$  to the helical axis (Fig. 9.2b) for a transformation from the *HMF* to the *MRF*( $X'$ ,  $Y'$ ,  $Z'$ ), the matrix  $R_2$  for the Euler rotation is given by:

$$R_2(\alpha'', \beta'', \gamma'') = R_2(0, \zeta, \theta) = \begin{bmatrix} \cos \zeta \cos \theta & \sin \theta & -\sin \zeta \cos \theta \\ -\cos \zeta \sin \theta & \cos \theta & \sin \zeta \sin \theta \\ \sin \zeta & 0 & \cos \zeta \end{bmatrix}, \quad (9.2)$$

where  $\theta$  varies continuously with rotational motion at the  $Z'$ -axis. It is emphasized that the direction of the tilt angle is important for determining the interhelical angle for molecules containing more than two helices. If the rotation axis inclines  $\chi$  to the magnetic field (the  $z$ -axis) (Fig. 9.2c) for transformation from the *MRF* to the *LF*( $x$ ,  $y$ ,  $z$ ), the matrix  $R_3$  of the Euler rotation is given by:

$$R_3(\alpha''', \beta''', \gamma''') = R_3(\Phi, \chi, 0) = R_3\left(\frac{\pi}{2}, \chi, 0\right) = \begin{bmatrix} 0 & \cos \chi & -\sin \chi \\ -1 & 0 & 0 \\ 0 & \sin \chi & \cos \chi \end{bmatrix} \quad (9.3)$$

Here,  $\phi$  is an arbitrary constant under the static condition and  $\phi = \pi/2$  is chosen. Consequently, a rotation matrix of  $R = R_3 R_2 R_1$  transforms the chemical-shift tensor from the PAF to the LF, as:

$$\tilde{\delta}^{\text{LF}} = R \cdot \tilde{\delta}^{\text{PAF}} \cdot R^{-1} \quad (9.4)$$

When the rotation axis inclines  $90^\circ$  to the magnetic field, the observed chemical-shift value  $(\delta_{zz})_{\chi=\pi/2} = \delta_{\perp}$  is expressed as

$$\begin{aligned} \delta_{\perp} = & \sin^2 \theta [\cos^2 \zeta (\delta_{11} \cos^2 \gamma + \delta_{33} \sin^2 \gamma - \delta_{22}) - (\delta_{11} \sin^2 \gamma + \delta_{33} \cos^2 \gamma - \delta_{22})] \\ & + \frac{1}{2} \sin 2\theta \cos \zeta \sin 2\gamma (\delta_{11} - \delta_{33}) + \delta_{11} \sin^2 \gamma + \delta_{33} \cos^2 \gamma \end{aligned} \quad (9.5)$$

On the other hand, when the rotation axis inclines  $0^\circ$  to the magnetic field, the observed chemical-shift value  $(\delta_{zz})_{\chi=0} = \delta_{\parallel}$  is expressed as

$$\delta_{\parallel} = -\cos^2 \zeta (\delta_{11} \cos^2 \gamma + \delta_{33} \sin^2 \gamma - \delta_{22}) + (\delta_{11} \cos^2 \gamma + \delta_{33} \sin^2 \gamma) \quad (9.6)$$

The chemical-shift anisotropy,  $\Delta\delta = \delta_{\parallel} - \delta_{\perp}$ , is obtained by combining Eqs. (9.5) and (9.6) as

$$\begin{aligned} \Delta\delta = & [(\delta_{11} \cos^2 \gamma + \delta_{33} \sin^2 \gamma) - \cos^2 \zeta (\delta_{11} \cos^2 \gamma + \delta_{33} \sin^2 \gamma - \delta_{22})] \\ & - \sin^2 \theta [\cos^2 \zeta (\delta_{11} \cos^2 \gamma + \delta_{33} \sin^2 \gamma - \delta_{22}) - (\delta_{11} \sin^2 \gamma + \delta_{33} \cos^2 \gamma - \delta_{22})] \\ & - \frac{1}{2} \sin 2\theta \cos \zeta \sin 2\gamma (\delta_{11} - \delta_{33}) - \delta_{11} \sin^2 \gamma - \delta_{33} \cos^2 \gamma \end{aligned} \quad (9.7)$$

Here, functions of  $\theta$  can be averaged over a cycle when the helical axis rotates rapidly about the axis parallel to the membrane normal that corresponds to the  $Z'$ -axis. In this case, we obtain an expression where the averaged anisotropy depends on the phase angle,  $\gamma$ , of the peptide plane about the helical axis, and the tilt angle,  $\zeta$ , of the helical axis from the rotation axis as

$$\overline{\Delta\delta} = \frac{3}{2} \sin^2 \zeta (\delta_{11} \cos^2 \gamma + \delta_{33} \sin^2 \gamma - \delta_{22}) + \left( \delta_{22} - \frac{\delta_{11} + \delta_{33}}{2} \right) \quad (9.8)$$

Since the C- and N-terminal regions of melittin adopt  $\alpha$ -helical structures, the phase angle,  $\gamma$ , varies by  $-100^\circ$  per consecutive residue in the direction toward the

C-terminus. Equation (9.8) indicates that the oscillations of  $\overline{\Delta\delta}$  of the each carbonyl carbon can be changed as a function of  $\gamma$  along the consecutive amino acid sequence in the  $\alpha$ -helical region. The amplitude of the oscillation depends on the tilt angle  $\zeta$ . We call this behavior as chemical-shift oscillation.

When an  $\alpha$ -helical peptide has a large tilt angle  $\zeta$ , the  $\Delta\delta$  value exhibits a large amplitude, as shown in Fig. 9.3. Using this property of  $\Delta\delta$ , the tilt angle  $\zeta$  of the  $\alpha$ -helical axis can be determined with respect to the bilayer normal by analyzing the anisotropic  $^{13}\text{C}$  chemical-shift values of the carbonyl carbon of consecutive amino acid residues in the  $\alpha$ -helical region (Fig. 9.3a). When a peptide forms an ideal  $\alpha$ -helical structure, it can be assumed that the interpeptide plane angle for consecutive peptide planes is  $100^\circ$ . This tilt angle can be accurately obtained by analyzing the root-mean-square deviation (RMSD) for the observed and calculated CSAs using Eq. (9.9).

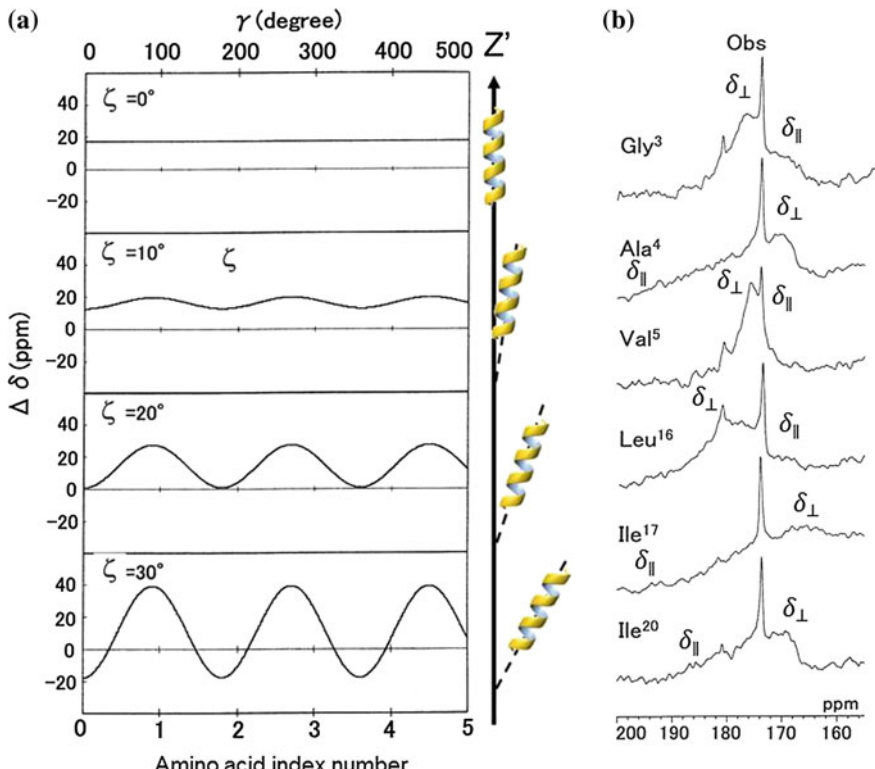


**Fig. 9.3** **a** Chemical-shift oscillation curves of chemical-shift anisotropy,  $\Delta\delta = \delta_{\parallel}/\delta_{\perp}$ , against the phase angle,  $\gamma$ , of the peptide plane for the amino acid residues as a function of the tilt angles,  $\zeta$ , of the  $\alpha$ -helical axis relative to the bilayer normal ( $Z'$ -axis) [4]. **b**  $^{13}\text{C}$  chemical-shift powder patterns of  $[1-^{13}\text{C}]\text{Gly}^3$ ,  $[1-^{13}\text{C}]\text{Ala}^4$ ,  $[1-^{13}\text{C}]\text{Val}^5$ ,  $[1-^{13}\text{C}]\text{Leu}^{16}$ ,  $[1-^{13}\text{C}]\text{Ile}^{17}$ , and  $[1-^{13}\text{C}]\text{Ile}^{20}$ -melittin-DMPG bilayer system at  $40^\circ\text{C}$  [54]

$$\text{RMSD} = \left[ \sum_i^N \{(\Delta\delta_{\text{obs}})_i - (\Delta\delta_{\text{calc}})_i\}^2 / N \right]^{1/2} \quad (9.9)$$

where  $(\Delta\delta_{\text{obs}})_i$  is the experimentally obtained chemical-shift anisotropy of the  $i$ th amino acid residue and  $(\Delta\delta_{\text{calc}})_i$  is the calculated chemical-shift anisotropy of the  $i$ th amino acid residues using the observed  $\delta_{11}$ ,  $\delta_{22}$ , and  $\delta_{33}$  values for the  $i$ th amino acid residue.  $N$  is the number of amino acid residues to be considered.

It is stressed that in chemical-shift oscillation analysis, lipid bilayers are not necessarily aligned with the magnetic field.

### 9.2.1.2 Orientation Dependence of Nuclear Dipolar Interactions

Similar information can be obtained by observing  $^{15}\text{N}-^1\text{H}$  dipolar interactions in the peptide backbone. Polarization inversion spin exchange at the magic angle (PISEMA), a type of separated local-field 2D NMR spectroscopy, provides excellent resolution in the dipolar dimension in the correlation spectra between  $^{15}\text{N}$  chemical-shift values and  $^{15}\text{N}-^1\text{H}$  dipolar interaction [13, 14]. PISEMA was developed based on the flip-flop Lee-Goldberg phase- and frequency-switched pulse sequence, which is used to spin-lock  $^1\text{H}$  spins along the magic angle to suppress homonuclear dipolar interactions. Sample heating is a serious problem in PISEMA, particularly when analyzing hydrated samples containing membrane proteins. This problem can be overcome by drastically reducing the radio frequency (rf) field [15, 16] or using a resonance coil designed for minimizing sample heating [17]. Offset problems encountered in PISEMA are overcome using the broadband PISEMA technique [18].

A characteristic circular pattern wheel, known as a polarity index slant angle (PISA), is observed in PISEMA ( $^{15}\text{N}$  chemical shifts,  $^1\text{H}-^{15}\text{N}$  dipolar interaction correlation) 2D NMR spectra when an  $\alpha$ -helix is formed in the membrane. The shape of the wheel is sensitive to the tilt angle of the  $\alpha$ -helix with respect to the bilayer normal [19–21] (Fig. 9.4). By examining the PISA wheel, one can evaluate the amino acid residues involved in the  $\alpha$ -helix, even if the amino acid sequence is not known. When the helical axis is parallel to the bilayer normal, all of the amino sites have an identical orientation relative to the direction of the applied magnetic field, and therefore, all of the resonances overlap with the same  $^1\text{H}-^{15}\text{N}$  dipolar couplings and  $^{15}\text{N}$  chemical-shift frequencies. Tilting the helix away from the membrane normal breaks the symmetry, introducing variation in the orientations of the amide N–H bond vectors relative to the field direction. This is manifested in the spectra as dispersions of both the  $^1\text{H}-^{15}\text{N}$  dipolar couplings and the  $^{15}\text{N}$  chemical-shift frequencies, as shown in Fig. 9.4b. Thus, the tilt angle of the helical axis can be accurately determined.

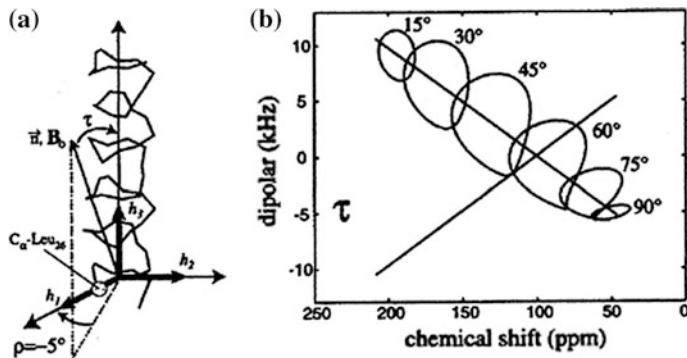


**Fig. 9.4** The generation of “PISA wheels.” **a** Definitions of  $\tau$  and  $\rho$  for an  $\alpha$ -helix.  $\tau = 0^\circ$  occurs when the helix axis,  $h_3$ , is parallel to  $B_0$ .  $\rho = 0^\circ$  occurs when the projection of  $B_0$  onto a plane perpendicular to,  $h_3$ , makes an angle of  $0^\circ$  with  $h_1$ , the radial axis of the helix that passes through the  $C\alpha$  carbon of Leu26 of the M2-TMP helix [22]. **b** Circles drawn for one of the dipolar transitions using average values for the  $^{15}\text{N}$  chemical-shift tensor elements ( $\sigma_{11} = 31.3$ ,  $\sigma_{22} = 55.2$ ,  $\sigma_{33} = 201.8$  ppm) and the relative orientations of the  $^{15}\text{N}-^1\text{H}$  dipolar and  $^{15}\text{N}$  chemical-shift tensor, given by  $\theta = 17^\circ$ , the angle of the peptide plane between  $\sigma_{22}$  and  $v$  (parallel to the N–H bond). Note that the center of the PISA wheel falls on a line that passes through the  $^{15}\text{N}$  isotropic chemical shift (96 ppm) at 0 kHz on the dipolar scale [22]

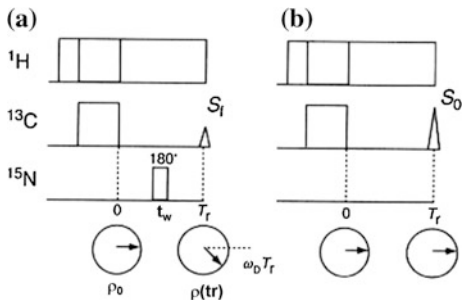
### 9.2.1.3 Interatomic Distance Measurements by REDOR

Solid-state NMR allows quite accurate determination of internuclear distances by looking at the recoupled dipolar interaction, thereby providing extensive information on the three-dimensional (3D) structures of biomolecules. The rotational echo double resonance (REDOR) [23] technique recouples the relatively weak heteronuclear dipolar interaction under the MAS condition by applying a  $\pi$  pulse synchronous with the rotor period. Consequently, the transverse magnetization cannot be refocused completely at the end of the rotor cycle, leading to a reduction of the echo amplitude. The extent of the reduction of the echo amplitude as a function of the number of rotor periods depends on the strength of the heteronuclear dipolar interaction. This method is extensively used to determine relatively remote interaction distances on the order of 2–8 Å.

#### Simple Description of the REDOR Experiment

Transverse magnetization which precesses about the static magnetic field due to dipolar interaction under the MAS condition moves back in the same direction at every rotor period because the integration of angular velocity ( $\omega_D$ ) due to dipolar interaction over one rotor period ( $T_r$ ) is zero. Consequently, the rotational echo signals are refocused at each rotor period (Fig. 9.5b). When a  $\pi$  pulse is applied to the  $S$  nucleus, which is coupled with the  $I$  nucleus, in one rotor period, the pulse

**Fig. 9.5** Pulse sequence to observe rotational echo. **a** Transverse magnetizations of  $^{13}\text{C}$  do not refocus at the rotor period in the REDOR pulse sequence. **b** Transverse magnetizations of  $^{13}\text{C}$  refocus at the rotor period in the rotational echo pulse sequence without  $180^\circ$  pulse of  $^{15}\text{N}$



plays a role in inverting the precession direction of the magnetization of the observed  $I$  nucleus. Consequently, the magnetization vector of the  $I$  nucleus cannot move back in the same direction after one rotor period, and therefore, the amplitude of the echo intensity ( $S_f$ ) decreases (Fig. 9.5a). The extent of the reduction of the rotational echo amplitude yields the interatomic distances. To evaluate the REDOR echo amplitude theoretically, one must consider the averaging precession frequency in the presence of a  $\pi$  pulse at the center of the rotor period over one rotor cycle as follows:

$$\begin{aligned} \overline{\omega_D(\alpha, \beta, t)} &= \mp \frac{1}{T_r} \left( \int_0^{\frac{T_r}{2}} \omega_D dt - \int_{\frac{T_r}{2}}^{T_r} \omega_D dt \right) \\ &= \pm \frac{D}{\pi} \sqrt{2} \sin 2\beta \sin \alpha, \end{aligned} \quad (9.10)$$

where  $\alpha$  is the azimuthal angle and  $\beta$  is the polar angle defined by the internuclear vector with respect to the rotor axis system. Therefore, the phase angle,  $\Delta\Phi(\alpha, \beta)$ , for the  $N_c$  rotor cycle can be given by:

$$\Delta\Phi(\alpha, \beta) = \overline{\omega_D(\alpha, \beta, t)} N_c T_r, \quad (9.11)$$

where  $N_c$  is the number of rotor cycles and  $T_r$  is the rotor period. Finally, the echo amplitude can be obtained by averaging over every orientation, as follows;

$$S_f = \frac{1}{2\pi} \int_{\alpha} \int_{\beta} \cos[\Delta\Phi(\alpha, \beta)] d\alpha \sin \beta d\beta \quad (9.12)$$

Therefore, the normalized echo difference,  $\Delta S/S_0$ , can be given by:

$$\Delta S/S_0 = (S_0 - S_f)/S_0 \quad (9.13)$$

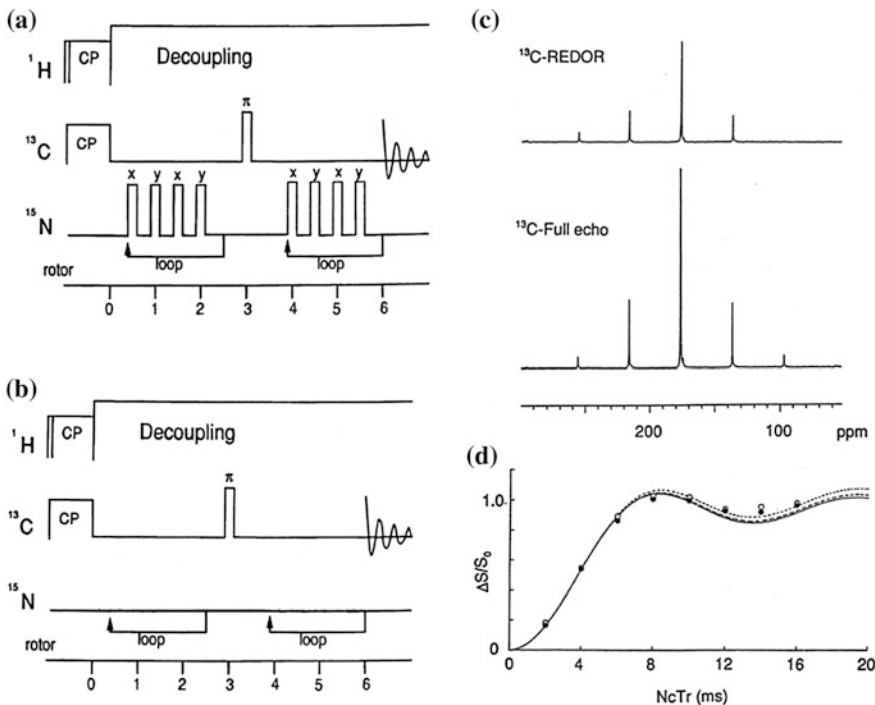


**Fig. 9.6** **a** Pulse sequence for REDOR experiments. **b** Pulse sequence for full-echo experiments. **c** <sup>13</sup>C-REDOR and full-echo spectra of [<sup>1</sup>-<sup>13</sup>C, <sup>15</sup>N]glycine. **d**  $\Delta S/S_0$  plots against  $N_c T_r$  values

Experimentally, REDOR and full-echo spectra are acquired for a variety of  $N_c T_r$  values and respective REDOR ( $S_f$ ) and full-echo ( $S_0$ ) amplitudes are evaluated (Fig. 9.6).

#### Rotational Echo Amplitude by the Density Operator Approach

The REDOR echo amplitude can be evaluated more rigorously by using density matrix operators and a pulse sequence for the REDOR experiment, as shown in Fig. 9.5a [24]. The time evolution of the density operator,  $\rho_0$ , under heteronuclear dipolar interaction during one rotor period can be considered by taking the pulse length into account. The average Hamiltonian in the rotating frame over one rotor period can be given by:

$$\begin{aligned}
\bar{\mathcal{H}} &= \frac{1}{T_r} \left[ \overline{\mathcal{H}_1(t)} \tau + \overline{\mathcal{H}_2(t)} t_W + \overline{\mathcal{H}_3(t)} \tau \right] \\
&= \frac{D}{4\pi} \left\{ \sin^2 \beta [\sin(2\alpha + \omega_r t_W) + \sin(2\alpha - \omega_r t_W) - 2 \sin 2\alpha] \right. \\
&\quad 2\sqrt{2} \sin 2\beta [\sin\left(\alpha + \frac{1}{2}\omega_r t_W\right) + \sin\left(\alpha - \frac{1}{2}\omega_r t_W\right) + 2 \sin 2\alpha] \\
&\quad - \sin^2 \beta [\sin(2\alpha + \omega_r t_W) + \sin(2\alpha - \omega_r t_W)] \frac{4\omega_r^2 t_W^2}{4\omega_r^2 t_W^2 - \pi^2} \\
&\quad + \sqrt{2} \sin 2\beta \left[ \sin\left(\alpha + \frac{1}{2}\omega_r t_W\right) + \left(\alpha - \frac{1}{2}\omega_r t_W\right) \right] \frac{2\omega_r^2 t_W^2}{\omega_r^2 t_W^2 - \pi^2} \} I_Z S_Z \\
&\quad + \frac{D}{4\pi} \left\{ \sin^2 \beta [\cos(2\alpha + \omega_r t_W) + \cos(2\alpha - \omega_r t_W)] \frac{2\pi\omega_r t_W}{4\omega_r^2 t_W^2 - \pi^2} \right. \\
&\quad - \sqrt{2} \sin 2\beta \left[ \cos\left(\alpha + \frac{1}{2}\omega_r t_W\right) + \cos\left(\alpha - \frac{1}{2}\omega_r t_W\right) \right] \frac{2\pi\omega_r t_W}{\omega_r^2 t_W^2 - \pi^2} \} I_z S_y \\
&= a I_z S_z + b I_z S_y
\end{aligned} \tag{9.14}$$

where  $\overline{\mathcal{H}_1(t)}$ ,  $\overline{\mathcal{H}_2(t)}$  and  $\overline{\mathcal{H}_3(t)}$  are the average Hamiltonian corresponding to the period  $T_r$  shown in Fig. 9.5a. The pulse length,  $T_w$ , is also considered in calculations used to analyze REDOR results. The density operator,  $\rho(T_r)$ , at  $T_r$  after evolution under the average Hamiltonian can be calculated as

$$\rho(T_r) = \exp(-i\bar{H}T_r)\rho_0 \exp(i\bar{H}T_r), \tag{9.15}$$

where  $\rho_0$  is considered to be  $I_y$  after the contact pulse. The transverse magnetization at  $T_r$  can then be given by:

$$\langle I_y(T_r) \rangle = T_r \{ \rho(T_r) I_y \} = \cos\left(\frac{1}{2} \sqrt{a^2 + b^2} T_r\right). \tag{9.16}$$

Echo amplitude in powder sample can be calculated by averaging over all orientation as follows:

$$S_f = \frac{1}{2\pi} \int_{\alpha} \int_{\beta} \langle I_y(T_r) \rangle \sin \beta d\beta d\alpha, \tag{9.17}$$

Therefore, the normalized echo difference,  $\Delta S/S_0$ , can be given by Eq. (9.13). When the length of  $\tau_{\omega}$  is zero, Eq. (9.16) can be simplified as follows:

$$\langle I_y(T_r) \rangle = \cos\left(\frac{D}{\pi}\sqrt{2} \sin 2\beta \sin \alpha T_r\right). \quad (9.18)$$

In this case, Eq. (9.17) is equivalent to Eq. (9.12) for  $N_c = 1$ .

### Echo Amplitude in Three-Spin System ( $S_1$ - $I_1$ - $S_2$ )

It is important to consider the case where the observed nucleus ( $I_1$ ) is coupled with two other heteronuclei ( $S_1$  and  $S_2$ ) [25]. The Hamiltonian in a three-spin system can be given by:

$$\begin{aligned} H(t) &= -\frac{\gamma_I \gamma_S h}{2\pi r_1^3} [3 \cos^2 \theta_1(t) - 1] I_{Z1} S_{Z1} - \frac{\gamma_I \gamma_S h}{2\pi r_2^3} [3 \cos^2 \theta_2(t) - 1] I_{Z1} S_{Z2} \\ &= -D_1 I_{Z1} S_{Z1} - D_2 I_{Z1} S_{Z2}, \end{aligned} \quad (9.19)$$

where  $r_1$  and  $r_2$  are the  $I_1$ - $S_1$  and the  $I_1$ - $S_2$  interatomic distances, respectively.  $\theta_1(t)$  and  $\theta_2(t)$  correspond to the angles between the magnetic field and the  $I_1$ - $S_1$  and the  $I_1$ - $S_2$  internuclear vectors, respectively. In the molecular coordinate system, the  $x$ -axis is along the  $I_1$ - $S_1$  internuclear vector, and the  $S_1$ - $I_1$ - $S_2$  plane is laid in the  $x$ - $y$  plane. The angle between  $I_1$ - $S_1$  and  $I_1$ - $S_2$  is denoted by  $\zeta$ . The coordinate system is transformed from the molecular axis system to the MAS system by applying a rotation transformation matrix  $R(\alpha, \beta, \gamma)$  with Euler angles  $\alpha, \beta, \gamma$ , followed by transforming from the MAS to the laboratory coordinate system by applying  $R(\omega_1 t, \theta_m, 0)$ . Finally,  $\cos \theta_1(t)$  and  $\cos \theta_2(t)$  are calculated as follows:

$$\begin{aligned} \cos \theta_1(t) &= (\cos \gamma \cos \beta \cos \alpha - \sin \gamma \sin \alpha) \sin \theta_m \cos \omega t \\ &\quad - (\sin \gamma \cos \beta \cos \alpha + \cos \gamma \sin \alpha) \sin \theta_m \sin \omega t + \sin \beta \cos \alpha \cos \theta_m \end{aligned}$$

and

$$\begin{aligned} \cos \theta_2(t) &= [(\cos \gamma \cos \beta \cos \alpha - \sin \gamma \sin \alpha) \cos \zeta \sin \theta_m \\ &\quad + (\cos \gamma \cos \beta \sin \alpha + \sin \gamma \cos \alpha) \sin \zeta \sin \theta_m] \cos \omega t \\ &\quad - [(\sin \gamma \cos \beta \cos \alpha + \cos \gamma \sin \alpha) \cos \zeta \sin \theta_m \\ &\quad + (\sin \gamma \cos \beta \sin \alpha - \cos \gamma \cos \alpha) \sin \zeta \sin \theta_m] \sin \omega t \\ &\quad + \sin \beta \sin \alpha \cos \theta \sin \zeta + \sin \beta \sin \alpha \cos \theta_m \sin \zeta \end{aligned} \quad (9.20)$$

where  $\theta_m$  is the magic angle between the spinner axis and the static magnetic field and  $\omega_r$  is the angular variation of the spinner rotating about the magic-angle axis. The four resonance frequencies in the system are given by:

$$\begin{aligned}
 \omega_{D1} &= (D1 - D2)/2 \\
 \omega_{D2} &= (D1 + D2)/2 \\
 \omega_{D3} &= -(D1 + D2)/2 \\
 \omega_{D4} &= -(D1 - D2)/2
 \end{aligned} \tag{9.21}$$

These dipolar transition frequencies are time-dependent and repeat the cycle during spinning. In the REDOR pulse sequence, a  $\pi$  pulse is applied in the center of the rotor period. In this case, the averaged angular velocity over one rotor cycle for each resonance is given by:

$$\overline{\omega_i(\alpha, \beta, \gamma, t)} = \frac{1}{T_r} \left( \int_0^{T_r/2} \omega_{Di} dt - \int_{T_r/2}^{T_r} \omega_{Di} dt \right) \tag{9.22}$$

The phase accumulation after the  $N_c$  cycle is given by:

$$\Delta\Phi_i(\alpha, \beta, \gamma, t) = \overline{\omega_i(\alpha, \beta, \gamma, T_r)} N_c T_r \tag{9.23}$$

Finally, the ENDOR echo amplitude after averaging over all Euler angles is calculated as

$$S_f = \frac{1}{8\pi^2} \sum_{i=1}^4 \int_{\alpha} \int_{\beta} \int_{\gamma} [\cos \Delta\Phi_i(\alpha, \beta, \gamma, t)] d\alpha \sin \beta d\beta d\gamma \tag{9.24}$$

The normalized echo difference,  $\Delta S/S_0$ , therefore strongly depends not only on the dipolar coupling of  $I_1$ - $S_1$  and  $I_1$ - $S_2$  but also on the angle  $S_1$ - $I_1$ - $S_2$  [25].

### Practical Aspects of a REDOR Experiment

It is emphasized that accurate interatomic distances are prerequisite to obtaining 3D structures of peptides, proteins, and macromolecules. Careful evaluation of the following points is the most important step to obtain reliable interatomic distances by REDOR experiments, although early paper did not necessarily take this into account. In practice, it is advisable to employ a standard sample such as [ $1\text{-}^{13}\text{C}$ ] glycine [25], whose C-N interatomic distance was determined to be 2.48 Å by a neutron diffraction study, to check that the correct parameters are set on spectrometer prior to beginning an experiment with the sample of interest.

The finite pulse length may affect the REDOR factor. Indeed, this effect is experimentally observed and can be calculated using Eq. (9.15). In one experiment, the REDOR parameter,  $\Delta S/S_0$ , was measured for 20% [ $1\text{-}^{13}\text{C}$ ,  $^{15}\text{N}$ ]Gly. These values were plotted for the length of the  $^{15}\text{N}$   $\pi$  pulse [13.0 μs for the experiment and 24.6 μs (to satisfy 10% rotor cycle)] as a function of  $N_c T_r$  with the calculated

lines using the  $\pi$  pulse length and finite length (13.0 and 24.6  $\mu$ s) of the  $\pi$  pulse (Fig. 9.6D). It was found that the finite length of the  $^{15}\text{N}$   $\pi$  pulse does not significantly affect the REDOR effect provided that the pulse length is less than 10% of the rotor cycle at rotor frequency of 4000 Hz. Using a much faster spinning rate, radio frequency (rf) irradiation occupies a significant fraction of the rotor period (10–60%), and thus, the  $\Delta S/S_0$  curve for REDOR deviates from that with an ideal  $\delta$ -function pulse [26].

With most spectrometers, it is very difficult to eliminate fluctuations in rf power during the acquisition of REDOR experiments. It is, therefore, very important for the rf power to be stabilized after waiting a certain period as otherwise the  $\pi$  pulse will deviate with time from the exact  $\pi$  pulse. Consequently, the utility of REDOR for providing relatively long interatomic distances diminishes if the rf power changes. Instability of the rf power must be compensated for by the pulse sequence in order to eliminate long-term fluctuation of amplifiers. The xy-4 and xy-8 pulse sequences have been developed for this purpose, and the xy-8 pulse is the best sequence to compensate for fluctuations in rf power [27].

Since the initial development of the REDOR technique, contributions of natural abundance nuclei have been considered as the major source of error in distance measurement [28]. The observed dipolar interaction modified by the presence of neighboring naturally abundant nuclei was originally taken into account by simply calculating the  $\Delta S/S_0$  values for the two isolated pairs and adding them proportionally to the natural abundance fraction [28]. Careful analysis of three-spin systems, however, indicates that this simple addition of the fraction in two-spin systems may result in serious overestimation of the natural abundance effect, yielding shorter distances [24]. Therefore, the most accurate way to address the natural abundance effect is to treat the whole spin system as a three-spin system by taking into account the neighboring carbons in addition to the labeled pair. In practice, contributions from naturally abundant nuclei can be ignored [25] for  $^{13}\text{C}$  REDOR but not for  $^{15}\text{N}$  REDOR, because the proportion of naturally abundant  $^{13}\text{C}$  nuclei is much higher than that of  $^{15}\text{N}$  nuclei.

$^{13}\text{C}$ ,  $^{15}\text{N}$ -doubly labeled samples are typically used in REDOR experiment to determine the interatomic distances between labeled nuclei. However, the dipolar interaction between labeled  $^{15}\text{N}$  nuclei in neighboring molecules should be taken into account as an additional factor contributing to the dipolar interaction of the pair under consideration. This contribution could be significant when the observed distance is quite large, because there are many contributions from nearby nuclei. This effect can be completely removed by diluting the labeled sample with a sample of the same compound with natural abundance of  $^{13}\text{C}$  and  $^{15}\text{N}$ . However, signal sensitivity will be sacrificed if the effect is to be completely removed, for example, by diluting the sample 1/49 [29]. Instead, it is advisable to evaluate the REDOR factors at infinitely diluted condition by extrapolating the data by stepwise dilution of the sample (i.e., 60, 30%) without losing sensitivity [25], given that a linear relationship between the REDOR factor and dilution can be ascertained by a theoretical consideration. Alternatively, the observed plots of  $\Delta S/S_0$  values against the corresponding NcTr values for the undiluted sample can be fitted by a theoretical

curve obtained from dipolar interactions among three-spin systems. However, the accuracy of this latter approach is not always equivalent to that of a dilution experiment.

The transverse magnetization of REDOR experiment decays as a function of the  $^1\text{H}$  decoupling field [30, 31]. Dipolar decoupling can be strongly hindered by molecular motion, if present, when the motional frequency is of the same order of magnitude as the decoupling field, thereby significantly shortening transverse relaxation times. Indeed, the  $T_2$  value of the carbonyl carbons in crystalline Leu-enkephalin is very short due to the presence of backbone motion [32]. This is a serious problem in REDOR experiments, especially for long-distance pairs, because the signal-to-noise ratio (S/N) deteriorates significantly. In this case, it is worth considering measuring the  $^{13}\text{C}$  REDOR signal under a strong decoupling field to elongate the transverse relaxation times. It is also useful to measure the distances at low temperature to reduce the motional frequency. It is cautioned, however, that crystalline phase transition could be associated with freezing of the solvent molecule as encountered using a variety of enkephalin samples [33].

The rotor of commercial NMR spectrometers is usually designed to allow as large sample volume as possible in order to achieve better sensitivity. This arrangement, however, can cause  $B_1$  inhomogeneity, resulting in a broad distribution of lengths of the  $90^\circ$  pulses. This problem is serious in REDOR experiments in which a number of  $\pi$  pulses are applied, and pulse errors can accumulate during acquisition to give serious errors. In particular, the samples located at the top or bottom of the sample rotor feel a significantly weaker rf field [24, 34]. This greatly reduces the REDOR factor for samples which utilize the entire sample rotor, as is the case for cylindrical rotors. This effect should be seriously taken into account prior to conducting a REDOR experiment with a commercial spectrometer. It is, therefore, strongly recommended to fill only the center part of the coil with sample, just for a multiple-pulse experiment to acquire accurate interatomic distances as accurately as possible using the REDOR method.

## 9.2.2 *Magic-Angle Spinning NMR*

### 9.2.2.1 CP-MAS NMR

MAS NMR [35] seeks to mechanically average anisotropic interactions to obtain high-resolution spectra in which resonance is resolved on the basis of isotropic chemical shift and, in favorable cases, J-couplings. To achieve this, the sample is rotated rapidly (kHz) in a static magnetic field at an angle  $54.7^\circ$  (the magic angle). Since the anisotropic interactions that give rise to the broadening observed in the NMR spectra of solid materials possess a  $(3\cos^2\theta - 1)/2$  dependence, a scaling of the anisotropic interaction is observed. When the sample rotation frequently exceeds the magnitude of the anisotropic interaction, this interaction is completely averaged and an anisotropic resonance is observed at its isotropic position.

When the sample rotation frequency is lower than that of the anisotropic interaction, incomplete averaging is lower than that of the anisotropic interaction. The resulting incomplete averaging is manifested in the solid-state NMR spectrum as a family of resonances separated from the isotropic resonance by multiples of the rotation frequency, known as spinning side bands.

Both  $^{13}\text{C}$  and  $^{15}\text{N}$  nuclei are frequently observed in membrane-associated peptides and proteins. CP techniques [36, 37] can thus be used to enhance the signal intensities of less abundant nuclei by transferring the polarization from abundant proton nuclei. Furthermore, combining CP, high-power proton decoupling, and MAS (CP-MAS) [38] enables the acquisition of high-resolution signals for biological molecules.

### 9.2.2.2 Correlation NMR Spectroscopy

The significant improvements in resolution afforded by MAS come at the expense of the information contained in the anisotropic interactions. A number of methods have thus been developed that permit selective reintroduction of these anisotropic interactions, thereby facilitating their analysis. These methods and their applications to biological systems have been extensively reviewed [4, 6].

The sequence of a protein backbone can be represented as  $\text{C}\alpha(i)-\text{N}(i)-\text{CO}$  ( $i+1$ )- $\text{C}\alpha(i+1)$ . Hence, to obtain sequential assignments using multidimensional correlation NMR, correlations must be established, for example,  $\text{C}\alpha(i) \rightarrow \text{N}(i) \rightarrow \text{CO}(i+1)$  (or vice versa). At the same time, the transfer should be restrained to this pathway to avoid misleading correlations over more than one amino acid. This is usually achieved using specific  $^{13}\text{C} \leftrightarrow ^{15}\text{N}$  CP techniques [39], which exploit a frequency-selected Hartmann–Hahn condition to reintroduce the heteronuclear dipolar  $^{13}\text{C}-^{15}\text{N}$  coupling at a lower order, which implies that this method should also work with very fast spinning frequencies. In a specific CP experiment, chemical-shift-dependent transfer characteristics are introduced using a controlled frequency offset in combination with relatively weak rf fields on the heteronuclei. Alternatively,  $\text{C}\alpha(i) \rightarrow \text{N}(i) \rightarrow \text{CO}(i+1)$  correlations may be brought about using the proton-assisted intensive nuclei CP sequence [40], a third-spin-assisted recoupling-based method [41].

### 9.2.2.3 PDSD and DARR 2D NMR Spectroscopy

Single amino acids can be identified by means of their characteristic chemical shift and connectivity patterns, for example, between carbon resonances. A number of methods are available for reintroducing homonuclear dipolar  $^{13}\text{C}-^{13}\text{C}$  couplings. A popular class of experiments relies on the proton-mediated reintroduction of carbon homonuclear dipolar couplings. This approach is usually referred to as longitudinal magnetization transfer by spin diffusion and facilitates zero-quantum flip-flop transition among  $^{13}\text{C}$  nuclei. In its basic form, this process is known as

proton-driven spin diffusion (PDSD) [42]. In PDSD, the decoupling field on the proton channel is switched off (while  $^{13}\text{C}$  magnetization is stored along the  $z$ -axis) during the spin diffusion mixing time to reintroduce heteronuclear dipolar couplings, thus increasing the efficiency of flip-flop transitions. This reintroduction occurs, however, only to higher order and scales inversely with the spinning frequency. Other methods, such as dipolar-assisted rotational resonance (DARR) [43, 44], the phase-alternated recoupling irradiation scheme [45], or mixed rotational and rotary resonance [46], outperform PDSD with increased spinning frequency because the heteronuclear dipolar couplings are reintroduced independent of the MAS frequency. However, because the flip-flop transition appears in the correlation terms of the effective Hamiltonian, the spin diffusion efficiency invariably decreases with increasing spinning frequency, although the transfer can still be efficient at very high MAS frequencies [47].

The DARR experiment can be used to determine the interatomic distance of carbon atoms as follows. First, spin diffusion among multiply labeled  $^{13}\text{C}$  spins can be characterized by a master equation as follows [48, 49]:

$$M(\tau_m) = [\exp(-R\tau_m)]M(0), \quad (9.25)$$

where  $M(\tau_m)$  represents the peak intensities for the labeled  $^{13}\text{C}$  spins at the mixing time  $\tau_m$ .  $M(0)$  is the initial peak intensities for the diagonal components. The initial buildup rate  $R_{j,k}$  for the direct polarization transfer can be given by [48]:

$$R_{j,k} = \frac{\gamma^4 \hbar^2}{15} \left( \frac{1}{r_{jk}^{\text{eff}}} \right)^6 \left( K_{\text{ZQ}}^{(j,k)}(\omega_R) + K_{\text{ZQ}}^{(j,k)}(-\omega_R) + \frac{1}{2} K_{\text{ZQ}}^{(j,k)}(2\omega_R) + \frac{1}{2} K_{\text{ZQ}}^{(j,k)}(-2\omega_R) \right) \quad (9.26)$$

$$\left( \frac{1}{r_{j,k}^{\text{eff}}} \right)^6 = \left( \sum_{m=1}^{N_j} \sum_{l=1}^{N_k} \frac{1}{r_{j,k,l,m}^6} \right) \quad (9.27)$$

where  $K_{\text{ZQ}}^{(j,k)}$  and  $r_{j,k,l,m}$  are the zero-quantum (ZQ) line-shape function and the distance between spin  $j$  in group 1 with  $N_l$  equivalent spins and spin  $k$  in group  $m$  with  $N_m$  equivalent spins. The zero-quantum line-shape function was calculated as [50, 51]:

$$K_{\text{ZQ}}^{(j,k)}(n\omega_R) = \frac{1}{2\pi} \int_{-\infty}^{\infty} F_j(\omega - n\omega_R) F_k(\omega) d\omega \quad (9.28)$$

where  $F_j(\omega)$  is the single-quantum (SQ) dipolar line-shape function of spin  $j$  under  $^{13}\text{C}-^1\text{H}$  dipolar coupling with  $^1\text{H}$  DARR recoupling field of MAS frequency,  $\omega_R$ .

Thus, interatomic distances can be obtained from the  $R_{j,k}$  value by varying the  $\tau_m$  values using Eq. (9.25) in DARR experiment, and DARR interatomic distance  $r_{j,k}^{\text{DARR}}$  can be obtained using Eqs. (9.26) and (9.27).

In PDSD and DARR experiments, dipolar truncation, which is the suppression of polarization transfer across small coupling by a larger coupling, does not strongly influence internuclear distances [52], and therefore, long internuclear distances are determined accurately. The effect due to multiple-spin labeling such as a change in transverse relaxation can be obtained by considering zero-quantum line-shape function [51].

### 9.3 Structure Determination of Membrane-Bound Peptides

The structures, topologies, and orientations of a number of membrane-bound peptides in lipid-bilayer environments have been investigated recently using solid-state NMR in order to understand their biological function. Solid-state NMR is particularly well suited for elucidating the dynamics, topologies, orientations, and high-resolution structures of peptides in bilayer environment using model and cell membranes. Peptides analyzed using this approach include venoms, antimicrobial peptides, and antibiotic peptides. In particular, chemical-shift oscillation analysis has allowed determination of the membrane-bound dynamic structures of melittin [7, 12, 53, 54], dynorphin [55], bombolitin [56], lactoferrampin [57], ECL-II of κ-opioid receptor [58], and alamethicin [59].

#### 9.3.1 Melittin

Melittin, a hexacosapeptide with the primary structure Gly-Ile-Gly-Ala-Val-Leu-Lys-Val-Leu-Thr-Gly-Leu-Pro-Ala-Leu-Ile-Ser-Trp-Ile-Lys-Arg-Lys-Arg-Gln-Gln-NH<sub>2</sub>, is the primary component of bee venom [60]. Melittin exhibits potent hemolytic activity [61] and induces voltage-dependent ion conductance across planar lipid bilayers at low concentration [62]. Melittin also causes selective micellization of lipid bilayers and membrane fusion at high concentrations [63]. As the temperature is lowered to approach the gel phase, the membrane breaks down into small particles. Upon raising the temperature above the gel-to-liquid crystalline phase-transition temperature ( $T_c$ ), the small particles reform into unilamellar vesicles and ultimately into multilamellar vesicles. It has been proposed that bilayer disks surrounded by a belt of melittin molecules are formed at temperature below the  $T_c$  [64].

Giant vesicles with diameters of  $\sim 20 \mu\text{m}$  were observed upon optical microscopic analysis of melittin-DMPC bilayers at  $27.9^\circ\text{C}$  [12]. When the temperature

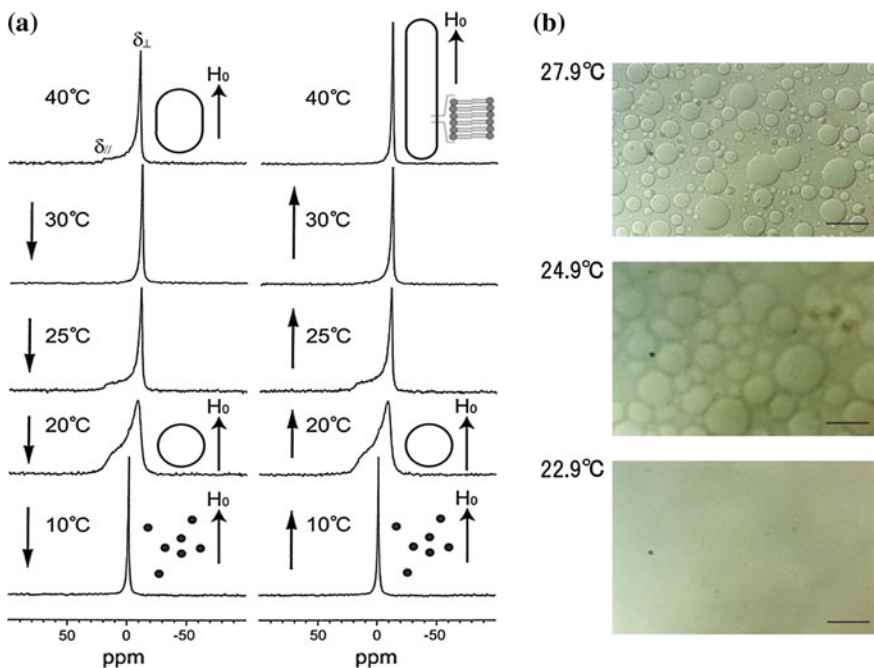


**Fig. 9.7** **a** Effect of temperature variation on <sup>31</sup>P-NMR spectra of melittin-DMPC bilayer systems. Arrows indicate the direction of the temperature variation.  $H_0$  indicates the direction of the static magnetic field. The shapes of the vesicles are also depicted on the right side of the spectra [53]. **b** Optical microscopic pictures of melittin-DMPC vesicle systems at 22.9, 24.9, and 27.9 °C [53]

was lowered to 24.9 °C ( $T_c = 23$  °C for neat DMPC bilayers), the surface of the vesicles became blurred, and dynamic pore formation was visible in microscopic images collected at different exposure times (Fig. 9.7b) [53]. These vesicles disappeared completely at 22.9 °C. It was thus found that melittin-lecithin bilayer systems undergo reversible fusion and disruption near the respective  $T_c$ . The fluctuation of lipids is responsible for membrane fusion above the  $T_c$ , whereas the association of melittin molecules causes membrane lysis below the  $T_c$ .

Static <sup>31</sup>P dipolar-decoupled (DD)-MAS spectra of melittin-DMPC bilayers hydrated with Tris buffer were recorded at various temperatures (Fig. 9.7a) [53]. Immediately after the sample was placed in the magnetic field, the <sup>31</sup>P-NMR spectrum of an axially symmetric powder pattern characteristic of the liquid-crystalline phase was recorded at 40 °C. The upper field edge ( $\delta_{\perp}$ ) was more intense than the lower field edge ( $\delta_{//}$ ) as compared with a normal axially symmetric powder pattern. This finding indicates that the DMPC bilayer is partially aligned with the applied magnetic field, with the bilayer plane assuming a parallel orientation by forming elongated vesicles (Fig. 9.7a). When the temperature was lowered to 30 °C, the intensity of the upper field edge of the powder pattern increased further, leading to a spectrum exhibiting almost complete alignment with the

magnetic field. At 25 °C, the axially symmetric powder pattern appeared again. At 20 °C, this spectrum changed to a broad envelope of the powder pattern, with round edges due to the presence of a large-amplitude motion in addition to a rotational motion about the molecular axis associated with lateral diffusion of the lipid molecules. At 10 °C, the isotropic  $^{31}\text{P}$ -NMR signal dominated near 0 ppm because of the isotropic rapid tumbling motion of small particles caused by melittin-induced lysis of the larger vesicles. The same axially asymmetric powder patterns reappeared when the temperature was raised from 10 to 25 °C as a result of fusion leading to the formation of larger spherical vesicles. At temperatures above 30 °C, a single perpendicular component at -12 ppm arose from the anisotropic  $^{31}\text{P}$  chemical-shift tensor of the liquid-crystalline bilayer. This result indicates that the lipid-bilayer surface orients parallel to the magnetic field with a higher order of alignment by forming longer elongated vesicles, which are referred to as magnetically oriented vesicle systems (MOVS) [12].

Melittin-induced changes in the morphology of a lipid bilayer are illustrated in Fig. 9.8. Microscopic observation clearly indicated that at temperatures above the  $T_c$ , melittin binds strongly to the vesicles and is distributed homogeneously. At temperatures close to the  $T_c$ , melittin molecules associate with each other, resulting in phase separation, as observed by fluorescence microscopy. Consequently, a large-amplitude fluctuation of lipid molecules occurs near the  $T_c$  as shown in Fig. 9.8.

It was shown that melittin forms a pseudo-transmembrane amphiphilic  $\alpha$ -helix [12]. However, melittin can remain in a homogeneous monomeric form in hydrophobic environments when the lipid bilayer enters the liquid-crystalline phase above the  $T_c$ . At temperatures close to the  $T_c$ , the hydrophilic sides of melittin molecules associate with one another such that the hydrophobic sides face the lipid molecules, which causes greater phase separation and partial disordering of the lipid bilayer. At temperature below the  $T_c$ , a large number of melittin molecules associate with each other. Consequently, small lipid-bilayer particles become surrounded by a belt of melittin molecules and are released from the vesicle, resulting in membrane disruption. Subsequently, entire vesicles dissolve in the buffer solution. At temperatures slightly above the  $T_c$ , a small number of associated melittin molecules may induce large-amplitude motion in liquid molecules in addition to motion about the molecular axis. This large-amplitude motion of lipid molecules may cause fluctuation on the surface of the vesicles, resulting in the mixing of lipids between adjacent vesicles and ultimately vesicle fusion.

Fully hydrated melittin-DMPC lipid bilayers also spontaneously align along a static magnetic field by forming elongated vesicles, with the long axis parallel to the magnetic field, as evidenced from static  $^{31}\text{P}$ -NMR spectra (Fig. 9.7a). Using this magnetic orientation property of the membrane, the structure, orientation, and dynamics of melittin have been extensively studied [12]. Static  $^{13}\text{C}$ -NMR spectra of [ $1\text{-}^{13}\text{C}$ ]Ile4-melittin bound to a DMPG bilayer hydrated with Tris buffer recorded at -60 °C show a broad asymmetric powder pattern characterized by  $\delta_{11} = 238$ ,  $\delta_{22} = 188$ , and  $\delta_{33} = 112$  ppm (with respect to TMS) (Fig. 9.1f). The presence of this broad signal indicates that any motion of melittin bound to the DMPG bilayer is

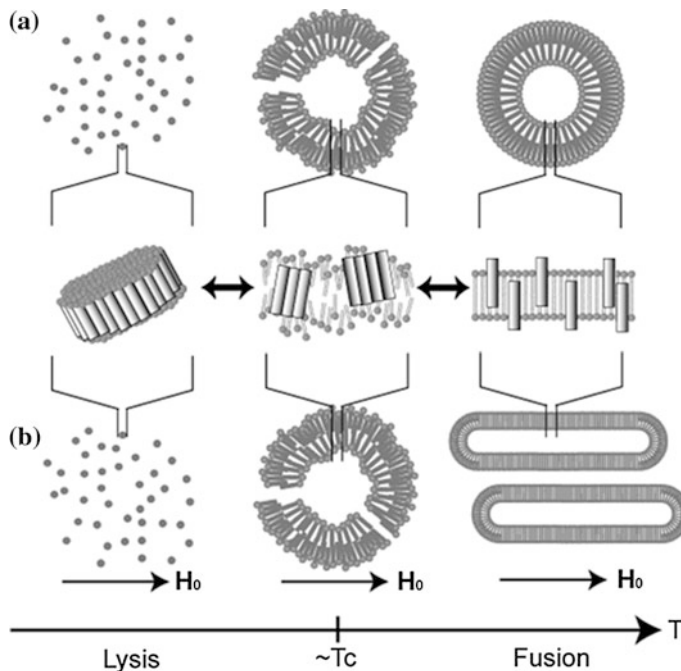


**Fig. 9.8** Schematic representation of the process of morphological changes in melittin-lecithin bilayer systems in the absence (a) and presence (b) of an applied magnetic field [53]

completely frozen at  $-60\text{ }^\circ\text{C}$ . A narrowed  $^{13}\text{C}$ -NMR experiment conducted at  $40\text{ }^\circ\text{C}$  (Fig. 9.1h) showed melittin in the magnetically oriented state. An axially symmetric powder pattern with an anisotropy of 33.3 ppm was recorded at  $40\text{ }^\circ\text{C}$  in the corresponding slow DD-MAS experiment (Fig. 9.1g). Because the line width due to the anisotropy at  $40\text{ }^\circ\text{C}$  was not as broad as that at  $-60\text{ }^\circ\text{C}$ , it was evident that the  $\alpha$ -helical segment underwent rapid reorientation ( $>20\text{ kHz}$ ) about the bilayer normal at  $40\text{ }^\circ\text{C}$  (Fig. 9.1c). The secondary structure of melittin bound to a DMPC bilayer can be determined based on conformation-dependent  $^{13}\text{C}$  chemical shifts referenced to those of model system [65, 66]. The isotropic  $^{13}\text{C}$  chemical shifts of the [ $1\text{-}^{13}\text{C}$ ]Gly3, [ $1\text{-}^{13}\text{C}$ ]Val5, [ $1\text{-}^{13}\text{C}$ ]Gly12, [ $1\text{-}^{13}\text{C}$ ]Leu16, and [ $1\text{-}^{13}\text{C}$ ]Ile20 residues in melittin were determined to be 172.7, 175.2, 171.6, 175.6, and 174.8 ppm (with respect to TMS), respectively, indicating that all of these residues are involved in the  $\alpha$ -helix [12].

The dynamic structure of melittin bound to MOVSs consisting of dipalmitoylphosphatidylcholine (DPPC) and dilauroylphosphatidylcholine (DLPC) was investigated by analyzing the  $^{13}\text{C}$  anisotropic and isotropic chemical shifts of selectively  $^{13}\text{C}$ -labeled carbonyl carbons of melittin under static and MAS conditions [7].

Axially symmetric chemical-shift powder patterns were observed for [ $1\text{-}^{13}\text{C}$ ]Gly3, [ $1\text{-}^{13}\text{C}$ ]Ala4, [ $1\text{-}^{13}\text{C}$ ]Val5, [ $1\text{-}^{13}\text{C}$ ]Gly12, [ $1\text{-}^{13}\text{C}$ ]Leu16, and [ $1\text{-}^{13}\text{C}$ ]Ile20. The lowest RMSDs were obtained at  $\gamma_{\text{G}3} = 71^\circ \pm 8^\circ$  and  $\zeta = 32^\circ \pm 4^\circ$  for the N-terminal  $\alpha$ -helix (Gly3, Ala4, Val5) and  $\gamma_{\text{L}16} = 80^\circ \pm 6^\circ$  and  $\zeta = 30^\circ \pm 3^\circ$  for the C-terminal  $\alpha$ -helix (Gly12, Leu16, Ile20) using Eq. (9.9). Practically, RMSD ( $\gamma, \zeta$ )s were obtained by varying  $\gamma(0^\circ\text{--}90^\circ)$  and  $\zeta(0^\circ\text{--}180^\circ)$  with respect to  $\gamma_{\text{G}3}$  for the N-terminal  $\alpha$ -helix and Leu16 for the C-terminal  $\alpha$ -helix.

Based on the symmetry relationship expressed in Eq. (9.8),  $\zeta$  or  $-\zeta$  cannot be distinguished because of the  $(3/2)\sin^2\zeta$  relation and  $\gamma$  and  $\gamma\text{-}180^\circ$  cannot be distinguished because of the  $\delta_{11}\cos^2\gamma + \delta_{33}\sin^2\gamma$  relation. Therefore, the possible  $(\gamma, \zeta)$  combinations to show minimum RMSD value can be determined according to the following relationship:

$$\begin{aligned}\text{RMSD}(\gamma, \zeta) &= \text{RMSD}(\gamma - 180^\circ, \zeta) \\ &= \text{RMSD}(\gamma - 180^\circ, -\zeta) \\ &= \text{RMSD}(\gamma, -\zeta)\end{aligned}\quad (9.28)$$

For the N- and C-terminal helices in the melittin–DPPC bilayer systems, the lowest RMSD values are given by:

$$\begin{aligned}(\gamma_{\text{G}3}, \zeta)_N &= (+76^\circ, \pm 36^\circ) \text{ or } (-84^\circ, \pm 36^\circ) \quad \text{and} \\ (\gamma_{\text{L}16}, \zeta)_C &= (+82^\circ, \pm 25^\circ) \text{ or } (-98^\circ, \pm 25^\circ).\end{aligned}\quad (9.29)$$

In this case, the interatomic distance between [ $1\text{-}^{13}\text{C}$ ]Val8 and [ $15\text{N}$ ]Leu13 was determined to be 4.8 Å by REDOR experiments [23, 67]. This distance allowed unique determination of the  $(\gamma_{\text{G}3}, \zeta)_N = (+76^\circ, -36^\circ)$  and  $(\gamma_{\text{L}16}, \zeta)_C = (-82^\circ, +25^\circ)$  values for melittin–DPPC bilayers, consistent with a larger kink angle (Fig. 9.9).

Analysis of the chemical-shift oscillation (Fig. 9.10) indicated that melittin molecules form two differently oriented  $\alpha$ -helices and diffuse laterally to rotate rapidly around the membrane normal, with tilt angle for the N-terminal helix of  $-33^\circ$  and  $-36^\circ$  and  $21^\circ$  and  $25^\circ$  for the C-terminal helix in DLPC and DPPC vesicles, respectively (Fig. 9.8). The results provided interhelical angles of  $126^\circ$  and  $119^\circ$  in DLPC and DPPC membranes, respectively. These analyses led to the conclusion that the  $\alpha$ -helices of melittin molecules penetrate the hydrophobic core of the bilayers incompletely as a pseudo-transmembrane structure, inducing fusion and disruption of the vesicles.

MD simulation for the melittin–DMPG system indicated that the basic residue Lys7 is located slightly within the lipid core region and interacts with one DMPG molecule to disturb the lower surface of the lipid bilayers, and this interaction is associated with melittin's membrane disruption activity (Fig. 9.7c) [54].

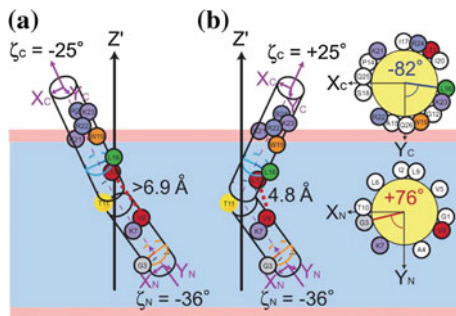


**Fig. 9.9** Schematic representation of the possible structure of melittin bound to the DPPC vesicle from the analysis of the  $^{13}\text{C}$  chemical-shift anisotropies. **a**  $(\gamma_{\text{G}3}, \zeta)_N = (+76^\circ, -36^\circ)$  and  $(\gamma_{\text{L}16}, \zeta)_C = (-82^\circ, -25^\circ)$ ; **b**  $(\gamma_{\text{G}3}, \zeta)_N = (+76^\circ, -36^\circ)$  and  $(\gamma_{\text{L}16}, \zeta)_C = (-82^\circ, +25^\circ)$ ; structure **b** is proved to be the actual structure based on the interatomic distance of  $4.8 \pm 0.2 \text{ \AA}$ , between [ $1^{13}\text{C}$ ]Val8 and [ $^{15}\text{N}$ ]Leu13 of melittin bound to the DPPC bilayers, determined by the REDOR measurements. The helical wheel representation is illustrated in the helical molecular frame (HMF). The  $Z'$ -axis is the rotation axis of a melittin molecule, which is parallel to the membrane normal [7]

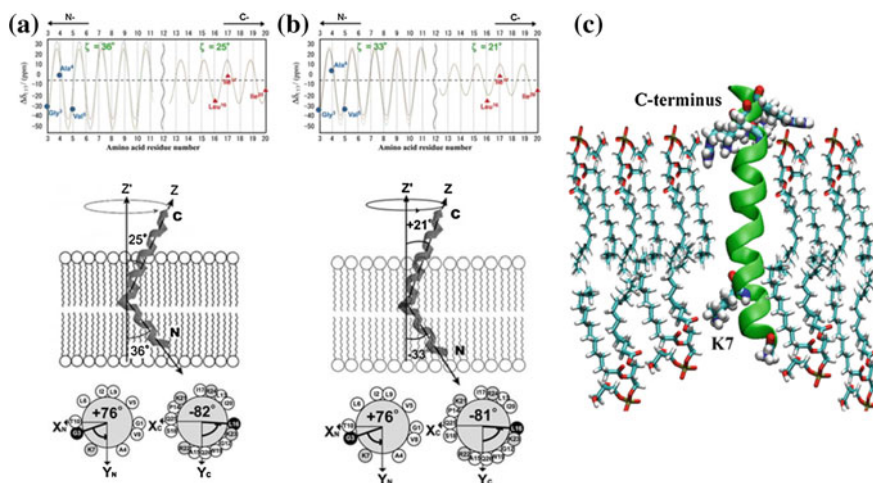


**Fig. 9.10** Schematic representation of the structures and orientations of melittin. **a** Bound to DPPC and **b** DLPC lipid bilayers. *Top* Chemical-shift oscillation curves for [ $1^{13}\text{C}$ ]Gly3, Ala4, Val5, Leu16, Ile17, and Ile20 of melittin in DPPC (**a**) and DLPC (**b**) lipid bilayers. *Bottom* The N- and C-terminal helices of melittin bound to DPPC and DLPC lipid bilayers are inserted into the bilayer with the tilt angle of  $36^\circ$  and  $33^\circ$  and  $(25^\circ$  and  $21^\circ$ ), respectively [4]. **c** Structure of melittin bound to DMPC bilayers obtained from MD simulation [54]

### 9.3.2 Alamethicin

Alamethicin is a 20-residue antibiotic peptide from *Trichoderma viride* [68]. The amino acid sequence is Ac-Aib-Pro-Aib-Ala-Aib-Ala-Gln-Aib-Val-Aib-Gly-Leu-Aib-Pro-Val-Aib-Aib-Gln-Gln-Phol in which 8  $\alpha$ -amino isobutyric acids (Aib) are included. In addition, the N-terminus is acetylated, and the C-terminus is terminated as an L-phenylalaninol residue [69]. Alamethicin consists of F30 and F50 types at a molar ratio of 0.85 and 0.12, respectively [70].

Alamethicin exhibits voltage-dependent ion channel activity in membranes [71]. Alamethicin has a high affinity for lipid bilayers and binds to the surface of lipid bilayers and inserts into the membrane. The orientation of alamethicin in a lipid bilayer depends upon the peptide-to-lipid (P/L) molar ratio [72], the type of lipid bilayer, and the membrane potential [73]. Various channel models have been proposed to determine its ion channel activity, such as the barrel-stave model [74]. Alamethicin channels are formed by parallel bundles of 3–12 transmembrane helical monomers surrounding a central water-filled pore [75]. The ion channel activity of alamethicin makes it a suitable model for investigating voltage-dependent ion channel proteins [76].

X-ray crystallographic data indicate that alamethicin assumes an overall helical structure with kink at Pro14, and the N- and C-termini assume  $\alpha$ - and  $3_{10}$ -helical structures, respectively [74]. Another study revealed that poly-Aib forms a  $3_{10}$ -helix [77].

The conformation and orientation of membrane-bound alamethicin have been studied using solid-state NMR spectroscopy with DMPC/DHPC bicelle systems. Analysis of the  $^{13}\text{C}$  chemical shifts of isotopically labeled alamethicin indicates that in lipid bilayers, the peptide forms an  $\alpha$ -helical structure oriented along the bilayer normal [78].

The conformation of alamethicin in mechanically oriented phospholipid bilayers has been studied using  $^{15}\text{N}$  solid-state NMR in combination with molecular modeling and MD simulations. Alamethicin variants labeled with  $^{15}\text{N}$  at different positions in combination with substitution of three Aib residues with Ala residues were examined. Anisotropic  $^{15}\text{N}$  chemical-shift data and  $^1\text{H}$ – $^{15}\text{N}$  dipolar couplings were determined for alamethicin with  $^{15}\text{N}$ -labeled Ala6, Val9, and Val15 incorporated into a phospholipid bilayer at a peptide-to-lipid molar ratio of 1:8. This study indicated that alamethicin assumes a largely linear  $\alpha$ -helical structure that spans the membrane, with the molecular axis tilted by 10–20° relative to the bilayer normal. In comparison, molecular modeling showed a straight  $\alpha$ -helix tilted by 17°, and a slightly kinked MD structure was tilted by 11° relative to the bilayer normal [79]. Measurement of the orientation-dependent  $^1\text{H}$ – $^{15}\text{N}$  dipole–dipole coupling,  $^{15}\text{N}$  anisotropic chemical shift, and  $^2\text{H}$  quadrupole coupling parameters for a single residue, analysis of the anisotropic coupling parameters for a single residue, analysis of the anisotropic interaction for the Aib8 residue, and analysis of the anisotropic interaction for the Aib8 residue together provided detailed information

regarding the helix-tilt angle, wobble, and oscillatory rotation around the helical axis in the membrane-bound state of alamethicin [80].

Proton-decoupled  $^{15}\text{N}$  solid-state spectra of a sample of alamethicin uniformly labeled with  $^{15}\text{N}$  and reconstituted into oriented palmitoyloleoylphosphatidylcholine (POPC) and DMPC membranes showed that alamethicin adopts a transmembrane orientation upon reconstitution into the POPC-oriented membrane [81]. Two-dimensional  $^{15}\text{N}$  chemical-shift  $^1\text{H}$ - $^{15}\text{N}$  dipolar-coupling solid-state NMR correlation spectroscopy (i.e., PISEMA) analysis suggested that in the transmembrane configuration, alamethicin adopts a mixed  $\alpha/3_{10}$ -helical structure with a tilt angle of  $8.9^\circ$  with respect to the bilayer normal [82].

Further detailed structural and orientational analyses of membrane-bound alamethicin have been carried out using solid-state NMR spectroscopy [4, 59].  $^{13}\text{C}$  chemical-shift interactions were observed in [1- $^{13}\text{C}$ ]-labeled alamethicin. The isotropic chemical-shift values indicated that the entire length of alamethicin forms a helical structure. The CSA of the carbonyl carbon of isotopically labeled alamethicin was also analyzed under the assumption that alamethicin molecules rotate rapidly about the bilayer normal of the phospholipid bilayer. It was concluded that the adjacent peptide plane forms an angle of  $100^\circ$  or  $120^\circ$  upon assumption of an  $\alpha$ - or  $3_{10}$ -helix, respectively. Anisotropic data were acquired for four and seven different residues at the N- and C-termini, respectively. The observed chemical-shift oscillation patterns for the  $^{13}\text{C}$  CSAs of the carbonyl carbons are shown in Fig. 9.11. The chemical-shift oscillation pattern clearly indicated that there are two helices with different tilt angles. RMSD analysis indicated that the dihedral angles of adjacent peptide planes for the N- and C-termini were found to be  $100^\circ$  and  $120^\circ$ , respectively. It was, therefore, determined that the N- and C-termini form an  $\alpha$ - and  $3_{10}$ -helix, respectively (Fig. 9.11) [4, 59].

Hexagonal alamethicin ion channel model is illustrated in Fig. 9.11c, d, based on the previously obtained structure by MD simulation [79]. Membrane-bound structure of alamethicin determined by solid-state NMR analysis is used as a component of hexagonal alamethicin oligomer [59]. It is of interest to note that Gln7 and Gln18 residues face to the inside of the ion channel, and thus, the inside of the helical bundle shows hydrophilic character suggesting the high ion conductivity inside the channel.

### 9.3.3 Bovine Lactoferrampin

Bovine lactoferrampin (LFampinB) is a recently discovered 17-residue antimicrobial peptide with the sequence Trp-Lys-Leu-Leu-Ser-Lys-Ala-Gln-Glu-Lys-Phe-Gly-Lys-Asn-Lys-Ser-Arg. This peptide corresponds to residues 268-284 of N1 domain of the multifunctional glycoprotein bovine lactoferrin [83]. LFampinB exhibits more potent antimicrobial activity than lactoferrin and kills a wide variety of organisms, ranging from the yeast *Candida albicans* to a number of bacteria,

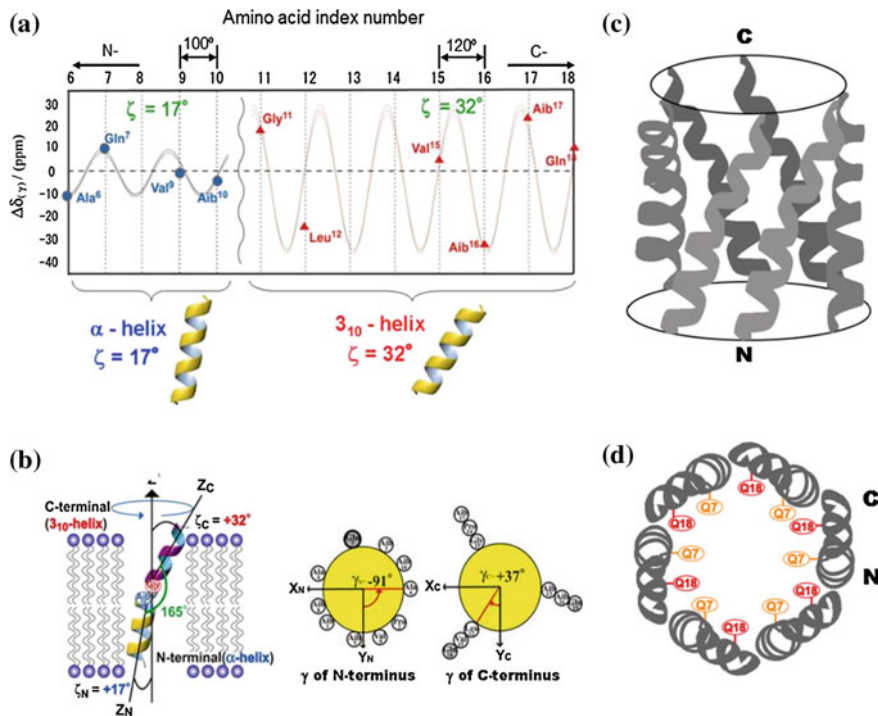


**Fig. 9.11** **a** Chemical-shift oscillation patterns of alamethicin. Chemical-shift oscillation curves were obtained from the chemical-shift anisotropies of the N-terminus (Ala6, Gln7, Val9, and Aib10) and the C-terminus (Val15, Aib16, Aib17, and Gln18). The tilt angles of the N- and C-termini were determined as  $17^\circ$  and  $32^\circ$ , respectively. The dihedral angles of peptide planes between  $n$  and  $n + 1$  residues of the N- and C-termini are analyzed to be  $\alpha$ -helix and  $3_{10}$ -helices, respectively. **b** Structure and topology of alamethicin bound to a DMPC bilayer, as determined from chemical-shift oscillation data [4, 59]. Side view (**c**) and top view (**d**) of hexameric oligomer of alamethicin in the membrane environment

including *Escherichia coli* [83–85]. LFampinB contains six basic amino acid residues and has a net charge of +5 at neutral pH. Solution-state NMR analysis revealed that LFampinB forms an amphipathic  $\alpha$ -helix from the N-terminus to Phe11 and that the C-terminal region remains unstructured, when the peptide is bound to neutral and acidic micelles [86].

The antimicrobial activity of LFampinB is believed to result from membrane defects caused by interaction of the peptide with the bacterial membrane, although the molecular mechanism has yet to be completely elucidated. To date, four major models have been proposed to explain the antimicrobial activity of LFampinB: the “aggregate,” “toroidal-pore,” “barrel-stave,” and “carpet” models (Fig. 9.12) [87]. In the aggregate model, peptides form a micelle-like structure with lipids and consequently translocate across the bilayer. In the toroidal-pore and barrel-stave models, the peptides orient in the transmembrane direction with respect to the

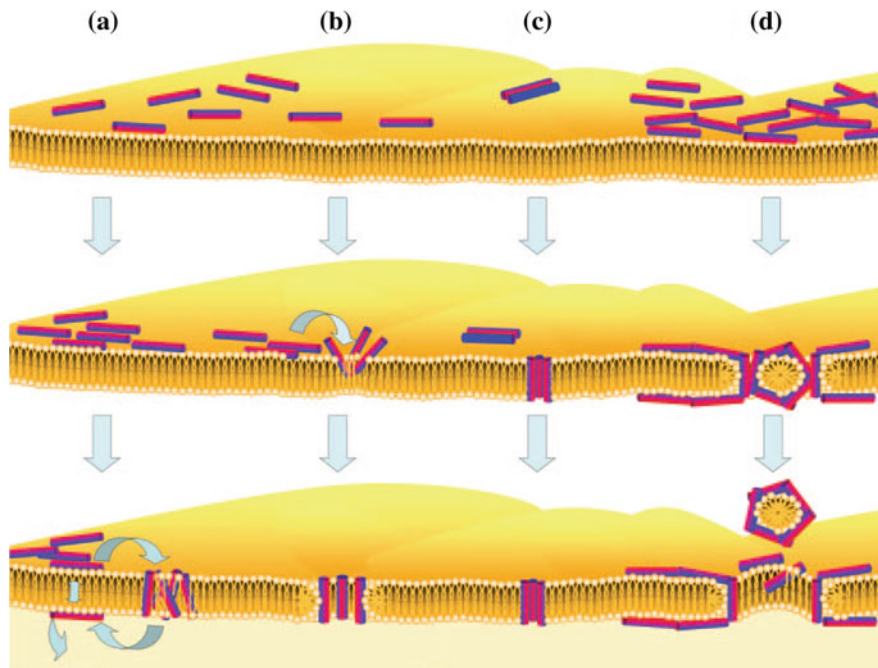


**Fig. 9.12** Schematic representation of action of antimicrobial peptides to membrane. **a** Aggregate model (polyphemusin). **b** Toroidal-pore model (melittin, magainin). **c** Barrel-stave model (alamethicin). **d** Carpet model (ovispirin) [87]

membrane surface. In the toroidal-pore model, the lipid head groups are oriented so as to form a pore in the core of the membrane. In the barrel-stave model, the peptides align to the lipid direction and form a bundle with each other to provide a pore [88–90]. In the carpet model, peptides align along the surface of the lipid-bilayer plane [91]. The peptide exhibits detergent-like activity that creates a defect in the lipid bilayer. Bovine lactoferricin (LFcinB) interacts strongly with the bacterial membrane by forming a pore that disrupts the intracellular ion balance, in the same manner as LFampinB derived from the N1-domain of lactoferrin [92]. Analysis of an antimicrobial peptide's structure and orientation with respect to the membrane surface is therefore important to gain insight into its antimicrobial activity.

$^{13}\text{C}$ - and  $^{31}\text{P}$ -NMR measurements, and  $^{13}\text{C}$ - $^{31}\text{P}$  REDOR experiments, and potassium ion-selective electrode and quartz-crystal microbalance analyses were carried out for LFampinB bound to mimetic bacterial membrane [57]. The  $^{31}\text{P}$ -NMR results indicated that LFampinB causes a defect in the mimetic bacterial membrane. Ion-selective electrode measurements showed that ions leak from mimetic bacterial membrane containing cardiolipin. Quartz-crystal microbalance measurements revealed that LFampinB has a greater affinity for acidic than for neutral phospholipids.  $^{13}\text{C}$  DD-MAS and static NMR spectra showed that

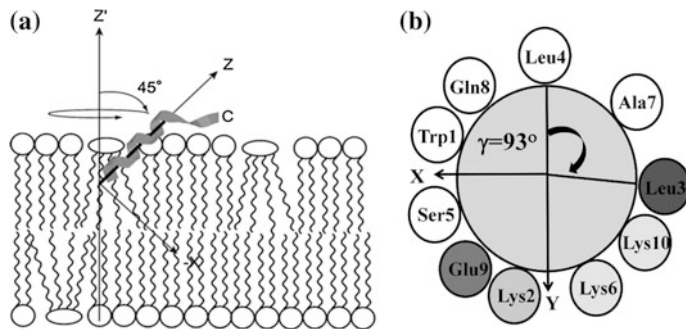


**Fig. 9.13** Schematic representation of membrane-bound structure for LFampinB. **a** Most probable alignment and structure bound to bacterial membrane. **b** Helix wheel and plane angle for carbonyl carbons. X-axis indicates the direction from bilayer normal to the helix axis. Carbonyl plane normal shows 93° from the Y-axis [57]

LFampinB forms an  $\alpha$ -helix in the N-terminal region and is tilted 45° relative to the bilayer normal. Dephasing patterns of the carbonyl carbon nucleus in LFampinB and the phosphorus nuclei of lipid phosphate groups were determined using  $^{13}\text{C}$ - $^{31}\text{P}$  REDOR and revealed that LFampinB localized in the interfacial region of the membrane (Fig. 9.13). MD simulations showed a tilt angle of 42° and a rotation angle of 92.5° for Leu3, both of which were in excellent agreement with experimental values [57].

## 9.4 Structure Determination of Membrane Proteins

Membrane proteins embedded in biological membranes account for 30% of the proteins encoded in the human genome and play an essential role in maintaining the homeostasis of cells, and knowledge of the structure of membrane proteins is extremely important to understanding their function. However, only about 1–2% of experimentally determined protein structures registered in the Protein Data Bank are membrane proteins. Solid-state NMR spectroscopy can provide structural information associated with the conformation, orientation, and dynamics of even insoluble biological macromolecules such as membrane proteins. Solid-state NMR spectroscopy does not require crystallization and is not restricted by the upper limits to molecular weight that affect X-ray crystallography and in solution NMR methods. Consequently, solid-state NMR can be directly applied to studies of the structure of membrane proteins reconstituted in lipid bilayers, over a broad range of lipid compositions, temperature, and pH. High-resolution structures of membrane proteins have recently been determined using MAS methods [93–97]. The structure of the G-protein-coupled chemokine receptor CXCR1 in liquid-crystalline phospholipid bilayers was determined using rotationally aligned NMR spectroscopy [93]. The trimeric structure of the transmembrane domain of the auto-transporter

adhesion protein YadA using the transmembrane domain of YadA in microcrystals was determined using solid-state MAS NMR [94]. This section reviews the high-resolution structures of various membrane proteins determined by solid-state MAS NMR analyses.

In solid-state NMR analyses of membrane proteins with slow tumbling motion in lipid environments, both spectral resolution and signal intensity are strongly affected by anisotropic spin interactions such as CSA, and by homo- and heteronuclear dipolar interactions. CP-MAS involving high-power proton decoupling can yield high-resolution solid-state NMR spectra for membrane protein samples. For sequential assignments and distance constraints of membrane protein structures, recoupling techniques can be combined with multidimensional NMR experiment under MAS conditions. PDSD involves spin diffusion between coupled  $^{13}\text{C}$  spins in the presence of dipolar coupling with a  $^1\text{H}$  spin bath [42, 98]. The technique was used to determine the 3D structure of selectively isotope-labeled SH3 protein without attenuation of long-distance correlations by dipolar truncation induced by strong dipolar coupling such as  $^{13}\text{C}$ - $^{13}\text{C}$  direct bonds [99]. DARR described by Takegoshi et al. [43, 44] induced spin diffusion between  $^{13}\text{C}$  spins enhanced by rf irradiation of the  $^1\text{H}$  spins with the same amplitude as the MAS frequency [43]. Consequently, under DARR conditions, the effects of dipolar truncation can be avoided even for uniformly labeled proteins, enabling the determination of long-range correlation [44, 100, 101]. DARR, as well as other recoupling techniques, can contribute significantly to the determination of sequential assignments and correlation of long-distance constraints in membrane protein structural analysis when combined with multidimensional NMR techniques. In addition,  $^{13}\text{C}$ - $^{13}\text{C}$  correlations based on dipolar interactions are also useful for determining distances between a ligand and neighboring residues of a membrane protein. The visual pigment rhodopsin containing the retinal chromophore is a member of the G-protein-coupled receptors (GPCRs) family. Upon the absorption of light, rhodopsin containing 11-*cis* retinal changes to meta-rhodopsin II (Meta II) with an all-*trans* configuration and a deprotonated Schiff base. This configurational change causes significant structural changes in the residues around the retinal chromophore. Smith et al. have been focusing on Tyr C $\zeta$  in bovine rhodopsin and have shown alteration of cross-peaks between  $^{13}\text{C}$ -labeled retinal, Met  $^{13}\text{C}\epsilon$ , and Tyr  $^{13}\text{C}\zeta$ . These NMR results identified the structural changes in the protein during the process of photo-activation [102, 103].  $^{13}\text{C}$ - $^{13}\text{C}$  correlations have also been used to characterize structure of the retinal-binding pocket in microbial rhodopsin. *Krokinobacter* rhodopsin 2 (KR2) from the marine flavobacteria *Krokinobacter eikastus* functions as a light-driven sodium ion pump, and its crystal structure under acidic condition has been determined [104]. Structural differences in the retinal-binding pocket of KR2 reconstituted into POPE/POPG membranes at acidic and neutral pH conditions were recently revealed using DARR NMR and  $^{15}\text{N}$  CP-MAS techniques [105]. DARR spectra obtained using a mixing time of 500 ms showed cross-peaks between retinal  $^{13}\text{C}$ -14, retinal  $^{13}\text{C}$ -20, Lys255  $^{13}\text{C}\epsilon$ , and Tyr218  $^{13}\text{C}\zeta$  (Fig. 9.14a). KR2 has 15 Tyr residues, and the interatomic distance between C $\zeta$  of Tyr218 and the C20 methyl carbon in retinal is within 5 Å.

The crystal structure data show that the next closest tyrosine is very far from C20 retinal [104]. Thus, the DARR spectra observed the cross-peak of Tyr218 in contact with retinal. The  $^{15}\text{N}$  NMR spectrum showed an unusual chemical-shift value of the protonated Schiff base in KR2, indicating that KR2 has an all-*trans* retinal configuration and a twist around the N-C $\epsilon$  bond. In addition, Tyr218 near the retinal formed a relatively weak hydrogen bond with Asp251. Apart from  $^{15}\text{N}$  Schiff base signal, the chemical-shift values of retinal  $^{13}\text{C}$ -14, retinal  $^{13}\text{C}$ -20, Lys255  $^{13}\text{C}$  $\epsilon$ , and Tyr218  $^{13}\text{C}$  $\zeta$  did not change under acidic condition (Fig. 9.14b), indicating that interaction between the protonated Schiff base and counter-ion is the main change in the retinal-binding pocket between acidic and neutral conditions.

Signal assignments of membrane proteins usually begin as a record of  $^{13}\text{C}$ - $^{13}\text{C}$  intraresidue correlations used to identify amino acids through side-chain correlation patterns. Adequate resolution of C-C correlations is key to a successful structure determination experiment, because the 5–70 ppm aliphatic region is the fingerprint region for residue types. Well-resolved  $^{13}\text{C}$ - $^{13}\text{C}$  correlations have recently been reported for a number of membrane proteins, including YadA [94], the potassium channel KcsA-Kv1.3 [106], human aquaporin-1 [107], DsbB [96], proteorhodopsin [108, 109], and sensory rhodopsin II (SRII) [110]. NCOCX (for inter-residue),

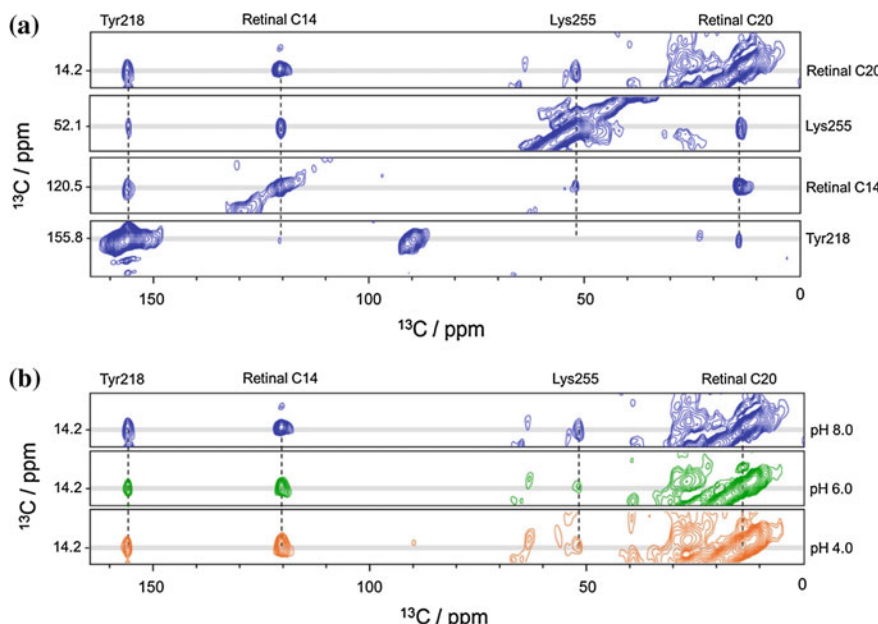


**Fig. 9.14**  $^{13}\text{C}$ - $^{13}\text{C}$  DARR spectra of wild-type KR2 in a POPE/POPG membrane in a Tris-NaCl solution. **a** Correlation peaks of labeled residues at pH 8.0. Cross-peaks and diagonal peaks are represented by the gray line. **b** Comparison of cross-peaks at pH 8.0 (top, blue), pH 6.0 (middle, green), and pH 4.0 (bottom, orange). All columns show correlations with retinal C20. Cross-peaks and diagonal peaks are represented by the gray line [105].

NCACX (for intraresidue), and CONCA (for inter-residue) with  $^{13}\text{C}$ - $^{13}\text{C}$  correlation have been used to construct spin systems for individual amino acid residues and connect the spin systems along the amino acid sequence. Dipolar-coupling data determined using recoupling technique, such as PDSD and DARR, can provide interatomic distances for structural constraints.  $^{13}\text{C}$ -based conformation-dependent chemical-shift tables can be used to correlate isotropic chemical shifts of amino acid residues with site-specific secondary structures [65, 66]. Backbone torsion angle ( $\phi$  and  $\psi$ ) can be estimated from corrected chemical shifts in sequential assignments using TALOS+ (torsion-angle likelihood obtained from shift and sequence similarity) software [111]. Structural calculations based on a large number of torsion-angle constraints and interatomic distances, together with the RMSD for backbone atoms, can provide an ensemble of structures.

Anabaena sensory rhodopsin (ASR) from Anabaena sp. PCC 7120 is a photoreceptor comprising seven-transmembrane helices and a retinal chromophore. ASR is believed to function in chromatic adaptation together with a soluble transducer protein [112]. The atomic resolution fine structure of ASR was recently determined using attentive solid-state MAS NMR spectroscopy. Uniformly and sparsely isotopically labeled ASR in DMPC/DMPA lipid bilayers provided high-resolution solid-state MAS NMR spectra at 800 MHz [95]. Well-resolved correlated peaks with high S/N ratios and narrow line width of 0.5 ppm were observed in 2D DARR  $^{13}\text{C}$ - $^{13}\text{C}$  correlated spectra of uniformly labeled ASR (Fig. 9.15) [113], indicating that the ASR sample was stable and characterized by excellent structural homogeneity in the membranes.  $^{15}\text{N}$  CP-MAS analysis indicated an all-trans configuration of retinal.

Sequential assignments for ASR were obtained using NCACX and NCOCX with DARR optimal short mixing times and CONCA from a single sample. The sequential assignments for the BC loop region in ASR are shown in Fig. 9.16. Although the X-ray structure of ASR [114] lacks the BC loop region, there are two short  $\beta$ -strands. Around 90% of the backbone and amino acid side chains could be assigned in experiments involving sparsely labeled ASR [95, 113, 115]. The water-accessible surface and transmembrane domain of the protein, as well as light-induced conformational changes, were characterized through H/D exchange experiments. The light-induced conformational changes occur in the cytoplasmic halves of helices F and G and at the ends of helices B and C [113, 116].

TALOS was used to determine dihedral restraints (186  $\phi$  and  $\psi$  pairs) from conformation-dependent N, C', C $\alpha$ , and C $\beta$  chemical shifts in ASR. Excellent spectral resolution allowed determination of a number of short, medium, and long interatomic distances by PDSD, CHHC, and a homogeneously broadened rotational resonance (HBR2) [117, 118]. In addition, paramagnetic relaxation enhancement (PRE) experiments with cross-linking, along with circular dichroism (CD) experiments, provided structural insights regarding trimer formation in lipid bilayers and intermonomer distance restraints based on interfacial contacts [119]. Starting from a calculated low-resolution template structure, a total of 1390 short- and 435 medium-range internuclear distances, long-range interhelical constraints, retinal–proton contacts, and intra- and intermonomer PREs with dihedral constraints

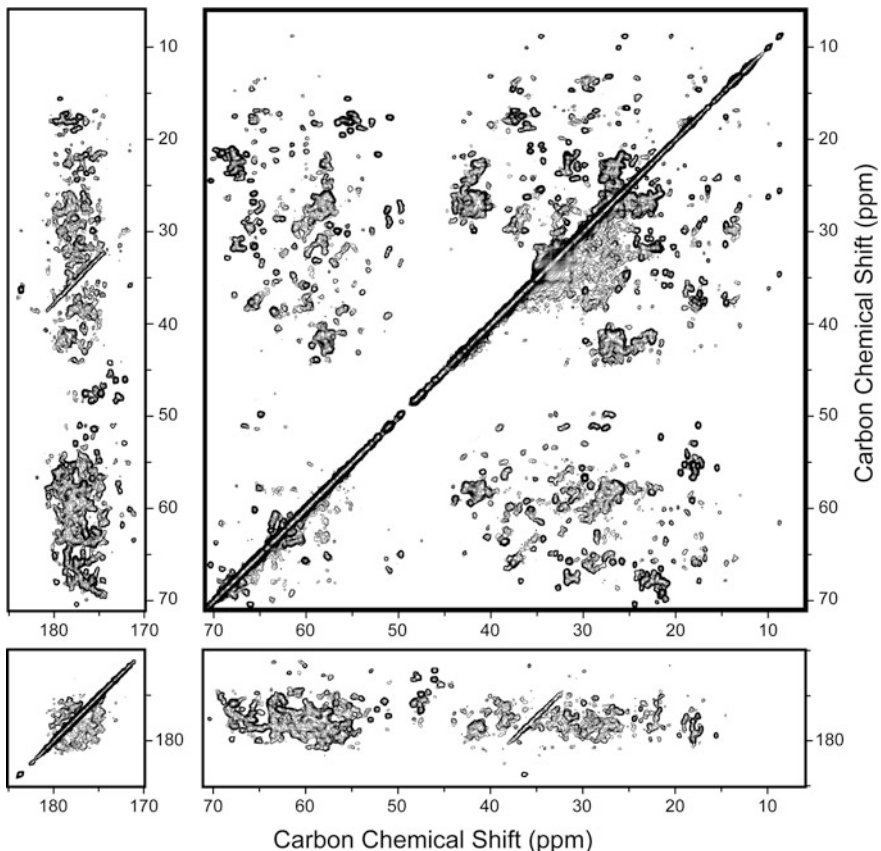


**Fig. 9.15** 2D  $^{13}\text{C}$ - $^{13}\text{C}$  correlation spectrum of *Anabaena* sensory rhodopsin (ASR) using solid-state NMR spectrometer at 800 MHz [113]

were used in the structural calculation [95] (Fig. 9.16). As a result, an ensemble of 10 structures was obtained with a backbone RMSD of 0.6 Å. This detailed trimeric structure of ASR in lipid environments differs notably from the crystal structure (Fig. 9.17). This structure will no doubt enhance understanding of the mechanism of the interaction between ASR (monomer) and the soluble transducer protein.

## 9.5 Conclusion

It is demonstrated that membrane-bound peptide rotates rapidly about the bilayer normal. Based on this dynamic structure characteristic of membrane-bound peptide, chemical-shift oscillation analyses can provide a detailed picture of the structure and orientation of membrane-bound peptides as combined with accurate

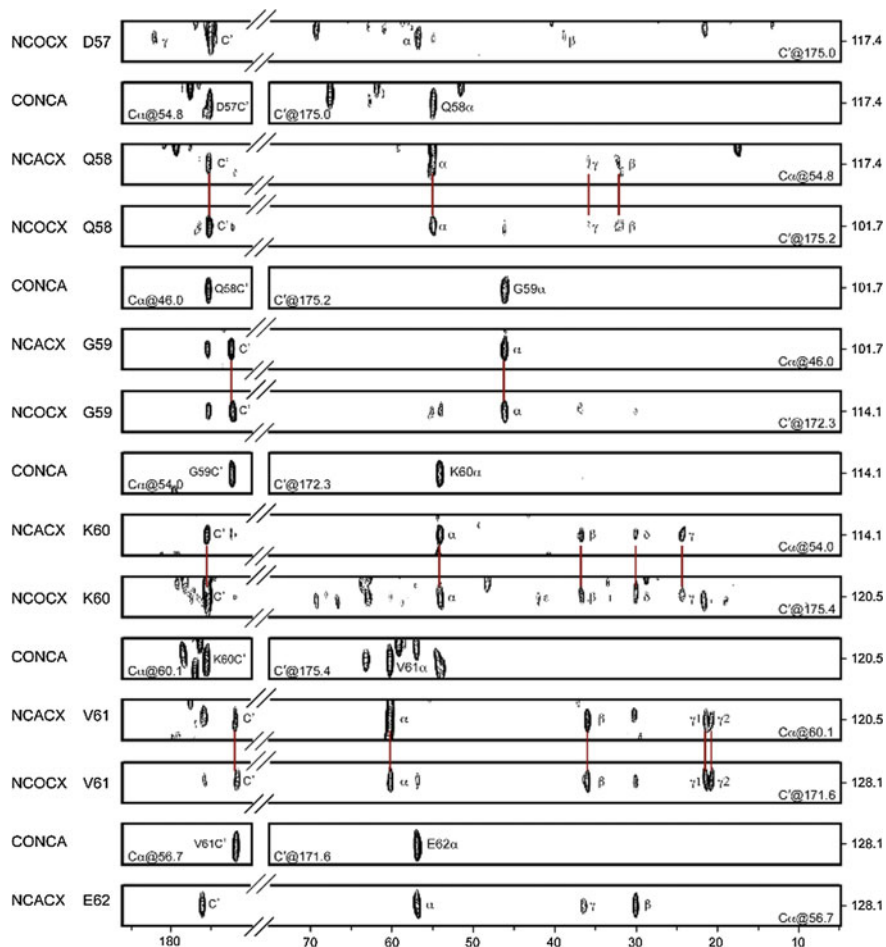


**Fig. 9.16** Sequential assignment from Asp57 to Glu62 in the BC loop of Anabaena sensory rhodopsin (ASR) [113]

internuclear distances. Using solid-state NMR analysis, melittin showed pseudo-transmembrane bending  $\alpha$ -helical structure which induces fusion and disruption of the vesicles. Membrane-bound alamethicin was found to be bending transmembrane structure, and the N- and C-termini form an  $\alpha$ - and  $3_{10}$ -helices, respectively. When hexagonal alamethicin oligomer channels are considered, Gln7 and Gln18 residues face to the inside of the channels that explain high ion conductivity of the ion channels. MAS NMR spectroscopy provides high-resolution NMR signals which permit the assignments of the nuclei in the particular amino acid residues. The chemical shifts and internuclear distance constraints can be used to determine the high-resolution structure of membrane proteins ASR to be trimer form in lipid environments.

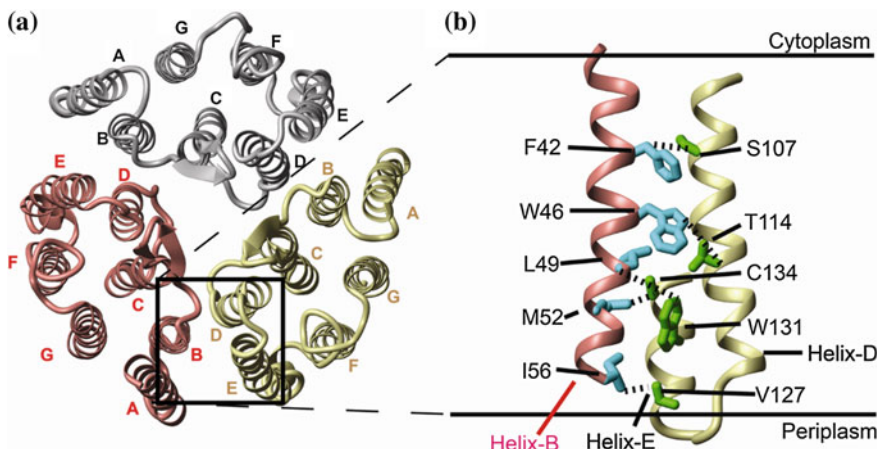


**Fig. 9.17** **a** Top view and **b** side view of the square part of the structure of *Anabaena* sensory rhodopsin (ASR) trimer, as determined by solid-state MAS NMR technique [95]

**Acknowledgements** This work was supported by grants-in-aid for Scientific Research in an Innovative Area (16H00756 to AN and 16H00828 to IK) and by a grant-in-aid for Scientific Research (C) (15K06963 to AN) and Research (B) (15H04336 to IK) from the Ministry of Education, Culture, Sports, Science and Technology of Japan.

## References

1. Opella, S.J., Marassi, F.M.: Structure determination of membrane proteins by NMR spectroscopy. *Chem. Rev.* **104**, 3587–3606 (2004)
2. Watts, A., Straus, S.K., Grage, S.L., Kamihira, M., Lam, Y.H., Zhao, X.: Membrane protein structure determination using solid-state NMR. In: Downing, A.K. (ed.) *Protein NMR. Techniques, methods in molecular biology*, vol. 278, pp. 403–473. Humana Press, Totowa (2004)
3. Saitô, H., Ando, I., Naito, A.: NMR constraints for determination of secondary structure. In: *Solid state NMR spectroscopy for biopolymers. Principles and Applications*, pp. 127–199. Springer, Berlin (2006)
4. Naito, A.: Structure elucidation of membrane-associated peptides and proteins in oriented bilayers by solid-state NMR spectroscopy. *Solid State Nucl. Magn. Reson.* **36**, 67–76 (2009)
5. Opella, S.J., Das, B.B.: Determination of the equivalence of solid-state NMR orientational constraints from magnetic and rotational alignment of the coat protein in a filamentous bacteriophage. In: Separovic, F., Naito, A. (eds.) *Advances in Biological Solid State NMR: Protein and Membrane-Active Peptides*, pp. 53–70. Royal Society of Chemistry, Cambridge (2014)
6. Naito, A., Kawamura, I., Javkhlanlugs, N.: Recent Solid-state NMR studies of membrane-bound peptides and proteins. *Annu. Rev. NMR Spectrosc.* **86**, 333–411 (2015)
7. Toraya, S., Nishimura, K., Naito, A.: Dynamic structure of vesicle-bound melittin in a variety of lipid chain lengths by solid-state NMR. *Biophys. J.* **87**, 3323–3335 (2004)

8. Marassi, F.M., Ramamoorthy, A., Opella, S.J.: Complete resolution of the solid-state NMR spectrum of a uniformly  $^{15}\text{N}$ -labeled membrane protein in phospholipid bilayers. *Proc. Natl. Acad. Sci.* **94**, 8551–8556 (1997)
9. Opella, S.J.: Solid-state NMR and membrane proteins. *J. Magn. Reson.* **253**, 129–137 (2015)
10. Weingarth, M., Buldus, M.: Introduction to Biological Solid-State NMR: Protein and Membrane Active Peptides, pp. 1–17. Royal Society of Chemistry, Cambridge (2014)
11. Ward, M.E., Brown, L.S., Ladizhansky, V.: Advanced solid-state NMR techniques for characterization of membrane protein structure and dynamics: application to *anabaena* sensory rhodopsin. *J. Magn. Reson.* **253**, 119–128 (2015)
12. Naito, A., Nagao, T., Norisada, K., Mizuno, T., Tuzi, S., Saitô, H.: Conformation and dynamics of melittin bound to magnetically oriented lipid bilayers by solid-state  $^{31}\text{P}$  and  $^{13}\text{C}$  NMR spectroscopy. *Biophys. J.* **78**, 2405–2417 (2000)
13. Wu, C.H., Ramamoorthy, A., Opella, S.J.: High-resolution heteronuclear dipolar solid-state NMR spectroscopy. *J. Magn. Reson.* **A109**, 270–272 (1994)
14. Ramamoorthy, A., Wei, Y., Lee, D.-K.: PISEMA solid-state NMR spectroscopy. *Annu. Rep. NMR Spectrosc.* **52**, 1–52 (2004)
15. Lee, D.K., Narasimhaswamy, T., Ramamoorthy, A.: PITANSEMA, a low-power PISEMA solid-state NMR experiment. *Chem. Phys. Lett.* **399**, 359–362 (2004)
16. Nishimura, K., Naito, A.: Dramatic reduction of the RF power for attenuation of sample heating in 2D-separated local field solid-state NMR spectroscopy. *Chem. Phys. Lett.* **402**, 245–250 (2005)
17. Nishimura, K., Naito, A.: Remarkable reduction of rf power by ATANSEMA and DATANSEMA separated local field in solid-state NMR spectroscopy. *Chem. Phys. Lett.* **419**, 120–124 (2006)
18. Gor'kov, P.L., Chekmenev, E.Y., Li, C., Cotton, M., Butfy, J.J., Traasch, N.J., Veglia, G., Brey, W.W.: Using low-E resonance to reduce RF heating in biological samples for static solid-state NMR up to 900 MHz. *J. Magn. Reson.* **185**, 77–93 (2007)
19. Yamamoto, K., Lee, D.K., Ramamoorthy, A.: Spectroscopy, broadband-PISEMA solid-state NMR spectroscopy. *Chem. Phys. Lett.* **407**, 289–293 (2005)
20. Marassi, F.M., Opella, S.J.: A solid-state NMR index of helical membrane protein structure and topology. *J. Magn. Reson.* **144**, 150–155 (2000)
21. Marrasi, F.M., Ma, C., Gesel, J.J., Opella, S.J.: Three-dimensional solid-state NMR spectroscopy is essential for resolution of resonances from in-plane residues in uniformly  $^{15}\text{N}$ -labeled helical membrane proteins in oriented lipid bilayers. *J. Magn. Reson.* **144**, 156–161 (2000)
22. Wang, J., Denny, J., Tian, C., Kim, S., Mo, Y., Kovacs, F., Song, Z., Nishimura, K., Gan, Z., Fu, R., Quine, J.R., Cross, T.A.: Imaging membrane protein helical wheels. *J. Magn. Reson.* **144**, 162–167 (2000)
23. Gullion, T., Schaefer, J.: Rotational-echo double-resonance. *J. Magn. Reson.* **81**, 196–200 (1989)
24. Naito, A., Nishimura, K., Kimura, S., Tuzi, S., Aida, M., Yasuoka, N., Saitô, H.: Determination of the three-dimensional structure of a new crystalline form of N-acetyl-Pro-Gly-Phe as revealed by  $^{13}\text{C}$  REDOR, X-ray diffraction, and molecular dynamics calculation. *J. Phys. Chem.* **100**, 14995–15004 (1996)
25. Naito, A., Nishimura, K., Tuzi, S., Saitô, H.: Inter- and intra-molecular contributions of neighboring dipolar pairs to the precise determination of interatomic distances in a simple [ $^{13}\text{C}$ ,  $^{15}\text{N}$ ]-peptide by  $^{13}\text{C}$ ,  $^{15}\text{N}$ -REDOR NMR spectroscopy. *Chem. Phys. Lett.* **229**, 506–511 (1994)
26. Jaroniec, C.P., Toung, B.T., Rienstra, C.M., Herzfeld, J., Griffin, R.G.: Recoupling of heteronuclear dipolar interactions with rotational-echo double-resonance at high magic-angle spinning frequencies. *J. Magn. Reson.* **146**, 132–139 (2000)
27. Gullion, T., Schaefer, J.: Elimination of resonance offset effects in rotational-echo double resonance NMR. *J. Magn. Reson.* **92**, 439–442 (1991)

28. Pan, Y., Gullion, T., Schaefer, J.: Determination of C-N internuclear distances by rotational-echo double-resonance NMR of solids. *J. Magn. Reson.* **90**, 330–340 (1990)
29. Garbow, J.R., McWherter, C.A.: Determination of the molecular conformation of melanostatin using  $^{13}\text{C}$ ,  $^{15}\text{N}$ -REDOR NMR spectroscopy. *J. Am. Chem. Soc.* **115**, 238–244 (1993)
30. Suwelack, D., Rothwell, W.P., Waugh, J.S.: Slow molecular motion detecting in the NMR spectra of rotating solids. *J. Chem. Phys.* **74**, 2559–2569 (1980)
31. Rothwell, W.P., Waugh, J.S.: Transverse relaxation of dipolar coupled spin systems under rf irradiation. *J. Chem. Phys.* **74**, 2721–2732 (1981)
32. Naito, A., Fukutani, A., Uitdehaag, M., Tuzi, S., Saitô, H.: Backbone dynamics of polycrystalline peptides studied by measurements of  $^{15}\text{N}$  NMR lineshapes and  $^{13}\text{C}$  transverse relaxation times. *J. Mol. Struct.* **441**, 231–241 (1998)
33. Kamihira, M., Naito, A., Nishimura, K., Tuzi, S., Saitô, H.: A high-resolution solid-state  $^{13}\text{C}$  and  $^{15}\text{N}$  NMR study on crystalline Leu- and Met-enkephalins: Distinction of polymorphs, backbone dynamics and local conformational rearrangements induced by dehydration or freezing of motion of bound solvent molecules. *J. Phys. Chem. B* **102**, 2826–2834 (1998)
34. Peersen, O.B., Groesbeek, M., Aimoto, S., Smith, S.O.: Analysis of rotational resonance magnetization exchange curves from crystalline peptides. *J. Am. Chem. Soc.* **117**, 7228–7237 (1995)
35. Andrew, E.R.: The narrowing of NMR spectra of solids by high-speed specimen rotation and resolution of chemical shift and spin multiplet structure for solids. *Prog. Nucl. Magn. Reson. Spectrosc.* **8**, 1–39 (1971)
36. Hartmann, S.R., Hahn, E.L.: Nuclear double resonance in the rotating frame. *Phys. Rev.* **128**, 2042–2053 (1962)
37. Pines, A., Gibby, M.G., Waugh, J.S.: Proton-enhanced NMR of dilute spins in solids. *J. Chem. Phys.* **59**, 569–590 (1973)
38. Schaefer, J., Stejeskal, E.O.: Carbon-13 nuclear magnetic resonance of polymers spinning at magic angle. *J. Am. Chem. Soc.* **98**, 1031–1032 (1976)
39. Baldus, M., Petokova, A.T., Herzfeld, J., Griffin, R.G.: Cross polarization in the tilted frame assignment and spectral simplification in heteronuclear spin system. *Mol. Phys.* **95**, 1197–1207 (1998)
40. Lewandowski, J.R., Paep, G.D., Griffin, R.G.: Proton assisted insensitive nuclei cross polarization. *J. Am. Chem. Soc.* **129**, 728–729 (2007)
41. Paep, G.D., Lewandowski, J.R., Loquet, A., Bockmann, A., Griffin, R.G.: Proton assisted recoupling and protein structure determination. *J. Chem. Phys.* **129**, 245101 (2008)
42. Grommek, A., Meier, B.H., Ernst, M.: Distance information from proton-driven spin diffusion under MAS. *Chem. Phys. Lett.* **427**, 631–637 (2006)
43. Takegoshi, K., Nakamura, S., Terao, T.:  $^{13}\text{C}-^1\text{H}$  dipolar-assisted rotational resonance in magic-angle spinning NMR. *Chem. Phys. Lett.* **344**, 631–637 (2001)
44. Takegoshi, K., Nakamura, S., Terao, T.:  $^{13}\text{C}-^1\text{H}$  dipolar-driven  $^{13}\text{C}-^{13}\text{C}$  recoupling without  $^{13}\text{C}$  rf irradiation in nuclear magnetic resonance of rotating solids. *J. Chem. Phys.* **118**, 2325–2341 (2003)
45. Weingarth, M., Demaco, D.E., Bodenhausen, G., Tekely, P.: Improved magnetization transfer in solid-state NMR with fast magic angle spinning. *Chem. Phys. Lett.* **469**, 342–348 (2009)
46. Scholz, I., Huber, M., Manolikas, T., Meier, B.H., Ernst, M.: MIRROR recoupling and its application to spin diffusion under fast magic-angle spinning. *Chem. Phys. Lett.* **460**, 278–283 (2008)
47. Weigarth, M., Masuda, Y., Takegoshi, K., Bodenhausen, G., Tekely, P.: Sensitive  $^{13}\text{C}-^{13}\text{C}$  correlation spectra of amyloid fibrils at very high spinning frequencies and magnetic fields. *J. Biomol. NMR* **50**, 129–136 (2011)
48. Egawa, A., Fujiwara, T., Mizoguchi, T., Kakitani, Y., Koyama, Y., Akutsu, H.: Structure of the light-harvesting bacteriochlorophyll c assembly in chlorosomes from *Chlorobium limicola* determined by solid-state NMR. *Proc. Natl. Acad. Sci.* **104**, 790–795 (2007)

49. Dumez, J.L., Emsley, L.: A master-equation approach to the description of proton-driven spin diffusion from crystal geometry using simulated zero-quantum lineshapes. *Phys. Chem. Chem. Phys.* **13**, 7363–7370 (2011)
50. Kubo, A., McDowell, C.A.: Spectral spin diffusion in polycrystalline solids under magic angle spinning. *Chem. Soc. Faraday Trans. I* **84**, 3713–3730 (1988)
51. Kubo, A., McDowell, C.A.:  $^{31}\text{P}$  spectral spin diffusion in crystalline solids. *J. Chem. Phys.* **89**, 63–70 (1988)
52. Grommek, A., Meier, B.H., Ernst, M.: Distance information from proton-driven spin diffusion under MAS. *Chem. Phys. Lett.* **427**, 404–409 (2006)
53. Toraya, S., Nagao, T., Norisada, K., Tuzi, S., Saitô, H., Izumi, S., Naito, A.: Morphological behavior of lipid bilayers induced by melittin near the phase transition temperature. *Biophys. J.* **89**, 3214–3222 (2005)
54. Norisada, K., Javkhlanlugs, N., Mishima, D., Kawamura, I., Saitô, H., Ueda, K., Naito, A.: Dynamic structure and orientation of melittin bound to acidic lipid bilayers, as revealed by solid-state NMR and molecular dynamics simulation. *J. Phys. Chem. B* **121**, 1802–1811 (2017)
55. Uezono, T., Toraya, S., Obata, M., Nishimura, K., Tuzi, S., Saitô, H., Naito, A.: Structure and orientation of dynorphin bound to lipid bilayers by  $^{13}\text{C}$  solid-state NMR. *J. Mol. Struct.* **749**, 13–19 (2005)
56. Toraya, S., Javkhlanlugs, N., Mishima, D., Nishimura, K., Ueda, K., Naito, A.: Dynamic structure of bombolitin II bound to lipid bilayers as revealed by solid-state NMR and molecular-dynamics simulation. *Biophys. J.* **99**, 3282–3289 (2010)
57. Tsutsumi, A., Javkhlanlugs, N., Kira, A., Umeyama, M., Kawamura, I., Nishimura, K., Ueda, K., Naito, A.: Structure and orientation of bovine lactoferrampin in the mimetic bacterial membrane as revealed by solid-state NMR and molecular dynamic simulation. *Biophys. J.* **103**, 1735–1743 (2012)
58. Kira, A., Javkhlanlugs, N., Miyamori, T., Sasaki, Y., Eguchi, M., Kawamura, I., Ueda, K., Naito, A.: Interaction of extracellular loop II of k-opioid receptor (196–228) with opioid peptide dynorphin in membrane environments as revealed by solid state nuclear magnetic resonance, quartz crystal microbalance and molecular dynamics simulation. *J. Phys. Chem. B* **2014**(118), 9604–9612 (2014)
59. Nagao, T., Mishima, D., Javkhlanlugs, N., Wang, J., Ishioka, D., Yokota, K., Norisada, K., Kawamura, I., Ueda, K., Naito, A.: Structure and orientation of antibiotic peptide alamethicin in phospholipid bilayers as revealed by chemical shift oscillation analysis of solid state nuclear magnetic resonance and molecular dynamics simulation. *Biochim. Biophys. Acta* **2015**(1848), 2789–2798 (2015)
60. Habermann, E., Jentsc, J.: Sequence analysis of melittin from tryptic and peptic degradation and products. *Hoppe-Seyler's Z. Phys. Chem.* **348**, 37–50 (1967)
61. Sessa, G., Free, J.H., Colacicco, G., Weissmann, G.: Interaction of a lytic polypeptide, melittin, with lipid membrane systems. *J. Biol. Chem.* **244**, 3575–3582 (1969)
62. Tosteson, M.T., Tosteson, D.C.: The sting melittin forms channels in lipid bilayers. *Biophys. J.* **36**, 109–116 (1981)
63. Dempsey, C.E.: The action of melittin on membrane. *Biochim. Biophys. Acta* **1031**, 143–161 (1990)
64. Dufourcq, J., Faucon, J.-F., Fourche, G., Dasseux, J.L., Le Maire, M., Gulik-Krywicki, T.: Morphological change of phosphatidylcholine bilayers induced by melittin: vesicularization, fusion, discoidal particles. *Biochim. Biophys. Acta* **859**, 33–48 (1986)
65. Saitô, H.: Conformation-dependent  $^{13}\text{C}$  chemical shifts: a new means of conformation characterization as obtained by high-resolution solid-state  $^{13}\text{C}$  NMR. *Magn. Reson. Chem.* **24**, 835–852 (1986)
66. Saitô, H., Ando, I.: High-resolution solid-state NMR studies of synthetic and biological macromolecules. *Annu. Rep. NMR Spectrosc.* **21**, 209–290 (1989)
67. Naito, A., Saitô, H.: Limit of accuracy of internuclear distances measured by REDOR. *Encycl. Nucl. Magn. Reson.* **9**, 191–283 (2002)

68. Meyer, C.E., Reusser, F.: A polypeptide antibacterial agent isolated from *Trichoderma viride*. *Experientia* **23**, 85–86 (1967)
69. Balasubramanian, T.M., Kendrick, N.C.E., Taylor, M., Marshall, G.R., Hall, J.E., Vodyanoy, J., Reusser, F.: Synthesis and characterization of the major component of alamethicin. *J. Am. Chem. Soc.* **103**, 6127–6132 (1981)
70. Vedovato, N., Baldini, C., Toniolo, C., Rispoli, G.: Pore-forming properties of alamethicin F50/5 inserted in a biological membrane. *Chem. Biodivers.* **4**, 1338–1346 (2007)
71. Mueller, P., Rudin, D.O.: Action potentials induced in biomolecular lipid membranes. *Nature* **217**, 713–719 (1968)
72. Dave, P.C., Billington, E., Pan, Y.-L., Straus, S.K.: Interaction of alamethicin with ether-linked phospholipid bilayers: oriented circular dichroism,  $^{31}\text{P}$  solid-state NMR, and differential scanning calorimetry studies. *Biophys. J.* **89**, 2434–2442 (2005)
73. Tieleman, D.P., Berendsen, H.J.C., Sansom, M.S.P.: Voltage-dependent insertion of alamethicin at phospholipid/water and octane/water interfaces. *Biophys. J.* **80**, 331–346 (2001)
74. Fox Jr., R.O., Richards, F.M.: A voltage-gated ion channel model inferred from the crystal structure of alamethicin at 1.5-Å resolution. *Nature* **300**, 325–330 (1982)
75. Pan, P., Tristram-Nagle, S., Nagle, J.F.: Alamethicin aggregation in lipid membranes. *J. Membr. Biol.* **231**, 11–27 (2009)
76. Sansom, M.S.: Alamethicin and related peptaibols—model ion channels. *Eur. Biophys. J.* **22**, 105–124 (1993)
77. Saitô, H., Tabetta, R., Formaggio, F., Crisma, M., Toniolo, C.: High-resolution solid-state  $^{13}\text{C}$ -NMR of peptides: A study of chain-length dependence for  $3_{10}$ -helix formation. *Biopolymers* **27**, 1607–1617 (1988)
78. Nagao, T., Naito, A., Tuzi, S., Saitô, H.: Conformation and orientation of biologically active peptide alamethicin in phospholipid bilayer by high-resolution solid state NMR spectroscopy. *Pept. Sci.* **1988**, 341–344 (1988)
79. Bak, M., Bywater, R.P., Hohwy, M., Thomsen, J.K., Adelhorst, K., Jakobsen, H.J., Sørensen, O.W., Nielsen, N.C.: Conformation of alamethicin in oriented phospholipid bilayers determined by  $^{15}\text{N}$  solid-state nuclear magnetic resonance. *Biophys. J.* **81**, 1684–1698 (2001)
80. Bertelsen, K., Paaske, B., Thøgersen, L., Tajkhorshid, E., Schiøtt, B., Skrydstrup, T., Nielsen, N.C., Vosegaard, T.: Residue-specific information about the dynamics of antimicrobial peptides from  $^1\text{H}$ – $^{15}\text{N}$  and  $^2\text{H}$  solid-state NMR spectroscopy. *J. Am. Chem. Soc.* **131**, 18335–18342 (2009)
81. Bechinger, B., Skladnev, D.A., Ogrel, A., Li, X., Rogozhkina, E.V., Ovchinnikova, T.V., O’Neil, J.D.J., Raap, J.:  $^{15}\text{N}$  and  $^{31}\text{P}$  solid-state NMR investigations on the orientation of Zervamicin II and alamethicin in phosphatidylcholine membranes. *Biochemistry* **40**, 9428–9437 (2001)
82. Salnikov, E.S., Friedrich, H., Li, X., Bertani, P., Reissmann, S., Hertweck, C., O’Neil, J.D.J., Raap, J., Bechinger, B.: Structure and alignment of the membrane-associated peptaibols ampullosporin A and alamethicin by oriented  $^{15}\text{N}$  and  $^{31}\text{P}$  solid-state NMR spectroscopy. *Biophys. J.* **96**, 86–100 (2009)
83. van der Kraan, M.I.A., Groenink, J., Nazmi, K., Veeman, E.C.I., Bolscher, J.G.M., Amerongen, A.V.N.: Lactoferrampin: A novel antimicrobial peptide in the N1-domain of bovine lactoferrin. *Peptides* **25**, 177–183 (2004)
84. van der Kraan, M.I.A., van Marle, J., Nazmi, K., Groenink, J., van’t Hof, W., Veerman, E.C. I., Bolscher, J.G.M., Amerongen, A.V.N.: Ultrastructural effects of antimicrobial peptides from bovine lactoferrin on the membranes of *Candida albicans* and *Escherichia coli*. *Peptides* **26**, 1537–1542 (2005)
85. van der Kraan, M.I.A., Nazmi, K., Teeken, A., Groenink, J., van’t Hof, W., Veeman, E.C.I., Bolscher, J.M.G., Amerongen, A.V.N.: Lactoferrampin, an antimicrobial peptide of bovine lactoferrin, exerts its candidacidal activity by a cluster of positively charged residues at the

- C-terminus in combination with a helix-facilitating N-terminal part. *Biol. Chem.* **386**, 137–142 (2005)
- 86. Haney, E.F., Lau, F., Vogel, H.J.: Solution structure and model membrane interactions of lactoferrampin, an antimicrobial peptide derived from bovine lactoferrin. *Biochim. Biophys. Acta* **1768**, 2355–2364 (2007)
  - 87. Janssen, H., Hamill, P., Hancock, R.E.W.: Peptide antimicrobial agents. *Clin. Microbiol. Rev.* **19**, 491–511 (2006)
  - 88. Matsuzaki, K., Murase, O., Fujii, N., Miyajima, K.: An antimicrobial peptide, magainin 2, induced rapid flip-flop of phospholipids coupled with pore formation and peptide translocation. *Biochemistry* **35**, 11361–11368 (1996)
  - 89. Katherine, A., Wildman, H., Lee, D.-K., Ramamoorthy, A.: Mechanism of lipid bilayer disruption by the human antimicrobial peptide, LL-37. *Biochemistry* **42**, 6545–6558 (2003)
  - 90. Steve, K.H., Luttko, L., Worcester, D.L., Huang, H.W.: Neutron scattering in the plane of membranes: structure of alamethicin pores. *Biophys. J.* **1996**(70), 2659–2666 (1996)
  - 91. Pouy, Y., Rapaport, D., Mor, A., Nicolas, P., Shai, Y.: Interaction of antimicrobial dermaseptin and its fluorescently labeled analogues with phospholipid membranes. *Biochemistry* **31**, 12416–12423 (1992)
  - 92. Umeyama, M., Kira, A., Nishimura, K., Naito, A.: Interaction of bovine lactoferricin with acidic phospholipid bilayers and its antimicrobial activity as studied by solid-state NMR. *Biochim. Biophys. Acta* **1758**, 1523–1528 (2006)
  - 93. Park, S.H., Das, B.B., Casagrande, F., Tian, F.Y., Nothnagel, H.J., Chu, M., Kiefer, H., Maier, K., De Angelis, A.A., Marassi, F.M., Opella, S.J.: Structure of the chemokine receptor CXCR1 in phospholipid bilayers. *Nature* **491**, 779–783 (2012)
  - 94. Shahid, S.A., Bardiaux, B., Franks, W.T., Krabben, L., Habeck, M., van Rossum, B.-J., Linke, D.: Membrane-protein structure determination by solid-state NMR spectroscopy of microcrystals. *Nat. Methods* **9**, 1212–1217 (2012)
  - 95. Wang, S., Munro, R.A., Shi, L., Kawamura, I., Okitsu, T., Wada, A., Kim, S.-Y., Jung, K.-H., Brown, L.S., Ladizhansky, V.: Solid-state NMR spectroscopy structure determination of a lipid-embedded heptahelical membrane protein. *Nat. Methods* **10**, 1007–1012 (2013)
  - 96. Tang, M., Nesbill, A.E., Sperling, L.J., Berthold, D.A., Schwieters, C.D., Gennis, R.B., Rienstra, C.M.: Structure of the disulfide bond generating membrane protein DsbB in the lipid bilayer. *J. Mol. Biol.* **425**, 1670–1682 (2013)
  - 97. Traaseth, N.J., Shi, L., Verardi, R., Mullen, D.G., Barany, G., Veglia, G.: Structure and topology of monomeric phospholamban in lipid membranes determined by a hybrid solution and solid-state NMR approach. *Proc. Natl. Acad. Sci. USA* **106**, 10165–10170 (2009)
  - 98. Suter, D., Ernst, R.R.: Spin diffusion in resolved solid-state NMR spectra. *Phys. Rev.* **32**, 5608–5627 (1985)
  - 99. Castellani, F., van Rossum, B., Diehl, A., Schubert, M., Rehbein, K., Oschkinat, H.: Structure of a protein determination by solid-state magic-angle-spinning NMR spectroscopy. *Nature* **420**, 98–102 (2002)
  - 100. Crocker, E., Patel, A.B., Eilers, M., Jayaraman, S., Getmanova, E., Reeves, P.J., Ziliox, M., Khorana, H.G., Sheves, M., Smith, S.O.: Dipolar assisted rotational resonance NMR of tryptophan and tyrosine in rhodopsin. *J. Biomol. NMR* **29**, 11–20 (2004)
  - 101. Marulanda, D., Tasayco, M.L., Cataldi, M., Arriaran, V., Polenova, Y.: Resonance assignments and secondary structure analysis of *E. coli* thioredoxin by magic spinning solid-state NMR spectroscopy. *J. Phys. Chem. B* **109**, 18135–18145 (2005)
  - 102. Eilers, M., Goncalves, J.A., Ahuja, S., Kirkup, C., Hirshfeld, A., Simmerling, C., Reeves, P.J., Sheves, M., Smith, S.O.: Structural transitions of transmembrane helix 6 in the formation of metarhodopsin I. *J. Phys. Chem. B* **116**, 10477–10489 (2012)
  - 103. Kimata, N., Pope, A., Eilers, M., Opefi, C.A., Ziliox, M., Hirshfeld, A., Zaitseva, E., Vogel, R., Sheves, M., Reeves, P.J., Smith, S.O.: Retinal orientation and interactions in rhodopsin reveal a two-stage trigger mechanism for activation. *Nat. Commun.* **7**, 12683 (2016)
  - 104. Kato, H.E., Inoue, K., Abe-Yoshizumi, R., Kato, Y., Ono, H., Konno, M., Hososhima, S., Ishizuka, T., Hoque, M.R., Kunitomo, H., Ito, J., Yoshizawa, S., Yamashita, K., Takemoto,

- M., Nishizawa, T., Taniguchi, R., Kogure, K., Maturana, A.D., Iino, Y., Yawo, H., Ishitani, R., Kandori, H., Nureki, O.: Structural basis for  $\text{Na}^+$  transport mechanism by a light-driven  $\text{Na}^+$  pump. *Nature* **521**, 48–53 (2015)
105. Shigeta, A., Ito, S., Inoue, K., Okitsu, T., Wada, A., Kandori, K., Kawamura, I.: Solid-state nuclear magnetic resonance structural study of the retinal-binding pocket in sodium ion pump rhodopsin. *Biochemistry* **56**, 543–550 (2017)
106. Lange, A., Giller, K., Hornig, S., Martin-Eauclaire, M.-F., Pongs, O., Becker, S., Baldus, M.: Toxin-induced conformational changes in a potassium channel revealed by solid-state NMR. *Nature* **440**, 959–962 (2006)
107. Emami, S., Fan, Y., Munro, R., Ladizhansky, V., Brown, L.S.: Yeast-expressed human membrane protein aquaporin-1 yields excellent resolution of solid-state MAS NMR spectra. *J. Biomol. NMR* **55**, 147–155 (2013)
108. Yang, J., Aslimovska, L., Glaubitz, C.: Molecular dynamics of proteorhodopsin in lipid bilayers by solid-state NMR. *J. Am. Chem. Soc.* **133**, 4874–4881 (2011)
109. Shi, L., Ahmed, M.A.M., Zhang, W., Whited, G., Brown, L.S., Ladizhansky, V.: Three-dimensional solid-state NMR study of a seven-helical integral membrane proton pump-structure insights. *J. Mol. Biol.* **386**, 1078–1093 (2009)
110. Etzkorn, M., Seidel, K., Li, L., Martell, S., Geyer, M., Engelhard, M., Baldus, M.: Complex formation and light activation in membrane-embedded sensory rhodopsin II as seen by solid-state NMR spectroscopy. *Structure* **18**, 293–300 (2010)
111. Shen, Y., Delaglio, F., Cornilescu, G., Bax, A.: TALOS+: a hybrid method for predicting protein backbone torsion angles from NMR chemical shifts. *J. Biomol. NMR* **44**, 213–223 (2009)
112. Jung, K.-H., Trivedi, V.D., Spudich, J.L.: Demonstration of a sensory rhodopsin in eubacteria. *Mol. Microbiol.* **47**, 1513–1522 (2003)
113. Shi, L., Kawamura, I., Jung, K.-H., Brown, L.S., Ladizhansky, V.: Conformation of a seven-helical transmembrane photosensor in the lipid environment. *Angew. Chem. Int. Ed.* **50**, 1302–1305 (2011)
114. Vogeley, L., Sineshchekov, O.A., Trivedi, V.D., Sasaki, J., Spudich, J.L., Luecke, H.: Anabaena sensory rhodopsin: a photochromic color sensor at 2.0 Å. *Science* **306**, 1390–1393 (2004)
115. Wang, S., Shi, L., Okitsu, T., Wada, A., Brown, L.S., Ladizhansky, V.: Solid-state NMR  $^{13}\text{C}$  and  $^{15}\text{N}$  resonance assignments of a seven-transmembrane helical protein Anabaena Sensory Rhodopsin. *Biomol. NMR Assign* **7**, 253–256 (2013)
116. Wang, S., Shi, L., Kawamura, I., Brown, L.S., Ladizhansky, V.: Site-specific solid-state NMR detection of hydrogen-deuterium exchange reveals conformational changes in a 7-helical transmembrane protein. *Biophys. J.* **101**, L23–L25 (2011)
117. Peng, X., Libich, D., Janik, R., Harauz, G., Ladizhansky, V.: Dipolar chemical shift correlation spectroscopy for homonuclear carbon distance measurements in proteins in the solid state: application to structure determination and refinement. *J. Am. Chem. Soc.* **130**, 359–369 (2007)
118. Lange, A., Luca, S., Baldus, M.: Structure constraints from protein-mediated rare-spin correlation spectroscopy in rotating solids. *J. Am. Chem. Soc.* **124**, 9704–9705 (2002)
119. Wang, S., Munro, R.A., Kim, S.Y., Jung, K.-H., Brown, L.S., Ladizhansky, V.: Paramagnetic relaxation enhancement reveals oligomerization interface of a membrane protein. *J. Am. Chem. Soc.* **134**, 16995–16998 (2012)

**Part II**

**Application to Life Science  
and Materials Science**

# Chapter 10

## NMR Studies on Silk Materials

Tetsuo Asakura and Yugo Tasei

**Abstract** A wide range of spectroscopic and imaging techniques have been applied to silk, but the most detailed picture of the structure and dynamics of silk in molecular level has been revealed from NMR, using both solid and solution state measurements. In this review, ten NMR techniques from solution NMR to solid-state NMR used to study the structure of dynamics of silk materials and the obtained typical results were reviewed.

**Keywords** Silk fibroin · In vivo NMR · Silk I\* and silk II ·  $^2\text{H}$  relaxation NMR  
 $^{13}\text{C}$  CP/MAS NMR ·  $^{13}\text{C}$ DDD/MAS NMR ·  $^{13}\text{C}$  refocused NMR  
REDOR · DARR ·  $^1\text{H}$  MQMAS NMR · NMR chemical shift calculation

### 10.1 Introduction

In nature, there are a variety of silkworms and spiders, each producing silk with a unique primary and higher order structures. Recently, these silks have received considerable attention as potentially valuable biomedical materials as well as textile materials [1]. An understanding of the structural and dynamical properties of natural silk materials is essential in development of these applications of silk. A wide range of spectroscopic and imaging techniques have been applied to silk, but the most detailed picture of the structure and dynamics of silk in molecular level has been obtained from NMR, using both solid and solution state measurements [2, 3]. For example, because of the composite structure of silk, comprising both crystalline and amorphous domains, well-known X-ray diffraction analysis only provides limited information.

Solution NMR can be applied to obtain the solution structure of the silk fibroin, SF (main component of the silk protein) including liquid SF stored in the silk gland in living silkworm that is described in Sect. 2.1 [4, 5] or using a combination of

---

T. Asakura (✉) · Y. Tasei  
Tokyo University of Agriculture and Technology, 2-24-16 Nakacho,  
Koganei, Tokyo, Japan  
e-mail: asakura@cc.tuat.ac.jp

well-developed multi-dimensional NMR techniques and isotope labeling techniques for elucidating the atomic level structure (Sect. 2.2) [6, 7]. In addition, the study on the solution structure and dynamics of water molecules interacted with silk materials is also possible using solution NMR which also gives us the important information in development of silk to biomaterials because the physical properties of silk depend on the interaction with water molecules largely (Sect. 2.3) [8, 9].

On the other hand, solid-state NMR is possible to study the structure and dynamics of silk materials in several forms, hydrogel, powder, film, fiber, and sponge, which is very useful in development of silk to biomaterials [1–3]. In general,  $^{13}\text{C}$  CP/MAS NMR which has been used most frequently as a solid-state NMR can be used to analyze the structure and dynamics of the rigid components with slow motion of the silk materials in the solid state. On the other hand,  $^{13}\text{C}$  refocused INEPT NMR can be used to obtain exclusively soft and mobile components in the materials.  $^{13}\text{C}$  DD/MAS NMR is possible to determine the fraction of both mobile and immobile components. Thus, the use of these three kinds of  $^{13}\text{C}$  solid-state NMR will be a powerful technique for study the structure and dynamics of swollen state of SF in water (Sects. 2.4 and 2.5) [9, 10]. The analysis is based on the conformation-dependent NMR chemical shift [2, 3, 11]. The  $^{13}\text{C}$  DARR (2.6) [12] and REDOR (Sect. 2.7) [13] experiments give cross-correlations based on the homo nucleus and the hetero nucleus dipolar interactions, respectively, which can be used to determine the structure of silk materials through the information about the inter-nuclear distances. For the purpose, selective stable isotope labeling of the silk samples is required [2, 3, 8, 10, 14]. Recently,  $^1\text{H}$  solid-state NMR with very fast spinning (more than 70 kHz spinning) has been developed, which is useful to obtain high resolution  $^1\text{H}$  solid-state NMR of silk materials [15, 16]. The  $^1\text{H}$  DQMAS NMR (Sect. 2.8) can be used to obtain  $^1\text{H}$ – $^1\text{H}$  distance information on silk materials and complex structure of SF and other molecules [17–19]. Finally, developments of the chemical shift calculation (Sect. 2.9) reveal inter-molecular arrangement as well as the conformation of a chain that deserves special mention. [17, 21] The agreement between the observed and calculated chemical shifts is excellent, which can be used to confirm the NMR peak assignments and to discuss the structure in detail. This is also used for the structural determination of silk. In this review, these nine NMR techniques (from Sects. 2.1 to 2.9) used to study the structure of dynamics of silk materials, and the obtained results were reviewed.

## 10.2 Results and Discussion

### 10.2.1 Dynamics of Silk Fibroin Stored in Living Silkworm

The shape and size of mature larva of *B. mori* silkworm are suitable to insert it into  $^{13}\text{C}$  solution NMR sample tube. Therefore, direct  $^{13}\text{C}$  NMR observation of SF stored in living silkworm was possible without extraction from the silkworm [4, 5].

Because the liquid SF extracted from the silk gland tends to change the structure easily by the external force such as shear stress during the extraction process or drying, [22] the in vivo NMR observation is very effective. A comparison of the conformation of SF stored in the silk gland among several kinds of wild and domestic silkworms and the study on the process of SF synthesis in silkworms are possible [4, 23]. Figure 10.1 shows a series of partially relaxed  $^{13}\text{C}$  solution NMR spectra of the middle silk gland portion of living *B. mori* silkworm [5]. Before NMR observation, the orifice of living silkworm spinneret was blocked, and therefore, the inner part of the silkworm was filled with liquid silk sufficiently. This treatment gives  $^{13}\text{C}$  solution NMR spectra of SF with sufficient S/N ratio in living silkworm within one day. The information on the structure and dynamics of SF stored in the middle gland can be obtained as follows. From the  $^{13}\text{C}$  chemical shifts of Ala and Ser carbon peaks, the solution conformation is basically random coil [11, 24]. In addition, from the narrow peak width, the segmental motion of the backbone chain is very fast. The relaxation study in Fig. 10.1 is possible to determine the motion of SF chain through the determination of the correlation time of SF molecule quantitatively and to obtain the information on the homogeneity of SF from view point of the dynamics. The mean correlation time of backbone motion of SF was determined to be  $2.2 \times 10^{-10}$  s, which corresponds to the correlation times of overall motion of typical low molecular weight compounds in water [5, 24]. In addition, it is noted that the dynamical structure of backbone and side chain of SF in the silk gland was uniform.

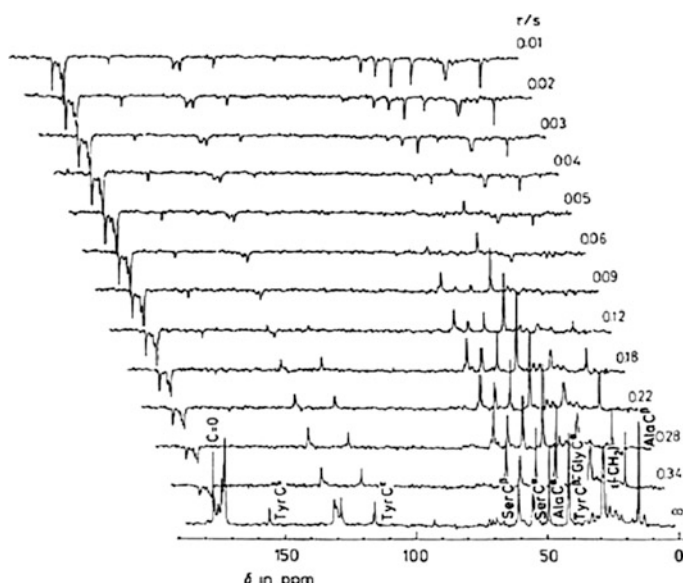


**Fig. 10.1** Partially relaxed  $^{13}\text{C}$  NMR spectra of middle silk gland portion of living *B. mori* mature larva at room temperature;  $\tau$  is delay time between the  $180^\circ$  and  $90^\circ$  pulses [5]

### 10.2.2 Solution Structure of Silk Fibroin at Atomic Level

It is possible to determine the solution structure of SF from the  $^1\text{H}$ ,  $^{13}\text{C}$ , and  $^{15}\text{N}$  solution chemical shifts by using TALOS program developed by NH group [25]. In general, the primary structure of SF is repeated in tandem [26]. Thus, typical sequence appeared in the SF repeatedly will be the target to determine the structure in atomic level. The sequential assignments of  $^1\text{H}$ ,  $^{13}\text{C}$ , and  $^{15}\text{N}$  nuclei of SF extracted from the silk gland were performed by 2D double resonance, and 3D double and triple resonance through bond correlation experiments; 2D  $^1\text{H}$ - $^{15}\text{N}$  heteronuclear single-quantum coherence (HSQC), 2D  $^1\text{H}$ - $^{13}\text{C}$  HSQC, 3D HNCO, 3D HCACO [27]. The torsion angle constraints for the backbone chain were derived from database analysis of the chemical shifts  $^{13}\text{C}\alpha$ ,  $^{13}\text{C}\beta$ ,  $^{13}\text{CO}$ ,  $^1\text{H}\alpha$ ,  $^1\text{HN}$ , and  $^{15}\text{N}$  using TALOS-N [6, 7].

Figure 10.2a shows five kinds of typical  $\beta$ -turns and the corresponding  $(\phi, \varphi)$  database for the  $(i+1)$  and  $(i+2)$  residues in  $\beta$ -turn structures formed with four amino acids  $(i-i+3)$ .

The  $(\phi, \varphi)$  plots of the 25 closest data base matches predicted for the GAGSGAGA motif using TALOS-N are shown in Fig. 10.2b [6]. Here the motif, GAGSGAGA is a typical sequence of crystalline domain of SF and appears frequently in the primary structure [26]. It is noted that the angles  $(\phi, \varphi)$  fall into well narrow regions for the  $(i+1)$  residue in typical type II  $\beta$ -turn structures. Figure 10.2c shows the model constructed using the average torsion angles for the best matches  $(\phi, \varphi)$  for the repeated GAGSGAG motif. This type II  $\beta$ -turn structure is essentially the same as Silk I\* structure (type II  $\beta$ -turn) in the solid-state reported previously [17, 28–30].

We reported previously molecular dynamic (MD) simulations of three dipeptides, Ac-X-NHMe ( $X = \text{G}, \text{A}, \text{S}$ ), in water to examine the favorable local conformation for the repeated sequence of the GAGSGA in water [31]. The conformational probability maps calculated for these three dipeptides indicate that the torsion angle of each Gly, Ala, and Ser residues in the repeated GAGSGA sequence with type II  $\beta$ -turn structure was basically in the energetically stable regions in water. The high possibility of the appearance of  $\beta$ -turn structure was also pointed out by the MD simulation of Ac-(AG)<sub>8</sub>-NHMe in water. This means that the time-averaged local structure of the silk fibroin in random coil form seems basically similar to those of type II  $\beta$ -turn structure in the solid-state. The amplitude and width of the structural fluctuations of these three residues are relatively large for random coil form in the diluted silk fibroin aqueous solution and such a fluctuation decreases by aggregation formation of the silk fibroin molecules with increasing the concentration [5]. The aggregates still keep high mobility as shown in Fig. 10.1 for SF stored in the silk gland of living silkworm. The generation of such aggregate of silk fibroin chain with type II  $\beta$ -turn conformation will be one of the origins of the nucleation to change the structure to  $\beta$ -sheet structure easily by external forces [22].

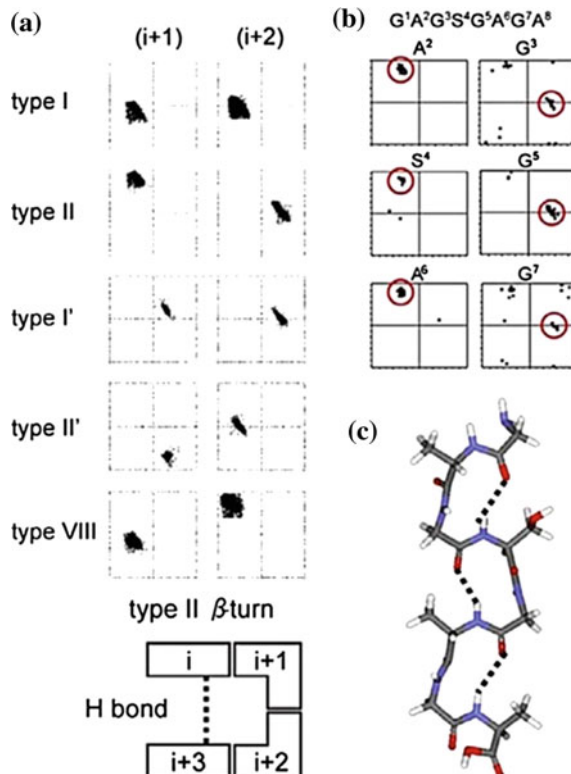


**Fig. 10.2** Torsion angle ( $\phi$ ,  $\psi$ ) maps for various types of  $\beta$ -turn structures and those predicted for repetitive sequence motifs GAGSGAG. The horizontal and vertical axes in each residue map show the predicted torsion angles  $\phi$  and  $\psi$  in each residue, respectively. **a** The ( $\phi$ ,  $\psi$ ) maps for typical type I, type II, type I', type II', and type VIII  $\beta$ -turns, and an illustration of the type II  $\beta$ -turn conformation; **b** the 25 best matches for torsion angles ( $\phi$ ,  $\psi$ ) for the GAGSGAG motifs obtained using the TALOS-N program; **c** a structural model constructed using the averaged ( $\phi$ ,  $\psi$ ) in the circle for each motif. Hydrogen bonds are assumed to exist between the HN of the  $i$ -th and the CO of the  $(i+3)$ -th residues for the GAGSGAG motifs [6]

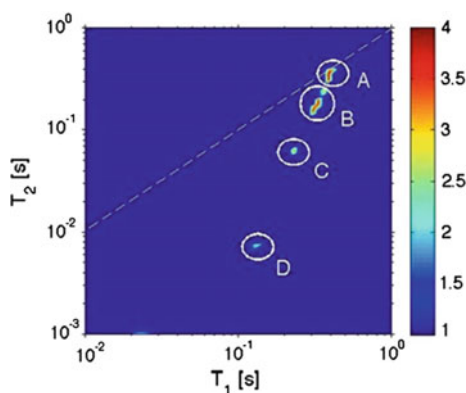
### 10.2.3 Dynamics of Water Molecules Interacted with Silk Fibroin

Generally, water in the SF-water system is divided into three categories: free water, freezing bound water, and non-freezing bound water which predominates in the plasticizing effect on the SF chains [32]. One might speculate that the hydration of SF may arise from water molecules penetrating into the relatively disordered domains, such as the non-crystalline domain, and increase chain motion due to disruption of the hydrogen bonding in these regions by the strong interaction of water molecules with polar groups of the SF chain. However, the hydration

mechanism of SF, including the microscopic interactions with water, is still not completely understood [33]. NMR relaxation has proven to be useful for monitoring the dynamics and distribution of water molecules interacting with SF.  $^1\text{H}$  pulsed NMR was used previously to study the dynamics of the non-freezing bound water molecules absorbed in SF fibers, films, and powders [34]. Recently, two-dimensional deuterium  $T_1-T_2$  ( $2\text{D } ^2\text{H } T_1-T_2$ ) NMR relaxation spectroscopy coupled with inverse Laplace transformation (ILT) has been used to monitor the dynamics of water molecules existing as multi-compartment systems [35, 36]. Therefore, this relatively new analytical technique can be used to monitor the dynamics of relatively mobile water (freezing bound water) molecules that interacted with the hydrated SF fiber.

Figure 10.3 shows the  $2\text{D } ^2\text{H } T_1-T_2$  correlation maps of the SF fiber in  $^2\text{H}_2\text{O}$  after immersing the fiber in  $^2\text{H}_2\text{O}$  for more than one day in NMR tube [8]. Four distinct reservoirs were observed. The dominant reservoir, A with  $T_1 \sim T_2$  values on the diagonal line can be assigned to bulk water outside of the fibers exhibiting highly isotropic fast motions. There are other reservoirs with smaller  $T_1$  and  $T_2$  values in the map. This means that the exchange among water molecules that interacted with the fiber becomes sufficiently slow in the NMR time scale and enables separated reservoirs to be observed in the map.  $T_2$  which is more sensitive to exchange and dynamical processes in the NMR relaxation times than  $T_1$  were significantly shorter than  $T_1$  values for the remaining three reservoirs, B–D. Thus, these water reservoirs may be assigned to exchangeable water molecules interacting with the SF fiber in three different degrees of binding interactions. The fraction of the reservoirs denoted A, B, C, and D was estimated to be 77, 21, 2, and 0.004%, respectively. Finally, the three reservoirs were assigned to B: water molecules trapped weakly on the surface of the fiber, C: bound water molecules located in the inner surface of the fiber, and D: bound water molecules located in the inner part of the fiber [8].

**Fig. 10.3**  $^2\text{H } T_1-T_2$  ILT correlation map of  $^2\text{H}_2\text{O}$  in hydrated SF fiber at 25 °C. The dotted line shows the relation of  $T_1 = T_2$  [8]

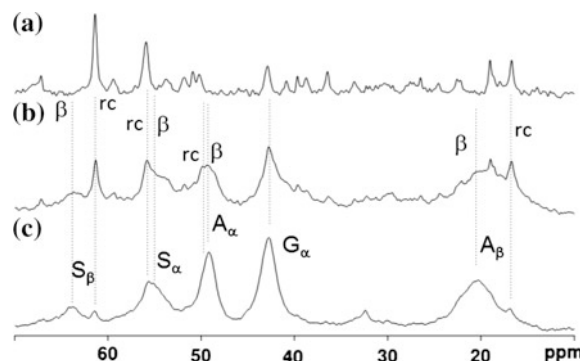


### 10.2.4 Dynamics of Hydrated Silk Cocoon, Sericin, and Fibroin

Changes in the local conformation and dynamics of the individual amino acid residues of silk proteins due to hydration are not currently well understood on the molecular level as well as change in the dynamics of water molecules. The  $^{13}\text{C}$  refocused INEPT ( $^{13}\text{C}$  r-INEPT), where the pulse sequence was developed for solution NMR, was used to detect the component of the hydrated silk proteins with fast motion by using J coupling [37]. In contrast,  $^{13}\text{C}$  CP/MAS NMR can observe the components of very slow motion. The  $^{13}\text{C}$  DD/MAS NMR can widely observe the both mobile and immobile domain. Thus, these three kinds of  $^{13}\text{C}$  NMR techniques,  $^{13}\text{C}$  r-INEPT,  $^{13}\text{C}$  CP/MAS, and  $^{13}\text{C}$  DD/MAS NMR, provide different perspectives on the dynamic behavior of hydrated silk samples and can be used together to characterize their local structure and conformations.

Figure 10.4 shows  $^{13}\text{C}$  r-INEPT, DD/MAS, and CP/MAS NMR spectra of natural abundance silk cocoon (SC) fiber in the hydrated state [9]. The SC consists of both SF and silk sericin (SS) components, and the fractions are about 75 and 25%, respectively. The  $^{13}\text{C}$  CP/MAS NMR spectrum of SC fiber (c) is similar to that of SF fiber, and the rigid domain in SC fiber comes mainly from SF fiber which is located at the inner part of the SC fiber. On the other hand, the mobile domain of the hydrated SC fiber comes mainly from the hydrated SS part on the surface of the SC fiber, and therefore, the  $^{13}\text{C}$  r-INEPT spectrum of the SC fiber (a) is similar to that of the SS powder. These data indicate that water molecules surrounded the SC fiber diffuse selectively to the SS domain coated the inner SF part of the SC fiber, and increase the mobility of the SS domains. This seems to be related to the roles of SC as waterproof barriers that keep the pupa dry and/or as humidity buffers that prevent the pupa from desiccating in molecular level as well as macroscopic level [38, 39].

**Fig. 10.4** a  $^{13}\text{C}$  r-INEPT, b  $^{13}\text{C}$  DD/MAS and c  $^{13}\text{C}$  CP/MAS NMR spectra of natural silk cocoon fiber in the hydrated state. Here, r is random coil, and  $\beta$  is  $\beta$ -sheet structure [9]



### 10.2.5 Fraction of Several Conformations of Silk Fibroin

It is possible to determine the fraction of several conformations of SF in the dry and hydrated states by deconvolution analysis of the  $^{13}\text{C}$  DD/MAS NMR at amino acid level on the basis of the conformation-dependent  $^{13}\text{C}$  NMR chemical shifts. From the primary structure of SF, it is known that Ser residues are present predominantly in the crystalline domains, Tyr predominantly in the non-crystalline domains, and Ala residues in both domains [26]. Thus, selective [ $3\text{-}^{13}\text{C}$ ] Ser, [ $3\text{-}^{13}\text{C}$ ] Tyr, and [ $3\text{-}^{13}\text{C}$ ] Ala labeling of SF are effective to analyze the conformation and dynamics of SF at amino acid level.

Figure 10.5 shows the deconvolution  $^{13}\text{C}$  DD/MAS NMR spectra of hydrated [ $3\text{-}^{13}\text{C}$ ] Ala-, [ $3\text{-}^{13}\text{C}$ ] Ser-, and [ $3\text{-}^{13}\text{C}$ ] Tyr-SF fiber to determine the fraction of different conformations of Ala, Ser, and Tyr residues in the dry and hydrated states [8, 10]. It is noted that the fraction of  $\beta$ -sheet of these residues in the SF fiber did not change significantly before and after hydration. Thus, the  $\beta$ -sheet structure which is main conformation of the SF fiber does not contribute to the hydration, and water molecules do not penetrate in the structure. In addition, there are two peaks in the random coil region. One is sharp peak with fast motion due to penetration of water molecules in the region and another is broad one with slow motion which indicates no penetration of water molecules. The fraction of sharp peak in total fraction of the hydrated SF fiber was determined to be 9, 11, and 6% for Ala, Ser, and Tyr residues, respectively. The previous speculation is that the hydration of SF may arise from water molecules penetrating into random coil region, such as the non-crystalline domain of SF fiber [32, 33]. However, the fraction of sharp peak of Ser residue is larger than that of Tyr residue by almost two times. The OH groups of Ser and Tyr residues will be the sites interacted with water, but the aromatic group of Tyr residue has hydrophobic character, which will keep out water molecules [10]. Thus, the hydration of SF fiber is independent of the crystalline and

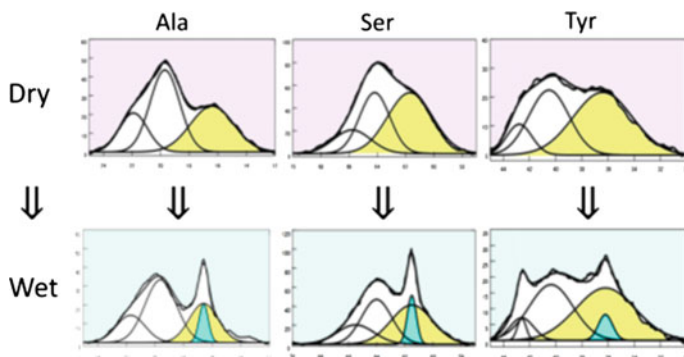


**Fig. 10.5** Observed and deconvoluted  $^{13}\text{C}$  DD/MAS NMR spectra of Ala, Ser, and Tyr C $\beta$  carbons of hydrated [ $3\text{-}^{13}\text{C}$ ] Ala-, [ $3\text{-}^{13}\text{C}$ ] Ser-, and [ $3\text{-}^{13}\text{C}$ ] Tyr-SF fiber in the dry and hydrated states, respectively [10]

non-crystalline domains and depends on the local environment of the individual amino acid. This information is the first detailed study of the effects of hydration on site-specific crystalline and non-crystalline domains of silk.

### 10.2.6 Domain of Silk Fibroin

The inter-distance information can be obtained by 2D  $^{13}\text{C}$ - $^{13}\text{C}$  correlation spectra with dipolar-assisted rotational resonance (DARR) [12, 40]. The complete spin connectivity within a given amino acid residue can be obtained from these spectra greatly aiding spectral assignment. In addition to the strong intra-molecular correlations for a given amino acid, the 2D  $^{13}\text{C}$ - $^{13}\text{C}$  correlation spectra also display inter-molecular interactions between residues. DARR was used here to assign two Ser C $\beta$  peaks, A and B in the  $\beta$ -sheet region of the powder sample of the crystalline fraction of SF. [41] In addition, the related information about the size of the domains A and B was also obtained [3, 20]. Here, the Ala-Gly-Ser-Gly-Ala-Gly chain of the sample was  $^{13}\text{C}$  uniformly labeled.

Figure 10.6 shows the correlations between Ala C $\beta$  and Ser C $\beta$  in the DARR spectrum at mixing time of 400 ms [41]. Here, the detailed assignment of the  $\beta$ -sheets A and B of Ala residues of the SF sample was already reported [3, 20, 42, 43]. Several correlations between Ser C $\beta$  peaks around 64 ppm and Ala C $\beta$  peaks at 19.6/21.7 ppm were detected. In a DARR spectrum, shorter inter-nuclear distances contribute more effectively to cross peak intensity. Therefore, one expects that the cross peak between Ser C $\alpha$ /C $\beta$  and Ala C $\beta$  carbons will be dominated by the inter-sheet rather than the intra-molecular contribution judging

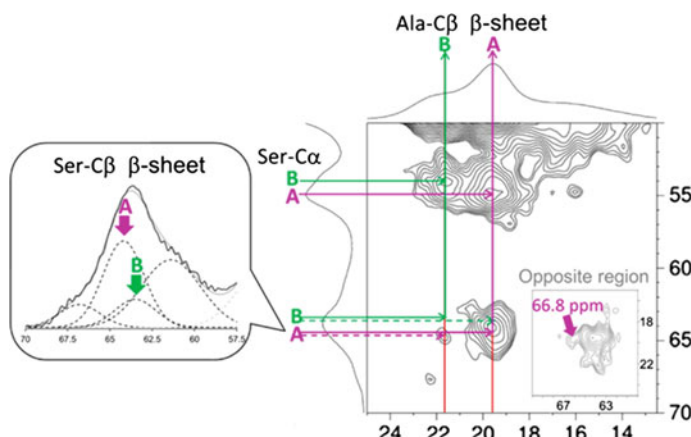


**Fig. 10.6** Ala C $\beta$ -Ser C $\alpha$ /C $\beta$  correlations in the 2D  $^{13}\text{C}$ - $^{13}\text{C}$  DARR spectrum of [U- $^{13}\text{C}$ ] crystalline fraction powder of SF with Silk II form at a mixing time of 400 ms [41]

from the sequence, Ala-Gly-Ser-Gly-Ala-Gly. In Fig. 10.6, the Ser C $\alpha$  peaks at 54.9 and 54.0 ppm (corresponding to geometries A and B, respectively) show correlations with the Ala C $\beta$  peaks at 19.6 and 21.7 ppm, also corresponding to geometries A and B, respectively [42, 43]. This observation supports the presence of separate A and B domains because any model that has alternating or statistically random A and B strands would have A-B interactions as the shortest inter-sheet distance. The Ser C $\beta$  peak at 64.2 ppm (geometry A) also has a strong cross peak with Ala C $\beta$  peak A, while the Ser C $\beta$  B peak has correlations that are too weak to interpret. However, correlations are also seen between geometries A and B, for Ser C $\beta$  A to Ala C $\beta$  B and between Ser C $\alpha$  and Ala C $\beta$ . If the two geometries A and B formed largely separate domains, inter-domain cross peaks could not be observed in the 2D DARR spectrum. Hence, it is concluded that the  $\beta$  sheets A and B form small domains with extensive inter-domain contact [41].

### 10.2.7 Inter-molecular Arrangement of Alanine Oligopeptide

Rotational echo double resonance (REDOR) is a commonly used solid-state NMR method for determining inter-atomic distance [13]. This is accomplished by preparing samples with isolated pairs of isotopic labels, which is required to obtain accurate distance results from REDOR experiments and subsequent analysis. The distance information derives from the dipole coupling of the spin pair which has a  $1/r^3$  distance dependence.

The structural analysis of Ala oligopeptides is important for understanding the crystalline region with  $\beta$ -sheet structure appeared frequently in silks from spiders and wild silkworms such as *Samia cynthia ricini*, *Antheraea pernyi*, and *Antheraea yamamai* [44–46]. Thus,  $^{13}\text{C}$ - $^{15}\text{N}$  REDOR was used here to determine the inter-molecular arrangement of Ala oligopeptide, A<sub>7</sub>. Figure 10.7 shows REDOR plot for determination of the inter-molecular distance between Ala<sup>4</sup> $^{13}\text{C}$  $\beta$  in one Ala<sub>7</sub> molecule and Ala<sup>5</sup> $^{15}\text{N}$  in the neighboring Ala<sub>7</sub> molecule [44]. This analysis showed that the inter-molecular distance between  $^{13}\text{C}$  and  $^{15}\text{N}$  nuclei is 3.8 ( $\pm 0.1$ ) Å. Then the inter-molecular arrangement of Ala<sub>7</sub> chains could be discussed together with other NMR structural information.

### 10.2.8 Complex between Silk Fibroin and Glycerin

$^1\text{H}$  NMR spectra in the solid-state were very broad because of strong dipolar coupling. [15] Recently, many works about high resolution  $^1\text{H}$  DQ solid-state NMR of hydrogen-bonded systems have been reported [15–18, 47]. We have developed a 1 mm microcoil MAS NMR probe-head that is limited for solid-state samples [48].

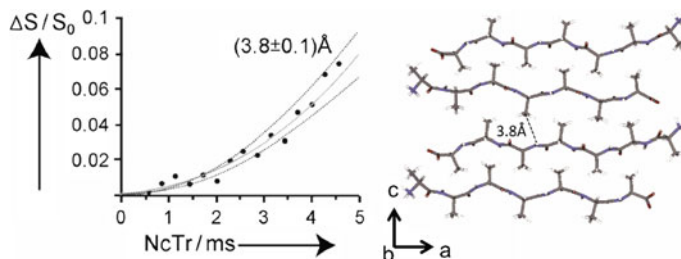


**Fig. 10.7** REDOR plot for determination of the inter-molecular distance between the  $^{13}\text{C}\beta$  carbon label in the  $\text{Ala}_4$  residue in one  $\text{Ala}_7$  molecule and the  $^{15}\text{N}$  label in the  $\text{Ala}_5$  residue in the neighboring  $\text{Ala}_7$  molecule.  $\text{Ala}_7$  molecules with a  $^{13}\text{C}$ -labeled  $\text{Ala}_4$  residue were surrounded by other  $\text{Ala}_7$  molecules with  $^{15}\text{N}$  labels in the  $\text{Ala}_5$  residues (molar ratio 1:3). The reduction in the intensity of the  $\text{C}\beta$  carbon signal (filled circle) is shown as a function of rotor cycle (NcTr). Dashed lines indicate the error margin [44].

By averaging residual dipolar couplings with the combined use of a microcoil-probe-head and ultrahigh field NMR, we can determine the  $^1\text{H}$  chemical shifts of SF in the solid state from the well-resolved  $^1\text{H}$  spectrum. Especially,  $^1\text{H}$  atoms are located on the surface of the SF molecules and sensitive to the inter-molecular arrangement in the solid state. Therefore, it is especially useful to obtain information on the inter-molecular arrangement of SF and also the complex structure between SF and other molecules.

In order to improve the stiff and brittle characteristics of pure SF film in the dry state, glycerin (Glyc) has been used as a plasticizer [49, 50]. However, there have been only limited studies on the structural characterization of the Glyc-blended SF film. Figure 10.8 shows the  $^1\text{H}$  DQMAS NMR spectrum of SF film containing 29 wt% Glyc [19]. The Ser H $\alpha$  peak of SF with Silk I\* form was clearly observed in the  $^1\text{H}$  DQMAS NMR spectrum. In addition, the NH peaks of Ala and Gly residues were separated clearly with chemical shift difference of more than 1 ppm due to the appearance of Silk I\* form [28–30]. In the Silk I\* conformation, the Gly NH contributed to intra-molecular hydrogen-bonding formation parallel to the SF chain, while Ala NH contributed to inter-molecular hydrogen-bonding formation perpendicular to the SF chain [28–30]. The latter inter-molecular hydrogen bonding was weaker than the intra-molecular hydrogen bonding judging from the NH chemical shifts; thus, the NH chemical shifts of Ala HN proton were 7.6 ppm and that of Gly HN proton 8.8 ppm [47]. Therefore, the inter-molecular hydrogen bonding was easy to break down by interaction with Glyc for the Silk I\* form.

The eight  $^1\text{H}$ - $^1\text{H}$  correlation signals (broken lines) between the OH or CH<sub>2</sub> groups of Glyc and SF were selected. Thus,  $^1\text{H}$  atomic distances of Glyc (CH<sub>2</sub>)-Ala H $\beta$ , Glyc (CH<sub>2</sub>)-Gly H $\alpha$ ①, Glyc (CH<sub>2</sub>)-Ser H $\alpha$ , Glyc (OH)-Ser H $\alpha$ , Glyc (OH)-Ala HN, and Glyc (OH)-Gly HN in Fig. 10.8 were considered to be within 4 Å. Here, the Glyc peaks were observed at 3.4 ppm (CH<sub>2</sub>) and 4.4 ppm (OH plus H<sub>2</sub>O). The observed signals reflecting the distance constraints could be used to prepare a

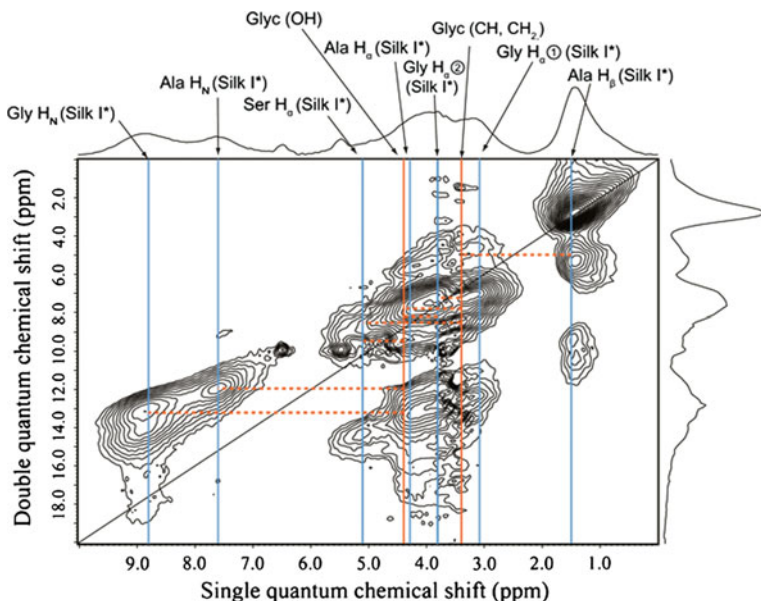


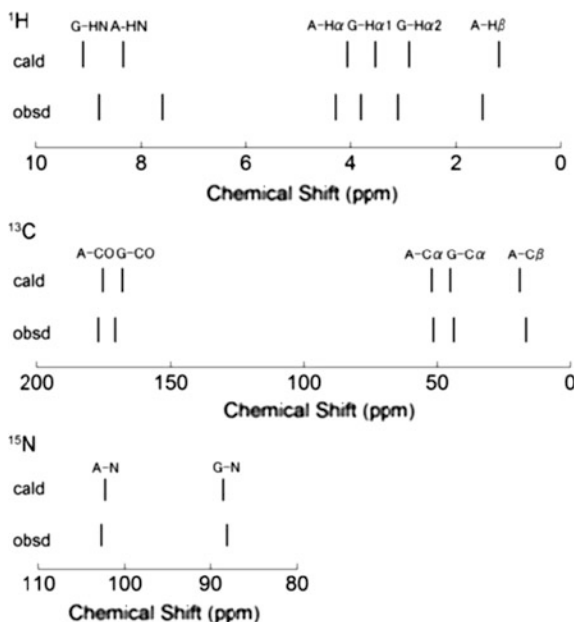
**Fig. 10.8**  $^1\text{H}$  DQMAS NMR spectrum of Glyc (29 wt%)-blended SF film together with the assignments. The  $^1\text{H}$  chemical shifts of random coil (red) and Silk I\* (blue) forms are shown together with the  $^1\text{H}$ - $^1\text{H}$  correlation signals (broken lines) [19]

structural model for the Glyc-SF complex. After MD calculation which satisfies the observed  $^1\text{H}$ - $^1\text{H}$  distance constraint in Glyc-blended SF film, the complex models between SF and Glyc were proposed [19].

### 10.2.9 Use of Chemical Shift Calculation for Verification of Silk Fibroin Structural Model

As mentioned above, the conformation-dependent  $^{13}\text{C}$  chemical shift coupled with selective labeling can be used effectively for determination of conformation of SF [2, 3]. The conformation-dependent  $^{15}\text{N}$  chemical shifts can be also used similarly [50]. On the other hand, rapid advance of the NMR chemical shift calculation is noticeable. For example, the geometry optimization by CASTEP and the GIPAW chemical shift calculation can reproduce the observed  $^{13}\text{C}$  and  $^{15}\text{N}$  NMR chemical shifts very well [16–18, 20, 21]. The  $^1\text{H}$  solid-state chemical shift is now possible to discuss the structure as mentioned in Sect. 2.8. With the combined use of a microcoil-probe-head and ultrahigh field NMR together with the geometry optimization by CASTEP and the GIPAW (gauge-including projector augmented wave) chemical shift calculation, we could determine the accurate  $^1\text{H}$  positions of small peptide molecules; such as Ala tripeptide and tetrapeptide with  $\beta$ -sheet

**Fig. 10.9** The stick spectra of the  $^1\text{H}$ ,  $^{13}\text{C}$ , and  $^{15}\text{N}$  chemical shifts calculated for  $(\text{Ala-Gly})_{15}$  in the Silk I\* form with inter-molecular arrangement. The observed chemical shifts are also shown [17]



structures [18]. Thus, this chemical shift calculation was applied to verify the Silk I\* model with inter-molecular arrangement proposed experimentally. The co-ordinate of inter-molecular co-ordinates has been reported for hetero atoms such as C, N, and O of  $(\text{Ala-Gly})_{15}$  with Silk I\* form as a model of SF together with  $^{13}\text{C}$  and  $^{15}\text{N}$  chemical shifts [28–30]. Figure 10.9 shows the stick spectra of the  $^1\text{H}$ ,  $^{13}\text{C}$ , and  $^{15}\text{N}$  chemical shifts calculated for  $(\text{Ala-Gly})_{15}$  with Silk I\* form together with the observed chemical shifts [17]. The agreement between the calculated and observed chemical shifts of all  $^1\text{H}$ ,  $^{13}\text{C}$ , and  $^{15}\text{N}$  nuclei is excellent, indicating that all the atomic-co-ordinate including  $^1\text{H}$  nuclei is highly correct [17, 28, 29]. The chemical shift calculation based on CASTEP and GIPAW methods was also applied to study more complexed structure of  $(\text{Ala-Gly})_{15}$  with Silk II form [20].

### 10.3 Conclusion

Some of recent NMR studies about silks performed in our laboratory were introduced in this Chapter. The majority of the NMR studies have been performed on fibroin and fibers produced by the domestic silkworm, *B. mori*, and to a lesser extent on fibroin produced by the wild silkworms, *S. c. ricini*. The combined use of isotopically labeled samples and NMR techniques has also been extremely advantageous in elucidating the silk structure and dynamics. Recently, much attention has been paid to silk from textile engineers to polymer chemists and

biomedical scientists. Thus, the atomic level information on the silk structure and dynamics summarized here will make a great contribution in many fields of silk application.

## References

- Asakura, T., Miller, T.: *Biotechnology of Silk*. Springer, Berlin (2014)
- Asakura, T., Suzuki, Y., Nakazawa, Y., Holland, G.P., Yarger, J.L.: Elucidating silk structure using solid-state NMR. *Soft Matter* **9**, 11440–11450 (2013)
- Asakura, T., Okushita, K., Williamson, M.P.: Analysis of the structure of *Bombyx mori* silk fibroin by NMR. *Macromolecules* **48**, 2345–2357 (2015)
- Asakura, T., Suzuki, H., Watanabe, Y.: Conformational characterization of silk fibroin in intact *Bombyx mori* and *Pilosamia cynthia ricini* silkworms by carbon-13 NMR spectroscopy. *Macromolecules* **16**, 1024–1026 (1983)
- Asakura, T.: Direct <sup>13</sup>C NMR observation of the silk fibroin in *Bombyx mori*. *Makromol. Chem. Rapid Commun.* **7**, 755–759 (1986)
- Suzuki, Y., Yamazaki, T., Aoki, A., Shindo, H., Asakura, T.: NMR study of the structures of repeated sequences, GAGXGA (X = S, Y, V), *Bombyx mori* liquid silk. *Biomacromolecules* **15**, 104–112 (2013)
- Suzuki, Y., Kawanishi, S., Yamazaki, T., Aoki, A., Saito, H., Asakura, T.: Structural determination of the tandem repeat motif in *Samia cynthia ricini* liquid silk by solution NMR. *Macromolecules* **48**, 6574–6579 (2015)
- Asakura, T., Isobe, K., Kametani, S., Ukpobor, O.T., Silverstein, M.C., Boutis, G.S.: Characterization of water in hydrated *Bombyx mori* silk fibroin fiber and films by <sup>2</sup>H NMR relaxation and <sup>13</sup>C solid state NMR. *Acta Biomater.* **50**, 322–333 (2017)
- Asakura, T., Endo, M., Tasei, Y., Ohkubo, T., Hiraoki, T.: Hydration of *Bombyx mori* silk cocoon, silk sericin and silk fibroin and their interactions with water as studied by <sup>13</sup>C NMR and <sup>2</sup>H NMR relaxation. *J. Mater. Chem. B* **5**, 1624–1632 (2017)
- Asakura, T., Isobe, K., Aoki, A., Kametani, S.: Conformation of crystalline and noncrystalline domains of [3-13C]Ala-, [3-13C]Ser-, and [3-13C]Tyr-Bombyx mori silk fibroin in a hydrated state studied with <sup>13</sup>C DD/MAS NMR. *Macromolecules* **48**, 8062–8069 (2015)
- Wishart, D.S.: Interpreting protein chemical shift data. *Prog. Nucl. Magn. Reson. Spectrosc.* **58**, 62–87 (2011)
- Takegoshi, K., Nakamura, S., Terao, T.: <sup>13</sup>C-<sup>1</sup>H dipolar-driven <sup>13</sup>C-<sup>13</sup>C recoupling without <sup>13</sup>C rf irradiation in nuclear magnetic resonance of rotating solids. *J. Chem. Phys.* **118**, 2325–2341 (2003)
- Gullion, T., Schaefer, J.: Rotational-echo double-resonance NMR. *J. Magn. Reson.* **81**, 196–200 (1989)
- Asakura, T., Watanabe, Y., Itoh, T.: NMR of silk fibroin. 3. Assignment of carbonyl carbon resonances and their dependence on sequence and conformation in *Bombyx mori* silk fibroin using selective isotopic labeling. *Macromolecules* **17**, 2421–2426 (1984)
- Schnell, I., Brown, S.P., Low, H.Y., Ishida, H., Spiess, H.W.: An investigation of hydrogen bonding in benzoxazine dimers by fast magic-angle spinning and double-quantum <sup>1</sup>H NMR spectroscopy. *J. Am. Chem. Soc.* **120**, 11784–11795 (1998)
- Brown, S.P.: Probing proton–proton proximities in the solid state. *Prog. Nucl. Magn. Reson. Spectrosc.* **50**, 199–251 (2007)
- Asakura, T., Suzuki, Y., Yazawa, K., Aoki, A., Nishiyama, Y., Nishimura, K., Suzuki, F., Kaji, H.: Determination of accurate <sup>1</sup>H positions of (Ala-Gly)<sub>n</sub> as a sequential peptide model of *Bombyx mori* silk fibroin before spinning (silk I). *Macromolecules* **46**, 8046–8050 (2013)

18. Asakura, T., Yazawa, K., Horiguchi, K., Suzuki, F., Nishiyama, Y., Nishimura, K., Kaji, H.: Intermolecular packing in *B. mori* silk fibroin: multinuclear NMR study of the model peptide (Ala-Gly)<sub>15</sub> defines a heterogeneous antiparallel antipolar mode of assembly in the silk II form. *Biopolymers* **101**, 13–20 (2014)
19. Asakura, T., Endo, M., Hirayama, M., Arai, H., Aoki, A., Tasei, Y.: Glycerin-induced conformational changes in *Bombyx mori* silk fibroin film monitored by <sup>13</sup>C CP/MAS NMR and <sup>1</sup>H DQMAS NMR. *Int. J. Mol. Sci.* **17**, 1517 (2016)
20. Asakura, T., Ohata, T., Kametani, S., Okushita, K., Yazawa, K., Nishiyama, Y., Nishimura, K., Aoki, A., Suzuki, F., Kaji, H., Ulrich, A.S., Williamson, M.P.: Intermolecular packing in *B. mori* silk fibroin: multinuclear NMR study of the model peptide (Ala-Gly)<sub>15</sub> defines a heterogeneous antiparallel antipolar mode of assembly in the silk II form. *Macromolecules* **48**, 28–36 (2015)
21. Yazawa, K., Suzuki, F., Nishiyama, Y., Ohata, T., Aoki, A., Nishimura, K., Kaji, H., Shimizu, T., Asakura, T.: Determination of accurate <sup>1</sup>H positions of an alanine tripeptide with anti-parallel and parallel β-sheet structures by high resolution <sup>1</sup>H solid state NMR and GIPAW chemical shift calculation. *Chem. Commun.* **48**, 11199–11201 (2012)
22. Asakura, T., Sato, Y., Aoki, A.: Stretching-induced conformational transition of the crystalline and noncrystalline domains of <sup>13</sup>C-labeled *Bombyx mori* silk fibroin monitored by solid state NMR. *Macromolecules* **48**, 5761–5769 (2015)
23. Asakura, T., Kawaguchi, Y., Demura, M., Osanai, M.: <sup>13</sup>C and <sup>31</sup>P NMR studies on sugar metabolism in *Bombyx mori* and *Philosamia cynthia ricini* larvae. *Insect Biochem.* **18**, 531–538 (1988)
24. Asakura, T., Watanabe, Y., Uchida, A., Minagawa, H.: Nmr of silk fibroin. 2. <sup>13</sup>C NMR-study of the chain dynamics and solution structure of *Bombyx-mori* silk fibroin. *Macromolecules* **17**, 1075–1081 (1984)
25. Shen, Y., Bax, A.: Protein backbone and sidechain torsion angles predicted from NMR chemical shifts using artificial neural networks. *J. Biomol. NMR* **56**, 227–241 (2013)
26. Zhou, C.Z., Confalonieri, F., Jacquet, M., Perasso, R., Li, Z.G., Janin, J.: Silk fibroin: structural implications of a remarkable amino acid sequence. *Proteins Struct. Funct. Genet.* **44**, 119–122 (2001)
27. Delaglio, F., Grzesiek, S., Vuister, G.W., Zhu, G., Pfeifer, J., Bax, A.: NMR pipe: a multidimensional spectral processing system based on UNIX pipes. *J. Biomol. NMR* **6**, 277–293 (1995)
28. Asakura, T., Ashida, J., Yamane, T., Kameda, T., Nakazawa, Y., Ohgo, K., Komatsu, K.: A repeated β-turn structure in Poly(Ala-Gly) as a model for silk I of *Bombyx mori* silk fibroin studied with two-dimensional spin-diffusion NMR under off magic angle spinning and rotational echo double resonance. *J. Mol. Biol.* **306**, 291–305 (2001)
29. Asakura, T., Yamane, T., Nakazawa, Y., Kameda, T., Ando, K.: Structure of *Bombyx mori* silk fibroin before spinning in solid state studied with wide angle x-ray scattering and <sup>13</sup>C cross-polarization/magic angle spinning NMR. *Biopolymers* **58**, 521–525 (2001)
30. Asakura, T., Ohgo, K., Komatsu, K., Kanenari, M., Okuyama, K.: Refinement of repeated β-turn structure for silk I conformation of *Bombyx mori* silk fibroin using <sup>13</sup>C solid-state NMR and X-ray diffraction methods. *Macromolecules* **38**, 7397–7403 (2005)
31. Yamane, T., Umemura, K., Asakura, T.: The structural characteristics of *Bombyx mori* silk fibroin before spinning as studied with molecular dynamics simulation. *Macromolecules* **35**, 8831–8838 (2002)
32. Hu, X., Kaplan, D.L., Cebe, P.: Dynamic protein–water relationships during β-sheet formation. *Macromolecules* **41**, 3939–3948 (2008)
33. Fu, C., Shao, Z., Fritz, V.: Animal silks: their structures, properties and artificial production. *Chem. Commun.* **43**, 6515–6529 (2009)
34. Asakura, T., Demura, M., Watanabe, Y., Sato, K.: <sup>1</sup>H pulsed NMR study of *bombyx mori* silk fibroin: dynamics of fibroin and of absorbed water. *J. Polym. Sci. Part B Polym. Phys.* **30**, 693–699 (1992)

35. Song, Y.-Q., Venkataraman, L., Hürlimann, M.D., Flaum, M., Frulla, P., Straley, C.: T<sub>1</sub>-T<sub>2</sub> correlation spectra obtained using a fast two-dimensional laplace inversion. *J. Magn. Res.* **154**, 261–268 (2002)
36. Ma, X., Sun, C., Huang, J., Boutis, G.S.: Thermal hysteresis in the backbone and side-chain dynamics of the elastin mimetic peptide [VPGVG]<sub>3</sub> revealed by <sup>2</sup>H NMR. *J. Phys. Chem. B* **116**, 555–564 (2012)
37. Burum, D.P., Ernst, R.R.: Net polarization transfer via a *J*-ordered state for signal enhancement of low-sensitivity nuclei. *J. Magn. Reson.* **39**, 163–168 (1980)
38. Horrocks, N.P., Vollrath, F., Dicko, C.: The silkworm cocoon as humidity trap and waterproof barrier. *Comp. Biochem. Physiol. Part A* **164**, 645–652 (2013)
39. Offord, C., Vollrath, F., Holland, C.: Environmental effects on the construction and physical properties of *Bombyx mori* cocoons. *J. Mater. Sci.* **52**, 10863–10872 (2016)
40. Takegoshi, K., Nakamura, S., Terao, T.: <sup>13</sup>C-<sup>1</sup>H dipolar-assisted rotational resonance in magic-angle spinning NMR. *Chem. Phys. Lett.* **344**, 631–637 (2001)
41. Okushita, K., Asano, A., Williamson, M.P., Asakura, T.: Local structure and dynamics of serine in the heterogeneous structure of the crystalline domain of *Bombyx mori* silk fibroin in silk II form studied by 2D <sup>13</sup>C-<sup>13</sup>C homonuclear correlation NMR and relaxation time observation. *Macromolecules* **47**, 4308–4316 (2014)
42. Asakura, T., Yao, J.: <sup>13</sup>C CP/MAS NMR study on structural heterogeneity in *Bombyx mori* silk fiber and their generation by stretching. *Protein Sci.* **11**, 2706–2713 (2002)
43. Asakura, T., Yao, J., Yaman, E.T., Umemura, K., Ulrich, A.: Heterogeneous structure of silk fibers from *Bombyx mori* resolved by <sup>13</sup>C solid-state NMR spectroscopy. *J. Am. Chem. Soc.* **124**, 8794–8795 (2002)
44. Asakura, T., Okonogi, M., Horiguchi, K., Aoki, A., Saito, H., Knight, D.P., Williamson, M. P.: Two different packing arrangements of antiparallel polyalanine. *Angew. Chem. Int. Ed.* **51**, 1212–1215 (2012)
45. Nakazawa, Y., Asakura, T.: Structure determination of a peptide model of the repeated helical domain in *Samia cynthia ricini* silk fibroin before spinning by a combination of advanced solid-state NMR methods. *J. Am. Chem. Soc.* **125**, 7230–7237 (2003)
46. Numata, K., Sato, R., Yazawa, K., Hikima, T., Masunaga, H.: Crystal structure and physical properties of *Antheraea yamamai* silk fibers: long poly(alanine) sequences are partially in the crystalline region. *Polymer* **77**, 87–94 (2015)
47. Yamauchi, S., Yamasaki, R., Takahashi, R., Asakura, T.: Microscopic structural analysis of fractured silk fibers from *Bombyx mori* and *Samia cynthia ricini* using <sup>13</sup>C CP/MAS NMR with a 1 mm microcoil MAS NMR probehead. *Solid State Nucl. Magn. Reson.* **38**, 27–30 (2010)
48. Lu, S., Wang, X., Lu, Q., Zhang, X., Kluge, J.A., Uppal, N., Omenetto, F., Kaplan, D.L.: Insoluble and flexible silk films containing glycerol. *Biomacromol* **11**, 143–150 (2010)
49. Pei, Y., Liu, X., Liu, S., Lu, Q., Liu, J., Kaplan, D.L., Zhu, H.A.: A mild process to design silk scaffolds with reduced  $\beta$ -sheet structure and various topographies at the nanometer scale. *Acta Biomater.* **13**, 168–176 (2015)
50. Asakura, T., Demura, M., Date, T., Miyashita, N., Ogawa, K., Williamson, M.P.: NMR study of silk I structure of *Bombyx mori* silk fibroin with <sup>15</sup>N- and <sup>13</sup>C-NMR chemical shift contour plots. *Biopolymers* **41**, 193–203 (1997)

# Chapter 11

## NMR Studies on Polymer Materials

Atsushi Asano

**Abstract** This chapter presents the NMR investigations of synthetic polymer materials, including polymer blends and alloys, polymer nanocomposites, rubbers and elastomers, and other semicrystalline polymers: polystyrene/poly(vinyl methyl ether), poly(methacrylic acid)/poly(vinyl acetate), and poly-3-hexylthiophene/phenyl-C<sub>61</sub>-butyric acid methyl ester blends, polyketone/polyamide alloy, poly(vinyl alcohol)/clay, polystyrene-poly(ethylene oxide) block copolymer/clay, nylon-6/clay, and poly(vinyl isobutyl ether)/poly( $\epsilon$ -L-lysine)/clay nanocomposites, and acrylonitrile butadiene rubbers are introduced. High-resolution solid-state <sup>13</sup>C NMR spectra are sensitive to the existence of interpolymer interaction, particularly hydrogen bonds make chemical shift value down-field shift. Hetero-correlation NMR spectroscopy shows a proof of existence of the interaction between component polymer and clay. Analysis of the <sup>1</sup>H spin-lattice relaxation ( $T_1^H$ ) behavior influenced by the spin diffusion provides the degree of homogeneity, domain size of component polymers, and phase separation process for polymer blends/alloys. Paramagnetic effect on  $T_1^H$  gives information of stability of an organic modifier on clay surfaces and of morphology of  $\alpha$  and  $\gamma$  crystalline phases of nylon-6 in nylon-6/montmorillonite nanocomposites. Finally, the degradation of rubbers is discussed by <sup>1</sup>H spin-spin relaxation ( $T_2^H$ ) analysis.

**Keywords** <sup>1</sup>H relaxation • Spin diffusion • Polymer blends • Nanocomposites  
Rubber • Paramagnetic effect

---

A. Asano (✉)

Department of Applied Chemistry, National Defense Academy,  
Hashirimizu 1-10-20, Yokosuka, Kanagawa 239-8686, Japan  
e-mail: asanoa@nda.ac.jp

## 11.1 Introduction

Characterization of morphology, molecular motion, or intermolecular interaction of polymer blends and alloys, nanocomposites, rubbers and elastomers, and some semicrystalline polymers using the solid-state  $^{13}\text{C}$  CPMAS (cross-polarization and magic-angle spinning) NMR is mainly described. The words “blend” and “alloy” are frequently used as the same meaning of “mixed component polymers.” On the other hand, polymer “alloy” is used for blend materials having superior mechanical properties after mixing of different component polymers in many cases. Hence, it is discriminated here that polymer blends indicate a simple mixing of polymers with regardless of having good physical properties and polymer alloys appear some improvement on mechanical/physical properties. The mechanical properties of polymer blends and alloys are significantly influenced by the degree of mixing as well as the characteristic property of a component polymer: this issue is described in Sect. 11.2. Similarly, the dispersion of fillers and the interaction between polymers and fillers for polymer nanocomposites are very important key points to show a great improvement such as gas barrier, impact strength, flame retardants, and thermal properties [1] (Sect. 11.3).

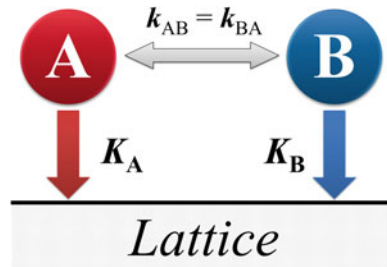
The density and the strength of the cross-links in rubbers and elastomers affect the molecular motion: for example, the existence of the cross-links resists being deformed. The rubbers without the cross-links are deformed easily by the fast MAS: a strong centrifugal force is produced by MAS. On the other hand, the cross-linked rubbers show the MAS rate dependence of  $^1\text{H}$  spin-lattice relaxation time ( $T_1^{\text{H}}$ ), indicating that the molecular motion is changed even if the rubbers are not deformed [2]. Thus, it is necessary to concern with the effects of MAS on molecular motion of rubbers and elastomers. On the one hand, many rubbers have a double bond in their unit, and it is easily oxidized and thermally damaged to produce a radical, resulting in the degradation/aging of rubbers [3]. The degradation causes the molecular motion change, and it results in shortening of  $^1\text{H}$  spin-spin relaxation time ( $T_2^{\text{H}}$ ): the investigation of aging is briefly described in Sect. 11.4.

## 11.2 Polymer Blends and Alloys

### 11.2.1 *Miscibility and Mobile Heterogeneity*

Different domain sizes of polymer blends are easily characterized distinctly by  $T_1^{\text{H}}$  and  $T_{1p}^{\text{H}}$ . Sensitive domain size for  $T_{1p}^{\text{H}}$  is one-order smaller than  $T_1^{\text{H}}$  [4]. The fast  $^1\text{H}$  spin diffusion averages various spin temperatures of almost all protons between component polymers in a homogeneous system. Thus, each  $^1\text{H}$  relaxation time obtained from the well-resolved  $^{13}\text{C}$  peaks of the respective component polymer has the identical value. On the other hand, in a heterogeneous blend, the individual  $^1\text{H}$  relaxation times of component polymers are not fully averaged each other because the large domain size does not allow to be averaged entirely each proton spin temperature.

**Fig. 11.1** Schematic illustration of the two-spin system. The arrow toward lattice represents the  $^1\text{H}$  spin-lattice relaxation rate:  $K_A = 1/T_{1A}$  and  $K_B = 1/T_{1B}$ . The  $^1\text{H}$  spin diffusion rate  $k_{AB}$  equals to  $k_{BA}$



The simple two-spin system is helpful to investigate the homogeneity of polymer blends and alloys [4–6]. Figure 11.1 shows the schematic illustration of the two-spin system of polymer blends consisted of polymers A and B. The  $^1\text{H}$  spin diffusion rate,  $k$ ,  $T_1$  rates ( $1/T_1$ ) of A-spin  $K_A$ , and  $K_B$  for B-spin are defined as shown in Fig. 11.1. The spin diffusion rates  $k_{ij}$  and  $k_{ji}$  between spin species  $i$  and  $j$  are assumed to be the same value  $k$  with each other. The proton fraction of the magnetization of polymer A,  $M_A$ , is  $f_A$  ( $=1-f_B$ ). The relaxation behavior connected by the  $^1\text{H}$  dipolar coupling between  $M_A$  and  $M_B$  is expressed by the simultaneous differential equations depending on time,  $t$ , as follows:

$$\begin{aligned}\frac{dM_A(t)}{dt} &= -(K_A + f_B k) \cdot M_A(t) + f_A k \cdot M_B(t) \\ \frac{dM_B(t)}{dt} &= -(K_B + f_A k) \cdot M_B(t) + f_B k \cdot M_A(t)\end{aligned}\quad (11.1)$$

These simultaneous differential equations are easily solved with the initial conditions of  $M_A(0) = M_A^0$  and  $M_B(0) = M_B^0$ .

$$\begin{aligned}M_A(t) &= a_+ e^{r_+ t} + a_- e^{r_- t} \\ M_B(t) &= b_+ e^{r_+ t} + b_- e^{r_- t}\end{aligned}\quad (11.2)$$

where

$$\begin{aligned}a_\pm &= \frac{1}{2} M_A^0 \{ 1 \pm R^{-1} (K_B + k - K_A) \}, \\ b_\pm &= \frac{1}{2} M_B^0 \{ 1 \pm R^{-1} (K_A + k - K_B) \}, \\ r_\pm &= \frac{1}{2} \{ -(K_A + K_B + k) \pm R \}, \quad \text{and} \\ R &= + \sqrt{[(K_A - K_B) + (f_B - f_A) k]^2 + 4 f_A f_B k^2}\end{aligned}$$

In the case that  $k$  is much slower than  $K_A$  and  $K_B$ , Eq. (11.2) becomes  $M_A(t) = M_A^0 \cdot e^{-K_A t}$  and  $M_B(t) = M_B^0 \cdot e^{-K_B t}$ , respectively. This indicates that the magnetizations  $M_A$  and  $M_B$  have the original relaxation rate  $K_A$  and  $K_B$ , respectively, even

though the mixed sample, namely a complete immiscible condition on a molecular level. On the other hand, when the  $^1\text{H}$  spin diffusion among the component polymers is sufficiently fast:  $k$  is much faster than  $K_A$  and  $K_B$ , the time-dependent magnetization  $M_A(t)$  will be simplified to  $M_A(t) = a_+ e^{r_+ t}$  with the parameters  $a_+ = M_A^0$ ,  $a_- = 0$ , and  $r_+ = -(f_A K_A + f_B K_B)$ . The similar equation for magnetization  $M_B(t)$  is also derived. Thus, the average relaxation rate  $K_{\text{ave}}$  for both magnetizations  $M_A$  and  $M_B$  is provided as

$$K_{\text{ave}} = f_A K_A + f_B K_B = f_A K_A + (1 - f_A) K_B \quad (11.3)$$

The average relaxation time  $T_{1\text{ave}}$  estimated from Eq. (11.3) would be measured in the system that the  $^1\text{H}$  spin diffusion fully and homogeneously occurs. The identical and single-exponential decay with  $K_{\text{ave}}$  for both polymers A and B is realized when the value of  $k$  is 10–100 times faster than the fastest  $K$  among the components [4, 7]. In a moderate rate case such as  $k$  is comparable to  $K$ , the observed  $T_1$  relaxations are followed the curvatures expressed by Eq. (11.2): non-single-exponential decay.

### 11.2.1.1 PS/PVME Blends

Polystyrene/poly(vinyl methyl ether) (PS/PVME) blends have well been known as a miscible polymer blend. In early 1970s, DSC and dielectric relaxation measurements had clarified that the PS/PVME blends show a single glass-transition and consist of a single phase [8–10]. The glass-transition temperature,  $T_g$ , of PVME is about 253 K while that of PS about 373 K. This large contrast of  $T_g$  induces a difference in dynamics between PS and PVME even in a homogeneous state: Kwei et al. called the phenomenon micro-heterogeneity on a segmental scale [9]. The molecular motion of component polymers in the several tens kilohertz range is influenced by blending. The change is appeared on the NMR spectra and the relaxation curves [11–13].

Figure 11.2 shows the  $^{13}\text{C}$  CPMAS NMR spectra of the PS, PVME, and PS/PVME = 5/5 blend at (a) 311 K and (b) 228 K, respectively [7]. The methine ( $\text{CH}$ ) and methoxy ( $\text{OCH}_3$ ) signals of PVME become broad after blending with PS. These linewidth changes indicate the reduction in the molecular motion owing to interacting with rigid PS. The gain of linewidth is due to the reduction in efficiency of  $^1\text{H}$  dipolar decoupling (DD). Namely, the molecular motion of pure PVME, that is much faster than the frequency of  $^1\text{H}$  DD, was decreased down to the comparable frequency level of  $^1\text{H}$  DD (about 55 kHz in this experiment) by blending with PS [11, 12]. This observation is related to the experimental temperature; the  $T_g$  of PS/PVME = 5/5 blend (about 259 K) is still much lower than the experimental

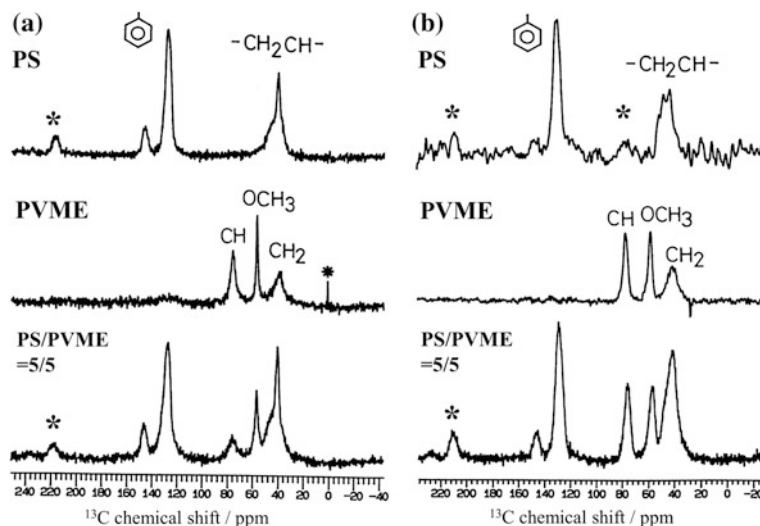
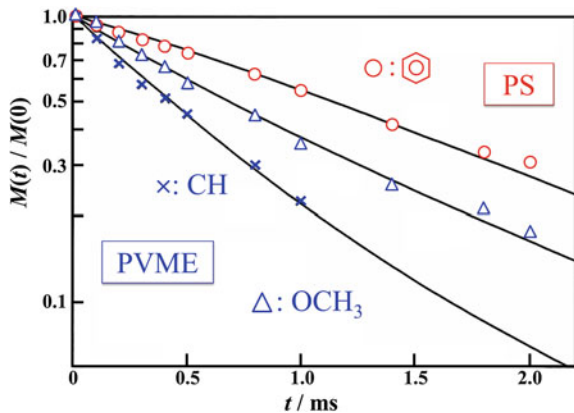


**Fig. 11.2** CPMAS  $^{13}\text{C}$  NMR spectra for pure PS, pure PVME, and the PS/PVME = 5/5 blend at **a** 311 K and **b** 228 K. An asterisk symbol in PVME of **a** comes from a silicon rubber seal. The other asterisks (\*) are the spinning side band. This figure is redrawn from the original source of Asano et al. [7]

temperature. Actually, such a line-broadening did not appear at 228 K because the molecular motion is frozen and the  $^1\text{H}$  DD works effectively. The motion around 50 kHz governs and influences the  $T_{1p}^{\text{H}}$  process severely; hence, the observed  $T_{1p}^{\text{H}}$  decays are modulated and show non-single-exponential even though the blends are homogeneous [4, 9].

Figure 11.3 shows  $T_{1p}^{\text{H}}$  decays obtained from each peak of PS and PVME in the PS/PVME = 5/5 blend [7]. The different and non-single-exponential  $T_{1p}^{\text{H}}$  decays for PVME are observed from the two signals, CH and  $\text{OCH}_3$  carbons. Usually, the  $T_{1p}^{\text{H}}$  decays in solid homopolymers are consistent with each other because of the fast  $^1\text{H}$  spin diffusion. However, the  $^1\text{H}$  spin diffusion even in pure PVME was so slow that the  $T_{1p}^{\text{H}}$  decays obtained from each signal were not averaged out. This phenomenon is due to the very fast molecular motion of PVME chains at 311 K. Therefore, the observed non-single-exponential  $T_{1p}^{\text{H}}$  decays in Fig. 11.3 are resulted in a three-spin system consisted of PS (A), side-chain (B), and main-chain (C) of PVME with insufficient  $^1\text{H}$  spin diffusion rates, not in phase separation: the decays in a case of phase separation are described in the next Sect. 11.2.2. To simulate the observed  $T_{1p}^{\text{H}}$  decays, the simultaneous differential Eqs. (11.1) are expanded to adapt the three-spin system as follows:

**Fig. 11.3**  $T_{1p}^H$  decays for the PS/PVME = 5/5 blend observed at 311 K. The open circles represent the decay of PS (red); the open triangles and crosses are  $\text{OCH}_3$  and CH of PVME (blue). The solid curves were the “best-fit” obtained from Eq. (11.4). This figure is redrawn from the original source of Asano et al. [7]



$$\begin{aligned}\frac{dM_A(t)}{dt} &= -(K_A + f_B k_{AB} + f_C k_{CA}) \cdot M_A(t) + f_A k_{AB} \cdot M_B(t) + f_A k_{CA} \cdot M_C(t) \\ \frac{dM_B(t)}{dt} &= -(K_B + f_A k_{AB} + f_C k_{BC}) \cdot M_B(t) + f_B k_{AB} \cdot M_A(t) + f_B k_{BC} \cdot M_C(t) \\ \frac{dM_C(t)}{dt} &= -(K_C + f_A k_{CA} + f_B k_{BC}) \cdot M_C(t) + f_C k_{CA} \cdot M_A(t) + f_C k_{BC} \cdot M_B(t)\end{aligned}\quad (11.4)$$

or

$$\frac{d}{dt} \begin{bmatrix} M_A(t) \\ M_B(t) \\ M_C(t) \end{bmatrix} = \begin{bmatrix} -\eta_A & f_A k_{AB} & f_A k_{CA} \\ f_B k_{AB} & -\eta_B & f_B k_{BC} \\ f_C k_{CA} & f_C k_{BC} & -\eta_C \end{bmatrix} \begin{bmatrix} M_A(t) \\ M_B(t) \\ M_C(t) \end{bmatrix} = \mathbf{AM}$$

where  $\eta_A$ ,  $\eta_B$ , and  $\eta_C$  are  $K_A + f_B k_{AB} + f_C k_{CA}$ ,  $K_B + f_A k_{AB} + f_C k_{BC}$ ,  $K_C + f_A k_{CA} + f_B k_{BC}$ , respectively. The solution of Eq. (11.4) is given by the numeric analysis; the magnetization  $M_i(t)$  is given by  $M_i(t) = \lambda_{Ai} \exp(\varepsilon_1 \cdot t) + \lambda_{A2} \exp(\varepsilon_2 \cdot t) + \lambda_{A3} \exp(\varepsilon_3 \cdot t)$ ,  $\lambda_{A1,2,3}$  and  $\varepsilon_{1,2,3}$  are eigenvectors and eigenvalues of matrix  $\mathbf{A}$  (11.4b) for  $M_A$ , respectively. The results of the numeric analysis with the initial condition of  $M_A(0): M_B(0): M_C(0) = f_A: f_B: f_C$  are drawn by the solid lines in Fig. 11.3. The solid lines are in excellent agreement with the observed  $T_{1p}^H$  decays. The estimated values are  $K_A = 0.40 \times 10^3 \text{ s}^{-1}$ ,  $K_B = 1.06 \times 10^3 \text{ s}^{-1}$ ,  $K_C = 1.85 \times 10^3 \text{ s}^{-1}$ ,  $k_{AB} = 1.0 \times 10^3 \text{ s}^{-1}$ ,  $k_{CA} = 1.1 \times 10^3 \text{ s}^{-1}$ , and  $k_{BC} = 100 \text{ s}^{-1}$ .

The value of  $k_{BC}$  is one-order smaller than those of  $k_{AB}$  and  $k_{CA}$ . This indicated that the interpolymer spin diffusion between PS and PVME is much faster and effective than the intrapolymer spin diffusion of PVME. Furthermore, the values of  $k_{AB}$  and  $k_{CA}$  are comparable to those of  $K_i$  values. This means that the interpolymer spin diffusion rate is not enough to average out the respective  $T_{1p}^H$  decays in the

PS/PVME blends as described above. It had been proved that the PS/PVME blends are homogeneous [8–10]. The disagreement of  $T_{1p}^H$  decays among PS and PVME was thus ascribed to the motional effects, namely motional heterogeneity. Actually, the  $T_{1p}^H$  decays observed at below 263 K showed the single-exponential decays with the same relaxation rate for both PS and PVME. This observation suggested that the  $^1\text{H}$  spin diffusion rate largely depends on the molecular motion. Therefore, it is noted to pay attention to the relationship between the experimental temperature and  $T_g$  of component polymers.

### 11.2.1.2 PMAA/PVAc Blends

The interpolymer hydrogen-bonding interaction between the COOH functional group of poly(methacrylic acid) (PMAA) and the CO functional group of poly(vinyl acetate) (PVAc) occurs in the blends [14, 16]. The exothermic interaction assists for the Gibbs free energy of mixing to be negative. The hydrogen-bonding interaction causes the lower-field shift and makes the feature of the NMR spectra at the interacted region complex and change. Figure 11.4 shows the observed solid-state  $^{13}\text{C}$  NMR spectra of PMAA/PVAc blends expanded at the COOH/CO region [14, 15]. At the left-hand side, decomposed spectra obtained from the least-square fit to the observed  $^{13}\text{C}$  NMR spectra by a sum of five Gaussian curves are summarized. The simulated spectra for blends obtained from the simple sum of each observed  $^{13}\text{C}$  NMR spectrum of pure PMAA and pure PVAc at the respective molar ratio are also displayed in the right-hand side.

The broad COOH line of pure PMAA is observed at 183 ppm, and the relatively narrow COO peak of PVAc is at 171 ppm. If there is no interpolymer interaction between the side chains of PMAA and PVAc, the observed NMR spectra should be reintroduced by the simple summation as shown in the right-hand side. However, the observed spectra of the PMAA/PVAc blends were obviously different from the simple summation. The observed spectra have a much more complicated envelope. The lineshape of the CO region in the blends was divided into apparently five peaks. Two peaks at around 187 and 179 ppm of those five peaks were clearly appeared, especially in the spectrum of the PMAA/PVAc = 1/1 blend. A peak at around 175 ppm was also clearly seen in the spectrum of the PMAA/PVAc = 3/1 blend, while the peak for the other blends was disappeared behind the broad envelope. These observations clearly suggested the existence of an interpolymer interaction. It was revealed that the peak at 179 ppm is associated with the PMAA-COOH carbon, which the carboxylic hydrogen interacts with PVAc-CO oxygen, and the interacted PVAc-CO carbon with PMAA-COOH is appeared at 175 ppm by the observations of composition dependent  $^{13}\text{C}$  spin-lattice relaxation time [14] and two-dimensional (2D) exchange  $^{13}\text{C}$  NMR [16]. The natural abundant 2D exchange  $^{13}\text{C}$  NMR spectrum showed the clear cross-peaks between  $\omega_1 = 175$  ppm and  $\omega_2 = 179$  ppm and between  $\omega_1 = 179$  ppm and  $\omega_2 = 175$  ppm

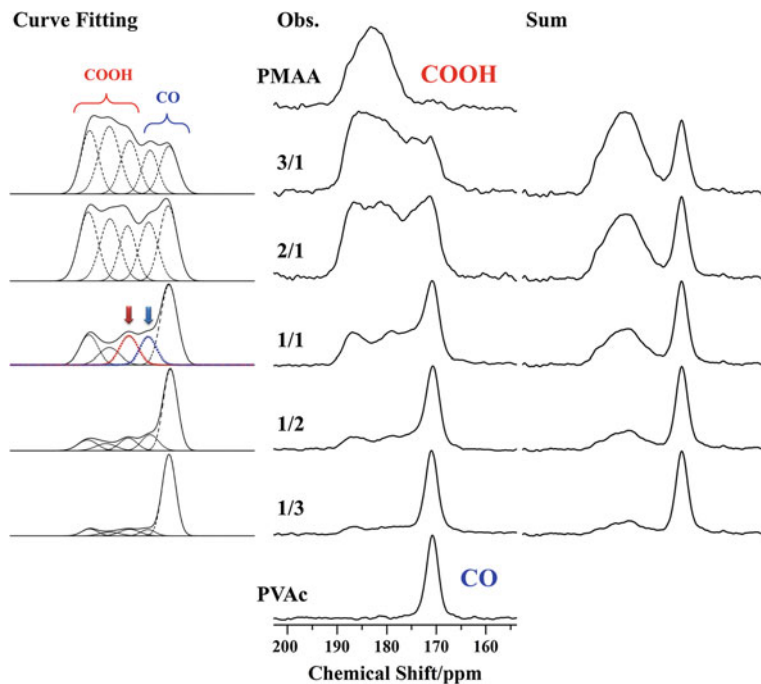


**Fig. 11.4** Observed CPMAS  $^{13}\text{C}$  NMR spectra (center) and the decomposed simulated spectra using five Gaussian curves (the left-hand side) of the expanded CO region in the PMAA/PVAc blends: a broken line depicts each decomposed peak and a solid line is the sum of those broken lines. The  $^{13}\text{C}$  NMR spectra obtained by the sum of those of pure PMAA and pure PVAc at the respective molar unit ratio are drawn on the right-hand side. This figure is redrawn from the original source of Asano et al. [14, 15]

with the same intensity. The distance between the interacted PMAA-COOH carbon and the PVAc-CO carbon was estimated to be 0.37 nm. The length of hydrogen bond was also estimated from the molecular mechanics calculation to be ca. 0.2 nm [16].

Figure 11.5 shows the observed  $T_1$  rates (a:  $1/T_1^{\text{H}}$  and b:  $1/T_{1\rho}^{\text{H}}$ ) of the PMAA/PVAc blends against the PMAA fraction: the fraction equals to the weight ratio of PMAA or unit  $^1\text{H}$  molar ratio because the unit weight and number of protons in a unit structure of PMAA is the same as those of PVAc [14]. This plot indicated that both original  $K$  values of pure PMAA and pure PVAc are averaged depending on the compositions in the blend. All the obtained  $K$  values of PMAA in the blends are in excellent agreement with those of PVAc. This result suggested that the complete averaging of the  $K$  values by the  $^1\text{H}$  spin diffusion occurs, and then, PMAA and PVAc are in close proximity with each other. Namely, the PMAA/PVAc blend is homogeneous on a scale of 20–50 nm for all compositions. Similarly, Fig. 11.5b shows that the observed  $T_{1\rho}^{\text{H}}$  rates of PMAA in the PMAA-rich/PVAc blends, which are the PMAA/PVAc = 3/1, 2/1 and 1/1 blends,

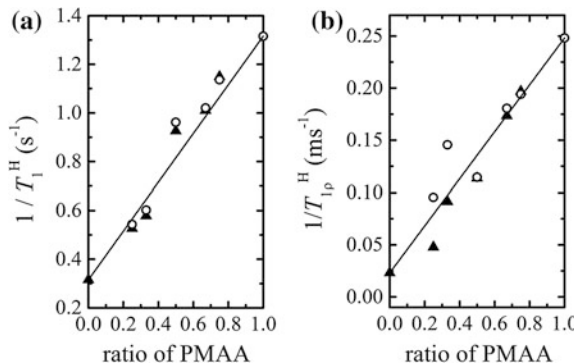


**Fig. 11.5** Observed  $1/T_1^H$  (a) and  $1/T_{1p}^H$  (b) values, namely the  $^1\text{H}$  relaxation rates  $K$ , against the  $^1\text{H}$  molar fraction  $f_{\text{PMAA}}$  of PMAA/PVAc blends: circle  $\text{CH}_2$  carbon of PMAA, triangle; OCH carbon of PVAc, and each solid straight line represents the calculated one from Eq. (11.3). Every error bar for each data point is covered with the symbols itself. In this case, PMAA weight ratio of the blends is equivalent to that of  $^1\text{H}$  molar fraction because both unit weight and number of protons in a unit structure of PMAA  $\text{[-(CH}_2\text{CCH}_3(\text{COOH})-]}$  are the same as those of PVAc  $\text{[-(CH}_2\text{CH(OOCCH}_3\text{)}-]}$ . This figure is newly drawn from the original source of Asano et al. [14, 15]

are fully consistent with those of PVAc. For the PMAA-poor (PMAA/PVAc-rich = 1/2 and 1/3) blends, both rates of PMAA and PVAc changed together and became close, although the  $T_{1p}^H$  rates of PMAA were different from those of PVAc. This plot indicated that the partially averaging of  $T_{1p}^H$  rates by the  $^1\text{H}$  spin diffusion occurs in the PMAA/PVAc-rich blends. These results showed that the PMAA-rich/PVAc blends are homogeneous on a scale of 2–5 nm as well as 20–50 nm, but the PMAA/PVAc-rich blends are inhomogeneous on the scale of 2–5 nm. The PMAA/PVAc-rich blends are probably homogeneous on a 5–10-nm scale because the  $T_{1p}^H$  rates are affected significantly by the  $^1\text{H}$  spin diffusion.

The solid straight lines in Fig. 11.5a and b were obtained using Eq. (11.3) with  $K$  values of pure PMAA and pure PVAc. The observed  $T_1^H$  rates were in good agreement with the calculated line. Similarly, the observed  $T_{1p}^H$  rates for PMAA-rich/PVAc blends are consistent with the calculated line. These agreements indicated that the molecular motions of both polymers in the blends are not changed drastically with each other comparing with those before mixing, and the very fast  $^1\text{H}$  spin diffusion occurs in the blends.

### 11.2.1.3 PK/PA Alloys

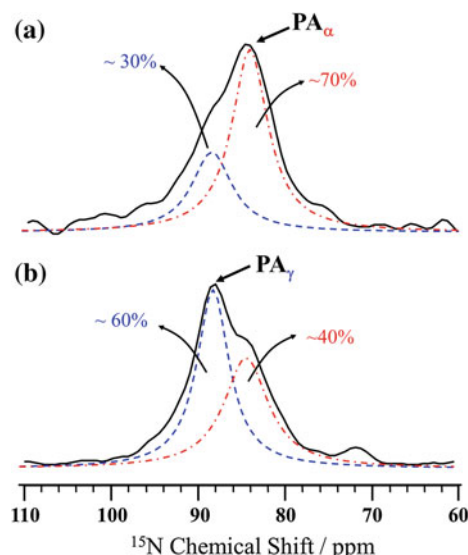
Polyketone/polyamide (PK/PA) alloys showed the superior impact resistance in the wet condition, particularly for the range of PK/PA = 1/9 to 7/3 [17]. The impact energy of  $25 \text{ kJ m}^{-2}$  under the dry condition became greater than  $160 \text{ kJ m}^{-2}$  under the over 1.5% humid condition. Interestingly, no improvement was seen for either

pure PA or pure PK. The three-dimensional (3D) morphology of the PK/PA alloys detected by the transmission electron microscope (TEM) analysis showed characteristic structure of lamellar-like structure with co-continuous spherical domains. It was clarified by the electron energy loss spectroscopy (EELS) measurement that the lamellar-like structure mainly originated in PK and the spherical domain came from PA [17–21]. Both 3D-TEM and EELS images also showed a characteristic spherical amorphous domain filled with lamellar structure. Furthermore, small angle X-ray scattering (SAXS) studies revealed that the long period of lamellae for PK-rich alloys is estimated to be ca. 14 nm but that for PA-rich alloys decreases from 14 to 9 nm gradually with the PA content [17, 19–21]. The long periods of both pure PK and pure PA were ca. 14 nm and ca. 8 nm, respectively. The lamellar network for the PA-rich alloys consisted of a mixture network of both PK and PA. Thus, the existence of both lamellae and co-continuous spherical amorphous region is strongly related to the improvement in the impact resistance.

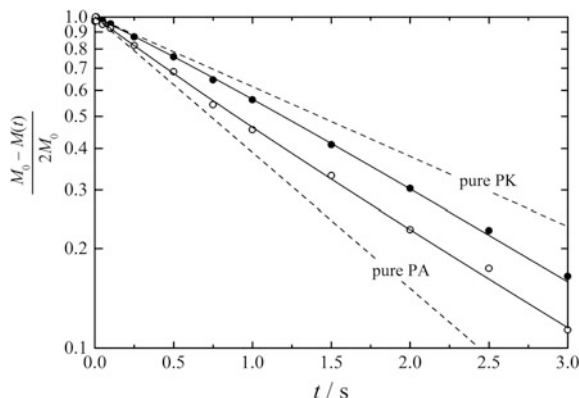
Because the solid-state NMR is sensitive to the conformational change in polymer chains, the NMR spectra give information of crystalline and amorphous phases with regardless of wet condition. Furthermore, the  $^1\text{H}$  spin diffusion analysis indirectly obtained from the  $T_1^{\text{H}}$  recovery curves gives information of the domain size of both polymers.

Figure 11.6 shows the  $^{15}\text{N}$  CPMAS NMR spectra of (a) the PK/PA = 6/4 alloy and (b) pure PA under the wet condition [17, 18]. The CP efficiency of the amorphous phase of PA was depressed because the amorphous phase was predominantly water absorbed. Thus, Fig. 11.6 is enhanced mainly the crystalline phase of PA. The geometry of the hydrogen bond is different between the between the  $\alpha$  and  $\gamma$  crystalline phases of PA. Such a difference influences the  $^{15}\text{N}$  chemical

**Fig. 11.6** Observed  $^{15}\text{N}$  CPMAS NMR spectra of **a** PK/PA = 6/4 alloy and **b** pure PA. This figure is redrawn from the original source of Asano et al. [17, 18]



**Fig. 11.7** Semilogarithmic plots of normalized  $T_1^H$  decay curves for PK (filled circle) and PA (empty circle) in the PK/PA = 6/4 alloy under the dry condition. Dashed straight lines represent  $T_1^H$  decay curves for pure PA and pure PK. The solid lines were obtained with Eq. (11.2). This figure is redrawn from the original source of Asano et al. [17]



shift values. The signal at 84 ppm is ascribed to the  $\alpha$  crystalline phase of PA and that at 89 ppm to the  $\gamma$  crystalline phase. Figure 11.6 clearly indicated that the PA in the PK/PA = 6/4 alloy changes remarkably from their  $\gamma$  crystalline phase to  $\alpha$  form. This observation suggested that PK induces the growth of the  $\alpha$  crystalline phase of PA in the blend rather than  $\gamma$  crystallites. The relative fraction of the  $\alpha$  crystalline phase of PA changed from 40 to 70% in the PK/PA = 6/4 alloy. The change in the crystalline form of PA is presumably related to the complicated morphology detected in the TEM image and to the high impact properties under the wet condition.

Figure 11.7 shows the  $T_1^H$  curves of both PK and PA observed in the PK/PA = 6/4 alloy under the dry condition [17]. The  $T_1^H$  curves of both pure PK and pure PA (dashed lines) show single-exponential decays with the  $T_1^H$  rates  $K_{PK}$  ( $= 1/T_1^H$ ) of  $0.485 \text{ s}^{-1}$  ( $T_1^H = 2.06 \pm 0.03 \text{ s}$ ) and  $K_{PA}$  of  $0.943 \text{ s}^{-1}$  ( $T_1^H = 1.06 \pm 0.01 \text{ s}$ ), respectively. For the PK/PA = 6/4 alloy, both  $T_1^H$  curves of PK and PA were in close together, indicating that the insufficient but moderately fast  $^1\text{H}$  spin diffusion occurs between PK and PA. The observed curves suggested that both PK and PA are not completely phase separated but are located in a region where both polymer protons diffuse each other to some extent. The solid lines show the least-squared fit curves using Eq. (11.2). Both PK and PA are the semicrystalline polymers, so there are four different phases in the alloy at least. However, the amorphous and crystalline phases in PK showed the identical  $T_1^H$  value and the same phenomenon was also detected for PA. This observation indicated that the fast  $^1\text{H}$  spin diffusion occurs between the crystalline and non-crystalline phases. This fact allowed us to analyze the observed  $T_1^H$  curves by the two-spin system using Eq. (11.2).

To obtain the information of domain size, the observed data points were fitted by Eq. (11.2) with  $f_{PA}$  of 0.548. The solid non-single-exponential lines were in good agreement with the observed  $T_1^H$  decay curves of both PK and PA in the PK/PA = 6/4 alloy. The  $K$  values obtained were  $0.53 \pm 0.02 \text{ s}^{-1}$  for PK and  $0.81 \pm 0.02 \text{ s}^{-1}$  for PA, respectively, and the  $^1\text{H}$  spin diffusion rate,  $k$ , of  $0.8 \pm 0.3 \text{ s}^{-1}$ .

This observation suggested that PA is dispersed and located in the PK matrix. The  $k$  value is comparable to the initial relaxation rate of both polymers, indicating that  $^1\text{H}$  spin diffusion is slow, but that the two polymers are not completely phase separated on a scale of several tens to several hundreds of nm. The estimated average domain size was approximately 150 nm, which is twice as large as the maximum diffusive path length with the assumption of the 3D diffusion model and the effective diffusion coefficient  $D_{\text{eff}}$  of ca.  $700 \text{ nm}^2\text{s}^{-1}$  estimated from both  $D_{\text{PK}} = 840 \text{ nm}^2\text{s}^{-1}$  and  $D_{\text{PA}} = 600 \text{ nm}^2\text{s}^{-1}$ : these  $D$  values were estimated from each  $^1\text{H}$  spin-spin relaxation rate of PK and PA [17, 22]. The value of 150 nm was comparable to the average overall size of the elliptical domains estimated from the 3D TEM images. Furthermore, the  $k$  value under the wet condition was consistent with that under the dry condition. Thus, the domain size under the wet condition did not change as compared to that under the dry condition.

The creation of the co-continuous spherical amorphous region and the existence of PK crystalline lamellae only in the PK/PA alloys were detected by 3D TEM images. The NMR studies revealed the conversion to the  $\alpha$  crystalline phase from the  $\gamma$  crystalline phase for PA in the PK/PA alloys and the selective occurrence of water absorption in the amorphous region of PA. Furthermore, SAXS analyses clarified that the long period of PK lamellae becomes wider by approximately 1 nm under the wet condition [17, 19–21]. These various morphological changes play an important role to exhibit high impact resistance and toughness in the PK/PA alloys under the wet condition. The combination of both rigidity of PK lamellae and elasticity of water-absorbing amorphous phase of PA is needed to obtain high impact properties, modulus, and toughness.

### 11.2.2 Phase Separation

Homogeneous single phase of a polymer blend for a lower critical solution temperature (LCST) phase diagram is thermodynamically unstable: the two types of the phase separation undergo and they are referred to the spinodal decomposition and the nucleation growth. The phase is easily collapsed when a blend is heat-treated above the LCST line, which is the binodal point. The homogeneous and transparent phase becomes heterogeneous and opaque in general. The concentration change during the spinodal decomposition at the initial stage is expressed by analyzing the  $^1\text{H}$  spin-lattice relaxation [4, 7, 15].

#### 11.2.2.1 PS/PVME Blends

The homogeneous phase of the PS/PVME blends is phase separated after heat treatment above 373–393 K (binodal point) because the PS/PVME blends exhibit the LCST phase diagram. Figure 11.8 shows the observed  $T_1^{\text{H}}$  decay curves of the PS/PVME = 5/5 blend, which is quickly cooled in liquid nitrogen to quench the

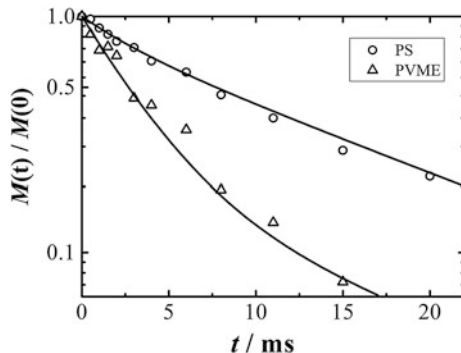


**Fig. 11.8** Observed  $T_{1p}^H$  decay curves for PS (circle) and PVME (triangle) in the phase-separated PS/PVME = 5/5 blend after 2 min of heating at 413 K. These decay curves were measured at 263 K. The solid lines are the “best-fit” curves from Eq. (11.5) with the parameters of  $\xi_x = 0.81 \pm 0.05$ ,  $\xi_y = 0.20 \pm 0.03$ ,  $T_{1x} = 15.3 \pm 0.6$  ms and  $T_{1y} = 3.1 \pm 0.2$  ms. This figure is redrawn from the original source of Asano et al. [4, 7]

phase separation progress after heating at 413 K for 2 min [7]. The  $T_{1p}^H$  decay curves were measured at 263 K to freeze the molecular motion of PVME and let the  $^1\text{H}$  spin diffusion work effectively. Before the heat treatment, both observed  $T_{1p}^H$  decays obtained from PS and PVME signals showed the same single-exponential curve. With increasing the heat treatment time, they deviated from the single exponential to show a double-exponential behavior.

A model based on a simple assumption for phase separation provides the double-exponential behavior [4, 7, 15]. The homogeneous polymer blend  $x/y$ , which  $x$  composition ratio is represented by  $\rho_x^0$ , is phase separated into the  $x$ -rich and the  $y$ -rich domains after the heat treatment. This model represents that the fast  $^1\text{H}$  spin diffusion occurs within each rich domain in the phase-separated blend; polymers  $x$  and  $y$  are homogeneously mixed in the respective  $x$ -rich and  $y$ -rich domains from the  $^1\text{H}$  spin diffusion point of view. There is no effective  $^1\text{H}$  spin diffusion between the  $x$ -rich and the  $y$ -rich domains because the sizes of both  $x$ -rich and  $y$ -rich domains become beyond 5 nm for  $T_{1p}^H$  or 50 nm for  $T_1^H$ . Each domain has an individual  $^1\text{H}$  spin-lattice relaxation time. In a word, the  $T_1$  value of polymer  $y$  in the  $x$ -rich domain has the same value as that of polymer  $x$ ,  $T_{1x}$ . Similarly, both polymers  $x$  and  $y$  in the  $y$ -rich domain have  $T_{1y}$ . According to this assumption, it is obvious that the relaxation curves observed from polymers  $x$  and  $y$  are expected to be the double-exponential decays as follows:

$$\begin{aligned} M_x(t) &= \xi_x \exp(-t/T_{1x}) + (1 - \xi_x) \exp(-t/T_{1y}) \\ M_y(t) &= \xi_y \exp(-t/T_{1x}) + (1 - \xi_y) \exp(-t/T_{1y}) \end{aligned} \quad (11.5)$$

where

$$\xi_x = \frac{\varphi_x \cdot r}{\rho_x^0}, \xi_y = \frac{(1 - \varphi_x) \cdot r}{1 - \rho_x^0}, \quad \text{and} \quad \rho_x^0 = \varphi_x \cdot r + \psi_x(1 - r).$$

Here,  $M_x(t)$  and  $M_y(t)$  represent the normalized magnetization. The parameters  $\xi_x$  and  $\xi_y$  are  $^1\text{H}$  molar fractions of polymers  $x$  and  $y$  in the  $x/y$  blend, respectively. The parameters  $\varphi_x$  and  $\psi_x$  are the concentration of polymer  $x$  in the  $x$ -rich and  $y$ -rich domains, respectively. The stoichiometric values  $\varphi_x$  and  $\psi_x$  of the two separated phases and the  $r$  value are easily deduced from the fractions  $\xi_x$  and  $\xi_y$ . The  $\varphi_x$  or  $\psi_x$  are any of  $^1\text{H}$  molar/weight/volume fractions, depending on the determination of the  $\rho_x^0$  value.

The solid lines in Fig. 11.8 were the “best-fit” curves obtained from Eq. (11.5). The adjusted values for  $\xi_X$  and  $\xi_Y$  were  $0.81 \pm 0.05$  and  $0.20 \pm 0.03$ , respectively, and  $T_{1X}$  and  $T_{1Y}$  were  $15.3 \pm 0.6$  ms and  $3.1 \pm 0.2$  ms. Here,  $X$  and  $Y$  represent PS and PVME, respectively. By using values of  $\xi_X$  and  $\xi_Y$ , the parameters of  $\varphi_X$ ,  $\psi_X$ , and  $r$  were calculated to be  $0.81 \pm 0.06$ ,  $0.20 \pm 0.03$ , and  $0.51 \pm 0.04$ , respectively.

The  $T_{1p}^H$  decays after heating at 413 K for 20 s, 40 s, 1 min, and 1.5 min were similarly examined. Thus, the gradual composition change for both PS-rich and PVME-rich phases and constancy of the fraction of the PS-rich domain  $r$  were found. For example, the values of  $\xi_X$ ,  $\xi_Y$ ,  $T_{1X}$ , and  $T_{1Y}$  at 1 min heat treatment were  $0.62 \pm 0.06$ ,  $0.40 \pm 0.05$ ,  $17.8 \pm 0.2$  ms, and  $6.7 \pm 0.2$  ms, respectively [7]. These values produced the  $\varphi_X$ ,  $\psi_X$ , and  $r$  to be  $0.62 \pm 0.05$ ,  $0.39 \pm 0.05$ , and  $0.51 \pm 0.05$ , respectively. The  $r$  value was not changed from 1 to 2 min heating. The PS composition in the PS-rich phase increased from 0.62 to 0.81, and that in the PVME-rich phase decreased from 0.39 to 0.20. This concentration analysis through  $T_{1p}^H$  curves during phase separation revealed that the spinodal decomposition undergoes for the PS/PVME blends with heat treatment at 413 K. The rate of the concentration change during the spinodal decomposition was verified by comparing to the results obtained from the other spectroscopy [23–25].

The appreciable change on the  $T_{1p}^H$  curves was not detected after further heating longer than 30 min. No change in  $T_{1p}^H$  curves indicated the end of the initial stage of the spinodal decomposition. After finishing of the initial stage, the morphological change occurs on a larger scale that is not reflected in  $T_1$ . The growth of domain size at the late stage of the phase separation of the PS/PVME blend had been revealed from the 2D exchange  $^{129}\text{Xe}$  NMR [26]. The 2D exchange  $^{129}\text{Xe}$  NMR showed that the cross-peaks, which are observed after heating 30 min, do not appear after 1200 min. The estimated average domain size was beyond 5000 nm at least.

### 11.2.2.2 P3HT/PCBM Blends

For rigid and immobile polymers, the CRAMPS spectrum with moderate MAS is also useful to detect high-resolution  $^1\text{H}$  NMR spectra. The domain size distribution for poly-3-hexylthiophene (P3HT) and phenyl-C<sub>61</sub>-butyric acid methyl ester (PCBM) blend, which is one of candidates for an organic photovoltaic device, was

analyzed via the direct  $^1\text{H}$  spin diffusion measurement and found that the size depends on spin-coating speed and thermal annealing significantly [27]. The observed  $^1\text{H}$  spin diffusion behavior was simulated by the linear combination of theoretical spin diffusion curves obtained from a rods-in-a-matrix or a lamellar model assumption with several domain sizes. The simulation gave the information of the domain size distribution: the as-cast P3HT/PCBM film has mainly less than 10 nm domains, but the size distribution shifts toward greater than 100 nm upon annealing at 413 K for 30 min [27].

The P3HT/PCBM blends showed the phase separation upon heat-treating at 423 K. Figure 11.9 shows the  $^1\text{H}$  CRAMPS NMR spectra of (a) P3HT/PCBM blend, (b) P3HT, and (c) PCBM [28]. Despite the existence of overlap of both  $^1\text{H}$  signals of P3HT and PCBM, the sinusoidal magnetization profile produced by the MREV8 preparation step gave the negative signal for PCBM and the positive signal for P3HT (dashed line in Fig. 11.9d). Figure 11.9e–h displays the  $^1\text{H}$  signal intensity change by the  $^1\text{H}$  spin diffusion during mixing time. The positive and negative magnetizations diffuse effectively each other when both polymers are miscible: the measured  $^1\text{H}$  spin diffusion curves are in consistent with each other. When the phase is heterogeneous, the identical  $^1\text{H}$  spin diffusion curves deviate and show characteristic curvature depending on the morphology. The  $^1\text{H}$  spin diffusion behaviors were satisfactorily explained by a two-phase model, which P3HT-rich

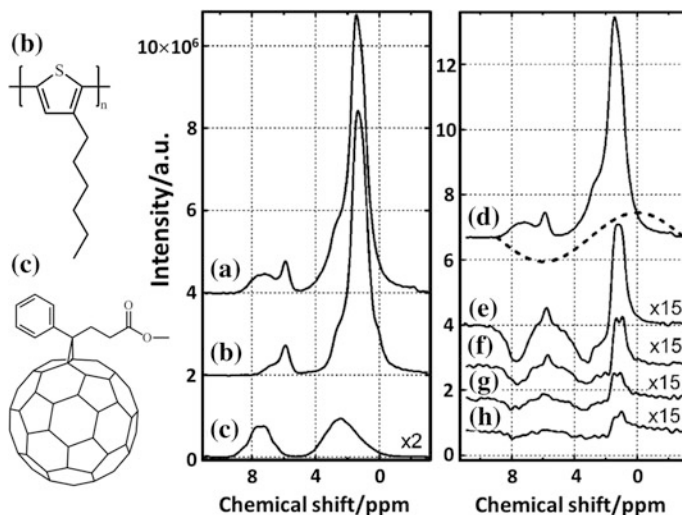


**Fig. 11.9** Stack plot of  $^1\text{H}$  CRAMPS NMR spectra: **a** P3HT/PCBM blend, **b** P3HT, and **c** PCBM: the chemical structures of **b** and **c** are depicted on the *left-hand side*. Spectrum **d** is the same as **a**, and the sinusoidal excitation profile (*dashed line*) by the MREV8 preparation is also depicted. Spectrum **e** was observed after mixing time of 2 ms subsequent the MREV8 preparation, **f** 60 ms, **g** 180 ms, and **h** 550 ms. The original source of this figure comes from Nieuwndaal et al. [28]

phase contains the grown up PCBM crystals (composition of 11% by mass in the phase) and PCBM-rich phase with 6% P3HT [28].

## 11.3 Polymer Nanocomposites

Organic polymer/inorganic clay nanocomposites have a potential to show a great improvement of gas barrier, mechanical or thermal properties, particularly in the exfoliate and the intercalated states [1]. Paramagnetic  $\text{Fe}^{3+}$ -ions which are naturally contained in montmorillonite (mmt) clay influenced on the  $T_1^{\text{H}}$  curves of a polymer in a polymer/mmt nanocomposite, and the analysis of the  $T_1^{\text{H}}$  curves gives morphological information [29, 30]. The interaction between inorganic fillers and polymers can be detected and analyzed by NMR techniques. In this section, the paramagnetic effect on  $T_1^{\text{H}}$  phenomenon is shown in the first. Next the investigation of the interaction between inorganic fillers and polymers is described. Finally, the morphological study for polymer nanocomposites is presented.

### 11.3.1 Paramagnetic Effect on Relaxation

#### 11.3.1.1 PVA/Montmorillonite Clay Nanocomposites

Figure 11.10 shows the  $T_1^{\text{H}}$  values obtained from the poly(vinyl alcohol) (PVA)/mmt nanocomposites [31]. The  $T_1^{\text{H}}$  recovery curves showed single-exponential function. Because PVA is severely moisture absorbed and the  $T_1^{\text{H}}$  is significantly sensitive to humidity, the nanocomposites and pure PVA was dried under vacuum at 353 K for 3 days after preparation and for 1 day in a sample rotor before measuring  $T_1^{\text{H}}$  to eliminate the effect of humidity: the  $T_1^{\text{H}}$  value under the humid condition becomes very short as compared to that under the dry condition. The original  $T_1^{\text{H}}$  value of PVA, which is represented by a cross, decreased steeply with the amount of mmt. The original  $T_1^{\text{H}}$  value of  $15.5 \pm 0.2$  s for PVA became half at only 2 wt% ( $7.9 \pm 0.3$  s) in the PVA/mmt nanocomposites. At beyond 6 wt%, the value became less than 2 s and saturated till 10 wt%. This phenomenon indicated that the mmt clay is well dispersed and exfoliated in the PVA matrix up to 10 wt%. The  $T_1^{\text{H}}$  value of the PVA neighboring  $\text{Fe}^{3+}$  ions becomes extremely short due to the paramagnetic effect. The effect of  $\text{Fe}^{3+}$  ions on  $T_1^{\text{H}}$  of PVA is, however, limited on a very short range. The very short  $T_1^{\text{H}}$  relaxation averages out the original  $T_1^{\text{H}}$  values of the bulk PVA by the fast  ${}^1\text{H}$  spin diffusion occurring among PVA protons. Therefore, the well dispersion is important to show the single-exponential decay and the extremely depression of  $T_1^{\text{H}}$  with the increment of mmt. At the excess amount than 10 wt% of mmt, such as 20 or 30 wt%, the  $T_1^{\text{H}}$  curves showed a non-single exponential, suggesting the poor dispersion of mmt in the PVA matrix.

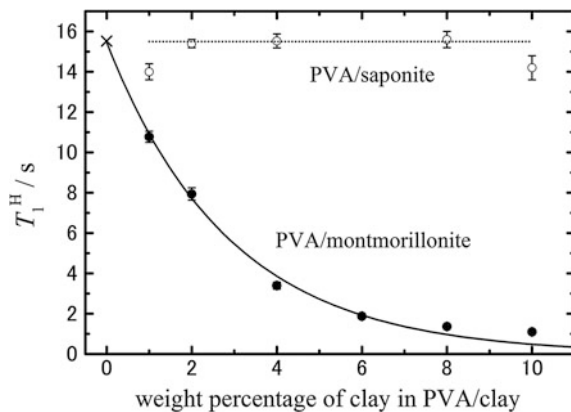


**Fig. 11.10** Observed  $T_1^H$  values of the PVA/mmt and PVA/saponite nanocomposites against the weight percentage of clay: pure PVA is represented by cross, PVA/mmt is solid circles and PVA/saponite open circles. The solid line is the “best-fit” curve to the observed data points using the simple-exponential decay function. The dotted-line is drawn to guide the reader’s eyes and represents the  $T_1^H$  value of 15.5 s. This figure is redrawn from the original source of Asano et al. [31]

In contrast, the  $T_1^H$  values of PVA in the PVA/saponite clay nanocomposites were not affected by the coexistence of the saponite clay. The saponite is artificial clay without any paramagnetic sources. This simple experiment suggested again that the effect of paramagnetic source on  $T_1^H$  is quite remarkable.

### 11.3.1.2 Nylon-6/mmt Nanocomposites

The influence of  $\text{Fe}^{3+}$  in the mmt clay layers on spins of a polymer is within about 0.4 nm of the clay surface [32]. The paramagnetic contribution to  $T_1^H$  can estimate from the approximate “sum-of-rates” equation as follows [29, 33]:

$$\frac{1}{T_1^{\text{para}}} = \frac{1}{T_1^H(\text{nanocomposite})} - \frac{1}{T_1^H(\text{polymer})} \quad (11.6)$$

where  $T_1^{\text{para}}$  is the paramagnetic contribution.

For nylon-6 (N6)/mmt nanocomposites, it was revealed that the  $T_1^{\text{para}}$  value changes by depending on the degree of mmt dispersion and exfoliation. The contribution ( $T_1^{\text{para}}$ ) hardly changes with magnetic field strength: the  $T_1^H$  of N6 depends on the magnetic field of course, 1.63 s for 7.05 T and 0.52 s for 2.35 T. The  $1/T_1^{\text{para}}$  rate for good dispersed mmt in the N6/mmt nanocomposite was  $1.05 \text{ s}^{-1}$  (7.05 T) to  $1.11 \text{ s}^{-1}$  (2.35 T) and  $0.45\text{--}0.46 \text{ s}^{-1}$  for a bad mmt dispersed N6/mmt nanocomposite [29, 33]. The difference of clay dispersion also related to the quality of the physical properties of a nanocomposite. For example, the tensile yield strength of

64 MPa for N6 became 85 MPa for the good dispersed and 69 MPa for the bad dispersed N6/mmt nanocomposites.

### 11.3.2 Interaction Between Polymers and Fillers

#### 11.3.2.1 Nylon-6/Montmorillonite Clay Nanocomposites

Figure 11.11 shows the  $^1\text{H}$  MAS NMR spectra of N6 and N6/mmt nanocomposites [29, 33, 34]. Due to the strong  $^1\text{H}$  homonuclear dipole interaction, the  $^1\text{H}$  MAS NMR spectrum of N6 shows very broad and featureless peak as shown in Fig. 11.11a. For N6/mmt nanocomposites, particularly the spectrum of Fig. 11.11c, there is a clear extremely narrow line sited on top of the broad  $^1\text{H}$  signal of N6; for spectrum in Fig. 11.11b, the narrow line is very small and less visible. Because a mmt contains paramagnetic  $\text{Fe}^{3+}$ -ions inside layers as described above, the NMR signals of the organic modifiers (OM) located on the clay surface, which is treated

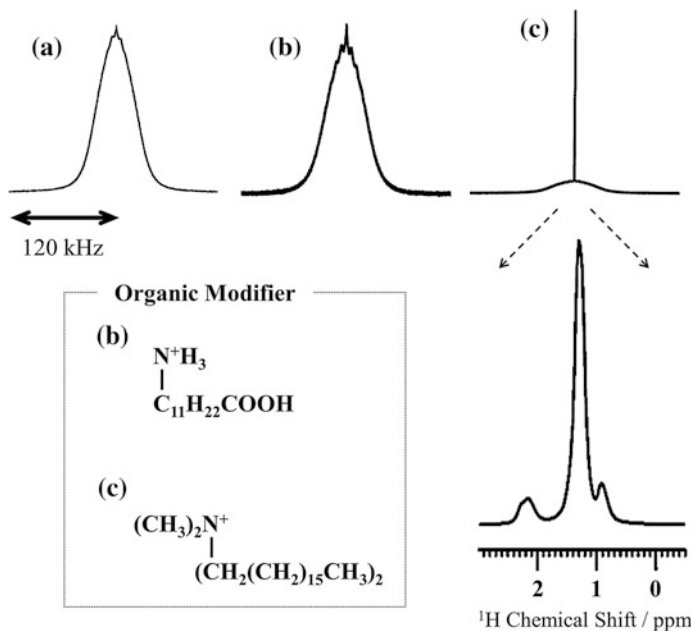


**Fig. 11.11**  $^1\text{H}$  MAS NMR signals of N6/mmt nanocomposites at MAS = 5 kHz: **a** N6, **b** in situ polymerized N6/mmt from a  $\epsilon$ -caprolactam solution in the presence of treated mmt, and **c** mechanical blending N6/mmt. Expanded narrow lines that sit on top of the broad N6  $^1\text{H}$  signal **c** are enlarged under the spectrum. The organic modifiers treated on mmt for **b** and **c** are also illustrated on the left-hand lower side. This figure is newly drawn using the original data of VanderHart et al. [29, 33, 34]

for clay layers to be exfoliated in and to interact with polymer chains in a nanocomposite, are significantly broaden and hard to be detected. Thus, the visible but very tiny peak sited on top of the N6  $^1\text{H}$  signal shown in Fig. 11.11b was not surprising feature; Fig. 11.11b indicated that the OM (b) is still located on the surface of clay layers.

On the other hand, the strong narrow peak measured in Fig. 11.11c suggested that the OM (c) is apart from the clay surface at least 2 nm: the paramagnetic effect is negligible beyond the distance [32]. The dissimilarity between Fig. 11.11b and c was related to processing condition. For an in situ polymerization from  $\epsilon$ -caprolactam, the sharp peak was invisible (Fig. 11.11b), but for mechanical mixing the sharp peak was visible (Fig. 11.11c). This observation indicated that the role of OM is different for the way of making nanocomposites even though both OM is mixed for clays to be compatible with polymer chains. The mmt layers in the N6/mmt nanocomposite shown in Fig. 11.11c were well dispersed, and the  $1/T_1^{\text{para}}$  rate was  $1.05 \text{ s}^{-1}$  at  $7.05 \text{ T}$ .

The chemical shifts for the sharp peaks were 0.9, 1.3, and 2.2 ppm, and they were associated with methyl, methylene, and protons on carbons attached to amine nitrogen, respectively. By comparing the relative signal intensities, the peak area integral of 2.2 ppm was 10% and the sum of other peaks 90%. This peak intensity ratio revealed that the OM (c) was degraded by removing  $\text{CH}_3$  functional group and changed to  $\text{CH}_3\text{N}(\text{CH}_2(\text{CH}_2)_{15}\text{CH}_3)_2$  [29, 33]. Therefore, the remained  $\text{CH}_3^+$ -cation on the mmt clay layers became a contact point between the anionic environment of clay surface and N6 as  $\text{CH}_3\text{N}^+\text{H}_2-(\text{CH}_2)_5\text{CO}-(\text{NH}-(\text{CH}_2)_5-\text{CO})_n-$ . The removal of a small cation from the OM (c) acts a very important role for clay layers to exfoliate in hydrophobic polymer chains and then the decomposed OM (c) dispersed in the N6 matrix.

For the in situ polymerized N6/mmt, in contrast, the role of the OM (b) with carboxyl group (COOH) was quite different from that of mechanical mixed N6/mmt. The ring-open polymerization of  $\epsilon$ -caprolactam starts with the reaction between the COOH group of the OM (b) and the amine group of  $\epsilon$ -caprolactam. The N6 chains were created on clay surface and aligned with the direction of clay layer, resulting in parallel orientation. This suggested the large amounts of the  $\gamma$  crystalline phase of N6 and the no dispersion of the OM (b) in the in situ polymerized N6/mmt nanocomposites.

### 11.3.2.2 PS-PEO Block Copolymer/Hectorite Clay Nanocomposites

The simplest idea for proving the existence of the interaction between inorganic fillers and polymers in the nanocomposites is to observe the hetero- or homonuclear correlation between their spins. Figure 11.12 shows the  $^{29}\text{Si}-^1\text{H}$  HETCOR spectra for PS-poly(ethylene oxide) (PEO) block copolymer and hectorite clay (HCT) nanocomposites: (a) PS30EO-HCT and (b) PS4EO-HCT [35]. The strong cross-peak appeared on the PEO  $^1\text{H}$  resonance position. This observation clearly indicated that the PEO chains are in the vicinity of HCT layers for PS4EO-HCT

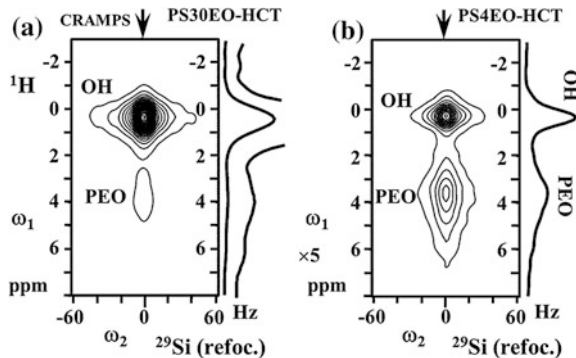


**Fig. 11.12**  $^{29}\text{Si}$ - $^1\text{H}$  HETCOR spectra for **a** PS30EO-HCT and **b** PS4EO-HCT with MAS = 5 kHz and frequency-switched Lee-Goldburg (FSLG)  $^1\text{H}$  decoupling: the numbers 30 and 4 indicate the number-average molecular weight ( $M_n$ ) of PS, corresponding to  $M_n$  = 30,000 and 4000, respectively. The arrows represent the center of the Si signal. The OH signal of  $\omega_1$  dimension comes from the clay surface. The source of this figure is Hou et al. [35]

nanocomposite. On the other hand, the absence of the cross-peak for PS30EO-HCT nanocomposite showed that the PEO chains are far from the HCT layers. These two observations suggested that PEO blocks of PS4EO do intercalate significantly into the silicate galleries, while the HCT clays are mostly aggregated in the PS30EO-HCT nanocomposite. This different result detected in the PS30EO nanocomposite was ascribed to the small fraction of PEO segments: a hydrophilic group of PEO was a key component to intercalate into the clay layers [35].

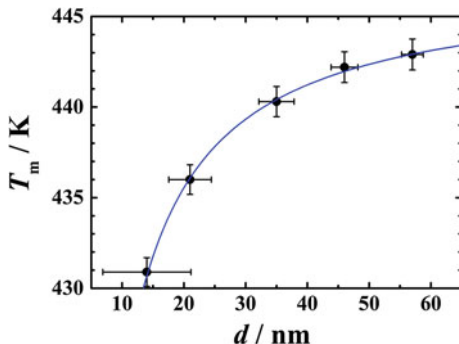
### 11.3.3 Morphology

#### 11.3.3.1 PVIBE/ε-PL/Saponite Clay Blends

The melting point ( $T_m$ ) of crystalline phase depends on the lamellar thickness as referred to the Gibbs–Thomson effect [36]. The  $T_m$  values of poly( $\epsilon$ -L-lysine) ( $\epsilon$ -PL) for poly(vinyl isobutyl ether) (PVIBE)/ $\epsilon$ -PL blends decreased with increase in the amounts of PVIBE, while the  $T_m$  values of PVIBE were not affected by the amounts of  $\epsilon$ -PL [37]. The decrease in  $T_m$  value was attributed to the decrease in crystal domain size of  $\epsilon$ -PL, which size was estimated from the  $T_1^{\text{H}}$  analysis.

Semicrystalline polymers PVIBE and  $\epsilon$ -PL have small crystal (CR) domain less than ca. 50 nm, so that the  $T_1^{\text{H}}$  of CR is consistent with that of non-crystalline phase (NC): the fast  $^1\text{H}$  spin diffusion occurs between CR and NC phases [37, 38]. The blends of PVIBE and  $\epsilon$ -PL were inhomogeneous, but the  $T_1^{\text{H}}$  curves could be reproduced by Eq. (11.2), suggesting that the moderate  $^1\text{H}$  spin diffusion occurs between PVIBE and  $\epsilon$ -PL. For the PVIBE/ $\epsilon$ -PL = 10/1 and PVIBE/ $\epsilon$ -PL/saponite

**Fig. 11.13** Relationship between the melting temperature,  $T_m$ , and the CR thickness of  $\epsilon$ -PL,  $d$ , for the PVIBE/ $\epsilon$ -PL blends. The solid line represents the Gibbs–Thomson relation expressed by  $446.8 \text{ (K)} - 220 \text{ (K nm)} / d \text{ (nm)}$ . The source of this figure is Asano et al. [37]



clay = 10/1/0.03 blends, however, the  $T_1^H$  curves of CR and NC for  $\epsilon$ -PL were not agree with each other. Therefore, the  $T_1^H$  curves for those blends were fitted by the three-spin system of Eq. (11.4). The  $T_1^H$  analyses gave the repeat length of both PVIBE and  $\epsilon$ -PL domains. The domain size of  $\epsilon$ -PL was estimated from the repeat length using the proton fraction in the blends. The CR size was finally calculated by using the crystallinity that was estimated from the  $^{13}\text{C}$  CPMAS NMR spectra editing using  $T_{1p}^H$  difference between CR and NC. The determined CR size of  $\epsilon$ -PL showed the PVIBE content dependence for the PVIBE/ $\epsilon$ -PL blends. The dependency is plotted in Fig. 11.13 and was fitted by the Gibbs–Thomson effect successfully on the assumption that the obtained CR size is comparable to the lamellar thickness [37].

For the PVIBE/ $\epsilon$ -PL/saponite clay = 10/3/0.09–10/5/0.15 blends, the CR size of  $\epsilon$ -PL was constant of ca. 33 nm. The value was in good agreement with that of the PVIBE/ $\epsilon$ -PL = 10/3 blend (35 nm). Furthermore, the  $T_m$  values for those of PVIBE/ $\epsilon$ -PL/saponite clay = 10/3/0.09–10/5/0.15 blends were constant of 439 K and the value was also consistent with that of the PVIBE/ $\epsilon$ -PL = 10/3 blend (440 K) within an experimental uncertainty. These results showed that clays influence the growth of CR. The constancy of  $T_m$  and CR size proved that the decrease in  $T_m$  is caused by the CR size [38].

### 11.3.3.2 Nylon-6/Montmorillonite Clay Nanocomposites

Thermal stability of the  $\alpha$  crystallite of N6 is better than that of  $\gamma$  crystallite. The N6 chain near the surface of the clay layers aligns parallel orientation; thus, the N6 chains create the  $\gamma$  crystalline phase in the N6/clay nanocomposites with the very slow cooling after the melting state of crystallites. With fast or natural cooling, both  $\alpha$  and  $\gamma$  crystallites exist in the N6/clay nanocomposites. The N6 located between the exfoliated mmt clay layers and the  $\gamma$  crystalline phase is placing closer to the clay surfaces, indicating that the  $T_1^H$  of the  $\gamma$  crystalline phase becomes shorter because of the paramagnetic effects. So, only if the  $\alpha$  crystalline phase were mostly well isolated from mmt clay surfaces would the  $T_1^H$  of these latter crystallites be notably longer than the average [29].

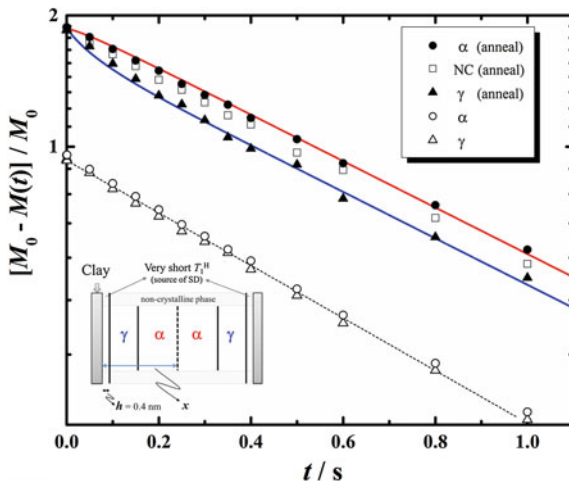


**Fig. 11.14** Observed  $T_1^H$  behaviors for the N6/mmt nanocomposites: open triangle and circle symbols are without annealing and those solid symbols with annealing at 487 K for 18 h. Open squares are the  $T_1^H$  behaviors observed from the non-crystalline phase (NC) of the annealed sample. The solid curves are obtained from the simplified spin diffusion (SD) computational model with two parameters of the clay layers' spacing ( $2x$ ) and the very short  $T_1^H$  value affected by the paramagnetic  $\text{Fe}^{3+}$ : N6 chains neighboring clay surface have such a short  $T_1^H$  and the range ( $h$ ) is assumed to be ca. 0.4 nm. This figure is newly drawn using the original data of VanderHart et al. [29]

Figure 11.14 shows the  $T_1^H$  curves observed from the N6/mmt nanocomposites with and without annealing [29]. The  $T_1^H$  behaviors of  $\alpha$  and  $\gamma$  crystalline phases without annealing are in excellent agreement with each other, even though the observed nanocomposites have substantial amounts of both crystallites. This observation indicated that the average distance from the clay surfaces is the same for both crystallites, indicating that not only  $\gamma$  crystallites located closer to the clay surfaces but also  $\alpha$  crystallite was in the close proximity. In contrast, the  $T_1^H$  behavior of  $\gamma$  crystalline phase with annealing was different from those of  $\alpha$  crystalline and non-crystalline phases (NC). The amounts of  $\alpha$  crystallites increased by ca. 30% after annealing. The initial slope of the  $\gamma$  crystalline phase was steeper than those of  $\alpha$  crystalline and NC phases; the protons in the  $\gamma$  crystalline phase are more rapidly decaying and influenced by the paramagnetic  $\text{Fe}^{3+}$  relative to the protons of the  $\alpha$  crystalline phase. This behavior strongly suggested that the  $\gamma$  crystalline phase is closer proximity to the clay surfaces than the  $\alpha$  crystalline phase.

To explain the observed  $T_1^H$  behaviors for both  $\alpha$  and  $\gamma$  crystalline phases, the simplified spin diffusion model was proposed: the inset shows the schematic illustration [29, 30]. Basics of this model are as follows: (1) the protons of N6 decay initially with the original  $T_1^H$ , (2) the very short  $T_1^H$  directly affected by the paramagnetic  $\text{Fe}^{3+}$  for the  $\gamma$  crystalline phase, which is directly contacting with the clay existed in the range of 0.4 nm, influences on the neighboring protons in the  $\gamma$

crystalline phase, and finally (3)  $^1\text{H}$  spin diffusion (SD) from the  $\gamma$  crystalline phase to the  $\alpha$  crystalline phase produces the relatively longer initial slope. The utilized parameters were the very short  $T_1^{\text{H}}$  value and the clay–clay spacing; the SD constant and the  $\gamma$  crystallite fraction are  $0.7 \text{ nm}^2\text{ms}^{-1}$  and 0.25, respectively. The simulated curves were in excellent agreement with observed data points. The estimated clay–clay spacing ( $2x$ ) of ca. 46 nm was comparable to that estimated from the TEM image [29, 32].

## 11.4 Rubbers and Elastomers

Rubbers and elastomers are one of indispensable materials for agricultural, medical, electrical appliances, and various engineering fields. The rubbery property of them, such as damping or sealing properties, is closely related to their molecular motion. For example, the relationship between rigidity and elasticity would be interpreted by the storage and loss moduli; the wet gripping performance or the rolling resistance for a tire is concerned with these parameters. Furthermore, the degradation of rubbers causes the significant change in molecular motion: the reduction in molecular motion occurs and rubbers become rigid and fragile. Thus, understanding of the molecular motion is very important to investigate the intrinsic rubbers character. To detect the change in the molecular motion,  $^1\text{H}$  spin-spin relaxation process of overall magnetizations detected by a low-resolution and low-field NMR is useful [39]. Here, the reduction in molecular motion caused by the thermal degradation is addressed briefly by describing an aging investigation for seal ability of rubbers [40].

Figure 11.15 shows (a) the relationship between the compression set and the acetone soluble fraction for acrylonitrile butadiene rubbers (NBR), which were used as sealing materials and (b) the correlation between the  $^1\text{H}$  spin-spin relaxation time ( $T_2^{\text{H}}$ ) and the compression set: the compression set (CS) is determined from the remaining permanent deformation after compression [40]. Larger CS value indicates that a sample is incurred severe damage much more and becomes rigid and non-flexible: the sample having the CS value of 80% is regarded to be degraded and out of the limitation for use. In particular, the elasticity and flexibility are essential for sealing materials. The used samples were kept at 333, 353, and 473 K up to 12,800 h in air to make reach higher CS value. The used two NBRs had different shapes and different acrylonitrile contents.

The symbols less than 10% of acetone soluble fraction and beyond 90% CS represent the aging period of 12,800 h at 80 and 100 °C. On the other hand, at 60 °C aging (open and solid circles), NBRs did not reach such a high CS and lower acetone soluble fraction region. Similar results were also observed for the correlation between the toluene swelling ratio and the CS. The acetone soluble fraction or the toluene swelling ratio relates to the amount of included plasticizer or of cross-link density, respectively. The less value of the acetone soluble fraction shows decrease in plasticizer by volatilization or bleed-out accompanied with

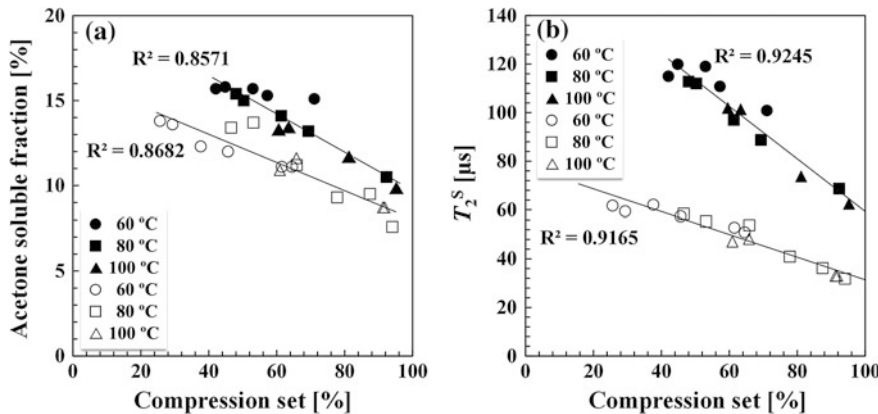


**Fig. 11.15** Relationship between the acetone soluble fraction and the compression set (a) and between the short  $T_2^H$  component ( $T_2^S$ ) and the compression set (b). Open symbols represent plate shape and 37% acrylonitrile content NBR, and solid symbols are O-ring and 46% acrylonitrile content NBR. The aging was executed under the air condition and up to 12,800 h at a constant temperature. Temperature was kept within  $\pm 1$  K for every aging period. The source of this figure is Numata et al. and arranged by AA [39, 40]

degradation. Similarly, the less value of the toluene swelling ratio indicates the increase in the cross-link density occurring during degradation. Thus, the good correlation between the acetone soluble fraction and the CS as shown in Fig. 11.15a indicates that the molecular interaction strengthened by the decrease in plasticizer concentration with aging reduces the molecular mobility.

The reduction in molecular motion causes the shortening of  $T_2^H$ . The observed  $T_2^H$  decays were fitted by the conventional double-exponential function, and the analysis gave the short  $T_2^H$  ( $T_2^S$ ) and long  $T_2^H$  ( $T_2^L$ ) values, and their fractions. Among the parameters,  $T_2^S$  values reflected the reduction in molecular motion caused by the high cohesion much better [40]. Figure 11.15b shows the good proportionality between the reduction in  $T_2^S$  values and the increase in CS for both NBRs. This observation strongly supported that the reduction in  $T_2^S$  represents the decrease in sealability of rubber materials in the thermal degradation process. The degradation by compression with long term, called as aging, causes the rigidness and brittleness of rubbers with changes in chemical structure and polymer segmental motion. It is very important to know aging process and its degree to ensure the lifetime of rubber products.

## 11.5 Conclusion

In this chapter, I described the characterization of polymer blends/alloys and nanocomposites via the high-resolution solid-state  $^{13}\text{C}$  NMR technique and of rubbers via the low-resolution  $^1\text{H}$  NMR method. To know morphology and/or

interaction between components is significant to understand the physical and chemical properties. Information of molecular motion would directly connect to the physical properties, such as flexibility, rigidity, entanglement of polymer chains, resistance for impact or friction. The analyses of NMR relaxation behaviors via the spin diffusion process or utilization of paramagnetic effect provided specific characterization on a molecular level such as domain size of crystalline phase or components, phase separation process, change in molecular motion of polymer chain, and the degree of dispersion of fillers. The correlation NMR spectroscopy directly proved the evidence of interaction between clay surfaces and polymer chains. Consequently, advanced solid-state NMR technique would certainly be useful and helpful for characterization of synthetic or natural polymers, amorphous or semicrystalline polymers, ordered and oriented polymers, and various polymer nanocomposites with organic or inorganic fillers.

## References

1. Pinnavaia, T.J., Beall, G.W. (eds.): *Polymer-Clay Nanocomposites*. Wiley, Chichester (2000)
2. Asano, A., Hori, S., Kitamura, M., Nakazawa, C.T., Kurotsu, T.: Influence of magic angle spinning on  $T_1^H$  of SBR studied by solid-state  $^1H$  NMR. *J. Polym. J.* **44**, 706–712 (2012)
3. bin Samusuri, A.: Degradation of Natural rubber and synthetic elastomers. In: Richardson, T. (ed.) *Shreir's Corrosion*, vol. 3, pp. 2407–2438. Elsevier, Durham (2010)
4. Asano, A., Takegoshi, K.: Polymer blends and miscibility. In: Ando, I., Asakura, T. (eds.) *Solid State NMR of Polymers*, pp. 351–414. Elsevier, Amsterdam (1998)
5. Solomon, I.: Relaxation process in a system of two spins. *Phys. Rev.* **99**, 559–565 (1955)
6. Stejskal, E.O., Schaefer, J., Sefcik, M.D., Mckay, R.A.: Magic-angle carbon-13 nuclear magnetic resonance study of the compatibility of solid polymeric blends. *Macromolecules* **14**, 275–279 (1981)
7. Asano, A., Takegoshi, K., Hikichi, K.:  $^{13}C$  c.p./m.a.s. n.m.r. study on the miscibility and phase separation of a polystyrene/poly(vinyl methyl ether) blend. *Polymer* **35**, 5630–5636 (1994)
8. Bank, M., Leffingwell, J., Thies, C.: The influence of solvent upon the compatibility of polystyrene and poly(vinyl methyl ether). *Macromolecules* **4**, 43–46 (1971)
9. Kwei, T.K., Nishi, T., Roberts, R.F.: A study of compatible polymer mixtures. *Macromolecules* **7**, 667–674 (1974)
10. Nishi, T., Kwei, T.K.: Cloud point curves for poly(vinyl methyl ether) and monodisperse polystyrene mixtures. *Polymer* **16**, 285–290 (1975)
11. Takegoshi, K., Hikichi, K.: Effects of blending on local chain dynamics and glass transition: polystyrene/poly(vinyl methyl ether) blends as studied by high-resolution solid-state  $^{13}C$  nuclear magnetic resonance spectroscopy. *J. Chem. Phys.* **94**, 3200–3206 (1991)
12. Menestrel, C.L., Kenwright, A.M., Sergot, P., Lauprêtre, F., Monnerie, L.: Carbon-13 NMR investigation of local dynamics in compatible polymer blends. *Macromolecules* **25**, 3020–3026 (1992)
13. Asano, A., Takegoshi, K.: Free volume study of amorphous polymers detected by solid state  $^{13}C$  NMR linewidth experiments. *J. Chem. Phys.* **115**, 8665–8669 (2001)
14. Asano, A., Eguchi, M., Shimizu, M., Kurotsu, T.: Miscibility and molecular motion of PMAA/PVAc blends investigated by high-resolution solid state CPMAS  $^{13}C$  NMR. *Macromolecules* **35**, 8819–8824 (2002)

15. Asano, A.: Polymer blends. In: Webb, G.W. (ed.) *Modern Magnetic Resonance*, pp. 627–631. Springer, Dordrecht (2006)
16. Asano, A.: Hydrogen-bond interaction of PMAA/PVAc blends: a natural abundant two-dimensional  $^{13}\text{C}$  exchange NMR investigation. *Polym. J.* **36**, 23–27 (2004)
17. Asano, A., Nishioka, M., Takahashi, Y., Kato, A., Hikasa, S., Iwabuki, H., Nagata, K., Sato, H., Hasegawa, T., Sawabe, H., Arao, M., Suda, T., Isoda, A., Mukai, M., Ishikawa, D., Izumi, T.: High impact properties of polyketone/polyamide-6 alloys induced by characteristic morphology and water absorption. *Macromolecules* **42**, 9506–9514 (2009)
18. Nishioka, M., Takahashi, Y., Kato, A., Hikasa, S., Iwabuki, H., Nagata, K., Asano, A.: Influence of water absorption on high-impact properties of polyketone/polyamide polymer alloy. *Kobunshi Ronbunshu* **66**, 570–576 (2009)
19. Takahashi, Y., Nishioka, M., Kato, A., Hikasa, S., Iwabuki, H., Nagata, K., Asano, A.: Nanostructure of polyketone/polyamide polymer alloy. *Kobunshi Ronbunshu* **66**, 577–584 (2009)
20. Kato, A., Nishioka, M., Tkhashi, Y., Suda, T., Sawabe, H., Isoda, A., Drozdova, O., Izumi, T., Nagata, K., Hikasa, S., Iwabuki, H., Asano, A.: Phase separation and mechanical properties of polyketone/polyamide polymer alloys. *J. Appl. Polym. Sci.* **116**, 3056–3069 (2010)
21. Kato, A., Isono, Y., Nagata, K., Asano, A., Ikeda, Y.: Study on polymeric nanocomposites by 3D-TEM and related techniques. In: Kumar, C.S.S.R. (ed.) *Transmission Electron Microscopy Characterization of Nanomaterials*, pp. 139–193. Springer, Berlin (2014)
22. Assink, A.: Nuclear spin diffusion between polyurethane microphases. *Macromolecules* **11**, 1233–1237 (1978)
23. Gelles, R., Frank, C.W.: Phase separation in polystyrene/poly(vinyl methyl ether) blends as studied by excimer fluorescence. *Macromolecules* **15**, 1486–1491 (1982)
24. Gelles, R., Frank, C.W.: Effect of molecular weight on polymer blend phase separation kinetics. *Macromolecules* **16**, 1448–1456 (1983)
25. Nishi, T., Wang, T.T., Kwei, T.K.: Thermally induced phase separation behavior of compatible polymer mixtures. *Macromolecules* **8**, 227–234 (1975)
26. Miyoshi, T., Takegoshi, K., Terao, T.:  $^{129}\text{Xe}$  n.m.r. study of free volume and phase separation of the polystyrene/poly(vinyl methyl ether) blend. *Polymer* **38**, 5475–5480 (1997)
27. Nieuwendaal, R.C., Ro, H.W., Germack, D.S., Kline, R.J., Toney, M.F., Chan, C.K., Agrawal, A., Gundlach, D., VanderHart, D.L., DeLongchamp, D.M.: Measuring domain sizes and compositional heterogeneities in P3HT-PCBM bulk heterojunction thin films with  $^1\text{H}$  spin diffusion NMR spectroscopy. *Adv. Func. Mater.* **22**, 1255–1266 (2012)
28. Nieuwendaal, R.C., Snyder, C.R., Kline, R.J., Lin, E.K., VanderHart, D.L., DeLongchamp, D.M.: Measuring the extent of phase separation in poly-3-hexylthiophene/phenyl-C61-butric acid methyl ester photovoltaic blends with  $^1\text{H}$  spin diffusion NMR spectroscopy. *Chem. Mater.* **22**, 2930–2936 (2010)
29. VanderHart, D.L., Asano, A., Gilman, J.W.: Solid state NMR investigation of paramagnetic nylon-6 clay nanocomposites. 2. Measurement of clay dispersion, crystal stratification, and stability of organic modifiers. *Chem. Mater.* **13**, 3796–3809 (2001)
30. Bourbigot, S., VanderHart, D.L., Gilman, J.W., Awad, W.H., Davis, R.D., Morgan, A.B., Wilkie, C.A.: Investigation of nanodispersion in polystyrene-montmorillonite nanocomposites by solid-state NMR. *J. Polym. Sci. Part B: Polym. Phys.* **41**, 3188–3213 (2003)
31. Asano, A., Shimizu, M., Kurotsu, T.: Effect of paramagnetic  $\text{Fe}^{3+}$  on  $T_1^{\text{H}}$  in PVA/montmorillonite-clay nanocomposites. *Chem. Lett.* **33**, 816–817 (2004)
32. VanderHart, D.L., Asano, A., Gilman, J.W.: Solid state NMR investigation of paramagnetic nylon-6 clay nanocomposites. 1. Crystallinity, morphology, and the direct influence of  $\text{Fe}^{3+}$  on nuclear spins. *Chem. Mater.* **13**, 3781–3795 (2001)
33. VanderHart, D.L., Asano, A., Gilman, J.W.: NMR measurements related to clay-dispersion quality and organic-modifier stability in nylon-6/clay nanocomposites. *Macromolecules* **34**, 3819–3822 (2001)

34. Asano, A.: Polymer blends and composites. In: Webb, G.W. (ed.) *Modern Magnetic Resonance*, 2nd edn. (ISBN 978-3-319-28388-3), Springer, Switzerland (2018), in press
35. Hou, S.-S., Bonagamba, T.J., Beyer, F.L., Madison, P.H., Schmidt-Rohr, K.: Clay intercalation of poly(styrene-ethylene oxide) block copolymers studied by two-dimensional solid-state NMR. *Macromolecules* **36**, 2769–2776 (2003)
36. Strobl, G.R.: *The Physics of Polymers*. Springer, Berlin (1997)
37. Asano, A., Murata, Y., Kurotsu, T.: Crystallinity and miscibility of poly(vinyl isobutyl ether)/poly( $\epsilon$ -L-lysine) blends by solid state  $^{13}\text{C}$  NMR study. *E-J. Soft Mater.* **3**, 1–8 (2007)
38. Asano, A., Tanaka, C., Kurotsu, T.: Melting point and domain size of PVIBE/ $\epsilon$ -PL/saponite clay investigated by solid-state  $^{13}\text{C}$  NMR. *Macromolecules* **41**, 9469–9473 (2008)
39. Asano, A.: NMR relaxation studies of elastomers. In: Webb, G.W. (ed.) *Annual Reports on NMR Spectroscopy*, pp. 1–72. Academic Press (Elsevier), Oxford (2015)
40. Numata, K., Kurokawa, H., Kawaguchi, S., Sekine, S., Nakazawa, Y., Asano, A.: Evaluation of sealability for aged rubber seals by spin–spin relaxation time. *Polym. Test.* **49**, 147–155 (2016)

# Chapter 12

## Solid-State $^2\text{H}$ NMR Studies of Molecular Motion in Functional Materials

Motohiro Mizuno

**Abstract** In this chapter, the analysis of molecular motion in solid materials, which is connected with the function of those materials, using  $^2\text{H}$  NMR spectroscopy is described. The line shape of a  $^2\text{H}$  NMR spectrum, which is dominated by the quadrupole interaction, is very sensitive to molecular motion. The mode and rate of molecular motion in the dynamic range of  $10^4$ – $10^7$  Hz can be obtained by the line shape analysis of a  $^2\text{H}$  NMR broad line spectrum of a powder sample using spectral simulation. Molecular motion in the order of  $10^3$  and  $10^8$  Hz can be analyzed by a line shape and line width of a  $^2\text{H}$  NMR Quadrupolar Carr-Purcell-Meiboom-Gill (QCPMG) spectrum. The analysis of molecular motion in paramagnetic materials is possible by simulation of the  $^2\text{H}$  NMR spectrum, including paramagnetic effects. The methods used to simulate these spectra are explained. In addition, the application of these methods to porous coordination polymer (PCP)/metal organic framework (MOF), proton-conducting material, and spin-crossover material is introduced.

**Keywords** Molecular motion • Paramagnetic effect • MOF/PCP  
Proton conduction • Spin-crossover

---

M. Mizuno (✉)

Department of Chemistry, Graduate School of Natural Science and Technology,  
Kanazawa University, Kakuma-Machi, Kanazawa, Ishikawa 920-1192, Japan  
e-mail: mizuno@se.kanazawa-u.ac.jp

M. Mizuno

Functional Supramolecular Materials Research Unit, Future Society Creation  
Research Core, Institute for Frontier Science Initiative, Kanazawa University,  
Kakuma-Machi, Kanazawa, Ishikawa 920-1192, Japan

## 12.1 Introduction

The function of solid materials is significantly affected by the structure and dynamics of local space, which is formed by molecules and ions in solid materials. Therefore, to develop innovative functional solid materials, the importance of material design based on detailed local structure and dynamics analysis is growing. Solid-state NMR spectroscopy is a very powerful tool for investigating molecular dynamics and local structure in solid materials. Solid-state  $^2\text{H}$  NMR spectroscopy is especially effective for the analysis of molecular motion in solid materials [1–3]. The nuclear spin quantum number of deuteron is  $I = 1$ , and the line shape of a  $^2\text{H}$  NMR spectrum of solid materials is mainly dominated by the quadrupole interaction. The change of the quadrupole interaction due to molecular motion creates the characteristic line shape of a  $^2\text{H}$  NMR spectrum. The mode and rate of molecular motion can be revealed by the line shape analysis of a  $^2\text{H}$  NMR broad line spectrum and a Quadrupolar Carr–Purcell–Meiboom–Gill (QCPMG) spectrum of a powder sample using spectral simulation [1–10].

For paramagnetic materials, because of the fast relaxation due to the interaction between the unpaired electron spin and resonant nuclei, the use of spin-lattice relaxation time ( $T_1$ ) and a two-dimensional exchange spectrum to study molecular dynamics is difficult. So, line shape analysis of one-dimensional NMR spectra becomes very important for studying molecular dynamics in paramagnetic materials. For the analysis of molecular motion in paramagnetic materials, the simulation of a  $^2\text{H}$  NMR spectrum, including not only the quadrupole interaction but also paramagnetic effects, is necessary [1, 11–16].

In this chapter, the methods used to simulate a  $^2\text{H}$  NMR spectrum are explained. The application of these methods to the analysis of molecular motion in functional materials is then introduced.

## 12.2 Measurements of Solid-State $^2\text{H}$ NMR Spectrum

To measure a solid-state  $^2\text{H}$  NMR spectrum, echo methods are usually used in order to avoid a rapid decrease in the NMR signal due to the quadrupole interaction. Figure 12.1a and b shows a quadrupolar echo sequence for the measurement of a  $^2\text{H}$  NMR broad line spectrum and the pulse sequence for a  $^2\text{H}$  NMR QCPMG spectrum, respectively [1–3, 10]. For the QCPMG measurement, echo signals are connected to form a single echo-train FID signal for Fourier transfer (Fig. 12.1c). Figure 12.2 shows a typical line shape of a  $^2\text{H}$  NMR broad line and QCPMG spectra of a powder sample without molecular motion. The broad line spectrum becomes a symmetric line shape with two horns (the Pake pattern) in the absence of molecular motion. The width of the two horns depends on the quadrupole coupling constant ( $e^2 qQ/h$ ) and on the asymmetry parameter ( $\eta$ ).

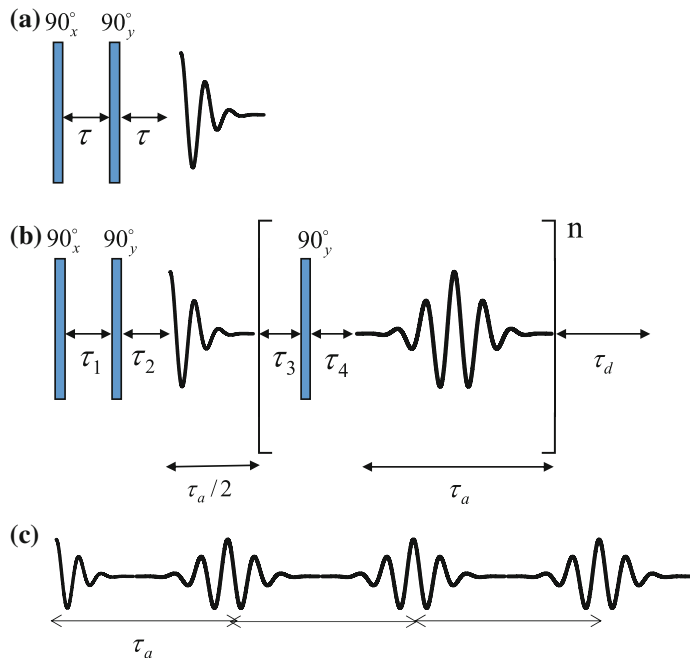


**Fig. 12.1** Pulse sequences for the  $^2\text{H}$  NMR broad line spectrum and the QCPMG spectrum. **a** Quadrupolar echo sequence, **b** QCPMG sequence, **c** NMR signal obtained by the QCPMG sequence

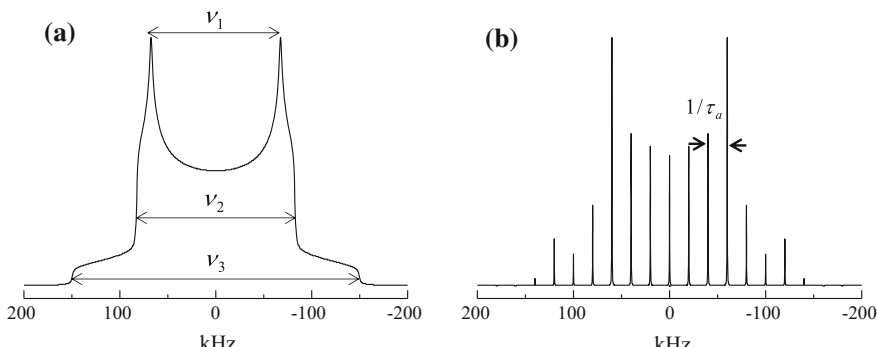
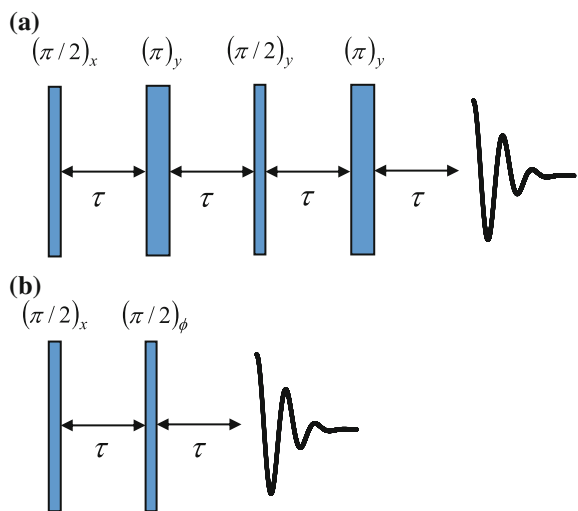


**Fig. 12.2** Typical line shape of a  $^2\text{H}$  NMR broad line spectrum and a QCPMG spectrum without molecular motion simulated by  $e^2qQ/h = 200$  kHz and  $\eta = 0.1$ . **a** Broad line spectrum, **b** QCPMG spectrum.  $v_1 = \frac{3e^2qQ}{4h}(1 - \eta)$ ,  $v_2 = \frac{3e^2qQ}{4h}(1 + \eta)$ ,  $v_3 = \frac{3e^2qQ}{2h}$

The QCPMG spectrum consists of sharp peaks separated by  $1/\tau_a$  where  $\tau_a$  is the detection period of each echo signal (Fig. 12.1b) and is similar to the spinning side-band pattern of the  $^2\text{H}$  NMR MAS spectrum. For paramagnetic materials, the interactions between deuteron and unpaired electrons cannot be negligible. Since

**Fig. 12.3** Pulse sequences of a  $^2\text{H}$  NMR broad line spectrum for paramagnetic materials.

**a** Shift-compensated quadrupolar echo sequence,  
**b** exorcycled quadrupolar echo sequence



the quadrupolar echo sequence only refocuses the dephasing of the quadrupole interaction, distortion of the line shape is caused by a paramagnetic shift [1, 11–16]. Hence the pulse sequences of Fig. 12.3 are used for the measurement of paramagnetic materials. Figure 12.3a is a shift-compensated quadrupolar echo sequence after inserting  $\pi$ -pulses in the quadrupolar echo sequence midway between the  $\pi/2$ -pulses to refocus the paramagnetic shift [11]. Figure 12.3b is an exorcycled quadrupolar echo sequence after selecting the coherence transfer pathway [12]. The signal intensity of the exorcycled quadrupolar echo sequence becomes half of that of the shift-compensated quadrupolar echo sequence. However, the exorcycled quadrupolar echo sequence that uses only two  $\pi/2$ -pulses is effective for materials with a very short spin-lattice relaxation time due to paramagnetic relaxation.

The  $^2\text{H}$  NMR spectra in this chapter were obtained by applying a resonance frequency of 45 MHz and a  $\pi/2$ -pulse of 2–3  $\mu\text{s}$ .

## 12.3 Simulation Methods of Solid-State $^2\text{H}$ NMR Spectrum

The calculation of a spectrum is performed by considering the  $^2\text{H}$  NMR frequency and the spin–spin relaxation rate at each deuteron site and the jump frequency of deuterons between sites. For diamagnetic materials, the  $^2\text{H}$  NMR frequency is dominated by the quadrupole interaction and the frequency at site  $i$  is written as [1, 2, 4, 17]

$$\omega_i = \pm \omega_{Q_i} \quad (12.1)$$

$$\omega_{Q_i} = \sqrt{\frac{3}{2}} \sum_{n,m=-2}^2 D_{0n}^{(2)*}(\psi, \theta, \phi) D_{nm}^{(2)*}(\alpha_{Q_i}, \beta_{Q_i}, \gamma_{Q_i}) \rho_{2m}^Q \quad (12.2)$$

$$\rho_{20}^Q = \sqrt{\frac{3}{8}} \frac{e^2 q Q}{\hbar}, \quad \rho_{2\pm 2}^Q = \frac{\eta e^2 q Q}{4 \hbar} \quad (12.3)$$

where  $D_{nm}^{(2)*}(\Omega)$  is the second-order Wigner rotation matrix.  $(\alpha_{Q_i}, \beta_{Q_i}, \gamma_{Q_i})$  and  $(\psi, \theta, \phi)$  are the Euler angles for transformation from the principal axes of the quadrupole tensor to the molecular axes and from the molecular axes to the laboratory axes, respectively.  $e^2 q Q / \hbar$  and  $\eta$  are the quadrupole coupling constant and asymmetry parameter, respectively. The echo signal  $G(t, \theta, \phi)$  is written as

$$G(t, \theta, \phi) = \mathbf{W} \hat{\mathbf{B}}_{\pi/2}^3 \exp[\hat{\mathbf{A}}t] \exp[\hat{\mathbf{A}}(\tau + t_{\pi/2})] \exp[\hat{\mathbf{A}}^*(\tau + t_{\pi/2})] \mathbf{1} \quad (12.4)$$

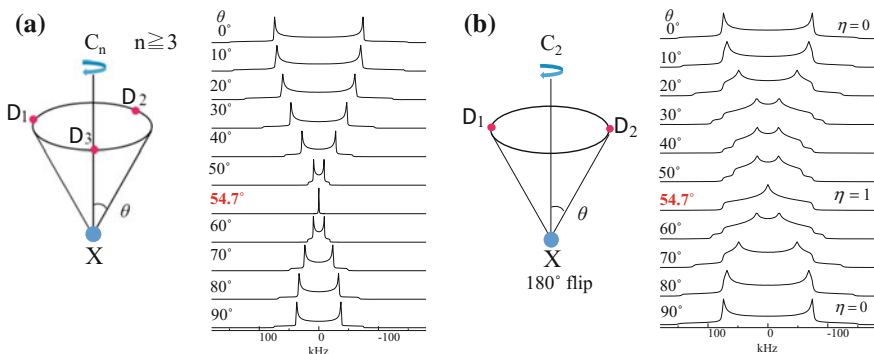
where  $\hat{\mathbf{A}}$  is the matrix with the elements  $i\omega_i - k_{ii} - R_2$  on the diagonal and  $k_{ij}$  off the diagonal.  $k_{ij}$  is the jumping rate between site  $i$  and  $j$ .  $R_2$  is the spin–spin relaxation rate [4, 5]. For the  $N$ -site jump,  $\hat{\mathbf{A}}$  becomes an  $N \times N$ -dimensional matrix and the relation  $k_{ii} = (N - 1)k_{ij}$  is established.  $\mathbf{W}$  and  $\mathbf{1}$  are a vector of site populations and a vector written as  $\mathbf{1} = (1, 1, 1)$ , respectively. The matrix for finite width of  $\pi/2$ -pulse  $\hat{\mathbf{B}}_{\pi/2}$  is written as [5]

$$\hat{\mathbf{B}}_{\pi/2} = \omega_1 \sin\left(t_{\pi/2} \sqrt{\omega_1^2 + \Omega_i^2/4}\right) / \sqrt{\omega_1^2 + \Omega_i^2/4} \quad (12.5)$$

where  $t_{\pi/2}$  and  $\omega_1 (= \gamma B_1)$  represent the width and the strength of the  $\pi/2$ -pulse, respectively.  $\Omega_i$  is the imaginary part of the  $i$ th eigenvalue of the matrix  $\hat{\mathbf{A}}$ . For the second  $\pi/2$ -pulse, the effect of pulse width becomes  $\hat{\mathbf{B}}_{\pi/2}^2$  because of the time evolution of multi-quantum coherence arising from the quadrupole interaction under the RF-field during  $t_{\pi/2}$ . Therefore,  $\hat{\mathbf{B}}_{\pi/2}^3$  is multiplied in Eq. (12.5) [5, 18]. The signal of the powder sample was calculated by

$$G(t) = \int_0^{2\pi} \int_0^\pi G(t, \theta, \phi) \sin\theta d\theta d\phi \quad (12.6)$$

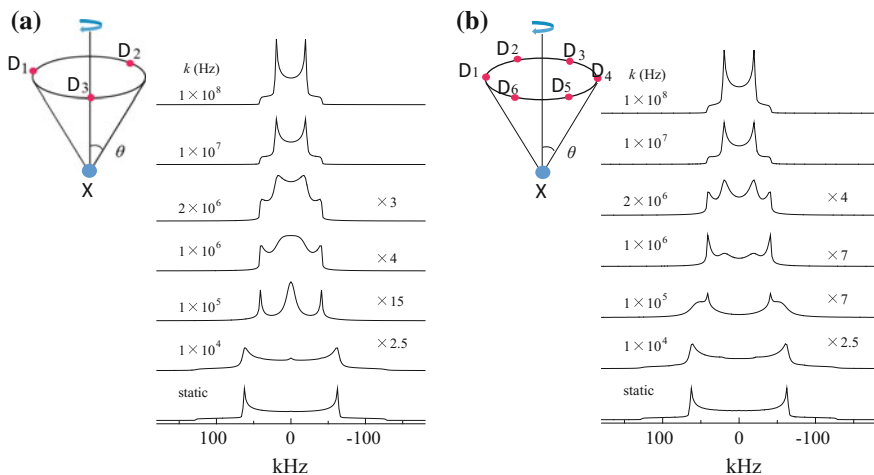
The broad line spectrum was obtained by the Fourier transformation of  $G(t)$ . The QCPMG spectrum can be obtained by the repeated calculation of time evolution due to  $\hat{\mathbf{A}}^*$  and  $\hat{\mathbf{A}}$  after calculation of Eq. (12.4).



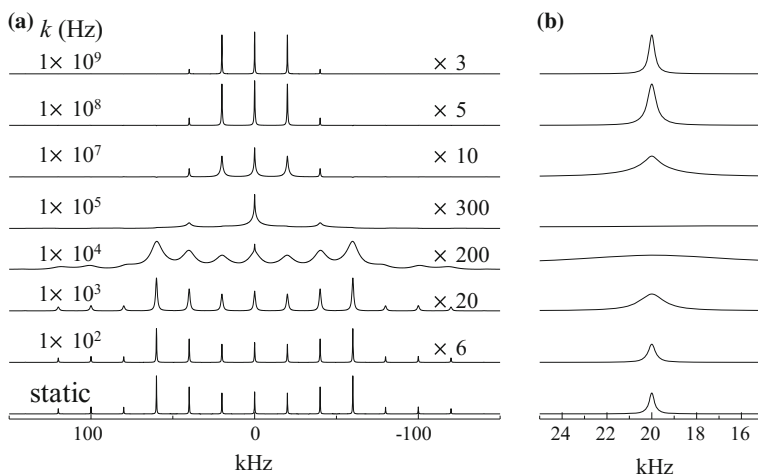
**Fig. 12.4** Simulation of a  $^2\text{H}$  NMR broad line spectrum in the presence of a fast  $n$ -site jump of the  $\text{X}-^2\text{H}$  axis around the  $n$ -hold axis. **a**  $n \geq 3$ , **b**  $n = 2$ .  $e^2 qQ/h = 200$  kHz,  $\eta = 0$ , rotational rate  $k = 1 \times 10^9$  Hz were used for the simulation

Figure 12.4 shows the simulation of a broad line spectrum in the presence of a fast  $n$ -site jump of the  $\text{X}-^2\text{H}$  axis around the  $n$ -hold symmetry axis. The principal  $z$ -axis of the quadrupole tensor was assumed to lie on the  $\text{X}-^2\text{H}$  axis.  $\theta$  is an angle between the  $\text{X}-^2\text{H}$  axis and the  $n$ -hold symmetry axis.  $k_{ij}$  was set as  $1 \times 10^9$  Hz. When the jumping rate is fast enough, the line shape of the spectrum becomes the same and  $\eta$  becomes 0 for the rotation of  $n \geq 3$ .  $e^2 qQ/h$  decreases as  $\theta$  approaches  $54.7^\circ$  and becomes 0 at  $\theta = 54.7^\circ$ . The line shape of the spectrum for the rotation of  $n = 2$ , which corresponds to the  $180^\circ$  flip motion, is different from that of  $n \geq 3$ .  $\eta$  increases as  $\theta$  approaches  $54.7^\circ$  and becomes 1 at  $\theta = 54.7^\circ$  for  $n \geq 3$ . The line shape of the  $^2\text{H}$  NMR spectrum with a large  $\eta$  is observed when a fast  $180^\circ$  flip of the water molecule occurs. Figure 12.5 shows the simulation of a broad line spectrum in the presence of a 3-site jump and a 6-site jump of the  $\text{X}-^2\text{H}$  axis around the  $n$ -hold axis with an intermediate rate. In the dynamic range of  $k = 10^4-10^7$  Hz, the line shape of the  $^2\text{H}$  NMR spectrum depends on the mode and rate of reorientational motion. Figure 12.6 shows a simulation of the QCPMG spectrum in the presence of a 3-site jump of the  $\text{X}-^2\text{H}$  axis around the  $n$ -hold axis with an intermediate rate. The pronounced decrease in the intensity of the QCPMG spectrum takes place in the dynamic range of  $k = 10^4-10^6$  Hz. The line broadening of each peak appears in the QCPMG spectrum in the presence of molecular rotation with an order of  $10^3$  and  $10^8$  Hz. Thus, by using a QCPMG spectrum, it is possible to obtain information of molecular motion in the order of  $10^3$  and  $10^8$  Hz, which is difficult to analyze using a broad line spectrum.

For paramagnetic materials, not only the quadrupole interaction but also the paramagnetic interaction affects the  $^2\text{H}$  NMR frequency, and the frequency at site  $i$  is written as [1, 13–16]



**Fig. 12.5** Simulation of a  $^2\text{H}$  NMR broad line spectrum in the presence of an  $n$ -site jump of the  $\text{X}-^2\text{H}$  axis around the  $n$ -hold axis with an intermediate rotational rate. **a**  $n = 3$ , **b**  $n = 6$ .  $e^2qQ/h = 170$  kHz,  $\eta = 0$ ,  $\theta = 70^\circ$  were used for the simulation



**Fig. 12.6** Simulation of a  $^2\text{H}$  NMR QCPMG spectrum in the presence of a 3-site jump of the  $\text{X}-^2\text{H}$  axis around a 3-hold axis with an intermediate rotational rate. **a** Whole spectrum, **b** expansion around 20 kHz.  $e^2qQ/h = 170$  kHz,  $\eta = 0$ ,  $\theta = 70^\circ$  were used for the simulation

$$\omega_i = \pm\omega_{Qi} - \sum_j \omega_{P_{ij}} + \omega_{CS_i} \quad (12.7)$$

$$\omega_{P_{ij}} = \sum_{n=-2}^2 D_{0n}^{(2)*}(\psi, \theta, \phi) D_{n0}^{(2)*}\left(\alpha_{P_{ij}}, \beta_{P_{ij}}, \gamma_{P_{ij}}\right) \rho_{20}^{P_{ij}} \quad (12.8)$$

$$\rho_{20}^{P_{ij}} = \left(\frac{\mu_0}{4\pi}\right) \frac{2\gamma_D B_0 g_j^2 \mu_B^2}{3k_B T r_{ij}^3} S(S+1) \quad (12.9)$$

where  $\omega_{P_{ij}}$  is the contribution of the dipolar interaction between the  ${}^2\text{H}$  nucleus and the  $j$ th paramagnetic ion and  $\omega_{CS_i}$  is the contribution of the isotropic paramagnetic shift (Fermi's contact shift).  $(\alpha_{P_{ij}}, \beta_{P_{ij}}, \gamma_{P_{ij}})$  are the Euler angles for transformation from the principal axes of the paramagnetic dipolar tensor to the molecular axes.  $r_{ij}$  is the distance between the  ${}^2\text{H}$  nucleus and the  $j$ th paramagnetic ion.  $T$ ,  $\gamma_D$ ,  $B_0$ ,  $\mu_B$ ,  $k_B$ ,  $S$ , and  $g_j$  are temperature, gyromagnetic ratio of the  ${}^2\text{H}$  nucleus, strength of the static magnetic field, Bohr magneton, Boltzmann constant, electron spin quantum number, and g-factor of the  $j$ th paramagnetic ion, respectively.

Equation (12.9) can be rewritten as Eq. (12.10) using magnetic susceptibility  $\chi_M$ ,

$$\rho_{20}^{P_{ij}} = \left(\frac{\mu_0}{4\pi}\right) \frac{2\gamma_D B_0 \chi_M}{N_A r_{ij}^3} \quad (12.10)$$

where  $N_A$  is Avogadro's constant. The anisotropic g-factor can be represented by

$$g_j^2 = g_{isoj}^2 + \sum_{n,m=-2}^2 D_{0n}^{(2)*}(\psi, \theta, \phi) D_{nm}^{(2)*}\left(\alpha_{g_j}, \beta_{g_j}, \gamma_{g_j}\right) \rho_{2m}^{g_j} \quad (12.11)$$

$$\rho_{20}^{g_j} = \sqrt{\frac{2}{3}\left(g_{zzj}^2 - \frac{1}{2}\left(g_{xxj}^2 + g_{yyj}^2\right)\right)}, \quad \rho_{2\pm 2}^{g_j} = \frac{1}{2}\left(g_{yyj}^2 - g_{xxj}^2\right) \quad (12.12)$$

$$g_{isoj}^2 = \frac{g_{xxj}^2 + g_{yyj}^2 + g_{zzj}^2}{3} \quad (12.13)$$

where  $(\alpha_{g_j}, \beta_{g_j}, \gamma_{g_j})$  are the Euler angles for transformation from the principal axes of the g-tensor to the molecular axes. Figure 12.7 shows the temperature dependence of the  ${}^2\text{H}$  NMR broad line spectrum for the  $[\text{Ni}(\text{D}_2\text{O})_6][\text{SiF}_6]$  crystal [15]. The spectrum was observed by a shift-compensated quadrupolar echo sequence. The spin quantum number of the  $\text{Ni}^{2+}$  ion is  $S = 1$ . Consequently, the line shape of the  ${}^2\text{H}$  NMR spectrum becomes asymmetric due to the paramagnetic interaction. For  $[\text{Ni}(\text{D}_2\text{O})_6]^{2+}$ , there are two molecular motions, a  $180^\circ$  flip of  $\text{D}_2\text{O}$  and the reorientation of  $[\text{Ni}(\text{D}_2\text{O})_6]^{2+}$  about the 3-fold axis (Fig. 12.8). In this temperature

**Fig. 12.7** Temperature dependence of a  $^2\text{H}$  NMR broad line spectrum for the  $[\text{Ni}(\text{D}_2\text{O})_6]\text{[SiF}_6]$  crystal [15]

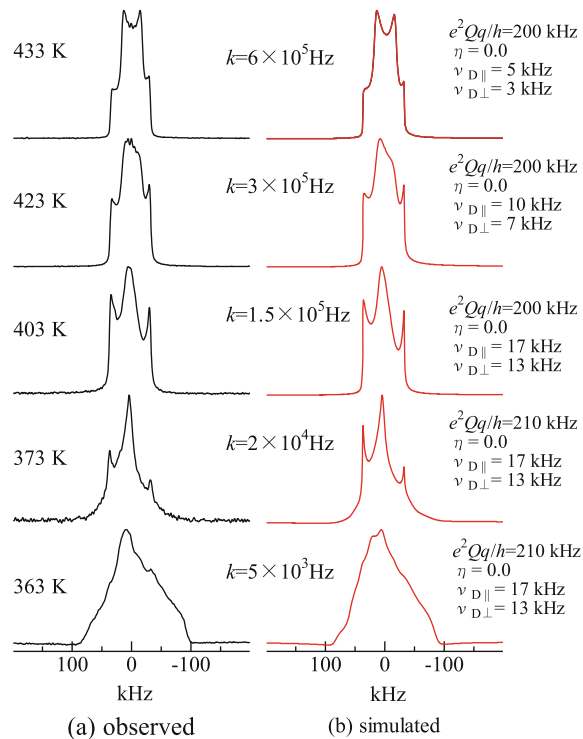
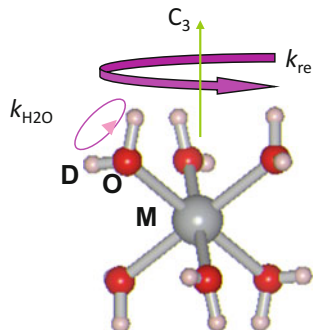


**Fig. 12.8** Reorientation of  $[\text{M}(\text{H}_2\text{O})_6]^{2+}$  ( $\text{M} = \text{Ni}^{2+}$ ,  $\text{Mn}^{2+}$ ) and 180° flip of  $\text{H}_2\text{O}$



range, the 180° flip of  $\text{D}_2\text{O}$  is in the fast motion limit and temperature variation of the spectral line shape is caused by reorientation of  $[\text{Ni}(\text{D}_2\text{O})_6]^{2+}$ . The principal axes system of the quadrupole tensor ( $x_p$ ,  $y_p$ ,  $z_p$ ) which is averaged by fast 180° flip of  $\text{D}_2\text{O}$  was assigned as follows: the  $z_p$ -axis is perpendicular to the water molecular plane, the  $y_p$ -axis lies in the water molecular plane, and the  $x_p$ -axis is parallel to the bisector of D-O-D plane. The rate of reorientation  $k$  was obtained at each temperature after fitting (Fig. 12.7).

In the case of a strong paramagnetic interaction, fast spin–spin relaxation due to the paramagnetic interaction affects the line shape of the spectrum. The anisotropic spin–spin relaxation rate due to the paramagnetic dipolar interaction can be written as [16]

$$\begin{aligned} R_{2i}^P = & \frac{4}{3} \left( \frac{\mu_0}{4\pi} \right)^2 \gamma_D^2 \mu_B^2 S(S+1) \\ & \times \sum_j g_j^2 \left\{ \frac{1}{6} |F_{20}^{ij}|^2 \left( 4\tau_e + \frac{\tau_e}{1 + (\omega_D - \omega_e)^2 \tau_e^2} \right) \right. \\ & \left. + \frac{1}{2} |F_{21}^{ij}|^2 \left( \frac{2\tau_e}{1 + \omega_e^2 \tau_e^2} + \frac{\tau_e}{1 + \omega_D^2 \tau_e^2} \right) + |F_{22}^{ij}|^2 \left( \frac{\tau_e}{1 + (\omega_D + \omega_e)^2 \tau_e^2} \right) \right\} \end{aligned} \quad (12.14)$$

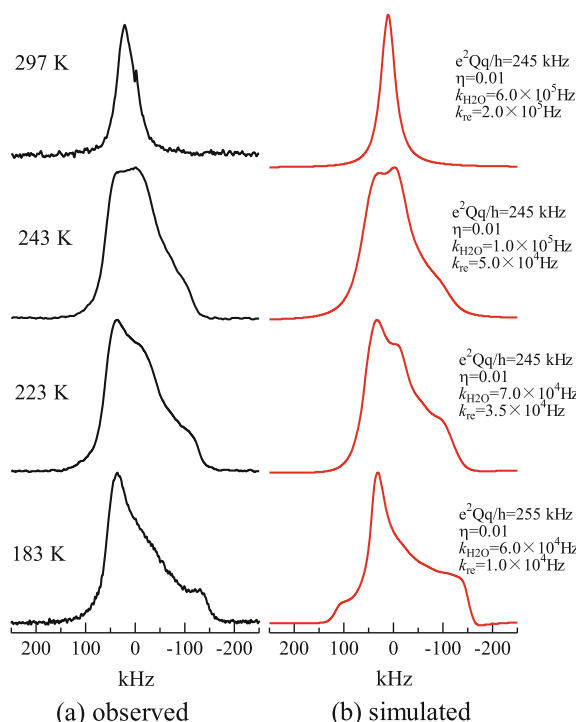
$$F_{2m}^{ij} = \sum_{n=-2}^2 D_{mn}^{(2)*}(\psi, \theta, \phi) D_{n0}^{(2)*}\left(\alpha_{P_{ij}}, \beta_{P_{ij}}, \gamma_{P_{ij}}\right) \rho_{20}^{D_{ij}} \quad (12.15)$$

$$\rho_{20}^{D_{ij}} = \sqrt{\frac{3}{2}} r_{ij}^{-3} \quad (12.16)$$

where  $\omega_D$  and  $\omega_e$  are angular NMR and ESR frequencies, respectively.  $\tau_e$  is the correlation time of the electron spin.

Figure 12.9 shows the temperature dependence of the  ${}^2\text{H}$  NMR spectrum for the  $[\text{Mn}(\text{D}_2\text{O})_6][\text{SiF}_6]$  crystal [16]. The spin quantum number of the  $\text{Mn}^{2+}$  ion is  $S = 5/2$ . Thus, the  $\text{Mn}^{2+}$  ion applies strong paramagnetic effects to the  ${}^2\text{H}$  NMR spectrum. The contribution of the paramagnetic dipolar interaction between the  ${}^2\text{H}$  nuclei and nearest neighboring  $\text{Mn}^{2+}$  ion exceeds 100 kHz, and even contribution from the second nearest-neighbor  $\text{Mn}^{2+}$  ion causes the frequency to become ca. 30 kHz. The spin-lattice relaxation time ( $T_1$ ) was  $\sim 70 \mu\text{s}$ . The exorcycled quadrupolar echo sequence was used to measure the spectrum of  $[\text{Mn}(\text{D}_2\text{O})_6][\text{SiF}_6]$ . For the simulation in Fig. 12.9, the contribution of  $\text{Mn}^{2+}$  in  $3^3$  hexagonal unit cells of the crystal (81  $\text{Mn}^{2+}$ ) is applied. The anisotropic spin–spin relaxation rate was calculated using a crystal structure and  $\tau_e = 3.0 \times 10^{-10} \text{ s}$  obtained by a  ${}^2\text{H}$  NMR  $T_1$  of  $[\text{Mn}(\text{D}_2\text{O})_6][\text{SiF}_6]$ . For  $[\text{Mn}(\text{D}_2\text{O})_6][\text{SiF}_6]$ , both the  $180^\circ$  flip of  $\text{D}_2\text{O}$  and reorientation of  $[\text{Mn}(\text{D}_2\text{O})_6]^{2+}$  affect the change in line shape of the  ${}^2\text{H}$  NMR spectrum in Fig. 12.9. Thus, a 6-site jump of deuteron around the  $C_3$  axis was assumed. The principal z-axis of the quadrupole tensor was assumed to lie on the O–D axis. From the simulation analysis, the rotational rates  $k_{180^\circ}$  and  $k_{\text{re}}$  were obtained for the  $180^\circ$  flip of  $\text{D}_2\text{O}$  and for the reorientation of  $[\text{Mn}(\text{D}_2\text{O})_6]^{2+}$ , respectively as shown in Fig. 12.9 [16].

**Fig. 12.9** Temperature dependence of a  $^2\text{H}$  NMR spectrum for the  $[\text{Mn}(\text{D}_2\text{O})_6]\text{[SiF}_6]$  crystal [16]



## 12.4 Analysis of MOF/PCP

Metal-organic frameworks (MOFs) or porous coordination polymers (PCPs) have attracted attention since they can be used to make tunable pore sizes and topologies, which lead to versatile architectures and applications, and have been actively studied due to their applications in gas storage, separation, catalysis, and chemical sensing. The dynamics of nano-spaces (rotation of bridging ligand, adsorbed molecules, etc.) in MOFs (PCPs) have been investigated by solid-state  $^2\text{H}$  NMR spectroscopy [19–24]. For  $[\text{Zn}_2(1,4-\text{ndc})_2(\text{dabco})]_n$  ( $1,4-\text{ndc}$ =1,4-naphthalenedicarboxylate, dabco=1,4-diazabicyclo[2]octane, Fig. 12.10) [20, 25], rotational motion of a naphthalene ligand before and after benzene adsorption was investigated. In this framework, paddle-wheel  $\text{Zn}^{2+}$  dimers are linked by 1,4-naphthalenedicarboxylate ions, resulting in regular square grid-type layers parallel to the ab plane, and these layers are pillared by 1,4-diazabicyclo[2]octane molecules (Fig. 12.10a). Rectangular channels of  $5.7 \times 5.7 \text{ \AA}^2$  run along the c direction. At 296 K, the naphthalene ring of the dicarboxylate ion is disordered over four positions which are defined by orientation angles of  $0^\circ$ ,  $70^\circ$ ,  $180^\circ$ , and  $250^\circ$  about the C1–C4 axis (Fig. 12.10b). The  $^2\text{H}$  NMR spectrum of the naphthalene ring was selectively observed by using  $[\text{Zn}_2([\text{D}_6]1,4-\text{ndc})_2(\text{dabco})]_n$  where only six hydrogens of the naphthalene ring were replaced by deuterons. Figure 12.11 shows  $^2\text{H}$  NMR spectra

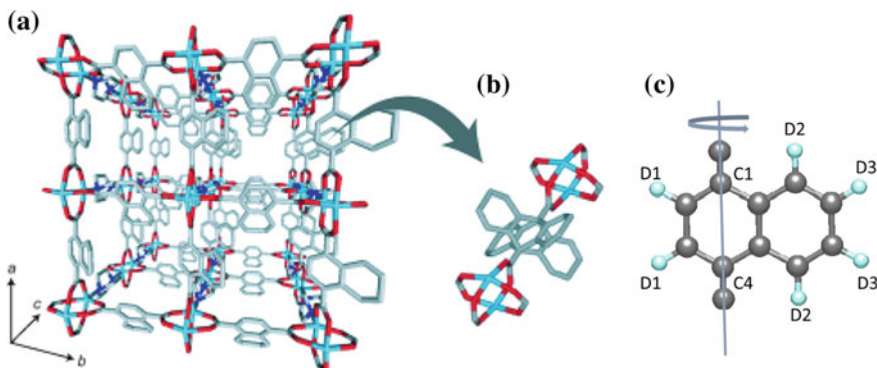


**Fig. 12.10** Crystal structure of  $[Zn_2(1,4\text{-ndc})_2(\text{dabco})]_n$  at 296 K. **a** The pillared layer structure viewed in the *c* direction. **b** Four-site disorder of the naphthalene ring. Hydrogen atoms are omitted; Zn blue, C gray, O red, N dark blue. Reproduced from Ref. [19] by permission of John Wiley & Sons Ltd. **c** Position of deuterons in the naphthalene ring

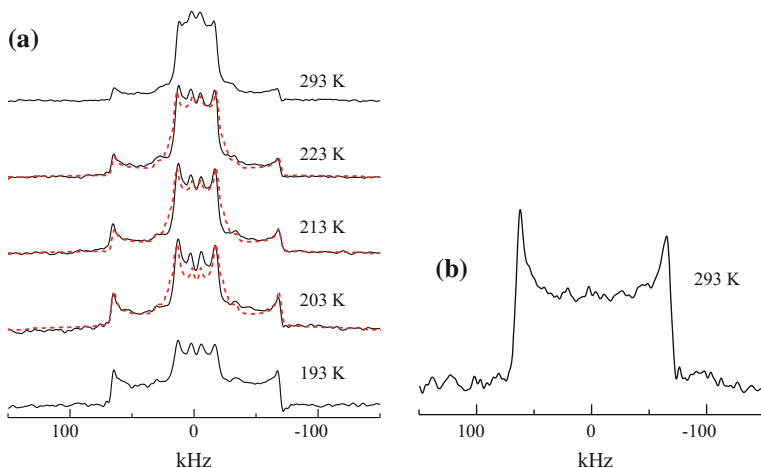


**Fig. 12.11**  $^2\text{H}$  NMR spectra of  $[Zn_2([D_6]1,4\text{-ndc})_2(\text{dabco})]_n$ . **a** Temperature dependence of a  $^2\text{H}$  NMR spectrum before benzene adsorption. **b**  $^2\text{H}$  NMR spectrum after benzene adsorption at 293 K. Broken lines are simulation spectra assuming the rotation of the naphthalene ring about the C1–C4 axis [19]

of  $[Zn_2([D_6]1,4\text{-ndc})_2(\text{dabco})]_n$  [20]. Figure 12.11a is the temperature dependence of the  $^2\text{H}$  NMR spectrum before the adsorption of benzene. Figure 12.11b is the  $^2\text{H}$  NMR spectrum after the adsorption of benzene at 293 K. The rapid rotation of the naphthalene ring around the C1–C4 axis takes place before the adsorption of benzene, even below room temperature, which can be ascertained from the line shape of the  $^2\text{H}$  NMR spectrum in Fig. 12.11a. In contrast, the naphthalene ring is static at room temperature after the adsorption of benzene. The broad component with peaks

at about  $\pm 60$  kHz in Fig. 12.11a corresponds to D2 of naphthalene (Fig. 12.10c). Since the C-D2 bonding direction corresponding to the principal axis direction of quadrupole interaction is almost consistent with the direction of rotational axis, rotation of the naphthalene ring around the C1–C4 axis does not affect the spectrum of D2. Inner components with peaks at  $\pm 15$  and  $\pm 5$  kHz correspond to D1 and D3. The broken lines in Fig. 12.11a represent the spectral simulation assuming rotation of the naphthalene ring among four positions in a disordered structure.  $e^2qQ/h = 180$  kHz and  $\eta = 0.02$  were used for the simulation. Euler angles were  $(\alpha_{Q1}, \alpha_{Q2}, \alpha_{Q3}, \alpha_{Q4}) = (0^\circ, 70^\circ, 180^\circ, 250^\circ)$  for four sites,  $\beta_Q = 56^\circ, 60^\circ$  for D1, D3 and  $\beta_Q = 0^\circ$  for D2 in Fig. 12.10c. Rotation rates ranging from  $3.0 \times 10^6$  Hz at 203 K to  $5 \times 10^7$  Hz at 223 K were determined from the fitting. The activation energy and the pre-exponential factor of the rotation of the naphthalene ring were obtained as  $53 \text{ kJ mol}^{-1}$  and  $9.5 \times 10^{19}$  Hz, respectively, from an Arrhenius plot of rotation rate.

## 12.5 Analysis of Solid Proton-Conducting Material

Anhydrous proton-conducting solids operating above  $100^\circ\text{C}$  are required for fuel cell applications. Heterocyclic organic molecules such as imidazole (Im) have attracted considerable attention for this purpose because they are non-volatile molecules with high boiling points. In such materials, proton transport occurs between Im molecules through a hydrogen-bonded chain. When proton conductivity is dominated by continuous proton transport in the hydrogen bond network between Im molecules (the Grotthuss mechanism), the reorientational motion of Im molecules is considered to play an important role [26]. For poly(vinylphosphonic acid) (PVPA) – Im composite material (PVPA/xIm, where  $x$  represents the number of moles of Im per mole of polymer repeat unit, Fig. 12.12), proton conductivity increased with increasing  $x$ , and a sudden increase in proton conductivity was observed in the range from  $x = 1$  to 2 [27]. In the PVPA/xIm composite, Im molecules are intercalated into host polymer PVPA and provide a migration path for excess protons caused by dissociation of the acid functions. The reorientational motion of Im molecules in the PVPA/xIm composite was investigated using  $^2\text{H}$  NMR.  $^2\text{H}$  NMR spectrum of the imidazole was selectively observed by using imidazole-d<sub>3</sub> (Im-d<sub>3</sub>), where only hydrogen bonded to carbon was replaced by deuterium. In polymer materials, dynamic inhomogeneity is closely related with these physical properties. In order to investigate the flexible region and the rigid region in PVPA/xIm, a combination of  $^2\text{H}$  NMR broad line spectra and QCPMG spectra is very effective.

The  $^2\text{H}$  NMR broad line and QCPMG spectra of PVPA/2Im-d<sub>3</sub> above  $30^\circ\text{C}$  are shown in Fig. 12.13 [28]. For the broad line spectrum, the spectral intensity around  $\pm 60$  kHz decreased and that of the central portion increased with increasing temperature. These changes in the line shape of the  $^2\text{H}$  NMR broad line spectrum are observed when the rate of isotropic rotation of molecules gradually increases.

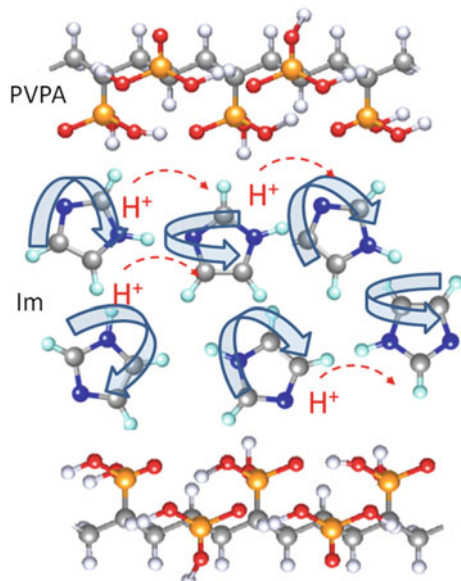


**Fig. 12.12** Poly(vinylphosphonic acid) (PVPA) – imidazole (Im) composite material (PVPA/xIm)

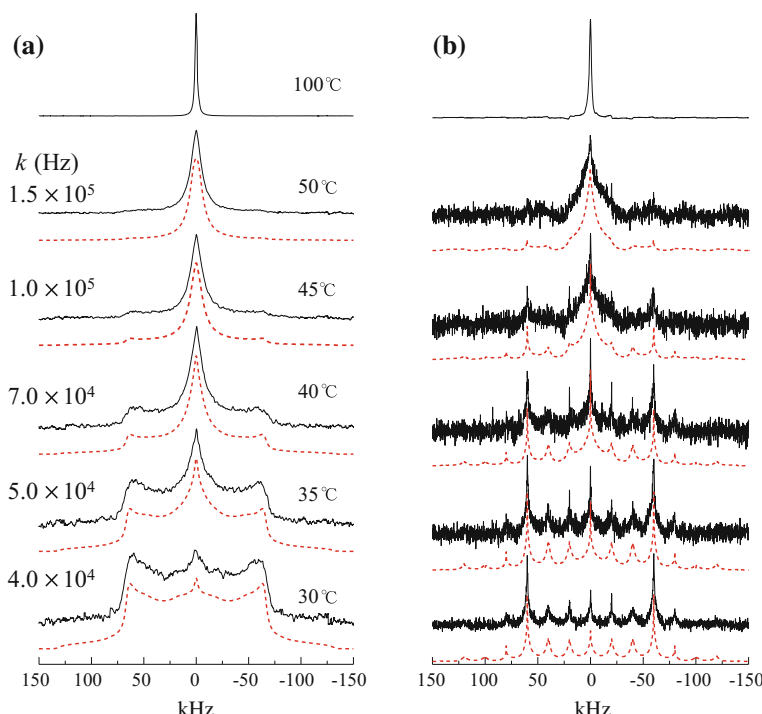
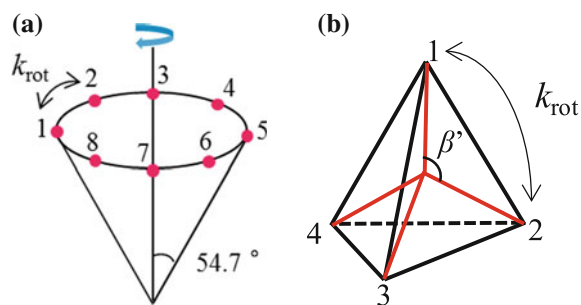


**Fig. 12.13** Temperature dependence of a <sup>2</sup>H NMR spectrum for PVPA/2Im [27]

**Fig. 12.14** Models of isotropic rotation. **a** 8-site jump on a cone at the magic angle model, **b** tetrahedral 4-site jump model



For the simulation of the  $^2\text{H}$  NMR spectrum due to the isotropic rotation of molecules, the multisite jump on the cone at the magic angle (Fig. 12.14a) and the tetrahedral jump (Fig. 12.14b) are conventional models [28, 29]. In polymers, there is often a large distribution of correlation time of molecular motion [30]. Simulation of the  $^2\text{H}$  NMR broad line and QCPMG spectra at 35 °C was performed using an eight-site jump on a cone at the magic angle (Fig. 12.14a) with a Gaussian distribution of the jumping rate  $k_{\text{rot}}$ . The observed and simulated spectra are shown in Fig. 12.15. The signal intensity was reduced by the molecular motion with an intermediate jumping rate. The reduction factor of signal intensity due to the eight-site jump on a cone at the magic angle was estimated. The distribution of the jumping rate used for the spectral simulation, the estimated reduction factor, and the resulting signal intensity are shown in Fig. 12.15e. The line width of the central portion of the observed broad line spectrum is broader than the simulation (Fig. 12.15a, b). The line broadening of the central component of the broad line spectrum indicates that the motion of Im molecules is not perfectly isotropic. Rather, there is pseudo-isotropic rotation with small anisotropy. Each peak of the observed QCPMG spectrum was broad, and the intensity of peaks within  $\pm 50$  kHz was weak relative to the simulated one. These differences between observed and simulated QCPMG spectra are caused by the rotational vibration of Im. Thus, the  $^2\text{H}$  NMR spectrum could be analyzed by three kinds of Im molecules, namely Im undergoing pseudo-isotropic rotation with small anisotropy, rotational vibration, and fast isotropic rotation. The Im molecules undergoing rotational vibration interact strongly with phosphonic acid, and their mobility is highly restricted in the tight segment. The Im molecules undergoing pseudo-isotropic rotation do not have a strong interaction with phosphonic acid and are relatively movable in the flexible segment. The Im molecules undergoing fast isotropic rotation are predicted to be in a flexible space around the end of PVPA chains. In order to investigate the rate and anisotropy of pseudo-isotropic rotation, and the ratio of three kinds of motions of the Im molecules in PVPA/xIm, simulations of the  $^2\text{H}$  NMR broad line and QCPMG spectra were performed. The line shape of the  $^2\text{H}$  NMR spectrum due to the isotropic rotation and the pseudo-isotropic rotation of the Im molecules was simulated by the tetrahedral jump model (Fig. 12.15b). The four deuteron sites were

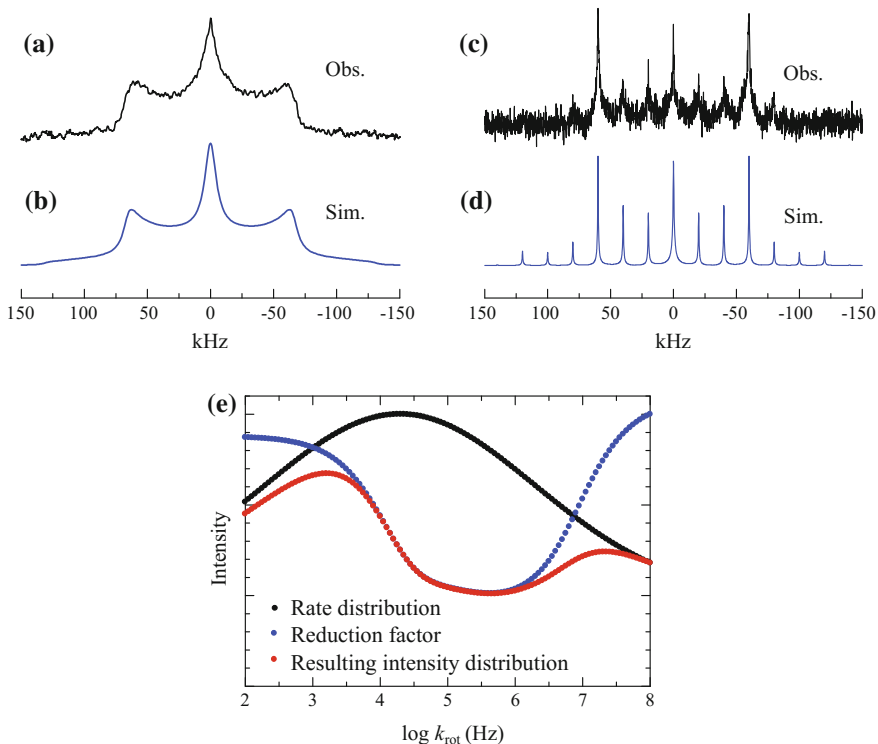


**Fig. 12.15** A  $^2\text{H}$  NMR *broad line* and a QCPMG spectrum at 35 °C for PVPA/2Im. **a** and **c** are observed *broad line* and QCPMG spectra, respectively. **b** and **d** are a simulation using the cone model at the magic angle (**a**) and a Gaussian distribution of the jumping rate. **e** is the distribution of the jumping rate, reduction factor and resulting signal intensity [27]

determined by Euler angles  $(\alpha, \beta)$  of Eq. (12.2) as  $(0^\circ, 0^\circ)$ ,  $(0^\circ, \beta')$ ,  $(120^\circ, \beta')$ , and  $(240^\circ, \beta')$ . Here, the anisotropy parameter  $A$  for molecular rotation is defined as [28]

$$A = \frac{1}{8} (2 + 3(3 \cos \cos^2 \beta' - 1)) \quad (12.17)$$

For the isotropic rotation,  $\beta'$  is  $109.4^\circ$  and  $A$  becomes 0. In the present work,  $\beta'$  changed in the range of  $109.4^\circ$ – $180^\circ$ , and the range of  $A$  was 0–1. As the  $A$  value increased, the line width of the central portion of the  $^2\text{H}$  NMR spectrum increased (see Fig. 12.16). The observed and simulated  $^2\text{H}$  NMR broad line and QCPMG spectra of  $x = 2$  at 35 °C are shown in Fig. 12.17. Simulation spectra were obtained by the superposition of three components: pseudo-isotropic rotation with small anisotropy, rotational vibration, and fast isotropic rotation of the Im molecules. The rate of rotational vibration ( $1.0 \times 10^4$  Hz), estimated by extrapolation from the rates at low temperatures, was used for the simulation. A rate of  $1.0 \times 10^8$  Hz was used for fast isotropic rotation. The rate  $k_{\text{rot}}$  and anisotropy parameter  $A$  of the

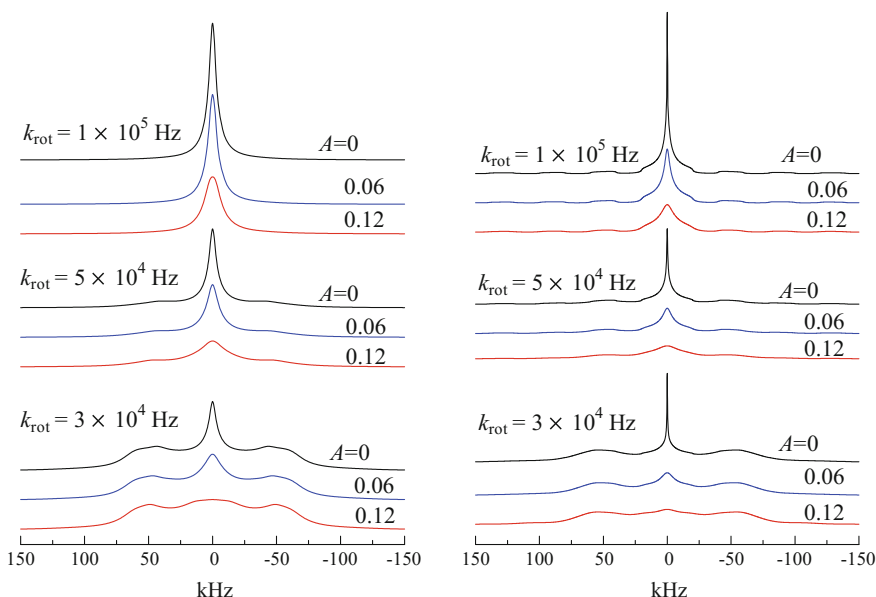


**Fig. 12.16** Anisotropy parameter  $A$  dependence of the  $^2\text{H}$  NMR spectrum for several motional rates. **a** Broad line spectra. **b** QCPMG spectra.  $k_{\text{rot}}$  is the jumping rate among four tetrahedral sites.  $e^2qQ/h = 176 \text{ kHz}$  and  $\eta = 0$  were used for simulation. Spin–spin relaxation time  $T_2$  values of 0.5 and 2.2 ms were used to simulate broad line and QCPMG spectra, respectively. To obtain a simulation of the broad line spectrum, a Lorentzian broadening factor of 3 kHz, which is same as that used for simulation of the rigid spectrum, was added for the Fourier transformation of the calculated time-dependent NMR signal [27]

pseudo-isotropic rotation and the ratio of each component which reproduced the  $^2\text{H}$  NMR broad line and QCPMG spectra simultaneously were determined. There was an extreme decrease in the intensity of the  $^2\text{H}$  NMR spectrum in the presence of molecular rotational motion at a rate of  $10^4$ – $10^5$  Hz. Therefore, although the abundance of Im undergoing pseudo-isotropic rotation exceeds 90%, the contribution of this component to the spectrum is strongly suppressed. The broken lines in Fig. 12.13 show the results of the spectral simulation.  $k_{\text{rot}}$  and  $A$  for the pseudo-isotropic rotation and the ratio of each component were estimated from a spectral simulation at each temperature. In the temperature range between 30 and 50 °C, the spectrum could be reproduced by  $A = 0.12$  for  $x = 2$ .  $A$  was 0.14 in the temperature range between 50 and 80 °C for  $x = 1$ . Thus, the rotation of Im molecules was more suppressed with  $x = 1$  than with  $x = 2$ . The efficient proton conduction accompanied by the pseudo-isotropic rotation of Im molecules exists for PVPA/2Im. The enhanced pseudo-isotropic rotation of Im molecules is correlated with an increase in the proton conductivity of PVPA/ $x$ Im.

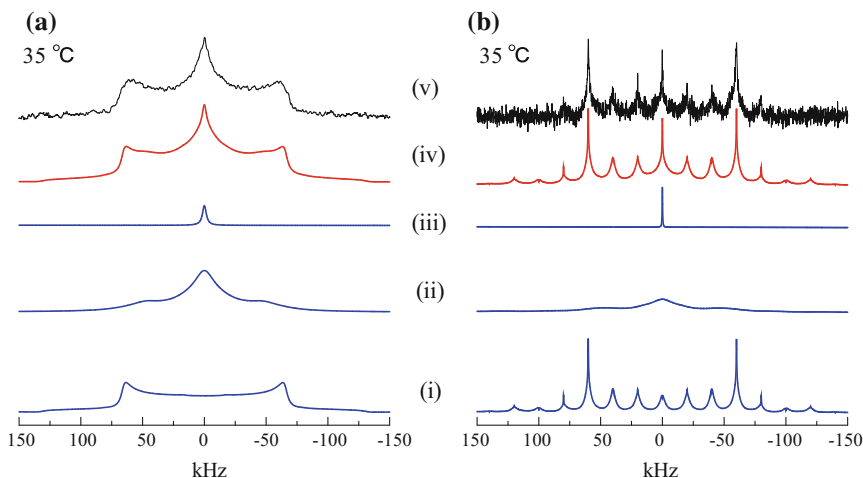


**Fig. 12.17** Observed and simulated  $^2\text{H}$  NMR spectra for  $x = 2$ . **a** and **b** are broad line spectra and QCPMG spectra at  $35\text{ }^\circ\text{C}$ , respectively. (i) Simulation spectra of the rotational vibration of Im with  $k_{\text{lib}} = 1 \times 10^4\text{ Hz}$  and  $\theta_{\text{lib}} = \pm 30^\circ$ ; (ii) simulation spectra of the pseudo-isotropic rotation of Im with  $k_{\text{rot}} = 5 \times 10^4\text{ Hz}$  and  $A = 0.12$ ; (iii) simulation spectra of the isotropic rotation of Im with  $k_{\text{iso}} = 1 \times 10^8\text{ Hz}$ ; (iv) superposition of (i), (ii), and (iii) components; (v) observed spectra.  $e^2qQ/\hbar = 176\text{ kHz}$  and  $\eta = 0$  were used for the simulation. The ratio of Im molecules undergoing pseudo-isotropic rotation, rotational vibration, and isotropic rotation was 96.2, 3.7, and 0.09, respectively [27]

## 12.6 Analysis of Spin-Crossover Material

The spin-crossover phenomenon is well known in  $\text{Fe}^{2+}$  coordination materials, whose electron configurations can move between paramagnetic high-spin (HS) and diamagnetic low-spin (LS) states under extrinsic stimuli, affording changes in magnetic, optical, dielectric and structural properties. When the cooperativity of the spin-crossover is large enough, these materials present a first-order spin transition with hysteretic behavior.

$\{\text{Fe(pz)}[\text{Pt}(\text{CN})_4]\}$  (pz = pyrazine) undergoes a first-order spin transition with a hysteresis of  $\sim 25\text{ K}$  width (transition temperatures:  $T_c = 285$  and  $309\text{ K}$  on cooling and heating, respectively) as shown in Fig. 12.18 [31]. The crystal structure of  $\{\text{Fe(pz)}[\text{Pt}(\text{CN})_4]\}$  can be described as 2D  $\{\text{Fe}[\text{Pt}(\text{CN})_4]\}_\infty$  layers connected along the (001) direction by pyrazine ligands, which occupy the apical positions of the Fe octahedrons (Fig. 12.19). The pyrazine rings are rotationally disordered in both spin states, and this is reflected in the appearance of electronic density corresponding to the carbon atoms of the pyrazine in two positions of the ring at  $90^\circ$  relative to each other.

The rotation of the pyrazine ligands in the LS and HS states was investigated by solid-state  $^2\text{H}$  NMR spectroscopy [31]. The  $^2\text{H}$  NMR spectrum of pyrazine was selectively observed by using  $\{\text{Fe}([\text{D}_4\text{pz}][\text{Pt}(\text{CN})_4]\}$  where only four hydrogens of

**Fig. 12.18** Temperature dependence of magnetic susceptibility for  $\{\text{Fe}(\text{pz})[\text{Pt}(\text{CN})_4]\}$  [30]

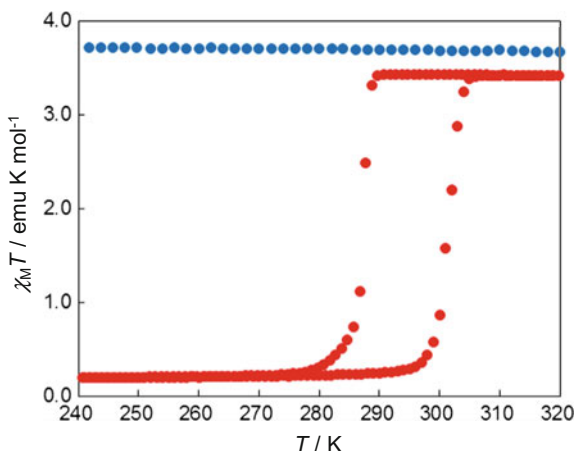
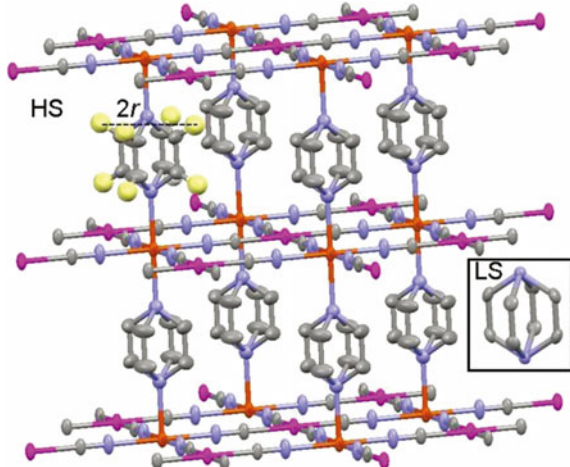
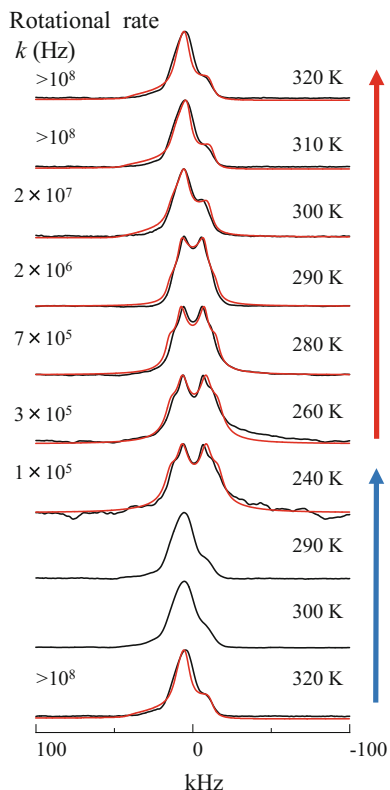


**Fig. 12.19** Crystal structure of  $\{\text{Fe}(\text{pz})[\text{Pt}(\text{CN})_4]\}$  in the HS state. Fe (orange), Pt (pink), N (blue), C (gray), H (yellow). The H atoms are omitted for clarity, except in one pz ring. Inset detail of the thermal ellipsoids of the pz carbon atoms in the LS state. Reprinted with the permission from ref. [30]. Copyright 2011 American Chemical Society



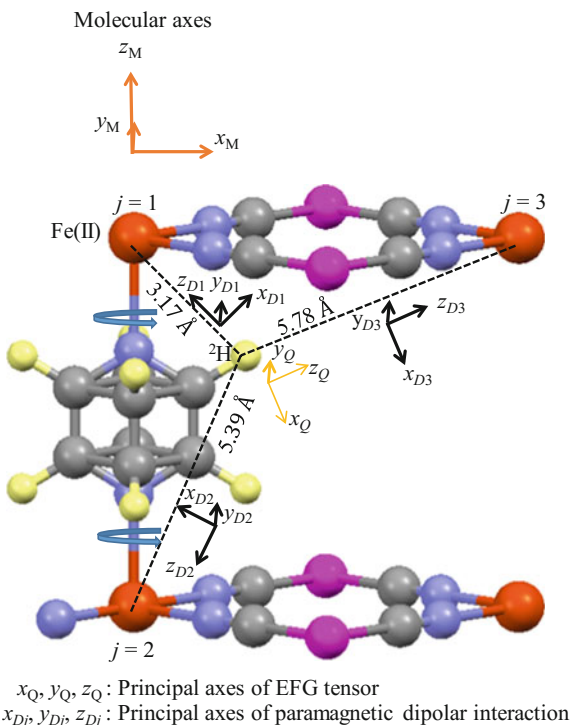
the pyrazine ring were replaced by deuterons. For the measurement of the  $^2\text{H}$  NMR spectrum in the HS state, a shift-compensated quadrupolar echo sequence was used. Figure 12.20 shows the temperature dependence of the  $^2\text{H}$  NMR spectrum for  $\{\text{Fe}([\text{D}_4]\text{pz})[\text{Pt}(\text{CN})_4]\}$ . In the diamagnetic LS state, the line shape of the  $^2\text{H}$  NMR spectrum is dominated by only the quadrupole interaction and becomes symmetric. In the paramagnetic HS state, however, not only the quadrupole interaction but also the paramagnetic interaction (dipolar interaction between  $^2\text{H}$  and paramagnetic  $\text{Fe}^{2+}$ ) affects the line shape of the  $^2\text{H}$  NMR spectrum. The dipolar interaction between  $^2\text{H}$  and paramagnetic ion causes the asymmetric  $^2\text{H}$  NMR line shape, since this interaction is anisotropic and the directions of its principal axes are different from those of the quadrupole interaction (Fig. 12.21). The spectra for the paramagnetic HS state were simulated as a four-site flip of pyrazine rings along the  $C_4$

**Fig. 12.20** Temperature dependence of a  $^2\text{H}$  NMR spectrum for  $\{\text{Fe}([\text{D}_4]\text{pz})[\text{Pt}(\text{CN})_4]\}$  [30]



axis, considering the contribution of the paramagnetic shift of three kinds of nearest-neighbor  $\text{Fe}^{2+}$  (Fig. 12.21).  $e^2qQ/h = 165 \text{ kHz}$  and  $\eta = 0$  were used for the simulation. The distance and angle between deuterium and  $\text{Fe}^{2+}$  for the simulation were extrapolated from the crystal structure of  $\{\text{Fe}(\text{pz})[\text{Pt}(\text{CN})_4]\}$ . The distances between deuterium and the first-, second-, and third-nearest  $\text{Fe}^{2+}$  are 3.17, 5.39, and 5.78 Å, respectively. Euler angles were  $(\alpha_{Q1}, \alpha_{Q2}, \alpha_{Q3}, \alpha_{Q4}) = (0^\circ, 90^\circ, 180^\circ, 270^\circ)$ ,  $\beta_Q = 60^\circ$  for the quadrupole interaction, and  $\beta_{Pi1} = 42.9^\circ$ ,  $\beta_{Pi2} = 23.7^\circ$ ,  $\beta_{Pi3} = 66.3^\circ$  for dipolar interactions between deuterium and three nearest-neighbor  $\text{Fe}^{2+}$ . The dipolar interactions between deuterium and  $\text{Fe}^{2+}$  were calculated using observed magnetic susceptibility values and Eq. (12.10). The anisotropic spin–spin relaxation was not considered for the simulation. It was determined that the rotation rate,  $k$ , of pyrazine was  $>10^8 \text{ Hz}$  at 300 and 290 K in the hysteresis loop. For comparison, the simpler two-fold jump model was also simulated with flip angles of both  $90^\circ$  and  $180^\circ$ , but these simulations failed to reproduce the measured spectra (Fig. 12.22). The contribution of the paramagnetic shift from nearest-neighbor iron ions to the  $^2\text{H}$  NMR spectrum was confirmed (Fig. 12.23). In the cooling process from 300 K, the rotation of pyrazine was remarkably suppressed by the spin transition below 280 K. The symmetric spectra for the diamagnetic LS state were

**Fig. 12.21** Principal axis systems of quadrupole interaction and paramagnetic dipolar interaction



$x_Q, y_Q, z_Q$ : Principal axes of EFG tensor  
 $x_{Dj}, y_{Dj}, z_{Dj}$ : Principal axes of paramagnetic dipolar interaction

**Fig. 12.22** Spectral simulation of two-fold jump model of the p<sub>z</sub> ring.  
 Reprinted with the permission from Ref. [30]. Copyright 2011 American Chemical Society

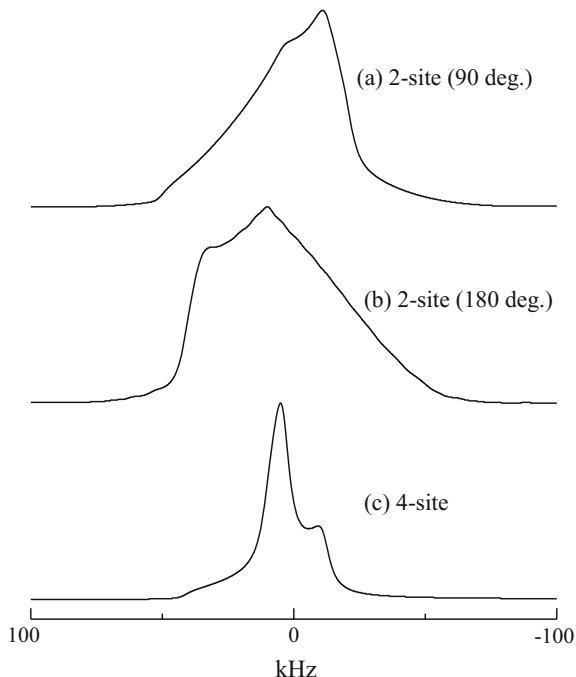
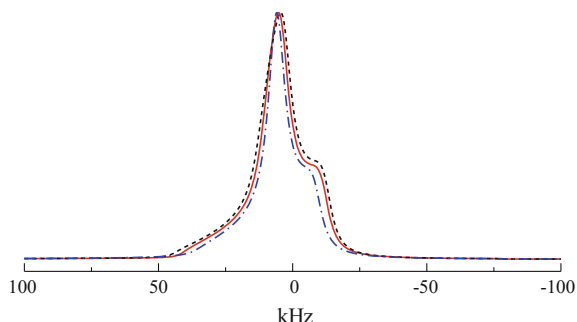


**Fig. 12.23** Contribution of paramagnetic shifts to the  $^2\text{H}$  NMR spectrum. Blue dashed line, black broken line, and red solid line show the simulation spectrum including one, two, and three nearest-neighbor iron ions, respectively



also analyzed as a 4-site flip motion and gave a rotational rate of  $3 \times 10^5$  Hz at 260 K. In the heating process from 260 to 300 K, the rotational rate gradually increased with heating ( $7 \times 10^5$  Hz at 280 K and  $2 \times 10^6$  Hz at 290 K), and then the shape returned to the initial distorted line shape at 300 K. The activation energy for the rotation of pyrazine was estimated to be  $33 \text{ kJ mol}^{-1}$  by an Arrhenius plot of  $k$ , with a pre-exponential factor of  $1.1 \times 10^{12}$  Hz.

Thus, as can be assessed from a  $^2\text{H}$  NMR investigation, the pyrazine ring rotates almost freely in the HS state, while rotation is suppressed in the LS state. The connection of the mobility with the switch of the spin state is expected, taking into account that spin-crossover is an entropy-driven phenomenon: the LS state is the ground state of the system at very low temperatures, while the HS state becomes the ground state at high temperatures. The difference in energy is thermally compensated by the higher entropy of the HS state, which mainly stems from electronic and vibrational contributions. In the case of  $\{\text{Fe(pz)}[\text{Pt}(\text{CN})_4]\}$ , the change in rotation velocity of the pyrazine rings may contribute considerably to this variation in entropy, thereby influencing the spin transition process.

## 12.7 Summary

Line shape analysis of a  $^2\text{H}$  NMR spectrum using spectral simulation is a powerful method for studying molecular motions in solid materials. The dynamics in nano-space of porous materials, which is correlated with their adsorption and reaction properties, can be analyzed by the  $^2\text{H}$  NMR spectral simulation method. The mode and rate of molecular motion over a wide dynamic range can be investigated using a broad line spectrum and a QCPMG spectrum. A combination of  $^2\text{H}$  NMR broad line spectra and QCPMG spectra is very effective for the analysis of dynamic inhomogeneity, which is closely related to the functions of polymers. The simulation of a  $^2\text{H}$  NMR spectrum, including the quadrupole interaction and paramagnetic effects, is indispensable for the analysis of molecular motion in paramagnetic materials. Although the point particle model, which ignores the delocalization of the unpaired electron and which was used to calculate the

paramagnetic dipolar interaction in this chapter, seems rather simple, the  $^2\text{H}$  NMR spectra of the paramagnetic metal complex were well reproduced by the simulation. Thus, the application of this simulation method to the analysis of various paramagnetic materials is expected.

## References

1. Vold, R.R.: Deuterium NMR studies of dynamics in solids and liquid crystals. In: Tycko, R. (ed.) Nuclear Magnetic Resonance Probes of Molecular Dynamics, pp. 27–112. Kluwer, Norwell (1994)
2. Vold, R.R., Vold, R.L.: Deuterium relaxation in molecular solids. In: Warren, W.S. (ed.) Advances in Magnetic and Optical Resonance, vol. 16, pp. 85–171. Academic Press Inc, San Diego (1991)
3. Schmidt-Rohr, K., Spiess, H.W.: Multidimensional Solid-State NMR and Polymers. Academic Press, London (1994)
4. Greenfield, M.S., Ronemus, A.D., Vold, R.L., Vold, R.R., Ellis, P.D., Raidy, T.E.: Deuterium quadrupole-echo NMR spectroscopy. III. Practical aspects of lineshape calculations for multiaxis rotational processes. *J. Magn. Reson.* **72**, 89–107 (1987)
5. Barbara, T.M., Greenfield, M.S., Vold, R.L., Vold, R.R.: Deuterium quadrupole echo NMR spectroscopy. I. Effects of chemical exchange during single and composite pulses. *J. Magn. Reson.* **69**, 311–330 (1986)
6. Long, J.R., Ebelhauser, R., Griffin, R.G.:  $^2\text{H}$  NMR line shapes and spin–lattice relaxation in  $\text{Ba}(\text{ClO}_3)_2 \cdot ^2\text{H}_2\text{O}$ . *J. Phys. Chem. A* **101**, 988–994 (1997)
7. Wittebort, R.J., Olejniczak, E.T., Griffin, R.G.: Analysis of deuterium nuclear magnetic resonance line shapes in anisotropic media. *J. Chem. Phys.* **86**, 5411–5420 (1987)
8. Hiyama, Y., Silverton, J.V., Torchia, D.A., Gerig, J.T., Hammond, S.J.: Molecular structure and dynamics of crystalline p-fluoro-D<sub>2</sub>L-phenylalanine. A combined X-ray/NMR investigation. *J. Am. Chem. Soc.* **108**, 2715–2723 (1986)
9. Araya, T., Niwa, A., Mizuno, M., Endo, K.: Dynamics of  $[\text{Zn}(\text{D}_2\text{O})_6]^{2+}$  in  $[\text{Zn}(\text{D}_2\text{O})_6][\text{SiF}_6]$  crystal as studied by 1D, 2D spectra and spin-lattice relaxation time of  $^2\text{H}$  NMR. *Chem. Phys.* **344**, 291–298 (2008)
10. Larsen, F.H., Jakobsen, H.J., Ellis, P.D., Nielsen, N.C.: Molecular dynamics from  $^2\text{H}$  Quadrupolar Carr–Purcell–Meiboom–Gill solid-state NMR spectroscopy. *Chem. Phys. Lett.* **292**, 467–473 (1998)
11. Shiminovitch, D.J., Rance, M., Jeffrey, K.R., Brown, M.F.: The quadrupolar spectrum of a spin  $I = 1$  in a lipid bilayer in the presence of paramagnetic ions. *J. Magn. Reson.* **58**, 62–75 (1984)
12. Antonijevic, S., Wimperis, S.: Refocussing of chemical and paramagnetic shift anisotropies in  $^2\text{H}$  NMR using the quadrupolar-echo experiment. *J. Magn. Reson.* **164**, 343–350 (2003)
13. Lin, T.-H., DiNatale, J.A., Vold, R.R.: Determination of molecular reorientation rates and electron-nuclear coupling in paramagnetic materials by deuterium solid echo NMR spectroscopy. *J. Am. Chem. Soc.* **116**, 2133–2134 (1994)
14. Mizuno, M., Hamada, Y., Kitahara, T., Suhara, M.: Deuterium NMR study of unstable phenomena and water molecular dynamics in samarium nitrate hexahydrate crystal. *J. Phys. Chem. A* **103**, 4981–4985 (1999)
15. Mizuno, M., Iijima, T., Suhara, M.: Dynamical Structure of Paramagnetic  $[\text{M}(\text{H}_2\text{O})_6][\text{SiF}_6]$  ( $\text{M}=\text{Fe}^{2+}$ ,  $\text{Ni}^{2+}$ ) crystal studied by means of  $^2\text{H}$  nuclear magnetic resonance. *J. Phys. Condens. Matter* **12**, 7261–7273 (2000)
16. Mizuno, M., Itakura, N., Endo, K.: Effects of strong paramagnetic interactions on solid-state deuterium NMR spectra. *Chem. Phys. Lett.* **416**, 358–363 (2005)

17. Rose, M.E.: Elementary Theory of Angular Momentum. Wiley, New York (1957)
18. Bloom, M., Davis, J.H., Valic, M.I.: Spectral distortion effects due to finite pulse widths in deuterium nuclear magnetic resonance spectroscopy. *Can. J. Phys.* **58**, 1510–1517 (1980)
19. Tanaka, D., Masaoka, S., Horike, S., Furukawa, S., Mizuno, M., Endo, K., Kitagawa, S.: Porous coordination polymer with  $\pi$  Lewis acidic pore surface,  $\{[\text{Cu}_3(\text{CN})_3\{\text{hat}-(\text{CN})_3(\text{OEt})_3\}] \cdot 3\text{THF}\}_n$ . *Angew. Chem. Int. Ed.* **45**, 4628–4631 (2006)
20. Horike, S., Matsuda, R., Tanaka, D., Matsubara, S., Mizuno, M., Endo, K., Kitagawa, S.: Dynamic motion of building blocks in porous coordination polymers. *Angew. Chem. Int. Ed.* **45**, 7226–7230 (2006)
21. Takamizawa, S., Nataka, E., Akatsuka, T., Miyake, R., Kakizaki, Y., Takeuchi, H., Maruta, G., Takeda, S.: Crystal transformation and host molecular motions in  $\text{CO}_2$  adsorption process of a metal benzoate pyrazine ( $\text{M}^{\text{II}} = \text{Rh}, \text{Cu}$ ). *J. Am. Chem. Soc.* **132**, 3783–3792 (2010)
22. Hijikata, Y., Horike, S., Tanaka, D., Groll, J., Mizuno, M., Kim, J., Takatade, M., Kitagawa, S.: Differences of crystal structure and dynamics between soft porous nanocrystal and bulk crystal. *Chem. Commun.* **47**, 7632–7634 (2011)
23. Zhu, K., Vukotic, V.N., O'Keefe, C.A., Schurko, R.W., Loeb, S.J.: Metal-organic frameworks with mechanically interlocked pillars: controlling ring dynamics in the solid-state via a reversible phase change. *J. Am. Chem. Soc.* **136**, 7403–7409 (2014)
24. Inukai, M., Fukushima, T., Hijikata, Y., Ogiwara, N., Horike, S., Kitagawa, S.: Control of molecular rotor rotational frequencies in porous coordination polymers using a solid-solution approach. *J. Am. Chem. Soc.* **137**, 12183–12186 (2015)
25. Chun, H., Dybtsev, D.N., Kim, H., Kim, K.: Synthesis, X-ray crystal structures, and gas sorption properties of pillared square grid nets based on paddle-wheel motifs: implications for hydrogen storage in porous materials. *Chem. Eur. J.* **11**, 3521–3529 (2005)
26. Bureekaew, S., Horike, S., Higuchi, M., Mizuno, M., Kawamura, T., Tanaka, D., Yanai, N., Kitagawa, S.: One-dimensional imidazole aggregate in aluminum porous coordination polymers with high proton conductivity. *Nature Mater.* **8**, 831–836 (2009)
27. Sevil, F., Bozkurt, A.: Proton conducting polymer electrolytes on the basis of poly(vinylphosphonic acid) and imidazole. *J. Phys. Chem. Solids* **65**, 1659–1662 (2004)
28. Mizuno, M., Iwasaki, A., Umiyama, T., Ohashi, R., Ida, T.: Local structure and dynamics of imidazole molecules in proton-conducting poly(vinylphosphonic acid)-imidazole composite material. *Macromolecules* **47**, 7469–7476 (2014)
29. Lee, Y.J., Murakhtina, T., Sebastiani, D., Spiess, H.W.:  ${}^2\text{H}$  solid-state NMR of mobile protons: it is not always the simple way. *J. Am. Chem. Soc.* **129**, 12406–12407 (2007)
30. Hansen, M.R., Graf, R., Spiess, H.W.: Solid-state NMR in macromolecular systems: insights on how molecular entities move. *Acc. Chem. Res.* **46**, 1996–2007 (2013)
31. Rodríguez-Velamazán, J.A., González, M.A., Real, J.A., Castro, M., Muñoz, M.C., Gaspar, A.B., Ohtani, R., Ohba, M., Yoneda, K., Hijikata, Y., Yanai, N., Mizuno, M., Ando, H., Kitagawa, S.: A switchable molecular rotator: neutron spectroscopy study on a polymeric spin-crossover compound. *J. Am. Chem. Soc.* **134**, 5083–5089 (2012)

# Chapter 13

## NMR Spectral Observations of the Gases in Polymer Materials

Hiroaki Yoshimizu

**Abstract** The gas transport properties of polymeric materials, including sorption, diffusion, and permeation, are closely related to the structural characteristics of the polymers. As a result, the analysis of polymers exposed to certain gases by NMR spectroscopy can determine detailed correlations between gas sorption and diffusion in the polymer and high-order structurers. One such method involving the analysis of  $^{129}\text{Xe}$  NMR chemical shifts is presented herein. This chapter also discusses the estimation of gas diffusion properties from the peak widths in the NMR spectra of polymers, as well as from data generated using pulsed field gradient NMR.

**Keywords**  $^{129}\text{Xe}$  NMR • PFG NMR • Polymer • Gas sorption • Gas diffusion

### 13.1 Introduction

The fuel sources used by humans have progressed through coal (a solid fuel) through petroleum (a liquid) to natural gas. At present, another gas, hydrogen, is one of the most important gaseous fuels associated with the pursuit of sustainable energy, so new technologies related to the controlled transport of gases are required. These technologies include the development of novel materials for applications such as transfer tubes, cylinders, gaskets, and permselective membranes. Advanced techniques for the characterization of such materials are also necessary. In particular, the development of polymeric materials acting as high-performance gas permeable membranes or barriers necessitates an understanding of the gas transport properties in such materials, including sorption, diffusion, and permeation. Conversely, because gas transport properties in a polymer are affected by both static and dynamic structural characteristics, it is possible to analyze the structures of macromolecules by assessing gas transport properties. Our own research group has

---

H. Yoshimizu (✉)

Graduate School of Engineering, Nagoya Institute of Technology,  
Nagoya, Aichi, Japan

e-mail: yoshimizu.hiroaki@nitech.ac.jp

been examining the applications of NMR techniques to the assessment of various structural properties of polymeric materials, focusing on the correlations of structure with gas transport characteristics. The present chapter discusses the manner in which the fine structure of polymeric solids can be characterized based on NMR spectroscopy, using gaseous probe molecules. One advantage of this NMR technique is that both gas transport properties and high-order structural information for the polymer can be obtained. For additional information, the reader is referred to our publications regarding the structural analyses of polymeric materials by means of  $^{129}\text{Xe}$  NMR spectroscopy [1–4].

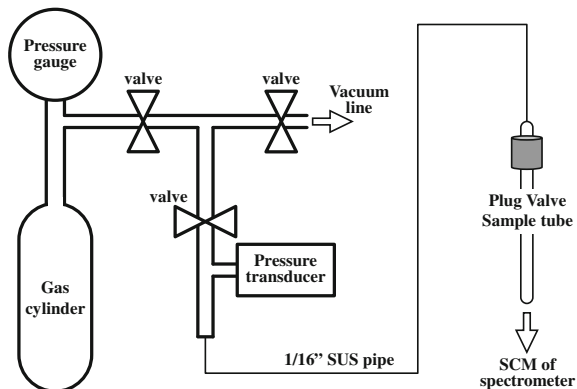
## 13.2 Basics of the NMR Analysis of Gas–Polymer Systems

This chapter does not address the newest and/or advanced NMR techniques but rather presents data primarily recorded using the single-pulse method in conjunction with standard commercial NMR spectrometers with typical solution NMR probes. The exception is that the analysis of relatively high-pressure gases requires special NMR tubes with thick, hardened walls. Fortunately, commercial NMR tubes that can withstand internal pressures up to approximately 1 MPa are readily available, and the development of improved tubes capable of safely containing pressures up to 10 MPa is anticipated in the near future.

### 13.2.1 Apparatus for the Preparation of NMR Sample Tubes Containing High-Pressure Gas Samples

Herein, the sample tubes and gaseous introduction apparatus are described. Our group typically uses commercially available NMR tubes with thick glass walls and a PTFE plug valve that can be easily and repeatedly connected to a narrow-bore stainless steel gas line. This valve is readily attached and removed, so that the sample gas (up to a pressure of approximately 1 MPa) can be easily introduced solely by operating the valve. Inserting and removing a polymer sample is also simple. Figure 13.1 shows a schematic diagram of an apparatus for introducing gas samples to NMR tubes of our own design. Using the integrated pressure gauge and transducer, the operator can introduce gas into the NMR tube to the desired pressure. The stainless steel gas line purposely has a length of several meters so that the sample tube can be situated within the field of the superconducting NMR magnet. This apparatus also allows for real-time monitoring of the pressure in the NMR tube throughout the trial, as well as variable temperature measurements. Following each experiment, the gas used for the measurements can be easily retrieved from the NMR tube by cooling an attached 50ml stainless steel gas storage cylinder with liquid nitrogen.

**Fig. 13.1** A schematic diagram of the laboratory-made apparatus employed for introducing gas into an NMR sample tube having thick walls and incorporating a plug valve



### 13.2.2 Gas Sorption Properties of Polymers

The gas transport properties of rubbery polymers can generally be described based on Fick's theory [5, 6] of gas–liquid systems, but this theory is not applicable in the case of glassy polymers. A glassy polymer is in a state of thermodynamic non-equilibrium and thus includes excess free volume (unrelaxed volume). While the gas sorption isotherms of rubbery polymers will increase in direct proportion to pressure, those of glassy polymers are typically concave along the pressure axis. This effect has been successfully explained by the dual-mode sorption model [7], in which the amount of gas adsorbed consists of the quantity predicted by Henry's law ( $C_D$ : where the subscript indicates "dissolved") and that predicted by the Langmuir mode ( $C_H$ : where the subscript indicates "hole"). This dual sorption is represented by the equation

$$C = C_D + C_H = k_D p + \frac{C'_H b p}{1 + b p}, \quad (13.1)$$

where  $C$  is the equilibrium sorption amount at a pressure,  $p$ , defined as the molar concentration of gas per unit volume of polymer (usually expressed in unit of  $\text{cm}^3$  (STP)/ $\text{cm}^3_{\text{polym}}$ ), corresponding to the density of the gas in the polymer. The hole saturation constant in the Langmuir sorption mode,  $C'_H$ , generally corresponds to the unrelaxed volume in the glassy polymer.

As an example, Fig. 13.2 shows the isotherms for the sorption of Xe in a polyphenylene oxide (PPO) sample at 25 °C, as obtained using the conventional gravimetric method ( $\diamond$ ) and a quantitative analysis of NMR signal intensity ( $\circ$ ). The data obtained from both methods are in good agreement and give almost the same line upon nonlinear least-squares regression with Eq. (13.1), as indicated by the solid curve in Fig. 13.2. This result suggests that NMR spectroscopy is a viable means of measuring gas sorption. There are two ways of the conversion from the NMR signal intensity to the absolute sorption amounts. One is using the sorption data obtained elsewhere, and another is using the intensity of the NMR peak which

**Fig. 13.2** Xe sorption isotherms of poly-2,6-dimethyl phenylene oxide (PPO) at 25 °C as obtained by NMR and conventional (gravimetric) methods

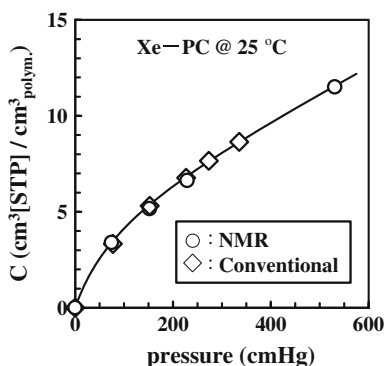
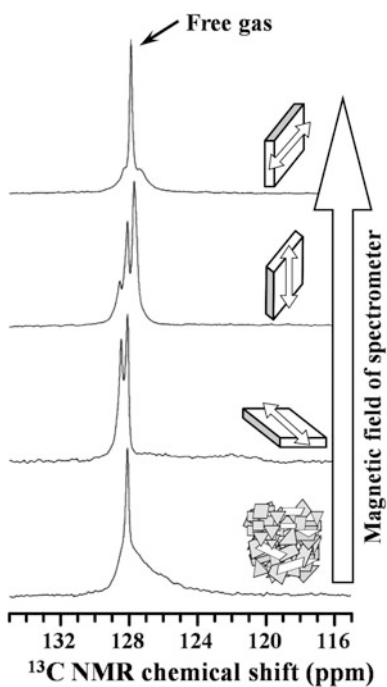


**Fig. 13.3** The 100 MHz  $^{13}\text{C}$  NMR spectra of  $^{13}\text{CO}_2$  in NMR sample tubes containing mono-axially drawn syndiotactic polystyrene (SPS) films at approximately 0.8 MPa and 25 °C. The inserted illustrations indicate the direction of the film relative to the magnetic field of the spectrometer.  $^{13}\text{C}$ -enriched carbon dioxide (approximately 98%) was employed in these trials



could be assigned to that of a free gas observed simultaneously. However, the assignment of free gas peak needs attentions. As a further example, the 100 MHz  $^{13}\text{C}$  NMR spectra of the  $^{13}\text{CO}_2$  in NMR sample tubes packed the drawn syndiotactic polystyrene (SPS) films at approximately 0.8 MPa and 25 °C are presented in Fig. 13.3. Each of these spectra was observed at the same temperature and pressure, but the direction of the film sample in the NMR tube was varied, as shown in the figure.  $^{13}\text{C}$ -enriched  $\text{CO}_2$  was used in this experiment, so the sharp peaks observed in each spectrum are readily assigned to the free gas in the tube. These peaks are split into doublets or triplets, with the exception of the spectrum obtained when

small pieces of the film are inserted into the tube at random. These results are primarily attributed to the anisotropic volume susceptibilities of the drawn SPS film samples. The CO<sub>2</sub> molecules at near the top and bottom edges, middle planes of the regularly stacked SPS films experience different magnetic field to some extent. But this susceptibility effect is sterically averaged when the small pieces of SPS films were randomly inserted into an NMR tube. This same effect will occur for any nuclei, so it must be taken into account during experimental analyses.

### 13.3 Characterization of the High-Order Structure of a Glassy Polymer Based on <sup>129</sup>Xe NMR Chemical Shifts

<sup>129</sup>Xe is an isotope with a natural abundance of approximately 26.4% and spin number  $I = 1/2$ . <sup>129</sup>Xe NMR allows for relatively high sensitivity, so Xe gas can be easily observed by NMR at relatively low pressures. The gyromagnetic ratio of <sup>129</sup>Xe is about 1.1 times that of <sup>13</sup>C, such that the resonant frequency for <sup>129</sup>Xe is close to that for <sup>13</sup>C, so <sup>129</sup>Xe spectroscopy can be performed using commercial spectrometers with standard multinuclear NMR probes. Furthermore, <sup>129</sup>Xe NMR is highly sensitive to the sorption environment due to the very high polarizability of the Xe atom. Therefore, the <sup>129</sup>Xe NMR chemical shifts are strongly correlated with the size and nature of micropores in the polymeric material, because interactions with the host system can modify the electron density of the Xe atom. This unique property has been demonstrated in studies utilizing inorganic cage compounds such as zeolites [8–12]. Recently, it was reported that various gas–polymer systems can be successfully characterized by <sup>129</sup>Xe NMR [13–22]. A review of this prior work is provided in references [1–4], but additional interpretations are presented herein.

The unrelaxed volume in a glassy polymer can play an important role in gas sorption by providing a source of microvoids, meaning the interspaces between polymer chains and <sup>129</sup>Xe NMR porosimetry can be applied for the determination of microvoid size in some glassy polymers. The chemical shift of Xe in a polymer is, in general, explained by Xe–Xe interactions as well as interactions between Xe and other atoms. These interactions increase when atomic distances are short, generating chemical shifts to lower-field values, the magnitudes of which depend on the size of the empty holes and the contribution of Xe–Xe interactions. The latter interactions will be proportional to the Xe density, meaning the extent of Xe sorption in the polymer. In the case of glassy polymers, a nonlinear relationship is observed between pressure and chemical shift, which is explained by assuming that the contributions of the Xe–Xe interactions at Henry and Langmuir sites are different. Specifically, the effect of the sorption amount at Langmuir sites on the <sup>129</sup>Xe NMR chemical shift is larger than that of sorption at Henry sites. This assumption is based on the dual-mode sorption model. That is, only a limited number of Langmuir sorption sites are formed, so that the extent of gas sorption at these sites is less than

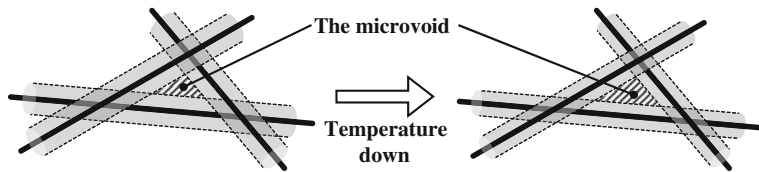


**Fig. 13.4** Schematic representation of the microvoid model (*slanted region*). The *solid line* indicates the center of the polymer chain. The *gray regions* along the *center line* indicate the occupied volume, with the free volume dependent on the molecular motions of the polymer chain. Details are provided in the text

that at Henry sites at high pressures, and gas molecules are preferentially adsorbed at the Langmuir sites. In addition, the disruption of Xe–Xe interactions by the molecular motions of polymer chain occurs much more frequently at Henry sites.

The above considerations are summarized by the model schematic shown in Fig. 13.4. Here, the straight bold line indicates the center line of a polymer chain, and the gray part along this line indicates the effective volume of the polymer chain including local molecular motions. This gray region therefore represents the volume occupied by the polymer and the free volume due to local molecular motions, which will be reduced with decreasing temperature. Because the larger segmental motions are frozen in the glassy state, the region that remains empty (the domain indicated by the slanted triangle) can be imagined as existing at the center of a triangle surrounded by three polymer chains. This domain can be defined as a microvoid, explaining why microvoids tend to expand with decreasing temperature. Previous studies of variable temperature measurements using PPO [21] and polycarbonate (PC) [23] have confirmed that the microvoid size as determined by analysis of  $^{129}\text{Xe}$  NMR chemical shifts increases with decreasing temperature. It is also evident that the temperature-extrapolated microvoids become smaller than a Xe atom as the temperature approaches the glass transition temperature of each polymer.

Since the Xe atoms in polymeric materials are in constant diffusive motion, the inter-atomic distance that affects the  $^{129}\text{Xe}$  NMR chemical shift can be related to the collision frequency of these atoms. A Xe atom contacting the gray region in Fig. 13.4 will collide with a polymer chain, and such collisions will occur repeatedly and continuously, such that the Xe atoms tortuously diffuse through the polymer. Xe atoms in this region will also collide with polymer chains much more frequently than with other Xe atoms. The scenario within a microvoid will be reversed, because of a lack of contact with polymer chains. These Xe atoms will collide with other Xe atoms more frequently. Experimental data are in good agreement with these predictions. The  $^{129}\text{Xe}$  NMR chemical shift of the Xe at Henry sites is predicted to be lower than that of Xe in Langmuir sites, indicating that the distance between Xe atoms and polymer chains at Henry sites is very short, such that they are almost in contact with one another. The chemical shift of the Xe at Langmuir sites is estimated to appear at high-field values, while Xe–Xe

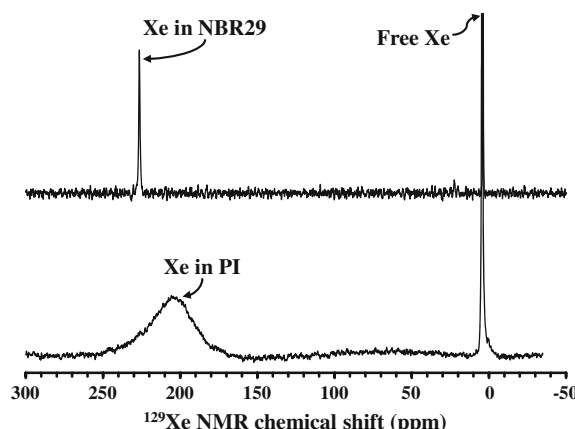
interactions will lead to significant low-field shifts. Thus, information regarding the microvoid structures in a glassy polymer can be obtained from the effect of the sorption amount on the  $^{129}\text{Xe}$  NMR chemical shift.

### 13.4 Characterization of the High-Order Structure of Rubbery Polymers from $^{129}\text{Xe}$ NMR Chemical Shifts

This section describes the analysis of rubbery polymers by  $^{129}\text{Xe}$  NMR. The micro-Brownian segmental motions of polymer chains are active in the rubbery state, meaning that the gray region in Fig. 13.4 expands and thus can be drawn without the slanted triangle (meaning the microvoid region). As discussed above, the gas sorption isotherms of glassy and rubbery polymers are different with one another, so it is necessary to use different analysis procedures and interpretations for each case.

As examples, the  $^{129}\text{Xe}$  NMR spectra of Xe in conjunction with a rubbery polymer (acrylonitrile–butadiene copolymer rubber with 29 mol% acrylonitrile, NBR29) and with a glassy polymer (polyimide, PI) at 25 °C are shown in Fig. 13.5. The sharp peaks observed at approximately 0 ppm are assigned to free Xe gas, and the associated chemical shifts are consistent with those of pure Xe gas at the same pressure and temperature. In contrast, the peaks assigned to Xe in these polymers are observed at approximately 205 ppm (in PI) and 228 ppm (in NBR29). Interestingly, the peaks obtained from the rubbery polymer are always sharper than those from the glassy material. This occurs because the gas diffusivity in a rubbery polymer is higher than that in a glassy polymer. This relationship between the peak width and diffusivity is discussed in more detail further on. The  $^{129}\text{Xe}$  NMR chemical shifts obtained from the rubbery polymer undergo a slight low-field shift

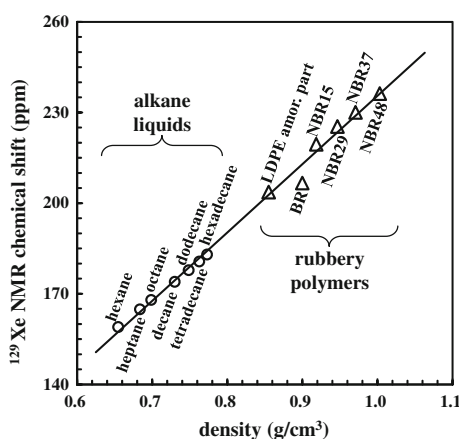
**Fig. 13.5** The 193.6 MHz  $^{129}\text{Xe}$  NMR spectra of free (gaseous) Xe and the Xe in acrylonitrile–butadiene copolymer rubber (with 29 mol% acrylonitrile; NBR29) and polyimide (PI) at 0.7 (NBR29) and 0.8 (PI) MPa and 25 °C



that is linearly correlated with increasing pressure. This linear shift can be explained by Henry's law, because the sorption amount will be proportional to the pressure. The variation in the chemical shift of the Xe-rubber polymer system is also considerably smaller than that in the Xe-glassy polymer system; in the range of Xe pressure from 0.1 to 0.8 MPa, a low-field shift of 2.9 ppm was observed for the Xe-NBR29 system, while the Xe-PI system showed a shift of 25 ppm. These data suggest that collisions between the Xe atoms tend to be disturbed by active micro-Brownian segmental motions.

The value of the  $^{129}\text{Xe}$  NMR chemical shift in a rubbery polymer extrapolated to a pressure value of nil depends on the degree of interaction between the Xe atoms and the polymer. This interaction becomes strong when the inter-atomic distance is short and, as a result, a low-field shift is induced. In Fig. 13.6, the extrapolated  $^{129}\text{Xe}$  NMR chemical shifts determined using liquid alkanes [24] and rubbery polymers are plotted against the host material densities. All these data are well represented by a single straight line, indicating that the  $^{129}\text{Xe}$  NMR chemical shift in a liquid or a rubbery polymer is useful for the estimation of density. It has been reported that, in the case of a liquid crystalline polyester with alkyl side chains, gas sorption only occurs within the aggregated side chain layer, allowing the density of this layer to be successfully estimated [20] even when conventional density measurements cannot be applied because of the coexistence of the polyester main chain. The density values estimated from the  $^{129}\text{Xe}$  NMR chemical shift in this case agreed with those predicted from X-ray structural analysis and gas solubility data. However, it should be noted that the  $^{129}\text{Xe}$  NMR peak generated by the PI appears at a higher-field position compared with that of the NBR29 (Fig. 13.5), although the density of PI ( $1.42 \text{ g/cm}^3$ ) is higher than that of NBR29 ( $0.947 \text{ g/cm}^3$ ). This result demonstrates that the density of a glassy polymer cannot always be estimated from the  $^{129}\text{Xe}$  NMR chemical shift. That is, the interpretation of the Xe data from a glassy polymer must take into consideration the effect of microvoids.

**Fig. 13.6**  $^{129}\text{Xe}$  NMR chemical shifts as a function of the density of various liquid alkanes and rubbery polymers at  $25^\circ\text{C}$

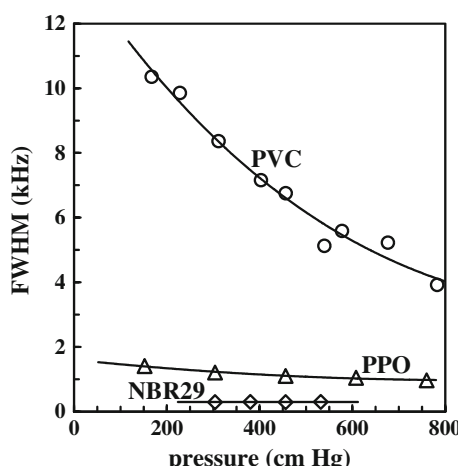


### 13.5 Analysis of Gas Diffusion Characteristics in Polymers Based on NMR Peak Width

During the technique described herein, small samples of polymeric solids are transferred into a sample tube and NMR spectra are acquired from the gas–polymer system without the use of deuterated solvents. Therefore, there is the possibility of significant sample inhomogeneity because of the anisotropic nature of the sample. Since the NMR peak width will be affected by inhomogeneity and by spin–spin relaxation, quantitative analysis of gas sorption in the polymer based on peak width is not possible. However, variations in the peak width with changes in temperature, pressure (which in turn affects the sorption amount), and polymer can be assessed. In this section, analyses based on the widths (as reflected in the full-width at half-maximum, FWHM) of NMR peaks generated by gases in polymers are described. As shown in Fig. 13.5, the FWHM of the Xe peaks obtained from a rubbery polymer is narrower than those obtained from a glassy polymer. This same effect is also observed during  $^1\text{H}$  NMR analyses using CH<sub>4</sub> [25]. The effects of pressure on the FWHM values of Xe peaks in conjunction with polyvinyl chloride (PVC), PPO, and NBR29 are summarized in Fig. 13.7. While the NBR29 spectra exhibit almost no FWHM changes with pressure, both the PVC and PPO undergo significant peak sharpening as the pressure is increased. The gas diffusion coefficients in these polymers as estimated from gas permeation, and sorption experiments are in the order PVC < PPO < NBR29. The FWHM values are also decreased by increasing the sample temperature, so it can be concluded that the FWHM of the peaks resulting from a gas in a polymer represents a measure of gas diffusivity.

The larger variation in the FWHM of peaks generated by glassy polymers can also be interpreted based on the dual-mode sorption model. The Xe atoms at Henry and Langmuir sorption sites are known to undergo rapid exchange, meaning that the

**Fig. 13.7**  $^{129}\text{Xe}$  NMR peak widths (FWHMs) obtained from analysis of poly(vinyl chloride) (PVC), PPO, and NBR29 at 25 °C as functions of Xe pressure. The solid curves indicate the results of curve fitting based on the dual-sorption model. Details are provided in the text



experimental FWHM values should be considered as the weighted averages of the fractions of the sorption amounts at both sites. Therefore, the experimentally observed FWHM (FWHM<sub>obs.</sub>) values can be described by the equation

$$\text{FWHM}_{\text{obs.}} = \phi_{\text{D}} \text{FWHM}_{\text{D}} + \phi_{\text{H}} \text{FWHM}_{\text{H}}, \quad (13.2)$$

where

$$\phi_{\text{D}} + \phi_{\text{H}} = C_{\text{D}}/C + C_{\text{H}}/C = 1, \quad (13.3)$$

and FWHM<sub>D</sub> and FWHM<sub>H</sub> are the virtual FWHM values of the peaks originating from the Xe at the Henry and Langmuir sites, respectively. The solid curves in Fig. 13.7 represent the fitting of the Xe sorption data using Eqs. (13.2) and (13.3). These results confirm that the value of FWHM<sub>D</sub> is much smaller than that of FWHM<sub>H</sub> for the Xe-PVC and PPO systems. In addition, similar results have been obtained for other Xe-glassy polymer systems, demonstrating that the diffusivity of a gas at Henry sites is much greater than that at Langmuir sites. The low diffusivity in glassy polymers can also be explained based on the effect of Langmuir sites, and the remarkably low diffusivity exhibited by PVC can likely be attributed to the presence of only a small number of isolated microvoids. The estimated FWHM<sub>H</sub> value for PPO also changes with temperature and with the sample preparation procedure (such as slow cooling and melt quenching), all of which can affect the gas diffusivity. In contrast, the FWHM<sub>D</sub> value shows only minimal variation. Together, these results indicate that the NMR peak width of a gas in a polymer can be applied to the characterization of the diffusivity of the gas in that material.

In an attempt to perform quantitative analysis based on peak widths, the spin–spin relaxation time ( $T_2$ ) of Xe in polymers was determined using the solid echo method. In some experiments, CH<sub>4</sub> was also used instead of Xe to confirm the universality of this method, since the sorption properties of CH<sub>4</sub> are similar to those of Xe but the diffusivity of CH<sub>4</sub> is higher than that of Xe due to molecular size effects. The experimental  $T_2$  values were readily determined from single exponential decay data and were found to correspond to the reciprocals of the FWHM values, demonstrating that FWHM data may be used to study diffusivity regardless of the nuclei being assessed. Figure 13.8 plots FWHM values against decay times obtained from solid echo experiments for CH<sub>4</sub> and Xe-PPO systems. In the case of PPO, both the peak intensity and FWHM are reduced during the  $T_2$  process. These findings indicate the distributions of  $T_2$ . If the only one component of  $T_2$  exists in the system, the peak intensity decays exponentially, but FWHM is not changed. The reciprocal value of FWHM is apparently related to  $T_2$ , and the change of FWHM during the  $T_2$  measurement, therefore, means the existence of the multi-component  $T_2$ . In other words, the diffusivity of the CH<sub>4</sub> and Xe in PPO over very short timescales is distributed to some extent, because the value of FWHM is influenced by diffusivity as mentioned above. The degree of reduction of the FWHM is therefore likely to be correlated with the distribution of diffusivity. Both optical and X-ray diffraction analyses demonstrated that the PPO was completely

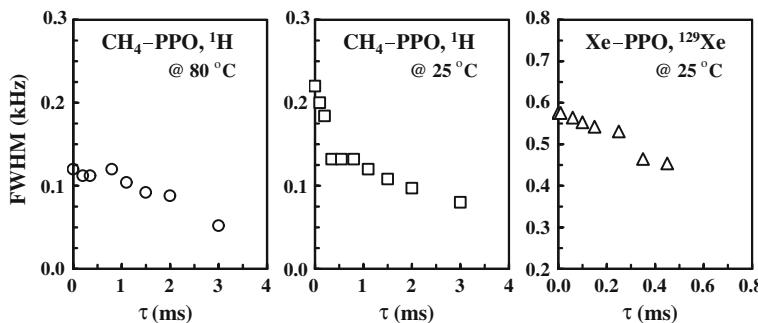
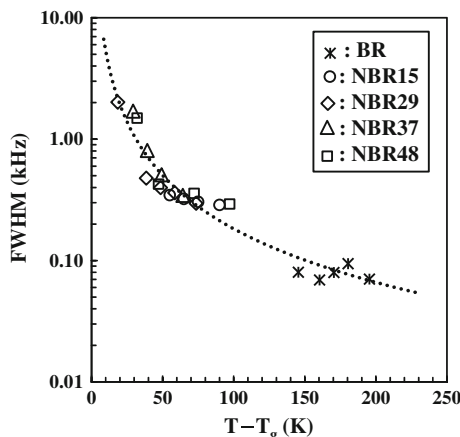


**Fig. 13.8**  $^1\text{H}$  and  $^{129}\text{Xe}$  NMR peak widths (FWHMs) obtained from  $\text{CH}_4$  and  $\text{Xe}$  in PPO as functions of the relaxation decay time,  $\tau$ , to determine spin–spin relaxation times by the solid echo method. Experimental conditions are indicated

amorphous. However, from the viewpoint of gas diffusivity, the amorphous structure of the PPO may have been slightly inhomogeneous, and it may be possible to detect this inhomogeneity on a very small timescale. The diffusing gas molecules can be expected to move through different regions of the samples in which the diffusivity varies, such that the observed diffusion behavior is actually an averaged value when the measurement is performed over a relatively long time span, or if the diffusivity of the gas is especially rapid. Since the observation time span used to assess the distribution of diffusivities is equal to an apparent  $T_2$ , this distribution will become narrower with increasing  $T_2$  values. Based on this discussion, the observed order of the reduction in FWHM values ( $\text{CH}_4$  at 80 °C <  $\text{CH}_4$  at 25 °C <  $\text{Xe}$  at 25 °C) is considered to be reasonable. It should also be noted that the fine high-order structure of PPO in the glassy state is inhomogeneous and thus will exhibit different gas diffusivities on the scale of several tens of nm based on the mean pathway length calculated using the diffusion coefficient and the apparent  $T_2$  at various experimental conditions. The glassy polymer PC, whose gas diffusion properties are lower than those of PPO, showed no change in FWHM values during solid echo measurements, indicating that the fine glassy state structure of PC is more homogeneous than that of PPO.  $T_2$  observations of gases in glassy polymers are therefore a useful means of characterizing the glassy state.

The FWHM values of the Xe peaks obtained from rubbery polymers are only minimally affected by pressure or by the  $^{129}\text{Xe}$  chemical shift, although the chemical shift is correlated with the density of the polymer, as discussed earlier. In general, the diffusion coefficient of a gas in a polymer has been understood based on the free volume theory [26]. Thus, in the case of rubbery polymers, the diffusion coefficient can be predicted from the  $^{129}\text{Xe}$  NMR chemical shift, while the FWHM values of the Xe peaks obtained from rubbery polymers also qualitatively correspond to the diffusivity. Despite this, the accuracy with which diffusion coefficients can be determined from FWHM data is less than that is possible using  $^{129}\text{Xe}$  NMR chemical shifts, because the FWHM is also affected by structural factors such as inhomogeneity due to

**Fig. 13.9** Plot of FWHMs as a function of the difference between observation ( $T$ ) and glass transition ( $T_g$ ) temperatures

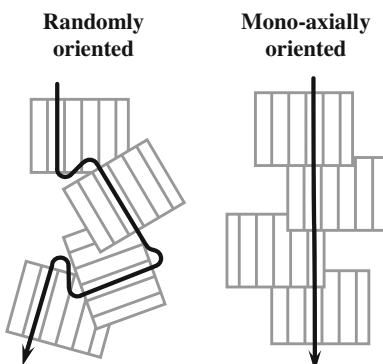


the volume susceptibility of the polymer pieces. However, the FWHM values of Xe peaks obtained from rubbery polymers exhibit an interesting trend with changes in temperature and type of polymer, indicating that the FWHM roughly correlates with the diffusivity of the Xe. Figure 13.9 shows a semilogarithmic plot of FWHM as a function of the difference between the experimental ( $T$ ) and glass transition ( $T_g$ ) temperatures. Although both density and  $T_g$  varied among the rubbery polymers employed to obtain these data, the FWHM values can be nearly normalized by the temperature difference ( $T - T_g$ ). This plot is similar to the temperature dependence of the shift factor,  $\alpha_T$ , which is derived from the well-known WLF equation [27]. Thus, the FWHM values in rubbery polymers, and by extension the Xe diffusivity, evidently are also affected by the polymer chain mobility.

### 13.6 Characterization of Oriented Structures by Pulsed Field Gradient NMR

It is known that self-diffusion coefficients can be determined by pulsed field gradient (PFG) NMR spectroscopy. Since this is a one-dimensional technique, the structural anisotropy of the polymeric material can be estimated from the anisotropic diffusion properties of gas and/or solvent molecules. As an example, the long-channel cavities in hexagonal columns composed of oriented polyester having dodecyl side chains have been successfully characterized using PFG NMR in conjunction with ethane as the probe molecule [28]. However, in many gas–glassy polymer systems, the gas diffusivity is too slow to determine the self-diffusion coefficient by the PFG method. In this section, a study [29] in which the gas diffusion anisotropy of molecularly oriented samples was determined is detailed. Figure 13.10 summarizes the gas diffusion paths in randomly and mono-axially oriented samples. Here, a single crystallite having anisotropic diffusivity is indicated by a striped square. When the

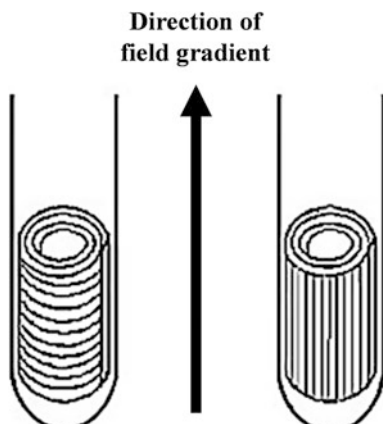
**Fig. 13.10** Schematic representing the model for the gas diffusion pathways (arrows) at a cross section in a polymer whose crystallites are arranged either randomly or mono-axially. The direction of gas diffusion is from *top to bottom*. The striped square indicates a single crystallite with anisotropic gas diffusion properties



crystallites are oriented randomly, the gas molecules must move tortuously, so diffusivity is low. In contrast, the diffusion pathway is relatively straight for long-range motion in the mono-axially oriented domains.

The form I crystal of poly 4-methyl-1-pentene (PMP) has four tetragonal 7/2 helical chains [30] and presents empty channel-like inter-chain spaces with mean diameters of approximately 0.4 nm along the helical axis of the PMP chains. It has been reported that only small gas molecules can penetrate into these spaces [16, 31]. Analyses using infrared dichroism and X-ray diffraction have confirmed that mono-axially oriented crystalline regions can be obtained by mono-axial drawing of a PMP film, with rod-like helical chains in these crystallites positioned parallel to the drawing direction. The relationship between the direction in which the film is positioned inside the NMR sample tube and molecular orientation is presented in Fig. 13.11, in which the drawing direction is indicated by stripes. Comparing the self-diffusion coefficients determined using two specially prepared sample tubes, information can be obtained concerning the anisotropy of the gas diffusivity. As an example, the  $^1\text{H}$  PFG NMR results obtained using  $\text{CH}_4$  in conjunction with a PMP

**Fig. 13.11** Schematic illustration of the directions of mono-axially drawn poly-4-methyl-1-pentene (PMP) films in NMR sample tubes. The drawing direction is indicated by *stripes*



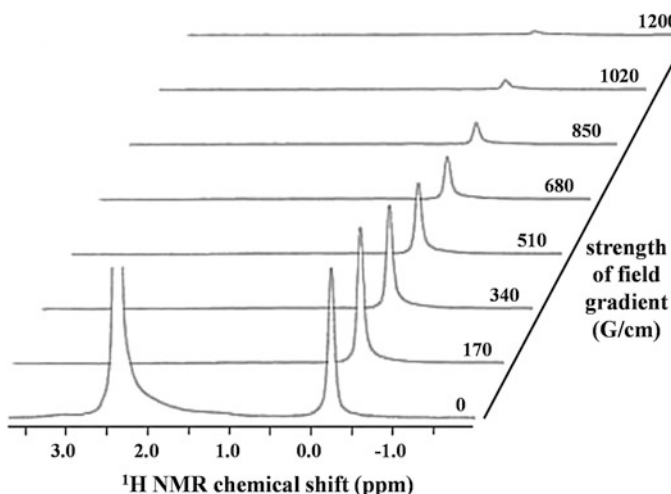


**Fig. 13.12** The 400 MHz  $^1\text{H}$  NMR spectra of the  $\text{CH}_4$  in an NMR tube packed with a drawn PMP film set perpendicular to the drawing axis (see the left side of Fig. 13.11), acquired at various PFG strengths ( $g$ ) at approximately 0.4 MPa and 25 °C. The PFG length ( $\delta$ ) and interval ( $\Delta$ ; the so-called diffusion and/or observation time) were 1.0 and 10 ms, respectively. A stimulated echo (STE) pulse sequence was used

film drawn perpendicular to the PFG direction (see the left side of Fig. 13.11) are shown in Fig. 13.12. The molecular mobility within the PMP film sample is too slow, such that peaks resulting from protons in the polymer are absent from the spectra. Therefore, all peaks in these spectra are assignable to  $\text{CH}_4$ . An intense peak appears in the low field at a PFG strength ( $g$ ) of 0 and can be assigned to free gaseous  $\text{CH}_4$ . This peak disappears upon applying the smallest  $g$  value of 170 G/cm, indicating rapid diffusion. In contrast, a relatively small peak appears in the high field, and the intensity of this peak decreases gradually with increasing  $g$ , meaning that this peak can be assigned to  $\text{CH}_4$  in the PMP film, having relatively low diffusivity. These findings demonstrate another application of PFG NMR as a technique for peak assignment.

In the case of undrawn PMP film, in which chains are randomly oriented in the crystallites, the same self-diffusion coefficient was obtained regardless of the direction in which the film was set in the NMR tube. However, the self-diffusion coefficient obtained when using drawn PMP film set parallel to the PFG direction (see the right side of Fig. 13.11) was approximately three times that obtained using a different orientation. This result indicates that the  $\text{CH}_4$  in a mono-axially oriented PMP film diffuses preferentially along the helical chains in the crystallites, as shown in Fig. 13.10. Similar studies using liquid crystalline polyesters [32] and polypeptides [33] have been reported elsewhere.

### 13.7 Summary

This chapter discussed the NMR spectroscopy data that can be obtained from numerous gas–polymer systems, in order to demonstrate that this technique allows the characterization of the fine structures and gas transport properties of polymeric materials.  $^{129}\text{Xe}$  NMR spectroscopy is one of the most powerful of these methods. In particular, the  $^{129}\text{Xe}$  NMR chemical shifts of polymeric materials can provide information regarding the density of rubbery polymers or the presence of microvoids in glassy materials, on both a qualitative and quantitative basis. In addition, the spectral intensity can be converted to units of gas sorption, and the peak width (equivalent to the spin–spin relaxation time) presents a measure of diffusivity. These features are independent of the nuclei being assessed, indicating that various gases can be applied. Because peak widths are typically in the range of several tens to tens of thousands of Hz, gas diffusivity can be observed on very short timescales. Furthermore, the PFG NMR analysis of gases in polymeric materials is useful for the determination of anisotropic gas diffusion properties and molecular orientations. In conclusion, the NMR spectral observation of gases in polymeric substances has significant potential as a means of studying both gas transport properties and fine high-order structures.

## References

1. Yoshimizu, H.: NMR characterizations of polymers using gases as probes. *J. Jpn. Soc. Color Mater.* **88**, 265–270 (2015). doi:[10.4011/shikizai.88.265](https://doi.org/10.4011/shikizai.88.265)
2. Yoshimizu, H.: Application of NMR spectroscopy to the characterization of gas separation membranes. *Sen'I Gakkaishi (J. Soc. Fiber Sci. Technol. Jpn.)* **68**, P\_323–P\_328 (2012). doi:[10.2115/fiber.68.P\\_323](https://doi.org/10.2115/fiber.68.P_323)
3. Yoshimizu, H.: Dependence of the amount of Xe sorption on the  $^{129}\text{Xe}$  NMR chemical shift in glassy polymers. In: Cheng, H.N., Asakura, T., English, A.D. (eds.) ACS Symposium Series 1077, pp. 509–523. American Chemical Society (2011). doi:[10.1021/bk-2011-1077.ch031](https://doi.org/10.1021/bk-2011-1077.ch031) (Chapter 31)
4. Yoshimizu, H., Suzuki, T., Tsujita, Y.: Characterization of polymers in the solid state by  $^{129}\text{Xe}$  NMR spectroscopy. *Sen'I Gakkaishi (J. Soc. Fiber Sci. Technol. Jpn.)* **60**, P\_498–P\_503 (2004). doi:[10.2115/fiber.60.P\\_498](https://doi.org/10.2115/fiber.60.P_498)
5. Kesting, R.E., Fritzsche, A.K. (eds.): *Polymeric Gas Separation Membranes*. Wiley Interscience, New York (1993)
6. Crank, J., Park, G.S. (eds.): *Diffusion in Polymers*. Academic Press, London (1968)
7. Micaels, A.S., Vieth, W.R., Barrie, J.A.: Solution of gases in polyethylene terephthalate. *J. Appl. Phys.* **34**, 1–12 (1963). doi:[10.1063/1.1729066](https://doi.org/10.1063/1.1729066)
8. Demarquay, J., Fraissard, J.:  $^{129}\text{Xe}$  NMR of xenon adsorbed on zeolites: relationship between the chemical shift and the void space. *Chem. Phys. Lett.* **136**, 314–318 (1987). doi:[10.1016/0009-2614\(87\)80258-0](https://doi.org/10.1016/0009-2614(87)80258-0)
9. Ripmeester, J.A., Ratcliffe, C.I., Tse, J.S.: The nuclear magnetic resonance of  $^{129}\text{Xe}$  trapped in clathrates and some other solids. *J. Chem. Soc. Faraday Trans. 1 Phys. Chem. Condens. Phases* **84**, 3731–3745 (1988). doi:[10.1039/F19888403731](https://doi.org/10.1039/F19888403731)

10. Fraissard, J., Ito, T.:  $^{129}\text{Xe}$  N.M.R. study of adsorbed xenon: a new method for studying zeolites and metal-zeolites. *Zeolites* **8**, 350–361 (1988). doi:[10.1016/S0144-2449\(88\)80171-4](https://doi.org/10.1016/S0144-2449(88)80171-4)
11. Ito, T., Springuel-Huet, M.A., Fraissard, J.:  $^{129}\text{Xe}$  N.M.R. study of xenon adsorbed on Na-Omega and Na and K ferrierite: Characterization of void spaces, defects, and intergrowth of ferrierite–mordenite structures. *Zeolites* **9**, 68–73 (1989). doi:[10.1016/0144-2449\(89\)90011-0](https://doi.org/10.1016/0144-2449(89)90011-0)
12. Ripmeester, J.A., Ratcliffe, C.I.: Application of xenon-129 NMR to the study of microporous solids. *J. Phys. Chem.* **94**, 7652–7656 (1990). doi:[10.1021/j100382a061](https://doi.org/10.1021/j100382a061)
13. Suzuki, T., Miyauchi, M., Takekawa, M., Yoshimizu, H., Tsujita, Y., Kinoshita, T.: Characterization of the microvoids in poly(2,6-dimethyl-1,4-phenylene oxide) by means of  $^{129}\text{Xe}$  NMR spectroscopy. *Macromolecules* **34**, 3805–3807 (2001). doi:[10.1021/ma001656f](https://doi.org/10.1021/ma001656f)
14. Suzuki, T., Miyauchi, M., Yoshimizu, H., Tsujita, Y.: Characterization of microvoids in glassy polymers by means of  $^{129}\text{Xe}$  NMR spectroscopy. *Polym. J.* **33**, 934–938 (2001). doi:[10.1295/polymj.33.934](https://doi.org/10.1295/polymj.33.934)
15. Suzuki, T., Yoshimizu, H., Tsujita, Y.: Characterization of microvoids in PPO/PS polymer blend by means of  $^{129}\text{Xe}$  NMR spectroscopy. *Desalination* **148**, 359–361 (2002). doi:[10.1016/S0011-9164\(02\)00730-0](https://doi.org/10.1016/S0011-9164(02)00730-0)
16. Suzuki, T., Tanaka, T., Nakajima, M., Yoshimizu, H., Tsujita, Y.: Characterization of the cavity in poly(4-methyl-1-pentene) crystal by gas permeation and  $^{129}\text{Xe}$  NMR measurements. *Polym. J.* **34**, 891–896 (2002). doi:[10.1295/polymj.34.891](https://doi.org/10.1295/polymj.34.891)
17. Suzuki, T., Yoshimizu, H., Tsujita, Y.: Analysis of gas transport properties of PPO/PS blends by  $^{129}\text{Xe}$  NMR spectroscopy. *Polymer* **44**, 2975–2982 (2003). doi:[10.1016/S0032-3861\(03\)00191-5](https://doi.org/10.1016/S0032-3861(03)00191-5)
18. Sivakumar, M., Suzuki, T., Yamamoto, Y., Mahesh, K.P.O., Yoshimizu, H., Tsujita, Y.: Structure and properties of the mesophase of syndiotactic polystyrene membrane: VII. Isothermal sorption behavior of xenon. *J. Membr. Sci.* **238**, 75–81 (2004). doi:[10.1016/j.memsci.2004.03.022](https://doi.org/10.1016/j.memsci.2004.03.022)
19. Tsukahara, T., Tsujita, Y., Yoshimizu, H., Kinoshita, T.: Structure, gas sorption, and gas diffusion of a low density liquid crystalline polyester. In: Pinnau, I., Freeman, B.D. (eds.) ACS Symposium Series 876, pp. 129–138 (2004). American Chemical Society (2004). doi:[10.1021/bk-2004-0876.ch008](https://doi.org/10.1021/bk-2004-0876.ch008) (Chapter 8)
20. Yoshimizu, H., Tsukahara, M., Suzuki, T., Toida, J., Ando, A., Watanabe, J., Tsujita, Y.: Layered structure and Xe sorption and diffusion properties of low-density liquid-crystalline polyesters with *n*-alkyl side chains. *J. Mol. Struct.* **739**, 19–26 (2005). doi:[10.1016/j.molstruc.2004.07.044](https://doi.org/10.1016/j.molstruc.2004.07.044)
21. Yoshimizu, H., Ohta, S., Asano, T., Suzuki, T., Tsujita, Y.: Temperature dependence of the mean size of microvoids of polyphenyleneoxide studied by analyses of Xe sorption and  $^{129}\text{Xe}$  NMR chemical shift. *Polym. J.* **44**, 821–826 (2012). doi:[10.1038/pj.2012.123](https://doi.org/10.1038/pj.2012.123)
22. Yoshimizu, H., Murakami, T., Suzuki, T., Tsujita, Y.: Characterization of the microvoids of a tetramethyl polycarbonate/polystyrene blend system using Xe sorption measurements and  $^{129}\text{Xe}$  NMR spectroscopy. *Polym. J.* **44**, 827–831 (2012). doi:[10.1038/pj.2012.128](https://doi.org/10.1038/pj.2012.128)
23. Higuchi, T., Yoshimizu, H.: Characterization of a glass state of polycarbonate by Xe sorption properties and Xe-129 NMR. *Polym. Prep. Jpn.* **61**, 4348–4349 (2012)
24. Stngle, T.R., Williamson, K.L.: Nuclear magnetic resonance of xenon absorbed in solid polymers: a probe of the amorphous state. *Macromolecules* **20**, 1428–1430 (1987). doi:[10.1021/ma00172a050](https://doi.org/10.1021/ma00172a050)
25. Yoshimizu, H., Okazawa, M., Jinno, S., Asano, T., Suzuki, T.: Characterizations of gas diffusion properties of polyphenyleneoxide in several glassy states by means of NMR spectroscopy. *Kobunshi Ronbunshu* **69**, 424–434 (2012). doi:[10.1295/koron.69.424](https://doi.org/10.1295/koron.69.424)
26. Bondi, A.: *Physical Properties of Molecular Crystals, Liquids, and Gasses*. Wiley, New York (1968)
27. Williams, M.L., Landel, R.F., Ferry, J.D.: The temperature dependence of relaxation mechanisms in amorphous polymers and other glass-forming liquids. *J. Am. Chem. Soc.* **77**, 3701–3707 (1955). doi:[10.1021/ja01619a008](https://doi.org/10.1021/ja01619a008)

28. Matsui, M., Yamane, Y., Kuroki, S., Ando, I., Fu, K., Watanabe, J.: Long-channel cavity and gas diffusion in liquid-crystalline polyester with *n*-alkyl side chains. *Ind. Eng. Chem. Res.* **44**, 8694–8698 (2005). doi:[10.1021/ie048785v](https://doi.org/10.1021/ie048785v)
29. Yoshimizu, H., Okumura, Y.: Gas transport properties of the crystalline phase controlled its orientation of poly(4-methyl-1-pentene). *Kobunshi Ronbunshu* **71**, 601–607 (2014). doi:[10.1295/koron.71.601](https://doi.org/10.1295/koron.71.601)
30. Kusanagi, H., Takase, M., Chatani, Y., Tadokoro, H.: Crystal structure of isotactic poly(4-methyl-1-pentene). *J. Polym. Sci. Polym. Phys. Edit.* **16**, 131–142 (1978). doi:[10.1002/pol.1978.180160112](https://doi.org/10.1002/pol.1978.180160112)
31. Yoshimizu, H., Fukatsu, H., Suzuki, T., Tsujita, Y., Kinoshita, T.: CO<sub>2</sub> permeation and diffusion properties of semicrystalline poly(4-methyl pentene-1) membranes. *Polym. J.* **30**, 981–984 (1998). doi:[10.1295/polymj.30.981](https://doi.org/10.1295/polymj.30.981)
32. Yoshimizu, H., Karakasa, T.: Magnetic orientation and gas diffusion properties of layered structures of liquid crystalline copolymers with alkyl side chains of different length. *Kobunshi Ronbunshu* **71**, 325–333 (2014). doi:[10.1295/koron.71.325](https://doi.org/10.1295/koron.71.325)
33. Iwamoto, J., Yoshimizu, H.: Structural analysis and gas diffusion properties of the solid oriented PBLG. In: Preparation 53rd Annual Meeting NMR Society Japan, pp. 348–349 (2014)

# **Chapter 14**

## **NMR Studies on Natural Product— Stereochemical Determination and Conformational Analysis in Solution and in Membrane**

**Nobuaki Matsumori and Michio Murata**

**Abstract** In this chapter we overview two topics on NMR methodologies for small molecules, mostly natural products; one is about the solution NMR-based methods used for stereochemical determination of natural products, and the other is on the solid-state and other techniques for investigating natural product-membrane interactions. Since important two methods for stereochemical analysis of natural products, namely the J-based configuration analysis (JBCA) and universal NMR database (UDB) methods, were reported in the 1990s, both methods have been widely used in the field of natural products. The newly coming RDC method is not the major method in the field of natural products yet, but will surely be an important tool for the stereochemical correlation between distant stereogenic centers, which could provide invaluable information as to the whole shape of natural products in solution. In the latter part of this chapter, we discuss the application of solid-state and other NMR techniques to membrane interaction analysis of natural products. In particular, we describe three examples of natural products that interact with biological membranes such as amphotericin B, erythromycin A, and theonellamide A. As shown in NMR studies of amphotericin B, natural products often reveal very high affinities for phospholipids and sterols in bilayer membranes. Solid-state NMR, therefore, provides a very promising approach toward the structure study of membrane-active complexes formed by natural products that have high affinity to lipids. In addition, solution NMR techniques can be applied to elucidate the

---

N. Matsumori  
Department of Chemistry, Graduate School of Sciences,  
Kyushu University, Fukuoka 819-0395, Japan

M. Murata (✉)  
Department of Chemistry, Graduate School of Science,  
Osaka University, Osaka 560-0043, Japan  
e-mail: murata@chem.sci.osaka-u.ac.jp

M. Murata  
Lipid Active Structure Project, Exploratory Research for Advanced  
Technology Organization (ERATO), Japan Science and Technology  
Agency (JST), Osaka University, Osaka 560-0043, Japan

structural features of membrane-bound small molecules such as antibiotic erythromycin A and membrane-disrupting cyclic peptide theonellamide A. Standard 2D  $^1\text{H}$ - $^1\text{H}$  experiments such as COSY (correlation spectroscopy), NOESY (nuclear Overhauser effect spectroscopy), and DOSY (diffusion-ordered spectroscopy) are often helpful in elucidating the membrane interaction between natural products and lipids.

**Keywords** Natural products • Stereochemical determination • Bicelles  
Solid-state NMR of membranes

## 14.1 Stereochemical Determination of Natural Products

In natural products chemistry, NMR spectroscopy is undoubtedly the most useful and important tool because NMR parameters provide fundamental information about not only the planar structures of natural products, but also their configuration and conformation [1]. In most cases, the molecular skeletons of natural products can be characterized by through-bond  $^1\text{H}$ - $^1\text{H}$  and  $^1\text{H}$ - $^{13}\text{C}$  correlation experiments such as COSY and HMBC. In addition, the evaluation of  $^1\text{H}$ - $^1\text{H}$  spin coupling constants ( $^3J_{\text{HH}}$ ), chemical shifts, and nuclear Overhauser effects (NOEs) allows the determination of the relative stereochemistry of cyclic compounds with rigid three to six-membered rings. In contrast, the relative configuration assignment of multiple-substituted acyclic chains and macrocycles as exemplified in Fig. 14.1 are more difficult, because the geometrical flexibility of such systems makes NOE intensities less reliable for stereochemical assignments. For example, assuming that a molecule has major and minor conformations and the interproton distance of interest is small in the minor conformation, the corresponding NOEs would be relatively strongly observed, even though the distance is out of NOE detection in the major conformation. This would cause misinterpretation of NOEs and mislead the stereochemical assignment of flexible natural products.

To address these issues in the relative configuration assignment of organic molecules, NMR-based approaches,  $J$ -based configuration analysis (JBCA) [2, 3], universal NMR database (UDB) [3–5], and theoretical calculation of NMR parameters [3, 6] were reported after the 1990s. More recently, residual dipolar couplings (RDCs) were utilized as a tool to determine the relative configuration of natural products [7, 8]. The modified Mosher's method involving the derivatization of chiral secondary alcohols and primary amines with  $\alpha$ -methoxy- $\alpha$ -trifluoromethyl- $\alpha$ -phenylacetic acid (MTPA) and comparison of chemical shifts has been widely used to determine absolute stereochemistry [9]. Although many other protocols such as circular dichroism measurement are also currently available [10], relative stereochemistry is mostly determined by the following methods: JBCA, UDB, and theoretical methods.

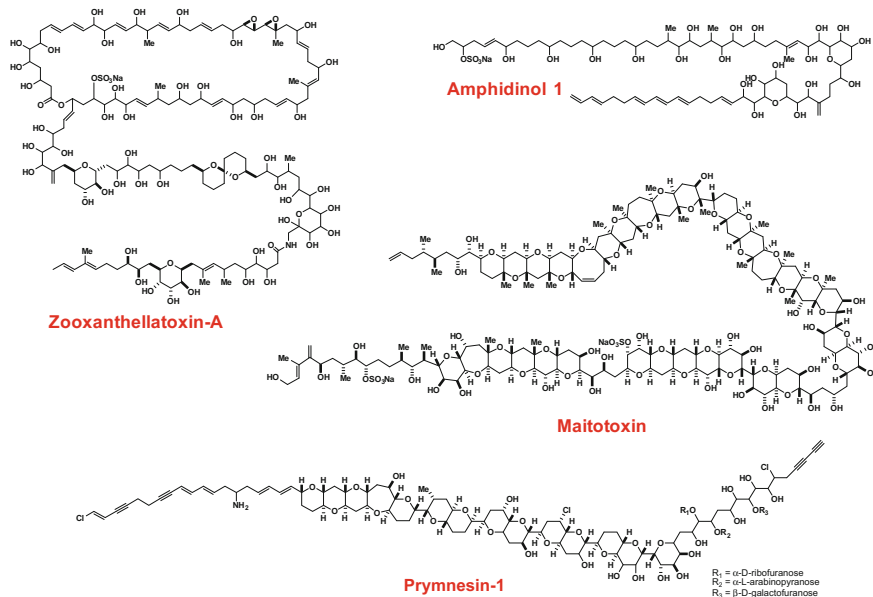


**Fig. 14.1** Representative marine natural products bearing multiple-substituted acyclic chains and macrocycles

### 14.1.1 JBCA Method

Until the 1990s, long-range C–H coupling constants ( $^{2,3}J_{\text{C},\text{H}}$ ) were seldom used for the conformational or configurational analysis of natural products, because, unlike biomolecules such as proteins and nucleic acids, it is difficult to achieve the isotopic enrichment of natural products. In the 1990s, more sensitive methods such as hetero-half-filtered TOCY (HETLOC) became available by detecting proton magnetization [11, 12]; this paved the way for the application of  $^{2,3}J_{\text{C},\text{H}}$  values in the conformational and configurational analysis of isotopically unenriched natural samples. Under these circumstances, the JBCA method was developed by Murata and co-workers in 1999 [2]. This method utilizes the empirical and qualitative Karplus-type dihedral angle dependence of not only  $^3J_{\text{H},\text{H}}$ , but also  $^{2,3}J_{\text{C},\text{H}}$  values (Fig. 14.2) to determine the relative stereochemistry of two adjacent or alternate stereocenters, commonly and frequently observed in the polysubstituted acyclic chains of natural products as shown in Fig. 14.1. In this section, basic concept of the JBCA method is briefly described.

As shown in Fig. 14.2,  $^3J_{\text{C},\text{H}}$  is known to follow a Karplus-type equation similar to  $^3J_{\text{H},\text{H}}$  [13]. In addition,  $^2J_{\text{C},\text{H}}$  also provides dihedral angle information when the  $\alpha$ -carbon has an electronegative substituent [14] (Fig. 14.2). In the JBCA method, the magnitude of coupling constants is qualitatively classified as small and large under the assumption that C–C bonds can be represented by three staggered

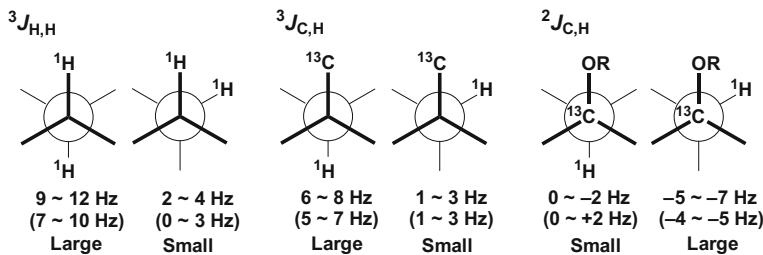


**Fig. 14.2** Empirical and qualitative Karplus-type dihedral angle dependence of coupling constants and their classification into large and small according to the magnitude of the absolute values. The parentheses indicate the values for 1,2-dioxygenated systems

rotamers (one *anti* and two *gauche*). This assumption is generally reasonable for acyclic carbon chains with less bulky substituents such as hydroxy and methyl groups, which hardly cause significant deviations from the staggered positions.

To assign the relative stereochemistry (*threo* and *erythro*) of a 1,2-dimethine system, six staggered rotamers possible in the *threo* and *erythro* diastereomers should be distinguished from one another (Fig. 14.3). Among these six rotamers, four rotamers, A-1, A-2, B-1, and B-2, can be specified using the qualitative magnitudes of  $^3J_{H,H}$ ,  $^2J_{C,H}$  and  $^3J_{C,H}$  values. However, two rotamers A-3 and B-3 with an H/H-*anti* orientation are still indistinguishable only from coupling constants. To identify these two *anti* conformers, the NOE information is obtained. In B-3 rotamer (Fig. 14.3), weak or no NOE (or ROE) should be observed between H-1 and H-4, whereas in A-3 rotamer, H-1 and H-4 should be closer to the NOE distance. Based on these criteria, all the six rotamers are distinguished, and their relative configuration (*threo* or *erythro*) can be determined accordingly.

The question is how many coupling constants are necessary to assign a specific rotamer out of the six rotamers. Because each rotamer shown in Fig. 14.3 can be defined by two *anti* arrangements, the coupling constants that specify two antiperiplanar relationships are enough to assign a single rotamer out of the six rotamers. For example, A-2 shown in Fig. 14.3 can be defined by the *anti* orientations of H-2/C4 and C1/H-3; therefore, two large  $^3J_{C,H}$  values for H-2/C4 and C1/H-3 are enough to specify this rotamer. Alternatively, for example, because the *anti* arrangement of H-2/C4 in A-2 rotamer is equivalent to the two *gauche* arrangements of H-2/H-3 and H-2/Y, the small  $^3J(H-2,H-3)$  and large  $^2J(H-2,C3)$  can compensate the lack of  $^3J(H-2/C4)$ . In this method, finding two antiperiplanar relations is the key to identify a specific rotamer. With this notion in mind, it is possible to assign the relative configuration of a rotamer by the step-by-step interpretation of coupling constants, as exemplified in Fig. 14.4, without referring to Fig. 14.3.

This analysis is applicable to methylene-spaced stereocenters such as 1,3-dimethine systems when prochiral methylene protons are stereospecifically labeled according to their chemical shifts. All the possible rotamers for a methine-methylene bond can be unambiguously distinguished using  $^3J_{H,H}$  and  $^{2,3}J_{C,H}$ . With

<b>A (Threo)</b>	<b>A-1</b>	<b>A-2</b>	<b>A-3</b>	
	$^3J$ (H-2, H-3) $^3J$ (H-2, C4) $^3J$ (C1, H-3)	Small Small Small	Large Large Large	Small Small Small
X=Me, Y=OR	$^3J$ (C <sub>X</sub> , H-3) $^2J$ (C3, H-2)	Large Small	Small Large	Small Large
X=OR, Y=OR	$^2J$ (C2, H-3) $^2J$ (C3, H-2)	Small Small	Large Large	Large Large
<b>B (Erythro)</b>	<b>B-1</b>	<b>B-2</b>	<b>B-3</b>	
	$^3J$ (H-2, H-3) $^3J$ (H-2, C4) $^3J$ (C1, H-3)	Small Large Small	Small Small Large	Large Small Small
X=Me, Y=OR	$^3J$ (C <sub>X</sub> , H-3) $^2J$ (C3, H-2)	Large Large	Small Small	Small Large
X=OR, Y=OR	$^2J$ (C2, H-3) $^2J$ (C3, H-2)	Small Large	Large Small	Large Large

**Fig. 14.3** JBCA for a 1,2-dimethine system. The expected magnitudes of coupling constants are listed for each rotamer. A combination of coupling constants can discriminate the rotamers except H/H-*anti* rotamers A-3 and B-3, which can be distinguished using NOEs

one methine–methylene relationship in hand, the same examination for the other methine–methylene relationship leads to the diastereomeric determination of the 1,3-dimethine via the stereospecific assignment of methylene protons. An example is shown in Fig. 14.5. The methylene protons on the C3 position are labeled as H3<sup>h</sup> (high-field proton) and H3<sup>l</sup> (low-field proton), respectively. For the C2–C3 bond, the observed coupling constants can specify the single rotamer (Fig. 14.5a). In this rotamer, the two antiperiplanar relations are H2/H3<sup>h</sup> and OH/H3<sup>l</sup>. Similarly, the rotamer for the C3–C4 bond was uniquely determined from the *anti* orientation for H3<sup>h</sup>/H4 and two *gauche* relations with respect to H3<sup>l</sup> (Fig. 14.5b). Then, the rotamers shown in Fig. 14.5a, b are connected at the C3 position so that the H3<sup>h</sup> and H3<sup>l</sup> in both the rotamers are consistent, thus establishing the diastereomeric relation between C2 and C4 as depicted in Fig. 14.5c.

The above analysis assumes a single and highly populated (>85%) rotamer in a C–C bond. However, this is not always the case for acyclic carbon chains. When multiple rotamers exist, averaged coupling constants, represented as medium *J* values, are observed owing to a conformational interconversion much faster than the NMR time scale. In most cases, the conformational equilibrium of a C–C bond

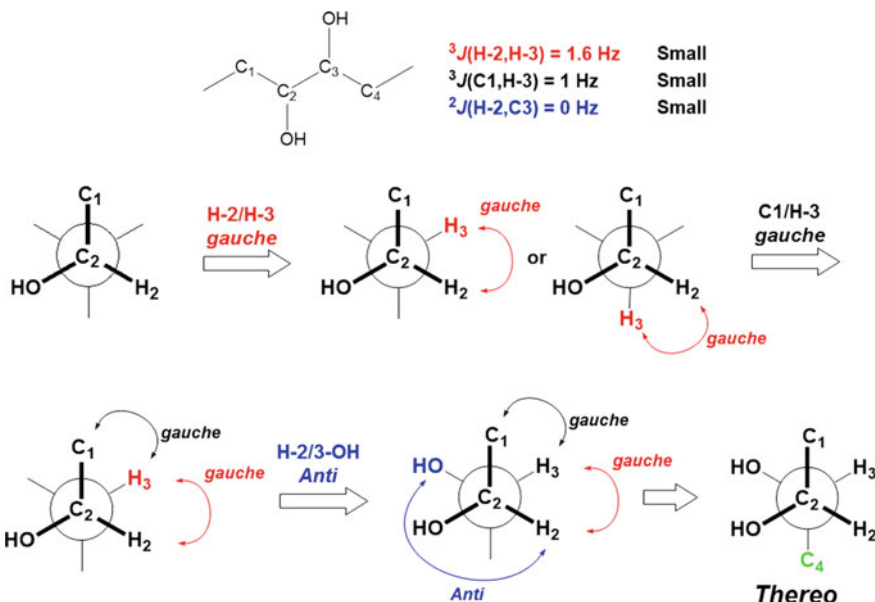


**Fig. 14.4** An example of the configuration assignment of a 1,2-dimethine system by the step-by-step interpretation of observed coupling constants. The H-3 position is determined by the two *gauche* relations of H-2/H-3 and C1/H-3. The 3-OH position is determined by *anti* H-2/3-OH relation derived from the small value of  $^2J(\text{H-2,C3})$ . Accordingly, the remaining C4 should be uniquely placed in the *anti* position of C1, and the relative configuration is assigned as *threo*

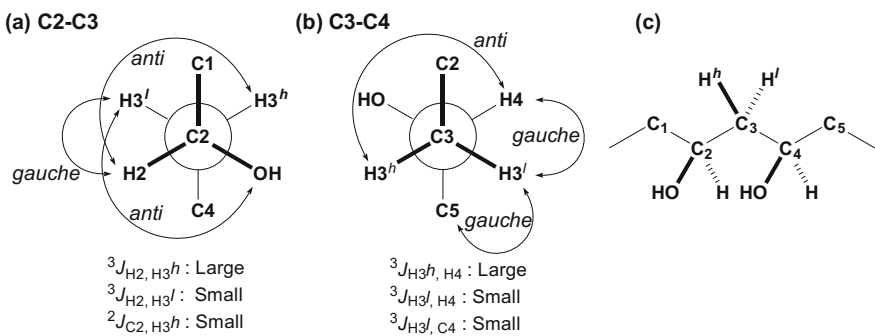
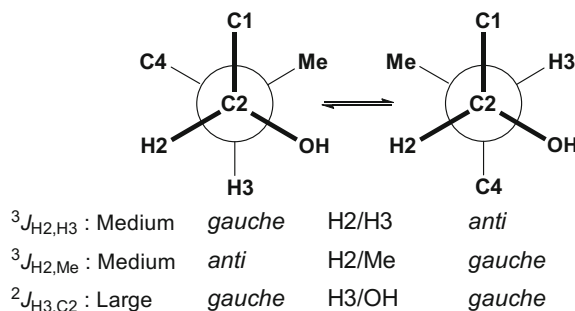


**Fig. 14.5** An example of stereochemical assignment of 1,3-stereocenters.  $\text{H}3^h$  and  $\text{H}3^l$  represent the diastereotopic methylene protons on C3 with chemical shifts at higher and lower fields, respectively

is assumed to be the interconversion between two major staggered rotamers. Figure 14.6 shows an example of relative stereochemistry determination in exchanging rotamers. The medium magnitude of  $^3J(\text{H-2,H-3})$  indicates the *gauche/anti* equilibrium of H-2/H-3 dihedral angles. The medium magnitude of  $^3J(\text{H-2,Me})$  is also indicative of equilibrium of *gauche/anti* between H2 and Me. The large

**Fig. 14.6** Stereochemical assignment of a C–C bond using the *J*-based method. A pair of equilibrating rotamers with *erythro* configuration can account for the observed coupling constants



value of  $^2J(\text{H-3,C2})$  further indicates two concurrent *gauche* arrangements of H-3/OH. These data indicate the equilibrium of two exchanging rotamers shown in Fig. 14.6, thus leading to the configuration assignment of the C–C bond as *erythro*.

When three staggered rotamers have comparable populations, all the *J* values fall into an intermediate category, and the *J*-based method cannot be applied to the system. If the population of a minor rotamer is less than ca. 10%, its contribution would be negligible, and the relative stereochemistry can be determined as the above discussed interconversion system between two major staggered rotamers.

Now that the introduction of  $^{2,3}J_{\text{C,H}}$  values provides a method for the stereochemical assignment in acyclic natural products, measurements of  $^{2,3}J_{\text{C,H}}$  are crucial for the success of this methodology. Since the 1990s, several practical methods have been proposed for the measurement of  $^{2,3}J_{\text{C,H}}$  [15], thanks to the introduction of inverse detection and pulse-field-gradient (PFG) technique. In the original paper reporting JBCA [2], two methods were used: HETLOC (hetero-half-filtered total correlation spectroscopy) [11, 12] and PS-HMBC (phase sensitive heteronuclear multiple bond correlation) [16]. The sensitivities of those methods are almost comparable to or slightly lower than conventional HMBC. The HETLOC experiment provides a  $^1\text{H}-^1\text{H}$  2D TOCSY-like spectrum, where each cross-peak is split by  $^1J_{\text{C,H}}$  along the  $F_1$  direction and dislocated by  $^{2,3}J_{\text{C,H}}$  along the  $F_2$  direction. This cross-peak feature of HETLOC allows efficient measurements of small  $^{2,3}J_{\text{C,H}}$  values. However, because HETLOC uses the TOCSY spin transfer, it cannot measure the coupling constants between protons and quaternary carbons or between protons and carbons belonging to different spin systems. To solve this problem, PS-HMBC experiments [16] were also introduced. In the PS-HMBC experiments, the relative cross-peak intensities arising from the same proton depend on the magnitude of  $^{2,3}J_{\text{C,H}}$  [16]. Therefore, the combined use of HETLOC and PS-HMBC can increase the number of observed  $^{2,3}J_{\text{C,H}}$  values. Several pulse sequences including *J*-HMBC [17], useful for estimating coupling constants between protons and quaternary carbons, were also reported for the estimation of  $^{2,3}J_{\text{C,H}}$  values. The *J*-HMBC signal amplitude of spectra shows the characteristic  $\sin(\pi^{2,3}J_{\text{C,H}}\tau)$ -dependence with increasing evolution time  $\tau$ , and thus accurate C–H coupling constants can be obtained by fitting a sine curve to the experimental data or by performing a 3D-version of *J*-HMBC.

The *J*-based method was first applied to maitotoxin [18] (Fig. 14.1), the largest secondary metabolite known to date, followed by dysiherbaine [19] and amphidinol 3 [20]. Since then, this method has been used for the structure determination of diverse natural products [3]. During the course of its application, this method has been modified according to each compound, thus becoming a robust method. For example, the application of the *J*-based method has been extended from stereocenters bearing methyl and hydroxy groups to those bearing amine and chloride groups [3].

### 14.1.2 UDB Method

Around the same time when the JBCA method was reported, Kishi et al. reported the UDB method, providing another powerful tool for determining relative stereochemistry [4, 5]. In the 1980s and 1990s, Kishi's group achieved the stereochemical assignments of multifunctional and complex acyclic natural products such as palytoxin [21], AAL toxins/fumonisins [22], and maitotoxin [23] through stereocontrolled synthesis. These studies demonstrated the following facts [4]: the NMR profiles of these natural products reflect the specific stereochemistry of the small substituents on the carbon backbone, independent of the other moieties in the molecules, and the steric and stereoelectronic interactions between the structural clusters separated by a two/more methylene bridge are negligible. Based on these experimental discoveries, they developed the principle of the UDB method for assigning the stereochemistry of (acyclic) compounds. A highly functionalized molecule can be considered as the sum of independent clusters of stereocenters (stereocluster), and the stereochemistry of each independent stereocluster can be determined from the NMR data ( $^{13}\text{C}$  chemical shifts were mainly used in the initial publications of UDB) comparison of the libraries of model compounds with stereochemically unknown natural products. One of the original demonstrations of this technique was carried out on the oasomycins [5]. To determine the stereochemistry of the stereocluster in the rectangle shown in Fig. 14.7, they built a library of model compounds with eight possible diastereoisomers (database 1) and compared their  $^{13}\text{C}$  chemical shifts with those of oasomycin B. According to Kishi's convention, the deviations ( $\Delta\delta$ ) are presented in a bar chart form (Fig. 14.7). Apparently, the deviations in  $^{13}\text{C}$  chemical shifts are the smallest in 1e, indicating that the relative stereochemistry at the C6–C9 of oasomycin B is the same as that of 1e.

Kishi's group created the libraries of stereoclusters (databases 2–5) and determined the stereochemistry of oasomycin (Fig. 14.8) [24]. Although the creation of a database requires the laborious organic synthesis of all the possible stereoisomers, once the database is available, it is universally applicable to the stereochemical determination of various natural compounds containing the stereocluster.

Later, Kishi's group created databases for contiguous polyols such as 1,2,3-triols, 1,2,3,4-tetraols, and 1,2,3,4,5-pentaols and extended the UDB method

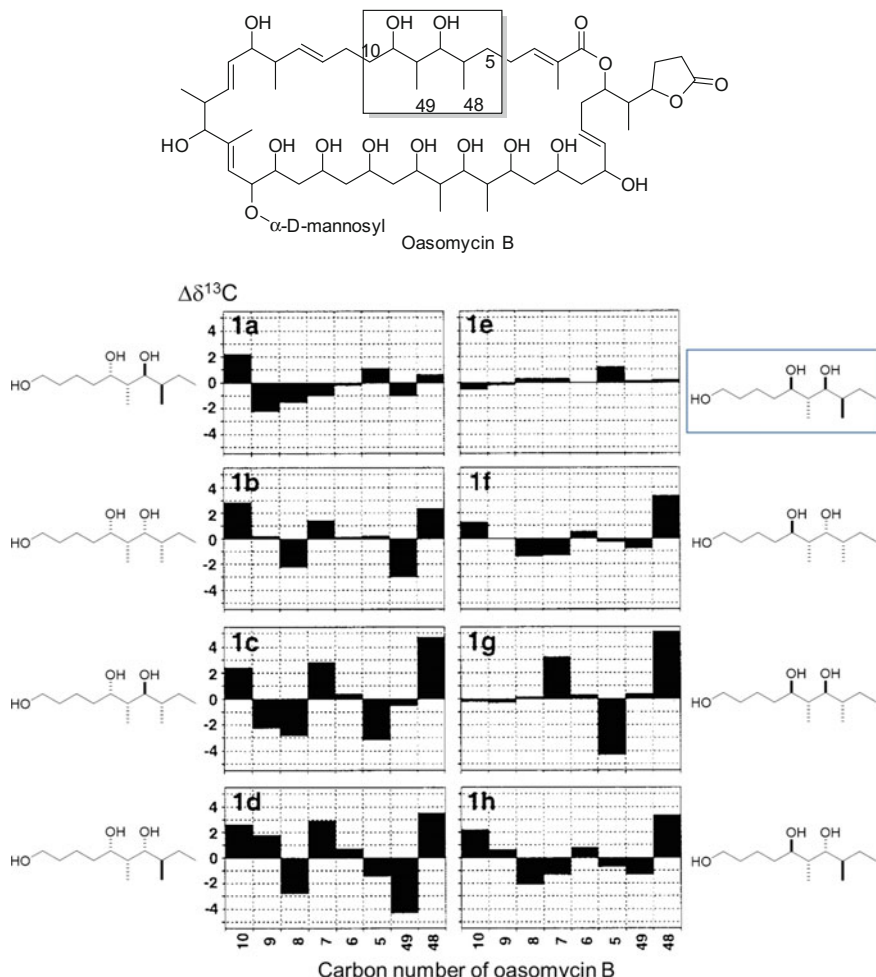


**Fig. 14.7** Application of UDB method to the stereochemical assignment of oasomycins. Difference in <sup>13</sup>C chemical shifts between oasomycin B and synthetic compounds **1a–h**. Reproduced with the permission from Ref. [5]. Copyright 1999 American Chemical Society

using profiles consisting of two or three contiguous  $^3J_{\text{H,H}}$  constants (Fig. 14.9) [25]. As exemplified for contiguous triols (Fig. 14.9), the internal and terminal  $^3J_{\text{H,H}}$  pairs are distributed in four areas depending on their relative stereochemistry, cf, *syn/anti*, *syn/syn*, *anti/anti*, and *anti/syn*. This indicates that a  $^3J_{\text{H,H}}$  profile can be used as a primary screening for predicting the stereochemistry of unknown polyols, whereas <sup>13</sup>C and <sup>1</sup>H chemical shift profiles are used to confirm the predicted stereochemistry.

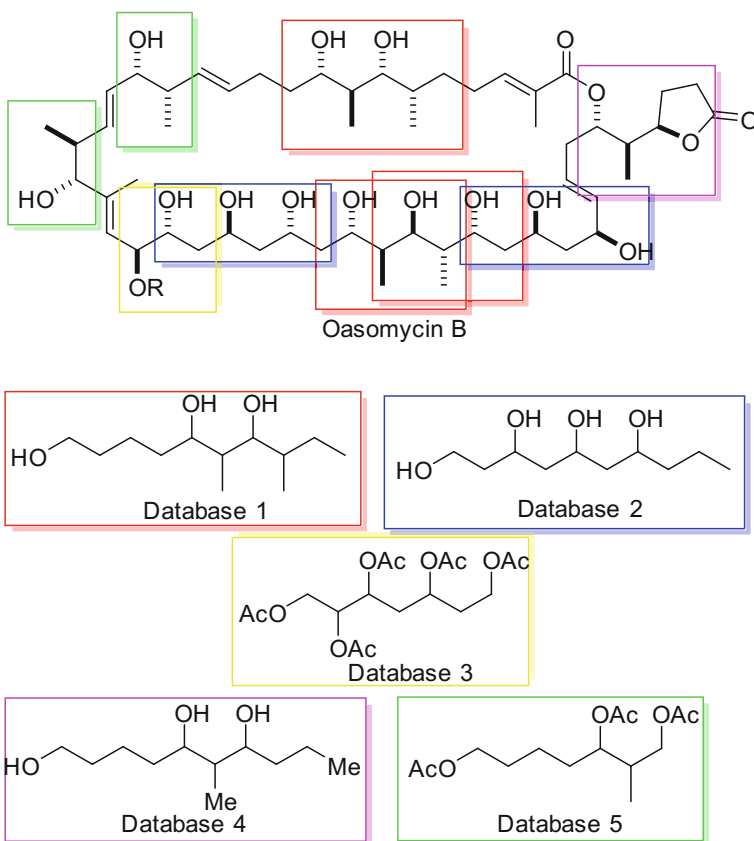
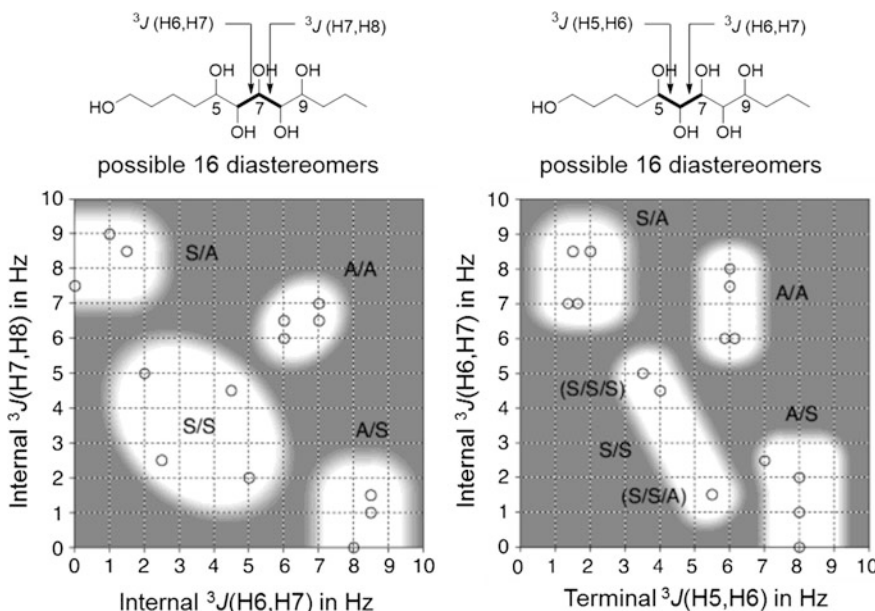


Fig. 14.8 Databases of stereoclusters to predict the stereochemistry of oasomycins

### 14.1.3 Calculations

One of the drawbacks of the JBCA method is that, unlike  $^3J_{\text{H,H}}$  values that have well-documented empirical and theoretical correlation with the dihedral angles, the use of  $^{2,3}J_{\text{C,H}}$  values for the analysis of relative configuration is accompanied by ambiguity in classifying a given value into large, medium, or small, because of the scarce accumulation of literature data, particularly for the stereocenters carrying less common substituents such as halogens. The NMR database method also faces the same difficult situation when NMR databases covering the stereocluster of interest are not available.

On the other hand, thanks to the developments in computational power and advances in quantum mechanical (QM) methods in the last two decades, experimental NMR parameters such as chemical shifts and coupling constants can be reproduced by calculations with a high accuracy. Hence, it is no surprise that theoretical



**Fig. 14.9** Two-dimensional representation of the internal (*left*) and terminal (*right*)  $^3J_{H,H}$  values observed for triols. The *x* and *y* axes represent the two contiguous  $^3J_{H,H}$  values indicated by the arrows. *S* = *syn* and *A* = *anti*. Reproduced with the permission from Ref. [25]. Copyright 2003 American Chemical Society

calculations are used to compensate not only the ambiguity in correlation between the experimental  $^{2,3}J_{C,H}$  data and dihedral angles in the JBCA method, but also the lack of experimental NMR databases for stereoclusters in the UDB method [3, 6].

A recent example of QM calculation that compensates the traditional JBCA method is shown in Fig. 14.10 [26]. Because some experimental  $^{2,3}J_{C,H}$  values for the C7–C10 of celebesides were difficult to categorize as small or large, a quantitative QM calculation was introduced in the JBCA method. The  $^3J_{H,H}$  and  $^{2,3}J_{C,H}$  values were calculated for each of the six staggered rotamers (three for each relative stereochemical arrangement) and compared with the experimental data [27]. In the calculation, constrained optimizations were performed for all the staggered rotamers in the simplified fragment (Fig. 14.10), and the gauge independent atomic orbital (GIAO) [28] method was applied to calculate the coupling constants. Then, the calculated and observed coupling constants were compared using the total absolute deviation (TAD) values (Table 14.1) derived from the equation  $(\sum |J_{\text{calc}} - J_{\text{exp}}|)$  for each stereoisomer. The rotamers exhibiting the lowest TAD values were A3 for the C7–C8 (5.5 Hz), B4 for the C8–C9 (5.5 Hz), and C1 for the C9–C10 (4.2 Hz), and C1 for the C9–C10 (4.2 Hz), corresponding to 7*S*<sup>\*</sup>,8*R*<sup>\*</sup>,9*S*<sup>\*</sup>,10*R*<sup>\*</sup> stereochemistry. This result confirmed the prediction by the conventional JBCA method. Thus, the quantitative approach based on a QM calculation is particularly helpful when the

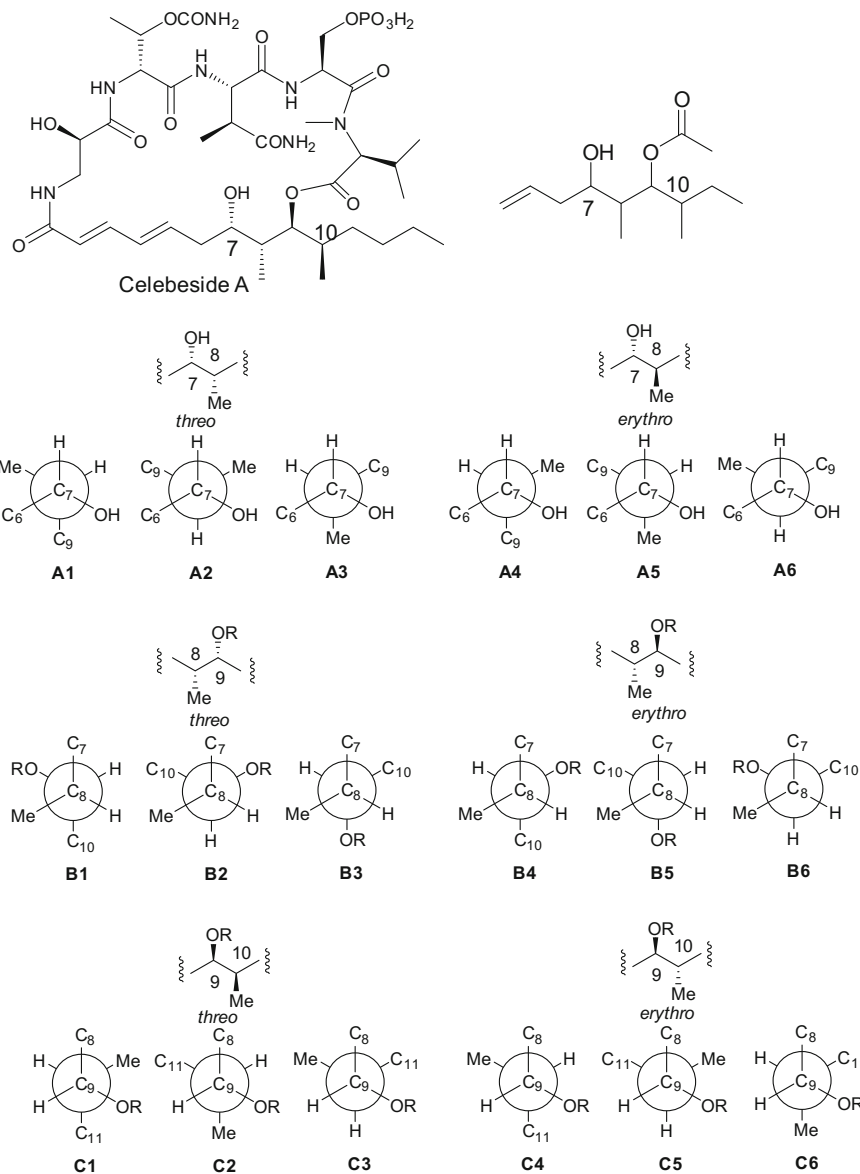


**Fig. 14.10** Structure of celebeside A and its simplified fragment containing the C7–C10 stereocenters for the calculation of coupling constants. Newman projections show all the possible staggered rotamers for *threo* and *erythro* diastereomers

experimental coupling constants are around the borderline between large and small classifications.

**Table 14.1** Calculated and observed coupling constants for the simplified fragment of celebeside A

	Calcd.						Experimental
	<i>threo</i>			<i>erythro</i>			
C7–C8	A1	A2	A3	A4	A5	A6	
$^3J(\text{H7,Me})$	2.7	4.0	4.3	2.9	4.2	5.1	5.5
$^3J(\text{H7,C9})$	4.9	0.4	2.1	5.6	1.5	0.1	3.1
$^3J(\text{H8,C6})$	4.4	1.7	0.5	0.7	5.2	5.7	2.6
$^3J(\text{H7,H8})$	8.0	7.5	2.2	2.4	4.1	6.1	1.0
TAD	8.0	11.7	<b>5.5</b>	8.4	8.7	11.8	
C8–C9	B1	B2	B3	B4	B5	B6	
$^2J(\text{H8,C9})$	-0.4	-4.8	-3.8	-4.1	-0.7	-5.2	-7.2
$^3J(\text{H9,C7})$	5.2	<b>5.5</b>	1.8	2.3	2.3	1.2	3.0
$^3J(\text{H9,Me})$	1.5	3.6	2.7	1.0	6.5	5.1	1.3
$^3J(\text{H8,H9})$	2.0	2.5	9.0	9.2	1.2	5.1	10.6
TAD	17.8	14.3	7.6	<b>5.5</b>	21.9	13.0	
C9–C10	C1	C2	C3	C4	C5	C6	
$^3J(\text{H9,Me})$	5.0	0.4	2.5	6.6	4.7	2.9	5.3
$^3J(\text{H9,C11})$	2.6	<b>6.2</b>	4.4	0.3	2.2	4.7	4.0
$^2J(\text{H10,C9})$	2.3	-2.0	-5.7	-2.1	-5.7	2.3	1.3
$^3J(\text{H9,H10})$	2.6	4.4	2.3	4.8	2.3	2.7	1.1
TAD	4.2	13.7	11.3	12.1	10.7	5.7	

Coupling constants were calculated using the density functional theory (DFT) method. TAD values were derived from the equation ( $\Sigma |J_{\text{calc}} - J_{\text{exp}}|$ ). The diastereomers with the lowest TAD values appear in italics

The other example is *in silico* compensation for the UDB method. The protocol, which was devised for flexible molecular systems by considering the contribution from all the significant conformers, consists of four steps [29]: (a) a conformational search of all the significantly populated conformers of each diastereomer, (b) QM geometry optimization of all the species, (c) GIAO calculations of all the obtained structures, (d) comparison of  $^{13}\text{C}$  chemical shifts between the Boltzmann-weighted average based on the calculated energies and observed data. Figure 14.11 shows an application of this protocol to the stereochemical assignment of the C2"–C3" of bonannione B [30]. The calculation was carried out for the three staggered rotamers around the C2"–C3" bond of each of the two possible diastereomers at C3" (**a** and **b**). For each rotamer, the geometry optimization followed by the GIAO  $^{13}\text{C}$  chemical shift calculation was carried out at the DFT level. The  $^{13}\text{C}$  chemical shifts for each stereoisomer were calculated as the Boltzmann-weighted average of the  $^{13}\text{C}$  chemical shifts for the three rotamers. Then, the calculated  $^{13}\text{C}$  chemical shifts were compared with the observed chemical shifts (Table 14.2); the chemical shift coincidence at the C4" and C5" between the calculated and experimental data indicates that the relative configuration of bonannione B is **a**.

**Fig. 14.11** Two possible stereoisomers at the C3'' of bonannione B

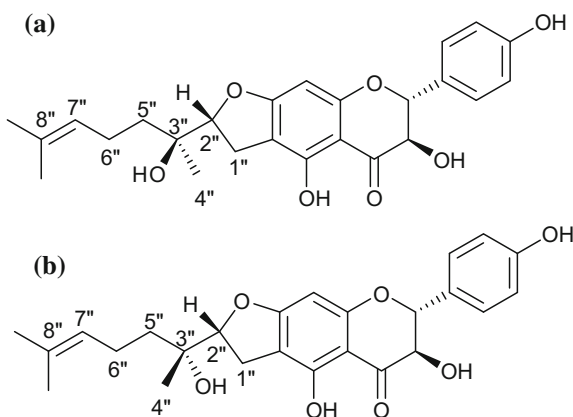


**Table 14.2** Calculated  $^{13}\text{C}$  NMR chemical shifts for possible stereoisomers **a** and **b**, and the  $^{13}\text{C}$  NMR data of bonannione B ( $\text{CDCl}_3$ )

	$^{13}\text{C}$ chemical shifts (ppm)		
	a	b	Obs.
1''	29.1	29.5	25.9
2''	94.0	94.0	91.3
3''	73.9	73.9	73.8
4''	23.1	19.7	22.4
5''	37.3	40.6	36.6
6''	24.8	25.0	21.8
7''	122.1	122.5	123.7
8''	128.7	128.0	132.0

#### 14.1.4 RDCs

As described above, the stereochemical assignments of organic molecules depend on chemical shifts, *J*-couplings, and NOEs, even though these NMR parameters do not provide long-range information. Therefore, it has been impossible to correlate distant stereocenters or stereocenters separated by a flexible linker, hindering the stereochemical determination of organic molecules with such stereocenters. This situation can be changed by introducing RDCs with angular information with respect to the direction of external magnetic field, thus allowing to correlate the distant moieties of a molecule. The RDC techniques were mostly developed in the biomolecular NMR field, where RDCs are frequently used to elucidate and refine the 3D structures of peptides, proteins, and nucleic acids. Lately, this approach has been used to determine the relative configurations of organic molecules. The basic principle and applications of RDCs to organic molecules are briefly described below; readers should refer to review papers for more details [7, 8].

Dipolar couplings are directly proportional to  $\left\langle \frac{3\cos^2\theta - 1}{2} \right\rangle \gamma_I \gamma_S / r^3$ , where  $\theta$  is the angle between the I–S interspin vector and magnetic field direction; bracket  $\langle \rangle$  indicates a time average of all the orientations sampled by the interspin vector;  $\gamma_I$  and  $\gamma_S$  are the magnetogyric ratios of the two spins I and S;  $r$  is the interspin distance. Thus, dipolar couplings provide structural information about the orientation and distance and are typically of the order of several kHz in solid-state samples. In liquid samples, the dipolar couplings are generally averaged to zero, and thus the orientation and distance information is lost, because the isotropic fast tumbling motion of the molecules nulls the time average term denoted by the bracket. To access the dipolar couplings in liquid NMR spectra without a significant loss in signal resolution, the solute molecules should be weakly aligned, which can be attained using alignment media such as liquid crystals or stretched polymer gels. In such alignment media, the solute molecules are weakly oriented, and the dipolar couplings are not averaged to zero, but scaled down from kHz to the order of several Hz. Such reduced dipolar couplings are known as RDCs.

For the application of RDCs to organic molecules, stretched polymer gels are most frequently used as the alignment media: polyacrylamide and polyacrylonitrile for water and polar organic solvents, and polystyrene for apolar organic solvents [8]. A preparation procedure involves the adding of a solvent to a dry polymer stick in an NMR tube. The swelling gel stretches along the NMR tube axis, and the polymer network also becomes anisotropic, preventing the solute samples from isotropic tumbling and consequently making the solute molecules weakly aligned (Fig. 14.12). To obtain RDCs, two measurements should be carried out: one in isotropic solution to obtain the scalar couplings  $J$ , and the other in anisotropic alignment media to obtain  $|J + 2D|$ .  ${}^1J_{C,H}/{}^1D_{C,H}$  can be measured by conventional HMQC or HSQC experiments without carbon decoupling during the acquisition.

To understand the basic principle of RDC application to stereochemical determination, the distinction of axial versus equatorial protons on a six-membered ring is exemplified in Fig. 14.13. Because all the axial C–H bonds are parallel or antiparallel, they give the same C–H RDCs. In the  $\alpha$  and  $\beta$  isomers of 4,6-*O*-ethylidene-*D*-glucopyranose [31], the RDC for the anomeric C–H bond in the  $\beta$  isomer should have the same size as those of the axial C–H bonds, whereas the  $\alpha$  isomer produces a different size of RDC, thus making it possible to discriminate the stereoisomers based on the size of RDC. Although for practical purposes, such a simple problem can be solved by measuring NOEs and/or  ${}^3J_{H,H}$  values without referring to RDCs, this demonstrates how RDCs make it possible to correlate the stereochemistry of the anomeric position even with the most distant stereocenter in the ketal moiety.

To determine the relative stereochemistry of complex molecules using RDCs, the conception of alignment tensor is generally introduced. In the case of a rigid molecule, the alignment tensor represents the distribution of the external magnetic field vector in a reference molecular frame. When more than five RDCs are observed for a rigid molecule, its alignment tensor can be obtained by fitting a molecular structure to the experimental RDC data. From thus obtained the

**Fig. 14.12** Schematic drawing of an anisotropic gel network in an NMR tube and its prevention of the isotropic motion of solute molecules

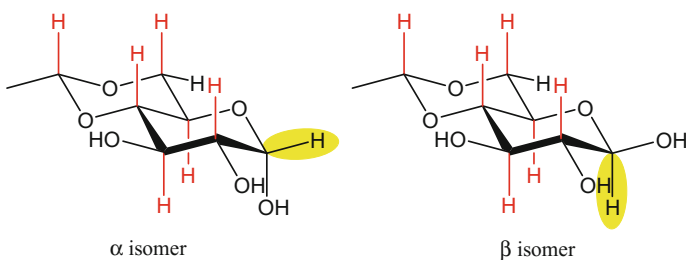
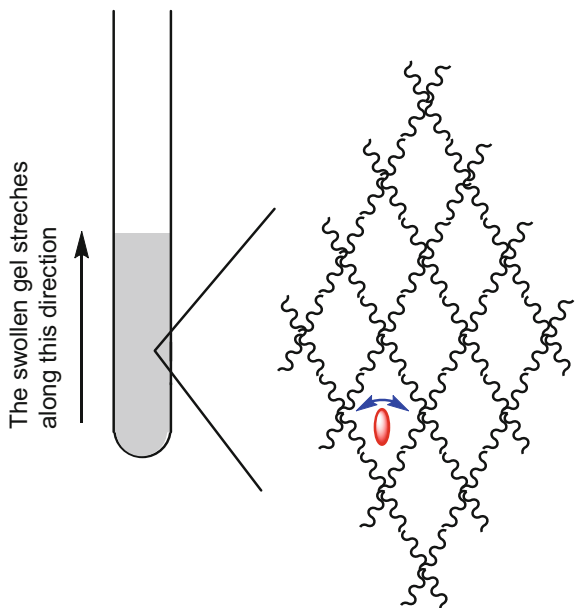
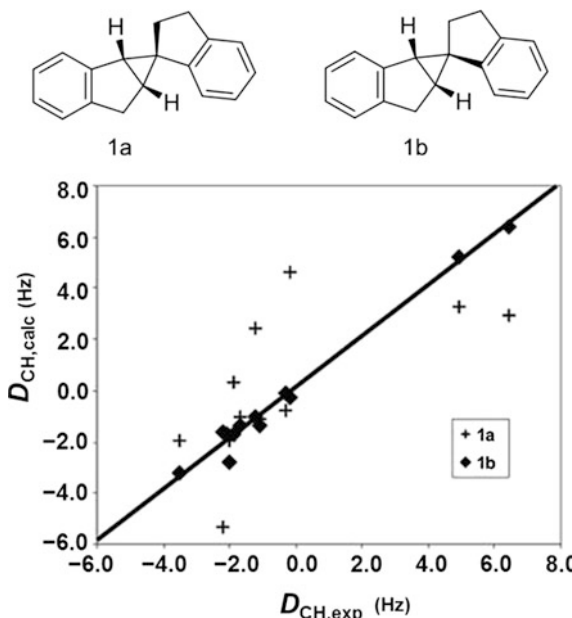


**Fig. 14.13**  $\alpha$  and  $\beta$  forms of 4,6-*O*-ethylidene-D-glucopyranose. The axial C-H bonds are highlighted in red, and the anomeric C-H bonds are shaded in yellow

best-fitting alignment tensor and molecular structure, it is also possible to back-calculate the RDCs; this should be completely consistent with the experimental RDCs when the input molecular structure is correct. In contrast, a molecular structure with a wrong stereochemistry will cause a poor agreement between the back-calculated and experimental RDCs (Fig. 14.14) [32]. In this manner, RDCs can be used for the verification and falsification of relative configuration. Then, the application of RDCs to stereochemical analysis has extended from cyclic rigid compounds to flexible acyclic natural products as demonstrated by the report from Griesinger's group on the stereochemistry of sagittamide A [33]; the combined use

**Fig. 14.14** Two possible diastereomers of spiroindene and the agreement of experimental versus back-calculated RDCs ( $D_{\text{CH},\text{exp}}$  and  $D_{\text{CH},\text{calc}}$ ) for the diastereomers



of coupling constants, NOEs, and RDCs allowed the successful determination of all the stereochemistry. Very recently, residual chemical shift anisotropy has also been applied to the stereochemical determination of organic molecules [34].

So far, however, the RDCs are not always generally used for the stereochemical determination of natural products, probably because of not only the requirement of slightly complex data analysis, but also the hesitation of mixing precious and small amount of natural products with alignment gel media.

## 14.2 NMR Methods for Examining the Conformation and Intermolecular Interactions of Natural Products in Membranes

To gain a deeper insight into the biological activities of natural products, it is crucial to obtain more precise information regarding their interactions with membrane lipids, but it has been hardly obtained even with the current technologies. The fluid mosaic model was proposed by Singer and Nicolson in 1972 [35]; a plasma membrane was thought to be a two-dimensional homogeneous fluid, mainly consisting of rapidly diffusing lipids and proteins. This vision has been revised by the concept of “lipid rafts,” where the lipid bilayers are heterogeneous in biological systems [36]. Some recent research results have demonstrated that certain physicochemical features of lipid rafts can be partly reproduced using artificial membranes

in the absence of proteins [37, 38], significantly accelerating biophysical and chemical studies on the atomic-level mechanism of lipid–lipid interactions in membranes [39–41]. The methodologies developed in these studies for lipids also help to examine the conformation of natural products associated with membranes. In this section, we would like to describe three examples of natural products that interact with biological membranes in exerting their activities, some of which can modify the domain formation of biological membranes.

During our research on amphotericin B (AmB), a clinically important antifungal drug, we learned that small molecules, particularly natural products, often show very high affinities for phospholipids and sterols in bilayer membranes when they induce membrane-disrupting activities [41]. Solid-state NMR, therefore, provides a very promising approach for the structural studies of complexes of natural products with membrane lipids. Furthermore, solution NMR techniques can be applied to characterize the structures of membrane-bound small molecules. Standard 2D  $^1\text{H}$ – $^1\text{H}$  experiments are often recorded with micelle suspensions or even with hydrated membrane dispersions. In this section, we would like to describe three examples for our and others' NMR studies on small molecule–lipid complexes.

### 14.2.1 Amphotericin B

As the first example, we selected a well-known antibiotic AmB. Although this antibiotic was discovered 70 years ago, it is still regarded as the drug of choice for the treatment of systemic fungal infections [42]. We became interested in the structure determination of the self-assembly formed by AmB and sterol, supposed to be the main responsible entity for the drug's fungicidal activity. First, we conducted the  $^{13}\text{C}$  NMR signal assignment of AmB in a membrane. The  $^{13}\text{C}$ – $^{13}\text{C}$  chemical shift correlation spectrum of uniformly  $^{13}\text{C}$ -labeled erythromycin A has been recorded using a method known as CMR7 based on  $^{13}\text{C}$ – $^{13}\text{C}$  magnetization transfer [43]. The same methodology was applied to AmB bound to a membrane (Fig. 14.15a). We prepared uniformly  $^{13}\text{C}$ -enriched AmB at 15% by feeding [ $^{13}\text{C}_6$ ] glucose to *Streptomyces nodosus* [44].  $^{13}\text{C}$ – $^{13}\text{C}$  cross-peaks were observed only for single-bond correlations with an incorporation pattern of biosynthetic precursors, acetates, and propionates [44] in hydrated 1,2-dilauroyl-*sn*-glycero-3-phosphocholine (DLPC) membrane (Fig. 14.15b).

With the chemical shift assignment in hand, we examined whether AmB spans the bilayer with a single or double molecular length (Fig. 14.15d) based on the interactions between AmB and the phosphate head group of DLPC. For this purpose,  $^{13}\text{C}$ – $^{31}\text{P}$  dipolar coupling was used [45–47]; usual REDOR pulse sequences could not be directly applied to uniformly  $^{13}\text{C}$ -labeled AmB because of homonuclear coupling interactions arising from  $^{13}\text{C}$ – $^{13}\text{C}$  spin networks. Homonuclear  $J$ -coupling is still active through the Hahn-echo refocusing routine, causing undesired phase modulations in the REDOR spectra. REDOR for X clusters (RDX) was thought to be the most suitable method for this purpose [48]; in this experiment,  $^{13}\text{C}$ – $^{13}\text{C}$  isotropic

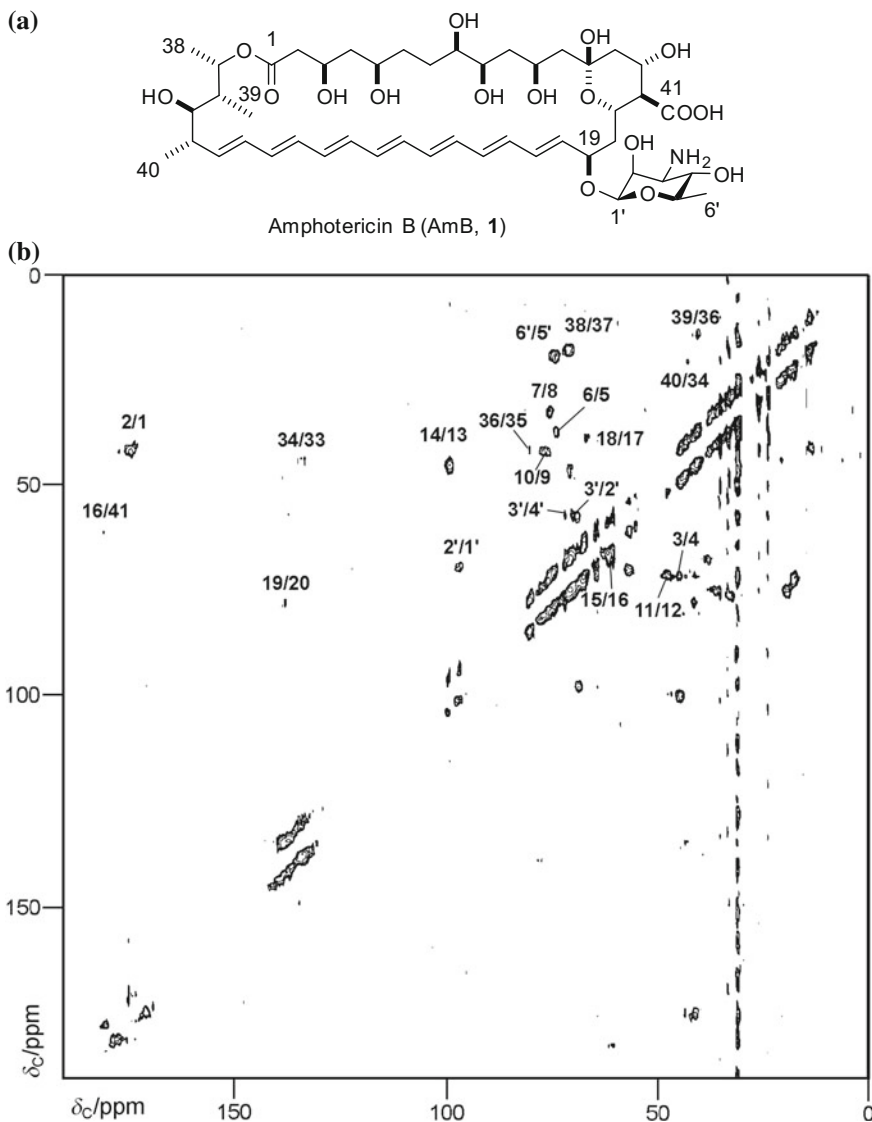


**Fig. 14.15** **a** Structure of AmB, **b** 2D  $^{13}\text{C}$ - $^{13}\text{C}$  correlation of  $^{13}\text{C}$ -enriched AmB in DLPC membrane at the AmB/DLPC molar ratio of 1:8 and 50 wt% hydrated with 10 mM HEPES/ $\text{D}_2\text{O}$  buffer. The spectrum was recorded with the magic-angle spinning at 7 kHz at 30°C. **c** The  $^{13}\text{C}$ - $^{31}\text{P}$  RDX spectrum of the same preparation as that shown in **(b)** with the magic-angle spinning at 7 kHz at 30°C. The *top trace* shows the REDOR difference spectrum,  $\Delta S$ , whereas the *bottom trace* shows the REDOR reference spectrum without  $^{31}\text{P}$  pulses. **d** Models showing the membrane interaction of AmB with a DLPC bilayer membrane as single-length (*left*) and double-length assemblies. Reprinted with the permission from Ref. [44]. Copyright 2006, with permission from Elsevier

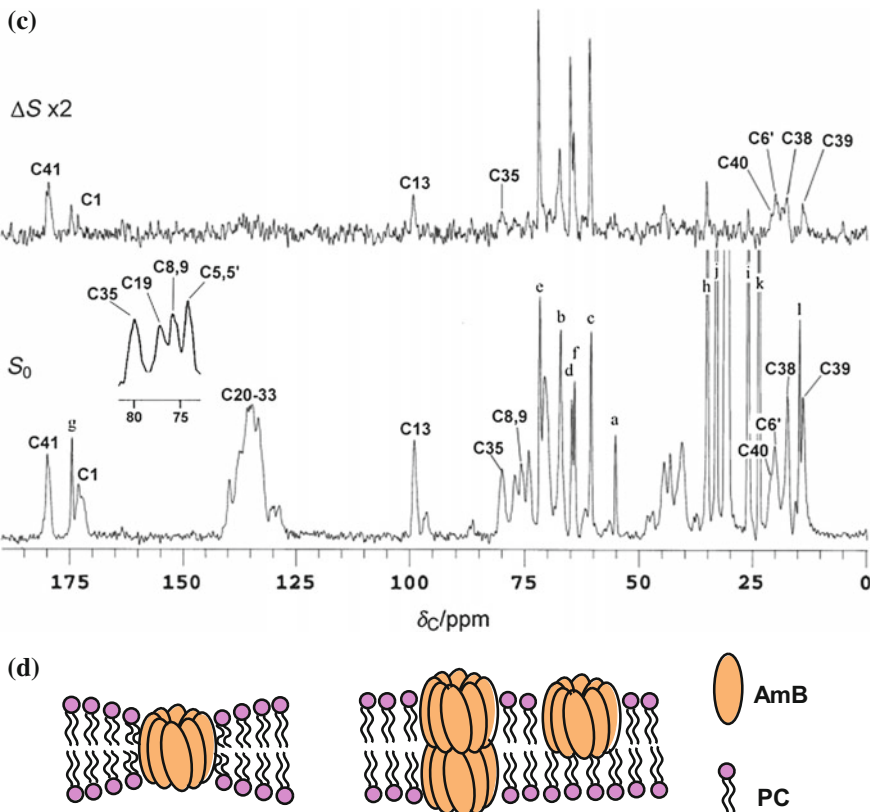


**Fig. 14.15** (continued)

*J* interactions are refocused by a combination of rotor-synchronized  $\pi$  and  $\pi/2$  pulses. In the spectrum shown in Fig. 14.15c, significant REDOR dephasing effects were detected for the  $^{13}\text{C}$  NMR signals near both the terminal ends of an AmB molecule, whereas the broad peaks due to seven double bonds (C20–C33) showed a marginal diphasic (Fig. 14.15c). These data indicate that AmB spans DLPC membranes with a single molecular length as depicted in Fig. 14.15d; the membrane thickness of DLPC is comparable to that of plasma membranes, thus indicating that single-length channels rather than double-length channels are responsible for the membrane-permeabilizing effect of AmB.

The selective activity for fungal membranes over human tissues is probably due to the more efficient formation of an ion-channel assembly in the presence of fungal ergosterol (Erg) over human cholesterol (Chol) [49]. To determine the structure of the bimolecular complex of AmB and Erg formed in a membrane,  $^{13}\text{C}\{^{19}\text{F}\}$  REDOR experiments were performed with C14- $^{19}\text{F}$ -labeled AmB and  $^{13}\text{C}$ -labeled Erg at the C4 and dimethyl terminus (C26/C27) positions [50]. The spectra showed the presence of a “head-to-tail” interaction of AmB and Erg (Fig. 14.16).

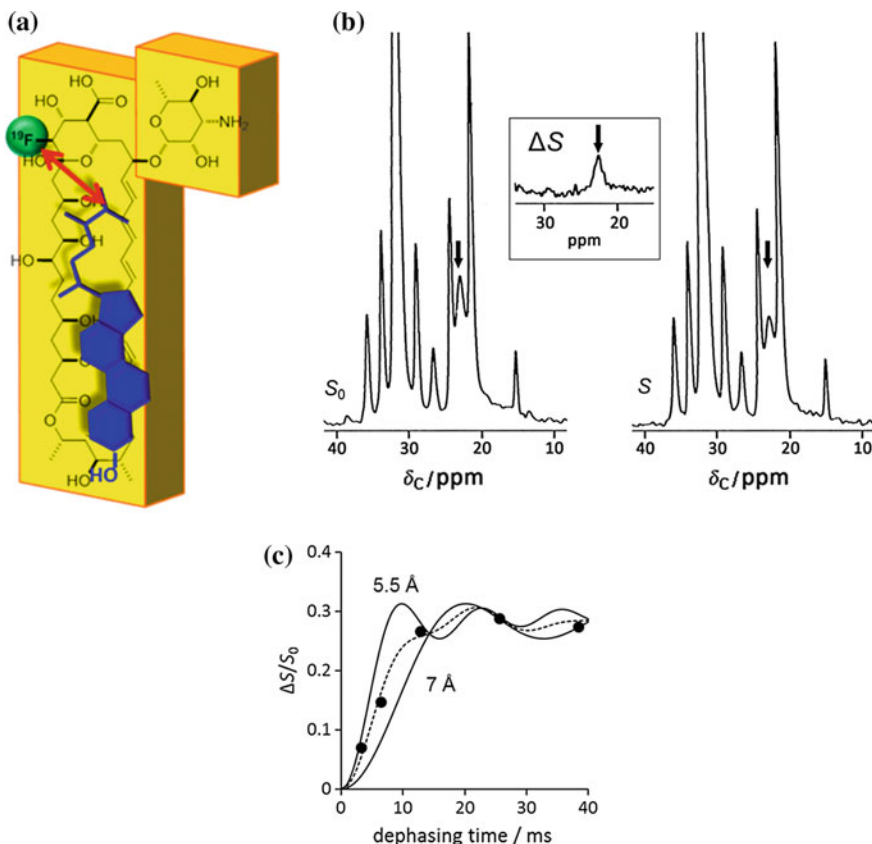


**Fig. 14.16** **a** A schematic model of AmB (yellow boxes) and Erg (blue) in antiparallel “head-to-tail” orientation. Red arrow indicates the pair of labeled atoms producing the REDOR dephasing. **b**  ${}^{13}\text{C}\{{}^{19}\text{F}\}$ REDOR spectra of nonirradiated (full-echo) ( $S_0$ ),  ${}^{19}\text{F}$ -irradiated experiments ( $S$ ), and difference spectrum ( $\Delta S$ ) focusing on the 26,27-dimethyl group of Erg at the ratio of 14-F AmB/26,27- ${}^{13}\text{C}_2$  Erg/POPC (1:1:9); hydrated POPC bilayers were prepared in 10 mM HEPES/D<sub>2</sub>O (50% wt) at 38 °C. Arrows indicate the C26/C27 signals. **c** Experimental  ${}^{13}\text{C}\{{}^{19}\text{F}\}$ REDOR dephasing values ( $\Delta S/S_0$ ) for the C26/C27 signal (filled circle), and simulation curves (solid lines) for the  ${}^{13}\text{C}-{}^{19}\text{F}$  distances of 5.5 and 7.0 Å, assuming that 30% of 26,27- ${}^{13}\text{C}_2$  Erg is involved in antiparallel pairing. A dashed line that was obtained as the average of two different curves simulated for distances 5.5 and 7.0 Å (1:1) fits the experimental data. Reprinted with the permission from Ref. [53]. Copyright 2016 American Chemical Society

A recent structure–activity relationship study [51, 52] showed that the tetracyclic core of Erg contacts the macrolide ring of AmB with a close face-to-face VDW force, indicating that the  $\alpha$ -face of an Erg core (Fig. 14.17c) interacts with AmB. Moreover, the REDOR experiments (Fig. 14.16c) showed that the dephasing effect reaches a plateau at the  $\Delta S/S_0$  ratio of 0.3, indicating that the parallel and antiparallel orientations of AmB–Erg occur at a 7:3 ratio in membrane assemblies [53]. Both the AmB–Erg orientations are mainly stabilized by a common interaction

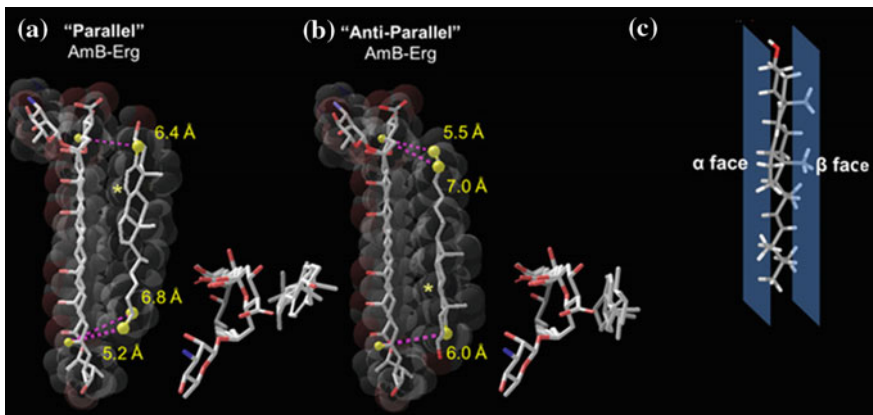


**Fig. 14.17** NMR-derived structures of AmB–Erg bimolecular complexes in parallel (**a**) and antiparallel (**b**) alignments. The images were generated by conformational search (Macromodel). \*C7 position of Erg. **c** Depicts the  $\alpha$ - and  $\beta$ -faces of Erg. Reprinted with the permission from Ref. [53]. Copyright 2016 American Chemical Society

mode such as face-to-face VDW. The structure of the stable complex (Fig. 14.17a, b) represents the face-to-face interaction that possibly accounts for the drug's selectivity of Erg over Cho; in complex 14.17a, the 7-axial hydrogen of Chol prevented close contact between the AmB macrocycle and alicyclic sterol core [52].

The structural study of AmB–Erg complex [53] has demonstrated that solid-state NMR techniques are useful to achieve the atomic-level interaction mode of small molecules in a membrane. Although numerous studies on solid-state NMR have been reported for membrane-active peptides (see Chap. 9) and membrane lipids, investigations on other small molecules such as natural products are rare. One of the reasons is the difficulty in preparing isotope-labeled compounds. As shown in these studies on AmB, if labeled compounds could be prepared, the structural information could also be obtained with atomistic resolution by solid-state NMR. Another important key to success is the mobility of membrane-bound molecules. In the AmB case, the ion-channel assemblies were regarded as immobile in the NMR timescale. When AmB is diluted with membrane phospholipids to 1:50 ratio, AmB starts moving in the membrane. In the former case, the accurate structure of the assembly could be elucidated using interatomic distances, and in the latter case, the orientation of the assembly could be deduced as reported recently [54].

#### 14.2.2 Erythromycin A

Erythromycin A (EA, Fig. 14.19) is an old antibiotic, but still widely prescribed. As a side effect known as phospholipidosis, the drug accumulates in lysosomal membranes and induces the excess accumulation of phospholipids [55, 56]. This is

caused by the inhibition of lysosomal phospholipase activity by EA [55]. Isotropic bicelles which are often applied to membrane-associated peptides and proteins [57, 58] have been used for the molecular characterization of the membrane-bound structure of EA [59]. First,  $^{31}\text{P}$  NMR spectra of a large oriented bicelle containing dimyristoyl phosphatidylcholine (DMPC), dihexanoyl phosphatidylcholine (DHPC), dimyristoyl phosphatidylglycerol (DMPG), and EA (the  $q$  value  $[\text{DMPC} + \text{DMPG}]/[\text{DMPC}] = 3.3$ ) were measured to confirm that the bicelle structure is maintained even at high contents of EA. The  $^1\text{H}$  NMR spectra of EA in bicelles comprising DMPC- $d_{54}$ , DHPC- $d_{22}$ , and DMPG- $d_{54}$  ( $q = 0.5$ ) showed that the conformation of bicelle-associated EA determined using NOEs and  $^3J_{\text{HH}}$  data (Fig. 14.19b) is consistent with the crystal structure of EA [60].

The relaxation parameter  $T_{1\text{M}}$  of EA protons in bicelles containing paramagnetic  $\text{Mn}^{2+}$  ions (Fig. 14.19a) was strongly shortened for the signals of the 7',8'-dimethyl group, indicating that the ammonium group in aqueous media has ionic interactions with the phosphate groups of the bicelle and come close to the water–lipid interface. On the other hand, the protons affected by 12-doxy-PSPC (Fig. 14.18) were positioned at 2, 13, 20, 1'', and 8'' (blue balls in Fig. 14.19a), indicating that these protons reside in the relatively deeper portion of the bicelle interior. Taken together, EA resides in the shallow and middle parts of membrane interior by placing the dimethylamine group close to the phosphate group and with slightly immersing the macrolide portion in the lipid bilayer [59].

EA was shown to dominantly partition to the flat bilayer area of the bicelle to interact more preferentially with acidic DMPG than with neutral DMPC and DHPC, and DMPG preferentially resides in the DMPC-rich bilayer of the bicelles owing to the better matching of acyl chain length to that of DMPC. The position and conformation of EA in bicelles shown in Fig. 14.20 suggest that the drug is a potential inducer of phospholipidosis; the possible mechanism for the inhibition of phospholipase activity is the binding of EA to negatively charged lysosomal membranes [55, 56]. This NMR-based study showed that the large macrolide moiety of EA comes close to the ester groups of phospholipids (Fig. 14.20), thus probably hindering the approach of lysosomal phospholipase to the C1' position of a lipid acyl chain. This led to the accumulation of phospholipids in the cell.

### 14.2.3 Theonellamide A

The next example is a cyclic peptide, which does not belong to typical membrane-active amphipathic peptides. In this section, we would like to describe some applications of solution NMR to membrane-bound molecules. Theonellamides (TNMs, Fig. 14.21) were isolated from the marine sponge *Theonella* sp. [61]. TNM homologs possess a bismacrocyclic skeleton that encompasses nonribosomal amino acid residues and a histidinoalanine tether. In vitro binding assays using a fluorescent derivative showed that the peptide specifically bound to  $3\beta$ -hydroxysterols such as cholesterol (Chol) and ergosterol

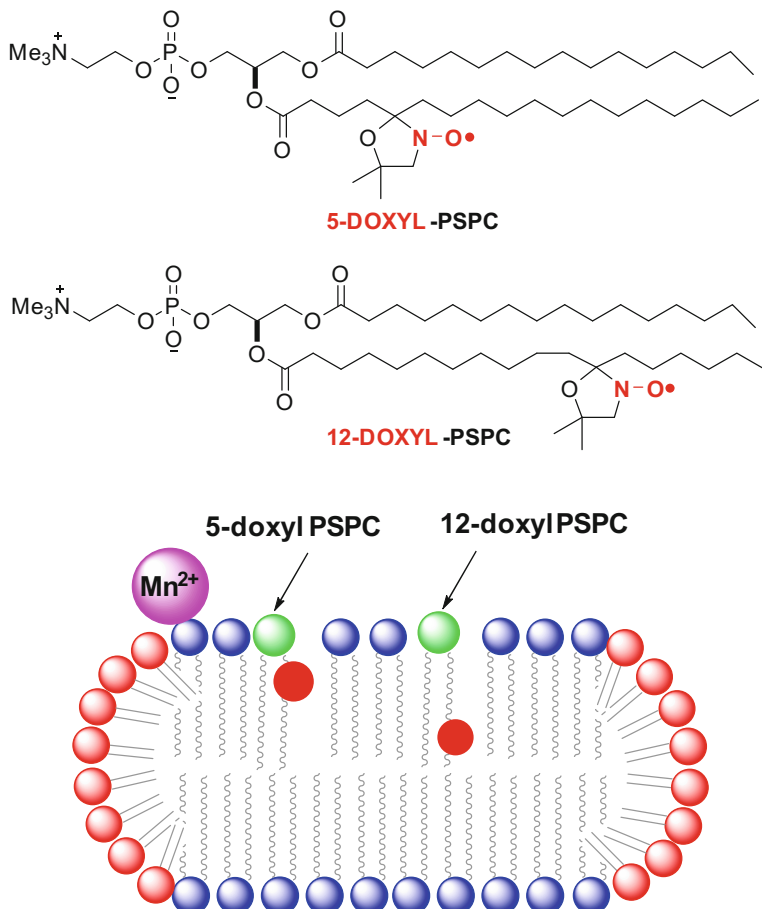


**Fig. 14.18** Interactions of paramagnetic DOXYL-PC and  $\text{Mn}^{2+}$  with an isotropic bicelle. Reproduced from Ref. [59b] by permission of The Royal Society of Chemistry

(Erg) [62]. The phenotypic changes in yeasts indicate that the membrane-related activity of TNM is distinct from that of polyene antifungals such as AmB. The  $^2\text{H}$  NMR spectra of deuterated-Chol and 3-*epi*-Chol showed that TNM-A significantly slows down the fast rotational motion of Chol and Erg, but not *epi*-cholesterol [63], indicating that 3 $\beta$ -hydroxysterol directly interacts with TNM-A in lipid bilayers.

To better understand the membrane-disrupting activity of TNM-A, solution NMR techniques were used for isotropic bicelles containing the peptide. In particular, several  $^1\text{H}$  NMR experiments were conducted to examine the interaction mode of TNM-A in model membranes. First, the aggregate formation of TNM-A was evaluated by diffusion-ordered spectroscopy (DOSY) [64]. Using the accurate viscosity values of deuterated solvent systems, the results indicate that TNM-A has the oligomeric states of 2–9 molecules (depending on peptide concentration) in an

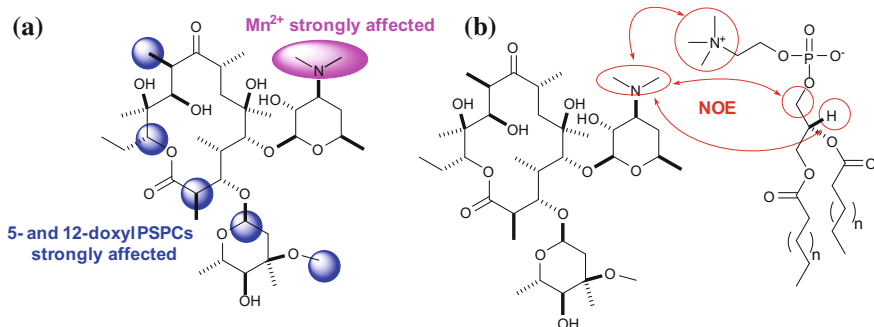


**Fig. 14.19** **a** Results of paramagnetic relaxation experiments for EA and **b** results of NOE experiments on EA-containing phospholipids. Reproduced from Ref. [59b] by permission of The Royal Society of Chemistry

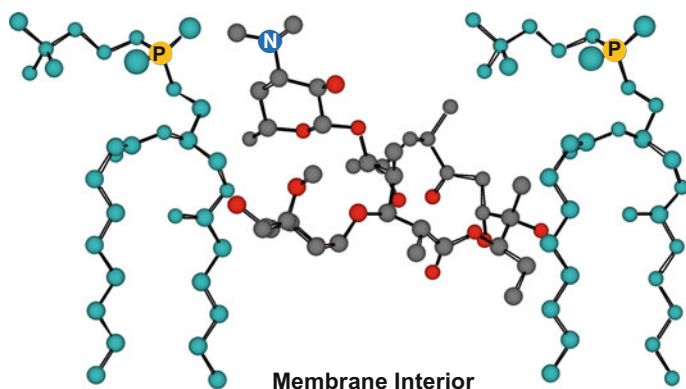


**Fig. 14.20** Hypothetical interaction of erythromycin A (EA) and interactions with membrane phospholipids (*light blue*). It is assumed that electrostatic interactions exist between the phosphate group of lipids and ammonium group of EA (see text). Reproduced from Ref. [59b] by permission of The Royal Society of Chemistry

aqueous environment, and this aggregation potential plays a role in the membrane-disrupting activity of the peptide [65]. Further, TNM-A was mixed with small DMPC-*d*<sub>54</sub>/DHPG-*d*<sub>22</sub> bicelles and subjected to <sup>1</sup>H NMR measurements in the presence of a paramagnetic quencher Mn<sup>2+</sup> [65] similar to erythromycin in the previous section (Fig. 14.22). In Chol-containing (10 mol%) bicelles, the <sup>1</sup>H signals of TNM-A were significantly broadened, indicating that the peptide efficiently associates with the Chol-containing bicelles. The addition of Mn<sup>2+</sup> to these bicelles also elicited a concentration-dependent decrease in the relative intensity of TNM-A signals, further indicating that the peptide completely stays near the surface of the bilayers where the Mn<sup>2+</sup> residing near the phosphate group effectively affects the

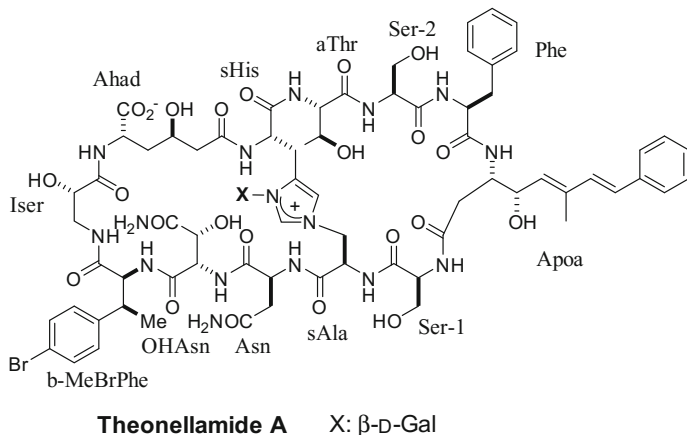


**Fig. 14.21** Structure of Theonellamide A (TNM-A)

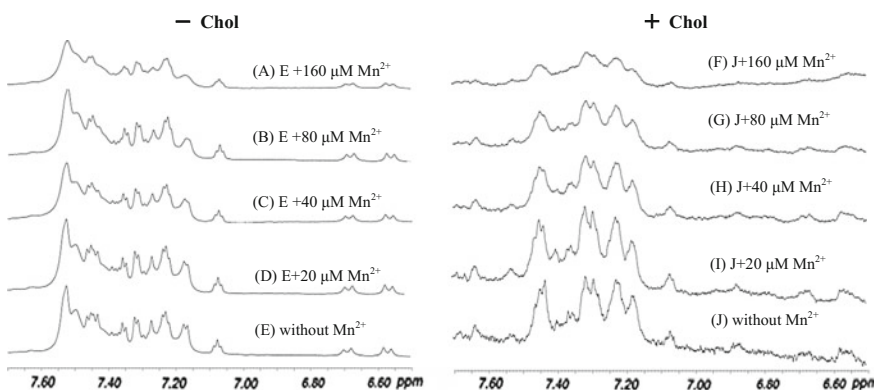


**Fig. 14.22**  $^1\text{H}$  NMR spectra of TNM-A incorporated in Chol-free (A–E) and Chol-containing (F–J) DMPC-*d*<sub>54</sub>/DHPC-*d*<sub>22</sub> bicelles ( $q = 0.5$ ) in  $\text{D}_2\text{O}$  (100 mM NaCl) without Mn<sup>2+</sup> (E, J) and with increasing concentrations of Mn<sup>2+</sup> (A–D and F–I). The amount of Chol added to bicelles was 10 mol% of DMPC-*d*<sub>54</sub>. Mn<sup>2+</sup>/TNM-A mol ratios: from the bottom to the top, 0:10, 1:10, 2:10, 4:10, and 8:10. The final concentrations of TNM-A and phospholipids (DMPC + DHPC) were 200  $\mu\text{M}$  and 160 mM, respectively. All the spectra were recorded with 512 scans at 310 K. Reproduced from Ref. [65]. Copyright 2016, with permission from Elsevier

relaxation process of  $^1\text{H}$  signals (Fig. 14.22). A comparison of the relative signal intensities with those of DMPC showed that the hydrophobic chains such as the Apoa and Phe groups of TNM-A bind at the lipid–water interface of the bilayer area of bicelles, close to the C2' portion of the phospholipid acyl chain (Fig. 14.23). This shallow penetration of TNM-A to lipid bilayers can induce an uneven membrane curvature and eventually disrupt the bilayer structure [65].

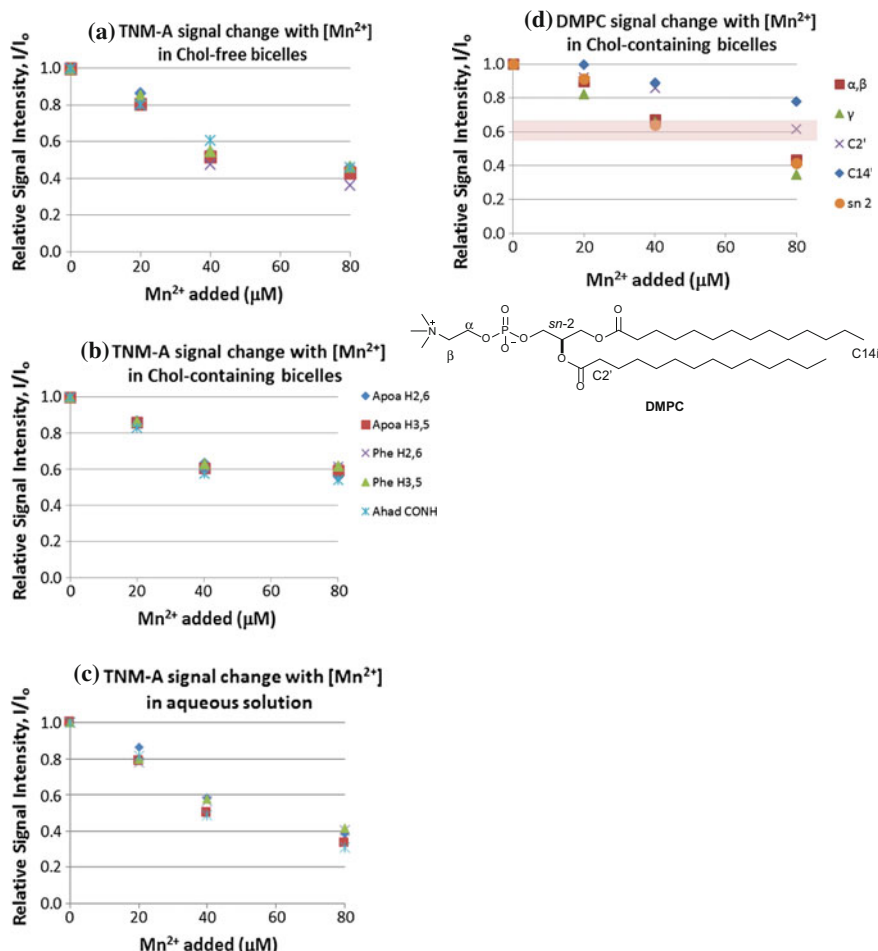


**Fig. 14.23** **a** Relative intensities ( $I/I_0$ ) of the  $^1\text{H}$  signals of TNM-A incorporated in Chol-free bicelles with increasing concentrations of  $Mn^{2+}$ . **b**  $Mn^{2+}$ -dependent  $I/I_0$  values of the same signals in Chol-containing bicelles. **c**  $Mn^{2+}$ -dependent  $I/I_0$  values of the same signals without bicelles. **d**  $Mn^{2+}$ -dependent  $I/I_0$  values of DMPC signals in Chol-containing bicelles. The  $I/I_0$  values were obtained from the ratio of the  $^1\text{H}$  peak intensities in the presence and absence of  $Mn^{2+}$  at the indicated amino acid residue of TNM-A and depth-dependent fragments of DMPC as shown in the figure. The concentrations of TNM-A and phospholipids (DMPC + DHPG) of bicelles were 200  $\mu M$  and 160 mM, respectively. A pink belt at  $I/I_0 = 0.6$  in panel (d) depicts the depth of hydrophobic residue of TNM-A shown in panel (b) penetrating into the  $C2'$  position of POPC molecules of Cho-containing bicelles

### 14.3 Summary and Outlook

In the former part of chapter, we overviewed four important methods used for the stereochemical determination of natural products on the basis of solution NMR techniques. The basic concepts of the JBCA and UDB methods were reported in the 1990s, and since then both the methods have been widely and frequently used in the field of natural products until today. The recent developments in computational methodology in predicting NMR data further compliment the ambiguity of interpreting coupling constants in the original JBCA method and the lack of literature database in the UDB method, thus further increasing the reliability of these methods. The newly developed RDC method, still less generalized in the field of natural products, will be an important tool, particularly for the stereochemical correlation between distant stereogenic centers, even though only RDC analysis is not sufficient to determine all the stereochemistry of natural products. In this context, it is important to understand the advantages and disadvantages of each methodology and select the optimal method or combine a few methods depending on the nature of the target organic molecules such as molecular size, complexity, type and distribution of functional groups, and sample quantity.

In the latter part of this chapter, we discussed the application of solid-state NMR techniques and solution NMR with bicelles to the analysis of membrane interactions of natural products [40, 49–67]. In particular, NMR-based studies of small molecules with lipids require site-specific isotope-labeled natural products. Closer collaborations between biophysicists and synthetic chemists will surely accelerate fundamental research on the structural biology of membrane lipids and mechanism-of-action studies of drugs and antibiotics. However, membrane lipids are highly mobile, and thus the conformation of small molecules bound to membranes also rapidly changes by interacting with lipids. The time constants of these interactions are usually much faster than the timescale of NMR experiments such as REDOR and  $^2\text{H}/^{31}\text{P}$  wide-line spectra. Therefore, realistic lipid behaviors should be deduced from these NMR data in combination with MD simulations as well as other modalities such as fluorescence microscopic techniques, X-ray/neutron scattering, and IR spectroscopy.

**Acknowledgements** We would like to thank Dr. Shigeru Matsuoka, the University of Tokyo, and Drs. Shinya Hashima, Hiroshi Tsuchikawa, and Yuichi Umegawa, Osaka University for valuable comments. Some of the research projects of the authors described in this review have been supported by JST ERATO lipid active structure projects (Grant Number JPMJER1005) and JSPS KAKENHI (Grant Numbers: 16H06315, 15H03121, and 25242073).

## References

1. Kwan, E.E., Huang, S.G.: Structural elucidation with NMR spectroscopy: practical strategies for organic chemists. *Eur. J. Org. Chem.* **2008**, 2671–2688 (2008)

2. Matsumori, N., Kaneno, D., Murata, M., Nakamura, H., Tachibana, K.: Stereochemical determination of acyclic structures based on carbon-proton spin-coupling constants. A method of configuration analysis for natural products. *J. Org. Chem.* **64**, 866–876 (1999)
3. Bifulco, G., Dambruoso, P., Lomez-Paloma, L., Riccio, R.: Determination of relative configuration in organic compounds by NMR spectroscopy and computational methods. *Chem. Rev.* **107**, 3744–3779 (2007)
4. Kobayashi, Y., Lee, J., Tezuka, K., Kishi, Y.: Toward creation of a universal NMR database for the stereochemical assignment of acyclic compounds: the case of two contiguous propionate units. *Org. Lett.* **1**, 2177–2180 (1999)
5. Lee, J., Kobayashi, Y., Tezuka, K., Kishi, Y.: Toward creation of a universal NMR database for the stereochemical assignment of acyclic compounds: proof of concept. *Org. Lett.* **1**, 2181–2184 (1999)
6. Micco, S.D., Chini, M.G., Riccio, R., Bifulco, G.: Quantum mechanical calculation of NMR parameters in the stereostructural determination of natural products. *Eur. J. Org. Chem.* **2010**, 1411–1434 (2010)
7. Thiele, C.M.: Use of RDCs in rigid organic compounds and some practical considerations concerning alignment media. *Concept Magn. Reson. A* **30A**, 65–80 (2007)
8. Kummerlöwe, G., Luy, B.: Residual dipolar couplings as a tool in determining the structure of organic molecules. *Trends Analyt. Chem.* **28**, 483–493 (2009)
9. Ohtani, I., Kusumi, T., Kashman, Y., Kakisawa, H.: High-field FT NMR application of Mosher's method. The absolute configurations of marine terpenoids. *J. Am. Chem. Soc.* **113**, 4092–4096 (1991)
10. (a) Seco, J.M., Quiñóa, E., Riguera, R.: The assignment of absolute configuration by NMR. *Chem. Rev.* **104**, 17–118 (2004); (b) Kong, L.Y., Wang, P.: Determination of the absolute configuration of natural products. *Chin. J. Nat. Med.* **11**, 193–198 (2013)
11. Kurz, M., Schmieder, P., Kessler, H.: HETLOC, an efficient method for determining heteronuclear long-range couplings with heteronuclei in natural abundance. *Angew. Chem. Int. Ed.* **30**, 1329–1331 (1991)
12. Wollborn, U., Leibfritz, D.: Measurement of heteronuclear long-range coupling constants from inverse homonuclear 2D NMR spectra. *J. Magn. Reson.* **98**, 142–146 (1992)
13. Hansen, P.E.: Carbon-hydrogen spin-spin coupling constants. *Prog. NMR Spectrosc.* **14**, 175295 (1981)
14. (a) Schwarcz, J.A., Cyr, N., Perlin, A.S.: Orientation effects and the sign of two-bond  $^{13}\text{C}$ – $^1\text{H}$  coupling. *Can. J. Chem.* **53**, 1872–1875 (1994); (b) Parella, T., Sanchez-Ferrando, F., Virgili, A.: Effect of hydroxyl and carbonyl groups on long-range proton-carbon coupling constants. *Magn. Reson. Chem.* **32**, 657–664 (1994); (c) Podlasek, C.A., Wu, J., Stripe, W.A., Bondo, P. B., Serianni, A.S.: [ $^{13}\text{C}$ ]Enriched methyl aldopyranosides: structural interpretations of  $^{13}\text{C}$ – $^1\text{H}$  spin-coupling constants and  $^1\text{H}$  chemical shifts. *J. Am. Chem. Soc.* **117**, 8635–8644 (1995)
15. Marquez, B.L., Gerwick, W.H., Williamson, R.T.: Survey of NMR experiments for the determination of nJ(C, H) heteronuclear coupling constants in small molecules. *Magn. Reson. Chem.* **39**, 499–530 (2001)
16. (a) Zhu, G., Bax, A.: Measurement of long-range  $^1\text{H}$ – $^{13}\text{C}$  coupling constants from quantitative 2D heteronuclear multiple-quantum correlation spectra. *J. Magn. Reson.* **104A**, 353–357 (1993); (b) Zhu, G., Live, D., Bax, A.: Analysis of sugar pucker and glycosidic torsion angles in a DNA G-tetrad structure by heteronuclear three-bond J coupling. *J. Am. Chem. Soc.* **116**, 8370–8371 (1994)
17. Willker, W., Leibfritz, D.: Determination of heteronuclear long-range H, X coupling constants from gradient-selected HMBC spectra. *Magn. Reson. Chem.* **33**, 632–638 (1995)
18. (a) Sasaki, M., Matsumori, N., Maruyama, T., Nonomura, T., Murata, M., Tachibana, K., Yasumoto, T.: The complete structure of maitotoxin. 1. Configuration of the C1–C14 side chain. *Angew. Chem. Int. Ed.* **35**, 1672–1675 (1996); (b) Nonomura, T., Sasaki, M., Matsumori, N., Murata, M., Tachibana, K., Yasumoto, T.: The complete structure of maitotoxin. 2. Configuration of the C135–C142 side chain and absolute configuration of the entire molecule. *Angew. Chem. Int. Ed.* **35**, 1675–1678 (1996); (c) Matsumori, N.,

- Nonomura, T., Sasaki, M., Murata, M., Tachibana, K., Satake, M., Yasumoto, T.: Long-range carbon-proton coupling constants for stereochemical assignment of acyclic structures in natural products: Configuration of the C5–C9 portion of maitotoxin. *Tetrahedron Lett.* **37**, 1269–1272 (1996)
19. Sakai, R., Kamiya, H., Murata, M., Shimamoto, K.: Dysiherbaine: a new neurotoxic amino acid from the Micronesian marine sponge *Dysidea herbacea*. *J. Am. Chem. Soc.* **119**, 4112–4116 (1997)
20. Murata, M., Matsuoka, S., Matsumori, N., Paul, G.K., Tachibana, K.: Absolute configuration of amphidinol 3, the first complete structure determination from amphidinol homologues: application of a new configuration analysis based on carbon-hydrogen spin-coupling constants. *J. Am. Chem. Soc.* **121**, 870–871 (1999)
21. Cha, J.K., Christ, W.J., Finan, J.M., Fujioka, H., Kishi, Y., Klein, L.L., Ko, S.S., Leder, J., McWhorter Jr., W.W., Pfaff, K.-P., Yonaga, M., Uemura, D., Hirata, Y.: Stereochemistry of palytoxin. 4. Complete structure. *J. Am. Chem. Soc.* **104**, 7369–7371 (1982)
22. (a) Boyle, C.D., Harmange, J.-C., Kishi, Y.: Novel structure elucidation of AAL toxin t-a backbone. *J. Am. Chem. Soc.* **116**, 4995–4996 (1994); (b) Boyle, C.D., Kishi, Y.: Absolute-configuration at the tricarballylic acid moieties of fumonisins b-1 and AAL toxin t-a. *Tetrahedron Lett.* **36**, 5695–5698 (1995)
23. (a) Zheng, W., DeMattei, J.A., Wu, J.-P., Duan, J. J.-W., Cook, L.R., Oinuma, H., Kishi, Y.: Complete relative stereochemistry of maitotoxin. *J. Am. Chem. Soc.* **118**, 7946–7968 (1996); (b) Cook, L.R., Oinuma, H., Semones, M.A., Kishi, Y.: The stereochemical assignment and conformational analysis of the V/W-ring juncture of maitotoxin. *J. Am. Chem. Soc.* **119**, 7928–7937 (1997)
24. Kobayashi, Y., Tan, C.-H., Kishi, Y.: Toward creation of a universal NMR database for stereochemical assignment: complete structure of the desertomycin/oasomycin class of natural products. *J. Am. Chem. Soc.* **123**, 2076–2078 (2001)
25. Higashibayashi, S., Czechtizky, W., Kobayashi, Y., Kishi, Y.: Universal NMR databases for contiguous polyols. *J. Am. Chem. Soc.* **125**, 14379–14393 (2003)
26. Plaza, A., Bifulco, G., Keffer, J.L., Lloyd, J.R., Baker, H.L., Bewley, C.A.: Celebesides A–C and theopapuamides B–D, depsipeptides from an Indonesian sponge that inhibit HIV-1 entry. *J. Org. Chem.* **74**, 504–512 (2009)
27. Bifulco, G., Bassarello, C., Riccio, R., Gomez-Paloma, L.: Quantum mechanical calculations of NMR J coupling values in the determination of relative configuration in organic compounds. *Org. Lett.* **6**, 1025–1028 (2004)
28. (a) Ditchfield, R.: Molecular-orbital theory of magnetic shielding and magnetic susceptibility. *J. Chem. Phys.* **56**, 5688–5691 (1972); (b) Wolinski, K., Hinton, J.F., Pulay, P.: Efficient implementation of the gauge-independent atomic orbital method for nmr chemical-shift calculations. *J. Am. Chem. Soc.* **112**, 8251–8260 (1990)
29. (a) Barone, G., Gomez- Paloma, L., Duca, D., Silvestri, A., Riccio, R., Bifulco, G.: Determination of the relative stereochemistry of flexible organic compounds by ab initio methods: conformational analysis and Boltzmann-averaged GIAO  $^{13}\text{C}$  NMR chemical shifts. *Chem. Eur. J.* **8**, 3233–3239 (2002); (b) Barone, G., Duca, D., Silvestri, A., Gomez-Paloma, L., Riccio, R., Bifulco, G.: Determination of the relative stereochemistry of flexible organic compounds by ab initio methods: conformational analysis and Boltzmann-averaged GIAO  $^{13}\text{C}$  NMR chemical shifts. *Chem. Eur. J.* **8**, 3240–3245 (2002)
30. Rosselli, S., Bruno, M., Maggio, A., Bellone, G., Formisano, C., Mattia, C.A., Di Micco, S., Bifulco, G.: Two new flavonoids from *Bonannia graeca*: a DFT-NMR combined approach in solving structures. *Eur. J. Org. Chem.* **2007**, 2504–2510 (2007)
31. Yan, J., Kline, A.D., Mo, H., Shapiro, M.J., Zartler, E.R.: A novel method for the determination of stereochemistry in six-membered chairlike rings using residual dipolar couplings. *J. Org. Chem.* **68**, 1786–1795 (2003)
32. Freudenberg, J.C., Spitteler, P., Bauer, R., Kessler, H., Luy, B.: Stretched poly(dimethylsiloxane) gels as NMR alignment media for apolar and weakly polar organic solvents: an ideal

- tool for measuring RDCs at low molecular concentrations. *J. Am. Chem. Soc.* **126**, 14690–14691 (2004)
33. Schuetz, A., Junker, J., Leonov, A., Lange, O.F., Molinski, T.F., Griesinger, C.: Stereochemistry of Sagittamide A from residual dipolar coupling enhanced NMR. *J. Am. Chem. Soc.* **129**, 15114–15115 (2007)
34. Nath, N., Schmidt, M., Gil, R.R., Williamson, R.T., Martin, G.E., Navarro-Vázquez, A., Griesinger, C., Liu, Y.: Determination of relative configuration from residual chemical shift anisotropy. *J. Am. Chem. Soc.* **138**, 9548–9556 (2016)
35. Singer, S.J., Nicolson, G.L.: The fluid mosaic model of the structure of cell membranes. *Science* **175**, 720–731 (1971)
36. Simons, K., Ikonen, E.: Functional rafts in cell membranes. *Nature* **387**, 569–572 (1997)
37. Maulik, P.R., Shipley, G.G.: *N*-palmitoyl sphingomyelin bilayers: structure and interactions with cholesterol and dipalmitoylphosphatidylcholine. *Biochemistry* **35**, 8025–8034 (1996)
38. Veach, S., Keller, S.: Separation of liquid phases in giant vesicles of ternary mixtures of phospholipids and cholesterol. *Biophys. J.* **85**, 3074–3083 (2003)
39. Quinn, P.J.: Lipid-lipid interactions in bilayer membranes: married couples and casual liaisons. *Prog. Lipid Res.* **51**, 179–198 (2012)
40. Simons, K., Sampaio, J.L.: Membrane organization and lipid rafts. *Cold Spring Harb. Perspect. Biol.* **3**, a004697 (2011)
41. Murata, M., Sugiyama, S., Matsuoka, S., Matsumori, N.: Bioactive structure of membrane lipids and natural products elucidated by a chemistry-based approach. *Chem. Rec.* **15**, 675–690 (2015)
42. Hartsel, S., Bolard, J.: Amphotericin B: new life for an old drug. *Trends Pharmacol. Sci.* **17**, 445–449 (1996)
43. Rienstra, C.M., Hatcher, M.E., Mueller, L.J., Sun, B., Fesik, S.W., Griffin, R.G.: Efficient multispin homonuclear double-quantum recoupling for magic-angle spinning NMR: <sup>13</sup>C–<sup>13</sup>C correlation spectroscopy of u-<sup>13</sup>C-erythromycin A. *J. Am. Chem. Soc.* **120**, 10602–10612 (1998)
44. Matsuoka, S., Ikeuchi, H., Umegawa, Y., Matsumori, N., Murata, M.: Membrane interaction of amphotericin B as single-length assembly examined by solid state NMR for uniformly <sup>13</sup>C-enriched agent. *Bioorg. Med. Chem.* **14**, 6608–6614 (2006)
45. Gullion, T., Schaefer, J.: Rotational-echo double-resonance NMR. *J. Magn. Reson.* **81**, 196–200 (1989)
46. Gullion, T., Schaefer, J.: Detection of weak heteronuclear dipolar coupling by rotational-echo double-resonance nuclear magnetic resonance. *Adv. Magn. Reson.* **13**, 57–83 (1989)
47. Hirsh, D.J., Hammer, J., Maloy, W.L., Blazyk, J., Schaefer, J.: Secondary structure and location of a magainin analogue in synthetic phospholipid bilayers. *Biochemistry* **35**, 12733–12741 (1996)
48. Mehta, A.K., Schaefer, J.: Rotational-echo double resonance of uniformly labeled <sup>13</sup>C clusters. *J. Magn. Res.* **163**, 188–191 (2003)
49. (a) Readjo, J.D., Bittman, R.: Equilibrium binding of amphotericin B and its methyl ester and borate complex to sterols. *Biochim. Biophys. Acta* **685**, 219–224 (1982); (b) Matsuoka, S., Murata, M.: Cholesterol markedly reduces ion permeability induced by membrane-bound amphotericin B. *Biochim. Biophys. Acta* **1564**, 429–434 (2002)
50. Umegawa, Y., Nakagawa, Y., Tahara, K., Tsuchikawa, H., Matsumori, N., Oishi, T., Murata, M.: Head-to-tail interaction between amphotericin B and ergosterol occurs in hydrated phospholipid membrane. *Biochemistry* **51**, 83–89 (2012)
51. Nakagawa, Y., Umegawa, Y., Takano, T., Tsuchikawa, H., Matsumori, N., Murata, M.: Effect of sterol side chain on ion channel formation by amphotericin B in lipid bilayers. *Biochemistry* **53**, 3088–3094 (2014)
52. Nakagawa, Y., Umegawa, Y., Nonomura, K., Matsushita, N., Takano, T., Tsuchikawa, H., Oishi, T., Matsumori, N., Murata, M.: Axial hydrogen at C7 position and bumpy tetracyclic core markedly reduce sterol's affinity to amphotericin B in membrane. *Biochemistry* **54**, 303–312 (2015)

53. Nakagawa, Y., Umegawa, Y., Matsushita, N., Yamamoto, T., Tsuchikawa, H., Hanashima, S., Oishi, T., Matsumori, N., Murata, M.: Structure of bimolecular complex between amphotericin B and ergosterol in membrane is stabilized by face-to-face Van der Waals interaction with their rigid cyclic cores. *Biochemistry* **55**, 3392–3402 (2016)
54. Yamamoto, T., Umegawa, Y., Yamagami, M., Tsuchikawa, H., Hanashima, S., Matsumori, N., Murata, M.: Perpendicular orientation of amphotericin B methyl ester in lipid bilayer elucidated by <sup>2</sup>H and <sup>19</sup>F solid-state NMR supports the barrel-stave model. *Biochemistry* (2017) (submitted)
55. Montenez, J.P., Van Bambeke, F., Piret, J., Brasseur, R., Tulkens, P.M., Mingeot-Leclercq, M.P.: Interactions of macrolide antibiotics (Erythromycin A, roxithromycin, erythromycylamine [Dirithromycin], and azithromycin) with phospholipids: computer-aided conformational analysis and studies on acellular and cell culture models. *Toxicol. Appl. Pharmacol.* **156**, 129–140 (1999)
56. Reasor, M.J., Kacew, S.: Drug-induced phospholipidosis: are there functional consequences? *Exp. Biol. Med.* **226**, 825–830 (2001)
57. Andersson, A., Biverstähl, H., Nordin, J., Danielsson, J., Lindahl, E., Mäler, L.: The membrane-induced structure of melittin is correlated with the fluidity of the lipids. *Biochim. Biophys. Acta* **1768**, 115–121 (2007)
58. Biverstähl, H., Lind, L., Bodor, A., Mäler, L.: Biophysical studies of the membrane location of the voltage-gated sensors in the HsapBK and KvAP K(+) channels. *Biochim. Biophys. Acta* **1788**, 1976–1986 (2009)
59. (a) Matsumori, N., Morooka, A., Murata, M.: Detailed description on conformation and location of membrane-bound erythromycin A using small bicelle. *J. Med. Chem.* **49**, 3501–3508 (2006); (b) Matsumori, N., Murata, M.: 3D structures of membrane-associated small molecules as determined in isotropic bicelles. *Nat. Prod. Rep.* **27**, 1480–1492 (2010)
60. Harris, D.R., McGeachin, S.G., Mills, H.H.: The structure and stereochemistry of erythromycin A. *Tetrahedron Lett.* **6**, 679–685 (1965)
61. Matsunaga, S., Fusetani, N., Hashimoto, K., Wälchli, M., Theonellamide, F.: A novel antifungal bicyclic peptide from a marine sponge *Theonella* sp. *J. Am. Chem. Soc.* **111**, 2582–2588 (1989)
62. Nishimura, S., Arita, Y., Honda, M., Iwamoto, K., Matsuyama, A., Shirai, A., Kawasaki, H., Kakeya, H., Kobayashi, T., Matsunaga, S., Yoshida, M.: Marine antifungal theonellamides target 3beta-hydroxysterol to activate Rho1 signaling. *Nat. Chem. Biol.* **6**, 519–526 (2010)
63. Espiritu, R., Matsumori, N., Murata, M., Nishimura, S., Kakeya, H., Matsunaga, S., Yoshida, M.: Interaction between the marine sponge cyclic peptide theonellamide A and sterols in lipid bilayers as viewed by surface plasmon resonance and solid-state <sup>2</sup>H nuclear magnetic resonance. *Biochemistry* **52**, 2410–2418 (2013)
64. Morris, K.F., Johnson Jr., C.S.: Diffusion-ordered two-dimensional nuclear magnetic resonance spectroscopy. *J. Am. Chem. Soc.* **114**, 3139–3141 (1992)
65. Cornelio, K., Espiritu, R.A., Todokoro, Y., Hanashima, S., Kinoshita, M., Matsumori, N., Murata, M., Nishimura, S., Kakeya, H., Yoshida, M., Matsunaga, S.: Sterol-dependent membrane association of the marine sponge-derived bicyclic peptide theonellamide A as examined by <sup>1</sup>H NMR. *Bioorg. Med. Chem.* **24**, 5235–5242 (2016)
66. Espiritu, R., Matsumori, N., Tsuda, M., Murata, M.: Direct and stereospecific interaction of amphidinol 3 with sterol in lipid bilayers. *Biochemistry* **52**, 2410–2418 (2014)
67. Espiritu, R.A., Cornelio, K., Kinoshita, M., Matsumori, N., Murata, M., Nishimura, S., Kakeya, H., Yoshida, M., Matsunaga, S.: Marine sponge cyclic peptide theonellamide A disrupts lipid bilayer integrity without forming distinct membrane pores. *Biochim. Biophys. Acta* **1858**, 1373–1379 (2016)

# Chapter 15

## Technical Basis for Nuclear Magnetic Resonance Approach for Glycoproteins

Koichi Kato, Saeko Yanaka and Hirokazu Yagi

**Abstract** *Glycophobia* in structural biology is strongly associated with the unpredictable, heterogeneous nature of protein glycosylation and the complex, flexible structures of the glycoprotein glycans. Moreover, glycoproteins cannot be produced by conventional bacterial expression systems. Nuclear magnetic resonance (NMR) spectroscopy assisted by other analytical and preparative techniques can now successfully address these issues. Recombinant glycoproteins can be expressed with stable isotope labeling using a variety of eukaryotic production vehicles. Glycoforms of glycoproteins can be remodeled by genetic engineering of the production vehicles as well as in vitro enzymatic reactions. Stable-isotope-assisted NMR techniques have provided detailed information regarding conformational dynamics and interactions of the carbohydrate chains in solution, giving insights into the functional mechanisms of glycoprotein glycans.

**Keywords** Glycoprotein · Oligosaccharide · Stable isotope labeling  
Eukaryotic expression system · NMR spectroscopy

---

K. Kato (✉) · H. Yagi

Graduate School of Pharmaceutical Sciences, Nagoya City University,  
3-1 Tanabe-dori, Mizuho-Ku, Nagoya 467-8603, Japan  
e-mail: kkato@phar.nagoya-cu.ac.jp

H. Yagi

e-mail: hyagi@phar.nagoya-cu.ac.jp

K. Kato · S. Yanaka

Okazaki Institute for Integrative Bioscience, Institute for Molecular Science,  
National Institutes of Natural Sciences, 5-1 Higashiyama Myodaiji,  
Okazaki 444-8787, Japan  
e-mail: saeko-yanaka@ims.ac.jp

## 15.1 Introduction

Advancements in biomolecular NMR spectroscopy have been driven by the constant development of methods for the expression of isotope-labeled biomacromolecules and novel hardware, exemplified by higher-field-strength magnets along with sophisticated measurement techniques. This progress has enabled high-throughput three-dimensional (3D)-structure determination of proteins, quantitative characterization of conformational dynamics of biomolecules on a broad range of timescales [1, 2], depiction of huge protein complexes beyond 1 MDa [3], and observation of protein behaviors in intracellular environments [4]. Advances in biomolecular NMR spectroscopy have also provided technical basis for high-throughput analyses of protein–ligand interactions using chemical libraries [5, 6]. To date, proteins subjected to NMR-based structural analysis have been conventionally produced using bacterial protein expression systems or cell-free expression systems [7]. Although more than half of proteins in nature are estimated to be modified with carbohydrate moieties [8], these recombinant proteins are not glycosylated by the aforementioned expression systems.

Carbohydrate chains have a significant impact on physicochemical and biofunctional properties of the carrier proteins [9]. Thermal stability and solubility of proteins are governed by the carbohydrate chains, which can also affect protein conformations, and thereby control their biological functions. Moreover, glycans directly involved in interactions with other proteins, which are collectively termed lectins, mediate a variety of biological processes involved in cell–cell communications, viral and bacterial infections, immune responses, and protein-fate determination. Therefore, without knowledge of the glycan structures, one can barely understand the functional mechanisms of glycoproteins in the biological context. However, despite their biological importance, structural biology studies of glycoproteins have been falling behind. Indeed, atomic coordinates of glycoproteins represent only 4% of the total entries in the Protein Data Bank, and most of these provide structural information on only one or two glycan residues (Fig. 15.1).

Besides the traditional application for the determination of the covalent structures of oligosaccharides [10–12], NMR spectroscopy can play versatile roles in characterizing dynamic conformations and interactions of oligosaccharides. In this chapter, we will outline the major obstacles in studying glycoproteins via NMR spectroscopy and the current state-of-the-art methodology for NMR-based structural glycobiology.

## 15.2 Enigmatic Aspects of Carbohydrate Structures

Needless to say, any structural biology studies presuppose the covalent structures of the target biomolecules, e.g., the amino acid sequences of proteins. An obvious example can be seen in structural genomics, in which accumulating genome

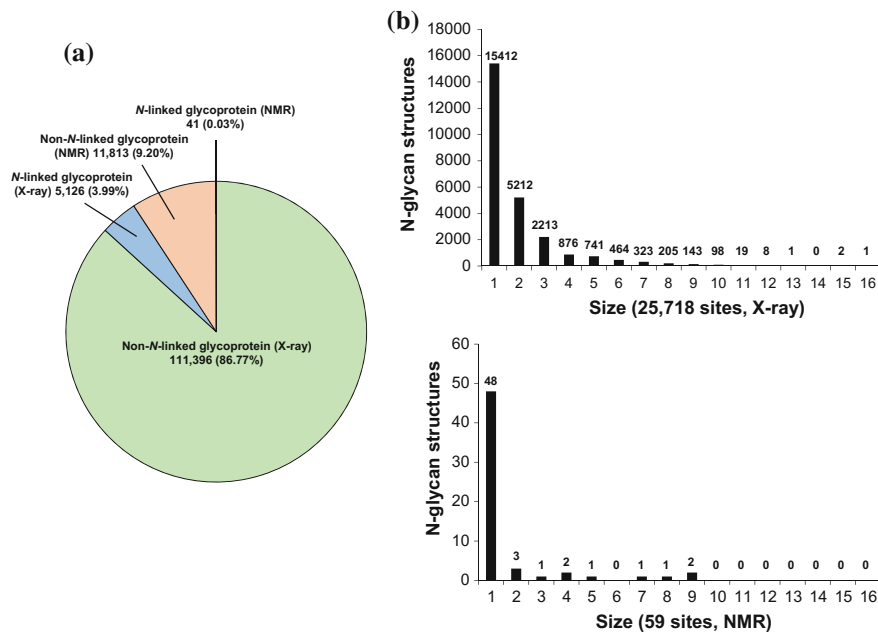


**Fig. 15.1** Current statistics regarding Protein Data Bank entries on *N*-linked glycoprotein structures (data were extracted on May 17, 2017). **a** Number and percentage of X-ray crystallography and NMR structures of *N*-linked glycoproteins. **b** Size distribution of *N*-glycans among glycoprotein structures revealed by X-ray crystallography (*top*) and NMR spectroscopy (*bottom*)

sequence data have prompted comprehensive structural determination of the encoded proteins. From this perspective, one of the biggest problems in structural biology of glycoproteins is that the covalent structures of glycans are not directly encoded in the genome. Although the necessary sequence for eukaryotic *N*-glycosylation, i.e., Asn-X-Ser/Thr/(Cys) in which X is not proline, is widely known, this is insufficient [9]. Furthermore, no consensus motif has been established for other glycosylation sites, despite a certain tendency of amino acid sequences in *O*-glycosylation sites [9]. Hence, glycosylation sites of a protein with a known amino acid sequence remain unpredictable. Moreover, it is much more difficult to deduce the sequence of carbohydrate moiety at each glycosylation site. Indeed, the carbohydrate moieties displayed at one site of protein often have a high degree of sequence divergence and heterogeneity, depending not only on the protein structure but also on physiological and pathological conditions [9]. In the case of immunoglobulin G (IgG), which is a major serum glycoprotein, its glycosylation depends on aging, pregnancy, delivery, and onset of connective tissue disease typified by rheumatoid arthritis [13–17]. Of course, recombinant glycoproteins produced in different production vehicles exhibit different glycoforms and even cell culture conditions affect the glycosylation profiles [18, 19].

The intrinsic complexity of oligosaccharide structures brings further difficulty in structural analysis of glycoproteins. The building blocks of sugar chains, i.e., monosaccharides, are structurally simple with little variation in their functional groups in comparison with amino acids [9]. However, unlike polypeptide chains and nucleic acids, sugar residues are connected through multiple types of glycosidic linkages, potentially giving rise to a wide variety of isomeric and branching structures. Indeed, the number of all possible isomers of a tetrasaccharide composed of four different monosaccharides was calculated to be 34,560, whereas only 24 different tetrapeptides are made from four different amino acid residues [20]. Glycosidic linkage isomerism is critical to glycoprotein functions, as best exemplified by infections with influenza viruses, which bind host cells by recognizing specific sialyl linkage isomers [21]. Paradoxically, the structural simplicity (or similarity) of sugar residues precludes structural analyses: Isomeric structures such as glucose, mannose, and galactose cannot be distinguished by conventional mass spectrometry (MS), whereas the little diversity of the functional groups causes a chemical shift degeneracy in NMR spectroscopy.

Another difficulty for structural analysis of glycoproteins is associated with the motional freedom of glycosidic linkages in the carbohydrate moieties, giving rise to conformational fluctuations. This flexible property of glycans, along with their structural heterogeneity, hampers crystallization of glycoproteins, and, even if it succeeds, interpretation of their electron densities is unavoidably ambiguous [22]. Moreover, a tricky problem is that mutational deglycosylation can cause unexpected or even undesirable modifications of the proteins, such as sulfation and nicks [23, 24].

All these characteristics of the carbohydrate chains make structural analysis of glycoproteins (and even oligosaccharides) a challenging task. Namely, one who attempts to perform structural glycobiology must conduct a series of analyses, from the determination of carbohydrate sequences to characterization of the conformational dynamics of target glycoproteins including their glycans. NMR spectroscopy plays a central role in addressing these issues because it can, in principle, characterize dynamic structures of heterogeneous biomacromolecules in solution. However, it should be noted that a variety of preparative and analytical techniques that complement NMR approach are indispensable for conducting structural analysis of glycoproteins. In the following sections, we will describe how one can perform structural glycobiology by NMR spectroscopy aided by these complementing methods.

### 15.3 Expression of Isotope-Labeled Glycoproteins

As glycoproteins cannot be produced by conventional protein expression systems such as *Escherichia coli*, appropriate eukaryotic vehicles have to be chosen for the production of NMR quantities of glycoproteins with stable isotope labeling. Typical choices would be cell lines derived from mammals. Several groups developed

metabolic isotope labeling of recombinant proteins using mammalian cells, including Chinese hamster ovary (CHO) cells, mouse hybridomas, and adenovirus vector-based mammalian cells [25–29]. In particular, uniform and amino acid-selective  $^{13}\text{C}$  and/or  $^{15}\text{N}$  labeling techniques were established using IgG as a model glycoprotein, yielding several NMR applications [27, 29]. The composition of the serum-free medium used for the production of isotopically labeled IgG is shown in Table 15.1. Amino acid-selective labeling is accomplished by replacing specific amino acid(s) with their isotope-labeled counterpart(s), although this often suffers from metabolic isotope scrambling and dilution. To suppress the undesirable metabolic processes, metabolic inhibitors such as  $\beta$ -chloro-L-alanine are often added to the medium [30].

For uniform  $^{13}\text{C}/^{15}\text{N}$  labeling of a glycoprotein, it is necessary to replace all the metabolic precursors with the isotope-labeled ones, which are commercially very expensive. A more practical approach is to use an isotope-labeled amino acid mixture derived from algae with the modification of the medium composition (Table 15.1). Using this protocol, uniformly  $^{13}\text{C}/^{15}\text{N}$ -labeled IgG glycoproteins were produced through mammalian cell culture. Figure 15.2A shows a  $^1\text{H}$ – $^{15}\text{N}$  HSQC spectrum of  $^{13}\text{C}/^{15}\text{N}$ -labeled human IgG-Fc obtained from CHO cells [31].

Isotope labeling of the carbohydrate moieties can be simply achieved by using  $^{13}\text{C}$ -labeled glucose as a metabolic precursor.  $^{13}\text{C}$ - and/or  $^{15}\text{N}$ -labeled glucosamine (but not *N*-acetylglucosamine) can be used for metabolic labeling of GlcNAc residues in the carbohydrate moieties of glycoproteins [32, 33].

In addition to mammalian cells, metabolic isotope labeling techniques have been developed for NMR applications in various eukaryotic expression systems including yeast, *Dictyostelium discoideum*, insects, and plants [34–39]. As an insect cell-based production vehicle, Sf9 cells infected with recombinant baculoviruses are widely used for the expression of membrane glycoproteins for NMR as well as crystallographic analyses [36, 40]. Recently, silkworms have been demonstrated as promising production vehicles for isotope-labeled recombinant glycoproteins [35]. In this approach, baculovirus-infected fifth instar larvae were reared with an artificial diet containing a protein mixture derived from *Candida utilis* grown in a culture medium containing  $^{15}\text{N}$ -labeled ammonium sulfate as a nitrogen source.  $^{15}\text{N}$ -enrichment level of recombinant human IgG achieved in this system was approximately 80%.

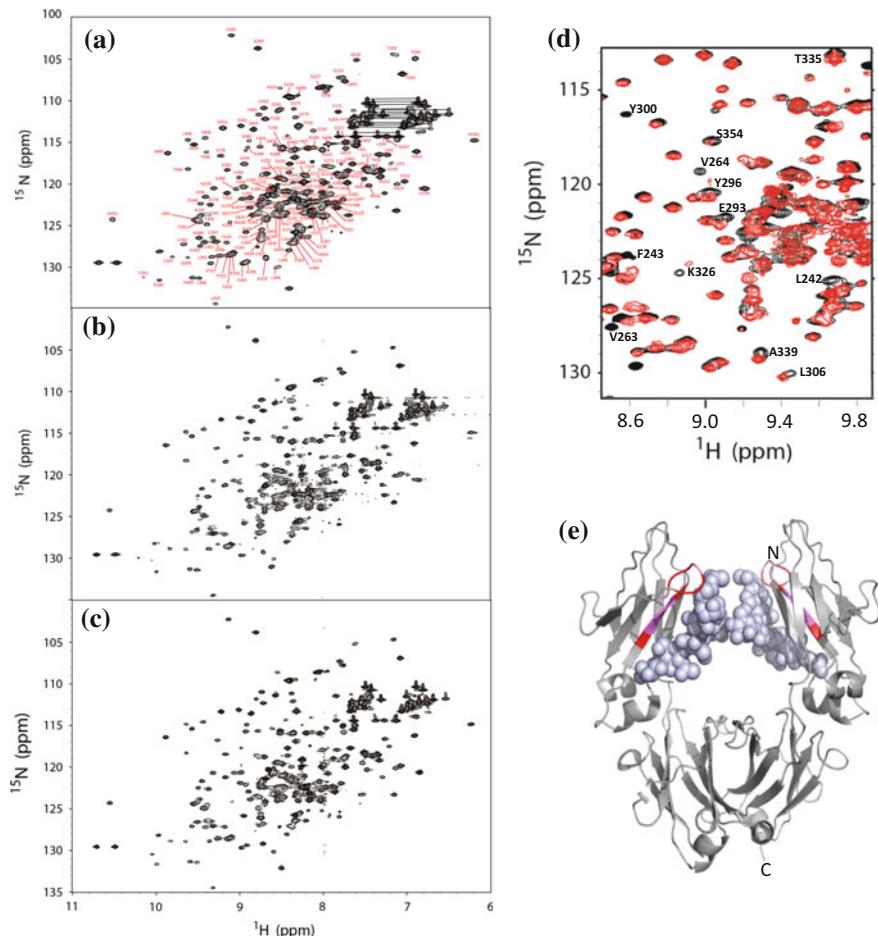
Plant expression systems are now attracting attention from pharmaceutical interests. Transgenic tobacco (*Nicotiana benthamiana*) was tested for the expression of  $^{15}\text{N}$ -labeled IgG [34]. Four-week-old seedlings of transgenic tobacco were placed in a drip hydroponic system and cultivated for 49 days with isotopically labeled Murashige and Skoog medium containing potassium nitrate ( $\text{K}^{15}\text{NO}_3$ ) and ammonium nitrate ( $^{15}\text{NH}_4^{15}\text{NO}_3$ ) as the major nitrogen sources. The degree of  $^{15}\text{N}$ -enrichment of recombinant human IgG thus produced was in the approximately 50–60% range.

Figure 15.2 compares the  $^1\text{H}$ – $^{15}\text{N}$  HSQC spectra of recombinant human IgG1-Fc expressed by transgenic tobacco and silkworm as well as CHO cells [31, 34, 35]. Although the spectra are similar, significant chemical shift differences were

**Table 15.1** Composition of the serum-free medium used for metabolic labeling of IgG glycoproteins (mg/L)

		Algal mixture	–	+
NaCl	6208	L-Arginine · HCl	76.1	–
KCl	388	L-Arginine	97.0	72.0
CaCl <sub>2</sub> (unhyd)	97	L-Asparagine · H <sub>2</sub> O	42.5	42.5
Ca(NO <sub>3</sub> ) <sub>2</sub> (unhyd)	33.7	L-Aspartic acid	9.7	–
MgSO <sub>4</sub> (unhyd)	69.0	L-Cystine · 2H <sub>2</sub> O	31.5	31.5
Na <sub>2</sub> HPO <sub>4</sub> (unhyd)	388.5	L-Cysteine · HCl · H <sub>2</sub> O	16.7	16.7
NaH <sub>2</sub> PO <sub>4</sub> (unhyd)	55.8	L-Glutamic acid	9.7	–
D-Biotin	0.11	L-Glutamine	450	450
D-Ca pantothenate	0.61	L-Histidine	27.7	15.5
Choline chloride	26.5	Glycine	9.9	–
Folic acid	0.97	L-Hydroxyproline	9.7	–
i-Inositol	18.0	L-Isoleucine	49.5	–
Nicotinamide	0.97	L-Leucine	49.5	13.1
p-Aminobenzoic acid	0.485	L-Lysine · HCl	54.8	–
Pyridoxal HCl	0.485	L-Methionine	14.6	–
Pyridoxine HCl	0.485	L-Proline	14.7	–
Riboflavin	0.146	L-Serine	29.6	–
Thiamin HCl	0.97	L-Threonine	48.0	–
Vitamin B12	0.0037	L-Valine	47.0	–
Glutathione (red)	0.485	L-Phenylalanine	22.8	–
Choline bitartrate	0.873	L-Tryptophan	7.3	7.3
Putrescine 2H <sub>2</sub> O	0.0125	L-Tyrosine	27.2	16.9
Sodium pyruvate	110.0	Algal mixture	–	867
Thymidine	0.0125			
Hypoxanthine	0.025			
Monoethanolamine	20.0			
Sodium selenite	0.0017			
Kanamycin sulfate	60.0			
Phenol red	5.0			
Glucose	2000			
Sodium succinate	50.0			
Succinic acid	37.5			
Bovine transferrin (holo)	5.0			
Bovine insulin	10.0			
HEPES	3570			
Sodium bicarbonate	1400			

observed for the amino acid residues in close proximity to *N*-glycans. The plant-derived IgG1-Fc exhibits  $\alpha$ 1,3-linked fucose and  $\beta$ 1,2-linked xylose residues in the common conserved Man<sub>3</sub>GlcNAc<sub>2</sub> core, whereas the insect cell-derived



**Fig. 15.2**  $^1\text{H}$ - $^{15}\text{N}$  HSQC spectra of isotope-labeled human IgG1-Fc are shown obtained from **a** CHO cells, **b** transgenic tobacco plants, and **c** silkworms. **d** Superposition of  $^1\text{H}$ - $^{15}\text{N}$  HSQC spectra of the uniformly  $^{15}\text{N}/^{13}\text{C}$ -labeled IgG1-Fc expressed by transgenic silkworm (red) and CHO cells (black). **e** Mapping of the amino acid residues with observable chemical shift changes [ $(0.2\delta_{\text{N}}^2 + \delta_{\text{H}}^2)^{1/2} > 0.1 \text{ ppm}$  and  $> 0.2 \text{ ppm}$  in pink and red, respectively] on the crystal structure [PDB code: 3AVE] [57]. The *N*-glycans are represented by gray sphere. The molecular graphics were generated with PyMOL [98]. In **(a)** backbone assignments are annotated by the resonance peaks with one-letter amino acid codes and the sequence numbers. Side-chain resonances corresponding to  $\text{NH}_2$  amides are connected by horizontal lines. Adapted from Refs. [31, 34, 35] with the modification

glycoprotein expresses paucimannose-type glycans as the major components (Fig. 15.3). Because these glycoforms are not expressed in mammalian vehicles, the observed spectral differences could be attributed to microenvironmental alterations caused by differential glycosylation.

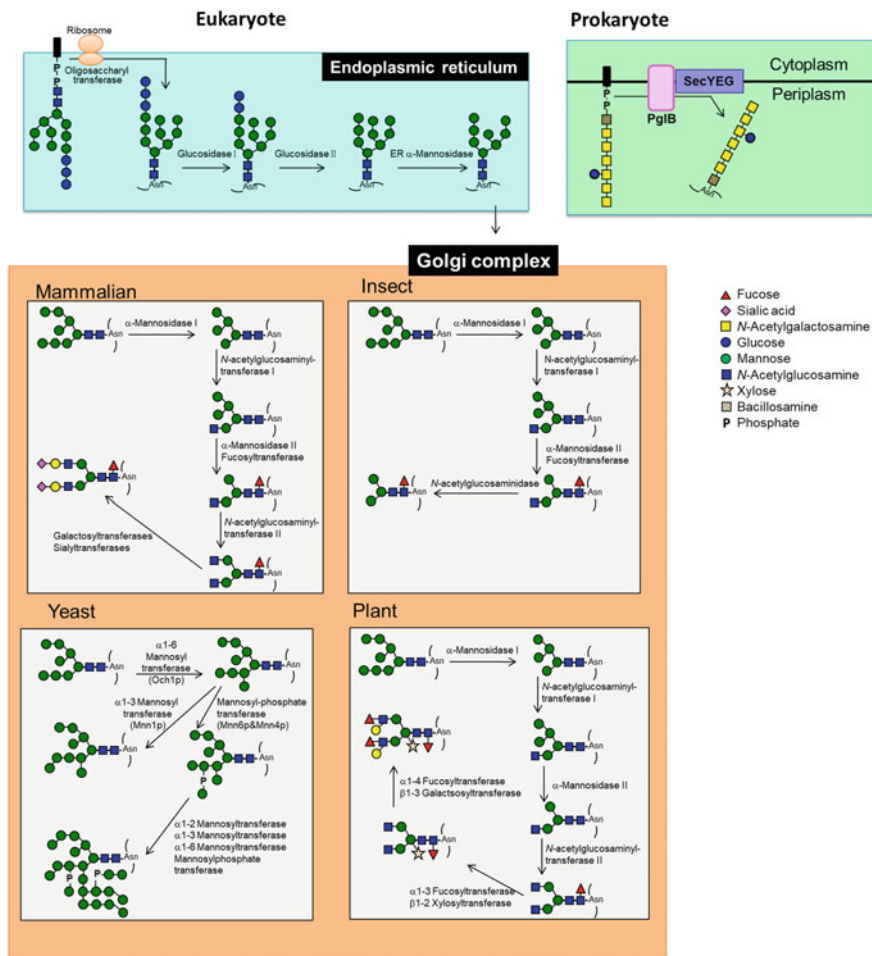


**Fig. 15.3** *N*-glycan processing pathways as the basis of glycoform-engineering strategies. Schematic drawing of the *N*-glycan processing pathway in the ER common to mammalian cells, insect, yeast, and plant, and the distinct pathways in the Golgi complex along with a prokaryotic *N*-glycan pathway exemplified by that in *C. jejuni*. Adapted from Ref. [94] with the modification

Yeast can also be employed for the expression of isotope-labeled recombinant glycroteins [37, 38, 41]. For example, *Pichia pastoris* strain GS115 was used for producing  $^{15}\text{N}$ -labeled human chorionic gonadotropin and human follicle-stimulating hormone [37]. From cultures of *P. pastoris* using  $^{15}\text{NH}_4\text{Cl}/\text{glucose-glycerol-methanol}$  as nitrogen and carbon sources, human chorionic gonadotropin was obtained with an  $^{15}\text{N}$  enrichment of 70%, with modification by the yeast-strain-specific high-mannose-type oligosaccharides ranging from  $\text{Man}_8\text{GlcNAc}_2$  to  $\text{Man}_{11}\text{GlcNAc}_2$ . Kamiya et al. [38, 41] described a method for the overexpression of uniformly  $^{13}\text{C}$ -labeled decasaccharides M8B and

undecasaccharide M9 using genetically engineered *Saccharomyces cerevisiae* cells grown in medium containing  $^{13}\text{C}$ -labeled glucose.

Deuteration is effective to suppress dipolar relaxation for dealing with larger biomacromolecules [42, 43]. However, one major problem in eukaryotic expression systems is difficulty in metabolic deuteration using heavy water because the cells cannot survive in such a milieu. Recently, using deuterated yeast extract, Grzesiek and coworkers successfully established a methodology for deuteration of recombinant proteins expressed in insect cells with a deuteration degree of >60% without any decrease in protein yield [44]. This line of study will open up new avenues for NMR analyses of larger glycoproteins expressed by eukaryotic expression systems.

Although *E. coli* lacks a protein glycosylation pathway, protein *N*-glycosylation has been found in a variety of bacteria including *Campylobacter jejuni*, which expresses proteins modified with the *N*-linked heptasaccharide, GalNAc $\alpha$ 1-4GalNAc $\alpha$ 1-4(Glc $\beta$ 1-3)GalNAc $\alpha$ 1-4GalNAc $\alpha$ 1-4GalNAc $\alpha$ 1-3Bac [45] (Fig. 15.3). A  $^{13}\text{C}/^{15}\text{N}$ -labeled recombinant protein produced in *E. coli* was successfully modified in vitro with this oligosaccharide by using enzymes from *C. jejuni* [46].

## 15.4 Glycosylation Profiling

Because the glycoform of a given glycoprotein is generally unpredictable, experimental glycosylation profiling is necessary for identifying its covalent structure. High-performance liquid chromatography (HPLC) mapping is a useful technique for the quantitative profiling of protein glycosylation. In particular, Takahashi and coworkers have developed 3D HPLC mapping using pyridyl-2-amination of *N*-linked oligosaccharides chemically or enzymatically cleaved from glycoproteins [47, 48] (Fig. 15.4). The fluorescence-labeled oligosaccharides are subjected to three different HPLC columns, i.e., diethylaminoethyl (DEAE), octadecylsilica (ODS), and amide, in a sequential manner, enabling identification of their structures based on their elution positions on the columns and reference to a database. A strength of this method is the ability to discriminate isomeric oligosaccharides by their differential elution times, primarily on the ODS column. Figure 15.4a illustrates a typical elution profile on an ODS column of the pyridylamino derivatives of *N*-glycans from human IgG1-Fc, which exhibit microheterogeneities resulting from the presence or absence of non-reducing terminal galactose residues [49].

MS also offers useful tools for rapid and sensitive profiling of glycosylation of glycoproteins. MS analyses enable site-specific glycosylation profiling as well as determination of entire molecular glycoforms of multiple glycosylated proteins including glycan combinations [50–53]. Although discrimination of isomeric oligosaccharides is not possible by conventional MS measurement, attempts have been made to achieve it by analyzing the fragmentation patterns observed in multistage tandem mass ( $\text{MS}^n$ ) spectra [54, 55].

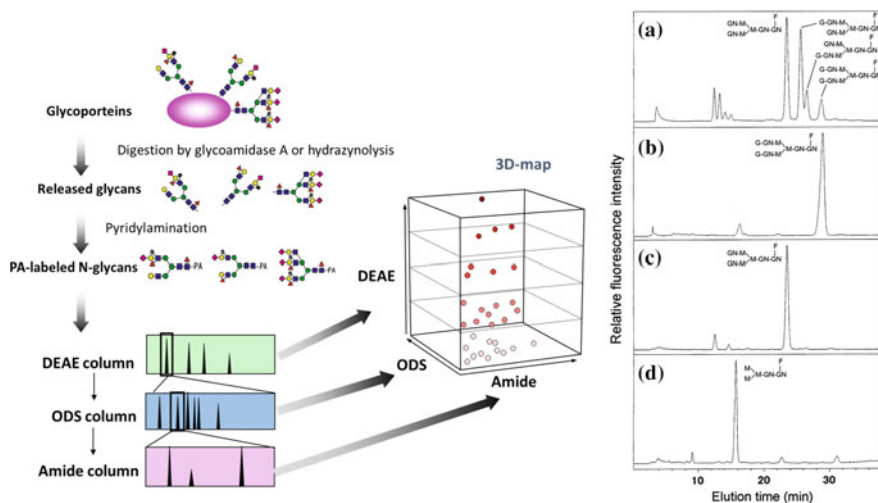


**Fig. 15.4** Scheme of *N*-glycosylation profiling based on the 3D HPLC map (*left*) and elution profiles on an ODS column of pyridylamino derivatives of the *N*-linked oligosaccharides released from the human IgG1-Fc glycoforms (*right*). **a** Non-treated Fc, **b** Fc(G2), **c** Fc(G0), and **d** Fc(M3). Key *F* fucose; *G* galactose; *GN* *N*-acetylglucosamine; *M* mannose. Partially adapted from Ref. [49] with the modification

## 15.5 Remodeling of Glycoprotein Glycoforms

Heterogeneous glycosylation hampers unambiguous structural studies of glycoproteins, making structural biologists *glycophobics*. To overcome this problem, various techniques have been applied for remodeling glycoprotein glycoforms to reduce glycan heterogeneity. Glycoform remodeling is also useful for systematic analyses of the structure–function relationships of glycoproteins, addressing the functional properties of individual glycoforms.

Glycosidase treatment has been traditionally used for trimming of glycoprotein glycans. Glycoproteins with a uniform glycan structure can also be prepared by *in vitro* enzymatic attachment of non-reducing terminal sugar residue(s) [49, 56]. Figure 15.4b, c shows elution profiles of *N*-glycans derived from digalactosyl (G2) and galactosyl (G0) glycoforms of human IgG1-Fc prepared by enzymatic galactosylation and degalactosylation, respectively. The IgG1-Fc glycans could be further trimmed into the trimannosyl core FucGlcNAc<sub>2</sub>Man<sub>3</sub> by *N*-acetylhexosaminidase treatment (Fig. 15.4d) and subsequently into the Fuc $\alpha$ 1 → 6GlcNAc disaccharide (FGN) with endo D treatment. The glycan could be completely eliminated by PNGase F treatment. Figure 15.5 compares the <sup>1</sup>H–<sup>15</sup>N HSQC spectra of a series of Fc glycoforms (G2, G0, M3, FGN, and deglycosylation), displaying progressive spectral changes of the polypeptide

backbone of Fc upon stepwise trimming of the glycans [49]. The results indicated that removal of the cleavage at the GlcNAc $\beta$ 1-4GlcNAc linkage of the Fc glycans conformationally affected areas proximal to the hinge region, including the Fc $\gamma$  receptor-binding sites, thereby impairing receptor binding. Therefore, the carbohydrate moieties of Fc play crucial roles in maintaining the structural integrity of the functional sites of IgG.

Another approach for controlling glycosylation is genetic engineering of glycoprotein-producing cells by knocking out genes responsible for specific processes during glycan formation. For example, CHO cells lacking FUT8, an enzyme catalyzing the transfer of fucose from GDP-fucose to GlcNAc in an  $\alpha$ -1,6 linkage, produce a completely non-fucosylated glycoform of IgG [57], which has a higher

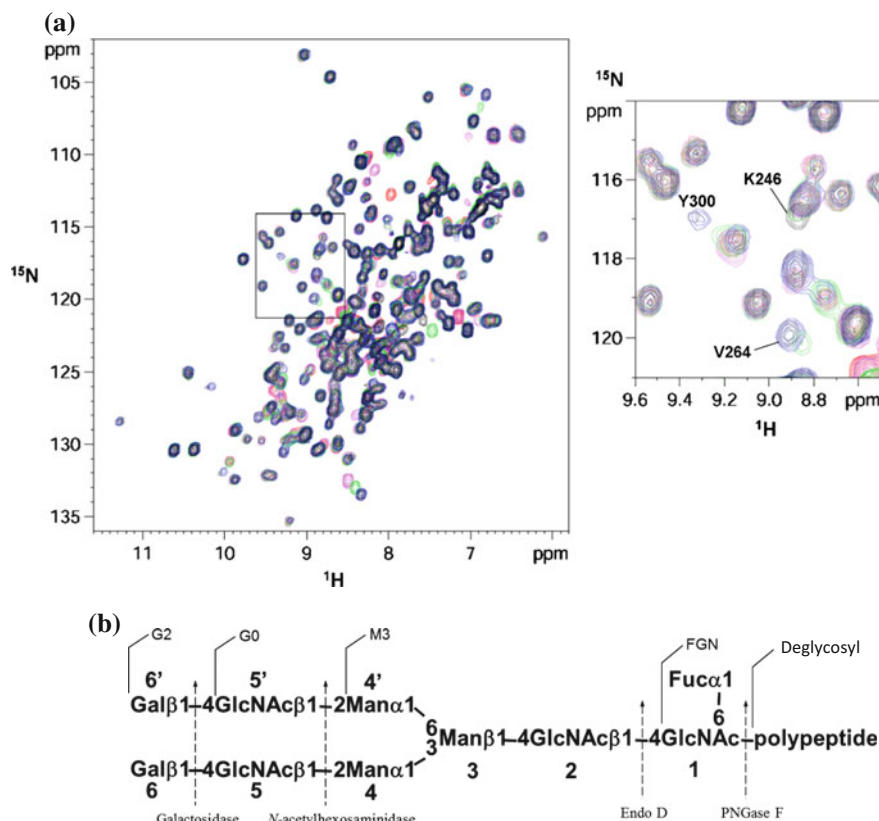


**Fig. 15.5** **a**  $^1\text{H}$ - $^{15}\text{N}$  HSQC spectral changes upon trimming of the carbohydrate chains of uniformly  $^{13}\text{C}$ / $^{15}\text{N}$ -labeled human IgG1-Fc. The spectra of the different glycoforms of Fc with different colors were superimposed. Black Fc(G2); blue Fc(G0); green Fc(M3); orange Fc(FGN); and red deglycosylated Fc. **b** The carbohydrate sequence attached to Asn297 of human IgG1-Fc. The arrows indicate the cleavage sites of the glycosidases used, and the resultant glycoforms are also shown. Adapted from Ref. [49] with the permission

affinity for Fc $\gamma$  receptor III on natural killer cells and consequently exerts an increased magnitude of antibody-dependent cell-mediated cytotoxicity (ADCC) [58–60]. Figure 15.6 compares the  $^1\text{H}$ - $^{15}\text{N}$  HSQC spectra of the fucosylated and non-fucosylated forms of IgG-Fc labeled with  $^{15}\text{N}$  at the amide groups of tyrosine residues, showing chemical shift perturbation and line broadening of the peak originating from Tyr296, which is proximal to the fucose residue (vide infra) [57].

Genetic engineering of *S. cerevisiae* by deletion of genes involved in *N*-glycan processing has enabled overexpression of homogeneous high-mannose-type oligosaccharides M9 and M8B with  $^{13}\text{C}$  labeling [38, 41] (Fig. 15.7). Several attempts have been made to produce recombinant proteins with human-like glycosylation in yeast [61–63]. Currently, sialylated biantennary *N*-glycans can be expressed by engineered *P. pastoris*, in which four genes responsible for yeast-specific glycosylation were knocked out and 14 heterologous genes involved in the biosynthesis of human-type glycosylation were introduced [62]. Furthermore, IgG modified with complex-type *N*-glycans could be expressed in silkworm by co-expression of human  $\beta$ 1,2-*N*-acetylglucosaminyltransferase II and  $\beta$ 1,4-galactosyltransferase [64]. This genetically engineered production vehicle may be used for the expression of isotope-labeled recombinant glycoproteins for NMR studies.

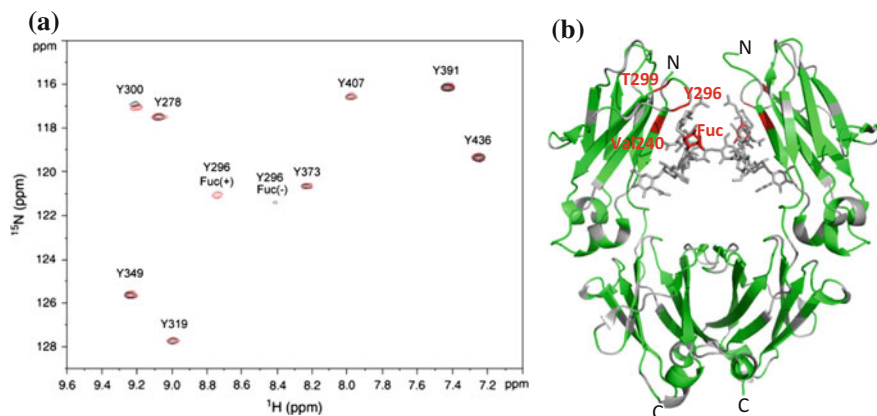


**Fig. 15.6** **a**  $^1\text{H}$ - $^{15}\text{N}$  HSQC spectral comparison between the fucosylated (red) and Fuc non-fucosylated (black) glycoforms of  $^{15}\text{N}$ -Tyr-labeled human IgG1-Fc. Tyr296 of non-fucosylated Fc exhibits a significant broadening of the HSQC peak. **b** Mapping on the crystal structure of fucosylated IgG-Fc of the amino acid residues showing the chemical shift difference between fucosylated and non-fucosylated IgG-Fc. The chemical shift differences are quantified for each residue according to the equation  $(0.2\delta_{\text{N}}^2 + \delta_{\text{H}}^2)^{1/2}$ , where  $\delta_{\text{N}}$  and  $\delta_{\text{H}}$  represent the differences in nitrogen and proton chemical shifts between fucosylated and non-fucosylated IgG-Fc. The amino acid residues showing and not showing observable chemical shift differences ( $>0.1$  ppm) are colored red and green on the crystal structure [PDB code: 3AVE] [57], respectively. The *N*-glycans are represented by stick models. The molecular graphics were generated with PyMOL [98]. Adapted from Ref. [57] with the permission

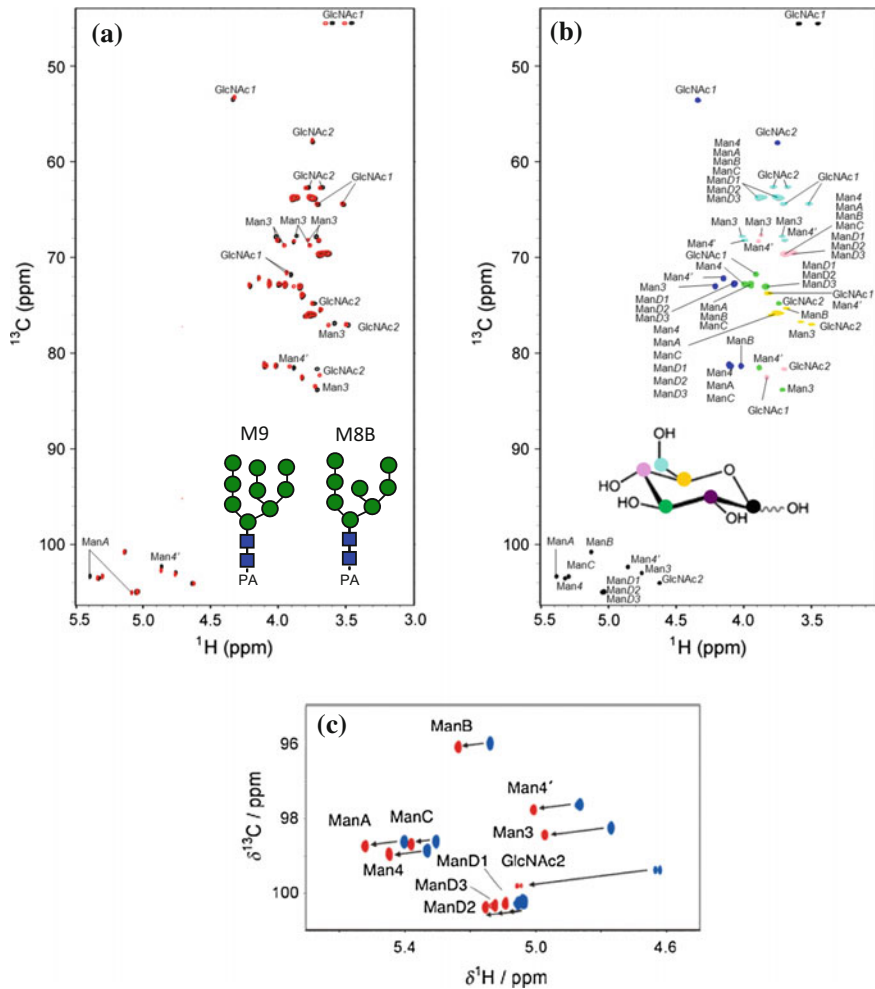


**Fig. 15.7** NMR spectra of the high-mannose-type undecasaccharide M9. **a**  $^1\text{H}$ - $^{13}\text{C}$  HSQC spectra of M9 (*black*) uniformly labeled with  $^{13}\text{C}$  compared with that of M8B (*red*). **b**  $^1\text{H}$ - $^{13}\text{C}$  HSQC spectra of M9, metabolically  $^{13}\text{C}$ -labeled with d-[1- $^{13}\text{C}$ ]glucose (*black*), d-[2- $^{13}\text{C}$ ]glucose (*blue*), d-[3- $^{13}\text{C}$ ]glucose (*green*), d-[4- $^{13}\text{C}$ ]glucose (*magenta*), d-[5- $^{13}\text{C}$ ]glucose (*orange*), or d-[6- $^{13}\text{C}$ ]glucose (*cyan*). The six spectra were superposed, and the  $^{13}\text{C}$ -labeled positions in the glucose isotopomers used as metabolic precursors are shown with *circles* in the *same colors* as the corresponding spectra. **c**  $^1\text{H}$ - $^{13}\text{C}$  HSQC spectra of M9, modified with a lanthanide chelating tag with  $\text{Tm}^{3+}$  (*red*) and  $\text{La}^{3+}$  (*blue*). Chemical shift differences induced by PCS are indicated by *arrows*. Adapted from the Refs. [38, 41, 69] with the permission

## 15.6 Spectral Observations and Assignments

Carbohydrate NMR spectral analyses are often hampered by peak overlapping, particularly when dealing with liberated oligosaccharides or solvent-exposed glycans. A straightforward approach for solving this problem is to employ a higher magnetic field so as to increase spectral resolution [65, 66]. Line narrowing of oligosaccharide CH peaks is expected in a higher magnetic field, because in systems where dipole–dipole interaction is a dominant relaxation mechanism,  $T_2$  longevity of the molecules with an appropriate motional correlation time increases in the higher field [67, 68]. Paramagnetic lanthanide probes can also be used for improving chemical shift dispersion. Figure 15.7c illustrates an HSQC spectrum of high-mannose-type undecasaccharide M9 with a lanthanide chelating tag covalently attached at its reducing terminus with La<sup>3+</sup> and Tm<sup>3+</sup> [69]. The overlapping peaks originating from the three non-reducing terminal mannose residues exhibit different pseudo-contact shifts (PCSs), dissolving the chemical shift degeneracy because their spatial arrangements are different with respect to the reducing terminus. PCS thus provides conformational information of the oligosaccharides (vide infra).

Although scalar connectivity-based techniques are applicable for spectral assignments of glycoprotein polypeptide chains, sequential assignments of the glycan remain partially dependent on nuclear Overhauser effect (NOE) connectivities. Therefore, selective isotope labeling of the carbohydrate moieties facilitates spectral assignments. Metabolic labeling using appropriate isotope-labeled metabolic precursors enables residue-specific and/or position-specific <sup>13</sup>C incorporation [28, 29]. Figure 15.7b shows superposition of six <sup>1</sup>H-<sup>13</sup>C HSQC spectra of M9 labeled with <sup>13</sup>C at different positions using six different glucose isotopomers as metabolic precursors [41]. Peak classification into the sugar residue types can be made based on differential protonation levels during metabolic labeling using perdeuterated <sup>13</sup>C-glucose as a metabolic precursor [38, 70]. In vitro enzymatic attachment of an isotope-labeled sugar onto the non-reducing end of the glycan is also useful for selective observation of NMR signals originating from the terminal sugar residues [33, 71, 72]. Yamaguchi et al. [73] proposed that <sup>13</sup>C-detected <sup>13</sup>C-<sup>13</sup>C NOE spectroscopy (NOESY) experiments are useful for spectral assignments of large glycoproteins because the observed peaks can be easily classified into monosaccharide types with specific linkage configurations by inspecting the intraresidue <sup>13</sup>C-<sup>13</sup>C connectivity patterns (Fig. 15.8).

Although carbohydrate hydroxyl groups are functionally crucial, as exemplified by hydrogen bonding, direct observation of their <sup>1</sup>H NMR signals is extremely difficult in aqueous solution. An indirect approach utilizes the H/D isotope effect on the <sup>13</sup>C chemical shift at <sup>13</sup>C-OH groups to estimate exchange rate for OH with the solvent in a 50/50 H<sub>2</sub>O/D<sub>2</sub>O solution at steady state [74, 75]. This technique is applicable for the estimation of the NH exchange rate of the acetamide group of *N*-acetylglucosamine residues of a glycoprotein with appropriate <sup>13</sup>C labeling (Fig. 15.9) [27]. Freedberg and coworkers used a <sup>1</sup>H-<sup>13</sup>C HSQC-total correlated

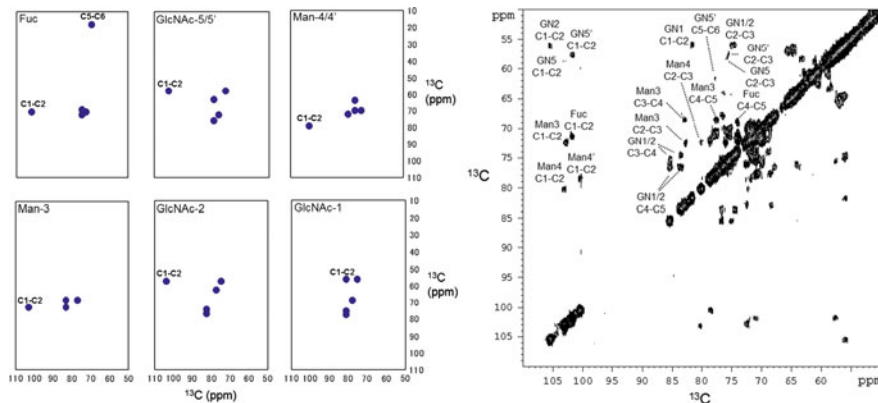


**Fig. 15.8** Two-dimensional  $^{13}\text{C}$ - $^{13}\text{C}$  NOESY patterns expected for the sugar residues in a biantennary complex-type oligosaccharide (*left*) and the oligosaccharide region of the two-dimensional  $^{13}\text{C}$ - $^{13}\text{C}$  NOESY spectrum of  $^{13}\text{C}$ -labeled mouse IgG2b-Fc (*right*). Adapted from Ref. [73] with the modification

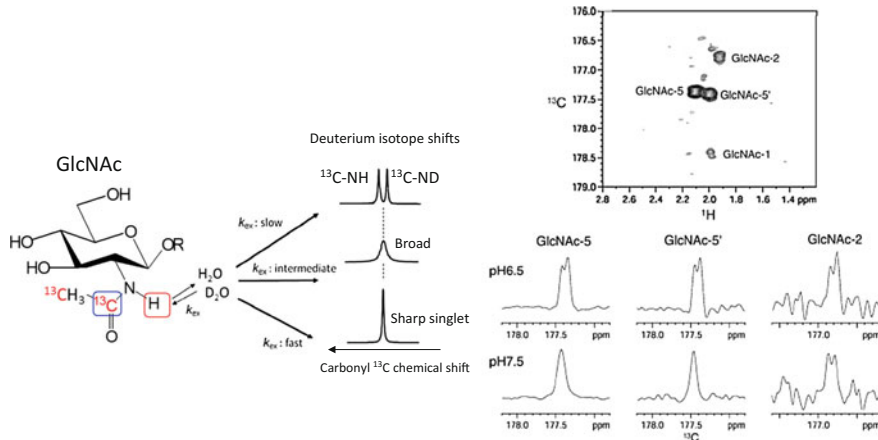


**Fig. 15.9** Schematic view of deuterium–hydrogen exchange of the amide group of GlcNAc residue on the *line shape* of the carbonyl  $^{13}\text{C}$  resonance due to deuterium isotope shift and (*left*) and 400 MHz 2D H(C)CO spectra of IgG-Fc showing the peaks from the GlcNAc acetamide groups. The Fc sample was dissolved in a sodium phosphate buffer  $\text{H}_2\text{O:D}_2\text{O} = 1:1$ . The nomenclature of oligosaccharide residues is represented in Fig. 15.5b. Adapted from Ref. [27] with the permission

spectroscopy (TOCSY)-based technique to measure OH exchange rates in a 50/50  $\text{H}_2\text{O/D}_2\text{O}$  solution, enabling quantitative characterization of transient hydrogen bonds involving the hydroxyl groups [76].

## 15.7 NMR Analyses of Dynamic Conformations and Interactions of Oligosaccharides

In the case of other biomolecules, conformations of oligosaccharides are primarily characterized based on NOE data complemented with those of *J* coupling and residual dipolar coupling [77–79]. NOE data are also used for probing carbohydrate–protein interactions. Figure 15.10a shows intramolecular NOE connectivities observed between the core fucose of biantennary complex-type glycan and the aromatic ring of its spatially proximal tyrosine residue (Tyr296) in human IgG1-Fc. Core fucosylation precludes optimum binding of IgG1 to Fc $\gamma$  receptor IIIa, which is mediated by the Tyr296 side chain, and thereby compromises ADCC activity [58]. This is, at least partially, attributed to steric masking of the functionally important tyrosine by the fucose. In the absence of the core fucose, Tyr296 gains motional freedom as exemplified by exchange line broadening of the  $^1\text{H}$ – $^{15}\text{N}$  HSQC peak originating from this tyrosine [57].

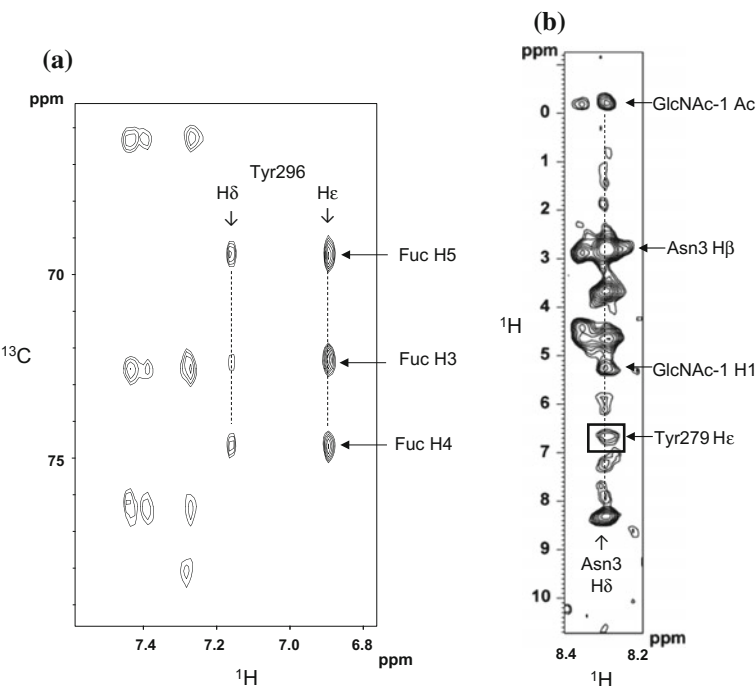


**Fig. 15.10** Parts of **a** 2D HSQC-NOESY spectrum of human IgG1-Fc (metabolically labeled with [ $^{13}\text{C}_6$ ]glucose) exhibiting intramolecular NOE connectivities between Tyr296 and the core fucose residue and **b**  $^{15}\text{N}$ -edited NOESY spectrum of the  $^{15}\text{N}$ -labeled Fc-derived heptapeptide carrying  $\text{Man}_3\text{GlcNAc}_2$  bound to the carbohydrate-binding domain of Fbs1 exhibiting intermolecular NOE peak (boxed) between Tyr279  $\text{H}\epsilon$  (Fbs1) and Asn3  $\text{H}\delta$  (glycopeptide). Adapted from Refs. [27, 69] with the permission

Glycoprotein recognition by lectins can be investigated by observing intermolecular NOEs using isotope-labeled oligosaccharides or glycopeptides [80, 81]. Figure 15.10B shows an  $^{15}\text{N}$ -edited NOESY spectrum indicating intermolecular NOE connectivities between the carbohydrate-binding domain of Fbs1, a cytosolic lectin, as well as the substrate recognition part of a multisubunit ubiquitin ligase and its cognate glycopeptide cleaved from metabolically  $^{13}\text{C}/^{15}\text{N}$ -labeled IgG [80]. In this specific case, the lectin contacts not only the innermost part of the glycan but also the side chain of the glycosylated asparagine. A glycan–polypeptide junction of glycoprotein is usually shielded from the solvent by spatially surrounding amino acid residues but can be exposed in its misfolded state and targeted for ubiquitin-mediated proteasomal degradation. Fbs1 captures the junction and protects it against attack by the cytosolic deglycosylation enzyme during ubiquitination of glycoprotein substrates. Because carbohydrate–lectin interactions are typically weak, with dissociation constants in the submillimolar range, transferred NOE and saturation transfer difference experiments are effective to characterize such weak interactions [82–84].

NOE-based conformational analysis of carbohydrate chains is hampered by low proton density, in comparison with that of protein. Moreover, conformational dynamics of carbohydrate chains hamper quantitative interpretation of NOE data. Recently, paramagnetism-assisted NMR approaches have been applied to conformational analysis of oligosaccharides [85–87]. In particular, PCS data, obtained employing paramagnetic lanthanide probes, are used as source of long distance (as far as 40 Å) information independent of the correlation time of the heterogeneous internal motion of oligosaccharides. Paramagnetic relaxation enhancements have also been used to characterize conformation and metal binding of oligosaccharides and their clusters [88–90].

Because oligosaccharides are extremely flexible molecules, NMR provides information averaged over their dynamic conformational ensembles. To address this issue, NMR data are treated as population-weighted averages of the possible conformers and reproduced by a population-optimized combination of selected low-energy conformers. In a recently proposed approach, NMR data are used for the validation of conformational ensembles derived from molecular dynamics (MD) simulation of flexible oligosaccharides that exhibit shallow and broad energy minima in their conformational space [69, 91–93]. In this approach, experimentally observed PCS data are compared with those back-calculated from the MD-derived conformational ensembles (Fig. 15.11). NMR validation showed that conformational spaces of the triantennary high-mannose-type oligosaccharides could be sufficiently explored by replica-exchange MD simulation with a total simulation time of several microseconds [69]. In conjunction with crystallographic data of lectin-bound oligosaccharides, carbohydrate recognition by lectins is characterized by conformational selection as well as induced-fit mechanisms [87, 93].

Oligosaccharides accommodated in a protein can be less mobile than liberated ones. As a typical example, the pair of biantennary oligosaccharides packed within the quaternary structure of IgG-Fc is visualized for the most part in the crystalline state [57, 58]. However, the terminal galactose residues exhibit different dynamic

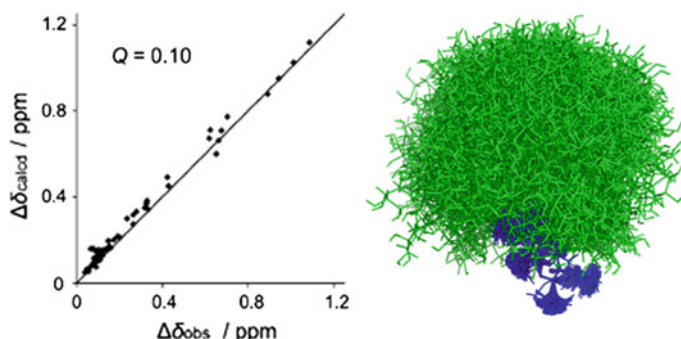


**Fig. 15.11** Conformational ensemble of M9 obtained from replica-exchange MD calculation validated by the PCS data (*left*) and the correlation between experimentally observed PCS values with  $\text{Tm}^{3+}$  and theoretical PCS data back-calculated from the ensemble model (*right*). Adapted from Ref. [69] with the permission

properties, which have been characterized on the basis of relaxation data [33, 71]. Therefore, the glycans attached to proteins can exhibit heterogeneous properties in terms of conformational dynamics.

## 15.8 Perspectives

NMR spectroscopy in conjunction with computational approaches has now successfully characterized dynamic conformational ensembles of oligosaccharides and glycoprotein glycans. This prompts us to improve functionality of carbohydrate chains by designing and optimizing their conformational spaces. To realize this glycoengineering, it is obviously necessary to create glycoproteins with tailored and even artificial glycoforms.

A hybrid approach combining cell engineering and chemoenzymatic techniques has the ability to deal with glycoform heterogeneity of glycoproteins in NMR structural glycobiology [94]. This line of technical development will realize isotope-labeled glycoproteins with tailored glycoforms. By installing glycosylation systems of *C. jejuni* and *S. cerevisiae* into *E. coli*, bacterial expression of recombinant glycoproteins having the core structure of eukaryotic glycans, i.e.,  $\text{Man}_3\text{GlcNAc}_2$ , has been achieved [95]. This glycan can be substituted with synthetic donor oligosaccharides by *in vitro* enzymatic transglycosylation catalyzed by endo- $\beta$ -N-acetylglucosaminidases, leaving the innermost GlcNAc residue as acceptor site [96].

Furthermore, synthetic approaches have been successfully developed to prepare glycoproteins involving chemical ligation of recombinant non-glycosylated peptides and chemically synthesized glycopeptides [97]. These technical advancements will open up new possibilities to create glycoproteins with artificial glycoforms.

NMR spectroscopy along with computational approaches will play critical roles in detailed characterization of dynamic conformations and interactions of those *neo-glycoproteins* for better understanding of the functional mechanisms of carbohydrate chains.

**Acknowledgements** We thank Mr. Masaki Kato (Structural Glycobiology Team, RIKEN) for statistic analysis of PDB data and Drs. Takumi Yamaguchi (School of Material Science, Japan Advanced Institute of Science and Technology) and Maho Yagi-Utsumi (Institute for Molecular Science, National Institutes of Natural Sciences) for useful discussion. This work was partly supported by the Nanotechnology Platform Program (Molecule and Material Synthesis) of MEXT, MEXT/JSPS Grants in Aid for Scientific Research (JP25102008, JP15K07935 and JP17H05893), the Japan Agency for Medical Research and Development, and the Cooperative Research Program of Institute for Protein Research, Osaka University, NMRCR-16-05.

## References

1. Boehr, D.D., Nussinov, R., Wright, P.E.: The role of dynamic conformational ensembles in biomolecular recognition. *Nat. Chem. Biol.* **5**, 789–796 (2009)
2. Kovermann, M., Rogne, P., Wolf-Watz, M.: Protein dynamics and function from solution state NMR spectroscopy. *Q. Rev. Biophys.* **49**, e6 (2016)
3. Rosenzweig, R., Kay, L.E.: Bringing dynamic molecular machines into focus by methyl-TROSY NMR. *Annu. Rev. Biochem.* **83**, 291–315 (2014)
4. Freedberg, D.I., Selenko, P.: Live cell NMR. *Annu. Rev. Biophys.* **43**, 171–192 (2014)
5. Skinner, A.L., Laurence, J.S.: High-field solution NMR spectroscopy as a tool for assessing protein interactions with small molecule ligands. *J. Pharm. Sci. US* **97**, 4670–4695 (2008)
6. Dias, D.M., Ciulli, A.: NMR approaches in structure-based lead discovery: recent developments and new frontiers for targeting multi-protein complexes. *Prog. Biophys. Mol. Biol.* **116**, 101–112 (2014)
7. Carlson, E.D., Gan, R., Hodgman, C.E., Jewett, M.C.: Cell-free protein synthesis: applications come of age. *Biotechnol. Adv.* **30**, 1185–1194 (2012)
8. Apweiler, R., Hermjakob, H., Sharon, N.: On the frequency of protein glycosylation, as deduced from analysis of the SWISS-PROT database. *Biochim. Biophys. Acta* **1473**, 4–8 (1999)
9. Varki, A., Cummings, R.D., Esko, J.D., Freeze, H.H., Stanley, P., Bertozzi, C.R., Hart, G.W., Etzler, M.E.: *Essentials of Glycobiology*, 2nd edn. Cold Spring Harbor Laboratory Press, New York (2009)
10. Bubb, W.A.: NMR spectroscopy in the study of carbohydrates: characterizing the structural complexity. *Concepts Magn. Resonance Part A* **19A**, 1–19 (2003)
11. Prestegard, J.H., Koerner, T.A.W., Demou, P.C., Yu, R.K.: Complete analysis of oligosaccharide primary structure using two-dimensional high-field proton NMR. *J. Am. Chem. Soc.* **104**, 4993–4995 (1982)
12. Vliegenthart, J.F.: High resolution  $^1\text{H}$ -NMR spectroscopy of carbohydrate structures. *Adv. Exp. Med. Biol.* **125**, 77–91 (1980)
13. Albrecht, S., Unwin, L., Muniyappa, M., Rudd, P.M.: Glycosylation as a marker for inflammatory arthritis. *Cancer Biomark.* **14**, 17–28 (2014)
14. Adamczyk, B., Albrecht, S., Stockmann, H., Ghoneim, I.M., Al-Eknah, M., Al-Busadah, K. A., Karlsson, N.G., Carrington, S.D., Rudd, P.M.: Pregnancy-associated changes of IgG and serum *N*-glycosylation in Camel (*Camelus dromedarius*). *J. Proteome Res.* **15**, 3255–3265 (2016)

15. Parekh, R.B., Dwek, R.A., Sutton, B.J., Fernandes, D.L., Leung, A., Stanworth, D., Rademacher, T.W., Mizuochi, T., Taniguchi, T., Matsuta, K., et al.: Association of rheumatoid arthritis and primary osteoarthritis with changes in the glycosylation pattern of total serum IgG. *Nature* **316**, 452–457 (1985)
16. Yamada, E., Tsukamoto, Y., Sasaki, R., Yagyu, K., Takahashi, N.: Structural changes of immunoglobulin G oligosaccharides with age in healthy human serum. *Glycoconj. J.* **14**, 401–405 (1997)
17. Kibe, T., Fujimoto, S., Ishida, C., Togari, H., Wada, Y., Okada, S., Nakagawa, H., Tsukamoto, Y., Takahashi, N.: Glycosylation and placental transport of immunoglobulin G. *J. Clin. Biochem. Nutr.* **21**, 57–63 (1996)
18. Park, S.S., Park, J., Ko, J., Chen, L., Mériege, D., Crouse-Zeineddini, J., Wong, W., Kerwin, B.A.: Biochemical assessment of erythropoietin products from Asia versus US Epoetin alfa manufactured by Amgen. *J. Pharm. Sci.* **98**, 1688–1699 (2009)
19. Zeck, A., Pohlentz, G., Schlothauer, T., Peter-Katalinic, J., Regula, J.T.: Cell type-specific and site directed N-glycosylation pattern of Fc $\gamma$ RIIIa. *J. Proteome Res.* **10**, 3031–3039 (2011)
20. Lindhorst, T.K.: Essentials of Carbohydrate Chemistry and Biochemistry, 3rd Completely Revised and Enlarged Edition edn. Wiley, London (2007)
21. de Graaf, M., Fouchier, R.A.: Role of receptor binding specificity in influenza A virus transmission and pathogenesis. *EMBO J.* **33**, 823–841 (2014)
22. Wormald, M.R., Petrescu, A.J., Pao, Y.L., Glithero, A., Elliott, T., Dwek, R.A.: Conformational studies of oligosaccharides and glycopeptides: complementarity of NMR, X-ray crystallography, and molecular modelling. *Chem. Rev.* **102**, 371–386 (2002)
23. Masuda, K., Yamaguchi, Y., Takahashi, N., Jefferis, R., Kato, K.: Mutational deglycosylation of the Fc portion of immunoglobulin G causes O-sulfation of tyrosine adjacently preceding the originally glycosylated site. *FEBS Lett.* **584**, 3474–3479 (2010)
24. Shibata-Koyama, M., Iida, S., Okazaki, A., Mori, K., Kitajima-Miyama, K., Saitou, S., Kakita, S., Kanda, Y., Shitara, K., Kato, K., Satoh, M.: The N-linked oligosaccharide at Fc $\gamma$ RIIIa Asn-45: an inhibitory element for high Fc $\gamma$ RIIIa binding affinity to IgG glycoforms lacking core fucosylation. *Glycobiology* **19**, 126–134 (2009)
25. Yamaguchi, Y., Kato, K.: Dynamics and interactions of glycoconjugates probed by stable-isotope-assisted NMR spectroscopy. *Methods Enzymol.* **478**, 305–322 (2010)
26. Sastry, M., Xu, L., Georgiev, I.S., Bewley, C.A., Nabel, G.J., Kwong, P.D.: Mammalian production of an isotopically enriched outer domain of the HIV-1 gp120 glycoprotein for NMR spectroscopy. *J. Biomol. NMR* **50**, 197–207 (2011)
27. Kato, K., Yamaguchi, Y., Arata, Y.: Stable-isotope-assisted NMR approaches to glycoproteins using immunoglobulin G as a model system. *Prog. Nucl. Magn. Reson. Spectrosc.* **56**, 346–359 (2010)
28. Yamaguchi, Y., Yagi, H., Kato, K.: Stable isotope labeling of glycoproteins for NMR study. In: *NMR in Glycoscience and Glycotechnology*, pp. 194–207. RSC Publishing, Cambridge (2017)
29. Kato, K., Yamaguchi, Y.: Glycoproteins and antibodies: solution NMR studies. In: *Encyclopedia of Magnetic Resonance*, vol. 3, pp. 1779–1790. Wiley, Chichester (2012)
30. Kato, K., Matsunaga, C., Igarashi, T., Kim, H., Odaka, A., Shimada, I., Arata, Y.: Complete assignment of the methionyl carbonyl carbon resonances in switch variant anti-dansyl antibodies labeled with [ $1^{-13}\text{C}$ ]methionine. *Biochemistry* **30**, 270–278 (1991)
31. Yagi, H., Zhang, Y., Yagi-Utsumi, M., Yamaguchi, T., Iida, S., Yamaguchi, Y., Kato, K.: Backbone  $^1\text{H}$ ,  $^{13}\text{C}$ , and  $^{15}\text{N}$  resonance assignments of the Fc fragment of human immunoglobulin G glycoprotein. *Biomol. NMR Assign.* **9**, 257–260 (2015)
32. Kato, K., Yamaguchi, Y.: Structural analyses of glycoconjugates by NMR. In: *Experimental Glycoscience*, pp. 45–50. Springer, Tokyo (2008)
33. Yamaguchi, Y., Kato, K., Shindo, M., Aoki, S., Furusho, K., Koga, K., Takahashi, N., Arata, Y., Shimada, I.: Dynamics of the carbohydrate chains attached to the Fc portion of immunoglobulin G as studied by NMR spectroscopy assisted by selective  $^{13}\text{C}$  labeling of the glycans. *J. Biomol. NMR* **12**, 385–394 (1998)

34. Yagi, H., Fukuzawa, N., Tasaka, Y., Matsuo, K., Zhang, Y., Yamaguchi, T., Kondo, S., Nakazawa, S., Hashii, N., Kawasaki, N., Matsumura, T., Kato, K.: NMR-based structural validation of therapeutic antibody produced in *Nicotiana benthamiana*. *Plant Cell Rep.* **34**, 959–968 (2015)
35. Yagi, H., Nakamura, M., Yokoyama, J., Zhang, Y., Yamaguchi, T., Kondo, S., Kobayashi, J., Kato, T., Park, E.Y., Nakazawa, S., Hashii, N., Kawasaki, N., Kato, K.: Stable isotope labeling of glycoprotein expressed in silkworms using immunoglobulin G as a test molecule. *J. Biomol. NMR* **62**, 157–167 (2015)
36. Walton, W.J., Kasprzak, A.J., Hare, J.T., Logan, T.M.: An economic approach to isotopic enrichment of glycoproteins expressed from SF9 insect cells. *J. Biomol. NMR* **36**, 225–233 (2006)
37. Blanchard, V., Gadkari, R.A., George, A.V., Roy, S., Gerwig, G.J., Leeflang, B.R., Dighe, R.R., Boelens, R., Kamerling, J.P.: High-level expression of biologically active glycoprotein hormones in *Pichia pastoris* strains—selection of strain GS115, and not X-33, for the production of biologically active N-glycosylated 15N-labeled pHCG. *Glycoconj. J.* **25**, 245–257 (2008)
38. Kamiya, Y., Yamamoto, S., Chiba, Y., Jigami, Y., Kato, K.: Overexpression of a homogeneous oligosaccharide with <sup>13</sup>C labeling by genetically engineered yeast strain. *J. Biomol. NMR* **50**, 397–401 (2011)
39. Cubeddu, L., Moss, C.X., Swarbrick, J.D., Gooley, A.A., Williams, K.L., Curmi, P.M., Slade, M.B., Mabbutt, B.C.: *Dictyostelium discoideum* as expression host: isotopic labeling of a recombinant glycoprotein for NMR studies. *Protein Exp. Purif.* **19**, 335–342 (2000)
40. Nettleship, J.E., Assenberg, R., Diprose, J.M., Rahman-Huq, N., Owens, R.J.: Recent advances in the production of proteins in insect and mammalian cells for structural biology. *J. Struct. Biol.* **172**, 55–65 (2010)
41. Kamiya, Y., Yanagi, K., Kitajima, T., Yamaguchi, T., Chiba, Y., Kato, K.: Application of metabolic <sup>13</sup>C labeling in conjunction with high-field nuclear magnetic resonance spectroscopy for comparative conformational analysis of high mannose-type oligosaccharides. *Biomolecules* **3**, 108–123 (2013)
42. Sattler, M., Fesik, S.W.: Use of deuterium labeling in NMR: overcoming a sizeable problem. *Structure* **4**, 1245–1249 (1996)
43. Kainoshio, M., Guntert, P.: SAIL—stereo-array isotope labeling. *Q. Rev. Biophys.* **42**, 247–300 (2009)
44. Opitz, C., Isogai, S., Grzesiek, S.: An economic approach to efficient isotope labeling in insect cells using homemade <sup>15</sup>N-, <sup>13</sup>C- and <sup>2</sup>H-labeled yeast extracts. *J. Biomol. NMR* **62**, 373–385 (2015)
45. Guarino, C., DeLisa, M.P.: A prokaryote-based cell-free translation system that efficiently synthesizes glycoproteins. *Glycobiology* **22**, 596–601 (2012)
46. Slyntko, V., Schubert, M., Numao, S., Kowarik, M., Aebi, M., Allain, F.H.: NMR structure determination of a segmentally labeled glycoprotein using in vitro glycosylation. *J. Am. Chem. Soc.* **131**, 1274–1281 (2009)
47. Takahashi, N., Nakagawa, H., Fujikawa, K., Kawamura, Y., Tomiya, N.: Three-dimensional elution mapping of pyridylaminated N-linked neutral and sialyl oligosaccharides. *Anal. Biochem.* **226**, 139–146 (1995)
48. Takahashi, N., Kato, K.: GALAXY(Glycoanalysis by the Three Axes of MS and Chromatography): a Web Application that Assists Structural Analyses of N-glycans. *Trends Glycosci. Glycotech.* **15**, 235–251 (2003)
49. Yamaguchi, Y., Nishimura, M., Nagano, M., Yagi, H., Sasakawa, H., Uchida, K., Shitara, K., Kato, K.: Glycoform-dependent conformational alteration of the Fc region of human immunoglobulin G1 as revealed by NMR spectroscopy. *Biochim. Biophys. Acta* **1760**, 693–700 (2006)
50. Yagi, H., Kuo, C.W., Obayashi, T., Ninagawa, S., Khoo, K.H., Kato, K.: Direct mapping of additional modifications on phosphorylated O-glycans of alpha-dystroglycan by mass

- spectrometry analysis in conjunction with knocking out of causative genes for dystroglycanopathy. *Mol. Cell. Proteomics* **15**, 3424–3434 (2016)
- 51. Masuda, K., Yamaguchi, Y., Kato, K., Takahashi, N., Shimada, I., Arata, Y.: Pairing of oligosaccharides in the Fc region of immunoglobulin G. *FEBS Lett.* **473**, 349–357 (2000)
  - 52. Thaysen-Andersen, M., Packer, N.H.: Advances in LC-MS/MS-based glycoproteomics: getting closer to system-wide site-specific mapping of the N- and O-glycoproteome. *Biochim. Biophys. Acta* **1844**, 1437–1452 (2014)
  - 53. Terral, G., Beck, A., Cianferani, S.: Insights from native mass spectrometry and ion mobility-mass spectrometry for antibody and antibody-based product characterization. *J. Chromatogr. B Analyt. Technol. Biomed. Life Sci.* **1032**, 79–90 (2016)
  - 54. Ito, H., Kameyama, A., Sato, T., Narimatsu, H.: Preparation of a glycan library using a variety of glycosyltransferases. *Methods Mol. Biol.* **534**, 283–291 (2009)
  - 55. Kato, K., Yamaguchi, Y., Takahashi, N., Nishimura, M., Iwamoto, S., Sekiya, S., Tanaka, K.: Discrimination of isomeric fragment ions observed in tandem mass spectra of biantennary oligosaccharides by use of selective isotope labeling. *J. Mass Spectrom. Soc. Jpn.* **52**, 284–288 (2004)
  - 56. Tanji, H., Ohto, U., Shibata, T., Miyake, K., Shimizu, T.: Structural reorganization of the Toll-like receptor 8 dimer induced by agonistic ligands. *Science* **339**, 1426–1429 (2013)
  - 57. Matsumiya, S., Yamaguchi, Y., Saito, J., Nagano, M., Sasakawa, H., Otaki, S., Satoh, M., Shitara, K., Kato, K.: Structural comparison of fucosylated and nonfucosylated Fc fragments of human immunoglobulin G1. *J. Mol. Biol.* **368**, 767–779 (2007)
  - 58. Mizushima, T., Yagi, H., Takemoto, E., Shibata-Koyama, M., Isoda, Y., Iida, S., Masuda, K., Satoh, M., Kato, K.: Structural basis for improved efficacy of therapeutic antibodies upon defucosylation of their Fc glycans. *Genes Cells* **16**, 1071–1080 (2011)
  - 59. Shields, R.L., Lai, J., Keck, R., O'Connell, L.Y., Hong, K., Meng, Y.G., Weikert, S.H., Presta, L.G.: Lack of fucose on human IgG1N-linked oligosaccharide improves binding to human Fc $\gamma$ RIII and antibody-dependent cellular toxicity. *J. Biol. Chem.* **277**, 26733–26740 (2002)
  - 60. Shinkawa, T., Nakamura, K., Yamane, N., Shoji-Hosaka, E., Kanda, Y., Sakurada, M., Uchida, K., Anazawa, H., Satoh, M., Yamasaki, M., Hanai, N., Shitara, K.: The absence of fucose but not the presence of galactose or bisecting N-acetylglucosamine of human IgG1 complex-type oligosaccharides shows the critical role of enhancing antibody-dependent cellular cytotoxicity. *J. Biol. Chem.* **278**, 3466–3473 (2003)
  - 61. Chiba, Y., Akeboshi, H.: Glycan engineering and production of ‘humanized’ glycoprotein in yeast cells. *Biol. Pharm. Bull.* **32**, 786–795 (2009)
  - 62. Hamilton, S.R., Davidson, R.C., Sethuraman, N., Nett, J.H., Jiang, Y., Rios, S., Bobrowicz, P., Stadheim, T.A., Li, H., Choi, B.K., Hopkins, D., Wischniewski, H., Roser, J., Mitchell, T., Strawbridge, R.R., Hoopes, J., Wildt, S., Gerngross, T.U.: Humanization of yeast to produce complex terminally sialylated glycoproteins. *Science* **313**, 1441–1443 (2006)
  - 63. Irani, Z.A., Kerkhoven, E.J., Shojaosadati, S.A., Nielsen, J.: Genome-scale metabolic model of *Pichia pastoris* with native and humanized glycosylation of recombinant proteins. *Biotechnol. Bioeng.* **113**, 961–969 (2016)
  - 64. Kato, T., Kako, N., Kikuta, K., Miyazaki, T., Kondo, S., Yagi, H., Kato, K., Park, E.Y.: N-glycan modification of a recombinant protein via coexpression of human glycosyltransferases in silkworm pupae. *Sci. Rep.* **7**, 1409 (2017)
  - 65. Kato, K., Sasakawa, H., Kamiya, Y., Utsumi, M., Nakano, M., Takahashi, N., Yamaguchi, Y.: 920 MHz ultra-high field NMR approaches to structural glycobiology. *Biochim. Biophys. Acta* **1780**, 619–625 (2008)
  - 66. Blundell, C.D., Reed, M.A., Overduin, M., Almond, A.: NMR spectra of oligosaccharides at ultra-high field (900 MHz) have better resolution than expected due to favourable molecular tumbling. *Carbohydr. Res.* **341**, 1985–1991 (2006)
  - 67. Canet, D., Robert, J.B.: Behaviour of the NMR relaxation parameters at high fields. In: NMR at very high field, vol. 25, pp 45–89. Springer, Berlin (1991)

68. Meersmann, T., Schwager, M., Varma, V., Bodenhausen, G.: Little-known advantages of very high fields in NMR. *J. Magn. Reson. Ser. A* **119**, 275–279 (1996)
69. Yamaguchi, T., Sakae, Y., Zhang, Y., Yamamoto, S., Okamoto, Y., Kato, K.: Exploration of conformational spaces of high-mannose-type oligosaccharides by an NMR-validated simulation. *Angew. Chem. Int. Ed. Engl.* **53**, 10941–10944 (2014)
70. Yamaguchi, Y., Takizawa, T., Kato, K., Arata, Y., Shimada, I.:  $^1\text{H}$  and  $^{13}\text{C}$  NMR assignments for the glycans in glycoproteins by using  $^2\text{H}/^{13}\text{C}$ -labeled glucose as a metabolic precursor. *J. Biomol. NMR* **18**, 357–360 (2000)
71. Barb, A.W., Prestegard, J.H.: NMR analysis demonstrates immunoglobulin G *N*-glycans are accessible and dynamic. *Nat. Chem. Biol.* **7**, 147–153 (2011)
72. Gilhespy-Muskett, A.M., Partridge, J., Jefferis, R., Homans, S.W.: A novel  $^{13}\text{C}$  isotopic labelling strategy for probing the structure and dynamics of glycan chains *in situ* on glycoproteins. *Glycobiology* **4**, 485–489 (1994)
73. Yamaguchi, Y., Walchli, M., Nagano, M., Kato, K.: A C-13-detection NMR approach for large glycoproteins. *Carbohydr. Res.* **344**, 535–538 (2009)
74. Hanashima, S., Kato, K., Yamaguchi, Y.:  $^{13}\text{C}$ -NMR quantification of proton exchange at LewisX hydroxyl groups in water. *Chem. Commun. (Camb.)* **47**, 10800–10802 (2011)
75. Pfeffer, P.E., Valentine, K.M., Parrish, F.W.: Deuterium-induced differential isotope shift C-13 NMR. 1. Resonance re-assignments of monosaccharides and disaccharides. *J. Am. Chem. Soc.* **101**, 1265–1274 (1979)
76. Battistel, M.D., Azurmendi, H.F., Freedberg, D.I.: Glycan OH exchange rate determination in aqueous solution: seeking evidence for transient hydrogen bonds. *J. Phys. Chem. B* **121**, 683–695 (2017)
77. Hadad, M., J., Zhang, W., Turney, T., Sernau, L., Wang, X., Woods, R.J., Incandela, A., Surjancev, I., Wang, A., Yoon, M.Y., Coscia, A., Euell, C., Meredith, R., Carmichael, I., Serianni, A.: NMR Spin-couplings in saccharides: relationships between structure, conformation and the magnitudes of JHH, JCH and JCC values. In: *NMR in Glycoscience and Glycotechnology*, pp. 20–100. RSC Publishing, Cambridge (2017)
78. Prestegard, J.H., Eletsky, A.: Paramagnetic, RDC and RCSA constraints in the structural analysis of glycans. In: *NMR in Glycoscience and Glycotechnology*, pp. 123–149. RSC Publishing, Cambridge (2017)
79. Schubert, M.: Insights into carbohydrate recognition by 3D structure determination of protein-carbohydrate complexes using NMR. In: *NMR in Glycoscience and Glycotechnology*, pp. 101–122. RSC Publishing, Cambridge. (2017)
80. Yamaguchi, Y., Hirao, T., Sakata, E., Kamiya, Y., Kurimoto, E., Yoshida, Y., Suzuki, T., Tanaka, K., Kato, K.: Fbs1 protects the malfolded glycoproteins from the attack of peptide: N-glycanase. *Biochem. Biophys. Res. Commun.* **362**, 712–716 (2007)
81. Nestor, G., Anderson, T., Oscarson, S., Gronenborn, A.M.: Exploiting uniformly  $^{13}\text{C}$ -labeled carbohydrates for probing carbohydrate-protein interactions by nmr spectroscopy. *J. Am. Chem. Soc.* **139**, 6210–6216 (2017)
82. Yamaguchi, Y., Kato, K.: Analyses of sugar–protein interactions by NMR. In: *Experimental Glycoscience*, pp. 121–123. Springer, Tokyo (2008)
83. Mayer, M., Meyer, B.: Group epitope mapping by saturation transfer difference NMR to identify segments of a ligand in direct contact with a protein receptor. *J. Am. Chem. Soc.* **123**, 6108–6117 (2001)
84. Jimenes-Barbero, J., Peters, T.: TR-NOE experiments to study carbohydrate-protein interactions. In: *NMR Spectroscopy of Glycoconjugates*, pp. 289–309. Wiley-VCH, Weinheim (2006)
85. Canales, A., Mallagaray, A., Pérez-Castells, J., Boos, I., Unverzagt, C., André, S., Gabius, H.-J., Cañada, F.J., Jiménez-Barbero, J.: Breaking pseudo-symmetry in multiantennary complex *N*-glycans using lanthanide-binding tags and NMR pseudo-contact shifts. *Angew. Chem. Int. Ed.* **52**, 13789–13793 (2013)
86. Kato, K., Yamaguchi, T.: Paramagnetic NMR probes for characterization of the dynamic conformations and interactions of oligosaccharides. *Glycoconj. J.* **32**, 505–513 (2015)

87. Kato, K., Yagi, H., Yamaguchi, T.: NMR characterization of dynamic conformations and interactions of oligosaccharides. In: *Modern Magnetic Resonance*. Springer, Berlin (2017, in press)
88. Yamaguchi, T., Kamiya, Y., Choo, Y.M., Yamamoto, S., Kato, K.: Terminal spin labeling of a high-mannose-type oligosaccharide for quantitative NMR analysis of its dynamic conformation. *Chem. Lett.* **42**, 544–546 (2013)
89. Yan, G., Yamaguchi, T., Suzuki, T., Yanaka, S., Sato, S., Fujita, M., Kato, K.: Hyper-assembly of self-assembled glycoclusters mediated by specific carbohydrate–carbohydrate interactions. *Chem. Asian J.* **12**, 968–972 (2017)
90. Demarco, M.L., Woods, R.J., Prestegard, J.H., Tian, F.: Presentation of membrane-anchored glycosphingolipids determined from molecular dynamics simulations and NMR paramagnetic relaxation rate enhancement. *J. Am. Chem. Soc.* **132**, 1334–1338 (2010)
91. Zhang, Y., Yamamoto, S., Yamaguchi, T., Kato, K.: Application of paramagnetic NMR-validated molecular dynamics simulation to the analysis of a conformational ensemble of a branched oligosaccharide. *Molecules* **17**, 6658 (2012)
92. Yamamoto, S., Zhang, Y., Yamaguchi, T., Kameda, T., Kato, K.: Lanthanide-assisted NMR evaluation of a dynamic ensemble of oligosaccharide conformations. *Chem. Commun.* **48**, 4752–4754 (2012)
93. Suzuki, T., Kajino, M., Yanaka, S., Zhu, T., Yagi, H., Satoh, T., Yamaguchi, T., Kato, K.: Conformational analysis of a high-mannose-type oligosaccharide displaying glucosyl determinant recognised by molecular chaperones using NMR-validated molecular dynamics simulation. *ChemBioChem* **18**, 396–401 (2017)
94. Kamiya, Y., Satoh, T., Kato, K.: Recent advances in glycoprotein production for structural biology: toward tailored design of glycoforms. *Curr. Opin. Struct. Biol.* **26**, 44–53 (2014)
95. Valderrama-Rincon, J.D., Fisher, A.C., Merritt, J.H., Fan, Y.Y., Reading, C.A., Chhiba, K., Heiss, C., Azadi, P., Aebi, M., DeLisa, M.P.: An engineered eukaryotic protein glycosylation pathway in *Escherichia coli*. *Nat. Chem. Biol.* **8**, 434–436 (2012)
96. Schwarz, F., Huang, W., Li, C., Schulz, B.L., Lizak, C., Palumbo, A., Numao, S., Neri, D., Aebi, M., Wang, L.X.: A combined method for producing homogeneous glycoproteins with eukaryotic N-glycosylation. *Nat. Chem. Biol.* **6**, 264–266 (2010)
97. Kajihara, Y., Tanabe, Y., Sasaoka, S., Okamoto, R.: Homogeneous human complex-type oligosaccharides in correctly folded intact glycoproteins: evaluation of oligosaccharide influence on protein folding, stability, and conformational properties. *Chemistry* **18**, 5944–5953 (2012)
98. DeLano, W.L.: The PyMOL Molecular Graphics System. DeLano Scientific, San Carlos (2002)

# Chapter 16

## NMR Studies on RNA

Taiichi Sakamoto, Maina Otsu and Gota Kawai

**Abstract** Basic methods for NMR analysis of RNA are presented for researchers who recently joined or want to join this field. This chapter includes design of RNA sequences, sample preparation, NMR measurements and analysis as well as structure calculation. Some examples are also shown.

**Keywords** RNA · In vitro transcription · Imino proton · Residual dipolar coupling

In this chapter, general methods for the RNA structure determination as well as some examples are shown. In the case of protein, the method for sequential assignment by using  $^{13}\text{C}/^{15}\text{N}$ -labelled protein samples and triple-resonance experiments is established and, furthermore, most of the processes are automated by the state-of-art programs. In contrast, the assignment method for RNA is still under development. Here, we focused on rather basic method for NMR analysis of RNA for researchers who recently joined or want to join this field. Please refer to the previous review articles for NMR analysis of RNA [1, 2].

### 16.1 Design of RNA Sequences

Because RNA consists of only four kinds of nucleotides, signal overlaps are always to be overcome. Thus, it is usually required to design shorter RNA fragments to be analysed by NMR. In many cases for stable isotopic labelling, the in vitro transcription using the T7 RNA polymerase is used. To increase the transcription efficiency, the 5' terminal must be a G residue, hopefully, GGG. This requirement limits the flexibility of the fragment design.

---

T. Sakamoto · M. Otsu · G. Kawai (✉)  
Department of Life and Environmental Sciences, Chiba Institute  
of Technology, Narashino 275-0016, Chiba, Japan  
e-mail: gkawai@sea.it-chiba.ac.jp

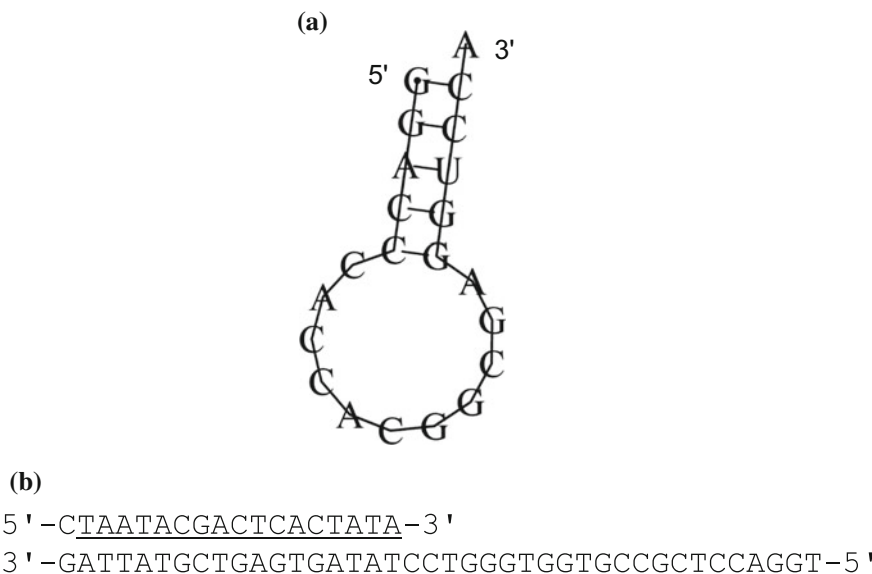


**Fig. 16.1** Design of RNA and DNA template. **a** The predicted secondary structure of a designed RNA. **b** An example of the template DNA for the in vitro transcription by the T7 RNA polymerase. Underlines indicate the T7 promoter

To design shorter fragments, it is recommended to check the possible secondary structure of the target RNA by the secondary structure prediction programs such as CentroidFold [3] or vsfold5 [4]. Figure 16.1 shows an example of the secondary structure predicted by vsfold5. For this RNA, two GC base pairs were added to its terminal to stabilize the structure as well as make the 5' terminal starting with GG. Sometimes, an A residue is added to the 3' terminal to stabilize the stem structure.

For larger RNA, it may be required to divide into several pieces to assign NMR signals and obtain structural restraints. Figure 16.2 shows an example of such division; to determine the structures of two types of dimer of 39nt RNA, two fragments are prepared [5]. By using the structures of each part, the overall structures were constructed. The constructed overall structure can be refined by RDC or other long-range information.

## 16.2 Sample Preparation

To prepare a large amount of RNA samples for NMR (100 nmol, for example), two methods, chemical synthesis and enzymatic synthesis (in vitro transcription) are available. Chemical synthesis is useful for the preparation of short RNAs (approximately less than 30 nucleotides), while in vitro transcription is suitable for

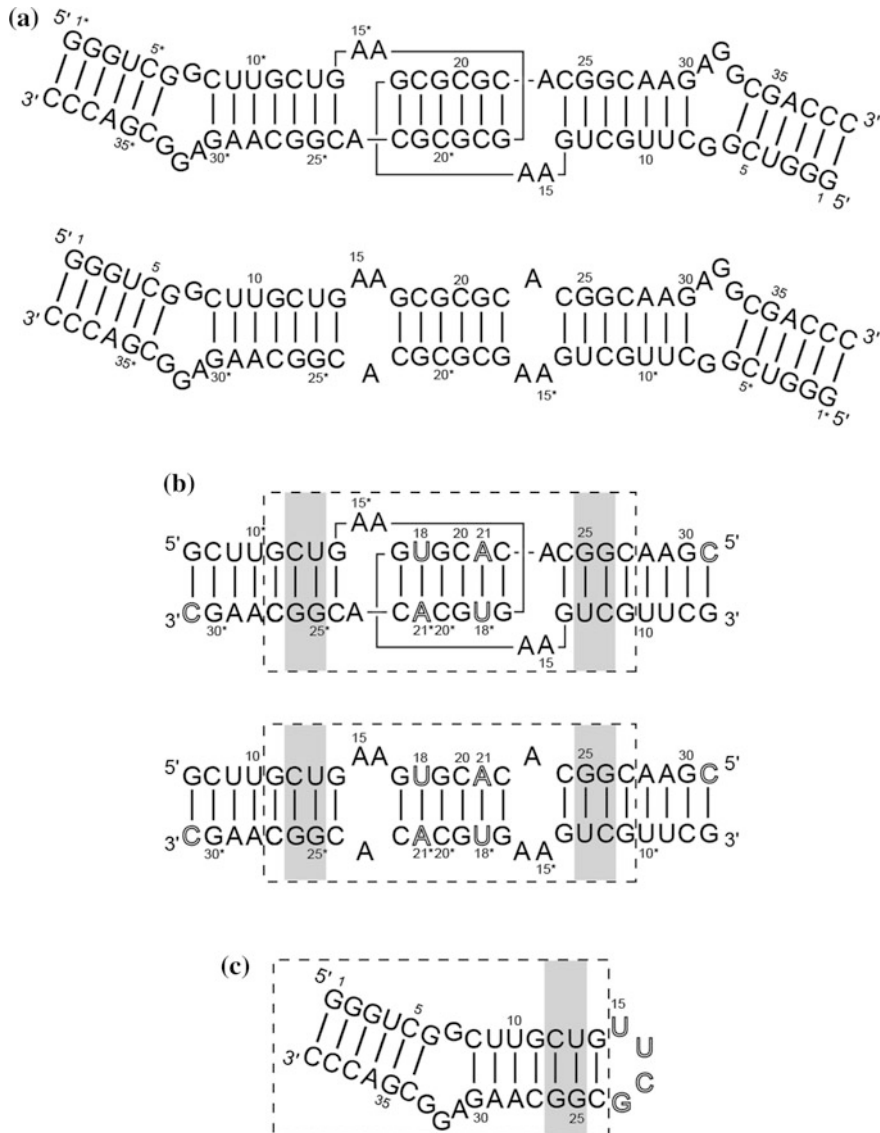


**Fig. 16.2** Design of RNA fragments for the NMR analysis of larger RNA. **a** Secondary structure of the target RNA, HIV-1 DIS, in the kissing dimer (*upper*) and extended-duplex dimer (*lower*) conformation. **b** A fragment containing the self-complementary loop. **c** A fragment containing the internal loop. Residues in the grey box will be superimposed for structure determination of the whole RNA. Reproduced from Ref. [5] by permission of Oxford University Press

long RNAs. Furthermore, chemical synthesis is useful for the site-specific labelling with stable isotopes; in vitro transcription is available for the uniform labelling or nucleotide-specific labelling.

### 16.2.1 *In Vitro Transcription*

Although T3 RNA polymerase, SP6 RNA polymerase and T7 RNA polymerase are commercially available for the in vitro transcription, T7 RNA polymerase-based in vitro transcription system is predominant for the preparation of NMR samples. The experimental procedure of in vitro transcription using T7 RNA polymerase was described previously [6], and some commercial kits, in which reaction buffers are optimized, are available (Epicentre Technologies Corp.). The promoter sequence of the template DNA is critical for recognition by the polymerase. Figure 16.1b shows an example of the DNA template: antisense strand (lower) and sense strand (upper).

Although the transcription efficiency depends on RNA sequence, T7 RNA polymerase-based in vitro transcription system is efficient, simple and cost effective for the preparation of RNA samples. Usually, 1–10 ml of reaction is needed to prepare 100 nmol of RNA sample which is the standard quantity of RNA for structure determination using NMR. On the other hand, it has some drawbacks as follows. Short RNAs less than 10 nucleotides are produced with only very low efficiency. The polymerase requires a guanosine at the 5' terminal of the transcript, and other nucleotides A, C and U cannot be incorporated. It prefers purine-rich sequences near the 5' end of RNA, such as GGG and GGA. Furthermore, 1 or 2 nucleotides of random sequences are added beyond the desired sequence, and it is difficult to purify the desired product away from these by-products. Thus, heterogeneity of the sample often leads to multiple sets of NMR signals and makes analysis of the spectra complicated. To avoid the heterogeneity, ribozymes can be applied for the removal of the additional nucleotides [7].

### 16.2.2 *Chemical Synthesis*

Although efficiency of chemical synthesis of RNA is not as high as that of DNA, solid-phase synthesis by phosphoramidite method has been established to produce large amounts of RNA. To synthesize the desired RNA, the phosphoramidite building blocks with 2'-*O*-butyldimethylsilyl as 2'-hydroxyl protecting group are sequentially coupled to the growing oligonucleotide chain in the order. The process is fully automated using a DNA/RNA synthesizer and purified RNAs which have desired sequences can be purchased from commercial companies. By using the [ $^{13}\text{C}/^{15}\text{N}$ ] phosphoramidite building blocks, labelled residues can be incorporated into specific positions of the RNA sequence.

### 16.2.3 Enzymatic Ligation

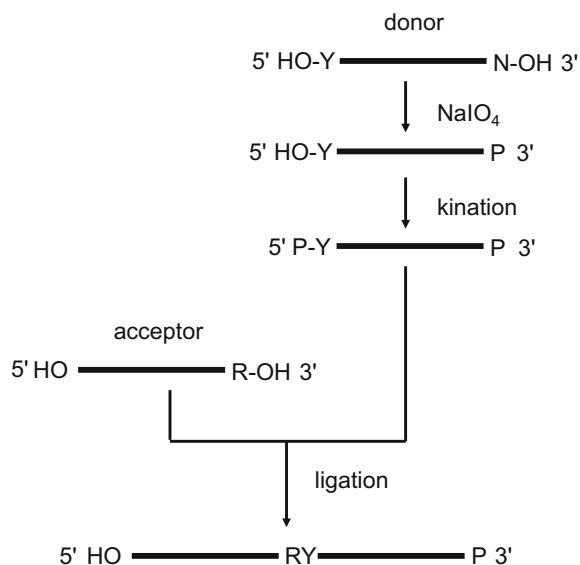
To incorporate labelled or modified nucleotides into RNA fragments at the specific positions in the sequence, enzymatic ligation using T4 RNA ligase can be used. For shorter RNA, typically shorter than 50 nt, residue specific labelling can be introduced by the chemical synthesis. Then, longer RNA with labelled or modified nucleotides can be prepared by ligating fragments.

To design the fragments to be used for ligation with T4 RNA ligase, it is required that the 5' fragment (acceptor) has a purine residue at the 3' terminal with 3'-OH and the 3' fragment (donor) has a pyrimidine residue at the 5' terminal with 5'-phosphate. To avoid the self-ligation of each fragment, acceptor and donor should have 5'-OH and 3'-phosphate, respectively as shown in Fig. 16.3. The 5'-phosphate can be added by kinase, and 3'-phosphate can be generated by the  $\text{NaIO}_4$  treatment [8]. This method was used for specific  $^{13}\text{C}/^{15}\text{N}$ -labelling of tRNA [9].

### 16.2.4 Artificial Base Pair System

The artificial base pair system is alternative way to incorporate modified nucleotides into RNA fragments at the specific positions in the sequence [10]. The artificial deoxynucleotide triphosphates, dDsTP and dPxTP can be used for conventional PCR reaction in which the Ds–Px base pair is formed and, starting from a small amount of the chemically synthesized DNA fragment with Ds in the specific position, fragments with Ds or Px were amplified. The amplified double-stranded

**Fig. 16.3** Scheme of the enzymatic ligation of RNA by T4 RNA ligase Y: pyrimidine, R: purine, N: any of A, C, G, U



fragment is used for in vitro transcription by T7 RNA polymerase, for example, and the artificial ribonucleotide triphosphate, N<sub>3</sub>-PaTP, is incorporated to the transcript. The N<sub>3</sub>-Pa base can react with variety of compounds by the click reaction. For example, spin-label such as (2,2,6,6-tetramethylpiperidin-1-yl)oxyl or TEMPO can be introduced into the specific position for the paramagnetic relaxation enhancement (PRE) measurement.

### 16.2.5 *Stable Isotopic Labelling*

Because proton signals of RNA are usually overlapped, stable isotopic labelling is required to separate the overlapped signals. Using commercially available <sup>13</sup>C and <sup>15</sup>N labelled NTPs (Taiyo Nippon Sanso Co.), stable isotopic labelled RNAs can be synthesized by using in vitro transcription system. The in vitro transcription system is useful for uniform labelling and nucleotide-specific labelling. The nucleotide-specific labelling is required for long RNAs to separate the overlapped signals. On the other hand, chemical synthesis with <sup>13</sup>C and <sup>15</sup>N labelled phosphoramidite building blocks has been carried out for site-specific labelling although chemical synthesis is available for short RNAs. To avoid the overlap of signals, the site-specific labelling or segmental labelling is required for long RNAs. Thus, for the site-specific labelling and segmental labelling, preparative ligation methods of a short RNA fragment containing isotope labelled nucleotides with the other RNA fragments have been developed [11–14]. Recently, a solid-liquid phase transcription method using automated robotic platform was developed for the synthesis of RNAs with site-selective labelling [15]. Furthermore, methods to incorporate labels at specific atomic positions within each nucleotide, such as 1',5',8-<sup>13</sup>C<sub>3</sub> guanosine residue, have been developed using recombinantly expressed enzymes and chemically synthesized ribose and nucleobase [16].

### 16.2.6 *Purification*

In the case of in vitro transcription, long by-products such as  $n + 1$  and  $n + 2$  products are synthesized. On the other hand, short by-products such as  $n - 1$  and  $n - 2$  products are produced in the case of chemical synthesis. For the purification of the desired RNA away from these by-products, preparative polyacrylamide gel electrophoresis (PAGE) under denaturing conditions with 7 M urea is widely used. This method has the advantage that single nucleotide resolution can be achieved for approximately less than 30 mer RNAs. After electrophoresis, RNA bands can be visualized by UV shadowing and cut out from the gel. Following the elution of the desired RNAs from the crushed gel (crush and soak procedure), the RNAs are purified using ethanol precipitation. For the folding of RNA conformation, the RNAs are annealed as follows. To obtain single-stranded RNAs, RNA samples are

incubated at around 95 °C and then snap-cooled on ice under low salt concentration. On the other hand, to obtain double-stranded conformation, the samples are cooled gradually after incubation at around 95 °C under high salt concentration. The conformation can be confirmed by native PAGE. To exchange buffer solution for NMR measurement, ultrafiltration membrane is useful, and the concentration of RNAs is estimated by UV absorption.

Alternative approach of purification is gel filtration chromatography. Although the gel filtration chromatography does not have single nucleotide resolution, it is useful to separate the desired long RNAs from the unincorporated nucleotides and short abortive by-products without denaturing RNA conformation [17, 18]. It is noted that it may be difficult to refold the conformation of long RNAs.

## 16.3 Measurements

Exchangeable imino protons and amino protons can be observed only in H<sub>2</sub>O containing 5% D<sub>2</sub>O, while non-exchangeable protons can be observed even in 100% D<sub>2</sub>O.

To obtain NMR restraints precisely and as much as possible, it is recommended to measure NMR spectra in 100% D<sub>2</sub>O because many ribose protons are overlapped with the water signal. However, it is also possible to analyse NMR signals of RNA only with spectra measured in H<sub>2</sub>O containing 5% D<sub>2</sub>O, especially for RNA with the stable isotopic labelling.

### 16.3.1 Exchangeable Protons

Imino proton signals of guanosine and uridine residues observed between 10 and 15 ppm contain valuable information about base pairing in the RNA molecule, because these signals are observable when the imino protons are involved in hydrogen bonding or protected from exchange with the bulk solvent water. Because of the fast exchange of imino and amino protons with water protons, presaturation of H<sub>2</sub>O signal cannot be used for solvent suppression to observe exchangeable base proton signals in RNA in contrast to NMR of proteins. Despite for the undesirable baseline distortions, the jump-and-return pulse sequence is useful for solvent suppression of RNA samples [19]. Furthermore, WATERGATE or similar solvent suppression schemes can be used to overcome the drawbacks of the jump-and-return pulse sequence [20].

The imino proton signals of A:U and G:C base pairs tend to be observed at 13–15 and 12–14 ppm, respectively, whereas imino protons of noncanonical base pairs (ex. G:U base pair) often show upfield chemical shifts (10–12 ppm) (Fig. 16.4). The chemical shifts of the imino proton signals depend strongly on the sequence of RNA. The analysis of imino proton signals is useful to elucidate secondary

structure of RNA. In addition, the conformational stability of RNA molecules can be investigated by following temperature-induced changes in the imino proton spectra. Amino proton signals of cytidine are observable when they are involved in hydrogen bonding, whereas those of guanosine and adenosine are hardly observed. By HNN-COSY experiment of  $^{15}\text{N}$ -labelled RNA, scalar couplings across an N–H $\cdots$ N-type hydrogen bond can be observed for the nitrogen and proton of the hydrogen-bond donor and the nitrogen of the hydrogen-bond acceptor [21].

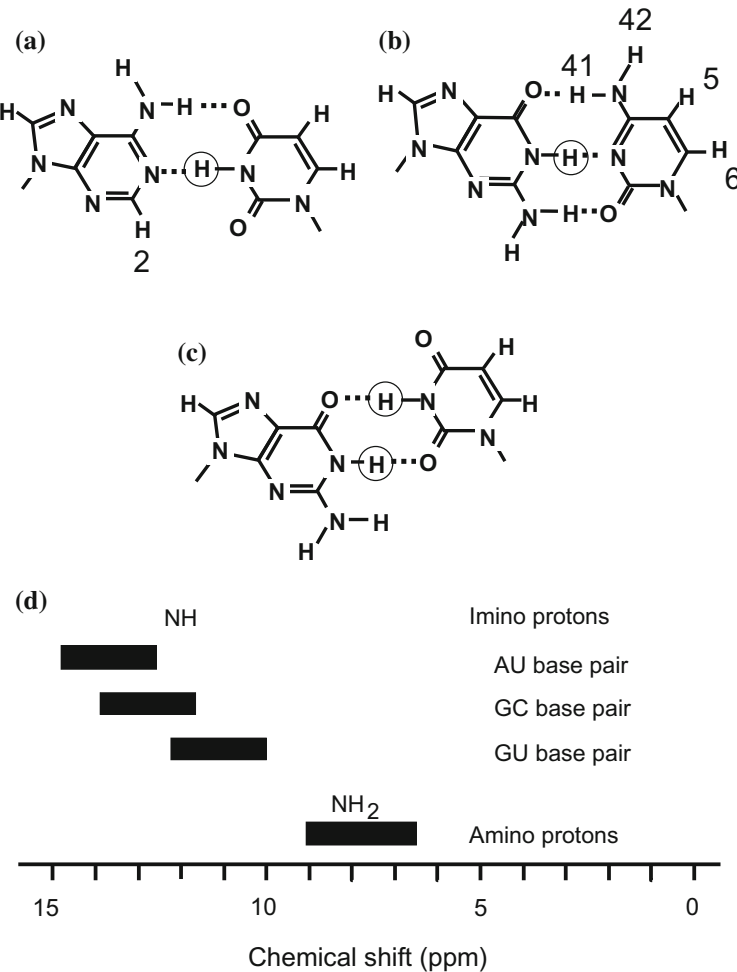


**Fig. 16.4** Imino protons in the typical base pairs of RNA. **a** A:U base pair. **b** G:C base pair. **c** G:U base pair. Imino protons are indicated by *circles*. **d** Distributions of proton chemical shifts for the exchangeable protons in RNA

### 16.3.2 Non-exchangeable Protons

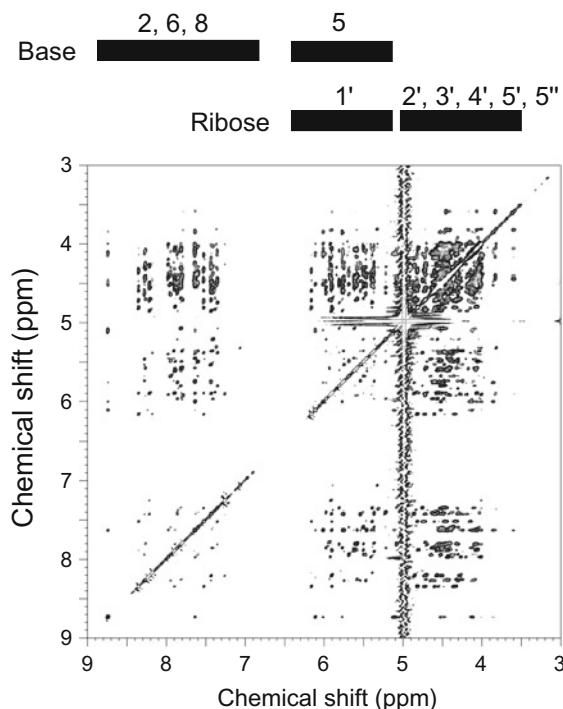
For measurement of NMR for non-exchangeable protons, D<sub>2</sub>O is the useful solvent because signals around water can be easily observed without water suppression pulse scheme. Solvent water H<sub>2</sub>O can be replaced with D<sub>2</sub>O by lyophilization or evaporation, because shorter RNA does not aggregate during such treatment in general. As shown in NOESY spectrum (Fig. 16.5), signals of H2', H3', H4', H5' and H5'' are overlapped at 3.5–5 ppm, while H1' and base protons can be observed separately.

In the case of <sup>13</sup>C(/<sup>15</sup>N)-labelled RNA, water signal can be suppressed effectively by the <sup>13</sup>C-edited experiments and the NMR analysis can be done with spectra measured in H<sub>2</sub>O.

### 16.3.3 Residual Dipolar Coupling

Residual dipolar couplings (RDCs) between spins i and j provide long-range constraints on the average orientation ( $\theta$ ) on the inter-nuclear bond vector relative to

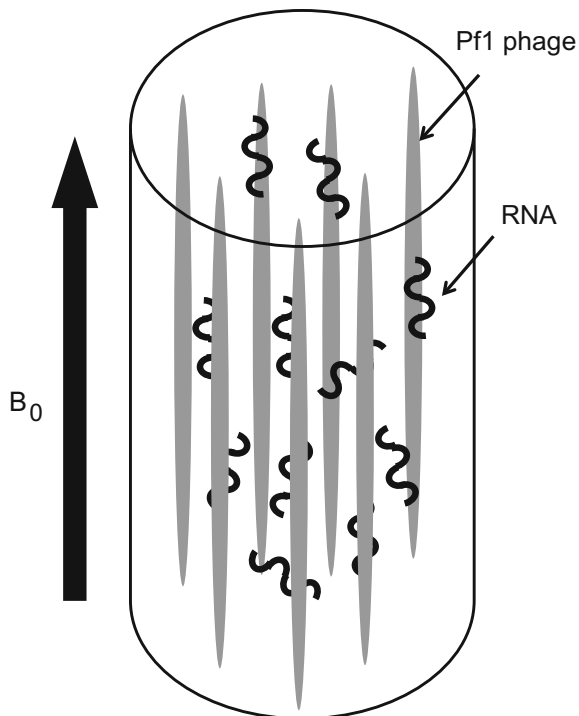
**Fig. 16.5** A 2D NOESY spectrum of a 22-mer RNA in D<sub>2</sub>O. Distributions of proton chemical shifts for the non-exchangeable protons in RNA were indicated on the top.



the applied magnetic field ( $B_0$ ) [22]. Because RNAs are usually elongated molecules, the long-range constraints are extremely useful to obtain information of global conformation of RNAs. Although several media can be applied, Pf1 filamentous phage has been generally used for alignment of RNAs (Fig. 16.6) [23, 24]. The negatively charged Pf1 phage is aligned in the magnetic field, which induces a slight alignment of RNA molecules. For the measurement of RDCs, 5–15 mg/ml of Pf1 phage is added to the stable isotope labelled RNAs. RDC can be measured as difference of coupling width (Hz) between with and without phage by undecoupled  $^{15}\text{N}-\text{H}$  SQC or  $^{13}\text{C}-\text{H}$  SQC spectrum. To avoid the overlap of signals, in-phase and anti-phase heteronuclear single quantum coherence (IPAP-HSQC) [25] or transverse relaxation optimized spectroscopy (TROSY) [26] can be used.

Furthermore, Al-Hashimi et al. have applied RDC for studying RNA structural dynamics [27, 28]. Inherent flexibility involving local motions of nucleotides residues and collective helix motions can be characterized over a wide range of timescales (<milliseconds).

**Fig. 16.6** Schematic representation of alignment of RNAs using Pf1 phage for RDC measurement. Pf1 phage is aligned in the magnetic field, which induces a slight alignment of RNA molecules



## 16.4 Signal Assignments

### 16.4.1 Exchangeable Protons

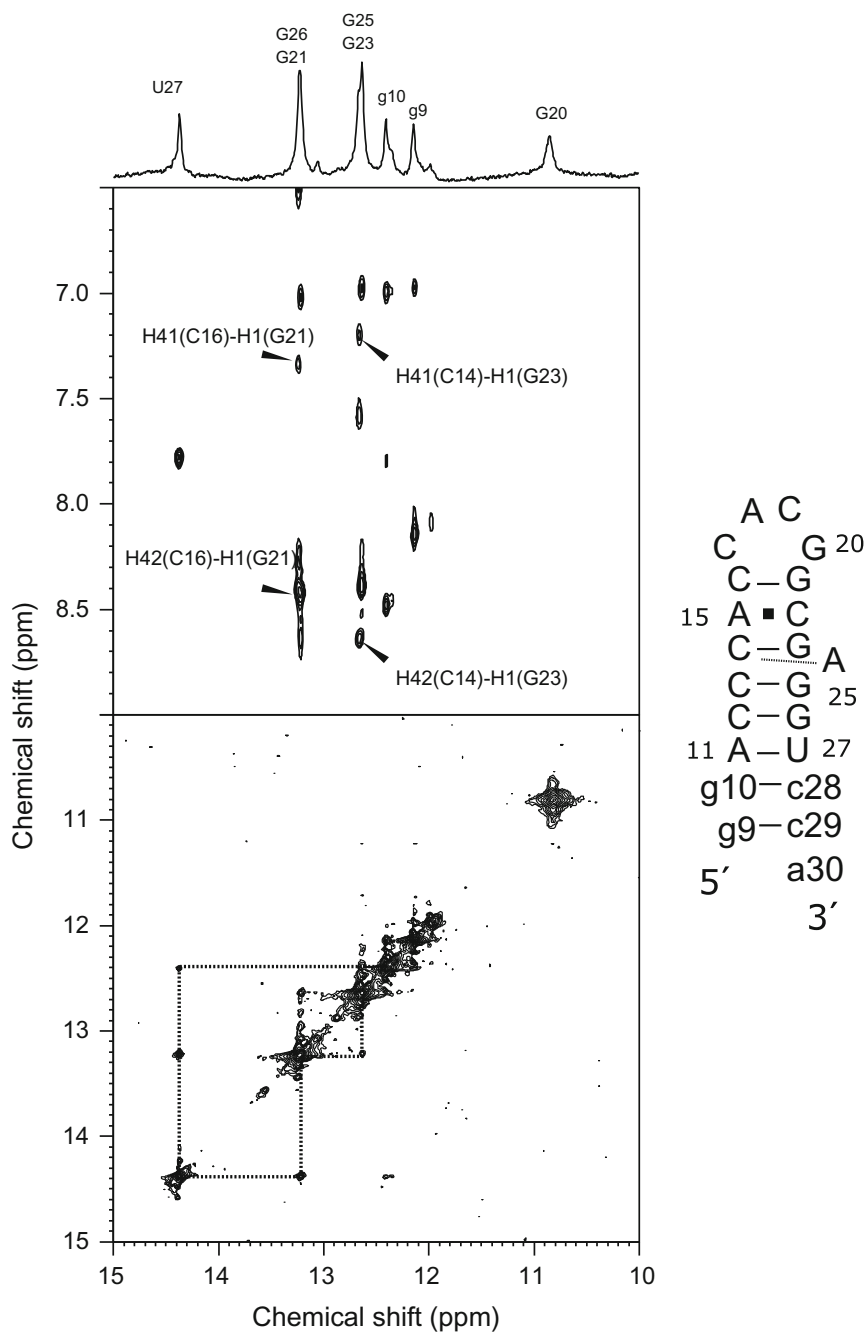
Based on the predicted secondary structure of RNA, the imino proton signals can be sequentially assigned along the stem sequence using the 2D NOESY spectrum (Fig. 16.7). A strong NOE crosspeak between the uridine H3 and the adenosine H2 can be observed in A:U base pairs. In G:C base pairs, NOE crosspeaks can be observed between the guanosine H1 and the amino protons of cytidine. Because one of the amino protons of cytidine in G:C base pair is close to H5 of the cytidine, H5/H6 signals can be assigned by following the NOE connectivity as H1(G)–H41/42(C)–H5(C)–H6(C). G:U base pairs, whose imino proton signals resonate higher field around 12–10 ppm, can be easily identified by a strong NOE crosspeak between the guanosine H1 and the uridine H3.

Heteronuclear multi-quantum coherence (HMQC) spectrum of  $^{15}\text{N}$ -labelled RNA is useful to assign the imino proton signals. Because the  $^{15}\text{N}$  chemical shift of guanosine N1 is around 150 ppm and that of uridine N3 is around 160 ppm, imino proton signals of guanosine and uridine can be clearly discriminated.

### 16.4.2 Non-exchangeable Protons

Although signals of ribose protons are highly overlapped, H1' signals can be observed separately from other ribose signals. Thus, sequential assignment of base and ribose H1' signals can be accomplished by the analysis of NOE connectivities in helical A-form RNA (Fig. 16.8). The H1' of residue  $i$  shows NOE crosspeaks to the H8/H6 of residue  $i$  (intra-residue) and residue  $i + 1$  (inter-residue), which enables sequential assignment of these signals along the RNA sequence. Figure 16.9 shows the region where NOEs used for the sequential assignment; NOE crosspeaks between purine base H2, H8, or pyrimidine base H6 and pyrimidine base H5 or ribose H1' are shown. Because the inter-residue H1'–H8/H6 distance is larger than 4 Å in helical A-form RNA, spin-diffusion-mediated NOEs, through strong NOE between H6/H8 and H2'/H3' protons, caused by long mixing time (>400 ms) of NOESY experiments may be useful for the sequential assignment. Furthermore, the inter-residue NOE crosspeaks between base protons are helpful for sequential assignment. Although NOEs between base protons and the sugar protons H4', H5' and H5'' can be observed, their assignment is difficult because of the low dispersion in most RNA sequences.

To perform the NOE-based assignment procedure, connectivities between non-exchangeable base protons and imino protons are important. The H5 proton of cytidine can be identified by NOE connectivities to the amino protons of cytidine in  $\text{H}_2\text{O}$  as described above. The pyrimidine H5 and H6 signals are easy to identify because of the strong NOE crosspeaks observed in NOESY experiment, which can



◀Fig. 16.7 Assignment of imino proton signals of a 22-mer RNA. Sequential connectivities is indicated by *lines* in the 2D NOESY spectrum and assignments are shown on the 1D spectrum. Secondary structure of the 22-mer RNA is shown. Reproduced from Ref. [29] by permission of Oxford University Press

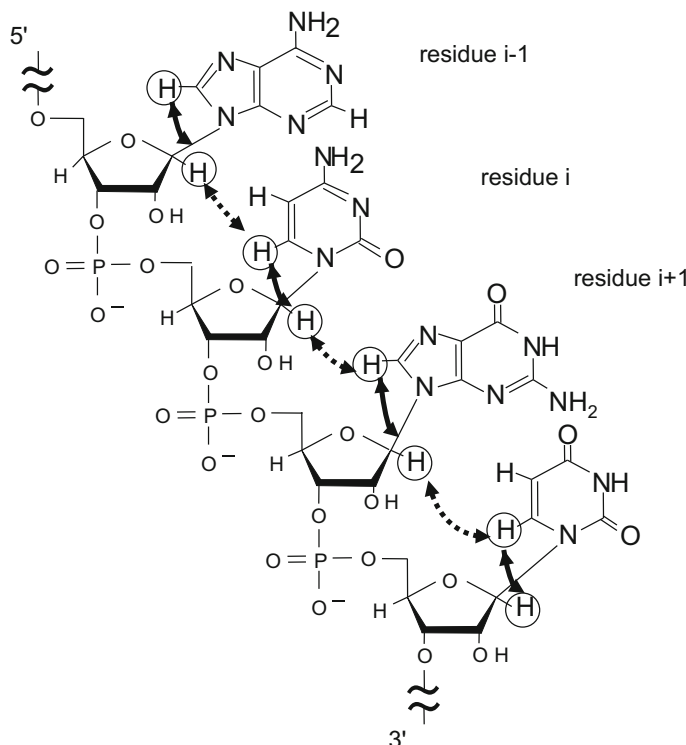


**Fig. 16.8** Schematic representation of NOE connectivities. The H1' of residue *i* shows NOE crosspeaks to the H8/H6 of residue *i* (intra-residue) and residue *i* + 1 (inter-residue). Intra-residue and inter-residue NOEs are shown by *arrow* and *dotted arrow*, respectively

be confirmed by TOCSY experiment. Signals of cytidine and uridine can be distinguished by the difference between the chemical shifts of the C5 resonances in a  $^{13}\text{C}$ - $^1\text{H}$  SQC (Fig. 16.10). Furthermore, H2 signals of adenosine can be identified by NOE contacts to the uridine imino protons in  $\text{H}_2\text{O}$ . The C2H2 region (150 ppm in  $^{13}\text{C}$ ) is well resolved in a  $^{13}\text{C}$ - $^1\text{H}$  SQC. In helical A-form RNA, the distance between H2 (*i*) and the H1' (*i* + 1) is shorter than 4 Å, and, thus, strong NOEs can be observed between them, which enable confirmation of sequential assignments.

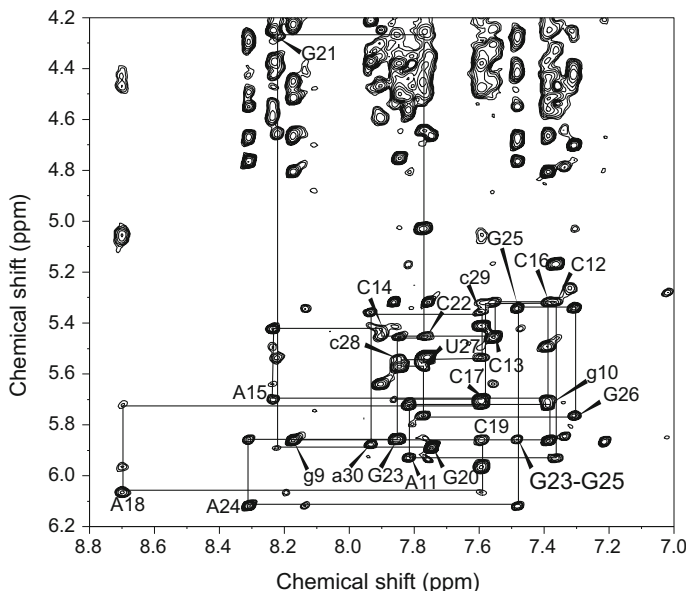


**Fig. 16.9** A 2D NOESY spectrum of a 22-mer RNA in  $\text{D}_2\text{O}$ . The region for crosspeaks between aromatic H6 and H8 and ribose H1' is shown. Sequential connectivities are indicated by *lines* and intra-residue NOEs are labelled. Reproduced from Ref. [29] by permission of Oxford University Press

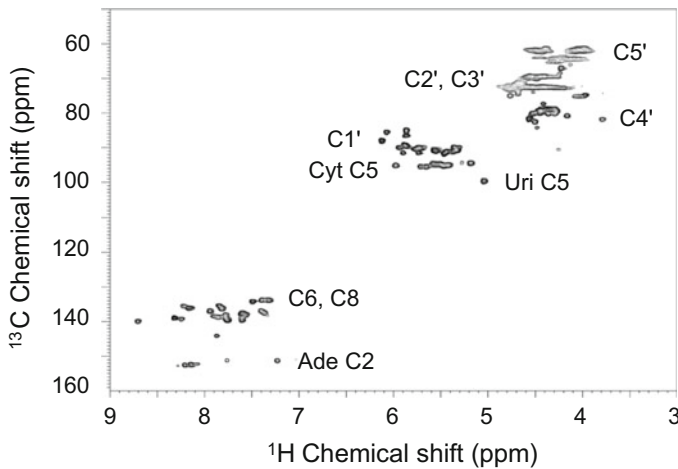


**Fig. 16.10**  $^{13}\text{C}$ - $^1\text{H}$  SQC spectrum of a 22-mer RNA C2 of adenosine (Ade), C5 of cytidine (Cyt) and uridine (Uri) can be assigned by their  $^{13}\text{C}$  chemical shift

**Table 16.1** Calculation protocol used for the structure determination of a 22nt RNA [29]

<i>Structure calculation without RDCs (CNS 1.1)</i>		
Hot steps	20,000 K	60,000 steps (60 ps)
Cooling steps	20,000–0 K	170,000 steps (170 ps)
<i>Refinement with RDCs (Xplor-NIH 2.38)</i>		
Refinement steps	2000–0 K	5000 steps (10 ps)

## 16.5 Structural Calculation

As a typical example of the RNA structure determination by NMR, the structure determination of a 22-mer RNA fragment is shown. The RNA obtained by SELEX against AML1 Runt domain contains a DNA mimicry motif [29]. The non-labelled sample (0.6 mM) and [uniform-<sup>13</sup>C/<sup>15</sup>N]-labelled sample (0.5 mM) were synthesized using T7 RNA polymerase. NMR spectra were measured using Bruker DRX-500 and DRX-600 spectrometers at 10 °C. Imino proton resonances of G and U residues were distinguished by the <sup>15</sup>N-<sup>1</sup>H SQC spectra and assigned by NOESY with mixing times of 150 ms using the jump-and-return scheme for water

**Table 16.2** Example of the constraints for structure determination [29]

<i>NOE distance restraints</i>	
Between exchangeable protons	1.8–6.0 Å
<i>From non-exchangeable protons</i>	
Strong	1.8–3.0 Å
Medium	1.8–4.0 Å
Weak	1.8–5.0 Å
Very weak	1.8–7.0 Å
<i>A-helix restraints for stem region</i>	
$\alpha$	$-62^\circ \pm 30^\circ$
$\beta$	$-174^\circ \pm 30^\circ$
$\gamma$	$49^\circ \pm 30^\circ$
$\delta$	$95^\circ \pm 30^\circ$
$\varepsilon$	$-158^\circ \pm 30^\circ$
$\zeta$	$-73^\circ \pm 30^\circ$
<i>Sugar packer restraints (<math>\delta</math> angle) based on DQF-COSY H1'-H2' crosspeak</i>	
Strong	$C2'\text{-}endo} \quad 145^\circ \pm 25^\circ$
No crosspeak	$C3'\text{-}endo} \quad 95^\circ \pm 30^\circ$
<i>Base pair restraints</i>	
<i>Hydrogen bond</i>	
N1–H3 (AU)	1.8–2.2 Å
H61–O4 (AU)	1.8–2.2 Å
H1–N3 (GC)	1.8–2.2 Å
O6–H41 (GC)	1.8–2.2 Å
H21–O2 (GC)	1.8–2.2 Å
<i>Base pair planarity</i>	
	N1–N3–C5

suppression. Base pairing schemes were established by 2D HNN-COSY experiments. HCCH-COSY and HCCH-TOCSY were used to assign sugar spin systems. H<sub>2</sub> protons of adenosines were assigned using HCCH-TOCSY and 2D SQC. NOE distance restraints from non-exchangeable protons were obtained using NOESY (mixing times of 100 and 400 ms) in D<sub>2</sub>O. Dihedral restraints were obtained from TOCSY (mixing time of 50 ms). Partial alignment for the RDC measurements was achieved by the addition of approximately 16.9 mg/ml of Pf1 phage (ASLA Ltd.) to [uniform-<sup>13</sup>C/<sup>15</sup>N]-labelled sample. Single-bond <sup>1</sup>H-<sup>13</sup>C RDC values for bases and ribose moieties were measured using non-decoupled <sup>13</sup>C-<sup>1</sup>H SQC.

NOE from non-exchangeable protons was assigned using Felix and ARIA in combination with CNS (version 1.1). Restraints were summarized in Table 16.2. A set of 100 structures was calculated using a simulated annealing protocol with CNS 1.1 utilizing 354 distance restraints and 80 dihedral restraints (Table 16.3) starting from an extended structure. The protocol used for the structure calculation was summarized in Table 16.1. The alignment tensor was obtained by the grid-search using the lowest energy structures for the first calculation without RDCs. The final 10 structures with the lowest total energy were chosen (Fig. 16.11), and the structural statistics were shown in Table 16.4.

It is noted that an improved method for structure calculations was proposed [30] in which the van der Waal radius was modified from 0.9 to 1.10.

**Table 16.3** Number of restraints used for the structure determination of a 22nt RNA [29]

Distance restraints	354
Total NOE	327
Intra-residue	133
Strong	44
Medium	42
Weak	3
Very weak	44
Inter-residue	194
Strong	21
Medium	36
Weak	10
Very weak	127
Hydrogen bonds	27
Dihedral angle restraints	72
Sugar pucker	19
C2'-endo	4
C3'-endo	15
Based on A-form geometry <sup>a</sup>	53
Base pair planarity	8
Residual dipolar coupling	10

<sup>a</sup>Restraints of angles  $\gamma$ ,  $\delta$ ,  $\epsilon$  and  $\zeta$  are used for the residue at 5'-terminal of helical A-form RNA, while those of angles  $\alpha$ ,  $\beta$ ,  $\gamma$  and  $\delta$  are used at 3'-terminal

**Fig. 16.11** Ensemble of 10 lowest energy structure of a 22-mer RNA G, A, C, and U are indicated by blue, red, yellow and green, respectively. Reproduced from Ref. [29] by permission of Oxford University Press. The corresponding secondary structure is shown in Fig. 16.7

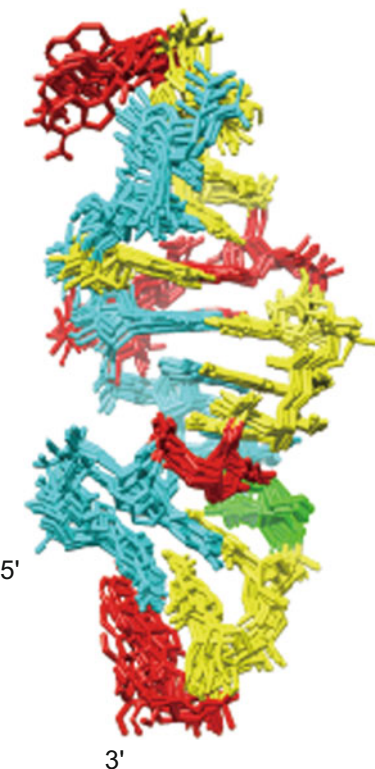


**Table 16.4** Structural statistics for a 22nt RNA [29]

<i>r.m.s. deviations from experimental restraints</i>	
Distance constraints ( $\text{\AA}$ )	$0.0592 \pm 0.0016$
Dihedral angle constraints ( $^\circ$ )	$0.0934 \pm 0.1826$
<i>r.m.s. deviations from idealized geometry</i>	
Bond lengths ( $\text{\AA}$ )	$0.0065 \pm 0.00019$
Bond angles ( $^\circ$ )	$1.1898 \pm 0.05405$
Improper ( $^\circ$ )	$1.0435 \pm 0.14214$
<i>Averaged pairwise r.m.s. deviation (<math>\text{\AA}</math>)</i>	
All RNA heavy atoms	0.825

## 16.6 Interaction Analysis and Structure Screening

NMR is a useful tool for the interaction analysis. The imino proton signals are often used for probes of interaction. Figure 16.12a shows the imino proton signals of a 32-mer RNA in the absence and presence of spermine (polyamine) [31]. In this case, addition of  $\text{Mg}^{2+}$  does not show significant change in spectrum but spermine shows drastic change, indicating that specific interaction between the RNA and

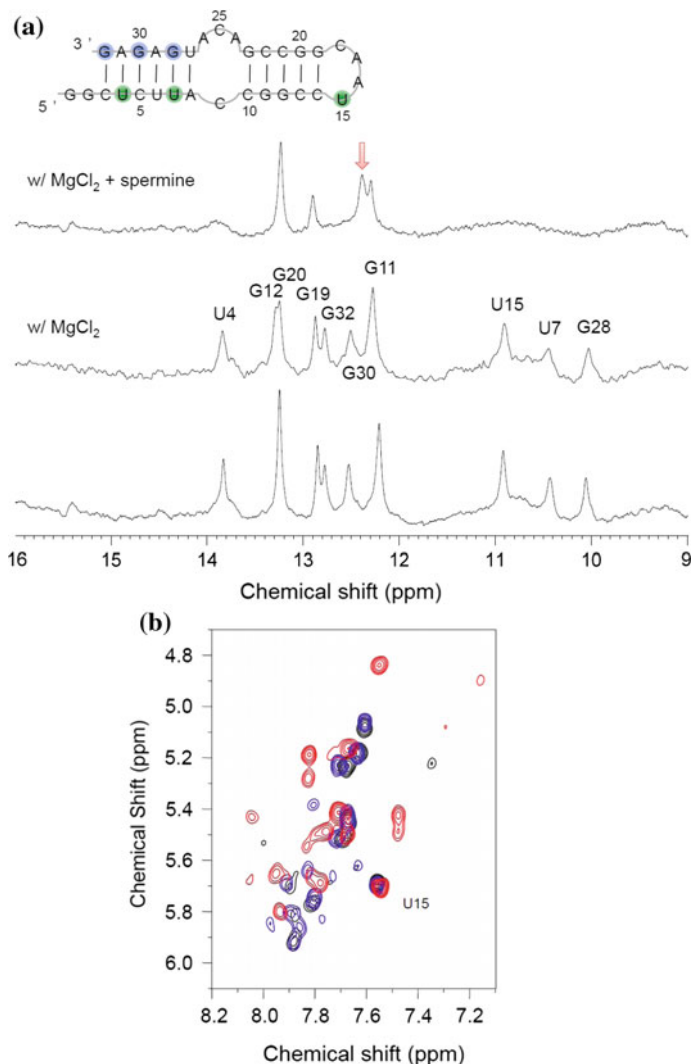


**Fig. 16.12** NMR spectra of a 32-mer RNA. **a** Imino proton spectra in  $\text{H}_2\text{O}$  (5%  $\text{D}_2\text{O}$ ) at 283 K. *Bottom* Spectrum of free RNA, *Middle* spectrum in the presence of 1 mM  $\text{MgCl}_2$ , *Top* spectrum in the presence of 1 mM  $\text{MgCl}_2$  and 5 mM spermine. *Shaded residues* in the secondary structure indicate the positions of disappeared resonances. Arrow indicates the newly appeared resonance in the presence of spermine. The RNA sample concentration was 0.12 mM. **b** HOHAHA spectra showing the H5–H6 crosspeaks of pyrimidine residues in  $\text{D}_2\text{O}$  at 298 K. *Black* free RNA. *Blue* in the presence of 1 mM  $\text{MgCl}_2$ . *Red* in the presence of 1 mM spermine and 1 mM  $\text{MgCl}_2$ . The RNA sample concentration was 0.02 mM. Reproduced from Ref. [31] by permission of Oxford University Press

spermine. In this case, a part of stem structure was changed and some base pairs were opened upon binding of spermine. The pyrimidine H5–H6 signals in TOCSY or HOHAHA spectra are also good probes of interaction. Figure 16.12b shows the drastic change of H5 and H6 chemical shift of the 32-mer RNA upon binding of spermine, indicating the conformational change [31].

High-throughput analyses such as high-throughput sequencing give a large number of information for novel functional RNA candidates. Thus, methods for high-throughput screening of RNA structure are required. Recently, two methods for RNA structure screening were proposed [32, 33]. The first method, In NMR tube transcription (INTT), is quite simple in which the transcription reaction by the T7 RNA polymerase is performed in the NMR tube and measures the NMR spectra of the transcript in the reaction mixture directly [32]. In the INTT method, neither purification nor specific skill for RNA handling is required. The limitation of INTT is the condition of measurement is fixed by the transcription reaction. The second one accelerates the screening process by direct buffer exchange and concentration of the transcription mixture [33]. In this case, any buffer condition suitable for NMR measurements of the target RNA can be used. The structural profiling ability was applied to the monitoring of the concentration of specifically folded RNA during the process of the systematic evolution of ligands by exponential enrichment (SELEX) method [34].

## 16.7 Perspective

Some systems to support NMR signal analysis for RNA have been developed, for example, Chess2FLYA [35] and RNA-PAIRS [36]. Such systems will accelerate the NMR analysis of RNA.

For larger RNA, methods to predict the structural domain in long sequence must be improved. GenoPoemics system for visualization of predicted secondary structures may be useful for such analysis [37].

## References

1. Varani, G., Aboul-ela, F., Allain, F.H.-T.: NMR investigation of RNA structure. *Prog. NMR Spectrosc.* **29**, 51–127 (1996)
2. Fürtig, B., Richter, C., Wöhner, J., Schwalbe, H.: NMR spectroscopy of RNA. *ChemBioChem* **4**, 936–962 (2003)
3. Sato, K., Hamada, M., Asai, K., Mituyama, T.: CentroidFold: a web server for RNA secondary structure prediction. *Nucleic Acids Res.* **37**, W277–W280 (2009)
4. Dawson, W., Fujiwara, K., Kawai, G.: Prediction of RNA pseudoknots using heuristic modeling with mapping and sequential folding. *PLoS ONE* **2**, 905 (2007)

5. Baba, S., Takahashi, K., Noguchi, S., Takaku, H., Koyanagi, Y., Yamamoto, N., Kawai, G.: Solution RNA structures of the HIV-1 dimerization initiation site in the kissing-loop and extended-duplex dimers. *J. Biochem.* **138**, 583–592 (2005)
6. Milligan, J.F., Groebe, D.R., Witherell, W.G., Uhlenbeck, O.C.: Oligoribonucleotide synthesis using T7 RNA polymerase and synthetic DNA templates. *Nucleic Acids Res.* **15**, 8783–8798 (1987)
7. Ferré-D’Amaré, A.R., Doudna, J.A.: Use of cis- and trans-ribozymes to remove 5' and 3' heterogeneities from milligrams of in vitro transcribed RNA. *Nucleic Acids Res.* **24**, 977–978 (1996)
8. Ohtsuki, T., Kawai, G., Watanabe, Y., Kita, K., Nishikawa, K., Watanabe, K.: Preparation of biologically active *Ascaris suum* mitochondrial tRNA<sup>Met</sup> with a TV-replacement loop by ligation of chemically synthesized RNA fragments. *Nucleic Acids Res.* **24**, 662–667 (1996)
9. Ohtsuki, T., Kawai, G., Watanabe, Y.: The minimal tRNA: unique structure of *Ascaris suum* mitochondrial tRNA<sup>Ser</sup><sub>UCU</sub> having a short T arm and lacking the entire D arm. *FEBS Lett.* **514**, 37–43 (2002)
10. Someya, T., Ando, A., Kimoto, M., Hirao, I.: Site-specific labelling of RNA by combining genetic alphabet expansion transcription and copper-free click chemistry. *Nucleic Acids Res.* **43**, 6665–6676 (2015)
11. Xu, J., Lapham, J., Crothers, D.M.: Determining RNA solution structure by segmental isotopic labelling and NMR: application to *Caenorhabditis elegans* spliced leader RNA 1. *Proc. Natl. Acad. Sci. USA* **93**, 44–48 (1996)
12. Kim, I., Lukavsky, P.J., Puglisi, J.D.: NMR study of 100 kDa HCV IRES RNA using segmental isotope labelling. *J. Am. Chem. Soc.* **124**, 9338–9339 (2002)
13. Tzakos, A.G., Easton, L.E., Lukavsky, P.J.: Complementary segmental labelling of large RNAs: economic preparation and simplified NMR spectra for measurement of more RDCs. *J. Am. Chem. Soc.* **128**, 13344–13345 (2006)
14. Kawahara, I., Haruta, K., Ashihara, Y., Yamanaka, D., Kuriyama, M., Toki, N., Kondo, Y., Teruya, K., Ishikawa, J., Furuta, H., Ikawa, Y., Kojima, C., Tanaka, Y.: Site-specific isotope labelling of long RNA for structural and mechanistic studies. *Nucleic Acids Res.* **40**, e7 (2012)
15. Liu, Y., Holmstrom, E., Zhang, J., Yu, P., Wang, J., Dyba, M.A., Chen, D., Ying, J., Lockett, S., Nesbitt, D.J., Ferré-D’Amaré, A.R., Sousa, R., Stagno, J.R., Wang, Y.X.: Synthesis and applications of RNAs with position-selective labelling and mosaic composition. *Nature* **522**, 368–372 (2015)
16. Longhini, A.P., LeBlanc, R.M., Becette, O., Salguero, C., Wunderlich, C.H., Johnson, B.A., D’Souza, V.M., Kreutz, C., Dayie, T.K.: Chemo-enzymatic synthesis of site-specific isotopically labelled nucleotides for use in NMR resonance assignment, dynamics and structural characterizations. *Nucleic Acids Res.* **44**, e52 (2016)
17. Lukavsky, P.J., Puglisi, J.D.: Large-scale preparation and purification of polyacrylamide-free RNA oligonucleotides. *RNA* **10**, 889–893 (2004)
18. McKenna, S.A., Kim, I., Puglisi, E.V., Lindhout, D.A., Aitken, C.E., Marshall, R.A., Puglisi, J.D.: Purification and characterization of transcribed RNAs using gel filtration chromatography. *Nat. Protoc.* **2**, 3270–3277 (2007)
19. Plateau, P., Gueron, M.: Exchangeable proton NMR without base-line distortion, using new strong-pulse sequences. *J. Am. Chem. Soc.* **104**, 7310–7311 (1982)
20. Piotto, M., Saudek, V., Sklenár, V.: Gradient-tailored excitation for single-quantum NMR spectroscopy of aqueous solutions. *J. Biomol. NMR* **2**, 661–665 (1992)
21. Dingley, A.J., Grzesiek, S.: Direct observation of hydrogen bonds in nucleic acid base pairs by internucleotide <sup>2</sup>J<sub>NN</sub> couplings. *J. Am. Chem. Soc.* **120**, 8293–8297 (1998)
22. Tjandra, N., Bax, A.: Direct measurement of distances and angles in biomolecules by NMR in a dilute liquid crystalline medium. *Science* **278**, 1111–1114 (1997)
23. Hansen, M.R., Mueller, L., Pardi, A.: Tunable alignment of macromolecules by filamentous phage yields dipolar coupling interactions. *Nat. Struct. Biol.* **5**, 1065–1074 (1998)

24. Hansen, M.R., Hanson, P., Pardi, A.: Filamentous bacteriophage for aligning RNA, DNA, and proteins for measurement of nuclear magnetic resonance dipolar coupling interactions. *Methods Enzymol.* **317**, 220–240 (2000)
25. Ottiger, M., Delaglio, F., Bax, A.: Measurement of J and dipolar couplings from simplified two-dimensional NMR spectra. *J. Magn. Reson.* **131**, 373–378 (1998)
26. Pervushin, K., Riek, R., Wider, G., Wüthrich, K.: Attenuated T2 relaxation by mutual cancellation of dipole-dipole coupling and chemical shift anisotropy indicates an avenue to NMR structures of very large biological macromolecules in solution. *Proc. Natl. Acad. Sci. USA* **94**, 12366–123671 (1997)
27. Bothe, J.R., Nikolova, E.N., Eichhorn, C.D., Chugh, J., Hansen, A.L., Al-Hashimi, H.M.: Characterizing RNA dynamics at atomic resolution using solution-state NMR spectroscopy. *Nat. Methods* **8**, 919–931 (2011)
28. Salmon, L., Yang, S., Al-Hashimi, H.M.: Advances in the determination of nucleic acid conformational ensembles. *Annu. Rev. Phys. Chem.* **65**, 293–316 (2014)
29. Nomura, Y., Tanaka, Y., Fukunaga, J., Fujiwara, K., Chiba, M., Iibuchi, I., Tanaka, T., Nakamura, Y., Kawai, G., Kozu, T., Sakamoto, T.: Solution structure of a DNA mimicking motif of an RNA aptamer against transcription factor AML1 Runt domain. *J. Biochem.* **154**, 513–519 (2013)
30. Bermejo, G.A., Clore, M., Schwieters, C.D.: Improving NMR Structures of RNA. *Structure* **24**, 806–815 (2016)
31. Oguro, A., Yanagida, A., Fujieda, Y., Amano, R., Otsu, M., Sakamoto, T., Kawai, G., Matsufuji, S.: Two stems with different characteristics and an internal loop in an RNA aptamer contribute to spermine-binding. *J. Biochem.* **161**, 197–206 (2016)
32. Okui, S., Kawai, g: In NMR tube transcription for rapid screening of RNA conformation. *Nucleosides Nucleotides Nucleic Acids* **34**, 103–113 (2015)
33. Helmling, C., Keyhani, S., Sochor, F., Fürtig, B., Hengesbach, M., Schwalbe, H.: Rapid NMR screening of RNA secondary structure and binding. *J. Biomol. NMR* **63**, 67–76 (2015)
34. Amano, R., Aoki, K., Miyakawa, S., Nakamura, Y., Kozu, T., Kawai, G., Sakamoto, T.: NMR monitoring of the SELEX process to confirm enrichment of structured RNA. *Sci. Rep.* **7**, 283 (2017)
35. Aeschbacher, T., Schmidt, E., Blatter, M., Maris, C., Duss, O., Allain, F.H.-T., Güntert, P., Schubert, M.: Automated and assisted RNA resonance assignment using NMR chemical shift statistics. *Nucleic Acids Res.* **41**, e172 (2013)
36. Bahrami, A., Clos II, L.J., Markley, J.L., Butcher, S.E., Eghbalnia, H.R.: RNA-PAIRS: RNA probabilistic assignment of imino resonance shifts. *J. Biomol. NMR* **52**, 289–302 (2012)
37. Nakamura, S.: A novel virtual spectrometry: visualized regulatory motifs on *ADM*, *rPolB* and *CD83* mRNAs in human-friendly manners. *J. Biochem.* **146**, 251–261 (2009)

# Chapter 17

## NMR Analysis of Molecular Complexity

Jun Kikuchi

**Abstract** NMR offers tremendous advantages in analysis of molecular complexity of natural mixtures, such as crude biological extracts, supramacromolecular complexes, and geochemical samples as well as intact cells and tissues. Here, I introduce recent applications of several NMR approaches for evaluation of human and environmental health (i.e., maintaining a homeostatic state) by metabolic profiling and data science. Further challenges in addressing macromolecular complexity include supramolecular structures, composition, and interactions of plant biomass, soil humic substances, and aqueous particulate organic matter. To support the study of these topics, I also introduce sample preparation techniques for molecular complexity studies as well as solid-state NMR approaches. Because solution and solid-state NMR can produce numerical matrix data (e.g., chemical shifts versus intensity) with high reproducibility and inter-institution convertibility, further data science approaches are desired, such as multivariate analysis and machine learning. Therefore, I also introduce informatics techniques for data pretreatment before solid-state NMR, for feature extraction from heterogeneously measured spectroscopic data and for extraction of submerged information using data science approaches.

**Keywords** Environmental homeostasis • Metabolic profiling • Data science

---

J. Kikuchi (✉)

RIKEN Center for Sustainable Resource Science, 1-7-22 Suehiro-cho,  
Tsurumi-ku, Yokohama, Kanagawa 230-0045, Japan  
e-mail: jun.kikuchi@riken.jp

J. Kikuchi

Graduate School of Medical Life Science, Yokohama City University,  
1-7-29 Suehiro-cho, Tsurumi-ku, Yokohama, Kanagawa 230-0045, Japan

J. Kikuchi

Graduate School of Bioagricultural Sciences, Nagoya University,  
1 Furo-cho, Chikusa-ku, Nagoya, Aichi 464-0810, Japan

## 17.1 Introduction

NMR is one of the most powerful tools available for molecular characterizations. Herein, I introduce the advantages of NMR analysis for challenging molecular complexity in biological extracts [1–3], biomacromolecular assembly [4–6], and crude biogeochemical samples [7–9] from natural ecosystems. First, NMR offers a wide variety of sample systems, from crude extracts to intact biological tissues [10–14], from small- to macromolecular complexes [15–18], and also in interaction studies [19–23]. Furthermore, NMR provides site- and atom-specific information [24–26], when assisted with stable isotopic tracing experiments [27, 28]. In addition, uniform, stable isotopic labeling in biological samples opens the availability of NMR for two- and three-dimensional experiments, similar to protein NMR [29, 30]. The interchangeability of spectral data among laboratories worldwide is a marked advantage of NMR-based approaches for cross-site analytical validity studies using careful parameter settings [31–34]. For this purpose, solid-state NMR, which approaches toward macromolecular complexes and low-solubility samples, has a unique advantage for various samples. This advantage is attributed to the feature that chromatography is not involved during measurement process for molecular complexity. Similar to the above, NMR's reproducibility and quantifying abilities are also major advantages [35–37]. In quantification, absolute measurements are not always important, but relative measurements within a variety of samples are a major concern. As solution and solid-state NMR produce highly reproducible numerical matrix data (e.g., chemical shifts versus intensity) with inter-institution convertibility, further analysis of such data using multivariate analysis and machine-learning approaches is desired.

## 17.2 Metabolomics and Metabolic Profiling for Small Molecular Complexity

### 17.2.1 Basic Knowledge for Small Molecular Profiling

Metabolites are the final products of biological processes, and metabolic profiling or metabolomics is the study of organic metabolites in cells, tissues, and biological fluids [38–40]. Metabolomics studies provide comprehensive datasets from target samples [41–43]. This section describes the range of samples, metabolites, and NMR experiments used in metabolomics studies.

Recently, solution NMR has been used for metabolic profiling in which NMR spectra of mixtures of small biological molecules are subjected to further multivariate analyses to identify metabolite biomarkers [44–48] and to evaluate nutrients in foods [49–52]. Innovations in nontargeted approaches to studying biological systems are important for better biomass production and sustainability of such systems.

Homeostasis is the maintenance of an internal physiological environment within a certain range against changes in the external environment. Pathological states collapse homeostasis and change metabolite compositions and/or profiles. Metabolomics has great potential in the diagnosis and monitoring of diseases using samples, such as blood, saliva, urine, and feces (Fig. 17.1). NMR metabolome analysis of the human superorganism has provided new insights into interactions between hosts and microorganisms during the establishment of immunological homeostasis in intestines [53–56]. Environmental homeostasis evaluation is growing in importance with declining environmental health. Environmental homeostasis can be evaluated at multiple levels using NMR [57–62].

### 17.2.2 Experimental Aspects of Sample Preparation

Sample preparation toward molecular complexity analysis is minimum laboratory experimental requirement due to unnecessary feature of column purification [63]. Solution NMR detects low-molecular-weight molecules, such as polar metabolites

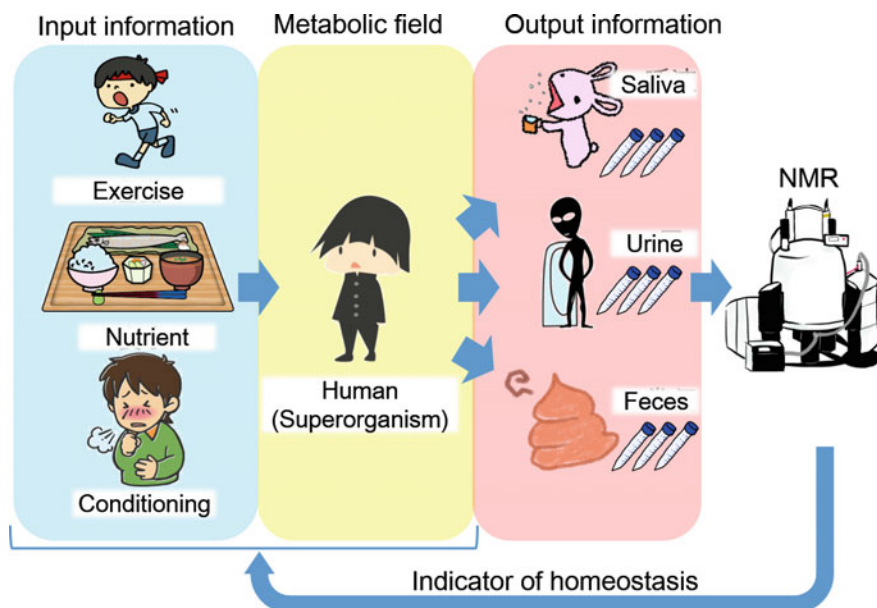


**Fig. 17.1** Conceptual figure to elucidate metabonomics as indicator of homeostatic response in the human superorganism from input to output information analyzed by NMR. Metabolic compositional changes in biological samples, such as saliva, urine, and feces, potentially contain abundant information regarding homeostatic state

in solvents, including deuterated water, methanol-d<sub>4</sub>, dimethyl sulfoxide-d<sub>6</sub>, and chloroform-d<sub>1</sub> (Fig. 17.2) [64]. Nonpolar metabolites, polymers, and extraction residues can be evaluated by solid-state NMR, as described in Sect. 17.3.

Hence, stable isotopic labeling, especially with <sup>13</sup>C, tremendously enhances NMR sensitivity and versatility in both solution [65, 66] and solid-state NMR of polysaccharides [67, 68]. For plant polysaccharides, there are two different strategies for stable isotopic labeling with <sup>13</sup>C; one is via photosynthesis using <sup>13</sup>C-labeled carbon dioxide and the other via uptake <sup>13</sup>C-labeled organic compounds from roots (Fig. 17.3) [69]. A cautionary note regarding the latter strategy is that <sup>13</sup>C-enrichments are concurrently decreased by photosynthetic <sup>12</sup>CO<sub>2</sub> incorporation. Also, note that there are biases in incorporations of <sup>13</sup>C (and <sup>12</sup>C) due to different metabolic activities. Metabolic flux analyses have indicated that nitrogen-rich amino acids, such as arginine and asparagine, are major metabolites synthesized in root and translocated to other tissues [70, 71].

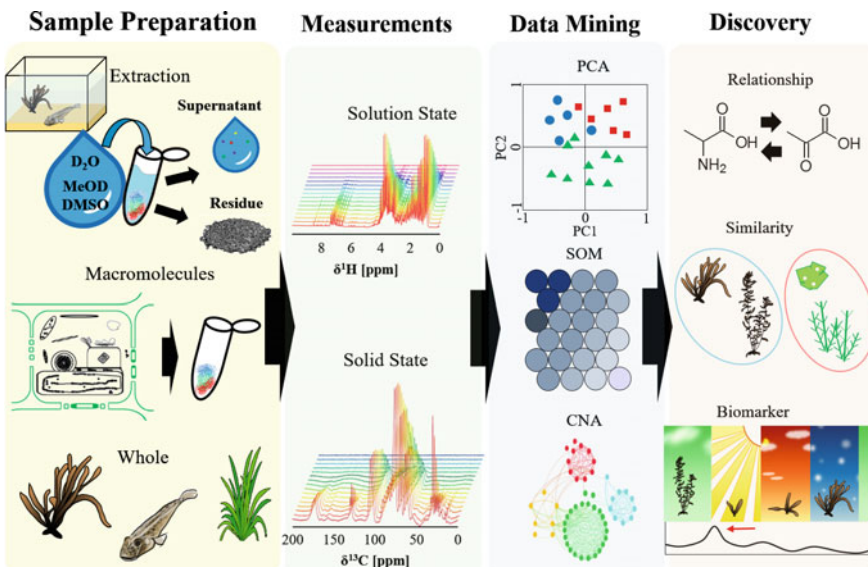


**Fig. 17.2** Scheme of NMR-based profiling approach for molecular complexity. Small (or macro) molecular mixtures are directly subjected to several NMR experiments without any chromatographic separation. The obtained crowded signals are digitized (occasionally binned) into numerical tabulation, and then, several data science approaches are applied, including principal component analysis (PCA), self-organization mapping (SOM), and correlation network analysis (CNA). Such data science approaches can extract useful information, such as key factor signals divided into homeostatic changes

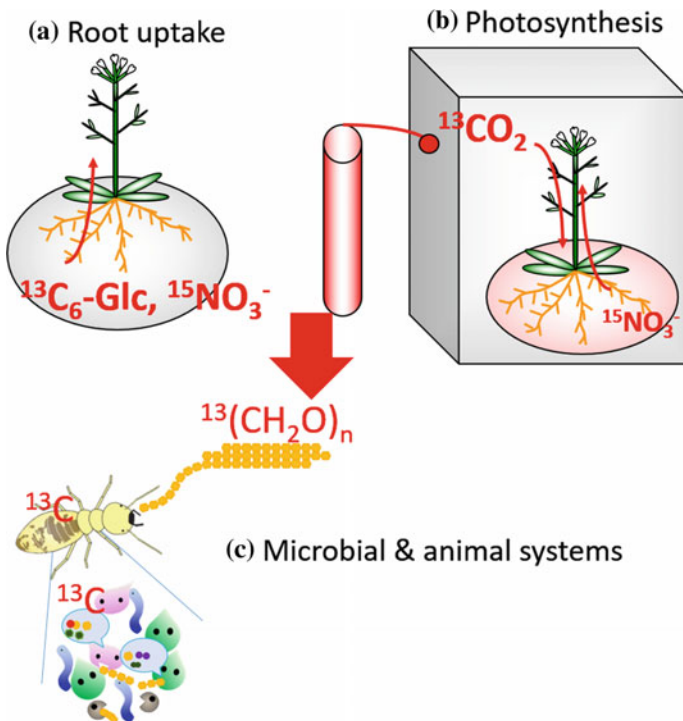


**Fig. 17.3** Schematic representation of stable isotopic labeling methods. **a** Both  $^{13}\text{C}$  and  $^{15}\text{N}$  nuclei are incorporated by plant root uptake when grown on agar plates containing  $^{13}\text{C}$  or  $^{15}\text{N}$ -labeled compounds. **b** Carbon nuclei are incorporated from  $^{13}\text{CO}_2$  through photosynthesis while  $^{15}\text{N}$  nuclei come from root incorporation. **c** Once  $^{13}\text{C}$ -feeds, such as  $^{13}\text{C}$ -cellulose, are prepared, animal and symbiotic microbiota can also be labeled in feeding experiments

### 17.2.3 NMR Measurements and Data Processing

#### 17.2.3.1 Useful Pulse Sequences

One-dimensional (1D) solution NMR is often used for metabolic analysis. However, mixture analysis using traditional 1D NMR spectra is difficult as signals overlap because of signal splitting by spin coupling. 2D  $J$ -resolved spectroscopy is used to determine spin–spin coupling constants that can then be used for structural analysis [72]. Multidimensional NMR is used to analyze correlation signals between homo- and heteronuclear experiments to identify metabolites. Heteronuclear single quantum coherence (HSQC) is a commonly used method in which metabolites can be identified by comparison with a chemical shift database and measured HSQC spectra. To increase identification accuracy, correlation spectroscopy (COSY), totally correlated spectroscopy (TOCSY), and single quantum–double quantum correlation spectroscopy (SQ-DQ) are used to confirm

correlation signals with adjacent atoms. Using HSQC-TOCSY and 3D HCCH-COSY together, adjacent correlation signals of annotated metabolites on HSQC spectra are easily confirmed [73].

### 17.2.3.2 Databases and Tools for NMR Analysis

Metabolite identification is one of the most important problems in metabolomics. Standard spectra and chemical shift databases typically are used to assign and annotate metabolic mixtures. Many chemical shift databases are available on the Internet, and using these services is simple and convenient. The Human Metabolome Database (HMDB) [74], Biological Magnetic Resonance Bank (BMRB) [75], and Madison Metabolomics Consortium Database (MMCD) [76] are commonly used chemical shift databases for metabolomics. Our laboratory developed the SpinAssign program, which can annotate metabolites in D<sub>2</sub>O and MeOD buffer using peak lists of <sup>1</sup>H–<sup>13</sup>C HSQC [77]. The *p* value has been adopted as a mathematical indicator for annotation evaluation (Fig. 17.4). A metabolomics database for NMR analysis (TOCCATA) has been recently developed [78]. In this database, highly reliable annotation is possible by database searching using TOCSY peaks for metabolites in a mixture. The Birmingham Metabolite Library (BML) contains <sup>1</sup>H and 2D *J*-resolved spectral data of metabolites, which can be used to annotate 2D *J*-resolved spectra of metabolic mixtures [79]. SpinCouple is an annotation tool for 2D *J*-resolved spectra of metabolic mixtures [37], in which the user can locate candidate compounds by entering <sup>1</sup>H chemical shifts, spin–spin coupling constants, and intensity values (Fig. 17.5). ECOMICS is a web tool for trans-omics research on environmental and metabolic systems together [80, 81]. Bm-Char in ECOMICS characterizes chemical structures from chemical shifts of biomass samples. FoodPro is a database and tool for evaluating the taste of food and predicting food taste based on similarities in food spectra measured by benchtop NMR [82].

### 17.2.3.3 Signal Assignments and Structure Elucidation

The evaluation of physical properties of compounds using theoretical values from quantum chemical calculations has been a topic of computer science research in recent years [83]. Theoretical values of NMR chemical shifts, spin coupling constants, and relationships between molecular structure and electronic states can be determined by solving equations, such as the Schrödinger equation, or by approximation using information on behaviors of atoms and electrons. Density functional theory (DFT) is used as a method through which the calculation time and accuracy are guaranteed to some extent; other calculation methods, basis sets, and solvents can be selected [84, 85].

Improvements in the accuracy of assigning NMR spectra of metabolic mixtures using theoretical chemical shifts have been recently reported. Misawa et al. have

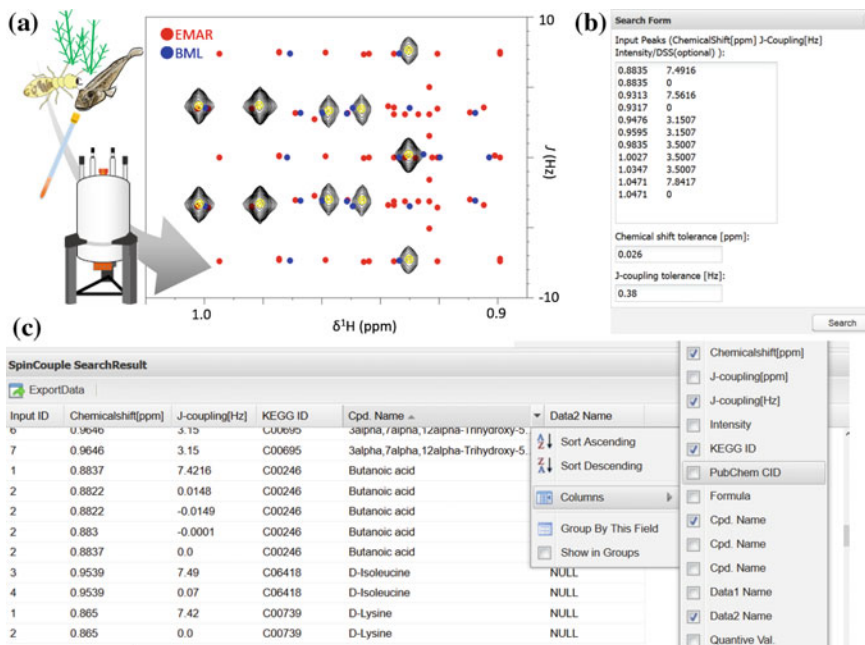


**Fig. 17.4** Schematic showing SpinCouple web tool. **a** An example of a biological extract's 2D  $J$ -resolved spectrum (black contour, methyl-expanded region) overlaid with BML (blue) and SpinCouple (red) database peaks. Examples of a query form **(b)** and results for the query **(c)** using SpinCouple (query peaks are highlighted in yellow on the methyl-expanded region of the 2D  $J$ -resolved spectrum). Reproduced from Ref. [48] with permission from the American Chemical Society

proposed a new annotation method using SENSI and quantum chemical calculations [86]. Komatsu et al. have assigned small biological molecules using 3D NMR and quantum chemical calculations [30]. In this study, correlation signals of methanol-soluble fractions in  $^{13}\text{C}$ -labeled land plants were detected using 3D-(H) CCH-TOCSY and  $^{13}\text{C}$ - $^{13}\text{C}$ -COSY (Fig. 17.6). Ito et al. have designed a new assignment method for NMR signals of metabolites using a fragment assembly approach and quantum chemical calculations [87]. In this study, metabolite structures are estimated by automatic chain assignments and fragment assembly (Fig. 17.7), and these structures are then evaluated by quantum chemical calculations and assigned. Note that careful setting of initial conformation to be made due for conformational dependence feature of theoretical calculation [88]. But anyhow, these results suggest that quantum chemical calculations can be used to assign NMR signals of biological metabolic mixtures.

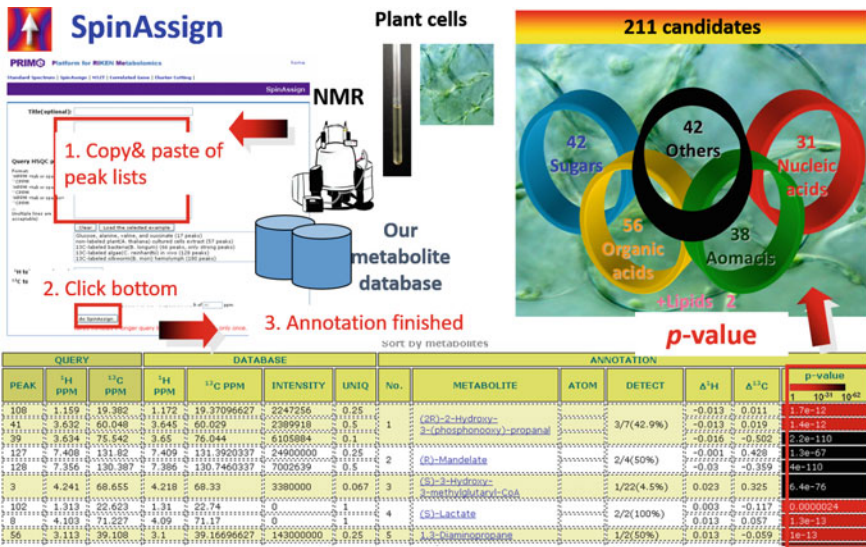


**Fig. 17.5** Schematic showing SpinAssign web tool. Peak picked  $^1\text{H}/^{13}\text{C}$  chemical shifts from biological extracts were input, then click bottom on the web, and finally annotation finished by searching the nearest candidate metabolites from our database. SpinAssign lists these candidate metabolites with precision indicated by calculated *p* values

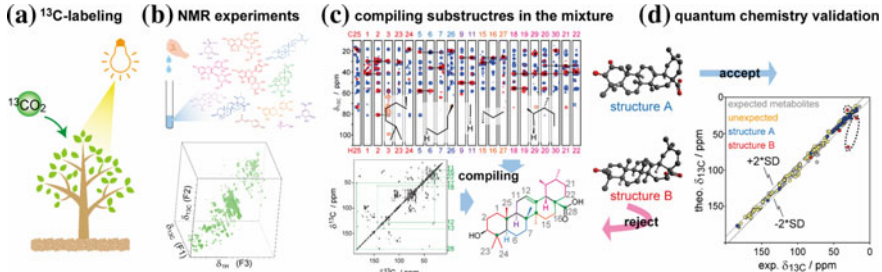


**Fig. 17.6** Assignments of secondary metabolite mixtures by 3D NMR and verification using quantum chemistry calculation. An ericaceous plant, *Rhododendron japonicum*, was cultivated in a chamber containing  $^{13}\text{C}$ -labeled carbon dioxide (a). Several 2D and 3D NMR experiments [(H) CCH-TOCSY, (H)CCH-COSY,  $^{13}\text{C}$ - $^{13}\text{C}$  TOCSY, and  $^{13}\text{C}$ - $^{13}\text{C}$  COSY] are conducted using MeOD extract (b). During this step, the 3D (H)CCH-TOCSY and (H)CCH-COSY spectra are useful for compiling substructures by  $^1\text{H}$  magnetization transfer through quaternary carbons (c). As a result, seven unexpected metabolites, including five terpenoids and two flavonoids, are elucidated as candidate metabolites and verified by the DFT method after conformational distribution analysis by molecular mechanics (d)

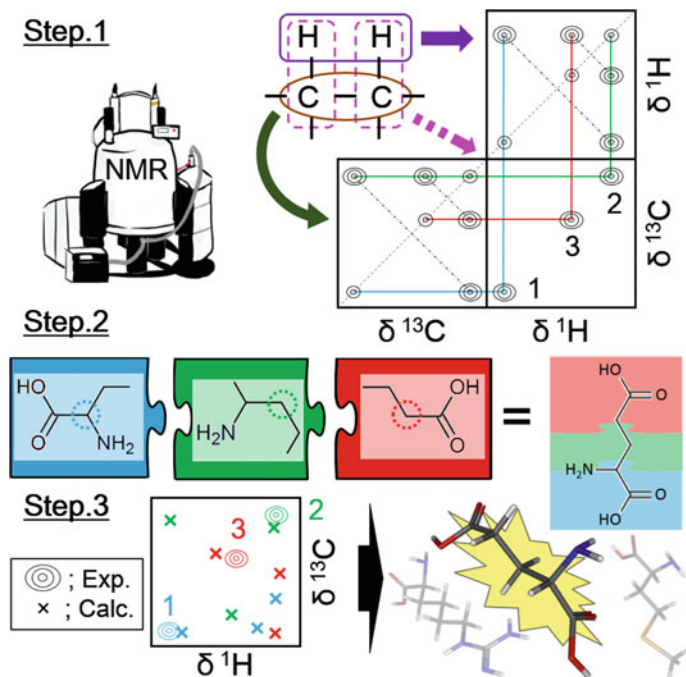


**Fig. 17.7** A strategy for assigning metabolites by fragment assembly and quantum chemical calculations. Correlation signals are detected with high sensitivity using labeled samples. Automatic chain assignments estimate the chemical backbone of metabolic mixtures (Step 1). Partial structures of each peak are estimated by most common substructure analysis, and the entire structure can be estimated by connecting fragments (Step 2). Theoretical NMR properties of the estimated structure are calculated using the QM method. Assignment allows comparison between experimental and theoretical chemical shifts (Step 3)

#### 17.2.3.4 Spectral Pretreatment for Data Science

As NMR spectra obtained experimentally might include useful and valuable information, analyses, such as multivariate statistical analysis and machine learning, should be incorporated into the analytical flow of metabolomics studies (Fig. 17.2). To enable appropriate analytical flow, data pretreatment and preprocessing, such as standardization of datasets, are very important.

Peak alignment, a computational approach for accurate peak alignments, is an important data pretreatment because NMR chemical shifts are altered by various factors, including pH, temperature, physicochemical interactions, background matrix, and ion intensity. The most commonly used method is spectral bucketing and binning. Binning denotes splitting a small bucket containing a range of variations for a specific peak shift, and the intensity of each bucket is calculated as the area under the curve. The drawback of the binning method is a considerable reduction in spectral resolution [89].

Scaling and normalization are also very important in data pretreatment and preprocessing. Extreme differences in scales between multiple parameters can obscure the data, leading to inadequate interpretation. Typically, an internal standard, such as 4,4-dimethyl-4-silapentane-1-sulfonic acid or trimethylsilane, is used for normalization between datasets. Z-scoring is an alternative method that uses a standard normal distribution with the average set as 0 and standard deviation as 1 [90]. However, the problem with this method for analyzing an entire spectrum is that noise is also normalized. Probabilistic quotient normalization (PQN) is a method that is not susceptible to outliers because a median of numerous estimated values is used [91].

### 17.2.3.5 Practical Aspects of Data Science

In metabolomic studies, the inclusion of multivariate analysis (also known as chemometrics, pattern recognition, and data mining) is absolutely imperative. Methods for multivariate analysis fall roughly into two categories: unsupervised (e.g., principle component analysis, PCA) and supervised (e.g., partial least squares, PLS). PCA is the most widely used method in the field of metabolomics. Typically, PCA is used for data overview and trend (or cluster) identification and is also used for dimension reductions in dataset preprocessing. Other representative, unsupervised, multivariate analyses include hierachal clustering (HCA) [92], *K*-means clustering [93], and self-organizing maps (SOM) [94].

Correlation-based analysis (identifying a linear relationship between two variables) is also widely used in metabolomic studies [95]. Correlation coefficients are usually visualized as heat map and network diagrams. Market basket analysis is a statistical approach for identifying co-occurrences of variables in datasets; this approach has recently been applied to metabolomic studies [96].

PLS is the most commonly used supervised, multivariate analysis in metabolomic studies. PLS and its related analyses are the most common classification and regression tools for analyzing metabolomic data. PLS-related analyses are powerful data-mining methods because they enable analysis of large, highly complex datasets with collinearity and noise. However, alternative “machine-learning” (ML) methods that are suitable for use in the field of metabolomics have been recently introduced [97].

## 17.2.4 Applications to Plant, Animal, and Microbial Systems

### 17.2.4.1 Application to Plant Systems

A variety of plants and algae are present in natural environments. These resources serve as primary producers and maintain ecosystems. Therefore, studies of compounds in plants and algae are expected to be useful not only in agricultural but in

other fields as well [16, 98]. Metabolic profiling using  $^1\text{H}$  NMR concurrently tracks changes in metabolites in plants and algae [99, 100]. Plants and algae are autotrophic organisms that cannot move on their own volition. Numerous organisms (e.g., grains, fruits, and seaweed) have been studied by this method using a variety of parts (e.g., roots, leaves, and stems) for analysis [101]. Characterization of differences based on geographical origin and plant varieties is possible using multivariable analysis, such as PCA. Such techniques can detect differences in the content and presence of low-molecular-weight molecules, such as amino acids, organic acids, and sugars. The evaluation of both low-molecular-weight molecules and polymers is possible using dimethylsulfoxide (DMSO) as the solvent [15].

#### 17.2.4.2 Application to Animal Systems

Plant-biomass eaters, such as termites, are among the most attractive living organisms for this kind of examination because of their considerable global impact on decay of dead plant materials. The primary constituent of plant biomass is cellulose, consisting of glucose linked by  $\beta$ -1,4-glucosidic bonds. Despite the fact that most animals cannot use this polysaccharide, termites are thought to be capable of hydrolyzing 74–99% of cellulose in woody materials. Therefore, this efficient cellulolytic system in termites has attracted many researchers and has been extensively studied in recent decades. An emerging technique for clarifying complex metabolic processes, such as cellulose digestion, involves the generation of comprehensive metabolite profiles (Fig. 17.8). We have recently demonstrated the utility of this technique in animal systems by feeding  $^{13}\text{C}$ -glucose and amino acids to *Bombyx mori* and monitoring time-dependent metabolic dynamics during insect morphogenesis [73].

In the context of symbiotic interactions, we have also successfully demonstrated the use of  $^{13}\text{C}$ -labeled compounds to illuminate the critical role of acetate [44] and reuterin [55] production by resident gut bacteria in mice. Advantages of the use of  $^{13}\text{C}$ -labeling methodologies in combination with multidimensional NMR analyses include the separation of crowded signals from metabolite mixtures and the opportunity to perform quantitative, multivariate analyses of time series in acquired data at an atomic level.

The growth and activity of these beneficial microbial symbionts is enhanced by functional foods, such as fructo-oligosaccharide (FOS) and galacto-oligosaccharides in the human gastrointestinal tract [56]. Therefore, evaluation of the effects of functional food on dietary interactive modulations of the host and beneficial microbial symbionts is important for human health [102]. In the initial stage of validation, evaluations are usually performed using animal experiments, such as mouse and rat [103]. However, animal experiments are time-consuming and have ethical issues, and thus, a simple and rapid method *in vitro* and without animal experiments has been sought as a better means for evaluating the effects of functional foods [104].

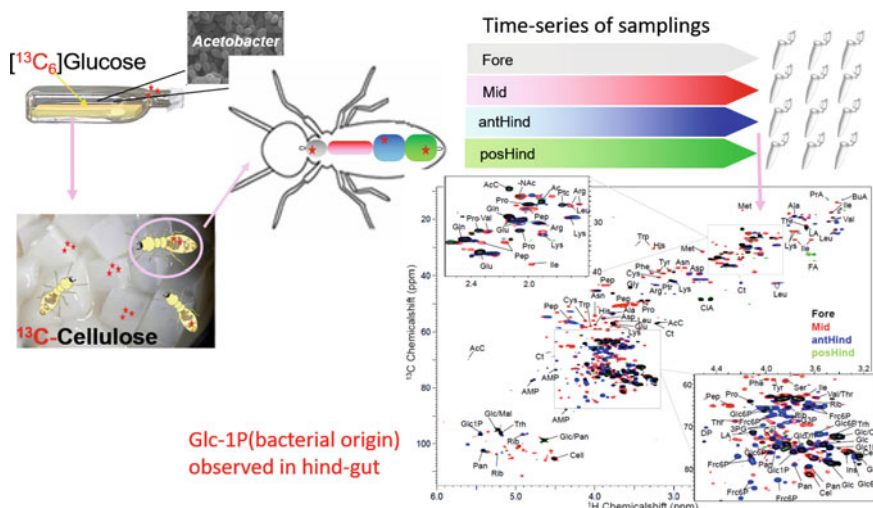


**Fig. 17.8** Schematic diagram of metabolic analysis of a  $^{13}\text{C}$ -cellulose-fed termite-symbiont system. From top to bottom: time series of samplings from a  $^{13}\text{C}$ -cellulose-fed termite-symbiont system; four types of digestive organ extracts are analyzed by  $^{13}\text{C}$ -HSQC

In contrast, an NMR-based metabolomics approach is widely used for investigating metabolic characterizations of animals and their intestinal symbiotic systems [105, 106]. Particularly in human studies, metabolic characterizations from non-invasive samples, such as urine, saliva, and feces, are well known to have a large quantity of vital and beneficial information regarding human health and disease.

We have described an advanced analytical approach for evaluating together the metabolic, mineral, and microbiota fluctuations of all fecal, urinary, and salivary samples from humans. These are then synchronously related with variations in dietary intakes under unlimited and uncontrolled diets using data-driven approaches [86, 96, 107].

#### 17.2.4.3 Application to Microbial Systems

Primordial microbial communities that perform anaerobic digestion are considered the most ancient metabolic communities. These communities became segregated from aerobic environments by the emergence of photosynthetic organisms that initially increased Earth's oxygen concentration. Many species in microbial communities of anaerobic environments, such as soil and aquatic bottom sediments, degrade biomass produced by photosynthetic organisms. Thus, anaerobic digestion remains essential to biogeochemical cycling of organic and inorganic matter. Among these, anaerobic microbial communities, which are responsible for digestion of plant saccharides into short chain fatty acids (SCFAs), have been

investigated in several systems, including the animal gut, waste management [68, 108], and soil from paddy fields [109].

Although  $^1\text{H}$ -NMR is easy to perform and versatile, its limited spectral resolution is insufficient to tackle the overlapping signals of saccharides. The introduction of  $^{13}\text{C}$ -nuclei to NMR analysis is a useful technological advance for the resolution of overlapping signals [110]. The advantages of  $^{13}\text{C}$ -labeling methods for NMR also include the characterization of compounds in complex components, determination of compound structures, and tracking of microbial metabolic pathways [111].

## 17.3 Biomass Profiling for Macromolecular Complexity

### 17.3.1 Basic Knowledge for Macromolecular Profiling

Plant biomass is the most abundant and important material in the terrestrial biosphere. Its major components are cellulose, hemicellulose, and lignin (Fig. 17.9). These components are all complex molecules and abundantly produced in plant cell walls. Cellulose is a linear condensation polymer that consists of  $\beta$ -1,4-linked D-glucose units with a degree of polymerization from 100 to 20,000. Hemicelluloses are branched, have molecular masses lower than cellulose, and mainly composed of glucose, mannose, galactose, xylose, and arabinose. Lignins are reticulated, cross-linked macromolecules composed of phenylpropanoid units, which include *p*-hydroxyphenyl, guaiacyl, and syringyl. These persistent substances have a highly formed, supramolecular structure that includes cellulose and hemicellulose cemented by lignin, called lignocellulose.

Comprehensive analysis of biological macromolecules performed without purification is the next frontier in the advancement of insights into living systems. Breakthrough technologies in basic biological research toward polysaccharide complexity can be produced using profiling approaches to biomass synthesis and degradation, as an intermediate-monitoring system. Innovation in “nontargeted” approaches for a wide range of biological systems in ecosystems is important for better biomass production and sustainability of such systems.

### 17.3.2 Experimental Aspects of Sample Preparation

As both solution and solid-state NMR methods have been developed for NMR analyses of polysaccharides, sample preparation procedures depend on which method is used (Fig. 17.10). In general, solution NMR possesses higher resolution than solid-state NMR but the former requires solubilization [11]. Solid-state NMR,

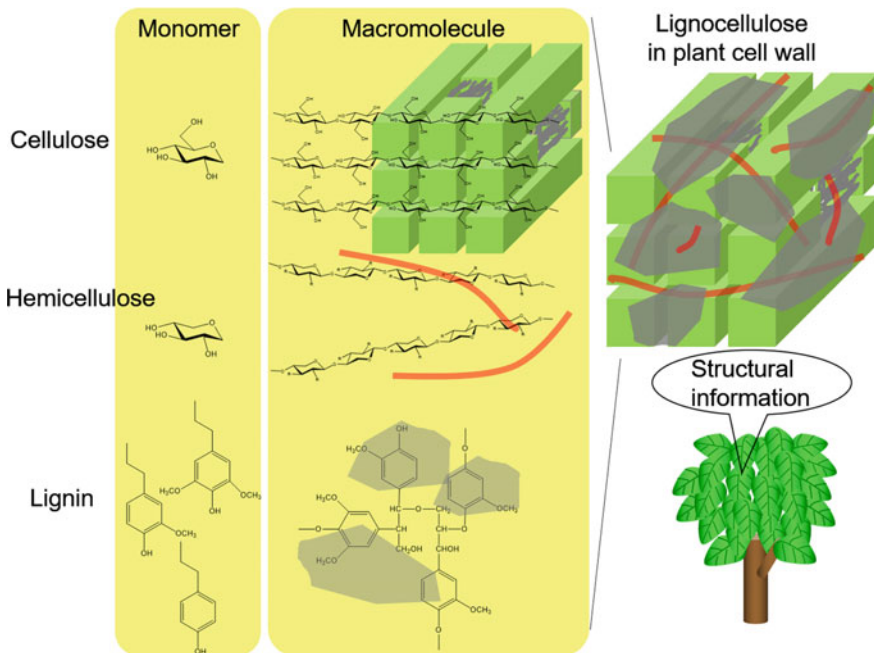


**Fig. 17.9** Diagram of lignocellulose structure. Lignocellulose of plant cell wall is composed of cellulose, hemicellulose, and lignin. Cellulose is composed of glucose units, hemicellulose mainly composed of xylose units, and lignin of phenolic units. Native cellulose has crystalline and amorphous regions. One of the main hemicelluloses is xylan, which is partially acetylated and partially substituted with sugar residues, such as arabinose, at the C2 and/or C3 positions. Lignin is a polymer based on syringyl, guaiacyl, and *p*-hydroxyphenyl moieties. Structural information of lignocellulose, namely at the supramolecular-level, is highly expected from biomass researchers during this half century

powerful for structure and dynamical analyses in native state polysaccharides, requires less sample preparation than solution state [112].

Some of the most common procedures for obtaining polysaccharide fractions are alcohol-insoluble residue (AIR)-based methods, in which ethanol solution, following methanol/chloroform solution are used to remove small molecules and lipids. First, dried plant material is ground to powder using a milling machine, and 70 or 80% ethanol solution (by vol) is added to remove polar metabolites. Then, starch is digested using  $\alpha$ -amylase, and proteins are digested using protease. As a result of these procedures, cell wall fractions are obtained.

As cell wall fractions barely dissolve into any organic solvent, grinding to a fine powder is essential for solubilization. Ball mill instruments are frequently used for cell wall solubilization.

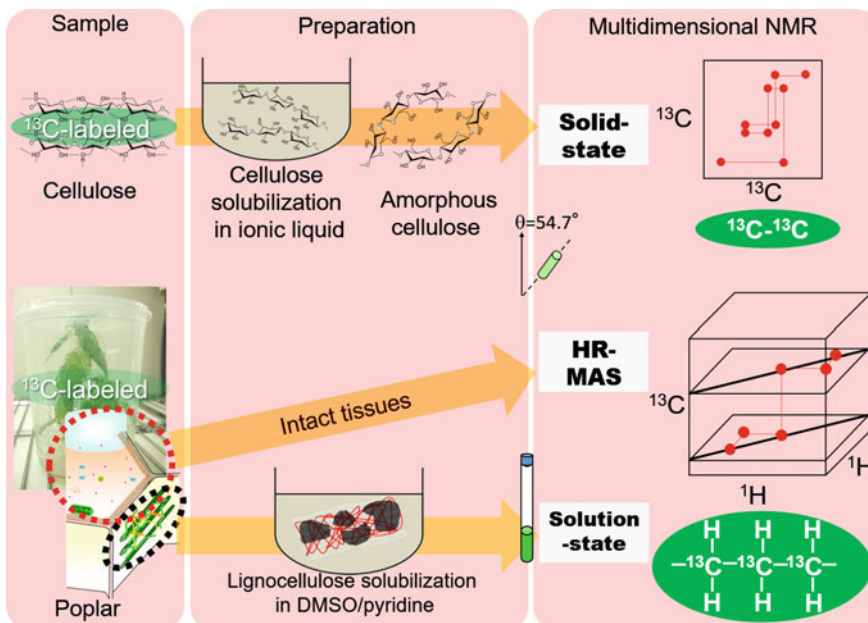


**Fig. 17.10** A combination of solubilization of lignocellulose and a multidimensional NMR technique has been applied for analyzing lignocellulose components. For NMR techniques,  $^{13}\text{C}$ -amorphous cellulose can be redissolved in ionic liquids (ILs). Alternatively, lignocellulose of  $^{13}\text{C}$ -poplar can be dissolved with DMSO/pyridine. Moreover, metabolites of intact tissues of  $^{13}\text{C}$ -poplar can be analyzed by high-resolution magic angle spinning (HR-MAS)

### 17.3.3 NMR Measurements and Data Processing

#### 17.3.3.1 Useful Pulse Sequences

Signals in  $^1\text{H}$  NMR spectra of polysaccharides, such as cell wall polysaccharides, in vascular plants are often broad-line shaped because of high sample viscosity. Thus,  $^1\text{H}$ - $^{13}\text{C}$  HSQC is used for cell wall composition analyses. Multidimensional NMR with  $^{13}\text{C}$ -labeled plants has provided a lot of detailed resonance assignments of plant cell wall, especially polysaccharides [113]. 3D HCCH-COSY experiments are powerful for resonance assignments of polysaccharides because crowded peaks from polysaccharides are separated into a 3D space (Fig. 17.11). Notably,  $^1\text{H}$ - $^{13}\text{C}$  HSQC-NOESY spectra provide intersugar correlations in polysaccharides that cannot be obtained with  $^1\text{H}$ - $^1\text{H}$  COSY,  $^1\text{H}$ - $^1\text{H}$  TOCSY,  $^1\text{H}$ - $^{13}\text{C}$  HSQC, or 3D HCCH-COSY spectra.

Solid-state NMR detects nonpolar polymers, and many pulse sequences for solid-state NMR have been developed. However, the application of multidimensional NMR pulse sequences has been delayed because anisotropic effects of dipole interactions are strong, and measuring the  $^1\text{H}$  detection type is very difficult. To

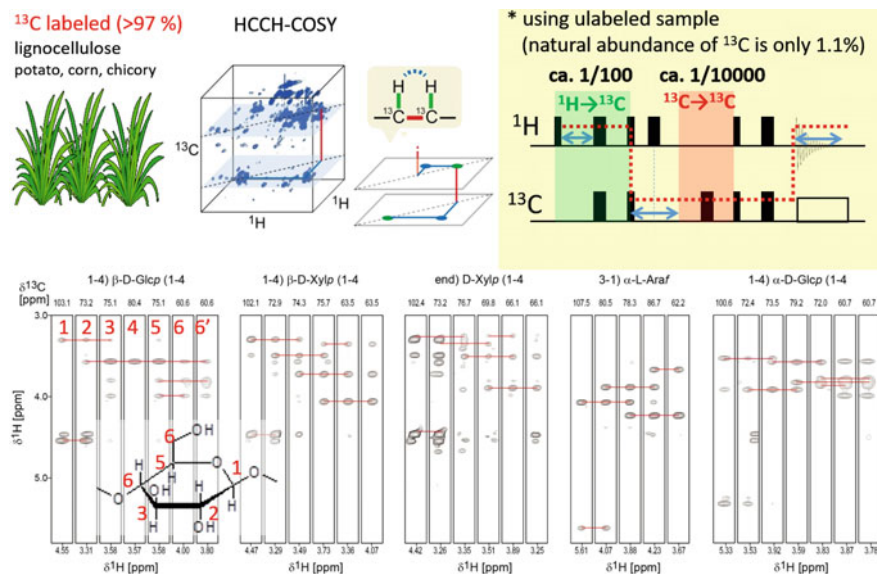


**Fig. 17.11** Multicomponent solution 3D HCCH-COSY approach for chemical assignments of <sup>13</sup>C-labeled lignocellulose. Because of low natural <sup>13</sup>C abundance (1.1%), plant samples must be enriched by <sup>13</sup>C stable isotopic labeling. Then, more NMR signals in the crowded sugar region can be assigned because of the high resolution provided by the combination of <sup>13</sup>C-labeling and 3D NMR techniques

overcome these problems, 1D cross-polarization magic angle spinning (CP-MAS) uses a greater number of scans to detect low-sensitivity <sup>13</sup>C, and 1D nonquaternary suppression (NQS)-MAS emphasizes quaternary carbons [114, 115].

There are several relaxation time constants, including longitudinal relaxation of <sup>1</sup>H (<sup>1</sup>H  $T_1$ ) and <sup>13</sup>C (<sup>13</sup>C  $T_1$ ), rotating-frame <sup>1</sup>H (<sup>1</sup>H  $T_{1\rho}$ ), transverse relation of <sup>1</sup>H (<sup>1</sup>H  $T_2$ ) and <sup>13</sup>C (<sup>13</sup>C  $T_2$ ), such that sensitive frequencies of molecular motion in each relaxation process are different. Note that relaxation time constants in <sup>1</sup>H represent types of molecular motion within domains caused by rapid <sup>1</sup>H-<sup>1</sup>H spin diffusion. In contrast, <sup>13</sup>C relaxation time constants represent local molecular motions of each nucleus.

In general, <sup>1</sup>H  $T_1$ , <sup>13</sup>C  $T_1$  and <sup>1</sup>H  $T_{1\rho}$  are longer, further <sup>1</sup>H  $T_2$  and <sup>13</sup>C  $T_2$  are shorter in cellulose than in matrix polysaccharides in hydrated plant cell walls. Hong and her coworkers have investigated differences in cell wall physicochemical properties via <sup>13</sup>C  $T_1$  and <sup>1</sup>H local  $T_{1\rho}$  (without spin diffusion using <sup>1</sup>H-<sup>1</sup>H homonuclear decoupling) using various *Arabidopsis* primary cell walls, including wild-type, chemically pectin-depleted, and homozygous mutants [116, 117].

Different relaxation times between each component can be used as spectral filtering techniques. Komatsu and Kikuchi have developed <sup>13</sup>C-<sup>13</sup>C correlation spectroscopy coupled with spectral filtering techniques to analyze matrix polysaccharides by removing signals from cellulose [118]. Dipolar dephasing is used as a

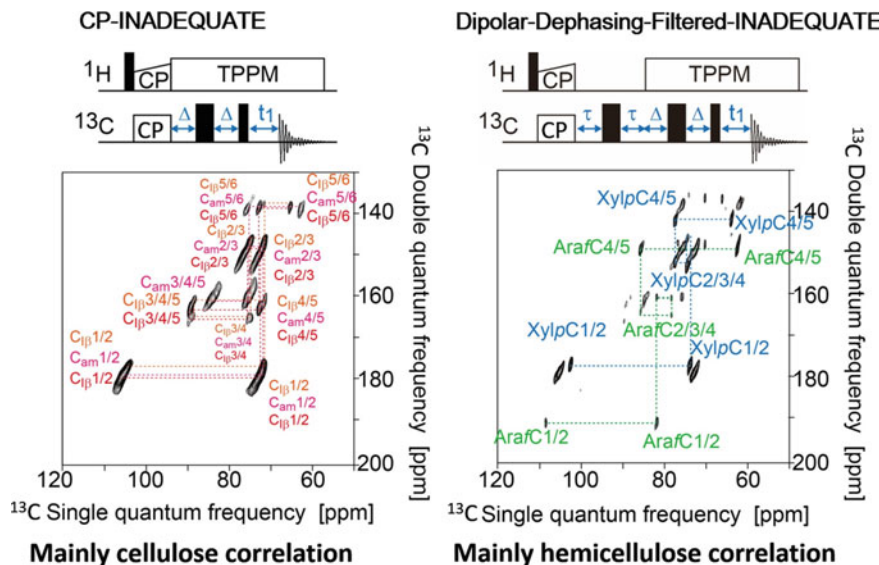


**Fig. 17.12** DDF-INADEQUATE pulse sequence successively detects and assigns hemicellulosic signals in lignocellulose (*Top*). Comparison of the pulse sequence of the CP-INADEQUATE and DDF-INADEQUATE experiments (*Bottom*). The CP-INADEQUATE spectrum mainly produces cellulose signals, whereas the DDF-INADEQUATE spectra, with a dephasing time of  $1/2\nu_{\text{MAS}}$ , completely dephases cellulose signals during this period. Each of the structural components is highlighted with different colors and abbreviations: crystalline cellulose I $\beta$  (red:  $\text{C}_{\text{I}\beta}$ ), Amorphous cellulose (pink:  $\text{C}_{\text{am}}$ ), Xylopyranose (blue:  $\text{Xylp}$ ), Arabofuranoside (green:  $\text{Araf}$ ), respectively

spectral filter in which coherence is dephased by  $^1\text{H}$ - $^{13}\text{C}$  dipolar interactions, and the amplitude strongly depends on molecular motion (Fig. 17.12).

Another option is to completely label the sample with  $^{13}\text{C}$ , allowing measurement at an abundance of 100 times the  $^1\text{H}$ - $^{13}\text{C}$  coupling detection rate and 10,000 times the  $^{13}\text{C}$ - $^{13}\text{C}$  coupling detection rate.  $^1\text{H}$ - $^{13}\text{C}$  coupling is used to evaluate crystalline polysaccharides, lipids, and low-molecular-weight molecules using double CP, solid-state HSQC, and high resolution (HR)-MAS (Fig. 17.13). Using  $^{13}\text{C}$ - $^{13}\text{C}$  coupling, the correlation signal between adjacent carbons is detected using dipolar-assisted rotational resonance (DARR), incredible natural abundance double quantum transfer experiment (INADEQUATE), and 3D  $^{13}\text{C}$ - $^{13}\text{C}$ - $^{13}\text{C}$  (CCC)-MAS [67].

### Peak Separation for Broad Macromolecular Spectra

Overlapping peaks in NMR spectra are one of the biggest problems encountered in the analysis of metabolic mixtures. Solid-state NMR typically has very low resolution, and thus, a single peak is more likely to contain multiple peaks derived from several chemical components. Peak separation techniques can be applied to address

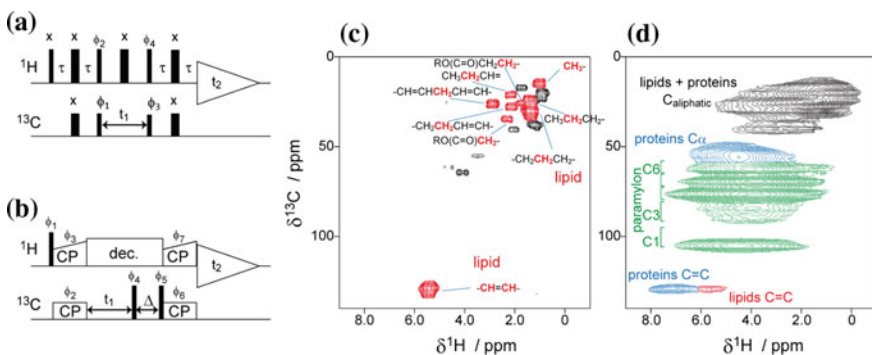


**Fig. 17.13**  $^1\text{H}$ -detected solid-state NMR spectra of *E. gracilis* cultured in high ammonium medium (31 mM). Examples of ssHSQC spectroscopy: **a** pulse sequence and **c** spectrum, and double CP, **b** pulse sequence and **d** spectrum. In pulse sequence diagrams, sharper and broader filled boxes represent  $90^\circ$  and  $180^\circ$  hard pulses, respectively.  $^{13}\text{C}$  resonance frequency, MAS frequency, and rotor diameter are 100 MHz, 60 kHz, and 1.3 mm, respectively. Reproduced from Ref. [101] with permission from the American Chemical Society

this problem. Multivariate curve resolution-alternating least squares (MCR-ALS) is a peak separation method based on optimization by iterative least squares, for calculating components [119]. Nonnegative matrix factorization (NMF) is an algorithm used for the analysis of matrices consisting of zero and/or positive values. This method decomposes multivariate and spectral data into a smaller number of basic functions, and extracts local features. NMF can be used for peak separations in solution- and solid-state NMR spectra [120].

### 17.3.4 Applications to Material, Biological, and Geochemical Systems

#### 17.3.4.1 Application to Cellulosic Material Systems

Cellulose is the most common chemical polymer on land and is an alternative energy and chemical resource with the greatest potential on Earth. PCA has been used to extract components from solid-state NMR spectra of bacterial cellulose. Polymers, such as cellulose, have several domain structures, and their structure and dynamics are reflected in the variety of solid-state spectra derived from different parameters [121].

Further statistical approaches have been used to characterize the heterogeneous structures of bacterial cellulose samples pretreated with four kinds of ionic liquids (ILs). Structural heterogeneity of these samples is measured by Fourier transform

infrared spectroscopy, as well as solid-state NMR methods, such as cross-polarization magic angle spinning and dipolar-assisted rotational resonance. The obtained data matrices are then evaluated by PCA. The measured one-dimensional data clearly reveals modification of crystalline cellulose; in addition, the statistical approach shows subtle structural changes that occur upon pretreatment with different ILs [122].

While crystalline cellulose has been investigated intensively, the structure of amorphous cellulose, even its local structures, has not been clarified. We thus prepared  $^{13}\text{C}$ -labeled amorphous cellulose and fully assigned  $^{13}\text{C}$  NMR chemical shifts by 2D  $^{13}\text{C}$ – $^{13}\text{C}$  correlation spectroscopy obtained both in IL-solution and in regenerated solid-states. On the basis of the assigned experimental  $^{13}\text{C}$  NMR chemical shifts, a candidate is proposed for local structures of amorphous cellulose via molecular dynamics and quantum chemistry computer simulations, which exhibit a twisted structure exposing more hydrophilic surfaces than extended crystalline cellulose [123].

Next, anaerobic digestion of biomacromolecules in various microbial ecosystems is influenced by variations in types, qualities, and quantities of chemical components. We have described a characterization strategy using NMR spectroscopy for targeting the input solid-insoluble biomass, catabolized soluble metabolites, and product gases.  $^{13}\text{C}$ -labeled cellulose produced by *Gluconacetobacter xylinus* is added as a substrate to stirred tank reactors and gradually degraded for 120 h. Time-course variations in structural heterogeneity of cellulose catabolism are determined using solid-state NMR, and soluble metabolites produced by cellulose degradation are monitored using solution NMR [68, 108].

#### 17.3.4.2 Application to Biological Systems

Plant biomass is one of the most abundant biomaterials in nature, and they predominantly consist of polysaccharides. Vascular plants have complex cell wall systems, including primary and secondary cell walls, which provide plants with mechanical strength, resistance to environmental stress, and a high level of tolerance toward microbial degradation. We have shown that cellulosic supramolecular structure of rice straw analyzed by  $^{13}\text{C}$ – $^1\text{H}$  HETCOR is altered using physical milling processes, and as a result, biomass degradation by paddy soil microbiota is affected [109].

Next, solution 2D  $^1\text{H}$ – $^{13}\text{C}$  NMR has been applied to DMSO-solubilized 13 cultivars of rice straw before and after dilute acid pretreatment to clarify general changes in the lignin and polysaccharide components. Most (15 of 16) peak intensities related to lignin aromatic regions, such as *p*-coumarate, guaiacyl, syringyl, and *p*-hydroxyphenyl, cinnamyl alcohol and methoxyl, increased or remained unchanged after pretreatment. In contrast, most (11 of 13) peak intensities related to lignin aliphatic linkages or ferulate bridge decreased [124].

A precipitate with high lignin content has been recovered from the supernatant of the liquid fraction of hydrothermally pretreated rice straw. The fates of lignin and polysaccharide components, during membrane separation and enzymatic hydrolysis, are evaluated in detail by 2D NMR and compositional analysis [125].

Furthermore, rice straw has been mechanically milled using a process consuming 1.9 MJ/kg-biomass, and 10 g/L of unmilled or milled rice straw used as the carbon source for methane fermentation in a digester containing carbon fiber textile as the supporting material. Solution NMR shows that lignin aromatic components, such as *p*-hydroxyphenyl (H), guaiacyl (G), and syringyl (S), are primarily retained, and the major lignin interunit structures, such as the  $\beta$ -O-4-H/G unit, are absent. This combinational process will aid in the complete utilization of rice straw [126].

Sorghum bagasse was fractionated by organosolv pretreatment using various types of solvents. 2D NMR has revealed that the black liquor fraction contains lignin aromatic regions, such as guaiacyl, syringyl, *p*-hydroxyphenyl, *p*-coumarate, and ferulate. Lignin in the black liquor lacked the aliphatic region,  $\beta$ -O-4 unit. Addition of 1-butanol or 1-pentanol is effective for removing *p*-coumarate, syringyl, and some guaiacyl from raw sorghum bagasse [127].

In contrast to these biomass degradation studies, we have focused that bacteria-derived enzymes can modify specific lignin substructures, that are potential targets for engineering plants with improved biomass processability. The Gram-negative bacterium *Sphingobium* sp. SYK-6 possesses a  $\text{Co}$ -dehydrogenase (LigD) enzyme that has been shown to oxidize the  $\alpha$ -hydroxy functionalities in  $\beta$ -O-4-linked dimers into  $\alpha$ -keto analogs that are more chemically labile. The possibility has been explored of using LigD for biosynthetically engineering lignin by expressing the codon-optimized ligD gene in *Arabidopsis thaliana*. 2D NMR analysis reveals a 2.1- to 2.8-fold increased concentration of G-type  $\alpha$ -keto- $\beta$ -O-4 linkages in cellulolytic enzyme lignins isolated from stem cell walls of LigD transgenic plants, indicating that the transformation is capable of altering lignin structure in the desired manner [128].

When look at the hydrosphere, there are plenty of polysaccharides serving as structural and storage materials in algae. Date et al. [92] have developed chemical profiling methods for macroalgae, using four *Chlorophyceae* (green algae), three red algae, and nine brown algae, by solution NMR as well as FT-IR. Solution NMR using a DMSO/pyridine solvent system identified neutral polysaccharides, such as agar and laminarin, in *Rhodophyceae* and *Phaeophyceae*, respectively. Wei et al. [120] have applied integrated analysis toward 107 algal samples using multi-instrumental data, including solid-state NMR, solution NMR, FT-IR, and ICP-OES, to characterize the samples based on their chemical diversity. Correlation analysis using multi-instrumental data provides chemotaxonomic clusters based on their chemical diversity, and these clusters agree with genetic linkages. Integrated analysis also indicates the relationships between alginate and ions, including iron, aluminium, and titan (Fig. 17.14).

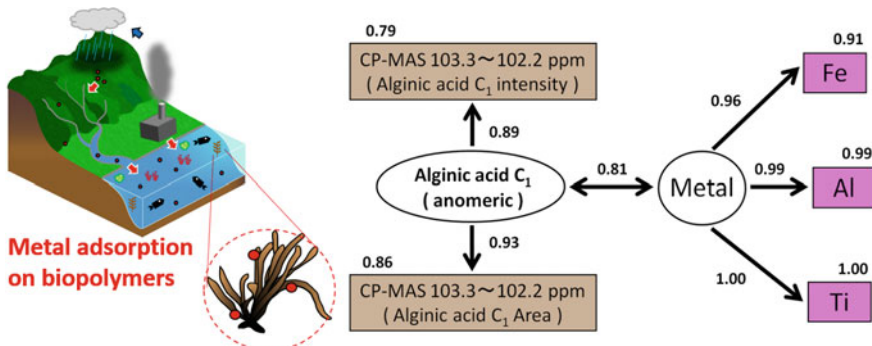


**Fig. 17.14** Integrated analysis of natural algae sample data using NMR and other instruments. The anomeric region ( $C_1$ ) of alginic acid in CP-MAS spectra was estimated by the peak separation method (MCR-ALS). The relationship between alginic acid and three metals was suggested by correlation network analysis (see in the text) and confirmed by structural equation modeling (SEM). Squares indicate observed variables, and circles indicate latent variables. The values on single-ended arrows indicate pass coefficients, and double-ended arrows indicate correlations. The values on observed variables are coefficient of determination ( $R^2$ ). Relationships of two latent variables were verified by confirmatory factor analysis. Reproduced from Ref. [71] with permission from the American Chemical Society

#### 17.3.4.3 Application to Geochemical Samples

A wide variety of microorganisms, including archaea, bacteria, fungi, plankton, and protists, are present everywhere on the globe (biosphere), such as in soil, sediment, underground, wetlands, rivers, and oceans. In soil environments, both solution and solid-state NMR measurements have been used in a study to characterize cellulosic supramolecular structures in rice straw and their degradation profiles as produced by a microbial community in a paddy field [109]. NMR-based metabolomics studies can also analyze the decomposition process of biochar [129] and fishes [94] in soil microbial communities.

The chemical components and structures of soil organic matter have been evaluated in numerous studies using NMR-based approaches. For instance, solution NMR has revealed that biomacromolecules derived from microorganisms and plants are major components in soil and aqueous humic substances [7, 130]. With the use of alkaline fractionation following a DMSO-solubilization protocol for humic substances, we have also revealed that eutrophied sediments from metropolitan sites exhibit high amounts of peptides as well as inorganic nitrogen (Fig. 17.15) [131]. Solid-state NMR is also a major tool used for the characterization of organic matter, such that a variety of solid-state NMR spectroscopies, including DP- and CP-MAS, DP- and CP-TOSS, and  $^1\text{H}$ - $^{13}\text{C}$  HETCOR, have been used to characterize chemical structures and composition of organic matter [21, 23, 132].

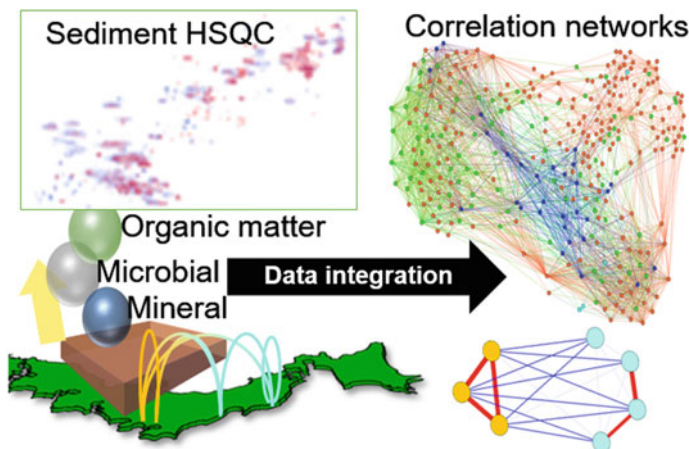


**Fig. 17.15** Integrative analysis of organic, inorganic, and microbial profiles in an estuarine environment. The organic matter profiles of geographically and seasonally varied sediments computed from HSQC spectra. Relationships between individual profiles are based on correlation analysis of integrated data obtained from heterogeneous measurements and visualized in a network diagram. Reproduced from Ref. [115] with permission from the American Chemical Society

## 17.4 Future Perspectives

In general, several analytical approaches tend to focus on a specific class of compounds or on a single compound important for evaluating foodstuff quality, nutritional properties, and sensory characteristics. This type of analysis, also called “target analysis,” usually requires specific extraction methods and sample pre-treatment. In contrast, NMR spectroscopy has earned an important role among the various techniques used to analyze molecularly complex samples owing to its high-throughput nature and high analytical precision. Many applications have been reported in the literature that show the potential of NMR-based approaches to investigating geographical origins, quality control, and processing of agricultural and fishery products. A further advantage of NMR-based approaches is the ease of sample preparation compared with that required for other analytical methods, which might involve derivatization and/or column chromatography. Therefore, if NMR users demonstrate the technology’s practicality for characterizing homeostasis and cost-effective instruments, such as benchtop NMR instruments, become available [133], NMR could be used on-site to evaluate ecosystem features almost directly.

## References

1. Lindon, J.C., Holmes, E., Nicholson, J.K.: Pattern recognition methods and applications in biomedical magnetic resonance. *Prog. Nucl. Magn. Reson. Spectrosc.* **39**, 1–40 (2001)

2. Nicholson, J.K., Lindon, J.C.: Systems biology: metabonomics. *Nature* **455**, 1054–1056 (2008)
3. Dunn, W.B., Broadhurst, D.I., Atherton, H.J., Goodacre, R., Griffin, J.L.: Systems level studies of mammalian metabolomes: the roles of mass spectrometry and nuclear magnetic resonance spectroscopy. *Chem. Soc. Rev.* **40**, 387–426 (2011)
4. Harris, D.M., et al.: Cellulose microfibril crystallinity is reduced by mutating C-terminal transmembrane region residues CES1A1A903V and CES3T942I of cellulose synthase. *Proc. Natl. Acad. Sci. U S A* **109**, 4098–4103 (2012)
5. Groger, C., Lutz, K., Brunner, E.: NMR studies of biomineralisation. *Prog. Nucl. Magn. Reson. Spectrosc.* **54**, 54–68 (2009)
6. Jantschke, A., et al.: Insight into the supramolecular architecture of intact diatom biosilica from DNP-supported solid-state NMR spectroscopy. *Angew. Chem. Int. Ed.* **54**, 15069–15073 (2015)
7. Goldberg, S.J., et al.: Refractory dissolved organic nitrogen accumulation in high-elevation lakes. *Nat. Commun.* **6**, 6347 (2015)
8. Hedges, J.I., et al.: Evidence for non-selective preservation of organic matter in sinking marine particles. *Nature* **409**, 801–804 (2001)
9. Gelinas, Y., Baldock, J.A., Hedges, J.I.: Organic carbon composition of marine sediments: effect of oxygen exposure on oil generation potential. *Science (New York, N.Y.)* **294**, 145–148 (2001)
10. Beckonert, O., et al.: High-resolution magic-angle-spinning NMR spectroscopy for metabolic profiling of intact tissues. *Nat. Protoc.* **5**, 1019–1032 (2010)
11. Kruger, N.J., Troncoso-Ponce, M.A., Ratcliffe, R.G.: 1H NMR metabolite fingerprinting and metabolomic analysis of perchloric acid extracts from plant tissues. *Nat. Protoc.* **3**, 1001–1012 (2008)
12. Beckonert, O., et al.: Metabolic profiling, metabolomic and metabonomic procedures for NMR spectroscopy of urine, plasma, serum and tissue extracts. *Nat. Protoc.* **2**, 2692–2703 (2007)
13. Frost, G., et al.: The short-chain fatty acid acetate reduces appetite via a central homeostatic mechanism. *Nat. Commun.* **5**, 3611 (2014)
14. Blaise, B.J., et al.: Metabotyping of *Caenorhabditis elegans* reveals latent phenotypes. *Proc. Natl. Acad. Sci. U S A* **104**, 19808–19812 (2007)
15. Mansfield, S.D., Kim, H., Lu, F.C., Ralph, J.: Whole plant cell wall characterization using solution-state 2D NMR. *Nat. Protoc.* **7**, 1579–1589 (2012)
16. Ward, J.L., Baker, J.M., Llewellyn, A.M., Hawkins, N.D., Beale, M.H.: Metabolomic analysis of *Arabidopsis* reveals hemiterpenoid glycosides as products of a nitrate ion-regulated, carbon flux overflow. *Proc. Natl. Acad. Sci. U S A* **108**, 10762–10767 (2011)
17. Choe, A., et al.: Sex-specific mating pheromones in the nematode *Panagrellus redivivus*. *Proc. Natl. Acad. Sci. U S A* **109**, 20949–20954 (2012)
18. Mao, J.D., Xing, B., Schmidt-Rohr, K.: New structural information on a humic acid from two-dimensional 1H-13C correlation solid-state nuclear magnetic resonance. *Environ. Sci. Technol.* **35**, 1928–1934 (2001)
19. Wang, T., et al.: Sensitivity-enhanced solid-state NMR detection of expansin's target in plant cell walls. *Proc. Natl. Acad. Sci. U S A* **110**, 16444–16449 (2013)
20. Simpson, A.J., Simpson, M.J., Soong, R.: Nuclear magnetic resonance spectroscopy and its key role in environmental research. *Environ. Sci. Technol.* **46**, 11488–11496 (2012)
21. Cao, X., Lattao, C., Pignatello, J.J., Mao, J., Schmidt-Rohr, K.: Sorption selectivity in natural organic matter probed with fully deuterium-exchanged and carbonyl-13C-labeled benzophenone and 1H-13C NMR spectroscopy. *Environ. Sci. Technol.* **48**, 8645–8652 (2014)
22. Feng, X., Simpson, A.J., Simpson, M.J.: Investigating the role of mineral-bound humic acid in phenanthrene sorption. *Environ. Sci. Technol.* **40**, 3260–3266 (2006)
23. Lattao, C., et al.: Sorption selectivity in natural organic matter studied with nitroxyl paramagnetic relaxation probes. *Environ. Sci. Technol.* **46**, 12814–12822 (2012)

24. Eisenreich, W., et al.:  $^{13}\text{C}$  isotopologue perturbation studies of *Listeria monocytogenes* carbon metabolism and its modulation by the virulence regulator PrfA. Proc. Natl. Acad. Sci. U S A **103**, 2040–2045 (2006)
25. Ohyama, K., Suzuki, M., Kikuchi, J., Saito, K., Muranaka, T.: Dual biosynthetic pathways to phytosterol via cycloartenol and lanosterol in Arabidopsis. Proc. Natl. Acad. Sci. U S A **106**, 725–730 (2009)
26. Peyraud, R., et al.: Demonstration of the ethylmalonyl-CoA pathway by using  $^{13}\text{C}$  metabolomics. Proc. Natl. Acad. Sci. U S A **106**, 4846–4851 (2009)
27. Kikuchi, J., Shinozaki, K., Hirayama, T.: Stable isotope labeling of *Arabidopsis thaliana* for an NMR-based metabolomics approach. Plant Cell Physiol. **45**, 1099–1104 (2004)
28. Tokuda, G., et al.: Metabolomic profiling of  $^{13}\text{C}$ -labelled cellulose digestion in a lower termite: insights into gut symbiont function. Proc. Biol. Sci. **281**, 20140990 (2014)
29. Mori, T., et al.: Multidimensional high-resolution magic angle spinning and solution-state NMR characterization of  $^{13}\text{C}$ -labeled plant metabolites and lignocellulose. Sci. Rep. **5**, 11848 (2015)
30. Komatsu, T., Ohishi, R., Shino, A., Kikuchi, J.: Structure and metabolic-flow analysis of molecular complexity in a  $^{13}\text{C}$ -labeled tree by 2D and 3D NMR. Angew. Chem. Int. Ed. **55**, 6000–6003 (2016)
31. Dumas, M.E., et al.: Assessment of analytical reproducibility of  $^1\text{H}$  NMR spectroscopy based metabolomics for large-scale epidemiological research: the INTERMAP Study. Anal. Chem. **78**, 2199–2208 (2006)
32. Viant, M.R., et al.: International NMR-based environmental metabolomics intercomparison exercise. Environ. Sci. Technol. **43**, 219–225 (2009)
33. Lacy, P., et al.: Signal intensities derived from different NMR probes and parameters contribute to variations in quantification of metabolites. PLoS ONE **9**, e85732 (2014)
34. Ward, J.L., et al.: An inter-laboratory comparison demonstrates that [H]-NMR metabolite fingerprinting is a robust technique for collaborative plant metabolomic data collection. Metabolomics **6**, 263–273 (2010)
35. Hao, J., et al.: Bayesian deconvolution and quantification of metabolites in complex 1D NMR spectra using BATMAN. Nat. Protoc. **9**, 1416–1427 (2014)
36. Gallo, V., et al.: Performance assessment in fingerprinting and multi component quantitative NMR analyses. Anal. Chem. **87**, 6709–6717 (2015)
37. Kikuchi, J., et al.: SpinCouple: development of a web tool for analyzing metabolite mixtures via two-dimensional J-Resolved NMR Database. Anal. Chem. **88**, 659–665 (2016)
38. Clayton, T.A., et al.: Pharmaco-metabonomic phenotyping and personalized drug treatment. Nature **440**, 1073–1077 (2006)
39. Schlipalius, D.I., et al.: A core metabolic enzyme mediates resistance to phosphine gas. Science (New York, N.Y.) **338**, 807–810 (2012)
40. Auro, K., et al.: A metabolic view on menopause and ageing. Nat. Commun. **5**, 4708 (2014)
41. Suhre, K., et al.: A genome-wide association study of metabolic traits in human urine. Nat. Genet. **43**, 565–569 (2011)
42. Kettunen, J., et al.: Genome-wide association study identifies multiple loci influencing human serum metabolite levels. Nat. Genet. **44**, 269–276 (2012)
43. Kettunen, J., et al.: Genome-wide study for circulating metabolites identifies 62 loci and reveals novel systemic effects of LPA. Nat. Commun. **7**, 11122 (2016)
44. Fukuda, S., et al.: Bifidobacteria can protect from enteropathogenic infection through production of acetate. Nature **469**, 543–547 (2011)
45. Furusawa, Y., et al.: Commensal microbe-derived butyrate induces the differentiation of colonic regulatory T cells. Nature **504**, 446–450 (2013)
46. Brindle, J.T., et al.: Rapid and noninvasive diagnosis of the presence and severity of coronary heart disease using  $^1\text{H}$ -NMR-based metabolomics. Nat. Med. **8**, 1439–1444 (2002)
47. Holmes, E., et al.: Human metabolic phenotype diversity and its association with diet and blood pressure. Nature **453**, 396–400 (2008)

48. Smith, M.I., et al.: Gut microbiomes of Malawian twin pairs discordant for kwashiorkor. *Science* (New York, N.Y.) **339**, 548–554 (2013)
49. Watanabe, M., Ohta, Y., Licang, S., Motoyama, N., Kikuchi, J.: Profiling contents of water-soluble metabolites and mineral nutrients to evaluate the effects of pesticides and organic and chemical fertilizers on tomato fruit quality. *Food Chem.* **169**, 387–395 (2015)
50. Tomita, S., et al.: A NMR-based, non-targeted multistep metabolic profiling revealed l-rhamnitol as a metabolite that characterised apples from different geographic origins. *Food Chem.* **174**, 163–172 (2015)
51. Tomita, S., et al.: A survey of metabolic changes in potato leaves by NMR-based metabolic profiling in relation to resistance to late blight disease under field conditions. *Magn. Reson. Chem.* **55**, 120–127 (2017)
52. Sekiyama, Y., Okazaki, K., Kikuchi, J., Ikeda, S.: NMR-based metabolic profiling of field-grown leaves from sugar beet plants harbouring different levels of resistance to Cercospora leaf spot disease. *Metabolites* **7**, 4 (2017)
53. Li, M., et al.: Symbiotic gut microbes modulate human metabolic phenotypes. *Proc. Natl. Acad. Sci. U S A* **105**, 2117–2122 (2008)
54. Sugahara, H., et al.: Probiotic *Bifidobacterium longum* alters gut luminal metabolism through modification of the gut microbial community. *Sci. Rep.* **5**, 13548 (2015)
55. Morita, H., et al.: Comparative genome analysis of *Lactobacillus reuteri* and *Lactobacillus fermentum* reveal a genomic island for reuterin and cobalamin production. *DNA Res.* **15**, 151–161 (2008)
56. Kato, T., et al.: Multiple omics uncovers host-gut microbial mutualism during prebiotic fructooligosaccharide supplementation. *DNA Res.* **21**, 469–480 (2014)
57. Bundy, J.G., et al.: Metabolic profile biomarkers of metal contamination in a sentinel terrestrial species are applicable across multiple sites. *Environ. Sci. Technol.* **41**, 4458–4464 (2007)
58. Collette, T.W., et al.: Impacts of an anti-androgen and an androgen/anti-androgen mixture on the metabolite profile of male fathead minnow urine. *Environ. Sci. Technol.* **44**, 6881–6886 (2010)
59. Ellis, R.P., et al.: (1)H NMR metabolomics reveals contrasting response by male and female mussels exposed to reduced seawater pH, increased temperature, and a pathogen. *Environ. Sci. Technol.* **48**, 7044–7052 (2014)
60. Samuelsson, L.M., Bjorlenius, B., Forlin, L., Larsson, D.G.: Reproducible (1)H NMR-based metabolomic responses in fish exposed to different sewage effluents in two separate studies. *Environ. Sci. Technol.* **45**, 1703–1710 (2011)
61. Whitfield Aslund, M.L., et al.: Earthworm sublethal responses to titanium dioxide nanomaterial in soil detected by (1)H NMR metabolomics. *Environ. Sci. Technol.* **46**, 1111–1118 (2012)
62. Yoshida, S., Date, Y., Akama, M., Kikuchi, J.: Comparative metabolomic and ionomic approach for abundant fishes in estuarine environments of Japan. *Sci. Rep.* **4**, 7005 (2014)
63. Sekiyama, Y., Chikayama, E., Kikuchi, J.: Profiling polar and semipolar plant metabolites throughout extraction processes using a combined solution-state and high-resolution magic angle spinning NMR approach. *Anal. Chem.* **82**, 1643–1652 (2010)
64. Sekiyama, Y., Chikayama, E., Kikuchi, J.: Evaluation of a semipolar solvent system as a step toward heteronuclear multidimensional NMR-based metabolomics for <sup>13</sup>C-labeled bacteria, plants, and animals. *Anal. Chem.* **83**, 719–726 (2011)
65. Kikuchi, J., Hirayama, T.: Practical aspects of uniform stable isotope labeling of higher plants for heteronuclear NMR-based metabolomics. *Methods Mol. Biol.* **358**, 273–286 (2007)
66. Tian, C., et al.: Top-down phenomics of *Arabidopsis thaliana*: metabolic profiling by one- and two-dimensional nuclear magnetic resonance spectroscopy and transcriptome analysis of albino mutants. *J. Biol. Chem.* **282**, 18532–18541 (2007)

67. Komatsu, T., Kobayashi, T., Hatanaka, M., Kikuchi, J.: Profiling planktonic biomass using element-specific, multicomponent nuclear magnetic resonance spectroscopy. *Environ. Sci. Technol.* **49**, 7056 (2015)
68. Yamazawa, A., Iikura, T., Shino, A., Date, Y., Kikuchi, J.: Solid-, solution-, and gas-state NMR monitoring of C-13-cellulose degradation in an anaerobic microbial ecosystem. *Molecules* **18**, 9021–9033 (2013)
69. Komatsu, T., Ohishi, R., Shino, A., Akashi, K., Kikuchi, J.: Multi-spectroscopic analysis of seed quality and 13C-stable-isotopologue monitoring in initial growth metabolism of *Jatropha curcas* L. *Metabolites* **4**, 1018–1033 (2014)
70. Ratcliffe, R.G., Shachar-Hill, Y.: Measuring multiple fluxes through plant metabolic networks. *Plant J.* **45**, 490–511 (2006)
71. Sekiyama, Y., Kikuchi, J.: Towards dynamic metabolic network measurements by multi-dimensional NMR-based fluxomics. *Phytochemistry* **68**, 2320–2329 (2007)
72. Fonville, J.M., et al.: Evaluation of full-resolution J-resolved 1H NMR projections of biofluids for metabolomics information retrieval and biomarker identification. *Anal. Chem.* **82**, 1811–1821 (2010)
73. Chikayama, E., Suto, M., Nishihara, T., Shinozaki, K., Kikuchi, J.: Systematic NMR analysis of stable isotope labeled metabolite mixtures in plant and animal systems: coarse grained views of metabolic pathways. *PLoS ONE* **3**, e3805 (2008)
74. Wishart, D.S., et al.: HMDB 3.0—The Human Metabolome Database in 2013. *Nucleic Acids Res.* **41**, D801–D807 (2013)
75. Ulrich, E.L., et al.: BioMagResBank. *Nucleic Acid Res.* **36**, D402–D408 (2008)
76. Cui, Q., et al.: Metabolite identification via the Madison metabolomics consortium database. *Nat. Biotechnol.* **26**, 162–164 (2008)
77. Chikayama, E., et al.: Statistical indices for simultaneous large-scale metabolite detections for a single NMR spectrum. *Anal. Chem.* **82**, 1653–1658 (2010)
78. Bingol, K., Zhang, F., Bruschweiler-Li, L., Brüschweiler, R.: TOCCATA: a customized carbon total correlation spectroscopy NMR metabolomics database. *Anal. Chem.* **84**, 9395–9401 (2012)
79. Ludwig, C., et al.: Birmingham metabolite library: a publicly accessible database of 1-D 1H and 2-D 1H J-resolved NMR spectra of authentic metabolite standards (BML-NMR). *Metabolomics* **8**, 8–18 (2012)
80. Kikuchi, J., Ogata, Y., Shinozaki, K.: ECOMICS: ECosystem trans-OMICS tools and methods for complex environmental samples and datasets. *J. Ecosyst. Ecogr.* **S2**, 001 (2011)
81. Ogata, Y., et al.: ECOMICS: a web-based toolkit for investigating the biomolecular web in ecosystems using a trans-omics approach. *PLoS ONE* **7**, e30263 (2012)
82. Chikayama, E., et al.: FoodPro: a web-based tool for evaluating covariance and correlation NMR spectra associated with food processes. *Metabolites* **6**, 36 (2016)
83. Willoughby, P.H., Jansma, M.J., Hoye, T.R.: A guide to small-molecule structure assignment through computation of ((1)H and (1)(3)C) NMR chemical shifts. *Nat. Protoc.* **9**, 643–660 (2014)
84. Lodewyk, M.W., Siebert, M.R., Tantillo, D.J.: Computational prediction of 1H and 13C chemical shifts: a useful tool for natural product, mechanistic, and synthetic organic chemistry. *Chem. Rev.* **112**, 1839–1862 (2012)
85. Odoh, S.O., Cramer, C.J., Truhlar, D.G., Gagliardi, L.: Quantum-chemical characterization of the properties and reactivities of metal-organic frameworks. *Chem. Rev.* **115**, 6051–6111 (2015)
86. Misawa, T., Komatsu, T., Date, Y., Kikuchi, J.: SENSI: signal enhancement by spectral integration for the analysis of metabolic mixtures. *Chem. Commun.* **52**, 2964–2967 (2016)
87. Ito, K., Tsutsumi, Y., Date, Y., Kikuchi, J.: Fragment assembly approach based on graph/network theory with quantum chemistry verifications for assigning multidimensional NMR signals in metabolite mixtures. *ACS Chem. Biol.* **11**, 1030–1038 (2016)

88. Chikayama, E., Shimbo, Y., Komatsu, K., Kikuchi, J.: The effect of molecular conformation on the accuracy of theoretical  $^1\text{H}$  and  $^{13}\text{C}$  chemical shifts calculated by ab initio methods for metabolic mixture analysis. *J. Phys. Chem. B* **120**, 3479–3487 (2016)
89. Anderson, P.E., Reo, N.V., DelRaso, N.J., Doom, T.E., Raymer, M.L.: Gaussian binning: a new kernel-based method for processing NMR spectroscopic data for metabolomics. *Metabolomics* **4**, 261–272 (2008)
90. Fukuda, S., et al.: Evaluation and characterization of bacterial metabolic dynamics with a novel profiling technique, real-time metabolotyping. *PLoS ONE* **4**, e4893 (2009)
91. Dieterle, F., Ross, A., Schlotterbeck, G., Senn, H.: Probabilistic quotient normalization as robust method to account for dilution of complex biological mixtures. Application in  $^1\text{H}$  NMR metabonomics. *Anal. Chem.* **78**, 4281–4290 (2006)
92. Date, Y., Sakata, K., Kikuchi, J.: Chemical profiling of complex biochemical mixtures from various seaweeds. *Polym. J.* **44**, 888–894 (2012)
93. Ogawa, D.M.O., et al.: Biogeochemical typing of paddy field by a data-driven approach revealing sub-systems within a complex environment—a pipeline to filtrate, organize and frame massive dataset from multi-omics analyses. *PLoS ONE* **9**, e110723 (2014)
94. Ogura, T., Hoshino, R., Date, Y., Kikuchi, J.: Visualization of microfloral metabolism for marine waste recycling. *Metabolites* **6**, 7 (2016)
95. Date, Y., Iikura, T., Yamazawa, A., Moriya, S., Kikuchi, J.: Metabolic sequences of anaerobic fermentation on glucose-based feeding substrates based on correlation analyses of microbial and metabolite profiling. *J. Proteome Res.* **11**, 5602–5610 (2012)
96. Shiokawa, Y., Misawa, T., Date, Y., Kikuchi, J.: Application of market basket analysis for the visualization of transaction data based on human lifestyle and spectroscopic measurements. *Anal. Chem.* **88**, 2714–2719 (2016)
97. Chatzimichali, E.A., Bessant, C.: Novel application of heuristic optimisation enables the creation and thorough evaluation of robust support vector machine ensembles for machine learning applications. *Metabolomics* **12**, 16 (2016)
98. Poulsen-Ellestad, K.L., et al.: Metabolomics and proteomics reveal impacts of chemically mediated competition on marine plankton. *Proc. Natl. Acad. Sci. U S A* **111**, 9009–9014 (2014)
99. Vergara, F., Kikuchi, J., Breuer, C.: Artificial autopolyploidization modifies the tricarboxylic acid cycle and GABA shunt in *Arabidopsis thaliana* Col-0. *Sci. Rep.* **6**, 26515 (2016)
100. Okamoto, M., Tsuboi, Y., Chikayama, E., Kikuchi, J., Hirayama, T.: Metabolic movement upon abscisic acid and salicylic acid combined treatments. *Plant Biotechnol.* **26**, 551–560 (2009)
101. Mochida, K., Furuta, T., Ebana, K., Shinozaki, K., Kikuchi, J.: Correlation exploration of metabolic and genomic diversity in rice. *BMC Genomics* **10**, 568 (2009)
102. van Duynhoven, J., et al.: Metabolic fate of polyphenols in the human superorganism. *Proc. Natl. Acad. Sci. U S A* **108**(Suppl 1), 4531–4538 (2011)
103. Hsieh, C.Y., et al.: Strengthening of the intestinal epithelial tight junction by *Bifidobacterium bifidum*. *Physiol Rep* **3**, e12327 (2015)
104. Date, Y., et al.: In vitro evaluation method for screening of candidate prebiotic foods. *Food Chem.* **152**, 251–260 (2014)
105. Vergara, F., Shino, A., Kikuchi, J.: Cannibalism affects core metabolic processes in *Helicoverpa armigera* larvae—a 2D NMR metabolomics study. *Int. J. Mol. Sci.* **17**, 1470 (2016)
106. Asakura, T., Sakata, K., Yoshida, S., Date, Y., Kikuchi, J.: Noninvasive analysis of metabolic changes following nutrient input into diverse fish species, as investigated by metabolic and microbial profiling approaches. *PeerJ* **2**, e550 (2014)
107. Misawa, T., Date, Y., Kikuchi, J.: Human metabolic, mineral, and microbiota fluctuations across daily nutritional intake visualized by a data-driven approach. *J. Proteome Res.* **14**, 1526–1534 (2015)
108. Yamazawa, A., et al.: Cellulose digestion and metabolism induced biocatalytic transitions in anaerobic microbial ecosystems. *Metabolites* **4**, 36–52 (2013)

109. Ogura, T., Date, Y., Kikuchi, J.: Differences in cellulosic supramolecular structure of compositionally similar rice straw affect biomass metabolism by paddy soil microbiota. *PLoS ONE* **8**, e66919 (2013)
110. Ogura, T., Date, Y., Tsuboi, Y., Kikuchi, J.: Metabolic dynamics analysis by massive data integration: application to tsunami-affected field soils in Japan. *ACS Chem. Biol.* **10**, 1908–1915 (2015)
111. Date, Y., et al.: New monitoring approach for metabolic dynamics in microbial ecosystems using stable-isotope-labeling technologies. *J. Biosci. Bioeng.* **110**, 87–93 (2010)
112. Dick-Perez, M., et al.: Structure and interactions of plant cell-wall polysaccharides by two- and three-dimensional magic-angle-spinning solid-state NMR. *Biochemistry* **50**, 989–1000 (2011)
113. Komatsu, T., Kikuchi, J.: Comprehensive signal assignment of  $^{13}\text{C}$ -labeled lignocellulose using multidimensional solution NMR and  $^{13}\text{C}$  chemical shift comparison with solid-state NMR. *Anal. Chem.* **85**, 8857–8865 (2013)
114. Mao, J.D., Schmidt-Rohr, K.: Accurate quantification of aromaticity and nonprotonated aromatic carbon fraction in natural organic matter by  $^{13}\text{C}$  solid-state nuclear magnetic resonance. *Environ. Sci. Technol.* **38**, 2680–2684 (2004)
115. Mao, J., Kong, X., Schmidt-Rohr, K., Pignatello, J.J., Perdue, E.M.: Advanced solid-state NMR characterization of marine dissolved organic matter isolated using the coupled reverse osmosis/electrodialysis method. *Environ. Sci. Technol.* **46**, 5806–5814 (2012)
116. Wang, T., Salazar, A., Zabotina, O.A., Hong, M.: Structure and dynamics of *Brachypodium* primary cell wall polysaccharides from two-dimensional  $^{13}\text{C}$  solid-state nuclear magnetic resonance spectroscopy. *Biochemistry* **53**, 2840–2854 (2014)
117. Wang, T., Park, Y.B., Cosgrove, D.J., Hong, M.: Cellulose-pectin spatial contacts are inherent to never-dried *Arabidopsis* primary cell walls: evidence from solid-state nuclear magnetic resonance. *Plant Physiol.* **168**, 871–884 (2015)
118. Komatsu, T., Kikuchi, J.: Selective signal detection in solid-state NMR using rotor-synchronized dipolar dephasing for the analysis of hemicellulose in lignocellulosic biomass. *J. Phys. Chem. Lett.* **4**, 2279–2283 (2013)
119. Ito, K., Sakata, K., Date, Y., Kikuchi, J.: Integrated analysis of seaweed components during seasonal fluctuation by data mining across heterogeneous chemical measurements with network visualization. *Anal. Chem.* **86**, 1098–1105 (2014)
120. Wei, F., Ito, K., Sakata, K., Date, Y., Kikuchi, J.: Pretreatment and integrated analysis of spectral data reveal seaweed similarities based on chemical diversity. *Anal. Chem.* **87**, 2819–2826 (2015)
121. Okushita, K., Komatsu, T., Chikayama, E., Kikuchi, J.: Statistical approach for solid-state NMR spectra of cellulose derived from a series of variable parameters. *Polym. J.* **44**, 895–900 (2012)
122. Okushita, K., Chikayama, E., Kikuchi, J.: Solubilization mechanism and characterization of the structural change of bacterial cellulose in regenerated states through ionic liquid treatment. *Biomacromol* **13**, 1323–1330 (2012)
123. Mori, T., et al.: Exploring the conformational space of amorphous cellulose using NMR chemical shifts. *Carbohydr. Polym.* **90**, 1197–1203 (2012)
124. Teramura, H., et al.: Changes in lignin and polysaccharide components in 13 cultivars of rice straw following dilute acid pretreatment as studied by solution-state 2D  $^1\text{H}$ - $^{13}\text{C}$  NMR. *PLoS ONE* **10**, e0128417 (2015)
125. Sasaki, K., et al.: Precipitate obtained following membrane separation of hydrothermally pretreated rice straw liquid revealed by 2D NMR to have high lignin content. *Biotechnol. Biofuels* **8**, 88 (2015)
126. Sasaki, K., et al.: Toward the complete utilization of rice straw: methane fermentation and lignin recovery by a combinational process involving mechanical milling, supporting material and nanofiltration. *Bioresour. Technol.* **216**, 830–837 (2016)
127. Teramura, H., et al.: Organosolv pretreatment of sorghum bagasse using a low concentration of hydrophobic solvents such as 1-butanol or 1-pentanol. *Biotechnol. Biofuels* **9**, 27 (2016)

128. Tsuji, Y., et al.: Introduction of chemically labile substructures into *Arabidopsis* lignin through the use of LigD, the calpha-dehydrogenase from *Sphingobium* sp. strain SYK-6. *Plant Biotechnol. J.* **13**, 821–832 (2015)
129. Ogura, T., et al.: Improvement of physical, chemical, and biological properties of aridisol from Botswana by the incorporation of torrefied biomass. *Sci. Rep.* **6**, 28011 (2016)
130. Mladenov, N., et al.: Dissolved organic matter quality in a shallow aquifer of Bangladesh: implications for arsenic mobility. *Environ. Sci. Technol.* **49**, 10815–10824 (2015)
131. Asakura, T., Date, Y., Kikuchi, J.: Comparative analysis of chemical and microbial profiles in estuarine sediments sampled from Kanto and Tohoku regions in Japan. *Anal. Chem.* **86**, 5425–5432 (2014)
132. Kaiser, E., Simpson, A.J., Dria, K.J., Sulzberger, B., Hatcher, P.G.: Solid-state and multidimensional solution-state NMR of solid phase extracted and ultrafiltered riverine dissolved organic matter. *Environ. Sci. Technol.* **37**, 2929–2935 (2003)
133. Mitchell, J., Gladden, L.F., Chandrasekera, T.C., Fordham, E.J.: Low-field permanent magnets for industrial process and quality control. *Prog. Nucl. Magn. Reson. Spectrosc.* **76**, 1–60 (2014)

# Chapter 18

## NMR of Paramagnetic Compounds

Yasuhiko Yamamoto and Tomokazu Shibata

**Abstract** Paramagnetic ions and molecules have been exploited quite extensively as extrinsic shift and relaxation probes for investigating the structure and dynamics of biological molecules. The prodigious growth of related research areas is easily discernible as the remarkably widening scope of application in diverse fields in life and material sciences. Sperm whale myoglobin (Mb) is well known as the first protein to have its three-dimensional structure revealed by X-ray crystallographic study and is also known as one of the first paramagnetic proteins studied by NMR. The heme Fe atom in Mb can exhibit a variety of oxidation, ligation, and spin states. In this chapter, Mb is selected as a reference paramagnetic compound to provide an overview of the relationship between the spectral features and the number of unpaired electrons, because the effects of a change in the spin quantum number  $S$ , i.e., the number of unpaired electrons, on NMR spectral parameters of a single compound can be readily understood. Field-dependent broadening of signals of proteins with a series of  $S$  values is also described.

**Keywords** Heme electronic structure · Myoglobin · Paramagnetic effect · Spin state · Unpaired electron

### 18.1 Introduction

The use of paramagnetic ions or molecules as extrinsic shift and relaxation probes for investigating the structures of biological molecules not only in solution, but also in solid states has been exploited much more than originally expected (see Chap. 15) [1–45]. In addition, dynamic nuclear polarization (DNP) ascribing to the magnetization transfer occurring from unpaired electrons to nuclei through stochastic

---

Y. Yamamoto (✉) · T. Shibata

Department of Chemistry, University of Tsukuba, Tsukuba 305-8571, Japan  
e-mail: yamamoto@chem.tsukuba.ac.jp

T. Shibata

e-mail: shibata@chem.tsukuba.ac.jp

modulation of the hyperfine interaction between electron and nuclear spins (see Chap. 4) is gaining increasing attention for a variety of applications, showing its potential in solution and solid-state NMR as well as in MRI [38, 46–49]. NMR study of paramagnetic compounds originated in solid-state physics in the middle of the 1950s [50, 51], and as is well known, the technique was soon introduced to chemistry and biochemistry. By 1970, the physical principles underlying the technique were well understood and the basic concepts of the technique, together with the theoretical framework for interpreting NMR parameters of paramagnetic compounds, had been well established [1, 2, 10, 52–61]. The prodigious growth of related research areas is easily witnessed by the remarkably widening scope of application in diverse fields in life and material sciences. A large number of reviews on NMR study of paramagnetic compounds have already appeared, some [10, 19, 62–64] comprehensive and others [3–9, 11–18, 20, 21, 23, 26–29, 38, 40, 65] more focused. Considering the aim of the present book, this chapter should serve as a reference source for active researchers and as an introduction to this subject for a novice, with particular emphasis on the experimental aspects. In view of the multiple purposes of the chapter, we selected hemoproteins, particularly sperm whale myoglobin [Mb (Fig. 18.1a)], as reference compounds. As is well known, Mb was the first protein to have had its three-dimensional structure revealed by X-ray crystallographic study [66]. Mb is also known as one of the first paramagnetic proteins studied by NMR [67], and paramagnetic hemoproteins such as Mb, cytochrome *c*, and hemoglobin were extensively investigated by Shulman [68], Wüthrich [69], Ogawa [70], La Mar [71], and Morishima [72] during the late 1960s to the late 1970s. In addition, paramagnetic Mb has been used for one of the landmark NMR measurements, which demonstrated that, in a magnetic field-oriented molecule, a

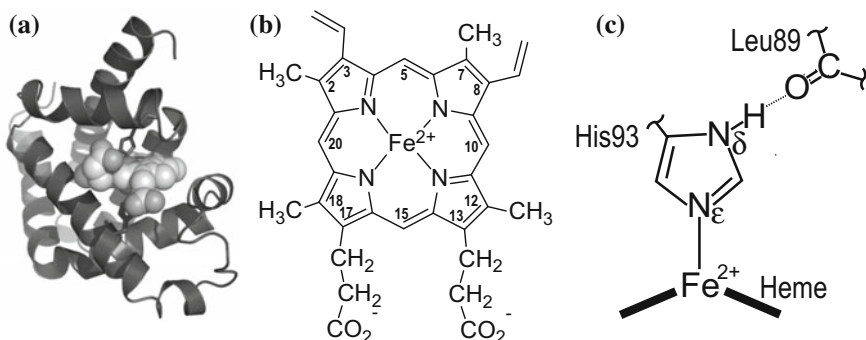


**Fig. 18.1** **a** Schematic representation of the structure of sperm whale myoglobin (Mb; Protein Data Bank ID 1A6M). The polypeptide chain is illustrated as a ribbon model, and the heme is drawn as a space-filling model. **b** Structure and numbering system of heme. **c** Schematic drawing of the heme coordination structure in deoxy Mb [76]. The hydrogen bonding interaction of His93 N<sub>δ</sub>H with the Leu89 carbonyl oxygen atom is represented by a broken line

magnetic dipole–dipole interaction does not average to zero [73] and yields a measurable dipolar coupling useful for refinement of structural and dynamic properties of molecules [74].

Mb is an oxygen ( $O_2$ ) storage hemoprotein with a molecular weight of about 17 kDa [75]. The heme cofactor (Fig. 18.1b) is buried inside the protein matrix composed of 153 amino acid residues, and its binding to the protein is stabilized by the coordination bond between the heme iron (Fe) atom and the nitrogen one ( $N_e$ ) of the proximal His (His93) [66, 76–78] (Fig. 18.1c), together with hydrophobic interaction of the heme cofactor with the surrounding amino acid residues in the heme pocket and the formation of salt bridges between the heme propionate groups and nearby polar amino acid side chains [76–78]. The heme Fe atom in Mb is generally in either the ferrous ( $Fe^{2+}$ ) or ferric ( $Fe^{3+}$ ) state. The numbers of electrons in the  $3d$  orbitals of  $Fe^{2+}$  and  $Fe^{3+}$  are six and five, respectively (inset of Fig. 18.2). Hence, the total spin quantum number  $S$  is the integer and half-integer for  $Fe^{2+}$  and  $Fe^{3+}$ , respectively. Depending upon the degree of spin pairing of electrons in the  $3d$  orbitals,  $Fe^{2+}$  can have 4, 2, or 0 unpaired electrons, corresponding to  $S = 2, 1,$  or 0, respectively, and  $Fe^{3+}$  corresponding to 5, 3, or 1 unpaired electron,  $S = 5/2,$   $3/2,$  or  $1/2,$  respectively. Based on an octahedral ligand field, the energy levels of the five  $3d$  orbitals are split into two groups in such a way that the levels of the  $d_{z^2}$  and  $d_{x^2-y^2}$  orbitals are higher than those of the other three orbitals,  $d_{xy}, d_{yz},$  and  $d_{xz}.$  The spin state of Mb depends on the chemical nature of the ligand. For heme  $Fe^{2+}$ , the deoxy form (deoxy Mb) is penta-coordinated with a high-spin configuration,  $S = 2,$  and the oxy form ( $MbO_2$ ) or carbonmonoxy form ( $MbCO$ ) possesses a low-spin configuration,  $S = 0.$  On the other hand, the binding of ligands of relatively weak field strength such as  $H_2O$  to heme  $Fe^{3+}$  gives high-spin state  $S = 5/2$  [ $metMb(H_2O)$ ], and low-spin state  $S = 1/2$  is obtained with a strong ligand such as  $CN^-$  [ $metMb(CN^-)$ ]. In addition, the binding of ligands of intermediate field strength such as  $N_3^-$  [ $metMb(N_3^-)$ ] exhibit a thermal equilibrium between  $S = 1/2$  and  $S = 5/2$  states. Complexes with  $S = 1$  and  $3/2$  are not so common and have been obtained in some particular systems such as  $Fe^{4+}$ -peroxo species ( $S = 1$ ) and  $Fe^{3+}$  species coupled with  $O_2^-$  ( $S = 3/2$ ) [79].

Aside from the importance of Mb in the early history of the NMR study of paramagnetic compounds, the significance of Mb in NMR studies is mainly two-fold, as follows. Firstly, as described above, the heme Fe atom in Mb can exhibit a variety of oxidation, ligation, and spin states, and hence, the effects of a change in the  $S$  value, i.e., the number of unpaired electrons, on NMR spectral parameters of a single compound, can be readily understood. Secondly, the relationship between the contact shift ( $\delta_c$ ), due to a delocalized unpaired electron, and a pseudo-contact one ( $\delta_{pc}$ ), due to a through-space dipolar interaction with the unpaired electron spin(s), as to paramagnetic shift ( $\delta_{para}$ ) is clearly reflected in the spectra of paramagnetic Mbs, and thus, a comprehensive description of the  $\delta_c$  value can be given in terms of delocalization of unpaired electron density from the paramagnetic center. We intend to portray a range of techniques applied to paramagnetic Mbs, which exhibit widespread utility in life and material sciences.

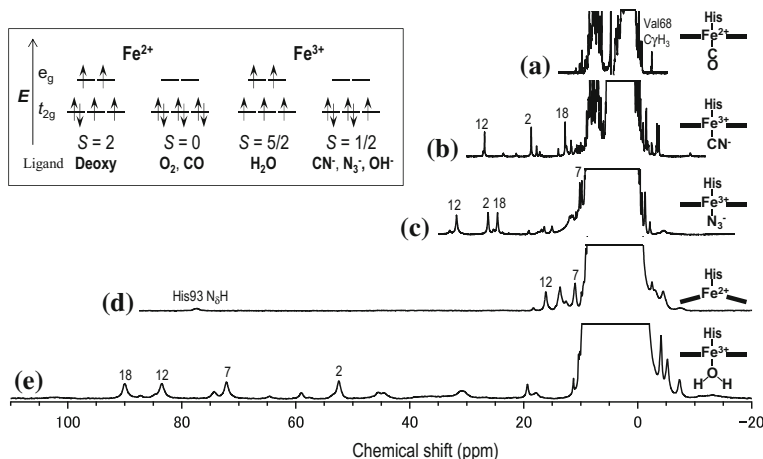


**Fig. 18.2** 400 MHz  $^1\text{H}$  NMR spectra of **a** carbonmonoxy form [Mb(CO)], **b** met-cyano form [metMb( $\text{CN}^-$ )], **c** met-azido form [metMb( $\text{N}_3^-$ )], **d** deoxy form (deoxy Mb) of Mb in 90%  $^1\text{H}_2\text{O}/10\% ^2\text{H}_2\text{O}$ , pH 7.4, at 25 °C, and **e** met-aquo form [metMb( $\text{H}_2\text{O}$ )] of the protein in 90%  $^1\text{H}_2\text{O}/10\% ^2\text{H}_2\text{O}$ , pH 6.5, at 25 °C. The heme Fe oxidation and ligation states of the proteins are schematically illustrated on the right-hand side of the spectra. The assignments of heme methyl proton signals, i.e., 2-, 7-, 12-, and 18- $\text{CH}_3$ , are indicated by the corresponding numbers in the spectra. In **(a)**, four signals are observed at  $\sim 3$  ppm. In **(b)**, the 7- $\text{CH}_3$  signal at  $\sim 5$  ppm is buried in the diamagnetic envelope, and in **(d)**, 2- and 18- $\text{CH}_3$  signals are not assigned yet. Assignments of the Val68  $\text{C}_7\text{H}_3$  signal of Mb(CO) and the His93  $\text{N}_\delta\text{H}$  proton signal of deoxy Mb are also indicated. In the inset, typical heme Fe oxidation, spin, and ligation states of the protein are illustrated. The intermediate spin complexes, i.e.,  $\text{Fe}^{2+} S = 1$  and  $\text{Fe}^{3+} S = 3/2$  complexes, are obtained in some particular systems [79]

## 18.2 Paramagnetic Effects

The theory behind NMR parameters in paramagnetic systems has been treated thoroughly elsewhere [2, 10, 13, 16]. Only a qualitative description of paramagnetic shifts and relaxation, which will suffice to allow an appreciation of the spectra presented, is given below.

### 18.2.1 Paramagnetic Shifts

Analysis of  $\delta_{\text{para}}$  in terms of the interaction between nuclear and electron spins provides a wealth of information about electronic and molecular structures [2, 8–21]. The observed shift ( $\delta_{\text{obs}}$ ) of a paramagnetic compound is given as in Eq. (18.1), where  $\delta_{\text{dia}}$  and  $\delta_{\text{para}}$  are the diamagnetic and paramagnetic contributions, respectively.

$$\delta_{\text{obs}} = \delta_{\text{dia}} + \delta_{\text{para}} \quad (18.1)$$

$\delta_{\text{dia}}$  is the shift that would have been observed if the molecule contained no unpaired electron, and  $\delta_{\text{para}}$  is expressed as the sum of  $\delta_c$  and  $\delta_{pc}$ ,

$$\delta_{\text{para}} = \delta_c + \delta_{pc} \quad (18.2)$$

$\delta_c$  reflects the electronic structure of the molecule, and the metal-centered  $\delta_{pc}$ , due to the magnetic dipolar field arising from delocalized unpaired electron(s) at the paramagnetic center, has been used extensively to refine the molecular structure (see Chap. 15 of this book).

In addition to  $\delta_{\text{para}}$  itself, its temperature dependence also provides valuable information about the molecule. Since both  $\delta_c$  and  $\delta_{pc}$  are proportional to the reciprocal of absolute temperature ( $T$ ), plots of  $\delta_{\text{obs}}$  against  $1/T$ , often called Curie plots, exhibit a straight line with the intercept at  $1/T \rightarrow 0$ , which is equal to  $\delta_{\text{dia}}$ . However, anomalous Curie plots are occasionally observed, and the thermodynamic nature of the thermal spin equilibrium in metMb(N<sub>3</sub><sup>-</sup>) [80] and the thermal equilibrium between <sup>5</sup>E,  $(d_{xy})(d_{xz})^2(d_{yz})(d_{z^2})(d_{x^2-y^2})$ , and <sup>5</sup>B<sub>2</sub>,  $(d_{xy})^2(d_{xz})(d_{yz})(d_{z^2})(d_{x^2-y^2})$ , states of high-spin heme Fe<sup>2+</sup> in deoxy Mb [81], have been quantitatively characterized through analysis of such anomalous temperature-dependent shift changes of the signals.

### 18.2.2 Paramagnetic Relaxation

The analysis of nuclear relaxation has provided a wealth of information about the structural and dynamic properties of molecules. In particular, in the case of paramagnetic metalloproteins, the dynamic nature of a molecule is sharply manifested in paramagnetic relaxation observed for paramagnetically shifted NMR signals [2, 10, 13, 14, 16].

The nuclear relaxation rate ( $R_{\text{obs}}$ ) in a paramagnetic system is expressed as the sum of diamagnetic ( $R_{\text{dia}}$ ) and paramagnetic ( $R_{\text{para}}$ ) terms,

$$R_{\text{obs}} = R_{\text{dia}} + R_{\text{para}} \quad (18.3)$$

$R_{\text{dia}}$  is the sum of the contributions of the dipole–dipole interaction ( $R_{\text{dia}}^{\text{DD}}$ ), chemical shift anisotropy ( $R_{\text{dia}}^{\text{CSA}}$ ), and others ( $R_{\text{dia}}^{\text{other}}$ ),

$$R_{\text{dia}} = R_{\text{dia}}^{\text{DD}} + R_{\text{dia}}^{\text{CSA}} + R_{\text{dia}}^{\text{other}}. \quad (18.4)$$

The contributions of  $R_{\text{dia}}^{\text{CSA}}$  to the nuclear spin–lattice ( $R_{1\text{dia}}$ ) and spin–spin ( $R_{2\text{dia}}$ ) relaxation rates ( $R_{1\text{dia}}^{\text{CSA}}$  and  $R_{2\text{dia}}^{\text{CSA}}$ , respectively) depend on the magnetic field strength and can be written as follows [56],

$$R_{1\text{dia}}^{\text{CSA}} = \frac{6}{40} \omega_I^2 \delta_z^2 \left( 1 + \frac{\eta^2}{3} \right) J(\omega_I) \quad (18.5)$$

$$R_{2\text{dia}}^{\text{CSA}} = \frac{1}{40} \omega_I^2 \delta_z^2 (3J(\omega_I) + 4J(0)) \quad (18.6)$$

$$J(\omega_I) = \frac{2\tau_r}{1 + \omega_I^2 \tau_r^2}, \quad (18.7)$$

where  $\delta_z$  is associated with the principal components of the chemical shift tensor,  $\eta$  is the asymmetric parameter of the molecule under consideration, and  $J(\omega_I)$  represents the spectral density function.

On the other hand,  $R_{\text{para}}$  is expressed as the sum of the contributions of metal-centered ( $R_{\text{para}}^{\text{MC}}$ ) and ligand-centered ( $R_{\text{para}}^{\text{LC}}$ ) dipolar terms, the contact hyperfine interaction ( $R_{\text{para}}^{\text{C}}$ ), and Curie spin relaxation ( $R_{\text{para}}^{\text{Curie}}$ ) [2], as illustrated in Fig. 18.3,

$$R_{\text{para}} = R_{\text{para}}^{\text{MC}} + R_{\text{para}}^{\text{LC}} + R_{\text{para}}^{\text{C}} + R_{\text{para}}^{\text{Curie}}. \quad (18.8)$$

Using the Solomon–Bloembergen equations [52, 82], together with the expression of  $R_{\text{para}}^{\text{Curie}}$  [83, 84] (see Chap. 15 of this book), paramagnetic

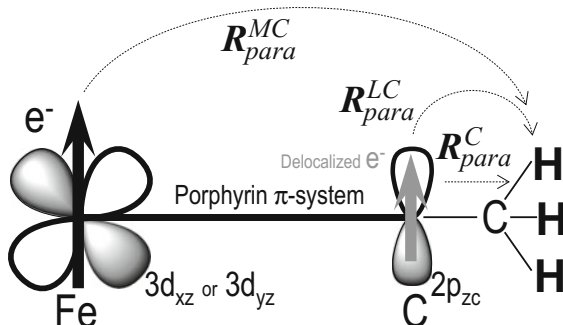


**Fig. 18.3** Schematic representation of paramagnetic relaxation mechanisms for heme  $\text{CH}_3$  protons. Paramagnetic metal-centered relaxation ( $R_{\text{para}}^{\text{MC}}$ ) is due to the dipole–dipole interaction between the nuclear spin and electron spin localized at heme Fe. Paramagnetic ligand-centered relaxation ( $R_{\text{para}}^{\text{LC}}$ ) is due to the dipole–dipole interaction between the nuclear spin and electron spins delocalized from heme Fe into the ligand atoms, and, in the case of the heme  $\text{CH}_3$  proton,  $R_{\text{para}}^{\text{LC}}$  due to the electron spin delocalized into the  $p_z$  orbital of the carbon atom to which  $\text{CH}_3$  is covalently attached is predominant. Paramagnetic contact relaxation ( $R_{\text{para}}^{\text{C}}$ ) arises from the contact hyperfine interaction between the nuclear spin and electron spin delocalized into the  $1s$  orbital of the  $\text{CH}_3$  hydrogen atoms. Curie spin relaxation ( $R_{\text{para}}^{\text{Curie}}$ ) arises from the dipole–dipole interaction between the nuclear spin and the time average of the electron magnetic moment (not shown)

contributions to the nuclear spin-lattice and spin-spin relaxation rates ( $R_{1\text{para}}$  and  $R_{2\text{para}}$ , respectively) in a paramagnetic system are expressed by

$$R_{1\text{para}} = \frac{2}{15} \left( \frac{\mu_0}{4\pi} \right)^2 \gamma_I^2 \beta_e^2 \mu_B^2 S(S+1) (\gamma_M^{-6} + \Sigma \rho^2 \gamma_L^{-6}) \\ \times \left[ \frac{\tau_{c2}}{1 + (\omega_I - \omega_S)^2 \tau_{c2}^2} + \frac{3\tau_{c1}}{1 + \omega_I^2 \tau_{c1}^2} + \frac{6\tau_{c2}}{1 + (\omega_I + \omega_S)^2 \tau_{c2}^2} \right] \\ + \frac{2}{3} S(S+1) \left( \frac{A}{\hbar} \right)^2 \left[ \frac{\tau_{e2}}{1 + (\omega_I + \omega_S)^2 \tau_{e2}^2} \right] \\ + \frac{2}{5} \left( \frac{\mu_0}{4\pi} \right)^2 \frac{\omega_I^2 \beta_e^4 \mu_B^4 S^2 (S+1)^2}{(3kT)^2 r_M^6} \left( \frac{3\tau_r}{1 + \omega_I^2 \tau_r^2} \right) \quad (18.9)$$

$$R_{2\text{para}} = \frac{1}{15} \left( \frac{\mu_0}{4\pi} \right)^2 \gamma_I^2 \beta_e^2 \mu_B^2 S(S+1) (\gamma_M^{-6} + \Sigma \rho^2 \gamma_L^{-6}) \\ \times \left[ 4\tau_{c1} + \frac{3\tau_{c2}}{1 + (\omega_I - \omega_S)^2 \tau_{c2}^2} + \frac{3\tau_{c1}}{1 + \omega_I^2 \tau_{c1}^2} + \frac{6\tau_{c2}}{1 + \omega_S^2 \tau_{c2}^2} + \frac{6\tau_{c2}}{1 + (\omega_I + \omega_S)^2 \tau_{c2}^2} \right] \\ + \frac{1}{3} S(S+1) \left( \frac{A}{\hbar} \right)^2 \left[ \tau_{e1} + \frac{\tau_{e2}}{1 + (\omega_I - \omega_S)^2 \tau_{e2}^2} \right] \\ + \frac{1}{5} \left( \frac{\mu_0}{4\pi} \right)^2 \frac{\omega_I^2 \beta_e^4 \mu_B^4 S^2 (S+1)^2}{(3kT)^2 r_M^6} \left( 4\tau_{c2} + \frac{3\tau_r}{1 + \omega_I^2 \tau_r^2} \right) \quad (18.10)$$

$$\tau_{c1}^{-1} = T_{1e}^{-1} + \tau_r^{-1} + \tau_{\text{ex}}^{-1} \quad (18.11)$$

$$\tau_{c2}^{-1} = T_{2e}^{-1} + \tau_r^{-1} + \tau_{\text{ex}}^{-1} \quad (18.12)$$

$$\tau_{c1}^{-1} = T_{1e}^{-1} + \tau_{\text{ex}}^{-1} \quad (18.13)$$

$$\tau_{c2}^{-1} = T_{2e}^{-1} + \tau_{\text{ex}}^{-1}, \quad (18.14)$$

where, in the present case,  $r_M$  and  $r_L$  are the distances between the proton of interest and the Fe atom, and between the proton and the pyrrole carbon atom, respectively,  $\rho$  is the unpaired electron density at the pyrrole carbon atoms (Fig. 18.1b),  $(\frac{A}{\hbar})$  is the apparent hyperfine coupling constant,  $\omega_I$  and  $\omega_S$  are the Larmor frequencies of the nucleus and electron, respectively,  $T_{1e}$  and  $T_{2e}$  are the electron longitudinal and transverse relaxation times, respectively, and  $\tau_{\text{ex}}$  is the electron exchange time. The other parameters are as usual. In large molecules with highly resolved NMR spectra,  $T_{1e}, T_{2e} \ll \tau_r$ , and at high magnetic field,  $\omega_I^2 T_{1e}^2 \ll 1$ ,  $1 < \omega_S^2 T_{1e}^2$ , and  $1 < \omega_S^2 T_{2e}^2$ , Eqs. (18.7) and (18.8) are reduced to the following equations [85, 86]

$$R_{1\text{para}} = \frac{2}{15} \left( \frac{\mu_0}{4\pi} \right)^2 \gamma_I^2 \beta_e^2 \mu_B^2 S(S+1) (\gamma_M^{-6} + \Sigma \rho^2 \gamma_L^{-6}) T_{1e} \quad (18.15)$$

$$\begin{aligned} R_{2\text{para}} &= \frac{7}{15} \left( \frac{\mu_0}{4\pi} \right)^2 \gamma_I^2 \beta_e^2 \mu_B^2 S(S+1) (\gamma_M^{-6} + \Sigma \rho^2 \gamma_L^{-6}) T_{1e} \\ &\quad + \frac{1}{3} S(S+1) \left( \frac{A}{\hbar} \right)^2 T_{1e} + \frac{4}{5} \left( \frac{\mu_0}{4\pi} \right)^2 \frac{\omega_I^2 \beta_e^4 \mu_B^4 S^2 (S+1)^2}{(3kT)^2 r_M^6} \tau_r \end{aligned} \quad (18.16)$$

Equation (18.16) dictates that  $R_{2\text{para}}$  depends on the field strength due to the contribution of  $R_{\text{para}}^{\text{Curie}}$ , the third term on the right-hand side of the equation (see Sect. 18.4.2).

### 18.3 $^1\text{H}$ NMR Spectra of Myoglobin with 0, 1, 4, or 5 Unpaired Electrons

In this section,  $^1\text{H}$  NMR spectra of Mbs in a variety of oxidation, ligation, and spin states are overviewed to understand the relationship between the number of unpaired electrons and the spectral features. In addition, 400, 600, and 800 MHz  $^1\text{H}$  spectra of each form of the protein are compared with each other to observe the field dependence of the spectral parameters.

#### 18.3.1 Overview

400 MHz  $^1\text{H}$  spectra of Mb(CO), metMb(CN<sup>-</sup>), metMb(N<sub>3</sub><sup>-</sup>), deoxy Mb, and metMb(H<sub>2</sub>O) are shown in Fig. 18.2. Heme methyl (CH<sub>3</sub>) proton signals are often used as sensitive probes for the heme electronic structures of hemoproteins [6, 14]. In addition to ready observation of the signals with three-proton intensity, the  $\delta_{\text{para}}$  values of the hemoprotein provide a measure of the nonequivalence of the four pyrrole environment of the porphyrin ring, i.e., the in-plane asymmetry of the heme electronic structure, because there is a CH<sub>3</sub> group on each pyrrole (Fig. 18.1b), and delocalization of unpaired electron(s) from the heme  $\pi$ -system to the s orbital of the CH<sub>3</sub> protons necessary for the Fermi contact interaction occurs effectively through hyperconjugation [2, 10]. Comparison of the  $\delta_{\text{para}}$  values of the heme CH<sub>3</sub> proton signals between heme model compounds and hemoproteins in every oxidation/spin state indicated that the spread of the four signals is always much larger in the protein environment [6]. The spread of the four heme CH<sub>3</sub> proton signals in model compound is due to intrinsic in-plane asymmetry of the heme electronic structure, and hence, the increase in the spread of the signals in the protein reflects the asymmetric nature of the heme–protein linkage, which is relevant to regulation of heme Fe reactivity, and hence the protein function [2, 6, 14].

In the presence of a large spread of the four heme  $\text{CH}_3$  proton signals, the average shift of the signals is used as a measure of the electronic nature of the heme Fe atom in the protein. The average shift of the signals of diamagnetic  $\text{Mb}(\text{CO})$  is  $\sim 3$  ppm [87] (trace 2a), and those of paramagnetic  $\text{metMb}(\text{CN}^-)$  and  $\text{metMb}(\text{H}_2\text{O})$  are  $\sim 14$  [88] and  $\sim 75$  ppm [89, 90], respectively (traces 2B and E, respectively). Thus, the average shift of the paramagnetically shifted heme  $\text{CH}_3$  proton signals is roughly proportional to the number of unpaired electrons, i.e., the  $S$  value. The average shift of the signals of  $\text{metMb}(\text{N}_3^-)$ , i.e.,  $\sim 23$  ppm [91] (trace 2c), is somehow between those of  $\text{metMb}(\text{CN}^-)$  and  $\text{metMb}(\text{H}_2\text{O})$ , because of the intermediate ligand field strength of  $\text{N}_3^-$ , which renders the energy difference between the  $\text{Fe}^{3+}$  low-spin ( $S = 1/2$ ) and high-spin ( $S = 5/2$ ) states comparable to the thermal energy [91–94]. Finally, among the physiologically active forms of the protein, deoxy Mb is the least understood in terms of the molecular properties of its heme active site [81, 95–97]. Despite extensive efforts, the ground-state electronic structure of the  $\text{Fe}^{2+}$  high-spin ( $S = 2$ ) state of deoxy Mb remains to be elucidated [81]. Due to out-of-plane displacement of the Fe atom from the porphyrin plane in the penta-coordinated heme complex in the protein [77] (Fig. 18.1c), the average shift of the four heme  $\text{CH}_3$  proton signals of deoxy Mb, i.e.,  $\sim 15$  ppm [96], is rather small, while the signal of the axial His93  $\text{N}_\delta\text{H}$  proton is observed at  $\sim 77$  ppm [98] (trace 2d).

### 18.3.2 Diamagnetic Carbonmonoxy Form [ $\text{Mb}(\text{CO})$ ]

$\text{Mb}(\text{CO})$  is often considered as a model of  $\text{Mb}(\text{O}_2)$  that tends to be spontaneously oxidized to  $\text{metMb}(\text{H}_2\text{O})$  through a reaction known as autoxidation. In the absence of a unpaired electron,  $\text{Mb}(\text{CO})$  is just like an ordinary diamagnetic protein. So the benefit of the higher resolution in the spectrum recorded at higher magnetic field strength can be clearly witnessed in Fig. 18.4. The ring current effect of the porphyrin moiety of heme is considerably greater than that of the phenyl group of such as phenylalanine. As a result, the Val68  $\text{C}_\gamma\text{H}_3$  proton signal is resolved at  $\sim -2.5$  ppm [99], and signals due to heme 5, 10, 15, and 20-H protons (Fig. 18.1b) are resolved in a downfield-shifted region, i.e.,  $>\sim 9.5$  ppm [87]. Hence, the porphyrin  $\pi$ -system of heme itself can be considered as a sort of intrinsic shift reagent. Furthermore, some NH protons involved in intramolecular hydrogen bonding are also resolved below  $\sim 9.5$  ppm [99, 100].

### 18.3.3 Paramagnetic Deoxy Form (Deoxy Mb) with $S = 2$

The His93  $\text{N}_\delta\text{H}$  proton signal is resolved at  $\sim 77$  ppm [98] and the heme  $\text{CH}_3$  proton ones in the range of  $<\sim 20$  ppm [96] (trace 2d). The line widths of signals due to the His93  $\text{N}_\delta\text{H}$  and heme  $\text{CH}_3$  protons of the protein in a 400 MHz spectrum

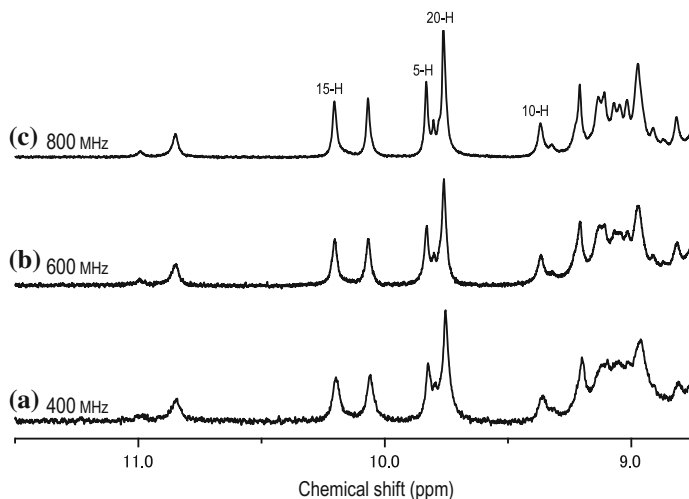


**Fig. 18.4** Portions, 8.8–11.5 ppm, of  $^1\text{H}$  NMR spectra of Mb(CO) in 90%  $^1\text{H}_2\text{O}/10\%$   $^2\text{H}_2\text{O}$ , pH 7.4, at 25 °C, recorded at  $^1\text{H}$  frequencies of 400 (a), 600 (b), and 800 MHz (c). Assignments of *meso* 5-, 10-, 15-, and 20-H proton (see Fig. 18.1b) signals are indicated in (c). The signals resolved below  $\sim 9.5$  ppm are due to NH protons involved in intramolecular hydrogen bonding [99, 100]

at 25 °C (trace 2d) are  $\sim 450$  and  $\sim 120$  Hz, respectively, and their relaxation times are  $<\sim 10$  ms. Consequently, as far as acquisition of only the paramagnetically shifted signals of the protein is concerned, the repetition time can be set considerably short, provided that the experimental setting is properly optimized. A drawback to such a measurement is that it will distort the spectral features of signals due to protein protons far away from the paramagnetic center because of the long relaxation times. A relatively large number of dummy scans prior to data acquisition will help to reduce the spectral distortion caused by short repetition times.

The unpaired electrons of the heme Fe atom of deoxy Mb are delocalized into the His93 imidazole through the Fe–His  $\sigma$  and  $\pi$  bonds, i.e.,  $\sigma$ - and  $\pi$ -delocalization, respectively [2, 10, 101]. The delocalization of the positive spin of an unpaired electron through the  $\sigma$ - and  $\pi$ -delocalization results in a net spin density of the opposite sign, that is, negative, and a positive spin on the His93  $\text{N}_e$  atom, respectively, and the spin on the His93  $\text{N}_e$  atom is further delocalized, through the  $\pi$  system of the imidazole ring, into the  $\text{N}_\delta$  atom, and then finally into the  $1s$  orbital of the His93  $\text{N}_\delta\text{H}$  hydrogen, through  $\sigma$  spin polarization [102]. As a result, the positive spin is delocalized into the  $1s$  orbital of the His93  $\text{N}_\delta\text{H}$  hydrogen through  $\sigma$ -delocalization, whereas the negative spin is delocalized through  $\pi$ -delocalization. Thus, the  $\delta_c$  value for the His93  $\text{N}_\delta\text{H}$  shift is determined as the difference between the  $\sigma$ - and  $\pi$ -delocalization, and hence, large positive  $\delta_c$  values

indicate that the  $\sigma$ -delocalization dominates over the  $\pi$ -delocalization [101]. The strength of the Fe–His bond is possibly affected by steric and electronic factors. La Mar and de Ropp [103] demonstrated, in a study involving horse radish ferrous peroxidase, that the proximal His  $N_{\delta}H$  proton shift is greatly affected by the hydrogen bond between the  $N_{\delta}H$  proton and a protein acceptor residue through its effect on the delocalization of the unpaired electron along the  $N_{\delta}$ –H bond, and that simultaneous consideration of changes of the stretching frequency of the Fe–His bond [104] and the axial His  $N_{\delta}H$  proton shift enables differentiation of the steric and electronic influences on the Fe–His bond [103]. In the case of deoxy Mb, the delocalization of the unpaired electron from the  $N_{\delta}$  atom to the 1s orbital of the  $N_{\delta}H$  hydrogen decreases with increasing strength of the His93–Leu89 H-bond because the interaction between the  $N_{\delta}H$  hydrogen and the unpaired electron density on the His93 imidazole ring is hampered by enhancement of polarization of the charge in the  $N_{\delta}$ –H bond. Furthermore, a change in the strength of the His93–Leu89 hydrogen bond (Fig. 18.1c) also influences the Fe–His bond strength in such a manner that the Fe–His bond becomes stronger with increasing His93–Leu89 hydrogen bond strength because of enhancement of the  $Fe \leftarrow His$   $\sigma$  donation. Consequently, the strengthening of the Fe–His bond through an increase in the His93–Leu89 H-bond strength results in an increase in the stretching frequency of the Fe–His bond and, inversely, a decrease in the His93  $N_{\delta}H$  shift [103].

In contrast to effective delocalization of unpaired electrons from the heme Fe atom to the His93 imidazole  $\pi$  system through the Fe–His bond, unpaired electron density delocalized from the Fe atom into the porphyrin  $\pi$  system in the penta-coordinated heme complex is considerably smaller than that in a hexa-coordinated one such as metMb(H<sub>2</sub>O) (see Sect. 18.3.6) due to the relatively weak electronic interaction between the Fe orbitals and the porphyrin  $\pi$  system in the former complex [102]. As a result, the heme CH<sub>3</sub> proton signals of deoxy Mb exhibit relatively small  $\delta_{para}$  values. In addition, the Val68 C<sub>γ</sub>H<sub>3</sub> proton signal is resolved in upfield-shifted region, i.e., <~−7 ppm [100], in the <sup>1</sup>H spectrum of deoxy Mb, due to magnetic anisotropy of the Fe<sup>2+</sup> high-spin state [95].

The signals of deoxy Mb increased dramatically with increasing the field strength (Fig. 18.5), and the field-dependent broadening was enhanced for signals of larger paramagnetic molecules [105]. According to the theory proposed by Gueron [83], there will be net polarization of the Fe electron spin magnetic moment that will be oriented along the direction of the external magnetic field. Modulation of this dipolar field due to the spin polarization (known as the “Curie spin”) through rotational diffusion will then introduce an extra field-dependent term into the expression for transverse relaxation (Eq. 18.16). Since the Curie spin contribution is proportional to the square of the magnetic field strength [83, 84], the benefit of higher resolution in a spectrum recorded at higher magnetic field strength is no longer expected for deoxy Mb.

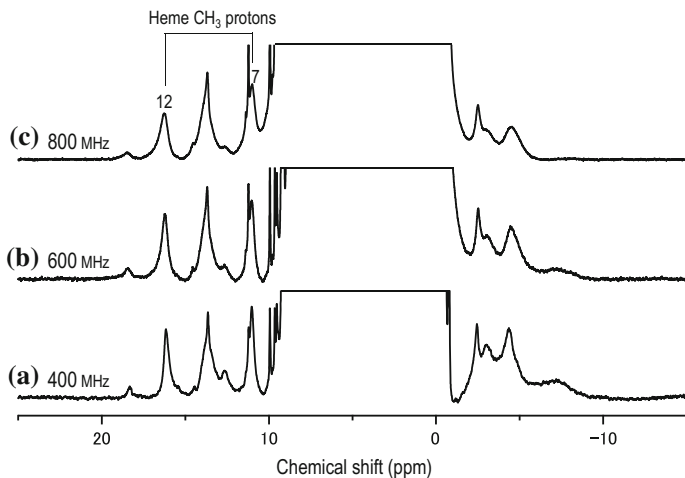


**Fig. 18.5** Portions,  $-15$  to  $25$  ppm, of  $^1\text{H}$  NMR spectra of deoxy Mb in  $90\%$   $^1\text{H}_2\text{O}/10\%$   $^2\text{H}_2\text{O}$ , pH  $7.4$ , at  $25$   $^\circ\text{C}$ , recorded at  $^1\text{H}$  frequencies of  $400$  (a),  $600$  (b), and  $800$  MHz (c). Assignments of heme  $7$ - and  $12\text{-CH}_3$  signals are indicated in (c) [96]

### 18.3.4 Paramagnetic Met-Cyano Form [MetMb(CN<sup>-</sup>)] with S = 1/2

Owing to the short spin-lattice relaxation time of electron ( $T_{1e}$ ), i.e.,  $\sim 2 \times 10^{-12}$  s [4, 20], and the large magnetic anisotropy of hexa-coordinated  $\text{Fe}^{3+}$  heme complexes with  $S = 1/2$  [106], metMb(CN<sup>-</sup>) exhibits well-resolved and relatively narrow signals useful for characterizing the electronic/molecular structure of its heme active site [14, 106]. The asymmetric nature of the heme–protein linkage can be readily characterized through analysis of the  $\delta_{\text{para}}$  values of the four heme CH<sub>3</sub> proton signals of metMb(CN<sup>-</sup>). The energy levels for the  $d_{xz}$  and  $d_{yz}$  orbitals are affected by the interaction with axial ligands, and a single unpaired electron resides in either the  $d_{xz}$  or  $d_{yz}$  orbital, whichever possesses the highest energy. Consequently, depending upon the relative energy of the  $d_{xz}$  and  $d_{yz}$  orbitals,  $\pi$  spin delocalization occurs into either pyrroles I, III or II, IV (Fig. 18.6). Since a diatomic cyanide ion is coordinated to the heme Fe atom with its orientation nearly normal as to the heme plane, its coordination does not affect the degree and pattern of the in-plane asymmetry of the heme electronic structure. Consequently, the energy levels for the  $d_{xz}$  and  $d_{yz}$  orbitals are predominantly affected by the orientation of the His93 imidazole ring, relative to the heme, through a repulsive interaction between the  $p_z$  orbital of the Fe-bound nitrogen atom of His93 imidazole and the  $d_{xz}$  or  $d_{yz}$  one of the heme Fe atoms (Fig. 18.6a). The Fe–His coordination bond is roughly along the heme normal, and hence, with the orientation of His93 imidazole, as shown in Fig. 18.6a [107], i.e., the projection of the His93 imidazole ring onto the heme plane is along the nitrogen atoms of pyrroles I and II, and the  $p_z$  orbital of the

Fe-bound nitrogen atom in the  $yz$  plane interact repulsively with the  $d_{yz}$  one, raising the energy level of  $d_{yz}$  orbital relative to that of the  $d_{xz}$  one (Fig. 18.6b). Consequently, the unpaired electron spin density delocalized from heme Fe atom into the pyrroles I and III  $\pi$ -system is much greater than that into pyrroles II and IV one, due to the unpaired electron delocalized from the singly occupied  $d_{yz}$  orbital directly to the former pyrroles. In contrast, the energy level of the  $d_{xz}$  orbital is higher than that of the  $d_{yz}$  one with the orientation of the His93 imidazole ring, of which the projection onto the heme plane is along the nitrogen atoms of pyrroles I and III, and the unpaired electron spin density delocalized from the heme Fe atom into the pyrroles II and IV  $\pi$ -system is greater than that into the pyrroles I and III one (Fig. 18.6c). Since the orientation of the His93 imidazole ring in Mb is similar to that illustrated in Fig. 18.6a [76, 77], the  $\delta_c$  values of the signals due to the heme  $\text{CH}_3$  groups at positions 2 and 12 are larger than those at positions 7 and 18.

The large magnetic anisotropy of metMb( $\text{CN}^-$ ) induces large  $\delta_{pc}$  values for signals arising from protons located close to the heme Fe atom, as can be witnessed by the observation of many resolved signals due to amino acid protons (Fig. 18.7). The combined use of NMR and X-ray studies allows determination of principal components and orientation, with respect to the heme, of the magnetic susceptibility tensor in the protein [106]. Formulation of the  $\delta_{pc}$  value is useful for detailed characterization of the local structure. In addition, due to the small Curie spin relaxation expected from the small  $S$  value, the signals of metMb( $\text{CN}^-$ ) exhibit

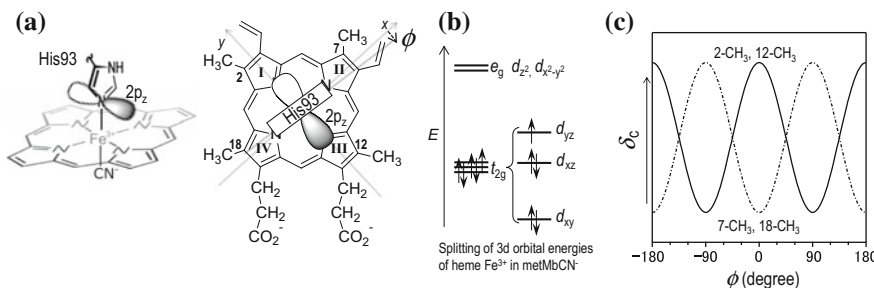


**Fig. 18.6** **a** Schematic representation of the orientation of the His93 imidazole ring and  $2p_z$  orbital of the His93  $N_e$  atom, with respect to the heme in Mb [76, 77]. Heme peripheral side chains are eliminated for clarity. Angle  $\phi$  is defined as the angle between the projection of the His93 imidazole plane onto the heme one and the  $\text{N}_{\text{II}}\text{--Fe}\text{--N}_{\text{IV}}$  axis. **b** Splitting of  $3d$  orbital energies of heme  $\text{Fe}^{3+}$  in metMb $\text{CN}^-$ . With  $\phi = \sim 0^\circ$ , the energy level of the  $3d_{yz}$  orbital is higher than that of the  $3d_{xz}$  one. Hence, electron spin density delocalized from the heme Fe atom into the pyrroles I and III  $\pi$ -system is much greater than that into the pyrroles II and IV one, due to unpaired electron delocalized from the singly occupied  $d_{yz}$  orbital directly to the former pyrroles. Coordination of  $\text{CN}^-$  with its orientation nearly normal to the heme plane does not significantly affect the energy levels of the  $3d_{yz}$  and  $3d_{xz}$  orbitals. **c** Semi-quantitative representation of the  $\phi$  dependence of the contact shift ( $\delta_c$ ) of heme 2- and 12- $\text{CH}_3$  (solid line), and 7- and 18- $\text{CH}_3$  (alternate long and short dash line) signals of metMb $\text{CN}^-$ . The  $\delta_c$  value was estimated with the assumption of fourfold symmetry in the electronic structure of the porphyrin moiety of heme

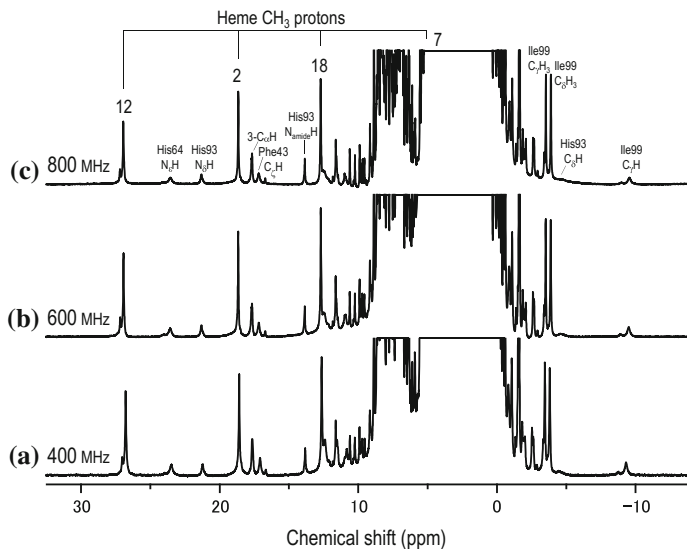


**Fig. 18.7** Portions,  $-13.9$  to  $32.5$  ppm, of  $^1\text{H}$  NMR spectra of metMb( $\text{CN}^-$ ) in  $90\%$   $^1\text{H}_2\text{O}/10\%$   $^2\text{H}_2\text{O}$ , pH  $7.4$ , at  $25^\circ\text{C}$ , recorded at  $^1\text{H}$  frequencies of  $400$  (a),  $600$  (b), and  $800$  MHz (c). Assignments of heme  $\text{CH}_3$  and some amino acid proton signals are indicated in (c)

small field-dependent broadening, i.e., the line widths of heme  $12\text{-CH}_3$  signals recorded at  $400$ ,  $600$ , and  $800$  MHz were  $39$ ,  $44$ , and  $66$  Hz, respectively (Fig. 18.7).

### 18.3.5 Paramagnetic Met-Azido Form [MetMb( $\text{N}_3^-$ )] with Mainly $S = \frac{1}{2}$

The met-azido derivatives of hemoproteins in general share the property that they exhibit a thermal equilibrium between low-spin,  $S = 1/2$ , and high-spin,  $S = 5/2$ , states, due to the intermediate field strength of  $\text{N}_3^-$  [92, 93]. Hence, changes in the population of the two spin states in the equilibrium provide a sensitive probe of the effective axial field strength. Among various techniques used to characterize the thermal spin equilibria in proteins, NMR is probably the most sensitive one and provides two separate probes of the average spin magnetization of the heme Fe atom, i.e., the heme  $\text{CH}_3$  proton and axial His93  $\text{N}_3^-$  proton  $\delta_{\text{para}}$  values [80, 91]. The thermal spin equilibrium in metMb( $\text{N}_3^-$ ) is manifested in the curvature or anti-Curie behavior of Curie plots, i.e., the plots of the  $\delta_{\text{obs}}$  values against the reciprocal of absolute temperature ( $1/T$ ), of these signals [80, 91]. Fitting of the Curie plots using the van't Hoff equation provides thermodynamic parameters of the equilibrium [80]. In the case of metMb( $\text{N}_3^-$ ), the high-spin contents at ambient

temperature are  $\sim 20\%$ , and the values of  $\sim -13 \text{ kJ mol}^{-1}$  and  $\sim -30 \text{ J } T^{-1} \text{ mol}^{-1}$  have been reported for the enthalpy change ( $\Delta H$ ) and molar entropy ( $\Delta S$ ), respectively [105].  $\Delta H$  is simply determined by the difference in thermodynamic energy between the low-spin and high-spin states, and  $\Delta S$  is determined by the structural and dynamic natures of the heme environment. The appreciable contribution of the high-spin state to the ground-state electron configuration of heme  $\text{Fe}^{3+}$  in metMb( $\text{N}_3^-$ ) leads to sizable Curie spin relaxation, which considerably broadens paramagnetically shifted signals with increasing magnetic field strength, e.g., the line width of the heme 12-CH<sub>3</sub> signal at 25 °C was  $\sim 140 \text{ Hz}$  at 400 MHz,  $\sim 160 \text{ Hz}$  at 600 MHz and  $\sim 200 \text{ Hz}$  at 800 MHz (Fig. 18.8).

### 18.3.6 Paramagnetic Met-Aquo Form [MetMb(H<sub>2</sub>O)] with S = 5/2

In the presence of five unpaired electrons in the system, the signals of metMb(H<sub>2</sub>O) are observed over the range of  $\sim 110$  to  $\sim -30 \text{ ppm}$  [89, 90]. Although the signals are considerably broad due to its relatively long  $T_{1e}$ , i.e.,  $< \sim 1 \times 10^{-10} \text{ s}$  [4, 20], owing to the large chemical shift range, the signals are fairly well separated (Fig. 18.9). In  $\text{Fe}^{3+}$  high-spin complexes, the relaxation process for the heme proton signals is modulated mainly by  $T_{1e}$ , which is in turn determined by modulation of the zero-field level of the complex [108, 109]. Some Mbs possess penta-coordinated

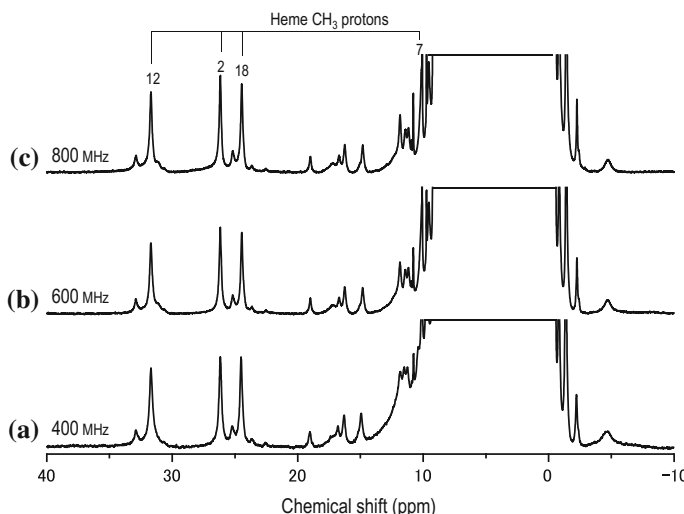


**Fig. 18.8** Portions,  $-10$  to  $40 \text{ ppm}$ , of  $^1\text{H}$  NMR spectra of metMb( $\text{N}_3^-$ ) in 90%  $^1\text{H}_2\text{O}/10\%$   $^2\text{H}_2\text{O}$ , pH 7.4, at 25 °C, recorded at  $^1\text{H}$  frequencies of 400 (a), 600 (b), and 800 MHz (c). Assignments of heme CH<sub>3</sub> signals are indicated in (c)

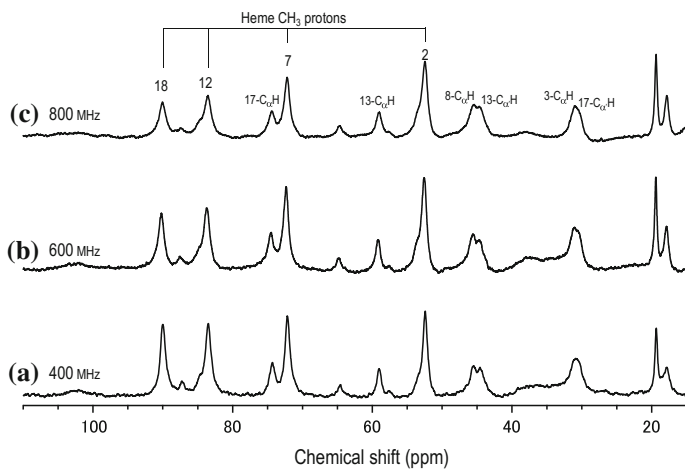


**Fig. 18.9** Portions, 15–110 ppm, of  $^1\text{H}$  NMR spectra of metMb( $\text{H}_2\text{O}$ ) in 90%  $^1\text{H}_2\text{O}/10\%$   $^2\text{H}_2\text{O}$ , pH 7.0, at 25 °C, recorded at  $^1\text{H}$  frequencies of 400 (a), 600 (b), and 800 MHz (c). Assignments of heme side chain proton signals are indicated in (c)

hemes in their  $\text{Fe}^{3+}$  high-spin complexes because of the absence of Fe-bound  $\text{H}_2\text{O}$  [110]. The heme proton signals of the Mbs with penta-coordinated  $\text{Fe}^{3+}$  high-spin hemes are narrower than those of the proteins with hexa-coordinated ones, because of the larger zero-field splitting in the former hemes, due to the lower symmetry in the ligand field around the heme Fe, which leads to the reduction of  $T_{1e}$  [110].

As indicated in trace 2e, signals resolved outside of the so-called diamagnetic envelope, i.e.,  $\sim 10$  to  $\sim 0$  ppm, are mostly due to heme peripheral side chain protons, and only a few signals due to amino acid protons are resolved. These spectral features indicated that  $\delta_c$  is large, while  $\delta_{pc}$  is relatively small. The  $\delta_{pc}$  contribution of metMb( $\text{H}_2\text{O}$ ) is due to magnetic anisotropy caused by zero-field splitting at the heme Fe and is in practice axially symmetric [111]. Since the Curie spin relaxation contribution is significant in high-spin metMb( $\text{H}_2\text{O}$ ), the line widths of paramagnetically shifted signals increased dramatically with increasing magnetic field strength, e.g., the line width of the heme 12- $\text{CH}_3$  signal at 25 °C was  $\sim 380$  Hz at 400 MHz,  $\sim 560$  Hz at 600 MHz, and  $\sim 950$  Hz at 800 MHz (Fig. 18.9).

## 18.4 NMR Measurements

### 18.4.1 NOEs in Paramagnetic Compounds

Despite the initial prejudice that the presence of unpaired electron(s) in paramagnetic molecules seriously diminishes the magnitude of NOEs through

“paramagnetic leakage,” and hence the observation of NOEs in paramagnetic systems is practically unrealistic, nowadays NOE measurements have been extensively applied for signal assignments and structural characterization in various paramagnetic systems [17]. The observation of relatively large NOEs in paramagnetic systems [88, 90, 107, 112, 113] could be rationalized on the basis of the nature of relaxation in the systems. The steady-state NOE in an isolated two-spin is given by Eq. (18.17)

$$\text{NOE}_{i \rightarrow j} = \frac{\sigma_{ij}}{\rho_j} \quad (18.17)$$

where  $\sigma_{ij}$  and  $\rho_j$  are the cross relaxation rate between the interacting protons,  $i$  and  $j$ , and the intrinsic spin–lattice relaxation rate of spin  $j$ , respectively. For paramagnetic system,  $\rho_j = \rho_{\text{dia}} + \rho_{\text{para}}$  ( $\rho_{\text{dia}}$  and  $\rho_{\text{para}}$  are the diamagnetic and paramagnetic contributions to  $\rho_j$ , respectively), and for a dominant paramagnetic relaxation ( $\rho_{\text{dia}} \ll \rho_{\text{para}}$ ), the steady-state NOEs are considerably reduced through paramagnetic leakage. Although the magnitude is relatively small, the observation of NOEs has been reported for most accessible oxidation and spin states of proteins.

Since  $\sigma_{ij}$  is given by

$$\sigma_{ij} = \frac{\hbar^2 \gamma_H^2}{10r^6} \left[ \frac{6\tau_c}{1 + 4\omega_H^2 \tau_c^2} - \tau_c \right] \quad (18.18)$$

where  $\gamma_H$  is the gyromagnetic ratio of proton,  $r$  is the distance between the protons,  $\tau_c$  is the correlation time that modulates the dipolar interaction between the two spins, and  $\omega_H$  is the Larmor frequency of proton. In the case of macromolecules, at high magnetic field and a long  $\tau_c$ , the molecular motion occurs in the slow motion limit ( $\omega_H^2 \tau_c^2 \gg 1$ ), and Eq. (18.19) is reduced to

$$\sigma_{ij} = -\frac{\hbar^2 \gamma_H^2 \tau_c}{10r^6} \quad (18.19)$$

Thus, the magnitude of the NOEs is simply proportional to  $\tau_c$ , and hence, as far as  $\sigma_{ij}$  is concerned, the observation of NOEs could be more promising for a larger molecule than for a small one. In practice, however, for a diamagnetic system with a large  $\tau_c$ , the detrimental effects of spin diffusion preclude the collection of any useful data in NOE studies. However, as demonstrated by La Mar and coworkers [90], paramagnetism not only undermines spin diffusion, and hence allows observation of specific NOEs for larger systems, but also improves the magnitude of NOEs with increasing  $\tau_c$ . Consequently, a large molecular size is likely to be an advantage rather than a disadvantage for observing useful NOEs in a paramagnetic system (Fig. 18.10).

The optimization of experimental parameters in 1D and 2D NOE measurements on rapidly relaxing systems, where  $\sigma_{ij}$  is much smaller than  $\rho_j$ , has been fully

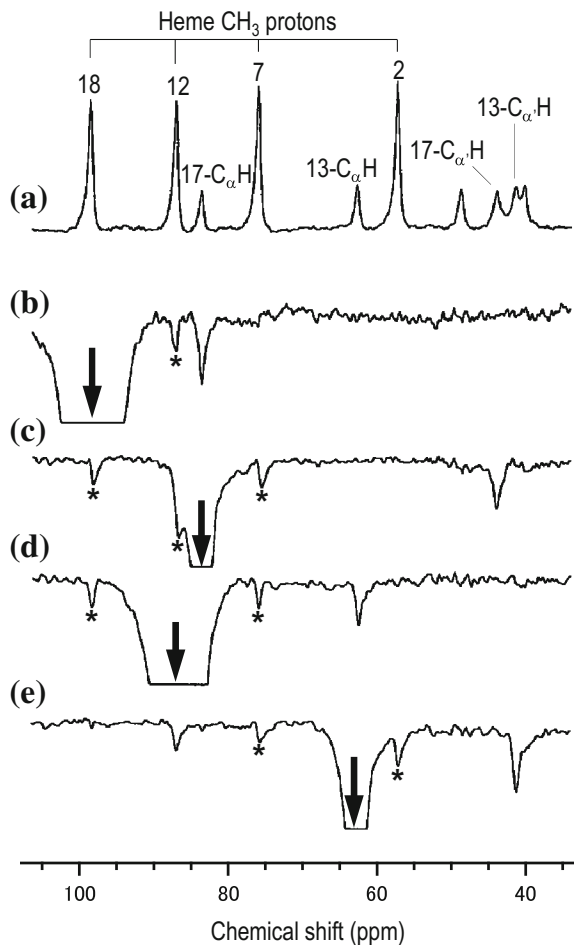


**Fig. 18.10** Downfield-shifted portions, 33–108 ppm, of the 500 MHz  $^1\text{H}$  NMR spectrum and NOE difference spectra of shark *Galeorhinus japonicas* metMb in  $^2\text{H}_2\text{O}$ , pH 7.0, at 35 °C. **a** Reference spectrum and **(b–e)** NOE difference spectra generated by subtracting the reference spectrum (**a**) from the spectrum recorded with saturation of the desired signal. Arrows indicate signals that are saturated, and peaks due to the decoupler pulse power spillage are indicated by asterisk. **b** Saturation of the 18- $\text{CH}_3$  signal exhibiting an NOE to a  $17-\text{C}_{\alpha}\text{H}$  one. **c** Saturation of  $17-\text{C}_{\alpha}\text{H}$  signal exhibiting an NOE to  $17-\text{C}_{\alpha}\text{H}$  one. **d** Saturation of the 12- $\text{CH}_3$  signal exhibiting an NOE to a  $13-\text{C}_{\alpha}\text{H}$  one. **e** Saturation of the 13- $\text{C}_{\alpha}\text{H}$  signal exhibiting an NOE to a  $13-\text{C}_{\alpha}\text{H}$  one. The spectra were taken from [91].

discussed [17, 90]. Considering  $\sigma_{ij} \ll \rho_j$  in a paramagnetic system, the magnitude of NOEs to be detected is quite small. In the spectrum of a paramagnetic molecule, fast relaxing signals exhibit large  $\delta_{\text{para}}$  and hence are resolved outside of the diamagnetic envelope. The observation of NOEs between a rapidly relaxing signal and a slowly relaxing one, resonating in the diamagnetic envelope, can be much more

effectively performed by conventional 1D NOE difference spectroscopy, provided that the signal-to-noise ratio of spectra is high enough to detect small NOEs. The accumulation of a large number of transients is a simple and easy approach to achieve a satisfactory signal-to-noise ratio. A short acquisition time due to a large spectral width and a relatively low digital resolution generally used for the observation of the spectra of a paramagnetic system, together with rapid repetition owing to fast paramagnetic relaxation, significantly contributes to effective data collection. In general, the detection of a small intensity change becomes more difficult as the signal broadens. Hence,  $T_2$  is often the determining factor for observing the effect; since  $T_2 \leq T_1$ , this is particularly true for signals with short  $T_1$ s.

Practically, there are also other limitations to the NOE method applied to paramagnetic systems. First, when saturating a fast relaxing signal by decoupler irradiation, the necessarily strong decoupler RF field irradiation can induce interfering off-resonance perturbations over a wide region of the spectrum [90]. In such a case, true NOEs may be difficult to distinguish from an off-resonance effect, often called “decoupler power spillage.” Comparison of the relative magnitudes of the effects under conditions of a reduced off-resonance effect and the determination of the actual power profile, as a function of offset, of the decoupler RF field irradiation can usually alleviate the problem. Second, observation of a small intensity difference in a broad signal demands a high dynamic range for the receiver and the digitizer. Selective excitation pulse sequences such as a simple 1–1 jump and return one [114] are helpful for suppressing the diamagnetic signals and allowing the full utilization of the dynamic range.

### 18.4.2 Hydrogen Exchange Rates

Biological macromolecules exhibit freedom of various structural changes, which are often relevant to their functions. Consequently, in order to elucidate the functions of the molecules, their static structures described by X-ray crystallographic coordinates must be augmented by their dynamic properties manifested in various spectroscopic data. Among a variety of spectroscopic techniques available for studies of their dynamic nature, NMR is quite unique in terms of not only its sensitivity as to dynamic structures exhibiting a wide range of timescales, but also its ability to provide information from which detailed descriptions of the dynamic structures of molecules in solution can be made.

Upon such dynamic studies involving NMR, it is important to consider the “NMR timescale.” For example, in the case of a molecule with interconvertible conformations, i.e., conformers I and II, which possibly exhibit two distinct NMR signals, whether or not we can observe two separate signals due to conformers I and II depends on the timescale of the interconversion. If the interconversion is sufficiently slow compared with the NMR timescale, signals I and II can be separately observed. On the other hand, if the interconversion is faster than the NMR timescale, a single signal representing the time-averaged conformation of conformers I

and II is observed. The NMR timescale of the interconversion between conformers I and II is given by the difference in resonance frequency between signals I and II ( $\Delta\delta_{I/II}$ ) and hence depends on magnetic field strength ( $B_0$ ) in such a manner that the NMR timescale increases with increasing  $B_0$  because  $\Delta\delta_{I/II}$  is proportional to  $B_0$ . Taking advantage of the large  $\delta_{\text{para}}$ , a paramagnetic counterpart possibly exhibits the  $\Delta\delta_{I/II}$  value that is large enough to allow observation of separate signals I and II. Thus, the NMR timescale can be controlled through the paramagnetic effect.

The exchange rates ( $k_{\text{ex}}$ ) of labile protons provide a wealth of information about the structural and functional features of proteins. For example, the X-ray structures of Mb [76, 77] suggested that the equilibrium structure does not possess channels large enough to permit ligand entry to and exit from the heme cavity. Theoretical calculations [115] have shown that the protein backbone and side chain motions of Mb modulate the energy barrier for  $O_2$  entry. Thus, the dynamics, as well as the structure of a protein, are relevant to its function [116, 117]. One of the most powerful methods for studying protein dynamics is the observation of the exchange behavior of labile protons, which are buried in the protein interior [118–120]. The timescale of exchange of labile protons can be considered as a measure of the local dynamic stability [116–120].

$k_{\text{ex}}$  is derived from solvent saturation transfer from the intrinsic spin-lattice relaxation time [ $T_{1(\text{int})}$ ] and the saturation factor ( $F$ ) given by [121]

$$F = \frac{I}{I_0} = T_{1(\text{int})}^{-1} \times \left( T_{1(\text{int})}^{-1} + \tau_i^{-1} \right)^{-1} \quad (18.20)$$

where  $I$  and  $I_0$  are the intensities of a labile proton signal with and without saturation of the  $^1H_2O$  signal, respectively.  $T_{1(\text{int})}$  is the intrinsic spin-lattice relaxation time, with which  $F$  is evaluated.  $\tau_i$  is the lifetime of the labile proton in the protein environment, and hence  $\tau_i^{-1} = k_{\text{ex}}$ . Consequently, independent measurements of  $T_{1(\text{int})}$  and  $F$  allow the determination of  $k_{\text{ex}}$ .

If  $T_{1(\text{int})}$  is independently known and remains constant over the pH range used,  $k_{\text{ex}}$  is obtained through Eq. (18.20').

$$k_{\text{ex}} = \tau_i^{-1} = T_{1(\text{int})}^{-1} \times (1 - F)F^{-1} \quad (18.20')$$

With the occurrence of exchange, and when  $T_{1(\text{int})}$  cannot be determined directly,  $k_{\text{ex}}$  is obtained through Eq. (18.21).

$$k_{\text{ex}} = T_{1(\text{int})}'^{-1} \times (1 - F) \quad (18.21)$$

where  $T_{1(\text{int})}'^{-1} = T_{1(\text{int})}^{-1} + \tau_i^{-1}$ . In such a case,  $T_{1(\text{int})}$  can be expressed as

$$T_{1(\text{int})}^{-1} = F \times T_{1(\text{int})}'^{-1} \quad (18.22)$$

$T_{1(\text{int})}$  can be measured as follows. At pH values where  $\tau_i$  of the labile proton is long compared with  $T_{1(\text{int})}$ , i.e.,  $T_{1(\text{int})} \ll \tau_i$ , a selective saturation recovery experiment with a pulse sequence for solvent suppression is performed. At pH values where  $\tau_i \approx T_{1(\text{int})}$ ,  $T_{1(\text{int})}^{\prime-1}$  is obtained by selective inversion recovery with the saturation of the  $\text{H}_2\text{O}$  signal at all times except during acquisition.

In general,  $k_{\text{ex}}$  is expressed as [118]

$$k_{\text{ex}} = k_A[\text{H}^+]^A + k_B[\text{OH}^-]^B + k_W[\text{H}_2\text{O}] \quad (18.23)$$

where  $k_A$ ,  $k_B$ , and  $k_W$  are the rate constants for  $\text{H}^+$ ,  $\text{OH}^-$ , and  $\text{H}_2\text{O}$  catalysis, respectively. Exponents  $A$  and  $B$  are at unity with  $k_A$  and  $k_B$  close to those observed for a model compound and are less than unity for protons buried in the protein interior and/or involved in hydrogen bonds [118]. When  $k_A$  and  $k_B$  are comparable in magnitude to each other, the pH value at the minimum  $k_{\text{ex}}$  is close to  $\sim 7$ . A change in either  $k_A$  or  $k_B$  alters the pH value at the minimum  $k_{\text{ex}}$  [118].

For example, the His93  $\text{N}_{\delta}\text{H}$  proton signal of deoxy Mb is observed at  $\sim 75$  ppm [96] (trace 2D). The His93  $\text{N}_{\delta}\text{H}$  proton of the protein is hydrogen-bonded to the carbonyl oxygen atom of Leu89, as illustrated in Fig. 18.1c, and exhibits  $T_{1(\text{int})} = \sim 15$  ms and  $k_{\text{ex}} = \sim 30 \text{ s}^{-1}$  at pH = 10.6 and 40 °C. Interestingly, the  $k_{\text{ex}}$  value of the His93  $\text{N}_{\delta}\text{H}$  protons of the subunits of the deoxy form of tetrameric human adult hemoglobin, i.e.,  $k_{\text{ex}} = \sim 10^{-4}\text{--}10^{-5} \text{ s}^{-1}$ , is several orders of magnitude smaller than that of deoxy Mb [122].

A 400 MHz  $^1\text{H}$  NMR spectrum of bovine metMbCN<sup>-</sup> at 25 °C is shown in Fig. 18.11. In the spectrum, His64  $\text{N}_{\epsilon}\text{H}$  and His93  $\text{N}_{\delta}\text{H}$  proton signals were

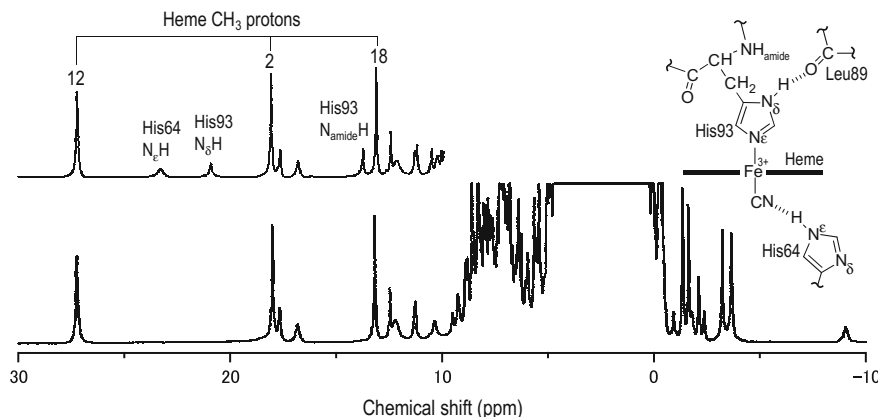


**Fig. 18.11** 400 MHz  $^1\text{H}$  NMR spectrum of bovine metMb ( $\text{CN}^-$ ) in 90%  $^1\text{H}_2\text{O}/10\%$   $^2\text{H}_2\text{O}$ , pH 7.0, at 25 °C. The downfield-shifted portion of the spectrum of the protein in  $^2\text{H}_2\text{O}$ , pH 7.0, at 25 °C is shown in the inset. Assignments of 2-, 12-, and 18- $\text{CH}_3$  signals and His64  $\text{N}_{\epsilon}\text{H}$ , His93  $\text{N}_{\delta}\text{H}$ , and His93  $\text{N}_{\text{amide}}\text{H}$  ones are shown in the spectrum. The location of these NH protons in the protein is shown in the inset. The spectra were taken from [123].

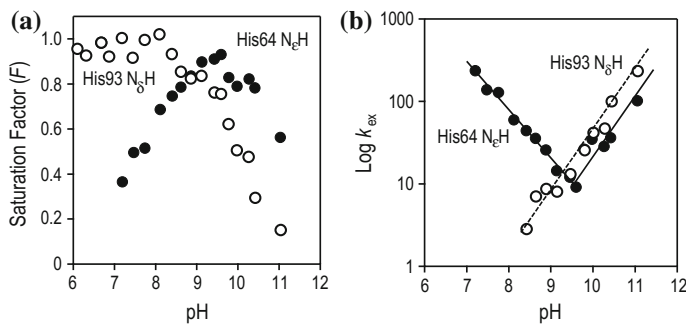


**Fig. 18.12** pH-profiles of **a** saturation factor ( $F$ ) and **b** logarithm of  $k_{\text{ex}}$  ( $\text{s}^{-1}$ ) for the His64 N<sub>e</sub>H (filled circle) and His93 N<sub>d</sub>H protons (open circle) in bovine metMbCN<sup>+</sup> in 90%  $^1\text{H}_2\text{O}/10\% ^2\text{H}_2\text{O}$  at 25 °C [123]. The exchange behavior of histidyl imidazole ring NH hydrogen atoms sharply reflects their local environment. The H<sup>+</sup> and OH<sup>-</sup> catalyses involve an attack at different sites of the neutral imidazole side chain, and both acid- and base-catalyzed exchanges were observed for the His64 N<sub>e</sub>H proton. On the other hand, only base-catalyzed exchange was observed for the His93 N<sub>d</sub>H proton because of the coordination of His93 to heme Fe, which precludes acid-catalyzed exchange

observed at 23.31 and 20.96 ppm, respectively, and exhibited  $T_{1(\text{int})}$  values of 8.4 and 22 ms, respectively [123]. The  $F$  values of the His64 N<sub>e</sub>H and His93 N<sub>d</sub>H protons of the protein at various pH values were measured (Fig. 18.12a), and then, the pH-profiles of the  $k_{\text{ex}}$  values of the protons were calculated from the  $F$  and  $T_{1(\text{int})}$  values [123] (Fig. 18.12b). The  $k_{\text{ex}}$  values of the His64 N<sub>e</sub>H and His93 N<sub>d</sub>H protons exhibited distinctly different pH-profiles. The pH-profile of the  $k_{\text{ex}}$  value of the His64 N<sub>e</sub>H proton reflected both acid- and base-catalyzed NH hydrogen exchange, with the minimum  $k_{\text{ex}}$  value at pH ~9.5. On the other hand, only the base-catalyzed exchange was manifested in the pH-profile of the  $k_{\text{ex}}$  value of His93 N<sub>d</sub>H hydrogen atom. Thus, the  $k_{\text{ex}}$  values of the NH protons provide valuable information about the dynamic nature of the heme cavity of the protein.

## 18.5 Concluding Remarks

This chapter has described the fundamentals of  $^1\text{H}$  NMR spectra of paramagnetic compounds. Using Mb as a reference compound, the spectral characteristics of paramagnetic compounds possessing a series of  $S$  values have been described in order to provide an overview of the effects of changes in the number of unpaired electrons on the spectral features. A few techniques applied to paramagnetic compounds, which provide widespread utility in life and material sciences, have also been described. As described in this chapter, the use of electron spin is opening up new horizons for NMR studies in life and material sciences.

**Acknowledgements** The authors are grateful to Professor Toshiyuki Tanaka (Graduate School of Life and Environmental Sciences, University of Tsukuba) for the use of a Bruker AVANCE III 800 spectrometer at TARA Center, University of Tsukuba.

## References

1. Wüthrich, K.: Structural studies of hemes and hemoproteins by nuclear magnetic resonance spectroscopy. *Struct. Bond.* **8**, 53–121 (1970)
2. La, M.G.N., Horrocks, W.D.W., Holm, R.H. (eds.): *NMR of Paramagnetic Molecules, Principles and Applications*. Academic Press, New York (1973)
3. Morrow, J.S., Gurd, F.R.N.: Nuclear magnetic resonance studies of hemoglobin: functional state correlations and isotopic enrichment strategies. *CRC Crit. Rev. Biochem.* **3**, 221–287 (1975)
4. Wüthrich, K.: *NMR in Biological Research: Peptides and Proteins*, Chap. 6. North-Holland Publishing, Amsterdam (1976)
5. Morishima, I., Ogawa, S., Inubushi, T., Iizuka, T.: Nuclear magnetic resonance studies of high-spin ferric hemoproteins. *Adv. Biophys.* **11**, 217–245 (1978)
6. La Mar, G.N.: Model compound as aids in interpreting NMR spectra of hemoproteins. In: Shulman, R.G. (ed.) *Biological Application of Magnetic Resonance*, pp. 305–343. Academic Press, New York (1979)
7. Inagaki, F., Miyazawa, T.: NMR analyses of molecular conformations and conformational equilibria with the lanthanide probe method. *Prog. NMR Spectrosc.* **14**, 67–111 (1981)
8. Keller, R.M., Wüthrich, K.: Multiple irradiation  $^1\text{H}$  NMR experiments with hemoproteins. *Biol. Magn. Reson.* **3**, 1–51 (1981)
9. Jarrettzky, O., Roberts, G.C.K.: *NMR in Molecular Biology*, Chap. III. Academic Press, New York, pp. 69–114 (1981)
10. Bertini, I., Luchinat, C.: *NMR of Paramagnetic Molecules in Biological Systems*. Benjamin/Cummings Publishing, Menlo Park (1986)
11. Satterlee, J.D.: MNR spectroscopy of paramagnetic haem proteins. *Annu. Rep. NMR Spectrosc.* **17**, 79–178 (1986)
12. Satterlee, J.D.: Proton NMR studies of biological problems involving paramagnetic heme proteins. *Met. Ions Biol. Syst.* **21**, 121–185 (1986)
13. Bertini, I., Turano, P., Vila, A.J.: Nuclear magnetic resonance of paramagnetic metalloproteins. *Chem. Rev.* **93**, 2833–2932 (1993)
14. Yamamoto, Y.: NMR study of active sites in paramagnetic haemoproteins. *Annu. Rep. NMR Spectrosc.* **36**, 1–77 (1998)
15. La Mar, G.N., Satterlee, J.D., de Ropp, J.S.: Nuclear magnetic resonance of hemoproteins. In: Kadish, K.M., Smith, K.M., Guilard, R. (eds.) *The Porphyrin Handbook*, pp. 185–298. Academic Press, San Diego (2000)
16. Bertini, I., Luchinat, C., Parigi, G.: *Solution NMR of Paramagnetic Molecules*. Elsevier, Amsterdam (2001)
17. de Ropp, J.S., Yu, L.P., La Mar, G.N.: 2D NMR of paramagnetic metalloenzymes: cyanide-inhibited horseradish peroxidase. *J. Biomol. NMR* **1**, 175–190 (1991)
18. Banci, L., Piccioli, M., Scozzafava, A.: Advances in the NMR investigation of paramagnetic molecules in solution. *Coord. Chem. Rev.* **120**, 1–28 (1992)
19. Ubbink, M., Worrall, J.A.R., Canters, G.W., Groenen, E.J.J., Huber, M.: Paramagnetic resonance of biological metal centers. *Annu. Rev. Biophys. Biomol. Struct.* **31**, 393–422 (2002)
20. Amesano, F., Banci, L., Piccioli, M.: NMR structures of paramagnetic metalloproteins. *Q. Rev. Biophys.* **38**, 167–219 (2005)

21. Bertini, I., Luchinat, C., Parigi, G., Pierattelli, R.: NMR spectroscopy of paramagnetic metalloproteins. *ChemBioChem* **6**, 1536–1549 (2005)
22. Tang, C., Iwahara, J., Clore, G.M.: Visualization of transient encounter complexes in protein-protein association. *Nature* **444**, 383–386 (2006)
23. Clore, G.M., Tang, C., Iwahara, J.: Elucidating transient macromolecular interactions using paramagnetic relaxation enhancement. *Curr. Opin. Struct. Biol.* **17**, 603–616 (2007)
24. Tang, C., Schwieters, C.D., Clore, G.M.: Open-to-closed transition in apo maltose-binding protein observed by paramagnetic NMR. *Nature* **449**, 1078–1082 (2007)
25. John, M., Schmitz, C., Park, A.Y., Dixon, N.E., Huber, T., Otting, G.: Sequence-specific and stereospecific assignment of methyl groups using paramagnetic lanthanides. *J. Am. Chem. Soc.* **129**, 13749–13757 (2007)
26. Pintacuda, G., John, M., Su, X.C., Otting, G.: NMR structure determination of protein-ligand complexes by lanthanide labeling. *Acc. Chem. Res.* **40**, 206–212 (2007)
27. Bertini, I., Luchinat, C., Parigi, G., Pierattelli, R.: Perspectives in paramagnetic NMR of metalloproteins. *Dalton Trans.* **29**, 3782–3790 (2008)
28. Clore, G.M., Iwahara, J.: Theory, practice, and applications of paramagnetic relaxation enhancement for the characterization of transient low-population states of biological macromolecules and their complexes. *Chem. Rev.* **109**, 4108–4139 (2009)
29. Otting, G.: Protein NMR using paramagnetic ions. *Annu. Rev. Biophys.* **39**, 387–405 (2010)
30. Bertini, I., Emsley, L., Lelli, M., Luchinat, C., Mao, J., Pintacuda, G.: Ultrafast MAS solid-state NMR permits extensive <sup>13</sup>C and <sup>1</sup>H detection in paramagnetic metalloproteins. *J. Am. Chem. Soc.* **132**, 5558–5559 (2010)
31. Iwahara, J., Clore, G.M.: Structure-independent analysis of the breadth of the positional distribution of disordered groups in macromolecules from order parameters for long, variable-length vectors using NMR paramagnetic relaxation enhancement. *J. Am. Chem. Soc.* **132**, 13346–13356 (2010)
32. Bertini, I., Giachetti, A., Luchinat, C., Parigi, G., Petoukhov, M.V., Pierattelli, R., Ravera, E., Svergun, D.I.: Conformational space of flexible biological macromolecules from average data. *J. Am. Chem. Soc.* **132**, 13553–13558 (2010)
33. Ravera, E., Salmon, L., Fragai, M., Parigi, G., Al-Hashimi, H., Luchinat, C.: Insights into domain-domain motions in proteins and RNA from solution NMR. *Acc. Chem. Res.* **47**, 3118–3126 (2014)
34. Yamaguchi, T., Sakae, Y., Zhang, Y., Yamamoto, S., Okamoto, Y., Kato, K.: Exploration of conformational spaces of high-mannose-type oligosaccharides by an NMR-validated simulation. *Angew. Chem. Int. Ed. Engl.* **53**, 10941–10944 (2014)
35. Brath, U., Swamy, S.I., Veiga, A.X., Tung, C.-C., Van Petegem, F., Erdélyi, M.: Paramagnetic ligand tagging to identify protein binding sites. *J. Am. Chem. Soc.* **137**, 11391–11398 (2015)
36. Schlagnitweit, J., Tang, M., Baias, M., Richardson, S., Schantz, S., Emsley, L.: Nanostructure of materials determined by relayed paramagnetic relaxation enhancement. *J. Am. Chem. Soc.* **137**, 12482–12485 (2015)
37. Matei, E., Gronenborn, A.M.: <sup>19</sup>F paramagnetic relaxation enhancement: a valuable tool for distance measurements in proteins. *Angew. Chem. Int. Ed. Engl.* **55**, 150–154 (2016)
38. Ravera, E., Luchinat, C., Parigi, G.: Basic facts and perspectives of Overhauser DNP NMR. *J. Magn. Reson.* **264**, 78–87 (2016)
39. Kato, K., Yamaguchi, T.: Paramagnetic NMR probes for characterization of the dynamic conformations and interactions of oligosaccharides. *Glycoconj. J.* **32**, 505–513 (2015)
40. Feintuch, A., Otting, G., Goldfarb, D.: Gd<sup>3+</sup> spin labeling for measuring distances in biomacromolecules: why and how? *Methods Enzymol.* **563**, 415–457 (2015)
41. Bertmer, M.: Paramagnetic solid-state NMR of materials. *Solid State Nucl. Magn. Reson.* **81**, 1–7 (2017)
42. Chen, J.L., Wang, X., Yang, F., Cao, C., Otting, G., Su, X.C.: 3D structure determination of an unstable transient enzyme intermediate by paramagnetic NMR spectroscopy. *Angew. Chem. Int. Ed. Engl.* **55**, 13744–13748 (2016)

43. Pilla, K.B., Otting, G., Huber, T.: Pseudocontact shift-driven iterative resampling for 3D structure determinations of large proteins. *J. Mol. Biol.* **428**, 522–532 (2016)
44. Orton, H.W., Kuprov, I., Loh, C.-T., Otting, G.: Using paramagnetism to slow down nuclear relaxation in protein NMR. *J. Phys. Chem. Lett.* **7**, 4815–4818 (2016)
45. Pilla, K.B., Otting, G., Huber, T.: 3D computational modeling of proteins using sparse paramagnetic NMR data. *Methods Mol. Biol.* **1526**, 3–21 (2017)
46. Can, T.V., Ni, Q.Z., Griffin, R.G.: Mechanisms of dynamic nuclear polarization in insulating solids. *J. Magn. Reson.* **253**, 23–35 (2015)
47. Su, Y., Andreas, L., Griffin, R.G.: Magic angle spinning NMR of proteins: high-frequency dynamic nuclear polarization and  $^1\text{H}$  detection. *Annu. Rev. Biochem.* **84**, 465–497 (2015)
48. Matsuki, Y., Idehara, T., Fukazawa, J., Fujiwara, T.: Advanced instrumentation for DNP-enhanced MAS NMR for higher magnetic fields and lower temperatures. *J. Magn. Reson.* **264**, 107–115 (2016)
49. Comment, A.: Dissolution DNP for *in vivo* preclinical studies. *J. Magn. Reson.* **264**, 39–48 (2016)
50. McConnell, H.M., Holm, C.H.: Proton resonance shifts in nickelocene. *J. Chem. Phys.* **27**, 314–315 (1957)
51. McConnell, H.M., Holm, C.H.: Proton resonance shifts in paramagnetic metal aromatic complexes. *J. Chem. Phys.* **28**, 749–750 (1958)
52. Bloembergen, N.: Proton relaxation times in paramagnetic solutions. *J. Chem. Phys.* **27**, 572–573 (1957)
53. McConnell, H.M., Chesnut, D.B.: Theory of isotropic hyperfine interactions in  $\pi$ -electron radicals. *J. Chem. Phys.* **28**, 107–117 (1958)
54. McConnell, H.M., Robertson, R.E.: Isotropic nuclear resonance shifts. *J. Chem. Phys.* **29**, 1361–1365 (1958)
55. Karplus, M.: Contact electron-spin coupling of nuclear magnetic moments. *J. Chem. Phys.* **30**, 11–15 (1959)
56. Abragam, A.: *The Principles of Nuclear Magnetism*. Oxford University Press, Oxford (1961)
57. Karplus, M., Fraenkel, G.K.: Theoretical interpretation of carbon-13 hyperfine interactions in electron spin resonance spectra. *J. Chem. Phys.* **35**, 1312–1323 (1961)
58. Fitzgerald, R.J., Drago, R.S.: Contact-shift studies and delocalization mechanisms of nickel (II)-benzylamine complexes. *J. Am. Chem. Soc.* **89**, 2879–2883 (1967)
59. Fitzgerald, R.J., Drago, R.S.: Contact-shift studies, delocalization mechanisms, and extended Hückel calculations of nickel(II)-alkylamine complexes. *J. Am. Chem. Soc.* **90**, 2523–2527 (1968)
60. Kurland, R., McGarvey, B.R.: Isotropic NMR shifts in transition metal complexes: the calculation of the Fermi contact and pseudocontact terms. *J. Magn. Reson.* **2**, 286–301 (1970)
61. Abragam, A., Bleaney, B.: *Electron Paramagnetic Resonance of Transition Metal Ions*. Oxford University Press, Oxford (1970)
62. Schwarzhans, K.E.: NMR spectroscopy of paramagnetic complexes. *Angew. Chem. Int. Ed. Engl.* **9**, 946–953 (1970)
63. Crans, D.C., Yang, L., Gaidamauskas, E., Khan, R., Jin, W., Simonis, U.: Applications of paramagnetic NMR spectroscopy for monitoring transition metal complex stoichiometry and speciation. In: Telser, J. (ed.) *Paramagnetic Resonance of Metallobiomolecules*, ACS Book Series 858, pp. 304–326. American Chemical Society, Washington (2003)
64. Bertini, I., Luchinat, C., Parigi, G., Ravera, E.: *NMR of Paramagnetic Molecules, Applications to Metallobiomolecules and Models*, 2nd edn. Elsevier Science, Amsterdam (2016)
65. Walker, F.A.: Magnetic spectroscopic (EPR, ESEEM, Mössbauer, MCD and NMR) studies of low-spin ferriheme centers and their corresponding heme proteins. *Coord. Chem. Rev.* **185–186**, 471–534 (1999)

66. Kendrew, J.C., Bodo, G., Dintzis, H.M., Parrish, R.G., Wyckoff, H., Phillips, D.C.: A three-dimensional model of the myoglobin molecule obtained by x-ray analysis. *Nature* **181**, 662–666 (1958)
67. Kowalsky, A.: Nuclear magnetic resonance studies of cytochrome *c*. Possible electron delocalization. *J. Biol. Chem.* **237**, 1807–1819 (1962)
68. Shulman, R.G., Wüthrich, K., Yamane, T., Antonini, E., Brunori, M.: Nuclear magnetic resonances of reconstituted myoglobins. *Proc. Natl. Acad. Sci. U S A* **63**, 623–628 (1969)
69. Wüthrich, K., Shulman, R.G., Peisach, J.: High-resolution proton magnetic resonance spectra of sperm whale cyanometmyoglobin. *Proc. Natl. Acad. Sci. U S A* **60**, 373–380 (1968)
70. Ogawa, S., Shulman, R.G., Yamane, T.: High resolution nuclear magnetic resonance spectra of hemoglobin. I. The cyanide complexes of  $\alpha$  and  $\beta$  chains. *J. Mol. Biol.* **70**, 291–300 (1972)
71. La Mar, G.N., Budd, D.L., Viscio, D.B., Smith, K.M., Langry, K.C.: Proton nuclear magnetic resonance characterization of heme disorder in hemoproteins. *Proc. Natl. Acad. Sci. U S A* **75**, 5755–5759 (1978)
72. Morishima, I., Iizuka, T.: Nuclear magnetic resonance studies of hemoproteins. Unusual temperature dependence of hyperfine shifts and spin equilibrium in ferric myoglobin and hemoglobin derivatives. *J. Am. Chem. Soc.* **96**, 5279–5283 (1974)
73. Tolman, J.R., Flanagan, J.M., Kennedy, M.A., Prestegard, J.H.: Nuclear magnetic dipole interactions in field-oriented proteins: Information for structure determination in solution. *Proc. Natl. Acad. Sci. U S A* **92**, 9279–9283 (1995)
74. Tjandra, N., Omichinski, J.G., Gronenborn, A.M., Clore, G.M., Bax, A.: Use of dipolar  $^1\text{H}$ - $^{15}\text{N}$  and  $^1\text{H}$ - $^{13}\text{C}$  couplings in the structure determination of magnetically oriented macromolecules in solution. *Nat. Struct. Biol.* **4**, 732–738 (1997)
75. Antonini, E., Brunori, M.: Hemoglobin and Myoglobin in Their Reactions with Ligands. North Holland Publishing, Amsterdam (1971)
76. Takano, T.: Structure of myoglobin refined at 2.0 Å resolution. I. Crystallographic refinement of metmyoglobin from sperm whale. *J. Mol. Biol.* **110**, 537–568 (1977)
77. Takano, T.: Structure of myoglobin refined at 2.0 Å resolution. II. Structure of deoxy myoglobin from sperm whale. *J. Mol. Biol.* **110**, 569–584 (1977)
78. Vojtechovský, J., Chu, K., Berendzen, J., Sweet, R.M., Schlichting, I.: Crystal structures of myoglobin-ligand complexes at near-atomic resolution. *Biophys. J.* **77**, 2153–2174 (1999)
79. Hong, S., Sutherlin, K.D., Park, J., Kwon, E., Siegler, M.A., Solomon, E.I., Nam, W.: Crystallographic and spectroscopic characterization and reactivities of a mononuclear non-haem iron(III)-superoxido complex. *Nat. Commun.* **5**, 5440–5446 (2014)
80. Neya, S., Funasaki, N.: Proton nuclear magnetic resonance investigation of the spin-state equilibrium of the  $\alpha$  and  $\beta$  subunits in intact azidomethemoglobin. *Biochemistry* **25**, 1221–1226 (1986)
81. Shibata, T., Kanai, Y., Nishimura, R., Xu, L., Moritaka, Y., Suzuki, A., Neya, S., Nakamura, M., Yamamoto, Y.: Characterization of ground state electron configurations of high-spin quintet ferrous heme iron in deoxy myoglobin reconstituted with trifluoromethyl group-substituted heme cofactors. *Inorg. Chem.* **55**, 12128–12136 (2016)
82. Solomon, I.: Relaxation processes in a system of two spins. *Phys. Rev.* **99**, 559–565 (1955)
83. Gueron, M.: Nuclear relaxation in macromolecules by paramagnetic ions: a novel mechanism. *J. Magn. Reson.* **19**, 58–66 (1975)
84. Vega, A.J., Fiat, D.: Nuclear relaxation processes of paramagnetic complexes the slow-motion case. *Mol. Phys.* **31**, 347–355 (1976)
85. Unger, S.W., Jue, T., La Mar, G.N.: Proton NMR dipolar relaxation by delocalized spin density in low-spin ferric porphyrin complexes. *J. Magn. Reson.* **61**, 448–456 (1985)
86. Yamamoto, Y.: Analysis of  $^{13}\text{C}$  relaxation of heme peripheral methyl group in ferric low-spin myoglobin. *J. Magn. Reson. B* **103**, 72–76 (1994)

87. Mabbutt, B.C., Wright, P.E.: Assignment of heme and distal amino acid resonances in the  $^1\text{H}$ -NMR spectra of the carbon monoxide and oxygen complexes of sperm whale myoglobin. *Biochim. Biophys. Acta* **832**, 175–185 (1985)
88. Emerson, S.D., La Mar, G.N.: Solution structural characterization of cyanometmyoglobin: resonance assignment of heme cavity residues by two-dimensional NMR. *Biochemistry* **29**, 1545–1556 (1990)
89. La Mar, G.N., Budd, D.L., Smith, K.M., Langry, K.C.: Nuclear magnetic resonance of high-spin ferric hemoproteins. Assignment of proton resonances in met-aquo myoglobins using deuterium-labeled hemes. *J. Am. Chem. Soc.* **102**, 1822–1827 (1980)
90. Unger, S.W., Lecomte, J.T.J., La Mar, G.N.: The utility of the nuclear Overhauser effect for peak assignment and structure elucidation in paramagnetic proteins. *J. Magn. Reson.* **64**, 521–526 (1985)
91. Yamamoto, Y., Chujo, R., Suzuki, T.: NMR study of *Galeorhinus japonicus* myoglobin.  $^1\text{H}$ -NMR evidence for a structural alteration on the active site of *G. japonicus* myoglobin upon azide ion binding. *Eur. J. Biochem.* **198**, 285–291 (1991)
92. Beetlesone, J., George, P.: A magnetochemical study of equilibria between high and low spin states of metmyoglobin complexes. *Biochemistry* **3**, 707–714 (1964)
93. Iizuka, T., Kotani, M.: Analysis of a thermal equilibrium phenomenon between high-spin and low-spin states of ferrimyoglobin azide. *Biochim. Biophys. Acta* **154**, 417–419 (1968)
94. Neya, S., Morishima, I.: Interaction of methemoglobin with inositol hexaphosphate. Presence of the T state in human adult methemoglobin in the low spin state. *J. Biol. Chem.* **256**, 793–798 (1981)
95. Yamamoto, Y., Iwafune, K., Chujo, R., Inoue, Y., Imai, K., Suzuki, T.:  $^1\text{H}$ -NMR comparative study of the active site in shark (*Galeorhinus japonicus*), horse, and sperm whale deoxy myoglobins. *J. Biochem.* **112**, 414–420 (1992)
96. La Mar, G.N., Davis, L., Johnson, R.D., Smith, W.S., Hauksson, J.B., Budd, D.L., Dalichow, F., Langry, K.C., Morris, I.K., Smith, K.M.: Nuclear magnetic resonance investigation of the electronic structure of deoxymyoglobin. *J. Am. Chem. Soc.* **115**, 3869–3876 (1993)
97. Bertin, I., Luchinat, C., Turano, P., Battaini, G., Casella, L.: The magnetic properties of myoglobin as studied by NMR spectroscopy. *Chem. Eur. J.* **9**, 2316–2322 (2003)
98. La Mar, G.N., Budd, D.L., Goff, H.: Assignment of proximal histidine proton NMR peaks in myoglobin and hemoglobin. *Biochem. Biophys. Res. Commun.* **77**, 104–110 (1977)
99. Thériault, Y., Pochapsky, T.C., Dalvit, C., Chiu, M.L., Sligar, S.G., Wright, P.E.:  $^1\text{H}$  and  $^{15}\text{N}$  resonance assignments and secondary structure of the carbon monoxide complex of sperm whale myoglobin. *J. Biomol. NMR* **4**, 491–504 (1994)
100. Yamamoto, Y.:  $^1\text{H}$  NMR probes for inter-segmental hydrogen bonds in myoglobins. *J. Biochem.* **120**, 126–132 (1996)
101. Bougault, C.M., Dou, Y., Ikeda-Saito, M., Langry, K.C., Smith, K.M., La Mar, G.N.: Solution  $^1\text{H}$  NMR study of the electronic structure and magnetic properties of high-spin ferrous or deoxy myoglobins. *J. Am. Chem. Soc.* **120**, 2113–2123 (1998)
102. Nishimura, R., Shibata, T., Tai, H., Ishigami, I., Yanagisawa, S., Ogura, T., Neya, S., Suzuki, A., Yamamoto, Y.: Effect of the electron density of the heme Fe atom on the Fe-histidine coordination bond in deoxy myoglobin. *Bull. Chem. Soc. Jpn.* **87**, 905–911 (2014)
103. La Mar, G.N., de Ropp, J.S.: Proton NMR characterization of the state of protonation of the axial imidazole in reduced horseradish peroxidase. *J. Am. Chem. Soc.* **104**, 5203–5206 (1982)
104. Matsukawa, S., Mawatari, K., Yoneyama, Y., Kitagawa, T.: Correlation between the iron-histidine stretching frequencies and oxygen affinity of hemoglobins. A continuous strain model. *J. Am. Chem. Soc.* **107**, 1108–1113 (1985)
105. Johnson, M.E., Fung, L.W.-M., Ho, C.: Magnetic field and temperature induced line broadening in the hyperfine-shifted proton resonances of myoglobin and hemoglobin. *J. Am. Chem. Soc.* **99**, 1245–1250 (1977)

106. Emerson, S.D., La Mar, G.N.: NMR determination of the orientation of the magnetic susceptibility tensor in cyanometmyoglobin: a new probe of steric tilt of bound ligand. *Biochemistry* **29**, 1556–1566 (1990)
107. Yamamoto, Y., Nanai, N., Chujo, R., Suzuki, T.: Heme methyl hyperfine shift pattern as a probe for determining the orientation of the functionally relevant proximal histidyl imidazole with respect to the heme in hemoproteins. *FEBS Lett.* **264**, 113–116 (1990)
108. La Mar, G.N., Walker, F.A.: Proton nuclear magnetic resonance line widths and spin relaxation in paramagnetic metalloporphyrins of chromium(III), manganese(III), and iron (III). *J. Am. Chem. Soc.* **95**, 6950–6956 (1973)
109. La Mar, G.N., de Ropp, J.S., Smith, K.M., Langry, K.C.: Proton nuclear magnetic resonance investigation of the electronic structure of compound I of horseradish peroxidase. *J. Biol. Chem.* **256**, 237–243 (1981)
110. Yamamoto, Y., Osawa, A., Inoue, Y., Chujo, R.: A  $^1\text{H}$ -NMR study of electronic structure of the active site of *Galeorhinus japonicus*. *Eur. J. Biochem.* **192**, 225–229 (1990)
111. Kao, Y.-H., Lecomte, J.T.J.: Determination of the zero-field splitting constant for proton NMR chemical shift analysis in metaquomyoglobin. The dipolar shift as a structural probe. *J. Am. Chem. Soc.* **115**, 9754–9762 (1993)
112. Trewella, J., Wright, P.E., Appleby, C.A.: Molecular basis for proton-dependent anion binding by soybean leghaemoglobin *a*. *Nature* **280**, 87–88 (1979)
113. Johnson, R.D., Ramaprasad, S., La Mar, G.N.: A method of assigning functionally relevant amino acid residue resonances in paramagnetic hemoproteins using proton NOE measurements. *J. Am. Chem. Soc.* **105**, 7205–7206 (1983)
114. Plateau, P., Guérón, M.: Exchangeable proton NMR without base-line distortion, using new strong-pulse sequences. *J. Am. Chem. Soc.* **104**, 7310–7311 (1982)
115. Case, D.A., Karplus, M.: Dynamics of ligand binding to heme proteins. *J. Mol. Biol.* **132**, 343–368 (1979)
116. Karplus, M., McCammon, J.A.: The internal dynamics of globular proteins. *CRC Crit. Rev. Biochem.* **9**, 293–349 (1981)
117. McCammon, J.A., Karplus, M.: The dynamic picture of protein structure. *Acc. Chem. Res.* **16**, 187–193 (1983)
118. Woodward, C.K., Hilton, B.D.: Hydrogen exchange kinetics and internal motions in proteins and nucleic acids. *Annu. Rev. Biophys. Bioeng.* **8**, 99–127 (1979)
119. Krishna, M.M.G., Hoang, L., Lin, Y., Englander, S.W.: Hydrogen exchange methods to study protein folding. *Methods* **34**, 51–64 (2004)
120. Anthos, N.J., Clore, G.M.: Visualizing transient dark states by NMR spectroscopy. *Q. Rev. Biophys.* **48**, 35–116 (2015)
121. Lecomte, J.T.J., La Mar, G.N.: Proton NMR study of labile proton exchange in the heme cavity as a probe for the potential ligand entry channel in myoglobin. *Biochemistry* **24**, 7388–7395 (1985)
122. Han, K.-H., La Mar, G.N.: Nuclear magnetic resonance study of the isotope exchange of the proximal histidyl ring labile protons in hemoglobin A. The exchange rates and mechanisms of individual subunits in deoxy and oxy-hemoglobin. *J. Mol. Biol.* **189**, 541–552 (1986)
123. Yamamoto, Y., Kurihara, N., Egawa, T., Shimada, H., Ishimura, Y.: Hydrogen bonding interaction of the amide group of Asn and Gln at distal E7 of bovine myoglobin with bound-ligand and its functional consequences. *Biochim. Biophys. Acta* **1433**, 27–44 (1999)

# Chapter 19

## NMR of Quadrupole Nuclei in Organic Compounds

Kazuhiko Yamada

**Abstract** General aspects of nuclear magnetic resonance (NMR) of quadrupole nuclei in organic solids, including theoretical background on quadrupole interactions and analysis of the characteristic line shapes that arise from quadrupole and/or chemical shift interactions, are described. Two theoretical approaches for spectral simulations, the perturbation method, and the direct diagonalization method, are discussed with examples of  $^{17}\text{O}$  ( $I = 5/2$ ),  $^{33}\text{S}$  ( $I = 3/2$ ), and  $^{79/81}\text{Br}$  ( $I = 3/2$ ) solid-state NMR analysis of organic compounds, as well as some examples of inorganic compounds with larger quadrupole interactions. When the magnitude of the quadrupole interactions is smaller than that of the Zeeman interactions, the perturbation method, in which equations can be definitively obtained to express the first- and second-order quadrupole interactions under static or magic-angle spinning conditions, is applicable. Otherwise, the direct diagonalization method, in which the combined Zeeman and quadrupole Hamiltonian is numerically calculated to derive probabilities for each transition, must be applied for spectral simulations. Several experimental techniques used to obtain NMR spectra broadened by large quadrupole interactions are briefly described.

**Keywords** Solid-state NMR • Quadrupole nuclei • Field-swept NMR  
Frequency-swept NMR

### 19.1 Introduction

Almost all the atoms in the periodic table exhibit nonzero spin quantum number ( $I$ ), and it is therefore theoretically possible to obtain NMR spectra for them. In fact, however, accessible NMR nuclei are typically limited to those with  $I = \frac{1}{2}$ , such as

---

K. Yamada (✉)

Interdisciplinary Science Unit, Multidisciplinary Sciences Cluster,  
Research and Education Faculty, Kochi University, Oko Campus,  
Nankoku, Kochi 783-8505, Japan  
e-mail: kyamada@kochi-u.ac.jp

$^1\text{H}$ ,  $^{13}\text{C}$ , and  $^{15}\text{N}$ . It is important to note that most of the atoms in the periodic table are quadrupole nuclei ( $I > 1/2$ ), which may give rise to additional nuclear spin interactions known as quadrupole interactions [1, 2]. The NMR experiments of quadrupole nuclei in organic compounds are much more difficult than those for inorganic compounds since the magnitude of the former quadrupole interactions tends to be larger, as will be discussed later. Nevertheless, thanks to recent developments in NMR technology, the number of accessible quadrupole nuclei of organic compounds has gradually increased, and the research areas to which solid-state NMR of quadrupole nuclei can be applied have undoubtedly expanded in the past decade.

Solid-state NMR spectra of quadrupole nuclei in organic compounds generally exhibit characteristic line shapes due to quadrupole interactions [3–5]. Unlike in cases where  $I = 1/2$ , sharp NMR signals may not be obtained, even if a standard magic-angle spinning (MAS) method is introduced. Thus, it is common to apply spectral simulation for such complicated NMR spectra in order to extract NMR parameters. More specifically, a theoretical NMR spectrum is calculated on the basis of Hamiltonians that express the proper nuclear spin interactions under the relevant experimental conditions, and the NMR parameters are input and varied until the theoretical line shape is in consistent with the experimental one. This is one of the most basic approaches for the analysis of NMR spectra of quadrupole nuclei in organic compounds. However, there is very little literature available in which the details of this technique are explained for graduated students and young scientists. Consequently, in this chapter, the experimental and theoretical aspects of solid-state NMR analysis of quadrupole nuclei in organic compounds, and spectral simulations in particular are presented. I hope that this review will serve as a guide for analyzing the NMR spectra of quadrupole nuclei in organic solids.

## 19.2 Theoretical Background of Quadrupole Interactions

In cases where  $I > 1/2$ , i.e., quadrupole nuclei, there is an additional nuclear spin interaction between the quadrupole moment and the electric field gradient (EFG) that a molecule forms [1, 2]. This nuclear spin interaction is called a quadrupole interaction and can be expressed by a second-rank tensor since it has anisotropy (in the same way as other nuclear spin interactions, such as chemical shift (CS) interactions, dipole–dipole interactions, and indirect spin–spin interactions). Two independent NMR parameters, termed the quadrupole coupling constant, denoted as  $e^2qQh^{-1}$  or  $C_Q$  (Hz), and the asymmetry parameter, denoted as  $\eta_Q$ , are generally used to describe such quadrupole interactions since the EFG tensor,  $\mathbf{V}$ , is traceless. For example, the EFG tensor in the principal axis system (the PAS frame) is diagonal:

$$\mathbf{V} = \begin{bmatrix} V_{XX} & 0 & 0 \\ 0 & V_{YY} & 0 \\ 0 & 0 & V_{ZZ} \end{bmatrix}. \quad (19.1)$$

where  $V_{XX} + V_{YY} + V_{ZZ} = 0$  with  $|V_{XX}| \leq |V_{YY}| \leq |V_{ZZ}|$ . According to the definition,

$$e^2 q Q h^{-1} = e Q h^{-1} \times V_{ZZ} \quad (19.2)$$

$$\eta_Q = \frac{V_{XX} - V_{YY}}{V_{ZZ}} \quad (19.3)$$

where  $0 \leq \eta_Q \leq 1$ . As can be seen, the former and the latter parameters describe the magnitude and symmetry of the EFG tensors, respectively.

The Hamiltonian representing a quadrupole interaction can be defined by

$$\mathcal{H}_Q = \frac{C_Q}{4I(2I-1)} \left[ \begin{array}{l} \frac{\sqrt{6}}{3} (3I_Z^2 - I^2) V_0 + (I_Z I_+ + I_+ I_Z) V_{-1} \\ -(I_Z I_- + I_- I_Z) V_{+1} + I_+^2 V_{-2} + I_-^2 V_{+2} \end{array} \right] \quad (19.4)$$

where  $I_{\pm}$  are the raising and lowering spin operators, and  $V$  is the EFG principal tensor component in the spherical tensor representation [2, 3]. Equation (19.4) can be further simplified when the magnitude of the Zeeman interactions is much larger than that of the quadrupole interactions, which is recognized as the high-field approximation:

$$\mathcal{H}_Q^{(1)} = \frac{\sqrt{6} C_Q}{12I(2I-1)} [3I_Z^2 - I(I+1)] V_0 \quad (19.5)$$

$$\mathcal{H}_Q^{(2)} = -\frac{1}{v_0} \left[ \frac{C_Q}{4I(2I-1)} \right]^2 \{ 2V_{-1} V_1 I_Z [4I(I+1) - 8I_Z^2 - 1] + 2V_{-2} V_2 I_Z [2I(I+1) - 2I_Z^2 - 1] \} \quad (19.6)$$

where  $v_0$  is the Larmor frequency. The former and the latter are called the first-order quadrupole interaction and the second-order quadrupole interaction, respectively. For spectral simulations, an adequate Hamiltonian must be chosen depending on the magnitude of the quadrupole interactions. For example, the first-order quadrupole Hamiltonian is required to describe the experimental NMR spectra broadened by smaller quadrupole interactions. It should be noted that the Larmor frequency is included in the denominator of Eq. (19.6), indicating that the magnitude of the second-order quadrupole interaction is inversely proportional to the strength of the external magnetic field. Thus, a stronger magnetic field could potentially allow the observation of NMR spectra broadened by larger quadrupole interactions.

It is important to note that these Hamiltonians can be obtained on the basis of perturbation theory, which is valid only when one interaction is much larger than the other. In other words, Eqs. (19.5) and (19.6) are not applicable when the

magnitude of the quadrupole interactions is comparable to or larger than that of the Zeeman interactions, even if a stronger magnetic field is used. In such cases, it is necessary to numerically solve the combined Zeeman and quadrupole Hamiltonians to derive transition probabilities. Thus, the full quadrupole Hamiltonian, i.e., Equation (19.4), combined with the Zeeman Hamiltonian,  $v_0 I_z$ , has to be diagonalized to find the eigenvalues, from which the transition amplitudes can be calculated for each transition. In this chapter, I call this the direct diagonalization method [6, 7].

To express the magnitude of quadrupole interactions, the quadrupole frequency,  $v_Q$ , may be used as an alternative to  $C_Q$  values:

$$v_Q = \frac{3C_Q\sqrt{1 + \eta_Q^2/3}}{2I(2I - 1)} \quad (19.7)$$

This frequency corresponds to the resonant frequency observed in NQR or zero-field NMR, which can be directly compared to the Larmor frequency. In summary, in order to correctly describe the experimental NMR spectra of quadrupole nuclei in spectral simulations, it is necessary to carefully select a proper theoretical model, i.e., the choice of the first- and/or second-order quadrupole Hamiltonians, or the direct diagonalization method, according to the situation in which the Larmor frequency should be compared to  $v_Q$  or  $C_Q$  values that one can predict from the spectral width of the experimental NMR spectra. In the next two sections, basic approaches to the analysis of one-dimensional NMR spectra of quadrupole nuclei on the basis of the perturbation method and the direct diagonalization method will be explained with some examples of solid-state NMR analysis results for quadrupole nuclei in organic compounds and inorganic compounds containing larger quadrupole interactions.

### 19.3 Simulating Solid-State NMR of Quadrupole Nuclei Based on the Perturbation Method

In this section, solid-state oxygen-17 [ $^{17}\text{O}$ ,  $I_s = 5/2$ , natural abundance = 0.038%,  $\gamma = 3.62808 \times 10^7 \text{ rad T}^{-1} \text{ s}^{-1}$ , and quadrupole moment ( $Q$ ) =  $-2.558 \text{ fm}^2$ ] NMR, which, I believe, will become a powerful tool for investigating physical and chemical properties in organic and biological chemistry, is reviewed with examples of spectral simulations based on the perturbation method [5]. Figure 19.1 shows the (upper) experimental and (lower) calculated  $^{17}\text{O}$  MAS spectra of  $^{17}\text{O}$ -enriched Fmoc-amino acid, measured at 11.7 T with a sample spinning frequency of  $19.9 \pm 0.2 \text{ kHz}$  [8]. The peak at approximately 380 ppm marked by an asterisk arises from the MAS rotor material,  $\text{ZrO}_2$ . If not preferable, the use of MAS rotors made of silicon nitride is highly recommended. The spectral assignment will be mentioned later. Figure 19.2 shows the (upper) experimental and (lower) calculated

$^{17}\text{O}$  stationary spectra of [ $^{17}\text{O}$ ]-Fmoc-amino acid, observed at 21.8 T [8]. As will be explained, the calculated total spectrum (site A + site B) is the sum of site A and site B sub-spectra with a 1:1 intensity ratio. Both the MAS and stationary  $^{17}\text{O}$  NMR spectra show characteristic line shapes, which are typically observed in solid-state NMR of half-integer quadrupole nuclei in organic compounds. To obtain experimental NMR parameters, a theoretical NMR spectrum is calculated using arbitrary NMR parameters, and the parameters are then suitably varied until the calculated NMR spectrum is consistent with the experimental one. It should be noted that the magnitude of a quadrupole interaction is expressed as a product of the quadrupole moment and the EFG, which is closely related to the molecular symmetry around the nuclei [see Eq. (19.2)]. For organic and biological compounds, molecular symmetries are generally low, which results in larger  $C_Q$  values compared with those of inorganic compounds. Therefore, the second-order quadrupole interaction, i.e., Equation (19.6), with the central transition  $m = -1/2 \Leftrightarrow m = 1/2$ , where  $m$  is quantum magnetic number, is often considered for spectral simulations of organic and biological solids. Although analysis of satellite transitions, which may appear at outside the frequency range that a conventional NMR instrument hardly accesses to, can yield the same results, the details are omitted due to space limitation. For organic and biological solids, the relevant  $^{17}\text{O}$  NMR parameters are the EFG and CS tensors. The following three situations are used to analyze the  $^{17}\text{O}$  NMR spectra of organic/biological compounds and to obtain  $^{17}\text{O}$  EFG and CS tensors from the experimental data: (1) stationary NMR spectra under the influence of second-order quadrupole interactions, (2) fast MAS NMR conditions under the influence of second-order quadrupole and CS interactions, and (3) stationary NMR spectra under the influence of second-order quadrupole and CS interactions.

**Fig. 19.1** Experimental and calculated  $^{17}\text{O}$  MAS spectra of [ $^{17}\text{O}$ ]-Fmoc-amino acid, measured at 11.7 T. The peak marked by asterisk arises from the MAS rotor material,  $\text{ZrO}_2$

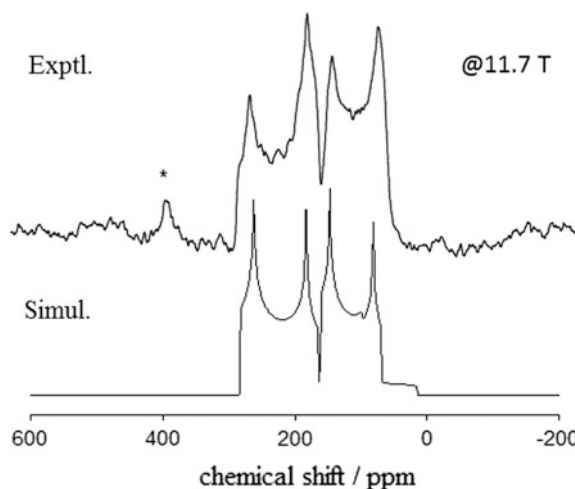
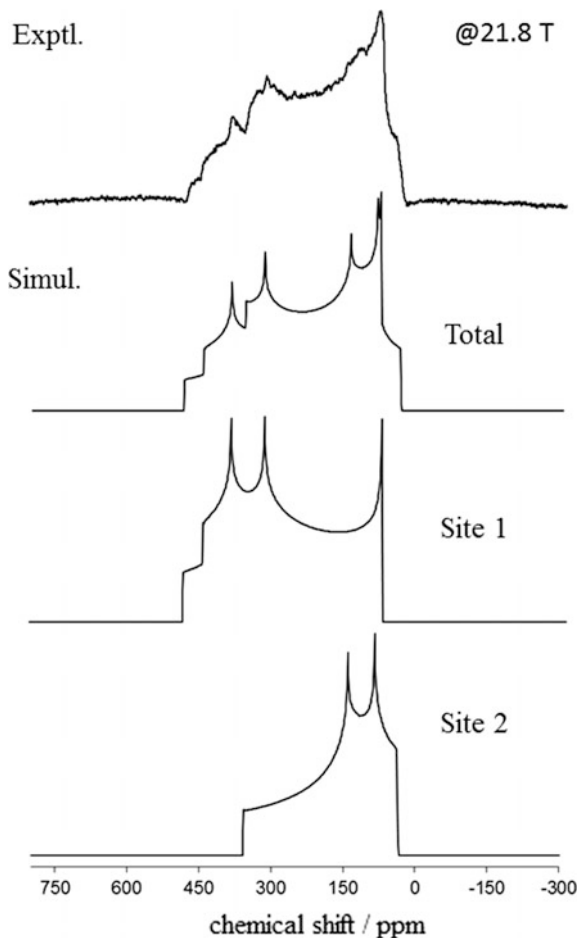


**Fig. 19.2** Experimental and calculated  $^{17}\text{O}$  stationary spectra of  $[^{17}\text{O}]\text{-Fmoc-amino acid}$ , observed at 21.8 T. The calculated total spectrum (site A + site B) is the sum of site A and site B sub-spectra with a 1:1 intensity ratio



### 19.3.1 Stationary NMR Spectra Under the Influence of Second-Order Quadrupole Interactions

In the cases of  $^{17}\text{O}$  ( $I = 5/2$ ) NMR, the Zeeman effect splits an energy level into six components in the presence of a static magnetic field [9]. The central transition, which is our main interest, is not affected by the first-order quadrupole interaction, resulting in no change in the resonant frequency. This implies that a sharp NMR signal is observed at the Larmor frequency. However, the second-order quadrupole interaction affects the energy levels involved in the central transition as well as the satellite transitions, indicating that, compared to the Larmor frequency, the resonant frequency,  $v_Q^{(2)}$ , is shifted according to

$$\begin{aligned} v_Q^{(2)} &= \left\langle -\frac{1}{2} \left| \mathcal{H}_Q^{(2)} \right| -\frac{1}{2} \right\rangle - \left\langle \frac{1}{2} \left| \mathcal{H}_Q^{(2)} \right| \frac{1}{2} \right\rangle \\ &= -\frac{1}{v_0} \left[ \frac{C_Q}{4I(2I-1)} \right]^2 \{ 2V_{-1}V_1[3-4I(I+1)] + V_{-2}V_2[3-4I(I+1)] \}. \end{aligned} \quad (19.8)$$

where the bra-ket is the energy level at  $m$ , and the  $V$  components are expressed in terms of the laboratory frame. In order to simulate stationary  $^{17}\text{O}$  NMR spectra, the  $V$  components in Eq. (19.8) have to be converted into ones expressed in terms of the PAS frame. For this purpose, it is convenient to use the following relationship:

$$V_i = \sum_{j=-2}^2 D_{j,i}^{(2)}(\phi, \theta, 0) V_j^{\text{PAS}} \quad (19.9)$$

where  $D_{j,i}^{(2)}$  is the Wigner rotation matrix, which is defined in the literature [2]. The orientation between the PAS and the laboratory frames used in this chapter is given in Fig. 19.3a (In the initial state of spectral simulation, orientations of EFG and CS tensors are assumed to be collinear, although CS and EFG tensors generally exhibit different orientations as shown in Fig. 19.3b). The orientation of a CS tensor ( $\delta_{11}$ ,  $\delta_{22}$ ,  $\delta_{33}$ ) will be discussed later.) For example,  $V_0$  can be rewritten as

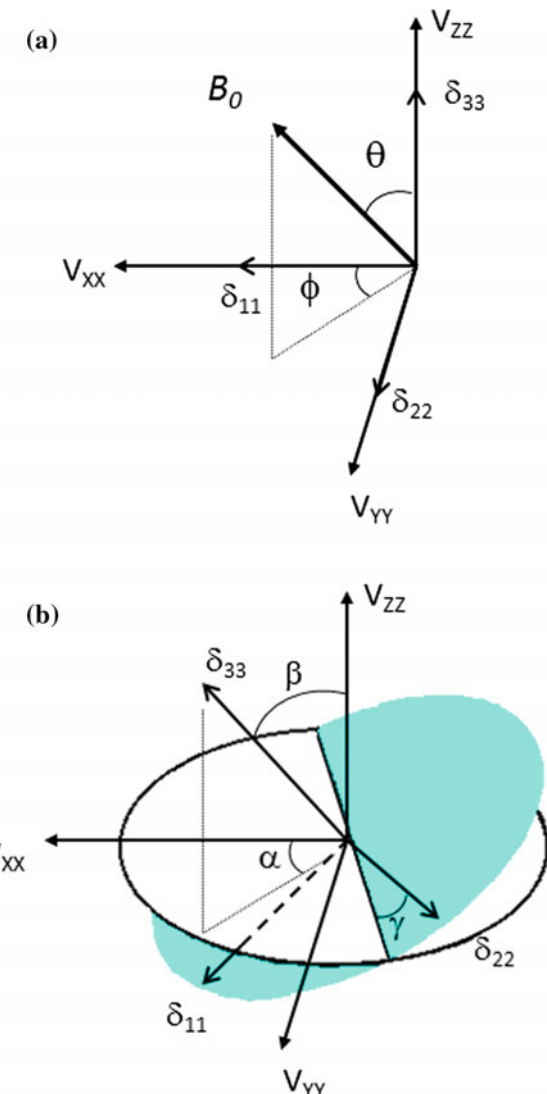
$$\begin{aligned} V_0 &= D_{-2,0}^{(2)}(\phi, \theta, 0) V_{-2}^{\text{PAS}} + D_{-1,0}^{(2)}(\phi, \theta, 0) V_{-1}^{\text{PAS}} + D_{0,0}^{(2)}(\phi, \theta, 0) V_0^{\text{PAS}} + D_{1,0}^{(2)}(\phi, \theta, 0) V_1^{\text{PAS}} \\ &\quad + D_{2,0}^{(2)}(\phi, \theta, 0) V_2^{\text{PAS}} \\ &= \sqrt{3/2}eQ[1/2(3\cos^2\theta - 1) + 1/2\eta_Q \sin^2\theta \cos 2\phi]. \end{aligned} \quad (19.10)$$

where  $V_0^{\text{PAS}} = \sqrt{3/2}eq$ ,  $V_{\pm 1}^{\text{PAS}} = 0$ , and  $V_{\pm 2}^{\text{PAS}} = 1/2eq$ . Similarly,  $V_{\pm 1}$  and  $V_{\pm 2}$  in the laboratory frame can be converted into the PAS frame, which are then inserted into Eq. (19.8). Thus, the NMR frequency arising from the second-order quadrupolar interaction under static conditions,  $v_{Q,\text{STATIC}}^{(2)}$ , can be obtained as

$$\begin{aligned} v_{Q,\text{STATIC}}^{(2)} &= -1/6v_0[3C_Q/2I(2I-1)]^2[I(I+1)-3/4][A\cos^4\theta + B\cos^2\theta + C] \\ A &= -27/8 + 9/4\eta_Q \cos 2\phi - 3/8(\eta_Q \cos 2\phi)^2 \\ B &= 30/8 - 1/2\eta_Q^2 - 2\eta_Q \cos 2\phi + 3/4(\eta_Q \cos 2\phi)^2 \\ C &= -3/8 + 1/3\eta_Q^2 - 1/4\eta_Q \cos 2\phi - 3/8(\eta_Q \cos 2\phi)^2. \end{aligned} \quad (19.11)$$

If the sample is a single crystal, the observed NMR frequency can be simply calculated with a single pair of  $\phi$  and  $\theta$  from the above equation. Crystalline or

**Fig. 19.3** **a** Initial alignment of the  $^{17}\text{O}$  EFG and CS tensors and direction of the external magnetic field,  $B_0$ . EFG and CS tensors are assumed to be collinear. **b** Euler angles relating EFG and CS tensors for the case that the orientations of EFG and CS tensors are different



Polymeric materials are used for most NMR experiments, and space-averaging in Eq. (19.11) yields the powder pattern. Figure 19.4a shows the calculated  $^{17}\text{O}$  stationary NMR spectra as a function of  $\eta_Q$  from 0 to 1.0 in steps of 0.2 [10]. These calculations were carried out using a  $C_Q$  value of 10 MHz and  $v_0$  of 100 MHz. The powder patterns exhibit complicated line shapes, and there is a dependence of the line shape on  $C_Q$ . In addition, there is a dependence of the spectral width on  $C_Q$  and  $v_0$ . For example, larger  $C_Q$  values give larger spectral widths, while higher  $v_0$  gives smaller width. Practically, computer simulation is required for extracting  $C_Q$  and

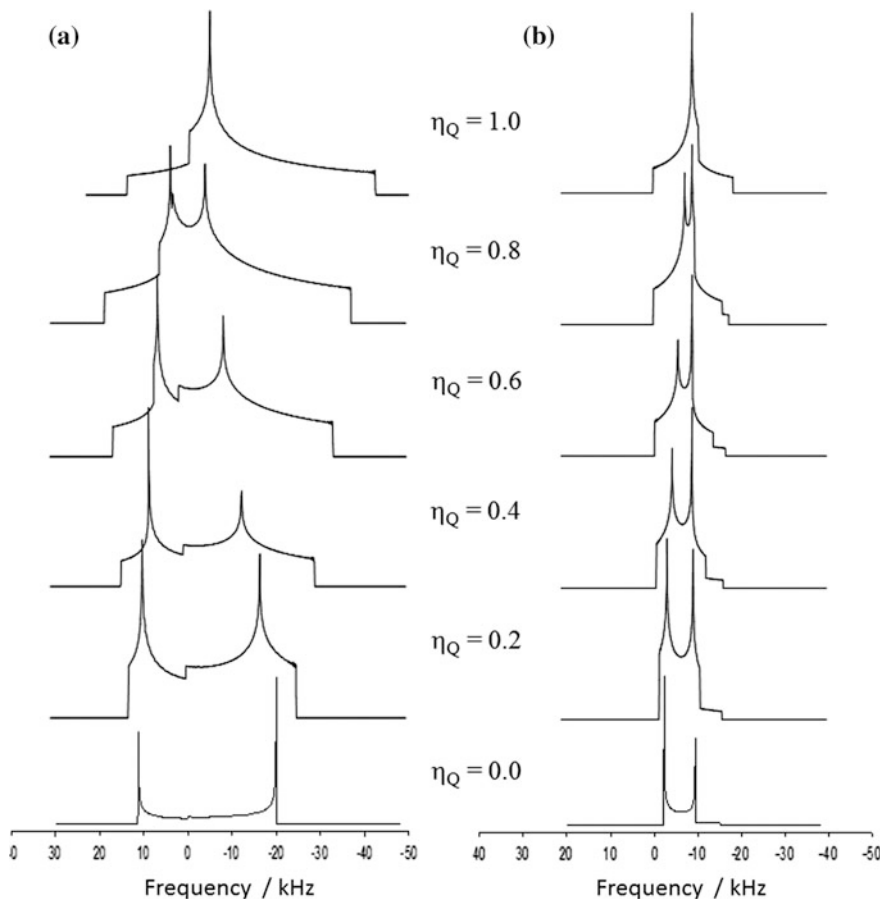


**Fig. 19.4** Dependence of  $\eta_Q$  on a stationary and b MAS NMR spectra of half-integer quadrupole nuclei, calculated by Eqs. (19.11) and (19.14)

$C_Q$  from experimental NMR spectra. As discussed above, substituting the appropriate  $C_Q$  values and  $\eta_Q$  into Eq. (19.11) with powder averaging yields a simulated NMR line shape, which is compared with the experimental one.

### 19.3.2 Fast MAS NMR Conditions Under the Influence of Second-Order Quadrupole and CS Interactions

It is well known that in the presence of second-order quadrupole interaction, high-resolution NMR spectra are not achievable by conventional MAS methods, even if the sample spinning frequency is sufficiently high compared to the spectral

width. This is because the second-order quadrupole interactions under MAS conditions are not simply proportional to the term  $3\cos^2\theta - 1$ , which can theoretically remove the first-order interactions such as dipole–dipole, CS, and first-order quadrupolar interactions [2].

This implies that only partial narrowing is achieved by the MAS method, and characteristic NMR line shapes still appear in the MAS NMR spectra.

To calculate the MAS NMR spectra of half-integer quadrupole nuclei, coordinate systems of the  $V$  component in Eq. (19.8) have to be changed stepwise from the laboratory frame to the MAS rotor frame and from the MAS rotor frame to the PAS frame. To do this, the following two relationships are used:

$$V_i = \sum_{j=-2}^2 \mathcal{D}_{j,i}^{(2)}(\omega_R t, \theta_M, 0) V_j^{\text{MAS}} \quad (19.12)$$

$$V_j^{\text{MAS}} = \sum_{k=-2}^2 \mathcal{D}_{k,j}^{(2)}(\phi, \theta, 0) V_k^{\text{PAS}} \quad (19.13)$$

where  $\omega_R$  and  $\theta_M$  are the sample spinning frequency and the magic angle of 54.7, respectively. In Eq. (19.13),  $\theta$  and  $\phi$  describe the direction of the MAS rotor with respect to the PAS frame in a similar manner to the orientation in Fig. 19.3a, and the third angle is set to zero since the experimental conditions are assumed to be in the fast MAS range, which means that the sample spinning frequency is high enough compared to the spectral width. In cases of slow or intermediate spinning ranges, however, the third angle in Eq. (19.13) becomes nonzero, and spinning side bands appear in the MAS NMR spectra, which makes it more difficult to analyze the line shape [11].

By inserting Eqs. (19.12) and (19.13) into Eq. (19.8), the frequency contribution from the second-order quadrupole interaction under the fast MAS condition,  $v_{Q,\text{MAS}}^{(2)}$ , can be expressed as

$$\begin{aligned} v_{Q,\text{MAS}}^{(2)} &= -1/6v_0[3C_Q/2I(2I-1)]^2[I(I+1)-3/4][D\cos^4\theta+E\cos^2\theta+F] \\ D &= 21/16 - 7/8\eta_Q\cos 2\phi + 7/48(\eta_Q\cos 2\phi)^2 \\ E &= -9/8 + 1/12\eta_Q^2 + \eta_Q\cos 2\phi + 7/24(\eta_Q\cos 2\phi)^2 \\ F &= 5/16 - 1/8\eta_Q\cos 2\phi + 7/48(\eta_Q\cos 2\phi)^2 \end{aligned} \quad (19.14)$$

Figure 19.4b shows the simulated  $^{17}\text{O}$  MAS spectra as a function of  $\eta_Q$  from 0 to 1 in steps of 0.2 [10]. These calculations were carried out using the same conditions as those used for the  $^{17}\text{O}$  stationary NMR spectra in Fig. 19.4a. The

spectral widths of the MAS NMR spectra are approximately one-third narrower than those of the stationary NMR spectra. Similar to the stationary NMR spectra, the MAS spectra exhibit characteristic line shapes from which information on  $C_Q$  and  $\eta_Q$  can be extracted. If there is a CS interaction, the anisotropy of the CS tensors is thought to be safely removed by MAS. Thus, the scalar value of  $\delta_{\text{iso}}$  should be added to Eq. (19.14) for the actual simulation. As an example, the analysis of the one-dimensional (1D)  $^{17}\text{O}$  MAS NMR spectrum in which two oxygen sites, C=O and COH, were assumed as shown in Fig. 19.1, yielded the following parameters: C=O:  $\delta_{\text{iso}} = 305 \pm 2$  ppm,  $C_Q = 7.90 \pm 0.08$  MHz,  $\eta_Q = 0.18 \pm 0.04$ ; COH,  $\delta_{\text{iso}} = 180 \pm 2$  ppm,  $C_Q = 7.05 \pm 0.08$  MHz,  $\eta_Q = 0.15 \pm 0.04$ . The frequency contribution from the second-order quadrupole interactions combined with the anisotropy of the CS interactions under slow/intermediate MAS conditions is given in the literature. A complicated line shape is expected to appear in the MAS NMR spectrum, so a computer simulation is not trivial [10].

High-resolution MAS NMR spectra of half-integer quadrupole nuclei are very often required for the purpose of site separation. Overlapping of multiple sites in MAS NMR spectra may result in complicated line shapes, and it is very difficult or nearly impossible to analyze such NMR spectra. To separate each site in the NMR spectra of quadrupole nuclei, the following standard experimental approaches based on a MAS method are commonly used, dynamic-angle spinning (DAS) [12], double rotation (DOR) [13], multiple-quantum MAS (MQMAS) [14], and satellite-transition MAS (STMAS) [15], all of which can remove second-order quadrupole interactions. MQMAS is the most widely used of these since it can be performed with a normal MAS probe. For example, Fig. 19.5 shows the contour plot of the two-dimensional (2D)  $^{17}\text{O}$  triple-quantum z-filtered MQMAS spectrum of [ $^{17}\text{O}$ ]-L-valine obtained with rotor synchronization for  $t_1$  increments with a MAS rate of 15.00.1 kHz [16]. The Y- and X-axes projections of the 2D MQMAS spectrum are shown on the side and at the top to the figure, respectively. As indicated in Fig. 19.5, four isotropic peaks, which arise from a pair of magnetically inequivalent carboxylate oxygen sites, are observed in the 2D MQMAS spectrum. The slice along the  $t_2$  direction (X-axis direction) of each peak corresponds to the 1D  $^{17}\text{O}$  MAS spectrum for each oxygen site, and spectral analysis can be performed easily. However, note that MQMAS spectra do not generally present quantitative information on peak intensities. Moreover, such cross-sectional spectra are often distorted by multiple-quantum effects. Therefore, spectral simulation of the 1D MAS spectrum is required to confirm the final  $^{17}\text{O}$  NMR parameters. The NMR parameters estimated from the analysis of MQMAS spectra may be used as the initial values for the simulations. Results for the combined analysis are given in Fig. 19.6, where the calculated spectrum is the sum of the O1, O2, O3, and O4 sub-spectra with a 1:1:1:1 intensity ratio.

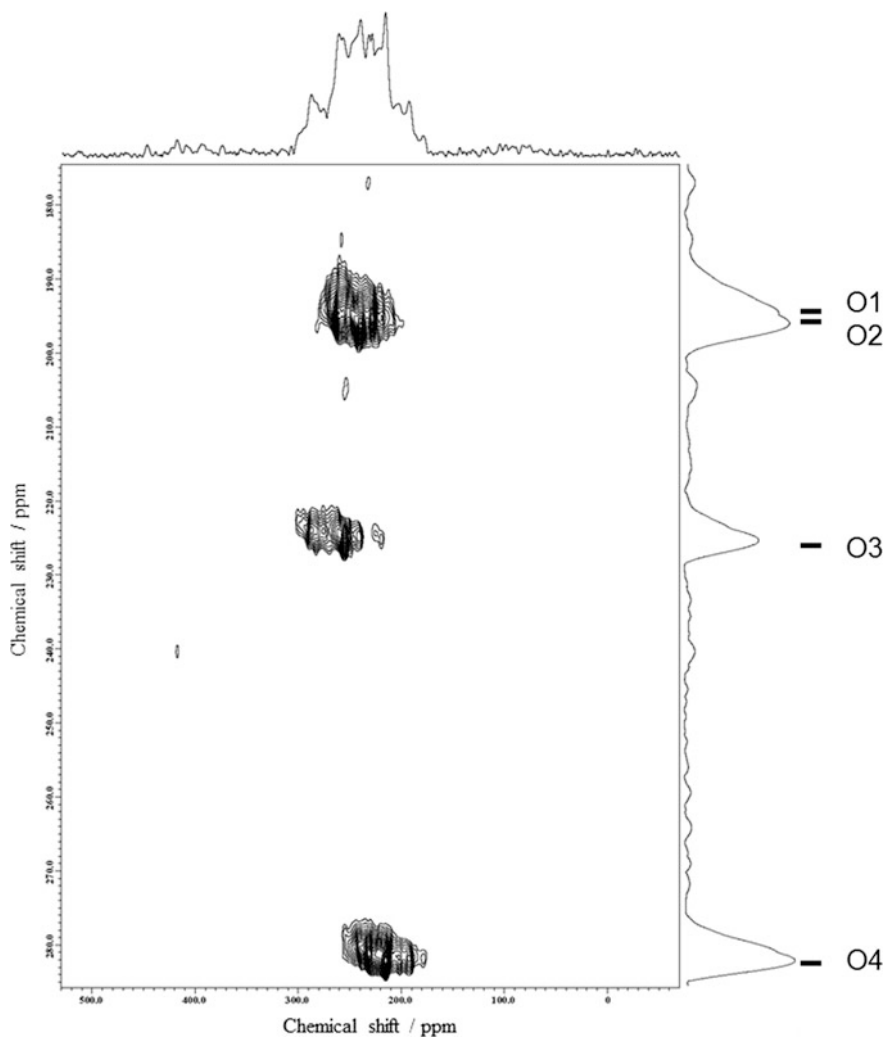
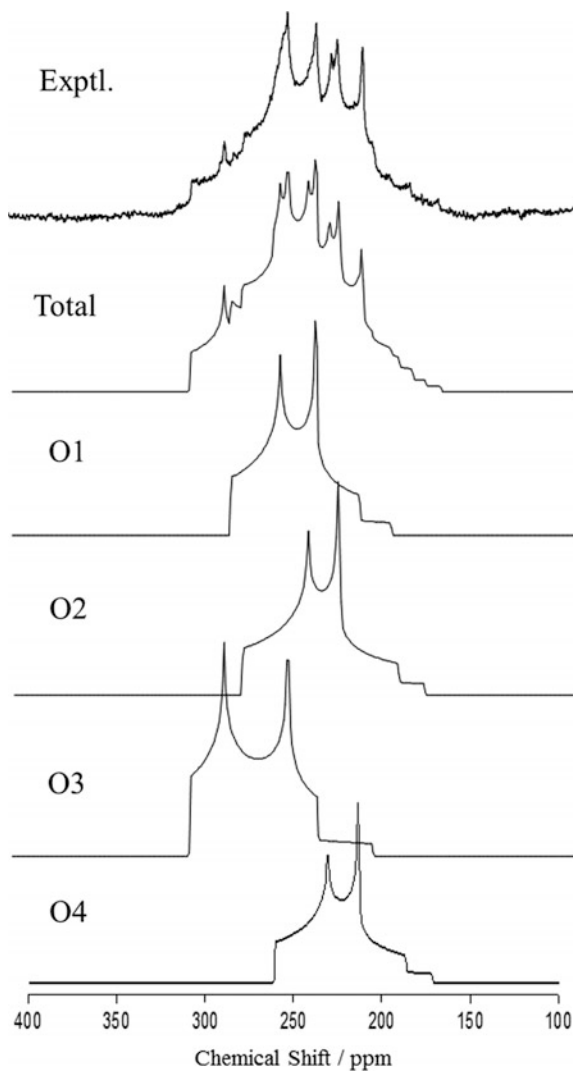


**Fig. 19.5** Contour plot of the  $^{17}\text{O}$  z-filter 3QMQMAS spectrum of  $[^{17}\text{O}]\text{-L-valine}$  recorded at 16.4 T

### 19.3.3 Stationary NMR Spectra Under the Influence of Second-Order Quadrupole and CS Interactions

One of the advantages of solid-state NMR is that tensor information on nuclear spin interaction can be obtained [2]. CS tensors ( $\delta_{11}, \delta_{22}, \delta_{33}$ ), EFG tensors ( $C_Q$  and  $C_Q'$ ), and the Euler angles ( $\alpha, \beta, \gamma$ ) showing the relative orientation between the two tensors, which will be explained later, are obtained by the analysis of  $^{17}\text{O}$  stationary

**Fig. 19.6** Experimental and calculated 1D  $^{17}\text{O}$  MAS spectra of  $[^{17}\text{O}]\text{-L-valine}$  recorded at 16.4 T. The calculated total spectrum is the sum of O1, O2, O3, and O4 sub-spectra with a 1:1 intensity ratio



NMR spectra of organic and biological compounds. To calculate stationary NMR spectra, one may simply add the following equation to express the anisotropy of CS interactions,  $v_{\text{CS}}$ , to Eq. (19.11):

$$v_{\text{CS}} = \delta_{11} \sin^2 \theta \cos^2 \phi + \delta_{22} \sin^2 \theta \sin^2 \phi + \delta_{33} \cos^2 \theta \quad (19.15)$$

where  $\theta$  and  $\phi$  describe the orientation of the magnetic field in the principal axis system of the CS tensor illustrated in Fig. 19.3a [1]. Very often, however, the CS and EFG tensors exhibit different orientations in the molecular frame of reference. This simply means that  $\theta$  and  $\phi$  in the above equation are not identical to those in

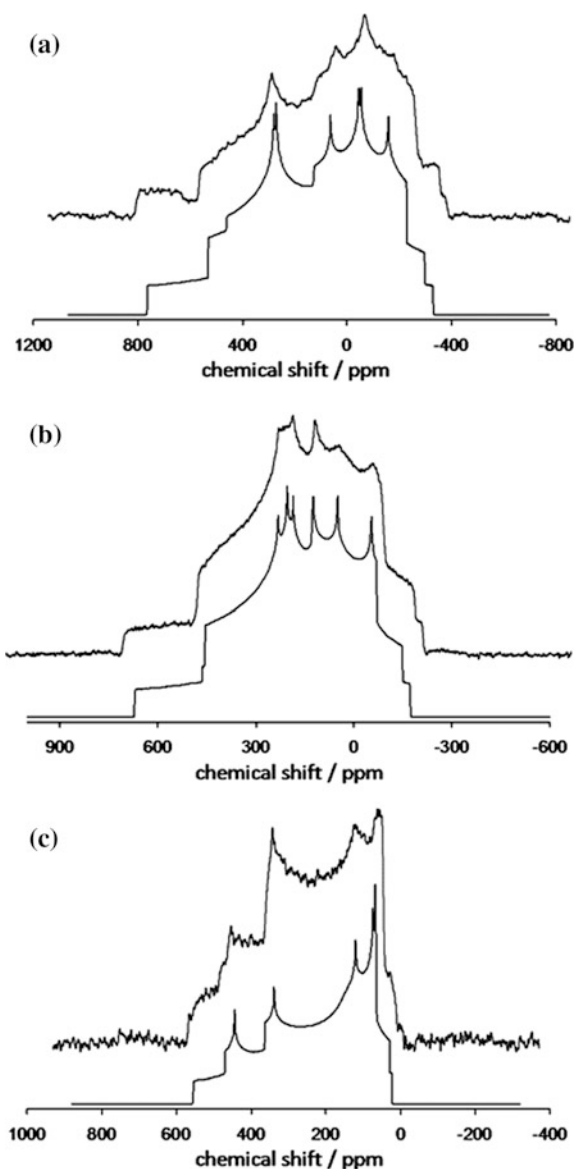
Eq. (19.11). Thus, it is helpful to use the relative orientation term between the two tensors, employing the three Euler angles ( $\alpha$ ,  $\beta$ ,  $\gamma$ ), as shown in Fig. 19.3b. The Euler angles describing the relative orientation of the two tensors depend critically on the choice of the initial frame, the definition of the Euler angles, and the rotational directions. Therefore, it is sometimes difficult or misleading to describe the reported tensor orientations in the literature. There are several different definitions in the literature concerning the Euler angles relating the EFG and CS tensors and the alignment of the two tensors in the magnetic field. Here the approach of Eichele et al. [17] is described, since I believe that this procedure is the most straightforward. The alignment of the two tensors in the magnetic field is illustrated in Fig. 19.3a. The transformation matrix of  $R(\alpha, \beta, \gamma)$  can be written as

$$R(\alpha, \beta, \gamma) = \begin{pmatrix} \cos \gamma \cos \beta \cos \alpha - \sin \gamma \sin \alpha & \cos \gamma \cos \beta \sin \alpha - \sin \gamma \cos \alpha & -\cos \gamma \sin \beta \\ -\sin \gamma \cos \beta \cos \alpha - \cos \gamma \sin \alpha & -\sin \gamma \cos \beta \sin \alpha - \cos \gamma \cos \alpha & \sin \gamma \sin \beta \\ \sin \beta \cos \alpha & \sin \beta \sin \alpha & \cos \beta \end{pmatrix}. \quad (19.16)$$

The directional cosines in Eq. (19.15) should be transformed according to the above transformation [3]. When  $(\alpha, \beta, \gamma) = (0, 0, 0)$ , the orientations of the CS tensor become coincident with those of the EFG tensor, *i.e.*, a simple addition of Eqs. (19.15)–(19.11) [18]. It is worth noting that the relative orientation of the two tensors can be expressed by different Euler angle sets. This is because the sign of the EFG tensors cannot be distinguished by conventional NMR experiments. For example, a 180° rotation around one of the three principal axis directions yields an identical NMR line shape. Thus, the sets of Euler angles  $(\alpha, \beta, \gamma)$ ,  $(\alpha, \beta, \gamma + 1 + 0)$ ,  $(\alpha, \beta + 1 + 0, -\gamma + 1 + 0)$ ,  $(-\alpha, \beta + 1 + 0, \gamma)$ ,  $(\alpha + 1 + 0, \beta + 1 + 0, -\gamma)$ , and so on will produce identical NMR line shapes.

As shown in Fig. 19.2, the NMR spectra could be analyzed by two oxygen sites, which are expected to arise from the carbonyl and hydroxyl oxygen atoms. The simulated total spectrum (C=O and COH) is the sum of C=O and COH sub-spectra with a 1:1 intensity ratio, where a stationary NMR line shape, arising from the sum of the CS and the second-order quadrupolar contributions (taking the relative orientations into consideration), as described above, is used for each sub-spectrum. Analysis of the 1D stationary  $^{17}\text{O}$  NMR spectrum yields the following NMR parameters: C=O,  $\delta_{11} = 478 \pm 9$  ppm,  $\delta_{22} = 409 \pm 9$  ppm,  $\delta_{33} = 28 \pm 9$  ppm,  $\alpha = 14 \pm 10^\circ$ ,  $\beta = 90 \pm 8^\circ$ ,  $\gamma = 134 \pm 10^\circ$ ; COH,  $\delta_{11} = 325 \pm 9$  ppm,  $\delta_{22} = 108 \pm 9$  ppm,  $\delta_{33} = 107 \pm 9$  ppm,  $\alpha = 10 \pm 15^\circ$ ,  $\beta = 12 \pm 8^\circ$ ,  $\gamma = -16 \pm 10^\circ$ . There are eight independent NMR parameters ( $\delta_{11}$ ,  $\delta_{22}$ ,  $\delta_{33}$ ,  $C_Q$ ,  $C_Q$ ,  $\alpha$ ,  $\beta$ ,  $\gamma$ ) for each oxygen site, so that many independent NMR parameters (in this case, a total of 16) have to be simultaneously used for spectral simulation. Using the results from the analysis of the  $^{17}\text{O}$  MAS experiments (see Fig. 19.1) that yield  $\delta_{\text{iso}}$ ,  $C_Q$ , and  $C_Q$  for each site, the number of independent NMR parameters can be reduced. Unfortunately, however, it is still not straightforward to analyze a stationary  $^{17}\text{O}$  NMR spectrum observed in a single magnetic field because slight

**Fig. 19.7** Experimental and calculated  $^{17}\text{O}$  stationary NMR spectra for [ $^{17}\text{O}$ ]-L-alanine hydrochloride, recorded at **a** 9.4, **b** 11.7, and **c** 21.6 T



changes in each NMR parameter have a significant effect on theoretical line shape. In particular, the Euler angles are critical. Thus, prior to computer simulation, it is advantageous to understand or predict the possible set of Euler angles for each functional group. An understanding of  $^{17}\text{O}$  NMR parameters, in particular tensor orientations, is very helpful for spectral simulations [5]. From my experience, it is also useful to use multiple magnetic fields, by which  $^{17}\text{O}$  stationary NMR line

### Theoretical calculations

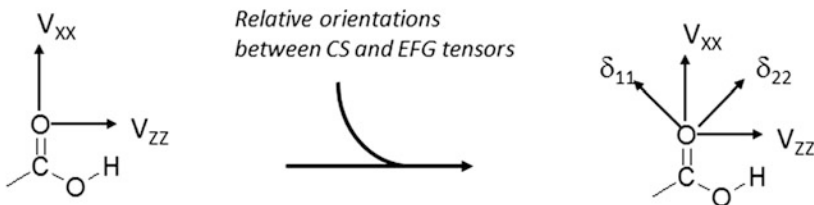


**Fig. 19.8** Schematic representation to obtain information on CS tensor orientation in terms of molecular frames

shapes are drastically changed. The simultaneous analysis of stationary NMR spectra observed in various magnetic fields, as shown in Fig. 19.7, is one of the most effective methods for extracting the  $^{17}\text{O}$  CS tensor components unambiguously [19].

It is important to note that the three Euler angles simply reveal the relative orientation between the two NMR tensors, but not physical properties. One may need the tensor orientation in terms of molecular frame. The ideal technique for obtaining orientation information on NMR tensors is single-crystal NMR experiments [20]. However, large single crystals suitable for NMR experiments are often difficult to obtain. In the case of  $^{17}\text{O}$  NMR, the need to introduce  $^{17}\text{O}$ -labels makes it even more difficult to grow large single crystals because of the small quantity of a labeled sample. An alternative method to establish the absolute tensor orientation in the molecular frame is to use quantum chemical calculations. It is assumed that the orientations of the  $^{17}\text{O}$  EFG tensors obtained from high-level quantum chemical calculations are correct. With the combined results of the absolute orientations of the EFG tensors and the Euler angles determined experimentally, it is feasible to determine the absolute orientations of the  $^{17}\text{O}$  CS tensors with respect to the molecular frame, as given in Fig. 19.8 [4].

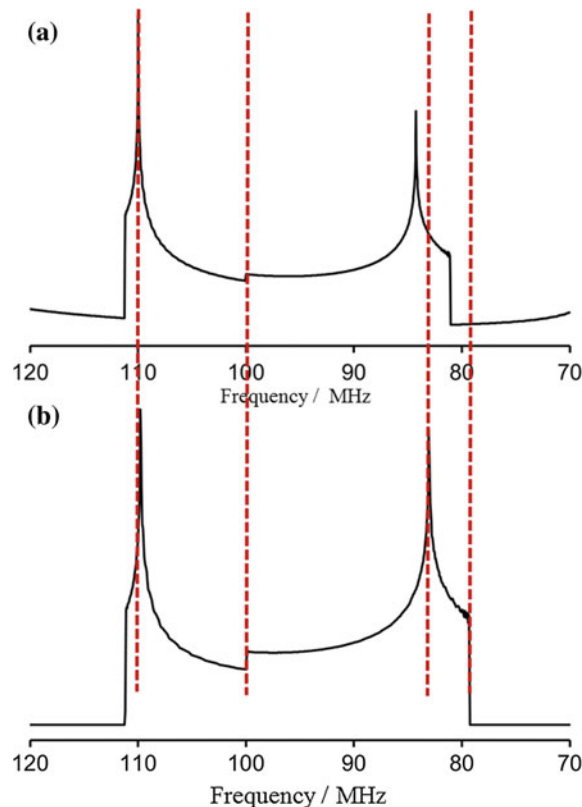
## 19.4 Solid-State NMR of Quadrupole Nuclei Based on Direct Calculation Methods

As mentioned, the perturbation method, i.e., Equations (19.5) and (19.6), cannot be used for spectral simulations, when the magnitude of the quadrupole interactions is comparable to or larger than that of the Zeeman interactions. In such cases, the direct diagonalization method is a promising approach to analyze NMR spectra broadened by quadrupole interactions. For simplicity, this section focuses on the cases in which a sample is static under the influence of quadrupole interactions. Figure 19.9 shows the stationary NMR spectra of a half-integer quadrupole calculated by (a) the direct diagonalization method and (b) the perturbation method [7]. These calculations were performed using  $C_Q = 150 \text{ MHz}$ ,  $\eta_Q = 0.1$ ,

$v_0 = 100$  MHz, and  $I = 3/2$ . In the later approach, only the central transition was considered for simplicity so that both edges, which should have contributions from satellite transitions, are quite different from those of the former. Similar line shapes in the range of the central transitions are observed in both NMR spectra, but the line width calculated by the perturbation method is, to some extent, expanded to the lower frequency. This difference is thought to be the main limit of the perturbation theory. Thus, it is potentially erroneous to apply the perturbation method when the magnitude of the quadrupole interactions is larger than that of the Zeeman interactions, or when the strength of the external magnetic field is lower even if the magnitude of the quadrupole interaction is not too large.

Traditionally, there are two experimental techniques to record solid-state NMR spectra broadened by large quadrupole interactions, i.e., frequency-swept NMR and field-swept NMR. A schematic representation of the two methods is given in Fig. 19.10. Both methods have advantages and disadvantages. For frequency-swept NMR, spectral analysis is straightforward, and experiments can be performed with a conventional NMR instrument under a static magnetic field using an NMR probe capable of varying irradiated and observed frequencies in a broad band. However, there may be a limitation in hardware, in particular, the capacity of the condensers

**Fig. 19.9** Theoretical NMR spectra of half-integer quadrupole nuclei, based on **a** the direct diagonalization method, **b** the perturbation method. See the text in the details



of NMR probes, which sets a limit to the observable frequency range. Conversely, for field-swept NMR, spectral analysis is complicated and time-consuming, and a variable superconducting magnet, which is not common in the research fields of chemistry and biochemistry, is required for the NMR measurements. However, there is no hardware-derived limit on the observable frequency range. Although both methods suffer from low sensitivity, one should choose the experimental techniques properly, depending on the sample situation. In the rest of this section, bromine and sulfur solid-state NMR are discussed as examples of frequency-swept NMR and field-swept NMR, respectively.

Bromine is the third-lightest halogen and plays important roles in a variety of materials including flame retardants, dye compounds, and gasoline additives. There are two NMR-accessible stable bromine isotopes:  $^{79}\text{Br}$  ( $I = 3/2$ , natural abundance = 50.54%,  $\gamma = 6.7228 \times 10^7 \text{ rad T}^{-1} \text{ s}^{-1}$ , and  $Q = 0.37 \times 10^{28} \text{ Qm}^{-2}$ ) and  $^{81}\text{Br}$  ( $I = 3/2$ , natural abundance = 49.46%,  $\gamma = 7.2468 \times 10^7 \text{ rad T}^{-1} \text{ s}^{-1}$ , and  $Q = 0.31 \times 10^{28} \text{ Qm}^{-2}$ ). Of these,  $^{79}\text{Br}$  may be more commonly used since its resonant frequency is very close to that of  $^{13}\text{C}$ , and KBr is used as a standard for adjusting the magic angle prior to MAS experiments. The magnitude of quadrupole interactions for  $^{79/81}\text{Br}$  depends on the bonding mode. In general, inorganic compounds or those forming ionic bonds in which molecular symmetry is high tend to have relatively small quadrupole interactions, while organic compounds or those forming covalent bonds exhibit much larger interactions, which increase spectral width. For example, the spectral width in  $^{79}\text{Br}$  NMR, whose  $C_Q$  value is more than 30 MHz, is spread in the order of megahertz, so it is not easy to observe the NMR spectra using conventional NMR instruments.

**Fig. 19.10** Two experimental techniques to record solid-state NMR spectra broadened by large quadrupole interactions: **a** frequency-swept types and **b** field-swept types of NMR experiments

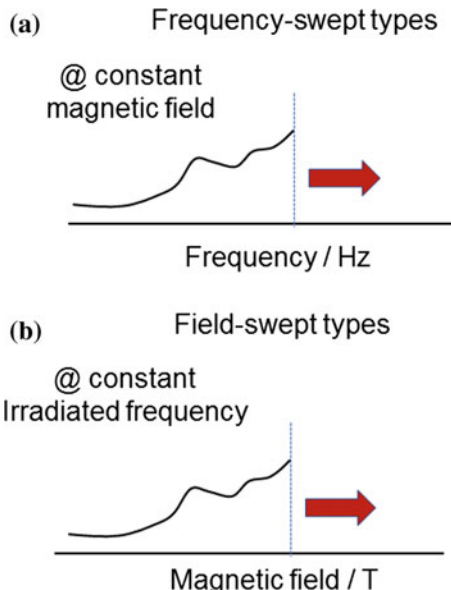
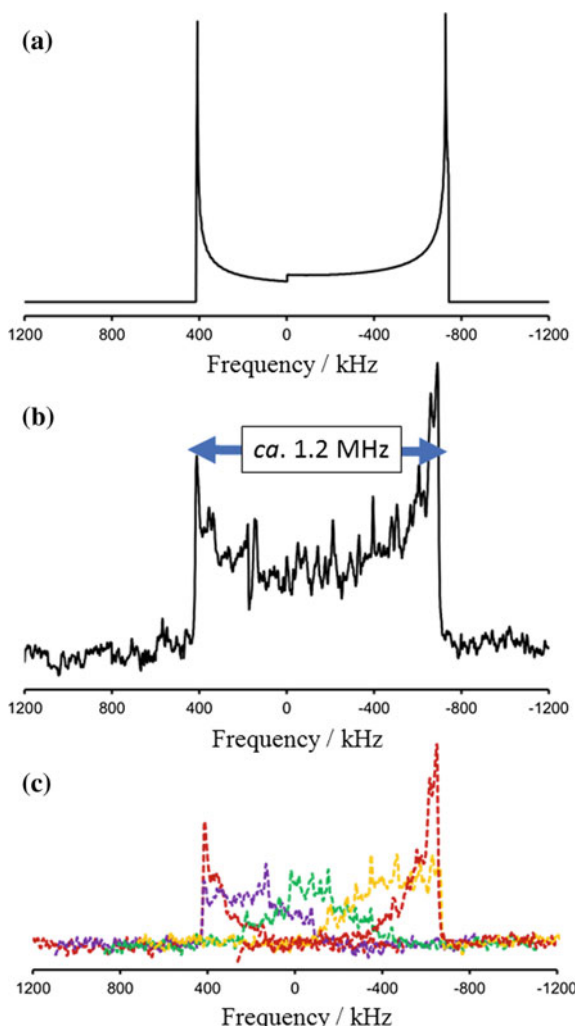


Figure 19.11 shows the (a) calculated and (b) experimental stationary  $^{79}\text{Br}$  frequency-swept NMR spectra of  $\text{SrBr 6H}_2\text{O}$  measured at 11.7 T [7]. The experimental spectrum is the sum of (c) five sub-NMR spectra, each of which were observed with the Oldfield echo [21] with steps of 300 kHz in the irradiation frequency. The spectral simulation based on the direct diagonalization method provides the following NMR parameters:  $C_Q = 33.2 \pm 0.5$  MHz and  $\eta_Q = 0.01 \pm 0.01$ . The line shape is insensitive to changes in the CS interactions, so the effect of the CS interactions (Eq. (19.15)) was safely ignored in the spectral simulation. As long as the tuning and matching of the NMR probe is achievable in the range of the spectral width for the experimental NMR, frequency-swept NMR is

**Fig. 19.11** **a** Calculated and **b** experimental stationary  $^{79}\text{Br}$  ( $I = 3/2$ ) frequency-swept NMR spectra. The experimental spectrum is the sum of **c** five sub-spectra



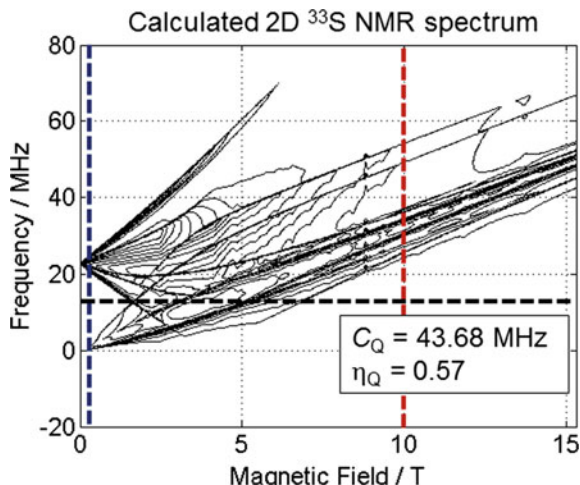
one of the best methods to record NMR spectra broadened by large quadrupole interactions.

Organosulfur compounds are essential for a variety of biological activities. For example, sulfur-containing methionine and cysteine are two of the twenty common amino acids in the human body, and a large number of organosulfur compounds such as penicillin have been marketed as drugs or used in drug development throughout history [22, 23]. Solid-state sulfur NMR ( $^{33}\text{S}$ ,  $I = 3/2$ , natural abundance = 0.75%,  $\gamma = 2.055 \times 10^7 \text{ rad T}^{-1}\text{s}^{-1}$ ,  $Q = -5.5 \times 10^{26} \text{ Qm}^{-2}$ ) has a long history, but still presents difficulties depending on the magnitude of quadrupole interactions, i.e., the bonding mode, and NMR researches concerning sulfur compounds that form covalent bonds are undeveloped in a similar manner to the cases of bromine NMR.

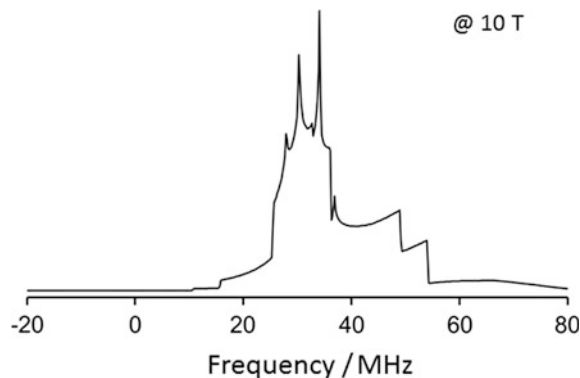
Figure 19.12 shows a calculated 2D solid-state  $^{33}\text{S}$  NMR spectrum of a typical compound containing covalent bonds [7]. The calculations were performed using the direct diagonalization method with  $C_Q = 43.68 \text{ MHz}$  and  $\eta_Q = 0.57$ , which were obtained from the analysis of the  $^{33}\text{S}$  NMR spectra of  $\alpha\text{-S}_8$  [6, 24]. It is convenient to use this figure to illustrate the relationship between frequency-swept and field-swept NMR. For example, the slices in the Y-axis direction correspond to frequency-swept NMR in a static magnetic field, while those in the X-axis direction correspond to field-swept NMR spectra at a certain irradiation frequency. Figure 19.13 shows the calculated  $^{33}\text{S}$  NMR spectrum sliced at 10 T in Fig. 19.12, which corresponds to a  $^{33}\text{S}$  NMR spectrum measured at 10 T. It is observed that the spectral width spread over 30 MHz, indicating that it is indeed very difficult or nearly impossible to record a  $^{33}\text{S}$  NMR spectrum under a moderate magnetic field.

Figure 19.14a shows the experimental field-swept  $^{33}\text{S}$  NMR spectrum of  $\alpha\text{-S}_8$  at the Larmor frequency of 16.2 MHz, acquired at 260 K [6]. Two sharp peaks are observed at approximately 1.3 and 1.4 T, and they are assigned to the NMR signals of  $^{65}\text{Cu}$  and  $^{63}\text{Cu}$ , respectively, in the transmitting and receiving antennae in the

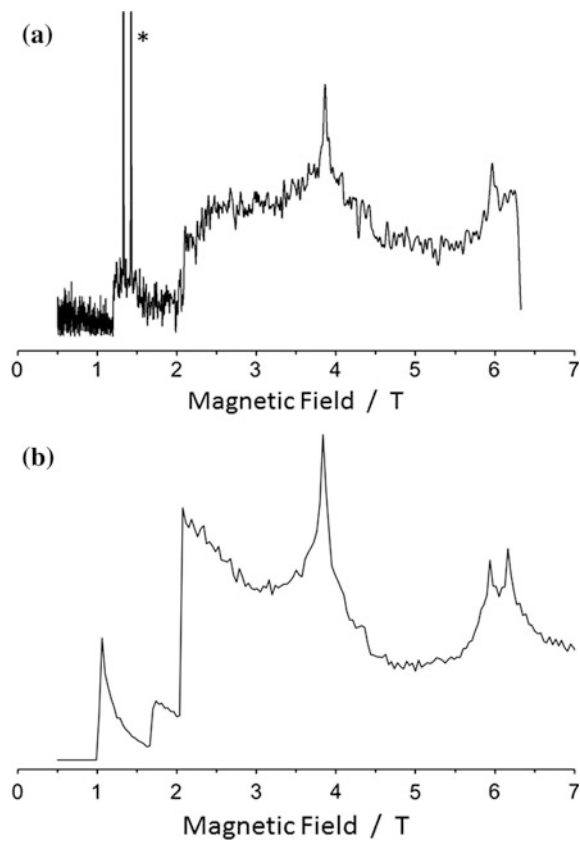
**Fig. 19.12** Calculated 2D solid-state  $^{33}\text{S}$  NMR spectrum using  $C_Q = 43.68 \text{ MHz}$  and  $\eta_Q = 0.57$ . The slices to Y-axis direction correspond to frequency-swept NMR spectra at static magnetic fields, while those to X-axis direction to field-swept NMR spectra at irradiated frequencies



**Fig. 19.13** Calculated frequency-swept  $^{33}\text{S}$  solid-state NMR spectrum at 10 T, which corresponds to the slice in the vertical red line in the NMR spectrum in Fig. 19.12

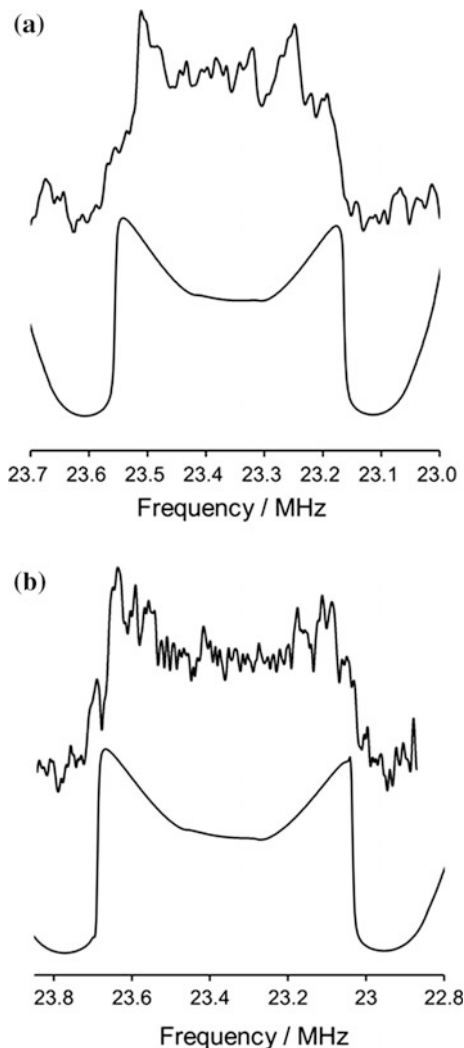


**Fig. 19.14** **a** Experimental and **b** best-fitted calculated field-swept  $^{33}\text{S}$  NMR spectra of  $\alpha\text{-S}_8$ , acquired at 16.2 MHz. Analyzing the NMR spectrum assuming that there was a single sulfur site gave  $C_Q = 43.68 \text{ MHz}$  and  $\eta_Q = 0.57$



NMR probe. The best-fitted calculated field-swept  $^{33}\text{S}$  NMR spectrum of  $\alpha\text{-S}_8$ , at a Larmor frequency of 16.2 MHz, is shown in Fig. 19.14b, which is the slice in the X-axis direction at 16.2 MHz in Fig. 19.12. As long as the sensitivity issue is

**Fig. 19.15** Experimental (upper trace) and best-fitted calculated (lower trace) frequency-swept  $^{33}\text{S}$  NMR spectra of  $[^{33}\text{S}]\text{-diphenyl disulfide}$ , acquired at **a** 0.50 and **b** 0.10 T



resolved and as long as a magnetic field can cover the range, there is no limitation in the spectral width, that is, the magnitude of the quadrupole interactions.

Very recently, a new type of frequency-swept solid-state  $^{33}\text{S}$  NMR that uses an extremely low magnetic field ( $\sim 0.10$  T) has been reported as an alternative to the above methods, which corresponds to the slice in the  $Y$ -axis direction at 0.10 T or lower in Fig. 19.12. The advantage of this method is that spectral width is expected to be much narrower than that at higher magnetic fields, i.e., the experimental conditions become much closer to those of zero-field NMR or NQR experiments where a sharp signal is generally observed at  $v_Q$ . It should be noted that NQR data

alone cannot yield EFG information since the spin number of  $^{33}\text{S}$  is 3/2 [see Eq. (19.7)].

The experimental and best-fit calculated  $^{33}\text{S}$  NMR spectra of [ $^{33}\text{S}$ ]-diphenyl disulfide observed at (a) 0.06 and (b) 0.10 T, which correspond to the Larmor frequencies of 0.1959 and 0.3265 MHz, respectively, are shown in Fig. 19.15 [25]. Unfortunately, the two sulfur sites in the disulfide bridge cannot be distinguished in the experimental NMR spectra due to poor spectral resolution. Assuming that there is a single sulfur site, the analysis of the NMR spectra with the aid of quantum chemical calculations yielded the following parameters:  $C_Q = 43.3 \pm 1.9$  MHz and  $\eta_Q = 0.70 \pm 0.20$ .

In a summary, the direct diagonalization method can be used to analyze NMR spectra of organic compounds broadened by large quadrupole interactions, for which the perturbation method is no longer valid. As mentioned, frequency-swept and field-swept NMR are useful techniques for recording such broadened NMR spectra, but both methods generally suffer from low sensitivity. I feel that field-swept NMR has many advantages for increasing signal sensitivities. This is because, in contrast to frequency-swept NMR, the resonant frequency can be fixed so that, for example, an NMR probe containing high-temperature superconducting (HTS) coils with an extremely high Q value, or a new technology called an optomechanics system [26], in which an NMR signal is detected by a receiver coil and transformed into laser radiation via a micro-condenser, can be potentially applied to field-swept NMR. Such developments are in progress in our group.

## 19.5 Conclusions

A general review of quadrupole solid-state NMR of organic compounds, in particular, on spectral simulation, has been presented. When the magnitude of the quadrupole interactions is smaller than that of the Zeeman interactions, the perturbation theory can be safely used to obtain numerical formulas to express the first- and second-order Hamiltonians of quadrupole interactions under static or MAS conditions. As examples, analysis of the solid-state  $^{17}\text{O}$  NMR spectra of organic compounds was explained in detail. Conversely, when the magnitude of the quadrupole interactions is comparable to or larger than that of the Zeeman interactions, the direct diagonalization method, in which a combined Zeeman and quadrupole Hamiltonian is numerically calculated to derive the eigenvalues, should be used for the spectral simulation because the perturbation theory is no longer valid in such cases. To record NMR spectra broadened by large quadrupole interactions, there are traditionally two experimental techniques: frequency-swept NMR and field-swept NMR. Examples of both methods were briefly introduced using results for  $^{79}\text{Br}$  and  $^{33}\text{S}$  solid-state NMR of organic compounds and those forming covalent bonds.

Recently, ultra-high field magnets made of HTS materials have been developed by NMR manufacturers. Unlike in the cases of low-temperature superconducting

(LTS) materials, HTS magnets are expected to make it possible to increase magnetic field strength and allow proton Larmor frequencies of more than 1.0 GHz, and HTS magnets of 1.2 GHz, which corresponds to 28.18 T, are expected to be commercially available very soon. At the present time, there are many undeveloped research areas in quadrupole nuclei NMR due to the fact that their quadrupole interactions are too large to be handled by the currently available magnetic field strengths. It is natural to expect that ultra-high field magnets will be helpful for recording NMR spectra broadened by large quadrupole interactions, because the magnitude of second-order quadrupole interactions is inversely proportional to the strength of the external magnetic field.

Unfortunately, however, even if ultra-high field magnets are applied, it is not always true that all the quadrupole nuclei in the periodic table can be observed because of the following two reasons: (1) From the perspective of NMR instrument manufacture, a change in materials from LTS to HTS wire rods, which would make it possible to increase magnetic fields beyond 1.0 GHz, is a challenge, but for NMR users, magnetic field strengths of 1.2–1.3 GHz are still not enough to observe NMR spectra of the quadrupole nuclei that current NMR instruments cannot access. For example, solid-state  $^{33}\text{S}$  NMR spectra of organic compounds are expected to exhibit spectral widths in excess of several megahertz, even if 1.3-GHz magnets are introduced. In fact, Larmor frequencies for low  $\gamma$  quadrupole nuclei may only increase by several megahertz as the strength increases from 1.0 to 1.3 GHz. (2) The effects of CS interactions in addition to quadrupole interactions should not be discounted, and, understandably, the magnitude of CS interactions is proportional to the strength of the external magnetic field. Therefore, application of higher magnetic fields may, in most cases, result in more broadened NMR spectra. It has been reported that the spectral width of solid-state  $^{17}\text{O}$  NMR spectra for an amino acid increases as the magnetic field strength increases since, at higher magnetic fields, the factor that determines spectral width is no longer quadrupole interactions, but CS interactions. Thus, alternative methods to the use of ultra-high magnetic fields are required to observe NMR spectra for all the quadrupole nuclei in the periodic table. I believe that field-swept NMR, in which there is no limitation on the observable frequency range as long as a magnetic field can cover the range, is the best candidate for this purpose. As mentioned already, this method currently suffers from low sensitivities, but the latest technology will potentially lead to hypersensitized NMR signals.

## References

1. Slichter, C.P.: Principles of Magnetic Resonance. Springer, Berlin (1990)
2. Mehring, M.: Principles of High-Resolution NMR in Solids. Springer, New York (1983)
3. Vega, A.J.: Quadrupolar nuclei in solids. In: Grant, D.M., Harris, R.K. (eds.) Encyclopedia of Nuclear Magnetic Resonance, pp. 3869–3889. Wiley, Chichester (1996)

4. Yamada, K., Dong, S., Wu, G.: Solid-State  $^{17}\text{O}$  NMR Investigation of the carbonyl oxygen electric-field-gradient tensor and chemical shielding tensor in amides. *J. Am. Chem. Soc.* **122**, 11602–11608 (2000)
5. Yamada, K.: Recent applications of solid-state  $^{17}\text{O}$  NMR. In: Webb, G.A. (ed.) *Annual Reports on NMR Spectroscopy*, Chapter 3, pp. 115–158. Academic Press, New York (2010)
6. Yamada, K., Kitagawa, K., Takahashi, M.: Field-swept  $^{33}\text{S}$  NMR study of elemental sulfur. *Chem. Phys. Lett.* **618**, 20–23 (2015)
7. Yamada, K.: Development of sulfur NMR in chemistry. *J. Cryo. Super. Soc. Jpn.* **51**, 64–70 (2016)
8. Yamada, K., Hashizume, D., Shimizu, T., Ohki, S., Yokoyama, S.: A solid-state  $^{17}\text{O}$  NMR, X-ray, and quantum chemical study of N-a-Fmoc-protected amino acids. *J. Mol. Struct.* **888**, 187–196 (2008)
9. Abragam, A.: *The Principles of Nuclear Magnetism*. Oxford University Press, Oxford (1961)
10. Yamada, K.: Solid-State NMR in half-integer quadrupolar spins: oxygen-17 solid-state NMR in organic compounds. *J. Spectrosc. Soc. Jpn.* **55**, 99–109 (2006)
11. Skibsted, J., Nielsen, N.C., Bildsoe, H., Jakobsen, H.J.: Satellite transitions in MAS NMR spectra of quadrupolar nuclei. *J. Magn. Reson.* **95**, 88 (1991)
12. Mueller, K.T., Sun, B.Q., Chingas, G.C., Zwanziger, J.W., Terao, T., Pines, A.: Dynamic-angle spinning of quadrupolar nuclei. *J. Magn. Reson.* **86**, 470 (1990)
13. Samoson, A., Kundla, E., Lippmaa, E.: High resolution MAS-NMR of quadrupolar nuclei in powders. *J. Magn. Reson.* **49**, 350–357 (1982)
14. Frydman, L., Harwood, J.S.: Isotropic spectra of half-integer quadrupolar spins from bidimensional magic-angle spinning NMR. *J. Am. Chem. Soc.* **117**, 5367–5368 (1995)
15. Gan, Z.: Isotropic NMR spectra of half-integer quadrupolar nuclei using satellite transitions and magic-angle spinning. *J. Am. Chem. Soc.* **122**, 3242–3243 (2000)
16. Yamada, K., Nemoto, T., Asanuma, M., Honda, H., Yamazaki, T., Hirota, H.: Both experimental and theoretical investigations of solid-state  $^{17}\text{O}$  NMR for L-valine and L-isoleucine. *Solid State Nucl. Magn. Reson.* **30**, 182–191 (2006)
17. Eichele, K., Wasylisen, R.E.: WSOLIDS NMR Simulation Package, Ver. 1.17.30 (2001)
18. Baugher, J.F., Taylor, P.C., Oja, T., Bray, P.J.: Nuclear magnetic resonance powder patterns in the presence of completely asymmetric quadrupole and chemical shift effects: application to metavanadates. *J. Chem. Phys.* **50**, 4914–4925 (1969)
19. Yamada, K., Shimizu, T., Yamazaki, T., Ohki, S.: Determination of the orientations for the  $^{17}\text{O}$  NMR tensors in a polycrystalline L-alanine hydrochloride. *Solid State Nucl. Magn. Reson.* **33**, 88 (2008)
20. Scheubel, W., Zimmerman, H., Haeberlen, U.: Oxygen-17 quadrupole coupling and nuclear magnetic shielding tensors in benzophenone. *J. Magn. Reson.* **63**, 544–555 (1985)
21. Kunwar, A.C., Turner, G.L., Oldfield, E.: Solid-state spin-echo Fourier transform NMR of potassium-39 and zinc-67 salts at high field. *J. Magn. Reson.* **69**, 124–127 (1986)
22. Barbarella, G.: Sulfur-33 NMR. *Prog. Nucl. Magn. Reson. Spectrosc.* **25**, 317–343 (1993)
23. Wagler, T.A., Daunch, W.A., Panzner, M., Youngs, W.J., Rinaldi, P.L.: Solid-state  $^{33}\text{S}$  MAS NMR of inorganic sulfates. *J. Magn. Reson.* **170**, 336–344 (2004)
24. O'Dell, L.A., Moudrakovski, I.L.: Testing the sensitivity limits of  $^{33}\text{S}$  NMR: an ultra-wideline study of elemental sulfur. *J. Magn. Reson.* **207**, 345–347 (2010)
25. Yamada, K., Aoki, D., Kitagawa, K., Takata, T.: Frequency-swept solid-state  $^{33}\text{S}$  NMR of an organosulfur compound in an extremely low magnetic field. *Chem. Phys. Lett.* **630**, 86–90 (2015)
26. Bagci, T., Simonsen, A., Schmid, S., Villanueva, L.G., Zeuthen, E., Appel, J., Taylor, J.M., Sørensen, A., Usami, K., Schliesser, A., Polzik, E.S.: Optical detection of radio waves through a nanomechanical transducer. *Nature* **507**, 81–85 (2014)

# Chapter 20

## Quadrupole Nuclei in Inorganic Materials

Toshikazu Takahashi

**Abstract** The solid-state NMR of quadrupolar nuclei is becoming more important to date. The anisotropy of quadrupolar coupling cannot be eliminated by magic-angle spinning. Although large quadrupolar couplings often prevent us to observe NMR signals of quadrupolar nuclei as sufficiently separated signals, the recent development of the equipment and methods including DNP, are spreading our opportunities of NMR observation to a wider range of materials and in deeper levels of information. The quadrupolar parameters, which can be taken from NMR spectra of quadrupolar nuclei, have a potential usefulness to distinguish atoms depending on their local electrostatic environment. MQMAS or STMAS enable us not only to observe quadrupolar nuclei in separated signals but also to get quadrupolar parameters and isotopic chemical shifts of each the separated signal component in a 2D spectrum. *J*- or *D*-HMQC, CP-HETCOR and related techniques provide us information about inter-atomic chemical bonding or geometrical correlations. When the sensitivity is insufficient, besides isotopes enrichment, for quadrupolar nuclei specifically, enhancement through intra-spin population transfer methods, RAPT, FAM, DFS, WURST and HS can be applied. WURST, when combined with QCPMG method, can provide us a method for obtaining NMR spectra for those nuclei having huge quadrupolar coupling that we cannot observe the whole signal shape by simple methods. This article is dealing with the NMR methods being standard at the present, or becoming standard in the near future, especially for the practical samples, for example, mixed samples or amorphous samples. A number of experimental hints and a couple of experimental examples of  $^{27}\text{Al}$  and  $^{17}\text{O}$  are described.

**Keywords** Quadrupolar interactions · MQMAS · STMAS · HMQC · HETCOR

---

T. Takahashi (✉)

Interdisciplinary Research Center for Catalytic Chemistry, National Institute of Advanced Industrial Science and Technology, 1-1-1 Higashi, Tsukuba, Ibaraki 305-8565, Japan  
e-mail: takahashi.toshikazu@aist.go.jp

## 20.1 Introduction

Quadrupolar nuclei, having spin quantum number  $I > 1/2$ , are consisting the majority of the periodic table of elements. Above 75% of naturally occurring elements have at least one isotope that has  $I > 1/2$ . Above 65% of the naturally occurring elements have only quadrupolar nuclei in their naturally occurring isotope lists [1]. Although the NMR spectra of quadrupolar nuclei have, relatively, not been frequently appeared in literature compared to those of the spin  $1/2$  nuclei such as  $^1\text{H}$ ,  $^{13}\text{C}$ ,  $^{15}\text{N}$ ,  $^{19}\text{F}$ ,  $^{31}\text{P}$ , and  $^{29}\text{Si}$ , now quadrupolar nuclei, such as  $^7\text{Li}$ ,  $^{11}\text{B}$ ,  $^{14}\text{N}$ ,  $^{17}\text{O}$ ,  $^{23}\text{Na}$ ,  $^{25}\text{Mg}$ ,  $^{27}\text{Al}$ ,  $^{39}\text{K}$ ,  $^{41}\text{Ca}$ ,  $^{95}\text{Mo}$ ,  $^{133}\text{Cs}$ , and  $^{139}\text{La}$ , are becoming more frequently investigated than before. Needless to say, quadrupolar nuclei are playing indispensable roles in organic, inorganic, or hybrid materials, those being used in our daily life. The NMR for quadrupolar nuclei, in its principle, has already established in very early time of NMR history [2–4]. Although, comparing to the spin  $1/2$  nuclei, there still remain some difficulties in the observations of the quadrupolar nuclei by NMR, the development of NMR equipment, especially in the magnetic field strength, which is still under development using high-temperature superconducting wire [5], and the increasing detection capabilities by the development of high-speed MAS [6], low noise circuits, and cryogenic circuits including probes [7] are expanding the range of observation opportunities for the quadrupolar nuclei in various materials. Software development including NUS [8] and related time-reducing technologies will also be important in the current development for the same purpose. Now the opportunity is spread to the materials of electric power storages, catalysts, intelligent components of the construction materials or glasses, shieling components of barrier films, and surface-modified or surface-anchored materials used for providing functional surfaces such as separation or detection of particular molecules, high-performance adsorption materials, rustproofed, anti-microbial or mold-prevention functions and so on.

Before the closing remarks in this section, the author will briefly comment about the recently developed dynamic nuclear polarization (DNP) technologies, because this new technology will be opening another step of opportunity for solid-state NMR of quadrupolar nuclei [9]. DNP is the name of methods for observing dynamically polarized nuclei, usually being conducted under low or very low temperatures, through achieving a larger magnetic polarization on nuclear spins compared to those in the high-field magnetic fields ordinary used in the current NMR apparatus. The magnetization transfer from long-lived triplet molecules, electron spins of organic radicals or para-hydrogen are used to promote large content of magnetic polarization on the nuclear spins. Among them, methods using organic radical polarizers (the source of nuclear polarization formation) are recently developed much, and the specific equipment for each liquid [10] and solid sample [11] is commercialized, currently (Dr. Fujiwara and Dr. Matsuki and their group in Osaka University with collaboration of JEOL are currently developing DNP MAS NMR equipment, See Chap. 4). For the liquid samples, the target sample mixed with an organic polarizer is frozen within a glassy spin-delivering solvent (having

protons in a suitable concentration and distribution) and stored in a medium magnetic field where the sample is irradiated microwaves to promote magnetization transfer from the much more polarized electron spins to the  $^1\text{H}$  nuclear spins. Then, after a time during which the nuclear spin polarization is sufficiently developed, the frozen solid sample is rapidly dissolved by a hot solvent, then whole the solution instantaneously transferred into the observation vessel set in a standard high-field NMR magnet through a transfer tube equipped between the two magnets. For the solid samples, high-field (currently 400–800 MHz) DNP MAS NMR equipment is developed and commercialized. This equipment is also using organic radicals as the polarizer, and solvents frozen in a glassy solid containing rich protons allowing the spin diffusion from the polarizer to the sample. The sample and the polarizer and the solvent are mixed and packed in the MAS rotor. Then, the sample in a rotor is loaded into the low-temperature MAS probe, the rotor rapidly frozen under magic angle spinning in the probe around 100 K. In the standard cases, the frozen sample is continuously irradiated by high-power microwaves to promote magnetization transfer from the electrons to nuclei. Although the sample should be mixed with organic radicals, and the enhancement coefficient is usually smaller than 100, which is much lower than the theoretical limit (660), the highly enhanced sensitivity will open a new era to the solid-state NMR. Although sometimes we should still need to prepare samples with some isotopes enriched, the development of NMR techniques is thus promising to the future development of material sciences and technologies as one of the key technologies of an observing and analysis tools for materials.

In this contribution, we will describe solid-state NMR of quadrupolar nuclei. The purpose of this contribution is not to provide a comprehensive knowledge about the NMR or that of quadrupolar nuclei. It is almost concentrated to help readers who will think and learn deeply about NMR and will do experiments to observe solid-state NMR of their objective materials and extract useful information from them and to develop knowledge of their own or, in some appropriate opportunity, sharing knowledge with somebody else around the reader.

## 20.2 Anisotropy of Quadrupolar Interaction

NMR is an observation method of magnetically active nuclei electromagnetically under the influence of Zeeman interaction. When a nuclear spin is put in a uniform magnetic field, the energy levels of a spin having spin quantum number  $I$  is quantized by that interaction energy and split into  $2I + 1$  states identified by the magnetic quantum number  $I_z$  (or  $m$ ) =  $-I, -I + 1, \dots, I$ . The energy difference between each of the neighboring two levels is  $\gamma\hbar H = \hbar\omega = h\nu$ , if there are no other interactions of significance. This interaction energy is called Zeeman energy, and the states are Zeeman states. Each the  $\hbar$  and  $h$  ( $= 2\pi\hbar$ ) is Planck constant used in combination with angular velocity or frequency, respectively.  $\gamma$  is the gyromagnetic (or magnetogyric) ratio of nucleus that is a specific constant depending on the

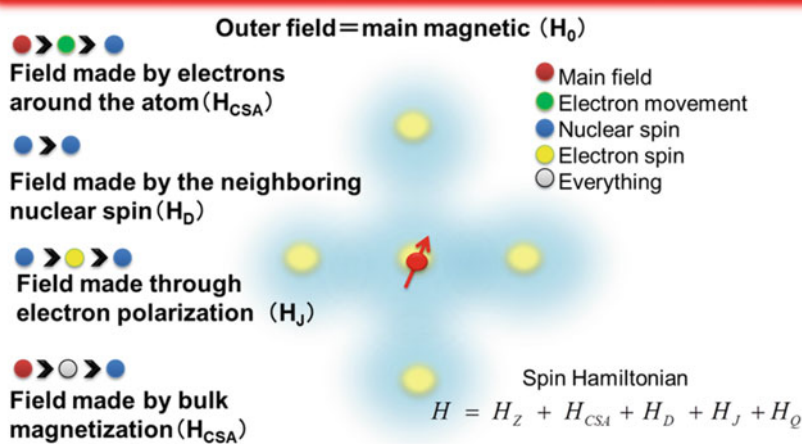


**Fig. 20.1** Various origins of primary and secondary magnetic fields that will affect the magnetic field on the location of the spin

particular nucleus.  $H$  is the magnetic field that the nucleus is feeling at a point during a time that the signal coherence continuing. The energy of Zeeman states of a quadrupolar nucleus can be described as

$$E = \gamma \hbar I_z H \quad (I_z = -I, -I+1, \dots, I) \quad (20.1)$$

We can detect nuclear spins through coherently observed electromagnetic waves emitted from the sample, just have been stimulated electromagnetically. The energy can be transferred into frequency domain through Fourier transformation of these emitted waves. In the spectrum of spins in a single magnetic environment, we can see a signal having the frequency that is corresponding to the energy difference between the two neighboring states [3].

$$\Delta E = \gamma \hbar H = h\nu \quad (20.2)$$

The NMR observation is based on the detection of this differential energy through an electromagnetic wave detection circuit including the sample. Here, the magnetic field  $H$  means not exactly the same to the main magnetic field we will apply to the sample using the magnet, however,  $H$  is including the secondary (and higher ordered) magnetic fields in that material induced by the main field (Fig. 20.1).  $H$  may include static and any fluctuated components, which means it is depending not only on the molecular structure but also on the orientation of the molecule relative to the field. Furthermore, it will be influenced by the relative distance and orientation of the neighboring molecules (Fig. 20.2). If these influences are directly added on the energy observed in the spectrum, NMR will be far

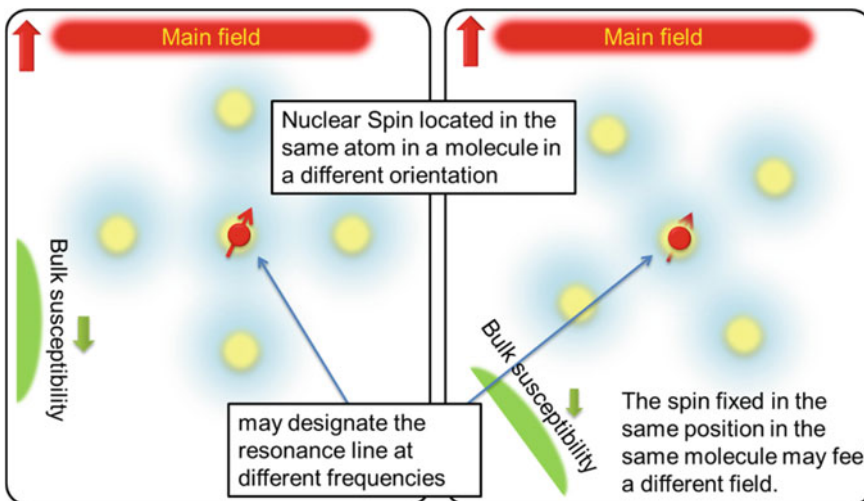


**Fig. 20.2** A spin within a same site of a same molecule will feel a different magnetic field depending on the orientation of the molecular axis relative to the field

from a method through which we can extract useful information because each molecule is under different magnetic environment at a time that will be observed at different frequencies. However, which is particularly characteristic to this method,<sup>1</sup> the observed energy is well averaged on each spin during a period of its coherence duration. In fact, this averaging duration may sustain several seconds that results in the spectrum as a signal with its width less than 1 Hz, meaning that the due time of the coherence sustaining is longer than 1 s ( $=1/(1 \text{ Hz})$ ). In the solid-state NMR, the typical line width is larger than 10 Hz even for crystallite samples, meaning the coherence time is shorter than 0.1 s ( $=1/(10 \text{ Hz})$ ). However, although there is no molecular movement around the spin that will average the field automatically as like as that in liquid-state NMR, the field averaging by certain mechanisms still works. This is obvious when we apply magic angle spinning to the sample for the observation of solid-state NMR. In this case, the orientation of the bulk magnetization anisotropy, most part of dipole–dipole interactions, and chemical shift anisotropies can be averaged so that we can observe the spins under these kinds of interactions as relatively sharp signals in the NMR charts.

The reason why the dipole–dipole interaction will be averaged by the MAS can be depicted in the Fig. 20.3. In a sufficiently strong magnetic field of  $+z$ -axis, every spin will be precessing around the main field vector in parallel or antiparallel directions in most of the time. In this situation, the average magnetic field produced by a spin will have a particular orientation dependence having the shape as like as that of  $d_z^2$  orbital. Under MAS conditions, from a fixed point of view on the spin A,

<sup>1</sup>The ESR and Mössbauer spectra also have similar characteristics.

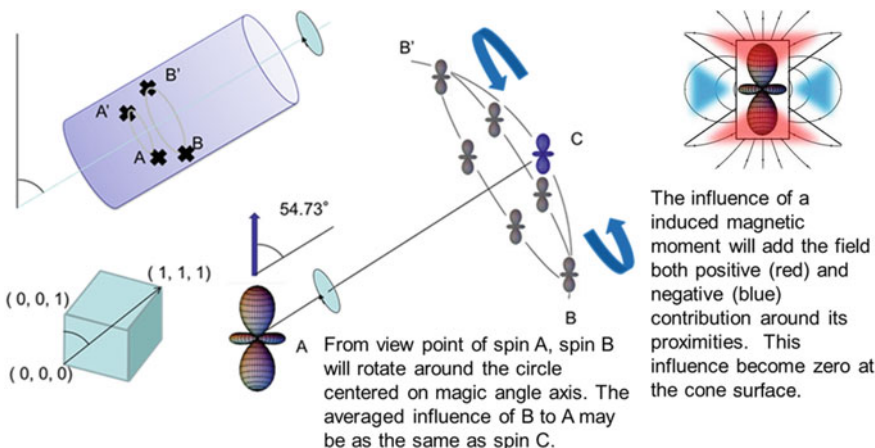


**Fig. 20.3** Magic angle spinning under strong field will cancel out the dipole–dipole interactions

the spin B interacting with this spin will be seen as rotating along a circle centered on the magic angle axis passing through the spin A. As a result, the magnetic field effect caused by spin B on the point spin A will be the same to those as if that of spin C may cause to spin A. Because a dipole moment does not have any  $z$ -axis component at the cone surface having magic angle relative to the  $z$ -axis (main field). Zero quantum contribution (chemical shift) of the dipole–dipole interaction between the two spins will be averaged out in this situation.

There are several numbers of anisotropic interactions that cannot be averaged completely by MAS. These interactions comprise the factors of ‘inhomogeneous broadening.’ One of the origins of inhomogeneous broadening is coming from an anisotropy in the magnetic susceptibility of a local magnetization source within the sample. The secondary magnetic field caused by a molecular residue will normally be cancelled out by orientation averaging caused by free molecular motions (typically in liquid states) or magic angle spinning (in solid samples). However, when the molecular residue has a relatively strong anisotropy in its magnetic susceptibility, a residual magnetic moment will appear which will not be averaged completely even after orientation averaging between the molecular axes and the magnetic field. These phenomena are called residual dipolar coupling (RDC) in liquid-state NMR [12], which is responsible for NOE interaction in the liquid state. In the solid-state NMR particularly, in some cases, this type of interaction causes splitting on the signals. These phenomena are obvious especially the relatively sharp signals of spin  $1/2$  nucleus, which has a strong dipole coupling to a quadrupolar nucleus [13–15]. These phenomena are called as residual dipolar shifts or splitting (RDS) in solid-state NMR [16, 17], however, the difference between them may exist only on the level of field averaging relative to the field difference. A large anisotropy on magnetic susceptibility produces small anisotropic field that causes small chemical shifts to the nuclei located on the close proximities of that

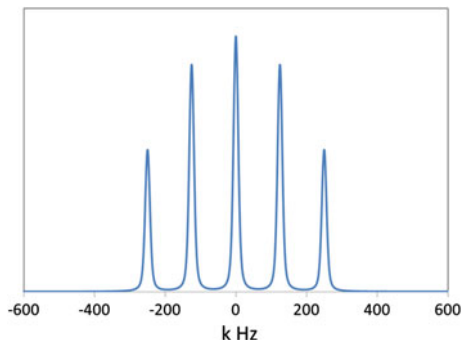
residue depending on the relative direction between the orientation vector connecting to the spin from the functional group (more exactly, the center of the source of the anisotropy) and the orientation of the group's residual magnetization orientation. In the liquid-state NMR, this interaction will effect only small chemical shifts on its close proximities which doesn't cause any broadenings to the signals, because the orientation averaging of a molecule within a liquid is perfect owing to the molecular motions, which are faster than  $10^{10}$  Hz. However, in some cases of larger molecular systems, the anisotropy of this interaction becomes obvious. Thus, RDC potentially causes both the line-broadenings and field-dependent shifts to the spins in the close proximities. A quadrupolar nucleus may, as like as a permanent RDC, have anisotropy that cannot be averaged by MAS. The main term being responsible to this line-broadening is the second-order quadrupolar interaction. In solid-state NMR including quadrupolar nuclei, we often encounter the RDC caused by pure dipole–dipole couplings and quadrupole–dipole couplings (sometimes called as quadrupole–dipole cross-term [16, 18]). Although RDC becomes relatively smaller in the higher magnetic fields, this kind of interactions makes one of the main reasons of line-broadening in solid-state NMR. Every kind of magnetic susceptibility anisotropies may cause such kind of inhomogeneous (being not care whether or not this term is suitable) broadenings on its surface by a similar mechanism.

Different from those nuclei having spin number 0 or 1/2, the charge distributions on a quadrupolar nucleus are not in perfect spherical symmetry. This situation leads to an interaction between a quadrupolar nucleus and an electrostatic field surrounding it mainly through the field's second-order gradient by the 3D space on that point the nucleus being located. Since the spin is one of the substantial properties of nuclei that interact with the magnetic fields exclusively, the nuclear spin may not interact with the electrostatic field directly. However, because of the strong binding between the nucleon spins inside a nucleus, the magnetic moment of a nucleus scarcely allows a single nucleon spin to interact with the exterior magnetic field as an independent spin. The nuclear spins do not indicate any sub-structures other than  $I_z$  dependence when it is investigated by the photons of their energy around Larmor-frequencies (typically several 10's of MHz to around 1 GHz), which are used in contemporary high-resolution NMR apparatus, and are having extremely low energy even compared to the environmental photons, i.e., environmental noise.<sup>2</sup> Consequently a spin behaves as like as a fixed magnetic moment in any electro-photonic experiments except for those using very high-energy photons of ranges of  $\gamma$ -ray frequencies as the incident light sources. In a literature [2], the authors described that within one nucleus, consisting of numbers of sub-particles such as quarks or gluons, the angular motion of the charges within the nucleus is strongly restricted by the nuclear spin that will restrict strongly the moving charges

---

<sup>2</sup>It is at least two orders lower even compared to the peak frequency of the Universe's 3.7 K background radiation, having its peak frequency at 160.2 GHz, which is around 2 orders lower to that of the earth's environmental temperatures.

**Fig. 20.4** A virtual spectrum of a spin 5/2 with  $2\omega_Q = 125$  kHz, Gaussian (20 kHz), and Lorentzian (10 kHz) broadening



distributed within the nuclei being under a higher spatial symmetry. This conjecture is reasonable considering the electric and the magnetic energy within a nucleus may be around  $10^{17}$  and  $10^9$  Hz, respectively. The deviation of the charge distribution within a nucleus will be minimized by taking a higher rotational symmetry. Comparing the energies, the deviation of the charge distribution within a nucleus will be the order of  $10^{-8}$  compared to the perfect sphere (10's cm /the earth's radius).<sup>3</sup>

A question will possibly be argued, why the non-spherical shape of the nuclei is possible, when the angular momentum state of that nuclei being zero, which is exclusively observed in the ground state of nuclei. Since, when a nucleus is in its ground state, it stands in the smallest angular momentum condition  $L = 0$ , in that state, the uncertainty of the orientation vector of this complex particle will be perfectly undeterminable compared to any of the exterior world frames, i.e., it exists in a perfect spherical symmetry. However, a small deviation from the spherical symmetry will be possible due to the perturbation of the magnetic interactions between the spin and the orbital within the nucleus, which causes the ground state nucleus mixing with the higher rotational quantum states with even angular momentum quantum numbers, for example,  $L = 2, 4$ . This will enable the shape of nucleus to subject a very small deviation from a perfect spherical symmetry observable from the exterior frames. The quadrupolar coupling that is observed in NMR spectra can be described as the small contribution of the higher orders of rotational states introduced by perturbation of magnetic interactions within a nucleus that interact with the second-order gradient of the external electric field.

The  $2I + 1$  energy levels of a quadrupolar nucleus with spin quantum number  $I$  can be confirmed by observing quadrupolar splitting of the NMR signals. Figure 20.4 demonstrates a static NMR spectrum, taken under a stable magnetic field, of a virtual single crystal sample containing a single site spin 5/2 nuclei. In a static field, each the spin will be observed as  $2I + 1$  signals separated by  $2\nu_Q$

---

<sup>3</sup>According to Cohen 1954, the order of quadrupolar interaction is as large as  $Q'_{jk}(\partial^2 V / \partial x_i \partial x_j) \sim e r_n^2 \left( \frac{e}{r_e^3} \right) = e V_0 (r_n / r_e)^2$ . The quadrupolar interaction is around  $10^{-8}$  compared to the electrostatic force between the charges within the nucleus.

(Quadrupolar frequency) approximately each the signal is corresponding to transition between the magnetic quantum number (also corresponding to the stationary states of observable  $I_z$ , with a  $z$ -axis taken to be parallel to the magnetic field)  $m$  and  $m + 1$  states. This separation frequency is corresponding to the first-order quadrupolar interaction energy. When the quadrupolar interaction is sufficiently small, the second-order shift can be negligible and the signals separated only by the influence of first-order quadrupolar interaction can be observed. The signal intensity of them is proportional to  $\zeta^2(m, m + 1) = I(I + 1) - m(m + 1)$ . For the case of  $I = 5/2$ , the ratio is 5:8:9:8:5. This ratio is confirmed experimentally for single crystal samples containing quadrupolar nuclei [19]. If the single crystal in the magnetic field is rotated around an axis for an angle, then the frequency splitting of the spin will be changed, however, that of central band changes only a small amount (by CSA or dipolar couplings or higher order of quadrupolar couplings). For the sample consisting of many numbers of crystallites, the signal will be observed in a different shape. The signal will be distributed along with the frequency range in which orientation dependence of the interaction sweeps spherically. The angular dependence of this frequency change is similar to those observed in a spin 1/2 nuclei having a chemical shift anisotropy (CSA). Indeed, as like as CSA, the first-order quadrupolar interaction can be cancelled by magic angle spinning. The signal position will be influenced by not only the first-order quadrupolar interaction but also the second-order quadrupolar interaction. This is obvious when the quadrupolar interaction runs high. The interaction anisotropy is much different from that of the chemical shift anisotropy and becomes one that cannot be averaged perfectly by magic angle spinning. Using this anisotropy positively, crystal structure analysis using NMR is possible and several numbers of groups are developing this method [20].

## 20.3 Orientation Dependence of Quadrupolar Interaction

In this part, we will follow the [Ref. 21]. The orientation dependency of the quadrupolar interaction can be described below. For simplicity, it is ordinarily described on its principal axis system (PAS) of the quadrupolar interaction. The quadrupolar interaction Hamiltonian ( $H_Q$ ) is written as,

$$\hat{H}_Q = \frac{eQ}{6I(2I-1)\hbar} \left\{ \sum_{\alpha, \beta=x, y, z} V_{\alpha, \beta} \left[ \frac{3}{2} (\hat{I}_\alpha \hat{I}_\beta + \hat{I}_\beta \hat{I}_\alpha) - \delta_{\alpha, \beta} I(I+1) \right] \right\}, \quad (20.3)$$

$$V_{\alpha, \beta} = \left. \frac{\partial^2 U}{\partial \alpha \partial \beta} \right|_{r=0}$$

where  $\delta_{\alpha, \beta}$  is Kronecker delta.  $U$  is the electric potential formed by the charge distributions outside of the nucleus, and  $V_{\alpha, \beta}$  are the Cartesian components of EFG at the origin. Because the matrix  $\mathbf{V} = \{V_{\alpha\beta}\}$  should be real and symmetry from its

definition, it will have three real eigenvalues and can be diagonalized by applying an orthogonal transformation  $T$ ,

$$V = T \begin{bmatrix} V_{xx} & 0 & 0 \\ 0 & V_{yy} & 0 \\ 0 & 0 & V_{zz} \end{bmatrix} T^{-1} \quad (20.4)$$

can be obtained in the newly defined coordination system  $(x, y, z)$ , determined also with the convention of  $|V_{xx}| \leq |V_{yy}| \leq |V_{zz}|$ . This new coordination system, of which the  $z$ -axis is set parallel orientation to the maximum electric field gradient, is called principal axis system (PAS) of the quadrupolar interaction. For simplicity, we will discuss the quadrupolar interaction based on this PAS, exclusively hereafter. The electrostatic force at the origin should be neutral because we are considering only the static charge distribution that should be balanced at the origin, so we obtain that the Laplacian of the field at the origin should be zero ( $V_{xx} + V_{yy} + V_{zz} = 0$ ). Thus, the independent components of this matrix will be reduced to two, quadrupolar coupling constant,  $eq$ , the largest component of the gradient tensor, and the asymmetric parameter,  $\eta$ , defined by

$$eq = V_{zz}, \quad \eta = \frac{V_{xx} - V_{yy}}{V_{zz}}. \quad (20.5)$$

If the sign of  $V_{zz}$  is positive, then those of  $V_{xx}$  and  $V_{yy}$  both are negative, or the other case of fully inverse signs is possible. In any cases,  $\eta$  varies from 0 to 1. If  $\eta$  is zero, then  $V_{xx} = V_{yy} = (-1/2)V_{zz}$ . If  $\eta = 1$ , then  $V_{xx} = 0$  and  $V_{yy} = -V_{zz}$ . Consequently,  $V_{xx}$  varies between  $-(1/2)V_{zz}$  and zero, and  $V_{yy}$  varies between  $-V_{zz}$  and  $(-1/2)V_{zz}$ . If the charge distribution around the nuclei is in axial symmetry, and if the polar orientations along with the symmetry axis are positively charged, then  $eq$  becomes positive and if negatively charged, negative. If the charge distribution around the nuclei is having a perfect tetrahedral or octahedral symmetry, then  $eq = 0$ . Thus, the orientation of the PAS is closely related to the coordination environment of the nuclei. Only the two parameters,  $eq$  and  $\eta$ , can be obtained in NMR experiments as the independent parameters of the electric field gradient.

The electronic field gradient can be rewritten by the spherical tensor expressions on the PAS in order to improve the visibility of the expressions in the intermediate calculations. In those expressions,

$$V_0^{\text{PAS}} = \sqrt{\frac{3}{2}}eq, \quad V_1^{\text{PAS}} = V_{-1}^{\text{PAS}} = 0, \quad V_2^{\text{PAS}} = V_{-2}^{\text{PAS}} = \frac{1}{2}eq\eta. \quad (20.6)$$

From now on, we will attempt to explain the anisotropy of quadrupolar interaction quantitatively to a certain level. As for the more generalized derivations of formula, we recommend the readers to refer to the documents [21] or books [22, 23]. The author has been given great numbers of help from these two books everywhere in this contribution.

When the quadrupolar interaction is relatively small compared to the Zeeman interaction, the quadrupolar interaction can be expressed correctly by using perturbation theory. Here we will express the Hamiltonian of the quadrupolar interaction by the first and the second order of perturbation to the Zeeman interaction as,

$$\hat{\mathcal{H}}_Q^{[1]} = \frac{eQ}{4I(2I-1)\hbar} \frac{\sqrt{6}}{3} [3\hat{I}_z^2 - I(I+1)] V_0, \quad (20.7)$$

and

$$\hat{\mathcal{H}}_Q^{[2]} = -\frac{1}{\omega_0} \left[ \frac{eQ}{4I(2I-1)\hbar} \right]^2 \times \left\{ \begin{array}{l} 2V_{-1}V_1\hat{I}_z[4I(I+1) - 8\hat{I}_z^2 - 1] \\ + 2V_{-2}V_2\hat{I}_z[2I(I+1) - 2\hat{I}_z^2 - 1] \end{array} \right\}. \quad (20.8)$$

The first-order quadrupolar interaction is independent to  $\omega_0$ , whereas the second-order interaction is proportional to  $C_Q^2/\omega_0$ . This is the reason why strong magnetic field is suitable for the observation of quadrupolar nuclei.

The shift of the first-order quadrupolar interaction for the transition energy from the  $m$  to  $m-1$  states, which are characterized by their magnetic quantum numbers is

$$\begin{aligned} \omega_{m,m-1}^{(1)} &= \langle m-1 | \hat{\mathcal{H}}_Q^{[1]} | m-1 \rangle - \langle m | \hat{\mathcal{H}}_Q^{[1]} | m \rangle \\ &= \frac{3eQ}{4I(2I-1)} \frac{\sqrt{6}}{3} (1-2m) V_0 \end{aligned} \quad (20.9)$$

Thus, the resonance frequency will split into  $2I+1$  lines separated by a constant,

$$2v_Q^{\text{PAS}} = \frac{3e^2qQ}{2I(2I-1)\hbar} = \frac{3C_Q}{2I(2I-1)}, 2\omega_Q^{\text{PAS}} = \frac{3\pi C_Q}{2I(2I-1)}. \quad (20.10)$$

The parameter  $2v_Q^{\text{PAS}}$ (or in angular velocity,  $2\omega_Q^{\text{PAS}}$ ), often called as quadrupolar splitting frequency and the  $C_Q$ , defined by  $C_Q = e^2qQ/h$  is called as quadrupolar coupling constant, which is also denoted as NQCC or QCC or  $C_q$  or  $C_{\text{qcc}}$  in literatures. Thus, the frequency of the central line does not shifted by the first-order interaction.

The second-order quadrupolar shift can be calculated as

$$\begin{aligned} \omega_{m,m-1}^{(2)} &= \langle m-1 | \hat{\mathcal{H}}_Q^{[2]} | m-1 \rangle - \langle m | \hat{\mathcal{H}}_Q^{[2]} | m \rangle \\ &= -\frac{2}{\omega_0} \left[ \frac{eQ}{4I(2I-1)\hbar} \right]^2 \times \left\{ \begin{array}{l} V_{-1}V_1[24m(m-1) - 4I(I+1) + 9] \\ + V_{-2}V_2[6m(m-1) - 2I(I-1) + 3] \end{array} \right\} \end{aligned} \quad (20.11)$$

In Eqs. 20.9 and 20.11, the anisotropic part of the interactions is included in terms correlated with  $V_0$ ,  $V_1$ ,  $V_{-1}$ ,  $V_2$ , and  $V_{-2}$ . These terms can be transferred to those in another coordination frame using Wigner rotation matrix elements [21] defined by the Euler angles,  $\alpha$ ,  $\beta$ , and  $\gamma$

$$V_i = \sum_{j=-2}^2 D_{j,i}^{(2)}(\alpha, \beta, \gamma) V_j^{PAS} \quad (20.12)$$

In a single crystal, the orientation-dependent quadrupolar splitting frequency can be written using the Euler angles as,

$$\omega_Q = \frac{3\chi}{2I(2I-1)} \left[ \frac{1}{2}(3\cos^2 \beta - 1) + \frac{1}{2}\eta \sin^2 \beta \cos 2\alpha \right], \quad (20.13)$$

where  $\chi$  is another quadrupolar coupling constant used with angular velocity,  $\chi = 2\pi C_Q$ . The first-order quadrupolar shift under static conditions is

$$\omega_{m-1,m}^{(1)\text{static}} = (1-2m)\omega_Q \quad (20.14)$$

The shift of the center band will become zero, and the other lines are equally separated. The separation frequency is dependent on the orientation. For the second-order shifts, the orientation dependency is expressed as,

$$\begin{aligned} \omega_{-1/2,1/2}^{(2)\text{static}} &= -\frac{1}{6\omega_0} \left[ \frac{3\chi}{2I(2I-1)} \right]^2 \left[ I(I+1) - \frac{3}{4} \right] \\ &\times [A(\alpha, \eta) \cos^4 \beta + B(\alpha, \eta) \cos^2 \beta + C(\alpha, \eta)] \end{aligned} \quad (20.15)$$

with

$$\begin{aligned} A(\alpha, \eta) &= -\frac{27}{8} + \frac{9}{4}\eta \cos 2\alpha - \frac{3}{8}(\eta \cos 2\alpha)^2 \\ B(\alpha, \eta) &= -\frac{30}{8} + \frac{1}{2}\eta^2 - 2\eta \cos 2\alpha + \frac{3}{4}(\eta \cos 2\alpha)^2 \\ C(\alpha, \eta) &= -\frac{1}{8} + \frac{1}{3}\eta^2 - \frac{1}{4}\eta \cos 2\alpha - \frac{3}{8}(\eta \cos 2\alpha)^2 \end{aligned} \quad (20.16)$$

Under MAS conditions, the first-order quadrupolar interaction becomes zero. The second-order quadrupolar interaction in the center band is

$$\begin{aligned} \omega_{-1/2,1/2}^{(2)\text{MAS}} &= -\frac{1}{6\omega_0} \left[ \frac{3\chi}{2I(2I-1)} \right]^2 \left[ I(I+1) - \frac{3}{4} \right] \\ &\times [D(\alpha, \eta) \cos^4 \beta + E(\alpha, \eta) \cos^2 \beta + F(\alpha, \eta)] \end{aligned} \quad (20.17)$$

with

$$\begin{aligned} D(\alpha, \eta) &= -\frac{21}{16} - \frac{7}{8}\eta \cos 2\alpha + \frac{7}{48}(\eta \cos 2\alpha)^2 \\ E(\alpha, \eta) &= -\frac{9}{8} + \frac{1}{12}\eta^2 + \eta \cos 2\alpha - \frac{7}{24}(-\eta \cos 2\alpha)^2 \\ F(\alpha, \eta) &= \frac{5}{16} - \frac{1}{8}\eta \cos 2\alpha + \frac{7}{48}(\eta \cos 2\alpha)^2 \end{aligned} \quad (20.18)$$

Here, the orientation of the magnetic field vector is described on the basis of the Cartesian coordinates of the PAS of the quadrupolar interaction.

Using MAS, the second-order effect to the line width is reduced to about 30% [24] that enables us to observe  $\text{Al}[\text{O}_4]$  and  $\text{Al}[\text{O}_6]$  in  $\gamma\text{-Al}_2\text{O}_3$  as separate signals in 400 MHz magnets (Fig. 20.5). One important thing should be pointed out. The second-order quadrupolar interactions are consisting of not only orientation-dependent terms but also an orientation-independent part that will result a field dependent permanent shift relative to the  $\delta_{\text{iso}}$  in the spectrum. For this reason, the peak positions of NMR signals of quadrupolar nuclei are field dependent. For a signal in which the environment of a quadrupolar nucleus has a certain deviation, when assuming a Gaussian distribution to the  $C_Q$ , the apparent signal will be distributed unsymmetrically in the frequency domain as can be seen in the Fig. 20.5 [25].

In Fig. 20.6 is illustrated the orientation dependence of the quadrupolar interactions with virtual quadrupolar nuclei each having 7 MHz of quadrupolar coupling

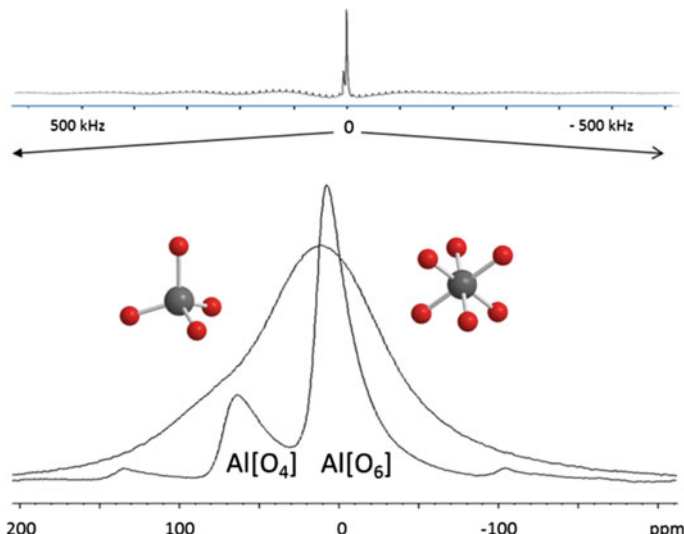
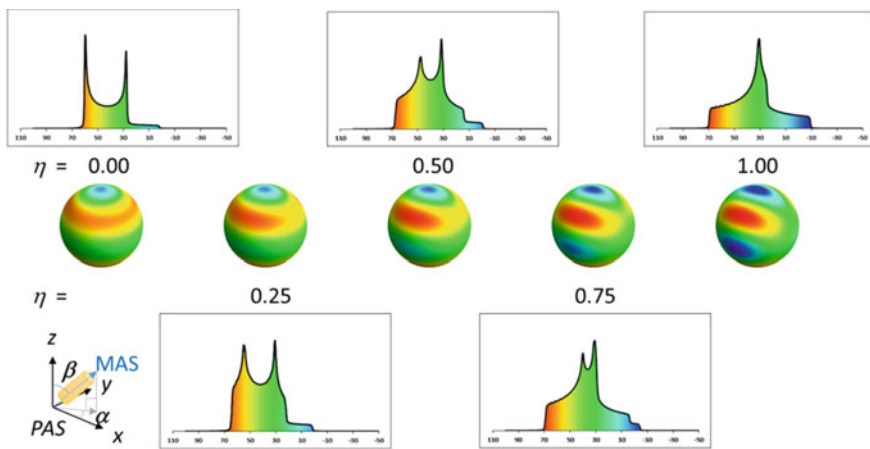


**Fig. 20.5** A typical 1D spectrum of a spin 5/2 nuclei. MAS NMR spectrum of  $\gamma\text{-Al}_2\text{O}_3$ . The whole range spectrum (upper) with a center expansion (lower) of MAS (relatively sharp) and non-MAS



Calculated center-band MAS spectra of  $^{27}\text{Al}$  species ( $\delta_{\text{iso}} = 70$  ppm,  $C_Q = 7$  MHz,  $\eta = \{0, 0.25, 0.5, 0.75, 1\}$ , exponential time constant = 100 Hz) in 400 MHz magnet with their MAS axis orientation dependence compared to the PAS.

**Fig. 20.6** Calculated MAS spectra of a spin 5/2 nuclei with the same  $C_Q$  and different  $\eta$ 's, with spherical maps of frequency-orientation relationship of the MAS axis to the PAS

constant,  $C_Q$ ,  $\delta_{\text{iso}}$  (70 ppm) and 6 different  $\eta$ 's. The  $\omega_0$  is  $104.6$  MHz/ $2\pi$  which is related to a  $\text{Al}[\text{O}_4]$  site in a silica-alumina compounds with relatively a large  $C_Q$ . The correspondence of resonance frequency in the MAS spectrum patterns and the MAS axis orientation dependences relative to the PAS are illustrated by colored spheres.

In the cases that both the quadrupolar interaction and the CSA and/or the other anisotropic interactions are comparable, numerical simulation will be needed for the analysis of the spectrum. For single crystal samples, the relative orientation between the two PAS of CS tensor and the EFG tensor is described by a set of Euler angles ( $\alpha$ ,  $\beta$ ,  $\gamma$ ), which can be obtained by fitting the simulation data to the experimental ones. However, for the amorphous or mixture solids, these parameters are rarely obtained separately.

## 20.4 Signal Separation Through Quadrupolar Coupling

Most of the spectrometry is being used for separation of the signals obtained from the objective materials to get information about the amounts and properties of particular ingredients. However, a large second-order quadrupolar interaction of a nucleus often prevents us to observe signals under different environments separately. As a result, there have been long demands for the observation of half-integer quadrupolar nuclei as well-separated, relatively narrow signals. For this purpose, several numbers of methods have been developed that may cancel the second-order quadrupolar broadenings in NMR. As systematical methods, double rotation

(DOR) and dynamic angle switching (DAS) were implemented both using specifically designed probes. Both of them are containing their particular advantages; however, here we have no space to deal with them further. Currently, multi-quantum MAS (MQMAS) is most frequently used for obtaining the quadrupolar parameter and a chemical shift, and obtaining separated signals depending on these parameters, because this method uses no special probes other than a normal MAS probe.

### 20.4.1 MQMAS

Frydmann and his coworker have first proposed MQMAS as a 2D NMR method [26] that can refocus anisotropic quadrupolar interactions in the F1 dimension (the second Fourier-transformed frequency dimension upon the parameter evolution time,  $t_1$ ). We use F2 dimension as the Fourier-transformed frequency dimension with the observation time,  $t_2$  in accordance with the commonly used convention) in a 2D map. The word ‘multi-quantum coherence’ is used first time by a Japanese researcher, Dr. Hatanaka as had been commented in a book [4]. Single quantum (SQ) coherence may be a single photon entangled state with a quadrupolar nucleus on its  $I_z = 1/2$  and  $-1/2$  Zeeman states. This coherence can be exclusively used for the observation of the CT band spectra. Similarly, MQ coherence means that an entangled state between  $+m$  and  $-m$  ( $m \leq I$ ) states of a quadrupolar spin with an MQ-energied photon that may have made by  $2m$  photons of incidental electromagnetic wave. Depending on the phase evolution frequency, we call the ‘coherence order’ of this entangled state,  $p$  (in the present case,  $|p| = 2m$ ). This method is based on the phenomena that the anisotropy of quadrupolar interaction of MQ coherence is proportional to that of SQ coherence in the frequency domain with a single universal ratio  $R(S, p)$ , described below,

$$R(S, p) = \frac{p[36S(S+1) - 17p^2 - 10]}{36S(S+1) - 27}, \quad (20.19)$$

which is depending only on the spin quantum number  $S$  and the coherence order  $p$ . Another important point is that  $R(S, p)$  can be selected negative for every combination of  $S$  and  $|p|$ . So, for a quadrupolar nucleus, when it experiences both the SQ and MQ coherences, in the time domain with each the time duration of  $1:R$ , all the nuclear spins under the identical orientation-dependent quadrupolar interactions, however under different orientations to the field, will evolve to refocus at the same time and form an echo signal. This echo is called isotropic quadrupolar echo. Based on these phenomena, controlling the evolution time of MQ coherence by changing the time between the excitation and conversion pulses, we can observe isotropic quadrupolar echo at a time depending on the  $C_Q$ ,  $\eta$  and  $\delta_{iso}$ . The resulted 2D data will contain the information of  $P_Q$  ( $P_Q$  = Quadrupolar parameter;  $P_Q^2 = C_Q^2(1 + \eta^2/3)$ ) and  $\delta_{iso}$  for each the separated signals. Numbers of introductions and

reviews of MQMAS are published. Here we describe the most frequently used  $z$ -filtered MQMAS [25, 27] in further detail. This most frequently used method is using symmetrical coherence pathways between  $p = 3 \rightarrow 0$  and  $-3 \rightarrow 0$  for the 3Q MQMAS. This method is suitable for cancelling the phase dispersive component in the finally obtained 2D map.

$Z$ -filtered MQMAS uses three pulses, two of which are at around the maximum strength to that probe, the third one is normally set to be a weak or selective pulse. Under MAS conditions, a strong pulse around  $180^\circ$  is first irradiated for the excitation of multi-quantum coherence. The second strong pulse around  $90^\circ$  is used to convert the MQ coherence into SQ coherence selecting that coherence through applying phase cycling. During the next waiting time, normally around  $20\ \mu\text{s}$ , the magnetization to be observed will be settled in the  $z$ -direction for avoiding appearance of dispersive components of the magnetization. The last weak or selective pulse will convert the magnetization to be the observable SQ coherence and the resulted signal will be observed as echoes with the coherence order  $|p| = 1$ . Fourier-transformed spectrum will show several numbers of slanted ridge-like peaks in the 2D map because each the peak is made by echo signals with those the starting time shifted sequentially (Fig. 20.6). These can be made parallel to the F2 axis by applying shearing to the 2D spectra. The quadrupolar parameter and the isotropic chemical shifts can be obtained from this finally obtained 2D map using the F1 and F2 value of the center of gravity of each peak by simple linear combination of these values. For the case of 3Q MQMAS ( $m' = 3/2$ ), the equations are

$$\delta_{\text{CS}} = \frac{10}{27} \delta_2^{\text{CG}} + \frac{17}{27} \delta_{\text{ISO}}^{\text{CG}} \quad (20.20)$$

$$\delta_{\text{QIS}} = \frac{17}{27} (\delta_2^{\text{CG}} - \delta_{\text{ISO}}^{\text{CG}}) \quad (20.21)$$

where  $\delta_2^{\text{CG}}$  and  $\delta_{\text{ISO}}^{\text{CG}}$  are the center of gravity of the 2D peak obtained by F2 and F1 value in the sheared 2D map, respectively.  $\delta_{\text{CS}}$  and  $\delta_{\text{QIS}}$  are the chemical shift and second-order quadrupolar shift of the peak. From these parameters, the quadrupolar parameter  $P_Q$  can also be calculated by the following equations,

$$P_Q^2 = (\delta_{\text{ISO}}^{\text{CG}} - \delta_2^{\text{CG}})^2 \cdot F(S) \cdot v_0^2 \times 10^{-6} \quad (20.22)$$

$$F(S) = \frac{680[2S(2S-1)^2]}{81[4S(S+1)-3]} \quad (20.23)$$

Here we will show an example of  $^{27}\text{Al}$   $z$ -filtered 3Q MQMAS chart. Zeolites and related materials are essential in catalysis and adsorbate materials. MQMAS is frequently used in the research of these materials sciences. Figure 20.7 shows  $^{27}\text{Al}$  MQMAS of ALPO-15 taken by using 4 mm MAS rotor spinning at 10 kHz within a MAS probe set in a 400 MHz magnet. You can see five peaks separately observed in the 2D map. In most of silica-alumina or alumino-silicate samples, 2D peaks of

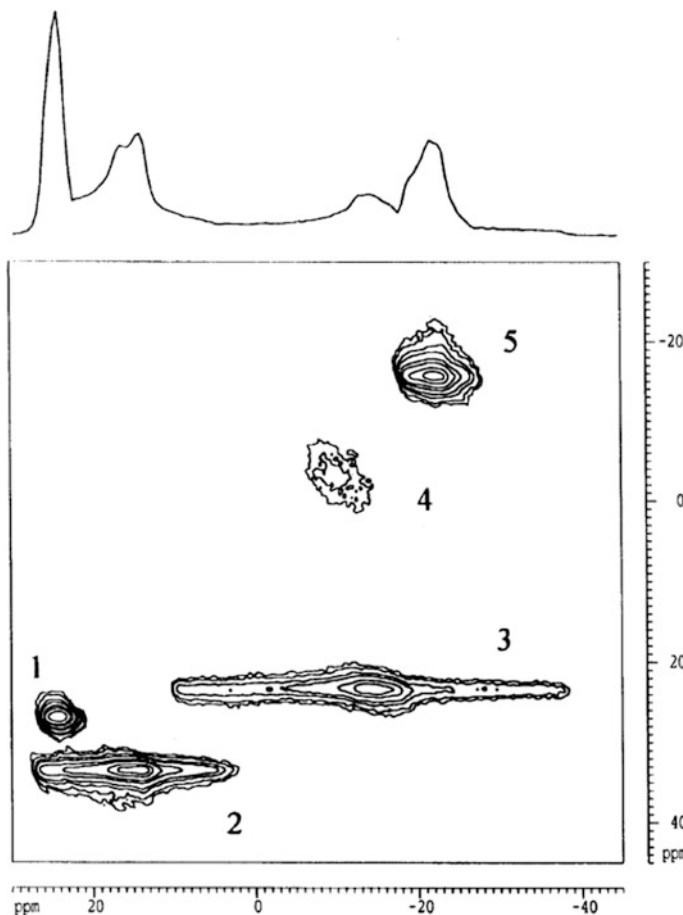


**Fig. 20.7** Z-filtered 3Q MQMAS spectrum of AlPO-14.  $^{27}\text{Al}$  3Q-MQMAS of AlPO-14. Two Al  $[\text{O}_4]$  (1,2), one Al  $[\text{O}_5]$  (3) and two Al  $[\text{O}_6]$  (4,5) sites are separately observed in this chart [27] (b). Copyright from Elsevier 4177351452113.

$^{27}\text{Al}$  signals of different coordination numbers can be observed separately. In some cases, we can recognize two or three peaks are included within the Al $[\text{O}_4]$ , Al $[\text{O}_5]$  or Al $[\text{O}_6]$  sites. From each the separated peak, with some help of spectral simulation softwares, we can obtain a set of quadrupolar parameters,  $C_Q$  and  $\eta$ , and an isotopic chemical shift,  $\delta_{\text{iso}}$  for each of the peaks.

There have been proposed a number of variations based on the same principle [28–32]. Each method has its own advantages and drawbacks. Among them, four pulse sequences, split-t1 type of MQMAS is useful for obtaining data which doesn't need shearing. SPAM may be useful in some cases for its ability to sensitivity enhancement. Although in both of these cases, the peak shape might be skewed a little. Note that in the former case, the parameter extraction should be performed in a different way [29].

### 20.4.2 STMAS

STMAS is a 2D NMR method that provides spectrum much looks like those spectra obtained by MQMAS, if we look at the result. However, this method is using different coherent pathway, compared to MQMAS, for the echo to be refocused [33]. STMAS uses spinning side bands of satellite transition (ST) bands, gathering them into a single peak in the F1 dimension of a 2D map, with an increment of  $t_1$  interval synchronized to the rotation period of the MAS rotor. STMAS uses coherent transfer echo that will form after the single pulse excitation of the ST bands and the following conversion pulse applied to the CT band. The initially excited nucleus will experience the two coherent states during the time domain and will make the coherence transfer echoes at a time. The advantage of STMAS compared to MQMAS is mainly in its higher sensitivity [34], since MQMAS adopts phase cycling that cancels the main part of the transiently obtained signals, resulting in the relatively lower overall sensitivity. A number of authors are describing the advantage of STMAS to MQAS on this point [35–37], although STMAS demands severer experimental settings in MAS rotation speed ( $\pm 2$  Hz) and MAS angle  $0.003^\circ$  than those demanded by MQMAS. These are needed for preventing loss of refocusing the ST band signals that are necessary for obtaining the coherent transfer echo. In many cases, samples showing less ST band signals are not suitable for the STMAS. Since the line shape especially in the F1 axis on the 2D chart will be broadening in those samples. A possible reason that would cause F1 broadening is molecular motion [38].

## 20.5 Signal Separation Through Correlations to Other Nuclei

NMR provides us extremely precise information of the nucleus observed in a particular frequency. What is the most unique property compared to the other spectroscopic method is the ability of correlation information between homo- or heteronuclei. In this section, we will describe the solid-state NMR using CPMAS and HMQC type coherence transfer methods.

Cross-polarization (CP) is a solid-state NMR method using magnetization transfer between two different nuclei under close proximities. When a pair of two  $I = 1/2$  spins, identified by  $i$  (initial) and  $f$  (final), are simultaneously irradiated and spin-locked at the same nutation rate,  $v_{1f} = v_{1i}$ , the relatively less abundant spin with low Larmor frequency will be magnetized by polarization transfer from the other abundant spin with high Larmor frequency. The condition,  $v_{1f} = v_{1i}$ , is called Hartman-Hahn matching condition, which allows magnetization transfer between the two nuclei through dipole-dipole interaction between them, and causes flip-flop between the two spins. CPMAS (or CPMAS or CP/MAS, meaning CP under magic angle spinning of the sample) is one of the most frequently used solid-state NMR

techniques used in the observation of a relatively rare nuclei with low Larmor frequency spin X (typically  $^{13}\text{C}$ ,  $^{15}\text{N}$ , etc.,) by using magnetization transfer from abundant nuclei with high Larmor frequency spins such as  $^1\text{H}$  or  $^{19}\text{F}$ . Under the MAS conditions, the Hartman-Hahn matching condition should be modified to,

$$\nu_{II} = \nu_{IS} \pm n\nu_R \quad (20.24)$$

where,  $\nu_{IS}$  and  $\nu_{II}$  is the nutation rate of the initially magnetized spin, and that of the target nuclear spin.  $\nu_R$  is the rotating rate of the sample and  $n$  is 0,1 or 2. Applying sub-miliseconds to milliseconds of spin-locking pulses to both the  $^1\text{H}$  channel and X channel simultaneously, magnetization transfer takes place during the pulse through dipole-dipole interaction between the two nuclei being under mutual spatial proximity. The heteronuclear dipolar interaction between spin  $I$  and  $S$  can be written in the following equation,

$$\omega_{IS} = \hbar\gamma_I\gamma_S \frac{1 - 3 \cos^2 \theta_{IS}}{r_{IS}^3} \quad (20.25)$$

where,  $\gamma_I$ ,  $\gamma_S$  are the gyromagnetic ratio of spin  $I$  and  $S$ , and  $r_{IS}$ ,  $\theta_{IS}$  are the distance and the relative angle between the two spins, respectively. The magnetization transfer will take place through the flip-flop interaction derived from this interaction.

The magnetization transfer in CPMAS is often treated in a simple thermodynamic transport model that consists of a magnetization buildup time ( $T_{IS}$ ) of the destination nuclei and the decay of the source, and sometimes, the decay of destination magnetization life time:  $T_{1\rho}$  (longitudinal relaxation time within a rotating frame). In some literature, this phenomenological treatment is used for the estimation of amount of nuclei those have long relaxation time, which makes the quantitative estimation difficult. This method will provide good estimation when there are no nuclei those will not receive any magnetization through CP. Theoretically, the magnetization transfer within a rotating sample including CPMAS is often explained using tilted rotating frame [39], and in some cases, with Floquet theory [40], which uses large matrix representation containing a number of rotary assisted states. In any cases, CPMAS is thought to be a rather complicated process. The explanation of this phenomenon needs precise estimation of RDC during the  $\nu_1$  field irradiated. In some ideal cases, where a dipolar interacting spin-pair is well isolated by the other spins, we can obtain dipolar coupling constant by performing Fourier transformation of the build-up curve as the time domain data. The dipolar coupling constant can be obtained from the peak distance appeared on the resulted pattern with a shape like a Pake doublet [41].

The pulse sequence used in the CPMAS is shown in Fig. 20.8.

The CPMAS including quadrupolar nuclei can be used as sensitivity enhancement in very limited cases. It's mainly because the spin-lock duration within quadrupolar nuclei is much shorter than that of spin 1/2 nuclei [42]. The sensitivity enhancement through CP can be observed only in the cases of nuclei with

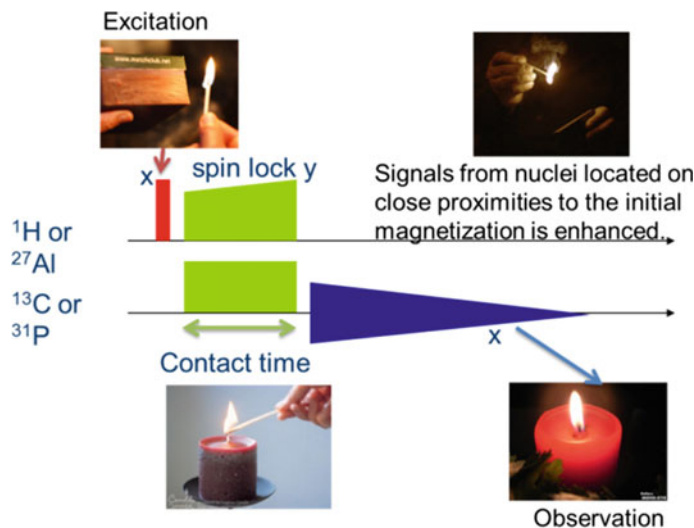


**Fig. 20.8** Pulse sequence of CPMAS with a schematic picture of magnetization transfers from the initial magnetization to the destination magnetization

sufficiently small quadrupolar couplings. In more general quadrupolar nuclei, a number of states having large anisotropic quadrupolar interaction exist and have intersystem crossings with the central transition band. The spin-lock state, which can be prepared on the CT band corresponding to  $m = 1/2$  between  $m = -1/2$  states, will be easily collapsed by the other states transitions within the same nucleus.

The matching condition of CPMAS with at least one quadrupolar nucleus included is apparently much different from those between spin 1/2 nuclei, because, the nutation of quadrupolar nuclei is much dependent on the  $C_Q$  and its orientation. If the  $C_Q$  is very small, close to zero, then the nutation rate is same as to that of liquid states. If the  $C_Q$  is sufficiently large, the nutation rate becomes  $2I + 1$  times faster than that of the liquid samples. An intermediate quadrupolar nucleus designates an intermediate effective nutation rate. Within this limit, the effective nutation rate of a quadrupolar nucleus varies. Under this situation, the matching condition should be changed to

$$\nu_{II} = -\nu_{IS}^{\text{eff}} + n\nu_R, \quad \nu_{IS} \leq \nu_{IS}^{\text{eff}} \leq (2I + 1)\nu_{IS}, \quad n = 1 \text{ (or } 2\text{).} \quad (20.26)$$

The only matching condition that can be used for the wide range of the samples is to set the effective nutation rate of the quadrupolar nuclei,  $\nu_{IS}^{\text{eff}}$ , to  $\nu_R - \nu_{II}$ , although in some cases, we can get CPMAS signal in the condition of  $n = 2$ ,  $\nu_{IS}^{\text{eff}} = 2\nu_R - \nu_{II}$ .  $\nu_{IS}^{\text{eff}}$  cannot be simply determined in precision by the spin-lock or nutation experiments. In most cases, we should search a range of frequencies to obtain a suitable nutation rate. For the case of magnetization transfer between two quadrupolar nuclei, both the nutation rates become  $\nu_1^{\text{eff}}$ .

The spin-lock of quadrupolar nuclei for a duration needed for the magnetization transfer is rather a problem. Alexander Vega introduced an adiabaticity parameter,  $\alpha$ , defined by

$$\alpha = \frac{v_1^2}{v_Q v_R}, \quad (20.27)$$

which can express the spin-lock efficiencies to the quadrupolar nuclei [43]. When this parameter is much larger than 1, then the spin-lock power is sufficiently strong for effectively delivering spin-locking power into whole range of the signal width. Contrary, when this parameter is much smaller than 1, then only a limited range of the nucleus within the signal can be spin-locked. The intermediate range,  $\alpha \sim 1$ , should not be used because in these regions, the RF field will interfere quadrupolar interaction and sample rotation to lead a complex magnetization movement. The shape analysis of the static CP signal obtained by applying this logic to expand the parameter  $\alpha$  to be orientation dependent, the spectral patterns of a quadrupolar nucleus taken under different conditions have been well simulated [44].

Even when the sensitivity is much lower compared to the direct excitation of the destination spins, the obtained signals will bear the information that the source spin handed the magnetization to the destination spin *via* through-space dipole interactions. Sometimes, the fact itself, that the magnetization has transferred thorough space, may bring us a critical information about the relationship of the two nuclei. Or, in other cases, we will be able to observe nuclei more clearly separated through these interactions. 2D spectra using these conditions may bring us the correlation map between the two nuclei if the spectrum successfully taken. The weak magnetizations of the source nuclei or weak spin-locking of them can be focused to nuclei under a particular environment. Using these methods, or combination of them, we will obtain the rich information of heteronuclear through-space correlations. Thus, the hetero-nuclear correlation (HETCOR) spectra combined with CPMAS enables us to observe the through-space correlation between the two hetero-nuclei visually in a 2D spectrum.

HMQC (hetero nuclear multiple quantum correlation) is another method to obtain heteronuclear correlations in a 2D spectrum. This method is originally used in liquid-state NMR that extracts heteronuclear interactions through *J*-coupling between them. When we apply a recoupling pulse during the magnetization transfer, this method can be used as *D*-HMQC method that is much useful for quadrupolar nuclei in general. In solid-state NMR, the coherence time duration ( $T_2$ ) is not in every case long enough for the magnetization transfer evolution *via J*-coupling. However, high-speed rotation and high magnetic fields together are lengthening the available coherence time and meanwhile narrowing the matching condition for the magnetization transfer *via* CP. Both these two conditions will increase the relative importance of HMQC compared to CP-HETCOR used in obtaining hetero-correlation spectra. When the value of *J*-coupling constant is roughly estimated, the only parameter to be adjusted for HMQC experiments is the inversion pulse for the observation nuclei, that makes preparative experiments

needed for HMQC easier than those for CP although the signal intensity of HMQC is comparably small or often smaller compared to that of CP, because HMQC actually extracts the dephased part of the signal using phase cycling.

We have no space to describe about non-half-integer quadrupolar nuclei in this article. Some useful information about quadrupolar nuclei with  $I = 1$ ,  $^2\text{H}$ ,  $^{14}\text{N}$  are described in Chaps. 6 and 12, respectively. 2D HETCOR experiments using  $D$ -HMQC type correlations are effectively used in  $^1\text{H}$  -  $^{14}\text{N}$  hetero-correlation and  $^{14}\text{N}$ - $^{14}\text{N}$  homo-correlation spectra [45]. These types of experiments require high speed rotation and strictly matched magic-angle conditions.

A number of researchers are combining MQMAS or STMAS with CPMAS, HMQC or SQ-DQ type correlation spectra for obtaining heteronuclear correlations information with much separated peaks [46, 47]. 1QCP-MQMAS, MQCP-MQMAS are one kind of these methods, which prepare firstly CP magnetization bearing 1Q or MQ coherence selected by phase cycling [46]. As for 1QCP-MQMAS method, the  $^1\text{H}$  initial magnetization is first moved to quadrupolar nuclei, then the resulted magnetization immediately flip back to  $z$ -axis, after a short wait, a normal MQMAS sequence is applied to the quadrupolar nuclei, with  $^1\text{H}$  decoupling during the MQ and SQ magnetization evolution and the acquisition time [46]. The other method is to obtain the correlation between the isotropically refocused quadrupolar signal with the chemical shift-solved  $^1\text{H}$  signals. The resulted magnetization is utilized as the initial 3Q magnetization then the second and the third pulse is irradiated consecutively to obtain MQMAS spectrum [47].

$^{27}\text{Al}$ - $^1\text{H}$  high-resolution, high-sensitivity correlation spectrum has been obtained through STMAS-CP using  $w$ -PMLG acquisition [48]. Because the  $T_1$  of quadrupolar nuclei is much shorter than that of spin 1/2 nucleus, it is advantageous to choose quadrupolar nuclei as the source magnetization.  $w$ -PMLG, or  $w$ -DUMBO aquisition is necessary for obtaining  $^1\text{H}$  magnetization well separated. Unless using such sequence the resulted  $^1\text{H}$  magnetization will be mixed up during the obser-vation period and will return to be observed as broad signals. We will also note that LG-CP should be considered to be used for the  $^1\text{H}$  signal separations [41].

## 20.6 Sensitivity Enhancement Through Population Transfer

For quadrupolar nuclei specifically, methods using the population transfer within a single nucleus can be used for the sensitivity enhancement of the MAS NMR. In this part we will introduce RAPT (rotation-assisted polarization transfer), FAM (fast amplitude modulation), DFS (double frequency sweep), HS (hyperbolic secant), and WURST (wide-band uniform-rate smooth truncation (WURST). Each of these methods listed here uses a different pulse sequence or a different shaped pulse. FAM and DFS can be also used in MQMAS as for 3Q-1Q conversion pulses.

Under MAS conditions, the ST band components of NMR signals will be observed as many spikelet peaks distributed in a wide range within that ST band (usually, MHz's or larger) (see Fig. 20.5). Although these spikelet signals are narrower than that of the CT signal, these signals are positively used in very limited cases, because these spikelet peaks are too small to gain a sufficient S/N ratio. The ST band coherence components of magnetization developed in a nucleus will experience one or two cycles of frequency oscillation, which sweeps a certain frequency range, during one MAS cycle. This swept frequency amplitude is depending on the relative orientation of PAS and the MAS axes. The spikelet peaks are emerging from the ST coherence in which the frequency sweep range is sufficiently small those can be averaged by MAS, contrary, some ST coherences experiencing larger frequency change during a MAS rotation period will be dephasing rapidly. The sensitivity enhancement methods listed above are all stimulate the spins under ST regions and sweep them out from the ST states (states with  $|m| > 1/2$ ) into the CT states ( $|m| = 1/2$ ) in a particular degree depending on the method and the conditions of the spins. Applying these pulses prior to the first stimulation pulse (90° pulse), we can obtain much larger signals in the CT band in many types of experiment except for the methods using the ST states directly, for example, MQMAS or STMAS.

RAPT and FAM are the methods proposed independently in relatively an early time [49, 50] and still developing in each. Both of them are using many numbers of short pulse trains with middle strength changing the frequency or amplitude alternatingly, respectively, for the population transfer from the ST to CT states in a quadrupolar nucleus. The pulse trains will provide a frequency distribution in a wide range of frequencies that spread to a large part of the ST bands. The efficiency of population transfer is depending on the applied frequency shifts of the pulse train among which, the population transfer will be maximized at the  $\pm 2v_Q$ . Because it will be vanished at the edge frequency of the ST bands, this observation can be utilized for the estimation of  $C_Q$  [51].

DFS, WURST, and HS are the methods using frequency sweeping pulses (more frequently called as adiabatic pulses). DFS [52] is based on the amplitude modulation by a frequency swept sine curve, resulting the pulse consists of up- and down- frequency sweeping components of relatively wide ranges in the frequency domain excluding the certain width of center region so as not to interfere the CT band signals. WURST [53] and HS [54] both are using similar phase modulations resulting one-direction (either up or down) frequency sweeping. Both the two shaped pulses, WURST and HS, have a common phase modulation pattern, a parabola curve rolled up within one phase period, that enables a uniform excitation or inversion of spins within a relatively wide range of frequencies. Each the shaped pulse is truncated by a different envelope shape. The truncation of the shape is important for cutting off the unexpected frequency extrema. The WURST is having the envelope shape closer to a rectangular shape, which can provide a wider range of frequency sweep width by using relatively a weaker pulse than that of HS, and HS may have sharper limits in the frequency domain. The usage of these pulses is different from that of DFS. When these pulses are applied to the population transfer

of quadrupolar nuclei, the frequency sweeping range is limited to a frequency span corresponding to one rotor cycle within a ST pulse region located at 150–250 kHz distant frequency higher or lower positions from the CT band. Applying 180° pulse to this limited region, during 1–3 rotation cycles, the highest population transfer is achieved so far. The theoretical background is not yet fully accounted. However, a large part of nuclei in ST states will pass through this frequency region, around  $v_Q$  distant from the CT band, 2 or 4 times during one rotor cycle.

Very recently, a new method that may elucidate the heteronuclear correlation between spin 1/2 and a half-integer quadrupolar spin, PT-*J*-HMQC and PT-*D*-HMQC, has been reported [55]. PT means population transfer that is performed by WURST pulses. This method is based on HMQC, with additional continuous irradiations of WRUST pulses to the quadrupolar nuclei during the spin evolution time. Those WURST pulses are applied synchronously to the rotation cycle. During this pulse period, the 3Q-coherence is continuously evolved on the quadrupolar nuclei to realize rapid growth of the correlation peaks through *J*-coupling with the spin 1/2 nuclei (PT-*J*-HMQC). When applying recoupling pulses to the spin 1/2 nuclei, the spin evolution through dipole–dipole interaction can be achieved (PT-*D*-HMQC). In this case, the growing up speed of the destination magnetization is accelerated only a little [55].

WURST can deliver RF powers uniformly to a relatively wide range of frequencies. Using this characteristics, it is used for excitation and inversion of signals spread in a relatively wide frequency range. This pulse is recently used in combination with CPMG. When the frequency sweeping pulses are applied in both the excitation and inversion pulses, every signal will be focused correctly [56], then also is used for signal acquisition of nuclei having vast  $C_Q$ 's such as  $^{71}\text{Ga}$ ,  $^{91}\text{Zr}$ , and  $^{59}\text{Co}$  with a help of VOCS type experiments [57].

## 20.7 Confronting the Real World, Real Materials

In solid-state NMR experiments for an objective sample, we should consider many parameters used in that experiment simultaneously. First of all, the rotor size selection is very important. If the larger rotor we use, we can obtain the higher sensitivity [58]. But, when we use the larger rotor, meanwhile we need a larger amount of that sample and also we should give up to apply strong RF field to the sample and also give up to rotate the sample under higher rotation speeds. The  $v_1$  homogeneity will also be hindered in the larger rotors. Generally, high-speed rotation and high-power decoupling pulses result good, however, the temperature rise of the sample will become high that will threaten the sample to potential thermal decompositions. Without saying, the probe specs, especially the endurable voltages and duty cycle limits are more important. Acquisition time and the frequency resolution, sampling time and the frequency width of the spectrum are in mutually reciprocal relationships, respectively. Especially for the 2D experiments, larger acquisition time in  $t_1$  (time in the parameter dimension) axis will take much

experimental time, hence we often minimize the number of  $t_1$  points. To achieve this, we should select short acquisition time in the  $t_1$  domain or long sampling interval along with  $t_1$ . Those conditions, when all the acquired data were finally Fourier transformed, will result in the lower resolution or narrower observation window in the  $F_1$  domain, respectively. Both of them prevent us from adjusting the phase properly in  $F_1$  domain. Especially if the line width along with the  $F_1$  domain is relatively large compared to the spectral width, we should observe in somewhat wider range than the frequency range in which all the signals are contained for the determination of the phase, especially the first-order phase/frequency coefficient,  $P_1$  (comparative to  $P_0$ ) properly. For this purpose, we should take excess numbers of  $t_1$  points. All of these trade-off conditions mentioned above are not limited to the experiments for the quadrupolar nuclei, but common to all the MAS NMR experiments. Thus, when we want to take NMR of a sample in a sufficiently high sensitivity, many numbers of trade-off factors should be considered in solid-state NMR experiments.

During our daily work using solid-state NMR, we may confront many types of problems to be overcome. First of all, we should pack the sample into the rotor properly. Very small unbalance of the weight distribution in the rotor will collapse the stable rotation of the rotor. The smooth rotation necessary for the observation of MAS NMR signals should be achieved prior to the signal observation. For some types of samples, this will be an extremely difficult task. Consequently, the sample packaging to the rotor is the first important task for obtaining MAS NMR spectra. The dense packing will be better for obtaining a good S/N ratio generally, however, in some cases, more sparse packing will be far easier than that of dense packing for obtaining a smooth, high-speed rotation of that rotor. In the latter case, the sample distribution within the rotor will be achieved during the rotation. For taking solid-state NMR, finely grained powder samples will be the most suitable for obtaining good spectra. However, this is not every time possible.

Generally, flowable samples should not be rotate within the rotor, because the convection flow within the rotor induced by the centrifugal force may push off the cap during rotation. There are many ideas and methods, special rotors and apparatus developed for gels, liquid crystals, liquid containing solids or solid containing liquids. A convenient way to take MAS NMR signals of these materials is available by using some tight packing rotor insert that can contain the liquid like samples within a rotor in the MAS experiment. Though the rotating speed will be limited, if we succeed in sampling, the rotor will start a stable spinning and MAS NMR signals can be taken using this rotor.

In the cases of samples emitting small amount of solvent vapor or other gases, such samples demand a special care. In those cases, using a cap having a central hole should be necessary for letting the gases escape from the rotor.

For the thin film samples, in most cases, the sample will be finely and regularly cut into small pieces. In some particular cases, stacked punched disk packing or scroll like packing to rotors are successfully used for their MAS NMR experiments. If the very first step of the rotation would help the achievement of a balanced mass distribution through centrifugal force, this kind of packing methods would work well, though the initiation of the smooth rotation is not always easy. In some case,

we can observe the chemical shift anisotropy of an oriented samples by comparing the NMR signals obtained with differently packed samples [59].

For the observation of conducting materials, sometimes dilution of the sample with insulation materials for example silica, alumina, etc., should be necessary. When we apply strong RF, the rotation of the sample possibly interrupted. In those cases we should dilute the sample further, or we should use a weaker pulse power or slower spinning speed or both.

Deeply dried samples such like silica, alumina, etc., would be inclined to be charged up electrostatically. These samples would not rotate in a strong magnetic field, possibly because of the force between the moving charges and the magnetic field (Lorentz force). In those cases, we need to use some static electricity eliminator during the sample packing within a dry box or similar apparatus.

Especially for the inorganic materials, the preparation and control of the sample conditions affect the resulted spectrum drastically. Sometimes, we should thoroughly dry up the sample under high-temperature and vacuum conditions, in some of those cases, we often obtain a complete different signals depending on the sample preparation conditions. In this section, we will discuss the  $^{27}\text{Al}$  NMR of zeolites and related silica-alumina materials in a little more detail. These materials are frequently used as catalysts or adsorbents. The surface conditions of these materials, especially for the amount of adsorbed water on the surface may often affect the activities of these materials.  $^{27}\text{Al}$ ,  $I=5/2$ ,  $v_0$  ( $^{27}\text{Al}$ ) /  $v_0$  ( $^1\text{H}$ ) = 0.26057 and natural abundance 100%. In the  $^{27}\text{Al}$  NMR spectra obtained in metal oxides such as silica, alumina, zeolites and silica-alumina ordinary shows signals from  $\text{Al}[\text{O}_4]$ ,  $\text{Al}[\text{O}_6]$  (Fig. 20.5), and less frequently from  $\text{Al}[\text{O}_5]$  sites separately [60]. However, the signal separation patterns of them are very sensitive to the moisture loaded on the surface of that sample. A simple assumption of the hydration mechanism of these materials will predict that  $\text{Al}[\text{O}_5]$  then  $\text{Al}[\text{O}_6]$  will appear stepwisely along with the hydration of the sample progressed as the  $\text{Al}[\text{O}_4]$  will decrease. However, at least from comparing the signal amounts of dried samples in different conditions, the amount of  $\text{Al}[\text{O}_4]$  and  $\text{Al}[\text{O}_6]$  increased and that of  $\text{Al}[\text{O}_5]$  decreased upon the hydration progressed. In addition to that, in some deeply dried silica-alumina samples including zeolites, we often cannot observe sufficient amount of  $^{27}\text{Al}$  signals including the Brønsted acid sites denoted as Al-OH-Si that can be working as a strong acid site. These observation has lead us to recognize that there are some ‘invisible’ aluminum species existing in the deeply dried zeolites or silica-alumina samples. Since the Brønsted acid sites, which can only be observed upon heating of oxonium,  $[\text{Al}^{\text{-}}\text{-O-Si}][\text{H}_3\text{O}^+]$ , or ammonium,  $[\text{Al}^{\text{-}}\text{-O-Si}][\text{H}_4\text{N}^+]$ , forms of the sites under vacuum, is one of the central importance in the catalytic science, many efforts have been made for the observation of these Brønsted sites. Comparing to the ordinary observed  $C_Q$ ’s of  $\text{Al}[\text{O}_4]$  sites (3 ~ 7 MHz), much larger a value,  $C_Q = 15.3$  MHz was found for the  $^{27}\text{Al}$  signal in the Brønsted acid sites in a dry HY zeolite that was measured by TRAPDOR (transfer population double resonance) [61]. In HZSM-5,  $C_Q \sim 16$  MHz is directly observed with a static sample by a help of signal enhancement with DFS [62]. An ab initio calculation of a model cluster structure taken from ZSM-5, the  $^{27}\text{Al}[\text{O}_4]$  signal at the Brønsted site

possibly exhibits very large  $C_Q$  values ( $\sim 20$  MHz) [63]. This is a very important knowledge that not every aluminium species can be observed in a NMR chart with a similar order of line-width.

In situ experiments are expected to provide very useful information for the material development and the reaction controlling in many fields of chemical systems. For this purpose, MAS probe with rotors having gas inlet and outlet, those can be operated under sample rotation within the rotor is under developing.

Hunger and his co-workers have first devised a MAS probe in which rotor equipped with in situ gas flow system inside [64]. For example, a partially protonated Na, HY zeolite (Faujasite) has been investigated using this apparatus. Under normal conditions, it shows both tetrahedral and octahedral Al sites. When the sample was heated and dried under continuous flow of dry air, almost all the  $^{27}\text{Al}$  signals of HY zeolite were disappeared. When water containing air was flowed inside the rotor, both the tetrahedral and octahedral coordinated Al species were recovered on the  $^{27}\text{Al}$  spectrum. Since not any Al was added or subtracted during these processes, this observation clearly shows that there exists Al species invisible in the NMR chart (Fig. 20.9). The differential area of  $^1\text{H}$  NMR signal is corresponding to the water adsorbed. Except for water, the amount of other components within the rotor do not change during this process. However, the structural change on the aluminium coordination environment affected both  $^1\text{H}$  and  $^{27}\text{Al}$  signals. Thus, the word ‘invisible’ exactly means ‘too broad to be observed’.

During the hydration of the sample, a part of adsorbed water molecules may construct the first, second and higher coordination shpere of the aluminium molecules in the sample. This change may introduce some molecular motions caused by reversible adsorption - desorption of water molecules on some local spots and/or the motion of the attached water molecules themselves. The strong dipole moment of water will affect the electrostatic environment of aluminium. These processes may cause motional averaging to the structure of aluminium coordination sphere and make it into a more relaxed one. The local environmental difference between species will shlink within a certain range and enables us to observe  $^{27}\text{Al}$  species rather simple and much more grouped. Although the above observation poses some limit to the observation of  $^{27}\text{Al}$  NMR within simple observation methods adoption, there are still existing other methods to observe such a broad signal especially in static experiments. In general cases, signals having a widgh wider than several numbers of rotor cycle frequencies should be observed in static conditions, not by MAS. In those cases, signal separation is mostly done by numerical methods.

As another example, we will describe about  $^{17}\text{O}$  NMR briefly.  $^{17}\text{O}$ ,  $I = 5/2$ ,  $v_0(^{17}\text{O}) / v_0(^1\text{H}) = 0.1356$  and natural abundance 0.037%. The quadrupole interaction of  $^{17}\text{O}$  species is much smaller than those of  $^{27}\text{Al}$  species ordinary, so the obser-  
vation of  $^{17}\text{O}$  species may be easier if the concentration of  $^{17}\text{O}$  is sufficient. Although it may take some cost, the  $^{17}\text{O}$  NMR with some isotope enrichment is widely investigated because oxides and hydroxides are important for ceramics, structue materials, electric materials, catalysts, and their supports. In solution

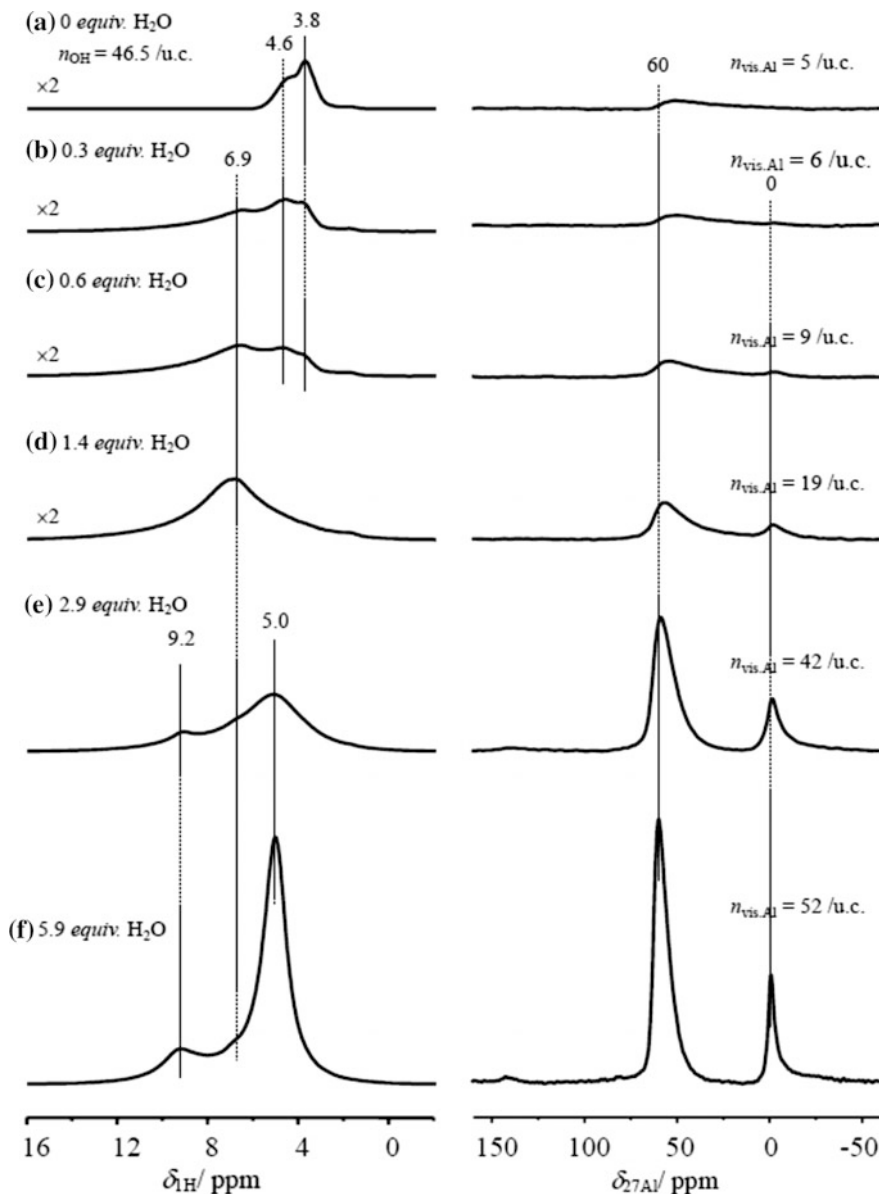


**Fig. 20.9** In situ MAS NMR of dried H, Na-Y zeolite upon hydration [65], as the hydration of the sample progressed, the signal area of proton is increasing and apparently, the signal area of <sup>27</sup>Al is also increasing although there are no change in the Al amount. Copyright permission was obtained personally from Dr. Jian Jiao

NMR, an oxygen species shows chemical shifts from 300 to  $-100$  ppm depending on its electronic states. For example, the oxo species may normally have very high-frequency chemical shifts at around 300 ppm or higher. Alkoxide ions show signals around 200 ppm. Contrary, the oxide species having two coordinated metals are not so high and can be observed ordinary under 100 to  $-100$  ppm [66]. The lowest frequency species are oxides having oxygens in their crystal's very high symmetrical positions. However, in most of the solid samples, the chemical shifts are no longer discriminative in the 1D solid-state NMR because of the ambiguity brought by the large quadrupole coupling of  $^{17}\text{O}$ . The typical value of quadrupolar coupling frequencies of  $^{17}\text{O}$  is around several MHz that will appear in the spectrum as a peak having several 10's kHz of the total line width. In contrast, the quadrupolar coupling frequencies of  $^{17}\text{O}$  can be separated by using MQMAS or STMAS [67].

As an example, we will see Zeolite materials here again. In the  $^{17}\text{O}$  NMR spectra of zeolite materials, it is of the primary importance that to separate the oxygen signals into the kinds of their neighboring two or three atoms. For example, a  $^{17}\text{O}$  MAS NMR signal obtained with a  $^{17}\text{O}$ -enriched zeolite, separately shows that the Si–O–Si and Si–O–Al signals. The signal from the Brønsted acid site has been also revealed [68]. In some special cases, further separation can also be obtained and the site dependent signal assignment is partially achieved, that means it will provide a further precision to the site specific observation of zeolites and related materials [69,70].

**Acknowledgements** The author is fully thanking to Prof. Naito, an editor of this book, for his kind and enduring help and encouragement; without his help, I couldn't complete my task. I thank Prof. Takegoshi for his frank and helpful discussion. I also thank to Dr. Hayashi who gave me instruction of the solid-state NMR especially in my launching days. I also thank to the committee members of Japanese Solid-state NMR and Material Forum (no English site, the site only in Japanese, <http://kuchem.kyoto-u.ac.jp/bun/forum/nmr.html>) and the Nuclear Magnetic Resonance Society of Japan (<http://www.nmrj.jp/index.php?page=index-e>) and people who have been gathering there and giving me a plenty of fruitful information and discussions. Finally, I would express another deep acknowledgement to National Institute of Industrial Science and Technology (AIST), and New Energy and Industry Technology Development Organization (NEDO) and people who are working there for their financial and everyday supports in everywhere.

## References

1. Man, P.P.: Quadrupole Coupling in NMR. <http://www.pascal-man.com>
2. Cohen, M.H., Reif, F.: Quadrupole effects in nuclear magnetic resonance studies of solids. In: Zeitz, F., Turnbull, D. (eds.) Solid State Physics, Advances in Research Applications, vol. 5, pp. 321–455. Academic Press, New York (1957)
3. Abragham, A.: Principles of Nuclear Magnetism. Oxford University Press, London (1961)
4. Slichter, C.P.: Principles of Magnetic Resonance. (Springer Series in Solid-State Science 1) Third Enlarged and Updated edn. Springer, New York (1996)
5. Hashi, K., Ohki, S., Matsumoto, S., Nishijima, G., Goto, A., Deguchi, K., Yamada, K., Noguchi, T., Sakai, S., Takahashi, M., Yanagisawa, Y., Iguchi, S., Yamazaki, T., Maeda, H.,

- Tanaka, R., Nemoto, T., Suematsu, H., Miki, T., Saito, K., Shimizu, T.: Achievement of 1020 MHz. *J. Magn. Res.* **256**, 30–33 (2015)
6. Nishiyama, Y., Endo, Y., Nemoto, T., Utsumi, H., Yamaguchi, K., Hioka, K., Asakura, T.: Very fast magic angle spinning  $^1\text{H}$ - $^{14}\text{N}$  2D solid-state NMR: sub-micro-liter sample data collection in a few minutes. *J. Magn. Reson.* **208**, 44–48 (2011). doi:[10.1016/j.jmr.2010.10.001](https://doi.org/10.1016/j.jmr.2010.10.001)
7. Mizuno, T., Takegoshi, K.: Development of a cryogenic duplexer for solid-state nuclear magnetic resonance. *Rev. Sci. Instrum.* **80**, 124072 (2009). doi:[10.1063/1.3263908](https://doi.org/10.1063/1.3263908)
8. Hyberts, S.G., Arthanari, H., Wagner, G.: Applications of non-uniform sampling and processing. *Top. Curr. Chem.* **316**, 125–148 (and references therein)
9. Barnes, A.B., De Paepé, G., van der Wel, P.C.A., Hu, K.-N., Joo, C.-G., Bajaj, V.S., Mak-Jurkauskas, M.L., Sirigiri, J.R., Herzfel, J., Temkin, R.J., Griffin, R.G.: High-field dynamic nuclear polarization for solid and solution biological NMR. *Appl. Magn. Res.* **34**(3–4), 237–263 (2008). doi:[10.1007/s00723-008-0129-1](https://doi.org/10.1007/s00723-008-0129-1)
10. Oxford Instruments: Hyper Sense DNP Polarizer. <https://www.oxford-instruments.com/products/spectrometers/nuclear-magnetic-resonance-nmr/hypersense>
11. Bruker Biospin: DNP NMR. [https://www.bruker.com/products/mr/nmr/dnp-nmr/overview.html?gclid=CPuNydr-6tQCFYcDKgod\\_OwAhg](https://www.bruker.com/products/mr/nmr/dnp-nmr/overview.html?gclid=CPuNydr-6tQCFYcDKgod_OwAhg)
12. Tolman, J.R., Flanagan, J.M., Kennedy, M.A., Prestegard, J.H.: Nuclear magnetic dipole interactions in field-oriented proteins: information for structure determination in solution. *Proc. Natl. Acad. Sci. U.S.A.* **92**, 9279–9283 (1995)
13. Hexem, J.G., Frey, M.H., Opella, S.J.: Influence of  $^{14}\text{N}$  on  $^{13}\text{C}$  NMR spectra of solids. *J. Am. Chem. Soc.* **103**, 224–226 (1981)
14. Naito, A., Gnanapathy, A.C., McDowell, C.A.: High resolution solid state  $^{13}\text{C}$  NMR spectra of carbons bonded to nitrogen in a sample spinning at the magic angle. *J. Chem. Phys.* **74**, 5393–5397 (1981)
15. Cavadini, S., Lupulescu, A., Antonijevic, S., Bodenhausen, G.: Nitrogen-14 NMR spectroscopy using residual dipolar splittings in solids. *J. Am. Chem. Soc.* **128**, 7706–7707 (2006)
16. McManus, J., Kemp-Harper, R., Wimperis, S.: Second-order quadrupolar-dipolar broadening in two-dimensional multiple-quantum MAS NMR. *Chem. Phys. Lett.* **311**(3), 292–298 (1999)
17. Wi, S-s, Frydman, L.: Residual dipolar couplings between quadrupolar nuclei in high resolution solid state NMR: description and observations in the high-field limit. *J. Chem. Phys.* **112**(7), 3248–3261 (2000)
18. Ashbrook, S.E., Wimperis, S.: Second-order cross-term interactions in high-resolution MAS NMR of quadrupolar nuclei. *Prog. Nucl. Magn. Reson. Spectrosc.* **55**, 160–181 (2009)
19. Man, P.P., Couty, R., Fraissard, J.: Determination of line intensities of  $^{27}\text{Al}$  in  $\text{Al}_2\text{O}_3$ . *J. Magn. Reson.* **86**, 613–617 (1990)
20. Bryce, D.L., Taulle, F.: NMR crystallography. *Acta Cryst.* **C73**, 126–127 (2017)
21. Man, P.P.: Quadrupolar interactions in solid-state NMR, general. In: Meyers, R.A. (ed.) *Encyclopedia of Magnetic Resonance*, pp. 12224–13365. Wiley, Chichester (1990)
22. MacKensie, K.J.D., Smith, M.E.: Multinuclear solid-state NMR of inorganic materials. In: Cahn, R.W. (ed.) *Pergamon Materials Series*, 6th edn. Elsevier, Oxford (2002)
23. Wasylissen, R.E., Ashbrook, S.E., Wimperis, S. (ed.) *NMR of Quadrupolar Nuclei in Solid Materials*. Wiley, Hoboken (2012)
24. Freude, D.: Quadrupolar nuclei in solid-state nuclear magnetic resonance. In: Meyers, R.A. (ed.) *Encyclopedia of Analytical Chemistry*, pp. 12188–12224. Wiley, Chichester (2000)
25. De-Lacaillerie, J.B.D., Fretigny, C., Massiot, D.: MAS NMR spectra of quadrupolar nuclei in disordered solids: the Czjzek model. *J. Magn. Reson.* **192**, 244–251 (2008)
26. Frydman, L., Harwood, J.S.: Isotropic spectra of half-integer quadrupolar spins from bidimensional magic-angle spinning NMR. *J. Am. Chem. Soc.* **117**, 5363–5364 (1995)
27. (a) Brown, S.P., Heyes, S.J., Wimperis, S., Two-dimensional MAS multiple-quantum NMR of quadrupolar nuclei. Removal of inhomogeneous second-order broadening. *J. Magn.*

- Reson. Ser. A **119**, 280–284 (1996); (b) Amoureux, J.-P., Fernandez, C., Steuernagel, S., Z Filtering in MQMAS NMR. J. Magn. Reson. Ser. A**123**, 116–118 (1996)
28. Massiot, D., Touzo, B., Trumeau, D., Coutures, J.P., Virlet, J., Florian, P., Grandinetti, P.J.: Two-dimensional MAS isotropin reconstruction sequences for quadrupolar nuclei. Solid State NMR **6**, 73–83 (1996)
29. Brown, S.P., Wimperis, S.: Two-dimensional MQ-MAS NR of quadrupolar nuclai. Solid State NMR **6**, 73–83 (1996)
30. Brown, S.P., Wimperis, S.: Two-dimensional MQMAS NMR of quadrupolar nuclei: a comparison of methods. J. Magn. Reson. **128**, 42–61 (1997)
31. Gan, Z.H., Kwak, H.T.: Enhancing MQMAS sensitivity using signals from multiple coherence transfer pathways. J. Magn. Reson. **168**, 346–351 (2004)
32. Amoureux, J.-P., Flambard, A., Delevoye, L., Montagne, L.: A very sensitive high-resolution NMR method for quadrupolar nuclei. Chem. Commun. **27**, 3573–3574 (2005)
33. Gan, Z.: Isotopic NMR spectra of half-integer quadrupolar nuclei using satellite transitions and magic-angle spinning. J. Am. Chem. Soc. **122**, 3242–3243 (2000)
34. Gan, Z., Gor'kov, T.A., Samoson, A., Massiot, D.: Seeking higher resolution and sensitivity for NMR of quadrupolar nuclei. J. Am. Chem. Soc. **124**, 5634–5635 (2002)
35. Amoureux, J.-P., Delevoye, L., Fink, G., Taulelle, F., Flambard, A., Montagne, L.: Unified representation of MQMAS and STMAS NMR of half-integer quadrupolar nuclei. Chem. Phys. Lett. **356**, 3200–3201 (2001)
36. Ashbrook, S.E., WImperis, S.: High-resolution NMR of quadrupolar nuclei in solids: the satellite-transition magic angle spinning (STMAS) experiment. Prog. Nucl. Magn. Reson. Spectrosc. **46**, 52–108 (2004)
37. Takahashi, T., Kanehashi, K., Shimoikeda, Y., Nemoto, T., Saito, K.: Practical comparison of sensitivity and resolution between STMAS and MQMAS for <sup>27</sup>Al. J. Magn. Reson. **198**, 228–235 (2009)
38. Antonijevic, S., Ashbrook, S.E., Biedasek, S., Walton, R.I., Wimperis, S., Yang, H.: Dynamics on the microsecond timescale in microporous aluminophosphate ALPO-14 as evidenced by <sup>27</sup>Al MQMAS and STMAS NMR spectroscopy. J. Am. Chem. Soc. **128**, 8054–8062 (2006)
39. Takegoshi, K., Nomura, K., Terao, T.: Rotational resonance in the tilted rotating frame. Chem. Phys. Lett. **232**, 424–428 (1995)
40. Marks, D., Vega, S.: A theory of cross-polarization NMR of non-spinning and spinning samples. J. Magn. Reson. Ser. A**118**, 157–172 (1996)
41. Van Rossum, B.-J., de Groot, C. P., Ladizhansky, V., Vega, S., de Groot, H. J. M.: A Method for measuring heteronuclear (<sup>1</sup>H-<sup>13</sup>C) distances in high speed MAS NMR. J. Am. Chem. Soc. **122**, 3465–3472 (2000)
42. Amoureux, J.-P., Pruski, M.: Theoretical and experimental assessment of single and multi-quantum cross-polarization in solid state NMR. Mol. Phys. **100**, 1595–1613 (2002)
43. Vega, A.: CP/MAS of S = 3/2 quadrupolar nuclei. Solid State NMR **1**, 17–32 (1992)
44. (a) Hayashi, S., Hayamizu, K.: Line-shapes in CP/MAS NMR of quadrupolar nuclei. Chem. Phys. Lett. **203**, 319–324 (1993);(b) Hayashi, S., Hayamizu, K.: Errata: line-shapes in CP/ MAS NMR of quadrupolar nuclei. Chem. Phys. Lett. **205**, 597 (1993)
45. Pandey, M.K., Amoureux, J.-P., Asakura, T., Nishiyama, Y.: Sensitivity enhanced <sup>14</sup>N/<sup>14</sup>N correlations to probe inter-beta-sheet interactions using fast magic angle spinning solid-state NMR in biological solids. Phys. Chem. Chem. Phys. **18**, 22583–22589 (2016)
46. (a) Pruski, M., Lang, D. P., Fernandez, C., Amoureux, J.P.: Multiple-quantum magic-angle spinning NMR with cross-polarization: Spectral editing of high-resolution spectra of quadrupolar nuclei. Solid State Nucl. Magn. Reson., **7**, 327–331 (1997); (b) Ashbrook, S. E., Wimperis, S.: Multiple-quantum cross-polarization and two-dimensional MQMAS NMR of quadrupolar nuclei, J. Magn. Reson. **147**, 238–249 (2000)
47. (a) Wang, S.H., De Paul, S.M., Bull, L.M.: High-resolution heteronuclear correlation between quadrupolar and spin-1/2 nuclei using multiple-quantum magic-angle spinning. J. Magn. Reson., **125** 364–368 (1997); (b) Fernandez, C., Morais, C., Rocha, J., Pruski, M.:

- High-resolution heteronuclear correlation spectra between  $^{31}\text{P}$  and  $^{27}\text{Al}$  in microporous aluminophosphates. Solid State NMR **21**, 61–70 (2002)
- 48 Siegel, R., Rocha, J., Mafra, L.: Combinating STMAS and CRAMPS NMR spectroscopy: High-resolution HETCOR NMR spectra of quadrupolar and  $^1\text{H}$  Nuclei in solids. Chem. Phys. Lett. **470**, 337–341 (2009)
  - 49 Kwak, H.-T., Prasad, S., Clark, T., Grandinetti, P.J.: Enhancing sensitivity of quadrupolar nuclei in solid-state NMR with multiple rotor assisted population transfers. Solid State NMR **24**, 71–77 (2003)
  50. Madhu, P.K., Goldbort, A., Frydman, L., Vega, S.: Sensitivity enhancement of the MQMAS NMR experiment by fast amplitude modulation of the pulses. Chem. Phys. Lett. **307**, 41–47 (1999)
  51. Kwak, H.-T., Prasad, S., Clark, T., Grandinetti, P.J.: Selective suppression and excitation of solid-state NMR resonances based on quadrupole coupling constants. J. Magn. Reson. **160**, 107–113 (2003)
  52. Kentgens, A.P.M., Verhagen, R.: Advantages of double frequency sweeps in static, MAS and MQMAS NMR of spin I=3/2 nuclei. Chem. Phys. Lett. **300**, 435–443 (1999)
  53. Kupče, Ě., Freeman, R.: Optimized adiabatic pulses for wideband spin inversion. J. Magn. Reson. Ser. A **118**, 299–303 (1996)
  54. Siegel, R., Nakashima, T.T., Wasylisen, R.E.: Sensitivity enhancement of NMR spectra of half-integer spin quadrupolar nuclei in solid using hyperbolic secant pulses. J. Magn. Reson. **184**, 83–100 (2007)
  55. Wang, Q., Li, Y., Trebosc, J., Lafon, O., Hu, B., Xu, J., Feng, N., Chen, Q., Amoureu, J. P., Deng, F.: Population transfer HMQC for half-integer quadrupolar nuclei. J. Chem. Phys. **142**, 094201 (2015)
  56. Luke A. O'Dell: The WURST kind of pulses in solid-state NMR. Solid State Nucl. Magn. Reson. **55–56**, 28–41 (2013)
  57. O'Dell L. A. Schurko, R. W.: QCPMG using adiabatic pulses for faster acquisition of ultra-wideline NMR spectra. Chem. Phys. Lett. **464**, 97–102 (2008)
  58. Pandey, M. K., Hashi, K., Ohki, S., Nishimjima, G., Matsumoto, S., Noguchi, T., Deguchi, K., Gotoh, A., Shimizu, T., Maeda, H., Takahashi, M., Yanagisawa, T., Suematsu, H., Saito, K., Miki, T., Nishiyama, Y.: 24T high-resolution and—sensitivity solid-state NMR measurements of low-gamma half-integer quadrupolar nuclei  $^{35}\text{Cl}$  and  $^{37}\text{Cl}$ . Anal. Sci. **32** (5), 1339–1345 (2016). doi: 10.1246/cl.160850
  59. Naito, A.: Structure elucidation of membrane-associated peptides and proteins in oriented bilayers by solid-state NMR spectroscopy. Solid State Nucl. Magn. Reson. **36**, 67–76 (2009)
  60. Klinowsky, J.: Solid-State NMR Studies of Molecular Sieve Catalysts. Chem. Rev. **91**, 1459–1479 (1991)
  61. Grey, C. P., Vega, A.J.: Determination of the Quadrupole Coupling Constant of the Invisible Aluminium Spins in Zeolite HY with  $^1\text{H}/^{27}\text{Al}$  TRAPDOR NMR. J. Am. Chem. Soc. **117**, 8232–8242 (1995)
  62. Kentgens, A. P. M., Iuga, D., Kalwei, M., Koller, H.: Direct observations of Brønsted acidic sites dehydrated zeolites, H-ZSM5 using DFS enhanced  $^{27}\text{Al}$  MQMAS NMR spectroscopy. J. Am. Chem. Soc. **123**, 2925–2926 (2001)
  63. Ehresmann, J.O., Wang, W., Herreros, B., Luigi, D.-P., Venkatraman, T. N., Song, W., Nicholas, J. B., Haw, J. F.: Theoretical and experimental investigation of the effect of proton transfer on the  $^{27}\text{Al}$  MAS NMR Line Shapes of zeolite-adsorbate complexes: An independent measure of solid acid strength. J. Am. Chem. Soc. **124**, 10868–10874 (2002)
  64. Hunger, M., Horvath, T.: A new MAS NMR probe for in situ investigations of hydrocarbon conversion on solid catalysts under continuous-flow conditions. J. Chem. Soc. Chem. Commun. 1423–1424 (1995)
  65. Jiao, J.: Chap. 8 Number and nature of framework aluminum atoms in non-hydrated zeolites Y studied by adsorption of probe molecules in Quantitative characterization of aluminum in non-hydrated zeolite catalysts by multi-nuclear solid-state NMR spectroscopy. Thesis at

- Universitet Stuttgart, (2006) which is presently accessible at [https://elib.uni-stuttgart.de/bitstream/11682/824/1/thesis\\_jiao.pdf](https://elib.uni-stuttgart.de/bitstream/11682/824/1/thesis_jiao.pdf)
- 66. Yamada, K. Chapter 3 - Recent Applications of Solid-State  $^{17}\text{O}$  NMR. Annual Rep NMR Spectrosc, pp 115–158 (2010)
  - 67. Ashbrook, S. E., Smith, M. E.: Solid state  $^{17}\text{O}$  NMR - an introduction to the background principles and applications to inorganic materials. Chem. Soc. Reviw. **35**, 718–735 (2006)
  - 68. Peng, L., Liu, Y., Kim, N., Readman, J. E., Grey, C. P.: Detection of Brønsted acid sites in zeolite HY with high-field  $^{17}\text{O}$ -MAS-NMR techniques. Nature Materials. **4**, 216–219 (2005)
  - 69. Peng, L., Huo, H., Gan, Z., Grey, C. P.:  $^{17}\text{O}$  MQMAS NMR studies of zeolite HY. Microporous and Mesoporous Materials. **109**, 156–162 (2008)
  - 70. Huo, H., Peng, L., Gan, Z., Grey, C. P.: Solid-State MAS NMR Studies of Brønsted Acid Sites in Zeolite H-Mordenite. J. Am. Chem. Soc. **134**, 9708–9720 (2012)

# Chapter 21

## Protein–Ligand Interactions Studied by NMR

Hidekazu Hiroaki and Daisuke Kohda

**Abstract** Various solution NMR experiments for studying protein–ligand interactions have become indispensable techniques in both academia and industry. In general, solution NMR is superior to other physico-chemical methods, in terms of its spatial resolution and the fact that protein modifications are not required. The applications are loosely classified into two categories, “ligand-based approach” and “protein-based approach.” Many unique experiments have been developed for the ligand-based approach, including STD, WaterLOGSY, DIRECTION, INPHARMA, ILOE, and trNOE. These experiments frequently comprise the important steps of a drug-discovery process, including ligand screening, pharmacophore mapping, and molecular design. This review provides a practicable classification of these experiments, to promote the selection of a suitable experiment depending on the purpose. In contrast, the variation of experiments in the protein-based approach is rather limited. The  $^1\text{H}$ – $^{15}\text{N}$ -HSQC-based NMR titration experiment and its variants are preferentially used for analyses of protein–ligand interactions. This review also discusses several practical aspects of the NMR titration experiment, including sample handling and data acquisition and analysis.

**Keywords** WaterLOGSY · INPHARMA · DIRECTION · NMR titration experiment · Fragment-based drug discovery (FBDD)

---

H. Hiroaki

Graduate School of Pharmaceutical Sciences, Nagoya University, Nagoya, Japan  
e-mail: hiroaki.hidekazu@f mbox.nagoya-u.ac.jp

D. Kohda (✉)

Medical Institute of Bioregulation, Kyushu University, Fukuoka, Japan  
e-mail: kohda@bioreg.kyushu-u.ac.jp

## 21.1 Overview

Solution NMR spectroscopy has recently become an indispensable analytical technique for studying protein–ligand interactions. The detection and quantitative analysis of protein–ligand interactions are important not only for basic research, but also for pharmaceutical industries. NMR provides comprehensive information about molecular interactions in solution at an atomic resolution. During the past decade, many different types of experiments have been devised for the analysis of protein–ligand interactions.

NMR experiments for protein–ligand interactions can be loosely classified into two categories, the “ligand-based” approach and the “protein-based” approach [1–4]. The ligand-based approach includes saturation transfer difference (STD) [5], water-ligand observed via gradient spectroscopy (WaterLOGSY) [6], diffusion-ordered spectroscopy (DOSY) [7, 8], difference of inversion-recovery rate with and without target irradiation (DIRECTION) [9], inter-ligand NOE for pharmacophore mapping (INPHARMA) [10], inter-ligand nuclear Overhauser experiment (ILOE) [11], and transferred NOE (trNOE) [12]. All of these experiments focus on the changes of the NMR signals derived from ligands, thus eliminating the need for isotopically labeled protein preparation.

The protein-based approach requires isotopic labeling of protein samples. After introducing suitably stable isotopes ( $^{15}\text{N}$ ,  $^{13}\text{C}$ , or both), heteronuclear correlation spectra, such as heteronuclear single quantum coherence (HSQC), are measured. Since the NMR chemical shift values are highly sensitive to the chemical and steric environments around nuclei in a molecule, the changes in position and intensity of the cross peaks in an HSQC spectrum monitor the binding of a ligand to the target protein. In addition, the amino acid residues involved in the molecular interactions in the protein can be identified. The identification of amino acid residues at the molecular interface is extremely useful for the design of new ligand molecules with higher affinity. Consequently, even at the early stage of drug screening projects, the protein-based approach is useful for validating the hit compounds.

In this review, we worked to concisely describe the merits and demerits of the “ligand-based” and “protein-based” approaches, according to the experimental purposes (Table 21.1). In addition, several practical aspects of the NMR experiments for protein–ligand interactions are described.

## 21.2 Ligand-Based Approach

In this section, we will focus on the six major methods of ligand-based NMR screening: STD, WaterLOGSY, ILOE, INPHARMA, DIRECTION, and trNOE. For all of the methods, no isotopically labeled protein sample is required, and usually a tenfold or larger molar excess of a ligand is added to the protein solution.

**Table 21.1** Purpose oriented classification of various solution NMR experiments that are useful for studying protein–ligand interactions

	Classification	Data acquisition	Number of ligands	Solvent	Protein: ligand ratio	Assignment of ligand signals	Protein sample	Key references
<i>Ligand screening</i>								
STD	Ligand-based	1D	1–several	100% $^2\text{H}_2\text{O}$	1: 20–100	Not required	Unlabeled	[5, 16–19, 24]
WaterLOGSY	Ligand-based	1D	1–several	5% $^2\text{H}_2\text{O}$ –95% $^1\text{H}_2\text{O}$	1: 20–100	Not required	Unlabeled	[6, 20–23]
DOSY	Ligand-based	2D	1–several	5% $^2\text{H}_2\text{O}$ –95% $^1\text{H}_2\text{O}$ /100% $^2\text{H}_2\text{O}$	1: 20–100	Not required	Unlabeled	[7, 8]
CSP/NMR titration	Protein-based	2D	1–several	5% $^2\text{H}_2\text{O}$ –95% $^1\text{H}_2\text{O}$	1: 0–20	Not required	$^1\text{H}/^{15}\text{N}$ -labeled, assignment not required	[33, 34]
<i>Pharmacophore determination</i>								
DIRECTION	Ligand-based	1D	1	100% $^2\text{H}_2\text{O}$	1: 20–100	Required	Unlabeled	[9]
INPHARMA	Ligand-based	2D	2	100% $^2\text{H}_2\text{O}$	1: 20–100	Required	Unlabeled	[10, 26–28]
<i>Ligand design</i>								
ILOE	Ligand-based	2D	2	100% $^2\text{H}_2\text{O}$	1: 20–100	Required	Unlabeled	[11, 29, 30]
trNOE	Ligand-based	2D	1	5% $^2\text{H}_2\text{O}$ –95% $^1\text{H}_2\text{O}$ /100% $^2\text{H}_2\text{O}$	1: 20–100	Required	Unlabeled	[31]
SAR-by-NMR	Protein-based	2D	2	5% $^2\text{H}_2\text{O}$ –95% $^1\text{H}_2\text{O}$	1: 0–20	Not required	$^1\text{H}/^{15}\text{N}$ -labeled, assignment required	[34]

(continued)

**Table 21.1** (continued)

	Classification	Data acquisition	Number of ligands	Solvent	Protein: ligand ratio	Assignment of ligand signals	Protein sample	Key references
<i>Ligand characterization (<math>K_D</math> determination)</i>								
CSP/NMR titration	Protein-based	2D	1	5% $^2\text{H}_2\text{O}$ –95% $^1\text{H}_2\text{O}$	1: 0–20	Not required	$^1\text{H}/^{15}\text{N}$ ( $^{13}\text{C}$ )-labeled, assignment required	—
<i>Ligand characterization (determination of the molecular interface)</i>								
CSP/chemical shift mapping	Protein-based	2D	1	5% $^2\text{H}_2\text{O}$ –95% $^1\text{H}_2\text{O}$	1: 0–20	Not required	$^1\text{H}/^{15}\text{N}$ ( $^{13}\text{C}$ )-labeled, assignment required	[35, 36]
Cross saturation	Protein-based	2D	1	80% $^2\text{H}_2\text{O}$ –20% $^1\text{H}_2\text{O}$	1: 0–20	Not required	$^2\text{H}/^{15}\text{N}$ -labeled, assignment required	[32, 37]

Among them, STD, WaterLOGSY, and DIRECTION are essentially one-dimensional (1D) NMR experiments, whereas ILOE, INPHARMA, and trNOE are two-dimensional (2D) NMR experiments.

### 21.2.1 Ligand Screening

In recent years, NMR experiments have been combined with a new drug discovery strategy, termed “fragment-based drug discovery” (FBDD) [13–15]. FBDD is one of the trends in lead generation in pharmaceutical industries. The FBDD approach finds one or several low molecular-weight compounds, called fragments, which weakly bind to the target protein. Both STD and WaterLOGSY are often used in the early stage of NMR-assisted FBDD. Weak interactions are usually difficult to detect by means other than the solution NMR method.

#### 21.2.1.1 Saturation Transfer Difference (STD)

For the STD experiment, the sample is set up as the mixture of a target protein (ca. 50  $\mu\text{M}$ ) and a tenfold to 40-fold molar excess of a ligand.  ${}^2\text{H}_2\text{O}$  (99.8%) is recommended as the solvent, in order to achieve higher spin saturation transfer efficiency. STD is the difference between an “on-resonance saturated” spectrum and an “off-resonance saturated” spectrum. To record the “on-resonance” spectrum, a selective pulse that excites the protein protons (i.e., nuclei of  ${}^1\text{H}$  atoms that give  ${}^1\text{H}$  resonances) is applied before the observed  $90^\circ$  pulse. After the  $90^\circ$  pulse, a weak spin-locking pulse and a water-suppression pulse are optionally applied before the NMR signal detection. To record the reference “off-resonance saturated” spectrum, the same selective excitation pulse is applied, but distant from the protein spectral region, leaving the protein protons unsaturated. Recently, technical improvements of the STD method have been made, which include (1) the saturation transfer double difference (STDD) experiment [16], (2) optimization of the excitation pulse bandwidth (WET-STD) [17], (3) STD with spectral editing (clean-STD) [18], and (4) quantitative STD [19]. STDD requires another reference sample (sample containing only the target protein). In exchange for the inconvenience of the requirement of the second NMR sample, STDD gives a higher signal-to-noise ratio by eliminating the background signals arising from the target protein. STDD is highly advantageous when the molecular size of the target protein is large.

#### 21.2.1.2 WaterLOGSY

WaterLOGSY is another important 1D NMR technique that is useful for discriminating whether the ligand of interest binds to the target protein. In contrast to STD, the solvent for WaterLOGSY is 90%  ${}^1\text{H}_2\text{O}$ –10%  ${}^2\text{H}_2\text{O}$ , because this experiment is

based on the magnetization transfers among protons in bulk solvent water molecules, the ligand, and the protein. Note that 10%  $^2\text{H}_2\text{O}$  is not specifically required for the WaterLOGSY experiment; instead, it is just necessary for the NMR spectrometer to stabilize (i.e., lock) the NMR frequency. WaterLOGSY works in the following manner: At the beginning of the pulse sequence, a selective pulse saturates the protons in the bulk water molecules. Then, the magnetization of the water protons transfers to the protein protons via two mechanisms: (1) The magnetization transfers to the surface protons of the target protein through the nuclear Overhauser effect (NOE) and (2) the exchange occurs between the bulk water protons and the exchangeable protons of the target protein, during the mixing time (typically 500 ms). Subsequently, the magnetization of the protein protons is transferred to the ligand protons in the bound state, through the NOE. A comprehensive review of this technique was written by Ramirez et al. [20]. In addition to the original WaterLOGSY experiment, several improvements in terms of the sensitivity were made, including polarization-optimized (PO) WaterLOGSY [21] and Aroma-WaterLOGSY [22] experiments. Furthermore, the radiation damping process was incorporated into the conventional WaterLOGSY experiment [23]. This modification resulted in a 13% sensitivity improvement, as compared to the PO-WaterLOGSY experiment.

### 21.2.1.3 STD Versus WaterLOGSY

STD and WaterLOGSY are often used to find a hit fragment in a mixture with non-hit fragments (up to 10 fragments). In the STD experiment, only the hit fragment gives a positive difference signal, and the signals from non-hit fragments are eliminated. In the WaterLOGSY experiment, the hit fragment gives a positive difference signal, whereas the non-hit fragments give negative signals. Thus, in terms of the interpretation of the experimental results, STD is simpler than WaterLOGSY. Ley et al. [24] proposed a simple but significant intensity improvement of the STD experiment, by using a shorter excitation pulse at an optimized excitation frequency. The sensitivities of STD and WaterLOGSY were compared in a realistic drug screening experiment [25]. The authors concluded that WaterLOGSY was more sensitive than STD in certain cases. Thus, the comparison of STD and WaterLOGSY is left for future evaluations.

## 21.2.2 *Pharmacophore Determination*

This section describes the medium-throughput NMR-based drug screening techniques, the DIRECTION [9] and INPHARMA [10] experiments. In contrast to the

two methods described above, these two experiments were developed to identify ligand protons in immediate contact with the target protein via NOE observation. Between the lead discovery and lead optimization processes of drug discovery, a core sub-structure that is common to related compounds with different affinities for the target protein should be experimentally determined. This sub-structure plays a central role in the molecular recognition, and is referred to as the “pharmacophore.” The spatial information from the DIRECTION and INPHARMA experiments is particularly useful to define pharmacophores. Pharmacophore identification leads to the further development of a series of derivative compounds, to find the best ligand.

### 21.2.2.1 DIRECTION

Mizukoshi et al. [9] developed a simple and accurate method to classify the ligand protons by their proximity to the target protein. The method is based on the difference in the longitudinal relaxation rates of the ligand protons, depending on the saturation state of the protein protons. The DIRECTION experiment involves a series of inversion-recovery 1D NMR experiments to determine the  $T_1$  values of the ligand protons, with and without additional excitation pulses on the protons of the target protein.

### 21.2.2.2 INPHARMA

The INPHARMA experiment is another important experiment used for pharmacophore mapping (Fig. 21.1) (see reviews, [10, 26]). The INPHARMA experiment is designed to identify spatially equivalent protons between two ligands that share the same binding pocket. Thus, the INPHARMA sample contains three components, ligand *a* of interest, a reference ligand *b* that is known to bind to the target protein, and the target protein itself. In the pulse sequence, the excited magnetization of ligand *a* transfers to the proximal protons in the ligand binding site of the target protein. During the long mixing time, ligand *a* dissociates and ligand *b* binds to the binding site. Then, the magnetization of the protein protons transfers to the proximal protons of ligand *b*. As a result, the spatially equivalent protons of ligand *a* and ligand *b* give a cross peak in the INPHARMA spectrum. The INPHARMA experiment was also shown to be useful for the binding-site identification of a protein target with multiple binding sites. Krimm prepared a set of reference molecules with known binding sites on glycogen phosphorylase and assigned the specific binding sites of several compounds unambiguously [27]. Skjærven et al. [28] developed a method to build a reliable protein–ligand complex model, by docking simulation assisted by INPHARMA-derived NOE constraints.

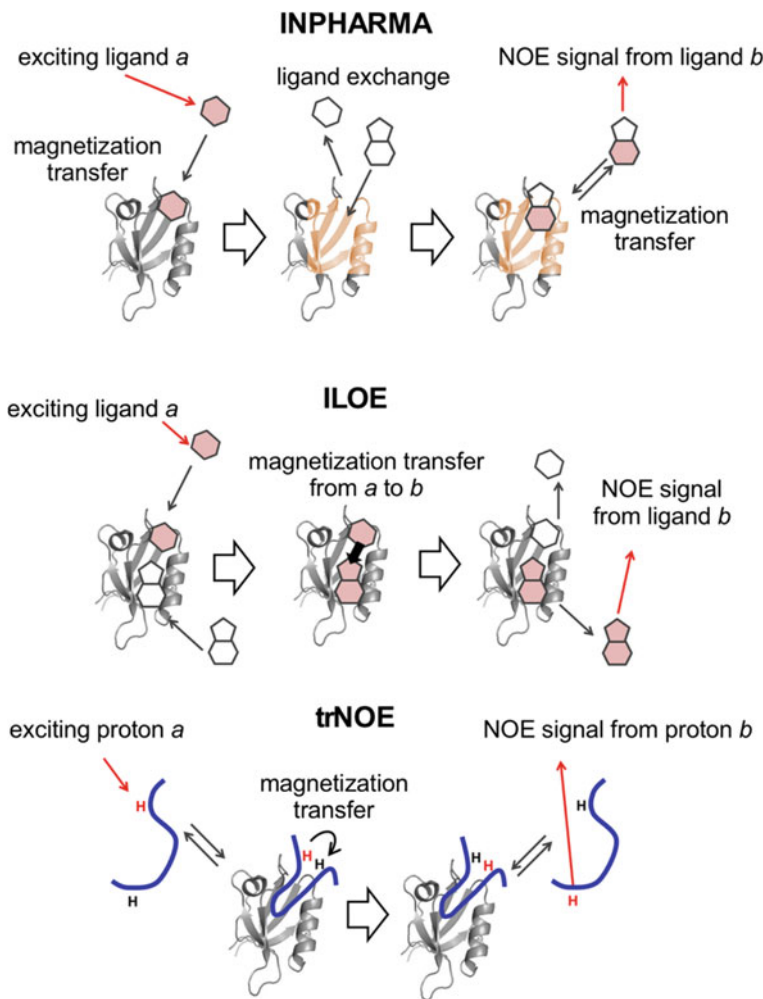


**Fig. 21.1** Basic principles of the operations of the ligand-based NMR experiments, INPHARMA, ILOE, and trNOE, for analyzing protein–ligand interactions. Note the routes of the magnetization transfer from proton to proton. The colored shapes and sites represent the ligands and protein parts “heated” by NMR pulse irradiation. The red H’s also represent the protons “heated” by irradiation

### 21.2.3 Structural Information-Driven Ligand Design

The nuclear Overhauser effect (NOE) is a phenomenon induced by through-space dipole-dipole interactions between two nuclear spins. The NOE effect is measured as the change in the signal intensity of one nuclear spin when another spatially close nuclear spin is saturated by irradiation. The NOE effect is proportional to the inverse of the sixth power of the distance between the two nuclei and hence

provides distance information between the two nuclei. NOE-based experiments thus furnish useful structural restraints for designing novel molecules with higher affinity to the target protein.

### 21.2.3.1 Inter-ligand Nuclear Overhauser Effect (ILOE)

The inter-ligand nuclear Overhauser effect (ILOE) experiment is a good example of the NOE-based experiment [11] (Fig. 21.1). As described, the FBDD approach is composed of the fragment screening step and the lead generation step from the fragments. NMR-assisted FBDD is a concept in which the NMR-derived information is used to promote the two FBDD steps. The first step is accelerated by several NMR screening experiments, including STD, WaterLOGSY, and NMR titration experiments. Once several fragments are identified, then linking the fragments into one novel molecule is the standard strategy in the second step of FBDD.

The ILOE experiment can facilitate the identification of a linking point in the fragment-based lead generation. The concept of the ILOE experiment is similar to that of INPHARMA. The ILOE sample contains two fragments and one target protein. In contrast to INPHARMA, two ligands *a* and *b* are assumed to bind side by side to the same binding site. In a 2D NOESY spectrum, an NOE cross peak between the two proximal protons, one in ligand *a* and the other in ligand *b*, is expected to be observed (Fig. 21.1). Two milestone papers were published by Sledz et al. [29] and Rega et al. [30]. Sledz et al. demonstrated the use of ILOE-based fragment linking to obtain a new tight inhibitor targeted to the *Mycobacterium tuberculosis* pantothenate synthetase ( $K_D = 880$  nM). Rega et al. employed an elegant application of SAR-by-ILOE [30], as an alternative strategy to SAR-by-NMR (described later). They succeeded in developing acylsulfonamide derivatives targeted to antiapoptotic Bcl-1 family proteins.

### 21.2.3.2 Transferred Nuclear Overhauser Effect (trNOE)

Transferred NOE is another NOE-based experiment that facilitates the design of new ligand molecules from linear flexible lead molecules, such as peptides (Fig. 21.1). In a small molecule, the peak intensity of one proton is increased when another proximal proton, within 4–5 Å, is irradiated by a selective pulse. This phenomenon is referred to as a positive NOE. In the presence of a protein, the small molecule is in an exchange equilibrium between the free state and the protein-bound state, which results in an apparent molecular mass increase. In the same NOESY spectrum, the peak intensity now decreases and a negative NOE is observed. The negative sign of the NOE effect confirms that the NOE arises from a fixed conformation of the flexible ligand in the bound state. One recent example is the determination of the CCR5-bound conformation of HIV-1 gp120 derived V2 peptide, which inhibits HIV infection [31]. The design of a new ligand with a fixed

conformation is usually advantageous to increase the affinity of a flexible ligand for the target protein, by the entropy reduction of the free state of the ligand. Thus, the distance information of the bound conformation provides invaluable hints for the design of a new lead compound.

### 21.2.3.3 Technical Comments on INPHARMA, ILOE and trNOE Experiments

Interestingly, the pulse sequence of the three experiments, INPHARMA, ILOE, and trNOE, is essentially the same standard 2D NOESY spectrum. The sample for trNOE contains only one ligand, whereas the samples of INPHARMA and ILOE contain two ligands, in addition to the target protein. The differences in the route of the magnetization transfer in the three experiments are illustrated in Fig. 21.1. The major difference in the concepts of INPHARMA and ILOE is the binding modes of the two ligands. The INPHARMA experiment is designed to find spatially equivalent atoms between the two ligands that compete directly for the same binding site. In contrast, the ILOE experiment is designed to detect inter-molecular NOEs between two ligands that simultaneously bind to the protein, side by side. In actual experimental set ups, the mixing time delay in the NOESY pulse sequence is different. INPHARMA uses a long mixing time (500 ms), whereas ILOE uses a short mixing time (80 ms). TrNOE typically requires a relatively long mixing time of 200–600 ms.

## 21.3 Protein-Based Approach for Protein–Ligand Interactions

In this section, we introduce the protein-based approach for protein–ligand interaction studies. The goals of the protein-based approach include: (1) the screening of ligands that weakly bind to the target, (2) the acquisition of information for the design of new lead compounds for FBDD, (3) the identification of the interface on the target protein molecule, (4) the detection of the conformational changes of the target protein upon ligand binding, and (5) the determination of the dissociation constant,  $K_D$ . To achieve these goals, the so-called NMR titration experiment, also known as the chemical shift perturbation (CSP) experiment, is most frequently used. For example, goals 1, 2, 4, and 5 are routinely achieved by the NMR titration experiment. Another useful protein-based method is the cross saturation experiment [32]. An overview of the two protein-based NMR experiments is illustrated in Fig. 21.2.

The NMR chemical shifts of some (but not all) chemical groups of the target protein are very sensitive to changes in the microscopic environments around the chemical groups. The nuclear spins of protons or other NMR-active nuclei located within or close to the ligand binding site can be used to monitor the binding of the

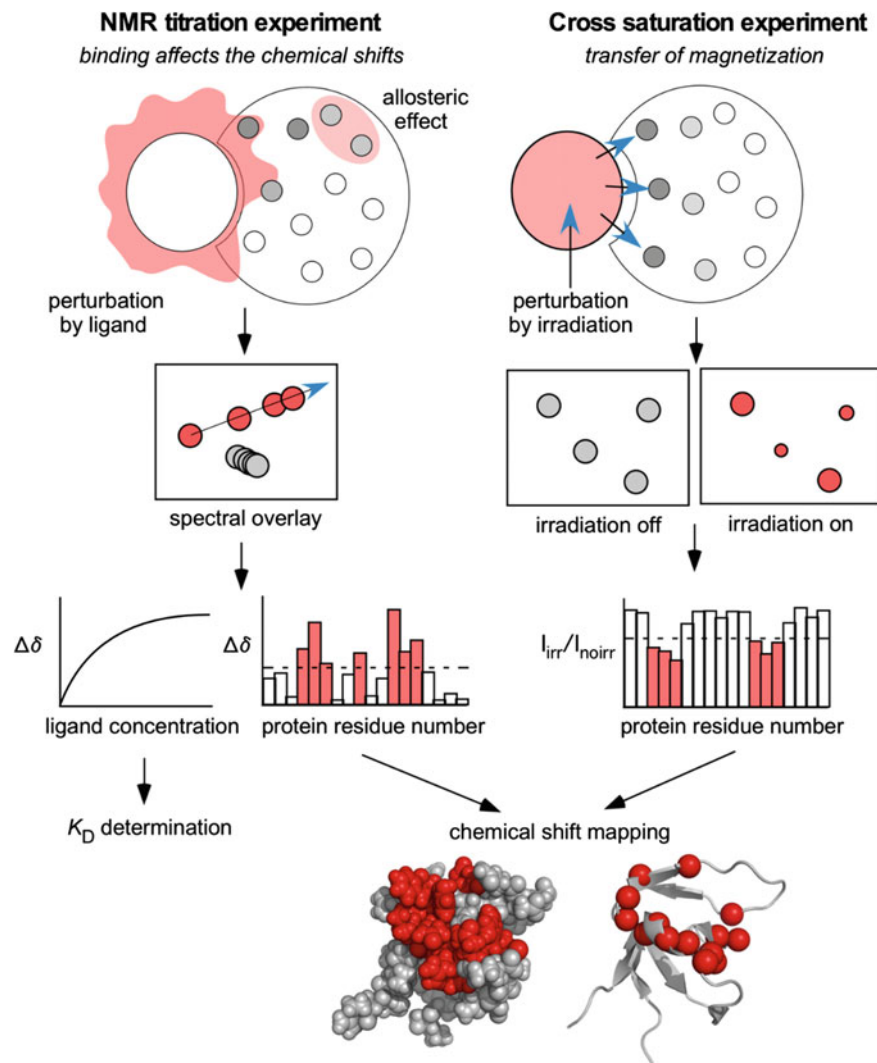


**Fig. 21.2** Basic principles of the operations of the protein-based NMR experiments, the NMR titration (alias, chemical shift perturbation) experiment and the cross saturation experiment

ligand to the protein. The comparison of two NMR spectra of the target protein recorded in the absence and presence of the ligand reveals the protein–ligand interactions. In practice, an NMR titration experiment involves repeated 2D NMR measurements with serial additions of the ligand stock solution to the protein sample.

The NMR titration and the cross saturation experiments are both 2D NMR experiments. The  $^1\text{H}$ – $^1\text{H}$  2D NMR spectrum is usable, but the incorporation of stable isotopes,  $^{15}\text{N}$  and/or  $^{13}\text{C}$ , is highly recommended, due to the heavy overlapping of the  $^1\text{H}$  signals of proteins. Note that if the heteronuclear  $^1\text{H}$ – $^{15}\text{N}$  or

$^1\text{H}$ - $^{13}\text{C}$  HSQC spectra show good cross peak dispersion, and at least some cross peaks are separately observed, then the signal assignment is not mandatory in the cases of goal 1 (ligand screening) and goal 5 ( $K_D$  determination).

### 21.3.1 Ligand Screening and NMR-Assisted Fragment-Based Drug Discovery

#### 21.3.1.1 HSQC-Based Ligand Screening

The chemical shift perturbations (CSPs) of the protein amide groups in  $^1\text{H}$ - $^{15}\text{N}$  HSQC spectra or the methyl groups in  $^1\text{H}$ - $^{13}\text{C}$  HSQC spectra are useful for monitoring protein-ligand interactions. A pair of HSQC spectra of the protein recorded in the absence and presence of the ligand is sufficient to detect the interaction of the ligand with the protein. In order to facilitate the screening, a cocktail of several different ligands can be used. In fact, using this cocktail technique, unexpected interactions of non-steroid anti-inflammatory drugs, diclofenac, and flufenamic acid, were discovered with the ZO-1 PDZ1 domain [33]. Here we provide another example of an NMR titration experiment, ZO-1 PDZ1, and the peptide derived from its physiological ligand claudin-3

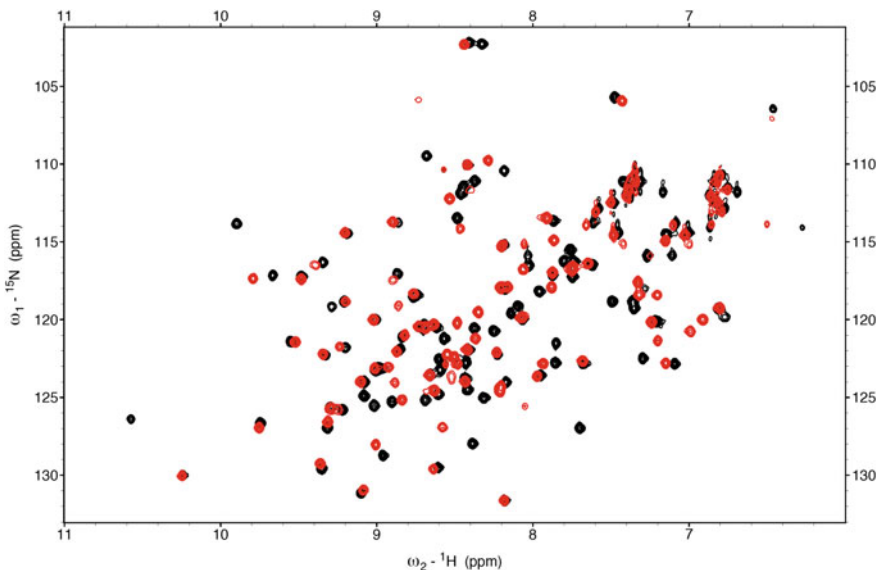


**Fig. 21.3** An example of the NMR titration experiment/chemical shift perturbation (CSP) experiment. The HSQC spectra of 0.1 mM of  $^{15}\text{N}$ -labeled mouse ZO1-PDZ1 domain with (red) or without (black) its physiological ligand-derived peptide, Pep-Claudin3, were recorded, and the two spectra were overlaid

(Fig. 21.3). As described, these NMR applications are often combined with FBDD approaches and are called NMR-assisted FBDD.

### 21.3.1.2 SAR-by-NMR

The “SAR-by-NMR” experiment proposed by Fesik et al. [34] is a pioneering method to design and synthesize a compound with improved affinity, from experimentally identified fragments. In brief, assume that two side-by-side ligand binding sites, *A* and *B*, are identified on a  $^{15}\text{N}$ -labeled protein, and all of the  $^1\text{H}$ – $^{15}\text{N}$  cross peaks or at least those close to the two binding sites are assigned. Next, a ligand *a* that binds to site *A* is discovered by the NMR titration, and then the chemical structure of ligand *a* is optimized to ligand *a'* with higher affinity. The CSPs of the protein amide groups provide a guide during the structural optimization, as a monitor of the fitness of the binding of fragment molecules into the binding site *A*. In parallel, a ligand *b* that binds to site *B* is discovered and optimized into ligand *b'*. Finally, a novel ligand *c* is generated by connecting ligand *a'* and ligand *b'* with an appropriate linker moiety.

## 21.3.2 Determination of the Molecular Interface and Exploring the Mode of Action

### 21.3.2.1 Chemical Shift Mapping

The second important use of the NMR titration experiment is to determine the molecular interface of the ligand binding site on the surface of the target protein. If the three-dimensional structure of the target protein has been determined by X-ray crystallography, solution NMR, or homology modeling, then the nuclei that show large chemical shift changes are mapped onto the surface of the target protein structure. Needless to say, the specific signal assignments of the amide groups or methyl groups in the corresponding HSQC spectrum must be accomplished beforehand. It might seem logical to perform mapping on an atom-to-atom basis, but residue-based coloring is better for easy interpretation. That is, the whole amino acid residues to which the amide or methyl groups belong are colored, for better visual effects. This application is referred to as “chemical shift mapping” (Fig. 21.2).

Chemical shift changes are normalized before mapping, according to the following equation:

$$\Delta\delta = [(\Delta\delta_{1\text{H}})^2 + (\Delta\delta_{15\text{N}}/w)^2]^{1/2} \quad (21.1)$$

where  $\Delta\delta_{^1\text{H}}$  and  $\Delta\delta_{^{15}\text{N}}$  are the chemical shift changes of the  $^1\text{H}$  and  $^{15}\text{N}$  chemical shifts of an amide N–H group, respectively, and  $w$  is the normalization weight. Usually,  $w = 5\text{--}7$  is used to balance the different ranges of the  $^1\text{H}$  and  $^{15}\text{N}$  chemical shift distributions of the amide cross peaks.

Each residue is colored differently, according to the amplitude of the normalized chemical shift change,  $\Delta\delta$ . The threshold value of the coloring is determined in an arbitrary fashion. A reasonable recommendation for determining the coloring threshold [35, 36] is as follows:

- (1) calculate the average,  $\Delta\delta_{\text{ave}}$ , and the standard deviation,  $\sigma$ , for all of the groups.
- (2) omit the groups with changes larger than  $\Delta\delta_{\text{ave}} + 3\sigma$ , and re-calculate a new average,  $\Delta\delta'_{\text{ave}}$ , and the standard deviation,  $\sigma'$ , using the rest of the groups.
- (3) color the residues with  $\Delta\delta$  larger than  $\Delta\delta'_{\text{ave}} + \sigma'$ .

In this protocol, step 2 helps to avoid the deleterious effects of groups with accidentally large chemical shift changes. Alternatively, the authors recommended only using groups on the surface-exposed residues.

A flaw of the quantitative CSP analysis is the lack of an obvious correlation between the amplitude of the CSP and the strength of the interaction. It is not always true that the residues with large CSPs are the critical residues in the molecular recognition. Positive and negative chemical shift changes are induced by various factors, and two opposing factors may cancel out to give nearly zero values accidentally. In such a case, the amino acid residue important for the molecular interactions exhibits a small CSP. In another case, the residues located far from the ligand binding site may exhibit large CSPs by allosteric conformational changes upon ligand binding. Therefore, one must recognize this limitation and cautiously interpret the chemical shift mapping. The cross saturation experiment largely resolves the chemical shift mapping problem, by using magnetization saturation transfer from the ligand to a highly deuterated protein sample [32, 37].

### 21.3.2.2 $K_D$ Determination by the NMR Titration

Here, we introduce a very basic mathematical analysis to determine the  $K_D$  values from the NMR titration experiment. In a system in a two-state exchange equilibrium between the ligand-free state and the bound state, with sufficiently fast association and dissociation, all of the cross peaks move smoothly during the ligand titration. Typically, the analysis is focused on a single cross peak that exhibits the largest CSP upon ligand binding in the  $^1\text{H}$ – $^{15}\text{N}$  (or  $^1\text{H}$ – $^{13}\text{C}$ ) HSQC spectrum.

In a simple two-state equilibrium and a single binding site model,  $K_D$  is defined by the following equation:

$$K_D = R \cdot L / RL \quad (21.2)$$

where  $R$  and  $L$  are the concentrations of the free protein (or free receptor) and the free ligand, respectively.  $RL$  represents the concentration of the complex. The total concentrations of the protein and the ligand,  $R_{\text{total}}$ , and  $L_{\text{total}}$ , are given by

$$R_{\text{total}} = R + RL \quad (21.3)$$

$$L_{\text{total}} = L + RL \quad (21.4)$$

The normalized chemical shift difference,  $\Delta\delta$ , and the maximum chemical shift change,  $\Delta\delta_{\text{max}}$ , are connected to each other by the following equation:

$$\Delta\delta = \Delta\delta_{\text{max}} \cdot (1/2R_{\text{total}})[(R_{\text{total}} + L_{\text{total}} + K_D) - \{(R_{\text{total}} + L_{\text{total}} + K_D)^2 - 4R_{\text{total}}L_{\text{total}}\}]^{1/2} \quad (21.5)$$

The normalized chemical shift change,  $\Delta\delta$ , is plotted against the total concentration of the ligand,  $L_{\text{total}}$ , to give a saturation curve. A non-linear least square fitting algorithm, with a given  $R_{\text{total}}$ , determines the  $K_D$  and  $\Delta\delta_{\text{max}}$  values. In some cases, several cross peaks can be collectively used to determine a single  $K_D$  value and a set of  $\Delta\delta_{\text{max}}$  values, by a global fitting algorithm. Of course, one would have to assume that these cross peaks monitor the same binding process. A suitable range of  $K_D$  values for the NMR titration experiment is usually between 1 mM and 1  $\mu\text{M}$ . If the affinity is weaker than  $K_D = 1 \text{ mM}$ , then the titration experiment would require too much of the ligand and is thus unfeasible. If the affinity is stronger than  $K_D = 1 \mu\text{M}$ , then the protein concentration must be reduced, which affects the sensitivity of the NMR measurement. Unfortunately, the precision of the  $K_D$  determination is not very high. This is because of the small number of titration data points, usually five to ten. Nevertheless, NMR-based  $K_D$  determination has tremendous merits, including (1) the protein and the ligand do not need to be immobilized to solid supports, beads, or sensor chip surfaces, (2) the protein does not need to be labeled with any fluorescent dyes, and (3) the exchange equilibrium of the protein–ligand interactions can be directly observed in solution.

## 21.4 Experimental Aspects of the NMR Study of Protein–Ligand Interactions

### 21.4.1 Stable Isotope Labeling

Most protein-based approaches for protein–ligand interactions rely on 2D heteronuclear chemical shift correlation experiments, such as a  $^1\text{H}$ – $^{15}\text{N}$  or  $^1\text{H}$ – $^{13}\text{C}$  HSQC spectrum. Usually, the cross peaks in a 2D  $^1\text{H}$ – $^1\text{H}$  NMR spectrum of the target protein are heavily overlapped. This signal overlapping problem can be solved by introducing a second heteronuclear dimension. The natural abundances of  $^{15}\text{N}$  and  $^{13}\text{C}$  are 0.4 and 1.1%, respectively. The first step of the protein-based

approach is to choose the isotope labeling strategy for the target protein. The most cost-effective isotope labeling is  $^{15}\text{N}$ -uniform labeling using the *Escherichia coli* (*E. coli*) expression system. *E. coli* cells grow in minimal media containing 2–4 g/L glucose ( $^{12}\text{C}_6$ - or  $^{13}\text{C}_6$ -if needed) as the sole carbon source and 0.5–1 g/L  $^{15}\text{N}$ -ammonium chloride as the sole nitrogen source. Trace amounts of vitamins, minerals, and nucleosides are often supplemented.

Other microorganism-based recombinant protein expression systems for isotope labeling have been developed. The systems include *Brevibacillus choshinensis* [38], *Pichia pastoris* [39, 40], *Schizosaccharomyces pombe* [41], and *Kluyveromyces lactis* [42]. These microorganisms can grow in minimal media containing simple nitrogen-source compounds, and thereby are cost-effective. If the target protein is difficult to produce in these microorganism-based expression systems, then the cell culture of a higher eukaryote is another choice. As for insect cells, the baculovirus-Sf9 insect cell [43] and *Drosophila* S2 cell [44] expression systems have been employed to prepare isotope labeled protein samples. With regard to plant cells, Ohki et al. [45] established an expression system using tobacco BY-2 cells. They demonstrated the preparation of sufficient amounts of  $^{15}\text{N}$ -labeled proteins, including dihydrofolate reductase, chicken calmodulin, porcine protein kinase C-dependent protein phosphatase-1 inhibitor, and bovine pancreatic trypsin inhibitor. As the nitrogen sources,  $\text{K}^{15}\text{NO}_3$  and  $^{15}\text{NH}_4^{15}\text{NO}_3$  were used. With regard to mammalian cells, Werner et al. [46] first reported the isotope labeling of GPCRs by using HEK293 cells. Sastry et al. [47] succeeded in preparing the isotopically labeled outer domain of the HIV-1 gp120 glycoprotein, using HEK293 cells and an adenovirus expression vector. The commercially available NMR-ready synthetic medium for mammalian cells, CGM-6000 (Cambridge Isotope Laboratory), was used. The main problem with these methods is the issue of cost. Recently, Egorova-Zachernyuk et al. [48] reported a cost-effective recipe for  $^{15}\text{N}$ -labeling, using HEK293 cells with yeast and algal auto-lysates.

Alternatively, several cell-free protein synthesis systems and many commercially available cell-free kits have been developed (reviewed in [49]). *E. coli* cell-free systems and wheat germ cell-free systems were used for highly automated protein production in several structural genomics projects. Depending on the purity of the cell-free extracts, some of these have limitations on their use for amino acid-specific labeling, because the cell-free extracts contain various metabolic enzymes in addition to all of the protein production machinery.

### 21.4.2 *Tips for the NMR Titration Experiment*

#### 21.4.2.1 *Sample Handling*

The chemical shift is very sensitive to environmental factors, such as pH and salt concentrations. Thus, accidental changes of the chemical shift values due to the unwanted solvent effects of the ligand solution must be taken into account during

the NMR titration experiments. In this case, the chemical shift changes cannot fit a saturation curve shape. As a control, titrations with the same solvent containing no ligand are helpful. Ideally, the ligand solution contains the identical solvent components at the same concentrations as in the protein solution, by dialysis or ultrafiltration. In practice, the volume change during titration should be, preferably, less than 10%, and the volume effect on the concentrations of the components must be corrected in the data analysis. To satisfy this prerequisite, the concentration of the ligand solution must be high enough to minimize the volume change. Alternatively, the protein solution and the ligand solution are premixed according to the pre-planned ratios in separate NMR tubes. In this case, a relatively large amount of the ligand is necessary, but the volume change does not matter. The latter method is also useful when the ligand solubility is limited by the saturating concentration. In drug screenings, candidate drug compounds are frequently hydrophobic, and consequently, DMSO or other organic solvents must be added to the water solution. Obviously, another titration experiment must be performed to exclude the side effects of the organic solvent inclusion. In the case of synthesized peptides, trifluoroacetic acid (TFA) is present in the lyophilized powder of the peptide, and must be neutralized before use. Sometimes, however, the neutralization by dialysis or ultrafiltration is difficult due to the small to medium size of the peptides.

A normal 5-mm-diameter NMR tube requires a sample volume of about 0.4 mL. A special micro NMR tube (Shigemi micro tubes, <https://www.shigeminmr.com/>) is useful to minimize the sample volume (Fig. 21.4). In normal use, an inner glass rod is inserted into an outer glass tube. A typical working sample volume is about 0.12–0.15 mL. For titration experiments, the inner glass rod is impracticable, but the outer glass NMR tube is still usable to reduce the sample volume to 0.25 mL. The addition of small volumes of the ligand solution is very difficult for beginners. First, the top of the NMR tube is tilted to the side, to the brink of spilling. A small volume of the ligand solution is added with a micropipette to the solution near the mouth of the NMR tube. Alternatively, a pair of capillary glass tubes (Drummond) tandemly connected by a rubber tube is useful to directly dispense a small volume of the

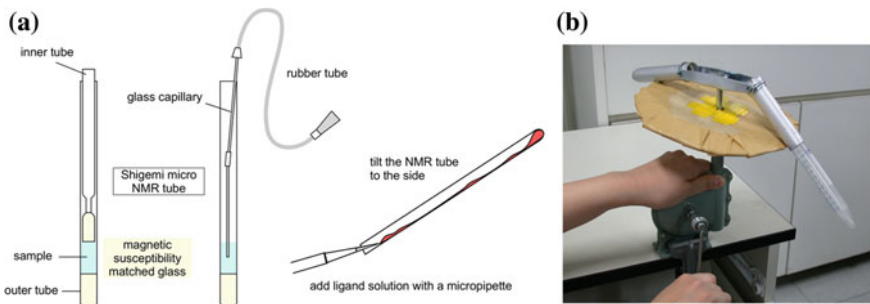


**Fig. 21.4** Sample handling tips for NMR titration study. **a** The tube-within-a tube method for sample volume minimization. The ligand is added via a glass capillary or micropipette. **b** Facilitation of sample mixing by centrifugation. Any solution stuck to the side of the tube is forced to the bottom upon centrifugation

ligand solution into the protein solution at the bottom of the NMR tube (Fig. 21.4a). It is convenient to use a wind-up type centrifuge apparatus specially adapted to an NMR tube, to drive the solution collected on the wall to the bottom of the NMR tube (Fig. 21.4b).

#### 21.4.2.2 Data Acquisition and Analysis

For the acquisition of the NMR titration experiment data, the most basic 2D experiment is HSQC. Between the measurements of HSQC spectra, measuring the 1D  $^1\text{H}$  spectra in an interleaved manner is recommended on a routine basis. The 1D spectra provide valuable information about the molar ratio of the ligand to the protein and allow monitoring to determine whether the desired amount of the ligand was correctly added to the sample. Although the HSQC recording does not require a very long measurement time, typically 10 min to 2 h, high-throughput screening is always a critical issue in industrial applications. SOFAST-HMQC is a variant of the  $^1\text{H}$ - $^{15}\text{N}$  HSQC experiment, designed to shorten the measurement time by up to several folds [50].

Solution NMR techniques can only effectively observe the NMR signals of relatively small proteins (i.e., molecular masses less than 30 kDa). In many practical cases, the sizes of the drug target proteins often exceed the molecular mass limit. In such cases, the use of a combination of transverse relaxation-optimized  $^1\text{H}$ - $^{15}\text{N}$  HSQC (TROSY- $^1\text{H}$ - $^{15}\text{N}$  HSQC) and deuterated protein samples in  $^1\text{H}_2\text{O}$  (to observe the backbone amide groups) can expand the molecular mass limit, up to 100 kDa [51]. Alternatively,  $^{13}\text{CH}_3$ -specific labeling is another solution. The incorporation of  $^{13}\text{CH}_3$ -methionine and the chemical methylation of the  $\varepsilon$ -amino group of lysine residues were demonstrated to be useful for this purpose [52, 53].

### 21.5 Other Complementary Methods for Protein–Ligand Interactions

In recent years, various methods other than NMR have been combined with FBDD and became indispensable core technologies for the early stages of drug discovery (see reviews, [54, 55]), especially for the development of protein-protein interaction modulators [56]. The methods include surface plasmon resonance (SPR), differential scanning fluorometry (DSF), and isothermal titration calorimetry (ITC) [57, 58]. The complementary use of these methods is always useful to confirm the binding of the ligand and the determined  $K_D$  values.

## 21.6 Perspective

This review summarized the recent developments in solution NMR techniques for analyzing protein–ligand interactions (Table 21.1). Solution NMR is an indispensable tool for detecting and analyzing protein–ligand interactions with various ranges of the dissociation constant,  $K_D$ . The versatility of NMR spectroscopy can affect the entire process of drug development, from upstream basic research to downstream clinical applications. Further developments and improvements of the solution NMR methods will create new trends in pharmaceutical applications, FBDD, protein–protein interaction inhibitor development, and peptide-mimetics strategies.

## References

1. Pellecchia, M., Sem, D.S., Wüthrich, K.: NMR in drug discovery. *Nat. Rev. Drug Discov.* **1**, 211–219 (2002)
2. Pellecchia, M., Bertini, I., Cowburn, D., Dalvit, C., Giralt, E., Jahnke, W., James, T.L., Homans, S.W., Kessler, H., Luchinat, C., Meyer, B., Oschkinat, H., Peng, J., Schwalbe, H., Siegal, G.: Perspectives on NMR in drug discovery: a technique comes of age. *Nat. Rev. Drug Discov.* **7**, 738–745 (2008)
3. Cala, O., Guilliére, F., Krimm, I.: NMR-based analysis of protein–ligand interactions. *Anal. Bioanal. Chem.* **406**, 943–956 (2014)
4. Hiroaki, H.: Recent applications of isotopic labeling for protein NMR in drug discovery. *Expert Opin. Drug Discov.* **8**, 523–536 (2013)
5. Viegas, A., Manso, J., Nobrega, F.L., Cabrita, E.J.: Saturation-transfer difference (STD) NMR: a simple and fast method for ligand screening and characterization of protein binding. *J. Chem. Educ.* **88**, 990–994 (2011)
6. Dalvit, C., Fogliatto, G., Stewart, A., Veronesi, M., Stockman, B.: WaterLOGSY as a method for primary NMR screening: practical aspects and range of applicability. *J. Biomol. NMR* **21**, 349–359 (2001)
7. Antalek, B.: Using pulsed gradient spin echo NMR for chemical mixture analysis: how to obtain optimum results. *Concepts Magn. Reson.* **14**, 225–258 (2002)
8. Chen, A., Shapiro, M.J.: Affinity NMR. *Anal. Chem.* **71**, 669A–675A (1999)
9. Mizukoshi, Y., Abe, A., Takizawa, T., Hanzawa, H., Fukunishi, Y., Shimada, I., Takahashi, H.: An accurate pharmacophore mapping method by NMR spectroscopy. *Angew. Chem. Int. Ed. Engl.* **51**, 1362–1365 (2012)
10. Sánchez-Pedregal, V.M., Reese, M., Meiler, J., Blommers, M.J.J., Griesinger, C., Carlonmagno, T.: The INPHARMA method: protein-mediated interligand NOEs for pharmacophore mapping. *Angew. Chem.* **117**, 4244–4247 (2005)
11. Becattini, B., Culmsee, C., Leone, M., Zhai, D., Zhang, X., Crowell, K.J., Rega, M.F., Landshamer, S., Reed, J.C., Plesnila, N., Pellecchia, M.: Structure-activity relationships by interligand NOE-based design and synthesis of antiapoptotic compounds targeting Bid. *Proc. Natl. Acad. Sci. U S A* **103**, 12602–12606 (2006)
12. Ni, F.: Recent developments in transferred NOE methods. *Prog. Nucl. Magn. Reson. Spectrosc.* **26**, 517–606 (1994)
13. Rees, D.C., Congreve, M., Murray, C.W., Carr, R.: Fragment-based lead discovery. *Nat. Rev. Drug Discov.* **3**, 660–672 (2004)

14. Ciulli, A., Williams, G., Smith, A.G., Blundell, T.L., Abell, C.: Probing hot spots at protein–ligand binding sites: a fragment-based approach using biophysical methods. *J. Med. Chem.* **49**, 4992–5000 (2006)
15. Orita, M., Warizaya, M., Amano, Y., Ohno, K., Niimi, T.: Advances in fragment-based drug discovery platforms. *Expert Opin. Drug Discov.* **4**, 1125–1144 (2009)
16. Claasen, B., Axmann, M., Meinecke, R., Meyer, B.: Direct observation of ligand binding to membrane proteins in living cells by a saturation transfer double difference (STDD) NMR spectroscopy method shows a significantly higher affinity of integrin alpha(IIb)beta3 in native platelets than in liposomes. *J. Am. Chem. Soc.* **127**, 916–919 (2005)
17. Furihata, K., Shimotakahara, S., Shibusawa, Y., Tashiro, M.: An effective pulse sequence for detecting a ligand binding with a protein receptor using a WET sequence and the repeated Z-filters. *Anal. Sci.* **26**, 1107–1110 (2010)
18. Bergeron, S.J., Henry, I.D., Santini, R.E., Aghdasi, A., Raftery, D.: Saturation transfer double-difference NMR spectroscopy using a dual solenoid microcoil difference probe. *Magn. Reson. Chem.* **46**, 925–929 (2008)
19. Kemper, S., Patel, M.K., Errey, J.C., Davis, B.G., Jones, J.A., Claridge, T.D.W.: Group epitope mapping considering relaxation of the ligand (GEM-CRL): including longitudinal relaxation rates in the analysis of saturation transfer difference (STD) experiments. *J. Magn. Reson.* **203**, 1–10 (2010)
20. Ramirez, B.E., Antanasićević, A., Caffrey, M.: Ligand screening using NMR. In: Anderson, W. (ed.) *Structural Genomics and Drug Discovery: Methods and Protocols*. *Methods Mol. Biol.* **1140**, 305–313 (2014)
21. Gossert, A.D., Henry, C., Blommers, M.J.J., Jahnke, W., Fernández, C.: Time efficient detection of protein–ligand interactions with the polarization optimized PO-WaterLOGSY NMR experiment. *J. Biomol. NMR* **43**, 211–217 (2009)
22. Hu, J., Eriksson, P.O., Kern, G.: Aroma WaterLOGSY: a fast and sensitive screening tool for drug discovery. *Magn. Reson. Chem.* **48**, 909–911 (2010)
23. Sun, P., Jiang, X., Jiang, B., Zhang, X., Liu, M.: Biomolecular ligands screening using radiation damping difference WaterLOGSY spectroscopy. *J. Biomol. NMR* **56**, 285–290 (2013)
24. Ley, N.B., Rowe, M.L., Williamson, R.A., Howard, M.J.: Optimising selective excitation pulses to maximise saturation transfer difference NMR spectroscopy. *RSC Adv.* **4**, 7347 (2014)
25. Antanasićević, A., Ramirez, B., Caffrey, M.: Comparison of the sensitivities of WaterLOGSY and saturation transfer difference NMR experiments. *J. Biomol. NMR* **60**, 37–44 (2014)
26. Carlomagno, T.: NMR in natural products: understanding conformation, configuration and receptor interactions. *Nat. Prod. Rep.* **29**, 536 (2012)
27. Krimm, I.: INPHARMA-based identification of ligand binding site in fragment-based drug design. *MedChemComm* **3**, 605 (2012)
28. Skjærven, L., Codutti, L., Angelini, A., Grimaldi, M., Latek, D., Monecke, P., Dreyer, M.K., Carlomagno, T.: Accounting for conformational variability in protein–ligand docking with NMR-guided rescoring. *J. Am. Chem. Soc.* **135**, 5819–5827 (2013)
29. Sledz, P., Silvestre, H.L., Hung, A.W., Ciulli, A., Blundell, T.L., Abell, C.: Optimization of the interligand Overhauser effect for fragment linking: application to inhibitor discovery against *Mycobacterium tuberculosis* pantothenate synthetase. *J. Am. Chem. Soc.* **132**, 4544–4545 (2010)
30. Rega, M.F., Wu, B., Wei, J., Zhang, Z., Cellitti, J.F., Pellecchia, M.: SAR by interligand nuclear overhauser effects (ILOEs) based discovery of acylsulfonamide compounds active against Bcl-xL and Mcl-1. *J. Med. Chem.* **54**, 6000–6013 (2011)
31. Cimbro, R., Peterson, F.C., Liu, Q., Guzzo, C., Zhang, P., Miao, H., Van Ryk, D., Ambroggio, X., Hurt, D.E., De Gioia, L., Volkman, B.F., Dolan, M.A., Lusso, P.: Tyrosine-sulfated V2 peptides inhibit HIV-1 infection via coreceptor mimicry. *EBioMedicine* **10**, 45–54 (2016)

32. Shimada, I.: NMR techniques for identifying the interface of a larger protein-protein complex: cross-saturation and transferred cross-saturation experiments. *Methods Enzymol.* **394**, 483–506 (2005)
33. Tanno, T., Goda, N., Umetsu, Y., Ota, M., Kinoshita, K., Hiroaki, H.: Accidental interaction between PDZ domains and diclofenac revealed by NMR-assisted virtual screening. *Molecules* **18**, 9567–9581 (2013)
34. Shuker, S.B., Hajduk, P.J., Meadows, R.P., Fesik, S.W.: Discovering high-affinity ligands for proteins: SAR by NMR. *Science* **274**, 1531–1534 (1996)
35. Schumann, F.H., Riepl, H., Maurer, T., Gronwald, W., Neidig, K.-P., Kalbitzer, H.R.: Combined chemical shift changes and amino acid specific chemical shift mapping of protein-protein interactions. *J. Biomol. NMR* **39**, 275–289 (2007)
36. Williamson, M.P.: Using chemical shift perturbation to characterise ligand binding. *Prog. Nuclear Magn. Reson. Spectrosc.* **73**, 1–16 (2013)
37. Shimada, I., Ueda, T., Matsumoto, M., Sakakura, M., Osawa, M., Takeuchi, K., Nishida, N., Takahashi, H.: Cross-saturation and transferred cross-saturation experiments. *Prog. Nucl. Magn. Reson. Spectrosc.* **54**, 123–140 (2009)
38. Tanio, M., Tanaka, T., Kohno, T.: <sup>15</sup>N isotope labeling of a protein secreted by *Brevibacillus choshinensis* for NMR study. *Anal. Biochem.* **373**, 164–166 (2008)
39. Rodriguez, E., Krishna, N.R.: An economical method for (<sup>15</sup>N)/(<sup>13</sup>C) isotopic labeling of proteins expressed in *Pichia pastoris*. *J. Biochem.* **130**, 19–22 (2001)
40. Sugiki, T., Ichikawa, O., Miyazawa-Onami, M., Shimada, I., Takahashi, H.: Isotopic labeling of heterologous proteins in the yeast *Pichia pastoris* and *Kluyveromyces lactis*. *Methods Mol. Biol.* **831**, 19–36 (2012)
41. Takegawa, K., Tohda, H., Sasaki, M., Idiris, A., Ohashi, T., Mukaiyama, H., Giga-Hama, Y., Kumagai, H.: Production of heterologous proteins using the fission-yeast (*Schizosaccharomyces pombe*) expression system. *Biotechnol. Appl. Biochem.* **53**, 227–235 (2009)
42. Sugiki, T., Shimada, I., Takahashi, H.: Stable isotope labeling of protein by *Kluyveromyces lactis* for NMR study. *J. Biomol. NMR* **42**, 159–162 (2008)
43. Strauss, A., Bitsch, F., Fendrich, G., Graff, P., Knecht, R., Meyhack, B., Jahnke, W.: Efficient uniform isotope labeling of Abl kinase expressed in Baculovirus-infected insect cells. *J. Biomol. NMR* **31**, 343–349 (2005)
44. Meola, A., Deville, C., Jeffers, S.A., Guardado-Calvo, P., Vasiliouskaite, I., Sizun, C., Girard-Blanc, C., Malosse, C., van Heijenoort, C., Chamot-Rooke, J., Krey, T., Guittet, E., Pêtres, S., Rey, F.A., Bontems, F.: Robust and low cost uniform <sup>15</sup>N-labeling of proteins expressed in *Drosophila* S2 cells and *Spodoptera frugiperda* Sf9 cells for NMR applications. *J. Struct. Biol.* **188**, 71–78 (2014)
45. Ohki, S., Dohi, K., Tamai, A., Takeuchi, M., Mori, M.: Stable-isotope labeling using an inducible viral infection system in suspension-cultured plant cells. *J. Biomol. NMR* **42**, 271–277 (2008)
46. Werner, K., Richter, C., Klein-Seetharaman, J., Schwalbe, H.: Isotope labeling of mammalian GPCRs in HEK293 cells and characterization of the C-terminus of bovine rhodopsin by high resolution liquid NMR spectroscopy. *J. Biomol. NMR* **40**, 49–53 (2008)
47. Sastry, M., Xu, L., Georgiev, I.S., Bewley, C.A., Nabel, G.J., Kwong, P.D.: Mammalian production of an isotopically enriched outer domain of the HIV-1 gp120 glycoprotein for NMR spectroscopy. *J. Biomol. NMR* **50**, 197–207 (2011)
48. Egorova-Zachernyuk, T.A., Bosman, G.J.C.G.M., DeGrip, W.J.: Uniform stable-isotope labeling in mammalian cells: formulation of a cost-effective culture medium. *Appl. Microbiol. Biotechnol.* **89**, 397–406 (2011)
49. Takeda, M., Kainosho, M.: Cell-free protein production for NMR studies. *Methods Mol. Biol.* **831**, 71–84 (2012)
50. Schanda, P., Kupče, Ě., Brutscher, B.: SOFAST-HMQC experiments for recording two-dimensional heteronuclear correlation spectra of proteins within a few seconds. *J. Biomol. NMR* **33**, 199–211 (2005)

51. Pervushin, K., Riek, R., Wider, G., Wüthrich, K.: Attenuated T2 relaxation by mutual cancellation of dipole-dipole coupling and chemical shift anisotropy indicates an avenue to NMR structures of very large biological macromolecules in solution. *Proc. Natl. Acad. Sci.* **94**, 12366–12371 (1997)
52. Amero, C., Schanda, P., Durá, M.A., Ayala, I., Marion, D., Franzetti, B., Brutscher, B., Boisbouvier, J.: Fast two-dimensional NMR spectroscopy of high molecular weight protein assemblies. *J. Am. Chem. Soc.* **131**, 3448–3449 (2009)
53. Ruschak, A.M., Velyvis, A., Kay, L.E.: A simple strategy for  $^{13}\text{C}$ ,  $^1\text{H}$  labeling at the Ile- $\gamma$ 2 methyl position in highly deuterated proteins. *J. Biomol. NMR* **48**, 129–135 (2010)
54. Lepre, C.A.: Practical aspects of NMR-based fragment screening. *Methods Enzymol.* **493**, 219–239 (2011)
55. Harner, M.J., Frank, A.O., Fesik, S.W.: Fragment-based drug discovery using NMR spectroscopy. *J. Biomol. NMR* **56**, 65–75 (2013)
56. Scott, D.E., Ehebauer, M.T., Pukala, T., Marsh, M., Blundell, T.L., Venkitaraman, A.R., Abell, C., Hyvönen, M.: Using a fragment-based approach to target protein-protein interactions. *ChemBioChem* **14**, 332–342 (2013)
57. Wielaens, J., Headey, S.J., Rhodes, D.I., Mulder, R.J., Dolezal, O., Deadman, J.J., Newman, J., Chalmers, D.K., Parker, M.W., Peat, T.S., Scanlon, M.J.: Parallel screening of low molecular weight fragment libraries: do differences in methodology affect hit identification? *J. Biomol. Screen.* **18**, 147–159 (2012)
58. Mashalidis, E.H., Śledź, P., Lang, S., Abell, C.: A three-stage biophysical screening cascade for fragment-based drug discovery. *Nat. Protoc.* **8**, 2309–2324 (2013)

# Chapter 22

## Protein Structure and Dynamics Determination by Residual Anisotropic Spin Interactions

Shin-ichi Tate

**Abstract** Proteins in a weakly aligned state restore the anisotropic nuclear spin interactions for dipoles and chemical shifts, which vanish in the rapidly tumbling molecules in an isotropic solution. The partly restored anisotropic nuclear spin interactions, also referred to as ‘residual anisotropic spin interactions’, observed in a protein provide additional structural information to refine its spatial structure and further elucidate its structure dynamics in a wider time range than that from the nuclear spin relaxations. The use of residual anisotropic nuclear spin interactions demands preparation for weakly aligning a protein to an appropriate extent to compromise between the sensitivity and the strength of the residual anisotropy. Various types of aligning media are devised for gaining the residual anisotropy for the proteins with different physical properties. The combined use of the residual anisotropic interactions with the other techniques including small angle X-ray scattering (SAXS), the paramagnetic relaxation enhancement (PRE) and the pseudo-contact shifts (PCS) paved the ways to elucidate a large amplitude motion of a protein such as domain rearrangement, which has remained elusive by the conventional NMR techniques primarily relying on the short-range structural information including NOEs and scalar nuclear spin couplings. This chapter describes the residual anisotropy in solution NMR, ranging from the theoretical basics on the residual anisotropic nuclear spin interactions to their application to the analyses of protein structure and dynamics.

**Keywords** RDC · RCSA · TROSY · Structure refinement · Structure dynamics

---

S. Tate (✉)

Department of Mathematical and Life Sciences, School of Science,  
Hiroshima University, Hiroshima, Japan  
e-mail: tate@hiroshima-u.ac.jp

S. Tate

Research Center for the Mathematics on Chromatin Live Dynamics (RcMcD),  
Hiroshima University, Hiroshima, Japan

## 22.1 Why Do We Need Residual Anisotropic Nuclear Spin Interactions in Solution NMR?

At present, a huge number of high-resolution crystal structures of proteins are available and the number is still growing. Although many people anticipated that the extensive collection of protein structures will comprehend the structure–function relationships of proteins, it is not supposed to be the case. The crystal structures and the solution structures of proteins determined by NMR unveil only limited states of the structures among of which they can adopt. The accurate views of protein structure dynamics are essential to deepen our understanding how proteins work. The functionally relevant protein dynamics may contain the motions in substantial amplitudes as associated with domain rearrangement (Fig. 22.1).

Crystal structures give us the details in protein–protein or protein–ligand interactions at atomic resolution. Machine learning on the interactions in the data base (PDB: Protein Data Bank) helps to improve the accuracy in the computer-based prediction for the molecular recognition by protein [1]. With the use of NMR chemical shift perturbations to identify the interacting surface in protein for its binding to target, we could model the complex structure of the protein with target, which relies on the experimental data but also supported by the supplemental structural information from the informatics [2]. Those approaches relying on the data base assume protein structure basically keeps the form in the crystal. The naïve assumption is not always valid for protein in binding to target: There are many examples demonstrating that proteins change the structures from those in crystals upon binding to target [3]. The structural change in protein is obvious in the cases for proteins comprising domains tethered by flexible linkers or intrinsically

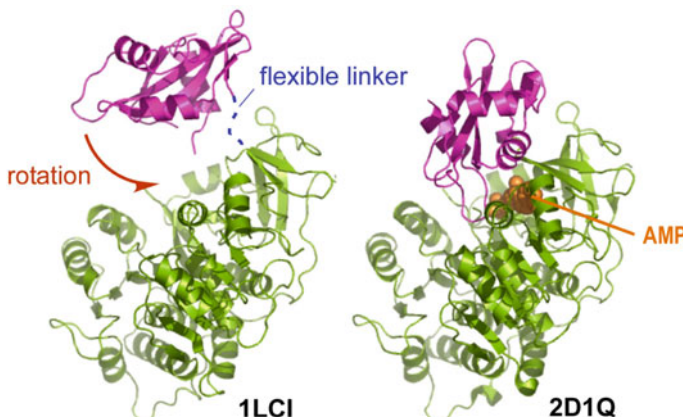


**Fig. 22.1** Protein domain rearrangement observed for Luciferase upon binding to ATP. PDB codes 1LCI and 2D1Q for apo- and AMP-bound forms, respectively. The relative domain orientation between the large and small domains is significantly changed by the ATP binding to luciferase

disordered regions (IDRs) [4]. The domain rearrangement of such multi-domain protein upon binding to target is functionally relevant [5, 6].

The structural change of protein associating with a large amplitude motion as found in domain rearrangement has been hard to analyze by conventional NMR approaches using the short-range structural parameters derived from NOEs and scalar couplings [7, 8]. Almost two decades ago, solution NMR introduced the anisotropic nuclear spin interactions to overcome the above limitations in analyzing the protein structure dynamics [9, 10]. Spatial anisotropy is an intrinsic physical property in the nuclear dipolar–dipolar interactions and in the magnetic shielding to nuclear spins observed as chemical shift anisotropy. The anisotropic nuclear spin interactions, however, are not observed for the proteins in an isotropic solution. In contrast, protein dissolved in an anisotropic medium as in the solution containing magnetically aligning liquid crystals can restore the anisotropic nuclear spin interactions [11]. The anisotropic nuclear spin interaction gives tensorial values that describe the orientation angles and the magnitudes of protein in reference to the external magnetic field [11]. The tensorial values can be used to determine the relative domain orientation in a multi-domain protein [12]. The introduction of the anisotropic nuclear spin interactions, therefore, made the analyses on the protein structural changes with large amplitudes feasible in solution NMR, which have never been accessed by the conventional NMR techniques. The anisotropic nuclear spin interactions observed for the proteins in anisotropic media are hereafter referred to as the ‘*residual*’ anisotropies, because a fraction of the anisotropies remain uncanceled in the observables.

The residual anisotropies can determine the relative domain orientations, while they cannot give the distances among them. The combinatorial use of the other methods, therefore, has to be applied to comprehend the domain dynamics of a protein, which requires the relative orientation of the domains and also their distances. For the purposes, we may combinatorically use electron spin resonance (ESR), fluorescence resonance energy transfer (FRET), and X-ray small angle scattering (SAXS) with the paramagnetic relaxation enhancements (PRE) and pseudo-contact shifts (PCS) in NMR, besides the residual anisotropies. In combining the other structural analyses described above, the residual anisotropies have significantly expanded the scope of NMR applications to grasp the protein structure dynamics more precisely on a wider range of time scales [13].

In this chapter, I will start from the brief description on the basic theories for the residual anisotropies and go to their application to structural analysis with stresses on the analyses of the protein motions with large amplitudes. In addition, I will also mention to our devised TROSY application to determine the molecular morphology of protein, which further could have moved forward the molecular size limitations in the application of the residual anisotropies [14, 15].

## 22.2 Theoretical Backgrounds of the Residual Anisotropies

Conventional NMR structure analysis relies on the short-range spin interactions does not give any global structural information required in determining protein morphology. The residual anisotropies, which become apparent for a ‘weakly’ aligning protein, give orientation angles of protein relative to the magnetic field, with which protein morphology can be determined.

Two different types of residual anisotropies are observable for the amide  $^1\text{H}$ - $^{15}\text{N}$  spin pair on a peptide plane in protein; one is the nuclear spin dipolar-dipolar interaction and the other is anisotropic shielding against the external magnetic field, which is called as chemical shift anisotropy (CSA) (Fig. 22.2).

These anisotropies are not observed on an NMR spectrum for protein in an isotropic solution, because each peptide plane in a rapidly tumbling protein experiences all the orientations to the magnetic field to average out the anisotropies. In contrast, a protein dissolved in an aligning medium becomes populated in a specific orientation thus partially retains the anisotropies [15].

In the presence of the magnetically aligned bicelle, protein stays in a confined cavity where protein still tumbles but frequently bumps to bicellar wall to make some of the protein orientations hindered, which leads to the incomplete cancelation of the anisotropies [16, 17]. This incomplete cancelation of the anisotropies of protein in an aligning bicellar solution gives the ‘residual’ anisotropies.

In a properly prepared aligning liquid crystalline solution, there is enough space for protein tumbling, and accordingly, protein under the condition still give high-resolution NMR signals. In a higher liquid crystalline concentration, the protein tumbling becomes severely limited to make NMR signals broadened to reduce the spectral resolution and sensitivity. In the experiments for observing the

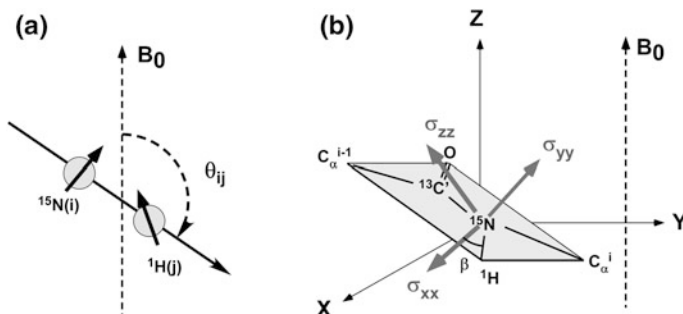


**Fig. 22.2** Two anisotropic nuclear spin interactions observed for the peptide bond. **a** Dipolar interaction between  $^1\text{H}$  and  $^{15}\text{N}$  nuclei in the amide bond. The strength of the anisotropy in the dipolar interaction depends on the orientation of the NH bond against the magnetic field,  $B_0$ . **b** Chemical shift anisotropy (CSA) for  $^{15}\text{N}$  nuclear spin in the peptide bond. The shielding anisotropy for  $^{15}\text{N}$  spin against the external magnetic field,  $B_0$ , is described by a tensorial value

residual anisotropies, we carefully adjust the aligning conditions to restore the significant anisotropies but to keep narrow spectral lines on an NMR spectrum, which condition is thus called as a ‘weak’ alignment [11].

Dipolar couplings have been a mainstay in solid-state NMR, which gave through-space interactions that arise between any two magnetically active nuclei. The weakly aligning condition has enabled to introduce the use of the dipolar couplings to solution NMR, which is referred to as residual dipolar couplings (RDCs). The commonly used through-space nuclear dipolar interactions in solution NMR are NOEs detected between protons within 5 Å [18]. NOEs give distance information between protons; however, they do not give any orientation angles between the proton pairs. In contrast, the magnitude of the dipolar coupling depends on the angle between the NH bond vector and the magnetic field,  $B_0$ , and the ensemble of the dipolar couplings for all the NH bonds in a protein determine the orientation of the molecular frame to the magnetic field (Fig. 22.2a).

Similar to the RDCs, the protein in a weakly aligning condition gives residual CSAs (RCSAs) that are observed as the chemical shift changes from the corresponding isotopic chemical shifts [19]. The CSA is another main observable in solid-state NMR, although it is not observed for protein in Brownian motion. In considering amide nitrogen ( $^{15}\text{N}$ ) and carbonyl carbon ( $^{13}\text{C}'$ ) in a peptide plane (Fig. 22.2b), their chemical shifts substantially change according to the orientation of the peptide plane against the magnetic field,  $B_0$ . In the case for amide  $^{15}\text{N}$  nucleus, if the peptide plan is in an orientation with  $\sigma_{zz}$  axis parallel to the magnetic field,  $B_0$ , the  $^{15}\text{N}$  nucleus shows high-field shift along  $^{15}\text{N}$  chemical shift axis (Fig. 22.2b). If the peptide plane stays to keep  $\sigma_{xx}$  axis parallel to the magnetic field, the  $^{15}\text{N}$  nucleus shows low-field shift (Fig. 22.2b). Each peptide plane orientation is defined in a molecular coordinate frame. A set of the RCSAs in a protein can determine the orientation of the molecular coordinate frame of a protein.

The combinatorial effects of the RCS and RCSA become apparent in a  $^1\text{H}-^{15}\text{N}$  TROSY correlation spectrum for the protein in a weakly aligning state [14, 20, 21]. The residual anisotropy appearing in a TROSY spectrum,  $\Delta\delta_{\text{TROSY}}$ , contains the RDC from a  $^1\text{H}-^{15}\text{N}$  spin pair and the RCSA from  $^{15}\text{N}$  nucleus in a peptide plain (Fig. 22.2b), which poses stronger structural information for determining the peptide plane orientation to the external magnetic field,  $B_0$ , over the sole RDC and RCSA. In addition to the richer structural information in  $\Delta\delta_{\text{TROSY}}$ , there is an advantage for this combinatorial residual anisotropy to be observed for even larger proteins over 100 kDa to which only TROSY can be applied in collecting the  $^1\text{H}-^{15}\text{N}$  correlation spectra [21].

### 22.2.1 Residual Dipolar Coupling, RDC

Residual dipolar coupling (RDC) gives the direction of the internuclear vector connecting a pair of nuclei against the external magnetic field,  $B_0$ . In the peptide bond of a protein isotopically enriched with  $^{15}\text{N}$ , the RDC observed for amide  $^{15}\text{N}$

nucleus defines the angle between the NH bond vector and a magnetic field (Fig. 22.2a).

The RDCs for amide  $^1\text{H}$ - $^{15}\text{N}$  spin pairs are of common choice in protein structure analysis, primarily due to the good spectral dispersion of the  $^1\text{H}$ - $^{15}\text{N}$  correlation spectrum. The RDCs are measured from a  $^1\text{H}$ - $^{15}\text{N}$  spectra collected without  $^1\text{H}$  decoupling during  $^{15}\text{N}$  nuclear spin evolution time,  $t_1$  (Fig. 22.3). In practice, the IP-AP HSQC is used to avoid unwanted signal overlaps that diminishes the accuracy in reading signal positions [22].

On a  $^1\text{H}$ -couple  $^1\text{H}$ - $^{15}\text{N}$  HSQC spectrum, each amide bond gives a pair of signals split along  $^{15}\text{N}$  dimension (Fig. 22.3). The split for a protein in an isotropic condition represents a single bond scalar coupling between  $^1\text{H}$  and  $^{15}\text{N}$  nuclei,  $^1J_{\text{NH}}$ , which is typically 93 Hz (Fig. 22.3a). The corresponding splits observed for a protein in a weakly aligning state vary residue by residue (Fig. 22.3b). The changes in  $^1J_{\text{NH}}$  values come from the overlaid contribution of the RDCs that become apparent in a weakly aligned state. As described above, the RDC varies according to the NH bond vector orientation to the magnetic field, and the observed change in  $^1J_{\text{NH}}$  value is different in each residue. The RDC is defined as  $^1J_{\text{NH}}$  (aligned state) —  $^1J_{\text{NH}}$  (isotropic state).

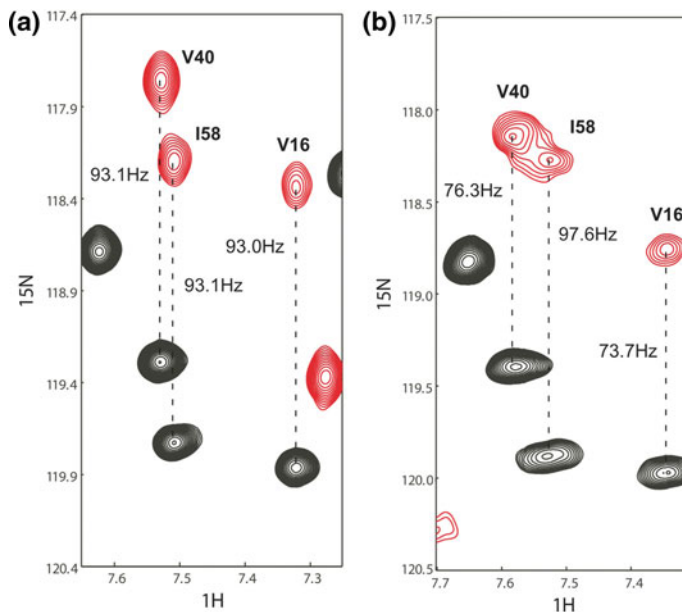


**Fig. 22.3** RDC measurement with  $^1\text{H}$ -coupled HSQC. Isotropic sample (a) and aligned sample (b). Split with for each paired signal corresponds to  $^1J_{\text{NH}}$ . The apparent  $^1J_{\text{NH}}$  is changed for aligned sample. The difference in  $^1J_{\text{NH}}$  defined as  $^1J_{\text{NH}}$  (align) —  $^1J_{\text{NH}}$  (isotropic) gives RDC

### 22.2.2 Theoretical Description on RDC

We focus only the amide  $^1\text{H}$ - $^{15}\text{N}$  spin pair in the following theoretical description of the RDC. In the following formulation, the indices  $i$  and  $j$  are used for  $^1\text{H}$  and  $^{15}\text{N}$  nuclei, respectively. The dipolar Hamiltonian to describe the dipolar coupling is written as below:

$$H_{ij}^D(t) = -\left(\frac{\mu_0}{4\pi}\right)\frac{\gamma_i\gamma_j h}{2\pi^2 r_{ij}^3} I_{iz} I_{jz} P_2(\cos \Theta(t)) \quad (22.1)$$

where  $\mu_0$  is the permeability in a vacuum,  $h$  is Planck's constant,  $r_{ij}$  is the distance between  $^1\text{H}$  and  $^{15}\text{N}$  atoms,  $\gamma_i$  and  $\gamma_j$  are the gyromagnetic ratios for  $^1\text{H}$  and  $^{15}\text{N}$  nuclear spin, respectively.  $I_{iz}$  and  $I_{jz}$  are the spin angular momentum operators for  $^1\text{H}$  and  $^{15}\text{N}$  nuclear spins, respectively. The angular part of the dipolar Hamiltonian is described by the second rank Legendre function,  $P_2(\cos \Theta(t))$ , where  $\Theta(t)$  is a time-dependent angle between the magnetic field,  $B_0$ , and the internuclear vector in the NH bond (Fig. 22.4a). In determining molecular orientation by the RDC, bond libration effect is negligible due to its faster motion over the protein tumbling that occurs on the nsec timescale. In considering the fast bond libration that happens in the psec time range, the time-averaged effective inter nuclear distance is used for  $^1\text{H}$ - $^{15}\text{N}$  bond length,  $r_{ij}$ ; which distance was estimated by NMR to be 1.04 Å, slightly longer than the static bond length 1.02 Å [23].

The experimentally measured RDCs,  $D_{ij}^{\text{res}}$ , is represented as the time-averaged value for the dipolar Hamiltonian, Eq. (22.1).

$$D_{ij}^{\text{res}}(t) = -\left(\frac{\mu_0}{4\pi}\right)\frac{\gamma_i\gamma_j h}{2\pi^2 r_{ij}^3} \langle P_2(\cos \Theta(t)) \rangle \quad (22.2)$$

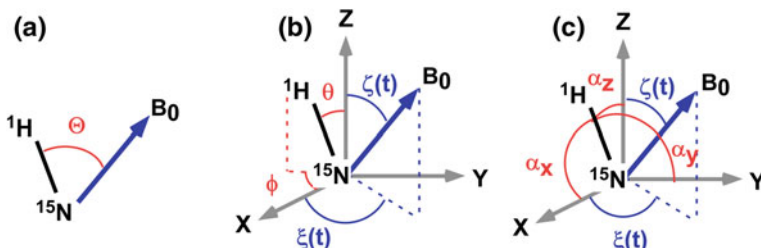


**Fig. 22.4** Three different representations for NH bond vector against a magnetic field. **a** Angle dependency of the  $^1\text{H}$ - $^{15}\text{N}$  RDC is described by  $\Theta$ , the angle between the NH bond vector and a magnetic field. **b** NH bond vector on a molecular coordinate system, whose direction is defined by polar angles  $(\theta, \phi)$ . Molecular reorientation relative to a magnetic field is described by the time-dependent polar angles  $(\xi(t), \zeta(t))$ . **c** NH bond vector is recast by direction cosines to three molecular axes

The angle bracket denotes the time-averaged value. When a protein rapidly tumbles in an isotropic solution, no residual anisotropy remains, thus leading to  $\langle P_2(\cos \Theta(t)) \rangle = 0$ . In an anisotropic condition, the molecular tumbling incompletely vanishes the time-averaged term, giving  $\langle P_2(\cos \Theta(t)) \rangle \neq 0$ . The magnitude of the RDC depends on the orientation of the NH bond vector against the magnetic field (Fig. 22.4a), and the order of the aligning magnitude of the protein in a liquid crystalline medium, which are described by the term  $\langle P_2(\cos \Theta(t)) \rangle$  in Eq. (22.2).

In using the RDCs as structural parameters, we have to define the orientation of each NH bond vector in the molecular coordinate frame, a Cartesian coordinate system in which all atomic positions in a protein are described.

The orientation of a NH bond vector in a protein is described by polar angles ( $\theta, \phi$ ) in the molecular coordinate system (Fig. 22.4b). The orientation of the magnetic field in the molecular coordinate system is described by the time-dependent polar angles, ( $\zeta(t), \xi(t)$ ) (Fig. 22.4b): The time-dependent polar angles describe the directional change of the magnetic field sensed by the tumbling protein.

The Legendre function  $P_2(\cos \Theta(t))$  is expanded by the spherical harmonics according to the spherical harmonic addition theorem [24]:

$$P_2(\cos \theta(t)) = \frac{4\pi}{5} \sum_{q=-2}^2 Y_{2q}^*(\theta, \varphi) Y_{2q}(\zeta(t), \xi(t)) \quad (22.3)$$

where the  $Y_{2q}$ 's are the normalized spherical harmonics. Using the relations in Eq. (22.3), the RDC ( $D_{ij}^{\text{res}}$  in Eq. (22.2) is expressed with the spherical harmonics:

$$D_{ij}^{\text{res}} = -\left(\frac{\mu_0}{4\pi}\right) \frac{\gamma_i \gamma_j h}{2\pi^2 r_{ij}^3} \frac{4\pi}{5} \sum_{q=-2}^2 Y_{2q}^*(\theta, \varphi) \langle Y_{2q}(\zeta(t), \xi(t)) \rangle \quad (22.4)$$

In Eq. (22.4), the five time-averaged spherical harmonics  $\langle Y_{2q}(\zeta(t), \xi(t)) \rangle$  with  $q = -2, -1, 0, 1, 2$  defines the orientation angles and its magnitudes for protein. Recasting these five terms makes more intuitively acceptable representation to describe the aligning state of protein, which is Saupe's order matrix. [25, 26]. The use of Saupe's order matrix reforms Eq. (22.4) as below:

$$D_{ij}^{\text{res}} = -\left(\frac{\mu_0}{4\pi}\right) \frac{\gamma_i \gamma_j h}{2\pi^2 r_{ij}^3} \frac{4\pi}{5} \sum_{k,l=x,y,z} S_{kl} \cos(\alpha_k) \cos(\alpha_l) \quad (22.5)$$

where  $S_{kl}$  is an element in Saupe's order matrix. The Saupe order matrix is a traceless, symmetric  $3 \times 3$  matrix: It comprises of five independent elements as described below. With Saupe's order matrix, each bond vector orientation is defined by direction cosines against the molecular coordinate axes with angles,  $\alpha_x, \alpha_y$ , and  $\alpha_z$  (Fig. 22.4c). Five elements in the Saupe order matrix are described by the time-averaged spherical harmonics  $\langle Y_{2q}(\zeta(t), \xi(t)) \rangle$  as described below:

$$\begin{aligned}
S_{xz} &= \sqrt{\frac{3}{8}} \sqrt{\frac{4\pi}{5}} (\langle Y_{21}(\xi(t), \zeta(t)) \rangle - \langle Y_{2-1}(\xi(t), \zeta(t)) \rangle) \\
S_{yz} &= i \sqrt{\frac{3}{8}} \sqrt{\frac{4\pi}{5}} (\langle Y_{21}(\xi(t), \zeta(t)) \rangle + \langle Y_{2-1}(\xi(t), \zeta(t)) \rangle) \\
S_{xy} &= i \sqrt{\frac{3}{8}} \sqrt{\frac{4\pi}{5}} (\langle Y_{22}(\xi(t), \zeta(t)) \rangle - \langle Y_{2-2}(\xi(t), \zeta(t)) \rangle) \\
S_{xx} - S_{yy} &= \sqrt{\frac{3}{2}} \sqrt{\frac{4\pi}{5}} (\langle Y_{22}(\xi(t), \zeta(t)) \rangle + \langle Y_{2-2}(\xi(t), \zeta(t)) \rangle) \\
S_{zz} &= \sqrt{\frac{4\pi}{5}} \langle Y_{20}(\xi(t), \zeta(t)) \rangle
\end{aligned} \tag{22.6}$$

The Saupe order matrix describes the orientation angles and the orders of the aligning magnitude of protein against the magnetic field,  $B_0$ . Diagonalization of the Saupe order matrix gives the alignment tensor. The alignment tensor consists of the principal values that represent the orders of the aligning magnitudes along principal axes and the angles of the tensorial axes defined in the molecular coordinate system, which angles define the orientation of protein to the magnetic field.

Z-axis of the alignment tensor is defined as the most ordered axis, and the others are defined according to the absolute magnitudes of the principal values,  $|S_{zz}| \geq |S_{yy}| \geq |S_{xx}|$ . An asymmetry,  $\eta = (S_{xx} - S_{yy})/S_{zz}$ , represents the deviation from the axially symmetric ordering. The orientation of the alignment tensor axes (the principal axes of the alignment tensor) is represented in the molecular coordinate system by the Euler angles.

In the alignment tensor axes system (alignment tensor frame), the RDC,  $D_{ij}^{\text{res}}$ , is rerepresented in a more simplified and intuitively acceptable form, in which two new parameters,  $A_a$  and  $A_r$ , are introduced.  $A_a$  and  $A_r$  are made of the nonzero average spherical harmonics:

$$\begin{aligned}
\langle Y_{20}(\xi(t), \zeta(t)) \rangle &= \sqrt{\frac{5}{4\pi}} S_{zz} = \sqrt{\frac{5}{4\pi}} A_a \\
\langle Y_{2\pm 2}(\xi(t), \zeta(t)) \rangle &= \sqrt{\frac{5}{24\pi}} (S_{xx} - S_{yy}) = \sqrt{\frac{15}{32\pi}} A_r
\end{aligned} \tag{22.7}$$

Using the parameters defined in Eq. (22.7),  $D_{ij}^{\text{res}}$  is transformed to the formulation that is readily applied to the structure analysis with the RDCs:

$$D_{ij}^{\text{res}} = - \left( \frac{\mu_0}{4\pi} \right) \frac{\gamma_i \gamma_j h}{2\pi^2 r_{ij}^3} \left[ A_a (3 \cos^2 \theta' - 1) + \frac{2}{3} A_r \sin^2 \theta' \cos 2\phi' \right] \tag{22.8}$$

where the polar angles ( $\theta', \phi'$ ) define the orientation of NH bond vector in the alignment tensor frame.  $A_a$  and  $A_r$  are the axial and rhombic components of the

ordering magnitudes, respectively. The orientation of alignment tensor is described in the molecular coordinate frame with the Euler angles ( $\alpha$ ,  $\beta$ ,  $\gamma$ ).

### 22.2.3 Residual Chemical Shift Anisotropy, RCSA

The other anisotropy associated with the amide  $^{15}\text{N}$  nucleus comes from the anisotropic nuclear shielding, or chemical shift anisotropy, CSA (Fig. 22.2b). CSA is not observed for a protein in isotropic solution; the peptide plane in a protein rapidly tumbling in an isotropic solution experiences entire direction relative to the magnetic field averages over the CSA to give an isotropic chemical shift,  $\delta_{\text{iso}}$ . In solid state where each molecule stays in a fixed direction to the magnetic field, we observe the three different components of the anisotropic chemical shifts for  $^{15}\text{N}$  nucleus in a peptide plane,  $\delta_{xx}$ ,  $\delta_{yy}$ , and  $\delta_{zz}$ , which reprints the directional dependent difference in the magnetic shielding (Fig. 22.2b) [27]. In a weakly aligned protein, the CSA is partially restored due to the incomplete directional averaging of the anisotropy, which causes chemical shift change form  $\delta_{\text{iso}}$  along  $^{15}\text{N}$  axis. This is the residual CSA (RCSA) (Fig. 22.5) [19].

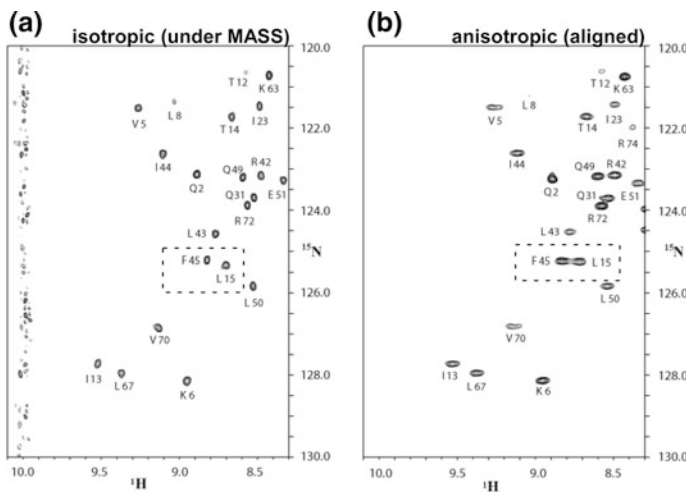


**Fig. 22.5**  $^{15}\text{N}$  chemical shift change induced by a weak alignment.  $^1\text{H}$ - $^{15}\text{N}$  HSQC spectra are compared for the sample of  $^{15}\text{N}$  labeled ubiquitin dissolved in 7.5% (w/v) DMPC/DHPC/CTAB ternary bicelle solution between isotropic and aligned states: **a** under the magic-angle sample spinning condition, giving an isotropic spectrum, **b** the aligned condition. Chemical shift changes along  $^{15}\text{N}$  axis caused by a weak alignment are clearly observed, for example the signals in dotted square. These spectral changes come from the incomplete cancellation of  $^{15}\text{N}$  chemical shift anisotropy (CSA) effect under a weak aligning condition. The change along  $^{15}\text{N}$  axis is the value for the residual CSA, RCSA.

The  $^{15}\text{N}$  RCSA is defined as  $\Delta\delta^{15}\text{N} = \delta^{15}\text{N}(\text{aligned}) - \delta^{15}\text{N}(\text{isotropic})$ . The magnitude of RCSA varies according to the peptide plane orientation to the magnetic field (Fig. 22.2b). In the peptide bond,  $^{13}\text{C}'$  also has also substantial CSA and the RCSA for  $^{13}\text{C}'$  can be used in the similar manner as in the  $^{15}\text{N}$  RCSA application [28].

The RCSA values,  $\Delta\delta^{15}\text{N}$ , relate the CSA tensor in each  $^{15}\text{N}$  nucleus to the molecular coordinate frame with Saupe's order matrix elements  $S_{ij}$ :

$$\Delta\delta^{15}\text{N} = \frac{2}{3} \sum_{i=x,y,z} \sum_{j=x,y,z} \sum_{k=x,y,z} S_{ij} \cos(\theta_{ik}) \cos(\theta_{jk}) \delta_{kk} \quad (22.9)$$

Here,  $\cos\theta_{ij}$ , denotes the direction cosine between  $i$ -axis in the molecular coordinate system and  $j$ -axis in the CSA tensor principal axis. The principal value for the CSA tensor axis  $k$  is denoted by  $\delta_{kk}$  ( $kk = xx$ ,  $yy$ , and  $zz$ ), the magnetic shielding magnitude along each principal axis (Fig. 22.2).

The alignment tensor is obtained through diagonalizing Saupe's order matrix, whose matrix elements are determined with a set of  $\Delta\delta^{15}\text{N}$  data using Eq. (22.9). In determining Saupe's order matrix, the pre-defined CSA tenor parameters including  $\beta$  angle to define the CSA tensor position in a peptide plane and two principal values  $\delta_{zz}$  and  $\delta_{xx}$  with assuming the isotropic shift  $\delta_{\text{iso}} = (\delta_{xx} + \delta_{yy} + \delta_{zz})/3 = 0.0$ : The  $\sigma_{yy}$  axis is normal to the peptide plane with the angle  $\beta = 19.6^\circ \pm 2.5^\circ$  (Fig. 22.2b) [29]. In determining the alignment tensor with the RDCs, the only pre-defined parameter is the libration average bond length, e.g.,  $\langle r_{\text{NH}} \rangle = 1.04 \text{ \AA}$ . In the case with the RCSA, the tensor determination is more pre-knowledge demanding.

The  $^{15}\text{N}$  CSA tensor value depends on the local backbone torsion angles [29]. The  $^{15}\text{N}$  CSA tensor values in protein have been reported by various methods including solid-state and solution NMR [19, 27, 29–32]. These data gave consensus  $^{15}\text{N}$  CSA tensor parameters for the residues in each type of the secondary structures such as  $\beta$ -helix and  $\beta$ -sheet. In determining the alignment tensor with the RCSAs, the secondary structure-specific  $^{15}\text{N}$  CSA tensor parameters will be used as pre-defined parameters. The use of the secondary structure-specific  $^{15}\text{N}$  CSA tensors gives the alignment tensors that can reproduce the experimentally observed  $\Delta\delta^{15}\text{N}$  values within the experimental errors.

At the end of this section, I briefly describe how the  $^{15}\text{N}$  CSA tensor parameters are determined by solution NMR, in which the weak alignment is essentially used.

We reported the  $^{15}\text{N}$  CSA tensor determined for the protein in a weakly aligning state in solution including a magnetically aligned bicelle [19]. In our approach, we applied magic-angle sample spinning (MASS) to collect the RCSA data,  $\Delta\delta^{15}\text{Ns}$ . The MASS to the magnetically aligned bicelles eliminates its magnetically induced ordering, and thus the protein in the bicellar solution completely averages out the anisotropies, while the protein stays in a weakly aligning state unless the MASS is applied [19]. As seen in Eqs. (22.5) and (22.9), the RDCs and RCSAs are represented by Saupe's order matrix. In the same sample, Saupe's order matrix elements,  $S_{ij}$ , are shared in the formula for RDC and RCSA as Eqs. (22.5) and (22.9),

respectively. Once the Saupe order matrix is determined by the RDCs using the relation in Eq. (22.5), which is directly used also in Eq. (22.9).

We can observe the RCSA,  $\Delta\delta^{15}\text{N}$ , values from the  $^{15}\text{N}$  chemical shift changes between the signals for the protein in a weakly aligned state and the same sample under the MASS (Fig. 22.5). The use of MASS is essential to measure the RCSA. Chemical shifts are quite sensitive to the chemical environment around the protein, which includes coexisting solute. In accurately measuring the RCSA, we need to keep the sample condition the same to remove the causes that change chemical shifts other than that from the alignment. The use of MASS to the weakly aligned sample fulfills this requirement in measuring the RCSA; the MASS eliminates the residual anisotropies with keeping the chemical environment the same.

With the RCSAs,  $\Delta\delta^{15}\text{Ns}$ , collected with the MASS and the Saupe order matrix determined by the RDCs, we can determine the  $^{15}\text{N}$  CSA tensors with the relation in Eq. (22.9). The  $^{15}\text{N}$  CSA tensor consists of five independent matrix elements, which therefore requires at least five  $\Delta\delta^{15}\text{Ns}$  to get the tensor determined. In using the single aligned sample, we only determine the averaged  $^{15}\text{N}$  CSA tensor over the residues at least five in the sample. Because of this requirement, the residues in the same type of secondary structure are used to give the secondary structure-specific  $^{15}\text{N}$  CSA tensor [19].

The residue-specific  $^{15}\text{N}$  CSA tensor can be determined, once we could collect the RCSAs and RDCs for the same sample at least five different aligning states, meaning protein has different orientation angles to the magnetic field. Those samples are not readily accomplished by merely changing the aligning media. The amino acid changes to loops in a protein, however, are demonstrated to significantly change the aligning states in the same bicelle medium. With the structurally innocent mutants, Bax and co-worker determined the residue-specific  $^{15}\text{N}$  CSA tensors in the protein GB3 based on the RDCs ad RCSAs for the protein in six different aligning states [29]. The RCSAs,  $\Delta^{15}\text{N}\delta$  values, for the protein in each aligning state were collected with the MASS. The Saupe order matrices determined from the RDCs were subjected to determine the residue-specific  $^{15}\text{N}$  CSA tensor with six different sets of the RCSAs using Eq. (22.9). The results have shown that the  $^{15}\text{N}$  CSA tensor shows only a moderate degree of variation from the average value, but it has larger magnitudes for the residue in  $\alpha$ -helix ( $\Delta\sigma = -173 \pm 7$  ppm) than  $\beta$ -sheet ( $\Delta\sigma = -162 \pm 6$  ppm) residues [29];  $\Delta\sigma$  is defined as  $(\sigma_{yy} - \sigma_{xx})/\sigma_{zz}$  [33]. The results ensure that the use of secondary structure-specific  $^{15}\text{N}$  CSA tensor is practically acceptable in the structure analysis using the RCSA.

## 22.3 Practical Procedures to Use the Residual Anisotropies

Measuring the residual anisotropies requires to achieve weak alignment of protein in solution to an appropriate extent to restores significant level of the anisotropies with keeping the spectral resolution high enough. The order of the alignment required for measuring residual anisotropies is approximately  $10^{-3}$ , giving around 20 Hz in maximum absolute magnitude for amide  $^1\text{H}$ - $^{15}\text{N}$  RDC. To prepare a weak alignment, we usually use liquid crystalline medium to assist protein to align to the magnetic field, because most of the proteins have too limited inherent magnetic susceptibility to make them spontaneously align even under the strong NMR magnetic field. Some of the proteins like heme-containing proteins tend to align without the aid of the magnetically aligning co-solute, due to its substantial magnetic susceptibility coming from a heme group [34]. The double-stranded DNAs also show spontaneous alignment in NMR magnet [35]. In this section, I will describe typical preparations for weakly aligning samples to measure the residual anisotropies.

### 22.3.1 Magnetically Aligning Liquid Crystalline Media

Magnetically ordering liquid crystalline media are commonly used in collecting the residual anisotropies. Discoidal phospholipid assembly, bicelle, is one of the prevailingly used materials for weakly aligning protein [36]. The discoidal bicelle is

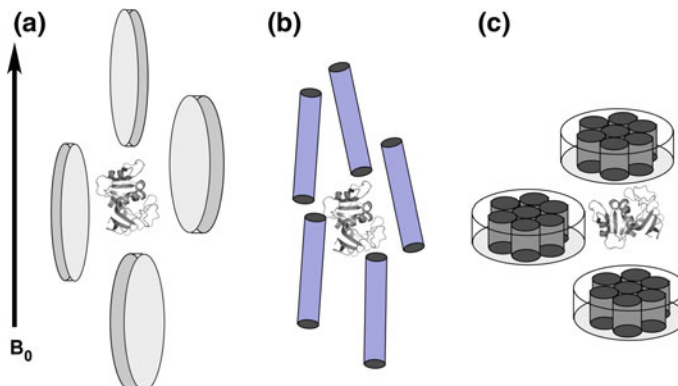


**Fig. 22.6** Weak alignment made by using various media. **a** Discoidal shape phospholipid bicelle medium, **b** rod-like filamentous phage and **c** purple membrane. Because of significant anisotropic magnetic susceptibility, the molecules spontaneously align in a magnetic field. Proteins in the aligning media are aligned through the collisional interaction or electrostatic interactions with the aligning molecules

composed of a mixture of dimyristoylphosphatidylcholine (DMPC) and dihexanoyl phosphatidylcholine (DHPC) in a ratio of 3:1. The phospholipid binary mixture forms lipid bilayer disks with 30–40 nm in diameter. Bicelle has substantial anisotropy in magnetic susceptibility that allows it for spontaneously align under NMR magnetic field: The normal of the discoidal bicellar surface orients perpendicular to the magnetic field (Fig. 22.6a).

In measuring the residual anisotropies, an appropriate amount of bicelle is put into protein solution to establish an ideal degree of aligning state; the higher concentration goes to higher alignment [17]. In NMR magnet, the bicelles transit into liquid crystalline phase, in which the discoidal molecules are ordered to arrange their bicellar normal perpendicular to the magnetic field. Bicelle has a discoidal shape with flat surface (Fig. 22.6a). In the liquid crystalline phase of the bicelles, proteins are entrapped in the cavities inside the bicellar liquid crystalline. Proteins in cavities bump to the bicellar walls and experience sterical limits for their tumbling. Under such conditions, proteins imperfectly average the anisotropic interactions to make the residual anisotropies observable [16, 37].

The aligning magnitude is tuned by the bicelle concentration; higher bicellar concentration will produce dense liquid crystalline phase, thus higher aligning magnitude. On the other hand, bicelle requires the minimal concentration to maintain the liquid crystalline phase; in lower bicellar concentration under the critical limit, bicellar solution becomes phase separated to be in a micelle state.

The bicelle made of DMPC/DHPC binary phospholipid has neutral charge on its surface, and it induces the residual anisotropy through the bumping of proteins to the bicellar walls. In using the charged bicelle made by doping charged molecule to the binary bicelle, the aligning property of proteins changes due to the additional electrostatic interactions between the charged bicellar wall and protein surface charge. Addition of SDS, sodium dodecyl sulfate, into binary phospholipid makes the bicelle negatively charged, while the doping CTAB, cetyl trimethyl ammonium bromide, makes it positively charged. This change in the aligning property allows for making various aligning states of protein to give more accurate orientational information.

The use of bicelle as aligning media has practical limitations in its application to protein research. One is the temperature required for keeping the bicelle in a liquid crystalline state is in a rather narrow range and limited in higher range, 27–45 °C. Some proteins may precipitate in such higher temperatures. Bicelle becomes unstable in the acidic or alkali conditions. It is only stable under the neutral condition. This also limits the solution conditions applied to prepare for protein samples. Additionally, stability of the liquid crystalline state of bicelle is sensitive to the salt conditions. We may have to care about the solution conditions to achieve the appropriate aligning condition. In some of the cases, the bicellar media cannot be used for the residual anisotropy measurement. This is why a variety of aligning media have been reported to overcome the limitations in the residual anisotropy experiments.

### 22.3.2 *Naturally Occurring Materials that Spontaneously Align in a Magnetic Field*

Spontaneously aligning molecules are also used as aligning media for observing the residual anisotropy. Rod-like filamentous phage and purple membrane constitute the representative examples for the application of the residual anisotropy.

Filamentous phage, which is made of a rod-like coat protein, is a well-known example of the naturally occurring molecule used for weak alignment [38]. Because of the highly anisotropic shape of the filamentous phage, it spontaneously aligns in a high magnetic field, with keeping its rod axis parallel to a magnetic field (Fig. 22.6b). Filamentous phage has negatively charged surface, and thus it induces protein alignment through electrostatic interactions with protein; the mechanism is different from that by the binary phospholipid bicellar medium. The order of alignment can be tuned by the concentration of the phage suspension in protein solution.

Purple membrane has two-dimensional crystal lattice structure of bacteriorhodopsin (bR) that is rich in  $\alpha$ -helices (Fig. 22.6c). Purple membrane constitutes of ordered  $\alpha$ -helices, and thus it has intrinsic high anisotropic magnetic susceptibility, which makes purple membrane spontaneously align in a high magnetic field.

Suspension of purple membrane is added into protein solution to make the protein weakly aligned. The aligning magnitude is tuned by the concentration of purple membrane in solution [39]. Protein in the solution of purple membrane is aligned through the electrostatic interactions with the negative charges on the discoidal surface.

Purple membrane and filamentous phage cannot be applied to basic proteins that are positively charged on their surfaces. The basic proteins tightly adsorb onto the negatively charged surfaces of those aligning molecules through the electrostatic interactions, which will induce the extreme ordering of proteins and thus prohibit observing high-resolution NMR signals.

Recently, additional spontaneous aligning media are reported to alleviate the limits by the existing aligning media, which include collagen gels and DNA nanotubes [40–42].

### 22.3.3 *Compressed Acryl Amide Gel*

The other method uses anisotropically compressed acrylamide gel. Acrylamide hydrogel has cavities to capture proteins within, whose cavity size is tuned by changing the ratios of the composing chemicals, acrylamide and bis-acrylamide. Acrylamide forms a linear polymer chain and bis-acrylamide makes bridge to link acrylamide liner polymers. The increased content of bis-acrylamide generates smaller cavity [43].

The acrylamide gel has a spatially isotropic cavity. Protein soaked in the gel retains isotropic tumbling and shows no residual anisotropies on its NMR spectrum. Weak alignment of protein in the gel is induced by generating the spatially anisotropic cavities in the gel.

In measuring the residual anisotropy with acrylamide hydrogen, a cast gel containing a protein solution is deformed inside an NMR sample tube (Fig. 22.7). There are two ways to make anisotropically compressed gel: One is to press the gel along the NMR tube (compressed gel), and the other is squeeze it in the lateral dimension, and thus it becomes stretched vertically (stretched gel) (Fig. 22.7).

In vertical compression, gel is cast to have a shorter diameter than the inner diameter for NMR sample tube. After inserting the cast gel, it is vertically compressed with glass rod in the Shigemi NMR tube [44, 45] (Fig. 22.7a). On the other hand, stretched gel is made from the cast gel having a slightly larger diameter than that the inner diameter of the tube; the gel is inserted into the tube by using tapered devise [46] (Fig. 22.7b). Because of the different direction to compress, these two preparations induce different protein orientation to each other.

The charge doping in the anisotropically compressed gel is also possible [47]. Negative charge is doped by replacing a part of acrylamide with acrylate, while a positive charge is introduced by adding DADMAC, diallyldimethylammonium chloride, in casting gel chip. The charge doping in the hydrogel changes aligning property through the additional electrostatic interaction between protein and the gel becomes active.

Acrylamide gel is neutral in charge and thus it aligns protein through collisional interaction between protein and anisotropically distributing acryl amide granules that exclude protein invasion within the compressed gel. The non-charged acrylamide gel is readily used for any types of protein, independent on the surface

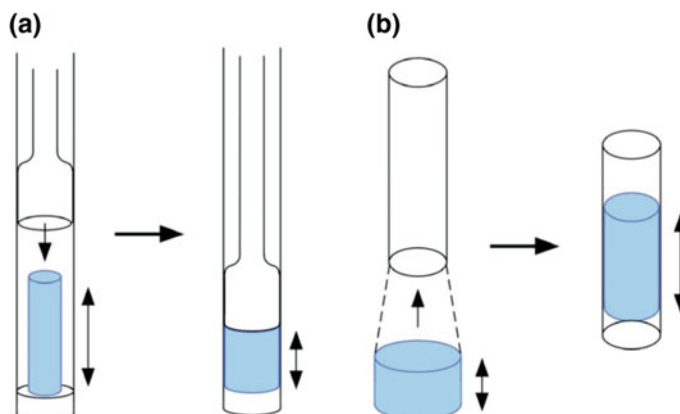


**Fig. 22.7** Anisotropically compressed gels to achieve weak alignment. **a** Vertically compressed gel. **b** Laterally compressed, thus, stretched gel. Cast gel chip (blue) is inserted into an NMR glass tube. In the vertical compression, the cast gel is pressed by a glass rod in NMR tube. These compressions induce spatially anisotropic cavities within the acrylamide gel

charge of protein. In working on the protein having significant surface charge, we carefully choose the doping to the hydro gel to avoid sticking protein to the gel by electrostatic interaction to keep the spectral resolution.

The aligning order of the magnitude is tuned by changing the concentration of acrylamide and/or the ratio of the composing chemicals and also the diameter of the cased gel chip. In addition, the extent of the charge doping may have to be considered in some cases. There are more parameters to adjust than those for the liquid crystalline media. We, therefore, need some trial experiments to gain the optimal gel condition to have the anisotropic spin interactions observable in enough spectral resolution. It is noted that the lateral compression using so-called Bax device can achieve rather uniform compression to give clear NMR signals for measuring the residual anisotropies [48], while the vertical compression is hard to get the uniformly compressed gel, which sometimes give seriously distorted NMR signals.

The great advantage for the use of the compressed gel is in the chemical stability of acrylamide gel. In using acrylamide gel for a weak alignment, we do not need to worry about the sample conditions including temperature, salt concentration, and solution pH. Under any sample conditions, we can align protein by the compressed gel. It is a keen difference from the limitation posed by using the other aligning materials including liquid crystalline media and the naturally occurring materials. The compressed gel can be applied as a universal media for weakly aligning protein. In particular, for the membrane proteins dissolved in detergents, the lipid bicelle is out of choice, and the spontaneous aligning molecules are also limited in use. In such cases, the use of acrylamide gel is the preferential choice of the aligning media to use the residual anisotropies [49].

### 22.3.4 Protein Structures in Weakly Aligned Media

Preparing for a weakly aligning protein is a prerequisite for the analysis of protein morphology by NMR. The protein morphology analysis needs the global structural information coming from the residual anisotropies. Because protein is dissolved in an artificial medium like magnetically ordering liquid crystalline solution, one may worry about the structural changes that may occur under such unusual condition: For example, the domain orientation in such an aligning medium represents the real state of the protein in an isotropic solution?

The mechanisms for aligning protein in magnetically aligned bicelle solution and rod-like filamentous phage suspension are well understood [16]. The observed RDCs can be reproduced with using the protein crystal structure by the simulation according to the aligning mechanism. The successful reproduction of the RDCs for the protein aligned by bicelle or filamentous phage supports that the proposed theory accurately describes the state of protein in the aligning media.

According to the theory, the observed residual anisotropies can be established by a small fraction of protein experiencing the rotational restriction through the collision between the protein and the magnetically aligning molecule. In using the

charged filamentous phage, the electrostatic interactions are also active in inducing the rotational restriction on the protein near the medium. The fraction for that is around 0.1% of the total number of protein molecules in the sample. In other words, the interactions have to be weak and transient. The inter-molecule interactions, therefore, do not actively align the protein but prohibit some fraction of the protein orientation near the medium. Under the condition, the aligning media do not induce artificial protein conformation or domain arrangement, because the prohibited orientation angles near the medium is solely determined by the intrinsic molecular shape of protein in the bulk solution.

The structural perturbation by the medium is easily monitored by the NMR spectral changes. If the medium tightly interacts with protein to change the structure, some of the chemical shifts should change from those found in an isotropic state.

The bicellar medium is in the liquid crystalline state over its phase-transition temperature. Under the temperature, it becomes a micelle solution that does not align in a magnetic field and thus does not induce protein alignment. If protein in this micelle solution does not show apparent spectral changes from the solution without containing micelle, we exclude the possibility that the bicelle induces a structural change to the protein through non-specific contacts.

In the case of the charged filamentous phage, the increased concentration of cations, which shield the surface charge on the phage, impairs the ordering of the media in a magnetic field. The magnitudes of the anisotropic spin interactions for the protein in the phage suspension, therefore, are proportion to the cation concentration. If the spectral changes show linear dependency on the cation concentration, we could rule out the structural changes caused by the interaction with the medium.

Using compressed acrylamide gel allows the direct spectral comparison between the samples in the reference gel (non-compressed gel) and the isotropic solution without gel to see if any structure change happens through the interaction with the gel.

In general, under weakly aligning conditions, the spectral changes caused by the interaction with the media are almost negligible, ensuring that no apparent structural changes happen to protein in the media, even in the cases of multiple domain proteins.

## 22.4 RDC-Based Domain Orientation Analysis

In this section, we will describe the experimental procedure to determine the domain orientation of a multi-domain protein, from the RDC data collection to the structure determination. In addition, the limitations in the RDC-based analysis will be discussed to emphasize the necessity of our TROSY-based DIORITE (Determination of Induced ORIentation by Trosy Experiment) approach.

### 22.4.1 Collecting the RDC Data

RDC is measured on a pair of  $^1\text{H}$  coupled HSQC spectra for the samples in isotropic and anisotropic states. The  $^1\text{H}$  coupled HSQC spectrum gives a pair of split peaks along  $^{15}\text{N}$  axis for each  $^1\text{H}-^{15}\text{N}$  correlation. The doubled number of peaks on a  $^1\text{H}$  coupled HSQC spectrum may give increased signal overlaps that obstacle the accurate reading of peak positions. To avoid this drawback, an NMR technique is used to separate the up- and down-field components into different 2D spectra, IPAP-HSQC [22]. IPAP-HSQC gives two separate spectra that have in-phase and anti-phase doubles, respectively. Addition or subtraction of the spectra will give two separate 2D spectra displaying only up-field or down-field components of each doublet. This signal separation reduces signal overlap on a  $^1\text{H}$  coupled HSQC spectrum and keeps the spectral resolution to the same extent as in the original HSQC spectrum (Fig. 22.3).

The separation width between the up- and down-field components measured from IPAP-HSQC spectra gives  $^1J_{\text{NH}}$  for isotropic sample and  $^1J_{\text{NH}} + D_{\text{NH}}^{\text{res}}$  for aligned sample. Therefore, the RDC,  $D_{\text{NH}}^{\text{res}}$ , is obtained by their difference.

### 22.4.2 Domain Orientation Analysis Based on the RDC Data

Here, we describe the domain orientation analysis based on the RDCs. The domain orientation analysis should be done for the protein whose structure is already known by X-ray. The primal interest of the analysis is in exploring the domain reorientation upon interaction with the other protein or ligand. In the cases, each domain is assumed to retain the same structure as in crystal.

As described in the theory section, the alignment tensor for a weakly aligned protein is determined based by the RDCs and its structure coordinate, Eq. (22.5). The Saupe order matrix consists of five independent elements. We therefore need more than five RDC data to determine the Saupe order matrix for the focusing part in a protein. The singular value decomposition (SVD) to the matrix relating the direction cosines to the observed RDCs will give the Saupe order matrix [25, 26, 50]. Diagonalizing the Saupe order matrix gives the alignment tensor frame orientation relative to the molecular coordinate system and the magnate of the aligning orders along each principal axis. As described in the theory part, the alignment tensor frame orientation is defined by the Euler angles ( $\alpha, \beta, \gamma$ ).

We consider a two-domain protein here. We also assume that the high-resolution structure of each domain is available, and each domain structure is the same as in the crystal. Based on the collected RDCs, the alignment tensor for each domain is independently determined according to the above procedure. As schematically drawn in Fig. 22.8, the determined tensor frames for each domain are used as a

guide to define solution domain orientation; one domain coordinate is rotated to make an overlay its tensor frame onto the other (Fig. 22.8). It is noted here, the RDCs do not provide any distance information between the domains. If the inter-domain segment is highly flexible, the additional distance restraints are required to build the entire structure, which should come from the other experiments like paramagnetic relaxation enhancement and/or small angle X-ray scattering (SAXS) [51–53].

Alignment tensor determined by the RDCs has four possible orientations. Inversion around each principal axis gives the same RDCs values. Therefore, the inversion is not discriminated experimentally. To alleviate this ambiguity in orientation angle, additional aligning states using different aligning media, including charged bicelle, or charged acrylamide gel, will be used. In analysing domain orientation, the structural restrictions, which include the length of the inter-domain linker or possible inter-domain steric clash, may define one inter-domain orientation even using a single aligning experiment [34, 54].

The alignment tensor magnitudes along each principal axis represent the extent of the aligning order. If the values differ between the domains, each domain tumbles differently. The aligning orders thus give the insight into the domain dynamics in a protein [34].

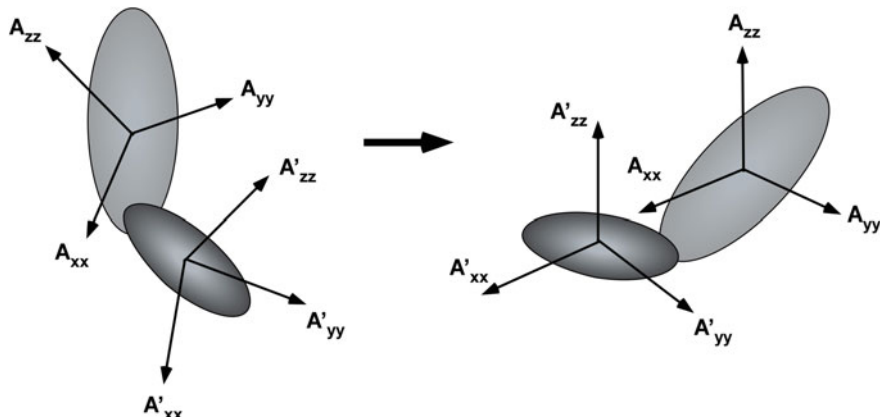


**Fig. 22.8** Schematic representation for the procedure to determine the relative domain orientation based on the alignment tensors for each domain. Sets of RDC data determine the alignment tensor for each domain, independently. The domain orientation of a protein is established by rotating one domain coordinate to make an overlay of its tensor frame on the other

### 22.4.3 *Significance of the Domain Orientation Analysis by RDCs*

The domain orientation analysis for protein in solution gives an invaluable outcome, even if its high-resolution crystal structure is available. There are some cases to show the different domain arrangements between solution and crystalline structures. The RDC analysis on maltose-binding protein (MBP) in the complex with  $\beta$ -cyclodextrin has shown that the relative domain orientation in solution was different from that in the crystal [55]. This may indicate the crystal contact causes a subtle change in domain orientation. Bacteriophage T4 lysozyme in solution was shown to have a more open conformation relative to the crystal structure, which was also analyzed by the RDCs [56]. This observation appears compatible with steric requirements for the ligand bindings.

These examples illustrate how the RDC-based domain analysis complements X-ray crystallography in determining the relative domain orientation or protein morphology. The significance of the RDC-based analysis is emphasized in exploring the domain rearrangement upon binding to the other protein or ligand. When the complex structure cannot be solved by X-ray, the complex structure is determined by the RDCs in a solution state with the structure in apo-form. This approach does not require tedious and time-consuming NOE analysis as required in conventional NMR structure determination, but just needs the backbone resonance assignments and a set of IPAP-HSQC spectra. The RDC based approach allows efficient structure determination of the protein in the complex with target.

### 22.4.4 *Molecular Size Limitation in the RDC-Based Approach*

The domain orientation analysis with the RDCs is now realized as a useful technique to elucidate overall protein morphology in solution, complementing the X-ray structure analysis. This approach has, however, severe size limitation. Here, this obstacle in the RDC application is discussed.

The size limitation comes from the rapid transverse relaxation rate of one of the split components observed on a 2D IPAP-HSQC spectrum. The high-field component shows faster transverse relaxation rate than that of the other. This component has even faster relaxation rate than that of HSQC counterpart. This is due to cross-correlated relaxation interference to amide  $^{15}\text{N}$  spin relaxation process; for the high-field component, the cross-correlated relaxation process additively affects, while for the low-field component, the interference reduces its relaxation rate. The transverse relaxation process of the HSQC signal is free from the interference.

In measuring the RDCs with IPAP-HSQC for high molecular weight protein, the high-field components of each amide spin pairs will broaden and severely reduce

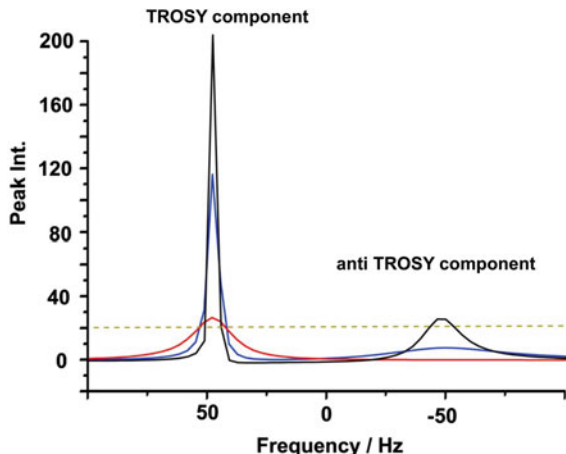
the signal intensities, thus, they will not be observed. In particular, the difficulty in observing the high-field component will be enhanced in an aligned state, due to the appearance of the residual dipolar interactions as relaxation causes. For proteins over 20 kDa, it is usually hard to observe the high-field component in an aligned state, thus making the RDC measurement impossible. The RDC-based domain orientation analysis with IPAP-HSQC is practically limited up to around 20 kDa.

Simulation of the line broadening on each component of a doublet according to molecular size is shown in Fig. 22.9. In this figure, the low-field component that shows a longer transverse relaxation time and the other having a shorter transverse relaxation time are named as TROSY and anti-TROSY, respectively. The slower transverse relaxation associated with the low-field component is due to the mechanism used in TROSY (Transverse Relaxation Optimized SpectroscopY) [21]. As demonstrated on the simulation, the anti-TROSY component shows severe broadening even for the medium-size protein, 20 kDa.

The difference in line widths between the TROSY and anti-TROSY components will become considerable for higher molecular weight proteins. As seen in the simulation, protein over 150 kDa gives severely broadened anti-TROSY signal, which already hard to observe. Protein with 800 kDa gives undetectable anti-TROSY signal. The size limitation in the RDC-based approach is clearly demonstrated in this simulation.

It should be noted, the TROSY component can remain observable in intensity even for 800 kDa protein (Fig. 22.9). This motivated us to devise an approach to determine an alignment tensor by using only TROSY components, which will push forward the molecular size limit in the existing RDC based experiments.

**Fig. 22.9** Simulation of the molecular size dependency of the TROSY and anti-TROSY components observed on a IPAP-HSQC spectrum. The data represent a slice peak along the  $^{15}\text{N}$  axis. This simulation assumed a 750-MHz experiment. Black, blue, and red lines are the simulated peaks for the sizes 20, 150, and 800 kDa, respectively. The dotted line is assumed the expected noise level



### 22.4.5 Existing Remedy for Overcoming the Size Limitation in the RDC-Based Approach

Some remedies are proposed to overcome the size limitation the RDC application. They all rely on the TROSY.

The difference in the transverse relaxation rates between the TROSY (low-field) and anti-TROSY (high-field) components split along the  $^{15}\text{N}$  axis are explained by the relaxation interference. The same effect is active in the split signals along  $^1\text{H}$  dimension. In observing the  $^1\text{H}$ - $^{15}\text{N}$  single bond correlation spectrum without decoupling during  $t_1$  and also  $t_2$  durations, each spin pair gives a quartet on a spectrum; split signals in both  $^1\text{H}$  and  $^{15}\text{N}$  dimensions. The pure TROSY signal is the one having the longest transverse relaxation time among the quartets. In using the protein labeled with  $^{15}\text{N}$  and  $^2\text{H}$ , where an unwanted relaxation process is diminished by breaking the  $^1\text{H}$ - $^1\text{H}$  dipolar interaction network in a protein, TROSY effect is enhanced, and it allows  $^1\text{H}$ - $^{15}\text{N}$  correlation spectrum for proteins over 100 kDa [21].

One proposed remedy is the combinatorial use of TROSY and HSQC. The difference between TROSY and HSQC signals along the  $^{15}\text{N}$  axis corresponds to a half of RDC. As discussed above, the transverse relaxation rate of the HSQC signal is slower than that for the anti-TROSY component in a IPAP-HSQC spectra. Therefore, the size limitation problem should be alleviated by replacing anti-TROSY signal with HSQC counterpart. For a 81.4-kDa protein, the transverse relaxation times for the TROSY, anti-TROSY, and HSQC signals are reported to be 65, 10, and 30 ms, respectively [57]. In considering the difference between the transverse relaxation times between TROSY and HSQC signals, the combinatorial use does not fully solve the problem, but just alleviate it.

Another remedy is the use of  $J$ -scaled TROSY, which is also referred to as  $J$ -enhanced (JE) TROSY [58, 59]. In this experiment, short  $J$ -evolution step is added in the standard TROSY, which induces  $J$ -dependent shift change from the standard TROSY shift. In the standard TROSY experiment, the shift difference between the signals along the  $^{15}\text{N}$  axis on the same  $^1\text{H}$  chemical shift corresponds to  $^1J_{\text{NH}}$ , while in the  $J$ -scaled TROSY, this shift difference is changed according to the additional duration for  $J$ -evolution. From the magnitude of the shift change induced by the applied  $J$ -evolution period, the apparent  $^1J_{\text{NH}}$  coupling value is estimated. If the  $J$ -evolution period is applied to allow full recovery of  $^1J_{\text{NH}}$  coupling, the observed signal position should be coincident with that of the HSQC signal. Usually, to gain the signal intensity for the observed signal on  $J$ -scaled TROSY, rather limited evolution time is set. In this  $J$ -evolution step, the coherences for TROSY and anti-TROSY are mixed; the equivalent mixing of the two gives the coherence for observed as HSQC signal. The more increased the contribution of the anti-TROSY coherence to the observed signal leads to more broadened signals observed. Therefore, in the  $J$ -scaled TROSY experiment, partial recovery of the  $J$ -modulation is used to maintain the signal intensities on the  $J$ -scaled TROSY spectrum in the observable level.

Signals observed on a  $J$ -scaled TROSY spectrum have longer transverse relaxation times than those of the signals on a HSQC spectrum. Their transverse relaxation times, however, are still shorter than those for real TROSY counterparts. The combined use of TROSY and  $J$ -scaled TROSY is indeed advantageous over the TROSY/HSQC combination. In determining more accurate RDCs,  $J$ -scaled TROSY requires more extent of the mixing of the anti-TROSY coherences, which will result in the lesser sensitive  $J$ -scaled TROSY signals. The use of  $J$ -scaled TROSY is not the complete remedy for the problem we concern.

In spite of the limitations in the existing approaches, they expanded the RDC application up to 50 kDa protein [60]. However, it is also reported that the rapid transverse relaxation of the non-TROSY component is already an obstacle in measuring the RDCs for 81.4-kDa protein [57]. The further expansion of the application limit is expected, and our DIORITE is one of the possible methods used for this purpose.

## 22.5 Alignment Tensor Determination Using Only TROSY

As discussed above, the molecular size limitation in the RDC-based domain orientation analysis is not completely overcome. Most of the biologically interesting multi-domain proteins tend to be over 100 kDa. The existing approaches are not supposed to be applied to such higher molecular weight protein. This is because they do not take fully advantages of TROSY spectroscopy, which adopts the signals with the longest transverse relaxation time. Our DIORITE approach uses the signals having the longest transverse relaxation times. This considerably diminishes the size limitation problem. In this section, we will describe the theoretical aspects of the TROSY-based alignment tensor determination, which will allow the domain orientation analysis for higher molecular weight.

### 22.5.1 Alignment-Induced TROSY Shift Changes

TROSY spectrum changes when protein is transferred from isotropic to anisotropic states. This TROSY shift change along the  $^{15}\text{N}$  axis contains the effects of two anisotropic spin interaction observed on a peptide plane;  $^1\text{H}-^{15}\text{N}$  dipolar interaction and  $^{15}\text{N}$  CSA. As depicted in Fig. 22.10, this alignment-induced TROSY shift change,  $\Delta\delta_{\text{TROSY}}$ , contains a half of RDC and the full RCSA effects. In a Cartesian representation using the Saupe order matrix, the following relation should hold:

$$\begin{aligned}\Delta\delta_{\text{TROSY}} &= -\frac{1}{2}\left(\frac{\mu_0}{4\pi}\right)\frac{\gamma_i\gamma_j h}{2\pi^2 r_{ij}^3} \frac{4\pi}{5} \sum_{kl=x,y,z} S_{kl} \cos(\alpha_k) \cos(\alpha_l) \\ &\quad + \frac{2}{3} \sum_{kl=x,y,z} \sum_{j=x,y,z} S_{kl} \cos(\theta_{kj}) \cos(\theta_{lj}) \delta_{jj} \\ &= \sum_{kl} S_{lk} \left\{ \frac{1}{2} D_{\text{NH}}^0 \cos(\alpha_k) \cos(\alpha_l) + \frac{2}{3} \Delta_{kl} \right\}\end{aligned}\quad (2.9)$$

$$\Delta_{kl} = \sum_{k,l=x,y,z} \sum_{j=x,y,z} S_{kl} \cos(\theta_{kj}) \cos(\theta_{lj}) \delta_{jj} \quad (2.10)$$

where  $\cos(\alpha_k)$  is the direction cosine for the NH bond vector relative the molecular axis  $k$  ( $k = x, y, z$ ).  $D_{\text{NH}}^0$  is the static dipolar coupling constant, which equals 23.0 and 21.7 kHz for assumed NH bond length 1.02 and 1.04 Å, respectively; in considering the bond libration effects, the effective NH bond length is to be 1.04 Å. The term  $\cos(\theta_{kj})$  is the direction cosine of the CSA principal axis  $j$  to the molecular axis  $k$ . The principal value of the CSA tensor along  $j$ -axis is denoted as  $\delta_{jj}$ . As done for the RDC, the SVD calculation to Eq. (22.9) gives the Saupe order matrix. At least, five  $\Delta\delta_{\text{TROSY}}$  data are required to determine the Saupe order matrix comprising five independent elements. The alignment tensor is obtained through the diagonalization of the Saupe order matrix.

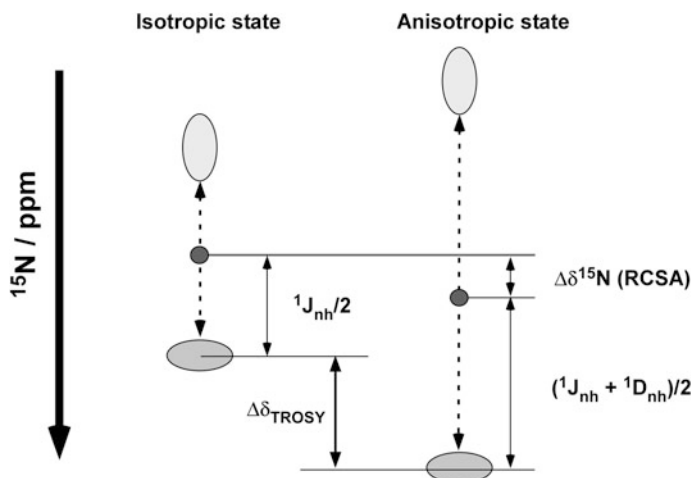


**Fig. 22.10** Schematic drawing of the relationship among the signals for  ${}^1\text{H}-{}^{15}\text{N}$  doublet in a  ${}^1\text{H}$  coupled HSQC spectra observed for protein in isotropic and aligned states.  $\Delta\delta_{\text{TROSY}}$  contains the contributions from a half of RDC and full RCSA

DIORITE is the algorithm to determine the alignment tensor solely from TROSY spectra. DIORITE is anticipated to give a more accurate alignment tensor over the  $^1\text{H}$ - $^{15}\text{N}$  RDCs, in particular the cases for the proteins over 50 kDa by taking advantage of the longest transverse relaxation time of the TROSY signal. DIORITE determines the alignment tensor based on two anisotropic spin interactions, including RDC and RCSA. As described in theory part, RCSA contains the tensorial value to define the orientation the peptide plane against the magnetic field, while RDC gives only the vectorial angle of the NH bond to the magnetic field. RDC value does not change if the peptide plane is rotated along the NH bond axis, while RCSA value significantly changes by the rotation. Because of the inclusion of RCSA, DIORITE can determine the peptide plane orientation. DIORITE is more informative over the RDC-based approach in determining the domain orientation in a protein.

### 22.5.2 CSA Tensor Parameters Used in DIORITE

DIORITE-based alignment tensor determination requires  $^{15}\text{N}$  CSA tensor value for each residue. As discussed in the part for the RCSA, it is not trivial to get accurate  $^{15}\text{N}$  CSA tensor value for each residue in a protein, because it sensitively changes according to the local structure which includes backbone torsion angle, hydrogen bonding, and so forth. In the DIORITE analysis,  $^{15}\text{N}$  CSA tensor for the residue has to be pre-defined as input parameters.

Recent reports on the residue-specific  $^{15}\text{N}$  CSA tensors determined for small proteins in solution had demonstrated that the  $^{15}\text{N}$  CSA tensor value is mainly determined by the backbone torsion angle. Based on the torsion angle dependency of  $^{15}\text{N}$  CSA tensor, we proposed the practical protocol for the DIORITE analysis that uses the secondary structure-specific  $^{15}\text{N}$  CSA tensors as pre-defined input from the structure.

The quality of the back-calculated  $\Delta\delta_{\text{TROSY}}$  values was assessed on ubiquitin. The values with the secondary structure-specific  $^{15}\text{N}$  CSA tensors and those with the residue-specific tensors were compared (Fig. 22.11); the residue-specific  $^{15}\text{N}$  CSAs used here were determined by a set of elaborate spin relaxation analyses by Bodenhausen and co-workers [61]. As demonstrated in the comparison, the use of the secondary structure-specific  $^{15}\text{N}$  CSA tensor gives consistent results with those with residue-specific values within an error range (Fig. 22.11). The DIORITE analysis using the secondary structure-specific  $^{15}\text{N}$  CSA tensors, therefore, can be applicable for exploring the domain orientation in a protein.

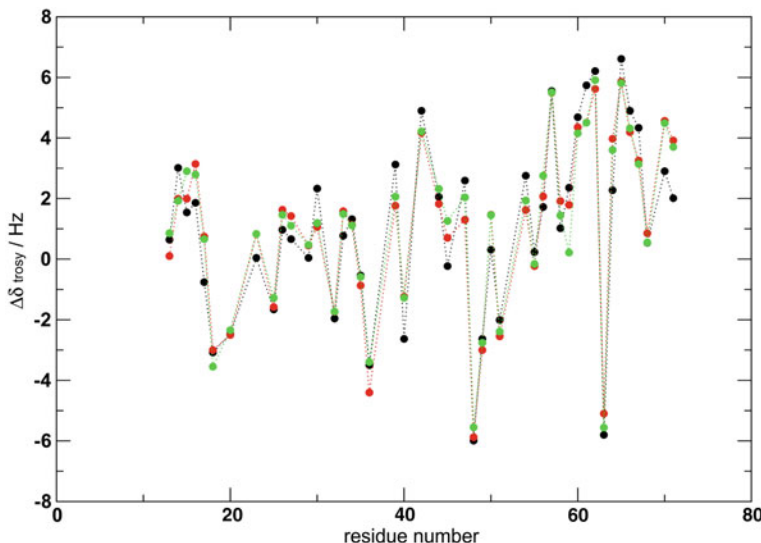


**Fig. 22.11** Comparison of the back-calculated  $\Delta\delta_{\text{TROSY}}$  obtained by DIORITE algorithm using the secondary structure-specific and the residue-specific  $^{15}\text{N}$  CSA tensors. Red and green circles are the values with secondary structure-specific and residue-specific tensors, respectively. *Black circles* are the observed  $\Delta\delta_{\text{TROSY}}$

### 22.5.3 DIORITE Analysis Using Different Magnetic Field Strengths

TROSY effect reduces line width along  $^{15}\text{N}$  dimension at a higher magnetic field; the original paper on TROSY has estimated the optimal frequency for obtaining the narrowest lines is around 1 GHz [62]. In this section, the optimal magnetic field strength for the DIORITE analysis will be discussed.

The alignment-induced TROSY shift change,  $\Delta\delta_{\text{TROSY}}$ , shows significant magnetic field dependency due to the RCSA contribution. The magnitude of RCSA is proportional to the applied magnetic field strength, while the RDC is independent on the applied magnetic field strength. The field dependency of the RCSA gives a peculiar profile to the  $\Delta\delta_{\text{TROSY}}$  value.

In a peptide plane, the least shielded  $^{15}\text{N}$  CSA tensor axis,  $\delta_{xx}$ , is close to the NH bond; the angle  $\beta$  ranges from  $15^\circ$  to  $20^\circ$  (Fig. 22.2b). The small  $\beta$  angle result in the cancelation between RDC and RCSA values to each other, making the observed  $\Delta\delta_{\text{TROSY}}$  value smaller than the corresponding RDC. In most of the residues in a protein, RDC and RCSA have an opposite sign to each other. Therefore,  $\Delta\delta_{\text{TROSY}}$  should be roughly equivalent to that a half of RDC minus RCSA in their absolute values. The value  $\Delta\delta_{\text{TROSY}}$  tends to be approximately one-third of the RDC in an absolute magnitude.

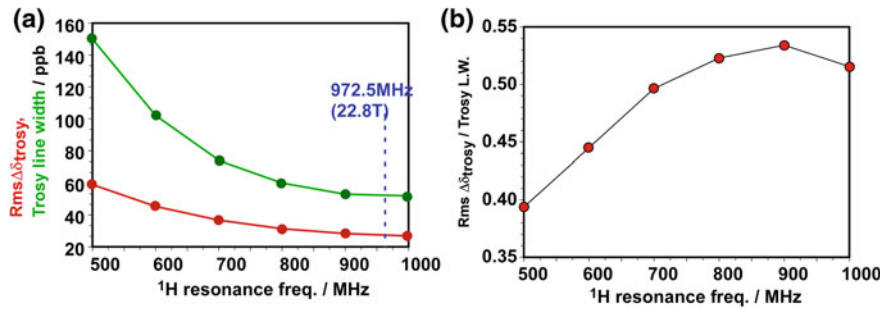


**Fig. 22.12** Field dependency of the TROSY line width and the root-mean-square (rms)  $\Delta\delta_{TROSY}$ . **a** TROSY line width (green) and rms  $\Delta\delta_{TROSY}$  (red) according to the magnetic field strength. **b** Field strength dependency of the effective resolution in measuring  $\Delta\delta_{TROSY}$

The inter cancelation effect depends on the magnetic field strength, but the dependency is not linear. Using ubiquitin, we simulated the root-mean-square (rms)  $\Delta\delta_{TROSY}$  values on different magnetic field strengths represented by  $^1\text{H}$  resonance frequencies, (Fig. 22.12). As seen in this simulation, the rms  $\Delta\delta_{TROSY}$ , which represents the average magnitude of  $\Delta\delta_{TROSY}$ , decreases up to 800 MHz and then increases according to the field strength (Fig. 22.12). In lower magnetic field strength, where the RCSA contribution is rather small and the  $\Delta\delta_{TROSY}$  is roughly approximated by a half of RDC. The increasing RCSA, which has an opposite sign to RDC, contribution overall decreases the RDC value but further enhancement of the RCSA contribution in a higher magnetic field becomes dominant in  $\Delta\delta_{TROSY}$  value, which may explain the profile (Fig. 22.12).

The condition for weak alignment is carefully tuned to avoid severe signal broadening. The alignment order is typically tuned to around  $10^{-3}$ , giving the maximal absolute magnitude of RDC around 20 Hz. Under the condition,  $\Delta\delta_{TROSY}$  is expected to give about 6 Hz. Even under the worst 800 MHz, the expected  $\Delta\delta_{TROSY}$  should be 5.5 Hz. The accuracy in reading peak positions at a signal-to-noise ration of 40:1 was estimated to be 0.6 Hz. Therefore, the experimental error in the observed  $\Delta\delta_{TROSY}$  is estimated to be 0.8 Hz, in considering the error propagation through subtracting the TROSY shift in an aligned state by that in an isotropic state. Accordingly, the expected  $\Delta\delta_{TROSY}$  is well resolved within the error in peak picking. It is noted that the estimated reading error in RDC should be 1.2 Hz due to twice subtraction required.

The resolution on TROSY spectrum also determines the validity of DIORITE at different magnetic field strength. Using the average  $^{15}\text{N}$  CSA tensor value estimated from ubiquitin, the dependencies of  $^{15}\text{N}$  TROSY line width and rms  $\Delta\delta_{TROSY}$  value are plotted against proton resonance frequencies, where the values are in ppb (parts per billion) units instead of Hz to compare them in the context of spectral resolution (Fig. 22.13a). In this simulation, the optimal frequency to minimize the  $^{15}\text{N}$  line width of the observed TROSY signal is 972.5 MHz, close but slightly different from the value by the simpler estimation in the original paper. In comparing the line

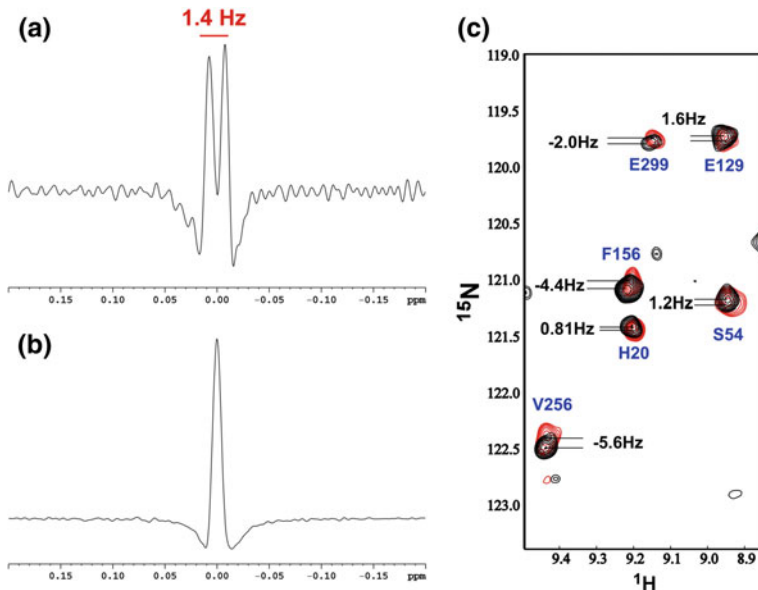


**Fig. 22.13** TROSY shift changes induced by weak alignment by using compressed acrylamide gel. TROSY shift changes are measured from the reference positions collected for the sample in an uncompressed gel that is made of the same chemical composition to that used for compressed gel. **a** <sup>1</sup>D <sup>1</sup>H residual quadrupole split observed in a compressed gel, **b** the residual quadrupole split is not observed in an uncompressed gel, showing that the gel can be used for the reference. **c** TROSY shift changes,  $\Delta\delta_{\text{TROSY}}$ , observed for a 38 kDa protein (MBP); a pair of TROSY spectra collected in compressed (red) and uncompressed gels (black)

width of TROSY signal, the rms  $\Delta\delta_{\text{TROSY}}$  value is less dependent on the magnetic field strength. The effective accuracy in observing  $\Delta\delta_{\text{TROSY}}$  value should be estimated by the value  $\Delta\delta_{\text{TROSY}}$  divided by the <sup>15</sup>N line width of TROSY signal (Fig. 22.13b). In the simulation, the optimal magnetic field strength for observing  $\Delta\delta_{\text{TROSY}}$  is around 900 MHz for <sup>1</sup>H resonance frequency. Therefore, the magnetic field strength for the maximal TROSY effect is almost optimal for the DIORITE analysis. DIORITE analysis, thus, can take full advantage of the TROSY effect on a 900 MHz NMR spectrometer that is now commercially available.

#### 22.5.4 Practical Aspects of the DIORITE Data Collection

DIORITE analysis uses TROSY chemical shift changes  $\Delta\delta_{\text{TROSY}}$  induced by weakly aligning protein [63, 64]. In general, chemical shift is very sensitive to the solution conditions, including temperature, sample concentration, pH, ionic strength, and co-solute. In measuring  $\Delta\delta_{\text{TROSY}}$ , we have to exclusively collect the

chemical shift changes caused by the alignment effects. For the purpose, anisotropically compressed polyacrylamide gel is the most appropriate medium for aligning protein. As described above, the anisotropically compressed gel (stretched gel) is made by inserting the cast gel chip having a little greater diameter than that of the inner diameter of NMR tube. The gel chip having the same diameter as that of NMR tube is not compressed after insertion, which can keep the isotropic cavity within. Protein in this non-compressed gel is not aligned and does not show any anisotropic spin interactions. The sample, therefore, can be used as the reference TROSY spectrum for measuring  $\Delta\delta_{\text{TROSY}}$ . Because the non-compressed gel consists of the same acrylamide composition, protein in this gel experiences the same chemical environments as in the compressed gel, which ensures that the observed TROSY shift changes solely come from the alignment effects. It is difficult in getting reference data with using the other aligning media, including bicelle, filamentous phage, and purple membrane. They cannot be the choice for DIORITE analysis.

In measuring  $\Delta\delta_{\text{TROSY}}$  values, a set of TROSY spectra for the aligned and isotropic samples are used (Fig. 22.13c). The formation of the anisotropic cavity in the stretched gel can be monitored by the split of the deuteron signal from HOD; the deuteron in the water molecule within an anisotropic cavity shows a doublet, residual quadrupolar coupling of the deuteron (Fig. 22.13a). The stronger anisotropy in a cavity gives a larger split. The water deuteron in the reference gel gives a singlet, confirming the cavity in the reference gel is isotropic (Fig. 22.13b).

In measuring NMR spectrum, water deuteron signal is used as a frequency lock to give the frequency standard. Because of the split of a deuteron signal in an aligned state, the resonance positions observed are biased; one of the doublet envelopes is used for the frequency lock, thus biasing the signals by a half of the split width. This offset should be subtracted from each signal position on the TROSY spectrum for protein in an aligned state.

### 22.5.5 DIORITE Analyses on MBP in Different Ligand Bound States

Here, we demonstrate the applications of the DIORITE analysis. Maltose-binding protein (MBP) has two domains. From a series of X-ray analysis, MBP is known to show domain reorientation upon binding to ligand, and the domain rotation angle depends on the size of ligand molecule.

MBP binds to  $\beta$ -cyclodextrin ( $\beta$ -CD) comprising of seven glucose units, and it shows a small change in the relative domain orientation from that in apo form as demonstrated by X-ray analysis. MBP also binds to different types of cyclodextrins comprising of the different number of glucose units;  $\alpha$ -CD (six glucose units),  $\gamma$ -CD (eight glucose units). We expected to see the domain rotation angle changes according to the size of the three types of CDs.

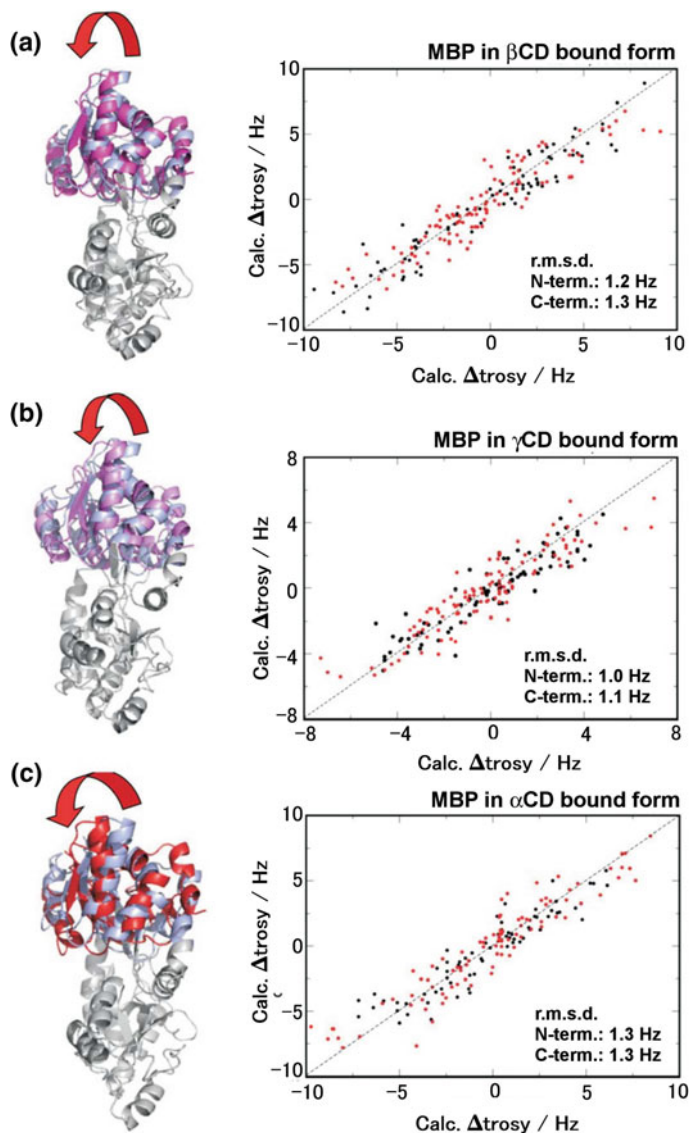


**Fig. 22.14** Domain rotation angle change according to the ligand size in maltose-binding protein (MBP). **a**  $\beta$ -CD, **b**  $\gamma$ -CD and **c**  $\alpha$ -CD complex states. The hinge rotation angles induced by ligand binding were  $13^\circ$ ,  $14^\circ$ , and  $22^\circ$  for the cases of  $\beta$ -CD,  $\gamma$ -CD, and  $\alpha$ -CD, respectively

Using the anisotropically compressed gel (stretched gel) and uncompressed reference gel, we collected a pair of TROSY spectra for each MBP in the complex with  $\alpha$ -,  $\beta$ - and  $\gamma$ -CD. Using the apo-form MBP X-ray coordinate, we analyzed the relative domain orientation using DIORITE; the model structure was constructed

based on the alignment tensors individually determined for N- and C-terminal domains. On each complex, the back-calculated and observed  $\Delta\delta_{\text{TROSY}}$  values were well correlated, suggesting the alignment tensors for each domain were well determined (Fig. 22.14).

The DIORITE analyses on the MBP complexes demonstrated that for the smallest ligand,  $\alpha$ -CD, the domain rotation angle was significantly larger than that for the  $\beta$ -CD complex structure. On the other hand, MBP in the complex with  $\gamma$ -CD retains almost the same domain orientation relative to the  $\beta$ -CD complex; the size over the  $\beta$ -CD does not change the domain rotation angle.

The example analyses demonstrated that the MBP showed significant domain reorientation according to the ligand size. It should be noted that the DIORITE analysis is very efficient to see this ligand-dependent domain reorientation; which requires just a pair of TROSY spectra collected for the sample in aligned and isotropic states.

## 22.6 Conclusion

X-ray structures are still exponentially accumulated every year. The huge collection of the protein coordinates should prompt the protein structure works using the existing protein coordinate data. In this review, we introduced protein structure analysis in solution with the assistance of protein structure data collected by X-ray crystallography.

There has been a lot of discussion on the significance of the solution structure determination by NMR. Most of the structures for single domain proteins or isolated domains have shown marginal structural deviations from the corresponding structures solved by X-ray. This diminishes the importance of NMR structure analysis, except for the case in which crystallization is hard. When X-ray structure is available on a type of protein behaving as an independent structural unit, the solution structure determination on the protein by NMR is not usually conducted, because the crystal structure should not largely differ from that in solution. Additionally, in most of the cases, the size limitation in NMR structure determination prohibits such solution structure analyses, even if they are required. NMR solution structure analysis, therefore, has been recognized as a complementary method in rather limited cases.

The situation seems different in the structure analysis of multiple domain proteins. There already appeared some examples to show the difference in the domain orientations of protein between solution and crystalline states. The kinds of example will be increased, because it is getting to know that many proteins have domains linked by seemingly flexible or unstructured linkers judged from the sequence. In the proteins, it is presumable that the domain arrangement tends to be defined artificially by crystal packing, thus not represent the protein morphology in a solution state.

The NMR techniques using a weak alignment have paved ways to directly determine the relative domain orientation in solution, which has not been ever done by the conventional NMR methods. Some variations of the methods were introduced in this review, with their limitations in practical applications. Our devised DIORITE approach has a significant advantage in the domain orientation analysis over the existing methods, when it is applied to the protein with high molecular weight. The domain orientation analysis by DIORITE will expand the X-ray structure assisted reach in exploring the protein morphological change in solution, which should have functional relevance.

The domain rearrangement in protein, or protein morphological change, upon binding to ligand or interaction with its partner protein will become much more important in discussing protein functional regulation, after getting the high-resolution crystal structure in a specific state, for example, apo form. The combined use of DIORITE with X-ray structure data may give vivid views how protein works in solution by changing its morphology. NMR is now becoming a complementary partner to X-ray crystallography in protein structure analysis, in particular, on higher molecular weight proteins.

## References

1. Morris, G.M., et al.: AutoDock4 and AutoDockTools4: automated docking with selective receptor flexibility. *J. Comput. Chem.* **30**, 2785–2791 (2009)
2. Dominguez, C., Boelens, R., Bonvin, A.M.: HADDOCK: a protein–protein docking approach based on biochemical or biophysical information. *J. Am. Chem. Soc.* **125**, 1731–1737 (2003)
3. de Vries, S.J., van Dijk, M., Bonvin, A.M.: The HADDOCK web server for data-driven biomolecular docking. *Nat. Protoc.* **5**, 883–897 (2010)
4. Fuxreiter, M.: Fuzziness: linking regulation to protein dynamics. *Mol. BioSyst.* **8**, 168–177 (2012)
5. Evenäs, J., Mittermaier, A., Yang, D., Kay, L.E.: Measurement of  $^{13}\text{C}\alpha$ – $^{13}\text{C}\beta$  dipolar couplings in  $^{15}\text{N}$ ,  $^{13}\text{C}$ ,  $^2\text{H}$ -labeled proteins: application to domain orientation in maltose binding protein. *J. Am. Chem. Soc.* **123**, 2858–2864 (2001)
6. Evenas, J., et al.: Ligand-induced structural changes to maltodextrin-binding protein as studied by solution NMR spectroscopy. *J. Mol. Biol.* **309**, 961–974 (2001)
7. Cavanagh, J., Fairbrother, W.J., Palmer III, A.G., Skelton, N.J.: Protein NMR spectroscopy, pp. 411–531. Academic Press, Cambridge (1996)
8. Wuthrich, K.: NMR of Proteins and Nucleic Acids. Wiley, Hoboken (1986)
9. Tjandra, N., Tate, S., Ono, A., Kainosho, M., Bax, A.: The NMR structure of a DNA dodecamer in an aqueous dilute liquid crystalline phase. *J. Am. Chem. Soc.* **122**, 6190–6200 (2000)
10. Tjandra, N., Bax, A.: Direct measurement of distances and angles in biomolecules by NMR in a dilute liquid crystalline medium. *Science* **278**, 1111–1114 (1997)
11. Bax, A.: Weak alignment offers new NMR opportunities to study protein structure and dynamics. *Protein Sci.* **12**, 1–16 (2003)
12. de Alba, E., Tjandra, N.: Residual dipolar couplings in protein structure determination. *Methods Mol. Biol.* **278**, 89–106 (2004)
13. Delaforge, E., et al.: Large-scale conformational dynamics control H5N1 influenza polymerase PB2 binding to importin  $\alpha$ . *J. Am. Chem. Soc.* **137**, 15122–15134 (2015)

14. Tate, S.-I.: Anisotropic nuclear spin interactions for the morphology analysis of proteins in solution by NMR spectroscopy. *Anal. Sci.* **24**, 39–50 (2008)
15. Prestegard, J.H., Bougault, C.M., Kishore, A.I.: Residual dipolar couplings in structure determination of biomolecules. *Chem. Rev.* **104**, 3519–3540 (2004)
16. Zweckstetter, M.: NMR: prediction of molecular alignment from structure using the PALES software. *Nat. Protoc.* **3**, 679–690 (2008)
17. Ottiger, M., Bax, A.: Characterization of magnetically oriented phospholipid micelles for measurement of dipolar couplings in macromolecules. *J. Biomol. NMR* **12**, 361–372 (1998)
18. Wüthrich, K.: NMR of proteins and nucleic acids, Chap. 7, pp. 117–129. John Wiley & Sons, Ltd, Hoboken (1986)
19. Kurita, J., Shimahara, H., Utsunomiya-Tate, N., Tate, S.: Measurement of <sup>15</sup>N chemical shift anisotropy in a protein dissolved in a dilute liquid crystalline medium with the application of magic angle sample spinning. *J. Magn. Reson.* **163**, 163–173 (2003)
20. Tate, S.-I., Shimahara, H., Utsunomiya-Tate, N.: Molecular-orientation analysis based on alignment-induced TROSY chemical shift changes. *J. Magn. Reson.* **171**, 284–292 (2004)
21. Pervushin, K., Riek, R., Wider, G., Wuthrich, K.: Attenuated T2 relaxation by mutual cancellation of dipole–dipole coupling and chemical shift anisotropy indicates an avenue to NMR structures of very large biological macromolecules in solution. *Proc. Natl. Acad. Sci. U S A* **94**, 12366–12371 (1997)
22. Ottiger, M., Delaglio, F., Bax, A.: Measurement of J and dipolar couplings from simplified two-dimensional NMR spectra. *J. Magn. Reson.* (San Diego, Calif.: 1997) **131**, 373–378 (1998)
23. Yao, L., Vögeli, B., Ying, J., Bax, A.: NMR determination of amide N–H equilibrium bond length from concerted dipolar coupling measurements. *J. Am. Chem. Soc.* **130**, 16518–16520 (2008)
24. Varshalovich, D.A., Mosjuklev, A.N., Khersonskii, V.K.: Quantum Theory of Angular Momentum. World Scientific Publishing Co. Pte. Ltd., Singapore (1998)
25. Saupe, A.: Recent results in the field of liquid crystals. *Angew. Chem. Int. Ed. Engl.* **7**, 97–112 (1968)
26. Saupe, A., Englert, G.: High-resolution nuclear magnetic resonance spectra of orientated molecules. *Phys. Rev. Lett.* **11**, 462–464 (1963)
27. Hiyama, Y., Niu, C.H., Silverton, J.V., Bavoso, A., Torchia, D.A.: Determination of <sup>15</sup>N chemical shift tensor via <sup>15</sup>N–<sup>2</sup>H dipolar coupling in Boc-glycylglycyl[<sup>15</sup>N glycine]benzyl ester. *J. Am. Chem. Soc.* **110**, 2378–2383 (1988)
28. Lundstrom, P., Hansen, D.F., Kay, L.E.: Measurement of carbonyl chemical shifts of excited protein states by relaxation dispersion NMR spectroscopy: comparison between uniformly and selectively (<sup>13</sup>C labeled samples. *J. Biomol. NMR* **42**, 35–47 (2008)
29. Yao, L., Grishaev, A., Cornilescu, G., Bax, A.: Site-specific backbone amide (<sup>15</sup>N) chemical shift anisotropy tensors in a small protein from liquid crystal and cross-correlated relaxation measurements. *J. Am. Chem. Soc.* **132**, 4295–4309 (2010)
30. Fushman, D., Tjandra, N., Cowburn, D.: An approach to direct determination of protein dynamics from <sup>15</sup>N NMR relaxation at multiple fields, independent of variable <sup>15</sup>N chemical shift anisotropy and chemical exchange contributions. *J. Am. Chem. Soc.* **121**, 8577–8582 (1999)
31. Boyd, J., Redfield, C.: Characterization of <sup>15</sup>N chemical shift anisotropy from orientation-dependent changes to <sup>15</sup>N chemical shifts in dilute bicelle solutions. *J. Am. Chem. Soc.* **121**, 7441–7442 (1999)
32. Cornilescu, G., Bax, A.: Measurement of proton, nitrogen, and carbonyl chemical shielding anisotropies in a protein dissolved in a dilute liquid crystalline phase. *J. Am. Chem. Soc.* **122**, 10143–10154 (2000)
33. Harris, R.K., Becker, E.D., Cabral de Menezes, S.M., Goodfellow, R., Granger, P.: NMR nomenclature: nuclear spin properties and conventions for chemical shifts. IUPAC Recommendations 2001. International Union of Pure and Applied Chemistry. Physical

- Chemistry Division. Commission on Molecular Structure and Spectroscopy. *Magn. Reson. Chem.* **40**, 489–505 (2002)
- 34. Tolman, J.R., Flanagan, J.M., Kennedy, M.A., Prestegard, J.H.: NMR evidence for slow collective motions in cyanometmyoglobin. *Nat. Struct. Biol.* **4**, 292–297 (1997)
  - 35. Williams, D.C., Cai, M., Clore, G.M.: Molecular basis for synergistic transcriptional activation by Oct1 and Sox2 revealed from the solution structure of the 42-kDa Oct1·Sox2·Hoxb1-DNA ternary transcription factor complex. *J. Biol. Chem.* **279**, 1449–1457 (2004)
  - 36. Ottiger, M., Bax, A.: Bicelle-based liquid crystals for NMR-measurement of dipolar couplings at acidic and basic pH values. *J. Biomol. NMR* **13**, 187–191 (1999)
  - 37. Berlin, K., O'Leary, D.P., Fushman, D.: Improvement and analysis of computational methods for prediction of residual dipolar couplings. *J. Magn. Reson.* **201**, 25–33 (2009)
  - 38. Hansen, M.R., Mueller, L., Pardi, A.: Tunable alignment of macromolecules by filamentous phage yields dipolar coupling interactions. *Nat. Struct. Biol.* **5**, 1065–1074 (1998)
  - 39. Sass, J., et al.: Purple membrane induced alignment of biological macromolecules in the magnetic field. *J. Am. Chem. Soc.* **121**, 2047–2055 (1999)
  - 40. Bellot, G., McClintock, M.A., Chou, J.J., Shih, W.M.: DNA nanotubes for NMR structure determination of membrane proteins. *Nat. Protoc.* **8**, 755–770 (2013)
  - 41. Douglas, S.M., Chou, J.J., Shih, W.M.: DNA-nanotube-induced alignment of membrane proteins for NMR structure determination. *Proc. Natl. Acad. Sci.* **104**, 6644–6648 (2007)
  - 42. Ma, J., Goldberg, G.I., Tjandra, N.: Weak alignment of biomacromolecules in collagen gels: an alternative way to yield residual dipolar couplings for NMR measurements. *J. Am. Chem. Soc.* **130**, 16148–16149 (2008)
  - 43. Naghash, H.J., Okay, O.: Formation and structure of polyacrylamide gels. *J. Appl. Polym. Sci.* **60**, 971–979 (1996)
  - 44. Ishii, Y., Markus, M.A., Tycko, R.: Controlling residual dipolar couplings in high-resolution NMR of proteins by strain induced alignment in a gel. *J. Biomol. NMR* **21**, 141–151 (2001)
  - 45. Tycko, R., Blanco, F.J., Ishii, Y.: Alignment of biopolymers in strained gels: a new way to create detectable dipole–dipole couplings in high-resolution biomolecular NMR. *J. Am. Chem. Soc.* **122**, 9340–9341 (2000)
  - 46. Chou, J., Gaemers, S., Howder, B., Louis, J., Bax, A.: A simple apparatus for generating stretched polyacrylamide gels, yielding uniform alignment of proteins and detergent micelles\*. *J. Biomol. NMR* **21**, 377–382 (2001)
  - 47. Meier, S., Häussinger, D., Grzesiek, S.: Charged acrylamide copolymer gels as media for weak alignment. *J. Biomol. NMR* **24**, 351–356 (2002)
  - 48. Liu, Y., Prestegard, J.H.: A device for the measurement of residual chemical shift anisotropy and residual dipolar coupling in soluble and membrane-associated proteins. *J. Biomol. NMR* **47**, 249–258 (2010)
  - 49. Opella, S.J., Marassi, F.M.: Structure determination of membrane proteins by NMR spectroscopy. *Chem. Rev.* **104**, 3587–3606 (2004)
  - 50. Losonczi, J.A., Andrec, M., Fischer, M.W., Prestegard, J.H.: Order matrix analysis of residual dipolar couplings using singular value decomposition. *J. Magn. Reson. (San Diego, Calif.)* **138**, 334–342 (1999)
  - 51. Clore, G.M., Schwieters, C.D.: Theoretical and computational advances in biomolecular NMR spectroscopy. *Curr. Opin. Struct. Biol.* **12**, 146–153 (2002)
  - 52. Kozak, M., Lewandowska, A., Oldziej, S., Rodziewicz-Motowidlo, S., Liwo, A.: Combination of SAXS and NMR techniques as a tool for the determination of peptide structure in solution. *J. Phys. Chem. Lett.* **1**, 3128–3131 (2010)
  - 53. Grishnev, A., Tugarinov, V., Kay, L.E., Trewhella, J., Bax, A.: Refined solution structure of the 82-kDa enzyme malate synthase G from joint NMR and synchrotron SAXS restraints. *J. Biomol. NMR* **40**, 95–106 (2008)
  - 54. Tolman, J.R., Al-Hashimi, H.M., Kay, L.E., Prestegard, J.H.: Structural and dynamic analysis of residual dipolar coupling data for proteins. *J. Am. Chem. Soc.* **123**, 1416–1424 (2001)

55. Skrynnikov, N.R., et al.: Orienting domains in proteins using dipolar couplings measured by liquid-state NMR: differences in solution and crystal forms of maltodextrin binding protein loaded with beta-cyclodextrin. *J. Mol. Biol.* **295**, 1265–1273 (2000)
56. Goto, N.K., Skrynnikov, N.R., Dahlquist, F.W., Kay, L.E.: What is the average conformation of bacteriophage T4 lysozyme in solution? A domain orientation study using dipolar couplings measured by solution NMR. *J. Mol. Biol.* **308**, 745–764 (2001)
57. Tugarinov, V., Kay, L.E.: Quantitative NMR studies of high molecular weight proteins: application to domain orientation and ligand binding in the 723 residue enzyme malate synthase G. *J. Mol. Biol.* **327**, 1121–1133 (2003)
58. Kontaxis, G., Clore, G.M., Bax, A.: Evaluation of cross-correlation effects and measurement of one-bond couplings in proteins with short transverse relaxation times. *J. Magn. Reson.* **143**, 184–196 (2000)
59. Bhattacharya, A., Revington, M., Zuiderweg, E.R.P.: Measurement and interpretation of  $^{15}\text{N}$ – $^1\text{H}$  residual dipolar couplings in larger proteins. *J. Magn. Reson.* **203**, 11–28 (2010)
60. Jain, N.U., Noble, S., Prestegard, J.H.: Structural characterization of a mannose-binding protein-trimannoside complex using residual dipolar couplings. *J. Mol. Biol.* **328**, 451–462 (2003)
61. Loth, K., Pelupessy, P., Bodenhausen, G.: Chemical shift anisotropy tensors of carbonyl, nitrogen, and amide proton nuclei in proteins through cross-correlated relaxation in NMR spectroscopy. *J. Am. Chem. Soc.* **127**, 6062–6068 (2005)
62. Pervushin, K., Riek, R., Wider, G., Wuthrich, K.: Attenuated T2 relaxation by mutual cancellation of dipole–dipole coupling and chemical shift anisotropy indicates an avenue to NMR structures of very large biological macromolecules in solution. *Proc. Natl. Acad. Sci. U S A* **94**, 12366–12371 (1997)
63. Tate, S.: Anisotropic nuclear spin interactions for the morphology analysis of proteins in solution by NMR spectroscopy. *Anal. Sci.* **24**, 39–50 (2008)
64. Tate, S., Shimahara, H., Utsunomiya-Tate, N.: Molecular-orientation analysis based on alignment-induced TROSY chemical shift changes. *J. Magn. Reson. (San Diego, Calif.)* **171**, 282–291 (2004)